

# IFMBE Proceedings

Lenka Lhotska · Lucie Sukupova ·  
Igor Lacković · Geoffrey S. Ibbott (Eds.)

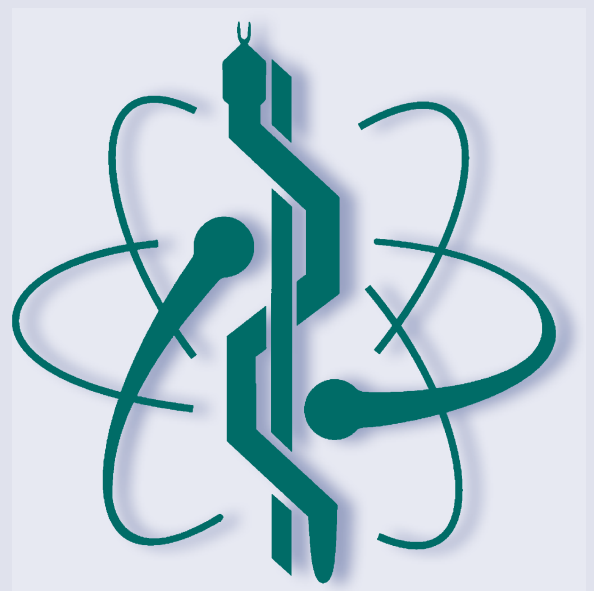
Volume 68/1

## World Congress on Medical Physics and Biomedical Engineering 2018

June 3–8, 2018, Prague,  
Czech Republic (Vol.1)



 Springer



---

# **IFMBE Proceedings**

Volume 68/1

*Series editor*

Ratko Magjarevic

*Deputy Editors*

Fatimah Ibrahim

Igor Lacković

Piotr Ładyżyński

Emilio Sacristan Rock



The International Federation for Medical and Biological Engineering, IFMBE, is a federation of national and transnational organizations representing internationally the interests of medical and biological engineering and sciences. The IFMBE is a non-profit organization fostering the creation, dissemination and application of medical and biological engineering knowledge and the management of technology for improved health and quality of life. Its activities include participation in the formulation of public policy and the dissemination of information through publications and forums. Within the field of medical, clinical, and biological engineering, IFMBE's aims are to encourage research and the application of knowledge, and to disseminate information and promote collaboration. The objectives of the IFMBE are scientific, technological, literary, and educational.

The IFMBE is a WHO accredited NGO covering the full range of biomedical and clinical engineering, healthcare, healthcare technology and management. It is representing through its 60 member societies some 120.000 professionals involved in the various issues of improved health and health care delivery.

#### IFMBE Officers

President: James Goh, Vice-President: Shankhar M. Krishnan

Past President: Ratko Magjarevic

Treasurer: Marc Nyssen, Secretary-General: Kang Ping LIN

<http://www.ifmbe.org>

More information about this series at <https://www.springer.com/bookseries/7403>

---

Lenka Lhotska • Lucie Sukupova  
Igor Lacković • Geoffrey S. Ibbott  
Editors

# World Congress on Medical Physics and Biomedical Engineering 2018

June 3–8, 2018, Prague, Czech Republic  
(Vol. 1)



*Editors*

Lenka Lhotska  
CIIRC  
Czech Technical University in Prague  
Prague  
Czech Republic

Lucie Sukupova  
Institute of Clinical and Experimental  
Medicine  
Prague  
Czech Republic

Igor Lacković  
Faculty of Electrical Engineering  
and Computing  
University of Zagreb  
Zagreb  
Croatia

Geoffrey S. Ibbott  
Department of Radiation Physics  
The University of Texas MD Anderson  
Cancer Center  
Houston, TX  
USA

ISSN 1680-0737 ISSN 1433-9277 (electronic)  
IFMBE Proceedings ISBN 978-981-10-9034-9 ISBN 978-981-10-9035-6 (eBook)  
<https://doi.org/10.1007/978-981-10-9035-6>

Library of Congress Control Number: 2018940876

© Springer Nature Singapore Pte Ltd. 2019, corrected publication 2022

Chapter "Evaluation of the Impact of an International Master of Advanced Studies in Medical Physics" has been changed as Open Access licensed under the terms of the Creative Commons Attribution 3.0 IGO License (<https://creativecommons.org/licenses/by/3.0/igo/>). For further details see license information in the chapter.

This work is subject to copyright. All rights are reserved by the Publisher, whether the whole or part of the material is concerned, specifically the rights of translation, reprinting, reuse of illustrations, recitation, broadcasting, reproduction on microfilms or in any other physical way, and transmission or information storage and retrieval, electronic adaptation, computer software, or by similar or dissimilar methodology now known or hereafter developed.

The use of general descriptive names, registered names, trademarks, service marks, etc. in this publication does not imply, even in the absence of a specific statement, that such names are exempt from the relevant protective laws and regulations and therefore free for general use.

The publisher, the authors and the editors are safe to assume that the advice and information in this book are believed to be true and accurate at the date of publication. Neither the publisher nor the authors or the editors give a warranty, express or implied, with respect to the material contained herein or for any errors or omissions that may have been made. The publisher remains neutral with regard to jurisdictional claims in published maps and institutional affiliations.

Printed on acid-free paper

This Springer imprint is published by the registered company Springer Nature Singapore Pte Ltd. part of Springer Nature

The registered company address is: 152 Beach Road, #21-01/04 Gateway East, Singapore 189721, Singapore

---

## Preface

This book presents the proceedings of the IUPESM World Congress on Biomedical Engineering and Medical Physics, a triennially organized joint meeting of medical physicists, biomedical engineers, and adjoining healthcare professionals. Besides the purely scientific and technological topics, the 2018 Congress will also focus on other aspects of professional involvement in health care, such as education and training, accreditation and certification, health technology assessment, and patient safety. The IUPESM meeting is an important forum for medical physicists and biomedical engineers in medicine and healthcare to learn and share knowledge, and to discuss the latest research outcomes and technological advancements as well as new ideas in both medical physics and biomedical engineering field.

Biomedical engineering and medical physics represent challenging and rapidly growing areas. Building on the success of the previous World Congresses, the aim of the World Congress 2018 is to continue in bringing together scientists, researchers, and practitioners from different disciplines, namely from mathematics, computer science, bioinformatics, biomedical engineering, medical physics, medicine, biology, and different fields of life sciences, so that they can present and discuss their research results. We hope that the World Congress 2018 will serve as a platform for fruitful discussions between all attendees, where participants can exchange their recent results, identify future directions and challenges, initiate possible collaborative research, and develop common languages for solving problems in the realm of biomedical engineering and medical physics.

Following a thorough peer-reviewed process, we have finally selected 498 papers. The Scientific Committee would like to thank the reviewers for their excellent job. The articles can be found in the proceedings and are divided into the main tracks and special sessions. The papers show how broad the spectrum of topics in biomedical engineering and medical physics is.

The editors would like to thank all the participants for their high-quality contributions and Springer for publishing the proceedings of the World Congress.

Prague, Czech Republic  
Prague, Czech Republic  
Zagreb, Croatia  
Houston, USA  
March 2018

Lenka Lhotska  
Lucie Sukupova  
Igor Lacković  
Geoffrey S. Ibbott

---

# Organizing Committees

---

## Congress Coordinating Committee

### Chair

Kin Yin Cheung, Chair, IOMP, Hong Kong

### Members

Howell Round, IOMP, New Zealand

Slavik Tabakov, IOMP, UK

Virginia Tsapaki, IOMP, Greece

James Goh, IFMBE, Singapore

Kang Ping Lin, IFMBE, Chinese Taipei

Herb Voigt, co-opted, IFMBE, USA †

Monique Frize, co-opted, IFMBE, Canada

---

## Congress Organizing Committee

### Co-chairs

Jaromir Cmiral, Czech Republic, BME

Libor Judas, Czech Republic, MedPhys

### Secretaries

Frantisek Lopot, Czech Republic, BME

Karel Nechvil, Czech Republic, MedPhys

### Members

#### Financial Committee Co-chairs

Martin Mayer, Czech Republic, BME

Vít Richter, Czech Republic, MedPhys

#### Scientific Committee Co-chairs

Lenka Lhotska, Czech Republic, BME

Lucie Sukupova, Czech Republic, MedPhys

#### Publicity Committee Chair

Martina Novakova, Czech Republic, BME, MedPhys

#### Education Committee Co-chairs

Jiri Hozman, Czech Republic, BME

Irena Koniarova, Czech Republic, MedPhys

---

## Financial Committee

### Co-chairs

Martin Mayer, Czech Republic, BME  
Vit Richter, Czech Republic, MedPhys

### Members

Jan Hanousek, Czech Republic, BME  
Anchali Krisanachinda, IOMP  
Mark Nyssen, IUPESM, IFMBE  
Vaclav Poljak, Czech Republic, MedPhys

---

## Scientific Committee

### Co-chairs

Geoffrey Ibbott, IOMP  
Lenka Lhotska, Czech Republic, BME  
Igor Lackovic, IFMBE  
Lucie Sukupova, Czech Republic, MedPhys

### Members

Magdalena Bazalova-Carter, Canada  
Carmel Caruana, Malta  
Tomas Cechak, Czech Republic  
Paul Chang, Singapore  
Kin Yin Cheung, Hong Kong, China  
Jiri Chvojka, Czech Republic  
Matej Daniel, Czech Republic  
Marie Davidkova, Czech Republic  
Harry Delis, IAEA  
Pavel Dvorak, Czech Republic  
Ludovic Ferrer, France  
Martin Falk, Czech Republic  
Christian Gasser, Sweden  
Csilla Gergely, France  
Susanna Guatelli, Australia  
Jens Haueisen, Germany  
Jan Havlik, Czech Republic  
Jiří Hozman, Czech Republic  
Marjan Hummel, The Netherlands  
Leonidas D. Iassemidis, USA  
Tom Judd, USA  
Peter Knoll, Austria  
Radim Kolar, Czech Republic  
Jana Kolarova, Czech Republic  
Christian Kollmann, Austria  
Irena Koniarova, Czech Republic  
David Korpas, Czech Republic  
Vladimir Krajca, Czech Republic  
Jan Kremlacek, Czech Republic

Petr Marsalek, Czech Republic  
Deborah Van Der Merwe, IAEA  
Karel Nechvil, Czech Republic  
Chris Nuggent, UK  
Pirkko Nykänen, Finland  
Hakan Nystrom, Sweden  
Pawel Olko, Poland  
Maria Perez, WHO  
Vaclav Porod, Czech Republic  
Kevin Prise, UK  
Ivo Provaznik, Czech Republic  
Jaroslav Ptáček, Czech Republic  
Vladimir Rogalewicz, Czech Republic  
Simo Saarakkala, Finland  
Ioannis Sechopoulos, The Netherlands  
Milan Sonka, USA  
Olga Stepankova, Czech Republic  
Lucie Sukupova, Czech Republic  
Krystina Tack, USA  
Annalisa Trianni, Italy  
Jiri Trnka, Czech Republic  
Virginia Tsapaki, Greece  
Adriana Velazquez, WHO  
Frantisek Vlcek, Czech Republic  
Jan Vrba, Czech Republic  
Kevin Warwick, UK  
Martha Zequera Diaz, Columbia

---

## **Program Committee**

### **Co-chairs**

Jaromir Cmiral, Czech Republic, BME  
Libor Judas, Czech Republic, MedPhys

### **Members**

Lenka Lhotska, Czech Republic, BME  
Frantisek Lopot, Czech Republic, BME  
Karel Nechvil, Czech Republic, MedPhys  
Martina Novakova, Czech Republic, BME  
Lucie Sukupova, Czech Republic, MedPhys

---

## **Publicity Committee**

### **Chair**

Martina Novakova, Czech Republic

**Members**

Pavla Buricova, Czech Republic  
Michele Hilts, Canada  
Jeannie Hsiu Ding Wong, Malaysia  
Akos Jobbagy, Hungary  
Luiz Kun, USA  
Pavla Novakova, Czech Republic  
Magdalena Stoeva, Bulgaria  
Tae-Suk Suh, Republic of Korea  
Jaw-lin Wang, Chinese Taipei

---

**Education Committee****Co-chairs**

Jiri Hozman, Czech Republic, BME  
Irena Koniarova, Czech Republic, MedPhys

**Members**

Jiri Kofranek, Czech Republic, BME  
Vladimír Krajca, Czech Republic, BME  
Simo Saarakkala, Finland, BME  
Ioannis Sechopoulos, The Netherlands, MedPhys

---

**Professional Standards Committee****Co-chairs**

David Korpas, Czech Republic, BME  
Libor Judas, Czech Republic, MedPhys

**Members**

John Damilakis, Greece, MedPhys  
Michele Hilts, Canada  
Jeannie Hsiu Ding Wong, Malaysia  
Tomas Kron, Australia, MedPhys  
Siew Lok Toh, Singapore, BME  
Yakov Pipman, USA, MedPhys  
Kang Ping Lin, Chinese Taipei, BME  
Jaroslav Ptacek, Czech Republic, MedPhys  
Christoph Trauernicht, South Africa, MedPhys

---

**Publication Committee****Chair**

Vladimir Marik, Czech Republic

**Co-chair**

Igor Lacković, Croatia



---

## **International Advisory Board (BME)**

### **Co-chairs**

James Goh, Singapore  
Ratko Magjarevic, Croatia

### **Members**

Guillermo Avendano C., Chile  
Paulo De Carvalho, Portugal  
Jaromir Cmiral, Czech Republic  
Fong Chin Su, Chinese Taipei  
David Elad, Israel  
Yubo Fan, China  
Mário Forjaz Secca, Portugal  
Monique Frize, Canada  
Birgit Glasmacher, Germany  
Peter Hunter, New Zealand  
Ernesto Iadanza, Italy  
Fatimah Ibrahim, Malaysia  
Timo Jämsä, Finland  
Akos Jobbagy, Hungary  
Eleni Kaldoudi, TBA  
Peter Kneppo, Czech Republic  
Shankar Krishnan, USA  
Eric Laciár Leber, Argentina  
Igor Lackovic, Croatia  
Piotr Ladyzynski, Poland  
Lenka Lhotska, Czech Republic  
Nigel Lovell, Australia  
Alan Murray, UK  
Marc Nyssen, Belgium  
Leandro Pecchia, UK  
Kang Ping Lin, Chinese Taipei  
Ichiro Sakuma, Japan  
Maria Siebes, The Netherlands  
Nitish Thakor, Singapore  
Herbert F. Voigt, USA  
Min Wang, Hong Kong

---

## **International Advisory Board (MP)**

### **Co-chairs**

Kin Yin Cheung, Hong Kong, China  
Slavik Tabakov, UK

### **Members**

Laila Al Balooshi, UAE  
Abdullah Al Hajj, KSA  
Huda Al Naemi, Qatar  
Rodolfo Alfonso Laguardia, Cuba  
Supriyanto Ardjo Pawiro, Indonesia

---

Eva Bezak, Australia  
Marco Brambila, Italy  
David Brettle, UK  
Arun Chougule, India  
John Damilakis, Greece  
Catherine Dejean, France  
Ludovic Ferrer, France  
Michelle Hilts, Canada  
Jeannie Hsiu Ding Wong, Malaysia  
Amaury Hornbeck, France  
Geoffrey Ibbott, USA  
Ahmed Ibn Seddik, Morocco  
Taofeeq Ige, Nigeria  
Petro Julkunen, Finland  
Simone Kodlulovich, Brazil  
Dimitri Kostylev, Russia  
Anchali Krisanachinda, Thailand  
James C L Lee, Singapore  
Melissa Martin, USA  
Rebecca Nakatudde, Uganda  
Herke Jan Noordmans, The Netherlands  
Fridtjof Nüsslin, Germany  
Yakov Pipman, USA  
Jaroslav Ptacek, Czech Republic  
Magdalena Rafecas, Germany  
Madan Rehani, USA  
Jose L. Rodriguez, Chile  
Howell Round, New Zealand  
Magdalena Stoeva, Bulgaria  
Tae-Suk Suh, Republic of Korea  
Lucie Sukupova, Czech Republic  
Virginia Tsapaki, Greece  
Graciela Velez, Argentina  
Ulrich Wolf, Germany

---

# Acknowledgements

---

## Organizing Societies



---

## International Societies



---

## Collaborating Institution



## Sponsors

**varian**



---

## About IFMBE

The International Federation for Medical and Biological Engineering (IFMBE) is primarily a federation of national and transnational societies. These professional organizations represent interests in medical and biological engineering. IFMBE is also a non-governmental organization (NGO) for the United Nations and the World Health Organization (WHO), where we are uniquely positioned to influence the delivery of health care to the world through biomedical and clinical engineering.

The IFMBE's objectives are scientific and technological as well as educational and literary. Within the field of medical, biological, and clinical engineering, IFMBE's aims are to encourage research and application of knowledge and to disseminate information and promote collaboration. The ways in which we disseminate information include the following: organizing World Congresses and Regional Conferences, publishing our flagship journal *Medical and Biological Engineering and Computing* (MBEC), our Web-based newsletter—IFMBE News, our Congress and Conference Proceedings, and books. The ways in which we promote collaborations are through networking programs, workshops, and partnerships with other professional groups, e.g., Engineering World Health.

### *Mission*

The mission of IFMBE is to encourage, support, represent, and unify the worldwide medical and biological engineering community in order to promote health and quality of life through the advancement of research, development, application, and management of technology.

### *Objectives*

The objectives of the International Federation for Medical and Biological Engineering shall be scientific, technological, literary, and educational. Within the field of medical, clinical, and biological engineering, its aims shall be to encourage research and the application of knowledge and to disseminate information and promote collaboration.

In pursuit of these aims, the Federation may, in relation to its specific field of interest, engage in any of the following activities: sponsorship of national and international meetings, publication of official journals, cooperation with other societies and organizations, appointment of commissions on special problems, awarding of prizes and distinctions, establishment of professional standards and ethics within the field, or in any other activities which in the opinion of the General Assembly or the Administrative Council would further the cause of medical, clinical, or biological engineering. It may promote the formation of regional, national, international, or specialized societies, groups or boards, the coordination of bibliographic or informational services, and the improvement of standards in terminology, equipment, methods and safety practices, and the delivery of health care.

In general, the Federation shall work to promote improved communication and understanding in the world community of engineering, medicine, and biology.

---

# Contents

## Part I Diagnostic Imaging

<b>Fast In Vivo High-Resolution Diffusion MRI of the Human Cervical Spinal Cord Microstructure</b> . . . . .	3
René Labounek, Jan Valošek, Jakub Zimolka, Zuzana Piskořová, Tomáš Horák, Alena Svátková, Petr Bednařík, Pavel Hok, Lubomír Vojtíšek, Petr Hluštík, Josef Bednařík and Christophe Lenglet	
<b>Image Quality Evaluation of Phase Contrast Mammographic Techniques</b> . . . . .	9
A. Daskalaki and N. Pallikarakis	
<b>Thermography Evaluation in Patients with Hypothyroidism and Fibromyalgia by Analyzing the Temperatures of the Palms of Hands</b> . . . . .	15
Ana Paula Christakis Costa, Joaquim Miguel Maia, Marcos Leal Brioschi and José Eduardo de Melo Mafra Machado	
<b>Material Analysis for a New Kind of Hybrid Phantoms Utilized in Multimodal Imaging</b> . . . . .	21
Manuel Stich, Karina Schuller, Anne Slawig, Klaus Detmar, Michael Lell, Sebastian Buhl and Ralf Ringler	
<b>Basic Study of the Imaging Conditions on Tumor Volume Measurement Using 3D-MR Imaging of the Liver While Patient Holds Breath</b> . . . . .	29
Shinichi Arao, Akihiko Tabuchi, Yasuhiko Okura, Hajime Harauchi, Atsushi Ono, Tatsuhiro Gotanda, Rumi Gotanda and Akiko Hayashi	
<b>Evaluation of Spatial Resolution of MRI, Optical CT and X-Ray CT Using MTF for Gel Dosimeter</b> . . . . .	35
Takaoki Takanashi and Hiraku Kawamura	
<b>Local Affine Transformation Method for Tomosynthesis</b> . . . . .	39
O. Morgun, K. Nemchenko and A. Vaisburd	
<b>Size and Shape of Spherical Objects on Full-Field Digital Mammography and Digital Breast Tomosynthesis Images</b> . . . . .	45
Hidetoshi Yatake, Yuka Sawai, Takahiro Kozuka, Yoshihiro Takeda, Mariko Kajihara, Toshizo Katsuda, Rumi Gotanda, Tatsuhiro Gotanda, Shuji Abe, Makoto Shimada, Nobuyoshi Tanki, Toshio Nishi and Hideo Inaji	
<b>Training Towards Precise Control Over Muscle Activity with Real Time Biofeedback Based on Ultrasound Imaging</b> . . . . .	49
Anna Sosnowska, Aleksandra Vuckovic and Henrik Gollee	
<b>On the CT Dose Index: Are we Meeting the Challenge?</b> . . . . .	53
Emmanuel Ramírez, Oriana Benavides, Alfonso Holguin, Carolina Castro and Wilson Lopera	

<b>Comparative Sequence Assessment of Optimised T2 and T2* Sequences for Quantification of Iron in Transfused Dependent Paediatric Sickle Cell Anaemia (SCA) Patients</b> . . . . .	57
Azza Ahmed, Amani Baldo, Hind Margani, Ahmed Fatah, Ibrahim Idris and Isam Salih	
<b>Quantitative Performance Evaluation of Mobile Cone-Beam CT for Head and Neck Imaging</b> . . . . .	63
Saowapak S. Thongvigitmanee, Walita Narkbuakaew, Sorapong Aootaphao, Chalinee Thanasupsombat, Kongyot Wangkaoom, Atthasak Kiang-ia, Jaturong Jitsaard, Thossapol Chunkiri, Puttisak Puttawibul and Pairash Thajchayapong	
<b>Prediction of Alzheimer’s Disease in Mild Cognitive Impairment Using Sulcal Morphology and Cortical Thickness</b> . . . . .	69
Maciej Plochanski and Lasse Riis Østergaard	
<b>Effect of Elimination of Noisy ECG Leads on the Noninvasive Localization of the Focus of Premature Ventricular Complexes</b> . . . . .	75
Elena Deutsch, Jana Svehlikova, Milan Tysler, Pavel Osmancik, Jana Zdarska and Peter Kneppo	
<b>Effect of Electrode Gel Application Between Patient’s Skin and Electrode Belt on Electrical Impedance Tomography of the Thorax</b> . . . . .	81
Kristyna Buzkova and Denisa Albrechtova	
<b>Capsaicin Effects on Human Facial and Neck Temperature</b> . . . . .	87
Jana Pokorná, Erik Staffa, Vladan Bernard and Vojtěch Mornstein	
<b>Assessment of Brain Water Content in Peripheral Inflammation by an Optimized Single-Voxel MR Spectroscopy Quantitation Technique</b> . . . . .	91
Abdul Nashirudeen Mumuni, John McLean, Rajeev Krishnadas, Maria Rosario Lopez-Gonzalez, Jonathan Cavanagh and Barrie Condon	
<b>Noninvasive Imaging of the Origin of Premature Ventricular Activity</b> . . . . .	97
Milan Tysler, Jana Svehlikova, Elena Deutsch, Pavel Osmancik and Robert Hatala	
<b>Quantitative Assessment of Strabismus and Selected Vision Related Anomalies</b> . . . . .	103
Shorav Suriyal, Christopher Druzgalski and Kumar Gautam	
<b>Phase-Contrast Breast-CT: Optimization of Experimental Parameters and Reconstruction Algorithms</b> . . . . .	109
Sandro Donato, Serena Pacile, Luca Brombal, Giuliana Tromba and Renata Longo	
<b>Response of CR Detector Plates for Use in Mammography Equipment</b> . . . . .	117
Mabel Bustos Flores and Arnaldo Prata Mourão	
<b>Towards In Vivo K-Edge X-Ray Micro-CT with the Pixirad-I/Pixie-III Detector</b> . . . . .	123
F. Brun, V. Di Trapani, D. Dreossi, L. Rigon, R. Longo and P. Delogu	
<b>Part II Image Processing</b>	
<b>Diffusion and Perfusion MR Parameters in Locally Advanced Rectal Cancer Management: An Explorative Study</b> . . . . .	129
Roberta Fusco, Mario Sansone, Alessandro Pepino and Antonella Petrillo	
<b>Mammographic Density Estimation Through Permutation Entropy</b> . . . . .	135
Adriana Antonelli, Gustavo Meschino and Virginia Ballarin	

<b>Multiregional Radiomics Phenotypes at MR Imaging Predict MGMT Promoter Methylation in Glioblastoma</b> . . . . .	143
Zhi-Cheng Li, Yinsheng Chen, Qiuchang Sun, Qihua Li, Lei Liu, Ronghui Luo, Hongmin Bai and Chaofeng Liang	
<b>Influence of Image Resolution Property on Aliasing Error of Digital Wiener Spectrum</b> . . . . .	147
Yasuyuki Kawaji, Tatsuhiko Gotanda, Tetsunori Shimono, Nobuyoshi Tanki, Toshizo Katsuda, Rumi Gotanda, Tadao Kuwano and Takuya Akagawa	
<b>Automatic Identification and Extraction of Pectoral Muscle in Digital Mammography</b> . . . . .	151
Ana L. M. Pavan, Antoine Vacavant, Allan F. F. Alves, Andre P. Trindade and Diana R. de Pina	
<b>Fully Automatic CAD System for Segmentation and Classification of Spinal Metastatic Lesions in CT Data</b> . . . . .	155
Jiri Chmelik, Roman Jakubicek, Jiri Jan, Petr Ourednicek, Lukas Lambert, Elena Amadori and Giampaolo Gavelli	
<b>A Classification and Segmentation Combined Two-Stage CNN Model for Automatic Segmentation of Brainstem</b> . . . . .	159
Huabei Shi, Jia Liu and Hongen Liao	
<b>Biometrics Based on Facial Landmark with Application in Person Identification</b> . . . . .	165
Aniwat Juhong, Boonchana Purahong, Supakorn Suwan and Chuchart Pitavirooj	
<b>A Computational Tool for Enhancing Ischemic Stroke in Computed Tomography Examinations</b> . . . . .	173
Allan Felipe Fattori Alves, Ana Luiza Menegatti Pavan, Rachid Jennane, Carlos Clayton Macedo de Freitas, Nitamar Abdala, João Maurício Carrasco Altemani and Diana Pina	
<b>Improving Priors for USTC via Transmission Tomography: A Simulation Study</b> . . . . .	177
Diego Armando Cardona Cardenas and Sergio Shiguemi Furuie	
<b>Brain Tumor Classification Using Convolutional Neural Network</b> . . . . .	183
Nyoman Abiwinanda, Muhammad Hanif, S. Tafwida Hesaputra, Astri Handayani and Tati Rajab Mengko	
<b>A Novel Method for 3D Reconstruction of Coronary Bifurcation Using Quantitative Coronary Angiography</b> . . . . .	191
Ioannis O. Andrikos, Atonis I. Sakellarios, Panagiotis K. Siogkas, Panagiota I. Tsompou, Vassiliki I. Kigka, Lampros K. Michalis and Dimitrios I. Fotiadis	
<b>Machine Learning Techniques for Classification of Breast Cancer</b> . . . . .	197
Ahmed Osmanović, Sabina Halilović, Layla Abdel Ilah, Adnan Fojnica and Zehra Gromilić	
<b>Segmentation and 3D-Modelling of Single-Rooted Teeth from CBCT Data: An Automatic Strategy Based on Dental Pulp Segmentation and Surface Deformation</b> . . . . .	201
Jerome Harrison, Steeve Chantrel, Matthieu Schmittbuhl and Jacques A. de Guise	



<b>A Three-Dimensional Quantification of Calcified and Non-calcified Plaque Based on Computed Tomography Coronary Angiography Images: Comparison with Virtual Histology Intravascular Ultrasound</b> . . . . .	207
Vassiliki I. Kigka, Antonis Sakellarios, George Rigas, Panagiota Tsobou, Ioannis O. Andrikos, Lampros K. Michalis and Dimitrios I. Fotiadis	
<b>Creation of Computational Breast Phantoms with Extracted Abnormalities from Real Patient Images</b> . . . . .	213
Nikolay Dukov, Zhivko Bliznakov, Ivan Buliev and Kristina Bliznakova	
<b>Metal Artifact Reduction by Morphological Image Filtering for Computed Tomography</b> . . . . .	219
Yakdiel Rodríguez-Gallo, Rubén Orozco-Morales and Marlen Pérez-Díaz	
<b>Fully Automatic CAD System for Spine Localisation and Vertebra Segmentation in CT Data</b> . . . . .	223
Roman Jakubicek, Jiri Chmelik, Jiri Jan, Petr Ourednicek, Lukas Lambert and Giampaolo Gavelli	
<b>Hyperdense Middle Cerebral Artery Segmentation in Non Contrast Computed Tomography</b> . . . . .	227
Nelly Gordillo, Alberto Davis, Felipe García, José Mejía and Xavier Aymerich	
<b>Joint Adaptive Beamforming to Enhance Noise Suppression for Medical Ultrasound Imaging</b> . . . . .	233
Acacio J. Zimbico, Diogo W. Granado, Fabio K. Schneider, Joaquim M. Maia, Amauri A. Assef, Nivaldo S. Junior and Eduardo T. Costa	
<b>Label-Free Nuclear Staining Reconstruction in Quantitative Phase Images Using Deep Learning</b> . . . . .	239
Tomas Vicar, Jaromir Gumulec, Jan Balvan, Michal Hracho and Radim Kolar	
<b>Performance Comparison of Segmentation Algorithms for Image Quality Degraded MR Images</b> . . . . .	243
Galip Ozdemir, Huseyin Nasifoglu and Osman Eroglu	
<b>Application of Low-Cost 3D Printing for Production of CT-Based Individual Surgery Supplies</b> . . . . .	249
Filip Górski, Radosław Wichniarek, Wiesław Kuczko, Jacek Banaszewski and Maciej Pabiszczak	
<b>Examination of the Spatial Structure of Pigs' Melanoma in Tissue Sections Based on Histology and Mass Spectrometry</b> . . . . .	255
Jiri Anyz, Lenka Vyslouzilova, Vratislav Horak, Olga Stepankova, Tomas Vaculovic and Vojtech Adam	
<b>Automatic Characterization of Plaques and Tissue in IVOCT Images Using a Multi-step Convolutional Neural Network Framework</b> . . . . .	261
G. A. Cheimariotis, M. Riga, K. Toutouzas, D. Tousoulis, A. Katsaggelos and N. Maglaveras	
<b>Iterative Methods for Fast Reconstruction of Undersampled Dynamic Contrast-Enhanced MRI Data</b> . . . . .	267
Hynek Walner, Michal Bartoš, Marie Mangová, Olivier Keunen, Rolf Bjerkvig, Radovan Jiřík and Michal Šorel	
<b>Multimodality Image Fusion of the Liver Using Structure-Guided Deformable Image Registration in Velocity AI—What Is the Preferred Approach?</b> . . . . .	273
S. Kuznetsova, P. Grendarova, N. Ploquin and K. Thind	

<b>First Validation of Semi-automatic Liver Segmentation Algorithm</b> . . . . .	279
Philipp Matthies, Jan Wuestemann, Francisco A. Pinto and Julius C. Neba	
<b>Image Quality Optimization and Soft Tissue Visualization in Cone-Beam CT Imaging</b> . . . . .	283
Aude Castonguay-Henri, Dmitri Matenine, Matthieu Schmittbuhl and Jacques A. de Guise	
<b>A Method to Detect Potentially Malignant Skin Lesions Through Image Segmentation</b> . . . . .	289
Carlos A. Wilches, Óscar J. Perdomo and César A. Perdomo	
<b>Part III Information Technology in Healthcare</b>	
<b>A Gait Character Analyzing System for Osteoarthritis Pre-diagnosis Using RGB-D Camera and Supervised Classifier</b> . . . . .	297
Xiwen Cui, Zhe Zhao, Cong Ma, Fang Chen and Hongen Liao	
<b>Architecture and Organization of a Computational System for the Management of Data from Individuals with Parkinson's Disease</b> . . . . .	303
João Paulo Folador, Luciene Chagas, Marcus Fraga Vieira and Adriano O. Andrade	
<b>Developing an Automated Clinical Trending Tool for the Neonatal Intensive Care Unit (NICU)</b> . . . . .	307
M. Frize, A. Esty, J. Gilchrist, J. Harrold and E. Bariciak	
<b>Data Analytics for Metabolic Syndrome Diagnostics</b> . . . . .	311
Ludmila Puzstová, František Babič and Ján Paralič	
<b>Medical Expert System with the Properties of Artificial Intelligence</b> . . . . .	315
Sergo Dadunashvili	
<b>A Simple Room Localization Method to Find Technology in a Big Trauma Center</b> . . . . .	321
J. Regolini, F. Frosini, E. Ciagli, A. Benassi, D. Cocchi, R. Miniati, P. Tortoli and A. Belardinelli	
<b>The Influence of the Voice Acquisition Method to the Mental Health State Estimation Based on Vocal Analysis</b> . . . . .	327
Yasuhiro Omiya, Naoki Hagiwara, Shuji Shinohara, Mitsuteru Nakamura, Masakazu Higuchi, Shunji Mitsuyoshi, Eiji Takayama and Shinichi Tokuno	
<b>Using Artificial Neural Network to Predict Functional Recovery of Patients Treated by Intravenous Thrombolysis in Acute Ischemic Stroke</b> . . . . .	331
Hung-Wen Chiu, Yu-Ting Huang and Chun-An Cheng	
<b>Estimation of the Heart Rate Variability Features via Recurrent Neural Networks</b> . . . . .	335
Mihaela Porumb, Rossana Castaldo and Leandro Pecchia	
<b>Study on Non-contact Heart Beat Measurement Method by Using Depth Sensor</b> . . . . .	341
Hirooki Aoki, Atsushi Suzuki and Tsuyoshi Shiga	
<b>Design Reflection on Mobile Electronic Data Capturing Forms in African Rural Settings</b> . . . . .	347
Ole Andreas Krumsvik, Ankica Babic and Alice Mugisha	

<b>Evaluation Methodology and Measurement of Physiological Data to Determine Operational Preparedness of Air Defense Staff: Preliminary Results . . . . .</b>	351
Vaclav Krivanek, Patrik Kutilek, Radek Doslak, Jan Farlik, Josef Casar, Jan Hejda, Slavka Viteckova, Petr Volf and Pavel Smrcka	
<b>A Multiple Criteria Decision Making System for Setting Priorities . . . . .</b>	357
Sergio Miranda Freire, Aline Nascimento and Rosimary Terezinha de Almeida	
<b>Towards Computer Supported Search for Semiological Features in Epilepsy Seizure Classification . . . . .</b>	363
Michaela Nova, Lenka Vyslouzilova, Zdenek Vojtech and Olga Stepankova	
<b>Scoring System for the One-Year Mortality Prediction of Sepsis Patients in Intensive Care Units . . . . .</b>	367
Javier E. García-Gallo, Nelson J. Fonseca-Ruiz and John F. Duitama-Muñoz	
<b>Computerized Cognitive Assessment System for Dementia Screening Application . . . . .</b>	371
Jia-Yun Wu, Sheei-Meei Wang, Kuo-Sheng Cheng and Pei-Fang Chien	
<b>Modeling Biological Data Through Dynamic Bayesian Networks for Oral Squamous Cell Carcinoma Classification . . . . .</b>	375
Konstantina Kourou, Costas Papaloukas and Dimitrios I. Fotiadis	
<b>A Process Modelling and Analytic Hierarchy Process Approach to Investigate the Potential of the IoT in Health Services . . . . .</b>	381
K. Tsiounia, N. G. Dimitrioglou, D. Kardaras and S. G. Barbounaki	
<b>A Virtual CPR (Cardio-Pulmonary Resuscitation) Learning System Using Motion Capture Device . . . . .</b>	387
Yasushi Yamauchi and Tae Hayashida	
<b>Usability of Electronic Patient Records for Assessment and Care Planning in Nursing Homes . . . . .</b>	393
Kate Shiells, Iva Holmerová and Olga Štěpánková	
<b>Data Security and Raw Data Access of Contemporary Mobile Sensor Devices . . . . .</b>	397
Till Handel, Max Schreiber, Katrin Rothmaler and Galina Ivanova	
<b>Security Mechanism for Medical Record Exchange Using Hippocratic Protocol . . . . .</b>	401
Jose Pirrone and Monica Huerta	
<b>An Engineering Module to Identify Potential Diabetes Patients and Preventive Measures for Diabetes in Developing Countries like Bangladesh . . . . .</b>	405
Md. Ashrafuzaman, Mohammad Tareq Alam and Md. Abdullah-Al-Harun	
<b>MULTISAB: A Web Platform for Analysis of Multivariate Heterogeneous Biomedical Time-Series . . . . .</b>	411
A. Jovic, D. Kukolja, K. Friganovic, K. Jozic and M. Cifrek	
<b>Technologies Catalog to Support the Identification of User Behavior During Usability Tests . . . . .</b>	417
Thâmmara Lariane Henriques Tito, Andrei Guilherme Lopes and Daniel Scherer	
<b>t-SNE Applied to Discriminate Healthy Individuals from Those with Parkinson's Disease Executing Motor Tasks Detected by Non-contact Capacitive Sensors . . . .</b>	421
Fábio Henrique M. Oliveira, Thaila Ferreira Zaruz, Marcus Fraga Vieira and Adriano O. Andrade	

<b>Electronic Delivery Book: Structured Database Enables Analysis of Perinatal Risk Factors</b> .....	427
Michal Huptych, Václav Chudáček, Ibrahim Abou Khashabh, Jiří Spilka, Miroslav Burša, Lukáš Hruban and Petr Janků	
<b>Wearable Cardiorespiratory Monitoring System for Unobtrusive Free-Living Energy Expenditure Tracking</b> .....	433
Ke Lu, Liyun Yang, Farhad Abtahi, Kaj Lindecrantz, Kristian Rødby and Fernando Seoane	
<b>Design Variations for Improved Usability of Mobile Data Capture in Rural Uganda</b> .....	439
Ole Andreas Krumsvik, Ankica Babic and Alice Mugisha	
<b>Advancing Medical Practice Through Computer Expert Systems</b> .....	445
K. I. Nkuma-Udah, G. Chukwudebe and E. Ekwonwune	
<b>Propose a Model of Multimedia Electronic Patient Record System for Sri Lankan Public Health Sector</b> .....	451
A. L. Pallewela and V. Parameshwaran	
<b>Multiple Sclerosis Application Design with Medical Expert Evaluation</b> .....	457
Aleksander Nygård Tonheim and Ankica Babic	
<b>Design Features for Usable Mobile Electronic Data Capturing Forms: The Form Developers' Perspective</b> .....	463
Alice Mugisha, Peter Wakholi and Ankica Babic	
<b>Task-Based Approach Recommendations to Enhance Data Visualization in the Kenya National Health Data Warehouse</b> .....	467
Milka Gesicho and Ankica Babic	
<b>Design of a Smart Multimodal Earthquake Response Mobile Application</b> .....	471
Allya Paramita Koesoema, Yoke Saadia Swito, Annisa Riyani, Masyithah Nur Aulia, Dody Qori Utama and Tauhid Nur Azhar	
<b>A Mobile App for the Self-management of Type 1 Diabetes as Tool for Preventing of Exercise-Associated Glycemic Imbalances</b> .....	475
Miloš Ajčević, Federica De Dea, Giovanni Barbieri and Agostino Accardo	
<b>An Online Service for Topics and Trends Analysis in Medical Literature</b> .....	481
Spyridon Kavvadias, George Drosatos and Eleni Kaldoudi	
<b>Part IV Modelling and Simulation</b>	
<b>Paced Electrical Field Modeling Within Ischemic Myocardium</b> .....	489
D. Korpas and P. Barta	
<b>Mathematical Modeling of Ocular Pulse Blood Filling in Rheophthalmography</b> .....	495
D. M. Shamaev, P. V. Luzhnov and E. N. Iomdina	
<b>Velocity Measurement at Carotid Siphon: Quantitative Comparison of Phase Contrast MRI and Computational Fluid Dynamics</b> .....	499
Chi Zhang, Jinfeng Yang, Ning Ding, Feiyan Chang, Sheng Xie, Deyu Li and Xiaoxu Hou	

<b>Proposal of Physical Model of Cardiovascular System; Improvement of Mock Circulatory Loop</b> . . . . .	505
Lukas Peter, Norbert Noury and Martin Cerny	
<b>Numerical Study on the Effects of Segmental Aqueous Humour Outflow on Ocular Drug Delivery</b> . . . . .	509
Ean Hin Ooi, Chai Yee Loke, Norlina Ramli and Amir Samsudin	
<b>Numerical Simulation of Fluid-Structure Interaction Under the Condition of Pulsatile Blood Flow of Renal Artery with Radiofrequency Electrode</b> . . . . .	515
Qun Nan, Yanyan Cheng, Zhen Tian, Tong Dong and Xiang Gao	
<b>In Vitro Evaluation of Hemodynamic Performance for Right Ventricular Outflow Tract Reconstruction with Trileaflet ePTFE Valved Conduit</b> . . . . .	519
Wei-Ling Chen, Chiu-Chin Wu and Chung-Dann Kan	
<b>Real-Time Monitoring of Yeasts Growth Based on Bioimpedance Spectroscopy</b> . . . . .	525
Marcos Antonio Salvino da Silva, Elizabeth Gomes Sanches, Alexandre Visintainer Pino and Marcio Nogueira de Souza	
<b>Agent-Based Model of the Budding Yeast Cell Cycle Regulatory Network</b> . . . . .	531
Carlos Castro, Dora-Luz Flores, Eunice Vargas, David Cervantes and Efren Delgado	
<b>Basic Concepts of Sensing Respiratory Sounds at the Surface of Human Chest</b> . . . . .	535
Vladimir Korenbaum, Alexandr Tagiltcev, Sergei Gorovoy, Anatoly Kostiv, Anton Shiryaev and Oksana Kabancova	
<b>Computational Modeling of Drug Delivery for Treatment of Age-Related Macular Degeneration</b> . . . . .	539
N. G. Dimitrioglou, M. E. Kavousanakis and D. T. Hatzivramidis	
<b>Numerical Simulation of Selective Withdrawal Pertinent to Efficient Cell Encapsulation</b> . . . . .	547
N. G. Dimitrioglou and D. T. Hatzivramidis	
<b>Simulation of Respiratory Impedance Variations During Normal Breathing Using a Morphometric Model of the Lung</b> . . . . .	553
Adam G. Polak and Zoltán Hantos	
<b>Discrete Event Simulation Model for the Analysis of Centralized Front Office Service in a Regional Hub Hospital</b> . . . . .	559
D. Cocchi, F. Frosini, E. Ciagli, P. Tortoli, C. Carpini, D. Cirone and A. Belardinelli	
<b>Numerical Study for Lung Microwave Ablation in Different Thermal and Electrical Properties</b> . . . . .	563
Zhen Tian, Yanyan Cheng, Tong Dong, Xiang Gao and Qun Nan	
<b>Use of Modelling Simulation to Monitor the Performance of a Pediatric Emergency Department</b> . . . . .	567
Giuliana Faiella, Marco Simonetti, Antonio D'Uffizi, Vincenzo Tipo, Mario Cesarelli and Fabrizio Clemente	
<b>Validation of SIMIND Monte Carlo Simulation Software for Modelling a Siemens Symbia T SPECT Scintillation Camera</b> . . . . .	573
John E. Ejeh, Johan A. van Staden and Hanlie du Raan	

<b>A Model Describing the Multiphasic Dynamics of Mixed Meal Glucose Responses in Healthy Subjects</b> . . . . .	577
Manuel Eichenlaub, Natasha Khovanova and John Hattersley	
<b>Geant4 Simulation for Commissioning of Proton Therapy Centre</b> . . . . .	583
Hong Qi Tan, Jun Hao Phua, Lloyd Tan, Khong Wei Ang, James Lee and Andrew Anthony Bettiol	
<b>3D Quantification of Biological Damage for a 160 MeV Proton Beam</b> . . . . .	589
Hong Qi Tan, Khong Wei Ang and Andrew Anthony Bettiol	
<b>Dynamic Effects of Obstructed Airways Mechanics on the Forced Expiratory Curve</b> . . . . .	593
Adam G. Polak, Dariusz Wysoczański and Janusz Mroczka	
<b>Electronic-Based Model of the Sensitive Type of Mycobacterium Tuberculosis</b> . . . . .	597
R. U. K. Raja Mohd Radzi, W. Mansor and J. Johari	
<b>RF Ultrasound Based Estimation of Pulsatile Flow Induced Microdisplacements in Phantom</b> . . . . .	601
Monika Zambacevičienė, Rytis Jurkonis, Sigita Gelman and Andrius Sakalauskas	
<b>Basic Cardiovascular Computer Model Shows System Degeneracy When Used in Reverse on Standard Measured Parameters</b> . . . . .	607
Borut Kirn	
<b>Quantifying the Spatial and Angular Distribution of Lethal Neutrons for Treating Planning</b> . . . . .	611
Jonathan Jian Wei Yeo, Hong Qi Tan, Khong Wei Ang, James Cheow Lei Lee and Andrew Anthony Bettiol	
<b>Effect of Left-Right Heart During Biventricular Assist Device Support by Speed Synchronization: A Computer Study</b> . . . . .	617
Phornphop Naiyanetr	
<b>PCA-QDA Model Selection for Detecting NS1 Related Diseases from SERS Spectra of Salivary Mixtures</b> . . . . .	623
N. H. Othman, Khuan Y. Lee, A. R. M. Radzol, W. Mansor and N. I. A. Hisham	
<b>A Novel Concept of the Management of Coronary Artery Disease Patients Based on Machine Learning Risk Stratification and Computational Biomechanics: Preliminary Results of SMARTool Project</b> . . . . .	629
Antonis I. Sakellarios, Nikolaos Tachos, Elena Georga, George Rigas, Vassiliki Kigka, Panagiotis Siogkas, Savvas Kyriakidis, Georgia Karanasiou, Panagiota Tsompou, Ioannis Andrikos, Silvia Rocchiccioli, Gualtriero Pelosi, Oberdan Parodi and Dimitrios I. Fotiadis	
<b>Estimating Cardiac Intensive Care Patients' Responsiveness to Late Conservative Fluid Management Using Systems Analysis</b> . . . . .	635
Katharina Bergmoser, Sonja Langthaler, Alexander Lassnig, Martin Horn and Christian Baumgartner	
<b>Non-invasive Quantification of Coronary Artery Disease in Arterial Bifurcations Using CCTA and CFD: Comparison to Fractional Flow Reserve Measurements</b> . . . . .	639
Panagiotis K. Siogkas, Antonis I. Sakellarios, Lampros K. Michalis and Dimitrios I. Fotiadis	

<b>Modelling Details for Electric Field Simulations of Deep Brain Stimulation</b> . . . . .	645
Johannes D. Johansson, Fabiola Alonso and Karin Wårdell	
<b>A Highly-Detailed 3D Model of the Human Atria</b> . . . . .	649
Sara Rocher, Alejandro López, Ana Ferrer, Laura Martínez, Damián Sánchez and Javier Saiz	
<b>The Correlation Between Central Corneal Thickness and Glaucomatous Optic Nerve Damage in a Human Eye</b> . . . . .	655
Chai Yee Loke, Ean Hin Ooi, Norlina Ramli and Amir Samsudin	
<b>Computer Simulation in the Analysis of Computed Tomography Exam Times</b> . . . . .	661
Rogerio Santos, Andrei Pires, Wagner Pereira and Renan Almeida	
<b>Genetic Algorithms Applied to Estimate 6-Parameters Model Which Define Analytical Function to Simulate the Motor Unity Force from Experimental Measures</b> . . . . .	665
J. P. Bermeo, F. Sanchez, J. Bravo, L. Bueno, J. D. Jara and R. Rodas	
<b>Quality Assurance in Medical 3D-Printing</b> . . . . .	669
Djim Kanters, Anke de Vries, Henk Boon, Joost Urbach, Arjen Becht and Homme-Auke Kooistra	
<b>Validation of Geant4 Nuclear Reaction Models for Hadron Therapy and Preliminary Results with BLOB</b> . . . . .	675
C. Mancini-Terracciano, B. Caccia, M. Colonna, M. De Napoli, A. Dotti, R. Faccini, P. Napolitani, L. Pandola, E. Solfaroli Camillocci, G. Traini and G. A. P. Cirrone	
<b>Prototype Measurement System for the Eye-Hand Coordination Test of the Developmental Test of Visual Perception</b> . . . . .	687
Daniel Alejandro Quiroga-Torres, Juan S. Lara, Antonio Miguel-Cruz and Adriana María Ríos-Rincón	
<b>The Implications of the Lead Theory on the Patch ECG Devices Positioning and Measurement</b> . . . . .	693
Ivan Tomasic, Aleksandra Rashkovska, Roman Trobec and Maria Lindén	
<b>VirRespir—An Application for Virtual Pneumonological Experimentation and Clinical Training</b> . . . . .	697
Krzysztof Zieliński, Anna Stecka and Tomasz Gólczewski	
<b>A Hybrid Cardio-Pulmonary Simulation Platform—An Application for Extracorporeal Assist Devices</b> . . . . .	703
Krzysztof Zieliński, Piotr Okrzeja, Anna Stecka, Maciej Kozarski and Marek Darowski	
<b>Different Methods of Arterial Compliance Estimation Tested with Reservoir-Wave Model of Arterial System</b> . . . . .	707
Marek Żyliński, Wiktor Niewiadomski, Marta Sadowiec and Gerard Cybulski	
<b>Breathing Experiments into the Simulated Avalanche Snow: Medical and Technical Issues of the Outdoor Breathing Trials</b> . . . . .	711
Lenka Horáková, Karel Sýkora, Ladislav Sieger and Karel Roubík	
<b>Technique and Gender Specific Conversion Coefficients for Estimation of Effective Dose from Kerma Area Product During X-Ray Radiography of Chest</b> . . . . .	719
Asen Dimov, Ivan Tsanev and Dimitar Penev	

<b>Design and Demonstration of a Complex Neonatal Physiological Model for Testing of Novel Closed-Loop Inspired Oxygen Fraction Controllers</b> . . . . .	725
Jakub Rafl, Thomas E. Bachman, Tomas Martinek, Leos Tejkl, Veronika Huttova, Petr Kudrna and Karel Roubik	
<b>Radionuclide Internal Dosimetry Using GATE and PENELOPE for Experimental Validation in Geometrical Phantoms</b> . . . . .	731
Nicollas Gonçalves Cavedini, Caroline Machado Dartora, Luís Vinícius de Moura, Marcelo Menna Barreto Schwarcke and Ana Maria Marques da Silva	
<b>Development of Low Cost Central Monitoring Platform by Modeling and Simulation for Patients Care in Low Middle Income Countries</b> . . . . .	737
Md. Ashrafuzzaman, Md. Sakib Abrar Hossain, A. F. M. Mohaimenul Joaa and Md. Tareq Aziz	
<b>Assistance Ratio: An Approach to Quantify the Hydraulic Load Distribution in LVAD Therapy</b> . . . . .	745
Philip von Platen, Daniel Rüschen, Steffen Leonhardt and Marian Walter	
<b>Analysis of Left Ventricular Unloading by Double Lumen Arterial Cannula During ECMO Assessed by Mathematical Modeling</b> . . . . .	749
Svitlana Strunina, Jiri Hozman and Petr Ostadal	
<b>Electromagnetic Compatibility of Cardiac Stimulation Technology in Relation to Human Body—The Introductory Study</b> . . . . .	755
Jan Morava, Aleš Richter and Pavel Kučera	
<b>Computational Fluid Dynamics Analysis of Coronary Stent Malapposition</b> . . . . .	761
Iuliana-Claudia Hudrea, Alin-Florin Totorean and Dan Gaita	
<b>Local Hemodynamics in Coronary Bypass in the Presence of Competitive Flow and Different Diameter Ratios Between Graft and Host Artery</b> . . . . .	767
Alin-Florin Totorean and Iuliana-Claudia Hudrea	
<b>The Electrical Conductivity of Human Cerebrospinal Fluid In Vivo</b> . . . . .	773
Juha Latikka and Hannu Eskola	
<b>Time-Efficient Fourier Domain Evaluation of Pharmacokinetic Model in Dynamic Contrast-Enhanced Magnetic Resonance Imaging</b> . . . . .	777
Michal Bartoš, Michal Šorel and Radovan Jiřík	
<b>Proton Therapy Treatment Plan Verification in CCB Krakow Using Fred Monte Carlo TPS Tool</b> . . . . .	783
M. Garbacz, G. Battistoni, M. Durante, J. Gajewski, N. Krah, V. Patera, I. Rinaldi, A. Schiavi, E. Scifoni, A. Skrzypek, F. Tommasino and A. Rucinski	
<b>Investigating Ballistic Gelatin Based Phantom Properties for Ultrasound Training</b> . . . . .	789
Mertcan Özdemir, Galip Özdemir and Osman Eroğul	
<b>Physical Breast Model as a Simulator of Pathological Changes</b> . . . . .	795
J. Biernat, M. Biernat, W. Łukasik, T. Pałko, A. Jung and M. Trzyzna	
<b>Activation Propagation in Cardiac Ventricles Using the Model with the Conducting System</b> . . . . .	799
Elena Cocherova, Jana Svehlikova and Milan Tysler	
<b>Comparison of ECREs Algorithm with Classical Method in Management of Diabetes Type 1 Exercise-Related Imbalances</b> . . . . .	803
Miloš Ajčević, Maria Pia Francescato, Mario Geat and Agostino Accardo	



<b>Application of Computational Aerodynamics on the Risk Prediction of PM2.5 in Congenital Tracheal Stenosis</b> . . . . .	807
L. M. Zhu, X. L. Gong, J. Y. Shen, L. P. Liu, J. F. Liu, J. L. Liu and Z. M. Xu	
<b>Hemodynamic Effects of Conduit Position on Systemic-to-Pulmonary Shunt: A Numerical Study Using Virtual Design</b> . . . . .	813
J. L. Liu, Q. Sun, Z. R. Tong, J. Y. Shen and J. F. Liu	
<b>Parameter Search to Find Ranges of Activation and Inhibition of Wound Healing Rate in a Mathematical Model with Introduced Photobiomodulation</b> . . . . .	819
Alistair McQueen, Jacquelyn Dawn Parente, Sean McGinty and Knut Moeller	
<b>The Effects of Expiratory Flow Limitation and Different Inspiratory and Expiratory Airway Resistances on Dynamic Hyperinflation of the Lungs: A Bench Study</b> . . . . .	823
Václav Ort and Lukáš Konupka	
<b>Part V BME and MP Education, Training and Professional Development</b>	
<b>A Novel Online Training Platform for Medical Image Interpretation</b> . . . . .	831
S. M. da Silva, S. C. M. Rodrigues, M. A. S. Bissaco, T. Scardovelli, S. R. M. S. Boschi, M. A. Marques, M. F. Santos and A. P. Silva	
<b>Biomedical Engineering Education in Georgia</b> . . . . .	837
Irine Gotsiridze and Giorgi Gigilashvili	
<b>Education System for Biomedical Technicians, Biomedical Engineers and Clinical Engineers in the Czech Republic</b> . . . . .	843
Jaromir Cmiral	
<b>Implementation of Project-Based Learning in Biomedical Engineering Course in ITB: Opportunities and Challenges</b> . . . . .	847
Agung W. Setiawan	
<b>Monte Carlo Simulation of a Linac Using PRIMO: User-Friendly Educational Tool Which Can Be Taken to the Cloud for Free</b> . . . . .	851
Angelina M. Bacala	
<b>Interdisciplinary Work as a Pedagogical Innovation for Biomedical Engineering and Health Science Students</b> . . . . .	855
William Ricardo Rodríguez Dueñas and Adriana María Ríos Rincón	
<b>Overseeing the Growth of Medical Physics: Indonesia Case</b> . . . . .	859
S. A. Pawiro, L. E. Lubis, A. N. Oktavianto and D. S. Soejoko	
<b>Enhance Medical Education and Training Using Interactive Autostereoscopic 3D Display by In Situ 3D Interaction</b> . . . . .	865
Guowen Chen, Cong Ma, Xinran Zhang and Hongen Liao	
<b>Public-Private Partnership Strategy in Acquiring Facilities for Radiotherapy Services and for Education and Training of Medical Physicists in Southern Philippines</b> . . . . .	869
Angelina M. Bacala and Agnette de Perio Peralta	
<b>Evaluation of the Impact of an International Master of Advanced Studies in Medical Physics</b> . . . . .	873
Giorgia Loreti, Hossein Aslian, Antonio Brito, Harry Delis, Renata Longo and Renato Padovani	

---

<b>UDA-<math>\mu</math>BioLab: Teaching Microcontrollers with Bioinstrumentation</b> . . . . .	877
O. Alvarado-Cando, H. Torres-Salamea and D. A. Almeida	
<b>Development of a Blended and eLearning Course on Anatomy and Physiology for Engineers in Indonesia: Lessons Learned and Future Developments</b> . . . . .	881
Yoke Saadia Swito, Allya Paramita Koesoema and Amanatullahy Pribadi	
<b>Cultural Aspects in Technology-Enhanced Education</b> . . . . .	885
Tatjana Welzer, Marjan Družovec and Aida Kamišalići	
<b>Correction to: Evaluation of the Impact of an International Master of Advanced Studies in Medical Physics</b> . . . . .	C1
Giorgia Loreti, Hossein Aslian, Antonio Brito, Harry Delis, Renata Longo and Renato Padovani	
<b>Author Index</b> . . . . .	889

---

**Part I**  
**Diagnostic Imaging**

# Fast In Vivo High-Resolution Diffusion MRI of the Human Cervical Spinal Cord Microstructure

René Labounek, Jan Valošek, Jakub Zimolka, Zuzana Piskořová, Tomáš Horák, Alena Svátková, Petr Bednařík, Pavel Hok, Lubomír Vojtíšek, Petr Hlušík, Josef Bednařík, and Christophe Lenglet

## Abstract

Diffusion Magnetic Resonance Imaging (dMRI) is a widely-utilized method for assessment of microstructural properties in the central nervous system i.e., the brain and spinal cord (SC). In the SC, almost all previous human studies utilized Diffusion Tensor Imaging (DTI), which cannot accurately model areas where white matter (WM) pathways cross or diverge. While High Angular Diffusion Resolution Imaging (HARDI) can overcome some of these limitations, longer acquisition times critically limit its applicability to clinical human studies. In addition, previous human HARDI studies have used limited spatial resolution, with typically a few slices and voxel size  $\sim 1 \times 1 \times 5 \text{ mm}^3$  being acquired in tens of minutes. Thus, we have optimized a novel fast HARDI protocol that allows collecting dMRI data at high angular and spatial resolutions in clinically-feasible time. Our data was acquired, using a 3T Siemens Prisma scanner, in less than 9 min. It has a total of 75 diffusion-weighted volumes and high spatial resolution of  $0.67 \times 0.67 \times 3 \text{ mm}^3$  (after interpolation in Fourier space) covering the cervical segments C4–C6. Our preliminary results demonstrate applicability of our technique in healthy

individuals with good correspondence between low fractional anisotropy (FA) gray matter areas from the dMRI scans, and the same regions delineated on T2-weighted MR images with spatial resolution of  $0.35 \times 0.35 \times 2.5 \text{ mm}^3$ . Our data also allows the detection of crossing fibers that were previously shown in vivo only in animal studies.

## Keywords

Diffusion MRI • HARDI • High-resolution imaging  
Cervical spinal cord

## 1 Introduction

DTI indirectly characterize white matter (WM) microstructure based on the diffusion properties of water molecules, but only models one pool of parallel fibers per voxel. Hence, HARDI approaches such as Q-ball imaging [1] or the ball-and-stick model [2], that enable to account for crossing fiber populations, could help better characterize complex WM configurations in the spinal cord. While these models have been preferentially utilized for in vivo imaging in the human brain, their application to the human spinal cord (SC) remains limited due to distortions, low signal to noise ratio (SNR) for higher  $b$ -values and long acquisition times.

Although Q-ball imaging of the cat SC showed the possibility to detect crossing WM fiber, such as the longitudinal and commissural tracts [3], so far, only a single study deals with the in vivo detection of multiple pathways in the human SC [4]. However, only 8 non-contiguous slices of the cervical and upper thoracic spine were captured with voxel size  $1 \times 1 \times 5 \text{ mm}^3$ , and scans thus suffered from partial volume effects which preclude the accurate delineation of SC sub-compartments. While previous animal studies have shown the feasibility of  $0.6 \times 0.6 \times 3 \text{ mm}^3$  spatial resolution [5, 6] at 3 T, their applicability to human HARDI

R. Labounek (✉) · J. Valošek · P. Hok · P. Hlušík  
University Hospital Olomouc, I. P. Pavlova 6, 779 00 Olomouc,  
Czech Republic  
e-mail: rene.labounek@gmail.com

R. Labounek · J. Valošek · P. Hok · P. Hlušík  
Palacký University Olomouc, Křížkovského 511/8, 771 47  
Olomouc, Czech Republic

J. Zimolka · Z. Piskořová  
Brno University of Technology, Antonínská 548/1, 601 90 Brno,  
Czech Republic

T. Horák · A. Svátková · P. Bednařík · L. Vojtíšek · J. Bednařík  
Central European Institute of Technology, Kamenice 753/5, 625  
00 Brno, Czech Republic

A. Svátková · P. Bednařík · C. Lenglet  
Center for Magnetic Resonance Research, Minneapolis, MN  
55455, USA

studies was critically limited by the required long scanning times (i.e. >30 min).

Our work is an extension of our preliminary (single subject) results [7], where we demonstrated the possibility to detect significant secondary fiber orientations in areas near the spinal nerve roots, by utilizing an innovative 3T HARDI protocol with spatial resolution  $0.67 \times 0.67 \times 3 \text{ mm}^3$  acquired in 10 min from contiguous slices of the lower cervical SC (i.e. C4–C6). Here, we aimed to demonstrate the feasibility of the proposed advanced protocol on 26 healthy individuals, and to discuss its benefits and limitations.

## 2 Materials and Methods

### 2.1 Data Acquisition Protocols

The data was collected on a 3T MRI scanner (Siemens Prisma) using a 64-channel head/neck and a 32-channel spine coils in 26 healthy subjects (13 women, mean age  $24.2 \pm 1.7$  years) who signed informed consent approved by the local ethics committee.

**T2-weighted sagittal images** (Fig. 1a) were acquired to cover the whole cervical SC with 30 contiguous slices using a turbo spin-echo sequence with TR = 8640 ms (repetition time), TE = 98 ms (echo time), 4 averages, GRAPPA = 2, field of view (FOV)  $250 \times 250 \text{ mm}^2$ , matrix size  $896 \times 896$  voxels, slice thickness 1.3 mm, voxel size  $0.28 \times 1.3 \times 0.28 \text{ mm}^3$ . The acquisition time (TA) was 8 min 49 s.

**T2-weighted axial images** (Fig. 1b) were acquired to cover the C3–C6 levels with 30 contiguous slices using a gradient recalled sequence with TR = 556 ms, TE = 17 ms,

2 averages, FOV  $180 \times 180 \text{ mm}^2$ , matrix size  $512 \times 512$  voxels, slice thickness 2.5 mm, voxel size  $0.35 \times 0.35 \times 2.5 \text{ mm}^3$ , TA = 5 min 37 s.

**ZOOMit HARDI dMRI images** (Fig. 1c, d) were acquired to cover the C4–C6 levels with 23 contiguous axial slices with TR = 4500 ms, TE = 73 ms, FOV =  $44 \times 129 \text{ mm}^2$ , matrix size  $68 \times 200$  voxels, slice thickness 3 mm, voxel size  $0.65 \times 0.65 \times 3 \text{ mm}^3$  after interpolation in Fourier space (original voxel size  $1.3 \times 1.3 \times 3 \text{ mm}^3$ ). 63 diffusion weighted images (42 gradient directions with  $b$ -value =  $1000 \text{ smm}^{-2}$  and 21 directions with  $b = 550 \text{ smm}^{-2}$ ) and 7 images ( $b_0$ ) with  $b = 0 \text{ smm}^{-2}$  were collected with anterior-posterior (AP) phase encoding. 5 additional  $b_0$  images were acquired using posterior-anterior (PA) phase encoding for a total TA = 8 min 32 s.

### 2.2 Data Processing and Registration

Sagittal and axial T2-weighted images were first bias-field corrected [8], and areas outside the body were removed. Sagittal T2-weighted images were resampled to spatial resolution  $0.28 \times 0.35 \times 0.28 \text{ mm}^3$ . The initial SC and cerebrospinal fluid (CSF) segmentation was performed utilizing the Spinal Cord Toolbox (SCT) `propseg` algorithm on the sagittal images. One axial slice containing the approximate center of the C2/C3 intervertebral disc was manually marked, and vertebral levels were labeled [9, 10]. The original axial and resampled sagittal T2-weighted images were then co-registered using the SCT multimodal registration algorithm [9] and the spinal cord and CSF segmentation [10] was repeated on the original axial image with prior knowledge from the previous segmentation of the sagittal

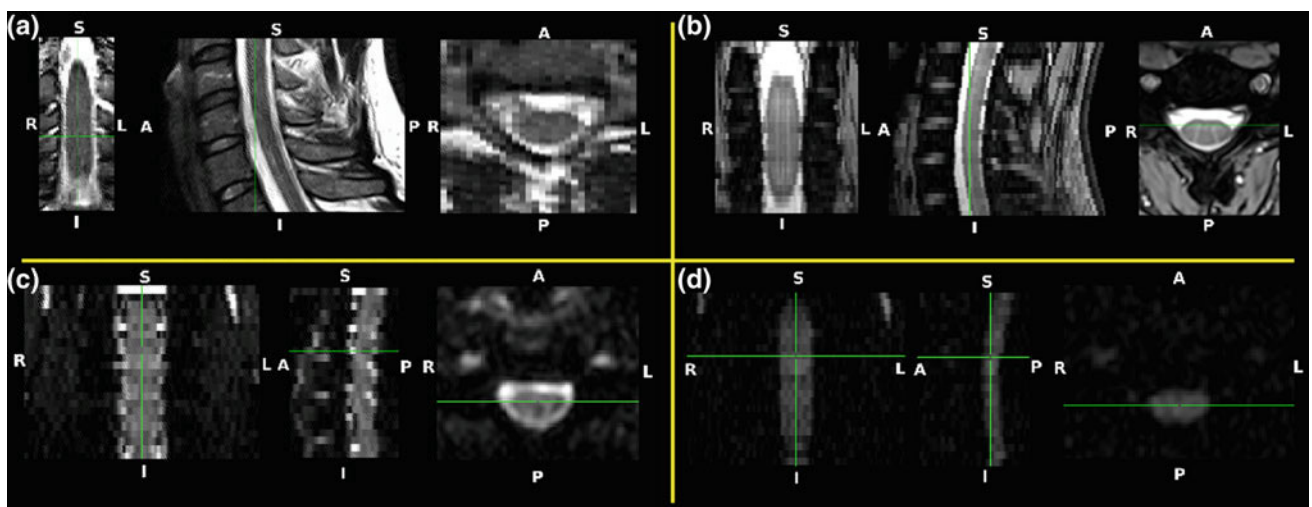


**Fig. 1** Spinal cord images in native space **a** T2-weighted images (sagittal acquisition) at C4–C6 levels **b** T2-weighted images (axial acquisition) at C3–C6 levels **c** dMRI AP  $b_0$  images (axial acquisition)

at C4–C6 levels **d** dMRI AP images with  $b$ -value =  $1000 \text{ smm}^{-2}$  and gradient  $\nu = [-0.91 \ -0.41 \ 0.06]$  (axial acquisition) at C4–C6 levels

images. Co-registered T2-weighted images were fused in the resampled sagittal space with non-linear weighted addition  $F = c_S * S + c_T * T$  where  $F$  is the T2-fused image,  $S$  is the resampled sagittal image,  $T$  is the registered axial image,  $c_S$  and  $c_T$  are spatially varying real coefficients (outside CSF and SC:  $c_S = 0.25$  and  $c_T = 0.75$ ; inside CSF:  $c_S = 0.125$  and  $c_T = 0.875$ ; inside SC:  $c_S = 0.1$  and  $c_T = 0.9$ ). The final SC and CSF segmentation and labeling [10] was performed on the fused T2-weighted image with prior knowledge of the 2nd segmentation.

The  $b_0$  images were extracted from the AP and PA dMRI acquisitions, and were affinely co-registered to correct for susceptibility artifacts using `topup` from FSL [11, 12]. A mean  $b_0$  image was calculated and co-registered to the space of the T2 axial images. Next, a mask of the SC was transformed into diffusion space from the fused T2-weighted images space. Together with the dMRI data and `topup` outputs, this mask was used as the input into `eddy` from FSL [12, 13] to correct eddy currents and motions.

DTI and ball-and-stick models [2] were separately estimated using `dtifit` and `bedpostx` from FSL [12],

providing estimates of primary and secondary fiber orientations as one diffusion tensor (`dtifit`) or as the additive three-compartment model of one isotropic diffusion compartment (i.e. ball) and two crossing diffusion tensors with 2nd and 3rd eigenvalues equal to 0 for each tensor (i.e. two sticks; `bedpostx`).

### 3 Results

Representative FA maps, estimated supra-threshold secondary fiber orientations and their associated volume fractions are shown in Fig. 2 in three different subjects. Areas with low FA that correspond to gray matter are correctly aligned with gray matter regions visible on T2-weighted axial images. As expected from the human SC anatomy, the secondary fiber orientations (with volume fraction around 30% of the measured dMRI signal) are mainly observable around the posterior horns of the SC. Their orientation follows the nerve roots, and crossing fibers are also detectable around the gray commissure. We have not detected crossing

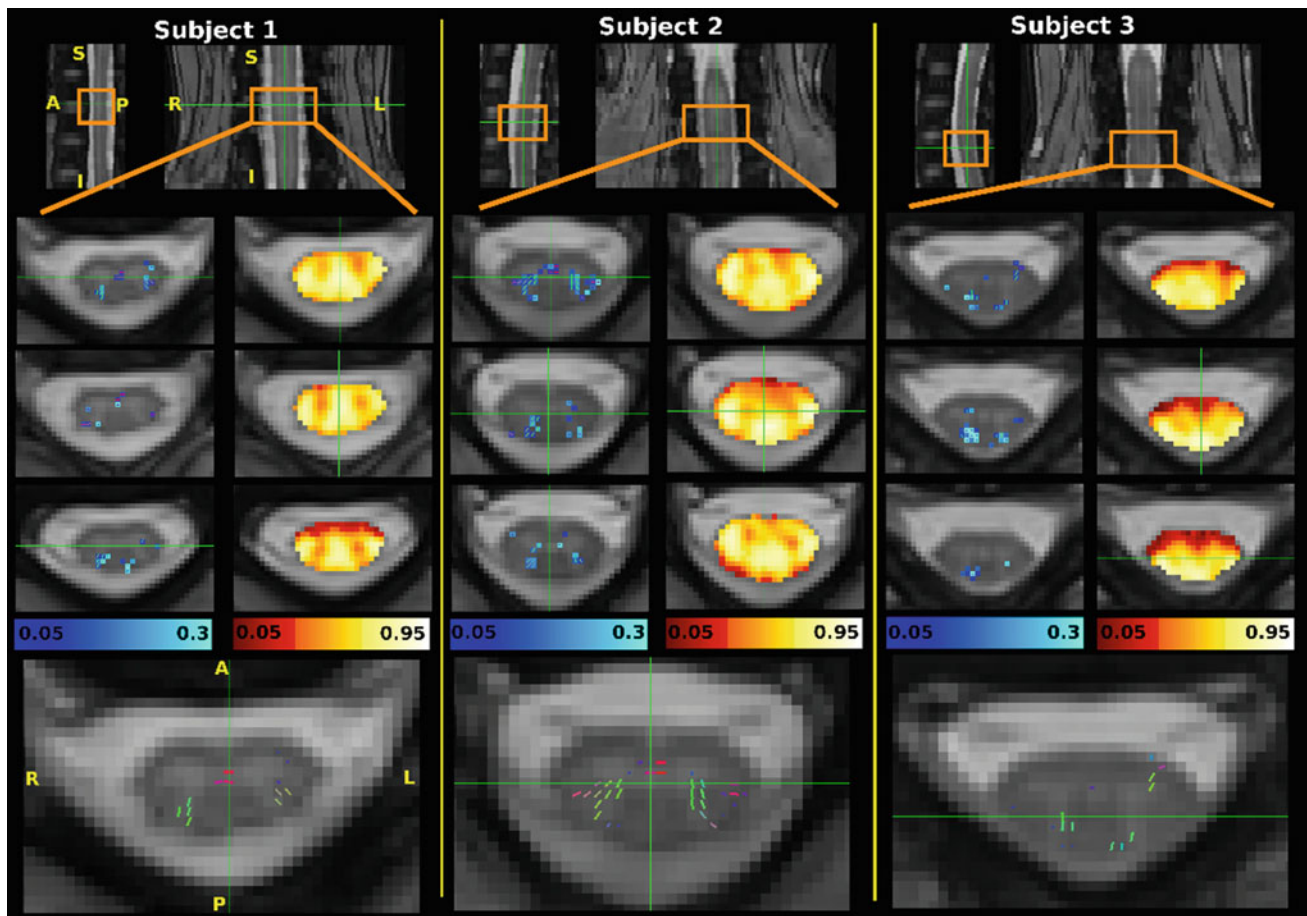
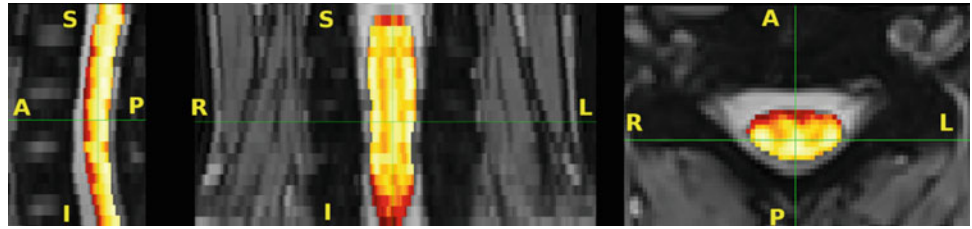


**Fig. 2** FA maps (red-yellow-white), 2nd fiber orientations and their volume fraction (blue) from slices near the C4–C6 areas are superimposed on axial T2-weighted images in native diffusion space for 3 different subjects. All slices are oriented as shown in subject 1



**Fig. 3** Increase noise (lower FA) in the anterior part of SC



fibers around the anterior horns, where they are also expected, probably due to lower signal quality (Fig. 3) at the anterior border of the SC and CSF.

## 4 Discussion

### 4.1 Contributions

We have shown that dMRI-derived microstructural parameters of the SC (Fig. 2) can be obtained using an advanced HARDI protocol, which improves spatial resolution, minimizes susceptibility artifacts, and can be obtained in less than 10 min while providing continuous coverage the cervical SC. The dMRI results are in good agreement with the expected locations of crossing fibers (horns of the SC), and also match well previously published data in the cat [3]. To the best of our knowledge, this is one of the very first demonstrations of in vivo high resolution HARDI in the human SC, with contiguous coverage at the C4–C6 levels and crossing fibers identification, obtained in under 10 min.

### 4.2 Limitations and Future Work

Although the FA maps were found to align very well with GM/WM borders on axial T2-weighted image (Fig. 2), the current study remains limited by the presence of unsuppressed artifacts in the anterior part of the SC (Fig. 3). ECG-triggering may help mitigate effects from cardiac pulsation as a potential source of this artifact, however, we cannot rule out registration issues as another possible explanation.

In addition, we are currently unable to accurately normalize single-subject fused T2-weighted images to the group-averaged SC PAM50 template [9] from SCT. This is needed for population studies of microstructural parameters, or to adequately use the atlas-based WM/GM segmentation from SCT, and might be due to the lower spatial resolution of the PAM50 atlas ( $0.5 \times 0.5 \times 0.5 \text{ mm}^3$ ) than our fused T2-weighted images ( $0.28 \times 0.35 \times 0.28 \text{ mm}^3$ ) [7]. Thus, a study-specific template created from our fused T2-weighted data may help overcome this limitation.

Finally, the SC segmentation fits an elliptical shape [10], which is appropriate in healthy subjects but, similarly to the

recent study by Martin et al. [14], fails in patients with SC compression. Thus, implementation of a more flexible method based on polynomials (e.g. b-splines or Bezier curves) segmentation may be necessary to study patients with compressive myelopathy. We plan to address these limitations in future work.

**Acknowledgements** We would like to express many thanks to Julien Cohen-Adad from Polytechnique Montréal in Canada for his help and insightful advice with optimal Spinal Cord Toolbox settings. We acknowledge the core facility Multimodal and Functional Imaging Laboratory, institution Masaryk University, CEITEC supported by the MEYS CR (LM2015062 Czech-BioImaging); special thanks to Veronika Fabíková and Petr Kudlička. This research was supported and funded by the Czech Health Research Council grants n. NV18-04-00159, NV16-30210A and NV17-29452A, and by the Ministry of Health of the Czech Republic project for conceptual development in research organizations, ref. 65269705 (University Hospital, Brno, Czech Republic). C.L. is partly supported by NIH grant P41 EB015894. Computational resources were supplied by the MEYS CR under the Projects CESNET (Project No. LM2015042) and CERIT-Scientific Cloud (Project No. LM2015085).

## References

1. Tuch, D.S.: Q-ball imaging. *Magn Reson Med* 52, 1358–72 (2004).
2. Behrens, T.E.J., Woolrich, M.W., et al.: Characterization and propagation of uncertainty in diffusion-weighted MR imaging. *Magn Reson Med* 50, 1077–88 (2003).
3. Cohen-Adad, J., Descoteaux, M., Rossignol, S., et al.: Detection of multiple pathways in the spinal cord using q-ball imaging. *Neuroimage* 42, 739–749 (2008).
4. Cohen-Adad, J., El Mendili M.M., Lehericy, S., et al.: Demyelination and degeneration in the injured human spinal cord detected with diffusion and magnetization transfer MRI. *Neuroimage* 55, 1024–1033 (2011).
5. Cohen-Adad, J., Benali, H., et al.: In vivo DTI of the healthy and injured cat spinal cord at high spatial and angular resolution. *Neuroimage* 40, 685–697 (2008).
6. Ellingson, B.M., Sulaiman, O., Kurpad, S.N.: High-resolution in vivo diffusion tensor imaging of the injured cat spinal cord using self-navigated, interleaved, variable-density spiral acquisition (SNAILS-DTI). *Magn Reson Imaging* 28, 1353–1360 (2010).
7. Zimolka, J., Piskořová, Z., et al.: HARDI dMRI imaging of cervical spinal cord. In: *Proceedings of the 23<sup>rd</sup> conference Student EEICT*. Brno University of Technology, Brno, pp 305–307 (2017).
8. Tustison, N.J., Cook, P.A., Gee, J.C.: N4ITK: improved N3 bias correction. *IEEE Trans Med Imaging* 29, 1310–1320 (2011).

9. De Leener, B., Lévy, S., et al.: SCT: Spinal Cord Toolbox, an open-source software for processing spinal cord MRI data. *Neuroimage* 145, 24–43 (2017).
10. De Leener, B., Cohen-Adad, J., Kadoury, S. Automatic Segmentation of the Spinal Cord and Spinal Canal Coupled with Vertebral Labeling. *IEEE Trans Med Imaging* 34, 1705–1718 (2015).
11. Andersson, J.L.R., Skare, S., Ashburner, J.: How to correct susceptibility distortions in spin-echo echo-planar images: Application to diffusion tensor imaging. *Neuroimage* 20, 870–888 (2003).
12. Jenkinson, M., Beckmann, C.F., et al.: *Fsl*. *Neuroimage* 62, 782–790 (2012).
13. Andersson, J.L.R., Sotiropoulos, S.N.: An integrated approach to correction for off-resonance effects and subject movement in diffusion MR imaging. *Neuroimage* 125, 1063–1078 (2016).
14. Martin, A.R., De Leener, B., et al.: A Novel MRI Biomarker of Spinal Cord White Matter Injury: T2\*-Weighted White Matter to Gray Matter Signal Intensity Ratio. *Am J Neuroradiol* 38, 1266–1273 (2017).



# Image Quality Evaluation of Phase Contrast Mammographic Techniques

A. Daskalaki and N. Pallikarakis

## Abstract

**Purpose:** Despite the technical improvements in breast imaging, early diagnosis and lower rate of missed lesions remain a primary goal against breast cancer. The aim of this paper is to investigate further the potential contribution of phase contrast imaging, combined with breast tomosynthesis (BT), in improving breast imaging outcomes and diagnosis.

**Methods:** A phantom composed of paraffin wax with three different embedded mammographic structures, spheres, fibers and  $\text{CaCO}_3$  powder, was constructed. Mammographic and BT images at two acquisition arcs were acquired, in phase contrast mode of two object to detector distances (ODD). The experiments were performed using synchrotron radiation at 20 keV within the conventional mean glandular dose (MGD) range. Evaluation metrics were introduced in order to assess quantitatively the detection of breast abnormalities and the image quality from different modalities.

**Results:** Visual and quantitative assessments of the images acquired showed that the increase of ODD resulted in superior contrast and stronger edge enhancement for all the features. BT images eliminated the overlapping effect and made possible the in depth localization of structures. In addition, BT images demonstrated higher values of all evaluation metrics compared with mammographic images especially for the narrow arc of  $15^\circ$ .

**Conclusions:** The results of this study showed that BT phase contrast imaging is a promising technique that can be proved important for the detection of small details in breast screening and diagnosing.

## Keywords

Phase contrast imaging • Breast phantoms  
Mammography • Breast tomosynthesis

## 1 Introduction

Cancer incidence and mortality statistics show that breast cancer is one of the most common types of cancer worldwide, accounting for 3 in 20 (15%) cancer deaths in females [1]. Mammography is the standard modality of breast screening and diagnosing. Although mammographic screening techniques have increased the image quality and despite the technical improvements in X-ray sources and digital detectors, the rate of missed lesions and false positives remains crucial [2–4].

In principle, mammography projects the compressed breast structure onto a two dimensional plane, based on X-ray tissue absorption. Anatomical structures can overlap resulting in poor visualization of useful diagnostic information and insufficient soft tissue contrast.

Ongoing research in innovative breast imaging modalities is growing in order to increase soft tissue contrast and spatial resolution [5–7]. Phase contrast imaging is such an emerging technique sensitive not only to attenuation but also to X-ray phase change arising at the boundaries of different refractive materials [8–10]. Tissues composed of low Z-elements, such as breast masses, produce low absorption contrast but considerable phase contrast, resulting in significant edge enhancement. Visibility of small and thin details that are not visible in absorption images will become detectable as a result of this edge enhancement effect due to phase shift between different materials.

This study focuses on the potentials of combining the advantages of BT and phase contrast effects for breast imaging. Specifically, the in depth information that BT provides, without overlapping anatomy, is combined with

---

A. Daskalaki (✉) · N. Pallikarakis  
Biomedical Technology Unit, School of Medicine, University of  
Patras, Patras, Greece  
e-mail: dasnatasa@upatras.gr

the edge enhancement effect resulting in a superior contrast and detectability of malignancies.

## 2 Materials and Methods

### 2.1 Hardware Phantom

For the needs of this study a phantom was constructed in our laboratory. The phantom consists of an outer cylinder of 5 cm radius and 2.8 cm thickness made of paraffin wax ( $C_{25}H_{52}$ , density:  $0.93 \text{ g/cm}^3$ ,  $\delta_{(20 \text{ keV})} = 5.53 \times 10^{-7}$ ), inside which are embedded three different types of abnormalities. Nylon spheres with sizes 4.8, 3.2 and 2.4 mm representing masses, nylon fibers with sizes 0.9, 0.7 and 0.5 mm, and  $CaCO_3$  powder representing microcalcifications ( $\mu Cs$ ). In order to avoid the presence of air bubbles in the base material, the paraffin wax was melted at  $70^\circ C$  under vacuum. During the solidification process four layers of the abovementioned abnormalities were embedded slowly. The aim of this arrangement was to produce areas with overlapping structures in order to facilitate a BT investigation.

### 2.2 Image Acquisition

All the experiments took place at the ELETTRA Synchrotron Trieste, at the SYRMEP beamline, especially designed for research in medical diagnostic radiology. The optics are based on a double-crystal Si (111) monochromator working in the energy area 18–35 keV. The X-ray beam provided at 20 m from the source is a laminar section with maximum area  $120 \times 4 \text{ mm}^2$ . The energy of the X-ray beam was 20 keV for all experiments performed. The phantom was placed on a metal plate moving vertically at each scan and able to rotate  $360^\circ$  fixed at 22.4 m from the source.

The detector was a Teledyne DALSA TDI CCD camera. Two object to detector distances (ODD) of 50 and 150 cm were used. With both arrangements, a free space propagation phase contrast imaging set-up was produced. The first set-up with ODD 50 cm resulted in images where the phase contrast contribution started to appear but cannot be fully seen, whereas the second one with ODD 150 cm resulted in images with strong edge enhancement. Two different modalities were used to produce images of  $4400 \times 2200$  pixels. The first one was a mammography mode, where 2D images were acquired. The second one was a BT mode at two different acquisition arcs: an acquisition arc of  $15^\circ$  and  $1^\circ$  increment resulting in 15 projections and an acquisition arc of  $44^\circ$  and  $2^\circ$  increment resulting in 23 projections [11]. The mean glandular dose (MGD) was in the range of 2.1–

2.6 mGy, in accordance with the European guidelines for quality assurance in breast cancer screening and diagnosing. For the BT mode, the MGD was equally distributed in the projections. The incident air kerma (K) was calculated in advance for all the cases in order to acquire an MGD in the above mentioned dose ranges. For the calculations, the following equation is used:

$$MGD = K \times g \times c \times s \quad (1)$$

where  $g$ ,  $c$  and  $s$  are conversion parameters depending on the breast thickness, the glandularity and the incident spectra respectively [12, 13].  $K$  is measured at the upper surface of the breast. In our study, where the base material of the phantom is paraffin wax, the equivalent breast thickness was calculated and found to be 2 cm.

Before reconstruction, a flat-field correction of the BT images was performed. Additional processing needed in order to correct the small vertical movements of the phantom during the BT acquisition arcs, was done using MATLAB 2013. For the reconstruction process an in-house platform was used [14] performing filtered back-projection. All the images were pre-filtered with the use of Ram-Lak filter. A pseudo-3D representation of the phantom was produced from the reconstructed axial planes at every 0.1 mm of the total volume.

### 2.3 Evaluation Metrics

In order to evaluate the image quality and the detection of breast abnormalities, two evaluation metrics were introduced. These metrics were based on the Contrast (C) and Signal to Noise Ratio (SNR), widely used for image quality assessments in conventional X-ray (attenuation based) imaging. For phase contrast imaging, where the edge enhancement needs to be taken into account in the calculations, these metrics are redefined as  $C_{PC}$  and  $SNR_{edge}$  respectively, based on Eqs. 2 and 3 [15].

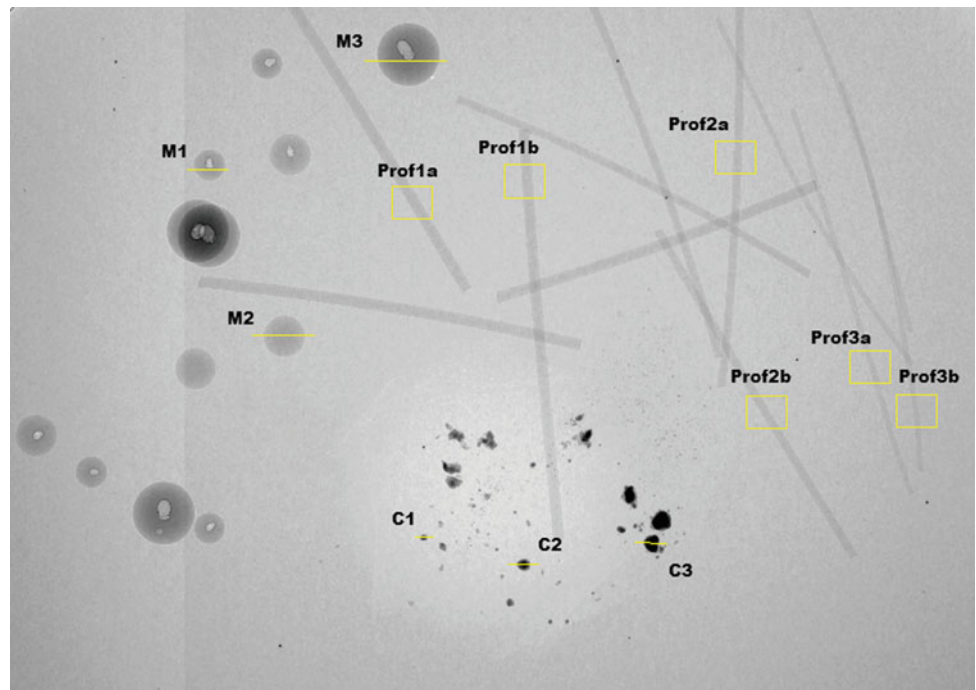
$$C_{PC} = \frac{I_{max} - I_{min}}{I_{back}} \times 100 \quad (2)$$

$$SNR_{edge} = \frac{I_{max} - I_{min}}{\sqrt{2} \times \sigma_{back}} \quad (3)$$

$$FOM = \frac{SNR}{\sqrt{MGD}} \quad (4)$$

where  $I_{max}$  and  $I_{min}$  are the maximum and minimum values of the intensity profiles.  $I_{back}$  and  $\sigma_{back}$  are the average intensity value and the standard deviation of the background ROI respectively, both calculated over the rectangle area (Fig. 1).

**Fig. 1** Projection of the phantom where the ROIs under investigation are illustrated



In order to examine the small variations of dose and allow the comparison of  $SNR_{edge}$ , at each experiment, a figure of merit (FOM) was introduced, where the  $SNR_{edge}$  was normalized to the square root of the MGD according to Eq. 4.

### 3 Results

Regions of interest as well as evaluation metrics were used for visual and quantitative assessment of the images acquired. Table 1 shows the FOM values calculated over the

ROIs presented in Fig. 1 for the six different imaging modalities investigated in this study.

As it can be seen in Fig. 2 last row, 2D images acquired with ODD 150 cm show a strong edge enhancement of the abnormalities that is barely seen in images acquired with ODD 50 cm. Actually, the edges in the latter case appear blurred, whereas in increased detector distance they appear sharp and with an improved contrast. In addition, according to Table 1, FOM values for the 2D images are higher at increased ODD for all findings. This improvement of FOM is significantly higher for masses, since it was calculated to be 43% on average, compared to 21% for  $\mu$ Cs and fibers.

**Table 1** Values of FOM for the ROIs presented in Fig. 1 at six different imaging modalities

2D FOM	ODD = 50 cm		ODD = 150 cm	
	Arc 15°	Arc 44°	Arc 15°	Arc 44°
M1	2.1	3.4	2.4	2.3
M2	1.5	2.7	2.6	1.5
M3	3.0	5.4	2.8	2.6
C1	5.8	8.9	7.9	8.1
C2	6.7	8.6	7.7	7.8
C3	8.3	8.6	11.4	12.4
Prof1a	3.3	4.2	3.4	3.4
Prof1b	3.3	4.7	3.5	3.3
Prof2a	3.3	4.5	3.3	3.1
Prof2b	3.6	4.2	4.0	3.4
Prof3a	3.6	4.3	3.4	3.3
Prof3b	3.1	3.8	3.5	3.2

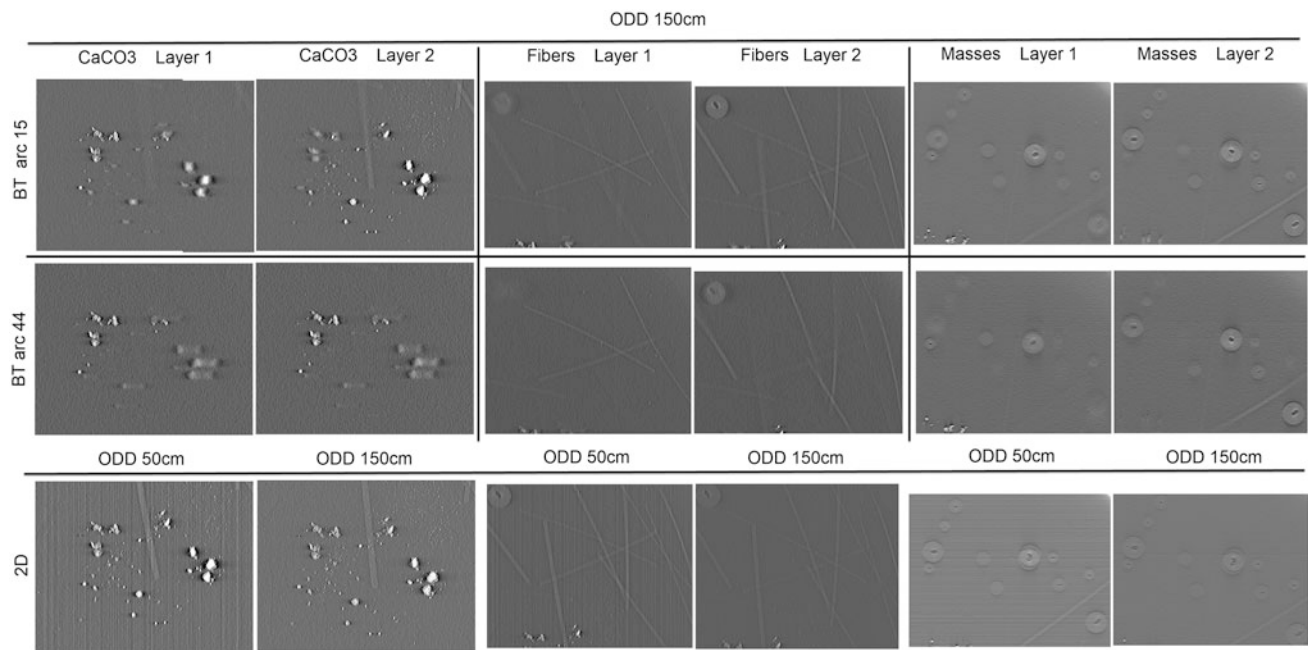


**Fig. 2** Regions of interest for  $\mu$ Cs, fibers and masses from phase contrast (ODD = 150 cm) BT planes and 2D images acquired with an ODD 50 cm and ODD 150 cm

The two first rows of Fig. 2 present phase contrast (ODD = 150 cm) BT planes with different cluster of  $\mu$ Cs, fibers and masses appearing in focus as we slice through the reconstructed volume. The first and second row of Fig. 2 present slices from the BT reconstructed volume acquired with an arc of  $15^\circ$  and an arc of  $44^\circ$ . Table 2 shows the contrast measurements of masses and  $\mu$ Cs for the different BT acquisitions.

Visual assessment of the BT volumes and quantitative results of FOM and contrast values, for the 2D cases, showed that the higher ODD results in improved phase contrast images and superior visualization of lesions. Moreover, BT slices acquired with the narrow arc of  $15^\circ$  exhibit higher FOM and contrast values for the total of the findings embedded in the phantom. BT slices resulted in an

improved detectability of small structures that were barely seen in 2D images.

#### 4 Discussion and Conclusion

This study evaluated the potentials of combining the advantages of BT and phase contrast for breast imaging. In order to do so, an in house constructed phantom was used. Visual assessment of the resulting images as well as FOM and Contrast measurements of the main structures embedded in the phantom showed that the increase of ODD results in improved image quality. In addition, the edge enhancement of the main findings becomes stronger and their appearance is sharper. These results may be critical in the detection of

**Table 2** Values of contrast for the ROIs presented in Fig. 1 for masses and  $\mu$ Cs, at four different BT configurations

ODD = 50 cm			ODD = 150 cm	
Contrast	Arc $15^\circ$	Arc $44^\circ$	Arc $15^\circ$	Arc $44^\circ$
M1	14	14	34	21
M2	22	13	44	24
M3	21	19	32	32
C1	115	91	187	135
C2	76	60	155	135
C3	123	118	131	151

small structures. For instance, the cluster of  $\mu$ Cs seen in Fig. 2 can be clearly depicted only in images acquired with high ODD, whereas in the rest it cannot be detected among the background noise. Moreover, the improvement of FOM was higher for masses, which may contribute in their detectability compared with attenuation based imaging, where it is difficult to be identified especially in dense breasts.

By comparing the 2D images with the respective BT slices, the latter resulted in an improved visualization of lesions. The biggest advantage of BT over mammography lies in the decrease of structural noise, a problem caused by overlying structures. Superposition of structures in the case of 2D imaging is resolved and illustrated at two separate BT planes (layer 1 and 2 in Fig. 2). Characteristic is the example of the two masses (4.8 mm) overlapping, which are illustrated separately in BT planes of Fig. 2. Moreover, according to Table 1, BT images resulted in higher FOM values compared with 2D images, especially for  $\mu$ Cs. All the above results conclude that BT phase contrast imaging is a promising technique that can be proved important for the detection of small details in breast screening and diagnosing.

A comparison of the two acquisition arcs chosen for phase contrast BT investigation showed that the narrow one ( $15^\circ$ ) resulted in higher values of FOM and contrast. The lesions appear sharper and the contrast of their edges is more intense. This is an important result for breast imaging, since the enhanced contrast of low contrast features as well as the clear visualization of  $\mu$ Cs needs to be improved. Moreover, the  $15^\circ$  arc BT resulted in out of plane artifacts less elongated as a result of the smaller arc. On the other hand, the contrast of those out of plane artifacts is higher in  $15^\circ$  arc BT, it may therefore be misinterpreted as in plane structures. This drawback is more intense for high contrast features, as it can be seen in Fig. 2. In addition, the case of the BT with the arc of  $44^\circ$  showed better in depth resolution, thus resulting in an improved in depth localization of features that might be helpful in biopsy guidance and breast operation planning. This indicates that further investigation for the optimal acquisition arc in the case of phase contrast BT is necessary and may trigger post image processing techniques.

## References

1. Cancer Research UK, <http://www.cancerresearchuk.org/>.
2. Pissano ED, Yaffe MJ. Breast cancer screening: Should tomosynthesis replace digital mammography. *JAMA*, 311(24), 2488–2489 (2014).
3. Rodriguez-Ruiz A, Castillo M, Garayoa J, Chevalier M. Evaluation of the technical performance of three different commercial digital breast tomosynthesis systems in the clinical environment. *Physica Medica*, 32, 767–777 (2016).
4. Gong X, Glick SJ, Liu B, Vedula A and Thacker S. Computer simulation study comparing lesion detection accuracy with digital mammography, breast tomosynthesis, and cone-beam CT breast imaging. *Med Phys* A33, 1041–52 (2006).
5. Russo P, Larobina M, Di Lillo F, Del Vecchio S, Mettievier G. Combined SPECT/CT and PET/CT for breast imaging. *Nucl Instr and Meth in Phys Res Sec A: Acceler, Spectr, Detect and Assoc Equip* 809, 58–66 (2016).
6. Tahir S, Bashir S, MacDonald CA, Petruccioli JC. Mesh-based phase contrast Fourier transform imaging. *Optics Communications*, 389, 103–109 (2017).
7. Schleede S, Bech M, Grandl S, Sztrokay A et al. X-ray phase-contrast tomosynthesis for improved breast tissue discrimination *European Journal of Radiology* 83, 531–539 (2014).
8. Bravin A, Coan P, Suotti P. X-ray phase contrast imaging: from preclinical applications towards clinics *Phys Med Biol*, 58, R1–R35 (2013).
9. Endrizzi M. X-ray phase contrast imaging. *Nuclear Inst. and Methods in Physics Research, A* 878, 88–98 (2018).
10. Szafranec MB, Konstantinidis AC, Tromba G, Dreossi D, Vecchio S et al. Synchrotron based planar imaging and digital tomosynthesis of breast and biopsy phantoms using a CMOS active pixel sensor. *Physica Medica*, 31, 192–198 (2015).
11. Daskalaki A, Bliznakova K, Pallikarakis N. Evaluation of the effect of silicone breast inserts on X-ray mammography and breast tomosynthesis images: A Monte Carlo simulation study. *Physica Medica*, 32, 353–361 (2016).
12. Dance DR, Skinner CL, Young KC, Beckett JR, and Kotre CJ. Additional factors for the estimation of mean glandular breast dose using the UK mammography dosimetry protocol. *Phys Med Biol*, 45, 3225–40 (2000).
13. Dance DR, Young KC, and Van Engen RE. Estimation of mean glandular dose for breast tomosynthesis: Factors for use with the UK, European, and IAEA breast dosimetry protocols. *Phys Med Biol*, 56, 453–71 (2011).
14. Kamarianakis Z, Buliev I, Pallikarakis N, A platform for Image Reconstruction in X-ray Imaging: Medical Applications using CBCT and DTS algorithms. *Computer Science Journal of Moldova*, 22(2) (65), 236–252 (2014).
15. Diemoz PC, Bravin A, Langer M and Coan P. Analytical and experimental determination of signal-to-noise ratio and figure of merit in three phase-contrast imaging techniques *Opt Expr*, 20(25), 27670–90 (2012).



# Thermography Evaluation in Patients with Hypothyroidism and Fibromyalgia by Analyzing the Temperatures of the Palms of Hands

Ana Paula Christakis Costa, Joaquim Miguel Maia, Marcos Leal Brioschi, and José Eduardo de Melo Mafra Machado

## Abstract

The objective of this work was to carry out a thermographic evaluation in patients with hypothyroidism (HP) and fibromyalgia (FM) by palms of the hands temperature analysis. The total of 136 electronic medical records of individuals belonging to a database of a thermography diagnostic clinic were selected. The inclusion criteria were: records containing anteroposterior (AP) orthostatic and AP cervical extension images; thermographic reports; male and female individuals; over 18 years old; groups with HP, FM and healthy individuals; laboratory and diagnostic reports; descriptive anamnesis of the patient's profile and preliminary questionnaire for FM criteria. Medical records were classified into three groups: group 1, with HP and FM (50 patients); group 2, with FM but no HP (56 patients); group 3, control (30 healthy individuals). All images selected in electronic records were studied through the Flir report software, with the demarcation of three points in thyroid gland region obtaining an average of temperature and one point on each palm of the hands. Temperature data of each group were statistically analyzed by Microcal Origin 6.0 software, where the obtained results for the thermal correlation between HP and FM, for the palms of the hands, were: group 1:  $31.0 \pm 1.5$  °C; group 2:  $30.7 \pm 2.0$  °C; and group 3:  $31.6 \pm 1.4$  °C. The Pearson linear correlation coefficient ( $\rho$ ) was 1, meaning that the

variables are correlated among themselves. It was concluded that if there is a variation in the metabolic activity of the thyroid gland in patients with FM, there is a variation in the temperature of the palms of the hands, for the groups studied.

## Keywords

Hypothyroidism • Fibromyalgia • Clinical thermography

## 1 Introduction

Infrared thermography is an additional image technique to help the diagnosis, monitoring and prognostic in the medicine [1], since there is a lack of methods in the clinical to associate skin temperature readings to abnormal physiological phenomena, once the temperature of the exposed body surface is highly dependent of environmental conditions and the individual's metabolism [1], however, the exam does not show anatomic abnormalities [2].

In the thermography, fibromyalgia (FM) shows a characteristic image pattern with broad and diffuse hyper-radiation on the cervicothoracic region (mantle sign), aspect of cooling of the extremities due to the Raynaud phenomenon in low level, and hyper-periocular radiation, resulting from palpebral venous congestion due to non-repairing sleep and fatigue (daytime tiredness). Thyroid gland does not appear in thermogram, being detectable when in hypermetabolism of nodules or the whole gland [3]. When treating FM along with hypothyroidism (HP—thyroid-stimulating hormone—TSH > 0.45 mU/L) it is possible to find similar clinical characteristics, such as: muscle pain, fatigue, exhaustion, reduction the ability of exercises and the cold intolerance. The characteristics of HP and FM may result from partial cell resistance to thyroid hormone [4, 5].

Based on the above arguments, the following research hypothesis was raised: is the non-invasive medical infrared

A. P. C. Costa (✉)

Graduate Program in Electrical and Computer Engineering (CPGEE), Federal University of Technology - Paraná (UTFPR), Curitiba, PR 80230-901, Brazil  
e-mail: anachristakis@gmail.com

J. M. Maia

Electronics Engineering Department (DAELN), Graduate Program in Electrical and Computer Engineering (CPGEE), Graduate Program in Biomedical Engineering (PPGEB) - Federal University of Technology - Paraná (UTFPR), Curitiba, PR 80230-901, Brazil

M. L. Brioschi · J. E. de Melo Mafra Machado

Faculty of Medicine at the University of São Paulo (FMUSP), São Paulo, SP 01246-903, Brazil

technique (MIT) effective in assessing thyroid gland temperature in HP and FM patients?

It is known that FM symptoms are similar to those of HP. Thus, in certain situations, patients are misdiagnosed, since FM diagnosis is essentially clinical and HP, laboratory. Therefore, in this paper, it was investigated thermal changes in thyroid gland topographic region of HP and FM patients by palms of the hands temperature analysis.

## 2 Methods

A total of 136 electronic files of individuals were selected, being 111 female and 21 male, who were attended in the period from 2014 to 2016 in a thermography clinic and who adopted the following criteria of inclusion: Records containing AP orthostatic and AP cervical extension images; Thermographic reports; Over 18 years old; Groups with HP, FM and healthy individuals; Laboratory reports for HP diagnosis (TSH > 0.45 mU/L); Radiological examination reports; Descriptive anamnesis of the patient's profile; Diagnosis according to the criteria of the American College of Rheumatology (ACR); And preliminary questionnaire for FM criteria that assists the medical professional in the disease's diagnosis, presenting the General Index of pain (IDG) and Severity of symptoms scale (EGS).

The medical records were classified into three groups: Group 1 (G1)—with HP and FM (50 patients,  $48.5 \pm 1.5$  years); Group 2 (G2)—with FM and no HP (56 patients,  $40 \pm 1.2$  years); and Group 3 (G3)—Control (30 healthy individuals,  $39.4 \pm 1.4$  years).

The Flir Report software were used to select the thermal data three points in thyroid gland topographic region, following its usual anatomical location (see Fig. 1), also performing an arithmetic average of the temperatures obtained. Repeating the same procedure, one points was bilaterally located in the central region of the palms of the hands (see Fig. 2).

The database thermal images were acquired using the FLIR T650SC infrared Camera (Flir Systems Inc. Nashua, NH, USA) with specification of: Resolution of  $640 \times 480$  pixels; Thermal sensitivity <20mk @ 30 °C; Field of view of  $25^\circ \times 19^\circ/0.25$  mm; Image frequency of 30 Hz; Spectral range of 7.5–14  $\mu\text{m}$ ; Spatial resolution of 0.68 mrad; Focus continuous, one shot or manual; Temperature range of  $-40^\circ\text{C}$  to  $+150^\circ\text{C}$ ;  $+100^\circ\text{C}$  to  $+650^\circ\text{C}$ ;  $+300^\circ\text{C}$  to 2,000 °C; Measurement accuracy of  $\pm 1^\circ\text{C}$  or  $\pm 1\%$  of reading; Temperature accuracy of  $\pm 2^\circ\text{C}$ ; Temperature resolution of 0.1 °C; Emissivity of 0.98; Reflection temperature of 20 °C; Atmospheric temperature of 23 °C; and Relative humidity of 50%. The individuals were positioned at 1 m from the camera, in an orthostatic position, and the AP images in cervical extension and AP upper orthostatic were obtained.

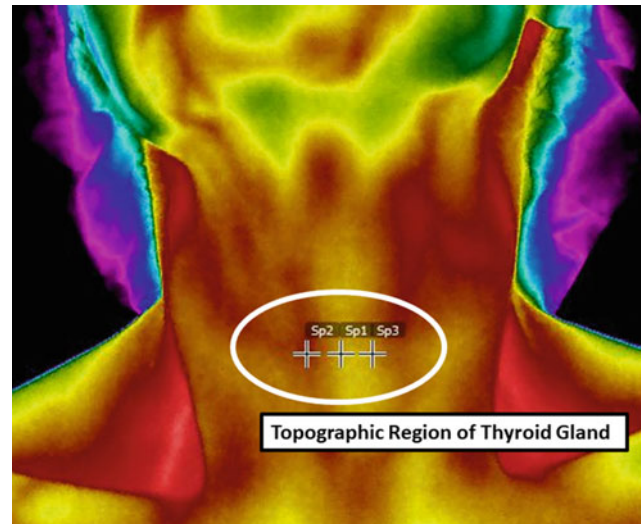


**Fig. 1** Topographic region of thyroid gland

The images were processed on the computer using the FLIR Reporter program (FLIR Tools, version 4.1.140661001) and the temperature data were obtained and analyzed by Microcal Origin 6.0 software, in which the average temperature  $T_m$  was found, for each group, as well as the correlations between groups, defined by  $\Delta 1$ .

Finally, Variance analysis (ANOVA) and Pearson's linear correlation coefficient (Pearson's  $\rho$ ) was calculated to evaluate the correlation degree and also the direction of this correlation. This work was approved by the Research Ethics Committee of the Federal University of Technology – Paraná (UTFPR), protocol number 1.054.356.

## 3 Results

The temperatures difference found in thyroid topographic region of these individuals by thermography was  $+1.09^\circ\text{C}$ . The mean temperature ( $T_m$ ) obtained for the groups were:  $31.7 \pm 1.6^\circ\text{C}$  for group 1,  $31.6 \pm 1.2^\circ\text{C}$  for group 2 and  $31.9 \pm 1.5^\circ\text{C}$  for group 3. Regarding  $\Delta 1$ , values were 0.1 °C between groups 1 and 2, 0.2 °C between groups 1 and 3 and 0.3 °C between groups 2 and 3 (Table 1).

ANOVA, when applied in all correlations, showed that the  $T_m$  were not different from each other and  $\rho = 0$ , indicating that these variables have no correlation.

When  $T_m$  of thyroid topographic regions was correlated with palms of hands's temperature, values were G1:  $31.0 \pm 1.8^\circ\text{C}$  ( $\rho = 1$ ); G2:  $30.7 \pm 2.0^\circ\text{C}$  ( $\rho = 0$ ) and G3:  $31.6 \pm 1.4^\circ\text{C}$  ( $\rho = 1$ ). It was reached, for  $\Delta 1$ , values 0.2 °C between groups 1 and 2; 0.4 °C between groups 1 and 3 and 0.6 °C between groups 2 and 3. ANOVA in all groups and their correlations showed that the samples were not different from each other (Table 2).

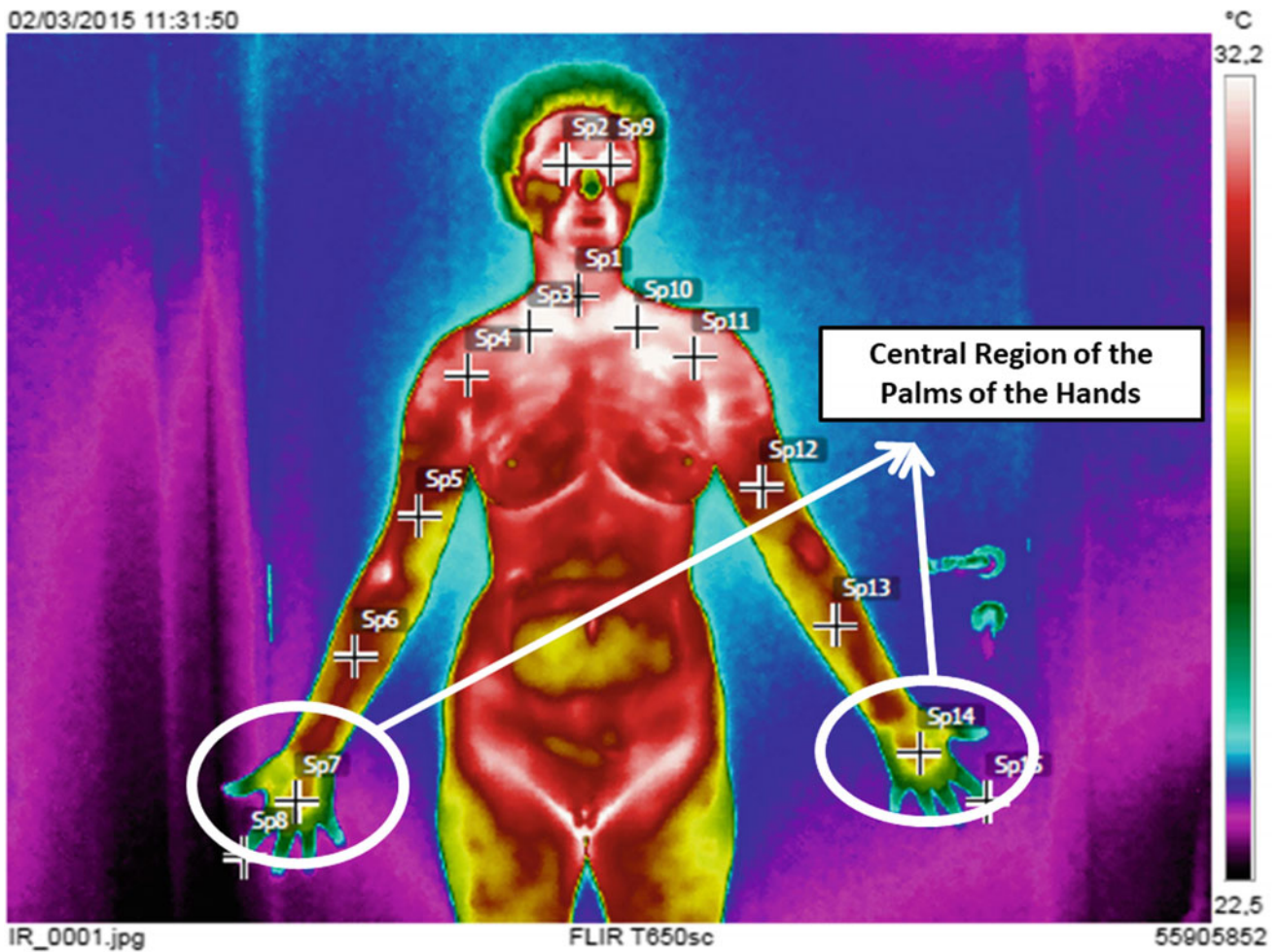


**Fig. 2** Central region of the palms of the hands

**Table 1** Average temperature of groups 1, 2 and 3

Group	Anatomic region	Average temperature (°C)	Temperature min (°C)	Temperature max (°C)	Standard deviation
Group 1	Thyroid gland	31.7	29.1	34.9	1.6
Group 2	Thyroid gland	31.6	28.0	34.0	1.2
Group 3	Thyroid gland	31.9	29.4	34.7	1.5

**Table 2** Average temperatures of thyroid gland topographic region versus palms of hands

Groups	Average temperature	Temperature min.	Temperature max.	Standard deviation
Group 1	31.0	27.6	34.8	1.8
Group 2	30.7	26.5	34.4	2.0
Group 3	31.6	27.6	33.9	1.4



## 4 Discussion

The obtained results for  $\Delta 1$ , 0.2 °C, 0.4 °C and 0.6, when analyzed the palms of the hands, disagree with those found in the literature, which claim that a variation of T of  $0.20 \pm 0.73$  °C show normality in the individual for the extremities regions [6]. Also, it was found evidence that values above 0.5 °C as indicative of painful dysfunction in the hand region [6], as in other studies that presented differences between 0.13 and 2.0 °C may mean some painful disorder [7]. In addition, a thermal difference of  $0.17 \pm 0.042$  °C for the human trunk region,  $0.20 \pm 0.073$  °C for the extremities and  $0.45 \pm 0.129$  °C at the fingers and toes, are also abnormality to the individuals studied [8].

In the anamnesis and in the questionnaire for preliminary FM criteria according to the Brazilian Association of Rheumatology (ACR) [3] applied to the studied groups, the following symptoms were observed: chronic pain in the body, showing more hyper-radiation regions when thermography was performed [3, 9]; depression; tiredness; non-repairing sleep with periocular congestion (confirmed by thermography); intestinal constipation; diarrhea; deflections; besides the correlation of chronic generalized pain, with myalgias, arthritis, arthrosis and rheumatism [4, 5, 10]. However, FM when analyzed by thermography, presents a characteristic image pattern with broad and diffuse hyper-radiation on the cervicothoracic region, called the “mantle signal”, where the brown fat activity can be analyzed; aspect of cooling of the extremities due to light Raynaud’s phenomenon; and periocular hyper-radiation, resulting from palpebral venous congestion due to non-repairing sleep and fatigue (tiredness) [1].

When treated, Raynaud’s phenomenon was observed in the results obtained by the analysis of the anamneses, applied questionnaires and thermographic results, which the individuals studied did not show the pathology. The presented differences of  $\Delta 1$  of 0.2 °C, 0.4 °C and 0.6 °C, of the palms of the hands region, were lower than the data presented in the literature for the diagnosis of Raynaud’s phenomenon [2, 11, 12].

The temperature difference found in thyroid region of FM patients by thermography was +1.09 °C and  $\rho = 0$  (zero), meaning that the Tm of the three groups have no correlation between themselves, being independent, so the variation in the metabolic activity of the thyroid gland will not impact the temperature in patients with FM. However, disagreeing with this finding, it was found in the literature using the same MIT evidence that values higher than 0.26 °C contribute to changes on thyroid metabolism [5]. Among dysfunctions that most point to similarity of symptoms with those of FM [5], HP (TSH > 0.45 mU/L) is one of them, and, in the literature, it can be found that this dysfunction

presents alterations in the hypophysis-hypothalamic axis where FM patients have less thyrotropin (TSH) and the hyperactivity of this axis may be genetically based or due to stress throughout life or due to a specific situation [3–5, 10]. HP was found in approximately 37% of the individuals studied, however, the symptoms that could be derived from this pathology were excluded by means of the study carried out in the anamneses and laboratory tests. In addition, in FM patients, pain is being investigated as changes in the hypothalamic-hypophysis-adrenal axis, excessive production of adrenocorticotrophic hormones (ACTH) and its hyperactivity, also, includes factors related to the genetic basis, stress throughout life [3] or physical trauma. Based on quantitative data and laboratory exams, were not observed in the instruments of anamnesis of this research, emotion factors that could trigger the FM.

## 5 Conclusion

The thermographic technique can be used to measure the temperature variation of thyroid gland topographic region. When analyzed the groups selected for this research, it was concluded that the variation in the metabolic activity of the thyroid gland does not depend on the thyroid dysfunction (HP) and FM. However, for the same study groups, variation in the metabolic activity of the thyroid gland exert an interaction on the variation of temperature rate of the palms of the hands ( $\rho = 1$ ).

**Acknowledgements** This research was supported by the Brazilian agencies CAPES, CNPq, Araucaria Foundation, FINEP and Brazilian Ministry of Health.

**Conflict of Interest Statement** The authors declare that they have no competing interests.

## References

1. Brioschi, M. L., Yeng, L. T., Araujo, J. O. de., Pezzucchi, M. Z., Teixeira, M. J.: Modulação da dor na síndrome fibromiálgica: um distúrbio termorregulatório?. *Pan American Journal of Medical Thermology* 1(2), 71–80 (2015).
2. Ring, E. F., Ammer, K.: Infrared thermal imaging in medicine. *Physiol Meas* 33(3), R 33–46 (2012).
3. Brioschi, M. L.: *Escore termográfico infravermelho para diagnóstico complementar da fibromialgia*. [Post-doctor degree thesis]. Faculdade de Medicina da Universidade de São Paulo. 165p. 2008.
4. Garrison, R. L., Breeding, P. C.: A metabolic basis for fibromyalgia and its relates disorder: The possible role of resistance to thyroid hormone. *Med Hypotheses* 61, 182–189 (2003).
5. Ramos, R. J. R.: *Fibromialgia: hipotireoidismo o transtorno de dolor persistente somatomorfo*. *Med Gen Y Fam* 5(4), 144–148 (2016).

6. Uematsu, S., Haberman, J., Pochaczewsky, R., Wexler, C. E., Goin, J., Abernathy, M.: Thermography as a diagnostic aid: A commentary on experimental methods, data interpretation and conclusions. *Themology* 1, 58 (1985).
7. Gratt, B. M., Sickles, E. A.: Electronic facial thermography: An analysis of asymptomatic Adult subjects. *J Orofac Pain* 9, 225–265 (1995).
8. Uematsu, S., Edwin, D. H., Jankel, W. R., Kozikowski, J., Trattner, M.: Quantification of thermal asymmetry. Part 1: Normal values and reproducibility. *J Neurosurg* 69, 552–555 (1988).
9. Brioschi, M. L.: Metodologia de normalização de análise do campo de temperaturas em imagem infravermelha humana. [Doctor degree thesis]. Universidade Federal do Paraná, Paraná (2011).
10. Rodriguez-Espinosa, J., Díaz-López, C., Guinot, M., Geli, C., Llobet, J. M., Rodriguez, A.: Disfunción tiroidea em mujeres com sospecha de fibromialgia. *Reumatol clin* 2, 70–77 (2006).
11. Rodriguez-Criollo, J. A., Jaramillo-Arroyave, D.: Fenómeno de Raynaud. *Rev Fac Med* 62(3), 455–464 (2014).
12. Ammer, K.: Temperature gradients in Raynaud's phenomenon. Comparison by gender, age class and finger involvement. *Thermology international* 20(3) (2010).

# Material Analysis for a New Kind of Hybrid Phantoms Utilized in Multimodal Imaging

Manuel Stich, Karina Schuller, Anne Slawig, Klaus Detmar, Michael Lell, Sebastian Buhl, and Ralf Ringler

## Abstract

The use of phantoms for medical imaging is of increasing importance, especially concerning hybrid imaging technologies. The purpose of this study was to find new materials suitable for hybrid phantoms which can be used in magnet resonance imaging, CT and nuclear medicine. Suitable phantom materials have to meet the requirements: tissue-equivalent relaxation and absorption/scattering coefficients, material stability/strength to reproduce tissue structures, no bacterial infestation of the material, cost-effective use. The material samples in this study were based on the basic components: carrageenan (3%, m/m), agarose (0.8–1.0%, m/m),  $\text{GdCl}_3$  (30–100  $\mu\text{mol/kg}$ ),  $\text{NaNO}_3$  (antiseptic

agent, <0.1%, m/m) and  $\text{H}_2\text{O}$ . Additional modifiers were added:  $\text{Ba}(\text{NO}_3)_2$ ,  $\text{SiO}_2$ ,  $\text{CuSO}_4$ ,  $\text{MgCl}_2$ . These modifiers influence the relaxation times and abortion characteristics. For tissue-equivalency,  $T_1/T_2$ -times and Hounsfield Units (HU) of material samples were compared to various human tissues after performing the following experiments: MR-relaxometry was measured using a 1.5T MRI scanner. HU were acquired at 80 kV/110 kV/130 kV using a CT scanner; for nuclear medicine, material samples (10 MBq, TC-99 m) were examined in a water-phantom utilizing a SPECT-system. Tissue structures, like soft-tissue, brain (gray/white matter), kidney and liver can be simulated with high accuracy in their relaxation times and HU-values using  $\text{Ba}(\text{NO}_3)_2$  as an additional modifier. This modifier meets all requirements and covers  $T_1/T_2$ -times of 700–1400 ms/50–80 ms and HU-values of 12–740 HU. Functional relationships were investigated by describing the  $T_1/T_2$ -times in dependency of the  $T_1/T_2$ -modifiers. Other modifiers did not meet all tissue-equivalent characteristics. Our gel-based approach can also be used in nuclear medicine to generate active tissue structures, e.g. hot nodules with TC-99 m.

M. Stich (✉) · K. Schuller · A. Slawig · R. Ringler  
X-Ray and Molecular Imaging Lab, Ostbayerische Technische Hochschule Amberg-Weiden, Hetzenrichter Weg 15, 92637 Weiden, Germany  
e-mail: m.stich@oth-aw.de

K. Schuller  
e-mail: ka.schuller@oth-aw.de

A. Slawig  
e-mail: a.slawig@oth-aw.de

R. Ringler  
e-mail: r.ringler@oth-aw.de

M. Stich · A. Slawig  
Institute for Diagnostic and Interventional Radiology, University Hospital Würzburg, Oberdürrbacher Str. 6, 97080 Würzburg, Germany

K. Detmar · M. Lell  
Institute for Radiology and Nuclear Medicine, Paracelsus Private Medical University, Prof.-Ernst-Nathan-Str. 1, 90419 Nuremberg, Germany  
e-mail: klaus.detmar@klinikum-nuernberg.de

M. Lell  
e-mail: michael.lell@klinikum-nuernberg.de

S. Buhl  
Molecular Diagnostics Lab, Ostbayerische Technische Hochschule Amberg-Weiden, Hetzenrichter Weg 15, 92637 Weiden, Germany  
e-mail: s.buhl@oth-aw.de

## Keywords

Multimodal imaging • Hybrid phantom • Carrageenan gel

## 1 Introduction

In this study new materials for hybrid phantoms are investigated, in terms of their suitability for magnetic resonance tomography, X-ray imaging and nuclear medicine. The main focus is the analysis and evaluation of suitable phantom materials, which have to meet the following requirements: (1) Tissue-equivalent relaxation properties. (2) Tissue-equivalent absorption properties for ionizing radiation in the energy range of 80–140 kV. (3) All tissue-equivalent properties from (1) and (2) have to be homogeneous in the

material. (4) The material needs to be sufficiently stable and have enough strength to reproduce also tissue structures of complex forms. (5) Easy handling and use. (6) Resistance to bacteria and other microorganisms. (7) Cost-effective manufacturing.

The objective of finding suitable materials for a hybrid phantom was approached by analyzing and evaluating existing MR-equivalent materials. Various possibilities have already been proposed in the literature, e.g.: agar [1, 2], agarose [3–8], Polyvinylalkohol [9, 10], TX-150 [11], TX-151 [12], gelatine [13, 14], polyacrylamide [15] and carrageen [16]. Some of the listed propositions can be excluded as they do not or only partially fulfill the requirements listed before. Mostly the concentrations necessary for tissue equivalent properties do not provide sufficient stability or vice versa [15, 17]. Handling, hardening and mold formation are further challenges [9, 10, 17].

A combination of carrageenan and agarose was found to be the most suitable material for a hybrid phantom to deliver enough material stability and adjust  $T_2$  time. Additionally, gadolinium ions were added as a  $T_1$  modifier. The effect of the  $T_2$  modifier on the  $T_1$  time is negligibly small [18]. Additionally, all modifiers for the  $T_1$ - and  $T_2$  relaxation times, will also affect the radiation attenuation properties. In order to fine tune a hybrid phantom, to provide tissue-equivalent properties, all effects needed to be considered. To ensure the equivalency to human tissue all material samples examined in this study were compared to different human tissues.

## 2 Materials and Methods

### 2.1 Composition of the Material Samples

The following materials supplied the basic components for all samples: (1) Carrageenan (carrageenan, kappa: Carl Roth, Germany); (2) Agarose (agarose standard Roti@garose, Carl Roth, Germany); (3) Gadolinium(III)-chloride hexahydrate (REacton|r, 99.9% REO, Alfa Aesar, Thermo Fisher, Germany); (4) Sodium azide ( $\text{NaN}_3$ , 98.0%, Carl Roth, Germany).

The mass fraction of carrageenan was 3.0% in all material samples. Agarose ( $\text{C}_{12}\text{H}_{18}\text{O}_9$ ,  $M = 306.27$  g) was used as a  $T_2$  modifier, and gadolinium(III)-chloride ( $\text{GdCl}_3$ ) as a  $T_1$  modifier. Different material samples were created with 0.4% and 0.8% (mass fraction) agarose, and 30, 50 or 100  $\mu\text{mol/kg}$   $\text{GdCl}_3$ . As an antiseptic agent, 0.03% (mass fraction) of sodium azide was added to all samples to prevent microbial infestation. These basic mixtures are combined with bi-distilled and deionized water to generate entities of 100 g each.

These basic components were mixed with the following additional modifiers: (1) Barium nitrate ( $\text{Ba}(\text{NO}_3)_2$ , 9.99%, Alfa Aesar, Thermo Fisher, Germany); (2) Silica ( $\text{SiO}_2$ , cristobalobalite flour, 8  $\mu\text{m}$ , Kremer Pigmente, Germany); (3) copper powder (Cu powder, >99.85, p.a., <63  $\mu\text{m}$ , Carl Roth, Germany); (4) copper(II)-sulphate ( $\text{CuSO}_4$ , 99%, Carl Roth, Germany); (5) Magnesium-chloride ( $\text{MgCl}_2$ , 98.5%, Carl Roth, Germany). These modifiers influence the relaxation times and change the absorption characteristics for ionizing radiation. They were chosen according to the following criteria: solubility in water, low toxicity, free electrons, electron spin, relaxation time, effective density and atomic number and current availability.

### 2.2 Sample Preparation

In a first step,  $\text{GdCl}_3$  was dissolved in water, and the mixture was heated to about 70 °C in a Pyrex-beaker. All the other components were added, except for  $\text{NaN}_3$ . The mixture was heated further to reach 90 °C and continuously stirred (e.g. using a magnetic stirrer). After bringing the mixture to a boil and completely dissolving the agarose, it was cooled down under room conditions for about 5 min. Finally,  $\text{NaN}_3$  was added under a sterile bench and the mixture was cooled further. After a solid structure has formed, the sample was wrapped in a plastic film to protect it against environmental influences. To form spherical material samples (diameter = 32 mm) for the measurements in nuclear medicine, the mixture was placed in a mold before cooling (see Suppl. 1).

### 2.3 MR-Relaxometry ( $T_1$ - and $T_2$ -Measurements)

The relaxation times of the material samples were measured in a 1.5T MR scanner (Magnetom Vision, Siemens, Erlangen, Germany) using a head-coil. Measurement parameters were: matrix size = 256 × 256, slice thickness = 10 mm, FOV (read) = 256 mm, FOV (phase) = 256 mm). The measurement was performed at  $25 \pm 1$  °C.

The  $T_1$  time was determined using an inversion recovery sequence. The repetition time (TR) and echo time (TE) were 5000 ms and 12 ms, respectively. Inversion times (TI) were chosen as: 24, 30, 40, 50, 60, 70, 80, 90, 100, 150, 200, 250, 300, 400, 500, 750, 1000, 1250, 1500, 1750, 2000, 2250, 2500, 2750, 3000 and 4000 ms. The flip angle was set to 180°.

The  $T_2$  time was determined using a spin echo sequence. Here, the repetition time (TR) was set to 5000 ms. The echo time (TE) was chosen as: 15, 22, 29, 39, 52, 69, 93, 125, 167, 224 and 280 ms. The flip angle was set to 90°. The

values for the MR signals  $S_{IR}(TI)$  (inversion recovery sequence) and  $S_{SE}(TE)$  (spin echo sequence) were calculated as the mean of a defined ROI ( $\sim 1000$  pixels). Assuming for  $T_2$ -weighted images:  $TE \approx T_2$  and for  $T_1$ -weighted images:  $TI \approx T_1$ , the measured signal can be fitted using the following equations (Eqs. 1 and 2) as:

$$S_{IR}(TI) = S_0 \left[ 1 - 2e^{-\frac{TI}{T_1}} + e^{-\frac{2TI}{T_1}} \right] + C, \quad (1)$$

$$S_{SE}(TE) = S_0 e^{-\frac{TE}{T_2}} + C. \quad (2)$$

Here,  $S_0$  is the initial signal intensity, proportional to the proton density  $\rho(x, y)$  of the tissue,  $C$  is the signal offset of the system. The measured and fitted signal are visualized in Suppl. 2 for all tested material samples. Material homogeneity was determined by evaluating the coefficient of variation in  $S_{IR}$  and  $S_{SE}$  signals in a rectangular ROI of  $\sim 1000$  pixel.

## 2.4 X-Ray Absorption (CT and SPECT-Measurements)

All material and tissue samples were measured at 80, 110 and 130 kV in a CT scanner (SOMATOM Emotion 6, Siemens Healthcare, Erlangen, Germany). The mean gray values of the acquired images were evaluated for all measured energies within a ROI ( $\sim 1000$  pixels). Material homogeneity measurements were performed by evaluating

the coefficient of variation for the HU-values in a rectangular ROI of  $\sim 1000$  pixel.

For investigation of material behavior in nuclear medicine, two spherical material samples were placed in a cylindrical water phantom as shown in Fig. 1a. Each material sample had a different material composition and consequently a different effective material density and atomic composition. In order to estimate the cross-section for the photo- and Compton effects, key numbers  $(Z^n/A)_{eff}$  ( $Z$ : atomic number,  $A$ : mass number) and  $\rho_{eff}$  were calculated. The product of the effective atomic-mass-ratio and the effective density  $\rho_{eff} \cdot (Z^n/A)_{eff}$  is proportional to the attenuation coefficient [19] and listed in Table 1. An activity of 10 MBq TC-99 m was introduced into both samples. In order to ensure a homogeneous distribution of the activity, TC-99 m was added in the liquid mixture just before the curing process began. An injection of the activity into the cured spheres does not ensure a homogeneous distribution. Measurements were performed using a SPECT system (PRISM1000, Intermedical) with the following acquisition parameters: matrix =  $128 \times 128$ , 60 angle positions, acquisition time/angle position = 30 s, zoom = 100%. The images were reconstructed using an iterative reconstruction algorithm (OS-EM) with a Butterworth filter (4th order, cutoff = 0.3, 8 iterations, 4 subsets, zoom = 100%). The intensities of both spheres were evaluated and compared to the effective values which are proportional to the linear attenuation coefficients [19] of the material composition.

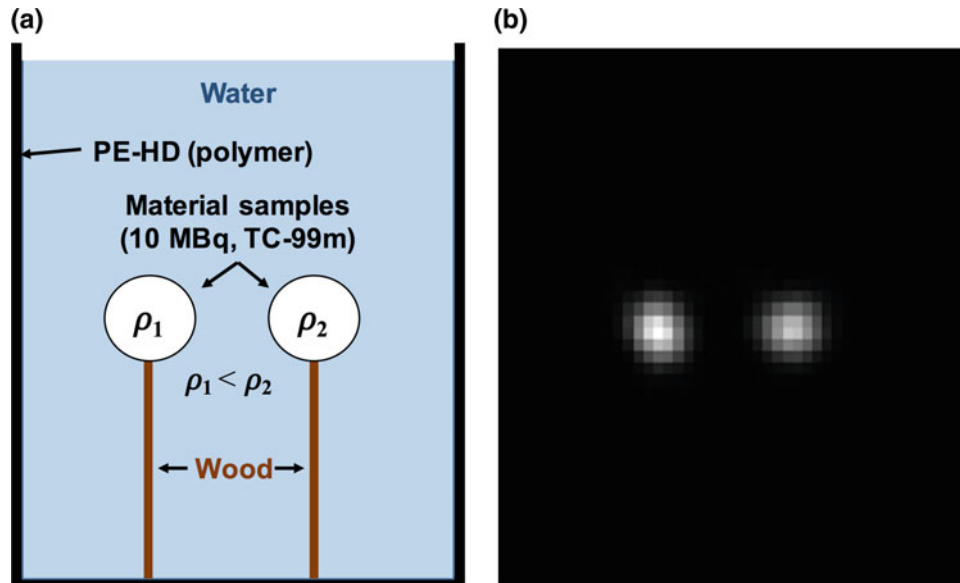


**Fig. 1** **a** Measurement setup for the investigation of the eligibility of the materials in nuclear medicine. Two spherical material samples were placed on two wooden sticks in a cylindrical phantom which is filled with water. Both spheres contain 10 MBq TC-99 m but differ in their material density. **b** Reconstructed SPECT data (coronal slice) of the

measurement setup shown in (a). The right sphere (3.09 g  $Ba(NO_3)_2$ ) with a higher material density and effective value shows smaller intensity values than at the left sphere (2.04 g  $Ba(NO_3)_2$ ) with a smaller material density and effective value

**Table 1** Effective density  $\rho_{eff}$  and effective value  $\rho_{eff} \cdot (Z^n/A)_{eff}$  ( $Z$ : atomic number,  $A$ : mass number) for Compton\* and photo effect\*\* were calculated for all tested material and various tissue structures (literature values). Hounsfield units (HUs) for the material and tissue samples (pig) were measured at 80, 110 and 130 keV

Material sample/Tissue	$\rho_{eff}$ (g/cm <sup>3</sup> )	$n = 1^*$	$n = 4^{**}$	CT values (HU)		
		$\rho_{eff} \cdot (Z^n/A)_{eff}$ (g/cm <sup>3</sup> )	$\rho_{eff} \cdot (Z^n/A)_{eff}$ (g/cm <sup>3</sup> )	80 kV	110 kV	130 kV
1.0% Agarose	1.00	0.55	229.81	42	40	39
0.8% Agarose	1.00	0.55	229.69	42	41	38
0.8% Agarose, 1.01 g Cu	1.09	0.60	365.45	146	85	78
0.8% Agarose, 5.00 g Cu	1.38	0.76	1030.48	532	384	336
0.8% Agarose, 1.01 g CuSO <sub>4</sub>	1.03	0.57	284.07	68	47	41
0, 8% Agarose, 5.00 g MgCl <sub>2</sub>	1.05	0.58	332.32	93	76	71
0.8% Agarose, 5.00 g SiO <sub>2</sub>	1.07	0.59	275.90	79	66	65
0.8% Agarose, 25.00 g SiO <sub>2</sub>	1.33	0.72	450.80	281	225	219
0.8% Agarose, 1.01 g Ba(NO <sub>3</sub> ) <sub>2</sub>	1.01	0.56	341.71	115	111	98
0.8% Agarose, 2.04 g Ba(NO <sub>3</sub> ) <sub>2</sub>	1.05	0.58	1022.19	375	352	321
0.8% Agarose, 3.09 g Ba(NO <sub>3</sub> ) <sub>2</sub>	1.07	0.59	1442.97	679	482	421
0.8% Agarose, 5.00 g Ba(NO <sub>3</sub> ) <sub>2</sub>	1.11	0.61	2227.81	1215	862	724
Liver	–	–	–	129	122	109
Kidney	–	–	–	105	99	96
Brain, matter	–	–	–	38	36	35
Bone, coronal	–	–	–	1334	1086	888
Lung	–	–	–	46	43	42
Muscle, skeletal	–	–	–	44	41	41
Soft tissue	–	–	–	54	51	51
Fat tissue	–	–	–	–84	–22	51

### 3 Results

#### 3.1 General Properties of the Material Samples

All samples formed a solid gel after curing times between 10 and 15 min, depending on the additional modifiers. Big and complex structures could be formed by pouring the gel into an appropriate mold. The total manufacturing time, including curing, was between 20 and 30 min. The manufacturing process and the handling of the material samples was simple and uncomplicated. Microbiological growth tests revealed that samples without sodium azide showed a microbiological infection, all samples with added sodium azide showed no such infestation. CT and MRI images showed homogeneous intensity values for most of the material samples. The variation coefficients of the examined samples were  $<0.3\%$ . Only the samples with the copper and silicon dioxide modifiers, showed higher variation coefficients  $\sim 1.2\%$ . An exception were material samples, containing copper and silicon dioxide showed inhomogeneity, which is mainly caused by small air inclusions occurring at the edges of the

sample. The material selection, proposed in this study proofed to be efficient in terms of material and manufacturing costs. Most of the material sample ingredients are standard substances in microbiology and relatively inexpensive. The manufacturing process can be performed using only standard equipment available in a standard university laboratory involved in microbiology.

#### 3.2 MR-Relaxometry ( $T_1$ - and $T_2$ -Measurements)

The relaxation times resulting from the measured and fitted signal intensities are visualized in Fig. 2. In addition to the relaxation times of the materials, Fig. 2 also shows the relaxation times of selected human tissues, according to literature [20–28]. At a constant agarose concentration and with increasing GdCl<sub>3</sub> concentration the  $T_1$  time decreases (Fig. 3a), but the  $T_2$  time is also affected (Fig. 3b). However, the relative change of the  $T_2$  is lower than that of the  $T_1$  time (Fig. 3a, b).

The  $T_1$  time at a constant agarose concentration, depends on GdCl<sub>3</sub> as well as on the barium nitrate concentration. The



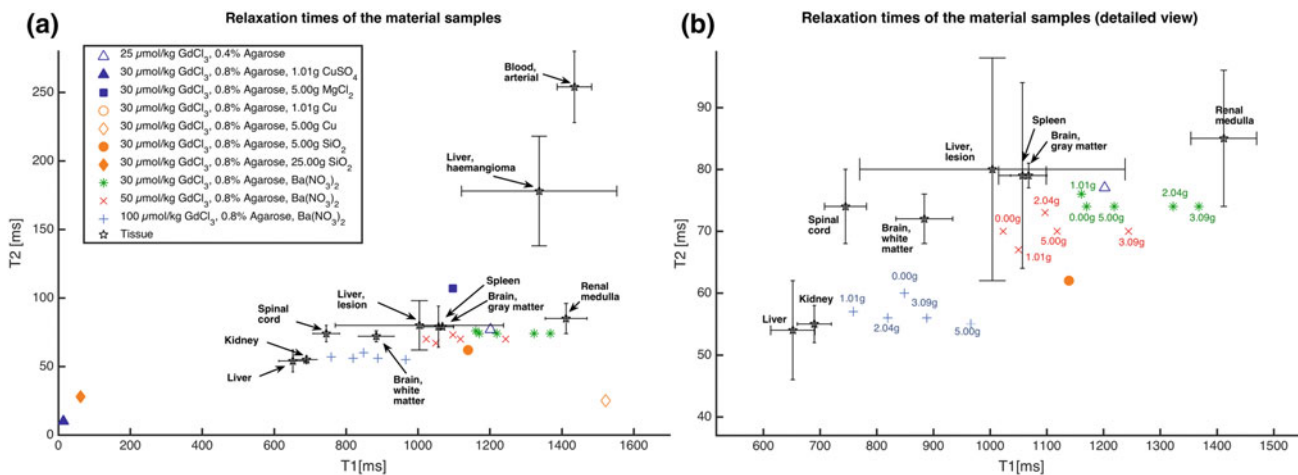


**Fig. 2**  $T_1$  and  $T_2$  times of the MR relaxometry experiments for the measured material samples and different tissues (a, b). The detailed view b shows the relaxation times for all samples with barium nitrate as an additional modifier. The numbers at the markers (+,  $\times$ ,  $\star$ ) indicate

the amount of barium nitrate contained in the sample. Relaxation times of human tissue structures are presented, according to literature values [20–28]

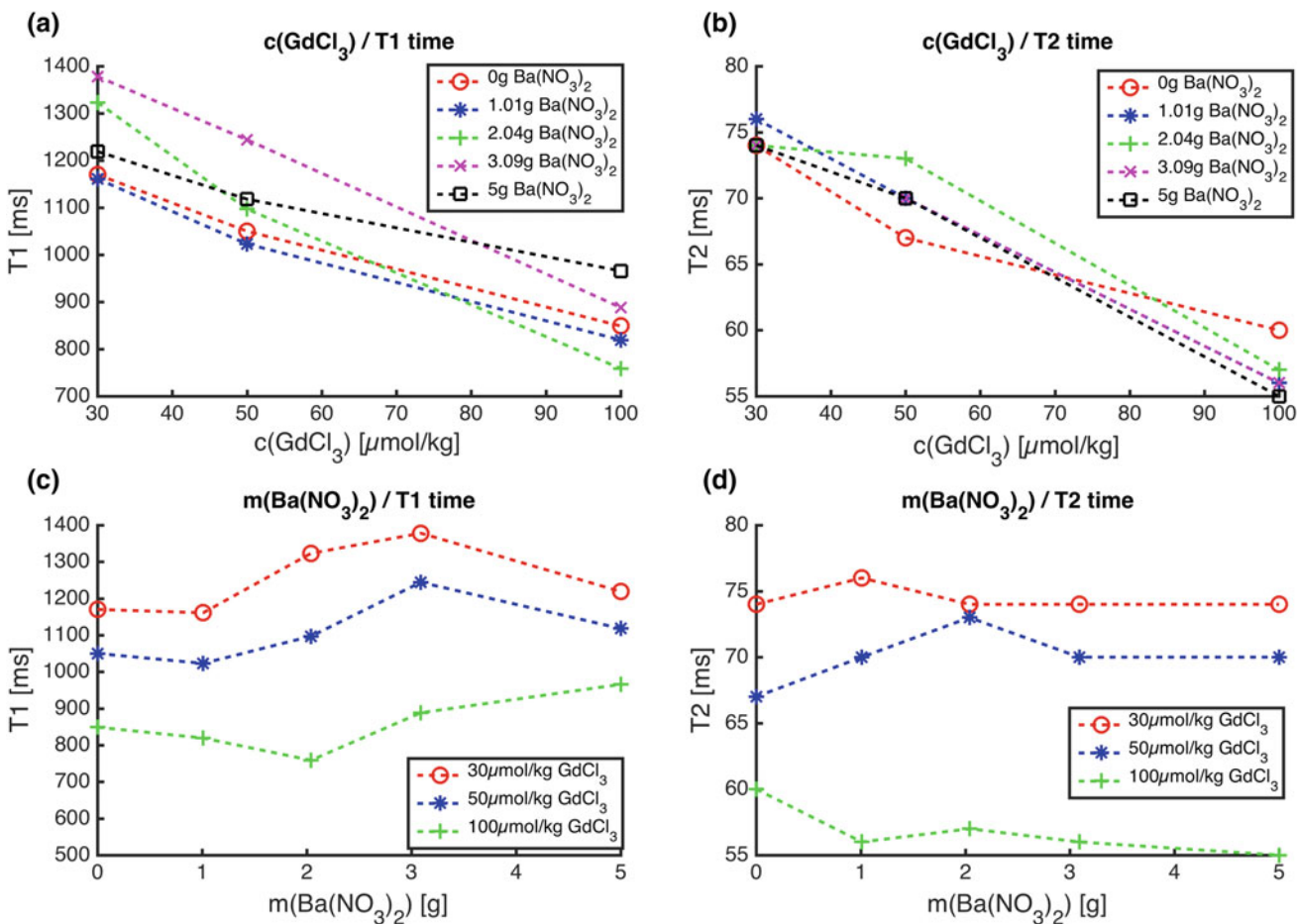


**Fig. 3** a  $T_1$  time as a function of the  $\text{GdCl}_3$  concentration (constant  $\text{Ba}(\text{NO}_3)_2$  concentrations). b  $T_2$  time as a function of the  $\text{GdCl}_3$  concentration (constant  $\text{Ba}(\text{NO}_3)_2$  concentrations). c  $T_1$  time as a function of the  $\text{Ba}(\text{NO}_3)_2$  concentration (constant  $\text{GdCl}_3$

concentrations). d  $T_2$  time as a function of the  $\text{Ba}(\text{NO}_3)_2$  concentration (constant  $\text{GdCl}_3$  concentrations). The data is represented for an overall constant agarose concentration of 0.8%

influence is shown in Fig. 3c for a constant  $\text{GdCl}_3$  concentration and Fig. 3d for a constant barium nitrate concentration. For barium nitrate a small to insignificant influence on the  $T_2$  time was measured. With an increase of the barium nitrate concentration at a constant concentration level of  $\text{GdCl}_3$  and agarose, the  $T_1$  time changes significantly, but the  $T_2$  time changes only slightly (Fig. 3c, d). Other additional modifiers, like copper and silicon dioxide influence both the transverse and the longitudinal relaxation time significantly (Fig. 2). The dependencies of the  $T_1$  and  $T_2$  times on the  $\text{Ba}(\text{NO}_3)_2$  and  $\text{GdCl}_3$  concentrations (at constant agarose concentration of 0.8%) are expressed by the following functional relationships, according to the  $\text{GdCl}_3$  and agarose dependency, analyzed by Yoshimura et al. [18].  $P_{T_1}(G, B)$  for the  $T_1$  time ( $x = 1$  for  $P_{T_x}(G, B)$ ) and  $P_{T_2}(G, B)$  for the  $T_2$  time ( $x = 2$  for  $P_{T_x}(G, B)$ ):

$$\begin{aligned}
 P_{T_x}(G, B) = & a_{(00, T_x)} + a_{(10, T_x)}B + a_{(01, T_x)}G + a_{(20, T_x)}B^2 \\
 & + a_{(11, T_x)}BG + a_{(02, T_x)}G^2 + a_{(30, T_x)}B^3 + a_{(21, T_x)}B^2G \\
 & + a_{(12, T_x)}BG^2 + a_{(40, T_x)}B^4 + a_{(31, T_x)}B^3G \\
 & + a_{(22, T_x)}B^2G^2.
 \end{aligned}
 \tag{3}$$

The variable  $B$  describes the barium nitrate quantity in g. The variable  $G$  is the  $\text{GdCl}_3$  concentration in  $\mu\text{mol}/\text{kg}$ . The polynomial coefficients  $a_{(mn, T_x)}$  of Eq. 3 are calculated for a 95% confidence interval using the MATLAB Curve Fitting Toolbox. For the  $T_1$ -fit a  $R^2$  value of 0.9876 ( $P_{T_1}(G, B)$ ) and for the  $T_2$ -fit a  $R^2$  of 0.9925 ( $P_{T_2}(G, B)$ ) was reached. The plotted regression polynomials are shown in Suppl. 3.

Figure 2 shows that the relaxation values of various test samples containing  $\text{Ba}(\text{NO}_3)_2$  are in the area of the relaxation times of human tissue. Tissue structures like gray and white matter, spleen, liver (lesion), kidney can be surrogated by the tested materials with maximum deviations in their  $T_1$  and  $T_2$  relaxation times  $<12\%$ . Liver tissue can be simulated with a deviation of 5% in the  $T_2$  time but with  $\sim 15\%$  deviation in the  $T_1$  time. An adaption of the  $\text{GdCl}_3$  and  $\text{Ba}(\text{NO}_3)_2$  concentration to reach the optimal relaxation times can be derived from Eq. 3.

### 3.3 X-Ray Absorption (HU-Measurements) and Attenuation in Nuclear Medicine

Material samples only consisting of the basic components provide HUs comparable to the HU values in biological tissue, e.g. lung, soft and muscle tissue, as well as brain matter. The maximum deviation in HU is  $\sim 10\%$  for brain matter. The deviation for the other tissues are smaller than 8%. Regarding the photo effect interaction, liver, kidney and bone tissue can be imitated using barium nitrate as an

additional modifier. The deviations are  $\sim 12\%$  for liver,  $\sim 10\%$  for kidney and  $\sim 9\%$  for bone tissue.

The following intensity values were measured with the SPECT system for samples containing different quantities of barium nitrate (0.8% agarose each): 67 (1.01 g  $\text{Ba}(\text{NO}_3)_2$ ), 193 (2.04 g  $\text{Ba}(\text{NO}_3)_2$ ), 271 (3.09 g  $\text{Ba}(\text{NO}_3)_2$ ), 405 (5.00 g  $\text{Ba}(\text{NO}_3)_2$ ). With increasing quantities of barium nitrate, the densities of the component mixtures and also the effective values ( $\rho_{\text{eff}} \cdot (Z^n/A)_{\text{eff}}$ ) raise. The analysis of the intensity values of the material samples, showed a good overall proportionality to the corresponding effective values of the materials (Table 1). Figure 1b visualizes this result qualitatively for two material samples with 2.04 g and 3.09 g  $\text{Ba}(\text{NO}_3)_2$ , respectively. The right sphere has a higher density than the left one. Consequently, the right sphere has a stronger attenuation of radiation and is represented darker in the image.

## 4 Discussion

This study analyzed different material combinations for a hybrid phantom. Material combinations were found to successfully mimic different tissue structures for three imaging modalities.

The investigated material samples utilizing only basic components or basic components with barium can be used to surrogate human tissue structures as gray and white matter, liver and kidney with a good overall agreement. White and gray brain matter can be surrogated by the basic component mixture of 100  $\mu\text{mol}/\text{kg}$   $\text{GdCl}_3/0.8\%$  agarose and 30  $\mu\text{mol}/\text{kg}$   $\text{GdCl}_3/0.8\%$  agarose, respectively. The difference in the  $\text{GdCl}_3$  quantity differentiates the relaxation properties, but does not influence the attenuation characteristics to ionizing radiation. Deviation in the HU-values between brain matter and the material sample are  $<10\%$ . Deviations in the relaxation times are  $<12\%$ .

Liver and kidney tissue can be simulated by adding 1.04 g barium nitrate to the basic component mixture. For both tissues, deviations in the HU-values  $\sim 10\text{--}12\%$  and the relaxation times can be simulated with an agreement  $>90\%$ . Only the  $T_1$  of liver tissue differs  $\sim 15\%$ . Equation 3 can be used to optimize the quantities of the components to reach even higher agreement in terms of the relaxation properties.

Gadolinium ions and agarose acted as a strong  $T_1$  and  $T_2$  modifiers, respectively. As the effect of each one on the other characteristic is insignificant they can be selectively tuned. This behavior of the modifiers is in accordance with former findings [18].

Adding additional modifiers, such as barium nitrate, leads to changes in the relaxation characteristics. As barium nitrate features less unpaired electrons, the  $T_1$  and  $T_2$  time are only



slightly affected, more so the  $T_1$  time than the  $T_2$  time. Nevertheless, the effect needs to be considered when fine tuning the properties. For other additional modifiers, similar behavior is assumed.

The found material combinations can also be used as phantoms in nuclear medicine. The attenuation properties of all combinations proposed to mimic different tissues, e.g. grey and white matter, liver, kidney, equal those of the actual tissues. Additionally, all, material compositions allow a homogeneous distribution of activity. Thus, even hot nodules can be simulated within a phantom in multimodal imaging.

As all material samples meet the physical requirements defined in the introduction tissue-equivalent surrogates for different organs can be constructed and combined in the desired fashion. Only drawback is composites including  $\text{SiO}_2$  and copper powder, which tend to form air bubbles, which hamper material homogeneity.

The analyses of relaxation times in high-field or ultra-high field MR remain an interesting object for future studies. Furthermore, an extension of possible applications for a hybrid phantom to other imaging modalities should be considered.

## 5 Conclusion

All in all, this study shows, that suitable material combinations are available to mimic human tissue for multi-modal imaging purposes. One phantom can be constructed and universally used for different imaging techniques.

**Acknowledgements** We gratefully thank the institute for radiology and nuclear medicine at the Paracelsus Private Medical University for providing their MR scanner for relaxometry measurements.

**Compliance with Ethical Standards** No humans or animals are involved in this study. The study was performed in compliance with ethical standards.

### Conflicts of Interest

The authors declare that they have no conflicts of interest.

## Electronic Supplementary Material

**Suppl. 1:** Figure of the material sample for MRI and CT measurements and spherical material sample for measurements in nuclear medicine.

University-Server URL:

[https://www.oth-aw.de/files/oth-aw/Personen/Stich/Suppl1\\_compressed.tif](https://www.oth-aw.de/files/oth-aw/Personen/Stich/Suppl1_compressed.tif)

**Suppl. 2:** Figure of the measured and fitted SIR and SSE signals for the basic component mixture with different modifiers.

University-Server URL:

[https://www.oth-aw.de/files/oth-aw/Personen/Stich/Suppl2\\_compressed.tif](https://www.oth-aw.de/files/oth-aw/Personen/Stich/Suppl2_compressed.tif)

**Suppl. 3:** Surface and contour plots of the regression polynomials  $P_{T_1}(G, B)$  for the  $T_1$  relaxation and  $P_{T_2}(G, B)$  for the  $T_2$  relaxation.

University-Server URL:

[https://www.oth-aw.de/files/oth-aw/Personen/Stich/Suppl3\\_compressed.tif](https://www.oth-aw.de/files/oth-aw/Personen/Stich/Suppl3_compressed.tif)

## References

1. R.-D. Vre, R. Grimee, F. Parmentier, J. Binet: The use of agar gel as a basic reference material for calibrating relaxation times and imaging parameters, *Magnetic Resonance in Medicine* 2, 176–179 (1985).
2. M. Buccioli, L. Ciraolo, B. Lehmann: Simulation of biologic tissues by using agar gels at magnetic resonance imaging, *Acta Radiologica* 30, 667–669 (1989).
3. M. D. Mitchell, H. L. Kundel, L. Axel, P. M. Joseph: Agarose as a tissue equivalent phantom material for nmr imaging, *Magnetic Resonance Imaging* 4, 263–266 (1986).
4. J. O. Christoffersson, L. Olsson, S. Sjoeborg: Nickel-doped agarose gel phantoms in mr imaging, *Acta radiologica* 32, 426–431 (1991).
5. F. Howe: Relaxation times in paramagnetically doped agarose gels as a function of temperature and ion concentration, *Magnetic resonance imaging* 6, 263–270 (1988).
6. K. A. Kraft, P. P. Fatouros, G. D. Clarke, P. R. S. Kishore: An mri phantom material for quantitative relaxometry, *Magnetic Resonance in Medicine* 5, 555–562 (1987).
7. W. Derbyshire, I. D. Duff: N.m.r. of agarose gels, *Faraday Discuss. Chem. Soc.* 57, 243–254 (1974).
8. I. Duff, W. Derbyshire: Nmr of frozen agarose gels, *Journal of Magnetic Resonance* (1969) 17, 89–94 (1975).
9. I. Mano, H. Goshima, M. Nambu, M. Iio: New polyvinyl alcohol gel material for mri phantoms, *Magnetic Resonance in Medicine* 3, 921–926 (1986).
10. K. C. Chu, B. K. Rutt: Polyvinyl alcohol cryogel: an ideal phantom material for mr studies of arterial flow and elasticity, *Magnetic Resonance in Medicine* 37, 314–319 (1997).
11. M. W. Groch, J. A. Urbon, W. D. Erwin, S. Al-Dooan: An mri tissue equivalent lesion phantom using a novel polysaccharide material, *Magnetic Resonance Imaging* 9, 417–421 (1991).
12. G. P. Mazzara, R. W. Briggs, Z. Wu, B. G. Steinbach: Use of a modified polysaccharide gel in developing a realistic breast phantom for mri, *Magnetic resonance imaging* 14, 639–648 (1996).
13. E. L. Madsen, G. D. Fullerton: Second annual meeting of the society for magnetic resonance imaging prospective tissue-mimicking

- materials for use in nmr imaging phantoms, *Magnetic Resonance Imaging* 1, 135–141 (1982).
14. J. Blechinger, E. Madsen, G. Frank: Tissue-mimicking gelatin-agar gels for use in magnetic resonance imaging phantoms, *Medical physics* 15, 629–636 (1988).
  15. F. De Luca, B. Maraviglia, A. Mercurio: Biological tissue simulation and standard testing material for mri, *Magnetic Resonance in Medicine* 4, 189–192 (1987).
  16. S. Ohno, H. Kato, H., T. Harimoto, Y. Ikemoto, K. Yoshitomi, S. Kadohisa, M. Kuroda, S. Kanazawa: Production of a human-tissue-equivalent MRI phantom: optimization of material heating, *Magnetic Resonance in Medical Sciences* 7, 131–140 (2008).
  17. A. Hellerbach, V. Schuster, A. Jansen, J. Sommer: Mri phantoms? Are there alternatives to agar?, *PLoS ONE* 8, 1–8 (2013).
  18. K. Yoshimura, H. Kato, M. Kuroda, A. Yoshida, K. Hanamoto, A. Tanaka, M. Tsunoda, S. Kanazawa, K. Shibuya, S. Kawasaki, Y. Hiraki: Development of a tissue-equivalent MRI phantom using carrageenan gel, *Magnetic Resonance in Medicine* 50, 1011–1017 (2003).
  19. H. Krieger: *Strahlungsmessung und Dosimetrie*. 2<sup>nd</sup> edn, Springer Spektrum (2013).
  20. S. J. Graham, G. J. Stanisz, A. Kecojevic, M. J. Bronskill, R. M. Henkelman: Analysis of changes in MR properties of tissues after heat treatment. *Magn. Reson. Med.* 42: 1061–1071 (1999).
  21. A. Cieszanowski, W. Szeszkowski, M. Golebiowski, D. K. Bielecki, M. Grodzicki, B. Pruszyński. *Eur Radiol* 12, 2273 (2012).
  22. T. Aherne, D. Tscholakoff, W. Finkbeiner, U. Sechtem, N. Derugin, E. Yee, C. B. Higgins: Magnetic resonance imaging of cardiac transplants: the evaluation of rejection of cardiac allografts with and without immunosuppression. *Circulation*. 74, 145–156 (1986).
  23. G. J. Stanisz, E. E. Odrobina, J. Pun, M. Escaravage, S. J. Graham, M. J. Bronskill, R. M. Henkelman: T1, T2 relaxation and magnetization transfer in tissue at 3T. *Magn. Reson. Med.*, 54: 507–512 (2005).
  24. S. C. Deoni, B. K. Rutt, T. M. Peters: Rapid combined t1 and t2 mapping using gradient recalled acquisition in the steady state, *Magnetic Resonance in Medicine* 49, 515–526 (2003).
  25. G. J. Stanisz, E. E. Odrobina, J. Pun, M. Escaravage, S. J. Graham, M. J. Bronskill, R. M. Henkelman: T1, T2 relaxation and magnetization transfer in tissue at 3T, *Magnetic Resonance in Medicine* 54, 507–512 (2005).
  26. C. M. J. de Bazelaire, G. D. Duhamel, N. M. Rofsky, D. C. Alsop: Mr imaging relaxation times of abdominal and pelvic tissues measured in vivo at 3.0 T: Preliminary results, *Radiology* 230, 652–659 (2004).
  27. M. A. Goldberg, P. F. Hahn, S. Saini, M. Cohen, P. Reimer, T. Brady, P. Mueller: Value of t1 and t2 relaxation times from echoplanar mr imaging in the characterization of focal hepatic lesions., *AJR. American journal of roentgenology* 160, 1011–1017 (1993).
  28. M. Barth, E. Moser: Proton nmr relaxation times of human blood samples at 1.5 t and implications for functional mri, *Cellular and molecular biology* 43, 783–791 (1997).

# Basic Study of the Imaging Conditions on Tumor Volume Measurement Using 3D-MR Imaging of the Liver While Patient Holds Breath

Shinichi Arao, Akihiko Tabuchi, Yasuhiko Okura, Hajime Harauchi, Atsushi Ono, Tatsuhiro Gotanda, Rumi Gotanda, and Akiko Hayashi

## Abstract

Tumor volumetric measurement using liver 3D-MR imaging tends to cause measurement errors because the liver moves with the diaphragm during imaging while the patient is holding the breath. The breath holding method of the patient when 3D-MR imaging for measurement of tumor volume was performed was discussed using a movable simulated tumor phantom. Furthermore, optimal imaging conditions (breath holding method, slice section, voxel setting and phase encoding direction) with the least influence by body motion were studied. Based on three breath holding methods, the simulated phantom was moved in the direction of the foot-head along the line of the MRI receiver coil. The image sequence was a 3D-T1 weighted fast field echo method. The imaging time was fixed at 20 s. As a result, the breath holding method with the smallest measured volume error is functional residual capacity (FRC) breath hold (0.1 mm/s). The optimum imaging condition is when the imaging section is set in the axial direction and the phase encoding direction is perpendicular to the moving direction with an iso voxel as small as possible. In the case where it is necessary to set the phase encoding in the direction parallel to the proceeding direction, imaging with the setting of rectangular voxel can suppress the measurement error of the volume. In order to measure accurate volume using liver 3D-MR imaging, it is necessary to know the direction of movement of the tumor during respiration and to set

appropriate breath holding method, section, phase encoding direction and voxel size.

## Keywords

MR-imaging • Breath hold • Tumor volume

## 1 Introduction

The stages of hepatocellular carcinoma (HCC) are classified in accordance with the cancer dimension, the number of cancer sites and whether the cancer cells remain in the liver. Also, in order to evaluate the treatment effectiveness, it is important to understand more accurately the time course of tumor volume [1]. There have been many reports so far that impacts due to body movement can be suppressed by immobilizing the patient, respiratory gated imaging, and imaging during breath holding [2–4]. In MRI imaging of the liver for measurement of tumor volume, fast 3D-MR imaging is conducted while the patient holds their breath, to prevent image quality from lowering due to influences of body movement. Still, even during breath holding, the liver moves slightly with the diaphragm in a vertical direction (foot-head direction). The speed of the movement of the liver during breath holding differs from the method used. It is reported that it is about 0.5 mm/s when stopped at maximum inspiration (MI breath hold), about 0.2 mm/s when stopped at maximum exhalation (ME breath hold), and about 0.1 mm/s when stopped at rest breathing (functional residual capacity phase: FRC breath hold) [5, 6]. The speed of movement caused by the breath holding method is likely to affect the measured tumor volume, but there are few reports on the effect of each method and method to reduce the effect. This study demonstrated the effects on the measurement of tumor volume due to changes in the speed of movement generated by differences in the breath holding methods during 3D-MR imaging, using self-produced phantoms. Then, the optimum imaging conditions (slice cross-section,

S. Arao (✉) · A. Tabuchi · A. Hayashi  
Kawasaki College of Allied Health Professions, Kurashiki,  
Okayama, Japan  
e-mail: arao@jc.kawasaki-m.ac.jp

H. Harauchi · A. Ono · T. Gotanda · R. Gotanda  
Kawasaki University of Medical Welfare, Kurashiki, Okayama,  
Japan

Y. Okura  
Hiroshima International University, Higashihiroshima, Hiroshima,  
Japan

voxel setting and phase encode direction setting) that resulted in the least impact due to body movement were discussed.

## 2 Materials and Methods

The simulated tumor phantom was made using an acrylic spherical container (one side of the lumen was 28 mm and volume was  $11,494 \text{ mm}^3$ ), which were filled with gadopentetate dimeglumine (Gd-DTPA) contrast agent dilute by 2 m mol/l with distilled water. To obtain a sufficient Signal to Noise Ratio (SNR), the simulated tumors were attached to a  $90 \text{ mm} \times 130 \text{ mm} \times 105 \text{ mm}$  poly vinyl chloride (PVC) container filled with poly vinyl alcohol (PVA). On the assumption of diaphragm movement speeds under each breath holding method, the phantoms were made to move along the line in the MRI receiver coil toward the foot-head direction at 0.5, 0.2 and 0.1 mm/s. Phantom movement was performed by connecting to the stage table of microdensitometer PDS-15 (manufactured by Konica Minolta Holdings). The simulated tumor phantom was towed toward the F-H direction. Figure 1 shows the location of the microdensitometer and movable seat.

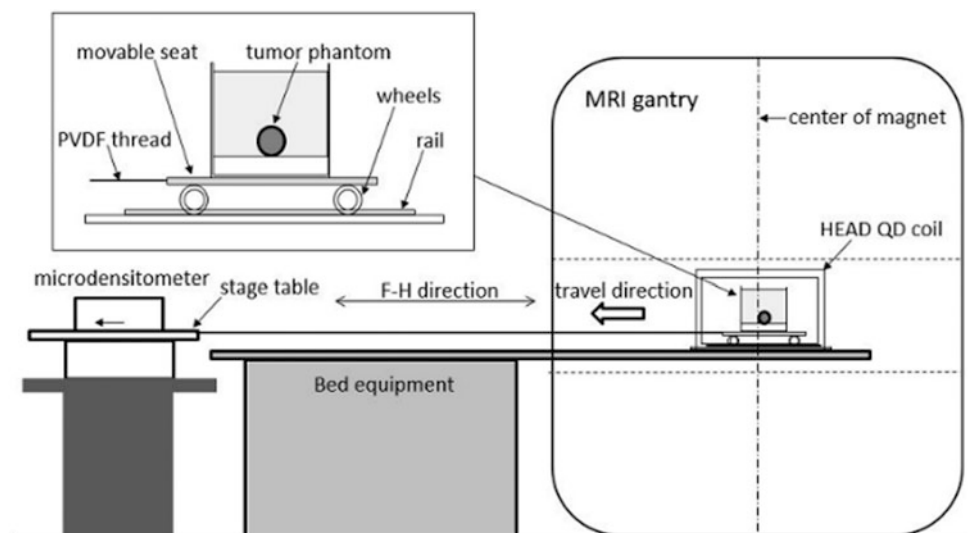
All examinations were performed using a Philips Intera Achieva 1.5-Tesla MR scanner (Intera Achieva 1.5T Philips, Netherlands). The imaging coil of the MRI used HEAD quadrature coil (HEAD QD coil). The image sequence, 3D-T1 weighted fast field echo method (3D-T1 FFE) was used. The voxel is an isovoxel, and it is set to 1.0 and 1.2 mm respectively considering the size of the simulated tumor and the imaging time. The repetition time (TR), effective echo time (TE<sub>eff</sub>), flip angle (FA) and number of excitation (NEX) were set so that the imaging time would be 20 s for all voxel conditions for the simulation of imaging

during breath holding. Imaging parameters for 1.0 mm iso voxel were: TR 4.6 ms, TE<sub>eff</sub> 2.28 ms, FA  $10^\circ$ , NEX 1 and 1.2 mm iso voxel were: TR 4.38 ms, TE<sub>eff</sub> 2.15 ms. The imaging cross-section were set to the cross-section (sagittal cross-section) parallel to the movement direction and the cross-section (axial cross-section) vertical to the movement direction. The phase encode directions in the sagittal cross-section was set to the direction parallel to the travel direction (foot-head (F-H)), and this in the axial cross-section was set to the direction vertical to the travel direction (right-left (R-L)). Figure 2 shows the relationship between the travel directions and imaging cross-sections and phase encode directions. In consideration of the amount of movement of the voxel, it was confirmed how much the volume measurement value fluctuation can be suppressed by changing the voxel to a rectangular voxel enlarged twice in the phase direction. The images were reconfigured into 3D images using the workstation (Virtual Place Raijin Plus AZE, Japan) and the volume of the simulated tumors were measured. The threshold value for creating the 3D images for volume measurement used the setting value so that the measured volume of simulated tumor would be the true value ( $11,494 \text{ mm}^3$ ) in the 3D image taken while the tumor remained still.

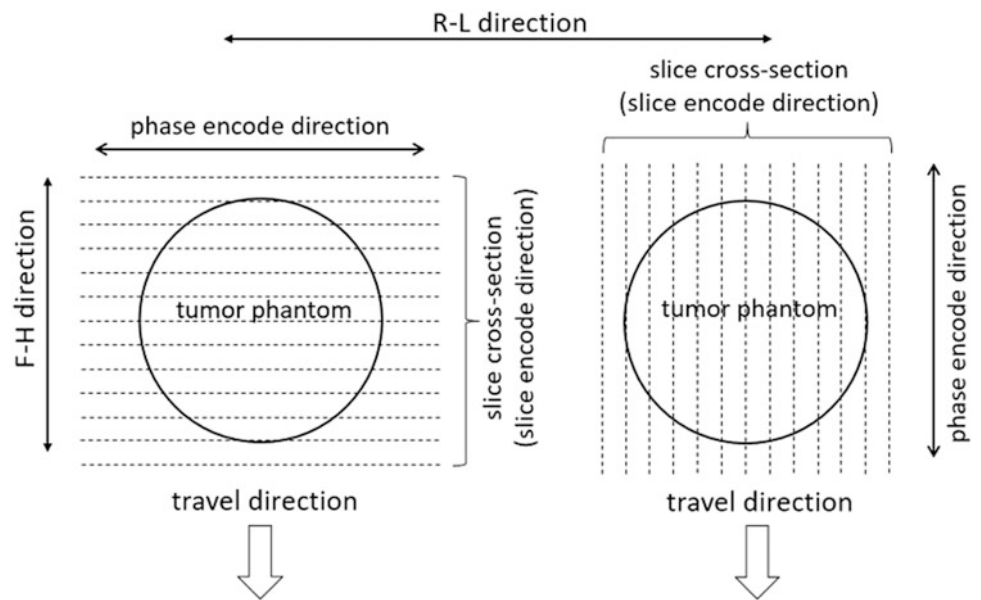
## 3 Results

Figure 3a shows an example of an image of a reconstructed simulated tumor in a stopped state and a traveled state. Figure 3b is a graph of the reduction rate of the simulated tumor volume when imaging is performed while moving the tumor with the image section set to the axial section with the iso voxel and the phase encoding direction set to R-L. At the moving speed of 0.1 and 0.2 mm/s, the

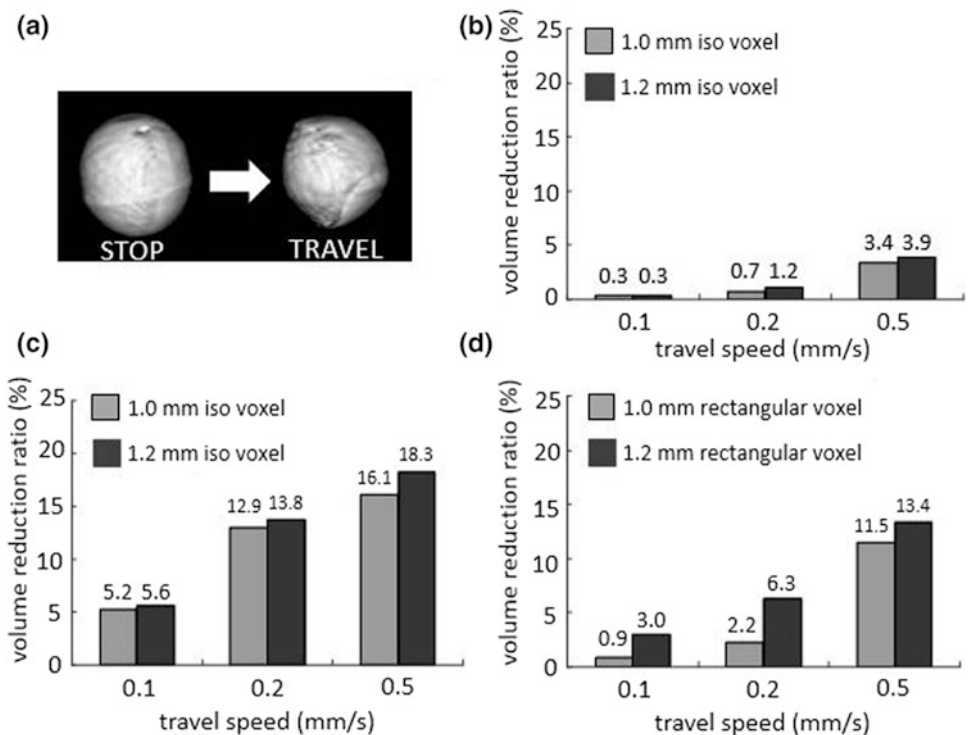
**Fig. 1** Outline of the movable seat and connection with the microdensitometer. The container is moved toward the direction indicated by the arrow along the line during imaging



**Fig. 2** The relationship between the travel direction and imaging cross-section and phase encode direction. Once the slice cross-section is determined, the phase encode direction is set to the direction parallel to the slice cross-section



**Fig. 3** The simulated tumor volume reduction ratio when images were taken during a travel. **a** 3D image of the simulated tumor. **b** Phase encode direction was set to R-L direction in the iso voxel. **c** Phase encode direction was set to F-H direction in the iso voxel. **d** Phase encode direction was set to F-H direction in the rectangular voxel



reduction ratio was 0.3–1.2%, but the reduction ratio was 3.4–3.9% at 0.5 mm/s. Figure 3c shows a graph of the reduction ratio of the simulated tumor volume when the imaging cross section is an iso voxel with a sagittal section and the phase encode direction is set in the F-H direction. The reduction ratio was higher than in the case where the imaging section was made axial and the phase encoding direction was set in the R-L direction. At the moving speed of 0.1 mm/s, the reduction ratio was 5.2–5.6%, but the

reduction ratio was 12.9–18.3% at 0.2 and 0.5 mm/s. Figure 3d shows the graph of the reduction ratio of the simulated tumor volume taken by setting the imaging cross-section to sagittal cross-section and phase encode to F-H directions in rectangular voxel where the voxel was expanded twice toward the phase direction. The reduction ratio was more suppressed compared to when the iso voxel was set. In all combinations, the reduction ratio when a large voxel size is increased.



## 4 Discussion

Under all conditions used for the verification, the larger the voxel size, the higher the volume reduction ratio was. This reflects that blurred areas due to movement became larger from the effect of partial volume effects, and the area was cut largely at the threshold value when it was converted into 3D images. The cut area was larger as the travel speed was faster, and the travel distance during imaging was longer. This is because the number of voxels, including blurred areas, increases due to a travel with the travel speed, and voxels which have signal strengths exceeding the threshold value would dramatically decrease. It becomes impossible that is, for slice encoding to catch up with movement speed. Hence, FRC breath hold (travel speed is about 0.1 mm/s) is the method with the least impact due to diaphragm movement as in the study by Tabuchi et al. [7, 8]. This study verified that breath holding at the rest expiratory level was the most suitable for an accurate volume measurement with improvement in image quality. Considering the short imaging time during breath holding, as the field of view (FOV) of the set voxel size is limited, there is a limit on reducing the dimension of the imaging target depending on the dimension of the imaging target, however, it is necessary to set as it small as possible within an allowable range. For setting the phase encode direction, the reduction ratio became higher when the slice cross-section was parallel to the travel direction, and the travel direction and the phase encode direction agreed. Under the setting, in addition to the impact due to the partial volume effects, a travel of an energized proton toward the phase encode direction causes a misregistration (intra-voxel dephasing) due to discrepant phase information. This results in large blurred areas and the number of voxels which are under the threshold value, causing a higher reduction ratio. In order to lower the reduction ratios under the imaging conditions, the phase encode direction should be set to the travel direction, and the rectangular voxel, which is expanded toward the travel direction should be applied. In the rectangular voxel, the energized proton is very likely to remain in one voxel even when the tumor travels during imaging, discrepant information on the phase tends not to occur and misregistration (intra-voxel dephasing) has a smaller impact, resulting in suppression of the volume reduction ratio. In the spherical tumor where the curved surface moves, as the number of voxels which contains the blurred area due to movement relatively decreases, the reduction ratio appeared to become lower. This study advanced the basic discussion on accurate volume evaluation on a moving object. The wall of the simulated tumor is made of acrylic, since no signal has

become an error factor for this measurement result. In this regard, improvement of the phantom will be necessary. As differences in the simulated tumor size and signal strength may affect the volume evaluation of the moving object, further validation is necessary.

## 5 Conclusion

In the MRI, imaging slice cross-sections can be set in accordance to the shapes and sizes of the imaging target and purposes of the examinations. The optimal imaging conditions for accurate tumor volume measurement of the 3D images created from 3D-MR imaging taken during breath holding are when the patient holds their breath at the rest expiratory level (FRC breath hold), and the slice cross-section and phase encode direction are set to the direction perpendicular to the movement direction, and images are taken in iso voxel as small as possible in that brief amount of time. When images are taken by setting the slice cross-section to the same direction as the movement direction, it is preferable to set the phase encode to the direction perpendicular to the movement direction. When it is necessary to set the slice cross-section to the same direction of the movement direction and to set the phase encode direction to the same direction of the movement direction depending on imaging targets, volume reduction due to movement can be suppressed by using the rectangular voxel which is expanded toward the travel direction, instead of expanding the voxel slice cross-section in iso voxel.

## References

1. Patrick T., Susan G.A., Elizabeth A.E., Jantien W., Richard S.K., Larry R., Jaap V., Martine V.G., Allan T.O., Michaele C.C., Steve G.G.: New Guidelines to Evaluate the Response to Treatment in Solid Tumors. *Journal of the National Cancer Institute* 92(3), 205–216 (2000).
2. Gaa J., Hatabu H., Jenkins R.L., Finn J.P., Edelman R.R.: Liver masses: replacement of conventional T2-weighted spin-echo MR imaging. *Radiology* 200(2), 459–464 (1996).
3. Rofsky N.M., Lee V.S., Laub G., Pollack M.A., Krinsky G.A., Thomasson D., Ambrosino M.M., Weinreb J.C.: Abdominal MR imaging with a volumetric interpolated breath-hold examination. *Radiology* 212(3), 876–884 (1999).
4. Augui J., Vignaux O., Argaud C., Coste J., Gouya H., Legmann P.: Liver: T2-weighted MR imaging with breath-hold fast-recovery optimized fast spin-echo compared with breath-hold half-Fourier and non-breath-hold respiratory triggered fast spin-echo pulse sequences. *Radiology* 223(3), 853–859 (2002).
5. Braun H.A., Cheney F.W., Loehnen C.P.: *Introduction to respiratory physiology*. 2nd ed. Little Brown and Company. Boston (1980).

6. Holland H.A., Goldfarb J.W., Edelman R.R.: Diaphragm and cardiac motion during suspended breathing: preliminary experience and implications for breath-hold MR imaging. *Radiology* 209(2), 483–489 (1998).
7. Tabuchi A., Katsuda T., Eguchi M., Gotanda T., Gotanda R., Mitani M., Takeda Y.: Functional residual capacity breath hold for subtraction image of dynamic liver MRI. *European Journal of Radiology* 71(3), 506–512 (2009).
8. Tabuchi A., Katsuda T., Gotanda R., Gotanda T., Mitani M., Takeda Y.: High resolution T2 weighted liver MR imaging using functional residual capacity breath-hold. *European Journal of Radiology* 72(2), 300–305 (2009).

# Evaluation of Spatial Resolution of MRI, Optical CT and X-Ray CT Using MTF for Gel Dosimeter

Takaoki Takanashi and Hiraku Kawamura

## Abstract

We have proposed a new gelatin phantom for evaluating the spatial resolution of Optical Computed Tomography (OCT), MRI and X-ray CT (X-CT) as a gel dosimeter readout device. In addition, MTF evaluation was conducted using the proposed gelatin phantom. Consequently, 0.19 (MRI), 1.07 (X-CT), 0.88 (0-D OCT), and 0.89 (2-D OCT) were obtained as a results of modulation transfer factor at 0.3 spatial frequency (cycle/mm).

## Keywords

Gel dosimeter • Optical CT • MTF

## 1 Introduction

Gel dosimetry uses a chemical dosimeter used for 3-D dosimetry [1, 2]. As gel dosimeters are mainly composed of water, they closely resemble human body tissue and are expected to have clinical applications in future radiation therapy. Before irradiation, it becomes possible to know the three dimensional dose distribution based on the radiotherapy plan. Currently, the development of gel dosimeters is underway for quality assurance in radiotherapy [3]. The dose evaluation method using MRI has been used to read irradiated information from the gel dosimeter in conventional research [4, 5]. Recently, gel dosimetry has been explored

with dye gels and radiochromic dosimeters. Radiochromic dosimeters, such as PRESAGE® [6], cannot be read by MRI because of their solid state. Therefore, we actively constructed Optical Computed Tomography (OCT) apparatuses. It is necessary to quantitatively compare and evaluate the results obtained using MRI with those obtained using OCT. A phantom is used to evaluate the MTF of the reading device, however, there is no phantom that can simultaneously evaluate all these devices. For example, the phantom of the needle for evaluating OCT [4, 7] cannot be scanned by MRI owing to the metallic artifacts. We created an original gelatin phantom to evaluate the spatial resolution of MRI, OCT, and X-ray CT(X-CT) using MTF. The phantom, not gel dosimeter, consists of a few air spaces, 0.3 mm in diameter, placed in spiral patterns to scan MRI, OCT, and X-CT. We obtained the MTF of each device from the slice image of the phantom imaged by each device.

## 2 Materials and Methods

### 2.1 Gelatin Phantom

A gelatin phantom was prepared using 94.7% w/w water and 5.3% gelatin (300 bloom). Water was heated to 40C, mixed with gelatin and heated to 50C on a hot plate/magnetic stirrer. After the solution became clear, it was cooled to 45C, and dispensed into a 75.5 mm diameter polyethyleneterephthalate (PET) jar. Next, 0.3-mm-diameter needles were inserted into the solution in a way that ensured that the needles did not overlap in the projected image from the radial direction (Fig. 1:left). Once the gelatin solidified after cooling, the needles were removed (Fig. 1:right).

### 2.2 Measurement

Measurement of this phantom by MRI, X-CT, and two in-house optical CT (0-D and 2-D OCT) was conducted

T. Takanashi · H. Kawamura (✉)  
3D Gel Dosimeter Research Laboratory, Innovation Center,  
RIKEN, 2-1, Hirosawa, Wako, Saitama, 351-0198, Japan  
e-mail: hiraku.kawamura@riken.jp;  
lhmspectroscopy@gmail.com

T. Takanashi  
e-mail: takaoki.takanashi@riken.jp

H. Kawamura  
Department of Radiological Sciences, Ibaraki Prefectural  
University of Health Sciences, 4669-2, Ami, Ami-Machi,  
Inashiki-Gun, Ibaraki 300-0394, Japan



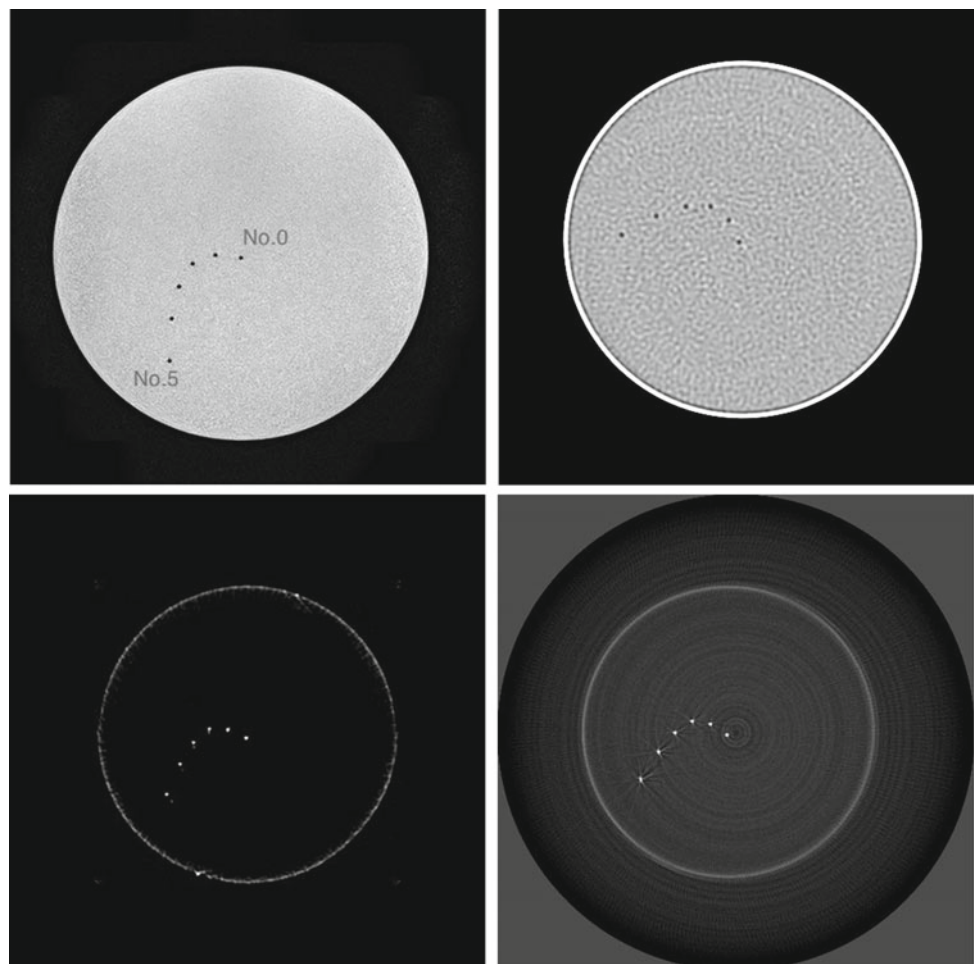


**Fig. 1** Needles with a diameter of 0.3 mm, arranged in a projected image not to overlap from the radial direction: left. (This is a prototype, and the number of needles is different from the one used for measurement.) Phantom that removed needle after gelatin solidified: right

(Fig. 2). The MRI using a 1.5 T MRI scanner (EXCELART Vantage, Toshiba Medical Systems, Tochigi, Japan). The MRI images acquired a field echo (FE) sequence under the following conditions: echo time was 15 ms, repetition time was 600 ms, flip angle was 25, number of images averaged was 10, slice thickness was 0.75 mm, field of view (FOV) was 94 mm  $\times$  94 mm, and matrix number was

400  $\times$  400 (pixel resolution was 0.235 mm  $\times$  0.235 mm). The CT images using 8 Data Acquisition System (ECLOS 8 DAS (Hitachi Medical Corporation, Tokyo, Japan)) were acquired under the following conditions: tube voltage was 120 kV, tube current was 175 mA, exposure time was 2 s, slice thickness was 0.75 mm, FOV was 100 mm  $\times$  100 mm, and matrix number was 512  $\times$  512 (pixel resolution

**Fig. 2** MRI image: upper left, X-CT image: upper right, OD-OCT image: lower left, and 2D-OCT image: lower right. Size and contrast are also adjusted for each images



was  $0.19 \text{ mm} \times 0.19 \text{ mm}$ ). The images were reconstructed with filtered back-projection (FBP). The selected reconstruction kernel of the CT was standard soft tissue.

The two original OCT apparatuses for gel dosimetry were constructed by us [8]. The first OCT system, called 0 dimensional (0D-OCT), which is categorized as a first-generation system, comprised of a single He-Ne laser, photodiode, and mechanical stages for moving and turning the sample as a gel dosimeter. For each scan, a set of  $360$  light intensity projections was acquired over  $2\pi$  for the reconstructed plane from the turned sample. In this system, the reconstructed image was acquired using the Mathematica software and the FBP method from the acquired raw data.

The reconstructed filter was Hann filter. The second OCT system is a 2D-OCT scanner that utilizes a light panel and a camera detector for a 2D acquisition. Projection data points amounting to  $317$  per  $2\pi$  for the reconstructed plane are acquired from the turned sample. The reconstructed image was acquired using the ImageJ software and the original FBP reconstructed program from the acquired raw data. The reconstructed filter was Shepp-Logan filter.

To evaluate the MTF, an analysis method of measuring MTF using a thin wire images from the CT and MRI was

used [9–11]. An point spread function (PSF) was obtained from the profiles of the images of thin air holes in the gelatin phantom. The PSF was smoothed and Fourier-transformed to obtain MTF curves.

### 3 Results and Discussion

MTF was evaluated for each of the six points (No.0 to No.5) of the gelatin phantom. In each modality, the MTF obtained for each point is shown in Fig. 3. In general, it is thought that an increase depends on the distance from the center; because the near center part reconstructed image have a higher Nyquist frequency than outer part. This tendency was particularly evident in 2-D OCT (Fig. 3: lower right), which affected by the depth of field. The significant increases in MTF can be confirmed in MRI No. 5 and No. 0, No. 3 of X-CT, which is thought to be the influence of the reconstruction kernel based on the high resolution function. Such an increase generates a signal distribution exceeding the original contrast owing to the use of a high resolution function in the original image, and causes obvious under-shoot and overshoot in the peripheral portion of the tissue.

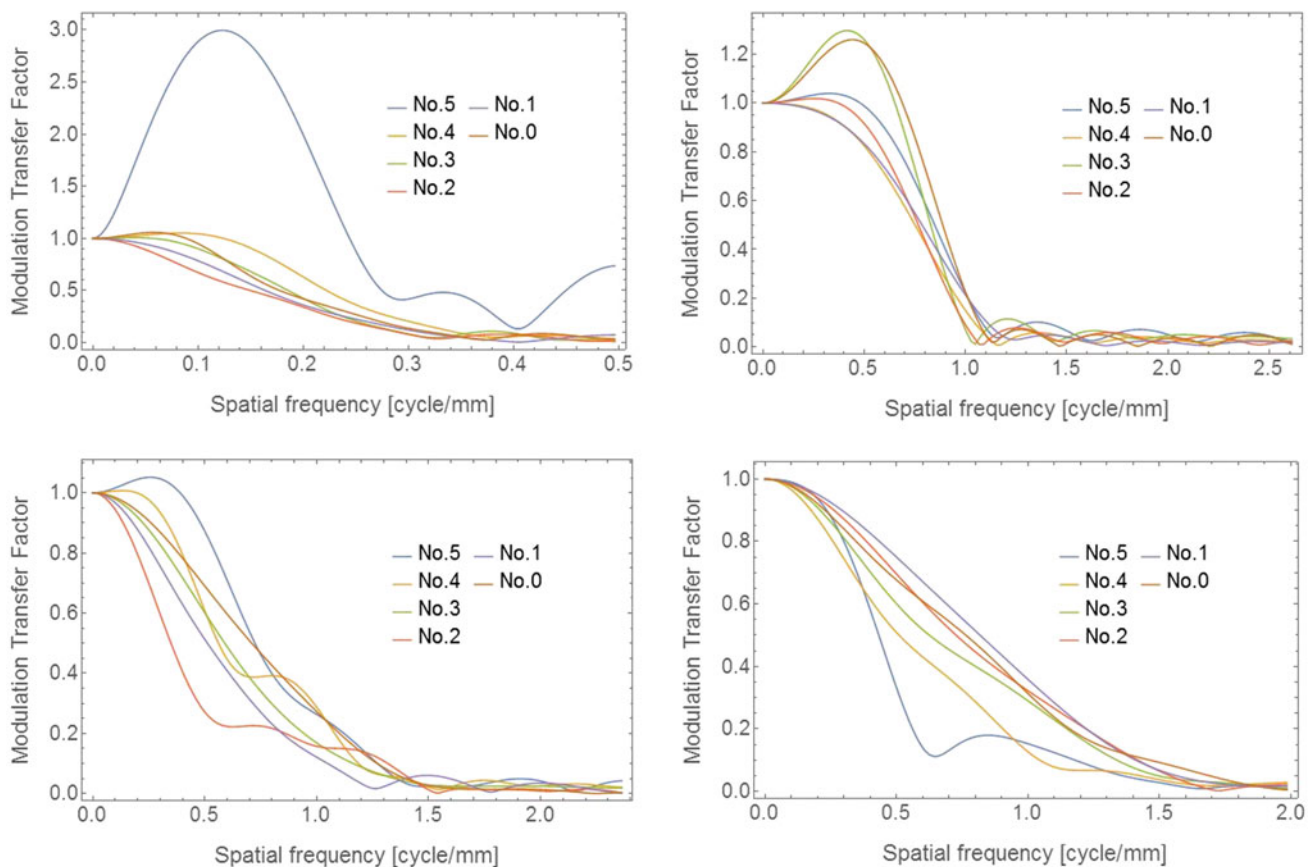


**Fig. 3** MTF curves for different distance from center. MRI: upper left, X-CT: upper right, 0D-OCT: lower left, and 2D-OCT: lower right

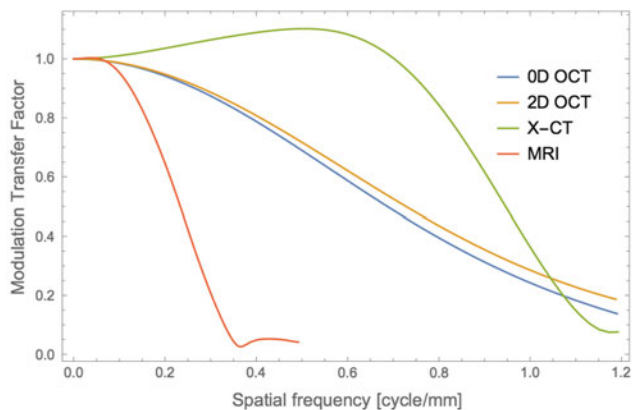


**Fig. 4** A comparison of each modalities of the MTF obtained from the point No. 0

On the other hand, the behaviour of the MTF of 2-D OCT shows that the resolution decreases as the distance from the centre increases, which can be explained, for optical reasons, as being caused by the difference in the matching of the refractive indices between the matching liquid and the gelatin.

A comparison of each of the modalities of the MTF obtained from the point (No. 0) close to the center is shown in Fig. 4. Consequently, 0.19 (MRI), 1.07 (X-CT), 0.88 (0-D OCT), and 0.89 (2-D OCT) were the obtained result of modulation transfer factor at 0.3 spatial frequency (cycle/mm). As expected, the spatial resolution of MRI was confirmed to be lower than that of other devices. Although this result is predictable, it is necessary to quantitatively compare the spatial resolution of each of the devices of MRI, X-CT, and OCT, using the new gelatin phantom. It is possible to simplify the evaluation of MTF.

## References

- Baldock C., De Deene Y., Doran S., Ibbott G., Jirasek A., Lepage M., McAuley KB., Oldham M., Schreiner LJ.: Polymer gel dosimetry. *Phys Med Biol.* 55(5):R1-63 (2010). <https://doi.org/10.1088/0031-9155/55/5/r01>. Epub 2010 Feb 11.
- Vandecasteele J., De Deene Y.: Evaluation of radiochromic gel dosimetry and polymer gel dosimetry in a clinical dose verification. *Phys Med Biol.* 58(18):6241-62 (2013). <https://doi.org/10.1088/0031-9155/58/18/6241>. Epub 2013 Aug 22.
- Watanabe Y., Nakaguchi Y.: 3D evaluation of 3DVH program using BANG3 polymer gel dosimeter. *Med Phys.* 40(8):082101 (2013).
- Maryanski MJ., Schulz RJ., Ibbott GS., Gatenby JC., Xie J., Horton D., Gore JC.: Magnetic resonance imaging of radiation dose distributions using a polymer-gel dosimeter. *Phys Med Biol.* 39(9):1437-55 (1994).
- Maryanski MJ., Gore JC., Kennan RP., Schulz RJ.: NMR relaxation enhancement in gels polymerized and cross-linked by ionizing radiation: a new approach to 3D dosimetry by MRI. *Magn Reson Imaging.* 11:253-258 (1993).
- P. Y. Guo, J. A. Adamovics, M. Oldham: Characterization of a new radiochromic three-dimensional dosimeter. *Med Phys.* 33(5): 1338-1345 (2006).
- Oldham M., Kim L.: Optical-CT gel-dosimetry. II: Optical artifacts and geometrical distortion. *Med Phys.* 31(5):1093-1104 (2004).
- Kawamura H., Takanashi T., Shimada Y., Sato Y., Abe S., Hara S.: Optical computed tomography for polymer gel dosimetry. *Igaku Butsuri.* 37(2): 111-116 (2017).
- Ichikawa K., Muramatsu Y. Hyoujun X Sen CT Gazou Keisoku, Ohmsha Japan (2009).
- Nickoloff EL: Measurement of the PSF for a CT scanner: appropriate wire diameter and pixel size. *Phys Med Biol.* 33(1): 149-155 (1988).
- Shashadhar M. Mohapatra, Jeff D. Turley, John R. Prince, Joseph C. Blechinger, and Don A Wilson: Transfer function measurement and analysis for a magnetic resonance imager. *Med Phys.* 18: 1114 (1991). <https://doi.org/10.1118/1.596622>.

# Local Affine Transformation Method for Tomosynthesis

O. Morgun, K. Nemchenko, and A. Vaisburd

## Abstract

In this report, a new method for image reconstruction for tomosynthesis is proposed. This technique consists in using local affine transformations and preliminary geometric calibration. The suggested approach makes it possible not to consider the geometry of the instrument and possible inaccuracies in determining the parameters of the investigation. As a result, this method allows achieving a higher tomography resolution. A comparison was made with the methods that are currently used in tomosynthesis. Experiments based on the results of real mammography researches were conducted.

## Keywords

Tomosynthesis • Mammography • Resolution  
Microcalcification

## 1 Introduction

Numerous studies of tomosynthesis techniques [1, 2] (comparing the diagnostic properties of standard flat 2D digital mammography with volumetric 3D digital breast tomosynthesis in phantoms and in clinical practice) showed that tomosynthesis has a significant advantage in detecting tumors (oncogenes), but significantly weaker than 2D mammography in microcalcification detection [3]. This contradiction is noticeable even more with a tomosynthesis angle increase.

Detailed studies have indicated inconsistent trends in tomosynthesis [4]—with a tomosynthesis angle increase, the detectability of tumors increases, and the microcalcification decreases in the same time [5]. The tendency of tumor identification growth with an increase of the angle is

explained by the tomosynthesis structure noise decrease at higher tomography resolution (i.e., the spatial resolution by the depth breast), since in each layer (breast is represented as a number of layers) is less than glandular tissue structure, and hence glandular tissue will not obscure the tumor, won't mimic for them [6]. In addition, an increase in the tomosynthesis angle makes it possible to reduce the contrast of artifacts, thereby improving the visibility of the objects in the explored layer.

On the other hand, the higher the tomosynthesis angle, the higher the path of X-ray radiation in the breast, which leads to a decrease in the number of quanta X-ray, thus to increase of (relative) quantum noise [5]. In addition, the passage of a longer length in the breast leads to the achievement of the energy of the X-ray quanta, and, consequently, to the decrease in the radiative contrast of microcalcification. Also, with the increase in the path length in the breast the level of the scattered X-ray increases as well, which reveals the detectability of microcalcification [7].

Thus, in the tomosynthesis there is a competition between the need for increasing the tomosynthesis angle for removing structure noise and providing high tomography resolution (by height) the need to provide high-quality images for projections made at a large angle, which requires to high increase in radiation exposure for these projections [8].

Separately, it worth mentioning that most types of existing mammographs with tomosynthesis have a stationary or a small variation angle ( $\pm 2.1^\circ$ ). This leads to the fact that with the increase of the tomography angle of X-ray, they fall not perpendicularly, thus deteriorating the performance characteristics of X-ray tube (even for needle phosphors [5]) and blurring the image, especially small details (microcalcification).

In addition to the physical reasons of the possible low quality of microcalcification reconstruction, a core role is played by pure mathematical reasons (reconstruction method and implementation). The fact is that the quality of the reconstructed images, and, consequently, the detection of

O. Morgun · K. Nemchenko · A. Vaisburd (✉)  
LRMT Ltd, Dostoevskogo Str. 1, Kharkiv, 61011, Ukraine  
e-mail: vaisburd.anton@gmail.com



microcalcification is influenced by the algorithm of tomography layers reconstruction [9–11], and the role of the geometrical calibration of the mammograph [12] is very important.

Based on the above-mentioned reasons, it can be concluded that the detection of tumors and microcalcification in a homogeneous structure, for example, in the breast with a high content of the adipose tissue and a small presence of glandular tissue, in standard 2D mammography more efficient than in the case of 3D tomosynthesis. Thus, we do not offer tomosynthesis in this case. Although for the breast with a high portion of glandular tissue tomosynthesis is necessary, as a way to reduce the contribution of structural noise. However, a comparative analysis of the quality of images in 3D and 2D modes is best performed for the homogeneous environment without structural noise, for example, using the phantom RMI-156 (GAMMEX, USA).

Thus, this work is devoted to solving the problems of increasing the tomography resolution at large angles of tomosynthesis with a minimum deterioration of the detectability of microcalcification in comparison with 2D images with identical dose loads on the breast.

## 2 A Description of the Proposed Tomosynthesis Technique

The main results of the work are based on the experimental studies conducted on a digital mammograph with a tomosynthesis function “Medima-3D” (Mosrentgenprom, RF), which is shown in Fig. 1a. One of the features of this device is the horizontal location of the patient, which makes it possible to carry out tomography wide-angle researches. When carrying out tomosynthesis, this device differs by two

principal properties from other similar used in practice devices [13].

Firstly, the source of X-ray performs a joint rotation around the breast. In contrast to fixed receiver [14], in this case, the X-ray radiation falls in perpendicularly projections on the needle-shaped phosphor receiver not only in direct, but also lateral projections. This allows to provide both a high quantum detection efficiency (about 78% at a frequency close to zero) and a high spatial resolution for projections made at a large angle. In this case, the maximum projection angle reaches a value of  $60^\circ$ , which made it possible to achieve a high tomography resolution on this device. Such an angle of  $60^\circ$  proved to be optimal, because a further increase in the projection angle leads, as noted above, to deterioration in the detectability of microcalcification.

Secondly, the feature of this device is a high spatial resolution in the image plane. This resolution reaches 20 pl/mm in all directions both along and across the scan (in the tomosynthesis mode, we perform  $2 \times 2$  binning). Such a high resolution is necessary to increase the detectability of microcalcification, the thin structure of glandular tissue and blood vessels. High resolution is achieved with the use of the discrete impulse scanning method [15].

When working in the tomosynthesis mode,  $N = 15$  two-dimensional indexed projections  $J_n$ , are produced, which are indexed by  $n = 0, \pm 1, \dots, \pm(N - 1)/2$ . To carry out the projection, the entire receiver-source system rotates around the axis passing through the breast at an angle multiple by about  $4.29^\circ$ . Thus, the outside projections are performed at an angle of  $\pm 30^\circ$ . The entire volume of the investigated object is divided into layers  $I_m$ ,  $m = 1 \dots M$ , which are subject to recovery. The number of layers  $M$  is determined by their thickness, which is determined by the magnitude of the tomographic resolution.

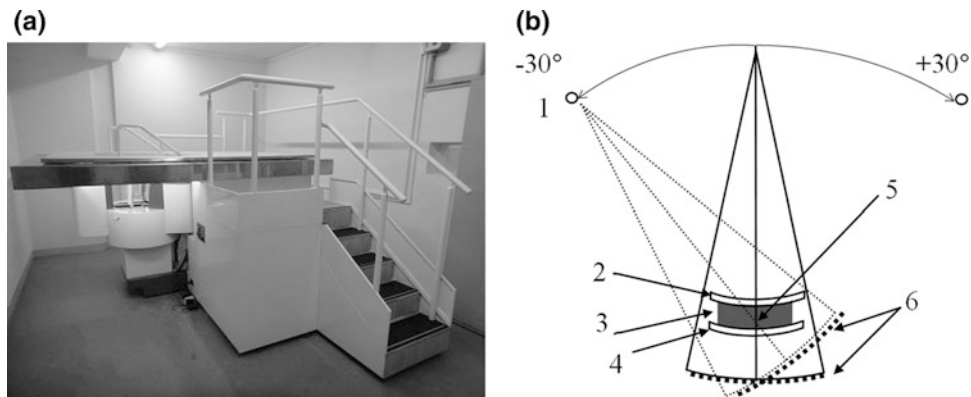


**Fig. 1** The appearance **a** and the principle of the action of the X-ray channel **b** of a digital mammograph with the tomosynthesis function “Medima-3D” (Mosrentgenprom). 1—moving source of X-ray; 2—

curved compression plate; 3—slightly compressed breast; 4 - curved support plate; 5 - the center of rotation; 6—curvilinear trajectories of receiver in 2D images

It is further assumed that each of the projections is a superposition of the projections of each of the layers:

$$J_n = \sum_{m=1}^{m=M} J_{nm} = \sum_{m=1}^{m=M} G_{nm} I_m \quad (1)$$

where  $J_{nm}$  is the  $n$ -th projection of the  $m$ -th layer, and  $G_{nm}$  are the direct projection operators that associate the pixels of the layer  $I_m$  with pixels of the projection  $J_n$ .

The central projections of the layers  $J_{0m}$  are considered as a target values in this work, and the following equation was obtained for them:

$$J_{0m} = \frac{1}{N} \sum_n F_{0n}(m) J_n - \frac{1}{N} \sum_n F_{0n}(m) \sum_{k \neq m} F_{0n}^{-1}(k) J_{0k}. \quad (2)$$

Here the operators

$$F_{0n}(m) = G_{0m} G_{nm}^{-1}, \quad (3)$$

describe the local affine transformations of the  $n$ -th projection into zero-projection and are determined from the prior information obtained from the preliminary calibration of the tomography system. This approach allows to get rid of the difficulties in determination of the geometric parameters of the system, which are used in other algorithms of tomosynthesis, and, as a result, get quite good recovery parameters.

In particular, this technique made it possible to achieve a layer thickness of 250  $\mu\text{m}$ , while not degrading the resolution in the layer as compared to classic 2D images.

As a criterion for tomography resolution (widely used by other authors [6, 10, 16]), the artifacts spreading function  $ASF(z)$  is used. Dependency of  $ASF(z)$  graphs for objects simulating microcalcification of size 540  $\mu\text{m}$  in the phantom

RMI-156 (GAMMEX, USA) are shown in Fig. 2. The theoretical dependence  $ASF(z)$  is determined by the formula

$$ASF(z) = \frac{1}{N} \sum_{n=-(N-1)/2}^{n=(N-1)/2} \sqrt{1 - \frac{(z - z_0)^2}{r^2} \sin^2(\alpha_n)}, \quad (4)$$

where the discrete angle  $\alpha_n = 60^\circ/(N - 1) \approx 4.29^\circ$  is the angle between the projections in the tomosynthesis. The calculation was carried out in a spherical-shaped microcalcification model with a radius  $r = 270 \mu\text{m}$ . From the figure, we can see a good correspondence between the half width at half-height ( $HWHH$ ) theoretical dependence and experimental data.

A comparison of the measured  $HWHH$  for the  $ASF(z)$  microcalcification with a diameter of 540  $\mu\text{m}$  in the RMI-156 phantom in our case and the approach of other authors [16] is presented in Table 1.

In our calculations, the depth of the tomography layer was assumed to be 250  $\mu\text{m}$ . Such a depth of the layer is determined from the result that, for smaller thicknesses, the  $HWHH$  of  $ASF(z)$  does not decrease, but as the depth of the layer increases, the growth of the  $HWHH$  of  $ASF(z)$  begins. Such a small value of the tomography resolution, compared with the studies [16], is primarily related to the large angle of maximum deviation for the supreme lateral projection of  $\pm 30^\circ$ . It is worth mentioning that other devices also use such angles [4–6, 17]. However, the simultaneous rotation of the receiver and the X-ray tube around the breast is used in the method investigated method, and this gives an advantage in the reconstruction of the layers compared with other techniques where stationary receivers [14] are used.

In addition to high tomography resolution, it is necessary to diagnose microcalcification no worse than in a flat 2D breast image, i.e. have a spatial resolution in the focal plane comparable to the spatial resolution for a flat 2D image. As a comparison criterion, we chose the analysis of the  $HWHH$  of densitograms of X-ray image built along the diameters of the microcalcification simulating objects with a diameter of 540 and 320  $\mu\text{m}$  of the RMI-156 phantom (Gammex, USA). Such densitograms were constructed both for an X-ray image in a flat 2D image and for an X-ray image obtained by 3D tomosynthesis in the focal layer at the same geometric position of the phantom, the voltage at the X-ray tube ( $U = 35 \text{ kV}$ ), and the total amount of electricity 60,8 mA.

Densitograms were constructed and compared both in the direction of the  $x$  axis (along the tomosynthesis direction) and along the  $y$  axis (across the direction of tomosynthesis). The results of the measurements presented in Fig. 3 and in Table 1b show a good correspondence between the geometric dimensions of microcalcification in both directions.

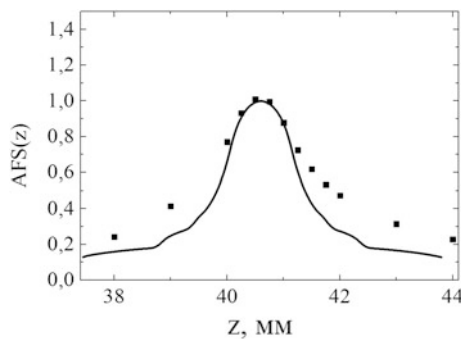
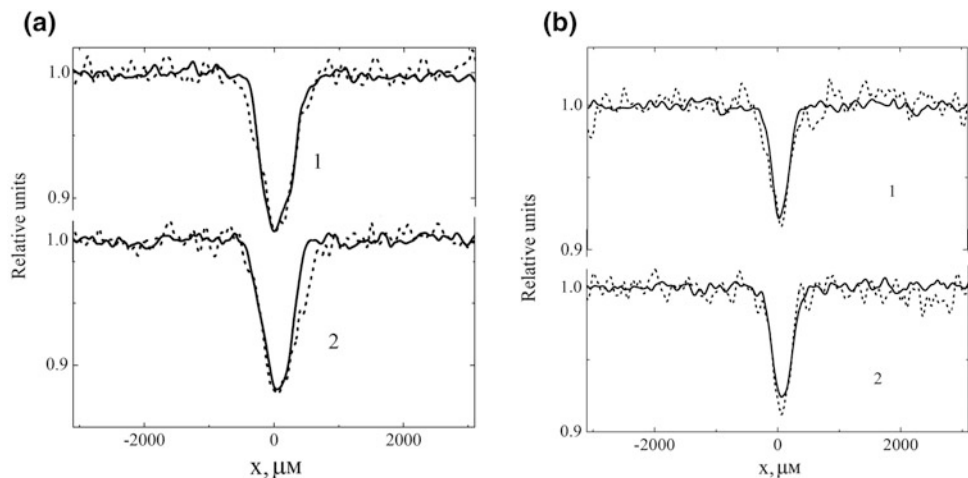


**Fig. 2** The  $HWHH$  of  $ASF(z)$  function is averaged over a group of six 540  $\mu\text{m}$  objects that mimic microcalcifications in the RMI-156 phantom. Solid line—calculation by formula (4). The relative  $MSE$  does not exceed 25%

**Table 1** Values *HWHH* of the *ASF(z)* (a) and densitogram (b) for the 540  $\mu\text{m}$  object

(a) <i>HWHH</i> of <i>ASF(z)</i>			(b) <i>HWHH</i> of densitogram		
This paper	2, 5 mm	Maximum projection angle— $60^\circ$	This paper	0.5 mm 0.5 mm	Along and across the direction of tomosynthesis
Ref. [16]	4, 1 mm	Maximum projection angle— $28^\circ$	Ref. [10]	0.69 mm 0.56 mm	Before processing After processing

**Fig. 3** Comparison of the densitograms of microcalcification in 2D (solid line) and 3D (dashed line) cases constructed along (1) and across (2) the direction of tomosynthesis for microcalcification with a size of 540  $\mu\text{m}$  (a) and 320  $\mu\text{m}$  (b). The relative *MSE* did not exceed 5%



### 3 Conclusion

The paper presents the results of a study of the technical parameters of images obtained on a digital X-ray mammographs, which uses new approaches of solving the tomosynthesis problem: impulse discrete scanning for obtaining flat 2D images, quasilocal affine transformations for restoring the three-dimensional structure of the breast in tomosynthesis. It is shown that joint application of these techniques allows to achieve a high tomography resolution (depth of the tomography layer  $\sim 250 \mu\text{m}$ , *HWHH* function  $\sim 2.5 \text{ mm}$ ); while the spatial resolution in the restored 3D layer remains at the level of a flat (2D) image with identical dose loads on the breast (phantom).

### References

- Mackenzie, A.: Effect of doze on the detection of micro-calcification clusters for planar and tomosynthesis imaging. In: Proc. of IWDM 2016, Malmo, Sweden, pp. 142–149.
- Timberg P., Baath M., Andersson I., Mattsson S., Tinberg A., Ruschin M.: Visibility of micro-calcification clusters and masses in breast tomosynthesis image volumes and digital mammography: a 4AFC human observation study. *Med. Phys.* 39(5), pp. 2431–7 (2010).
- Cockmartin L.: Comparison of digital reast tomosynthesis and 2D digital mammography using a hybrid performance tes. *Phys. Med. Biol.* 60(10), pp. 3939–3958 (2015).
- Goodsitt M.: Digital breast tomosynthesis: studies of the effects of acquisition geometry on contrast-to-noise ratio and observer preference of low-contrast objects in breast phantom images. *Phys. Med. Biol.* 59, pp. 5883–5902 (2014).
- Chan H.P.: Digital breast tomosynthesis: Observer performance of clustered microcalcification detection on breast phantom images acquired with an experimental system using variable scan angles, angular increments, and number of projection views. *Radiology* 273(3), pp. 675–685 (2014).
- Sechopoulos I., Ghetti C.: Optimization of the acquisition geometry in digital tomosynthesis of the breast. *Med. Phys.* 36, pp. 1199–1207 (2009).
- Wu G., Mainprize J., Boone J., Yaffe M.: Evaluation of scatter effects on image quality for breast tomosynthesis. *Med. Phys.* 3 (10), pp. 4425–32 (2009).
- Chawlaa A., Lo J., Baker J., Samei E.: Optimized image acquisition for breast tomosynthesis in projection and reconstruction space. *Med. Phys.* 36(11), pp. 4859–4869 (2009).
- Zhao B.: Experimental validation of a three-dimensional linear system model for breast tomosynthesis. *Med. Phys.* 36(1), pp. 240–251 (2009).
- Mota A.: 3D Total Variation Minimization Filter for Breast Tomosynthesis Imaging. Proc. of 13th Int. Workshop IWDM. Malmo, Sweden. pp. 484–492 (2016).
- Lu Y.: Adaptive diffusion regularization for enhancement of microcalcifications in digital breast tomosynthesis (DBT) reconstruction. Proc. SPIE 7961, Medical Imaging 2011: Physics of Medical Imaging, 796117 (March 16, 2011). <https://doi.org/10.1117/12.878096>.
- Li X., Zhang D., Liu B.: A generic geometric calibration method for tomographic imaging systems with flat-panel detectors-A detailed implementation guide. *Med. Phys.* 37(7), pp. 3844–3854 (2010).

13. Vadantham S., Karrelas A., Vijaraghavan G., Kopaks D.: Digital Breast Tomosynthesis: State of the Art. *Radiology* 277(3), pp. 663–684 (2015).
14. Sompel D., Brady S.M., Boone J.: Task-based performance analysis of FBP, SART and ML for digital breast tomosynthesis using signal CNR and Channelized Hotelling Observers. *Med. Im. An.* 15, pp. 53–70 (2011).
15. Morgun O.N.: A device for visualization of a patient's breast by X-ray radiation in the mode of tomosynthesis or mammorphy. Patent for invention of the Russian Federation No. 2553505.
16. Tucker A., Lu J., Zhou O.: Dependency of image quality on system configuration parameters in a stationary digital breast tomosynthesis system. *Med. Phys.* 40(3), pp. 031917 (2013). <https://doi.org/10.1118/1.4792296>.
17. Zhang Y.: Comparative study of limited-angle cone-beam reconstruction methods for breast tomosynthesis. *Med. Phys.* 33(10), pp. 3781–379 (2006).
18. Kononchuk R.D., Morgun O.N., Nemchenko K.E.: Spatial resolution in the direction of scanning in receivers using the accumulation of a signal with a time delay. *Medical Technology* 5, pp. 22–25 (2014).



# Size and Shape of Spherical Objects on Full-Field Digital Mammography and Digital Breast Tomosynthesis Images

Hidetoshi Yatake, Yuka Sawai, Takahiro Kozuka, Yoshihiro Takeda, Mariko Kajihara, Toshizo Katsuda, Rumi Gotanda, Tatsuhiko Gotanda, Shuji Abe, Makoto Shimada, Nobuyoshi Tanki, Toshio Nishi, and Hideo Inaji

## Abstract

This study assessed the accuracy of shape and size representation of spherical objects on full-field digital mammography (FFDM) and digital breast tomosynthesis (DBT) images. Six 5-mm-thick polymethylmethacrylate slabs were positioned on the breast support table with 9 aluminum spherical objects of 30 ( $\pm 0.1$ ) mm diameters between the first and second slabs. X-ray imaging was performed using FFDM and DBT (angular range 15°–40°, with correction of magnification), and repeated with the objects placed between the third and fourth slabs, and subsequently between the fifth and sixth slabs. The aspect ratio of the spherical objects and longer diameter were measured to evaluate the shape and size, respectively. A Steel-Dwass test was performed for comparative analysis. A  $P$  value  $<0.05$  was considered significant. No significant differences in the aspect ratio of the spherical objects imaged using FFDM, DBT15°, or DBT40° images were observed (overall median: 1.02, overall range: 1.00–1.06). The longer diameter on the FFDM was increasingly magnified (median, range) with increasing distances of 20 mm (32.5, 31.8–33.5 mm) and 40 mm (33.6, 32.9–34.7 mm) between the breast support table and object center. However, in the case of DBT, the longer diameter was approximately the same as that of the

actual object (overall, 30.4, 30.0–31.7 mm). At each height, the longer diameter was significantly different between the FFDM and DBT15° images and between the FFDM and DBT40° images (all  $P = 0.001$ ), with no significant difference in that between the DBT15° and DBT40° images. The size on the FFDM images was magnified as compared to the size of the actual objects, and that on the DBT images was approximately the same as that of the actual objects. Thus, preoperative tumor size determination using FFDM images should be avoided.

## Keywords

Tumor size • Tumor shape • Full-field digital mammography • Digital breast tomosynthesis

## 1 Introduction

Accurate size measurement of preoperative invasive breast cancer is mandatory for staging as well as determining modal status. According to “TNM Classification of Malignant Tumors, eighth edition”, physical examination and imaging, e.g., mammography are the standard procedure for assessing T categories [1]. In general, preoperative tumor size measurement is performed using mammography and ultrasonography because these are more objective than physical examination. The shape and size of the subjects must therefore be represented accurately on these images.

It has been reported that there is a difference in the level of accuracy of size representation between the tumor size assessed using FFDM and/or DBT with the pathological tumor size [2–7]. A study has reported that the relationship between the mammographic size and the pathological size was almost exactly 1:1 [2]. However, the majority of studies have reported that tumor size was either under- or overestimated on FFDM images [3–7]. In addition, pathological specimens are reduced at the time of size measurement.

H. Yatake (✉) · Y. Sawai · T. Kozuka · T. Nishi · H. Inaji  
Kaizuka City Hospital, Osaka, Japan  
e-mail: yatakehidetoshi@yahoo.co.jp

H. Yatake · Y. Takeda  
Okayama University, Okayama, Japan

M. Kajihara  
Fujifilm Medical Corporation, Tokyo, Japan

T. Katsuda · N. Tanki  
Butsuryo College of Osaka, Osaka, Japan

R. Gotanda · T. Gotanda  
Kawasaki University of Medical Welfare, Okayama, Japan

S. Abe · M. Shimada  
Osaka Women’s and Children’s Hospital, Osaka, Japan

A consensus regarding this has not been obtained to date because of conflicting reports and biases in the evaluation.

The present study physically assessed the accuracy of shape and size representation of spherical objects on full-field digital mammography (FFDM) and digital breast tomosynthesis (DBT) images in order to resolve this contrariety and bias.

## 2 Materials and Methods

Six 5-mm-thick polymethylmethacrylate (99.9%) slabs were positioned on the breast support table with 9 aluminum (99.99%) spherical objects of 30 ( $\pm 0.1$ ) mm diameters (Fig. 1) placed between the first and second slabs such that the distance between the support table and the center of the sphere was 20 mm (Fig. 2).

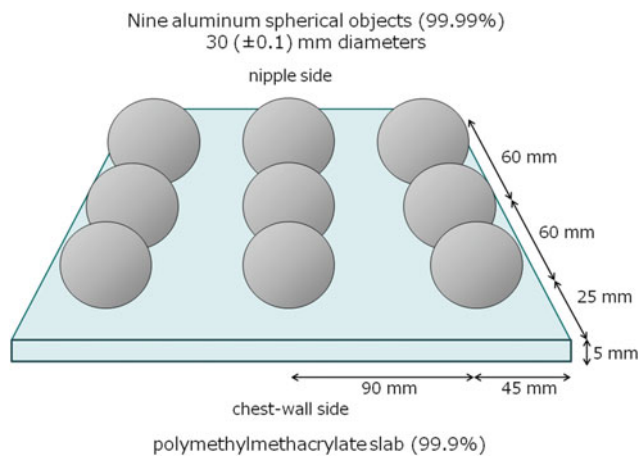


**Fig. 1** Schematic showing the placement of the nine aluminum spheres

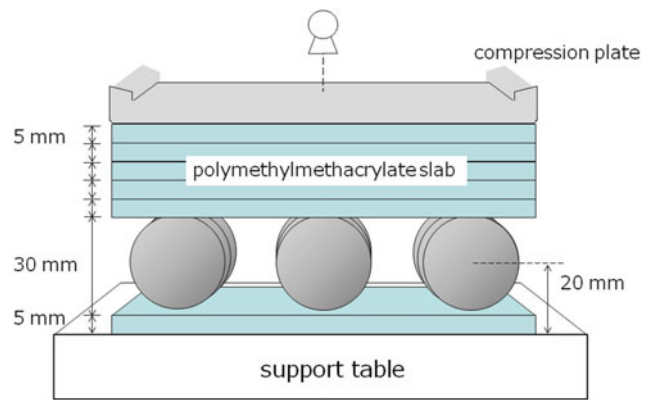


**Fig. 2** Schematic showing the placement of the nine aluminum spheres and six polymethylmethacrylate slabs

X-ray imaging was then performed (AMULET Innovality; Fujifilm, Japan) using FFDM and DBT (angular range 15°–40°, with correction of magnification), and repeated with the objects placed between the third and fourth slabs (support table—spherical object center distance: 30 mm), and subsequently between the fifth and sixth slabs (support table—spherical object center distance: 40 mm). Exposure conditions and reconstruction protocols for FFDM, DBT 15°, and DBT 40° images are shown in Table 1.

Assuming that round shapes would deform into an ellipse, the aspect ratio (longer diameter to shorter diameter ratio) and longer diameter of the spherical objects were measured to evaluate the shape and size, respectively. Measurements were made on digital images using image processing software (ImageJ 1.50i; NIH, Bethesda, MD). Measurements on DBT images were performed in the slice with the reconstructed focal planes. When the aspect ratio and longer diameter were measured, each threshold was used by auto mode on the image processing software.

**Table 1** Exposure conditions and reconstruction protocols for full field digital mammography (FFDM), digital breast tomosynthesis (DBT) 15° and DBT 40°

Images	FFDM	DBT 15°	DBT 40°
Target/filter	W/Rh	W/AI	W/AI
Tube voltage (KVp)	28	27	28
Effective mAs	44	26	29
Angular range	N/A	15°	40°
Slice interval (mm)	N/A	1.0	1.0
Reconstruction method	N/A	ISR*	ISR*

ISR\*: Iterative Super-Resolution reconstruction

A Steel-Dwass test was performed for comparative analysis between FFDM, DBT 15°, and DBT 40° (aspect ratio and longer diameter, respectively). *P*-values less than 0.05 were considered significant. All statistical analyses were performed with R version 2.8.1.

### 3 Results

The aspect ratios of the spherical objects (overall median, overall range) on the FFDM, DBT 15°, and DBT 40° images were approximately the same as the actual object (on the FFDM, 1.02, 1.00–1.06; on the DBT, 15°, 1.02, 1.00–1.06; on the DBT, 40°, 1.01, 1.00–1.06). Furthermore, no significant differences in the aspect ratios of the spherical objects were observed between any of these image types (Fig. 3).

The longer diameter of the spherical objects on the FFDM images were increasingly magnified (median, range) with increasing distances of 20 mm (32.5 mm, 31.8–33.5 mm), 30 mm (33.1 mm, 32.3–34.1 mm), and 40 mm (33.6 mm, 32.9–34.7 mm) between the breast support table and object center. In the case of DBT, however, the longer diameter was approximately the same as that of the actual object (overall, 30.4 mm, 30.0–31.7 mm) (Fig. 4).

At each height, the longer diameter on FFDM was significantly greater than that on DBT15° (all  $P = 0.001$ ) and than that on DBT40° images (all  $P = 0.001$ ), with no significant difference between the DBT15° and DBT40° images.

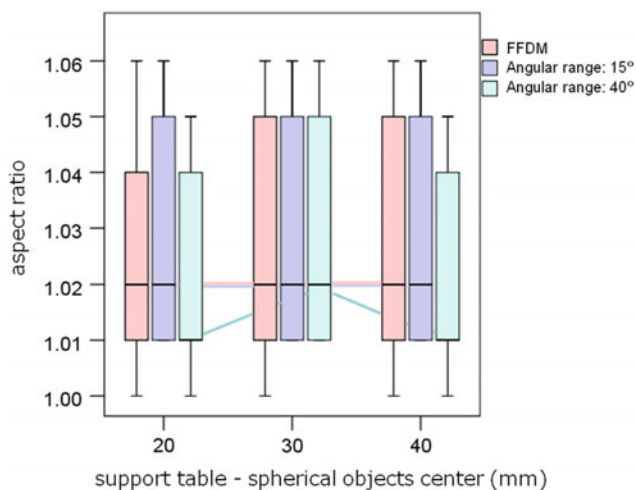


**Fig. 3** The aspect ratios of the spherical objects on the FFDM, DBT 15°, and DBT 40° images

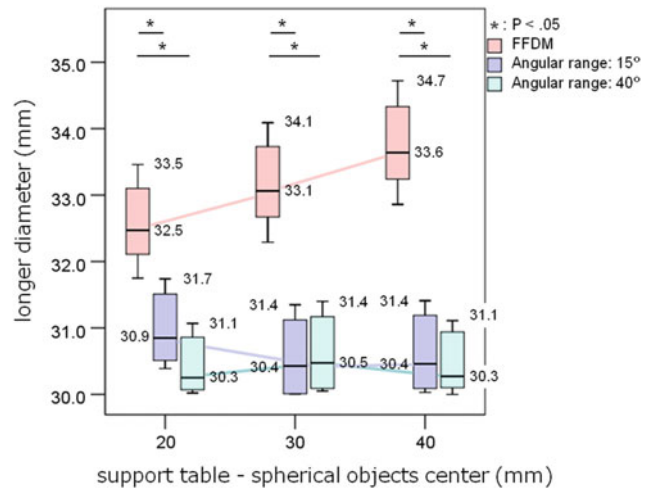


**Fig. 4** The sizes of the spherical objects on the FFDM, DBT 15°, and DBT 40° images

### 4 Discussion

The results of the present study show that there was no significant difference between the aspect ratios of the spherical objects on the FFDM and DBT images. In addition, FFDM and DBT images were not highly deformed (at a maximum 1.06). Therefore, it is reasonable to suppose that DBT images reconstruct favorably. The maximum longer diameter of the spherical objects on the DBT images was 31.7 mm. However, the longer diameter of the spherical objects on the FFDM images were increasingly magnified (34.7 mm at a maximum; support table—spherical object center, 40 mm) with increasing distance between the breast support table and object center.

Fornvik et al. reported that in comparison to the resected tumor specimen, tumor size is clinically overestimated on FFDM images, and DBT is superior to FFDM in the assessment of breast tumor size and stage [3]. This conclusion supports the results of the present study. In contrast, in some cases, tumor size has been shown to be underestimated on both FFDM and DBT images [3]. Further, Hieken et al. [5] and Pierie et al. [7] reported that tumor size was underestimated only in FFDM. However, the tumor size on FFDM images should be magnified and represented depending on the variations in the distance between the tumor and film/detector and compression of the breast during examination. The results of the present study demonstrated that the subjects on FFDM magnified and represented; therefore, this is inconsistent with the reports suggesting that tumor size evaluated using FFDM was underestimated.

The studies showing underestimation of tumor size using FFDM have some limitations. Fornvik et al. discussed that DBT was only performed when the tumor was either minimally visible or not visible on FFDM images. Furthermore, the presence of extensive calcification representing ductal carcinoma in situ (DCIS) but also containing invasive components may be difficult to assess pathologically. Additionally, in cases where the maximum tumor extent lies in the orthogonal plane of slicing, it may be difficult to measure the true tumor extent [3]. In addition, Pierie et al. [7] pointed out that they performed measurements on the tumoral opacity and disregarded spicules, which may only represent fibrosis, and that this is the possible reason for the underestimation of tumor size using FFDM in their study. Although the limitations of these reports may be the reason why measurement on FFDM underestimates the tumor size compared to histological size, the exact reason is still not clear. The present study physically assessed the representation accuracy of objects such as a tumor on FFDM and DBT images in order to create some consensus.

The limitations of the present study were as follows. First, X-ray images of the spherical objects were taken using the equipment with the correction function of magnification percentage turned on. This function corrects the slice cross-section of DBT so as to prevent the enlargement ratio of each slice image from being differently represented in accordance with the distance. This corrects for differences in distances between the slice cross section and detector. However, this function is not installed in all DBT devices. Therefore, when a DBT device not equipped with this function is used, the object is magnified and represented according to the distance from film/detector, such as in FFDM. Second, on both FFDM and DBT, clinical tumor size may be more extended by compressing the breast with a compression plate than the findings of the present study. In addition, in case of spread of the tumor along the direction of breast compression during examination, images acquired using these modalities do not capture the maximum tumor size. Therefore, the present study physically demonstrates that the object size on the FFDM was increasingly magnified with increasing distance between the breast support table and object center, whereas in case of DBT, it was approximately the same as that of the actual object.

## 5 Conclusion

The size on the FFDM image was magnified as compared to the actual object, whereas on the DBT image, the represented size was closer to that of the actual object. Thus, the results of the present study indicate that preoperative tumor size determination using FFDM images should be avoided.

**Disclosures of Conflicts of Interest** H.Y. disclosed no relevant relationships. Y.S. disclosed no relevant relationships. T.K. disclosed no relevant relationships. Y.T. disclosed no relevant relationships. M.K. Activities related to the present article: disclosed no relevant relationships. Activities not related to the present article: employment at Fujifilm Medical Corporation, Tokyo, Japan. Other relationships: disclosed no relevant relationships. T.K. disclosed no relevant relationships. R.G. disclosed no relevant relationships. T.G. disclosed no relevant relationships. S.A. disclosed no relevant relationships. M.S. disclosed no relevant relationships. N.T. disclosed no relevant relationships. T.N. disclosed no relevant relationships. H.N. disclosed no relevant relationships.

## References

1. James D. Brierley MKG, Christian Wittekind. Union for International Cancer Control. TNM classification of malignant tumours, 8th Edition. UK: Wiley Blackwell; 2017.
2. Flanagan FL, McDermott MB, Barton PT, Pilgram TK, Dehdashti F, Wick MR, et al. Invasive breast cancer: mammographic measurement. *Radiology*. 1996;199(3):819–23.
3. Fornvik D, Zackrisson S, Ljungberg O, Svahn T, Timberg P, Tingberg A, et al. Breast tomosynthesis: Accuracy of tumor measurement compared with digital mammography and ultrasonography. *Acta Radiol*. 2010;51(3):240–7.
4. Bosch AM, Kessels AG, Beets GL, Rupa JD, Koster D, van Engelshoven JM, et al. Preoperative estimation of the pathological breast tumour size by physical examination, mammography and ultrasound: a prospective study on 105 invasive tumours. *Eur J Radiol Open* 2003;48(3):285–92.
5. Hieken TJ, Harrison J, Herreros J, Velasco JM. Correlating sonography, mammography, and pathology in the assessment of breast cancer size. *Am J Surg* 2001;182(4):351–4.
6. Pain JA, Ebbs SR, Hern RP, Lowe S, Bradbeer JW. Assessment of breast cancer size: a comparison of methods. *Eur J Surg Oncol* 1992;18(1):44–8.
7. J.P.E.N Pierie CIP, Levert LM, de Hooge P. Clinical assessment, mammography and ultrasonography as methods of measuring the size of breast cancer: a comparison. *Breast*. 1998;7(5):247–50.

# Training Towards Precise Control Over Muscle Activity with Real Time Biofeedback Based on Ultrasound Imaging

Anna Sosnowska, Aleksandra Vuckovic, and Henrik Gollee

## Abstract

Automated algorithms for analysis of B-mode muscle ultrasound videos are computationally expensive. Thus, we propose a technique based on the comparison of pixels intensities between frames, that processes ultrasound recordings almost instantaneously, without special processing hardware. We verify the suitability of this method for feedback training of muscle activation. 15 able-bodied volunteers took part in the study practising contractions of different torque outputs of the gastrocnemius muscle. Within 3 s of each trial, they received visual feedback reflecting the ultrasound video analysis, visualizing how close their attempt was to the target, allowing them to modify their strategy for the next trial. A tendency to get closer to the target contraction intensity was recorded for 60.1%, 74.4%, 67.8% of trials for *minimal*, *weak* and *medium* contractions, respectively. Considering the number of successful trials (within 10% of the target), 11 participants improved in the second session in the *weak* and 10 in the *medium* contraction task. We demonstrated that the method provides easily interpreted semi-real time feedback of muscle activation that could help with muscle training.

## Keywords

Ultrasound imaging • Biofeedback • Muscle training

## 1 Introduction

Neuromuscular disorders such as stroke, spinal cord injury or peripheral nerve damage can result in partial paralysis and loss of functional activity of specific body parts. While the signals from the central nervous system are affected, the main muscles operate correctly and recovering patients can re-learn to use them [1], which can be augmented by providing feedback about the muscle behaviour.

Muscular activity is commonly measured by surface electromyography (sEMG), however it is susceptible to motion artifacts and cross-talk from various muscles [2]. Due to background noise, sEMG is not sensitive enough to register weak muscle activations and not suitable to evaluate deep muscles.

Ultrasound imaging (USI) enables to monitoring muscles during movement in real-time and to record videos for off-line analysis. This non-invasive, inexpensive technique can detect the activity of deeper structures, differentiate small contractions, and precisely identify which muscle is activated. Advancements in image processing have enabled us to automatically analyse videos, using feature tracking based on optical flow or cross-correlation approaches [3, 4] and feature detection in single USI image [5]. These methods proved reliable and suitable to study various muscle architecture changes. However, all of them are used offline or require specialist processing hardware, as they are very computationally expensive, with processing times on standard hardware ranging from minutes [4] to hours [3] to analyse video recordings of only 10 s duration.

To overcome this issue a new method was developed to allow basic processing of ultrasound videos instantly after the recording. The technique is based on comparing pixel intensity between successive frames in the identified region of interest (ROI) containing the muscle. The output allows precise identification of the instances when the muscle gets activated.

A. Sosnowska (✉) · A. Vuckovic · H. Gollee  
Centre for Rehabilitation Engineering, The University of Glasgow,  
University Avenue, Glasgow, G12 8QQ, UK  
e-mail: a.sosnowska.1@research.gla.ac.uk



The aim of this study is to develop and test a USI system which provides feedback of the contraction intensity to the user in almost real time, to facilitate muscle training and help with practising precise movements.

## 2 Materials and Methods

### 2.1 Participants and Measurement Procedure

**Participants.** Fifteen able-bodied participants (7 male, 8 female, age  $30.3 \pm 9.8$  years) were recruited for this study, that was approved by the Ethics Committee at the College of Science and Engineering, University of Glasgow.

**Experimental design.** Participants were seated in an upright position with the right foot resting on the dynamometer force platform. The leg was supported at the thigh so the lower leg was parallel to the ground, with the ankle in the neutral position. An ultrasound probe was positioned over the medial gastrocnemius muscle. The participant was facing a 19" computer screen positioned about 0.5 m away, where experimental cues and feedback were displayed.

**Experimental procedures.** Initially, baseline USI was recorded when the muscle was relaxed, and the maximum voluntary contraction (MVC) determined by pushing on the force platform as strongly as possible. The tasks involved contractions of the gastrocnemius muscle of different intensities (i) at 25% MVC—*medium*, at 10% MVC—*weak*, and at smallest possible intensity—*minimal*. For the *minimal* tasks, participants were instructed to initiate contraction only up to the point when they became aware of activating muscle.

The tasks consisted of 15 trials, lasting 10 s each. During the first 5 trials (Training), participants practised the contractions while observing feedback on the generated torque to learn how to differentiate between different intensities. During the following 10 trials (Feedback training), participants attempted the tasks and received USI based biofeedback (displayed on the screen) in form of a bar, the size of which was proportional to the value of detected muscle movement. This procedure was completed for all three intensities and repeated at two separate sessions, separated by two days.

**Data collection.** Ultrasound images were recorded in B-mode at a rate of 40 frames/s, using a computer-based ultrasound system (Echoblaster 128; Telemed, Lithuania) with a 96-element linear array transducer operating at a frequency of 6 MHz and a 50 mm scanning depth (LV7.5/60/96). A digital output signal from the ultrasound system was used to synchronize data collection. Ankle torque and joint position measurements were taken with a

Biodex System 3-PRO (Biodex Medical Systems Inc., USA) dynamometer at a sample rate of 40 Hz.

### 2.2 Analysis Methods

**Ultrasound image processing.** The ultrasound videos were processed using custom C++ software that extracted the pixel intensity for each of the 96 transducer elements resulting in a frame of  $96 \times 884$  pixels. Using MATLAB software (The Mathworks, USA), the intensities were converted into grayscale values between 0 and 1. For an initial frame the ROI was selected by a polygon, containing the gastrocnemius muscle but excluding the aponeuroses. This was only done once for the baseline recording, and then used throughout the experiment.

In the selected ROI, the intensities of corresponding pixels were subtracted between adjacent frames, and the absolute difference values were summed over the entire region which was then scaled by the number of pixels within the ROI, giving the *normalised pixel difference*. This value would be 1 if all pixels within the ROI had changed between frames, and zero if there was no difference between pixels. Analysing the normalised pixel difference allowed detection of changes in muscle activation and differentiation between types of contractions. With this very simple technique, processing of a typical 10 s video took about 3 s on a standard laptop (Lenovo Thinkpad T440) with an Intel i5 processor.

**Ultrasound based feedback.** The baseline video was used to determine the value of normalised pixel difference when no movement was happening and to establish a threshold to detect muscle contraction by using the mean +3 SD to account for periodic activity of the capillaries and physiological changes in the muscles not associated with the contraction. The maximum value of normalised pixel difference was found by analysing videos of MVC. Processing of trials enabled detection whether muscle activation occurred. During the *minimal* contractions, the trial was considered successful when the contraction threshold was exceeded and the value of the first peak corresponding to initial muscle activation stayed within 25% of the maximum. For *weak* and *medium* contractions, the target value was determined during the training session, when real-time torque feedback from the dynamometer was available. The value of the normalised pixel difference for the final successful trial was used. The maximum peak (highest muscle activation) was selected as the target value for the feedback session, and trials within  $\pm 10\%$  were considered *successful*, within  $\pm 30\%$  were *acceptable*, while others were *unsuccessful*. Due to the small processing times, using this algorithm it is possible to

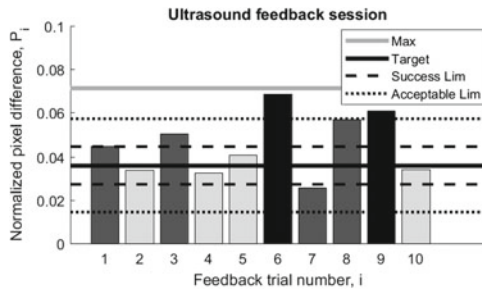


**Fig. 1** Example of ultrasound imaging based feedback as presented to the participant (white bars—successful, gray bars—acceptable, black bars—unsuccessful)

present feedback to the participant as bar graphs within 3 s after the trial concludes. A typical example for 10 completed trials is shown in Fig. 1.

**Outcome measures.** The outcome of trials was presented in terms of normalised pixel difference ( $P_i$  for trial  $i$ ,  $P_{max}$  for MVC test,  $P_{tgt}$  for target value). Then, the result of trial  $i$  relative to MVC is  $P_i/P_{max}$ , while the difference from the target relative to MVC is  $v_i$  (Eq. 1), and  $|v_i|$  is its absolute value. To compare between successive trials, difference relative to MVC is used ( $\Delta v_i$ , Eq. 2).

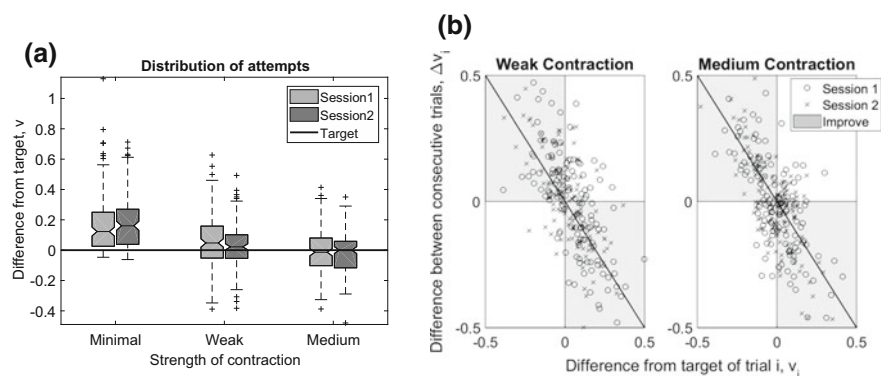
$$v_i = \frac{P_i}{P_{max}} - \frac{P_{tgt}}{P_{max}} \quad (1)$$

$$\Delta v_i = v_{i+1} - v_i = \frac{P_{i+1}}{P_{max}} - \frac{P_i}{P_{max}} \quad (2)$$

When assessing the success rates of using the feedback, we considered:

- *number of successful and unsuccessful trials* within each session
- *distribution of trials* considering variability within each session, represented by the difference from the target value relative to MVC ( $v_i$ )

**Fig. 2** **a** Distribution of attempts for the whole group, **b** Difference between trials in approaching the target for weak and medium contraction tasks



- *trial-to-trial improvement* within 1 session by comparing the difference from target between consecutive trials ( $\Delta v_i$ ) and absolute difference from target ( $|v_i|$ ).

### 3 Results

Considering the number of successful trials, 47% of 15 participants improved in the second session for the minimal contraction task, compared to 73% and 67% for weak and medium. Only 1 person had more unsuccessful trials in the second session for weak and medium, as opposed to 3 people in minimal contraction task. The distribution of attempts for all participants is shown in Fig. 2a representing difference  $v$  from target relative to the normalised pixel difference recorded for MVC. The biggest variability was noted for the minimal contraction. For weak and medium contractions, the variability decreased in second session with the mean approaching the target.

The expected tendency from trial to trial was to get closer to the target or follow a trial below the target ( $v_i < 0$ ) with one above ( $v_{i+1} > 0$ ) (or opposite). It means that the participant was able to use feedback to increase/decrease outcome, even if difference from the target increased. It was recorded for 74.4% and 67.8% of trials for weak and medium contractions. Figure 2b shows the difference ( $v_i$ ) from the target for trial  $i$  against the difference between 2 consecutive trials ( $\Delta v_i$ ). Results in the 1st and 3rd quadrant correspond to correct tendency. For minimal movement, improvement was considered when approaching the baseline and this happened for 60.1% of trials.

Analysing solely the tendency to approach the target, the absolute difference from target ( $|v_i|$ ) was plotted in Fig. 3 for the minimal movement task. The fitness of lines is characterised by following  $R^2$  values and p-value significance levels:  $R^2 = 0.059$ ,  $p = 0.0121$  for session 1, and  $R^2 = 0.089$ ,  $p = 0.0015$  for session 2. This indicates that

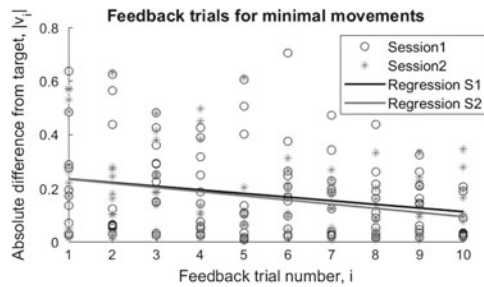


**Fig. 3** Regression of feedback trials for minimal contraction task

there is a very weak but statistically significant correlation between progressing in session and decreasing difference from target. For medium and weak contraction tasks, there was a decreasing trend consistent between 2 sessions (line gradient of  $-0.0033$  and  $-0.0032$  for session 1 and 2).

## 4 Discussion and Conclusions

We investigated the ability to learn to precisely control muscle activity using ultrasound based biofeedback and analysed learning within one biofeedback session and whether it transfers to the repeated sessions. As expected the trials were more successful and variability between trials decreased for *weak* and *medium* contraction tasks in the second session indicating that prolonged use of feedback was beneficial and participants learnt to perform more consistently. For *minimal movement* there was no overall improvement in terms of variability. In the majority of cases, the participant was able to apply information from the feedback to modify their attempts successfully. It was hypothesised that from trial to trial participants would get closer to the target (Fig. 3) and it was confirmed that for minimal movement learning was slow but consistent across the whole group.

To the best of our knowledge, ultrasound based biofeedback presented in near real-time, requiring no specialist computational hardware, has not previously been

developed. Feedback bars shown to participants enabled them to increase their awareness of muscle behaviour and to learn to reproduce contractions of different intensities. This approach could provide the basis for a feedback system for muscle training and rehabilitation. It would be especially advantageous when practising activations of deep muscles, for example in shoulder and neck, that cannot be assessed easily with any other method. The limitation of the algorithm is that feedback corresponds to the initial change in a muscle, reflecting the change in intensity of pixels, related to the change in torque, but not necessarily leading to development of a proportional torque. While it works well for detecting the onset of muscle activity, it would be beneficial to analyse whole contractions. In addition, processing time could be reduced further and the effect of more training sessions should be evaluated to assess learning outcomes of using the feedback over a longer period of time.

**Conflict of Interest** The authors declare that they have no conflict of interest.

## References

1. S. Arzillo, K. Gishen, and M. Askari, "Brachial plexus injury: treatment options and outcomes." *J Craniofac Surg*, vol. 25, no. 4, pp. 1200–1206, 2014.
2. J.-Y. Guo, Y.-P. Zheng, Q.-H. Huang, and X. Chen, "Dynamic monitoring of forearm muscles using one-dimensional sonomyography system." *J Rehabil Res Dev*, vol. 45, no. 1, pp. 187–195, 2008.
3. J. Darby, E. F. Hodson-Tole, N. Costen, and I. D. Loram, "Automated regional analysis of B-mode ultrasound images of skeletal muscle movement," *J Appl Physiol*, vol. 112, no. 2, pp. 313–327, 2012.
4. N. J. Cronin, C. P. Carty, R. S. Barrett, and G. Lichtwark, "Automatic tracking of medial gastrocnemius fascicle length during human locomotion," *J Appl Physiol*, vol. 111, no. 5, pp. 1491–1496, 2011.
5. M. Rana, G. Hamarneh, and J. M. Wakeling, "Automated tracking of muscle fascicle orientation in B-mode ultrasound images," *J Biomech*, vol. 42, no. 13, pp. 2068–2073, 2009.



# On the CT Dose Index: Are we Meeting the Challenge?

Emmanuel Ramírez, Oriana Benavides, Alfonso Holguin, Carolina Castro, and Wilson Lopera

## Abstract

The computed tomography dose index (CTDI), has long been recognised as a metric to quantify the radiation output from a CT examination that is easily measured and that captures the majority of the scatter tails for even wide X-ray beam widths. International standards now require manufacturers to display the pitch-normalised metric (CTDI<sub>vol</sub>) prior to scan initiation and the radiology community has become very familiar to typical values of this metric. However, it has been suggested that modern developments in CT technology permit patient doses to be determined in a more adequate way that allows representing the risks to patients, and that is now time to forgo the use of the CTDI (or variants) for CT dose optimisation. In this work, we explore the main problems concerning the use of the CTDI<sub>vol</sub> as a relevant dose index through a retrospective study of 20 of the most common CT examinations at a South American imaging centre including adult and paediatric patients using a total of three CT scanners. Applicable results were compared with diagnostic reference levels (DRL's) from European and North American countries. Our research shows that although CT technology is changing at a quick pace, CTDI<sub>vol</sub> keeps being a practical and valuable method for the task of dose optimisation because is well established and uniformly adopted.

## Keywords

Computed tomography • CT dose index • Radiation dose

## 1 Introduction

Computed tomography (CT) is essential for diagnosis, screening, therapy and management of patient care. In hospitals and emergency departments, CT significantly impacts diagnostic confidence and admission decisions [1]. However, this benefits come with a considerable increase utilisation and an increment in population being exposed to ionizing radiation.

Exposure to radiation however, is believed to carry a small, but non-zero, risk of radiation-induced cancer [2] and there is a realisation that the image quality at CT often exceeds the level required for a confident diagnosis and that patient doses are higher than necessary. This concern was emphasized by the Food and Drug Administration regarding the exposure of paediatric and adult patients to radiation at CT [3].

Modern CT scanners report patient dose indexes of the volume CT dose index (CTDI<sub>vol</sub>) and the dose-length product (DLP) that are measured in 16- and 32-cm-diameter acrylic phantoms [4]. The CTDI<sub>vol</sub> (mGy) was first introduced in 1891 by Shope et al. [5] as an index that quantifies the relative intensity of the radiation that is incident on the patient, however, is not intended to represent doses to any particular patient or organ. The product of CTDI<sub>vol</sub> and scan length, known as DLP (mGy · cm) is used to quantify the total amount of radiation patients receive during a CT scan [6]. These dose parameters are also suggested for dose optimisation purposes by various international organisations [7, 8] usually named dose reference levels (DRL's) or guidance levels that assist the optimisation of patient protection whilst at the same time permit comparisons of the performance of different CT scanners and techniques.

The advances in dose descriptors made great sense at the time due to the small heat capacities and slow CT equipment available. However, it has been suggested that recent technological developments in CT and dosimetry permit patient doses to be determined in a more adequate way and that

E. Ramírez (✉) · O. Benavides · A. Holguin · C. Castro  
Departamento de Imágenes Diagnósticas, Fundación Valle del Lili, Cali, Colombia  
e-mail: emmanuel.ramirez@correounivalle.edu.co

E. Ramírez · W. Lopera  
Departamento de Física, Universidad del Valle, A.A. 25360 Cali, Colombia

measurements of  $CTDI_{vol}$  (or variants) may not be as accurate as desirable [9]. On the other hand, some argue that replacement of these metrics is unnecessary and remain suitable for dose optimisation and quality assurance purposes [10].

The objective of the present study was to review some of the main challenges concerning the use of the  $CTDI_{vol}$  as a relevant dose descriptor for dose optimisation purposes carrying a retrospective analysis of 20 of the most common CT examinations at a large academic medical centre in South America.

## 2 Methods

This retrospective data analysis was approved by our Institutional Review Board (IRB) which waived the requirement for informed consent. All of the CT examinations performed in our centre included in this study were divided into four main groups: head, neck, chest and abdomen. Five protocols were selected for the main groups: adult head, child head ears, sinuses and head with contrast for the head region; adult neck, cervical spine, neck/chest and neck/chest/abdomen for the neck region; adult chest, chest/abdomen, lung nodule, thoracic aorta and child chest for the chest region and multiphase liver, bladder, abdomen, dynamic pancreas and pelvis for the abdomen region. All patients that underwent the selected CT imaging examinations during the data collection period (January to December 2016) were identified and included in this study. “CT Imaging Data Sheets” were available at each of the three CT scanners where this examinations were performed. Patient and exam information (e.g. age, sex, scan model and  $CTDI_{vol}$ ) were recorded by the radiologist and technologist responsible for the case. The data sheets were routinely collected from the scan room, and the data were recorded and analysed by diagnostic medical physicist and research fellows using an Excel<sup>®</sup> spreadsheet (Microsoft Corp., Redmond, WA). A total of three scanners used at our institution were included: one Biograph mCT (Siemens Medical Solutions, Inc., Forchheim, Germany), one Aquillion ONE (Toshiba Medical Systems, Inc., Otawara-shi, Japan) and one LightSpeed VCT (General Electric Medical Systems, Waukesha, WI). Our clinical practice evaluates image quality (e.g. noise and uniformity) as a function of scanner outputs and slice width (e.g. current-exposure time product and peak voltage). We then adjust our protocols accordingly, such that similar levels of image quality are produced in all of our scanners. In the cases where an examination was performed using a multiphase protocol, data were recorded for the phase that used the larger  $CTDI_{vol}$ . In all cases, only protocols using the same phantom size (16 or 32 cm) to compute the  $CTDI_{vol}$  were compared. Each scanner was randomly assigned an index

number, either 1, 2, or 3, and will be referred to by its assigned index from this point on.

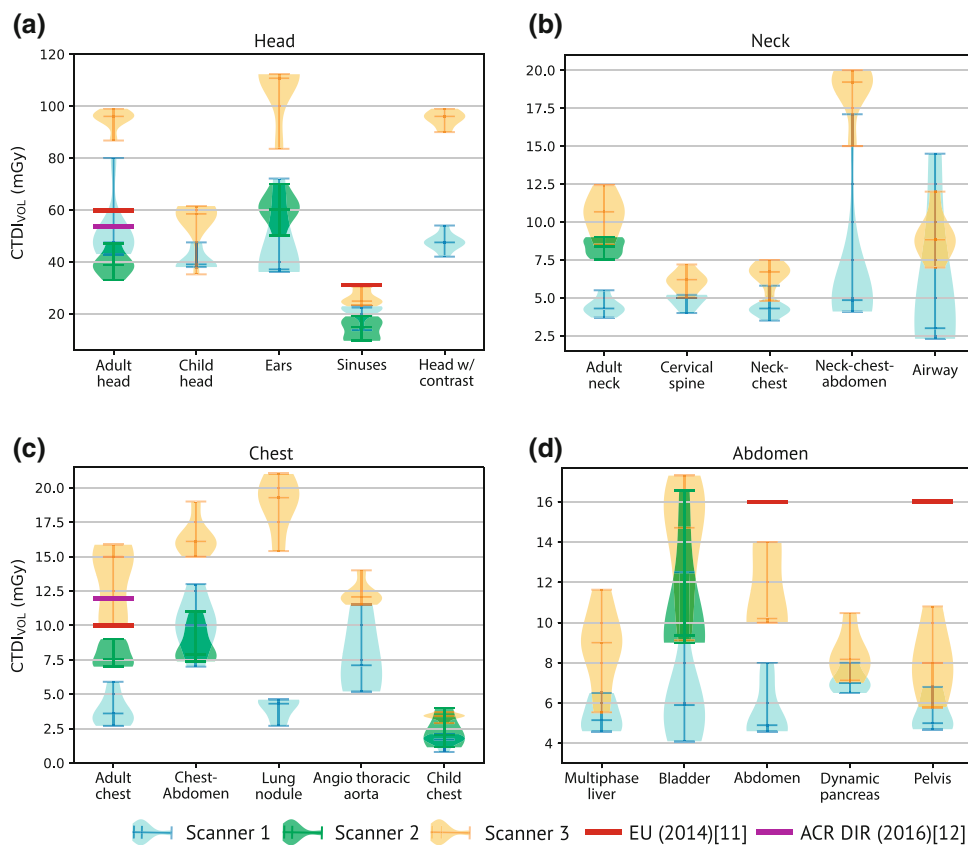
## 3 Results and Discussion

Between January and December 2016, 3157 patients underwent CT examinations resulting in 1289 head examinations, 79 neck examinations, 930 chest examinations and 859 abdomen examinations. 1981 male and 1176 females were included with an average age of  $50 \pm 19$  years (range, 0–97 years). Figure 1 shows the data distribution of  $CTDI_{vol}$  values for all three scanners. In each anatomic region, data distribution is displayed for a single CT examinations as beanplots with error bars showing the maximum and minimum values recorded as well as mean values (midline) for all protocols. The figure also shows DRL’s for selected protocols from the European Commission (EU) [11] and the American College of Radiology (ACR) [12]. DRL’s values (mGy) are 60, 31, 10 and 16 for the EU in adult head, sinuses, adult chest, abdomen and pelvis examinations respectively and 56 and 12 for the ACR in adult head and adult chest respectively. In some cases, the resulting  $CTDI_{vol}$  values obtained in scanner 2 for some examinations were not enough to be included in this study.

The maximum and minimum  $CTDI_{vol}$  (mGy) values registered for the selected protocols were 10.4–81.5, 5.4–70.2 and 24.9–112.7 in the head region (Fig. 1a), 2.1–17.2, 7.5–9.1 and 4.9–20.1 in the neck region (Fig. 1b), 1.1–13.2, 2.8–19.2 and 1.4–22.4 for the chest region (Fig. 1c) and 4.2–12.4, 9.1–16.5 and 5.6–17.6 for the abdomen region (Fig. 1d) in scanners 1, 2 and 3 respectively.

It can be seen from Fig. 1 that, for most protocols, there is a considerable difference in  $CTDI_{vol}$  values. For example,  $CTDI_{vol}$  values for head with contrast (Fig. 1a) from scanner 3 is approximately twice that of scanner 1. With the exception of protocols like sinuses, cervical spine, neck/chest, child chest and dynamic pancreas, this relatively large variation appears fairly consistent for other pairwise scanner comparisons across most protocols. The reason of this variations rely on the relatively large variation of our patients weight and chest-abdomen sizes in comparison to head sizes. Although this study did not include patients size and weight information and did not exclude any specialised examinations, we can conclude that the highest doses occur when scanning adult chest-abdomen regions of oversized (120-kg) patients, and the lowest doses when scanning paediatric patients. Scanner 3 delivered the highest doses indexes, by a relatively large margin for all protocols in terms of mean  $CTDI_{vol}$  values. Although data values recorded for head protocols show low variations in its distribution (Fig. 1a), this values are higher than any other

**Fig. 1** CTDI<sub>vol</sub> data distribution for all CT scanners displayed as beanplots for **a** head, **b** neck, **c** chest, and **d** abdomen regions. DRL's from the European Commission (solid lines) and the American College of Radiology (dashed lines) are also shown for selected CT examinations. In each case, the error bars show the maximum and minimum values recorded as well as the mean (midline) for each CT protocol



protocols due to the high radiation levels required for head imaging. As expected, patient weight is more important in determining mean CTDI<sub>vol</sub> values in body imaging than in head imaging.

Dose indexes values for scanner 2 are not enough to be compared with scanner 1, however, data distribution shows that these values are closer to scanner 2 than those of scanner 3. A drawback of our study is that we did not compare the choice of reconstruction algorithms, as its well know that the use of iterative reconstruction algorithms significantly reduce the mean CTDI<sub>vol</sub> values compared to the use of filtered back projection algorithms [13].

With the exception of adult head for scanner 3, all DRL's values compared were higher than mean CTDI<sub>vol</sub> values in our centre. Whilst there are no formal National DRL's with which to compare our results, data suggest that a future multi-institutional study providing National DRL's could show smaller values than those previously reported by the EU and ACR.

There has been increasing concern regarding the use of CTDI metrics in the CT physics community due to the ever-increasing collimated beam widths used in modern commercial CT scanners [10].

Multi-detector row CT systems have opened the field for other, as well as improved, applications. Radiation dose data indicate that manufacturers are focusing their efforts toward

improving image quality with reduced radiation doses compared with the doses required with the older-generation equipment in recognition of the idea that dose reduction has been an important issue for users in the past years. On the other hand, the ease and speed with which the CT systems with more advanced technology can be operated allow more use, and the exposure factors applied are usually higher than those actually required to acquire an image with diagnostic confidence.

DRL's and guidance levels in the basic safety standards [14] were produced before the introduction and clinical use of modern CT scanners. Therefore, the need to develop new values that account for such innovations seems valid. Continuing developments in CT scanner technology will no doubt further extend the indications for and scope of CT examinations. Ongoing clinical studies, similar to this one, to monitor associated patient doses can play a role in achieving excellent imaging at reasonable patient doses.

## 4 Conclusions

This study showed that there is a noticeable variation among modern MDCT scanners when considering CTDI<sub>vol</sub> values for similar CT protocols. Variation in dose indexes between and within specific protocols suggests room for improvement

with technique modification to balance image quality and radiation dose. Low-tube-voltage CT may be useful for reducing CT dose indexes and therefore, radiation doses among paediatric and adult patients.

Comparison of the results reported in our study and in other studies in the literature with the European and North American DRL's revealed the need for revision of these values. This need for revised dose values has arisen in part from the improved technology of the newer CT units that facilitates lower patient doses.

**Conflict of Interest** The authors declare that they have no conflict of interest.

## References

- Pandharipande, P V et al. (2015) CT in the emergency department: a real-time study of changes in physician decision making *Radiology* 278 3:812–821.
- The 2007 Recommendations of the International Commission on Radiological Protection. ICRP publication 103. *Ann ICRP* 37 2-4:1–332.
- US Food and Drug Administration (2010) Initiative to reduce unnecessary radiation exposure from medical imaging Center for Devices and Radiological Health.
- McNitt-Gray M F (2002) AAPM/RSNA physics tutorial for residents: topics in CT: radiation dose in CT *Radiographics* 22 6:1541–1553.
- Shope T B et al. (1891) A method for describing the doses delivered by transmission X-ray computed tomography *Med Phys* 8 4:488–495.
- Task Group on Control of Radiation Dose in Computed Tomography (2000) Managing patient dose in computed tomography *Ann ICRP* 30:7–45.
- International Commission on Radiological Protection (2000) Managing patient dose in computed tomography *Annals of the ICRP* 30 4:7–45.
- European Guidelines on Quality Criteria for Computed Tomography (1999) Report EUR 16262. Brussels, Belgium: European Commission.
- Boone J M (2007) The trouble with CTDI100 *Med Phys* 34 4:1364–1371.
- Brenner D J et al. (2006) It is time to retire the computed tomography dose index (CTDI) for CT quality assurance and dose optimization. *Med Phys* 33 5:1189–1191.
- European Commission (2014). Radiation Protection No. 180 Diagnostic reference levels in thirty-six European countries (Part2/2). EC website. Accessed December 4, 2017.
- Kanal, K. M., Butler, P. F., Sengupta, D., Bhargavan-Chatfield, M., Coombs, L. P., & Morin, R. L. (2017). US diagnostic reference levels and achievable doses for 10 adult CT examinations. *Radiology*, 284(1), 120–133.
- Matsunaga Y et al. (2015) Survey of volume CT dose index in Japan in 2014 *Brit J Radiol* 88 1052: 20150219.
- FAO, IAEA, NEMOECI ILO, and WHO PAHO (1996) International basic safety standards for protection against ionizing radiation and for the safety of radiation sources (IBSS) IAEA safety series 115.

# Comparative Sequence Assessment of Optimised T2 and T2\* Sequences for Quantification of Iron in Transfused Dependent Paediatric Sickle Cell Anaemia (SCA) Patients

Azza Ahmed<sup>1</sup>, Amani Baldo<sup>2</sup>, Hind Margani<sup>3</sup>, Ahmed Fatah<sup>4</sup>, Ibrahim Idris<sup>5</sup>, and Isam Salih<sup>6</sup>

## Abstract

Despite the fact that Sickle Cell Anaemia (SCA) patients undergo blood transfusion to reduce the risk of some complications associated with the disease, however, regular blood transfusion inevitably causes iron overload. In Sudan, the levels of iron in blood-transfused patients are regularly monitored using the serum ferritin, which is widely known to be an unreliable marker for body iron balance. The use of magnetic resonance imaging techniques such as the T2 and T2\* sequences have demonstrated promising results in estimating iron concentration in transfused dependent patients Wood (Blood 106:1460–1465, 2005, [1]). There is however little data on the literature that systematically compared T2 and T2\* in sickle cell anaemia (SCA) Wood (Am J Hematol 90:806–810, 2015, [2]). The aims of this work are to investigate two optimised T2 and T2\* sequences, determine their viability for the quantification of iron in transfused dependent SCA and compare them to the standard serum ferritin method. The two optimised sequences were subsequently investigated on livers of 10 volunteers and 25 SCA paediatric patients using a 1.5T Philips scanner located at Al Ateeba Hospital in Khartoum State-Capital of Sudan. Ethical approval for the study was obtained

from the National Ministry of Health-Health Research Council-Sudan. Linear correlation was found between T2\* and serum ferritin ( $R^2 = 0.949$ ,  $P < 0.001$ ), T2 and serum ( $R^2 = 0.946$ ,  $P < 0.001$ ) and T2 and T2\* measurements ( $R^2 = 0.921$ ,  $P = 0.789$ ). The results demonstrate that both of the optimised T2 and T2\* sequences could provide reliable measurements in the quantification of range of iron concentrations on transfused dependent paediatric SCA patients.

## Keywords

MRI • Iron concentrations • Sickle cell anaemia (SCA) Paediatric patients

## 1 Introduction

Anemic patients who undertake regular blood transfusion, such as those with sickle cell, thalassemia, aplastic anaemia, can develop iron overload in their organs such as the heart and liver [3, 4]. Excess iron in the body may be reversible by administration of iron chelating agents. Traditionally, chelation therapy is used when the ferritin levels exceed 1,000 ng/ml. Despite the improvement in therapeutic options, many patients however still die due to several other factors such as difficulties in assessing hepatic and cardiac iron overload and problems with long term compliance to treatment regimens [5].

Serum ferritin levels have historically and are still used clinically to estimate total amount of iron stored in the body [6, 7]. The studies been conducted on the measurements of plasma iron showed a high correlation was obtained between the serum ferritin and liver iron concentrations. Despite of this, other factors can influence the serum ferritin concentrations such as malnutrition, and vitamin C deficiency. Inflammation, disseminated malignancy and chronic

A. Ahmed (✉) · I. Idris · I. Salih  
Sudan Atomic Energy Commission, Al Gamah Street, 3001  
Khartoum, Sudan  
e-mail: azzasabo@hotmail.com

A. Baldo · H. Margani  
Jaffar Bin Auf Paediatric Hospital, Hospitals Road, Khartoum,  
Sudan

A. Fatah  
Al Ateeba Hospital, 37, Amarat Street, 907 Khartoum, Sudan

I. Idris  
College of Science, Al Imam Mohamed Ibn Saud Islamic  
University, 11642 Riyadh, Saudi Arabia

I. Salih  
Department of Physics, Taibah University, Almadinah  
Almunawara, 41477 Saudi Arabia

diseases can also cause large amount of ferritin to be release in the circulation, making a single elevated reading unreliable [8–11]. Another major drawback of the serum ferritin method is its lack of specificity and inter-patient variability.

The use of Magnetic Resonance Imaging (MRI) relaxation techniques to estimate liver iron concentrations has been studied for over 20 years [2]. The literature demonstrated great potential of the use of MRI because it is widely accessible, non-invasive and provides reproducible results [12, 13]. Accurate MRI measurements of the hepatic iron levels can further allow better diagnosis and management of the disease and will potentially improve the mortality rates in transfused dependent anemia patients. On the other hand, the accuracy of relaxometry measurements on subjects is affected by factors involving the acquisition techniques of the MRI images. Non-optimised protocols, presence of image artifacts, unawareness of variability of measurements and poor data analysis can all result in misleading diagnosis and inappropriate management of the treatment of patients with iron overload.

Several comparative sequence studies have been reported in the literature to assess the performance of T2 and T2\* MRI sequences in relation to the quantification of iron in patients. Much of the reported work involving comparative sequence testing was based on arbitrary and non-optimised settings and thus did not provide definitive assessments [14].

Without systematic optimisation of the existing sequences and identifying their performance limitations, it is for example difficult to discriminate between these sequences.

The general objective of the research is to identify the performance of optimized MRI techniques in the quantification of liver iron concentrations on transfusion dependent patients with sickle cell anemia, and to determine their feasibility of use for the first time in Sudan as an alternative technique to the standard serum ferritin method.

## 2 Materials and Method

### 2.1 Study Population

10 Health volunteers (15–20 years old, 3 Females/7males) and 25 patients (12–19 years old, 14 Females/11 males) were involved in both serum ferritin, and T2 and T2\* sequences measurements. All patients are currently admitted to the hospital and regularly receiver iron chelation treatment.

### 2.2 Serum Ferritin

The serum ferritin reagent was manufactured by Roche (REF 03737551190). Serum analysis was conducted by cobas e 411 device.

### 2.3 Magnetic Resonance Imaging

Livers of volunteers and patients were scanned using 1.5T Philips scanner located at Al Ateeba Hospital in Khartoum State, Capital of Sudan.

The T2-TSE parameters were determined as follow: 20 echoes (TE/ES: 4.4/4.4 ms), acquisition voxel =  $2 \times 2 \times 10$  mm; repetition time (TR) 245 ms, field of view (FOV) 25 cm, giving a matrix size of  $124 \times 125$ ; receiver bandwidth 1581.3 Hz, and an total acquisition time = 27 s. As for the T2\* sequence, the parameters were: 15 echo times (TE/ES: 3.7/1.7 ms); acquisition voxel =  $1 \times 1 \times 12$  mm; TR of 100 ms, FOV 25 cm, with a matrix size  $252 \times 250$ ; receiver bandwidth 148.2 Hz and a total acquisition time of 8 s.

Seven of the patients were not able to breath-hold, and thus respiratory triggering was implemented. The acquisition time obtained was 3 min and 21 s for T2, and 1 min and 12 s for T2\* sequence.

The new T2-TSE and T2\* sequences were previously optimised for four parameters which were: 1-Three different shim techniques (default, auto and volume); 2-Four pixel sizes (ranging between  $1 \times 1$  and  $4 \times 4$  mm); 3-Three slice thickness (8–12 mm); 4-Four repetition times (TR) (ranging between 100 to 500 ms) on gadolinium phantoms with different concentrations to mimic human subjects with wide range of iron concentrations, and also on volunteers. To validate the new sequences, their optimum levels of their four parametric performances were then tested on livers of the SCA paediatric patients and compared to the standard MRI acquisition parameters used at the hospital for both T2 and T2\* sequences.

The acquired images from each of the two sequences were analysed by drawing a circular region of interest (ROI) using a personally written Matlab code (version 2015b). From the phantom images, the ROI was chosen around each of the eight bottles, and for both the volunteers and patients' the ROI was chosen away from the vascular structure to avoid artefacts contribution from blood. Average



signal intensity of the pixels within the highlighted area was calculated for each of the acquired images on the series of increasing TE values. The signal intensities were then plotted versus their corresponding TEs from which exponential decay curves were derived. Magnitude measurements of T2 and T2\* values were calculated from the series of TE images using the following equation:

$$S = S_0 \exp^{-T2^*/TE} \quad (1)$$

where S is the final signal intensity measurement and  $S_0$  is the initial signal intensity measurement. TE is the echo time.

All data points at noise level were removed using the truncation method to provide more reproducible and accurate measurements.

## 2.4 Image Resolution Index

Image quality grading was utilized by assigning five points scale that was adapted from Willinek et. al. [15]. A score of 5 indicate excellent diagnostic quality that is, uniform contrast over the entire field of view, with no apparent artifacts or signal intensity variations. A score of 4 indicate good diagnostic quality with mild artifacts and/or signal intensity variations without impaired image interpretation. A score of 3 is assigned for moderate diagnostic quality—and artefact (s) and/or signal intensity variations interfere with image interpretation. A score of 2 indicate poor diagnostic quality—with noticeable artifacts and/or signal intensity variations, with questionable diagnostic quality. A score of 1 indicated non-diagnostic image quality.

## 3 Results and Discussion

Serum ferritin for the volunteers ranged from 5.5–86.8 ng/ml. For the patients the ferritin levels were 179–2000 ng/ml.

Figure 1a shows a rather linear decreased correlation between serum ferritin of all the studied subjects and T2 measurements. All data points are shown to be scattered around the fitted lines and appear polynomial ( $R^2 = 0.754$ ). However, it was noticed that for serum ferritin of 1000 ng/ml and above, this relationship becomes more linear. Figure 1b, shows more linear relationship between the serum ferritin measurements of above 1000 ng/ml and T2, with an improved correlation coefficient ( $R^2 = 0.946$   $P < 0.001$ ).

Figure 2a is a representation of the relation of the serum ferritin for all subjects (volunteers and patients) against their

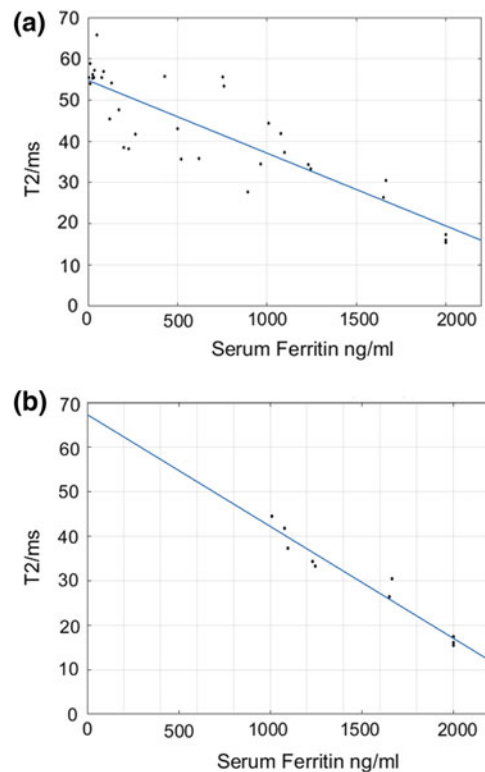


**Fig. 1** **a** Serum Ferritin versus T2 measurements for all subjects (volunteers and patients). **b** Serum Ferritin of Patients  $\geq 100$  ng/ml versus their corresponding T2 measurements

corresponding T2\* measurements. Data points are widely dispersed up to 1000 ng/ml ( $R^2 = 0.509$ ). This can be explained that T2\* cannot be measured accurately for low ferritin iron concentration below this value due to the limitations in the used echo time and echo spacing in the sequence. Also, the longest used TE should be approximately 2-fold longer than the longest T2\*, however, this is not always practical in part because T2\* images can degrade at longer TEs [16, 17]. In our situation the longest TE that was used was 27.5 ms which is shorter than the T2\* values recorded for normal volunteers.

In Fig. 2b, the relationship between the serum ferritin of values of 1000 ng/ml and above became more linear. The Figure demonstrates a significantly improved correlation coefficient ( $R^2 = 0.949$ ,  $P < 0.001$ ).

The comparative assessment between T2\* and T2 sequences for all subjects is shown on Fig. 3a. Early data points appear more scattered around the curve than the later ones ( $R^2 = 0.513$ ). For serum ferritin of 1000 ng/ml and above, there is a high agreement between the two sequences as represented in Fig. 3b ( $R^2 = 0.921$ ,  $P = 0.789$ ). This

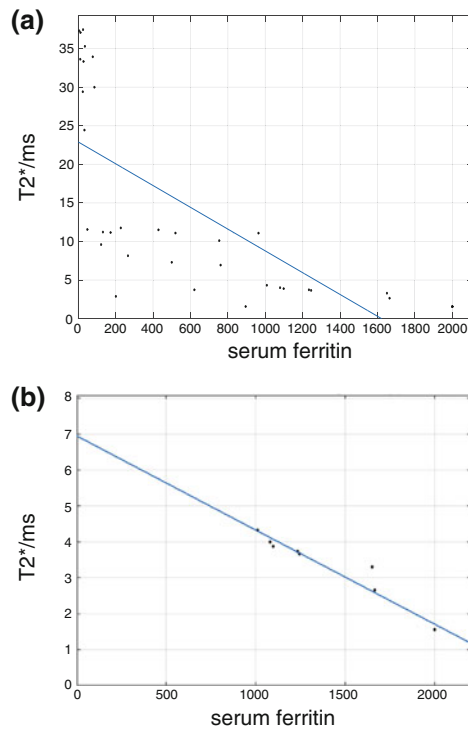


**Fig. 2** **a** Serum Ferritin versus T2\* measurements of all subjects (volunteers and patients). **b** Serum Ferritin of patients  $\geq 100$  ng/ml versus their corresponding T2\* measurements

result agrees with the finding of Wood JC et al. [2] that showed a high agreement between his studied R2 and R2\* values of 102 patients with iron overload (Their recorded R2 = 0.94).

Figures 4a and b are acquired images of the same sickle cell patient using the optimised T2 and T2\* sequences respectively.

Some of the T2-TSE images that were acquired appeared with artefacts (also known as banding artefact). Banding artefacts are caused by periodic trains of RF pulses which interfere with spin echoes and produce a pattern of fine lines. These were tested and found to be present for even longer TR of up to 500 ms. In the future, it has been suggested to use non-selective refocusing train to reduce on this banding artefact [18].

In 10 of the T2\* images, an artefact, caused by field inhomogeneity appeared in the stomach of the patients involved. This artefact were created by susceptibility effects secondary to bowel gas. Reducing TE in the future may reduce this effect.

Table (1) below presents the average image resolution index with the standard deviation for the 10 volunteers and 25 sickle cell patients.

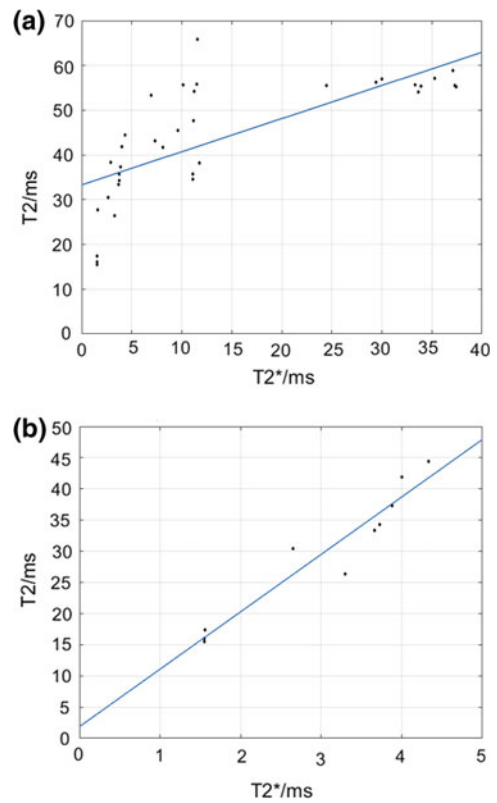


**Fig. 3** **a** T2\* versus T2 measurements of all subjects (volunteers and patients). **b** T2\* versus T2 measurements of patients with serum ferritin  $\geq 1000$  ng/ml

**Table 1**

T2-TSE (average rating $\pm$ SD)	T2* (average rating $\pm$ SD)
$3.77 \pm 1.011$	$3.45 \pm 0.801$

## 4 Conclusion

The results show good agreement between the serum ferritin and T2, serum ferritin and T2\*, and T2 and T2\* sequences. Our study did not include patients with known diseases such as malnutrition, and vitamin C deficiency, inflammation, or any known disease that could cause unreliability in the serum ferritin measurements. It would be interesting in the future to recruit larger population of patients, including patients with these conditions and understand more fully the effect their disease will have on the serum ferritin results. Another advantage of the MRI techniques is that while the serum ferritin method gives as indication of the quantity of iron on the overall body, MRI techniques can provide information about iron quantities and distribution of not only livers but also on the hearts and pancreas of transfused dependent patients. This may help on improving the overall



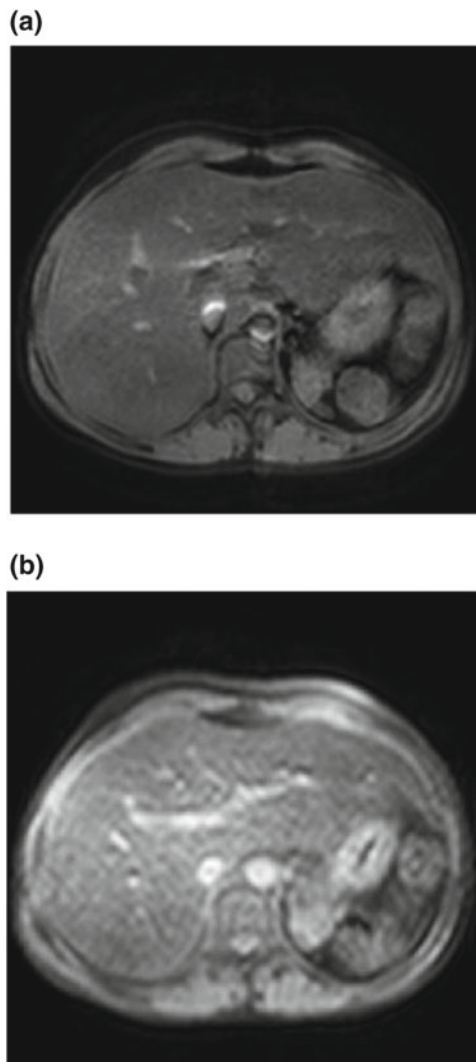


**Fig. 4** **a** Image of a patient acquired using T2-TSE sequence. **b** Image of the same patient acquired using T2\* sequence

treatment plans of patients and avoid the occurrence of siderosis and heart failure.

In conclusion, MRI techniques involving T2 and T2\* sequences provide reliable measurements and could be replaced by serum ferritin method, especially for ferritin values greater than 1000 ng/ml. Our new sequences provide adequate images with adequate acquisition time. Future studies will also include conducting T2 and T2\* measurements in higher population of sickle cell anemia patients and establish for the first time in Sudan a calibration curve between serum ferritin and these new sequences.

**Conflict of Interest** The authors declare there is no conflict of interest.

## References

1. Wood JC, Enriquez C, Ghugre NJ, Tyzka N, Carson S, Nelson MD, and Coates TD. MRI R2 and R2\* mapping accurately estimates hepatic iron concentration in transfusion-dependent thalassemia and sickle cell disease patients. *Blood* 2005;106:1460–1465.
2. Wood JC, Pressel S, Rogers ZR, Odame I, Kwiatkowski JL, Lee MT, Owen WC, Cohen AR, Pierre ST, Heeney MM, Schultz WH, Davis BR, Ware RE. Liver iron concentration measurements by MRI in chronically transfused children with Sickle Cell Anemia: Baseline Results from the TWITCH Trial. *Am J Hematol*. 2015;90:806–810.
3. Gordeuk VR, Bacon BR, Brittenham GM. Iron Overload: causes and consequences. *Annu Rev Nutr* 1987;7:485–508.
4. McLaren GD, Muir WA, Kellermeyer RW. Iron overload disorders: natural history, pathogenesis, diagnosis, and therapy. *Crit Rev Clin Lab Sci* 1983;19:205–66.
5. He T, Gatehouse PD, Anderson LJ, Tanner M, Keegan J, Pennell DJ, Firmin DN. Development of a novel optimized breath hold technique for myocardial T2 measurement in thalassemia. *J Magn Reson Imaging* 2006;24:580–585.
6. Brittenham G, Cohen A, McLaren C, et al. Hepatic iron stores in plasma ferritin concentration in patients with sickle cell anemia and thalassemia major. *Am. J. Hematol* 1993;42:81–85.
7. Prieto J, Barry M, Sherlock S. Serum ferritin in patients with iron overload and with acute and chronic liver diseases. *Gastroenterology* 1975;68:525–533.
8. Kolnagou A, Eracleous E, Economides Ch, Kontoghiorghes GJ. Low serum ferritin levels are misleading for detecting excess cardiac iron loading and increase of risk of cardiomyopathy in thalassemia patients. The importance of cardiac iron overload monitoring using magnetic resonance imaging T2 and T2\*. *Hemoglobin*. 2006;30:219–227.
9. Nielsen P, Gunther U, Durken M, Fischer R, Dullmann J. Serum ferritin iron in iron overload and liver damage: correlation to body iron stores and diagnostic relevance. *J Lab Clin Med* 2000;135(5):413–418.
10. Wood JC and Ghurge N. Magnetic resonance imaging assessment of excess iron in thalassemia, sickle cell disease and other overload diseases. *Hemoglobin*. 2008;32(1–2):85–96.
11. Correlation between serum ferritin levels and liver iron concentration determined by MR imaging: impact of hematologic disease and inflammation. *MagnReson Imaging*. 2007 Feb;25(2):228–31.
12. Modell B, Khan M, Darlison M, Westwood MA, Ingram D, Pennell DJ. Improved survival of thalassemia major in the UK and relation of T2\* cardiovascular magnetic resonance. *J. Cardiovascular Magnetic Resonance* 2008;10:42.
13. Isreal J, Unger E, Buetow K, Brown T, Blumberg B, London WT. Correlation between liver iron content and magnetic resonance imaging. *MagnReson Imaging* 1989;7:629–634.
14. Wood JC, Duessel MO, Auguilar M, Nick H, Nelson MD, Coates TD, Pollack H and Moates R. Cardiac Iron Determines Cardiac T2\*, T2 and T1 in the Gerbil Model of Iron Cardiomyopathy. *Circulation* 2005;112:535:543.
15. Willinek WA, Gieseke J, Kukuk GM, Nelles M, Konig R, Morakkabati-Spitz N, Traber F, Thomas D, Kuhl CK, Schild HH. Dual-source parallel radiofrequency excitation body MR imaging compared with standard MR imaging at 3.0 T: initial clinical experience *Radiology*. 2010;256(3):966–975. <https://doi.org/10.1148/radiol.10092127>.

16. Ghurge N.R, Enriquez C.M, Coates T.D, Nelson M.D, Wood J. C. Improved R2\* Measurements in Myocardial Iron Overload. *J MagnReson Imaging*. 2006; 23:9–16.
17. Positano V, Salani B, Pepe A, Santarelli MF, De Marchi D, Ramazzotti A, et al. Improved T2\* assessment in liver iron overload by magnetic resonance imaging. *MagnReson Imaging*. 2009;27:188–97.
18. He T, Gatehouse PD, Anderson LJ, Tanner M, Keegan J, Pennell DJ, Firmin DN. Development of a novel optimised breath hold technique for myocardial T2 measurement in thalassemia. *J Magn Reson Imaging* 2006;24:580–585.

# Quantitative Performance Evaluation of Mobile Cone-Beam CT for Head and Neck Imaging

Saowapak S. Thongvigitmanee<sup>✉</sup>, Walita Narkbuakaew<sup>✉</sup>, Sorapong Aootaphao<sup>✉</sup>, Chalinee Thanasupsombat<sup>✉</sup>, Kongyot Wangkaoom, Atthasak Kiang-ia, Jaturong Jitsaard, Thossapol Chunkiri, Puttisak Puttawibul, and Pairash Thajchayapong<sup>✉</sup>

## Abstract

Cone-beam computed tomography (CBCT) has become increasingly popular in dental and maxillofacial imaging due to its accurate 3D information, minimal radiation dose, and low machine cost. In this paper, we propose the newly developed mobile CBCT scanner which combines the benefits of CBCT and mobility to extend its applications to head and neck imaging and allow faster access to a patient at various clinical sites. With the large area detector, only a single rotation is needed to reconstruct the field-of-view of almost the entire head. Our filtered back-projection reconstruction and artifact reduction algorithms were based on a graphics processing unit to speed up the calculations. The quantitative performance was evaluated in terms of radiation doses and image quality. The radiation doses were measured using both CT dose index and dose area product (DAP) and compared with other CBCT and multi-slice CT (MSCT) machines. Then, we analyzed image quality using the standard cone-beam phantom. The effective doses radiated from the proposed mobile CBCT machine were within the range of 0.1–0.2 mSv, while the normalized DAP measurements were within the range

of 46–144 mGy cm<sup>2</sup>, which are significantly below the achievable dose of 250 mGy cm<sup>2</sup>. The overall image quality of the proposed scanner was mostly comparable to other MSCT and CBCT scanners. Geometric accuracy of the reconstructed images provided the errors less than 0.16 mm or 0.12%. Due to low radiation dose, high accuracy and adequate image quality as compared to others, the proposed mobile CBCT has high potential for diagnosis and treatment planning in head and neck applications.

## Keywords

Cone-beam CT • Image quality • Radiation dose

## 1 Introduction

Cone-beam CT (CBCT) has become increasingly popular in dental and maxillofacial applications due to its low cost, small machine size, and 3D data information [1, 2]. Unlike 2D radiography, CBCT can provide accurate 3D complete data without distortion and superposition of anatomical structures. Although typical medical CT scanners can be used for dental and maxillofacial applications, their radiation doses delivered to a patient are quite high [1, 2].

Following the first CBCT scanner made in Thailand for dental and maxillofacial applications, called DentiiScan [3–6], the mobile CBCT scanner called MobiiScan has also been researched and developed for the first time in Thailand to improve the affordability and availability of the mobile CBCT machines in the country. The advantage of low radiation exposure in CBCT still remains in this scanner. Due to its mobility purpose, it allows better and faster access to a patient at various clinical sites, for example, in the operating room for pre- and post-operation without moving a patient out of the operating room. At the moment, the proposed mobile CBCT scanner is aimed toward cranio-maxillofacial imaging, skull fractures and ENT (Ear, Nose, and Throat) applications.

S. S. Thongvigitmanee (✉) · W. Narkbuakaew · S. Aootaphao  
C. Thanasupsombat · K. Wangkaoom  
X-Ray CT and Medical Imaging Laboratory, Biomedical  
Electronics and Systems Research Unit, National Electronics  
and Computer Technology Center, Khlong Luang, 12120,  
Pathumthani, Thailand  
e-mail: saowapak.thongvigitmanee@nectec.or.th

A. Kiang-ia · J. Jitsaard · T. Chunkiri  
Medical Devices Laboratory, Biomedical Engineering Research  
Unit, National Metal and Materials Technology Center, Khlong  
Luang, 12120, Pathumthani, Thailand

P. Puttawibul  
Faculty of Medicine, Prince of Songkla University, Hat Yai,  
90112, Songkla, Thailand

P. Thajchayapong  
National Science and Technology Development Agency, Khlong  
Luang, 12120, Pathumthani, Thailand

Apart from the introduction of the new mobile CBCT machine, another aim of this work is to analyze its radiation doses and image quality as the first step before scanning human subjects. For radiation doses, we focus on both CTDI (computed tomography dose index) and DAP (dose area product) measurements [7, 8]. Image quality is evaluated using the standard cone-beam phantom in terms of high contrast resolution, uniformity, noise and geometric accuracy. Comparison with other CBCT and CT machines is studied as well.

## 2 Materials and Methods

### 2.1 The Proposed Mobile CBCT

The proposed mobile CBCT machine (MobiiScan) in Fig. 1 used a cone-shaped X-ray beam projecting toward a large X-ray flat panel detector located on the opposite site of the so-called gantry. This gantry system performed only one complete  $360^\circ$  rotation around a patient's head in the supine position to collect raw projection data at each angle. Our modified 3D cone-beam reconstruction process based on the FDK (Feldkamp-Davis-Kress) algorithm [9] together with scatter artifact reduction, truncation reduction and noise suppression was computed using a graphics processing unit (GPU) [3, 4] to rapidly reconstruct cross-section images with the maximum field-of-view (FOV) of 22.5 cm in diameter and 19 cm in height. A variety of preset configuration



**Fig. 1** The proposed mobile CBCT

protocols was available for both pediatric and adult protocols with the voxel size of 0.3–0.5 mm.

To acquire high quality 3D images, the flat panel detector used in this system was based on amorphous-silicon thin-film-transistor arrays coupled to a Cesium-Iodide (CsI) scintillator with the size of 40 cm  $\times$  30 cm. The reconstruction time required about 140–150 s. In addition to reconstruction, our in-house viewer software, called MobiiView, can display 3D reconstructed images in different 2D and 3D views. Three-dimensional surface and volume rendering of a patient's facial bones and skull can be quickly displayed from the volumetric data. Not only viewing the 3D images, the MobiiView provides a variety of tools to enhance visualization, diagnosis and treatment planning, such as distance/angle/density measurements, intensity-profile plotting, window/level adjustment, slice thickness adjustment, annotation, and matrix display.

### 2.2 Radiation Dose

In this study, CTDI and DAP measurements were considered. For CTDI, a 16-cm-diameter cylindrical CTDI phantom and an air ionization chamber (10  $\times$  6 – 0.6 CT, Radcal Corp., USA) in conjunction with a Radcal digitizer module (Accu-Gold +) were used. The factors to convert from dose-length product (DLP) to effective dose are equal to 0.0021 and 0.0040 to represent the adult head scan and the 5-year-old head scan, respectively. These CTDI measurements were compared with one CBCT machine, 3D Accuitomo 170 (Morita MFG. Corp., Japan), and one multi-slice CT machine, GE Discovery CT750HD (GE Medical Systems, USA). The DAP measurements were acquired from the DAP meter (DAPcheck Plus, Radcal Corp., USA). Furthermore, we normalized the doses to the beam area of 4  $\times$  4 cm<sup>2</sup> for comparison with others [7, 8].

### 2.3 Image Quality

An image quality phantom used in this study is the QRM cone-beam phantom produced by QRM GmbH, Germany. The diameter of the phantom imitates the typical size of a human head at 16 cm. The QRM phantom was scanned at different sections to cover high contrast resolution, uniformity, noise, and geometric sections. Like CTDI measurements, image quality was compared with other CBCT and MSCT scanners.

High contrast resolution was measured by reading bar patterns twice and one week apart via our viewer software, MobiiView. Uniformity and noise were automatically computed from five regions of interest at the center and peripheral areas by our in-house automated analysis

computer program over five consecutive image slices around the isocenter. Furthermore, linear measurements were performed using our in-house automated analysis program to automatically measure in the anterior-posterior and left-right directions for five consecutive image slices in each protocol. To measure geometric accuracy in the coronal plane, the QRM phantom was rotated by  $90^\circ$  such that the geometric section was appeared in the coronal view and distances in the top-bottom and left-right directions were measured. Likewise, to measure image accuracy in the sagittal plane, the similar process was applied and the top-bottom and

anterior-posterior directions were considered. All protocols were scanned, thus resulting in the total of 180 measurements for geometric accuracy.

### 3 Results

The settings of all different configuration protocols and scanners are shown in Table 1. It is noted that the GE MSCT was selected for the facial bone protocol and its FOV length was set to 18.8 cm to fairly compare its CTDI with the

**Table 1** Configuration protocols in CBCT and medical CT machines

Machine/Protocol	kV	mA	mAs	FOV (Dia × H)	Voxel/Pixel size (mm)
MobiiScan, Child Bone 0.3 mm	90	6	28.08	120 mm × 120 mm	0.3
MobiiScan, Child Bone 0.4 mm	90	6	28.08	160 mm × 168 mm	0.4
MobiiScan, Child Bone 0.5 mm	90	4	18.72	180 mm × 170 mm	0.5
MobiiScan, Adult Bone 0.3 mm	90	8	46.08	165 mm × 120 mm	0.3
MobiiScan, Adult Bone 0.4 mm	90	8	46.08	220 mm × 188 mm	0.4
MobiiScan, Adult Bone 0.5 mm	90	8	33.84	225 mm × 190 mm	0.5
Morita 3D Accuitomo 170 (CBCT)	80	5	87.5	170 mm × 120 mm	0.25
GE Discovery CT750HD (MSCT)	120	200	–	220 mm × 188 mm	0.43

**Table 2** Radiation dose calculations using CTDI and DAP

Machine/Protocol	CTDI <sub>vol</sub> (mGy)	DLP (mGy cm)	Effective dose (mSv)	Actual DAP (mGy cm <sup>2</sup> )	Normalized DAP (mGy cm <sup>2</sup> )
MobiiScan, Child Bone 0.3 mm	2.347	28.158	0.113	714.80	79.42
MobiiScan, Child Bone 0.4 mm	2.697	45.307	0.181	1343.00	79.00
MobiiScan, Child Bone 0.5 mm	1.817	30.892	0.124	887.90	46.43
MobiiScan, Adult Bone 0.3 mm	4.716	77.817	0.163	1834.00	143.84
MobiiScan, Adult Bone 0.4 mm	4.987	93.762	0.197	3302.00	126.39
MobiiScan, Adult Bone 0.5 mm	3.278	62.288	0.131	2193.00	80.29
Morita 3D Accuitomo 170 (CBCT)	9.356	112.272	0.236	–	–
GE Discovery CT750HD (MSCT)	85.144	1600.714	3.362	–	–

**Table 3** High contrast resolution, uniformity, and noise of different machines

Machine/protocol	High contrast res (lp/cm)	Deviation from center	% Cupping	Avg noise	% Noise
MobiiScan, Child Bone 0.3 mm	11.0	1.61	−0.16	63.21	6.37
MobiiScan, Child Bone 0.4 mm	8.5	−10.88	−1.10	64.88	6.51
MobiiScan, Child Bone 0.5 mm	7.0	13.10	1.33	49.04	5.04
MobiiScan, Adult Bone 0.3 mm	11.5	8.48	0.85	58.41	5.93
MobiiScan, Adult Bone 0.4 mm	9.0	−5.32	−0.55	57.12	5.85
MobiiScan, Adult Bone 0.5 mm	7.0	6.22	0.64	36.96	3.82
Morita 3D Accuitomo 170 (CBCT)	10.0	−80.90	−19.39	30.22	6.07
GE Discovery CT750HD (MSCT)	8.5	−4.93	−0.48	26.14	2.52

**Table 4** Geometric accuracy in the axial planes

Machine/protocol	Axial, L-R			Axial, A-P		
	Actual (mm)	Abs error (mm)	Error (%)	Actual (mm)	Abs error (mm)	Error (%)
MobiiScan, Child Bone 0.3 mm	100	0.10	0.10	100	0.09	0.09
MobiiScan, Child Bone 0.4 mm	140	0.06	0.04	140	0.08	0.06
MobiiScan, Child Bone 0.5 mm	140	0.03	0.02	140	0.04	0.02
MobiiScan, Adult Bone 0.3 mm	140	0.04	0.03	100	0.09	0.09
MobiiScan, Adult Bone 0.4 mm	140	0.06	0.04	140	0.06	0.05
MobiiScan, Adult Bone 0.5 mm	140	0.05	0.03	140	0.08	0.06
Morita 3D Accuitomo 170	140	0.74	0.53	140	0.73	0.52
GE Discovery CT750HD	140	0.10	0.07	140	0.08	0.05

**Table 5** Geometric accuracy in the coronal and sagittal planes

Machine/protocol	Coronal, L-R		Coronal, T-B		Sagittal, A-P		Sagittal, T-B	
	Abs error (mm)	Error (%)	Abs error (mm)	Error (%)	Abs error (mm)	Error (%)	Abs error (mm)	Error (%)
MobiiScan, Child Bone 0.3 mm	0.07	0.07	0.10	0.10	0.07	0.07	0.05	0.05
MobiiScan, Child Bone 0.4 mm	0.16	0.12	0.10	0.07	0.06	0.04	0.09	0.06
MobiiScan, Child Bone 0.5 mm	0.08	0.06	0.08	0.06	0.08	0.06	0.06	0.04
MobiiScan, Adult Bone 0.3 mm	0.08	0.08	0.09	0.09	0.05	0.05	0.02	0.02
MobiiScan, Adult Bone 0.4 mm	0.05	0.04	0.12	0.08	0.10	0.07	0.09	0.06
MobiiScan, Adult Bone 0.5 mm	0.10	0.07	0.12	0.08	0.06	0.04	0.07	0.05

“Adult Bone, 0.4 mm” protocol. Table 2 summarizes the CTDI and DAP measurements. The DAP measurements were normalized to the  $4 \times 4 \text{ cm}^2$  beam area for comparison to other machines. From the results, the normalized doses were between 46 and 144  $\text{mGy cm}^2$ , which are far below the proposed achievable dose of  $250 \text{ mGy cm}^2$  [7].

Table 3 shows the high contrast resolution, uniformity and noise of different CBCT and MSCT machines. The percentages of cupping and noise were compensated with the gray scale value of air ( $-1000$  for all except  $-150$  for the Morita). Tables 4 and 5 show geometric accuracy for six configuration protocols in six different directions. In addition, geometric accuracy of one CBCT and one MSCT was compared in the axial planes as shown in Table 4.

and image quality of the reconstructed images acquired from the machine. The MobiiScan machine provided much lower effective doses than the Morita CBCT and GE MSCT machines. Furthermore, the normalized DAP measurements confirms the low doses of the proposed mobile CBCT scanner. The overall image quality of the proposed scanner was mostly comparable to the GE MSCT and Morita CBCT scanners. The maximum geometric error was 0.16 mm or 0.12%, thus all protocols yielded high accuracy. The low radiation dose, high image quality and high accuracy results confirm that the proposed mobile CBCT scanner has the high potential to visualize high-contrast morphology for diagnosis and treatment planning in cranio-maxillofacial, skull fractures, and ENT applications.

## 4 Conclusions

This paper introduced a novel mobile CBCT scanner, MobiiScan, developed in Thailand. To ensure its radiation safety and performance, we investigated the radiation doses

## References

1. De Vos W, Casselman J, and Swennen GRJ. Cone-beam computerized tomography (CBCT) imaging of the oral and maxillofacial region. A systematic review of the literature. *Int J Oral Maxillofacial Surgery*. 2009;38:609–625.



2. Ludlow JB, and Ivanovic M. Comparative dosimetry of dental CBCT devices and 64-slices CT for oral and maxillofacial radiology. *Oral Surgery, Oral Medicine, Oral Pathology, Oral Radiology and Endodontology*. 2008;106(1):106–114.
3. Thongvigitmanee SS, Pongnapang N, Aootaphao S, Yampri, Srivongsa T, Sirisalee P, Rajruangrabin J, and Thajchayapong P. Radiation dose and accuracy analysis of newly developed cone-beam CT for dental and maxillofacial imaging. *Proc. of the IEEE Engineering in Medicine and Biology Society*. 2013;2356–2359. <https://doi.org/10.1109/embc.2013.6610011>.
4. Aootaphao S, Thongvigitmanee SS, Rajruangrabin J, Yampri P, Srivongsa T, and Thajchayapong P. Fast scatter correction for cone-beam computed tomography using the statistical method. *Proc. of the IEEE Nuclear Science Symposium and Medical Imaging Conference*. 2013. <https://doi.org/10.1109/nssmic.2013.6829350>.
5. Kosalagood P, Silkosessak OC, Pittayapat P, Pisarnurakit P, Pauwels R and Jacobs R. Linear measurement accuracy of eight cone beam computed tomography scanners. *Clinical Implant Dentistry and Related Research*. 2014;1–11. <https://doi.org/10.1111/cid.12221>.
6. Khongkhunthian P, Jomjunyong K, and Reichart PA. Accuracy of cone beam computed tomography for dental implant treatment planning. *CMU J Nat Sci* 2017;16(1):51–62.
7. Holroyd JR, and Walker A. Recommendations for the design of X ray facilities and the quality assurance of dental cone beam CT (computed tomography) systems—a report of the HPA working party on dental cone beam CT. HPA-RPD-065. Health Protection Agency; 2010.
8. Pauwels R, Theodorakou C, Walker A, Bosmans H, Jacobs R, Horner K, Bogaerts R, and The SEDENTEXCT Project Consortium. Dose distribution for dental cone beam CT and its implication for defining a dose index. *Dentomaxillofacial Radiology*. 2012;41(7):583–593.
9. Feldkamp LA, Davis LC, Kress JW. Practical cone-beam algorithm. *Journal of the Optical Society of America A* 1984;1(6):612–619.

# Prediction of Alzheimer's Disease in Mild Cognitive Impairment Using Sulcal Morphology and Cortical Thickness

Maciej Plocharski and Lasse Riis Østergaard  
for the Alzheimer's Disease Neuroimaging Initiative

## Abstract

Mild cognitive impairment (MCI) is an intermediate condition between healthy ageing and dementia. The amnesic MCI is often a high risk factor for subsequent Alzheimer's disease (AD) conversion. Some MCI patients never develop AD (MCI non-converters, or MCI<sub>nc</sub>), but some do progress to AD (MCI converters, or MCI<sub>c</sub>). The purpose of this study was to predict future AD-conversion in patients with MCI using machine learning with sulcal morphology and cortical thickness measures as classification features. 32 sulci per subject were extracted from 1.5T T1-weighted ADNI database MRI scans of 90 MCI<sub>c</sub> and 104 MCI<sub>nc</sub> subjects. We computed sulcal morphology features and cortical thickness measurements for support vector machine classification to identify structural patterns distinguishing future AD conversions. The linear kernel classifier trained with these features was able to predict 87.0% of MCI subjects as future converters, (89.7% sensitivity, 84.4% specificity, 0.94 AUC), using 10-fold cross-validation. These results using sulcal and cortical features are superior to the state-of-the-art methods. The most discriminating predictive features were observed in the temporal and frontal lobes in the left hemispheres, and in the entorhinal cortices, which is consistent with literature. However, we also observed structural changes in the cingulate and calcarine cortices, suggesting that the limbic and occipital lobe atrophy may be linked to AD conversion.

Data used in preparation of this article were obtained from the Alzheimer's Disease Neuroimaging Initiative (ADNI) database ([adni.loni.usc.edu](http://adni.loni.usc.edu)). As such, the investigators within the ADNI contributed to the design and implementation of ADNI and/or provided data but did not participate in analysis or writing of this report. A complete listing of ADNI investigators can be found at: [http://adni.loni.usc.edu/wp-content/uploads/how\\_to\\_apply/ADNI\\_Acknowledgement\\_List.pdf](http://adni.loni.usc.edu/wp-content/uploads/how_to_apply/ADNI_Acknowledgement_List.pdf).

M. Plocharski (✉) · L. R. Østergaard  
Department of Health Science and Technology, Aalborg University, Aalborg, Denmark  
e-mail: [mpl@hst.aau.dk](mailto:mpl@hst.aau.dk)

## Keywords

MRI • Alzheimer's disease • Mild cognitive impairment  
Sulcal morphology • Cortical thickness • SVM  
classification

## 1 Introduction

Early diagnosis of Alzheimer's disease (AD) is considered to have a great impact on developing treatment for AD. AD is a progressive neurodegenerative disorder, characterized by an accumulation of amyloid- $\beta$  deposits and hyperphosphorylated tau proteins in the brain, which leads to a gradual gray matter loss, a decline in cognitive functions, and eventually death. Some of the symptoms, such as short-term memory loss, coincide with mild cognitive impairment (MCI), widely regarded to be a transitional condition between normal ageing and dementia [1]. MCI is characterized by a cognitive decline greater than what is expected for a person's age and education level, but which does not significantly interfere with daily life [2]. Even though some MCI patients never develop AD, and some even return to normal over time, there is a significant risk of converting to AD. It is estimated that up to 50% of MCI individuals do indeed convert to AD within 5 years [2]. Amnesic MCI is therefore regarded as a substantial AD risk factor.

Magnetic resonance imaging (MRI) is an imaging modality used for diagnosing AD atrophy and monitoring its progression. The atrophy in the entorhinal cortex, the hippocampus, and the medial temporal lobe is the most principal characteristic of AD [3]. Decrease in the cortical thickness at the early stages of AD has been observed in the medial temporal lobe [4, 5], in the entorhinal and perirhinal cortices [6, 7]. Patterns of atrophy in the entorhinal cortex have also been observed in MCI [8]. Distinguishing AD from MCI using MRI has received a great amount of attention [9–12]. Numerous approaches using structural



imaging for predicting conversion to AD have been suggested [9, 10, 12, 13]. Querbes et al. [9] built feature vectors for classification with mean thickness values of neuroanatomical cortical regions. Eskildsen et al. [10, 12] used cortical thickness patterns to predict AD in MCI subjects by identifying cortical regions discriminative for separating MCI converters from non-converters. Misra et al. [13] defined statistically different brain regions, which were highly discriminating between MCI converters and non-converters.

Morphology of the cerebral sulci had been shown to be a promising neurological biomarker in AD and MCI. Sulcal depth reductions [14, 15] and an increase in sulcal width [14, 16] due to gray matter atrophy and cortical thickness reduction have been observed in AD. The purpose of this study was to combine sulcal features and cortical thickness measures to distinguish between MCI converters and non-converters and investigate the ability of such features to predict AD.

## 2 Methods

### 2.1 Data

Data used in the preparation of this article were obtained from the Alzheimer’s Disease Neuroimaging Initiative (ADNI) database (adni.loni.usc.edu). The ADNI was launched in 2003 as a public-private partnership, led by Principal Investigator Michael W. Weiner, MD. The primary goal of ADNI has been to test whether serial magnetic resonance imaging (MRI), positron emission tomography (PET), other biological markers, and clinical and neuropsychological assessment can be combined to measure the progression of mild cognitive impairment and early Alzheimer’s disease.

360 1.5T pre-processed T1-weighted MP-RAGE MRI scans were obtained from the ADNI database. The scans consisted of 85 cognitively normal subjects (CN), 90 MCI subjects who later converted to AD (referred to as MCI converters, or MCIC), 104 MCI subjects who remained stable (MCI non-converters, or MCInc), and 81 AD patients. The CN group consisted of healthy controls without significant impairment in cognitive functions. The AD subjects had been scanned 24 months after the AD diagnosis. We selected the MCIC subjects from the ADNI database at 12 months prior to the AD-conversion diagnosis. The ADNI database contains MRI scans of MCI subjects scanned at baseline, after 6 months, 12 months, 18 months, 24 months, 36 months, and 48 months. A clinical diagnosis was made at each of these time points to identify MCI subjects who converted to AD.

The MCIC subject group used in this study consisted of scans at baseline ( $n = 27$ ), 6 months ( $n = 24$ ), 12 months ( $n = 26$ ), 18 months ( $n = 12$ ), and 24 months ( $n = 1$ ). The MCInc group consisted of 104 scans of subjects who did not

**Table 1** Demographic characteristics of the subjects included in this study. Age, Mini-Mental State Exam (MMSE) score, and Clinical Dementia Rating (CDR) are represented as mean values and their standard deviations

	CN	AD	MCIC	MCInc
Number	85	81	90	104
Male/female	47/38	40/41	53/37	64/40
Average age (years)	$76.1 \pm 5.0$	$77.8 \pm 7.5$	$75.8 \pm 6.5$	$75.7 \pm 7.7$
MMSE (score)	$29.0 \pm 1.1$	$19.3 \pm 5.3$	$26.2 \pm 2.2$	$27.2 \pm 1.9$
CDR	$0.0 \pm 0.0$	$1.32 \pm 0.6$	$0.5 \pm 0.0$	$0.5 \pm 0.0$

progress to AD over the course of the ADNI study. Table 1 shows the subjects’ demographic characteristics. The general inclusion criteria for the groups were: *Cognitively normal controls*: MMSE score: 24–30 (inclusive), CDR: 0; non-depressed, non-demented, with no MCI. *Mild cognitive impairment*: MMSE score: 24–30 (inclusive), CDR: 0.5, general cognition and functional performance sufficiently preserved so that an AD diagnosis could not be made at the time of the visit. *Alzheimer’s disease*: MMSE score: 20–26 (inclusive), CDR: 0.5 or 1.0; subjects met NINCDS/ADRDA criteria for probable AD.

### 2.2 Feature Extraction, Selection and Classification

32 cortical sulci (Fig. 1) were extracted from the T1-weighted MR images in BrainVISA 4.4.0, a fully automatic anatomical segmentation pipeline, which recognizes, labels and extracts cortical sulci. The images had been normalized and resampled to  $1 \text{ mm}^3$  voxels in SPM12 (Statistical Parametric Mapping software package). Sulcal morphology features were computed for each sulcal mesh using MATLAB R2016b (described in detail in our previous study [15]). In total, 320 sulcal morphology features were extracted from each subject: sulcal depth, length, mean curvature, mean Gaussian curvature, medial surface area. Regional cortical thickness measurements were generated with FreeSurfer, version 5.3.0.

Feature selection was performed by means of forward selection, where each iteration of either adding to or removing a feature from the SVM classifier was evaluated on the classification accuracy and a balance index  $B$  of 0.4 [17]. The balance index, defined by Eq. 1, permits feature extraction that maximize the classification accuracy and at the same time maintains a low difference between the true positives and true negatives in each group. Feature normalization was applied to rescale the features to the range of [0, 1]. SVM classifiers with linear and a Gaussian radial basis function kernel were chosen, due to their performance in

**Fig. 1** The 32 cortical sulci extracted from the 360 subjects in BrainVISA 4.4.0 for the subsequent sulcal feature extraction and classification

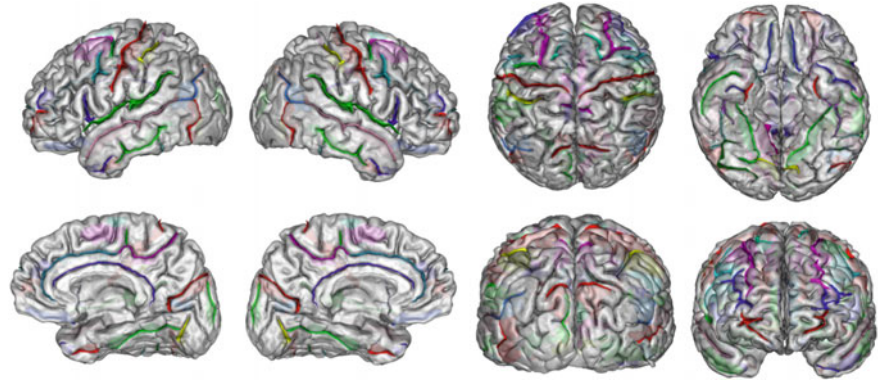


**Table 2** Classification results obtained with the feature selection distinguishing MCIc from MCInc

Classification	Accuracy		Sensitivity		Specificity		AUC	
	Linear	Gaussian	Linear	Gaussian	Linear	Gaussian	Linear	Gaussian
	SVM (%)	SVM (%)	SVM (%)	SVM (%)	SVM (%)	SVM (%)	SVM	SVM
MCIc versus MCInc	87.0	84.2	89.7	82.3	84.4	86.7	0.94	0.92
CN versus AD	86.7	86.8	80.4	82.0	92.6	92.0	0.97	0.97
MCInc versus AD	80.1	75.2	88.4	81.6	68.5	65.6	0.87	0.87
MCIc versus AD	76.2	73.5	84.6	79.0	65.6	67.0	0.85	0.85
MCInc versus CN	68.7	73.0	79.0	80.0	56.8	63.9	0.77	0.76
MCIc versus CN	83.4	79.0	88.9	90.0	77.5	66.8	0.95	0.94

classifying AD in high dimensional feature spaces [17, 18]. Each feature was separately tested for inclusion in the model with a 10-fold cross-validation. The best feature was identified, then added to the model, and all the remaining features were individually tested in conjunction with the previously selected feature, until the classification accuracy would no longer increase.

$$B = \frac{|(1 - \text{Specificity}) - (1 - \text{Sensitivity})|}{|(1 - \text{Specificity}) + (1 - \text{Sensitivity})|} \quad (1)$$

### 3 Results

The selected features ( $n = 22$ ) provided the highest MCIc versus MCInc classification accuracy of 87.0%, 89.7% sensitivity, and 84.4% specificity, with an AUC of 0.94, were obtained with the linear kernel SVM. The same anatomical feature combination was applied for the 10-fold cross-validated classifications: CN versus AD, MCInc versus AD, MCIc versus AD, MCInc versus CN, and MCIc versus CN. These classification results are shown in Table 2. Figure 2 illustrates the ROC curves for the six classifications using the features selected in the MCIc versus MCInc classification. The temporal lobe was the most discriminating anatomical region, where discriminating features were

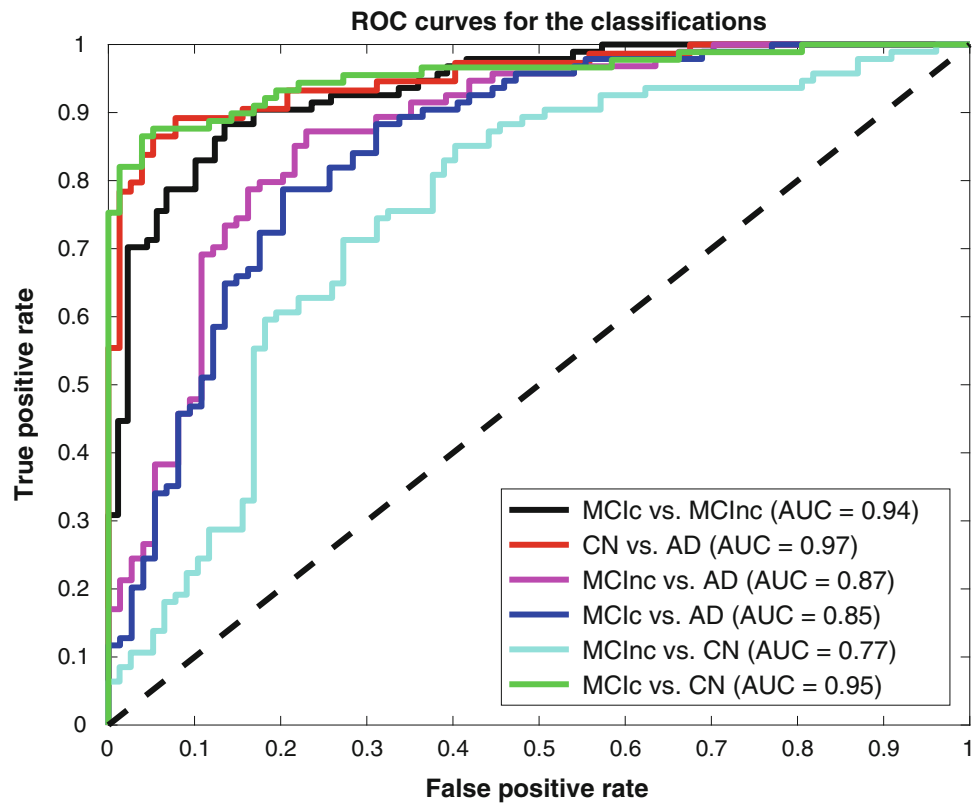
selected both from the cortical regions and from the sulci located either in the temporal lobe, or between the temporal and occipital lobes. We observed cortical thickness reductions in MCIc subjects in the temporal and frontal cortices (middle temporal gyrus, orbital operculum, caudal middle frontal gyrus, medial orbitofrontal cortex), as well as in the entorhinal cortex. Structural changes were also present in the cingulate and calcarine cortices in the form of reductions in sulcal depth (calcarine sulcus) and in cortical thickness (pericalcarine cortex, caudal anterior cingulate, isthmus of cingulate cortex).

### 4 Discussion

The purpose of this paper was to use sulcal morphology features and cortical thickness measurements for classification of MCI converters and non-converters. We previously showed that sulcal features can successfully be used for classification of AD [15, 19]. It was hypothesized that features distinguishing MCIc from MCInc can be successfully applied to classify AD from CN.

The MCIc versus MCInc classification resulted in 87.0% accuracy, 89.7% sensitivity, and 84.4% specificity, with an AUC of 0.94, obtained with a linear kernel SVM. Zheng et al. [20] extracted correlative features from MR images and achieved a 79.37% accuracy with a combination of cortical

**Fig. 2** The ROC curves for the six classifications using the linear kernel SVM and the features selected in the MCIc versus MCIc classification



thickness measurements and apolipoprotein information. Eskildsen et al. [10] used cortical thickness patterns for predicting AD in MCI subjects. They obtained a 72% accuracy for AD-conversion in MCI subjects selected at 12 months prior to AD diagnosis [10]. Eskildsen et al. [21] showed the accuracy to improve as the time to AD-conversion from MCI decreased, from 70% at 3 years before AD diagnosis, to 76% at 6 months. Misra et al. [13] achieved a high cross-validated classification accuracy of 81.5%, using statistically different brain regions to differentiate MCIc and MCIc. However, caution must be taken while comparing our results to literature. 10-fold cross-validation is a well-established statistical method for validating a predictive model by partitioning the original data into a training set to train the model, and a test set to evaluate its classification performance due to absence of sufficient amounts of data to separately test the performance of the classifier. We therefore acknowledge that these results may be more biased than if a separate test dataset was available.

Accuracy of 86.7% was obtained for CN versus AD classification, using the features discriminating MCIc from MCIc. The selected features were mostly identified in the temporal lobe (thickness of the middle temporal gyrus, the entorhinal cortex, sulcal features from the collateral fissure or the posterior occipito-temporal lateral sulcus), but also in parietal, frontal, occipital, and limbic nodes. The same feature combination has been used for the classifications of

MCIc versus AD, MCIc versus AD, MCIc versus CN, and MCIc versus CN. The atrophic patterns reflected in the selected features provided high accuracies for the MCIc versus AD (80.1%) and MCIc versus CN (83.4%), which were not unexpected for these two classification scenarios. However, we also obtained relatively high accuracies for MCIc versus AD (76.2%) and MCIc versus CN (68.7%) classifications, where one would not expect to detect notable changes in the degree of brain atrophy. The most discriminating features for AD prediction were selected from the entorhinal cortices, and from the temporal and frontal lobes. The left hemisphere was more affected by atrophy in MCIc. Atrophy in these regions is consistent with AD and MCI studies. However, the observed structural changes in the cingulate and calcarine cortices may suggest that the atrophy in the limbic and occipital lobes may be one of the underlying causes of conversion from amnesic MCI to AD.

There are some potential limitations to this study. Although the classification based on sulcal and cortical thickness features demonstrated promising results, the method is limited by the relatively low number of converter and non-converter subjects, necessitating the use of cross-validation. Moreover, in this paper the term “AD conversion” was applied to an MCI subject who fulfilled the AD diagnostic criteria at a subsequent clinical visit. We selected the MCIc subjects from the ADNI database at 12 months

prior to the conversion diagnosis. Progression from MCI to the state where a patient fulfills the AD diagnostic criteria is a gradual decline, not instantaneous. Thus, the actual stage of the disorder can be expected to vary between patients at the time of the AD diagnosis. Moreover, a similar uncertainty can be expected from the term "MCI non-converter". The MCInc group consisted of participants who maintained the MCI diagnosis during the course of the ADNI study. However, we cannot exclude the possibility that those subjects did later progress to AD after study conclusion.

**Acknowledgements** Support for this research was provided by The Lundbeck Foundation. Data collection and sharing for this project was funded by the Alzheimer's Disease Neuroimaging Initiative (ADNI) (National Institutes of Health Grant U01 AG024904) and DOD ADNI (Department of Defense award number W81XWH-12-2-0012). ADNI is funded by the National Institute on Aging, the National Institute of Biomedical Imaging and Bioengineering, and through generous contributions from the following: AbbVie, Alzheimer's Association; Alzheimer's Drug Discovery Foundation; Araclon Biotech; BioClinica, Inc.; Biogen; Bristol-Myers Squibb Company; CereSpir, Inc.; Eisai Inc.; Elan Pharmaceuticals, Inc.; Eli Lilly and Company; EuroImmun; F. Hoffmann-La Roche Ltd and its affiliated company Genentech, Inc.; Fujirebio; GE Healthcare; IXICO Ltd.; Janssen Alzheimer Immunotherapy Research & Development, LLC.; Johnson & Johnson Pharmaceutical Research & Development LLC.; Lumosity; Lundbeck; Merck & Co., Inc.; Meso Scale Diagnostics, LLC.; NeuroRx Research; Neurotrack Technologies; Novartis Pharmaceuticals Corporation; Pfizer Inc.; Piramal Imaging; Servier; Takeda Pharmaceutical Company; and Transition Therapeutics. The Canadian Institutes of Health Research is providing funds to support ADNI clinical sites in Canada. Private sector contributions are facilitated by the Foundation for the National Institutes of Health ([www.fnih.org](http://www.fnih.org)). The grantee organization is the Northern California Institute for Research and Education; the study is coordinated by the Alzheimer's Disease Cooperative Study at the University of California, San Diego. ADNI data are disseminated by the Laboratory for Neuro Imaging at the University of Southern California.

**Conflict of Interest** The authors declare that they have no conflict of interest.

## References

- Morris, J.C. and Cummings, J., 2005. Mild cognitive impairment (MCI) represents early-stage Alzheimer's disease. *Journal of Alzheimer's Disease*, 7(3), pp. 235–239.
- Gauthier, S., Reisberg, B., Zaudig, M., Petersen, R.C., Ritchie, K., Broich, K., Belleville, S., Brodaty, H., Bennett, D., Chertkow, H. and Cummings, J.L., 2006. Mild cognitive impairment. *The Lancet*, 367(9518), pp. 1262–1270.
- Chan, D., Fox, N.C., Scahill, R.I., Crum, W.R., Whitwell, J.L., Leschziner, G., Rossor, A.M., Stevens, J.M., Cipelotti, L. and Rossor, M.N., 2001. Patterns of temporal lobe atrophy in semantic dementia and Alzheimer's disease. *Annals of neurology*, 49(4), pp. 433–442.
- Jack, C.R., Petersen, R.C., Xu, Y., O'Brien, P.C., Smith, G.E., Ivnik, R.J., Tangalos, E.G. and Kokmen, E., 1998. Rate of medial temporal lobe atrophy in typical aging and Alzheimer's disease. *Neurology*, 51(4), pp. 993–999.
- Cho, H., Jeon, S., Kang, S.J., Lee, J.M., Lee, J.H., Kim, G.H., Shin, J.S., Kim, C.H., Noh, Y., Im, K. and Kim, S.T., 2013. Longitudinal changes of cortical thickness in early-versus late-onset Alzheimer's disease. *Neurobiology of aging*, 34(7), pp. 1921–e9.
- Braak, H. and Braak, E., 1991. Neuropathological staging of Alzheimer-related changes. *Acta neuropathologica*, 82(4), pp. 239–259.
- Krumm, S., Kivisaari, S.L., Probst, A., Monsch, A.U., Reinhardt, J., Ulmer, S., Stippich, C., Kressig, R.W. and Taylor, K.L., 2016. Cortical thinning of parahippocampal subregions in very early Alzheimer's disease. *Neurobiology of aging*, 38, pp. 188–196.
- Cho, Y., Seong, J.K., Jeong, Y., Shin, S.Y. and Alzheimer's Disease Neuroimaging Initiative, 2012. Individual subject classification for Alzheimer's disease based on incremental learning using a spatial frequency representation of cortical thickness data. *Neuroimage*, 59(3), pp. 2217–2230.
- Querbes, O., Aubry, F., Pariente, J., Lotterie, J.A., Démonet, J.F., Duret, V., Puel, M., Berry, I., Fort, J.C., Celsis, P. and Alzheimer's Disease Neuroimaging Initiative, 2009. Early diagnosis of Alzheimer's disease using cortical thickness: impact of cognitive reserve. *Brain*, 132(8), pp. 2036–2047.
- Eskildsen, S.F., Fonov, V., Coupé, P., Østergaard, L.R. and Collins, D.L., 2011. Prediction of Alzheimer's disease in subjects with mild cognitive impairment using structural patterns of cortical thinning. In 15th Nordic-Baltic Conference on Biomedical Engineering and Medical Physics (NBC 2011) (pp. 156–159). Springer, Berlin, Heidelberg.
- Westman, E., Muehlboeck, J.S. and Simmons, A., 2012. Combining MRI and CSF measures for classification of Alzheimer's disease and prediction of mild cognitive impairment conversion. *Neuroimage*, 62(1), pp. 229–238.
- Eskildsen, S.F., Coupé, P., Fonov, V.S., Pruessner, J.C. and Collins, D.L., 2015. Structural imaging biomarkers of Alzheimer's disease: predicting disease progression. *Neurobiology of aging*, 36, pp. S23–S31.
- Misra, C., Fan, Y. and Davatzikos, C., 2009. Baseline and longitudinal patterns of brain atrophy in MCI patients, and their use in prediction of short-term conversion to AD: results from ADNI. *Neuroimage*, 44(4), pp. 1415–1422.
- Im, K., Lee, J.M., Seo, S.W., Kim, S.H., Kim, S.I. and Na, D.L., 2008. Sulcal morphology changes and their relationship with cortical thickness and gyral white matter volume in mild cognitive impairment and Alzheimer's disease. *Neuroimage*, 43(1), pp. 103–113.
- Plocharski, M., Østergaard, L.R. and Alzheimer's Disease Neuroimaging Initiative, 2016. Extraction of sulcal medial surface and classification of Alzheimer's disease using sulcal features. *Computer methods and programs in biomedicine*, 133, pp. 35–44.
- Hamelin, L., Bertoux, M., Bottlaender, M., Corne, H., Lagarde, J., Hahn, V., Mangin, J.F., Dubois, B., Chupin, M., De Souza, L.C. and Colliot, O., 2015. Sulcal morphology as a new imaging marker for the diagnosis of early onset Alzheimer's disease. *Neurobiology of aging*, 36(11), pp. 2932–2939.
- Garde, A., Voss, A., Caminal, P., Benito, S. and Giraldo, B.F., 2013. SVM-based feature selection to optimize sensitivity–specificity balance applied to weaning. *Computers in biology and medicine*, 43(5), pp. 533–540.
- Cai, K., Xu, H., Guan, H., Zhu, W., Jiang, J., Cui, Y., Zhang, J., Liu, T. and Wen, W., 2017. Identification of early-stage Alzheimer's disease using sulcal morphology and other common neuroimaging indices. *PloS one*, 12(1), p.e0170875.
- Andersen, S.K., Jakobsen, C.E., Pedersen, C.H., Rasmussen, A. M., Plocharski, M. and Østergaard, L.R., 2015. June. Classification of Alzheimer's disease from MRI using sulcal morphology. In

- Scandinavian Conference on Image Analysis (pp. 103–113). Springer, Cham.
20. Zheng, W., Yao, Z., Hu, B., Gao, X., Cai, H. and Moore, P., 2015. Novel cortical thickness pattern for accurate detection of Alzheimer's disease. *Journal of Alzheimer's Disease*, 48(4), pp. 995–1008.
  21. Eskildsen, S.F., Coupé, P., García-Lorenzo, D., Fonov, V., Pruessner, J.C., Collins, D.L. and Alzheimer's Disease Neuroimaging Initiative, 2013. Prediction of Alzheimer's disease in subjects with mild cognitive impairment from the ADNI cohort using patterns of cortical thinning. *Neuroimage*, 65, pp. 511–521.



# Effect of Elimination of Noisy ECG Leads on the Noninvasive Localization of the Focus of Premature Ventricular Complexes

Elena Deutsch<sup>✉</sup>, Jana Svehlikova<sup>✉</sup>, Milan Tysler<sup>✉</sup>, Pavel Osmancik<sup>✉</sup>,  
Jana Zdarska<sup>✉</sup>, and Peter Kneppo

## Abstract

High frequency of the premature ventricular complexes (PVCs) can lead to the development of the left ventricular dysfunction. Preoperative noninvasive localization of the PVC focus can decrease the time of the invasive electrophysiological study and improve the success rate of the radiofrequency ablation. Body surface potential (BSP) maps, patient-specific inhomogeneous torso model and inverse solution in terms of single dipole model were used for noninvasive localization of the PVC focus in five patients. BSP maps were computed for the initial 20 ms time interval of the ventricular activation (QRS complex in the ECG) from five selected PVCs in each patient. The inhomogeneous torso model included surfaces of torso, lungs, heart cavities and outflow tracts. To investigate whether the exclusion of the noisy ECG leads improves the accuracy of the inverse solution, the leads with the signal-to-noise ratio (SNR) less than the defined threshold value were excluded from the inverse computations. Four levels of the SNR were defined: 10, 20, 30, 40 dB. Locations of the PVC foci were computed by the inverse solution and compared with the catheter positions during successful radiofrequency ablation performed within invasive electrophysiological study. Removal of noisy ECG leads did not improve the PVC localization when the noisy ECG leads were located in left anterior torso region.

## Keywords

Body surface potential mapping • Inverse problem of electrocardiography • Premature ventricular complexes  
Ectopic activity • Noninvasive localization

## 1 Introduction

Premature ventricular complexes (PVCs) in patients with underlying chronic structural disease increase the risk of sudden cardiac death and total cardiac death. The PVC focus can be located anywhere in the ventricles and adjacent structures. Usually, anti-arrhythmic therapy is used in these patients. However, when the patient does not respond to the pharmacological treatment, a catheter radiofrequency ablation (RFA) is performed during the invasive electrophysiological (EP) study. Accurate localization of the PVC focus is highly important for successful RFA [1]. Therefore, a preoperative noninvasive estimation of the PVC focus location using a novel method of electrocardiographic imaging [2, 3] can decrease the time of the invasive EP procedure and improve the ablation success rate.

This novel method requires solution of the inverse problem of electrocardiography, which uses multiple ECG leads signals to compute BSP maps representing the electrical activity of the heart, realistic 3D torso model and a model representing the cardiac electrical generator. Because the inverse problem is ill-posed slight inaccuracies or disturbances of the input data might lead to significant changes in the obtained inverse results [4]. Therefore, we can suspect that noisy ECG signals can lead to faulty results of the inverse solution. In this study we will evaluate whether exclusion of the noisy leads can improve the accuracy of the inverse solution.

E. Deutsch (✉) · M. Tysler · P. Kneppo  
Czech Technical University in Prague, nam. Sitna 3105, 27201  
Kladno, Czech Republic  
e-mail: elena.deutsch@fbmi.cvut.cz

J. Svehlikova · M. Tysler  
Institute of Measurement Science SAS, Dubravska Cesta 9, 84104  
Bratislava, Slovakia

P. Osmancik · J. Zdarska  
University Hospital Kralovske Vinohrady, Charles University and  
Cardiocenter, Srobarova 50, 10034 Prague, Czech Republic

## 2 Materials and Methods

The study population consisted of two male (Pat004—77Y, Pat006—51Y) and three female (Pat005—43Y, Pat007—54Y, Pat009—74Y) patients with frequent PVCs. The study complied with the Ethical Principles for Medical Research Involving Human Subjects as stated in the Declaration of Helsinki and received approval from the Ethic Committee of the University Hospital Kralovske Vinohrady, where the data were collected after obtaining written informed consent from the study participants.

All patients underwent BSP mapping, full torso computed tomography (CT) scanning and intracardiac EP study.

### 2.1 Body Surface Potential Mapping

High-resolution multichannel ECG system ProCardio-8 [5] was used to record ECGs and compute integral BSP maps. Disposable pre-gelled Ag/AgCl electrodes with active adapters were applied to record limb leads and 96 chest leads. Chest electrodes were evenly distributed over the torso and organized in 12 strips of 8 electrodes. The sampling frequency was 1 kHz, data resolution was 16 bit. The ECG recording time was up to 10 min.

Processing of the multichannel ECGs to obtain BSP maps included baseline correction by applying the Lynn's high-pass filter [6]. In each patient five PVCs were chosen for further analysis.

In order to study the effect of the noisy leads removal on the inverse solution, assessment of the present noise had to be performed. For each PVC, the noise in the signal was evaluated as follows: (1) time interval with no physiological signal (amplitude close to zero), usually during the compensatory pause, was selected; (2) linear two-point baseline correction was applied to this interval to correct baseline

wandering and shift the signal closer to zero; (3) root mean square of the signal was calculated as a noise estimator ( $RMS_{noise}$ ) for each of the 96 chest leads.

Then, the PVC signal was processed using two-point baseline correction with points before and after the whole PVC beat. Time interval of 20 ms duration was selected at the beginning of the PVC to represent the pathological activity of the ectopic focus [7]. Root mean square of the signal ( $RMS_{signal}$ ) was evaluated for each of the 96 leads. Signal to noise ratio (SNR) was assessed using the equation:

$$SNR = 20 \log(RMS_{signal}/RMS_{noise}), \quad (1)$$

where

SNR—signal to noise ratio in dB for each lead;

$RMS_{signal}$ —root mean square of the 20 ms PVC signal in each lead;

$RMS_{noise}$ —root mean square of the noise signal in each lead.

Four levels of the SNR were studied: 10, 20, 30, 40 dB. If the SNR on the lead was less than the studied SNR level, the electrode was excluded. Therefore, amount and configuration of the leads varied between the beats and between studied levels of the SNR (see Fig. 1). If the position of the lead was missing in the CT, the lead was excluded as well. From the used leads the integral BSP map was computed for each SNR and each PVC as:

$$ibspm = \int_I \phi(t) dt, \quad (2)$$

where

$ibspm$ —integral BSP map,

$\phi(t)$ —BSP map in time instant  $t$ ,

$I$ —examined time interval.

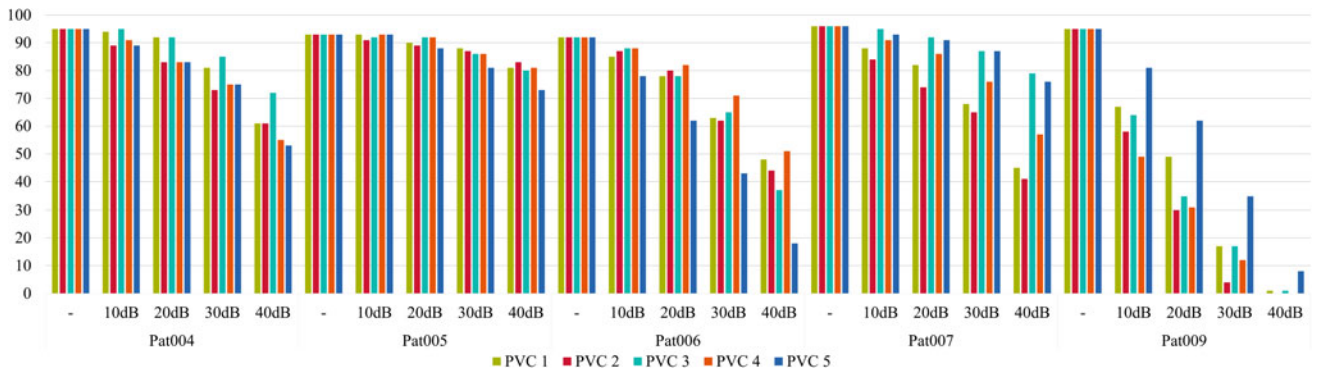


**Fig. 1** Number of ECG leads for all patients, for each of 5 selected PVCs and 5 lead sets: full set, leads with SNR > 10 dB, with SNR > 20 dB, with SNR > 30 dB and with SNR > 40 dB

## 2.2 Computed Tomography

Computed tomography scanning was performed for the whole torso using Siemens Somatom Definition system immediately after the BSP mapping. ECG electrodes were still attached to the torso in order to determine their precise positions. CT scanning had 0.3 mm slice thickness and was used to obtain inhomogeneous patient-specific 3D torso model using TomoCon PACS<sup>®</sup> software. The torso model included geometries of torso, lungs, heart atria and ventricles (epi- and endocardial surfaces), aorta and pulmonary artery. Conductivities of its compartments were assigned so that the lungs conductivity was assumed to be four times lower than the torso conductivity, and the conductivity of the heart cavities (right and left atria, right and left ventricles), aorta and pulmonary artery was assumed three times higher than the torso conductivity [8].

## 2.3 Electrophysiological Study

On the same day of the BSP mapping and CT scanning procedures or the next day, an invasive intracardiac EP study was performed using the cardiac mapping and navigation system (CARTO 3<sup>®</sup> Biosense Webster Inc.) to reveal the position of the premature ectopic activity and navigate the ablation catheter. All patients underwent the EP study under mild conscious sedation with fentanyl. Intracardiac electrograms were recorded using the electrophysiological recording system (LabSystem PRO, Boston Scientific).

Invasive localization of the PVC focus was determined by activation mapping and confirmed by pace mapping. After localization of the pathological ectopic focus RFA was performed using an open irrigated ablation catheter (Thermocool Navistar, Biosense Webster Inc.) in the power-control mode (25–40 W, flow 15–20 ml/min, max. temperature 43 °C). In order to ensure the complete destruction of the ventricular ectopic focus, after the last energy application and 15 min monitoring the patients were challenged with isoproterenol.

## 2.4 Inverse Solution

Inverse solution based on single dipole model of the cardiac electrical generator was used for noninvasive localization of the PVC focus. Integral BSP maps computed from the measured multichannel ECGs and patient-specific inhomogeneous torso geometry were used as input data for the inverse solution. It was assumed that the area of the ectopic focus can be represented by a single dipole and its electrical activity is defined by the integral BSP map computed from the initial 20 ms time

interval of the PVC. All possible positions of the equivalent dipole generator  $G'$  were supposed in a regular 3 mm cubic grid throughout the whole volume of the ventricular myocardium model. For each of these positions, parameters of the dipole were computed by the inverse solution using the equation:

$$G' = B^+ ibspm, \quad (3)$$

where

$G'$ —equivalent integral dipole generator,

$B^+$ —pseudo-inverse of the transfer matrix  $B$  representing the relation between the equivalent dipole generator and potentials on the torso.

The location of the PVC focus was determined as the position of the equivalent dipole generator best representing the measured electrical field according to the criterion of minimal relative residual error ( $RRE$ ) between the input integral BSP map ( $ibspm$ ) and map ( $gm$ ) computed from the equivalent dipole generator  $G'$ :

$$RRE = \frac{\sqrt{\sum_{i=1}^n (ibspm_i - gm_i)^2}}{\sqrt{\sum_{i=1}^n ibspm_i^2}}, \quad (4)$$

where  $n$  is the number of points in the maps.

In each patient the inverse solution was calculated for 5 PVCs from selected ECG leads (based on the SNR). For each PVC 5 lead configurations were used: all available leads, and leads having SNR > 10, SNR > 20, SNR > 30, and SNR > 40 dB.

## 2.5 Evaluation of the Inverse Solution

The locations of the equivalent dipoles obtained from the inverse solution were compared with the positions of the ablation points obtained during the intracardiac EP study. In order to make the comparison unbiased, the positions obtained from the EP study were evaluated by the physician and technician who performed the study, and the locations of the inverse solution were evaluated by the technicians who performed the non-invasive localization. The locations of the equivalent dipoles and ablation points were characterized depending on their position in the heart chambers and assigned to appropriate segments. The LV was divided into 17 segments according to the American Heart Association recommendations [9]. The right ventricular outflow tract (RVOT) was displayed in the superior view and divided into 12 segments. If the segments of the equivalent dipole and the ablation point were the same, the result of the inverse solution was marked as correct.



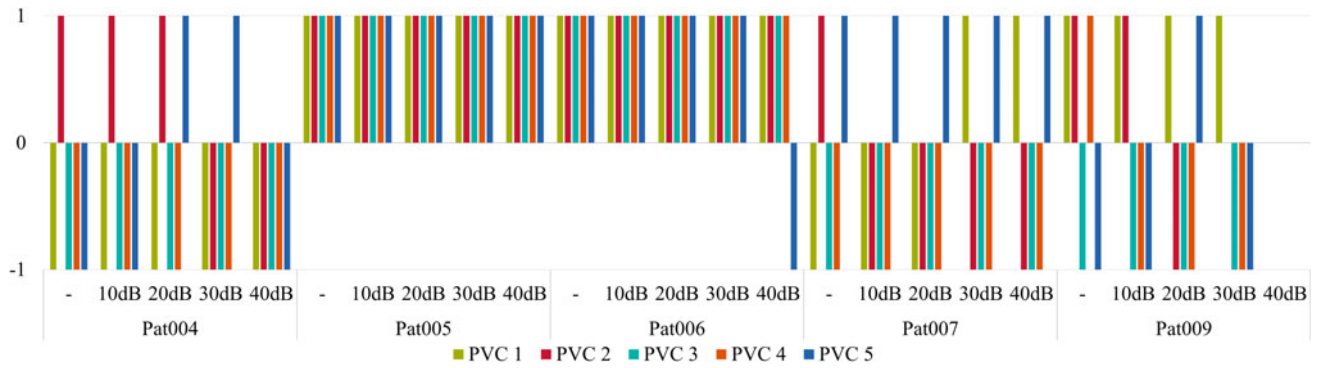


**Fig. 2** Correctness (correct +1, incorrect -1) of the inverse solution for all patients and each of 5 PVCs for 5 lead sets: full set; leads where SNR > 10, SNR > 20, SNR > 30, SNR > 40 dB

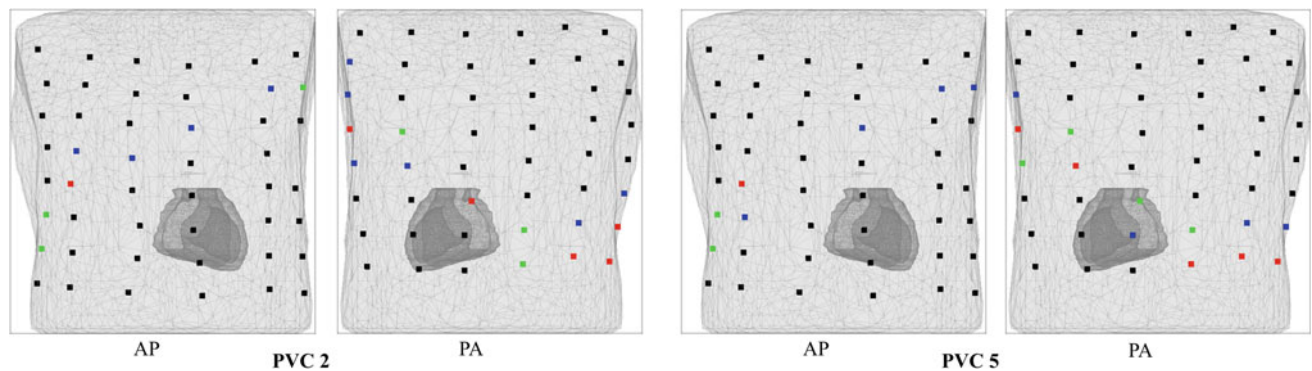


**Fig. 3** Torso model of the patient Pat004 in anterior-posterior (AP) and posterior-anterior view (PA) with leads used in evaluation of PVC 2 and PVC 5 with different SNR levels. Black: SNR > 30 dB, Blue: SNR > 20 dB, Green: SNR > 10 dB, Red: SNR < 10 dB

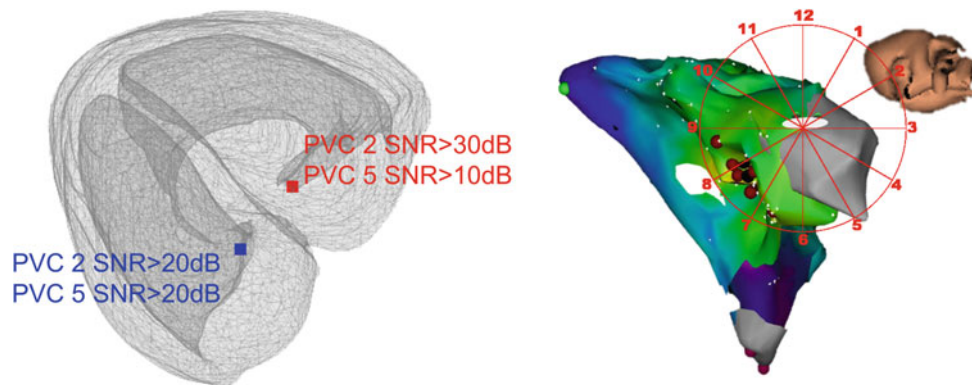


**Fig. 4** Results for Pat004. Superior view. Left: Model of the heart ventricles with positions of the inverse solutions obtained for PVC 2 and PVC 5 using different SNR levels. Blue: correct results, Red:

incorrect results. Right: Endocardial model of the right ventricle. Ablation points are marked by red markers

### 3 Results

Number of ECG leads for each of 5 lead sets (full set, and leads having SNR > 10, SNR > 20, SNR > 30, and SNR > 40 dB) is given in Fig. 1. The correctness of the

inverse solution for all patients, for each of the five analyzed PVCs and each lead set (full set and 4 sets with leads above selected SNR) is presented in Fig. 2.

Patient Pat005 had correct inverse solutions in all cases (5 PVCs, for all analyzed SNRs), patient Pat006 had correct

inverse solutions in all cases, except PVC 5 with SNR > 40 dB, when most leads were removed (78 out of 96).

Removal of the noisy ECG leads not located in the left anterior torso region (heart region) improved the PVCs localization whereas the elimination of the noisy ECG leads in the heart region caused up to 2 cm shift of the inverse PVC focus localization. One example is presented in Pat004 showing that elimination of the electrodes located precordially near the heart region (see Fig. 3, PVC 2) worsened the inverse localization (Fig. 4, PVC 2). In contrast, removal of the noisy leads from the back (see Fig. 3, PVC 5) improved the results of the inverse solution (see Fig. 4, PVC 5).

## 4 Conclusion

Small disturbances in the input data can lead to faulty results of the inverse solution due to the ill-posedness of the problem. Measurements in real patients are usually impaired by noise. Assessment of the noisy ECG leads elimination effect on the inverse solution was performed for the following SNR for each of five selected beats: 10, 20, 30, 40 dB.

When considering individual BSP maps, exclusion of noisy ECG leads did not improve the PVC focus localization if the noisy leads were located in the heart region—on left anterior torso surface. The inverse solution obtained using also noisy ECG leads in this region provided more accurate results when compared with the inverse solution computed from the input BSP map obtained only from ECG leads with high SNR level. Limitation of the study is the small number of evaluated patients. Validity of the results could be verified after more patient records will be available.

**Acknowledgements** This work was supported by research grants 17110/122/1222100G000 from the Department of BMT FBME CTU, Czech Republic, APVV-14-0875 from the Research and Development Agency, and 2/0071/16 from the VEGA Grant Agency in Slovakia.

**Conflict of interest** The authors declare that they have no conflict of interest.

## References

1. Noheria, A., Deshmukh, A., Asirvatham, S.: Ablating Premature Ventricular Complexes: Justification, Techniques, and Outcomes. *Methodist DeBakey Cardiovascular Journal* 11(2), 109–120, (2015).
2. Wissner, E., Saguner, A.M., Metzner, A., Chmelesky, M., Tsyganov, A., Deiss, S., Maurer, T., Kuck, K.-H.: Radiofrequency ablation of premature ventricular contractions originating from the aortomitral continuity localized by use of a novel noninvasive epicardial and endocardial electrophysiology system. *HeartRhythm Case Reports* 2(3), 255–257, (2016).
3. Milanic, M., Jazbinšek, V., MacLeod, R.S., Brooks, D.H., Hren, R.: Assessment of regularization techniques for electrocardiographic imaging. *Journal of Electrocardiology* 47(1), 20–28, (2014).
4. Greensite, F.: The mathematical basis for imaging cardiac electrical function. *Critical Reviews in Biomedical Engineering*, 22(5–6), 347–99, (1994).
5. Rosík, V., Karas, S., Hebláková, E., Tyšler, M., Filipová, S.: Portable device for high resolution ECG mapping. *Measurement Science Review* 7(6), 57–61 (2007).
6. Berbari, E., Bronzino, J.: *The biomedical engineering handbook*. 2nd edn. CRC Press, Boca Raton FL (2000).
7. Punshchikova, O., Svehlikova, J., Kneppo, P., Maksymenko, V., Tysler, M.: Noninvasive localization of the ectopic focus using time integral ECG mapping. *Experimental and Clinical Cardiology* 20 (7), 1564–1570 (2014).
8. Punshchikova, O., Svehlikova, J., Tysler, M., Grunes, R., Sedova, K., Osmancik, P., Zdarska, J., Herman, D., Kneppo, P.: Influence of torso model complexity on the noninvasive localization of ectopic ventricular activity. *Measurement Science Review* 16(2), 96–102 (2016).
9. Cerqueira, M.D., Weissman, N.J., Dilsizian, V., Jacobs, A.K., Kaul, S., Laskey, W.K., et al.: Standardized myocardial segmentation and nomenclature for tomographic imaging of the heart: A statement for healthcare professionals from the cardiac imaging committee of the council on clinical cardiology of the American Heart Association. *Circulation* 105(4), 539–542, (2002).

# Effect of Electrode Gel Application Between Patient's Skin and Electrode Belt on Electrical Impedance Tomography of the Thorax

Kristyna Buzkova and Denisa Albrechtova

## Abstract

Electrical impedance tomography (EIT) is a non-invasive, radiation-free imaging method that can be used for bed-side monitoring of the distribution of ventilation in lungs. However, using EIT for lung monitoring in research and clinical practice is still limited by many methodical issues. In this case study, we analyzed the possible effect the application of electrode gel between the subject's skin and the electrode belt can have on the EIT lung image. If the gel is wrongly applied, it can create a conductive connection between neighboring electrodes and distort the EIT signal. Our pilot study first minimized several unpredicted factors causing changes in EIT image and then confirmed that the conductive connection of the electrodes can lead to significant changes in the evaluated distribution of ventilation. Based on our preliminary findings, a greater study will follow with the aim of providing an official recommendation of how the gel should be applied to avoid possible errors that could lead to inaccurate conclusions about patients' health status.

## Keywords

Electrical impedance tomography • Electrode belt  
Electrode gel

## 1 Introduction

Electrical impedance tomography (EIT) is a non-invasive diagnostic technique that can be used for functional lung monitoring. EIT has many advantages for use in clinical practice such as no radiation and possibility of continuous bed-side monitoring [1, 2]. However, EIT still has many methodical unclarities that prevent the clinicians from

implementing EIT into clinical practice as a standard lung-monitoring tool. Main factors that influence the EIT lung image, the following can be listed: movement of the patient, position of the patient and position (level and rotation) of the electrodes around the patient's chest. Another factor that could have an impact on the final EIT image is an amount and way of application of electrode gel between the patient's skin and the electrode belt, which is used by many commercial EIT systems, such as PulmoVista 500 (Dräger Medical, Lübeck, Germany) [2, 3].

The aim of this study was to analyze the possible impact of various ways of application and amount of the conductive electrode gel between the patient's skin and electrode belt and to contribute by these findings to the standardization of the methodology of EIT use for lung monitoring in both research and clinical practice. No study was found dealing with this issue.

One of the most frequently used devices in clinical practice is EIT system PulmoVista 500 (Dräger Medical, Germany). Electrode belt with 16 integrated electrodes is used for monitoring. The manufacturer of the EIT system PulmoVista 500 mentions in the user manual that it is necessary to use the electrode gel in case that the skin is dry or the electrical contact between the skin and electrodes is unstable or not sufficient (the contact resistance between the skin and the electrode must be smaller than 300  $\Omega$ ) [2]. However, the manufacturer does not mention how the gel should be applied and what amount of the gel should be used. The manufacturer only describes that the application of the gel can have an impact on impedance of the chest since it influences the electrical resistance between the skin and electrodes, and specifically the chest impedance at the end of exhalation. The issue can be raised once the operator applies the gel to the whole belt, causing the electrodes to electrically connect. The question is whether the caused inductive connection between two or more electrodes could affect the EIT signal and could lead to misinterpretation of the final EIT lung image. This error could cause incorrect evaluation of the patient medical conditions.

K. Buzkova (✉) · D. Albrechtova  
Faculty of Biomedical Engineering, Department of Biomedical Technology, Czech Technical University, Prague, Czech Republic  
e-mail: buzkokri@fbmi.cvut.cz

## 2 Methods

This prospective intervention study consisted of a series of pilot measurements performed in a Faculty of Biomedical Engineering, Czech Technical University in Prague. The study is part of a greater research dealing with methodical unclarity of the EIT for lung monitoring and was approved by ethical committee of Faculty of Biomedical Engineering, Czech Technical University in Prague. The pilot measurements were all performed on a male volunteer (25 years, 172 cm, 70 kg). The effect of amount and way of application of electrode gel was analyzed by the creation of a conductive connection between the neighboring electrodes. The scheme of the positions of the electrodes on the electrode belt is shown in Fig. 1. Three forms simulated the conductive connection, electrode gel was applied: (1) between the first and second electrode, (2) between the first and the eighth electrode (half of the electrode belt), (3) between the first and the sixteenth electrode (the whole electrode belt). Moreover, one measurement was performed with no conductive connection between any of the electrodes, to create a reference.

When performing the first set of the pilot measurements, we discovered several other influencing factors that we had to minimize in order to obtain valuable and comparable results. These factors were a leakage of the electrode gel from beneath the electrode belt, irregular breathing habit of the subject, and movement of the belt on the subject's body. Those factors are described below.

### 2.1 Minimizing the Factors Influencing EIT Signal

The first factor that interfered with the measurement protocol and therefore influences the EIT signal was the fact that the layer of gel applied on the electrodes was pushed outside of the belt, when the belt was tightly around the subject's chest.

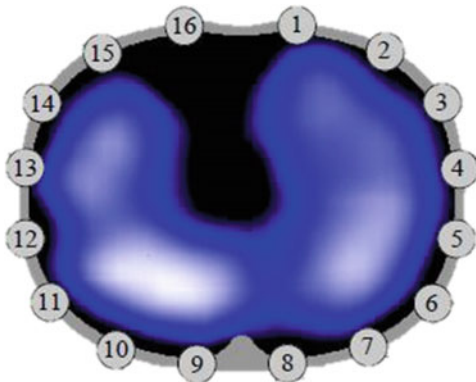


**Fig. 1** Schematic position of the 16 electrodes on the electrode belt of EIT system PulmoVista 500 (Dräger Medical, Germany) [based on 3]

When the gel is pushed out from underneath the belt, it can lead to a decrease of the conductive connection between the electrodes that we tried to simulate. Therefore, we placed gauze between the belt and the subject to maintain the layer of the gel in place.

Another factor that could decrease the reproducibility of the measurements was irregular breathing of the subject. Therefore, the subject used a mask and was breathing with a ventilation support (Avea, Carefusion, USA). The patient was conscious and adapted to the breathing efforts managed by the ventilator. Used ventilation mode was volume-controlled (VCV), respiratory rate (RR) was set to 15/min, tidal volume ( $V_T$ ) was 0.75 L and positive end-expiratory pressure (PEEP) was set to 3 cm  $H_2O$ . The subject set RR and  $V_T$  by himself prior the measurement, so the parameters were reflecting his natural breathing habits. The comparison of the breathing cycles when breathing spontaneously and with ventilation support is shown in Fig. 2. It is evident that values of the tidal volumes were more constant when compared to the spontaneous breathing.

The last factor that could have an adverse impact on the EIT signal was a possible cranial and caudal shift of the belt on the subject's body. When a greater amount of the gel was applied, the belt did not remain on the same place, but was moving caudally and cranially during the breathing cycle. The manufacturer [3] warns that certain constant position of the belt must be kept in order to obtain valid EIT signal. The constant position of the belt was therefore maintained using a bandage over the belt around the subject's chest.

### 2.2 Set of Pilot Measurements

Based on the adverse effect of the factors mentioned above, series of pilot measurements was performed. The measurements were designed to gradually, one by one, eliminate the adverse effects.

All measurements had following procedure in common. Adequate electrode belt size (medium) was chosen for the subject. The belt was always placed in the fifth intercostal space in the medioclavicular line. The subject was lying in supine position, not talking and not moving during the EIT monitoring. Every monitoring took approx. 3 min. In the beginning of every pilot measurement, the reference measurement was obtained with no electrodes connected. A good quality signal was ensured by applying the gel directly beneath the electrodes with a high contact resistance. Two electrodes were then connected by the conductive gel, then 8 electrodes (the half of the belt) and finally all 16 electrodes (whole length of the belt). Every time the belt was taken off to apply the gel, the same steps were followed to place the belt in the exact same position. Three sets of these measurements were performed as described above:



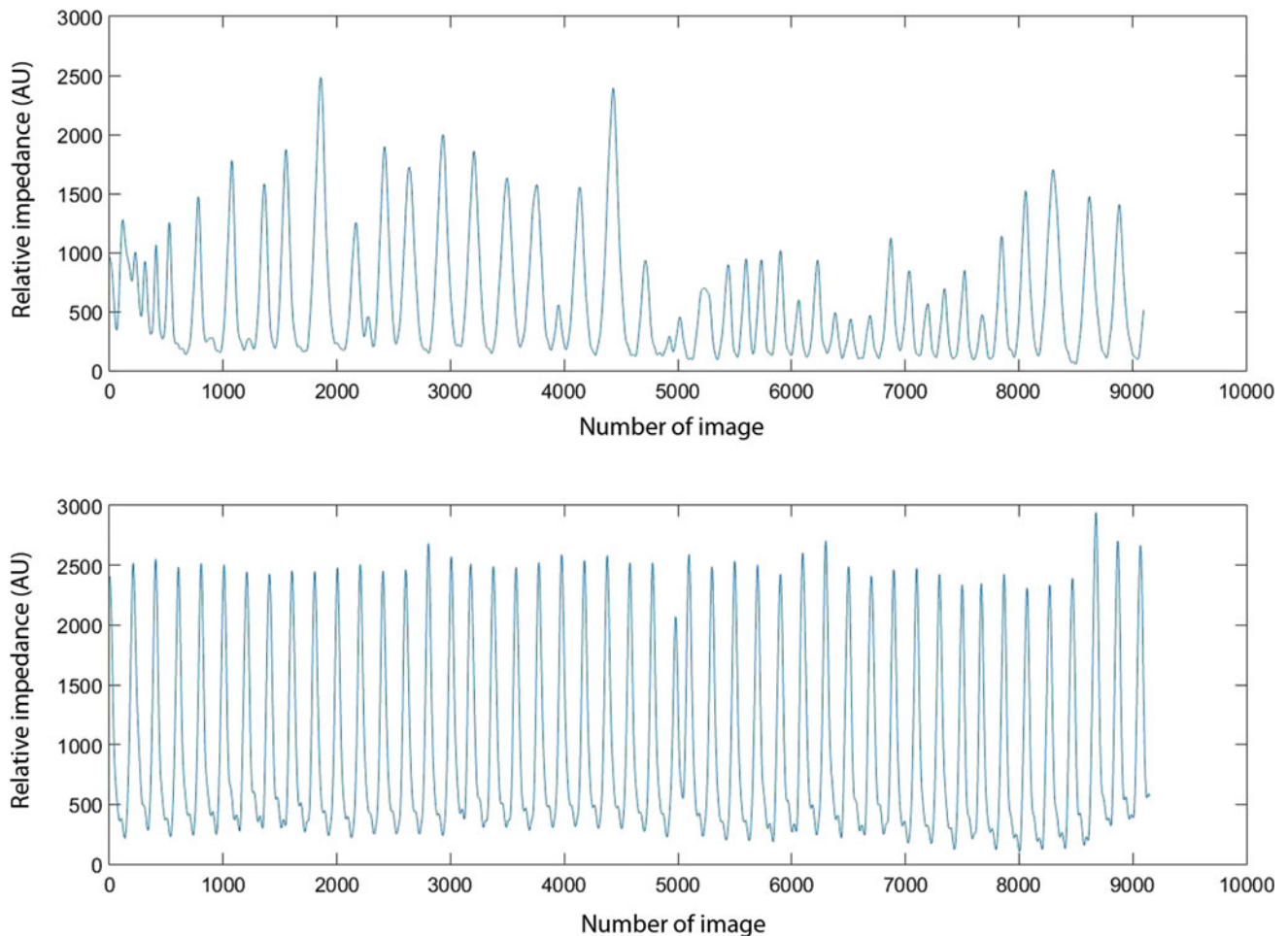


**Fig. 2** Relative impedance of spontaneous breathing (upper figure) and of breathing with a ventilation support (lower figure)

(1) standard measurement using gel, (2) the gauze was used to maintain the gel layer in place, (3) measurement using gauze and ventilation support, (4) measurement using gauze, ventilation support and a bandage over the belt.

### 2.3 Data Analysis

Measured data were analyzed using Dräger EIT Data Analysis Tool and Matlab R2015a (Mathworks). Distribution of ventilation was analyzed in two types of regions of interest (ROI)—layers and quadrants. Average images were generated from every EIT signal and changes of relative impedance of lungs were evaluated. Also, center of ventilation (CoV) and center of gravitation (CoG) was calculated

as described in literature [4–9]. The parameters are used to represent a potential shift of the ventilation in the lungs in both  $x$  (lateral direction) and  $y$ -axis (ventro-dorsal direction). These values were then compared to analyze the differences in the EIT images of lungs for the described situations (no connection, 2 electrodes connected, 8 electrodes connected and 16 electrodes connected).

## 3 Results

Distribution of ventilation for layers and quadrants for measurements using gauze, ventilator and bandage are shown on Fig. 3. Differences between CoG and CoV for the same cases are summarized in Table 1.

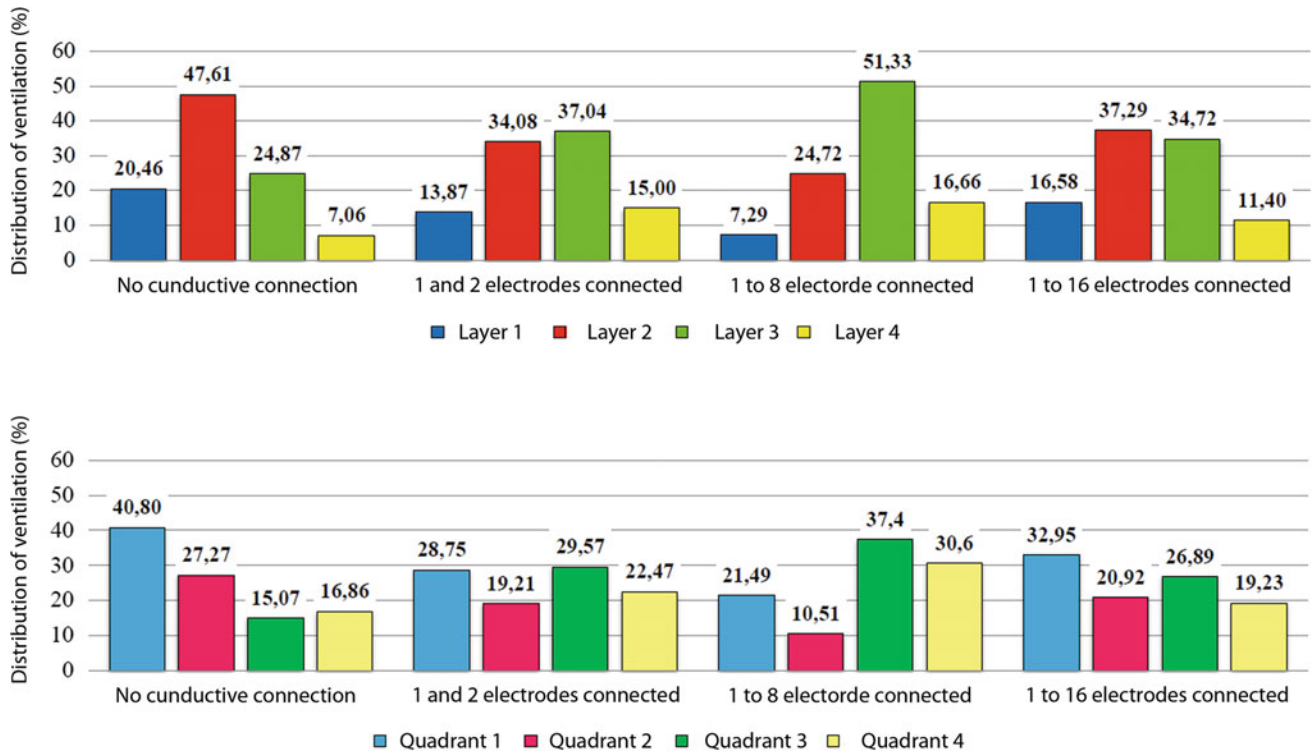


**Fig. 3** Distribution of ventilation for measurements using gauze, ventilator and bandage for layers (upper part) and quadrants (lower part)

**Table 1** CoG and CoV (%) for the final series of measurements (using gauze, ventilator and bandage). CoG\_x represents shift in lateral direction, CoG\_y in ventro-dorsal direction

Type of measurement	CoG_x (%)	CoG_y (%)	CoV (%)
No conductive connection between neighboring electrodes	46.1	43.0	39.2
Conductive connection between electrodes 1 and 2	47.7	52.5	56.3
Conductive connection between electrodes 1 and 8	40.8	51.6	53.3
Conductive connection between electrodes 1 and 16	48.8	44.2	41.7

## 4 Discussion

The main finding of this study is that amount of gel and way of its application between the subject's skin and the electrode belt can significantly influence the EIT of the thorax. In the results section, we showed mainly the results of the final pilot experiment, where we minimized as many adverse factors as possible. In the previous experiments, the differences between the obtained values were even greater, but we assumed that the differences were mostly caused by the described adverse factors, not by the application of the gel and the caused conductive connection.

In Fig. 3, we focused mainly on layers 1 and 4 (dorsal and ventral parts), since those are the most important from the diagnostic point of view (atelectasis and hyperinflation occurs most frequently in these areas) [3]. More than 9% difference of the distribution of ventilation in layer 1 is

shown when comparing no conduction and conductive connection on the whole belt (electrodes 1–16). For layer 4, the difference was more than 4% for no connection and connection between electrodes 1 and 2.

CoG\_x showed the greatest change when comparing no connection and connection between electrodes 1 and 8 (46.1 vs. 40.8%). This shift can be clearly explained since the whole left half of the belt (right part in the image) was conductively connected and thus the ventilation image seems to be influenced by this. The biggest difference in CoG\_y is in situation with no connection and 1 and 2 electrodes connected (43.0 vs. 52.5%). This could be a proof that connection of only two neighboring electrodes out of 16 could have a significant impact on the analyzed EIT image of lungs.

For CoV, the greatest changes were found when comparing no connection and connection between electrodes 1 and 2 (39.2 vs. 56.3%).

Based on these preliminary results from the pilot experiments, we assume that even connection of two neighboring electrodes can cause great impact on the EIT image and can potentially lead to inaccurate medical decisions. It is hard to assume and more data would be needed to conclude whether the distribution of ventilation seems decreased or increased in the areas where the electrodes are conductively connected. The differences that we discovered are hard to be statistically analyzed, since this was just a case study. In order to conclude this, greater study with tens of subjects needs to be performed and is planned to be realized in 2018/2019. This study will have a goal to provide an official recommendation for research and clinical practice describing how the electrode gel should be applied for lung monitoring by EIT.

## 5 Conclusion

The aim of this case study was to analyze the impact that the conductive connection of the neighboring electrodes can have on the EIT signal and image. Based on our results, we assume that the way gel is applied can have a significant adverse impact on the EIT image, but it is yet impossible to quantify this impact. The best option to avoid any such impact is to apply the electrode gel separately underneath every electrode, avoiding the creation of a conductive connection between the electrodes. The complex study will be following up describing the possible impacts of the outlined phenomenon more precisely.

**Acknowledgements** The study was supported by the grant SGS16/258/OHK4/3T/17.

**Conflict of Interest Declaration** The authors state that there are no conflicts of interest regarding the publication of this article.

## References

1. Holder D.: Electrical impedance tomography: methods, history, and applications. Philadelphia: Institute of Physics Pub. 2005.
2. Leonhardt S., Lachmann B.: Electrical impedance tomography: the holy grail of ventilation and perfusion monitoring? *Intensive Care Medicine*. Col. 38, issue 12, 917–1929, 2012.
3. Teschner E, Imhoff M. Electrical impedance tomography: The realization of regional lung monitoring. Dräger Medical GmbH EIT Booklet, Germany, 2011.
4. Frerichs I. et al.: Monitoring perioperative changes in distribution of pulmonary ventilation by functional electrical impedance tomography. *Acta Anaesthesiologica Scandinavica*, Volume 42, 721–726, 1998.
5. Frerichs I. et al: Lung Volume Recruitment after Surfactant Administration Modifies Spatial Distribution of Ventilation. *American Journal of Respiratory and Critical Care Medicine*, Volume 174, 772–779, 2006.
6. van Heerde M. et al.: Spontaneous breathing during high-frequency oscillatory ventilation improves regional lung characteristics in experimental lung injury. *Acta Anaesthesiologica Scandinavica*, Volume 54, 1248–1256, 2010.
7. Radke O. C. et al.: Spontaneous Breathing During General Anesthesia Prevents the Ventral Redistribution of Ventilation as Detected by Electrical Impedance Tomography. *Anesthesiology*, Volume 116, 1–8, 2012.
8. Sobota V., Roubik K. (2016) Center of Ventilation—Methods of Calculation Using Electrical Impedance Tomography and the Influence of Image Segmentation. In: Kyriacou E., Christofides S., Pattichis C. (eds) XIV Mediterranean Conference on Medical and Biological Engineering and Computing. IFMBE Proceedings, vol 57. Springer, Cham, 2016.
9. Leupschen H. et al.: Protective ventilation using electrical impedance tomography. *Physiological Measurement*, Volume 28, 247–260, 2007.



# Capsaicin Effects on Human Facial and Neck Temperature

Jana Pokorná, Erik Staffa, Vladan Bernard, and Vojtěch Mornstein

## Abstract

Capsaicin is an alkyl-amide that can be found in chilli peppers as its main irritant component with some analgesic properties. It has also many other properties, so it may help to control peripheral nerve pain as well as can be helpful during chemotherapy and radiotherapy. Capsaicin, as an irritant compound, affects body temperature. This study was aimed to specify what is its effect to facial and neck temperature. To obtain temperature distribution images the Workswell WIC 640 infrared camera was used in order to measure and visualize temperature. Facial and neck temperatures were measured before and after ingestion of about teaspoonful of Jalapeño chilli pepper extract of 6.000–8.000 SHU. Finally, surface body temperature was affected by ingestion of chilli pepper extract. Using the appropriate amount of capsaicin can be helpful in medicine but the individual variability of physiological reactions to this irritant substance must be considered.

## Keywords

Capsaicin • Chilli pepper • Thermal camera imaging Thermography

## 1 Introduction

### 1.1 Function of Capsaicin in Human Body

Capsaicin is a chilli pepper extract with analgesic properties. Capsaicin is a neuropeptide releasing agent selective for primary sensory peripheral neurons. Used topically, capsaicin aids in controlling peripheral nerve pain. In addition,

capsaicin may be useful in controlling chemotherapy- and radiotherapy-induced mucositis [1].

Capsaicin is associated with many enzymatic, cytoskeletal, and osmotic changes, as well as disruption of mitochondrial respiration, impairing nociceptor function for extended periods of time. Intracerebral or subcutaneous administration of capsaicin decreases core temperature, as a result of heat loss responses such as cutaneous vasodilation [2, 3]. Hence, capsaicin has physiological actions, including unique thermoregulatory actions [4].

## 2 Methods

### 2.1 Infrared Thermography in Medicine

Infrared thermography is a method of temperature measurement using a contactless machine called infrared camera. Since the time of Hippocrates, temperature is considered to be one the most important indicator of health.

All objects with temperature above absolute zero emit electromagnetic radiation, which is known as infrared radiation or thermal radiation [5–7]. Wavelength of this radiation lies within a range of 0.75–1000  $\mu\text{m}$ . This wide range can be further subdivided into three smaller groups (near, medium and far infrared). According to thermal radiation theory, blackbody is considered as a hypothetical object that absorbs all incident radiation and radiates a continuous spectrum according to Planck's law [8]. Integrating Planck's law for all frequencies, we get Stefan–Boltzman's law—Eq. (1), which describes the total emissive power from a blackbody [7].

$$E = \sigma T^4 \quad (1)$$

There  $E$  means the total emissive power ( $\text{W}/\text{m}^2$ ),  $\sigma$  is the Stefan Boltzman's constant and  $T$  is the absolute temperature (K). For real surfaces the Stefan Boltzman's law is modified to the following form:

J. Pokorná (✉) · E. Staffa · V. Bernard · V. Mornstein  
Faculty of Medicine, Department of Biophysics, Masaryk  
University, Brno, Czech Republic  
e-mail: 419334@mail.muni.cz

$$E = \varepsilon\sigma T^4 \quad (2)$$

where  $\varepsilon$  is the emissivity of the emitting surface at a fixed wavelength and absolute temperature  $T$ . For a perfect blackbody emissivity is unity, but for real materials emissivity is always less than unity [7].

Thermography is a very good method for temperature measurement especially on surfaces with very high emissivity, as human body is for example.

## 2.2 Facial and Neck Temperature Measurement

To measure and visualize the facial and neck temperature of observed persons, the Workswell WIC 640 infrared camera was used.

Workswell WIC is stationary LWIR thermal camera for precise non-contact temperature measurements in laboratory environments. Camera with resolution  $640 \times 512$ px and with thermal sensitivity up to  $\leq 0.03$  °C was used. For the intense of this study, camera was connected by a USB3 interface, which is the best option for laboratory usage. WIC infrared camera was calibrated properly during the manufacture process and its calibration certificate is available.

Facial and neck temperatures were measured before and after ingestion of about teaspoonful of Jalapeño chilli pepper extract (1.17 grams) of 6.000–8.000 SHU. This amount of Jalapeño chilli pepper extract is containing about 0.0587 grams of pure capsaicin.

Compared to other chillies, the jalapeño heat level varies from mild to hot depending on cultivation and preparation [9, 10]. All of the capsaicin and related compounds are concentrated in vesicles found in the placenta membrane surrounding the seeds; the vesicles appear white or yellow and fluoresce in the range of 530–600 nm when placed in violet light [10].

Measurement was performed for 2 min and 30 s for every of the 12 volunteers (4 males and 8 females) aged 20–

30 years. And the measurement evaluation was performed every 30 s.

As it is very important to keep the measurement condition same during the whole experiment, all the observed people were sitting about one meter far away from the camera lens. Temperature was 23.3 °C and humidity was 40.2% in the room where the measurement took place. The both parameters were kept constant during the measurement.

## 3 Results

### 3.1 Infrared Thermography

The temperature increase of different parts of the face depends on individual physiology of volunteers participating in the study and is observable almost immediately after ingestion of the Jalapeño chilli pepper extract. Usually, the more the observed person likes a hot taste subjectively, the smaller temperature increase is observable.

In general, temperature rise was observed between 1 and 2 °C in oral region, between 0 and 1.5 °C in frontal region, between 0 and 1 °C in canthi, between 1 and 0.9 °C in the neck, and 0.2–0.6 °C in the nose region after 2 min. It was confirmed there is an obvious relation between the temperature rise and subjective perception of the hot taste. Facial temperature of people who like hot taste rises slower and less in comparison with the other people.

In the following Table 1 you can find a summary of evaluation of temperature changes of observed people

In the pictures below, there can be found an example of the two measured persons (Figs. 1 and 2).

In the images, there are obvious lines of the measured areas. To quantify each region temperature changes, mean temperature was considered as the most important. Minimum and maximum temperature of each region were available and considered as important too, but those

**Table 1** Evaluation of temperature rises after 2 min for the 12 observed subjects

Measurement	1	2	3	4	5	6	7	8	9	10	11	12
Hot taste sympathies	Yes	Yes	No	No	No	No	Yes	No	No	Yes	No	No
Frontal region (°C)	0	0	0	0	1	0.7	0	1.5	0.7	0.7	1	0.2
Nose region (°C)	1	1	0.2	1.5	0.8	1.5	0.3	2	2	0.6	1.3	1.6
Oral region (°C)	1	1.5	0.4	1.8	1.8	1.3	2	1	1.4	1.2	0.9	1.3
Canthi (°C)	0	0.8	0	1	0.9	0.7	0.6	1.3	1	1	0.9	0.5
Neck region (°C)	0.6	0.9	0	0.9	0	0.3	0.4	0.5	0.6	0.5	0.2	0.2
Mean (°C)	0.52	0.84	0.12	1.04	0.9	0.9	0.66	1.26	1.14	0.8	0.86	0.76
Max (°C)	1	1.5	0.4	1.8	1.8	1.5	2	2	2	1.2	1.3	1.6
Min (°C)	0	0	0	0	0	0.3	0	0.5	0.6	0.5	0.2	0.2

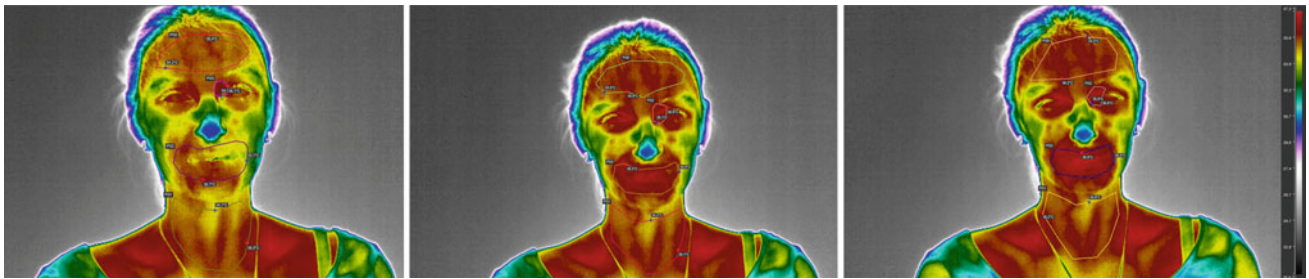


**Fig. 1** Measurement of the women in time: 0 min–1 min–2 min

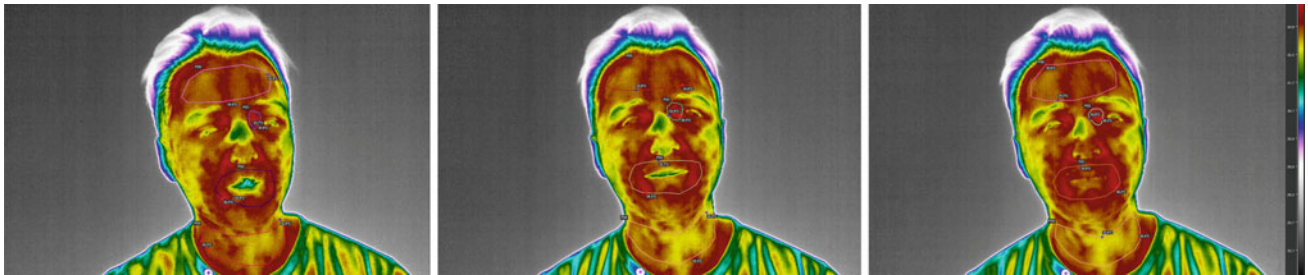


**Fig. 2** Measurement of the man in time: 0 min–1 min–2 min

temperature pieces of information were not classified as statistically important.

For the thermograms analysis, Workswell CorePlayer was used. It is a computer application which allows to analyse thermograms individually, use different measurement tools and change the measurement parameters if needed.

To minimize the problems with the floating uncertainty of measuring of the WIC infrared camera, all the measurements were made at one time.

To summarize results of the study, temperature rise after ingestion of about teaspoon of chilli pepper extract was obvious in the all measured cases. Only the growth steepness was different for everybody. Those differences are probably caused by an individual taste and thermoregulation specifics of every person participating this study.

Human body has very high emissivity. What is also important, human's body reflected temperature has very little significance (due to the high emissivity) so there was no need to change this parameter during the measurement.

## 4 Conclusion

Generally speaking, capsaicin alkylamide affects surface body temperature. The temperature rise is probably caused by a psychosomatic reaction—brain submits a signal for vasodilatation in the specific body region. Using the appropriate amount of capsaicin can be helpful in medicine

but we must consider individual variability of physiological reactions to this irritant substance which are also represented by the observed skin temperature changes. To make the measurements as accurate as possible, it is important to stick to certain principles.

Firstly, during the time of measurement, it was important to keep the climatic condition constant in the laboratory, so the windows were closed, and door was opened only in necessary cases like for entering and exiting the room. Otherwise, the air flow might change the temperature and humidity in the laboratory.

Secondly, acclimatization of everyone who was going to be measured was very important part of the experiment. Temperature is the primary displayed parameter of thermal camera, so it is important to be acclimatized before the measurement. Practically, every volunteer must rest at least for 10 min in the room of the measurement, but the ideal time would be probably even longer, about half an hour.

Measurement of infrared radiation by a thermal camera can sometimes be influenced not only by the subject directly measured but also by ambient influences such as heating in the room for example. It was therefore important to make measurements as far away as possible from heat source and certainly without a glossy background.

Theoretically, this research can be a basis for further experiments. In the future, there might be a need of determining the procedure for choosing the optimal dose of a local anaesthetics on a basis of capsaicin individually (the reaction to this substance is shown to be individual).

Furthermore, other studies of the organism thermal reaction on capsaicin are planned. Another study of the chilli pepper with different SHU will be realized soon, as it is important to find out, how a temperature response of the organism depends on the capsaicin concentration.

**Conflict of Interest Declaration** The authors declare that they have no conflict of interest.

---

## References

1. Capsaicin (Code C339). In: NCI Thesaurus [online]. U.S.: National cancer institute, 2014. Accessible from: [lurl.cz/ltbQq](http://lurl.cz/ltbQq).
2. Jancsó-Gábor, Aurelia, J. Szolcsányi and N. Jancsó. Irreversible impairment of thermoregulation induced by capsaicin and similar pungent substances in rats and guinea-pigs. *J. Physiol.* 1970, 206 (3), 495–507.
3. Issekutz B Jr, Lichtneckert I, Nagy H. Effect of capsaicin and histamine on heat regulation. *Arch. Int. Pharmacodyn. Ther.* 1950; 81:35–46.
4. Szolcsanyi J. Capsaicin and sensory neurones: a historical perspective. *Prog. Drug Res.* 2014; 68:1–37.
5. B.F. Jones, A reappraisal of the use of infrared thermal image analysis in medicine, *IEEE Transactions on Medical Imaging* 17 (1998) 1019–1027.
6. X. Maldague, *Theory and Practice of Infrared Technology for Nondestructive Testing*, first ed., John Wiley and Sons, New York, 2001.
7. M.F. Modest, *Radiative Heat Transfer*, second ed. Academic Press, California, 2003.
8. J. Steketee, Spectral emissivity of the skin and pericardium, *Physics in Medicine & Biology* 18 (1973) 686–694.
9. González-Zamora, Alberto, Erick, Sierra-Campos, J. Luna-Ortega, Rebeca Pérez-Morales, Juan Ortiz and José García-Hernández. Characterization of Different Capsicum Varieties by Evaluation of Their Capsaicinoids Content by High Performance Liquid Chromatography, Determination of Pungency and Effect of High Temperature. *Molecules.* 2013, 18(11), 13471–13486. <https://doi.org/10.3390/molecules181113471>. ISSN 1420-3049. Accessible from: <http://www.mdpi.com/1420-3049/18/11/13471/>.
10. Bosland, Paul; Coon, Danise; Cooke, Peter H. (June 2015). “Novel Formation of Ectopic (Nonplacental) Capsaicinoid Secreting Vesicles on Fruit Walls Explains the Morphological Mechanism for Super-hot Chile Peppers”. *Journal of the American Society for Horticultural Science.* 140 (3): 253–256.

# Assessment of Brain Water Content in Peripheral Inflammation by an Optimized Single-Voxel MR Spectroscopy Quantitation Technique

Abdul Nashirudeen Mumuni<sup>1</sup>, John McLean, Rajeev Krishnadas, Maria Rosario Lopez-Gonzalez, Jonathan Cavanagh, and Barrie Condon

## Abstract

Increased brain water content (BWC) of up to 12% has been reported in brain inflammatory disease. However, no study has assessed variation of BWC in peripheral inflammatory disease, such as psoriasis. BWC, as one of the reference standards in quantitative magnetic resonance spectroscopy (MRS), has not been considered by previous studies mostly due to the challenge of acquiring the water signal within tolerable times in patients, for accurate estimation of BWC. In this study, we developed a technique of BWC quantification by optimizing the standard MRS acquisition from which unsuppressed water spectra were extracted by post-processing. The extracted in vivo unsuppressed water signal was adjusted for all necessary correction factors and calibrated against a reference signal deduced from voxel position-dependent polynomial equations derived from head coil sensitivity maps obtained from phantom experiments. Experiments were conducted on psoriasis patients and controls, comprising 16 (8 males, 8 females) participants in each group. CHES water-suppressed spectra were recorded from the anterior cingulate cortex and bilateral hippocampi of participants using the standard PRESS sequence. BWC did not vary significantly ( $p > 0.05$ ) between patients and controls, across all the brain regions of both patients and controls, and in patients at baseline and post anti-inflammatory medication. BWC in this study compared with published estimates, indicating that the technique is accurate. The results further indicate that BWC is unaltered in peripheral inflammation, and thus support the use of BWC as an

internal reference standard for absolute quantitative MRS studies of peripheral inflammation.

## Keywords

Magnetic resonance spectroscopy • Brain water content Reference standard • Inflammation • Psoriasis CHES • PRESS • Hippocampus • Anterior cingulate cortex

## 1 Introduction

Inflammation is a defensive mechanism of body tissues against harmful agents. Inflammatory response could however sometimes result in auto-immune diseases such as multiple sclerosis (MS) and psoriatic arthritis (PsA). PsA is an inflammation of the skin, causing plaques, whereas MS affects the brain.

Brain water content could increase up to 12% in MS [1], but this observation has not been reported for PsA even though evidence exists for the involvement of the brain in PsA [2]. To the best of the authors' knowledge, no magnetic resonance spectroscopy (MRS) study has reported on BWC in PsA.

Current MRS techniques of measuring BWC involve placing an external reference next to the head or performing a separate reference scan [3–5]. Unfortunately, this defeats the full benefit of using BWC as an internal reference concentration and also potentially introduces more errors into the BWC estimate, depending on the type of external reference used and its position in the head coil [6].

Ideally, quantitative MRS involving the BWC as a reference should be such that both metabolite and water signals are acquired from the same voxel position, simultaneously. BWC estimated from such an acquisition should be well adjusted to a level of accuracy that compares with known values of BWC in comparable study subjects.

A. N. Mumuni (✉) · J. McLean · M. R. Lopez-Gonzalez  
B. Condon  
Institute of Neurological Sciences, Southern General Hospital,  
Glasgow, UK  
e-mail: mnashiru@uds.edu.gh

R. Krishnadas · J. Cavanagh  
Institute of Health and Wellbeing, University of Glasgow,  
Glasgow, UK



This paper therefore describes a novel technique that optimizes the MRS acquisition of the water signal within clinical scan times, tolerable to patients, and yet offers accurate BWC estimate. Exploratory analyses were also conducted to assess BWC in the anterior cingulate cortex (ACC) and bilateral hippocampi of PsA patients, at baseline compared to post-anti-inflammatory medication and healthy volunteers.

## 2 Methods

### 2.1 Subjects

Following ethical approval of the study by the West of Scotland Research Ethics Committee 4 (WoSREC4), PsA patients (8 males/8 females, mean age  $\pm$  SD =  $46 \pm 10$  years) and healthy volunteers (8 males/8 females, mean age  $\pm$  SD =  $39 \pm 12$  years) were recruited into the study. All volunteers had no neurological or psychiatric disorders, and contraindications for magnetic resonance imaging (MRI). Each participant gave informed consent before study entry. Both groups had a baseline MRS scan, and 6–8 weeks later, only the PsA patients had MRS scan again after receiving intravenous anti-inflammatory medication (Etanercept).

### 2.2 MRI/MRS Acquisition

Phantom calibration and human brain scans were performed in separate sessions on a 3 T GE Signa HD MRI/MRS scanner equipped with an eight-channel receive-only head coil.

A standard MRS pulse sequence on the scanner acquires 16 unsuppressed-water spectral averages (NSA) prior to the acquisition of metabolite spectra. By a user-defined number of radiofrequency excitations (NEX) for a particular MRS acquisition, the total number of spectral lines stored in the data frame ( $N_{Total}$ ) can be calculated from:

$$N_{Total} = (16/NEX) + (NSA/NEX) \quad (1)$$

Thus,  $(16/NEX)$  from Eq. 1 can be extracted and post-processed to yield the unsuppressed-water peak area.

#### In Vitro Experiments

MRS was conducted on an axial MRI of a GE MRS phantom using a PRESS localization sequence ( $TE/TR = 35/2000$  ms, NSA = 64, NEX = 8, voxel size,  $VOI = 20.0 \times 20.0 \times 20.0$  mm<sup>3</sup>, CHESS water suppression).

From the isocenter of the image (using on-screen voxel coordinates display as a guide), three slices were selected towards the superior (S) end, and another three slices

towards the inferior (I) end of the image. Each slice was 20.0 mm thick, and so the VOI size was fitting for the slice thickness, making it possible to make acquisitions across every point on the image. Spectra were thus recorded in a two-dimensional plane (RL-AP axis) along the SI direction. This resulted in a three-dimensional coil signal sensitivity map. Fewer voxel positions were however possible towards the S and I ends due to the spherical geometry of the phantom. The number of voxel positions (from S to I) were 19, 27, 32, 31, 26 and 17; thus, a total of 152 acquisitions were made.

The unsuppressed-water peak area,  $A_u$  from each acquisition was obtained from  $(16/NEX)$  in Eq. 1, and was corrected for coil loading effect ( $10^{(TG/200)}$  [7]), relaxation effects ( $T_1 = 3.3$  s and  $T_2 = 2.5$  s [6]), and voxel size (VOI); the result was a corrected in vitro unsuppressed-water peak area,  $A_{phan}$ :

$$A_{phan} = \frac{A_u \times K_{TG}}{VOI \times [1 - \exp(-TR/T_1)] \times \exp(-TE/T_2)} \quad (2)$$

A surface plot of  $A_{phan}$  versus the RL and AP coordinates was performed for each slice. The plots were fitted to polynomial functions of up to 5th-degree. Analysis were done in MATLAB.

#### In Vivo Experiments

Spectra (PRESS, CHESS water suppression, NSA = 128, NEX = 8) were acquired from the ACC ( $TE/TR = 35/2000$  ms) and bilateral hippocampi ( $TE/TR = 144/2000$  ms) on axial MRI of the brain. Voxel sizes were adjusted for subject's brain size; ACC voxels ranged between 8.0 and 14.5 mL, while hippocampal voxels ranged between 5.3 and 13.2 mL.

### 2.3 Correction Factors in the Calibration of the In Vivo Water Signal Against $A_{phan}$

CSF contamination of voxels was eliminated as previously described [8], to yield tissue fraction,  $f_{tissue}$ . Voxel size variations was accounted for by the respective voxel size,  $VOI_{brain}$  for each acquisition. Coil loading by the brain was corrected by  $K_{TG\_brain}$  from each acquisition. Effect due to temperature difference between the phantom ( $T_{phantom}$ ) and brain was corrected for, by the correction factor,  $k_{temp}$ :

$$k_{temp} = (273.2 + T_{phantom})/310.2 \quad (3)$$

During the in vitro experiments,  $T_{phantom} = 18$  °C, so  $k_{temp}$  was approximately 0.94.

Using CHESS water suppression for the acquisitions, and not setting  $TE = 0$  ms and  $TR = 5 \times T_1$  of water (which is

about 3000 ms) for optimum signal recovery, meant that only about 45% of the unsuppressed-water signal partially recovered between successive  $TR$  times. A partial recovery constant,  $k_{pr}$  was therefore necessary to correct both this and  $T_1$  relaxation effects:

$$k_{pr} = (A_{TE=23;TR=15000}) / (A_{TEacq;TRacq}) \quad (4)$$

$A_{TE=23;TR=15000}$  is the maximum recovered signal without CHES, and  $A_{TEacq;TRacq}$  is the signal acquired with CHES.  $TE = 23$  ms was the lowest achievable value on the scanner because gradients had to be turned ON; therefore,  $TE$  could not practically be equal to 0 ms.

## 2.4 Spectral Analysis

Raw signals from the eight channels of the head coil were eddy-current corrected, combined [9] and Fourier transformed to frequency domain water peak for phase and baseline correction. The water peak was fitted to a Lorentzian line shape, and its area was estimated using the Levenberg-Marquardt method of nonlinear least squares minimization [10]. Analysis were performed using the SAGE software (version 7).

## 2.5 Quantification of Brain Tissue Water Content (BWC)

BWC was estimated from:

$$BWC = \frac{A_{brain}}{A_{phan}} \times \frac{k_{TG\_brain}}{VOI_{brain}} \times \frac{f_{tissue}}{R_{2\_tissue}} \times \frac{k_{pr}}{k_{temp}} \quad (5)$$

$A_{brain}$  is the in vivo unsuppressed-water peak area,  $A_{phan}$  is the reference unsuppressed-water peak area obtained by substitution of the in vivo voxel coordinates of  $A_{brain}$  into the appropriate position-dependent polynomial equation from the in vitro experiments, and  $R_{2\_tissue}$  is the tissue  $T_2$  relaxation correction factor. BWC was expressed in mol/kg wet weight by multiplying Eq. 5 by the concentration of water (55.51 mol/L), and then dividing the result by the density of water at 37 °C (which is 0.9934 g/mL).

## 2.6 Statistical Analysis

BWC variation in patients was assessed by paired t-test, BWC difference between patients and controls was assessed by two-sample t-test, and variation of BWC in the brain regions of interest was assessed by one-way ANOVA. Statistical significance was set at  $p < 0.05$ . All tests were performed using Minitab software (version 17).

## 3 Results

### 3.1 In Vitro Experiments

The generic polynomial function for the sensitivity map of any given slice was given by:

$$\begin{aligned} A_{phan} = SI_{a:b}(x, y) = & A + Bx + Cy + Dx^2 + Exy + Fy^2 \\ & + Gx^3 + Hx^2y + Ixy^2 + Jy^3 + Kx^4 + Lx^3y + Mx^2y^2 \\ & + Nxy^3 + Oy^4 + Px^5 + Qx^4y + Rx^3y^2 \\ & + Sx^2y^3 + Txy^4 + Uy^5 \end{aligned} \quad (6)$$

$SI_{a:b}(x, y)$  is the calculated in vitro unsuppressed-water peak area ( $A_{phan}$ ),  $a:b$  is the range of possible voxel positions within an in vivo slice,  $x$  and  $y$  are respectively the RL and AP coordinates of the in vivo voxel. The coefficients of the polynomial function are listed in Table 1.

### 3.2 In Vivo Experiments

Mean  $\pm$  SE BWC in the ACC of PsA patients did not vary significantly ( $p = 0.35$ ) between baseline, PsA-1 ( $39.3 \pm 1.6$  mol/kg) and post-medication, PsA-2 ( $41.2 \pm 2.5$  mol/kg); both baseline ( $p = 0.63$ ) and post-medication ( $p = 0.14$ ) estimates compared with those for the control group ( $37.4 \pm 2.8$  mol/kg). There were no gender differences ( $p > 0.05$ ) in average BWC in both groups.

Mean  $\pm$  SE BWC (mol/kg) in the left and right hippocampi are shown in Table 2. Variation of BWC was assessed in the ACC, left and right hippocampus by group comparison of estimates from all three brain regions, as



**Table 1** Coefficients of the polynomial fits to the inter-slice spatial RF sensitivity maps of the receiver coil

Slice	Coefficient of polynomial fit																					
	A	B	C	D	E	F	G	H	I	J	K	L	M	N	O	P	Q	R	S	T	U	
55S	1.70e8	-2.56e7	-3.58e7	2.85e5	-2.26e6	-1.03e6	5475	1.61e4	-6.38e4	-8980	6.29	154.90	204	-581.30	3.53	0	0	0	0	0	0	0
35S	3.85e8	2.00e6	2.74e6	3.82e5	1.90e5	2.81e5	-1862	-1769	-333	154.10	-141	-95.34	-180.40	-92.04	-85.59	0.10	-1.14	-1.83	-1.11	-0.71	-0.65	-0.65
15S	4.38e8	4.44e6	-4.88e6	1.42e5	1.27e5	2.29e5	-3.552	5595	-2579	8341	-35.04	-111.30	-31.44	-45.52	81.44	0.40	-1.36	-0.91	-0.51	-0.12	0.25	0.25
15I	4.29e8	1.07e6	-1.39e7	1.71e5	2637	-1.04e5	-3161	8353	2611	8594	-60.11	6.90	139.60	49.45	170.10	0.94	-1.63	-0.44	1.24	0.23	0.87	0.87
35I	2.03e8	1.55e6	-8.06e6	1.38e5	-5660	8.05e5	-85.29	7320	-9696	3.65e4	0.66	-101.70	10.02	-254.10	503.80	-0.87	-1.17	-1.35	-0.54	-1.73	2.29	2.29
55I	9.53e7	1.41e6	-6.90e5	8.11e5	2.69e4	9.55e5	-6520	4.66e4	2025	2.64e4	37.21	-109.90	576	30.68	185.20	0	0	0	0	0	0	0

**Table 2** BWC estimates in the hippocampi compared

Hippocampus	Control group (C)	Pre-medicated patients (PsA-1)	Post-medicated patients (PsA-2)	C versus all PsA	C versus PsA-1	C versus PsA-2
Left (L)	35.5 ± 1.8	36.1 ± 1.6	37.0 ± 1.7	$p = 0.75$	$p = 0.78$	$p = 0.53$
Right (R)	34.3 ± 2.2	34.1 ± 1.2	35.4 ± 1.6	$p = 0.59$	$p = 0.92$	$p = 0.69$
L versus R	$p = 0.57$	$p = 0.10$	$p = 0.88$			

**Table 3** Variation in regional BWC in the three voxel positions

Subjects	ACC	Left hippocampus	Right hippocampus	p-value
Controls	35.9 ± 2.7	35.9 ± 1.4	34.3 ± 1.9	0.86
PsA-1	36.6 ± 3.1	37.2 ± 1.8	34.1 ± 1.1	0.63
PsA-2	41.9 ± 2.8	35.8 ± 1.7	35.4 ± 1.4	0.11

shown in Table 3. No comparison was significant ( $p > 0.05$ ) in Tables 2 and 3.

## 4 Discussion

To quantify BWC, Dreher and Leibfritz [11] implemented a two-scan method without water suppression involving a short echo time ( $TE = 18$  ms) PRESS localization sequence. Prior to the standard single-voxel PRESS localization sequence, two scans were performed: the chemical shift inversion pulse was turned off in the first scan, and then was turned on in the next scan, both scans yielding the time domain (TD) datasets  $S_A$  and  $S_B$ , respectively. They suggested that BWC could be estimated from the signal sum  $S_A + S_B$ . However, this method doubles the minimum total measurement time, and significantly reduces the unsuppressed water signal intensity.

Christiansen et al. [5] quantified brain tissue water content by acquiring the unsuppressed-water signal and referencing it to a signal acquired from an external water bag. In a group of healthy subjects aged 10–70 years, they estimated cerebral water content in the range of 35.8–39.6 (mean = 36.9) mol/kg wet weight for four brain regions: frontal, temporal, occipital and basal ganglia, selecting predominantly grey and white matter tissues in separate cases. They did not find significant variation in water content among the four regions, as in this study.

## 5 Conclusions

The method presented in this paper limits BWC quantification to a single MRS acquisition, from which the partially recovered water signal can be optimized and referenced to a mathematically deduced unsuppressed-water peak area using a standard 3-dimensional function that defines the in vivo

voxel position. Sensitivity of the technique to measuring subtle variations in BWC was assessed in this study. Future studies will consider brain tumors where variations in BWC are substantial.

**Acknowledgements** This study was funded by the Scottish Imaging Network: A Platform for Scientific Excellence (SINAPSE), University of Glasgow, and Sackler Institute of Psychological Research.

**Conflict of Interest** The authors declare that they have no conflict of interest.

## References

1. Laule, C., et al.: Water content and myelin water fraction in multiple sclerosis. A T2 relaxation study. *Journal of Neurology* 251(3), 284–93 (2004).
2. Mumuni, A.N.: Brain involvement in peripheral inflammatory disease. *EC Psychology and Psychiatry* 5(1), 27–29 (2017).
3. Brief, E., et al.: Absolute metabolite concentrations calibrated using the total water signal in brain 1H MRS. *NMR in Biomedicine* 22(3), 349–354 (2009).
4. Whittall, K.P., et al.: In vivo measurement of T2 distributions and water contents in normal human brain. *Magnetic Resonance in Medicine* 37(1), 34–43 (1997).
5. Christiansen, P., et al.: MR-visible water content in human brain: a proton MRS study. *Magnetic Resonance Imaging* 12(8), 1237–44 (1994).
6. Tofts, P.: *Quantitative MRI of the brain: measuring changes caused by disease*. John Wiley & Sons Ltd, Chichester, England (2003).
7. Helms, G.: A precise and user-independent quantification technique for regional comparison of single volume proton MR spectroscopy of the human brain. *NMR in Biomedicine* 13(7), 398–406 (2000).
8. Mumuni, A.N. and McLean, J.: Voxel segmentation-based partial volume correction using FSL: theory and implementation. *EC Proteomics and Bioinformatics* 1(1), 19–26 (2017).
9. Wright, S.M. and Wald, L.L.: Theory and application of array coils in MR spectroscopy. *NMR in Biomedicine* 10(8), 394–410 (1997).
10. Press, W.H., et al.: *Numerical Recipes in C: The art of scientific computing*. Cambridge University Press, Cambridge (1992).

11. Dreher, W. and Leibfritz, D.: New method for the simultaneous detection of metabolites and water in localized in vivo  $^1\text{H}$  nuclear magnetic resonance spectroscopy. *Magnetic Resonance in Medicine* 54(1), 190–5 (2005).

# Noninvasive Imaging of the Origin of Premature Ventricular Activity

Milan Tysler<sup>ID</sup>, Jana Svehlikova<sup>ID</sup>, Elena Deutsch<sup>ID</sup>, Pavel Osmancik<sup>ID</sup>, and Robert Hatala<sup>ID</sup>

## Abstract

The localization and imaging of the origin of premature ventricular complex (PVC) before the electrophysiological study (EPS) can significantly shorten the time needed for the ablation procedure. In this paper, a method allowing noninvasive localization of the PVC origin by solving the inverse problem of electrocardiography and finding a dipolar source best representing the initial ectopic activity is presented. It requires measurement of body surface potential (BSP) maps and a model of the patient torso obtained from CT. To test the method, 96 ECG leads were measured in 5 patients and 128 leads in another 2 patients. BSP maps from the initial interval of several PVCs were used to solve the inverse problem using inhomogeneous (IT) or simplified homogeneous (HT) patient specific torso model. All measured ECG leads, as well as only selected 64, 48 or 32 leads of the 96 lead set were used for the inverse computations. The inversely obtained dipole locations were compared with the catheter positions during successful ablation within the EPS. In five patients the PVC origin was found in the right ventricular outflow tract (RVOT), in the remaining two patients it was in the left ventricle (LV). The noninvasive method localized the PVC origins in correct heart segments in all but one patient with localization

errors of up to about 2 cm. In one patient the true origin in RVOT was localized in LV but still within 2 cm from the true position. The employment of the more detailed IT torso model did not bring significant improvement of the localization but the dispersion of solutions from different PVCs increased. The use of subsets of 48 or less ECG leads resulted in increased number of incorrect localizations. If the IT torso model was employed, there were a few incorrect localizations also when 64 ECG leads were used.

## Keywords

Ventricular arrhythmia • Body surface potential mapping  
Inverse problem of electrocardiology • Dipole model  
Noninvasive localization of ectopic focus • ECG imaging

## 1 Introduction

Patients with frequent ventricular arrhythmias that do not respond to pharmacological treatment are indicated for catheter ablation of the arrhythmogenic tissue during an electrophysiological study (EPS) [1]. The localization of the origin of premature ventricular complexes (PVCs) before the EPS can shorten the time and significantly increase the efficacy of the procedure. In this paper, we present a method intended for noninvasive localization of the origin by solving the inverse problem of electrocardiology and finding an equivalent dipolar electrical generator that best represents the initial ectopic activity [2]. Such solution requires measurement of body surface ECG potentials (BSPs) in many torso points and individual 3D model of the patient torso as a volume conductor.

The aim of the study was to test if a simplified homogeneous torso (HT) model is sufficient for the inverse solution or if an inhomogeneous torso (IT) has to be used. The possibility to reduce the number of surface ECG leads without significant decrease of the accuracy or stability of

M. Tysler (✉) · J. Svehlikova  
Department of Biomeasurements, Institute of Measurement  
Science, Slovak Academy of Sciences, Bratislava, Slovakia  
e-mail: tysler@savba.sk

E. Deutsch  
Faculty of Biomedical Engineering, Czech Technical University  
in Prague, Kladno, Czech Republic

P. Osmancik  
3rd Faculty of Medicine, Charles University and Cardiocenter,  
University Hospital Kralovske Vinohrady, Prague, Czech  
Republic

R. Hatala  
Department of Arrhythmias, National Institute of Cardiovascular  
Diseases, Bratislava, Slovakia

the inverse solution was also checked for solutions with both, HT and IT torso models.

## 2 Materials and Methods

### 2.1 ECG Measurement and CT Scanning

Seven patients were included in the study, 3 men and 4 women, age from 18 to 77 years. Five patients were treated in the University Hospital Královské Vinohrady in Prague where 96 ECG leads, organized in 12 vertical strips with 8 electrodes were recorded. Another 2 patients were treated in the National Institute of Cardiovascular diseases in Bratislava where 128 ECG leads were measured using 16 strips with 8 electrodes (Fig. 1). In both hospitals, the ProCardio 8 system [3] developed in the Institute of Measurement Science SAS was used for ECG measurement and processing. ECG signals were recorded using Ag/AgCl electrodes with active adapters and sampled at 1 kHz with 16-bit resolution. The record length was several minutes, depending also on the occurrence of the PVCs.

After ECG recording, the patients with placed ECG electrodes underwent CT scanning of the whole torso using the Siemens Somatom Definition system. From the obtained CT scans patient-specific HT and IT torso model was created using extended TomoCon PACS<sup>®</sup> software [4] (Fig. 2). The

lungs, heart ventricles and atria, aorta and pulmonary artery were defined in the IT models and different electrical conductivities were assigned to lungs and structures filled with blood.

### 2.2 Noninvasive Localization of the PVC Origin

BSP maps from the initial interval from 5 to 25 ms of selected PVCs and individual HT or IT torso models were used to localize the origin of the PVC by solving the inverse problem. Assuming that the area activated during the initial time interval is small enough to be represented by a single dipole in a predefined position in the ventricles, the inverse solution can be computed using the equation:

$$G' = \mathbf{B}^+ im \quad (1)$$

where  $G'$  is dipolar equivalent electrical generator,  $\mathbf{B}^+$  is pseudo-inverse of the transfer matrix  $\mathbf{B}$  representing the relation between the equivalent generator and potentials on the torso, and  $im$  is integral BSP map.

The equivalent generator  $G'$  was computed for all positions in a regular 3 mm grid throughout the ventricular myocardium. The resultant location of the ectopy origin was determined as the dipole position for which the agreement between the measured integral BSP map  $im$  and map generated by the computed equivalent dipolar generator  $G'$  was

**Fig. 1** Example of anterior (left) and posterior (right) placement of 128 ECG leads using 16 vertical strips with 8 electrodes in patient P004

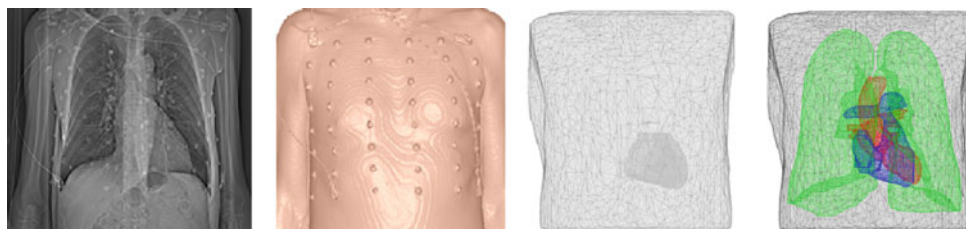
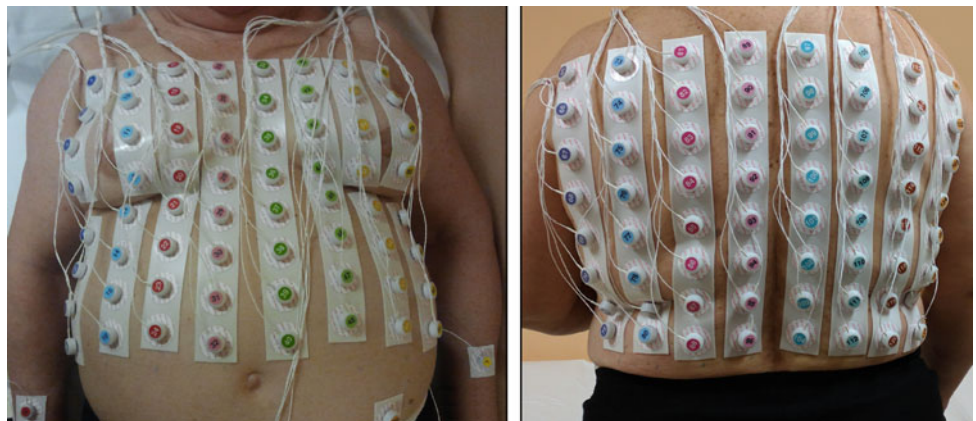


**Fig. 2** Example of construction of the torso models for Pat004. From left to right: CT scan of the patient torso, torso surface with identified 96 electrode positions, homogeneous torso model HT with marked heart region, inhomogeneous torso model IT

best (according to the criterion of minimal value of the relative residual error).

In this study, the inverse solution was computed using both, HT and IT torso models and all 96 or 128 measured ECG leads, as well as only selected 64, 48 or 32 leads of the 96 lead set to check if it is possible to reduce the number of ECG leads without significant decrease of the accuracy or stability of the inverse solution.

### 2.3 The EPS and the Ablation Procedure

The EPS and catheter ablation were performed using 3-dimensional electroanatomic mapping (CARTO<sup>®</sup>, Biosense Webster Inc.) in Prague and navigation and visualization technology (EnSite NavX, St. Jude Medical) in Bratislava. The right ventricle was mapped via standard femoral approach, the left ventricle via a trans-septal approach. The target site for the radiofrequency ablation was determined by activation mapping and confirmed by pace mapping. After the target site was located, radiofrequency catheter ablation was performed using an open irrigated ablation catheter (Thermocool Navistar, Biosense Webster Inc.). Usually several ablations in neighboring points had to be performed. After the last energy application patients were monitored for 15 min with isoproterenol challenge to ensure complete removing of the ectopy. The ablation point was considered to be the true position of the PVC origin.

### 2.4 Evaluation of the Noninvasive Localization of the PVC Origin

Each resultant inversely obtained dipole location was compared with the catheter position during the successful ablation. However, the precise merging of the torso and heart

model geometry obtained from CT with the geometry of heart chambers obtained by intracardiac mapping during the EPS was not possible due to the measurement errors and available graphical outputs of the intracardiac mapping. The estimated residual error of the merging was of the order of 1 cm. Evaluation of the “correctness” of the inverse solution was based on the dipole position within particular anatomical structures of the heart and its distance from the ablation point was estimated manually using the graphical outputs of the intracardiac mapping.

## 3 Results

During the EPS, in three patients from Prague and both patients from Bratislava the PVC origin was found in some part of the right ventricular outflow tract (RVOT), in the remaining two patients it was in basal part of the left ventricle (LV). When all ECG leads were used, in all patients except Pat005 the noninvasive method localized the PVC origins in correct heart areas (Table 1) with estimated localization errors of up to about 2 cm.

In patient Pat005 the PVC origin in the RVOT (Fig. 3) was localized in basal anterior LV when using HT torso model but still within 2 cm from the true position.

The use of inhomogeneous torso model IT did not significantly improve the localization accuracy but the dispersion of solutions from individual PVCs increased (examples in Figs. 3, 4 and 5).

The decrease of the number of ECG leads used in the inverse computations (by omitting some strips of electrodes in several variations) resulted in increased dispersion of locations obtained from different PVCs, especially if the IT torso model was employed. The number of incorrect localizations increased when 48 or less ECG leads were used. If the IT torso model was employed there were a few incorrect localizations also when 64 ECG leads were used (example in Fig. 5).

**Table 1** Positions of the catheter during successful ablation and localizations of PVC origins obtained by inverse solutions from 96 or 128 ECG leads using both, HT and IT torso models

Patient	Leads	Ablation position	Solution using HT	Solution using IT
Pat004	96	septal RVOT	septal RVOT	posterior RVOT
Pat005	96	left lateral RVOT	<u>basal anterior LV</u>	left lateral RVOT
Pat006	96	basal inferior LV	basal inferior LV	basal inferior LV
Pat007	96	septal RVOT	septal RVOT	septal RVOT
Pat009	96	basal anterior LV	basal anterior LV	basal anterior LV
P001	128	left lateral RVOT	left lateral RVOT	left lateral RVOT
P004	128	anterolateral RVOT	left lateral RVOT	left lateral RVOT



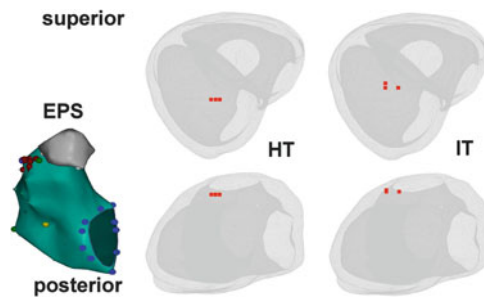


**Fig. 3** Results for patient Pat005, superior view (top) and posterior view (bottom). Left: Ablation points (red markers) in the RVOT. Center and right: results of the inverse solution (red squares) for five selected PVCs as obtained with the use of HT and IT torso models (Color figure online)

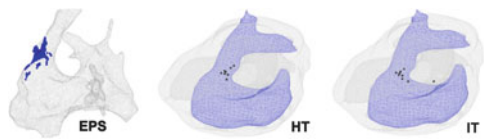


**Fig. 4** The early activated area in the RVOT (left lateral view) in patient P001. Left: The RVOT surface activated within the first 20 ms as it was recorded by the NavX system. Center and right: Right ventricular chamber and RVOT reconstructed from the patient CT. Positions of the PVC origin (marked by dots) computed by the inverse solution from 10 ectopic beats using both, HT and IT torso models. Light gray area corresponds to the contour of the whole ventricular myocardium

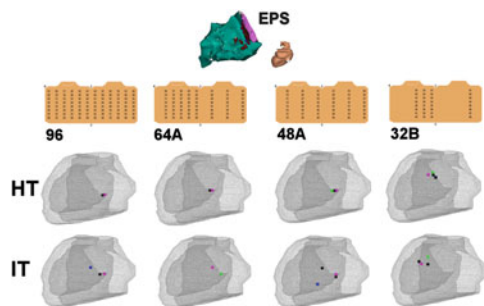


**Fig. 5** Results for patient Pat006 (posterior view). Top: Ablation points in basal inferior LV (red markers) in the CARTO picture of the LV. Bottom: Inverse localization of the PVC origin from 5 ectopic beats when using HT or IT torso models and 96, 64, 48, or 32 leads (shown above) (Color figure online)

## 4 Discussion and Conclusions

It is widely accepted [5] that realistic patient-specific geometry should be used for accurate inverse solution in electrocardiology. Despite potentially better localization accuracy, results of this study did not demonstrate significantly more “correct” results when IT torso models were used. Moreover, their use

caused higher sensitivity of the inverse solution to variations and noise in the input signals.

The number of ECG leads required for acceptable inverse solution was estimated to 24–64 if they are placed non-uniformly on anterior and posterior torso with a higher density on the left anterior chest [6]. In our earlier simulation study 32 leads were sufficient for robust localization of single dipolar source [7]. However, these results were not confirmed on real data used in this study and the number of incorrect results increased even if 48 or 64 leads were used. Limitation of the study is that only a few lead sets created from 96 leads by omitting a few strips of electrodes were evaluated.

If 96 or 128 ECG leads and the HT torso model were used, the inverse localization of the PVC origin was quite stable when individual ectopic beats were evaluated. Reduction to 64 leads used in the inverse computations preserved acceptable stability and accuracy of the localization. With 96 or 128 ECG leads and the IT torso model, the PVC origin localization from different ectopic beats was less stable and already reduction to 64 ECG leads resulted in several incorrect localizations in some patients.

**Acknowledgements** This work was supported by grants APVV-14-0875 from the Slovak Research and Development Agency and 2/0071/16 from the VEGA grant agency in Slovakia and by grants 13/229/OHK/4/3T/17 from SGS CVUT and PRVOUK P35 in Czech Republic.

**Conflict of Interest** The authors declare that they have no conflict of interest.

## References

1. Bogun, F., Crawford, T., Reich, S., et al.: Radiofrequency ablation of frequent, idiopathic premature ventricular complexes: Comparison with a control group without intervention. *Heart Rhythm* 4(7), 863–867 (2007).
2. Punshchikova, O., Svehlikova, J., Kneppo, P., Maksymenko, V., Tysler, M.: Noninvasive Localization of the Ectopic Focus Using Time Integral ECG Mapping. *Experimental and Clinical Cardiology*, 20(7): 1564–1570 (2014).
3. Kadanec, J., Zelinka, J., Bukor, G., Tyšler, M.: ProCardio 8 - system for high resolution ECG mapping. In: Maňka, J., Tyšler, M., Witkovský, V., Frollo, I. (eds.) MEASUREMENT 2017, Proceedings of the 11th International Conference on Measurement, pp. 263–266. Institute of Measurement Science, Slovak Academy of Sciences, Bratislava (2017).
4. TatraMed Software, TomoCon PACS. <http://www.tatramed.sk/pacsItem?element=3&parentId=18&type=19>, last accessed 2018/02/05.
5. Rahimi, A., Wang, L.: Sensitivity of noninvasive cardiac electrophysiological imaging to variations in personalized anatomical modeling. *IEEE Transactions on Biomedical Engineering* 62(6), 1563–1575 (2015).
6. Hoekema, R., Uijen, G.J., van Oosterom, A.: On selecting a body surface mapping procedure. *Journal of Electrocardiology* 32 (2), 93–101 (1999).



7. Kneppo P., Tyšler M., Turzová M.: Simulation study of possibilities of using limited lead mapping data for inverse solution based on multipole cardiac generator. In: Morucci, J.P., Plonsey, R., Coatrieux, J.L., Laxminarayan, S. (eds.) IEEE Engineering in Medicine and Biology (pp. 2002–2003). IEEE Inc., Piscataway (1992).

# Quantitative Assessment of Strabismus and Selected Vision Related Anomalies

Shorav Suriyal, Christopher Druzgalski, and Kumar Gautam

## Abstract

Decreased vision, double vision, eye fatigue and strain associated with strabismus often require no-surgical or surgical options which may lead to overcorrection or under correction with a need for a follow up surgery. Therefore, quantitative assessment of the degree of strabismus can serve as very useful tool for deciding on therapeutic options and evaluation of their outcomes. Further, US focused statistics indicate that 4% of the population has strabismus while some global estimates attribute this anomaly only to 0.034% of world population. These contrasting statistics further lead to a necessity of having a uniform quantitative tool for a broader application to determine the scope and the degree of this anomaly in different populations. At this point variety of tests are used including Hirschberg test, Cover test, and Central Corneal Light Reflex Ratio. Therefore, the developed technique allows automatic quantitative detection of a presence of possible strabismus and calculation of linear and vertical deviations of eyes in digital images. In particular, the proposed algorithm was structured in seven stages: (1) face matching (2) face detection and alignment (3) extraction of region of interest (4) locating the iris of both eyes and their center positions (5) selection of reference points in the eyes (6) calculation of linear and vertical deviations (7) making prediction using pre-trained regression model. This methodology has 93% of accuracy, 84% of sensitivity and 30% of specificity as tested on 128 images. In particular, the outcome encompasses a methodology for two graphical user interfaces which have real time as well as local image processing capability; a bounding box approach to make the face of a person aligned; and determination of numerical linear and vertical deviations of the eyes in millimeters. While the deviation of normal eyes is close to

zero, the higher numbers indicate pre-strabismus or strabismus conditions respectively.

## Keywords

Strabismus analysis • Machine learning • Exotropia  
Hypertropia • Purkinje image

## 1 Introduction

Ophthalmologic imaging encompassing assessment of angular deviation of eyes becomes a useful tool in evaluation of long term changes associated with strabismus. Moreover, it becomes technique of choice in quantitative evaluation of strabismus and its early detection. The employed techniques includes image processing of regular photographic images, Purkinje image analysis, or other techniques [1–3]. In particular, his paper focuses on calculating the deviation of strabismus through various computer vision techniques and also provide a machine learning model that takes deviations as input and predicts the type of strabismus from a list of 4 main categories. These authors focus their interest on deviation of light reflection from the eyes when it moves in a certain direction.

The main stages in the methodology of this project include the following steps. The first step is to perform calibration of the camera used in the study with the help of a checkerboard structure. This calibration process is done using a graphical user interface. More details of graphical interface are discussed in the last section of this paper. The next step is to extract facial features using histogram of oriented gradients method. These features will be used for facial recognition. Next, an extraction of the region of interest from the face image is done with the help of HAAR features. Following that the center of the iris is located. This is done with the help of Hough transform. In order to determine this, a range of radius of the iris is provided to the Hough transform function. This radius range varies from

S. Suriyal (✉) · C. Druzgalski · K. Gautam  
Department of Electrical Engineering, California State University,  
CSULB, 1250 Bellflower Blvd, Long Beach, CA 90804, USA  
e-mail: shoravsuriyal@yahoo.com

person to person due to difference in their eye size. Once the center of iris is found, two reference points one for each eye are selected and their location is fixed for every individual's face. Next step is to find the distance between the centers of the irises of both the eyes and the reference points. Once those distances are found one can calculate their difference which gives the final deviation value.

The next section of the paper briefly describes the approach which made the detection of iris more robust to noise. Due to noise in the eye images, one may have some false detection of the iris attributes. Since Hough transform approach is considered as one of the most efficient tools to find the geometric shapes in an image still often it's unable to overcome the noise in the image. This problem arises due to the fact that a range of radius in which Hough transform finds a range of circles is supplied. Since this range of radius differs from person to person if one tries to come up with a common radius range that covers most people faces. By doing this, the Hough transform technique detects other circular like false objects in the background leading to false circle detection error.

This paper also discusses a machine learning approach which involves training on images of people faces to predict the type of strabismus using logistic regression model. This model was trained on 128 images of people faces. Image data collection and its filtering process begins with web scraping of image database on web. Filtering is required because the image dataset is not according to the condition that will be discussed later in this paper. The image dataset also included images of five healthy subjects taken in real time. The images in the dataset are classified under two categories namely strabismus and non-strabismus. Once this logistic regression model is trained on the images it can be used as a classifier.

---

## 2 Strabismus Analysis Procedure

For this experimental and computational project, Canon EOS M3 camera was used to capture images of the target facial areas. This study requires snapshot of people's faces to evaluate the degree of strabismus, primarily the eye region. First, the camera was calibrated using a checkerboard structure with the help MATLAB camera calibrator application [4]. The important step in this study involves initiation with collecting pictures, developing an algorithm to quantifying and measuring the horizontal and vertical deviation in eyes, to ultimately construct a measure for strabismus. Thus, steps involved in this study are broadly listed and defined as: A: Data collection, B: Image Processing, C: Estimation of deviation in eyes, D: Graphical User Interface.

### 2.1 Data Collection

Data collection is an important step in machine learning to make a model learn and predict using the input data. A set of taken experimental images was complemented by two sources used for data collection namely: ImageNet website and Google Image Search [5, 6]. The dataset consists of images of people's faces of different age groups. The faces also include some people with strabismus. This type of data is more diverse as it has people of various ethnicities contributes to machine learning model being more robust and not specific to one group of population. Since the dataset consists of images that are random in nature meaning they are inconsistent in the condition when images were taken. Images have different background and lighting conditions and even the people's faces are oriented at different angles. Due to this randomness in the images, we removed many images that do not fit used dataset and finally there were 123 images analyzed. Still this dataset represented sufficient images to train a logistic regression model. The condition used for removing bad images from the dataset included the following: the eye of the person should not be occluded with any object or it should not be partially closed, background noise should be reduced, face of the person should not be tilted too much that can lead to improper detection of face and eyes by the algorithm used in this study. The more details on face alignment is given in next part of this section. In some cases, face is also covered with various mask-like objects that can also hinder the algorithm developed for these studies. Once the dataset is ready and cleaned it can be used for extracting features of interest (Fig. 1).

### 2.2 Image Processing

The first step in image processing is to find the face in the input image. For this task the computer vision technique for extracting facial features known as HAAR features was used [7]. This technique involves series of steps until it reaches the final stage of its detection. These steps involved selecting the appropriate filter that runs over the entire input image pixel by pixel and performs convolution. With the help of HAAR features, one can not only extract the face from the image but also make a bounding box structure on the image around the face which is later used in aligning face in the image. Next step is to find the eyes in the extracted face. Again, we apply the HAAR features to extract the eyes from the face. Then we crop the extracted eyes from the image. We then further segment the eyes into left and right eye. These left and right eyes are further used in extracting the iris.



**Fig. 1** Shows a glimpse of used dataset after performing filtering

Once both the left and right eyes as separated in distinct images next step is to extract the iris from both the left and right eye. In order to do that Hough transform technique was used for finding the circular region in the eye [8]. Hough transform involves mapping x-y plane to parametric plane. One can find any arbitrary shape using Hough transform technique. In order to find the iris with this technique, one needs to supply a range of radius to the Hough transform function. The difficulty in doing that it causes false circle detection in the eye. To overcome this problem a simple technique was used and it is discussed below:

The result from the Hough transform technique includes a list of radius values and center points of all the detected circles that fall under the range of radius supplied as input argument. Since every individual has different iris size so in order to make a generalized iris detector, a range of radius values that covers most of the people's eyes was selected. Let's say one wants to remove the false circle detection in person's left eye image, then first the mid-point in left eye image must be determined and then the Hough transform

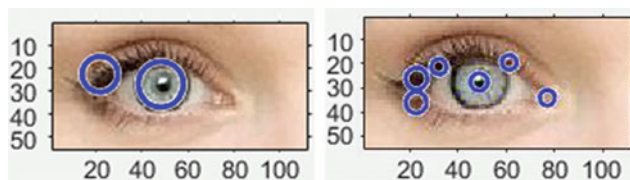


**Fig. 2** Illustrates the false circle detection in eye images

technique applied to the eye image which gives a list of all the radius values and center coordinates of all the circles detected including the false circle and the actual iris (Fig. 2).

After that the distances between all the center points and the mid-point are found utilizing earlier distances that are stored in an array. After that the minimum value of distance in that array can be found, so the center point that corresponds to that minimum distance value is the correct center point of the iris. This way the entire false circle can be removed.

So now once the center point of the iris can be found and the next step is to find a reference point that will be used to calculate the final deviation. For the reference point, caruncle of both the left and right eyes was chosen as shown in the Fig. 3.

Next step is to find the horizontal and vertical deviation values. Specifically, the distance between both caruncle point and center of iris for both the eyes is determined. This gives two deviation values. After that both these deviation are subtracted to get our final horizontal deviation. In order to find the vertical deviation of eyes the y coordinates of center point of both irises are subtracted. These deviation values will vary if they are not calculated under certain conditions.

The conditions that must be taken into consideration while taking picture of a person are as follows: face should be straight w.r.t the camera and both eyes should be focused on the camera. In order to align the face in front of the camera, a bounding box approach was used which helps a



**Fig. 3** Illustrates reference point selection in the cropped eye portion of image

person to align the face. This bounding box will appear in real-time while a person is taking the picture. After this step, two values of deviation are obtained, one is a horizontal deviation and other is a vertical deviation. These sets of two values are used to train a machine learning model to predict whether person has strabismus or not.

### 2.3 Estimation of Deviation

The final value of deviation can be found in two different units. First one is deviation in millimeters and second one is deviation in degrees. Since the whole experiment is done using a calibrated camera so one can easily find the final deviation value in millimeters. This is also discussed in the previous section B. Now in order to find the value of deviation in degrees, the below eye model was implemented in this project (Fig. 4).

Above model shows the position of left and right eye of the subject in front of the calibrated camera.  $W1$  and  $W2$  are the angles that right and left eye make w.r.t the camera. The known parameters are: distances between point  $P$  and left, right eye and value of  $D$  are known. Equation used for computing angular deviation is given below:

$$W1 = 90^\circ - \tan^{-1} \frac{D}{\text{distance between } p \text{ and right eye}} \quad (1)$$

$$W2 = 90^\circ - \tan^{-1} \frac{D}{\text{distance between } p \text{ and left eye}} \quad (2)$$

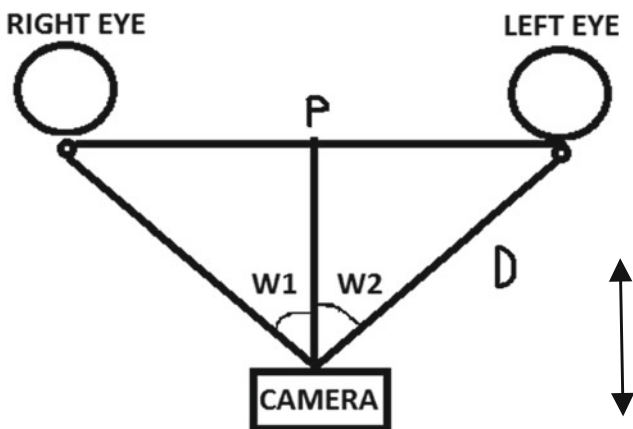


**Fig. 4** Shows model for calculating angular deviation from top view

Once the value of  $W1$  and  $W2$  are calculated one can find the final deviation by:

$$\text{Final deviation} = \text{absolute value of } (W1 - W2) \quad (3)$$

The degree of deviation is less than one degree for a normal person without strabismus [11].

### 2.4 Graphical User Interface

There are two user interfaces that were developed in Matlab to be run using the developed algorithm.

1. First interface has real time processing capability. It uses a built in camera in the laptop or desktop or it can be any USB camera attached to the computer for taking images. Once the image is taken from the interface, it is passed on to image processing part of the program written in Matlab.
2. The second user interface provides support for taking images from local hard drive of the system. User can upload images from the system stored hard drive and then perform same set of image processing operation as done for the 1st user interface (Fig. 5).

## 3 Prediction and Results

The prediction is based on the probability of the outcome from the machine learning model and what type of input data applies to the model. In this study, logistic regression was utilized to train a machine learning model [9]. The image database was divided into testing and training phases. In training phase 100 images were taken to train the model and in testing phase 28 images were used from the image database to test the model. These images contain both the strabismus and non-strabismic individuals of various age groups. Once the picture of person is taken, the face is cropped out and send for image processing. The image processing involves techniques such as HAAR features, Histogram Equalization and Hough transform. Once the image processing is done two sets of values are obtained including horizontal and vertical deviations. Then all the deviation values are stored in an Excel sheet automatically using a script written in Matlab. Inside the Excel



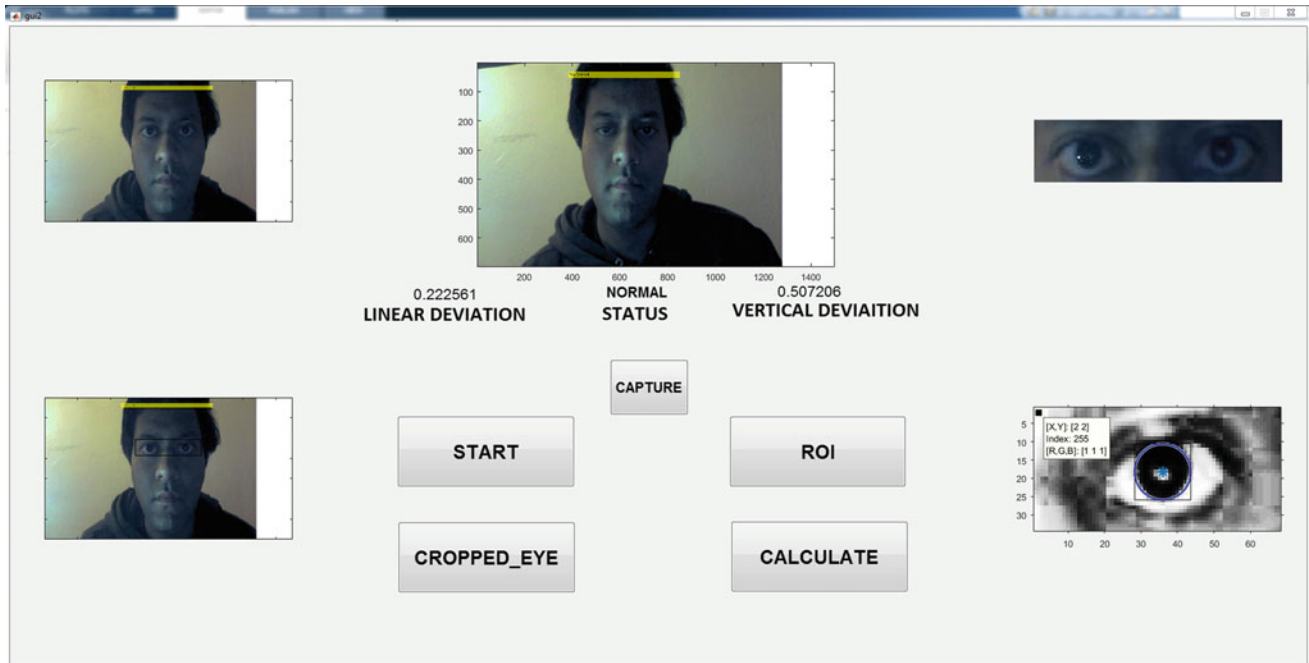


**Fig. 5** Illustrates first graphical user interface for real time image processing capability

sheet three columns are set namely: horizontal deviation, vertical deviation and output label. For training purpose the output label column is filled manually with 0 or 1 value. Value 0 signifies that person does not have strabismus and 1 for person having strabismus. This logistic regression model takes this Excel sheet as input and try to learn from the data inside it. Further, this regression model uses natural logarithmic function to find the coefficients. These coefficients help in predicting the future results from the logistic equation. In order to find the probability of the outcome being normal or strabismic, logistic regression uses concept of odds ratio. This odds ratio is the ratio of event happening over it's not happening.

$$Odds = \frac{P(y = \frac{1}{x})}{1 - P(y = \frac{1}{x})} \quad (4)$$

With the help of above Odds ratio, logistic function can be created by taking the logarithm of Odd function [10].

$$Logit(P(x)) = \ln\left(\frac{P(y = \frac{1}{x})}{1 - P(y = \frac{1}{x})}\right) \quad (5)$$

Here  $x$  is a feature and  $y$  is the outcome of an event.

Above logit function is linear w.r.t  $x$  so one can easily write it in another form. This is also known as sigmoid function. This sigmoid function is used to convert the output value to probability between 0 and 1.

$$P\left(y = \frac{1}{x}\right) = \frac{1}{1 + e^{-(w^T x)}} \quad (6)$$

Here  $w$  represents the gradient value. Once model is trained with data of all the images from the Excel sheet, one comes up with an optimized value of gradient that we can be used to give the prediction. The training accuracy of the developed model comes out to be 93% (Table 1).

The above results in the table suggest that the developed method works well when one uses it under defined above set of conditions. The table also shows that the person with deviation value less than 1 mm is non-strabismic or simply indicating normal in this aspect vision (Fig. 6).

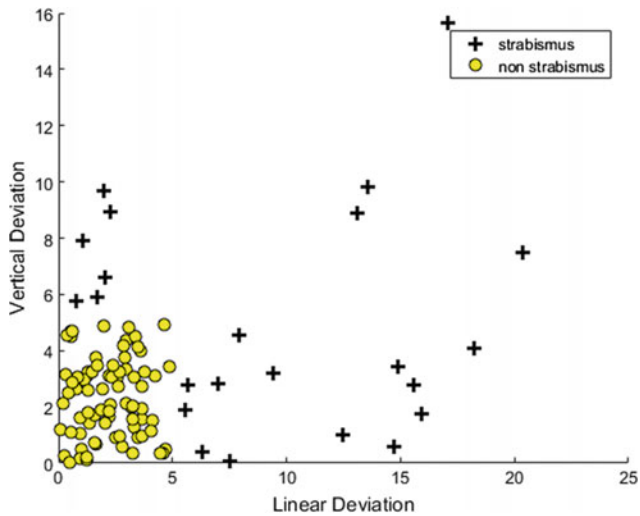
Since this was not verified on a large number of subjects with strabismus it would not be appropriate to state that this prediction is 100% correct. The documented work presented here is more of a demonstration to show that the method can be applied on a large scale to people having some degree of strabismus. Even with the image data utilized there might be some individuals with strabismus but the problem is that some of these images were not taken under sufficient conditions including lighting and position.

## 4 Conclusion

The outcome of these studies demonstrates the application of developed computer vision algorithms needed to provide

**Table 1** Shows the deviation value results of five healthy subjects

S.no	Horizontal deviation (mm)	Vertical deviation (mm)	Age
Subject 1	0.74	0.85	25
Subject 2	0.48	0.34	26
Subject 3	0.19	0.32	26
Subject 4	0.41	0.62	25
Subject 5	0.36	0.78	31

**Fig. 6** Illustrates the data points obtained by applying developed algorithm on all 128 images

clinically applicable tool for calculating the deviation of eyes for people with strabismus. These studies provide a machine learning tool that can be trained with a large number of images and thus can be used as a classifying tool. This type of method for finding the deviation in eyes can be done at ease at home or any place with the help of a laptop. With the help graphical user interface one can take picture of the face in real time, and see the result of the deviation value inside the interface. This provides a convenient and affordable way for a person to prescreen for possibility of strabismus and eventually recommending consultation with a physician. Therefore, this strabismus analysis can be an effective tool for measuring linear and vertical deviation in the eyes and it serves as a clinically applicable tool for early detection of strabismus.

**Conflict of Interest** The authors declare that they have no conflict of interest.

## References

- Jian-Nan, Peng-Yi, Si-Yi, Chuang, & Ying. (2009). Key Techniques of Eye Gaze Tracking Based on Pupil Corneal Reflection. *Intelligent Systems, 2009. GCIS '09. WRI Global Congress on*, 2, 133–138.
- Khumdat, N., Phukpattaranont, P., & Tengtrisorn, S. (2013). Development of a computer system for strabismus screening. *Biomedical Engineering International Conference (BMEiCON)*, 2013 6th, 1–5.
- Varier, D., & Krishnamoorthy, V. (2014). An electrooculogram based real time system for measurement and analysis of visual stimuli for detecting strabismus and nystagmus. *Advances in Computing, Communications and Informatics (ICACCI)*, 2014 International Conference on, 1125–1130.
- Mathworks. (2017). Single Camera Calibration App. [Online]. <https://www.mathworks.com/help/vision/ug/train-a-cascade-object-detector.html>.
- ImageNet. (n.d.). Face Synsets. [Online]. Available: <http://www.image-net.org/synset/textnet/api.org.geturls?wnid=n09618957>.
- Google. (n.d.). Face (Image Search). [Online]. Available: [https://www.google.com/search?biw=944&bih=947&tbm=isch&sa=1&q=face&oq=face&gs\\_l=psy-ab.3..0j0i67k112j0.4914.5199.0.5434.4.4.0.0.0.228.430.2-2.2.0....0...1.1.64.psy-ab..2.2.430....0.3TXAw0gbymM](https://www.google.com/search?biw=944&bih=947&tbm=isch&sa=1&q=face&oq=face&gs_l=psy-ab.3..0j0i67k112j0.4914.5199.0.5434.4.4.0.0.0.228.430.2-2.2.0....0...1.1.64.psy-ab..2.2.430....0.3TXAw0gbymM).
- P. Viola and M. Jones, “Rapid object detection using a boosted cascade of simple features,” presented at the IEEE Computer Society Conf. Computer Vision and Pattern Recognition, 2001.
- Fitriyani, N., Yang, C., & Syafrudin, M. (2016). Real-time eye state detection system using haar cascade classifier and circular hough transform. *Consumer Electronics, 2016 IEEE 5th Global Conference on* 1–3.
- Seddik, A., & Shawky, D. (2015). Logistic regression model for breast cancer automatic diagnosis. *SAI Intelligent Systems Conference (IntelliSys)*, 2015, 150–154.
- Pavlyshenko, B. (2016). Machine Learning, Linear and Bayesian Models for Logistic Regression in Failure Detection Problems.
- Economides, J., Adams, D., & Horton, J. (2016). Variability of Ocular Deviation in Strabismus. 63–69.



# Phase-Contrast Breast-CT: Optimization of Experimental Parameters and Reconstruction Algorithms

Sandro Donato, Serena Pacile<sup>\*</sup>, Luca Brombal, Giuliana Tromba, and Renata Longo

## Abstract

X-ray breast computed tomography (breast-CT) is a new emerging technique for breast imaging however its application is still limited because of low spatial resolution and high delivered dose. In this framework, synchrotron radiation provides ideal X-ray imaging conditions. Tunable and monochromatic laminar X-ray beam, along with large propagation distance, allows acquiring images with high quality, low scatter and dose reduction, due to the selection of the most suitable energy for the given thickness and breast composition. Moreover, the high spatial coherence permits to exploit the phase-contrast effects enabling a better image quality and soft tissue contrast. At the Elettra synchrotron facility, in Italy, a project for in vivo low-dose, high-contrast and high-resolution breast-CT is under development using a high-efficiency photon-counting detector. Due to the vertical size of the beam ( $\sim 3.5$  mm) the scan requires a sequence of vertical steps. Thus reducing the number of projections is essential to shorten the total acquisition time. Optimized preprocessing algorithms (phase-retrieval) and the state of the art of tomographic reconstruction methods are crucial to improve image quality. In this work, performances of standard and iterative reconstruction algorithms at different experimental conditions are compared, evaluating quantitatively the image quality in terms of Contrast-to-Noise ratio and edge sharpness. Preliminary results suggest that, in the light of a clinical exam where a short scan time is desirable, the

projection number can be reduced without a major loss in image quality by applying FBP based reconstruction algorithms and phase-retrieval pre-processing.

## Keywords

Breast-CT • Phase-Contrast • Reconstruction algorithms

## 1 Introduction

Breast cancer is one of the most common cancer in women worldwide. It also represents about a quarter of all cancers in women and the second leading cause of cancer related death [1]. The importance of early detection leads to an increasing interest in the development of novel tools and imaging techniques that may supplement or replace mammography, overcoming its limited specificity [2]. In the last few decades an increased effort in the transition from mammography to three-dimensional (3D) imaging has been made in clinical practice with the realization of 3D mammographic systems, such as tomosynthesis [3, 4] and breast-CT dedicated scanners [5, 6]. Tomosynthesis, when combined to digital mammography, leads to a significant increase in the breast cancer detection rate but at the cost of increased glandular dose [4, 7]. Cone breast CT [8] is a promising technique because it has full 3D capability with near-isotropic resolution but still limited because of low spatial resolution and high delivered dose.

In this framework, synchrotron radiation provides ideal X-ray imaging conditions. The possibility to tune monochromatic X-rays enables the selection of the most suitable energy for a given thickness and breast composition. This point represents a great benefit for both image quality and dosimetry in radiological applications [9]. The high spatial coherence enables the detection of phase effects which can be exploited for imaging biological tissues [10]. In the simplest phase sensitive imaging configuration, the so-called propagation-based imaging technique (PB-CT), to detect phase effects, it is sufficient to place the sample at a

S. Donato (✉) · L. Brombal · R. Longo  
INFN Sezione Di Trieste, Trieste, Italy  
e-mail: sandro.donato@elettra.eu

S. Pacile<sup>\*</sup>  
Department of Engineering and Architecture, University of Trieste, Trieste, Italy

S. Pacile<sup>\*</sup> · G. Tromba  
Elettra-Sincrotrone Trieste S.C.p.A, Basovizza, Trieste, Italy

suitable distance from the detector. From the acquired projections, phase information can be exploited to improve signal-to-noise ratio of the projection by applying the phase retrieval algorithm [11].

Phase-contrast imaging has been shown to provide enhanced soft-tissue contrast and improved better visualization and characterization of lesions in breasts [12, 13]. Different feasibility studies have been recently conducted for evaluating the potentials of PB-CT to the characterization of breast tissue specimens [14–16].

In this context, the SYRMA-3D (SYnchrotron Radiaton for Mammography) aims to setup the first clinical protocol of PB-CT at the Elettra synchrotron light source in Trieste (Italy). To achieve high image quality at low delivered dose ( $\sim 5$  mGy mean glandular dose), both the experimental setup and the data processing include a number of innovative elements: novel high-efficiency CdTe photon-counting detector, dedicated pre-processing procedure, Phase Retrieval (PhR) algorithm and Monte Carlo model for the mean glandular dose estimation [17]. Recently, a work showing the first characterization of the imaging system and the first images of breast specimens have been published showing encouraging results in terms of image quality and delivered dose [18].

At present, a great effort is being made to reduce the total scan time which, due to the limited vertical size of the beam ( $\sim 3.5$  mm), the maximum frame rate of the detector (33 fps) and the selected number of projections (1200 per scan), currently is of the order of ten minutes. Considering the actual beam size and that the frame rate cannot be further increased, reducing the number of projections is the only way to shorten the total duration time of the exam. Furthermore, the role of the reconstruction algorithms in the image quality must be evaluated and discussed. In the following the image quality is established using two common metrics, namely the edge sharpness and the Contrast-to-Noise Ratio (CNR). This study is carried out using a surgical breast specimen to simulate conditions as close as possible to a clinical exam.

## 2 Materials and Methods

### 2.1 Breast Tissue Sample

The image reported in this study was acquired to guide the pathologist in the localization of lesions for the histological examination, according to the standard procedures of the Pathology Unit of the Academic Hospital of Cattinara, Trieste University, accredited by JCI (Joint Commission International). The sample was derived from surgical material sent to the Pathology Unit according to local guidelines for histological examination. The Directive 2004/23/EC of

the European Parliament and of the Council of 31 March 2004 on setting standards of quality and safety for the donation, procurement, testing, processing, preservation, storage and distribution of human tissues were followed. For breast-CT acquisition, the sample was formalin fixed and sealed hermetically in a polyethylene container. The dimensions of the specimen, containing an infiltrating ductal carcinoma, were approximately 10 cm by 8.5 cm and the thickness was of about 4 cm.

### 2.2 Experimental Setup and Acquisition Parameters

Breast-CT scans were performed the SYRMEP (SYnchrotron Radiation for MEDical Physics) beamline of Elettra. X-rays are generated by a bending magnet in the energy range from 8.5 to 40 keV, while energy is selected using a Si (111) double-crystal monochromator with resolution of  $\Delta E/E \approx 10^{-3}$ . The beam cross-section at sample position is  $220$  (horizontal)  $\times$   $3.5$  mm (vertical, Gaussian shape, FWHM). CT projections are acquired using a photon-counting detector (PIXIRAD-8), made up by 8 adjacent modules with a CdTe sensor, a pixel spacing of  $60$   $\mu\text{m}$  and a global active area of  $246 \times 25$  mm<sup>2</sup> ( $4096 \times 476$  pixels). It is placed in the beamline patient room 32 m far away from the X-ray source. Sample is attached to a rotating bed in correspondence of an ergonomic aperture devoted to host the breast of the patient. The sample-to-detector distance is 1.6 m that allows to detect phase-contrast effects.

Due to the small beam divergence ( $\sim 7$  mrad), scans were done over 180 degrees, at the maximum frame rate of the detector in dead-time-free mode [19], collecting 1200 equally-spaced projections at three different energies (32, 35 and 38 keV) of the same region of the tissue. The photon beam was filtered with Aluminum sheets of different thickness to deliver a fixed Mean Glandular Dose (MGD) of 5 mGy, that is a dose comparable with a two views mammographic exam. The MGD's was calculated according an ad hoc developed model [17] based on a MonteCarlo simulation developed and validated for this program [20].

### 2.3 Data Pre-processing and Reconstruction

Starting from the original stacks of projections, two new datasets with 600 and 900 images were generated by means of linear interpolation, preserving the delivered MGD. Raw collected images undergo to an optimized pre-processing procedure that performs dynamic flat fielding equalization [21], fix gaps around adjacent modules, applies despeckle and dynamic ring removal filters. Subsequently a

single-distance phase-retrieval algorithm, based on the Homogeneous Transport of intensity equation (TIE-Hom [11]), is applied. The algorithm requires as input parameter the  $\delta/\beta$  ratio, whereas  $\delta$  and  $\beta$  denote, the phase-shift and the absorption components of the complex refractive index  $n = 1 - \delta + i\beta$ , respectively. We used two distinct  $\delta/\beta$  ratios, the first value is theoretical value [22] of breast tissue in air ( $\delta/\beta \sim 2300$ , hereafter single material PhR), while the latter considers an adipose/glandular tissues interface ( $\delta/\beta = 870, 978, 1083$  for 32, 35 and 38 keV, respectively, hereafter two material PhR). Then the slices have been reconstructed with an in-house built software [23] using different GPU-based reconstruction algorithms: standard Filtered Back Projection (FBP), Simultaneous Iterative Reconstruction Technique (SIRT) using 1000 iterations, Simultaneous Algebraic Reconstruction Technique (SART) with 50 iterations, and Minimum Residual Filtered Back Projection method (MR-FBP).

## 2.4 Quantitative Analysis

Quantitative analysis was conducted to study the influence of each parameter (energy,  $\delta/\beta$  ratio, number of projections and reconstruction algorithm) on the quality of the reconstructed images. We evaluated image quality using two estimators: Contrast-to-Noise Ratio (CNR) and edge sharpness. CNR helps to evaluate the visibility of low-contrast structures and is defined as:

$$CNR = \frac{|S_g - S_a|}{\sqrt{(\sigma_g^2 + \sigma_a^2)/2}} \quad (1)$$

where  $S$  is the mean value of a homogeneous region of interest (ROI),  $\sigma$  is the associated standard deviation and the subscripts  $g$  and  $a$  refer to glandular and adipose tissues. The CNR was measured taking the average CNR of four non-overlapping pairs of square ROIs (showed with square boxes in Fig. 1), where for each pair one ROI is selected within the glandular tissue and the other within the adipose tissue.

Edge sharpness was evaluated by fitting an error function (erf) in a profile (shown with the magenta line in Fig. 1) of the interface between adipose and glandular tissue, across a sharp step-wedge (produced by a surgical cut during the preparation for formalin fixation), calculating the derivative of this function (a Gaussian) and measuring the full width at half maximum value (FWHM). The error associated to the measured resolution is derived from the parameter uncertainty with the error propagation rules.

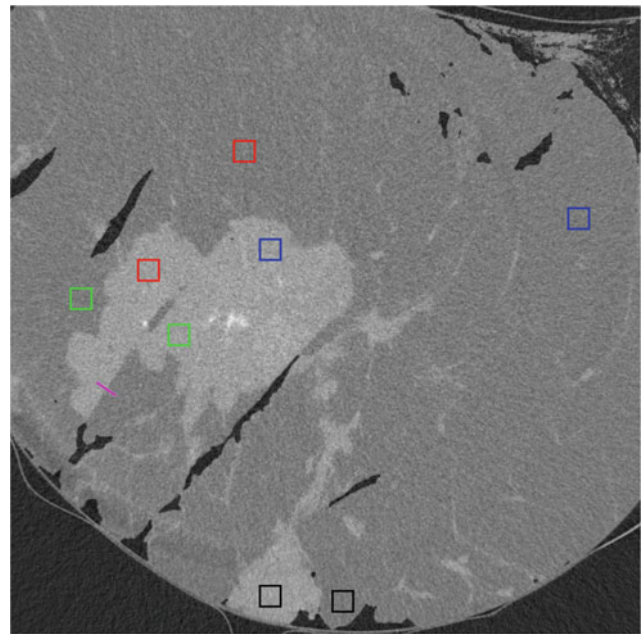


**Fig. 1** Slice of the central region of the breast tissue at 32 keV reconstructed with FBP, using 1200 projections and  $\delta/\beta = 2308$ . Squares represent ROIs for the evaluation of the CNR. Different colors indicate a different couple of glandular-adipose uniform regions. The magenta line refers to the edge used for spatial resolution evaluation

## 3 Results and Discussion

Results of the quantitative analysis, for the single and two material PhR, are reported in Tables 1 and 2, respectively. In Table 1 the CNR and FWHM for all the energies, projection numbers and reconstruction algorithms, when the single material PhR is applied, are reported. Comparing the algorithms while keeping the number of projection fixed, it can be noted that SIRT reconstructions have the best CNR but the poorest resolution, while FBP gives the best spatial resolution with the lowest CNR (Fig. 2a-d). Furthermore, regardless of the reconstruction algorithm, reducing the number of projections the spatial resolution worsens; on the contrary the CNR remains constant if FBP is applied while it increases for the other algorithms (see Fig. 3). Comparing the energies, it is shown that the 38 keV reconstruction gives the lowest CNR while the values at 32 and 35 keV are comparable.

When the two materials PhR is applied (Table 2), CNR and FWHM show similar dependence on the reconstruction algorithms and projection numbers as observed in Table 1. Contrarily, the CNR shows a little energy dependence and its values are compatible within the statistical uncertainty for all the energies.

**Table 1** Values of CNR and FWHM for single material PhR, at different energies, number of projections and reconstruction algorithm

N <sub>proj</sub>	Algorithm	E = 32 keV		E = 35 keV		E = 38 keV	
		CNR	FWHM (mm)	CNR	FWHM (mm)	CNR	FWHM (mm)
1200	FBP	3.62 ± 0.15	0.13 ± 0.03	3.55 ± 0.26	0.11 ± 0.06	3.11 ± 0.22	0.13 ± 0.03
	MR-FBP	4.31 ± 0.14	0.15 ± 0.02	4.18 ± 0.26	0.12 ± 0.05	3.72 ± 0.21	0.13 ± 0.02
	SART	3.29 ± 0.13	0.17 ± 0.02	3.65 ± 0.36	0.12 ± 0.05	3.17 ± 0.16	0.13 ± 0.02
	SIRT	7.02 ± 0.18	0.25 ± 0.01	7.03 ± 0.38	0.21 ± 0.03	6.30 ± 0.29	0.25 ± 0.01
900	FBP	3.65 ± 0.15	0.15 ± 0.03	3.62 ± 0.33	0.13 ± 0.06	3.18 ± 0.29	0.16 ± 0.03
	MR-FBP	4.92 ± 0.11	0.19 ± 0.02	4.87 ± 0.32	0.14 ± 0.04	4.32 ± 0.27	0.18 ± 0.02
	SART	4.38 ± 0.22	0.17 ± 0.02	4.24 ± 0.31	0.20 ± 0.03	3.52 ± 0.27	0.18 ± 0.02
	SIRT	7.21 ± 0.23	0.27 ± 0.01	7.32 ± 0.42	0.22 ± 0.03	6.49 ± 0.36	0.28 ± 0.02
600	FBP	3.56 ± 0.05	0.16 ± 0.02	3.52 ± 0.25	0.17 ± 0.07	3.15 ± 0.27	0.18 ± 0.05
	MR-FBP	6.11 ± 0.28	0.22 ± 0.01	6.22 ± 0.28	0.18 ± 0.03	5.60 ± 0.39	0.21 ± 0.02
	SART	5.64 ± 0.33	0.22 ± 0.01	5.89 ± 0.42	0.22 ± 0.03	5.19 ± 0.23	0.22 ± 0.01
	SIRT	7.59 ± 0.53	0.28 ± 0.01	8.09 ± 0.29	0.27 ± 0.02	7.28 ± 0.43	0.31 ± 0.01

**Table 2** Values of CNR and FWHM for two materials PhR, at different energies, number of projections and reconstruction algorithm

N <sub>proj</sub>	Algorithm	E = 32 keV		E = 35 keV		E = 38 keV	
		CNR	FWHM (mm)	CNR	FWHM (mm)	CNR	FWHM (mm)
1200	FBP	1.88 ± 0.11	0.09 ± 0.02	2.02 ± 0.17	0.09 ± 0.11	1.88 ± 0.15	0.09 ± 0.04
	MR-FBP	2.44 ± 0.11	0.13 ± 0.02	2.51 ± 0.18	0.10 ± 0.07	2.38 ± 0.15	0.11 ± 0.03
	SART	1.86 ± 0.11	0.17 ± 0.03	20.1 ± 0.16	0.11 ± 0.07	2.04 ± 0.20	0.11 ± 0.03
	SIRT	4.37 ± 0.13	0.20 ± 0.02	4.51 ± 0.31	0.17 ± 0.04	4.25 ± 0.24	0.18 ± 0.02
900	FBP	1.91 ± 0.12	0.09 ± 0.03	2.07 ± 0.21	0.12 ± 0.11	1.95 ± 0.20	0.14 ± 0.05
	MR-FBP	2.93 ± 0.11	0.18 ± 0.03	3.04 ± 0.25	0.12 ± 0.06	2.85 ± 0.21	0.14 ± 0.03
	SART	2.66 ± 0.08	0.17 ± 0.04	2.69 ± 0.22	0.12 ± 0.06	2.37 ± 0.22	0.14 ± 0.02
	SIRT	4.59 ± 0.11	0.21 ± 0.02	5.38 ± 0.35	0.18 ± 0.04	4.49 ± 0.32	0.21 ± 0.02
600	FBP	1.86 ± 0.03	0.14 ± 0.03	2.01 ± 0.17	0.13 ± 0.10	1.92 ± 0.17	0.15 ± 0.06
	MR-FBP	3.87 ± 0.06	0.22 ± 0.02	4.01 ± 0.23	0.15 ± 0.05	3.83 ± 0.29	0.18 ± 0.02
	SART	3.57 ± 0.17	0.22 ± 0.02	3.91 ± 0.28	0.17 ± 0.05	3.45 ± 0.20	0.17 ± 0.02
	SIRT	5.03 ± 0.15	0.23 ± 0.01	5.39 ± 0.25	0.21 ± 0.04	5.12 ± 0.35	0.24 ± 0.02

In general, comparing results at different  $\delta/\beta$ , the single material approach produces a higher CNR (40% in average) and a worst spatial resolution (20% in average). These effects can be seen in Fig. 4 that compares FBP reconstructions with different  $\delta/\beta$  ratio. The one with a lower  $\delta/\beta$  ratio has sharpen edges, but it looks noisy. On the contrary, the appearance of the slice at higher  $\delta/\beta$  is better (higher visibility of glandular blanches). In order to better visualize results reported in the tables, scatter plots of the FWHM vs CNR at 32 keV for both  $\delta/\beta$  ratios are presented in Fig. 5. In a recent work [24] it was established that if an insufficient CNR is detected, a radiologist judges an image as

meaningless for the diagnosis process. Beyond a level of CNR considered acceptable, the radiologists prefer the images having the highest edges sharpness (i.e. the lowest value of FWHM). Therefore, as an example, SIRT algorithm produces a major CNR increment while introducing a substantial blurring (see Fig. 2d) has not to be considered for our study. The SART algorithm, while enhancing CNR with good spatial resolution, introduces a texturized noise in the reconstruction (see Fig. 2c). The MR-FBP, at least for 900 and 1200 projections, shows a spatial resolution comparable to FBP, giving at the same time a better CNR (see Fig. 2a–b).

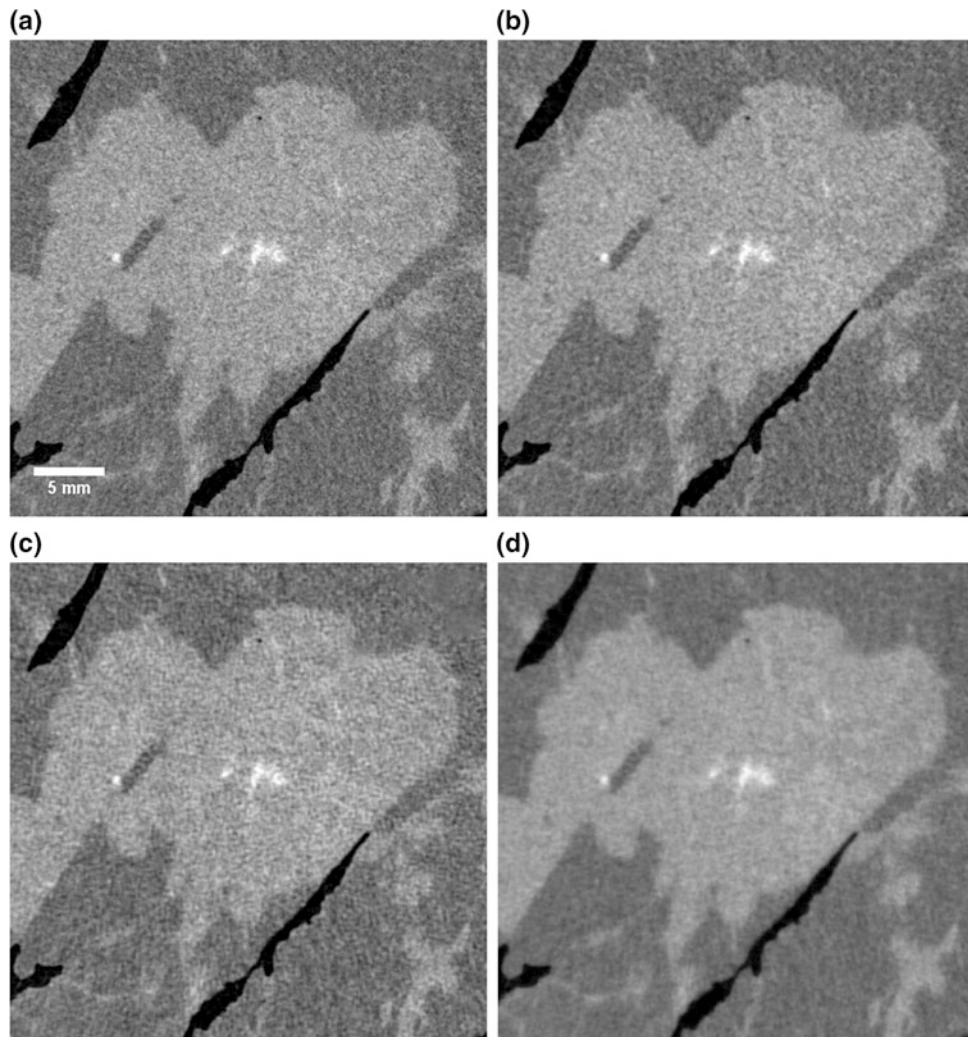


**Fig. 2** Detail of the central region of a slice reconstructed with FBP (a), MR-FBP (b), SART (c) and SIRT (d) algorithms, acquired at 32 keV using 1200 projections and  $\delta/\beta = 2308$  (slices are showed with the same grayscale range). The white pixels indicate a calcification inside the lesion (bright gray) surrounded by adipose tissue (dark gray).

Sharp edges and air (black regions) are a result of the surgical cuts done for clinical assessment. FBP slice **a** appears sharper than the ones resulting from other reconstructions, but at the same time with higher noise, while SIRT slice **d** is clearer visible, i.e. with more CNR, but more blurred

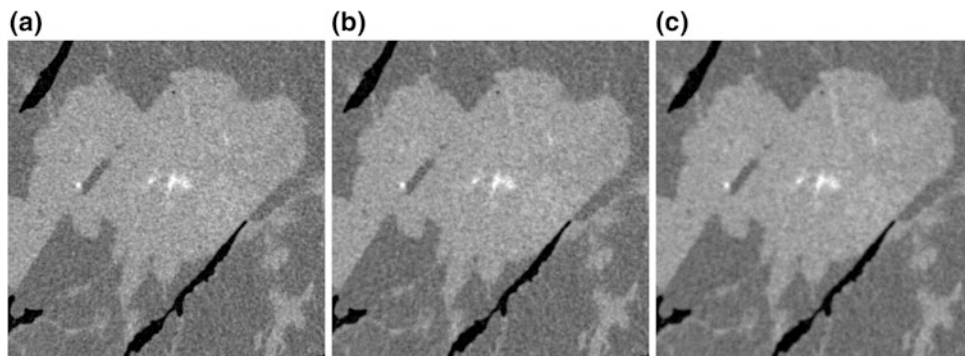


**Fig. 3** Different panels shown MR-FBP slices with different number of projections, 1200 (a), 900 (b) and 600 (c), respectively. With non-standard reconstruction algorithms, reducing the number of projections increases the CNR and decreases the spatial resolution



**Fig. 4** FBP reconstructions, at 32 keV and 1200 projections, with two materials **a** and single material **b** PhR

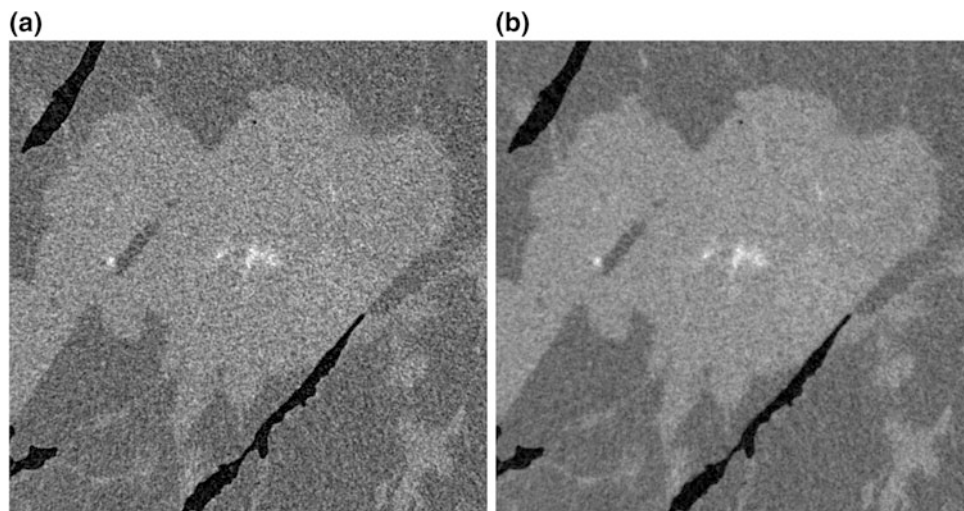
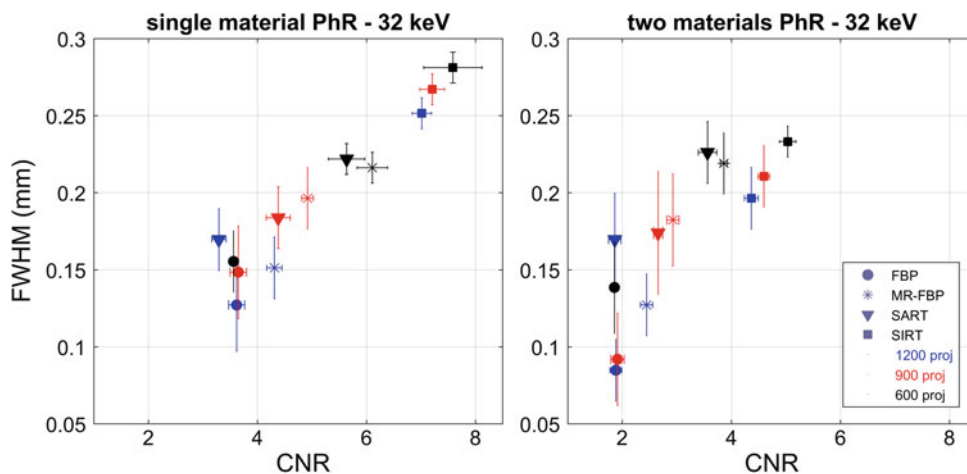


**Fig. 5** Scatter plot of the FWHM and CNR at 32 keV with single material PhR (left) and two materials PhR (right). Different symbols denote different algorithms, while colors indicate the number of projections used for reconstruction (1200 in blue, 900 in red, 600 in black)



## 4 Conclusions

In this study we report PB-CT images of a large ( $\sim 10$  cm in diameter) breast specimen acquired with a delivered dose (5 mGy MGD) lower than (or comparable to) available clinical systems but with higher spatial resolution (60  $\mu$ m pixel size and FWHM down to 100  $\mu$ m). Two different sets of  $\delta/\beta$  ratio are compared, showing that, for a given CNR, the single material approach results in a better spatial resolution (see Fig. 3).

The performances of different reconstruction algorithms were investigated: in general, an increase in CNR is related to a decrease of the spatial resolution. The best spatial resolution is obtained using the FBP while similar performances, with a slight increase in CNR, are produced by the MR-FBP. On the contrary, the iterative algorithms produce a major increase in CNR but they introduce either a textured noise (SART) or an excessive blurring (SIRT).

In the selected energy range (32–38 keV) the CNR is slightly energy dependent, reporting the highest values for energies lower or equal 35 keV.

In the light of a clinical breast-CT exam, where a short scan time is desirable, the projection number can be reduced down to 900 without a major loss in image quality by applying the FBP-based reconstruction algorithms and single material PhR.

In this work preliminary results are presented and a wider study comprising several breast samples, a larger energy range and an image scoring by radiologists is ongoing to perform the final tuning of phase retrieval and reconstruction parameters.

**Acknowledgements** Funding: This work was conducted within the SYRMA-3D project, which is funded by Istituto Nazionale di Fisica Nucleare (National Scientific Committee 5 for Technological and Inter-Disciplinary research) and supported by Elettra-Sincrotrone Trieste S.C.p.A. S. Donato was partially supported by Consorzio per la Fisica Trieste. The authors acknowledge Prof. F. Zanconati MD and Dr



Deborah Bonazza MD for providing and preparing the breast specimen. Authors want also to thank all the participant of the SYRMA-3D collaboration for their support and useful discussions. We thank the staff of the SYRMEP beamline for the precious help during the experimental activity.

**Compliance with Ethical Requirements** The authors declare that they have no conflict of interest.

## References

1. Siegel, R.L., Miller, K. D., Jemal, A.: Cancer statistics, 2016. CA: a cancer journal for clinicians 66, 7–30 (2016).
2. Sprague, B. L., Arao, R. F., Miglioretti, D. L., et al.: National performance benchmarks for modern diagnostic digital mammography: Update from the breast cancer surveillance consortium, 283, 59–69 (2017).
3. Teertstra, H.J., Loo, C.E., van den Bosch, M.A.A.J., et al.: Breast tomosynthesis in clinical practice: initial results. European Radiology 20, 16–24 (2010).
4. Sechopoulos, I.: A review of breast tomosynthesis. Part I. The image acquisition process. Med. Phys. 40, 014301–12 (2013).
5. O’Connell, A.M., Karellas, A., Vedantham, S.: The potential role of dedicated 3D breast CT as a diagnostic tool: review and early clinical examples. Breast J. 20, 592–605 (2014).
6. Zhao, B., Zhang, X., Cai, W., Conover, D., Ning, R.: Cone beam breast CT with multiplanar and three dimensional visualization in differentiating breast masses compared with mammography. Eur. J. Radiol. 84, 48–53 (2015).
7. Olgar, T., Kahn, T., Gosch, D.: Average glandular dose in digital mammography and breast tomosynthesis. Rofo, 184 (10), 911–918 (2012).
8. Lindfors, K.K., Boone, J.M., Nelson, T.R., Yang, K., Kwan, A.L., Miller, D.F.: Dedicated breast CT: initial clinical experience. 246 (3), 725–33 (2008).
9. Fedon, C., Rigon, L., Arfelli, F., et al.: Dose and diagnostic performance comparison between phase-contrast mammography with synchrotron radiation and digital mammography: a clinical study report. JMI (2018) in press.
10. Beltran, M.A., Paganin, D.M., Siu, K. K.W., et al.: Interface-specific x-ray phase retrieval tomography of complex biological organs, Phys.Med.Biol. 56(23), 7353–69 (2011).
11. Paganin, D., Mayo, S., Gureyev, T. E., Miller, P. R., and Wilkins, S. W.: Simultaneous phase and amplitude extraction from a single defocused image of a homogeneous object. J. Microsc. 206(1), 33–40 (2002).
12. Longo, R., Tonutti, M., Rigon, L., et al.: Clinical study in phase-contrast mammography: image-quality analysis. Philos. Trans. A. Math. Phys. Eng. Sci. 372, 20130025 (2010).
13. Coan, P., Bravin, A., Tromba, G.: Phase-contrast x-ray imaging of the breast: recent developments towards clinics. J. Phys. D: Appl. Phys 46(49) 494007 (2013).
14. Zhao, Y., Brun, E., Coan, P., Huang, Z., et al.: *High-resolution, low-dose phase contrast X-ray tomography for 3D* diagnosis of human breast cancers. Proc. Nat. Acad. Sci. 109(45), 18290–18294 (2012).
15. Nesterets, Y.I., Gureyev, T.E., Mayo, S.C., et al.: A feasibility study of x-ray phase-contrast mammographic tomography at the imaging and medical beamline of the Australian synchrotron. J. Synchron. Rad. 22, 1509–1523 (2015).
16. Baran, P., Pacilè, S., Nesterets, Y., et al.: Optimization of propagation-based x-ray phase-contrast tomography for breast cancer imaging. Phys. Med. Biol. 62, 2315–2332 (2017).
17. Mettievier, G., Fedon, C., Di Lillo, F., et al.: Glandular dose in breast computed tomography with synchrotron radiation. Phys. Med. Biol. 61(2), 569 (2016).
18. Longo, R., Arfelli, F., Bellazzini, et. al: Towards breast tomography with synchrotron radiation at Elettra: first images. Phys. Med. Biol. 61(4), 1634 (2016).
19. Delogu, P., Golosio, B., Fedon, C., et al.: Imaging study of a phase-sensitive breast-CT system in continuous acquisition mode. J. Instr. 12(01), C01016 (2017).
20. Fedon, C., Longo, F., Mettievier, G., Longo, R.: Geant4 for breast dosimetry: parameters optimization study. Phys. Med. Biol. 60 (16), N311 (2015).
21. Delogu, P., Brombal, L., Di Trapani, V., Donato, et al.: Optimization of the equalization procedure for a single-photon counting CdTe detector used for ct. J. Instr. 12(11), C11014 (2017).
22. TS\_imaging Homepage: <https://ts-imaging.net/Services/Simple/ICUtilXdata.aspx>.
23. Brun, F., Pacilè, S., Accardo, A., et al.: Enhanced and flexible software tools for x-ray computed tomography at the Italian synchrotron radiation facility Elettra. Fundam. Inform. 141(2–3), 233–243 (2015).
24. Pacilè, S., Brun, F., Dullin, C., et al.: Clinical application of low-dose phase contrast breast CT: methods for the optimization of the reconstruction workflow. Biomed. Opt. Expr. 6(8), 3099–3112 (2015).

# Response of CR Detector Plates for Use in Mammography Equipment

Mabel Bustos Flores and Arnaldo Prata Mourão

## Abstract

Worldwide, breast cancer is the second leading cause of cancer death among women, overcome only by melanoma cancer. In Brazil, the detectors commonly used in CR mammography are photostimulable phosphor plates, whose response to radiation varies in relation to the parameters applied to the X-ray tube for the acquisition of mammographic images. The high incidence of this disease makes it important to analyze and monitor the entire mammography system to ensure optimal performance, seeking to make your diagnosis early, increasing the chances of the patient's healing. The objective of this study is to evaluate the response of a CR plate for the variation of voltage and time applied. For this purpose, four X-ray beams were selected and a successive exposition of the CR plate was made, varying the exposure time. Then, with a solid-state detector, the air kerma was measured for the 30 kV X-ray beam previously used, and subsequently, with the acquired images, the intensity value recorded by the CR plate was correlated with the value of measured air kerma, obtaining the response curve in relation to the exposure time and the air kerma. The determination of these response curves will help to know the performance of the CR plate, which will allow selecting the most suitable parameters within the sensitivity range of the CR plate for the acquisition of mammographic images.

## Keywords

Mammography • Computed radiography • X radiation

M. B. Flores (✉) · A. P. Mourão  
 Department of Nuclear Engineering, School of Engineering,  
 Federal University of Minas Gerais, Av. Antônio Carlos,  
 Belo Horizonte, MG 131270-901, Brazil  
 e-mail: mbustos@ufmg.br; mabelita.bfm@gmail.com

A. P. Mourão  
 Federal Center for Technological Education of Minas Gerais,  
 Center for Biomedical Engineering, Av. Amazonas,  
 Belo Horizonte, MG 30421-169, Brazil

## 1 Introduction

In global statistics, breast cancer is one of the leading causes of cancer death in women [1]. In 2012, more than 1.67 million new cases and more than 521 thousand deaths were estimated for the world, corresponding to 14.7% of cancer deaths in women [2]. In Brazil, according to INCA, more than 57 thousand new cases of breast cancer were estimated by 2016 [3].

In developed countries, at the same time that the incidence tends to increase, mortality is declining due mainly to the timely detection and the best conditions for the treatment of this disease [4].

Indications for the presence of breast cancer may be based on 4 types of records that appear on mammographic images: the morphology characteristic of a tumor mass, with irregular margins; the presence of calcifications; distortions in the patterns of normal tissues generated by the disease; asymmetries between the corresponding regions of the left and right breasts [5].

Mammography is basically an X-ray image of the breast, is the main tool used in early detection programs and plays a relevant role in the diagnosis of breast cancer as well as its location in biopsy and therapy procedures [6].

The X-ray detection of these structures presents difficulties, the most important ones are because they present an attenuation very similar to the tissues in which they are immersed and to the superposition of tissues that occurs when projecting the mammary volume in an image 2D [5].

The quality of the images acquired with these systems depends on several parameters such as the voltage and current applied to the X-ray tube and the characteristics of the detector used [4].

The objective of this work was to evaluate some parameters of image quality, such as saturation time and spatial resolution of CR plates. For the evaluation of this last parameter, a basic test object was suggested for the qualitative evaluation of the resolution.

## 2 Methodology

A CR plate was used to perform this study, which was exposed on a X-ray mammography device. The main characteristics of this equipment will be presented below.

### 2.1 Mammographic System

The mammographic system consists of a mammograph VMI, model Graph Mammo AF (see Fig. 1a), which has a rotating anode and an anode/filter combination Mo/Mo [7]; a CR plate for mammography of size  $18 \times 24 \text{ cm}^2$ , model Regius RP6M110, manufactured by Konica Minolta (see Fig. 1b), and its respective scanning unit, model Regius 110 HQ (see Fig. 1c). For this plate, according to the manufacturer, this digitizing unit has a reading function with a pixel size of  $43.75 \mu\text{m}$  and a digital gradation level of 4096 levels (12 bits) [8].

### 2.2 Caracterización de la respuesta de la placa CR y dosimetría

To know the response of the CR plate with respect to the intensity of darkening as a function of the exposure time, 4 voltages were selected, trying to cover the entire range of voltages available in the mammograph, from 20 to 35 kV, thus knowing the response of the CR plate when low, intermediate and high voltages are applied.

For the acquisition of the images, the direct exposure of the CR plate was carried out, applying the voltages of 20, 25, 30 and 35 kV, varying the time from 0.5 s and in increments

of 0.5 s until obtaining the first saturated image, maintaining the current at 70 mA and the focus-detector distance at 53 cm and without the use of additional filters.

After performing each of the exposures of the CR plates, it was read in its corresponding digitizing unit, obtaining 25 images for each CR plate, which were saved in unprocessed format, that is to say, without any program of improvement of image quality. The size of the images obtained was  $4040 \times 5416$  pixels, with a resolution of  $22.86 \text{ pixel mm}^{-1}$ .

These images were analyzed using ImageJ software by selecting ROIs of  $1 \text{ cm}^2$  in the central region of the CR plate to evaluate the variation of the recorded intensity, in grayscale, and then to perform a correlation of the exposure time for each voltage and determine the best fit curve.

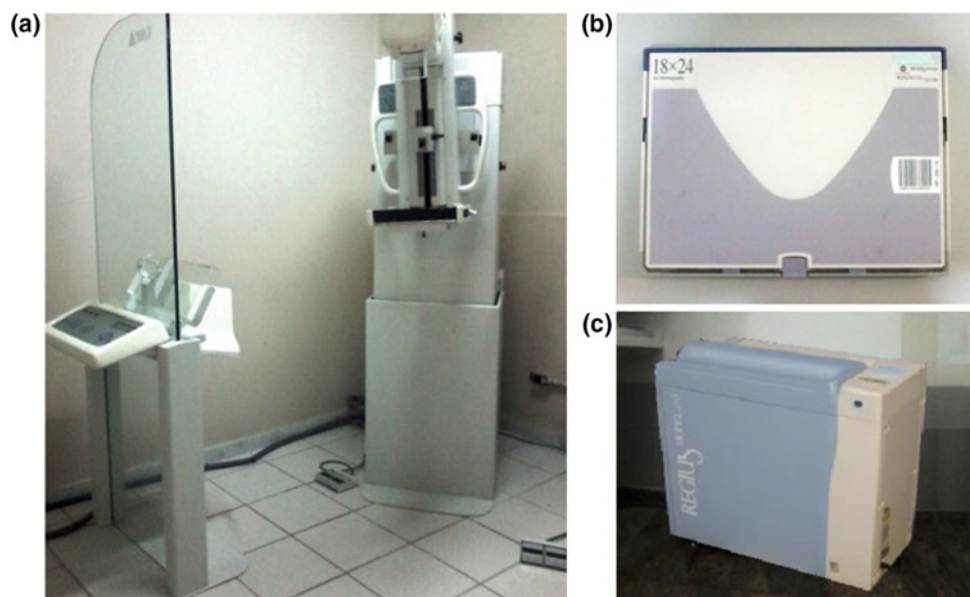
The voltage of 30 kV was selected to study the response of the CR plate in relation to the air kerma, this voltage was selected because the one that does not saturate so quickly compared to the 35 kV curve and could be used to perform a diagnostic test.

To obtain this response curve, an Accu Dose Radcal solid-state detector was used, which was placed directly on the breast support to obtain the values of the air kerma [9] applying the same parameters previously mentioned for the curve of 30 kV.

With this procedure, 4 values of the air kerma were obtained, which were correlated with the intensity values, in gray scale, to obtain the kerma—intensity calibration curve and to determine the maximum and minimum dose values present in the images. It should be noted that the measurement of the air kerma does not represent the typical exposure to the output of a breast.

Next, the image obtained with the voltage of 30 kV and saturation time of 1.0 s was selected to evaluate the

**Fig. 1** Mammographic system  
A: Mammograph VMI Graph Mammo AF (a), CR plate Regius RP6M110 (b) and scanning unit Regius 110 HQ (c)



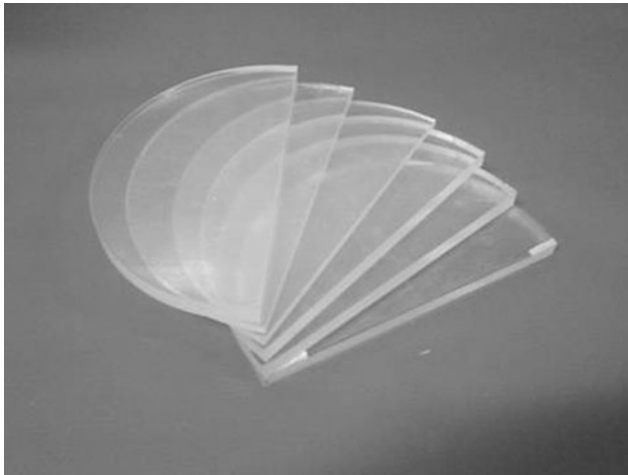
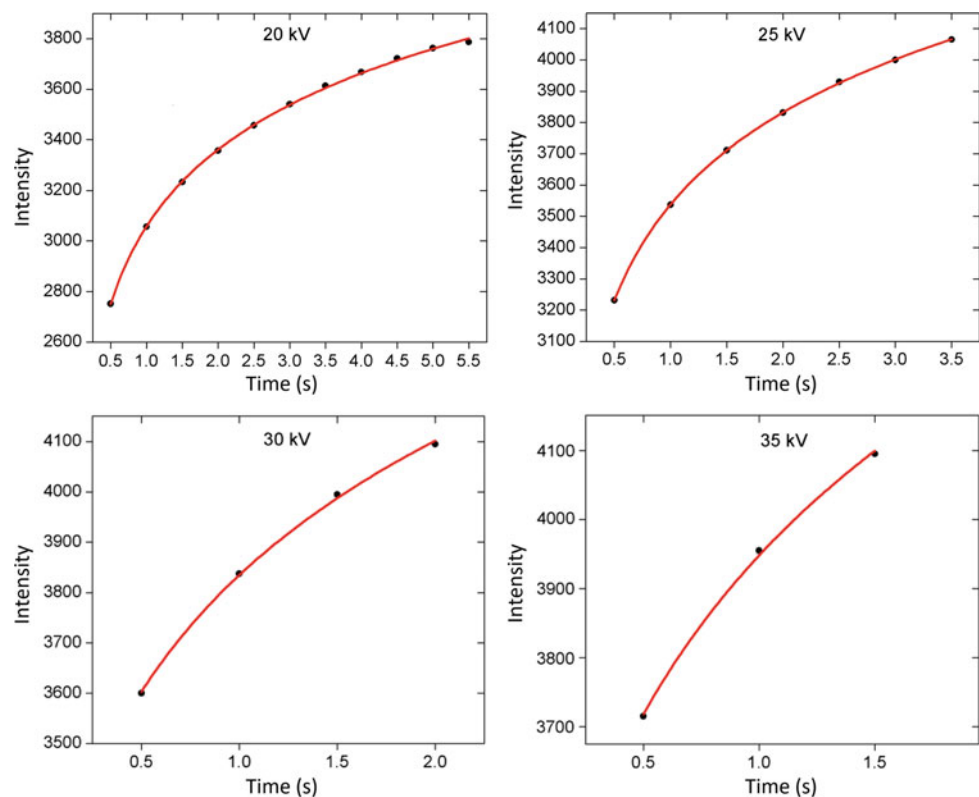


**Fig. 2** PMMA plates used to simulate a compressed breast of 50 mm thick

percentage distribution of the intensity, recognizing the regions where the maximum and minimum values are found. For this, ROIs of  $1 \text{ cm}^2$  were selected on the regions of maximum and minimum intensity, the maximum value was correlated with the value of 100% and the minimum value with 0%, and consecutively the other percentage values were calculated in all the regions. Subsequently, the maximum and minimum intensity values were used to estimate the air kerma in these regions and compare it with the air kerma that was measured to perform the correlation of intensity—air kerma.

**Fig. 3** Curve of response of the intensity to the variation of time for the voltages of 20, 25, 30 and 35 kV



To perform the dosimetry with a compressed breast phantom, GAFCHROMIC XR-QA2A® radiochromic film strips of  $25 \times 5 \text{ mm}^2$  in size were exposed using a voltage of 30 kV, varying from 0.5 to 2.5 s the exposure time, current 70 mA to obtain the scanning value of the strips and be able to calculate the optical density, and in this way obtain the calibration curve correlating the values of the air kerma measured in the same positions with the detector solid-state and radiochromic films.

To represent a compressed breast, a 50 mm breast phantom made of plates with 6 plates of Polymethylmethacrylate (PMMA) of 10 and 5 mm thickness was designed to measure the input and output dose and inside of the phantom using radiochromic film strips (see Fig. 2).

With the same parameters of voltage and current used for the calibration of the radiochromic films and setting the exposure time in 2.5 s, we proceeded to position the compressed breast phantom together with a radiochromic film strip at the same time to estimate the input and output dose and inside the phantom at 10, 20, 30 and 40 mm thick. Finally, with the calibration curve, the dose was calculated in all positions.

### 3 Results

By relating the recorded intensity to the exposure time for each voltage (see Fig. 3), the mathematical behavior of the curve could be determined to estimate the saturation time corresponding to each voltage.

**Table 1** Estimated the saturation time for each voltage

Voltage (kV)	Saturation time (s)
20	10.84 ± 0.03
25	3.75 ± 0.03
30	1.98 ± 0.01
35	1.48 ± 0.05

The curve that best describes this behavior is presented in Eq. 1.

$$I = a - b \cdot \ln(t+c) \quad (1)$$

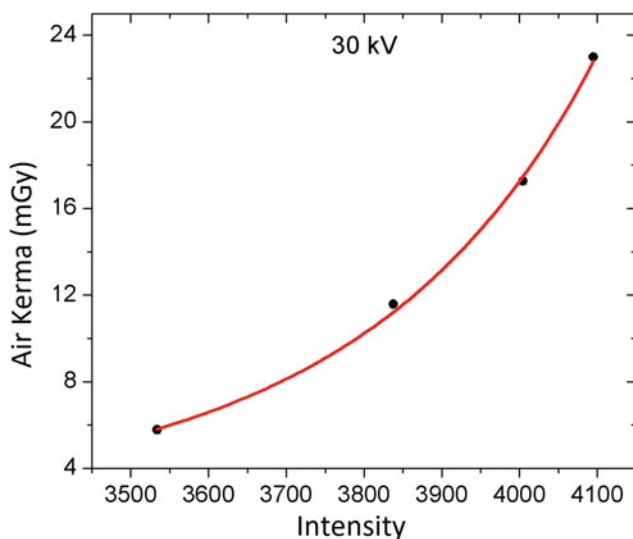
where,  $I$  is the recorded intensity with the exposure time  $t$ ,  $a$ ,  $b$  and  $c$  are the values of the constants. The values of the constants and the saturation times for each voltage are shown in Table 1.

It can be observed in Fig. 3, that applying the 20 kV voltage the CR plate does not saturate the 4095 as expected, but it does so at 3800, approximately at 10 s, while with the other voltages this does is fulfilled.

Next, the response of the CR plate in relation to the air kerma was determined for a 30 kV voltage when a variation in the exposure time is made (see Fig. 4) and the best fitting curve presented in the Eq. 2.

$$k = \exp(a + b \cdot I + c \cdot I^2) \quad (2)$$

where,  $k$  is the air kerma (mGy),  $I$  is the intensity and  $a$ ,  $b$  and  $c$  are the coefficients.

**Fig. 4** Behavior of the air kerma to the variation of intensity for the voltage of 30 kV

In this behavior it can be evidenced that, as the air kerma increases as a result of the increase in the exposure time, the value of the intensity increases more and more slowly until reaching the value 4095 in the gray scale; it is from this value that the CR plate loses sensitivity due to the saturation of its pixels.

Subsequently, the image obtained with the tension of 30 kV and exposure time 1.0 s was selected to analyze the percentage distribution of the intensity in the entire CR plate (see Fig. 5) and determine the air kerma corresponding to the minimum and maximum values of intensity.

It can be observed in Fig. 5, that in the region closest to the chest wall of the patient is where the highest intensity values for this image are found, of 3790 on the gray scale, which represent 100% and go decreasing in the direction of the corners furthest away from the patient until reaching near the minimum intensity value, value of 80 on the gray scale, represented by 0%.

Table 2 shows the air kerma values measured with the solid state detector and the air kerma values estimated from the adjustment curve (Eq. 2) for the maximum and minimum intensity values found in the digital image.

It should be noted that the region where the air kerma was measured is close but it is not the same where the maximum intensity value was found.

Finally, the dose was estimated at the entrance, exit and after each centimeter of thickness of the compressed breast phantom, using the calibration curve that correlates the optical density (OD) with the dose measured with the solid state detector (see Fig. 6) presented in Eq. 3.

$$OD = ak^b \quad (3)$$

where,  $OD$  is the optical density,  $k$  is the air kerma (mGy), and  $a$  and  $b$  are the coefficients.

According to Table 3, the maximum and minimum dose would be in the entrance and exit of the phantom, respectively, the input dose, on average, decreases by a factor of 0.5 to each centimeter of thickness of the PMMA phantom, that is to say that only 2.4% of the estimated dose at the entrance of the breast phantom is recorded at the exit of the object.



**Fig. 5** Distribution of the registered intensity with the exposure time of 1.0 s and the voltage of 30 kV

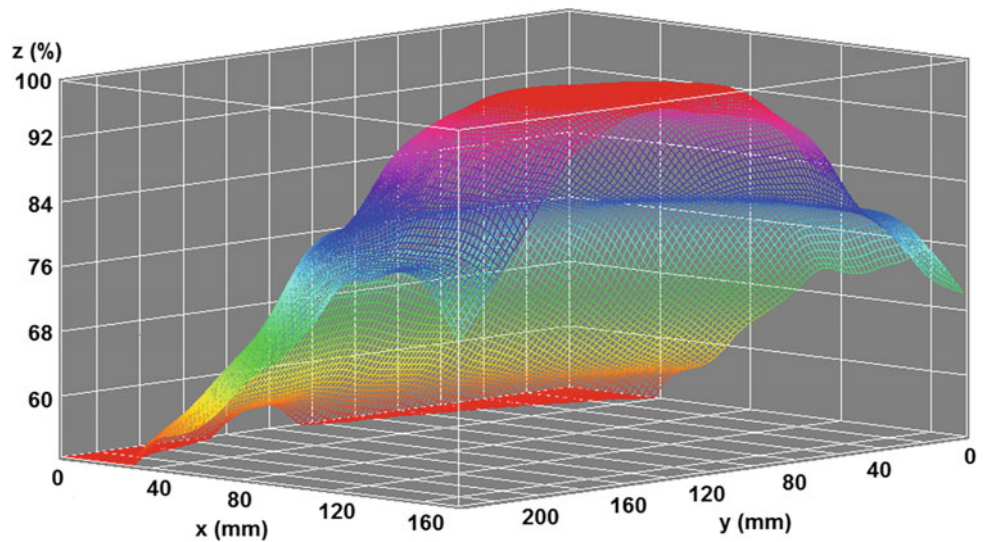


**Table 2** Value of the air kerma measured in the center of the CR plate and the estimated values of the air kerma in the regions of maximum and minimum intensity

Applied voltage (kV)	Air kerma measured (mGy)	Air kerma maximum (mGy)	Air kerma minimum (mGy)
30	11.58 ± 0.02	12.56 ± 0.03	3.04 ± 0.03

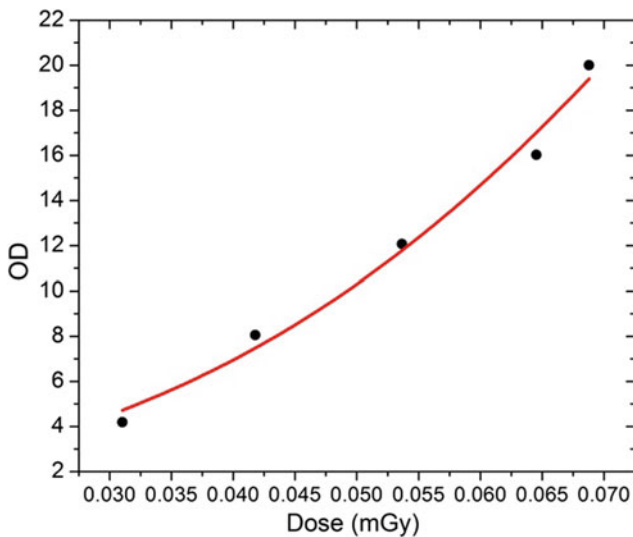


**Fig. 6** Behavior of the OD to the variation of the air kerma

#### 4 Conclusions

The CR digital mammography system is widely used in Brazil and the knowledge of the characteristics and the response of the CR plates when different exposure parameters are applied are essential to obtain good quality images in order to reduce the energy deposited in the patient.

The logarithmic behavior of the recorded intensity, in this work, exhibits a saturation region occurring at lower exposure times for higher X-ray tube supply voltage values. While the behavior of the air kerma with respect to the intensity recorded by the CR plate has an exponential behavior, which increases more slowly the closer it is to the saturation value of the intensity.

When the CR plate operates in regions close to saturation, the plate enters a process of loss of sensitivity, which must be avoided, since the patient can receive an unnecessary

**Table 3** Estimated dose at the entrance, exit of the phantom and at 10, 20, 30, 40 mm of thickness inside the object

Thickness (mm)	Dose (mGy)
Entrance of the phantom	27.15
10	10.46
20	3.44
30	2.06
40	0.92
Exit of the phantom	0.66



amount of deposited energy, also compromising the quality of the image.

The distribution of intensity shows that the region closest to the chest wall of the patient is the one that receives the greatest exposure, because in this region it is where the maximum intensity values were found, as expected. The estimated value of the air kerma that would correspond to the maximum intensity value is greater than the value of the air kerma measured with the solid state detector; this may be due to the fact that the region that presented the maximum values is not the same as the region where the detector was positioned.

In this work was also presented the estimate of the input and output dose and within the phantom of compressed breast, with which it was possible to estimate the rate of decrease of the dose at different thicknesses and the percentage of dose in the exit of the breast phantom.

**Acknowledgements** The authors are grateful to the Fundação de Amparo à Pesquisa do Estado de Minas Gerais (FAPEMIG) and the Nacional de Desenvolvimento Científico e Tecnológico (CNPq) for the support.

## References

1. Oliveira, M., Nogueira, M. S., Guedes, E., Andrade, M. C., Peixoto, J. E., Joana, G. S., Castro, J. G.: Average glandular dose and phantom image quality in mammography. *Nuclear Instruments and Methods in Physics Research Section A* 580(1), 574–577 (2007).
2. IARC, Cancer Today Homepage, <http://gco.iarc.fr/today>, last accessed 2017/09/23.
3. Ministério da Saúde, Instituto Nacional do Câncer Homepage, <http://www2.inca.gov.br/wps/wcm/connect/tiposdecancer/site/home/mama>, last accessed 2018/01/10.
4. Parkin, D. M., Bray, F. I., Devesa, S. S.: Cancer burden in the year 2000. The global picture. *European Journal of Cancer* 37(8), 4–66 (2001).
5. Dance, D. R., Christofides S., Maidment, A. D. A., McLean, I. D., Ng, K. H.: *Diagnostic radiology physics: A handbook for teachers and students*. Vienna: IAEA (2014).
6. Oliveira, M. A., Dantas, M. V. A., Santana, P. C., Squair, P. L., Gomes, D. S., Nogueira, M. S.: Assessment of glandular dose and image quality in mammography using computerised radiography employing a polymethylmetacrilate breast simulator. *Radiation Measurements* 46(12), 2081–2085 (2011).
7. VMI Indústria e Comércio LTDA: Manual do usuário aparelho de mamografia mod. Graph Mammo AF. Código 0043\_01/02 (2002).
8. Konica Minolta INC.: Regius Model 110HQ Homepage, <http://www.konicaminolta.com/healthcare/products/mammo/model110hq/>, last accessed 2017/08/25.
9. Van Engen, R., Bouwman, R., Dance, D., Heid, P., Lazzari, B., Marshall, N., Young, K.: Protocol for the quality control of the physical and technical aspects of digital breast tomosynthesis system. EUREF, European Guidelines for Quality Assurance in Breast Cancer Screening and Diagnosis (2013).

# Towards In Vivo K-Edge X-Ray Micro-CT with the Pixirad-I/Pixie-III Detector

F. Brun, V. Di Trapani, D. Dreossi, L. Rigon, R. Longo, and P. Delogu

## Abstract

X-ray spectral computed microtomography ( $\mu$ -CT) has gained considerable interest in recent years thanks to the development of Photon Counting X-ray Detectors (PCXD). Through the energy-based discrimination of the photons, obtained by setting up the discriminator threshold at different levels, PCXDs allow measuring photon energies with an accuracy appropriate for several practical applications. The major potentials of this approach are multiple contrast images (sometimes referred to as “color” or “spectral” images), obtained by using a single polychromatic source. In contrast to multiple acquisitions with different tube spectra, photon-counting spectral CT eliminates the risk of misregistration due to motion between consecutive scans and it allows for the elimination of dark noise in the image by rejecting all the events below the signal threshold. Of particular importance is the application of spectral CT in preclinical models where small animals are scanned and an effective discrimination among e.g. soft-tissue, bone and K-edge contrast agents can be in principle performed in a single shot. While spectral CT is considered very promising, its practical application has

been hampered by the charge sharing issue that negatively affects the energy resolution of PCXDs. However, latest generations of PCXDs implement solutions to cope with the charge sharing effects, thus allowing sharp color sensitivity. This work presents a comparison of K-edge spectral CT images acquired with the Pixirad-I/Pixie-III detector with and without the application of a charge sharing recovery solution. When a solution for the charge sharing issue is considered both the spatial accuracy and energy resolution are preserved, thus allowing accurate K-edge subtraction imaging.

## Keywords

Computed tomography • K-edge imaging  
Photon counting detectors • Energy resolution

## 1 Introduction

The availability of  $\mu$ -CT has increased over the last decade and it has shown its utility in many biomedical (mainly preclinical) applications. Micro-CT instruments have evolved from custom-made to commercially available scanners designed for e.g. small animal imaging, either ex vivo or in vivo. The strengths of  $\mu$ -CT lie in its high resolution, relatively low cost, and scanning efficiency. However, the primary limitations of  $\mu$ -CT imaging for biomedical applications are the associated radiation dose and relatively poor soft tissue contrast.

Since the X-ray tube has a polychromatic spectrum, it is desirable to obtain spectral or multi-energy  $\mu$ -CT images with therefore additional information about the composition of the scanned material [1]. One of the most useful potentials in the biomedical field is, perhaps, the ability to reconstruct virtual non-contrast images. In fact, in medical X-ray imaging it is common practice to use contrast pharmaceuticals containing highly attenuating heavy elements such as iodine, barium or gadolinium to highlight parts of the

F. Brun (✉) · L. Rigon · R. Longo  
Sezione di Trieste, Istituto Nazionale di Fisica Nucleare (INFN),  
Via A. Valerio, 2-34127 Trieste, Italy  
e-mail: francesco.brun@ts.infn.it; fbrun@units.it

V. Di Trapani · P. Delogu  
Dipartimento di Scienze Fisiche, della Terra e dell’Ambiente,  
Università degli Studi di Siena, Presidio San Niccolò, Via Roma,  
56-53100 Siena, Italy

V. Di Trapani · P. Delogu  
Sezione di Pisa, Istituto Nazionale di Fisica Nucleare (INFN),  
Largo B. Pontecorvo, 3-56127 Pisa, Italy

D. Dreossi  
Elettra - Sincrotrone Trieste S.C.p.A., S.S. 14 km 163.5 in Area  
Science Park, 34149 Basovizza, Trieste, Italy

L. Rigon · R. Longo  
Dipartimento di Fisica, Università degli Studi di Trieste, Via A.  
Valerio 2, 34127 Trieste, Italy

anatomy or to derive functional information. Each of these heavy elements has a characteristic jump in their attenuation (opacity) of X-rays with energies above the binding energy of their K-shell electrons. This jump, also known as the K-edge, is used to identify specific heavy elements in multi-energy X-ray imaging techniques. The consideration of a specific heavy element's K-edge in multi-energy X-ray imaging is widely known as K-edge imaging. Conventional K-edge imaging requires measurements taken at X-ray energies either side of the respective K-edge.

The most promising approach for K-edge spectral  $\mu$ -CT with conventional sources is provided by energy discriminating Photon Counting X-ray Detectors (PCXDs) [2] since they acquire perfectly registered data over multiple energy bins with a single scan. The reconstruction process attempts to recover the attenuation coefficient for each specific energy bin (range) enabling high fidelity K-edge imaging with a polychromatic X-ray source and, ideally, emulating K-edge imaging results produced with a tunable, monochromatic, synchrotron source. In contrast to the dual energy CT systems (dual source and tube voltage switching), photon-counting spectral CT eliminates the risk of misregistration due to motion between the energy images and can achieve accurate spectral separation between the images without requiring heavy prefiltration. Many more potential applications exist and, in principle, it should also allow for scans with much lower doses of contrast medium.

While spectral imaging with PCXDs is considered very promising, its practical application has been hampered by the charge sharing issue. The sharing is due to the finite size of the charge cloud and the unavoidable diffusion process occurring during its transport from the conversion point to the collecting pixel anode [3]. Latest generations of PCXDs implement solutions to cope with the charge sharing effects, thus allowing sharp color sensitivity.

This work presents a comparison of K-edge spectral CT images acquired by the Pixirad-I/Pixie-III detector [4] with and without the application of a charge recovery solution. When such a solution for the charge sharing issue is considered both the spatial accuracy and energy resolution are preserved. Accurate K-edge subtraction imaging is therefore feasible.

## 2 Materials and Methods

### 2.1 Hardware Setup

A micro-focus Hamamatsu X-ray source (tube voltage: 20–90 kV, tube current: 0–200  $\mu$ A, maximum output: 8 W, X-ray focal spot size: 5  $\mu$ m) and a CdTe Pixirad-I/Pixie-III detector (sensitive area:  $31.7 \times 25.0$  mm<sup>2</sup> organized as a  $512 \times 402$  pixels on a square matrix at 62  $\mu$ m pitch) were

used. The detector can be configured with the two modalities hereafter described.

*NONPI*. This modality does not consider solutions for the charge sharing effects. This means that the Pixie-III chip is actually used as in the previous generations (Pixie-II and Pixie-I) of the detector.

*NPISUM*. In Neighbor Pixel Inhibit—Pixel Summing Mode (NPISUM) the hit event is allocated to the pixel receiving the highest fraction of the total charge and then the signals of the 4 neighbor pixels are summed up to correctly evaluate the total energy of any event involving up to 4 pixels [4].

### 2.2 Test Object

A simple test object has been prepared where 5 pipettes can be inserted. Four inserts were used to hold pipettes composed of different dilutions of an iodine-based contrast agent (Bayern Ultravist® 370 0.5M) and deionized water was used in the fifth pipette as a reference. The different dilutions with water are: 0.25M, 0.125M, 0.063M, 0.050M. Iodine was considered because it is a widely exploited contrast agent having a K-edge at 33.2 keV.

### 2.3 Acquisitions

To minimize the total scanning time, a number of 360 tomographic projections were acquired in continuous mode, i.e. the detector acquires the images while the sample freely rotates continuously over the rotating stage. A source-to-sample distance of 170 mm and a source-to-detector distance of 240 mm were considered, thus a resulting magnification factor of 1.4 and a nominal isotropic voxel size of 43  $\mu$ m is achieved. The tube settings were: voltage = 50 kV, current = 160  $\mu$ A, 1 mm Al filter. The detector settings were: exposure time of 1 s, 2 color mode, threshold  $E_1 = 27.0$  keV, threshold  $E_2 = 33.2$  keV. With these settings the detector outputs two images in a single shot, denoted as “low” (27.0–33.2 keV) and “high” (from 33.2 keV).

### 2.4 Image Processing and Reconstruction

Digital pre-processing of the detector raw data was necessary. A custom outlier removal digital filter has been introduced in the reconstruction pipeline based on the automatic identification of the outliers (both bright and dark values) and replacement with the median gray level of the  $5 \times 5$  neighborhood. Prior to flat fielding, a ring removal filtering has been also applied. Cone beam reconstruction with the conventional FDK method [5] has been applied. Digital pixel-by-pixel subtraction of the “low” and “high” datasets,

i.e. the subtraction of attenuation coefficients, has been performed.

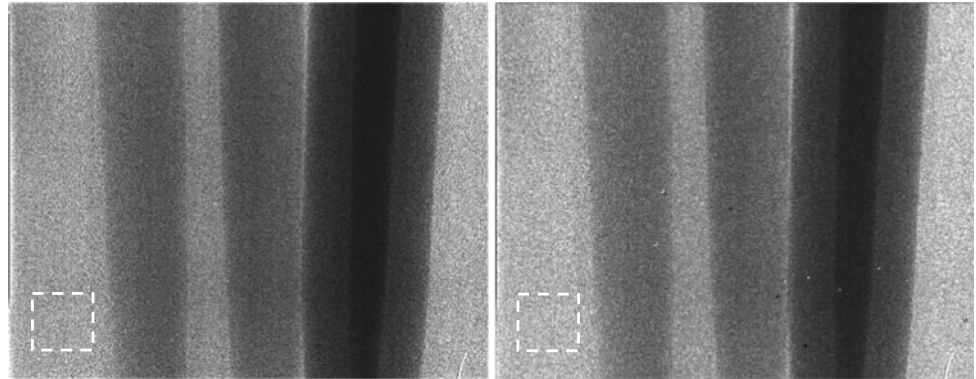
### 3 Results and Discussion

Figure 1 reports a raw projection acquired by the detector in NONPI and NPISUM modes. The noise model of the two cases seems to be visually different and a few hot/dead pixels appear in the NPISUM case. This latter aspect is probably due to limitations of the charge recovery hardware implementation of Pixie-III in some pixels. These outlier pixels have to be handled during the reconstruction pre-processing since they would produce severe streak and ring artifacts in the reconstructed CT slices. For this reason, the custom outlier removal filter has been included prior to the actual reconstruction.

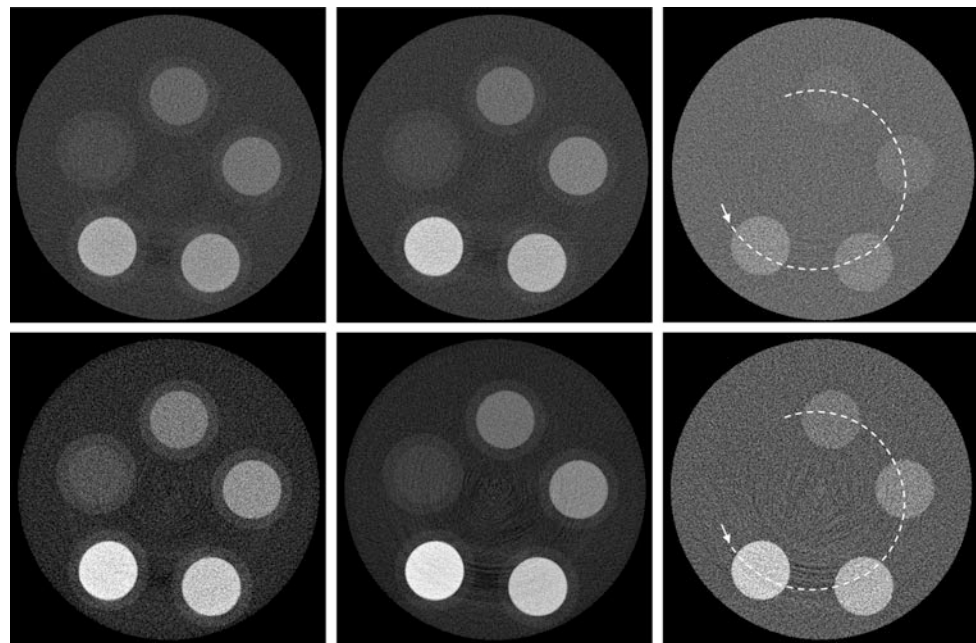
The Signal-to-Noise Ratio (SNR) of the flat-corrected images evaluated as the ratio of the mean value to the standard deviation within the highlighted Region-of-Interest (ROI) reported in Fig. 1 was used to compare the acquired projections. A  $SNR = 23.2$  was computed for the NPISUM case while a lower value ( $SNR = 19.5$ ) was recorded for the NONPI case.

Figure 2 reports the same reconstructed slice for both the “low” and “high” datasets in NONPI and NPISUM modes. Additional artifacts are noticeable in the NPISUM reconstructed images due to a different noise model and an imperfect correction of the hot/dead pixels. Figure 2 reports also the subtraction between the “high” and “low” images for both the NONPI and NPISUM. It can be visually noticed a higher Contrast-to-Noise Ratio (CNR) for each concentration of iodine. Even a very low concentration, such as the 0.05 M solution, can still be appreciated.

**Fig. 1** A raw projection in NONPI mode (on the left) and NPISUM mode (on the right). The noise model seems visually different and a few hot/dead pixels appear in the NPISUM case

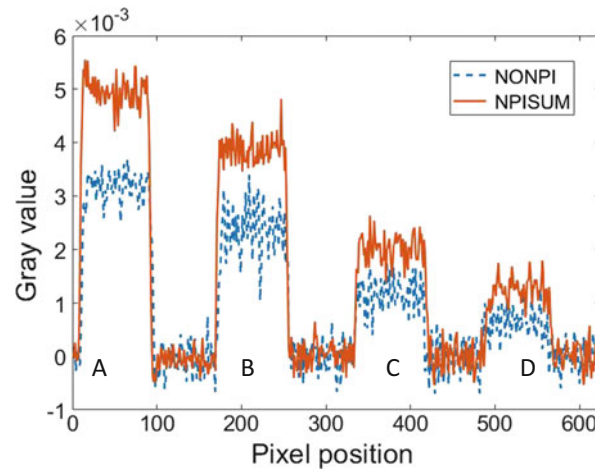


**Fig. 2** “Low” (left column), “high” (middle column) and K-Edge subtracted (right column) reconstructed slice for the NONPI mode (top row) and NPISUM mode (bottom row)





**Fig. 3** Line profile of the dashed segments highlighted in Fig. 2 and values for CNR



ROI	NONPI	NPISUM
A	2.08	4.28
B	1.65	3.41
C	0.87	1.87
D	0.51	1.19

To quantitatively confirm the differences, Fig. 3 reports the line profile along the dashed segments highlighted in Fig. 2 as well as the values for CNR defined as:

$$CNR_i = \frac{|\mu_i - \mu_b|}{\sqrt{\frac{\sigma_i^2 + \sigma_b^2}{2}}}$$

where  $\mu$  and  $\sigma$  are the average and standard deviation of gray levels within a selected ROI  $i$  and the background  $b$ . Four different ROIs having size  $50 \times 50$  pixels inside each pipette have been considered. It can be noticed a significant increment in CNR (a factor 2) when applying the NPISUM mode.

## 4 Conclusion

Practical applications of spectral CT with photon counting X-ray detectors have been hampered by the charge sharing issue. Promising results were observed with the Pixirad-I/Pixie-III detector when taking advantage of its NPISUM mode. The underlying charge sharing recovery algorithm sums up the signals of 4 neighbor pixels to correctly evaluate the total energy. This modality ensures that both the spatial accuracy and energy resolution are preserved, thus allowing accurate K-edge subtraction imaging with conventional sources. While long exposure times were considered in the presented application, a faster acquisition can be expected by exploiting a different X-ray tube. Experiments are going on with an X-ray source having

larger focal spot (around  $30 \mu\text{m}$ ) and a maximum beam current of 1.0 mA. If considering also a short scan scheme (i.e. an acquisition over  $180^\circ$  plus twice the cone angle) as well as iterative reconstruction algorithms capable to better perform when dealing with a reduced number of projections, it should be feasible to propose a fast acquisition protocol compatible with in vivo imaging of small animals.

**Acknowledgements** The KEST project, funded by INFN - Istituto Nazionale di Fisica Nucleare (National Scientific Committee 5 for Technological and Interdisciplinary research) is acknowledged.

**Conflicts of Interest** The authors declare that they have no conflict of interest.

## References

1. Fredenberg, E. *Spectral and dual-energy X-ray imaging for medical applications*, Nuclear Instruments and Methods in Physics Research, Section A: Accelerators, Spectrometers, Detectors and Associated Equipment, 878, pp. 74–87 (2018).
2. Ballabriga, R. et al. *Review of hybrid pixel detector readout ASICs for spectroscopic X-ray imaging*, Journal of Instrumentation, 11 (1), art. no. P01007 (2016).
3. Gimenez, E.N. et al.: *Study of charge-sharing in MEDIPIX3 using a micro-focused synchrotron beam*, Journal of Instrumentation, 6 (1), art. no. C01031 (2011).
4. Bellazzini, R. et al. *PIXIE III: A very large area photon-counting CMOS pixel ASIC for sharp X-ray spectral imaging*, Journal of Instrumentation, 10 (1), art. no. C01032 (2015).
5. Feldkamp, L., Davis, L., and Kress, J., *Practical cone-beam algorithm*, Journal of the Optical Society of America A, 1 (6), pp. 612–619 (1984).

---

**Part II**  
**Image Processing**



# Diffusion and Perfusion MR Parameters in Locally Advanced Rectal Cancer Management: An Explorative Study

Roberta Fusco, Mario Sansone, Alessandro Pepino, and Antonella Petrillo

## Abstract

**Background:** Diffusion Weighted (DW) and Dynamic Contrast Enhanced (DCE) MRI have been used in therapy assessment of several tumors. **Purpose:** The aim of this paper is to explore the possibility to apply DW- and DCE-MRI in Locally Advanced Rectal Cancer (LARC) to predict complete pathological response (CPR) to short-course radio-therapy (SCRT). **Methods:** 34 patients with LARC underwent DCE and DW-MRI before and after SCRT. Afterwards, patients were surgically treated. Pathological responses were registered. Tumor Regression Grade (TRG) on a scale from 1 to 5 on the surgical sample was used to classify the response. Two groups (CPR = 1 complete pathological response and CPR = 0 partial response) were identified. The discriminative power of several features from DW and DCE MRI has been investigated. Specifically, diffusion features from the intra-voxel incoherent motion (IVIM) model have been computed by means of Siemens MR Body Diffusion ToolBox; in addition, diffusion kurtosis parameters have been estimated. As regards DCE features, we used the Standard Index of Shape (SIS) which our group has proposed in previous works. DW features and SIS have been evaluated on a statistical basis (Wilcoxon-Mann-Whitney test for two independent samples, Area Under Curve of Receiver Operating Characteristics). **Results:** All diffusion features showed a significant variation after therapy; however, this difference was not significant to predict complete response. SIS was the only feature to show statistical significant difference between

the two groups. ROC and tree-based analysis revealed an optimal cut-off of 78.26 with specificity and sensitivity of 0.93 and 0.86 respectively.

## Keywords

DCE-MRI • DW-MRI • LARC

## 1 Introduction

Rectal cancer is one of the most spread cancers among men [1]. Commonly used therapy involves radio-chemo therapy (CRT) followed by total mesorectal excision (TME) [2]. It has been observed that short course radiotherapy (SCRT) can have similar effects compared to conventional chemo-radio-therapy (CRT) [3].

In order to tailor the therapy to each specific patient is important to have non-invasive instruments for assessing the therapy response. In particular it is important to distinguish between complete response, which might lead to a conservative wait and see surgical approach, and partial response. MRI has been widely used in this field: specifically, diffusion weighted (DW-MRI) and dynamic contrast enhanced (DCE-MRI) have gained an increasing success [1, 4]. In fact, these two methods can provide useful ‘functional’ information not available with other methods.

In particular, DW-MRI gives information about the water diffusion (brownian motion). DW-MRI can be analyzed using a well known bi-exponential model known in literature as intra-voxel incoherent motion (IVIM) [5]. Model fitting provides an estimates of a few important tissue parameters. Another emerging model is the diffusion kurtosis which provides a measure of the non-gaussianity of the water diffusion [6].

As regards DCE-MRI, several methods have been proposed for analyzing time-intensity course of injected contrast agent: they can be subdivided into model-based [7] and model-free [8]. Our group has previously proposed a

R. Fusco · A. Petrillo  
Diagnostic Imaging Division, National Cancer Institute of Naples  
“Pascale Foundation”, via Mariano Semmola,  
80100 Naples, Italy

M. Sansone (✉) · A. Pepino  
Department of Electrical Engineering and Information  
Technologies (DIETI), University of Naples “Federico II”,  
via Claudio 21, 80131 Naples, Italy  
e-mail: msansone@unina.it

model-free based method for rectal cancer therapy evaluation which has been called standard index of shape (SIS) [9].

The aim of this study is to evaluate the discriminative power of IVIM and kurtosis parameters and SIS for the prediction of complete response to SCRT.

## 2 Methods

### 2.1 Patients

Thirty-four consecutive patients (age: 48–83, 26 male 8 female) at our institution have been included in the study. They all had a diagnosis of Locally Advanced Rectal Cancer (LARC). They underwent short-course radiotherapy before surgical resection: details in therapy can be found in [1]. Each patient underwent MR studies before and after SCR: baseline, on average 23.8 days before starting radiotherapy and delayed, on average 61.0 days after the end of SCR.

### 2.2 Specimens Evaluation

Histopathological analysis has been performed using the Mandard system by an expert pathologist blinded to the results of MRI. Tumor Regression Grade has been assessed per each specimen. A score of TRG = 1 meant complete pathological response (CPR) i.e. absence of tumoral cells. TRG from 2 to 4 meant an increasing number of tumoral cells with respect to fibrotic tissue; TRG = 5 meant no therapy effect. More details on the scoring system can be found in [1].

### 2.3 Imaging

All examinations were performed at our institution using a Magnetom Symphony scanner 1.5T (Siemens Medical Systems, Erlangen, Germany).

#### 2.3.1 Diffusion weighted MRI

DW-MRI imaging has been performed using the following DW-EPI sequence parameters: TR/TE = 2700/83 ms/ms, FOV = 136 × 160 mm × mm, matrix size = 230 × 272, ST = 4 mm (TR repetition time, TE echo time, FOV field of view, ST slice thickness).  $b$ -values were the following 0, 50, 100, 150, 300, 600, 800 s/mm<sup>2</sup>. Gradient directions were all three axis, direct trace imaging; voxel size was 1.7 × 1.7 × 4~mm<sup>3</sup>.

#### 2.3.2 Dynamic Contrast Enhanced MRI

DCE-MRI imaging has been performed using the following FLASH 3D sequence parameters: TR/TE/FA = 9.8/4.76/25

ms/ms/deg, FOV = 330 × 247 mm×mm, ST = 3 mm. Temporal resolution was 35 s between two consecutive images. Voxel size 0.64 × 0.48 × 3 mm<sup>3</sup>.

## 2.4 Feature Extraction

Regions of interest (ROIs) were manually drawn appropriately by an expert radiologist. While IVIM analysis has been performed both before and after short-course radiotherapy, SIS has been evaluated only at the second MR examination because it involves a comparison of before—after therapy.

### 2.4.1 IVIM Parameters

Intravoxel incoherent motion parameters have been computed using the Siemens software MR Body Diffusion Toolbox. The IVIM model corresponds to the following bi-exponential equation [5]:

$$S(b) = S(0) * \exp(-bD)[(1-f) + f \exp(-bD^*)] \quad (1)$$

and the parameters have the following meanings:  $S(b)$  is the MR signal when a specific gradients  $b$ -value is used,  $f$  is the perfusion fraction (corresponding to the fraction of capillary vessels in the voxel),  $D$  is the diffusion coefficient (mm/s<sup>2</sup>) (Brownian motion coefficient),  $D^*$  is the pseudo-diffusion coefficient (mm/s<sup>2</sup>) (due to the motion of water in capillary vessels).

The Siemens software allowed ROI drawing and output ROI-averaged parameters.

### 2.4.2 Diffusion kurtosis Parameters

Under appropriate assumptions, DW signal can be modeled as [6]:

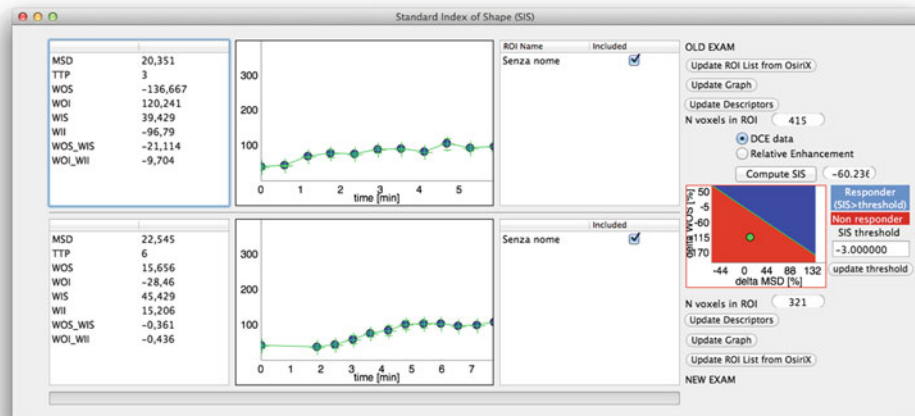
$$S(b) = S(0) * \exp\left(-bD + \frac{1}{6}b^2D^2K\right) \quad (2)$$

in which  $D$  is again the apparent diffusion coefficient and  $K$  is the kurtosis. Diffusion Kurtosis parameters have been computed using the Siemens software MR Body Diffusion Toolbox.

### 2.4.3 Standard Index of Shape

This model-free DCE parameter has been developed by our group in previous studies [1, 9–11]. The software for SIS computation has been developed at our institution (see Fig. 1); it is an Osirix plugin available upon request. SIS analysis involves the use of both before and after therapy MR exams. ROIs have been drawn manually by an expert radiologist. The software outputs ROI-averaged DCE-MRI semi-quantitative parameters and the SIS parameters which is a synthesis of the comparison between before/after therapy DCE-MRI.

**Fig. 1** SIS Osirix plugin developed at our institution



## 2.5 Statistical Analysis

We performed mono- and multi-parametric analysis on each single DW feature for discriminating the two patient groups (CPR = 1 complete pathological response and CPR = 0 incomplete pathological response).

All tests have been considered significant for  $p < 0.05$ . All statistical analysis have been performed in R [12].

### 2.5.1 Mono-parameter Analysis

First, the Wilcoxon-Mann-Withney test for two independent unmatched samples has been applied to each feature extracted from the before-therapy MR session. This has been done, in order to see if CPR could be predicted by some before-therapy feature. In this case we used only IVIM + kurtosis based features.

Second, we considered both before and after therapy features. Relative differences between before and after therapy MR have been evaluated using the following formula:

$$\frac{X_{post} - X_{pre}}{X_{pre}} \quad (3)$$

where  $X_{pre}$  is a generic feature evaluated before therapy while  $X_{post}$  is the same feature evaluated after therapy. In this case the Wilcoxon-signed-rank (paired data) test has been applied to relative differences.

ROC analysis was also made for the calculation of the best cut-off.

### 2.5.2 Multi-parametric Analysis

Further, classification and regression trees (CART) have been applied to all features [13]. Both the before-only and before-after features were analysed. CART is a particular type of non-linear classifier whose main advantage is that provides *binary rules* that are human interpretable.

## 3 Results

The result of the Wilcoxon-Mann-Withney test suggested that the groups CPR = 0 and CPR = 1 were not significantly different for all the IVIM + kurtosis features calculated on the pre-SCRT alone except the average and the standard deviation of  $D^*$ . ROC analysis of these two features provided AUC 0.71 and 0.77, specificity and sensitivity 0.89, 0.57 and 0.51, 1.00 respectively.

Moreover, *none* of the relative differences *pre-post* of all IVIM + kurtosis features resulted significant at the Wilcoxon signed-rank test.

However, the SIS resulted in a significant difference between CPR = 0 and CPR = 1. In Fig. 2a the results of ROC analysis for SIS have been reported. The area under curve (AUC) was 0.89 while the best cut-off (Youden index) was 78.26 while specificity and sensitivity were 0.93 and 0.86 respectively. A further analysis based on CART provided results (see Fig. 2b) in line with the previous analysis and also the cut-off were coincident.

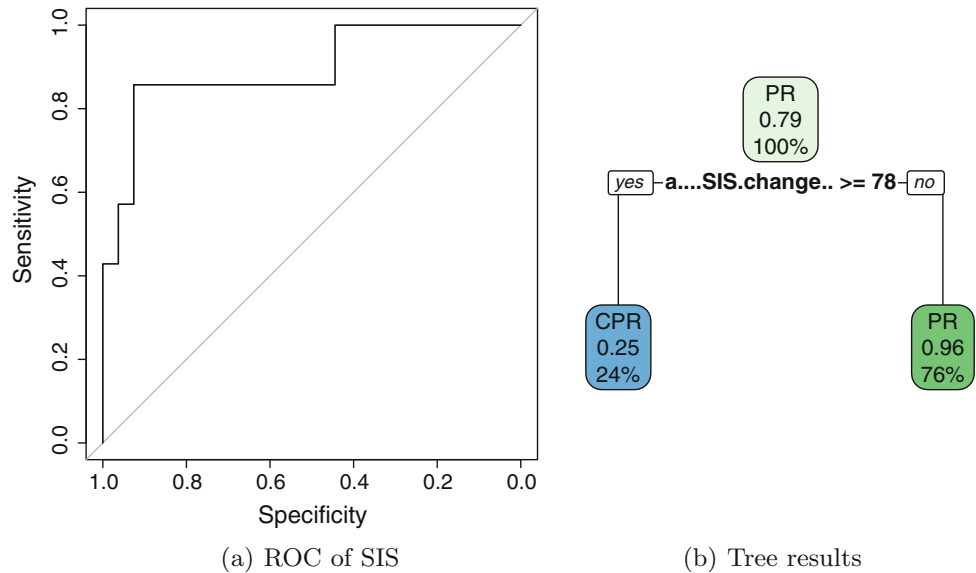
## 4 Discussion

The aim of this study was to explore the possibility to predict, using DW- and DCE-MRI parameters, the Complete Pathologic Response of LARC patients to short-course radiotherapy.

Although all patients showed a modification in diffusion related parameters (IVIM + kurtosis) after therapy, the variation was not significant (with the exception of two features average and standard deviation of  $D^*$  with a low accuracy measured by ROC AUC) for distinguishing between CPR = 0 and CPR = 1.

In contrast, our previously proposed index, Standard index of Shape (SIS), showed a better behaviour: it was

**Fig. 2** Receiver Operating Characteristic of the SIS parameter alone (a). Tree analysis reveals that SIS is indeed the most important feature in separating complete pathological response (CPR) from pathological response (PR) (b): each node of the tree reports the class contained in that node, the probability assigned to that class, the percentage of subjects in the node



significantly different between CPR 0 and 1. Both conventional statistical analysis (Wilcoxon test) and tree based classification (CART) agreed upon the superiority of SIS.

One limit of this study is the set of  $b$ -values used for the diffusion kurtosis modelling: it should be pointed out that kurtosis imaging might require higher  $b$ -values; however, as this is an explorative study we attempted the kurtosis modelling aware of the possible limitations. In addition, although SIS has proven to be a relevant variable for complete response detection its interpretation is not completely clear, which will be the aim of future studies.

**Acknowledgements** This work has been partially funded by the project n. BioMatMRI—000010—ALTRI-2017-M-SANSONE\_001\_001 at the Department of Electrical Engineering and Information Technologies (DIETI) of the University “Federico II”, Naples Italy.

#### Conflict of Interest

The authors declare that they have no conflict of interest.

## References

1. A. Petrillo, R. Fusco, V. Granata, S. V. Setola, M. Sansone, D. Rega, P. Delrio, F. Bianco, G. M. Romano, F. Tatangelo, A. Avallone, and B. Pecori, Mr imaging perfusion and diffusion analysis to assess preoperative short course radiotherapy response in locally advanced rectal cancer: Standardized index of shape by dce-mri and intravoxel incoherent motion-derived parameters by dw-mri. *Med Oncol*, vol. 34, p. 198, Nov 2017.
2. G. Tong, G. Zhang, J. Liu, Z. Zheng, Y. Chen, and E. Cui, A meta-analysis of short-term outcome of laparoscopic surgery versus conventional open surgery on colorectal carcinoma. *Medicine (Baltimore)*, vol. 96, p. e8957, Dec 2017.
3. B. Ma, Q. Xu, Y. Song, P. Gao, and Z. Wang, Current issues of preoperative radio(chemo)therapy and its future evolution in locally advanced rectal cancer. *Future Oncol*, vol. 13, pp. 2489–2501, Nov 2017.
4. R. Fusco, M. Petrillo, V. Granata, S. Filice, M. Sansone, O. Catalano, and A. Petrillo, Magnetic resonance imaging evaluation in neoadjuvant therapy of locally advanced rectal cancer: A systematic review. *Radiol Oncol*, vol. 51, pp. 252–262, Sep 2017.
5. D. Le Bihan, E. Breton, D. Lallemand, P. Grenier, E. Cabanis, and M. Laval-Jeantet, Mr imaging of intravoxel incoherent motions: application to diffusion and perfusion in neurologic disorders. *Radiology*, vol. 161, pp. 401–7, Nov 1986.
6. D. H. J. Poot, A. J. den Dekker, E. Achten, M. Verhoye, and J. Sijbers, Optimal experimental design for diffusion kurtosis imaging. *IEEE Trans Med Imaging*, vol. 29, pp. 819–29, Mar 2010.
7. S. P. Sourbron and D. L. Buckley, Classic models for dynamic contrast-enhanced mri. *NMR Biomed*, vol. 26, pp. 1004–27, Aug 2013.
8. A. Fabijańska, A novel approach for quantification of time-intensity curves in a dce-mri image series with an application to prostate cancer. *Comput Biol Med*, vol. 73, pp. 119–30, 06 2016.
9. A. Petrillo, R. Fusco, M. Petrillo, V. Granata, M. Sansone, A. Avallone, P. Delrio, B. Pecori, F. Tatangelo, and G. Ciliberto, Standardized index of shape (sis): a quantitative dce-mri parameter to discriminate responders by non-responders after neoadjuvant therapy in larc. *Eur Radiol*, vol. 25, pp. 1935–45, Jul 2015.
10. A. Petrillo, R. Fusco, M. Petrillo, V. Granata, P. Delrio, F. Bianco, B. Pecori, G. Botti, F. Tatangelo, C. Caracò, L. Aloj, A. Avallone, and S. Lastoria, Standardized index of shape (dce-mri) and standardized uptake value (pet/ct): Two quantitative approaches to discriminate chemo-radiotherapy locally advanced rectal cancer responders under a functional profile. *Oncotarget*, vol. 8, pp. 8143–8153, Jan 2017.
11. M. Petrillo, R. Fusco, O. Catalano, M. Sansone, A. Avallone, P. Delrio, B. Pecori, F. Tatangelo, and A. Petrillo, Mri for assessing response to neoadjuvant therapy in locally advanced rectal cancer using dce-mr and dw-mr data sets: A preliminary report. *Biomed Res Int*, vol. 2015, p. 514740, 2015.

12. R Development Core Team, *R: A Language and Environment for Statistical Computing*. R Foundation for Statistical Computing, Vienna, Austria, 2008. ISBN 3-900051-07-0.
13. W.-Y. Loh, Classification and regression trees. *Wiley Interdisciplinary Reviews: Data Mining and Knowledge Discovery*, vol. 1, no. 1, pp. 14–23, 2011.



# Mammographic Density Estimation Through Permutation Entropy

Adriana Antonelli, Gustavo Meschino, and Virginia Ballarin

## Abstract

The American College of Radiology, through its committee on BI-RADS (Breast Imaging Study Data and Reporting System), has concluded that breast density is more clinically important as an indicator of concealment of possible breast lesions than as a quantifier of cancer risk, due to the lack of robust descriptors for detecting diverse types of density. In this work, new descriptors for mammographic density estimation based on the Permutation Entropy (PE) algorithm are developed and assessed. PE is a measure of complexity initially proposed for chaotic time series, particularly in the presence of dynamic and observational noise. We propose different novel algorithms to adapt the concept of PE from time series to images, to characterize the level of roughness. Once the characteristic vector for each mammogram was obtained, we trained a multilayer feedforward neural network as a classifier, to evaluate the potentiality of the set of descriptors as mammographic density characterizers, in accordance with the BI-RADS nomenclature. The results show that these descriptors have remarkable success rates in the classification of densities and especially they generalize with good coincidence percentages for cases of extreme densities. The categorization of extremely dense breasts is of special interest because of their clinical importance to assign more intensive monitoring or more complex studies to the patients who present it.

## Keywords

Mammographic density • Permutation entropy  
Medical image processing

## 1 Introduction

Of all known cancers, breast cancer represents the first cause of cancer death in Argentinian women. In a global comparison, Argentina is one of the countries with the highest incidence and mortality rates for malignant breast tumors [1, 2].

Breast cancer is difficult to prevent and has multiple risk factors: age, overweight, sedentary lifestyle, family history, breast density, exposure to hormonal treatments. The modification of these factors may take several decades to become evident. Efforts to achieve disease control should focus on the early detection and implementation of treatments [3].

The mammary density is the proportion of fibroglandular tissue in relation to the amount of adipose tissue in the composition of a breast. Many studies indicate that it is an important indicator of the development of a breast cancer [3–5]. This predictor has the advantage of being detected on mammograms. It is used for monitoring and more complex interventions, such as ultrasound or magnetic resonance imaging, could be required in patients with high density. The problem in mammographic density is not only the increased risk of breast cancer, but also a marked decrease in the sensitivity of mammography versus detection by simple inspection of nodules. Women with dense tissue in 75% or more have a risk of breast cancer higher than the risk among women with little or no dense tissue [6]. The sensitivity of mammograms decreases linearly according to the increase in density [7].

There are different methods to measure the degree of breast density. The most used is the BI-RADS classification [8], where the density has 4 levels. These levels are subjectively indicated by an expert, by visual inspection of the

A. Antonelli (✉) · G. Meschino · V. Ballarin  
Institute of Scientific and Technological Research in Electronics,  
Mar del Plata, Argentina  
e-mail: adriana\_antonelli@hotmail.com

G. Meschino  
e-mail: gmeschin@fi.mdp.edu.ar

V. Ballarin  
e-mail: vballari@fi.mdp.edu.ar

G. Meschino · V. Ballarin  
Department of Electronics and Computer Engineering, University  
of Mar del Plata, Mar del Plata, Argentina



mammogram. However, several studies indicate that the density indicated by experts does not match with the obtained by some well-known automatic measurement systems [9].

In this work, we propose texture indicators as density quantifiers to quantify fibroglandular tissue in mammograms. Different techniques are studied to obtain a new descriptor in mammography densities, called Permutation Entropy. Usually, it is used as a temporal indicator to determine the level of disorder in a series of data. However, there are works that seek to adapt the algorithm for computing this descriptor in digital images [10–12], with the objective of quantifying the level of roughness in the texture of the processed image.

Some advantages of our method are simplicity, extremely fast computation, robustness, and invariance respect to nonlinear monotonous transformations [13].

## 2 Materials and Methods

### 2.1 BI-RADS Classification and Breast Density

The atlas of the Breast Imaging Reporting and Data System (BI-RADS®) was proposed by the American College of Radiology (ACR) as a standardized method for reporting imaging studies of the breast, specifically in mammograms, ultrasound images and magnetic resonances. Writing of a mammography report is done according to the lexicon defined in BI-RADS. Each characteristic present in mammograms must be described in the report according the BI-RADS reporting system. This work only uses the characteristic about breast tissue, described in Table 1.

This terminology does not refer to isolated mammographic findings, but to the degree of radiographic attenuation presented for the mammary tissue. The obscured areas of mammography belong to the adipose tissue, while the fibroglandular tissue is observed as whitish plaques.

The mammographic sensitivity to detect non-calcified lesions decreases as the density category increases. In Fig. 1 are examples of classification according to the terminology described in Table 1.

In the previous BI-RADS editions, the assignment of the breast composition was based in numerical categories according the percentage of fibroglandular tissue in the

breast composition: Density 1 (<25% fibroglandular tissue), Density 2 (25–50%), Density 3 (50–75%) and Density 4 (>75%). In the fifth and, to date, last edition of BI-RADS, the use of percentages is discouraged, because in individual cases it is more important to take into account the chance that a mass can be obscured by fibroglandular tissue than the percentage of breast density as an indicator for breast cancer risk. Then, breast density is clinically more important as an indicator of concealment of possible breast lesions than classifying patients in two general groups: patients who require further monitoring and more complex studies and patients who do not require those. In this way, the assignment of the breast composition is changed into a, b, c and d-categories and depends on the degree of concealment that the radiologist considers.

In this sense, BI-RADS indicates that radiologists should continue using the numerical density categories in mammography reports as they have always done, but more publications with robust data about breast density depending on the volume of the breast are expected [8].

### 2.2 Permutation Entropy (PE) for Temporal Series and Images

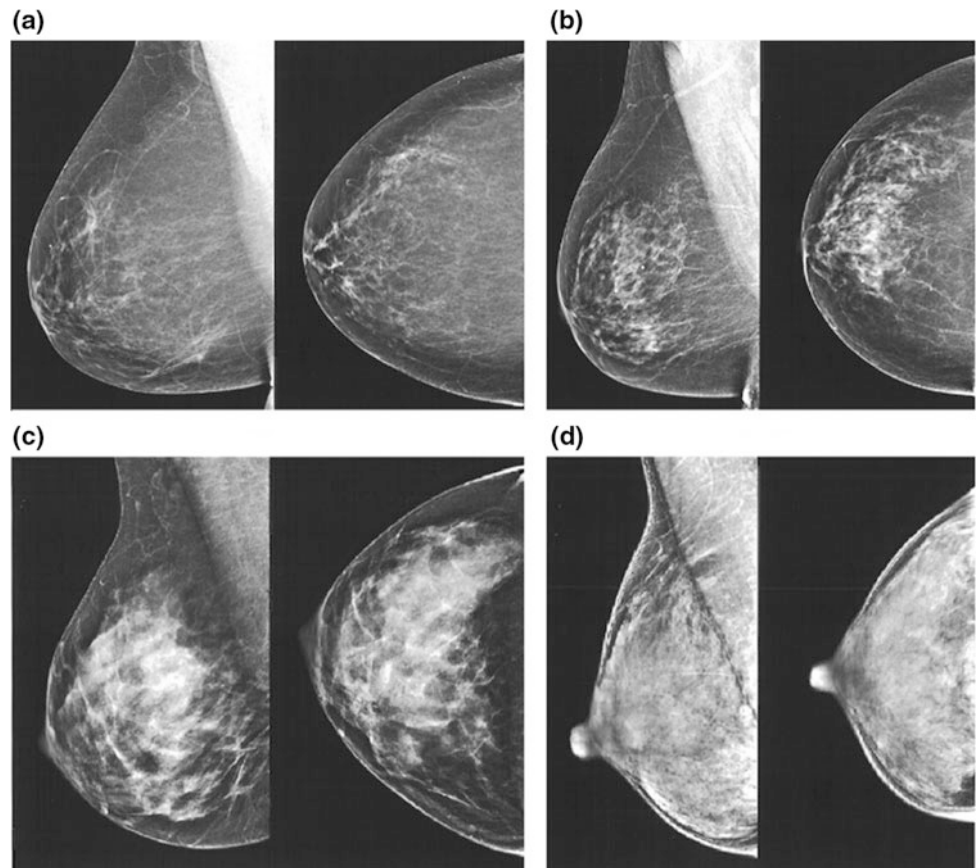
PE is a complexity measures developed for time series. The definition directly applies to arbitrary real-world data and is particularly useful in the presence of dynamical or observational noise. It is a powerful tool for time series analysis, since it allows to describe the probability distributions of the possible state of a system, and therefore the information it encodes. Research related to the so called complex systems are widely spread [14].

PE is based on comparison of neighboring values. Consider a time series  $x(t)$ ,  $t = 1, \dots, T$ , with  $\pi$  of order  $n$  are the permutations of order  $n$  which are considered here as possible order types of  $n$  different numbers, it is processed with delay  $\tau$  to complete series of data, then,  $x(t)$  is takes with a vector of dimensions  $n$  and delay  $\tau$ . This vector is called *embedding vector*. PE are calculated for different embedding dimension and delays, but the original work developed by Bandt and Pompe [13] recommends for practical purposes  $n = 3, \dots, 7$  and  $\tau = 1$ . Each of this *embedding vector* represent a pattern of order.  $n!$  possible patterns orders can exist. For a sufficiently large sequence in compare with  $n!$ , it is

**Table 1** Terminology to describe breast tissue in the BI-RADS reporting system [8]

Incubency	Characteristic	Terminology
Breast tissue	Breast composition	A. Breasts are almost entirely fatty B. Scattered areas of fibroglandular density C. Breasts are heterogeneously dense, which may obscure small masses D. Breasts are extremely dense, which lowers the sensitivity of mammography

**Fig. 1** Mammographic density categorization according BI-RADS reporting system in 4 categories: **a**, **b**, **c** and **d**. Images obtained from the 5th edition of the BI-RADS Atlas [8]



possible to calculate the frequencies of occurrence of any pattern of order. These occurrences are stored in a histogram, called *permutation histogram*, whose associated Shannon Entropy determines PE of  $x(t)$ .

There are many variants of this algorithm in the field of temporal signal processing.

The concept of PE for time series naturally matches with one of several interpretations of texture image: array of pixels whose relationship is the spatial variation of its gray intensities [15].

### 2.3 Image Database

168 mammograms from different patients were obtained from the Digital Database for Screening Mammography (DDSM) database) [16]. The original images were acquired by different scanners (DBA M2100 ImageClear, Howtek 960, Lumisys 200, Laser and Howtek MultiRad850) with different spatial resolution levels (frequency sampling of 42, 43.5 and 50  $\mu\text{m}$ ), considering gray levels of 12 or 16 bits. All mammograms have their relevant report, describing the breast tissue according to a specialist using the numerical BI-RADS reporting system (Density1 to Density4).

The images obtained from the database correspond to 40 mammograms with Density1, 40 with Density2, 44 with Density3 and 44 with Density4.

To appreciate the robustness and simplicity of the descriptors, we do not apply any preprocessing on the images.

The region of interest of each mammography (glandular tissue) was selected to apply the algorithms. Rectangular images with varied sizes were obtained. The size resulted for each rectangular image was approximately  $70 \times 100$  pixels. Figure 2 shows examples for each type of mammographic density processed by the algorithms.

### 2.4 Proposed Descriptors

We developed 15 algorithms to obtain roughness descriptors of gray images. We propose two ways to process the image pixels: the first one consider that the image is a unidimensional series of pixels, transforming the matrix of pixels in a vector; the second way process the image without losing space information about the relative position of pixels in the matrix, then process the pixel and its 2D close environment. The algorithms developed are explain in Table 2.

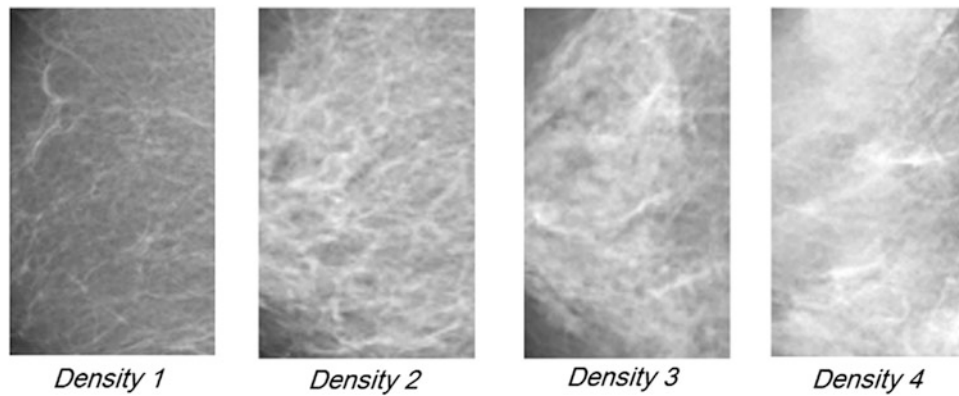


**Fig. 2** Glandular tissue of 4 kind of mammographic densities

**Table 2** Algorithms developed

Name	Description
Permutation Entropy (PE)	The pixels of images are disposed as a vector. The algorithm described in Sect. 2.2 is applied
Weighted PE (WPE)	The same algorithm to PE but assigning weights for each extracted embedding vector when computing the relative frequencies associated with every pattern of order
PE with threshold (UPE)	The same procedure as PE and WPE, but one pixel is different to its neighbor if the distance between them exceeds a certain threshold value. We obtain two algorithms called UPE and UPEw
PE of binarized image (PET)	Clustering the matrix of pixels in $n$ different classes. Then, each pixel is replaced to a class which depends on the range of gray levels that the pixel belongs. The PE algorithm process this thresholded image to obtain a new algorithm called PET
PE of filtered image	Three different low pass space filters are applied in the original image. The PE algorithm is implemented on each of these filtered images to obtain 3 new algorithms
PE of averages values (APE)	The image is divided in square submatrix of embedding size, the average submatrix value is calculated and stored in a new matrix location consistence with its previously place occupied for submatrix in the original image. The WPE is calculated with this new matrix, obtaining a new algorithm called APEw
PE of matrix entropies (MPE)	Each pixel is replaced to PE, WPE or UPE value of its close environment. Then, we obtain three new matrices which store entropies values. On each matrix is apply PE and WPE algorithms to obtain 6 news algorithms called MPE, MWPE, MUPE, MPEw, MWPEw and MUPEw respectively

A preliminary analysis of the application is required to determine the algorithms to be used. Those algorithms that could separate different roughness were selected.

The hypothesis was: it is expected to get comparable results of entropy for extreme densities (Density1 and Density4), because both have similar gray values for close pixels, leading to low entropies values. The same for Density2 and Density3, but, in this case, big variation between close pixels are observed, then higher entropies values will be obtained.

The 15 algorithms were used on all 168 mammograms. Input parameters were initially heuristically defined: *delay*  $\tau = 1$  and *embedding*  $3 \leq n \leq 7$ . In the practice, certain algorithms show better results to  $n > 7$ , where increase the dynamic range of results. In consequence, we increase the embedding range to  $3 \leq n \leq 10$ .

Based on the results, we selected 11 descriptors. Certain algorithms cannot discriminate the roughness present in the

different kind of densities; therefore, they were not used for obtaining descriptors. The selection criterion was to take the parameter  $n$  when the dynamical range was the biggest.

## 2.5 Density Classifier

The descriptor vector (11 elements) of each mammography was used to train a multilayer artificial neuronal network as a density classifier. In this instance, we considered this classification technique, but other could have been used. All the implementation was made in MATLAB in this prototype study.

A network with 11 inputs and 4 outputs (density categories) was proposed. Weights were adjusted during training by backpropagation.

The training was stopped considering the generalization capacity of the network, according to validation data. The

average training time was 2 s. A set with data test is kept for monitoring the training steps. The percentages assigned to each data subset were: 70% training (118 images), 15% validation (25 images), and 15% testing (25 images). The selection was random.

The number of neurons in the hidden layer was determined considering 2–10 neurons.

The follow steps were necessary to determinate the neurons number:

- Less than 4 neurons, class Density1 can be discriminated from Density4, and both can be discriminate of the rest, but classes Density2 and Density3 cannot be individually recognized.
- Between 4 and 7 neurons, Density2 and Density3 started to be recognized, but with low percentage of success (less of 60%).
- 8 neurons in the hidden layer was the number selected, because percentages greater than 80% success was robustly obtained.

Hold-out cross validation was carried out to estimate the error, considering 100 training cycles with random selection of test data.

### 3 Results and Discussion

Figure 3 shows the entropies values obtained with MUPE algorithm in 23 different mammograms. The maximal dynamic range is for  $n = 7$ , then the descriptor chosen for this algorithm is MUPE(7).

In this figure, the entropies of mammographic densities with Density1 and Density4 (red and black) show lower

values than categories 2 and 3 (blue and yellow) for all *embedding* values. Following this example, it is possible to select the descriptor of each algorithm. Table 3 shows the 11 descriptors selected form 15 algorithms assessed.

Table 4 shows the confusion matrix resulting from training. Density3 classification was the least efficient and scattered errors in all the remaining classes. A success of 78.57% is obtained for class Density2, but in this case the network only confuses with Density3, as expected. Then, the greatest number of errors are observed in the densities Density2 and Density3. These results were expected due to the similarity of the entropy of mammograms with these densities. However, the training resulted in a greater number of successes for classes Density1 and Density4, accordingly to the extreme densities.

The most important indicator of the performance of the network is the generalization ability to classify new data. Table 5 shows the confusion matrix of the test data.

The subset Density1-Density4 or Density2-Density3 are quantified with similar entropy values, due to the nature of their roughness. Then, images labeled as Density3 are classified as Density2 in 60% of cases. The network obtained is not a good generalizer to discriminate between mammograms Density2-Density3 but is more effective in classifying and generalizing extreme densities.

Through the cross validation a test error of 24.42% was obtained. Although improvements were seen in the qualification, the tests were prevailed for classes Density2 and Density3. The persistence of this error is attributed to several factors, one of which is the considerable intra- and inter-observer variability between two adjacent categories that are presented in the mammographic images studied. On the other hand, a very small difference is observed between the denser breast of the lower density and the less dense

**Fig. 3** Results of algorithm MUPE for 23 random mammograms from the database. Red: Density1, Blue: Density2, Yellow: Density3, Black: Density4

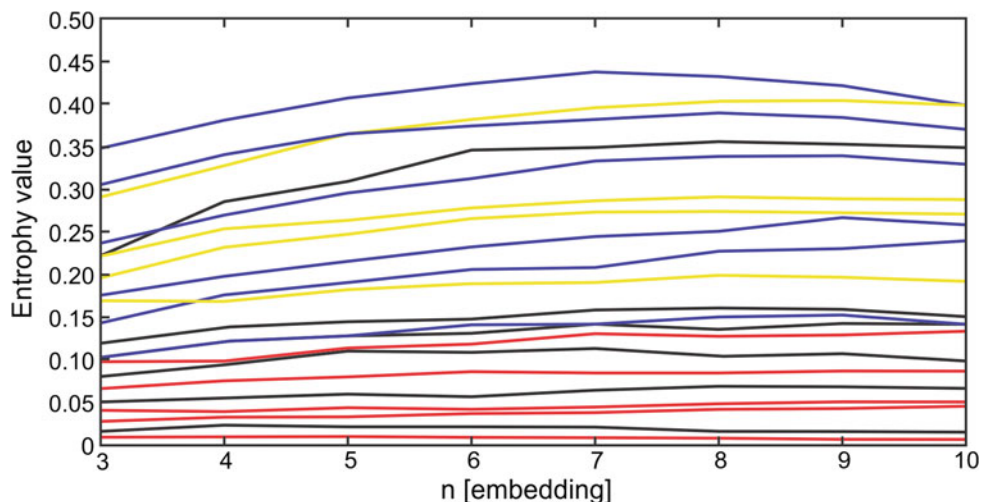


**Table 3** Descriptors selected to represent mammographic density in a mammography

Algorithm	Optimal descriptor
Permutation entropy	PE(7)
Weighted PE (WPE)	WPE(7)
PE with threshold (UPE)	UPE(7)
WPE with threshold (UPE)	UPEw(7)
PE of thresholdized image (PET)	PET(7)
PE of filtered image	–
PE of averages values (APE)	–
PE of matrix entropies (MPE)	MPE(10); MWPE(9); MUPE(7); MPEw(10); MWPEw(8); MUPEw(7)

**Table 4** Training data confusion matrix

MAMMOGRAPHY...	Classified as Density1	Classified as Density2	Classified as Density3	Classified as Density4
Labelled as Density1	26 <b>89.65%</b>	0 <b>0.00%</b>	1 <b>2.86%</b>	1 <b>3.85%</b>
Labelled as Density2	1 <b>3.45%</b>	22 <b>78.57%</b>	6 <b>17.14%</b>	0 <b>0.00%</b>
Labelled as Density3	0 <b>0.00%</b>	6 <b>21.43%</b>	27 <b>77.14%</b>	0 <b>0.00%</b>
Labelled as Density4	2 <b>6.90%</b>	0 <b>0.00%</b>	1 <b>2.86%</b>	25 <b>96.15%</b>

**Table 5** Test data confusion Matrix

MAMMOGRAPHY...	Classified as Density1	Classified as Density2	Classified as Density3	Classified as Density4
Labelled as Density1	7 <b>87.50%</b>	0 <b>0.00%</b>	0 <b>0.00%</b>	0 <b>0.00%</b>
Labelled as Density2	0 <b>0.00%</b>	3 <b>100%</b>	3 <b>60.00%</b>	0 <b>0.00%</b>
Labelled as Density3	0 <b>0.00%</b>	0 <b>0.00%</b>	2 <b>40.00%</b>	1 <b>11.11%</b>
Labelled as Density4	1 <b>12.50%</b>	0 <b>0.00%</b>	0 <b>0.00%</b>	8 <b>88.89%</b>

breast of the higher density. These factors limit the clinical relevance of the classification of the breast density of each woman, evidencing the need of more robust indicators.

Mammograms categorized as Density1, which was classified by the neural network as a case of Density4, the error is attributed to the sensitivity of the entropy descriptors used. Entropy values are due to the homogeneous distribution between the shades of gray that make up the glandular tissue.

A single classifier was tested, but the study should be continued considering other techniques and eventually in combination with descriptors from other paradigms.

## 4 Conclusion

New descriptors based on the PE algorithm were developed and tested for the mammary density characterization obtained from mammography.

The results obtained are consistent with those expected due to the characteristics of the algorithms implemented and the information obtained by the data base. Highest density images are those that requires particular care due to the masking of possible injuries. In this sense, the proposed



method provides the highest percentages of quality in the classification, estimated by cross-validation (96.15%).

Faced with the need for more robust descriptors to relate the mammary density as an indicator of risk of breast cancer, and because of the absence of a robust descriptor to categorize mammographic density according to BI-RADS mammographic reporting system, EP-based descriptors could be a viable alternative for the detection of different densities in mammograms.

We conclude that descriptors presented are of interest for quantification of mammary tissue density by mammography. They are calculated based on the epidemiological primary control examination, and for their potential, as well as other potential descriptors, but also as possible individual descriptors by analyzing their ability to discriminate through other techniques, that were not studied in this work and that are matter of immediate future work.

**Conflicts of Interest** The authors declare that they have no conflict of interest.

## References

1. "Ministerio de Salud Presidencia de la Nación-Cáncer de mama." [Online]. Available: <http://www.msal.gob.ar/index.php/component/content/article/48/246-cancer-de-mama#panel-7> [Accessed: 01-Jun-2017].
2. S. Antoni, I. Soerjomataram, B. Miller, F. Bray, and J. Ferlay, "An assessment of GLOBOCAN methods for deriving national estimates of cancer incidence," *Bull. World Health Organ.*, vol. 94, no. 3, pp. 174–184, Mar. 2016.
3. M. Viniestra, M. Paolino, and S. Arrossi, *Cáncer de mama en Argentina: organización, cobertura y calidad de las acciones de prevención y control*. 1a ed.-Buenos Aires: Organización Panamericana de la Salud-OPS, 2010.
4. L. Yaghjian, G. A. Colditz, B. Rosner, and R. M. Tamimi, "Mammographic breast density and breast cancer risk: interactions of percent density, absolute dense, and non-dense areas with breast cancer risk factors," *Breast Cancer Res. Treat.*, vol. 150, no. 1, pp. 181–189, 2015.
5. V. Paulina Neira, "Densidad mamaria y riesgo de cáncer mamario," *Rev. Médica Clínica Las Condes*, vol. 24, no. 1, pp. 122–130, 2013.
6. N. F. Boyd, H. Guo, L. J. Martin, L. Sun, J. Stone, E. Fishell, R. A. Jong, G. Hislop, A. Chiarelli, S. Minkin, and M. J. Yaffe, "Mammographic Density and the Risk and Detection of Breast Cancer," *N. Engl. J. Med.*, vol. 356, no. 3, pp. 227–236, 2007.
7. L. Aibar, A. Santalla, M. S. López-Criado, I. González-Pérez, M. A. Calderón, J. L. Gallo, and J. F. -Parra, "Clasificación radiológica y manejo de las lesiones mamarias," *Clin. Invest. Ginecol. Obstet.*, vol. 38, no. 4, pp. 141–149, 2011.
8. E. Ruj, *BI-RADS®. Sistema de informes y registro de datos de estudios por imágenes de la mama*, 5ta ed. 2016. American College of Radiology. Mamografía, Ecografía, Resonancia Magnética, Seguimientos y vigilancia de los resultados, Diccionario. Ediciones Journal.
9. O. M. Ruiz, C. R. Castellano, P. M. Angulo Aguilar, V. S. Nieto, A. A. Gil, R. Moreno de la Presa, and J. M. Pinto Varela, "Valoración de las categorías BI-RADS® de la densidad mamaria entre radiólogos y respecto a un método cuantitativo de medición," *Rev. Senol. y Patol. Mamar.*, vol. 27, no. 4, pp. 157–162, 2014.
10. Y. Li, C. Qian, and Y. Fan, "Unsupervised texture segmentation using permutation entropy and grey-level feature," *Proc. World Congr. Intell. Control Autom.*, vol. 2, pp. 9845–9848, 2006.
11. H. V. Ribeiro, L. Zunino, E. K. Lenzi, P. A. Santoro, and R. S. Mendes, "Complexity-entropy causality plane as a complexity measure for two-dimensional patterns," *PLoS One*, Published online 2012 Aug 14. <https://doi.org/10.1371/journal.pone.0040689>.
12. L. Zunino and H. V. Ribeiro, "Discriminating image textures with the multiscale two-dimensional complexity-entropy causality plane," *Chaos, Solitons and Fractals*, vol. 91, pp. 679–688, 2016.
13. C. Bandt and B. Pompe, "Permutation entropy: a natural complexity measure for time series," *Phys. Rev. Lett.*, vol. 88, no. 17, p. 174102, Apr. 2002.
14. M. Zanin, L. Zunino, O. A. Rosso, and D. Papo, "Permutation entropy and its main biomedical and econophysics applications: A review," *Entropy*, vol. 14, no. 8, pp. 1553–1577, 2012.
15. A. P. Antonelli, G. J. Meschino, and V. L. Ballarin, "Permutation entropy: Texture characterization in images," 2017 XVII Workshop on Information Processing and Control (RPIC), Mar del Plata, 2017, pp. 1–7.
16. M. Heath, K. Bowyer, D. Kopans, R. Moore, and P. Kegelmeyer, "The digital database for screening mammography," *Proc. Fifth Int. Work. Digit. Mammogr.*, pp. 212–218, 2000.



# Multiregional Radiomics Phenotypes at MR Imaging Predict MGMT Promoter Methylation in Glioblastoma

Zhi-Cheng Li, Yinsheng Chen, Qiuchang Sun, Qihua Li, Lei Liu, Ronghui Luo, Hongmin Bai, and Chaofeng Liang

## Abstract

This study aimed to build a reliable radiomics model from magnetic resonance imaging (MRI) for pretreatment prediction of MGMT methylation status in Glioblastoma. High-throughput radiomics features were automatically extracted from multiparametric MRI, including location features, geometry features, intensity features and texture features. A machine learning method was used to select a minimal set of all-relevant features. Based on these selected features, a radiomics model were built by using a random forest classifier for MGMT methylation prediction from a primary cohort (133 patients) and tested on an independent validation cohort (60 patients). Predictive models combing radiomics features and clinical factors were built and evaluated. The radiomics model with 6 all-relevant features allowed pretreatment prediction of MGMT methylation (AUC = 0.88, accuracy = 80%). Combing clinical factors with radiomics features did not benefit the prediction performance. The proposed radiomics model could provide a tool to guide preoperative patient care and made a step forward radiomics-based precision medicine for GBM patients.

## Keywords

Radiomics • Glioblastoma • MRI • MGMT methylation

Z.-C. Li (✉) · Q. Sun · Q. Li · L. Liu · R. Luo  
Shenzhen Institutes of Advanced Technology, Chinese Academy of Sciences, Shenzhen, China  
e-mail: zc.li@siaat.ac.cn

Y. Chen  
Department of Neurosurgery/Neuro-oncology, Sun Yat-sen University Cancer Center, Guangzhou, China

H. Bai  
Department of Neurosurgery, Guangzhou General Hospital of Guangzhou Military Command, Guangzhou, China

C. Liang  
Department of Neurosurgery, The 3rd Affiliated Hospital of Sun Yat-sen University, Guangzhou, China

## 1 Introduction

Glioblastoma Multiforme (GBM) is the most common malignant primary brain tumor in adults. The poor prognosis (median survival less than 15 months) is mainly due to the genomic heterogeneity [1]. Among all identified genetic alterations in GBM, *O*<sup>6</sup>-methylguanine-DNA methyltransferase (MGMT) promotor methylation has been so far the only one used as a molecular marker in clinical settings. GBM Patients with methylated MGMT are more sensitive to temozolomide (TMZ) and radiotherapy, hence have improved prognosis [2]. Therefore, the detection of MGMT promotor methylation status is of importance for GBM patients. Currently, the detection techniques have focused on genomic approaches, requiring biopsies and invasive surgeries to extract small portions of tumor. Although tissue is accessible in most patients undergoing gross total resection, tumor heterogeneity poses clear barriers to biopsy-based method. Medical imaging has great potential to address the tumor heterogeneity problem and provide a holistic view of the tumor in a non-invasively and repeated way. Identification of possible association between imaging phenotypes and MGMT methylation status has undoubted clinical benefits.

To explore the correlation between medical image and underlying genetic characteristics, an emerging technique, radiomics, has been proposed. Radiomics refers to a process of converting image into minable data through extracting high-throughput quantitative imaging features, and analyzing these data for predicting genomic patterns and clinical outcomes [3]. Early evidence has shown the correlation between MRI features and MGMT methylation in GBM [4]. However, these studies extract only a small number of simple features, which cannot fully describe the intratumoral heterogeneity. Recent studies have revealed the multiregional and microenvironmental heterogeneity in GBM [5]. It highlights the value of multiregional image analysis in spatially distinct habitats, some of which harbor heterogeneous tumor populations. To our knowledge, little work has

been done on a radiomics model linking multiparametric and multiregional MRI phenotypes with MGMT methylation status in GBM.

In this work, we propose a MR radiomics model for pretreatment prediction of MGMT promotor methylation status in GBM. The aim was to build a reliable multiregional and multiparametric MRI radiomics model for pretreatment prediction of MGMT promotor methylation status in GBM.

## 2 Materials and Methods

### 2.1 Study Cohort

In this retrospective multicenter study, 193 patients was recruited. The training cohort of 133 patients comprised 57 from TCIA and 76 from Guangzhou General Hospital of Guangzhou Military Command. Another cohort of 60 patients comprising 39 from The 3rd Affiliated Hospital of Sun Yat-Sen University and 21 from Sun Yat-Sen University Cancer Center were used for independent validation. The inclusion criteria were: (1) newly diagnosed GBM and (2) pretreatment MR imaging including T1-weighted, T1-weighted contrast-enhanced, T2-weighted, and T2-weighted FLAIR (T1w, T1c, T2w, and FLAIR) and (3) available MGMT methylation status. Institutional Review Board (IRB) approval for TCIA data was not required. IRB approvals from the three local institutions were obtained, and informed patient consent was waived. The clinical variables included age, sex, and Karnofsky performance score (KPS).

### 2.2 Image Preprocessing and Tumor Subregions Segmentation

Based on T1w, T1c, T2w and FLAIR images, we aimed to automatically segment the brain into five classes: the non-tumor region and four tumor subregions including necrosis, edema, non-enhancement area, and enhancement area. Before segmentation, images were preprocessed for standardization across multicenter subjects. First, N4ITK was applied to the images to correct the bias field distortion. After skull stripping and isotropic voxel resampling into  $1 \times 1 \times 1 \text{ mm}^3$ , rigid registration was performed with the mutual information similarity metric using T1c as a template. An efficient landmark-based approach with piecewise intensity mapping was used for intensity standardization in the same modality across multicenter subjects [6]. Then, a convolutional neural network (CNN)-based method was used to automatically segment the images into five classes [7]. To train the CNN model, real patient MR data sets from the 2015 brain tumor segmentation challenge (BRATS 2015) were used.

### 2.3 Multiregional MRI Radiomics Feature Extraction

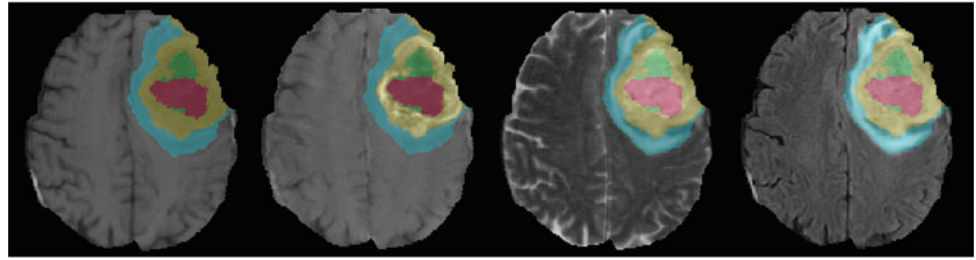
High-throughput imaging features can be extracted based on the segmented tumor subregions. To characterize the tumor heterogeneity, we extracted four groups of features, including (1) location features, (2) geometry features, (3) intensity features, and (4) texture features. The features (2–4) were extracted from four modalities within six extraction subregions, including necrosis, enhancement area, non-enhancement area, edema, solid core (the whole tumor except edema) and whole tumor. The features extracted were summarized in Table 1.

The location features were defined as the locations of the tumor geographic epicenter according to the Vasari guideline.

**Table 1** A summary of the radiomics features

Feature classes		Feature names
Location features		Regions: frontal, temporal, insular, parietal, occipital, brainstem, cerebellum; sides: right, left, bilateral
Intensity features		MaxValue, MedianValue, MinValue, MeanValue, energy, entropy, variance, kurtosis, root mean square, skewness, standard deviation, mean absolute deviation
Texture features	GLCM	Contrast, correlation, difference entropy, entropy, informational measure of correlation, sum average, sum entropy, sum variance, variance, difference variance, autocorrelation, cluster prominence, energy, cluster shade, dissimilarity, inverse difference normalized, homogeneity, maximum probability, inverse difference moment normalized
	GLRLM	Short run emphasis, long run emphasis, gray-level non-uniformity, run-length non-uniformity, low gray-level run emphasis, high gray-level run emphasis, short run low gray-level emphasis, short run high gray-level emphasis, gray-level variance, long run low gray-level emphasis, run-length variance, long run high gray-level emphasis, run percentage
	GLSZM	Small zone emphasis, large zone emphasis, gray-level non-uniformity, zone-size non-uniformity, low gray-level zone emphasis, high gray-level zone emphasis, small zone low gray-level emphasis, small zone high gray-level emphasis, gray-level variance, large zone low gray-level emphasis, zone-size variance, large zone high gray-level emphasis, zone percentage
	NGTDM	Coarseness, contrast, busyness, complexity, strength

**Fig. 1** Segmentation of the tumor subregions from T1, T1c, T2 and FLAIR



They comprised of 7 locations with different sides of right, left and bilateral, resulting in 21 location features. The geometry features described the three-dimensional shape characteristics of tumor subregions. In total 28 geometry features were extracted. The intensity features described the first-order statistical distribution of the tumor subregion intensities. We extracted 288 intensity features in total. The texture features described the high-order spatial distributions of the intensities. 1248 texture features were computed from all 6 extraction subregions and 4 modalities. Finally, for each patient 1705 quantitative imaging features were extracted from multiple tumor regions in multiparametric MR images.

## 2.4 Feature Selection and Classification Model

Having high-dimensional imaging features, we aimed to develop a stable multivariate model for predicting MGMT methylation status. Before model building, a feature selection was required to improve both the reliability and interpretability. Here a machine learning-based algorithm, Boruta, was used to select all-relevant features and generate a classification model [8]. Boruta was a wrapper algorithm for all-relevant feature selection, where relevant features were searched in a top-down way by comparing the importance of the original features with the importance achieved by artificially added random features. A random forest algorithm was performed in each iteration to evaluate the classification and measure the feature importance, and irrelevant features were eliminated progressively. To obtain statistically significant results, the algorithm repeatedly calculated all possible subsets of the features and finally select the minimal set of the most relevant features for an optimal classification. The R package Boruta was used to build the model. Furthermore, a combined model based on radiomics features and clinical factors (sex, age and KPS) was also built.

## 2.5 Statistical Analysis

All statistical analysis was done with R software, version 3.4.0 (<https://www.r-project.org>). The statistical significance levels were set at 0.05. The predictive models were trained

on the primary cohort and tested on the independent validation cohorts. The performance was assessed using accuracy, sensitivity, specificity, and area under the receiver operating characteristic (ROC) curve (AUC) (Fig. 1).

## 3 Results and Discussions

There was no significant difference in patient and tumor characteristics between the primary and validation cohorts ( $P = 0.56-0.85$ ). For both radiomics models, 6 all-relevant features were selected by the Boruta algorithm. The selected features included: (1) Skewness from core area in T1w, (2) Energy from edema in T1w, (3) Contrast calculated by GCLM matrix from necrosis in FLAIR, (4) Gray-level Variance calculated by GLSZM matrix from enhanced area in T1c, (5) Low Gray-level Zone Emphasis calculated by GLSZM matrix from T2w, and (6) Business calculated by NGTDM matrix from core area in T2w. Our study was based on 1705 quantitative features derived from multiple 3D tumor subregions in multiparametric MR images, allowing for a more comprehensive characterization of the intratumor heterogeneity. This may offer penitential to improve the prediction performance.

The radiomics model with 6 relevant features achieved an AUC of 0.95, an accuracy of 87%, a sensitivity of 0.84 and a specificity of 0.89 in the primary cohort. The predictive performance was further confirmed in the validation cohort with an AUC of 0.88, an accuracy of 80%, a sensitivity of 0.70 and a specificity of 0.86. The ROC curve of the 6-feature radiomics models were shown in Fig. 3. In previous studies, the AUCs ranged from 0.75 to 0.85 while the accuracies ranged from 58 to 73.6%. To the best of our knowledge, our study was the first multicenter study with an independent validation cohort, and our all-relevant radiomics model achieved higher accuracy (80%) and AUC (0.88) compared with previous models. For the combined model, the same 6 all-relevant features were selected after Boruta selection. Therefore, the combined model achieved the same performance as the radiomics model. Our results highlight the value of radiomics feature rather than clinical factor in methylation prediction (Fig. 2).

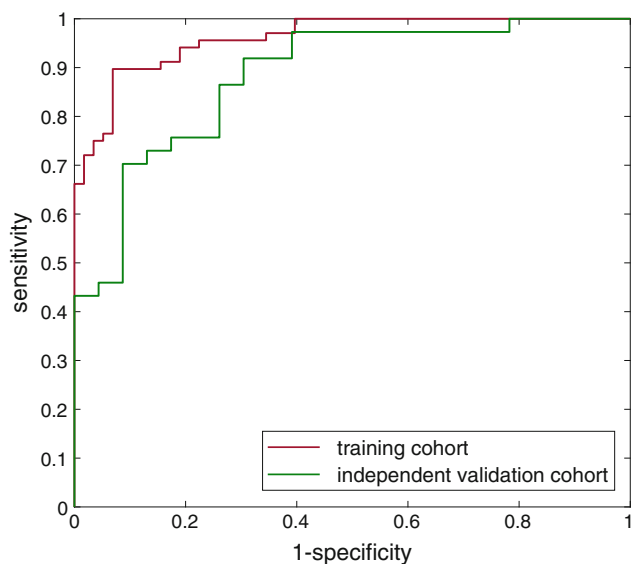


**Fig. 2** ROC curve of the radiomics model

## 4 Conclusions

The presented multiregional and multiparametric MRI radiomics model has the potential to non-invasively detect MGMT methylation status in GBM. The model may serve as a potential imaging biomarker to guide preoperative patient care and made a step forward radiomics-based precision medicine for GBM patients.

**Acknowledgements** This work was supported by the National Natural Science Foundation of China (No.61571432), and Shenzhen Basic Research Project (JCYJ20170413162354654).

**Conflict of Interest** The authors declare that they have no conflict of interest.

## References

- Ostrom, Q.T., Gittleman, H., Xu, J. et al: CBTRUS statistical report: primary brain and other central nervous system tumors diagnosed in the United States in 2009–2013. *Neuro-Oncology* 18:v1-75 (2016). <https://doi.org/10.1093/neuonc/now207>
- Weller, M., Stupp, R., Reifenberger, G. et al: MGMT promoter methylation in malignant gliomas: ready for personalized medicine? *Nat. Rev. Neurol.* 6:39–51 (2010). <https://doi.org/10.1038/nrneurol.2009.197>
- Lambin, P., Leijenaar, R.T., Deist, T.M. et al: Radiomics: the bridge between medical imaging and personalized medicine. *Nat. Rev. Clin. Oncol.* 14:749–762 (2017). <https://doi.org/10.1038/nrclinonc.2017.141>
- Korfatis, P., Kline, T.L., Coufalova, L. et al: MRI texture features as biomarkers to predict MGMT methylation status in glioblastomas. *Med. Phys.* 43:2835–2844 (2016) <https://doi.org/10.1118/1.4948668>
- Patel, A.P., Tirosh, I., Trombetta, J.J. et al: Single-cell RNA-seq highlights intratumoral heterogeneity in primary glioblastoma. *Science* 344:1396–1401 (2014). <https://doi.org/10.1126/science.1254257>
- Ltjnen, J.M., Wolz, R., Koikkalainen, J.R. et al: Fast and robust multi-atlas segmentation of brain magnetic resonance images. *Neuroimage* 49:2352–2365 (2010). <https://doi.org/10.1016/j.neuroimage.2009.10.026>
- Pereira, S., Pinto, A., Alves, V., Silva, C.A. Brain tumor segmentation using convolutional neural networks in MRI images. *IEEE. T. Med. Imaging.* 35:1240–1251 (2016) <https://doi.org/10.1109/tmi.2016.2538465>
- Kursa, M.B., Rudnicki, W.R.: Feature selection with the Boruta package. *J. Stat. Softw.* 36:1–13 (2010). <https://doi.org/10.18637/jss.v036.i11>

# Influence of Image Resolution Property on Aliasing Error of Digital Wiener Spectrum

Yasuyuki Kawaji, Tatsuhiro Gotanda, Tetsunori Shimono, Nobuyoshi Tanki, Toshizo Katsuda, Rumi Gotanda, Tadao Kuwano, and Takuya Akagawa

## Abstract

The noise properties of a radiography system are commonly described by its wiener spectrum (WS). The two-dimensional discrete Fourier transform (2D-DFT) methods is the most commonly used and accepted techniques for measuring the digital WS. The 2D-DFT method has been adopted by the International Electrotechnical Commission (IEC) as a noise-power spectrum. However, the digital WS contains the effects of aliasing error, and this error depends on the presampled modulation transfer function (MTF) of the digital radiography (DR) system. The aim of this work was to show the influence of the aliasing error of the digital WS when the image resolution property was changed. We examined the influence of the aliasing error using simulated noise images. Two types of noise images with same pixel size and different presampled MTFs were generated by using ImageJ (National Institutes of Health: NIH). These images were used to simulate the image resolutions of an indirect/direct flat panel detector (FPD). The theoretical WS of the simulation noise image can be derived from a standard deviation  $\sigma$  of the Gaussian filter and added noise. Simulated noise images were analysed using

the 2D-DFT method. The WS values calculated from those simulation images were compared with the theoretical WS values. The WS values in the indirect and direct FPD increased, compared to the theoretical WS values. The average relative differences for frequencies up to the Nyquist frequency were 27.9% and 85.2%, respectively. The results showed that the degree of the influence of the aliasing error of the digital WS depends largely on the presampled MTF of the DR system. Therefore, we should take into account the impact of the aliasing error of the digital WS, in the comparison between DR systems with different presampled MTFs.

## Keywords

Digital wiener spectrum • Two-dimensional discrete fourier transform method • Aliasing error

## 1 Introduction

Noise analysis is very important for the evaluation of the performance of digital radiography (DR) systems and for the optimum selection of the exposure parameters used in the creation of clinical digital images. The wiener spectrum (WS) of a DR system is generally used to describe its noise properties [1–7]. The most commonly used and accepted techniques for measuring the digital WS is the two-dimensional discrete Fourier transform (2D-DFT) methods. The International Electrotechnical Commission (IEC) has adopted the 2D-DFT method as a noise power spectrum, which is an important factor for the determination of detective quantum efficiency (DQE) of DR systems [8]. However, the WS value obtained from these methods, referred to as “digital WS”, contains the effect of aliasing error. The aliasing error of the WS can significantly degrade the DQE [9]. This aliasing error depends on the resolution property of the DR system. To the best of our knowledge, there is little research on them.

Y. Kawaji (✉) · T. Shimono  
Faculty of Health Sciences, Department of Radiological Science,  
Junshin Gakuen University, Fukuoka, Japan  
e-mail: kawaji.y@junshin-u.ac.jp

T. Gotanda · R. Gotanda  
Faculty of Health Science and Technology, Department of  
Radiological Technology, Kawasaki University of Medical  
Welfare, Kurashiki, Japan

N. Tanki · T. Katsuda  
Faculty of Health Sciences, Butsuryo College of Osaka, Sakai,  
Japan

N. Tanki · T. Kuwano  
Division of Radiological Health Supporting Sciences, Graduate  
School of Health Science, Okayama University, Okayama, Japan

T. Akagawa  
Department of Radiology, Tokushima Red Cross Hospital,  
Komatsushima, Japan



We examined the influence of the aliasing error of the WS using a simulated noise image when the presampled modulation transfer function (MTF) was changed. Two types of simulated images modelled on the resolution property of indirect and direct flat panel detectors (FPD) were generated. The WS of simulated noise images were analysed using the 2D-DFT method. Simulation noise images can be used to derive the WS theoretically from a standard deviation  $\sigma$  of the Gaussian filter, added noise and pixel size of the image. The WS values obtained using the 2D-DFT method were compared with the theoretical WS values.

## 2 Materials and Methods

We examined the influence of the aliasing error of the WS using simulated noise images when the resolution property was changed.

### 2.1 Image Simulation

The simulated noise images were generated using ImageJ 1.46r (National Institutes of Health, USA). The images were  $2\text{ K} \times 2\text{ K}$ , 16-bit, with  $100\ \mu\text{m}$  pixels. All pixel values of the image were set to 1000. Gaussian noise was added to the images with a standard deviation of 31.62. Further, a blurring process was performed on these images by using a Gaussian filter. The blur of each image was controlled by a standard deviation  $\sigma$  of the Gaussian filter. In the version of image  $j$  used in this study, the  $\sigma$  is the standard deviation multiplied by 2.5. Two types of simulated images modelled on the resolution property of indirect and direct FPD were generated. The  $\sigma$  was set to 0.75 and 0.25 for the indirect and direct FPD, respectively. The frequency response of Gaussian filter can be calculated by taking the Fourier transform of the filter. The spatial frequency response of the filter  $G(u)$  is given by the following Eq.:

$$G(u) = e^{-\left(\frac{\sigma^2}{25} \cdot u^2\right)} \quad (1)$$

where  $u$  is the discrete spatial frequency,  $\sigma$  is the standard deviation of the Gaussian filter. The presampled MTF of simulated noise images can be calculated from  $G(u)$  and sinc function of pixel size, using the following Eq.:

$$MTF_{presampled}(u) = G(u) \times \text{sinc}(\pi \cdot d \cdot u) \quad (2)$$

where  $d$  is the pixel size. Figure 1 shows presampled MTFs of each simulated image in this study.

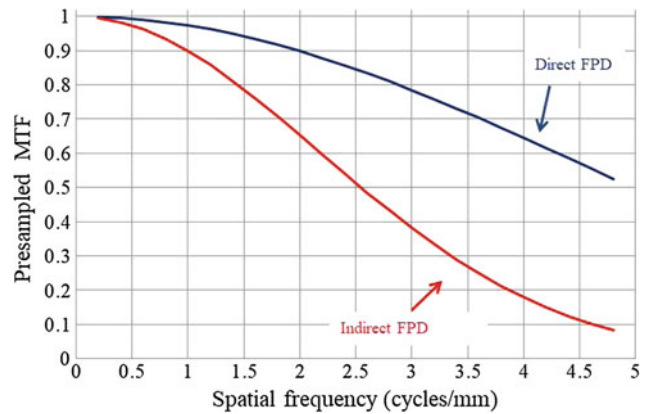


Fig. 1 Presampled MTF of simulated noise images with the resolution property of indirect and direct FPD in this study

### 2.2 WS Analysis

The WSs of simulated noise images were analysed using the 2D-DFT method [7]. The WS was calculated from a  $1\text{ K} \times 1\text{ K}$  pixel region extracted from the center of the flood image. Regions of interest (ROIs) of size  $128 \times 128$  pixels were then extracted from the image by using a half overlapping pattern. A 2D second-order polynomial was fitted to each ROI and subtracted. The 2D fast Fourier transform was applied to each ROI, and the squared modulus was added to the WS ensemble. Finally, the WS was calculated by dividing the ensemble by the mean square value of the linearized  $1\text{ K} \times 1\text{ K}$  pixel region. The WS data at discrete frequencies were obtained by binning all WS data points within an interval of  $0.2\text{ mm}^{-1}$  around the specified frequencies.

### 2.3 Theoretical WS

The simulated noise images have white noise with uniform noise property at all spatial frequencies, and the standard deviation is 31.62. The known WS of images are  $1.00e^{-5}$ , which is the inverse of the signal value per unit area ( $0.01\text{ mm}^2$ ). Theoretical WS can be calculated from the known WS and the presampled MTF using the following Eq. [10]:

$$WS_{theoretical}(u) = 1.00e^{-5} \cdot MTF_{presampled}(u)^2 \quad (3)$$

where  $u$  is the discrete spatial frequency. The WS values obtained using the 2D-DFT method were compared with the theoretical WS values.



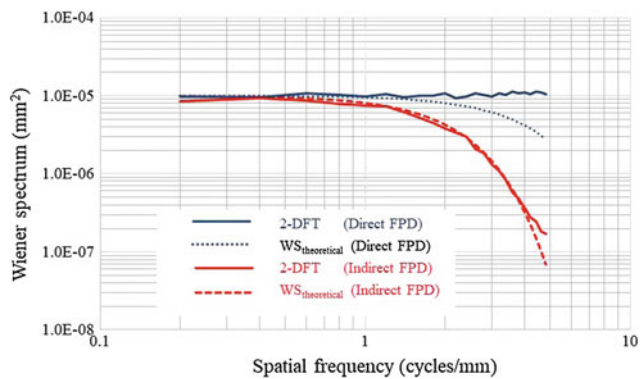


**Fig. 2** Comparison of WS values obtained from the 2D-DFT method and theoretical WS values

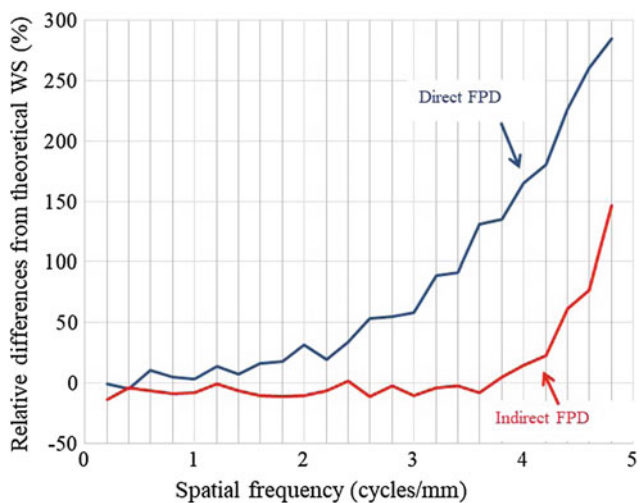


**Fig. 3** Relative differences from the theoretical WS

### 3 Results

Figure 2 shows the comparison of WS values obtained from the 2D-DFT method and theoretical WS values. The WS values in the indirect and direct FPD increased, compared to the theoretical WS values. The WS values in the indirect FPD increased compared to the theoretical WS at 4 cycles/mm. In the direct FPD, The WS increased at 2.5 cycles/mm.

Figure 3 shows the relative differences from theoretical WS. The maximum relative differences of indirect and direct FPD were 146% and 284.4%, respectively. The average relative differences for frequencies up to the Nyquist frequency were 27.9% and 85.2%, respectively.

### 4 Discussion

As shown in Fig. 2.3, the WS values were affected in the high-frequency domain. Large differences were observed in measurement accuracy when the presampled MTF of simulated noise images was different. The average relative difference for frequencies up to the Nyquist frequency of the direct FPD is larger than that of the indirect FPD. This is because these images have spatial frequency components exceeding the Nyquist frequency and the images with a high-presampled MTF contain high-spatial-frequency components. Consequently, the digital WS of digital systems with high resolution property, such as a direct FPD, are more susceptible to aliasing errors, because the 2D-DFT method cannot remove the effect of aliasing error.

According to the results of this simulation study, the degree of the aliasing error of the digital WS depends considerably on the presampled MTFs of the DR system. The result of this study represents the result of only the quantum noise region. The noise in a clinical digital radiography system contains three main components, namely, quantum noise, structural noise, and electric noise. For further study, it is necessary to consider the condition including these three main components.

### 5 Conclusion

We examined the influence of the aliasing error of the WS using simulated noise images when the presampled MTF was changed.

The results show that,

1. The degree of the aliasing error of the digital WS depends considerably on the presampled MTFs of the DR system.
2. The impact on the aliasing error of the digital WS for the comparison of DR systems with different presampled MTFs should be taken into account.

**Conflict of interest** The authors declare that they have no conflict of interest.

### References

1. Doi, K. Holje, G. Loo, L. N. *et al.*: MTF's and Wiener spectra of radiographic screen – film systems. HHS Publication FDA, 82 - 8187, pp. 14–38 (1982).
2. Giger, M. L., Doi, K. Metz, C. E.: Investigation of basic imaging properties in digital radiography. 2. Noise Wiener spectrum. Medical Physics, 11, 6, pp. 97–805 (1984).

3. Dobbins, JT: Effects of undersampling on the proper interpretation of modulation transfer function, noise power spectra, and noise equivalent quanta of digital imaging systems. *Med Phys* 22, 171–81(1995).
4. Williams, MB. Mangiafico, P, A. Simoni, P, U.: Noise power spectra of images from digital mammography detectors. *Med Phys*; 26(7), pp. 1279–93 (1999).
5. Samei, E. Performance of digital radiographic detectors: quantification and assessment methods. In: Samei, E. Flynn, M, J. editors. *Syllabus: advances in digital radiography-categorical course in diagnostic radiology physics*. Oak Brook: Radiological Society of North Americap. 37–4, (2003).
6. Neitzel, U. Gu'nther-Kohfahl, S. Borasi, G. Samei, E.: Determination of the detective quantum efficiency of a digital X-ray detector: comparison of three evaluations using a common image data set. *Med Phys*, 31(8). pp. 2205–11 (2004).
7. Dobbins, J, T III. Samei, E. Ranger, N, T. Chen, Y.: Intercomparison of methods for image quality characterization. II. Noise power spectrum. *Med Phys*, 33(5), 1466–75 (2006).
8. IEC62220-1: Medical electrical equipment characteristics of digital x-ray imaging devices – Part 1; Determination of the detective quantum efficiency (2003).
9. Zhao, W and Rowlands, J,A.: Digital radiology using active matrix readout of amorphous selenium: Theoretical analysis of detective quantum efficiency. *Medical Physics* 24, pp. 1819–1833 (1997).
10. Kunitomo, H. Ichikawa, K. Higashide, *et al.*: Investigation of error factors in analysis of digital noise power spectrum. *Nihon Hoshasen Gijutsu Gakkai Zasshi*. 20; 66 (7), pp. 734–42 (2010).



# Automatic Identification and Extraction of Pectoral Muscle in Digital Mammography

Ana L. M. Pavan, Antoine Vacavant, Allan F. F. Alves, Andre P. Trindade, and Diana R. de Pina

## Abstract

Mammography is a worldwide image modality used to diagnose breast cancer and can be used to measure breast density (BD). In clinical routine, radiologist perform image evaluations through BIRADS assessment. However, this method has inter and intraindividual variability. An automatic method to measure BD could relieve radiologist's workload by providing a first aid opinion. However, pectoral muscle (PM) is a high density tissue, with the same imaging characteristics as fibroglandular tissues, which makes its automatic detection a challenging task. The aim of this work is to develop an automatic algorithm to segment and extract PM in digital mammograms. A hybrid methodology has been developed using Hough transform, to find the edge of the PM, and active contour, to segment PM muscle. Seed of active contour is applied automatically in the edge of PM found by Hough transform. An experienced radiologist manually performed the PM segmentation. Manual and automatic methods were compared using the Jaccard index and Bland-Altman statistics. The comparison between methods presented a Jaccard similarity coefficient greater than 90% for all analyzed images. The Bland-Altman statistics compared the segmented PM area and showed agreement between both methods within 95% confidence interval. The method proved to be accurate and robust, segmenting rapid and free of intra and inter-observer variability.

## Keywords

Mammography • Pectoral muscle • Hough transform and active contour

## 1 Introduction

Mammography is a worldwide image modality used to diagnose breast cancer, even in asymptomatic women. Due to its large availability, mammograms can be used to measure breast density and to predict cancer development [1]. Women with increased mammographic density have a four- to sixfold increase in their risk of developing breast cancer [1, 2]. In clinical routine, radiologist perform image evaluations through BIRADS (Breast Imaging Reporting and Data System) assessment. However, this subjective method shows variable intra- and inter-observer agreement [3, 4].

Furthermore, BIRADS categories are too rough to follow breast evolution in individual women [3]. For this reason, tasks such as selection of women who may benefit from supplemental screening exams and prediction of breast cancer risk, may be challenging with only subjective density assessment [2, 5]. Therefore, studies have been made to accurately quantify mammographic breast density. An automatic objective method to measure breast density could relieve radiologist's workload by providing a first aid opinion. Semi-automated and automated algorithms have been developed to achieve objective breast density measurements [2, 3, 5–8].

Algorithms are applied in digital mammograms in crano-caudal (CC) and medio-lateral oblique (MLO) views. However, pectoral muscle (PM) is a high density tissue, with similar image characteristics as fibroglandular tissues [9]. Furthermore, patient positioning during mammograms acquisition may cause variations in texture, size, position, intensity and shape of PM [10]. It is consequently hard to automatically quantify mammographic breast density. The

A. L. M. Pavan · A. F. F. Alves (✉)  
Department of Physics and Biophysics, Biosciences Institute of Botucatu, São Paulo State University, Distrito de Rubião Junior S/N, Botucatu, São Paulo, 18618-000, Brazil  
e-mail: allan@ibb.unesp.br

A. Vacavant  
Department Institut Pascal, UMR 6602, UCA/SIGMA, CNRS, Université Clermont Auvergne, 63171 Aubière, France

A. P. Trindade · D. R. de Pina  
Department of Tropical Diseases and Diagnostic Imaging, Botucatu Medical School, Univ Estadual Paulista, Distrito de Rubião Junior S/N, Botucatu, São Paulo, 18618-000, Brazil  
e-mail: drpina@fmb.unesp.br

success of automatic methodology depends on accurate differentiation between PM and breast tissue mass [11].

Therefore, it is necessary to use a pre-processing tool to segment the PM, which may erroneously be quantified as fibroglandular tissue. Methods such as line detection [11, 12], statistical techniques [11, 13], application of active contours [11, 14], wavelets [11, 15] and based on pixel intensity [16] have been proposed in literature. However, it is reported variability in the success rate and in the accuracy of methods [17]. Therefore, there is no specific method used widely by researchers. The aim of this work is to develop an automatic algorithm to segment and extract PM in digital mammograms. The developed method could be used to standardize PM segmentation. The methodology, presented in Sect. 2, is based on Hough transform and active contour. Section 3 is dedicated to compare PM segmentation results from the proposed algorithm with manual segmentation.

## 2 Methodology

### 2.1 Dataset

The present study was developed with ethical approval from the authors' institutions under protocol number 50547315.8.0000.5411.

Women aged 18 years or older undergoing screening mammography between 2013 and 2015 at Botucatu Medical School were included. For the purpose of this work, only medio-lateral oblique view were selected. A total of thirty mammograms were evaluated. Mammograms of all BIR-ADS tissue density classes were included.

The mammography system used was a Senographe 600T (GE Healthcare, Milwaukee, WI) with a CR-85X image digitizer (Agfa-Gevaert Group, Mortsel, BE). An Agfa image plate ( $18 \times 24 \text{ cm}^2$  or  $24 \times 30 \text{ cm}^2$ ) with a pixel pitch of  $50 \mu\text{m}$  was employed. A Mo/Mo anode/filter combination was used for all X-ray exposures.

### 2.2 Developed Algorithm

The algorithm, developed in Matlab® platform, uses image processing tools to automatically segment and extract the PM of digital mammograms. Firstly, it applies thresholding technique in original image, shown in Fig. 1a, to remove non-biological information, resulting in Fig. 1b.

All mammograms must be in the same orientation. In this work, we have chosen that PM occupies the top left corner of the image. It is necessary to standardize image orientation because Canny method and Hough transform steps utilizes parameters which depends on PM position. Pectoral muscle forms a roughly triangular shape in this area of image.

Therefore, algorithm detects the presence or absence of breast tissue in the top left corner by summing pixel's intensity in a triangle area. Figure 1b shows an example where sum is equal to zero meaning that image needs to be re-orientated. In this case, image is flipped and the PM occupies the top left corner of the image, as represented in Fig. 1c.

In the next step, the quadrant containing the PM is selected and edges are detected using the Canny method. Figure 1d shows the quadrant containing PM and the lines representing detected edges by Canny. Then, Hough transform is applied in resulting Canny image to find edge of the PM. For this step, features as size and angular orientation of edges were used to detect only PM limits. The green line in Fig. 1e shows edge of PM detected by Hough transform. An active contour model, based on Mumford–Shah segmentation techniques and the level set, is then applied to segment PM area. The seed area used by active contour [18] is the triangle defined by PM edge line previously detected. The area segmented by active contour is extracted from original image, resulting in Fig. 1f.

### 2.3 Validation

To validate the developed automatic method, an experienced radiologist manually performed the PM segmentation in the same mammograms assessed by algorithm. Both methods, manual and automatic, were compared using the Jaccard index and Bland-Altman statistics.

## 3 Results and Discussion

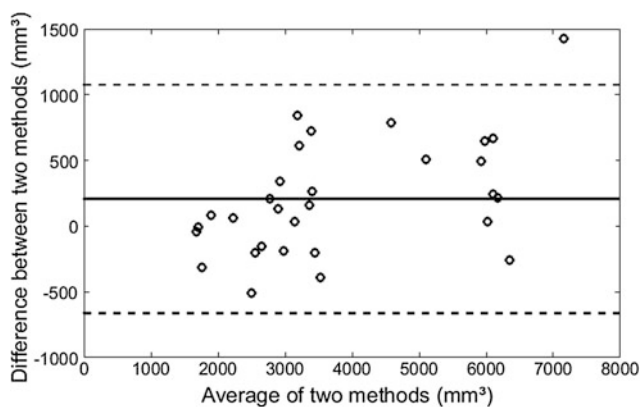
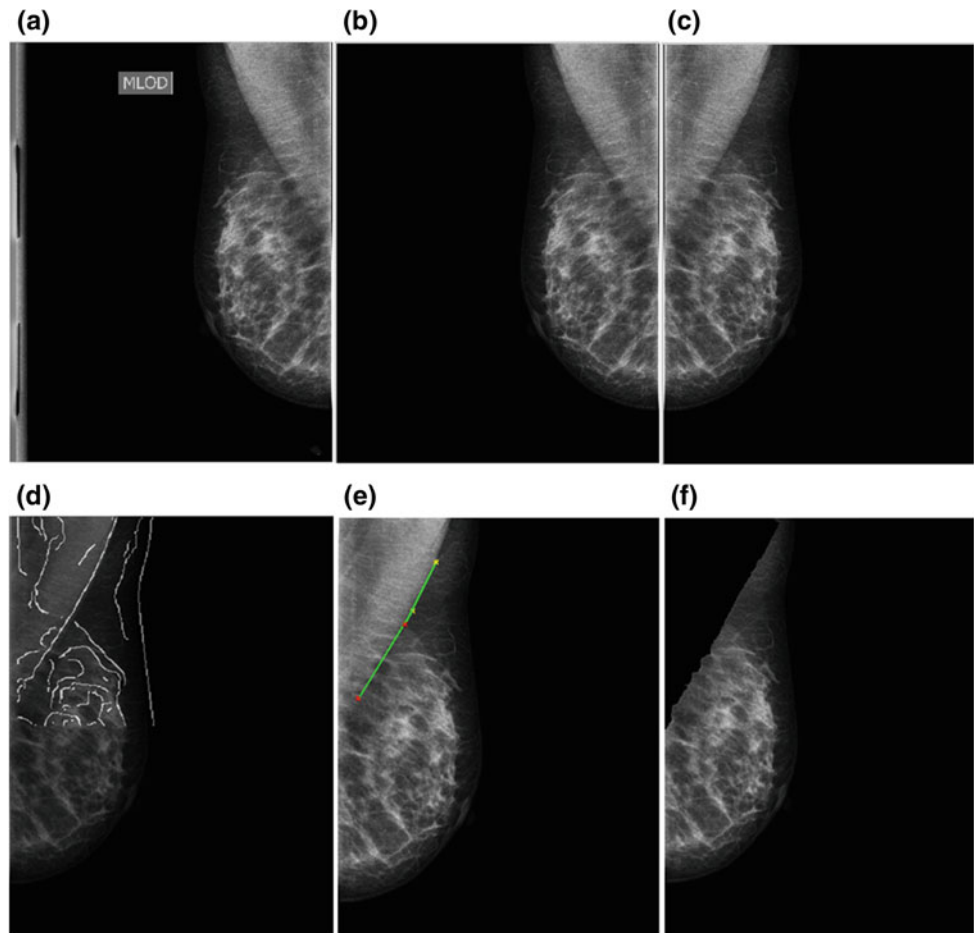
The Bland-Altman statistics compared both methods in relation to area ( $\text{mm}^2$ ) of segmented PM, as shows Fig. 2. The analysis revealed strong agreement and low dispersion between variables within 95% confidence interval, enhancing the accuracy of segmentation compared to the manual method. Thus, the method proved to be accurate and robust, segmenting rapidly and freely from intra and inter-observer variability.

Figure 3 shows segmentation performed by automatic (a) and manual (b) methods.

The comparison between manual and developed automatic method presented a mean Jaccard similarity coefficient of 92% with 3.1% of standard deviation, showing the efficiency and accuracy of segmentation using the proposed method. This result agrees with literature that shows accuracy greater than 90% [19].

Pectoral muscle segmentation has been reported to be a challenging task in dense breasts, where a significant part of the breast is made up of fibrous and glandular tissues [11, 19]. Therefore, it is important to note that our methodology was

**Fig. 1** Steps of developed method to extract pectoral muscle: **a** Original image, **b** extraction of non-biological tissues, **c** image flip, **d** Canny method to detect lines, **e** Hough transform to delineate roughly pectoral muscle edge and **f** result image after active contour application



**Fig. 2** Bland-Altman comparing total area segmented by both manual and automatic methods

applied in all breast category showing good results. The limitation of our method is that in breasts not correctly positioned, the PM makes a fold making it difficult to extract lines with Hough transform. In this study, such cases were excluded. Further studies should be done to overcome this issue.

The use of methodologies combining different computational tools has been reported to have better results when

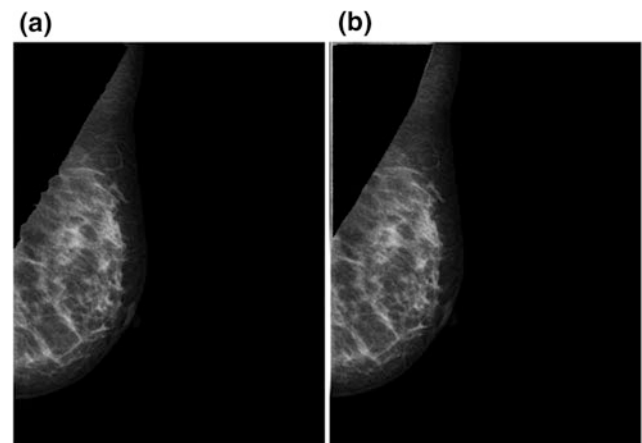


**Fig. 3** Comparison between segmentation by **a** automatic and **b** manual methods

compared with only one method [20]. In the present study, we developed an automatic algorithm using hybrid methodology which allows to segment PM more robust and faster when compared with manual segmentation.

## 4 Conclusion

The proposed method may be used reliably to segment PM in digital mammography in clinical routine. The segmentation of the PM is very important for further quantifications of fibroglandular tissue volume present in the breast. Literature shows that when using both views, MLO and CC, breast density estimation has better results when compared with only one view [2]. In future works, we will quantify breast density in MLO mammograms resulted from this study using our methodology described in [21]. Therefore, we believe that breast density quantification will present results with better accuracy.

**Conflict of Interest Statement** The authors declare that there is no conflict of interest for this study.

## References

- Lu, L.J., et al., Comparison of breast tissue measurements using magnetic resonance imaging, digital mammography and a mathematical algorithm. *Phys Med Biol*, 2012. **57**(21): p. 6903–27.
- Gubern-Merida, A., et al., Volumetric breast density estimation from full-field digital mammograms: a validation study. *PLoS One*, 2014. **9**(1): p. e85952.
- Wang, J., et al., Agreement of mammographic measures of volumetric breast density to MRI. *PLoS One*, 2013. **8**(12): p. e81653.
- Seo, J.M., et al., Automated volumetric breast density estimation: a comparison with visual assessment. *Clin Radiol*, 2013. **68**(7): p. 690–5.
- van der Waal, D., et al., *Comparing Visually Assessed BI-RADS Breast Density and Automated Volumetric Breast Density Software: A Cross-Sectional Study in a Breast Cancer Screening Setting*. *PLoS One*, 2015. **10**(9): p. e0136667.
- Alonzo-Proulx, O., R.A. Jong, and M.J. Yaffe, *Volumetric breast density characteristics as determined from digital mammograms*. *Phys Med Biol*, 2012. **57**(22): p. 7443–57.
- Kallenberg, M.G., et al., *Automatic breast density segmentation: an integration of different approaches*. *Phys Med Biol*, 2011. **56**(9): p. 2715–29.
- van Engeland, S., et al., *Volumetric breast density estimation from full-field digital mammograms*. *IEEE Trans Med Imaging*, 2006. **25**(3): p. 273–82.
- Feudjio, C.K., et al., *Automatic extraction of pectoral muscle in the MLO view of mammograms*. *Phys Med Biol*, 2013. **58**(23): p. 8493–515.
- Vikhe, P.S. and V.R. Thool, *Detection and Segmentation of Pectoral Muscle on MLO-View Mammogram Using Enhancement Filter*. *J Med Syst*, 2017. **41**(12): p. 190.
- Ganesan, K., et al., *Pectoral muscle segmentation: a review*. *Comput Methods Programs Biomed*, 2013. **110**(1): p. 48–57.
- Kwok, S.M., et al., *Automatic pectoral muscle segmentation on mediolateral oblique view mammograms*. *IEEE Trans Med Imaging*, 2004. **23**(9): p. 1129–40.
- Wang, L., et al., *Automatic pectoral muscle boundary detection in mammograms based on Markov chain and active contour model*. *Journal of Zhejiang University SCIENCE C*, 2010. **11**(2): p. 111–118.
- Ferrari, R., et al., *Identification of the breast boundary in mammograms using active contour models*. *Med Biol Eng Comput.*, 2004. **42**(2): p. 201–208.
- Ferrari, R.J., et al., *Automatic identification of the pectoral muscle in mammograms*. *IEEE Trans Med Imaging*, 2004. **23**(2): p. 232–45.
- Saltanat, N., M.A. Hossain, and M.S. Alam, *An efficient pixel value based mapping scheme to delineate pectoral muscle from mammograms*. *IEEE Fifth International Conference on Bio-Inspired Computing: Theories and Applications*, 2010: p. 1510–1517.
- Taghanaki, S.A., et al., *Geometry-Based Pectoral Muscle Segmentation From MLO Mammogram Views*. *IEEE Trans Biomed Eng*, 2017. **64**(11): p. 2662–2671.
- Chan, T.F. and L.A. Vese, *Active contours without edges*. *IEEE Trans Image Process*, 2001. **10**(2): p. 266–77.
- Mustra, M., M. Grgic, and R.M. Rangayyan, *Review of recent advances in segmentation of the breast boundary and the pectoral muscle in mammograms*. *Med Biol Eng Comput*, 2016. **54**(7): p. 1003–24.
- Rampun, A., et al., *Fully automated breast boundary and pectoral muscle segmentation in mammograms*. *Artif Intell Med*, 2017. **79**: p. 28–41.
- Pavan, A.L.M., et al., *Fibroglandular Tissue Quantification in Mammography by Optimized Fuzzy C-Means with Variable Compactness*. *Innovation and Research in BioMedical engineering*, 2017. **48**(4): p. 228–233.



# Fully Automatic CAD System for Segmentation and Classification of Spinal Metastatic Lesions in CT Data

Jiri Chmelik, Roman Jakubicek, Jiri Jan, Petr Ourednicek, Lukas Lambert, Elena Amadori, and Giampaolo Gavelli

## Abstract

Our contribution presents a research progress in our long-term project that deals with spine analysis in computed tomography (CT) data. A fully automatic computer-aided diagnosis (CAD) system is presented, enabling the simultaneous segmentation and classification of metastatic tissues that can occur in the vertebrae of oncological patients. The task of the proposed CAD system is to segment metastatic lesions and classify them into two categories: osteolytic and osteoblastic. These lesions, especially osteolytic, are ill defined and it is difficult to detect them directly with only information about voxel intensity. The use of several local texture and shape features turned out to be useful for correct classification, however the exact determination of relevant image features is a difficult task. For this reason, the feature determination has been solved by automatic feature extraction provided by a deep convolutional neural network (CNN). The achieved mean sensitivity of detected lesions is greater than 92% with approximately three false positive detections per lesion for both types.

## Keywords

CAD • Convolution neural network • Spine analysis  
Metastasis • CT data

## 1 Introduction

Systems for automatic computer aided diagnosis (CAD) are increasingly important in all fields of clinical medicine, especially in fields where large amounts of data (CT, MRI, multi-modal data, longitudinal studies, etc.) must be processed. CAD systems help medical staff to decrease the duration of the routine steps that are required for assessment of a large amount of images or signals. The lower time requirements and high sensitivity of CAD also help to avoid mistakes caused by the fatigue of the operator. This paper aims to discuss the detection, segmentation and classification of metastatic bone lesions that are situated in vertebral bodies due to cancerous cells spreading from primary tumour site. It was proven that up to 70% of all metastases are situated in bone structures and up to 20% of them are formed in the spine [1, 2].

Some of the recent methods that have enabled the detection of sclerotic or lytic bone lesions in thoraco-lumbar spine are described below. The authors in [3] proposed a CAD based on pre-segmentation by watershed, graph cut and level set algorithms, followed by a support vector machines (SVM) based classifier trained on several experimentally-devised image features. This approach was improved by a superior meta-analytic convolutional neural network (CNN) that enabled the reduction of false positive detection of sclerotic lesions [4, 5]. Another approach was published in [6], where authors used three independent classification methods based on Markov random fields, three-layer perceptron, and graph cut algorithm. More extensive reviews of recent methods can be found in [7].

In this paper we propose a fully automatic and fast CAD system designed for the detection, segmentation, and

---

J. Chmelik (✉) · R. Jakubicek · J. Jan  
Faculty of Electrical Engineering and Communication,  
Department of Biomedical Engineering, Brno University of  
Technology, 61600 Brno, Czech Republic  
e-mail: chmelikj@feec.vutbr.cz

P. Ourednicek  
Department of Medical Imaging, St. Anne's University Hospital  
Brno and Faculty of Medicine Masaryk University, 65691 Brno,  
Czech Republic

L. Lambert  
First Faculty of Medicine, Department of Radiology, Charles  
University in Prague and General University Hospital in Prague,  
12808 Prague, Czech Republic

E. Amadori · G. Gavelli  
Radiologia, Istituto Scientifico Romagnolo per lo Studio e la Cura  
dei Tumori, Istituto di Ricovero e Cura a Carattere Scientifico,  
47014 Meldola, Italy

classification of lytic and sclerotic lesions in the spine in CT data. Our system is composed of a specific adaptive data pre-processing steps followed by a from scratch trained CNN classifier. The main contribution of our system is its usability on whole-spine scans instead of thoraco-lumbar only, enabling the detection of small lesions (depending on CT data resolution), reduced dependence on a CT scan protocol, and fast processing. We decided to design our CNN rather than transfer some of the existing models to ensure low computational demands; the proposed CNN requires significantly less amount of computational operations and trainable parameters than most of the existing models.

## 2 Materials and Methods

The proposed CAD system was implemented in the MATLAB programming interface with the MatConvNet toolbox [8], using the NVIDIA Titan Xp graphical processor unit (GPU). The computational effort of the CAD system was 4 min per whole-spine CT data (24 vertebrae). On the standard PC without any GPU the computational effort was 19 min.

### 2.1 Used Dataset

The proposed CAD system was learned and evaluated on our dataset of 17 cases that contained 88 cervical, 204 thoracic, and 85 lumbar heavily pathologically-affected vertebrae. The dataset was obtained by a Philips iCT 256 CT scanner with ‘pixel spacing’ 0.651 mm, ‘slice thickness’ 0.670 mm, and ‘spacing between slices’ 0.335 mm.

Both types of lesions were manually annotated by two independent radiologists, where the first expert annotated 1,046 osteolytic lesions and 755 osteoblastic lesions. The second expert labelled 1,205 osteolytic and 878 osteoblastic lesions.

### 2.2 Data Pre-processing

The available dataset was firstly pre-processed in several steps:

1. removal of surrounding tissues in the neighbourhood of the individual vertebral body utilised by the spine segmentation algorithm (developed in the earlier phase of our project);
2. data re-sampling and Gaussian filtering in accordance of the physical resolution of the data (enables processing of CT data with different protocols);
3. slice-by-slice data centring by subtraction of the mean intensity value measured in the spinal cord (reducing influence of inter-patient variances, beam hardening, and different CT protocols); and,
4. extraction of three mutually orthogonal slices, where each classified voxel is situated in their centre (reducing computational complexity in comparison with full 3-D neighbourhood).

### 2.3 Convolutional Neural Network—Architecture and Learning

The proposed CNN was designed specifically for the purpose of segmentation by voxel-wise classification. CNN architecture is composed of 17 layers in the training phase, which is depicted in more detail in Fig. 1. The first part of CNN contains three convolutional layers; the first two convolutions extract low-level image features and the third convolution combines them to create more complicated high-level features. The final FC layer classifies an input feature vector to one of the interest classes.

The learning dataset contained 120,000 samples with a balanced representation of classes: 60% of randomly picked samples were used for training, 20% for validation, and 20% for the testing of the CNN.

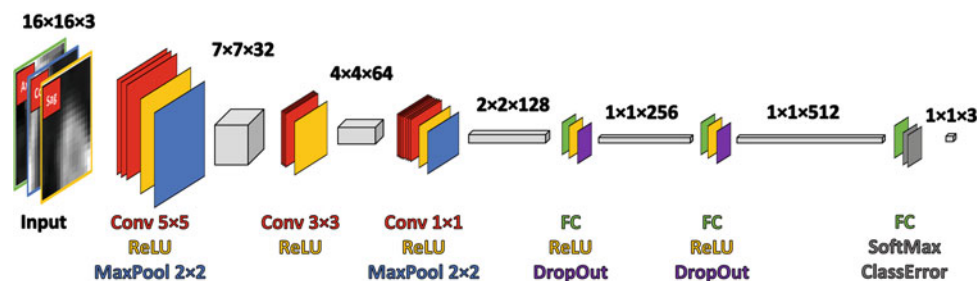


**Fig. 1** Scheme of the proposed CNN with actual data sizes. Input data contains a stack of three mutually orthogonal slices. Red boxes represent convolutional layers, yellow boxes ReLU activation layers,

blue boxes MaxPool layers, purple boxes DropOut layers, and grey boxes represent layers of objective functions. Grey blocks are output volumes

### 3 Results and Discussion

The final CAD system has been evaluated on the rest of the available database (~45 million of samples, which not overlaps with the learning dataset). Evaluation has been performed by two methodologies, most frequently used by other authors. The first, the ‘voxel-wise’ method, evaluates the correct classification of each voxel, which is more useful for technical comparison of CAD systems. The second, the ‘object-wise’ method, is more interpretable as a clinical validation, because it evaluates the correct detection and classification of whole lesions. In accordance to the same evaluation conditions as other published methods, detected lesions with one voxel intersection with golden standard have been taken as correct.

Results of the voxel-wise evaluation are presented in Table 1. Using the available method of authors Jan et al. [6], this evaluation has been done directly from our dataset. It is obvious that the proposed CAD system has the highest sensitivity for both types of lesions, even in comparison with the inter-rater agreement. A low inter-rater agreement is probably caused by voxel-wise annotation, where two experts are not able to label the exact same shape of lesions on the level of single voxels. On the other hand, experts have the highest specificity, which means that they have a great agreement in healthy tissue. The proposed CAD system achieved specificity greater than 0.8 for both types of lesions, which is positive based on the single voxel evaluation.

Table 2 summarises results achieved using object-wise methodology. The proposed CAD system correctly detected over 90% of all lesions with a volume greater than 1.42 mm<sup>3</sup>, which is the best sensitivity in comparison with other authors. The lower sensitivity of the inter-rater agreement could be caused by very small lesions missed by one of the experts. From the false positive (FP) counts point of view, it is evident that the proposed CAD also detected a large amount (~3.0 per lesion) of false candidates, especially small lesions. It is important to notice that our database includes small lesions (greater than 1.42 mm<sup>3</sup>) in

**Table 1** Achieved results of the proposed CAD system by voxel-wise evaluation in comparison to the inter-rater agreement and other recently published methods. Mean sensitivity (TPR), specificity (TNR), accuracy (ACC) and F1-score (F1) for osteolytic (osteoblastic) voxels are presented

Authors	TPR (–)	TNR (–)	ACC (–)	F1 (–)
Inter-rater	0.46 (0.53)	0.97 (0.95)	0.96 (0.94)	0.27 (0.45)
Jan et al. [6]	0.33 (0.41)	0.86 (0.94)	0.83 (0.90)	0.13 (0.22)
Proposed CAD	0.71 (0.75)	0.84 (0.83)	0.84 (0.84)	0.20 (0.27)

**Table 2** Achieved results of the proposed CAD system by the object-wise evaluation in comparison to the inter-rater agreement and other recently published methods. Mean sensitivity (TPR) and false positive detection (FP) for osteolytic (osteoblastic) lesions are presented

Authors	# Lesions	TPR (–)	FP (count per lesion)
Inter-rater	1046 (755)	0.63 (0.73)	0.02 (0.02)
Yao et al. [3]	16 (372)	0.94 (0.84)	5.90 (1.30)
Jan et al. [6]	1046 (755)	0.70 (0.80)	1.50 (1.50)
Roth et al. [4, 5]	–(532)	–(0.70)	–(0.30)
Proposed CAD	1046 (755)	0.94 (0.92)	3.30 (2.80)

comparison with other authors, whose databases contain only large lesions greater than 300 mm<sup>3</sup>. If we only validated the large lesions from our database, we achieved 0.99 sensitivity with ~0.95 FP, which is better than most published algorithms. Another important parameter is the slice thickness that was 0.670 mm in our database, whereas other authors used slice thickness up to 5 mm. In accordance to RECIST 1.1 guideline [9], only lesions with the longest diameter greater than twice the slice thickness are considered as measurable by CT. In this case we validated only large and medium lesions greater than 14.2 mm<sup>3</sup>, and we still achieved very high (0.98) sensitivity with FP (~1.5 per lesion) compared to other published methods. Authors [4, 5] achieved the lowest FP (0.3 per lesion) from all mentioned algorithms, but at the cost of a significantly lower sensitivity (0.70).

The proposed CNN contained ~850 k of parameters (par.) and it required ~5 M of operations (ops.) per one single forward pass. Both values are significantly lower than most of the existing CNN models (e.g. AlexNet—65 M par./2G ops., GoogleNet—8 M par./3G ops., VGG-19—155 M par./39G ops., ResNet-152—65 M par./23G ops., Inception-v4—35 M par./18G ops. [10]), which ensured a low computational complexity (4 min per patient) of the proposed method.

### 4 Conclusion

In this paper we presented a fully automatic CAD system for osteolytic and osteoblastic lesion detection, segmentation, and classification based on specific pre-processing and the CNN classifier. We tested the CAD system on our dataset of 17 cases, where we achieved a sensitivity above 0.90 with ~3.0 false positive detections per lesion for lesions greater than 1.42 mm<sup>3</sup>. The CAD system was compared

with results of other recently published methods with consideration of CT slice thickness according to RECIST 1.1 guidelines, where our CAD system achieved a distinctly higher sensitivity (0.98) with comparable ( $\sim 1.5$ ) false positive detections per lesion. Considering the relatively low sensitivity of the inter-rater agreement and fast computation (4 min), the proposed CAD system in combination with an appropriate expert validation seems to be a suitable tool that could significantly help the radiologists diagnose not only the initial state of bone metastases, but also follow up the response to applied treatment.

**Acknowledgements** The Titan Xp GPU used for this research was donated by the NVIDIA Corporation.

**Conflict of Interest** This research project is partly supported by Philips Healthcare Netherlands.

**Ethical Approval** All procedures performed in studies involving human participants were in accordance with the ethical standards of the institutional and/or national research committee and with the 1964 Helsinki declaration and its later amendments or comparable ethical standards (Institutional Review Board of the IRST Meldola, Prot. N. 343/V. 3, issued 10 January 2012).

## References

1. Gasbarrini, A., Cappuccio, M., Mirabile, L., Bandiera, S., Terzi, S., Barbanti Bròdano, G., Boriani, S.: Spinal metastases: treatment evaluation algorithm. *European Review for Medical and Pharmaceutical Sciences* 8(6), 265–274 (2004), <http://www.europeanreview.org/article/145>
2. Kakhki, V.R.D., Anvari, K., Sadeghi, R., Mahmoudian, A.S., Torabian-Kakhki, M.: Pattern and distribution of bone metastases in common malignant tumors. *Nuclear Medicine Review* 16(2), 66–69 (2013), <http://doi.org/10.5603/NMR.2013.0037>
3. Yao, J., Burns, J.E., Summers, R.M.: Computer aided detection of bone metastases in the thoracolumbar spine. In: Li, S., Yao, J. (eds.) *Spinal Imaging and Image Analysis. Lecture Notes in Computational Vision and Biomechanics*, vol 18, pp. 97–130. Springer, Cham (2015), [https://doi.org/10.1007/978-3-319-12508-4\\_4](https://doi.org/10.1007/978-3-319-12508-4_4)
4. Roth, H.R., Yao, J., Lu, L., Stieger, J., Burns, J.E., Summers, R. M.: Detection of sclerotic spine metastases via random aggregation of deep convolutional neural network classifications. In: Yao, J., Glocker, B., Klinder, T., Li, S. (eds.) *Recent Advances in Computational Methods and Clinical Applications for Spine Imaging*, pp. 3–12. Springer, Cham, 1 edn. (2015), <http://doi.org/10.1007/978-3-319-14148-0>
5. Roth, H.R., Lu, L., Liu, J., Yao, J., Seff, A., Cherry, K., Kim, L., Summers, R.M.: Improving computer-aided detection using convolutional neural networks and random view aggregation. *IEEE Transactions on Medical Imaging* 35(5), 1170–1181 (2016), <http://doi.org/10.1109/TMI.2015.2482920>
6. Jan, J., Novosadova, M., Demel, J., Ourednicek, P., Chmelik, J., Jakubicek, R.: Combined bone lesion analysis in 3d ct data of vertebrae. In: *Proceedings of the 37th Annual International Conference of the IEEE Engineering in Medicine and Biology Society*, pp. 6374–6377. IEEE, Milano (2015), <http://ieeexplore.ieee.org/document/7319851/>
7. Chmelik, J., Jakubicek, R., Jan, J.: Tumorous spinal lesions: Computer aided diagnosis and evaluation based on ct data—a review. *Current Medical Imaging Reviews* 13(4), 1–10 (2017), <https://doi.org/10.2174/1573405613666170331102245>, [Manuscript in press]
8. Vedaldi, A., Lenc, K.: Matconvnet—convolutional neural networks for matlab. In: *Proceeding of the 23rd ACM International Conference on Multimedia*, pp. 689–692. ACM, Brisbane (2015), <http://www.acmmm.org/2015/proceedings/>
9. Eisenhauer, E., Therasse, P., Bogaerts, J., Schwartz, L., Sargent, D., Ford, R., Dancey, J., Arbuck, S., Gwyther, S., Mooney, M., et al.: New response evaluation criteria in solid tumours: revised recist guideline (version 1.1). *European journal of cancer* 45(2), 228–247 (2009), <http://dx.doi.org/10.1016/j.ejca.2008.10.026>
10. Canziani, A., Paszke, A., Cullurciello, E.: An analysis of deep neural network models for practical applications. *arXiv preprint arXiv:1605.07678* (2016), <https://arxiv.org/abs/1605.07678>

# A Classification and Segmentation Combined Two-Stage CNN Model for Automatic Segmentation of Brainstem

Huabei Shi, Jia Liu, and Hongen Liao

## Abstract

Accurate segmentation of brainstem in MRI images is the basis for treatment of brainstem tumors. It can prevent brainstem from being damaged in neurosurgery. Brainstem segmentation is dominantly based on atlas registration or CNN using patches at present. Nevertheless, the prediction time and the false positive of brainstem segmentation is relatively high. We proposed a classification and segmentation combined two-stage CNN model of brainstem segmentation to improve the prediction accuracy and reduce computation time. Firstly, a classification-CNN model was used to classify MRI images to estimate whether transverse section images exist brainstem. In the view of classified images, a segmentation CNN model to segment brainstem is used to analysis the whole image rather than patches. In addition, considering segmentation based the whole image is a big problem of class unbalance, we settle this problem by changing loss function and giving the label coefficients to get more accurate results. This method provides higher segmentation precision and consume less time for the segmentation task of brainstem than current methods.

## Keywords

Deep learning • Image classification • Brainstem segmentation

## 1 Introduction

Human brainstem is a complex structure with several small nuclei and neural pathways. It not only serves as a conduit for motor and sensory information, but also the location of multiple primary nuclei that control or modulate a vast array of vital functions including homeostasis, consciousness, locomotion, reflexive and emotive behaviors [1]. Accurate segmentation of brainstem in MRI images not only can prevent brainstem from being damaged in neurosurgery, but also is the basis for treatment of brainstem tumors [2, 3]. Currently, brainstem segmentation is mainly based on atlas registration or CNN using patches, which need long prediction time and get high false positive.

A popular approach for brain image segmentation is not just the use of (population specific) atlases [4], but pattern recognition methods are also used [5], sometimes in combination with an atlas-based approach [6]. To obtain anatomically correct segmentations, these methods both require a standard atlas or database and segment images by computing some multidimensional vectors. The value of each pixel will not be considered in segmentation, because they segment images base on images rather than pixels.

The explicit definition of such spatial and intensity features could be avoided by using convolutional neural networks (CNNs) [7]. Moeskops et al. [8] presented a method for the automatic segmentation of anatomical MR brain images into a number of classes based on a multi-scale CNN. Each pixel in the image is classified to different brain tissues classes by using the net. Information about each pixel is provided in the form of image patches where the pixel of interest is in the center. But for larger images ( $512 \times 512$  pixels), it takes a long time for CNN to classify only one pixel at a time.

Nie et al. [9] proposed to utilize the fully convolutional networks (FCNs) to do a pixel-level segmentation for the brain image. Considering segmentation task-based whole image is a big challenge of class unbalance, they extract

Huabei Shi and Jia Liu contributed equally to this work.

H. Shi (✉) · J. Liu · H. Liao  
Department of Biomedical Engineering, School of Medicine,  
Tsinghua University, Beijing, 100084, China  
e-mail: shb16@mails.tsinghua.edu.cn

H. Liao  
e-mail: liao@tsinghua.edu.cn



patches as a size of  $64 \times 64$  for both original images and manually segmented image. The method based on patch is more efficient than based on pixel. However, the segmentation results may be false positive for patch with similar pixels, due to the absence of the whole image information.

In this paper, we propose a classification and segmentation combined two-stage CNN model (CSCNN-F) of brainstem segmentation to improve the prediction accuracy and reduce computation time. Firstly, a classification-CNN model (CCNN) was used to classify each MRI image to judge whether the transverse section images have brainstem. Based the classified images, we proposed a segmentation-CNN model (SCNN) to segment brainstem based on the whole image rather than patches.

## 2 Method

### 2.1 The Classification-CNN

The current methods, those segment brainstem, put a set of images into their net without considering whether image contains brainstem. Although processing can be accelerated by GPU, it is undisputed a waste of time and resources on segmenting images without brainstem. And if the algorithm is not robust enough, these transverse section images will have a high rate of false-positive result. In order to avoid those preceding problems, the first module of image processing in this paper is a classification-net, to obtain images that contains brainstem. Compared with classifying each pixel in the image, it's uncomplicated to classify image based on its abstract information.

The structure of CCNN is outlined in Fig. 1. This binary CNN only has two convolution and pooling layers. The first convolution layer with big kernel size  $11 \times 11$  and strides 5 is to refine the MR image rapidly. After the maxpooling with kernel size  $2 \times 2$ , the second convolution obtain overall information of image and transfer these information to the fully-connect layer. Using softmax activation function and binary-crossentropy loss function, the CCNN output two

probability values finally, presenting whether images contain brainstem.

For CNN, different convolution times will extract different scales' feature [10]. There are more image details in the shallow convolution layers, and deep convolution layers have more abundant overall information of image, as shown in Fig. 2. In order to classify MR images accurately, features should be refined by using least convolution and pooling layers. This is the reason why we adopt those big kernel size and strides. Assuming the convolution kernel as a size of  $3 \times 3$  and strides 1, like VGG, the net need four convolution layers to gain similar feature at least. The increase of layers will greatly multiply the number of parameters, and make the binary-CNN easy to overfitting. So CCNN is better than VGG on the small dataset. Results of different kernel size are compared in Fig. 2.

### 2.2 The Segmentation-CNN

Inspired by works [11], the SCNN was designed, as shown in Fig. 1. Considering that brainstem contains less 700 pixels in an image ( $1 \text{ mm} \times 1 \text{ mm}$ ,  $512 \times 512$  pixels), we propose a model with three convolution layer groups and three de-convolution groups. For small organs like brainstem, too many convolution and de-convolution layers can impair feature and the accuracy of segmentation result.

The input of SCNN is a whole MR image ( $512 \times 512$  pixels) rather than patches extracted from image, and details will be discussed in Sect. 2.3. The first layer consisted two convolutional layers with kernel size  $3 \times 3$  and a max-pooling layer with kernel size  $2 \times 2$  will produce feature maps of size  $256 \times 256 \times 32$ . These feature maps are put into the second layer which also contain two convolution layers and a maxpooling layer, leading to feature maps of size  $128 \times 128 \times 64$ . In the final convolution layer, 128 convolutional kernels with size  $3 \times 3$  is applied to the outputs of the second layer.

On the fourth layer, the output feature maps from the third layer group are up-sampled through a de-convolution layer with

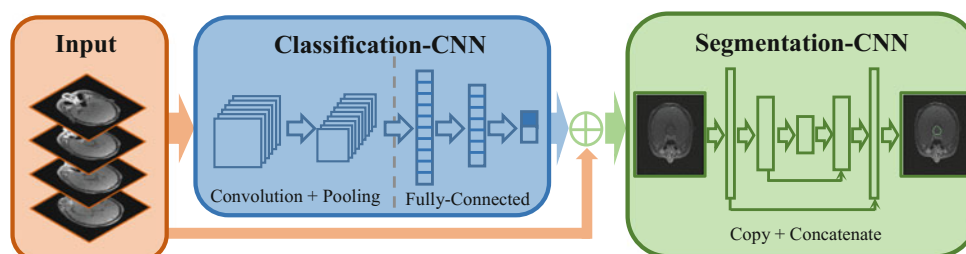


**Fig. 1** The process of classification and segmentation combined two-stage CNN model. Input MR images will be classified firstly, then the SCNN segments brainstem based classified images



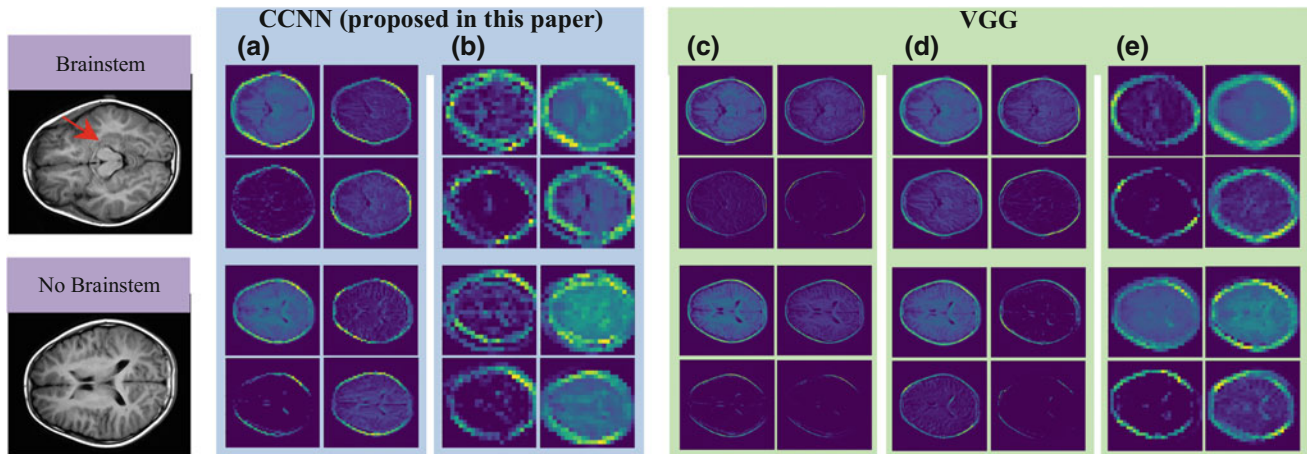


**Fig. 2** The results of different convolution layers. There is the image with brainstem in first row and the image without brainstem in second row. **a, b** columns are results of first convolution layer and second

convolution layer in our binary-CNN. **c–e** columns are results of first convolution layer, second convolution layer and fourth convolution layer in VGG

64 filters of size  $3 \times 3$ . Then concatenate these feature to the outputs of the second layer and put result to the fifth layer. In this way, SCNN can utilize both the details and the global information of images. Repeating this process, the net has a layer with one filter at last to reshape the feature maps. The loss function and activation function will be mentioned in Sect. 2.3.

### 2.3 The Segmentation-CNN Loss Function

Essentially, segmenting image is the classification of each pixel and there may be unbalance between the positive and negative samples. For the segmentation of brainstem, pixels which represent brainstem are positive samples while other pixels are negative samples. In a  $512 \times 512$  pixels ( $1 \text{ mm} \times 1 \text{ mm}$ ) image, the number of positive samples is about 500-700 pixels and the number of negative samples is greater than 200,000 pixels, this kind of unbalanced class is a big issue. At present, lots of methods keep class balance through extracting patches from image and reducing the proportion of negative samples. SCNN solved this problem by changing loss and giving the label weight coefficients to get more accurate results rather than extracting patches.

In this paper, we use ReLU, softmax activation function and Adam optimizer. In addition, we have optimized the mean square error loss function. Formulas are shown as follows:

$$\operatorname{argmin}_{\omega} \frac{1}{N \cdot M} \cdot \sum_{i=1}^N \sum_{j=1}^M \left( L'_{ij}(\omega, x) - \theta \cdot L_{ij}(\omega, x) \right)^2 \quad (1)$$

$$L'_{ij}(\omega, x) = \max(L_{ij}(\omega, x), 0) \quad (2)$$

where  $M, N$  is the number of pixels in length and width of the image.  $L_j(\omega, x)$  is the value for each pixel in label.  $L'_j(\omega, x)$  is the value for each pixel computed by the softmax activation function.  $x$  is the grayscale value for each pixel in image.  $\omega$  is network parameters.  $\theta$  is the weight of train-data label. The value of  $\theta$  depends on the proportion of the number of positive samples to negative samples.

## 3 Experiments and Results

### 3.1 Training Details

We trained classification and segmentation combined two-stage CNN model on a GeForce GTX 1080 GPU and download 210 cases of head MRI images from IDA database [12]. IDA provides systems and resources to help collect, manage and share data from clinical trials and clinical research studies. We selected 168 cases as the training and validation set randomly, and put the others into the test set. Besides experiment enhance the training dataset.

In training phase, the CCNN with epoch = 60 takes 1 h and the SCNN with epoch = 100 takes 8.5 h. In testing phase, the classify accuracy, segment accuracy and time were observed.

**Table 1** Accuracy of classification nets: AlexNet, VGG and CCNN

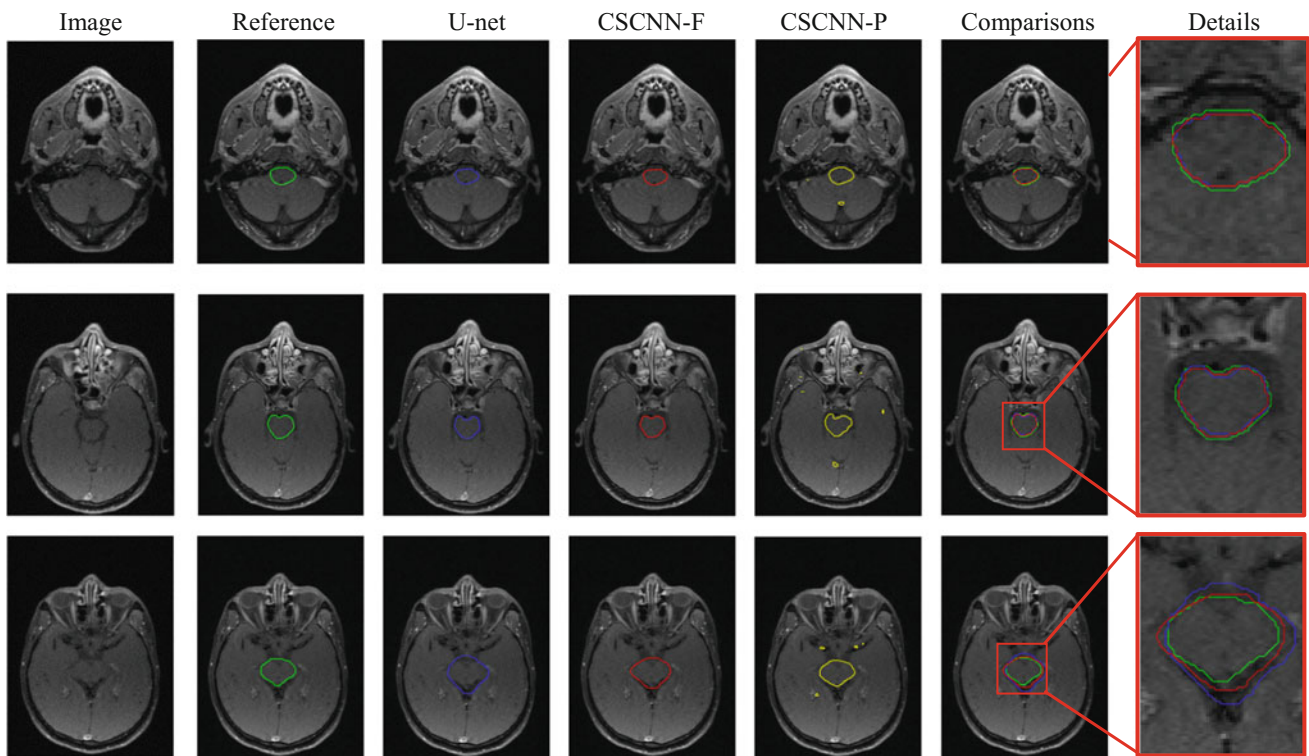
Parameters	Net		
	AlexNet [13]	VGG [14]	CCNN
Accuracy (%)	98.12	94.23	<b>98.45</b>
False positive (%)	0.51	0.44	<b>1.10</b>
False negative (%)	1.33	5.32	<b>0.44</b>

**Table 2** Accuracy of different segmentation nets

Parameters	Net				
	U-net [11]	CSCNN-F	SCNN-F	CSCNN-P	SCNN-P
Dice coefficient	0.9133	<b>0.9219</b>	0.9194	0.9117	0.9026
Jaccard index	0.8672	<b>0.8903</b>	0.8824	0.8364	0.8543
Conformity coefficient	0.8661	<b>0.8767</b>	0.8624	0.8721	0.8523
Average perpendicular distance	0.2869	<b>0.2192</b>	0.2276	0.2787	0.3093

**Table 3** Running time of different nets to segment 50 MR images

Parameters	Net				
	U-net [11]	CSCNN-F	SCNN-F	CSCNN-P	SCNN-P
Classify time (s)		<b>0.2530</b>		0.2646	
Segment time (s)	1.2551	<b>0.3062</b>	1.1835	0.5414	1.5187
Total time (s)	1.2551	<b>0.5592</b>	1.1835	0.8060	1.5187

**Fig. 3** Segmentation comparisons. (1) The first column shows MR image. (2) The second column shows label created by doctors. (3) The 3th-5th columns show segmentation results of U-net, CSCNN-F and CSCNN-P. (4) The last two column shows results of reference, U-net and CSCNN-F

### 3.2 Accuracy and Running Time

The false positive in the form indicate that CCNN classify the no-brainstem image as images contain brainstem. The false negative is opposite to the false positive.

The bold column in Table 1 is result of the method proposed in this paper. Result of CCNN simulation shows that the false negative is significantly smaller than the false

positive. It means the net may put images without brainstem into the SCNN rather than ignore images contain brainstem.

The bold column in Table 2 is result of the method proposed in this paper. Compared with CSCNN-F, the differences of third to fifth columns are whether there is a CCNN and segment MR images based on the full image or patches. The last letter of nets' name (-F, -P) in Tables 2 and 3 means how nets process MR images, based on full

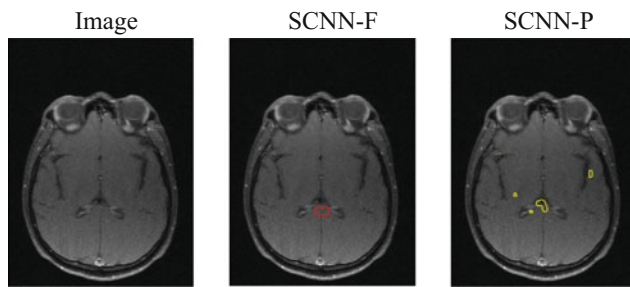


**Fig. 4** Results of the segmentation model without CCNN

images or patches extracted from images. Actually, many current nets [10] are like SCNN-P based patches, but in this paper we segment brainstem based full images (CSCNN-F).

Table 3 shows classifying images cost less time than segmenting images. The CCNN can save time in whole model.

According to Fig. 3, we can find that method proposed in this paper is superior to U-net in details and have higher accuracy. And CSCNN-P segment MR images based on patches [10], there will be a great false positives because of no global information. And as shown in Fig. 4, the SCNN may get wrong result on images without brainstem. We will avoid this mistake by adding CCNN.

## 4 Conclusion

The consequence demonstrated that our method can get better segmentation accuracy and less running time for the segmentation task of brainstem than many current methods. Method proposed in this paper not only improve the accuracy of the image with brainstem, but also can avoid misjudgment in the image without brainstem. The application of segmentation can assist preoperative planning and surgical navigation perfectly. And we will do more works about segmenting brainstem with tumors in the future.

**Acknowledgements** The authors acknowledge supports from Beijing Municipal Science & Technology Commission (Z151100003915079), Beijing National Science Foundation (7172122, L172003), National Natural Science Foundation of China (81427803, 81771940), and National Key Research and Development Program of China (2017YFC0108000).

## References

1. P. Fazio, M. Schain, K. Varnäs, C. Halldin, L. Farde and A. Varrone, Mapping the distribution of serotonin transporter in the human brainstem with high-resolution pet: validation using postmortem autoradiography data. *NeuroImage*, vol. 49, no. 1, pp. 133–313(2016).
2. H. Liao: Integrated diagnostic and therapeutic techniques: Toward an intelligent medical system, *Computerized Medical Imaging and Graphics*, Vol. 38, No.5, pp. 421–422 (2014).
3. H. Liao, T. Inomata, I. Sakuma and T. Dohi: 3-D Augmented Reality for MRI-guided Surgery using Integral Videography Autostereoscopic Image Overlay, *IEEE Transactions on Biomedical Engineering*, Vol.57, No.6, pp. 1476–1486(2010).
4. F. Chen, D. Wu, H. Liao: Registration of CT and Ultrasound Images of the Spine with Neural Network and Orientation Code Mutual Information, *Lecture Notes in Computer Science 9805*, pp. 292–301 (2016).
5. L. Wang, Y. Gao, F. Shi, G. Li, J. H. Gilmore, W. Lin and D. Shen, Learning-based multi-source integration framework for segmentation of infant brain images. *NeuroImage*, vol. 108, pp. 160–172(2015).
6. P. Anbeek, I. Isgum, B. J. van Kooij, C. P. Mol, K. J. Kersbergen, F. Groenendaal, M. A. Viergever, L. S. de Vries and M. J. Benders, Automatic segmentation of eight tissue classes in neonatal brain MRI. *PLOS ONE*, vol. 8, no. 12, p. e81895(2013).
7. F. Chen, J. Liu, Z. Zhao and H. Liao. 3D Feature-Enhanced Network for Automatic Femur Segmentation. *IEEE Journal of Biomedical and Health Informatics*, pp (99):1–1(2017).
8. P. Moeskops, M. Viergever and M. Mendrik, Automatic Segmentation of MR Brain Images With a Convolutional Neural Network. *IEEE Transactions on Medical Imaging*, 35(5):1252–126(2016).
9. D. Nie, L. Wang, Y. Gao and D. Shen, Fully convolutional networks for multi-modality isointense infant brain image segmentation. *IEEE, International Symposium on Biomedical Imaging*. 1342(2016).
10. F. Ciompi, B. de Hoop, S. J. van Riel, K. Chung, E. T. Scholten, M. Oudkerk, P. A. de Jong, M. Prokop and B. van Ginneken, Automatic classification of pulmonary peri-fissural nodules in computed tomography using an ensemble of 2D views and a convolutional neural network out-of-the-box. *Med Image Anal*, vol. 26, no. 1, pp. 195–202(2015).
11. Ronneberger O, Fischer P, Brox T. U-Net: Convolutional Networks for Biomedical Image Segmentation. *Medical Image Computing and Computer-Assisted Intervention — MICCAI 2015*. Springer International Publishing, 2015:234–241..
12. Image & Data Archive (IDA). Available online: <https://ida.loni.usc.edu/login.jsp?project=ABVIB>.
13. Krizhevsky A, Sutskever I, Hinton G E. ImageNet classification with deep convolutional neural networks. *International Conference on Neural Information Processing Systems*. Curran Associates Inc. 2012:1097–1105.
14. Simonyan K, Zisserman A. Very Deep Convolutional Networks for Large-Scale Image Recognition. *Computer Science*, 2014.

# Biometrics Based on Facial Landmark with Application in Person Identification

Aniwat Juhong, Boonchana Purahong, Supakorn Suwan, and Chuchart Pitavirooj

## Abstract

This paper presents a novel technique for face recognition based on facial landmarks extracted automatically. Our landmarks are those associated with eyes mouth and nose. To extract facial landmarks, we first use Haar cascade algorithm to detect the face ROI following by Haar cascade algorithm for the eye, mouth and nose ROI determination. To find landmark associated with the eye, we convert eye ROI image to binary image using thresholding algorithm. To exclude the eyebrow region, we apply horizontal radon transform. The project data will then be used to separate the eyebrow region from the eye region. To detect eye-related landmark, vertical radon transform is applied. With the vertical projection data, the outermost pixel can be identified and the associated eye landmark can be determined. The similar technique can then be used to identify landmarks associated with the nose and mouth area. Given the correspond landmarks on the reference face and the query face, geometric transformation can be determined using normal equation bases on minimized mean squared error. The two faces are then aligned. To provide the quantitative measurement, the two aligned face are converted to edge image using canny edge algorithm. The distance map error between the two aligned edge facial images is then used to identify the query face. The purposed algorithm for person identification was tested on the face database resulting in a very high accuracy.

## Keywords

Facial landmarks • Haar cascade • Face recognition

## 1 Introduction

Humans have used biometric characteristics for century to either confirm or determine the identity of an individual. Biometric characteristics are mostly popular used in security systems over the traditional secure measures, internet access computer system security, secure electronic, passport control, banking, mobile phone, credit card, secured access to building, health and social services, parenthood determination, terrorist determination and corpse identification. Many biometric features of human are typical invariant, easy to acquire and unique for each individual. These features includes DNA [1], ear [2], face [3], fingerprint [4], gait [5], hand and finger geometry [6], Iris [7], keystroke [8], odor [9], palmprint [10], voice [11], etc. Among all, face recognition is the most widely-used for person identification. Face recognition is technology measures and matches the unique characteristics for the purpose of personal identification to apply in many applications such as face recognition system at airport, patient identification, access control and so forth. Sometimes in traditional methods, face recognition misses matching because there are invariance factor resulted from human pose, hair-style, acne arising, fatter etc. Hence face recognition based on facial geometric landmarks was developed and seems promising to solve these problems. Recently, there are many attempts to develop face recognition based on geometry. Panagiotis B. Perakis et al. [1] developed novel method for 3D landmark detection. 3D facial Landmarks Model (FLM) was proposed. Although it was claimed to have high accuracy result but the 3D technique require high specification, spending long time to process, and it has a high cost.

This paper developed 2D technique to identify person using facial biometric. The technique extracts landmark associated with facial anatomical landmark including nose,

A. Juhong (✉) · B. Purahong · S. Suwan · C. Pitavirooj  
King Mongkut's Institute of Technology Ladkrabang, Bangkok,  
Thailand  
e-mail: Aniwat\_BMEKMITL@hotmail.com

B. Purahong  
e-mail: yuna001@gmail.com

S. Suwan  
e-mail: supakorn1582@gmail.com

C. Pitavirooj  
e-mail: chuchartpitavirooj@gmail.com



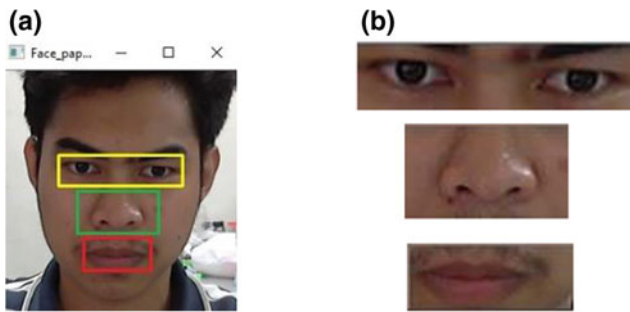


**Fig. 1** Defined ROI of facial components by Haar cascade algorithm eye and mouth. The extracted landmark can be used to estimate geometric transformation. The 2D query face image are aligned the reference image. Distance map error between the edged images of the two aligned image in region of interest are used for person identification.

## 2 Facial Biometrics Based on Facial Landmarks Extraction

Our facial biometric is based on facial landmarks which are the important fiducial points on the face including those associated with eyes, mouth and nose. To extract landmarks, we first applied Haar cascade algorithm to extract the region of interest of 2D face image as shown in Fig. 1. To find landmark associated with the eye, we can convert eye ROI

image to binary image using thresholding algorithm. The result is illustrated in Fig. 2b. The thresholding ROI is further used to identify landmark associated with eye using radon transform. To exclude the eye-bow region, we first applied horizontal radon transform. The results of radon transform shown in Fig. 2c. The horizontal radon transform data is used to distinguish between eye region and eyebrow region. To detect eye related landmark, vertical radon transform is applied. With the vertical radon, outermost pixel can be identified and the associated eye landmark can determine as shown in yellow dot in Fig. 3a.

To extract the nose related landmark, we convert the nose ROI to binary image and apply vertical radon transform. The outermost pixel can be identified and the associated nose landmark, as shown in Fig. 4. Figure 5 shows the similar algorithm that is applied to detect mouth-related landmark.

The extracted fiducial facial landmark points for sample image are shown in Fig. 6.

## 3 Affine Transformation and Image Registration

Image registration is used for person identification. To align query face image against the reference image in the database, the fiducial points are extracted. The fiducial points on the query palm and the reference face are then used to estimate

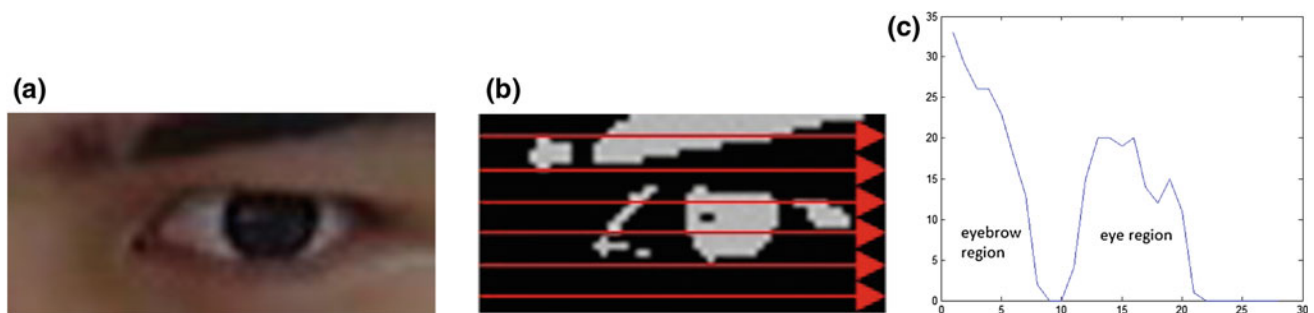


**Fig. 2** Horizontal radon transform technique to exclude eye-bow region

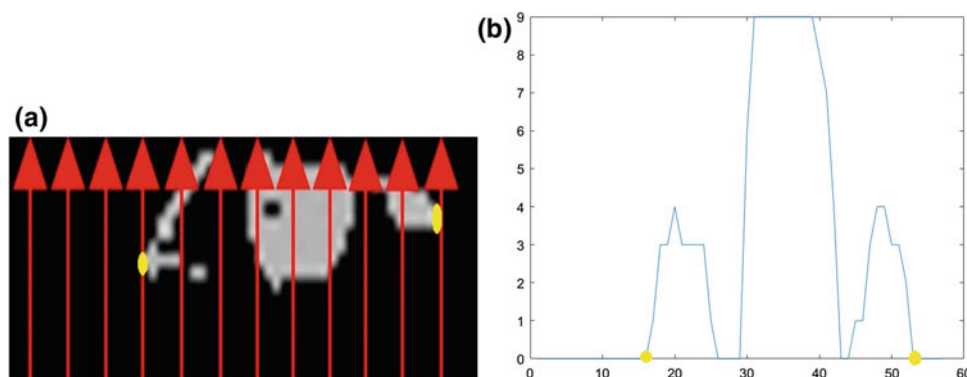


**Fig. 3** Vertical radon transform to extract fiducial point as associated with eye



**Fig. 4** Vertical radon transform of nose ROI



**Fig. 5** Vertical radon transform of mouth ROI

**Fig. 6** Fiducial facial landmark points [12]



the affine transformation matrix based on the corresponding key points by equation

$$Z = (X^T X)^{-1} (X^T Y) \quad (1)$$

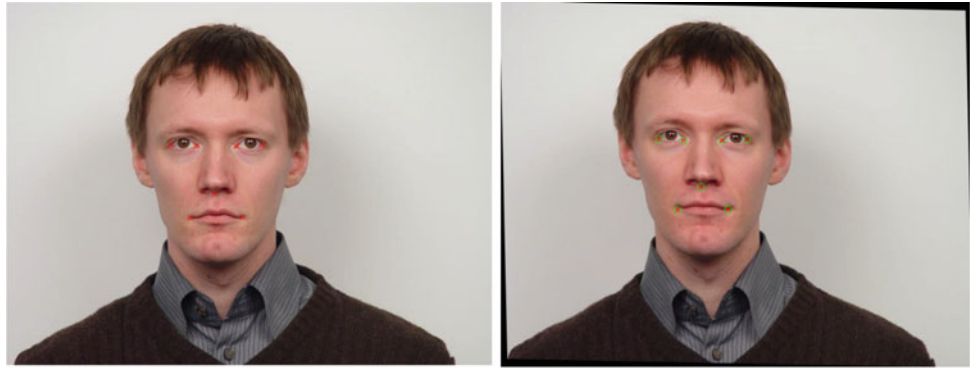
where  $Z$  is the affine transformation matrix.  $X$  and  $Y$  are the corresponding key points of reference and inquiry facial image respectively. The registration of the inquiry against the reference landmark point are shown in Fig. 7.

## 4 Person Identification

To identify person based on extracted fiducial point the face image that used to align the reference image against the query image, the face region of interest is determined using facial border point. Facial border point, P1, P2, P3, P4, P5 and P6, are shown in Fig. 8. The definitions of facial border points are as follows:



**Fig. 7** Face registration (circle dot: landmark of reference image, cross dot): landmark of query image



(a) Face registration of corresponding person



(b) Face registration of different person

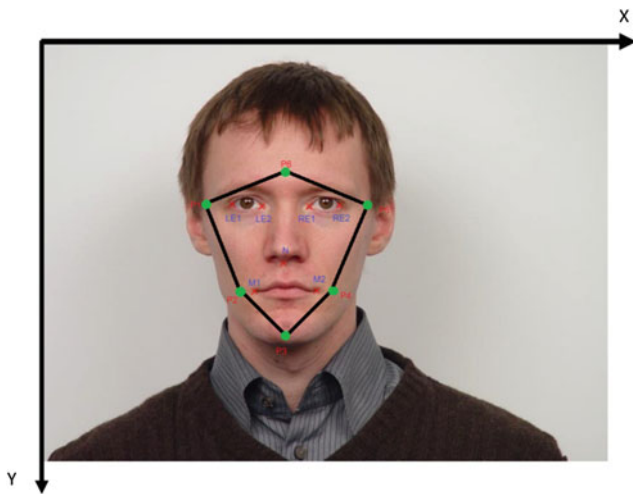


**Fig. 8** Facial border points which are defined by facial land marks

P1 is defined by coordinate

$$\left( X1 - \frac{X5 - X1}{2}, Y1 \right) \quad (2)$$

P2 is defined by coordinate

$$\left( X6 - \frac{X5 - X6}{2}, Y6 \right)$$

P3 is defined by coordinate

$$\left( \frac{X5 + X6}{2}, \frac{Y6 + Y7}{2} + 1.3 \times \left( \frac{Y6 + Y7}{2} - Y5 \right) \right)$$

P4 is defined by coordinate

$$\left( X7 + \frac{X7 - X5}{2}, Y7 \right)$$

P5 is defined by coordinate

$$\left( X4 + \left( \frac{X4 - X5}{2} \right), Y4 \right)$$

P6 is defined by coordinate

$$\left( \frac{X2 + X3}{2}, \frac{Y2 + Y3}{2.5} \right)$$

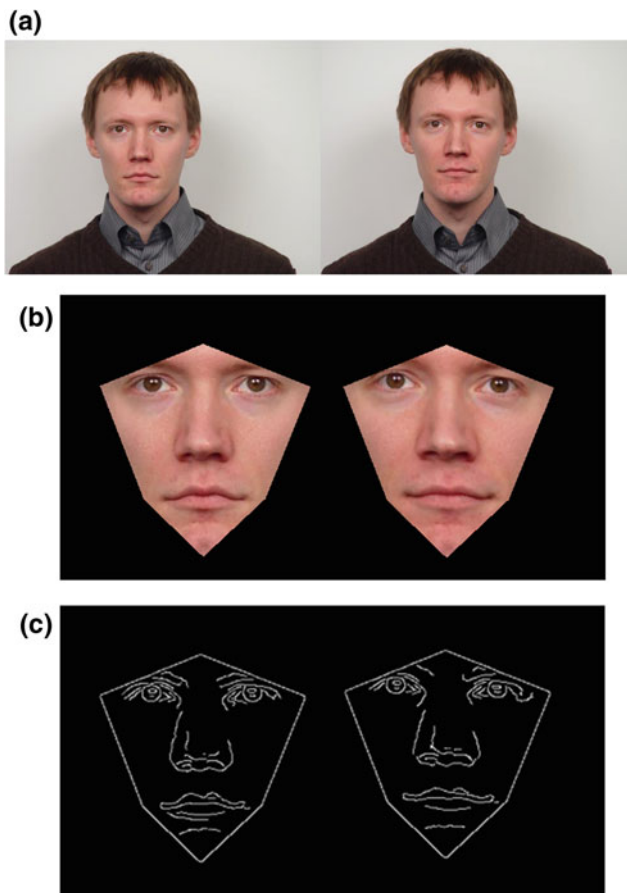


**Fig. 9** **a** Face region of interface pair of reference and inquiry image, **b** Registered image that was cropped by facial border, **c** Candy edge image

where

$X_1, Y_1$  is the coordinate of left eye outer landmark point (LE1),  
 $X_2, Y_2$  is the coordinate of left eye inner landmark point (LE2),  
 $X_3, Y_3$  is the coordinate of right eye outer landmark point (RE1),  
 $X_4, Y_4$  is the coordinate of right eye inner landmark point (RE2),

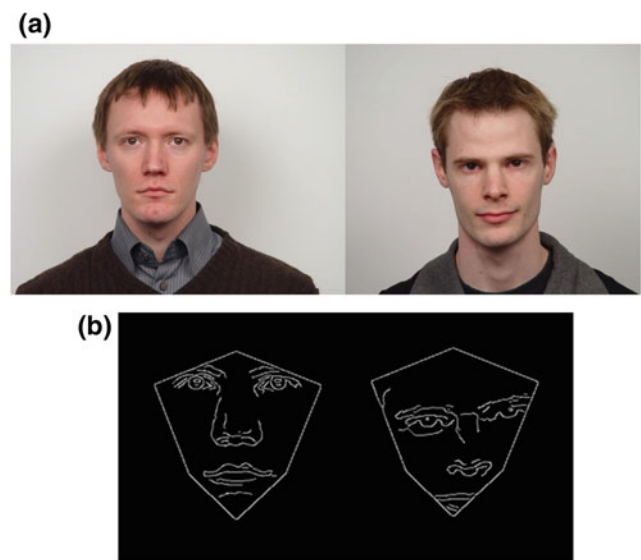


**Fig. 10** Instance of inter-subject experiment, **a** Face region of interface pair of reference and inquiry image, **b** Candy edge image

$X_5, Y_4$  is the coordinate of nose landmark point (N),  
 $X_6, Y_6$  is the coordinate of mouth right landmark point (M1),  
 $X_7, Y_7$  is the coordinate of mouth left landmark point (M2).

Canny edge detection is further applied on the face region of interest as shown in Fig. 9. Distance map error [13] is then applied on the edge image between the query face image and reference face image and used for person identification.

## 5 Experimental and Result

We test our algorithm using the face images from The IMM frontal face database [12]. The 12 different frontal human faces were test in this paper. Figure 10 shows the sample of inter-subject experiment between reference1 face image and inquiry 1 face image. The Table 1 shows distance map error result. The diagonal elements of Table 1 yield the minimum average error as it is the corresponding person testing.

**Table 1** Distance map error between reference image and inquiry image (unit in pixel)

	Inquiry 1	Inquiry 2	Inquiry 3	Inquiry 4	Inquiry 5	Inquiry 6	Inquiry 7	Inquiry 8	Inquiry 9	Inquiry 10	Inquiry 11	Inquiry 12
Reference 1	1.1031	7.6327	2.3476	6.2590	3.4981	8.7250	8.1061	3.7435	5.9527	8.8830	2.7224	7.7370
Reference 2	4.0402	1.0091	3.3838	5.0467	2.0334	3.3107	2.4510	3.9172	1.7237	5.7649	4.1483	3.6673
Reference 3	2.1925	7.0573	1.0553	6.4426	3.8738	8.2823	7.7334	2.7209	5.6591	8.5805	3.7714	7.1571
Reference 4	3.2228	4.1096	3.2261	2.3742	3.8855	8.1194	5.4883	3.9181	3.5970	8.1102	2.6196	2.6357
Reference 5	3.7662	6.1084	3.7464	8.1942	2.0491	9.0517	8.0889	5.6782	2.3737	8.9252	3.3574	5.5044
Reference 6	2.4588	2.3671	2.4785	6.2899	1.8382	1.3731	3.0810	2.7948	2.1106	6.3690	3.2143	2.8065
Reference 7	2.9677	2.6116	2.7620	3.4465	2.6706	2.1221	1.1443	2.0279	2.4312	4.0674	2.6031	1.6466
Reference 8	2.8397	7.6907	3.1888	9.0009	4.3047	9.0385	8.7261	0.6006	6.1368	9.5963	3.7668	7.5503
Reference 9	4.7200	2.9431	3.8637	3.4694	3.0486	3.3911	3.3978	4.2568	2.1146	3.3877	4.2969	3.9930
Reference 10	4.5125	3.5567	4.2424	4.2360	3.4551	3.6777	3.7396	2.9159	3.2017	2.2249	3.2755	2.5453
Reference 11	4.0944	6.5979	5.3017	8.6095	4.5158	7.6166	8.2496	5.8887	3.0959	7.2863	1.7845	6.1930
Reference 12	3.0793	3.2370	2.8673	4.8710	3.3231	5.3110	2.5974	2.2147	2.9096	7.2691	2.6357	1.9395

## 6 Conclusion

This paper presents a novel technique for face recognition that related with facial landmark extraction, canny edge detection and distance map error. The projection technique is applied to extract facial landmarks after that these landmarks are used to defined facial border for obtaining face region only. The Canny edge is then applied to get edge image from face region image. Eventually, distance map error is performed with edge image. The result of person identification is successful and very promising.

---

## References

1. D. Bozinov and P. -M. Seidel, "Iterative gridding for automated microarray image analysis," *Signals, Systems and Computers*, 2004. Conference Record of the Thirty-Eighth Asilomar Conference on, vol. 2, pp. 1635–1638, 7–10 Nov. 2004.
2. K. H. Pun and Y. S. Moon, "Recent advances in ear biometrics," *Automatic Face and Gesture Recognition*, 2004. Proceedings. Sixth IEEE International Conference on, pp. 164–169, 17–19 May 2004.
3. P. J. Phillips, Hyeonjoon Moon, et al., "The FERET evaluation methodology for face-recognition algorithms," *Pattern Analysis and Machine Intelligence*, IEEE Transactions on, vol. 22, no. 10, pp. 10901104, Oct 2000.
4. S. Pankanti, S. Prabhakar and A. K. Jain, "On the individuality of fingerprints," *Pattern Analysis and Machine Intelligence*, IEEE Transactions on, vol. 24, no. 8, pp. 1010–1025, Aug 2002.
5. D. K. Wagg and M. S. Nixon, "On automated model-based extraction and analysis of gait," *Automatic Face and Gesture Recognition*, Proceedings. Sixth IEEE International Conference on, pp. 11–16, May 2004.
6. R. Sanchez-Reillo, C. Sanchez-Avila and A. Gonzalez-Marcos, "Biometric identification through hand geometry measurements," *Pattern Analysis and Machine Intelligence*, IEEE Transactions on, vol. 22, no. 10, pp. 1168–1171, Oct 2000.
7. Lye Wil Liam, A. Chekima, Liau Chung Fan and J. A. Dargham, "Iris recognition using self-organizing neural network," *Research and Development*, 2002. SCOREd 2002. Student Conference on, pp. 169172, 2002.
8. Enzhe Yu and Sungzoon Cho, "GA-SVM wrapper approach for feature subset selection in keystroke dynamics identity verification," *Neural Networks*, 2003. Proceedings of the International Joint Conference on, vol. 3, pp. 2253–2257, 20–24 July 2003.
9. T. Nakamoto and T. Moriizumi, "Odor sensor using quartz-resonator array and neural-network pattern recognition," *Ultrasonics Symposium*, 1988. Proceedings., IEEE 1988, vol. 1, pp. 613–616, 2–5 Oct 1988.
10. Lei Zhang and D. Zhang, "Characterization of palmprints by wavelet signatures via directional context modeling," *Systems, Man, and Cybernetics, Part B: IEEE Transactions on*, vol. 34, no. 3, pp. 13351347, June 2004.
11. P. J. Besl, "Geometric modeling and computer vision," *Proceedings of the IEEE*, vol. 76, no. 8, pp. 936–958, Aug 1988.
12. [http://www2.imm.dtu.dk/pubdb/views/publication\\_details.php?id=394](http://www2.imm.dtu.dk/pubdb/views/publication_details.php?id=394).

# A Computational Tool for Enhancing Ischemic Stroke in Computed Tomography Examinations

Allan Felipe Fattori Alves, Ana Luiza Menegatti Pavan, Rachid Jennane, Carlos Clayton Macedo de Freitas, Nitamar Abdala, João Maurício Carrasco Altemani, and Diana Pina

## Abstract

Stroke is a cardio-vascular disease that currently ranks in the fifth position among all causes of death worldwide. Computed tomography is the first radiologic examination performed in emergency decisions to diagnose stroke. The earliest signs of ischemic stroke are quite subtle in CT, thus image-processing tools can be used to enhance ischemic areas and to aid physicians during diagnosis. This study aimed to enhance the ischemic stroke visual perception in computed tomography examinations. A cohort of 45 exams were used during this study, with 28 patients previously diagnosed with ischemic stroke and 17 control patients. Stroke cases were obtained within 4.5 h of symptom onset and with mean NIHSS of  $13.6 \pm 5.5$ . The complete series of non-enhanced images were obtained in DICOM format and all processing was performed in Matlab software R2017a. The main steps of the computed algorithm were as follows: an image averaging was performed to reduce the noise and redundant information within each slice; then a variational decomposition model was applied to keep the relevant component for our analysis; then three different segmentation methods were used to enhance the ischemic stroke area. The segmentation methods used were expectation maximization method, K-means and mean-shift.

We determined a test to evaluate the performance of six observers (physicians) in a clinical environment with and without the aid of enhanced images. According to the opinion of the observers who participated in this study the enhanced images were particularly useful when displayed together with the original images. The overall sensitivity of the observer's analysis changed after the evaluation of the enhanced images with the expectation maximization method. The overall specificity also increased. The improvement was even more remarkable for the three least experienced physicians.

## Keywords

Stroke • Image processing • Computational algorithm  
Enhanced images

## 1 Introduction

Stroke is one of the biggest causes of deaths being responsible for 6.5 million cases worldwide only in 2013 [1]. The evaluation and initial treatment of patients is difficult and require a high efficiency to avoid cerebral damage [2, 3]. Multiple medical imaging modalities are capable to diagnose early signs of stroke such as Magnetic Resonance Image (MRI) and Computed Tomography (CT). Standard MRI sequences are relatively insensitive to the changes of acute ischemia [4], but diffusion-weighted imaging appears as a sensitive and specific sequence to determine acute infarct location [5]. Some MRI disadvantages limits its assessment on a large number of patients, such as the higher cost, its long acquisition time and the increased vulnerability to motion artifacts [2]. Compared to MRI, CT is more accessible, less expensive and faster.

Computed Tomography scans are usually the first radiologic examination performed in emergency decisions concerning stroke. CT is sufficient to identify contraindications to fibrinolysis treatment, allowing patients with ischemic

A. F. F. Alves (✉) · A. L. M. Pavan  
Physics and Biophysics, São Paulo State University, Botucatu,  
Brazil  
e-mail: allan@ibb.unesp.br

R. Jennane  
Laboratory I3MTO, University of Orleans, Orléans, France

C. C. M. de Freitas · D. Pina (✉)  
Tropical Diseases and Diagnostic Imaging, São Paulo State  
University, Botucatu, Brazil  
e-mail: drpina@fmb.unesp.br

N. Abdala  
Diagnostic Imaging, UNIFESP, São Paulo, Brazil

J. M. C. Altemani  
Radiology, UNICAMP, Campinas, Brazil

stroke to receive intravenous therapy [6]. The earliest signs of ischemic stroke are quite subtle on CT. Usually, after 1 to 4.5 h of symptoms onset, a slight hypodense area of infarction in either the cortices or the basal ganglia can become visible.

In this paper, a novel approach to enhance the visual perception of ischemic stroke in CT is proposed. This enhancement aims to enable less experienced viewers, to reliably detect early signs of stroke in clinical routine. Our new contribution consists in combining efficiently different image processing techniques to enhance the visual insight of ischemic stroke in CT images. We tested three different segmentation methods to determine which performs better to enhance ischemic stroke in computed tomography examinations.

## 2 Methods

### 2.1 Patients and Image Selection

The study was approved by the local institutional ethics committee. We collected retrospective CT scans of patients with mean age of  $68.89 \pm 10.41$  years for stroke and  $66.76 \pm 9.36$  for control. Certified stroke cases were confirmed with the clinical reports including histological, pathological and clinical results. Stroke cases were obtained within 4.5 h of symptom onset and with mean NIHSS of  $13.6 \pm 5.5$ . After this selection, a set of 45 CT examinations were used, from those 28 cases were from patients with acute ischemic stroke, and 17 cases were from normal patients. CT scans were obtained from the database of the Botucatu Medical Hospital, Brazil, where they were acquired on a multislice CT scanners with 120 kVp, 1 s of exposure time, and 0.5 mm thickness.

### 2.2 Developed Approach

We developed a computational algorithm in Matlab software R 2017a. to enhance the diagnosis of ischemic stroke in CT scans. Firstly, to reduce noise and redundancies, a projection of the slices from a specific brain region is performed. This brain region is the same evaluated in the ASPECTS method [7], being at the level of the thalamus and basal ganglion and adjacent to the most superior margin of the ganglionic structures. This step is followed by a band-pass filtering to remove undesired structures from the slice. Then, to enhance the contrast of the projection obtained, a variational model (VM) decomposition is used [8]. Finally, three different segmentation methods are applied to the relevant component

from VM decomposition to segment and emphasize the ischemic stroke region.

To improve the contrast of the projection, a Variational Model (VM) [8, 9] decomposition was applied to decompose the image into different components. The image  $P$  was modeled as the sum of three terms:  $P = u + v + w$ . In this sense,  $v$  is the smooth second order part,  $u$  is related to contours and  $w$  is linked to fine textures. Our primary interest is in the  $v$  component since it is related to contrast and brightness of the image.

## 2.3 Segmentation Methods

### Expectation Maximization Method

Expectation Maximization (EM) is a segmentation method that assigns the pixel intensities of the image into different clusters using a probabilistic distribution such as a mixture of Gaussian distributions [10, 11]. The mixture model is composed of a sum of  $K$  Gaussian distributions, each distribution with its own parameters  $\theta_k = \{\mu_k, \alpha_k\}$  ( $\mu_k$  is the mean and  $\alpha_k$  is the standard deviation). The algorithm is iterative and starts from some initial estimate and then proceeds to an iteratively update until convergence is detected. Each iteration consists of an Expectation (E-step) and an Maximization (M-step) step [12]. In the E step, the membership weights ( $w_{ik}$ ) for all data points,  $x_i$  ( $1 \leq i \leq N$ ) and mixture components,  $k$  ( $1 \leq k \leq K$ ) are computed:

$$w_{ik} = (z_{ik} = 1 | x_i, \theta) = \frac{p_k(x_i | z_k, \theta_k) \cdot \alpha_k}{\sum_{m=1}^K p_m(x_i | z_m, \theta_m) \cdot \alpha_m} \quad (1)$$

where  $p_k(x | z_k, \theta_k)$  are the density mixture components,  $z = (z_1, \dots, z_k)$  is a vector of  $K$  binary variables that are mutually exclusive. The membership weights are defined such that  $\sum_{k=1}^K w_{ik} = 1$ . Next, in the M-step the membership weights are used to calculate the new parameters values of  $\theta_k$ . Let  $N_k = \sum_{i=1}^N w_{ik}$ , and consider:

$$\alpha_k^{new} = \frac{N_k}{N}, \quad 1 \leq k \leq K \quad (2)$$

$$\mu_k^{new} = \frac{1}{N_k} \sum_{i=1}^N w_{ik} \cdot x_i, \quad 1 \leq k \leq K \quad (3)$$

After computing all new parameters, the M-step is completed and then the algorithm returns to compute new membership weights in the E-step. This EM cycle is repeated until new parameters no longer change by a significant amount. Each pair of E and M steps are considered one iteration. Thus, in the final assignment, each pixel of the final image will belong to only one cluster.



## K-means

K-Means is a clustering segmentation method similar to EM. The goal is to choose cluster centers that minimize the total squared distance between each point and its closest center. Each data value is assigned to the nearest partition based upon a similarity parameter, in this approach the Euclidean distance of intensity [13]. At every step of the algorithm, partitions are then recalculated based on these hard assignments. The values of the partitions can alter at each successive step. K-Means algorithms are typically faster when compared to other clustering algorithms [14].

## Mean Shift

The mean shift segmentation method is an extension of the discontinuity-preserving smoothing algorithm [15]. Each pixel is associated with a joint domain located in its neighborhood. The algorithm delineates the cluster by grouping pixels that are closer than  $h_s$ , which is the spacial domain bandwidth and  $h_r$ , the range domain bandwidth. Each pixel element will be assigned to a partition. The mean shift generates partitions characterized by a nonparametric model. We used the approach described by Comaniciu et al. [15] with a different selection of spatial and range domains. The best results were achieved with  $(h_s, h_r) = (16, 4)$ .

## 2.4 Observers Evaluation

A test was established to evaluate the performance observers in a clinical environment based on a scoring system [16]. Four resident radiologists from first, second and third year of residence and two experienced radiologists worked as observers. For each case, each observer was required to give a score relating to the presence of acute stroke (definitely absent: 1, absent: 2, uncertain: 3, present: 4 and definitely present: 5). We also measured both sensitivity and specificity of the performance of the observers before and after the enhanced images for the three different segmentation methods.

## 3 Results

In this study, the results show the sensitivity and specificity obtained for each observer both before and after evaluating the enhanced images. We tested the observer's ability to detect ischemic stroke both with and without the aid of enhanced images. Overall results with the three different image segmentation methods are displayed in Table 1.

Representative examples of images both before and after the application of the algorithm are presented in Fig. 1. Enhanced images were obtained after the band-pass filtering, followed by the VM decomposition and the segmentation with EM method.

## 4 Discussion and Conclusion

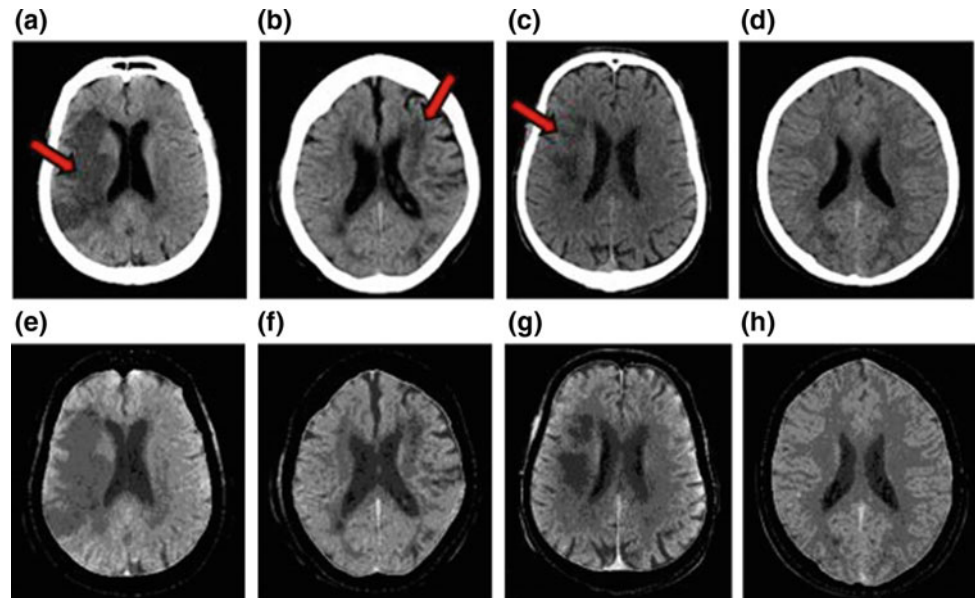
In this paper, we proposed a novel approach to enhance the visual perception of ischemic stroke in CT scans. We combined different image processing techniques to achieve our main goal, which is to enable less experienced radiologists to improve their sensitivity and specificity scores. The Variational Model decomposition helped to enhance the contrast and the brightness of the images.

With the observer's evaluation, we examined the impact of enhanced images on the score of diagnosis. We tested the three different segmentation methods. The Expectation Maximization method provided the best results among all observers. Regarding the EM method the overall sensitivity of the observer's analysis was 63.9% and changed to 78.9% after the evaluation of the enhanced images. The specificity was 67.4% and increased to 78.2%. Considering the three least experienced the improvement was even more remarkable from 46.2 to 69.9% for sensitivity and from 57.6 to 71% for specificity. In general, all observers agreed that the proposed approach helps to clarify difficult cases of acute ischemic stroke. We demonstrated that enhanced images improved physician's performance to diagnose early signs of acute ischemic stroke. These results show the importance of a computational tool to assist neuroradiology decisions, especially in critical situations such as ischemic stroke.

**Table 1** Sensitivity and specificity before and after the enhanced images for the three different segmentation methods. The overall results accounts for the average among all observers

	Sensitivity		Specificity	
	Before	After	Before	After
Overall				
EM	63.9	78.9	67.4	78.2
K-means	63.9	74.2	67.4	71.5
Mean-shift	63.9	69.5	67.4	72.3

**Fig. 1** Average images for three different patients with stroke (a–c) and one control (d). Red arrows indicate the region of ischemic stroke. Enhanced images by the EM approach are shown in (e–g) for stroke patients and one control (H) (Color figure online)



## References

1. Benjamin, E.J., et al., *Heart Disease and Stroke Statistics—2017 Update: A Report From the American Heart Association*. Circulation, 2017.
2. Jauch, E.C., et al., *Guidelines for the early management of patients with acute ischemic stroke: a guideline for healthcare professionals from the American Heart Association/American Stroke Association*. Stroke, 2013. **44**(3): p. 870–947.
3. Amar, A.P., *Brain and vascular imaging of acute stroke*. World Neurosurg, 2011. **76**(6 Suppl): p. S3–8.
4. Mohr, J.P., et al., *Magnetic Resonance Versus Computed Tomographic Imaging in Acute Stroke*. Stroke, 1995. **26**(5): p. 807–812.
5. Fiebach, J.B., et al., *CT and Diffusion-Weighted MR Imaging in Randomized Order: Diffusion-Weighted Imaging Results in Higher Accuracy and Lower Interrater Variability in the Diagnosis of Hyperacute Ischemic Stroke*. Stroke, 2002. **33**(9): p. 2206–2210.
6. Wu, H.-Q., et al., *The association between retinal vasculature changes and stroke: a literature review and Meta-analysis*. International Journal of Ophthalmology, 2017. **10**(1): p. 109–114.
7. Huisa, B.N., et al., *Alberta Stroke Program Early CT Score (ASPECTS) in patients with wake-up stroke*. J Stroke Cerebrovasc Dis, 2010. **19**(6): p. 475–9.
8. Bergounioux, M., et al., eds. *Variational methods in imaging and geometric control*. 2016, de Gruyter: France.
9. Bergounioux, M., *Mathematical Analysis of a Inf-Convolution Model for Image Processing*. Journal of Optimization Theory and Applications, 2016. **168**(1): p. 1–21.

# Improving Priors for USTC via Transmission Tomography: A Simulation Study

Diego Armando Cardona Cardenas and Sergio Shiguemi Furuie

## Abstract

The current USCT-algorithms have limitations due to the object size and contrast to be reconstructed. To avoid USCT-algorithms divergence, it is common to initialize USCT-algorithms with a priori anatomical information of the reconstructing region. This information can be obtained from transmitted signals. Our work presents, on simulated medium, an alternative to the Modified Median Filter (MMF) that improves the transmission reconstructed image, and aims to offer a better a priori information to USCT-algorithms. Herein, it was used: 64 transducers (100 kHz) distributed around the medium; Two sets of data were generated: the first with speed of sound between [1400 1680] m/s and the second with speed of sound between [1350 1730] m/s simulating a higher contrast medium; Simultaneous Algebraic Reconstruction Technique (SIRT) as the transmission reconstruction algorithm; a Matlab toolbox (k-wave) for data generation of ultrasound propagation on heterogeneous medium; Spatial filters (mean, median, Gaussian), the original MMF over several thresholds and its modification proposed here (m-MMF), which eliminates the need of threshold. Normalized Root Mean Square Error was utilized over the reconstructing objects for evaluation. Comparing the SIRT reconstructions performance, better results were found when any studied filter is executed with the SIRT compared to none. Among the filters, the m-MMF yielded better results than the other studied filters, and more importantly, the improvements were higher for high contrast. The investigation suggests that

the use of specific filters on Transmission reconstruction algorithm for USCT improve the extraction of information of the medium that might be valuable as priors for USCT of high contrast heterogeneous medium.

## Keywords

Image reconstruction • Transmission tomography  
Simultaneous algebraic reconstruction technique  
Ultrasoundography • Modified median filter

## 1 Introduction

Today, Ultrasound Tomography (USCT) is presented as a promising low-cost alternative for medical imaging such as breast tomography [1, 2]. Although the USCT has had many advances in recent years, the developed algorithms for this methodology have limitations due to the contrast and size of the objects to be reconstructed [3, 4]. Among some alternatives to overcome these limitations and thus avoid the divergence of USCT-algorithms, we will focus on initialization of algorithms with a priori information of the region to be reconstructed. This a priori information can be obtained from transmitted data. In order to improve the extraction of this information from the transmission algorithms, aiming to offer better information to initialize USCT-algorithms, our work presents, on simulated medium, an alternative to the Modified Median Filter (MMF) [5] that improves the transmission reconstructed image.

## 2 Transmission Algorithms and Filters

The transmission algorithms assume that the sound propagation is given in a straight line and the reconstruction is based on finding the  $\mathbf{q}$  in the linear equation

D. A. C. Cardenas (✉) · S. S. Furuie  
School of Engineering, University of Sao Paulo, Sao Paulo, Brazil  
e-mail: dacadas@gmail.com

S. S. Furuie  
e-mail: sergio.furuie@usp.br

$$\mathbf{b} = H \cdot \mathbf{q} \quad (1)$$

where  $\mathbf{b}$  is a measurement related vector and  $H$  is a “known” distance matrix that represents the spatial length, in each pixel, of the propagation in straight line between the emitter and receiver transducers. To solve and find  $\mathbf{q}$ , it is common to use “Algebraic Reconstruction Technique” such as Simultaneous Algebraic Reconstruction Technique (SIRT) [6], which is an iterative method and finds an approximate solution of  $\mathbf{q}$ . The reconstructed image is noisy because the model is inaccurate for ultrasound, for example the physical phenomenon propagation in straight line. This noise could generate misinterpretations of represented structures within the reconstructed image. In order to control the noise level in the images generated by SIRT, Whiting [5] proposed the Modified Median Filter (MMF), which consists in the implementation of the mean or median filter depending on the range of pixel values in the window filter (Fig. 1). The criterion on which filter to apply is given by comparing the difference between the second highest and second lowest intensity values of the filter window, centered on the pixel, with an empirical value. In case this value is exceeded, the pixel intensity will be the median window value. Otherwise, the pixel intensity will be replaced by the mean window value.

The fact that the MMF filter requires an empirical value turns it into a dependent filter on a parameter. Consequently, the filter parameter should be previously determined or optimized. Aiming to eliminate this dependence, in this work is proposed an alternative to the MMF (m-MMF), which consists in modifying the pixel value for the mean

value between the second highest and second lowest intensity values of filter window.

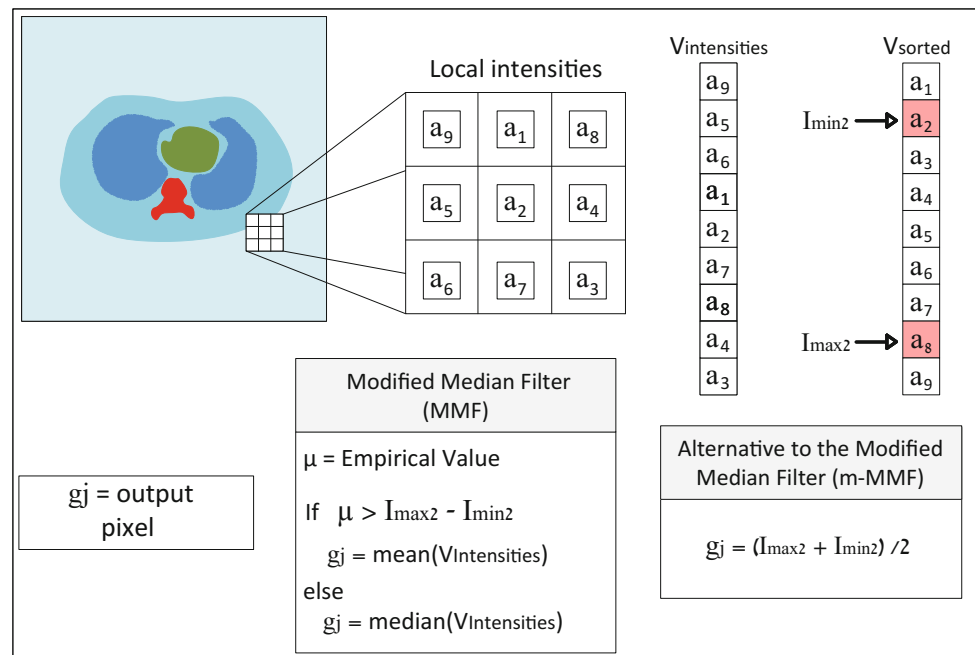
### 3 Method

This work presents an alternative to the MMF that improves the image reconstructed by transmission algorithms. The method proposed was divided into three parts: First, in **Model Generation**, where the medium and its physical properties was defined; Second, in **Simulation**, ultrasound wave propagation in the medium was simulated in order to provide information for the transmission algorithm; and finally, in **Simultaneous Algebraic Reconstruction Technique and m-MMF**, the application of the SIRT, as the Transmission algorithm, together with several spatial filters, including the m-MMF proposed here, was executed.

#### 3.1 Model Generation

In this stage, medium physical properties, size of simulated area and work frequency are defined. Thus, to ensure wave penetration in high contrast, it was chosen a central frequency equal to 100 kHz. The simulated space was defined as a square area equivalent to 441 cm<sup>2</sup> whose size in pixels is 96 × 96 pixels (Fig. 2). This space has water properties and the simulated objects were inserted in it. The model was designed in Microsoft office Visio 2016 and it is assumed that the density ( $\rho = 1000 \text{ kg/m}^3$ ), attenuation ( $\alpha = 0.0022 \text{ dB}/(\text{cm}/\text{MHz}^1)$ ) and the dependence

**Fig. 1** Modified Median Filter (MMF) and its alternative proposed here (m-MMF)



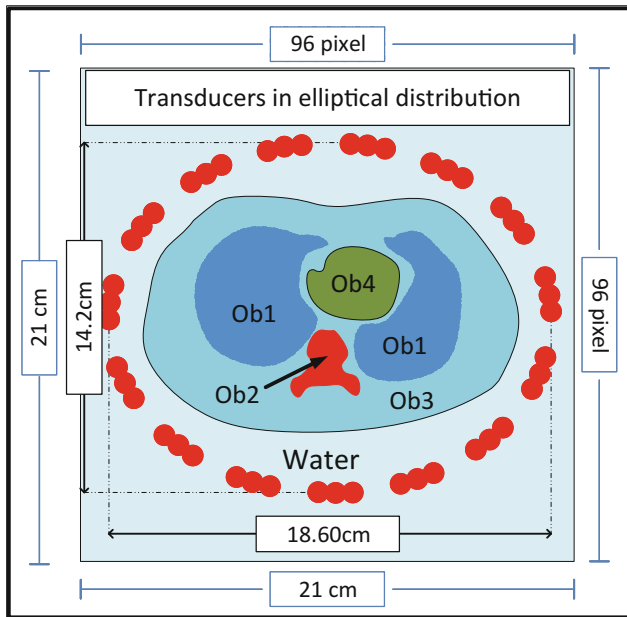


**Fig. 2** Original simulated medium

**Table 1** Object properties in simulated medium

Simulated object	Speed $c$ (m/s)
Water	1540
Ob1	$1450 - v$
Ob2	$1630 + v$
Ob3	1520
Ob4	1570

frequency factor ( $\gamma = 1.05$ ) are equal for all objects into the medium. The sound speed is shown in Table 1, where the term  $v$  will be changed according to the desired contrast. Two sets of data were generated: the first with speed of sound between  $[1400 - 1680]$  m/s ( $v = 50$  m/s) and the second with speed of sound between  $[1350 - 1730]$  m/s in a higher contrast medium ( $v = 100$  m/s). Finally, in order to simulate noise in the received signals, the speed sound and density values were subject to an additive normal random noise with standard deviation of 1% of assigned values.

### 3.2 Simulation

As shown in the Fig. 2, the transducers here simulated are mono-elements uniformly distributed along the perimeter of an elliptical area. This elliptical area simulates a tank where the objects were submerged. The total number of simulated transducers was 64. A Tone Burst signal of one oscillation was used at a frequency of 100 kHz and amplitude of 0.1 MPa. The Matlab Toolbox k-wave [7] was used to simulate the

ultrasonic waves propagation into the heterogeneous medium. To make the simulation, a single transducer is selected as emitter while all other transducers “receive” for a period of time (TR receptors). A new transducer is chosen, and the process is repeated until all transducers have emitted.

### 3.3 Simultaneous Algebraic Reconstruction Technique and m-MMF

To generate the reconstructions, it was selected the Simultaneous Algebraic Reconstruction Technique (SIRT) as the Transmission algorithm with a small relaxation parameter equal to  $\lambda = 0.05$ . The measuring vector  $\mathbf{b}$  is equivalent to the difference in time between receiving an ultrasound signal in a homogeneous medium and in a heterogeneous medium. Since SIRT is an iterative method,  $\mathbf{q}$  is initialized with  $\mathbf{0}$ . The reconstruction is executed for 16 sweeps (here, a sweep is the cycle of processing that considers the transmission of all defined transducers in turn). After each sweep, a spatial filter with size  $3 \times 3$  pixel window is applied on the reconstructed image. The analyzed filters are mean, median, Gaussian ( $\sigma = 1$  and  $\sigma = 1.5$ ) [8], the alternative of the Modified median filter (m-MMF), proposed here, and the traditional MMF with different empirical values ( $[4.5, 9, 13.5, 18, 22.5, 27, 31.5, 36, 40.5, 45, 49.5]$  m/s). Two restrictions were enforced in the reconstruction. First, the analyzed TR-receptors were selected as the receptors that are within the area between  $\pm$  a viewing angle ( $\Theta$ ). This angle was defined as  $\Theta = 22.5^\circ$ . Second, the lower and upper limits of reconstruction speed were set as  $-200$  m/s and  $+200$  m/s of lowest and highest expected values. This means that if the set of data analyzed is  $[1350 - 1730]$  m/s and one pixel gets a value, for instance, that is out of the interval  $[1150 - 1930]$  m/s, a value that is closer to the limits is set. Figure 3 shows a flowchart that describes the applied process.

## 4 Results

To evaluate all simulations, it was utilized the Normalized Root Mean Square Error (NRMSE) over the objects to be reconstructed. The NRMSE metric estimates normalized errors between the ideal ( $\mathbf{g}$ ) and the reconstructed image ( $\mathbf{q}$ ), and is defined as:

$$NRMSE = \sqrt{\frac{\sum_{j=1}^J (\mathbf{g}_j - \mathbf{q}_j)^2}{\sum_{j=1}^J (\mathbf{g}_j)^2}}. \quad (2)$$

The Table 2 presents the filter type, the empirical value used (when necessary) and the respective metric evaluated in

**Fig. 3** Flowchart that describes the process applied

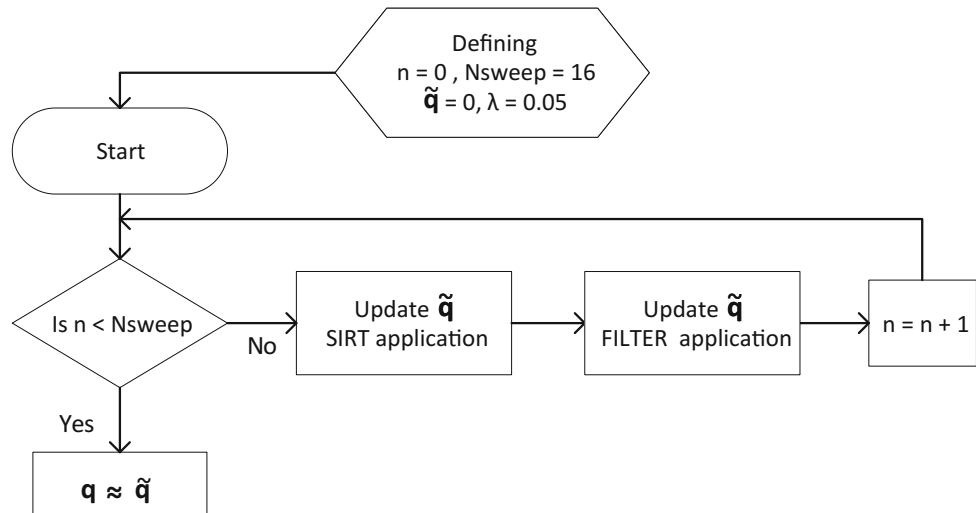


**Table 2** NRMSE (%) evaluated over the objects to be reconstructed (Fig. 2). The ob1 is the cold object and ob2 is the hot object

Filter	Empirical value (m/s)	NRMSE (%)				
		[1400 1680]		-	[1350 1730]	
		Cold	Hot		Cold	Hot
None	-	3.96	6.28		6.68	9.02
Mean	-	3.47	5.73		5.41	7.02
Gauss ( $\sigma = 1, 0$ )	-	3.47	5.69		5.42	7.05
Gauss ( $\sigma = 1, 5$ )	-	3.47	5.71		5.41	7.03
Median	-	3.48	5.64		5.54	7.21
m-MMF	-	3.48	5.64		5.41	6.84
MMF	4.5	3.47	5.65		5.53	7.22
	9.0	3.46	5.65		5.51	7.22
	13.5	3.46	5.66		5.50	7.26
	18.0	3.44	5.67		5.47	7.29
	22.5	3.44	5.68		5.46	7.32
	27.0	3.45	5.70		5.45	7.33
	31.5	3.45	5.73		5.46	7.31
	36.0	3.46	5.75		5.44	7.34
	40.5	3.47	5.73		5.45	7.35
45.0	3.48	5.73		5.44	7.32	
49.5	3.48	5.73		5.43	7.34	

the last sweep, and the Fig. 4 shows some reconstructions. Onwards, ob1 is the cold object (the largest object and with lowest velocity) and ob2 is the hot object (the object with highest velocity).

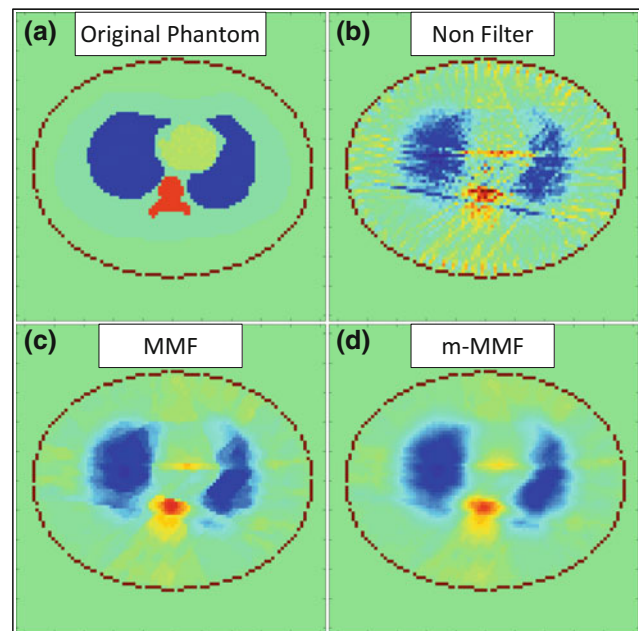


**Fig. 4** Image reconstructed: Original Phantom with data contrast equal to [1350-1730] (a), and its reconstructions with No Filter (b) and using MMF (c) and m-MMF (d)

## 5 Discussion and Conclusions

Comparing the SIRT reconstructions performance, it is possible to see better results when any filter is executed with SIRT. Among the filters, the m-MMF yielded better results than the other studied filters, and more importantly, the improvements were higher for high contrast.



Furthermore, the proposed approach does not depend on any parameter such as threshold. The investigation, based on simulations, suggests that the use of filters on Transmission algorithm for Ultrasound Tomography bring improvements in the extraction of information of the medium that might be valuable as priors for USCT of high contrast heterogeneous medium.

**Acknowledgements** We would like to acknowledge the financial support from FAPESP, grant number 2014/50889-7 and 2018/04290-7.

**Conflict of Interest Declaration** The authors declare that they have no conflict of interest.

---

## References

1. Wiskin, J., Borup, D., Johnson, S. (2011). Inverse scattering theory. In *Acoustical Imaging* (pp. 53–59). Springer, Dordrecht.
2. Huthwaite, P., Simonetti, F. (2011). High-resolution imaging without iteration: A fast and robust method for breast ultrasound tomography. *The Journal of the Acoustical Society of America*, 130(3), 1721–1734.
3. Cavicchi, T. J., Johnson, S. A., O'Brien, W. D. (1988). Application of the sinc basis moment method to the reconstruction of infinite circular cylinders. *IEEE transactions on ultrasonics, ferroelectrics, and frequency control*, 35(1), 22–33.
4. Lavarello, R., Oelze, M. (2008). A study on the reconstruction of moderate contrast targets using the distorted Born iterative method. *IEEE transactions on ultrasonics, ferroelectrics, and frequency control*, 55(1).
5. Whiting, P. T. (1992). Resolution enhancement of seasat scatterometer data (Doctoral dissertation, Brigham Young University. Department of Electrical and Computer Engineering).
6. Andersen, A. H., Kak, A. C. (1984). Simultaneous algebraic reconstruction technique (SART): a superior implementation of the ART algorithm. *Ultrasonic imaging*, 6(1), 81–94.
7. Treeby, B. E., Cox, B. T. (2010). k-Wave: MATLAB toolbox for the simulation and reconstruction of photoacoustic wave fields. *Journal of biomedical optics*, 15(2), 021314–021314.
8. Gonzalez, R. C., Woods, R. E. (2008). *Digital image processing*, 3rd Edition, Prentice Hall, ISBN: 9780131687288.

# Brain Tumor Classification Using Convolutional Neural Network

Nyoman Abiwinanda, Muhammad Hanif, S. Tafwida Hesaputra, Astri Handayani, and Tati Rajab Mengko

## Abstract

Misdiagnosis of brain tumor types will prevent effective response to medical intervention and decrease the chance of survival among patients. One conventional method to differentiate brain tumors is by inspecting the MRI images of the patient's brain. For large amount of data and different specific types of brain tumors, this method is time consuming and prone to human errors. In this study, we attempted to train a Convolutional Neural Network (CNN) to recognize the three most common types of brain tumors, i.e. the Glioma, Meningioma, and Pituitary. We implemented the simplest possible architecture of CNN; i.e. one each of convolution, max-pooling, and flattening layers, followed by a full connection from one hidden layer. The CNN was trained on a brain tumor dataset consisting of 3064 T-1 weighted CE-MRI images publicly available via figshare Cheng (Brain Tumor Dataset, 2017 [1]). Using our simple architecture and without any prior region-based segmentation, we could achieve a training accuracy of 98.51% and validation accuracy of 84.19% at best. These figures are comparable to the performance of more complicated region-based segmentation algorithms, which accuracies ranged between 71.39 and 94.68% on identical dataset Cheng (Brain Tumor Dataset, 2017 [1], Cheng et al. (PLoS One 11, 2017 [2])).

## Keywords

Training loss • Training accuracy • Validation loss  
Validation accuracy • Overfitting

## 1 Introduction

On 2016, brain tumor was the leading cause of cancer-related death in children (ages 0–14) in the United States and ranked above Leukemia [3]. Brain and CNS tumors are also the third most common cancer occurring among teenager and adolescents (ages 15–39) [4]. Different types of brain tumors require different medical interventions. In conventional computer-aided diagnosis systems, the tumor mass itself has to be identified and segmented before it can be classified into different types. Upon tumor mass segmentation, the segmented region is then subjected to feature extraction and classification.

Recent studies of identification and segmentation of brain tumor [5, 6] found no universal system for accurate tumor detection system regardless of its location, shape, and intensity [6]. There are numerous proposed algorithms in recent studies for feature extraction and classification of brain tumors. Grey-level co-occurrence matrix (GLCM) [7–9] is commonly used for extraction of low-level features. Several other feature extraction algorithms which attempt to handle the complex texture of brain tumor are Neural Network [9, 10], Bag-of-Words (BoW) [2, 8], and Fisher Vector [2]. One recent study showed that by using a combination of adaptive spatial pooling and fisher vector algorithm, brain tumor classification into Glioma, Meningioma, and Pituitary can be achieved with 71.39–94.68% accuracy [2].

Conventional brain tumor classification methods commonly involve region-based tumor segmentation prior to feature extraction and classification. In this paper, we propose an automatic brain tumor segmentation/classification method based on Convolutional Neural Networks. CNN consists of a convolutional network to perform automatic segmentation

N. Abiwinanda (✉) · M. Hanif · S. T. Hesaputra · A. Handayani  
T. R. Mengko  
Bandung Institute of Technology, Bandung, West Java 40134,  
Indonesia

e-mail: abiwinanda@outlook.com

M. Hanif  
e-mail: mhaniffarhat@gmail.com

S. T. Hesaputra  
e-mail: tafwidahesaputra@gmail.com

A. Handayani  
e-mail: a.handayani@stei.itb.ac.id

T. R. Mengko  
e-mail: tmengko@stei.itb.ac.id

and feature extraction, followed by a conventional neural network to perform classification task. The well-known basic architecture of CNN involves a Rectified Linear Unit (ReLU), a convolution, and a pooling layer [11]. In contrast to conventional methods which require prior segmentation of tumor mass, our CNN approach does not involve region-based pre-processing step. We validate our algorithm on the same dataset which was used in previous publications [1, 2].

## 2 Previous Work

Various methodologies have been developed in the past years to recognize brain tumor in MRI images. These methods are ranging from classical image processing to neural network based machine learning approach. Jun Cheng et al. [2] developed a tumor classification method that consists of two phases: offline database building and online retrieval. In the offline database phase, the brain tumor images are processed in sequential steps. The steps are consisted of tumor segmentation, feature extraction, and distance metric learning. In the online learning, the input brain image will be processed similarly and compare the extracted feature with the learned distanced metrics which are stored in the online database. This method does not use neural network approach but could achieve a classification accuracy of 94.68%. On the other hand, Gawande and Mendre [12] used Deep Neural Network using autoencoders in order to classify the brain tumor. Image segmentation and feature extraction had been implemented on the image before it was processed by DNN layers. The texture and intensity based features of the image were extracted with help of Gray Level Co-occurrence Matrix (GLCM) and Discrete Wavelet Transform (DWT). In the final step, DNN layers which consist of two autoencoders and one softmax layer were performed for classification. Furthermore, Pereira et al. [13] also exploring the used of Convolutional Neural Networks (CNN) with small  $3 \times 3$  kernels in order to get to the deeper architecture and avoid the overfitting. They also investigated the use of intensity normalization as the pre-processing step before getting into the CNN layers. In this study, inspired by those works, we investigate and explore the implementation of deep CNN on classifying several brain tumor type diagnosis problems in order to get better accuracy result.

## 3 Method

### 3.1 Convolutional Neural Network

CNN convolution layer is a network where an image will be convolved with filters to produce feature maps. This feature

maps will be forwarded to the next convolution layer to receive or extract another higher level features from the input image. Between convolution layers, non-linearity functions and down sampling operation is used to add non-linearity and reduced the dimensionality of the image respectively. Max-pooling usually used as the down sampling operation as it reduced the dimension while preserving the dominant feature in the feature maps. Just after the last convolution layer or before the first layer of the neural network, flattening layer exist to vectorize the feature maps. In the neural network or classification phase, the flatten input vector will be forwarded into the network to produce a number at each output neurons. This number tells how much an input vector is classified as a certain class. Usually a softmax activation function is used at the output layer to normalize the output sum such that all numbers at the output neuron will add up to one.

In the training phase, CNN use a learning or optimizer algorithm to update the filters at the convolution layers and weights at the neural network or fully connected layer. The learning algorithm takes a classification error or loss as an input and back propagates the error into the network to update the filters and the weights.

### 3.2 CNN Architecture

In this paper, we use five different architectures to test the accuracy of brain tumor classification. There are already well defined CNN architecture such as AlexNet [14], VGG16 [15], and ResNet [16] but the architecture that are implemented in this paper are much simpler than the one mentioned. The CNN architecture that are implemented in this paper are summarize in the Fig. 1a–e.

### 3.3 Hyper-parameters Optimization

Hyper-parameter is a parameter in deep learning process whose value can be set and tuned before the learning process. This parameter will determine the algorithm to be used in the learning process. Different model training algorithms need different hyper-parameters that also affecting the result of the learning process too. Hyper-parameter optimizer has to be chosen and tuned so that the classifier will have the most optimal way to solve the problem.

In this study, we will use ‘adam’ optimizer in the learning process which is a method for stochastic optimization by utilizing the stochastic gradient descent principle. ‘Adam’ optimizer which stands for adaptive moment estimation is chosen because of its advantage that can handle sparse gradients on noisy problems.

**Fig. 1** a–e The proposed Convolutional Neural Network Architecture 1–5

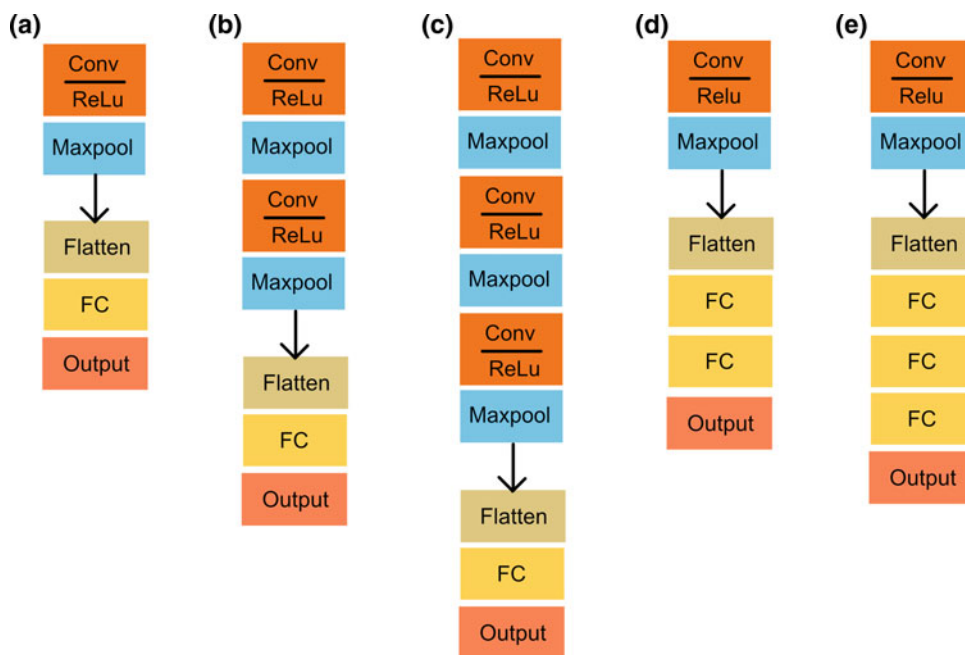
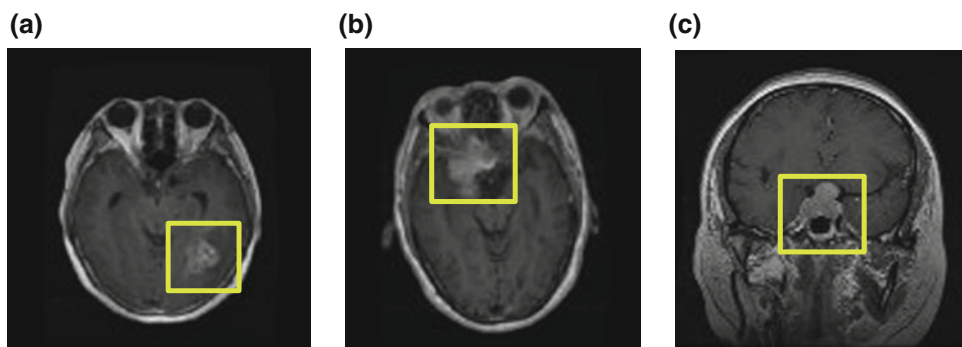


**Fig. 2** a Glioma, b Meningioma, c Pituitary (each labeled in green)



## 4 Data

In this paper, our CNN is trained using 3064 T-1 weighted CE-MRI of brain tumor images. The dataset is provided by Jun Cheng and was previously used in his paper [1, 2]. This dataset consists of 708 images with glioma, 1426 images with meningioma, and 930 images with pituitary tumors. In our training phase, we equalize the amount of images that are used to train the CNN for each class or type of tumors. Out of all available images, we only used 700 images from each class where 500 of those images were used for training phase and the other 200 images were used for validation phase. The dataset was originally provided in matlab.mat format where each file stores a struct containing a label which specify the type of tumor for a particular brain image, patient ID, image data in  $512 \times 512$  uint16 format, vector storing the

coordinates of discrete points on tumor border, and a binary mask image with 1 s indicating tumor region. In our paper we only make use the label and image data in the.mat files therefore our brain tumor classifier is a simple CNN network which only takes image as an input. Figure 2a–c represent example of the dataset from each of the classes.

## 5 Result

In our experiment, the hyperparameter at each layer such as number and size of filters in the convolution layers, size of maxpooling kernel, number of neurons in the fully connected layers are held fixed. Only the depth of the architecture are varied between different architectures. The architecture and hyperparameter that are used are served in Table 1.

**Table 1** Architecture 1–5

Architecture 1			Architecture 2		
Layer (type)	Output Shape	Param #	Layer (type)	Output Shape	Param #
conv2d_6 (Conv2D)	(None, 62, 62, 32)	896	conv2d_7 (Conv2D)	(None, 62, 62, 32)	896
max_pooling2d_6 (MaxPooling2)	(None, 31, 31, 32)	0	max_pooling2d_7 (MaxPooling2)	(None, 31, 31, 32)	0
flatten_6 (Flatten)	(None, 30752)	0	conv2d_8 (Conv2D)	(None, 29, 29, 32)	9248
dense_11 (Dense)	(None, 64)	1968192	max_pooling2d_8 (MaxPooling2)	(None, 14, 14, 32)	0
dense_12 (Dense)	(None, 3)	195	flatten_4 (Flatten)	(None, 6272)	0
Total params: 1,969,283 Trainable params: 1,969,283 Non-trainable params: 0			dense_10 (Dense)	(None, 64)	401472
			dense_11 (Dense)	(None, 3)	195
			Total params: 411,811 Trainable params: 411,811 Non-trainable params: 0		
Architecture 3			Architecture 4		
Layer (type)	Output Shape	Param #	Layer (type)	Output Shape	Param #
conv2d_1 (Conv2D)	(None, 62, 62, 32)	896	conv2d_3 (Conv2D)	(None, 62, 62, 32)	896
max_pooling2d_1 (MaxPooling2)	(None, 31, 31, 32)	0	max_pooling2d_3 (MaxPooling2)	(None, 31, 31, 32)	0
conv2d_2 (Conv2D)	(None, 29, 29, 32)	9248	flatten_3 (Flatten)	(None, 30752)	0
max_pooling2d_2 (MaxPooling2)	(None, 14, 14, 32)	0	dense_7 (Dense)	(None, 64)	1968192
conv2d_3 (Conv2D)	(None, 12, 12, 32)	9248	dense_8 (Dense)	(None, 64)	4160
max_pooling2d_3 (MaxPooling2)	(None, 6, 6, 32)	0	dense_9 (Dense)	(None, 3)	195
flatten_1 (Flatten)	(None, 1152)	0	Total params: 1,973,443 Trainable params: 1,973,443 Non-trainable params: 0		
dense_1 (Dense)	(None, 64)	73792			
dense_2 (Dense)	(None, 3)	195			
Total params: 93,379 Trainable params: 93,379 Non-trainable params: 0					
Architecture 5					
Layer (type)	Output Shape	Param #			
conv2d_1 (Conv2D)	(None, 62, 62, 32)	896			
max_pooling2d_1 (MaxPooling2)	(None, 31, 31, 32)	0			
flatten_1 (Flatten)	(None, 30752)	0			
dense_1 (Dense)	(None, 64)	1968192			
dense_2 (Dense)	(None, 64)	4160			
dense_3 (Dense)	(None, 64)	4160			
dense_4 (Dense)	(None, 3)	195			
Total params: 1,977,603 Trainable params: 1,977,603 Non-trainable params: 0					

Sizes of the input images that are forwarded into the network are  $64 \times 64$ . The original images are in the size of  $512 \times 512$ . This reduction is performed because of computational cost reason. All architectures are compiled without a GPU therefore to speed up the training phase smaller image size is used.

All convolution layers in the architectures use 32 filters of size  $3 \times 3$ . We use ReLu as our activation function as it already the standard activation function used in image classification task. The size of the maxpool kernel is  $2 \times 2$

and all the fully connected layer (called ‘dense’ in keras) use 64 neurons.

Finally, there are 3 neurons in the output layer since we try to classify an image with three types of brain tumors (glioma, meningioma, and pituitary). The activation functions that are used at the output layer are softmax so that all three output neurons are summed up to one.

Based on Table 1, each of architecture produces different numbers of params and features depending on the depth of the convolution layer and the fully connected network. The

architecture with deeper layers of convolution will have fewer numbers of the trainable params.

Implementation of the above architectures will produce four parameter values that will describe the success of the classifier model in classifying the input image. The four parameter values are loss and accuracy from the training set and validation set. Accuracy is defined as the percentage of the correct guesses by the classifier either for the training set input or the validation set input. Loss is defined as feasible error that represents the price paid for inaccuracy of predictions in classification problem. We use cross-entropy loss calculation. The cross-entropy loss calculation can be represented in the mathematical form [17] below:

$$H(y, \hat{y}) = \sum_i y_i \log \frac{1}{\hat{y}_i} = - \sum_i y_i \log \hat{y}_i \quad (1)$$

$y_i$  represents the result of the classifier output from class  $i$ . While  $\hat{y}_i$  represents the expected output from class  $i$ . The classification accuracy of each architecture are presented in Figs. 3, 4, 5, 6 and 7.

Based on Figs. 3, 4, 5, 6 and 7, the values of loss and accuracy vary according to the implementation of the architecture. The classifier model is said to be ‘good fit’ if the accuracy of training set and validation set tend to increase for every epoch of training. However, if the accuracy of validation set tends to decrease while the accuracy of training set increases, then the classifier model is estimated to have overfitting. Overfitting happens when the model learns the detail and noise in the training data thus reducing its ability to generalize other datasets well [18].

By looking at the result of each architectures, we could see that all architecture’s validation loss shows an increasing trend with respect to the number of epoch except for

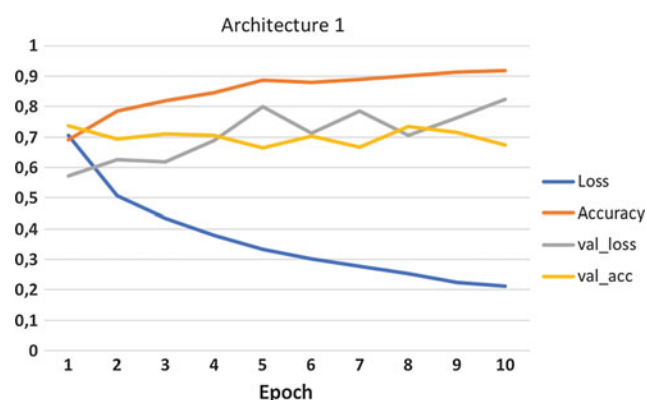


Fig. 3 Accuracy and loss of architecture 1

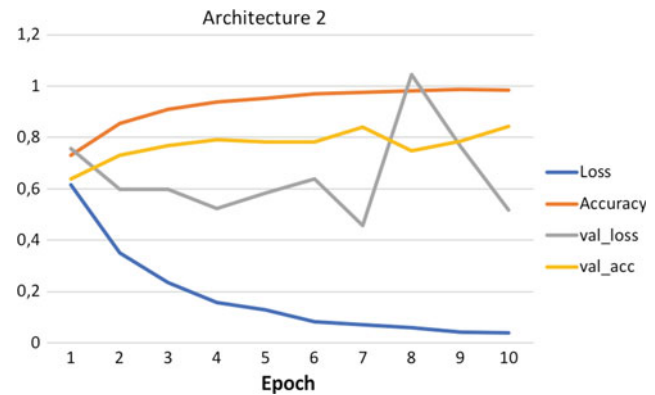


Fig. 4 Accuracy and loss of architecture 2

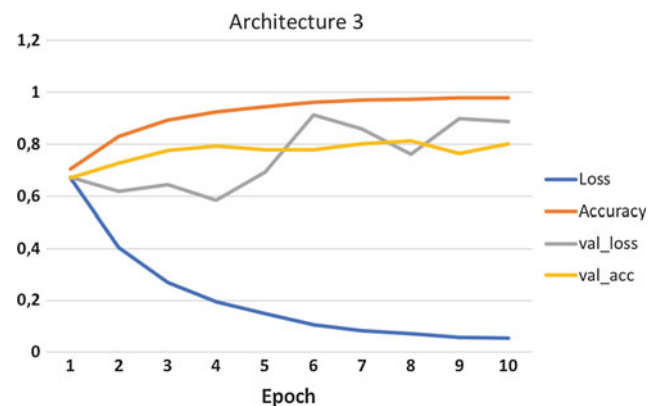


Fig. 5 Accuracy and loss of architecture 3

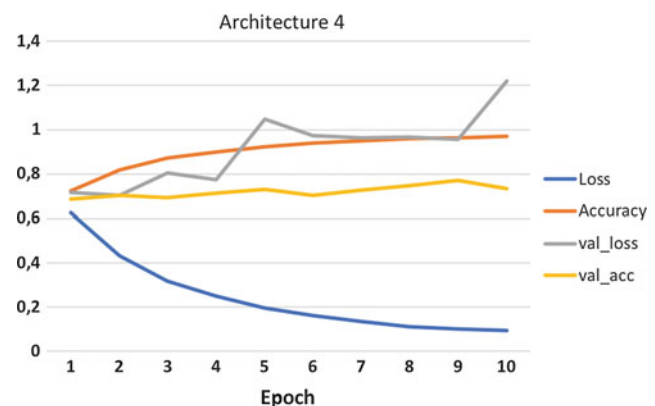


Fig. 6 Accuracy and loss of architecture 4

architecture 2. This indicates that architecture 2 is the best architecture out of the five architectures at generalizing the brain tumor images. The decreasing pattern in the validation loss indicates that using the available training images, architecture 2 could classify the unknown images in the



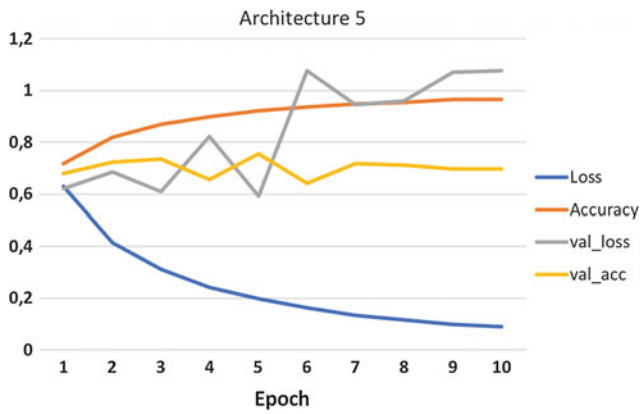


Fig. 7 Accuracy and loss of architecture 5

validation set with medium performance. We conclude a medium performance since the validation loss does not show a perfect decreasing pattern as the number of epoch increase. In the last epoch, architecture 2 could achieve a validation accuracy of 84.19%.

Based on the best architectural choice on the previous part, we try to vary the number of the filter in the convolution layer into 64 filters and 128 filters we called it as architecture 6 and architecture 7 respectively. In this experiment, we will identify the effect of the filter numbers in the convolution layer on the accuracy of the validation set. The architecture and hyper parameters that are used are served in the Table 2.

After implementation of those architectures, the classification accuracy of those architectures are presented in Figs. 8 and 9.

From the result, the architecture that has the highest validation accuracy is still architecture 2 with 32 filters in the convolution layers. Although an increase in the number of filters in the convolution layer does not necessarily contribute to better CNN performance, in our case the number of filter in a convolution layer does influence the accuracy of the classifier. We stick or recommend the use of architecture 2 to classify a brain tumor since it has the highest validation accuracy.

Table 2 Architecture 6–7

Architecture 6			Architecture 7		
Layer (type)	Output Shape	Param #	Layer (type)	Output Shape	Param #
conv2d_1 (Conv2D)	(None, 62, 62, 64)	1792	conv2d_1 (Conv2D)	(None, 62, 62, 128)	3584
max_pooling2d_1 (MaxPooling2D)	(None, 31, 31, 64)	0	max_pooling2d_1 (MaxPooling2D)	(None, 31, 31, 128)	0
conv2d_2 (Conv2D)	(None, 29, 29, 64)	36928	conv2d_2 (Conv2D)	(None, 29, 29, 128)	147584
max_pooling2d_2 (MaxPooling2D)	(None, 14, 14, 64)	0	max_pooling2d_2 (MaxPooling2D)	(None, 14, 14, 128)	0
flatten_1 (Flatten)	(None, 12544)	0	flatten_1 (Flatten)	(None, 25088)	0
dense_1 (Dense)	(None, 64)	802880	dense_1 (Dense)	(None, 64)	1605696
dense_2 (Dense)	(None, 3)	195	dense_2 (Dense)	(None, 3)	195
Total params: 841,795 Trainable params: 841,795 Non-trainable params: 0			Total params: 1,757,059 Trainable params: 1,757,059 Non-trainable params: 0		

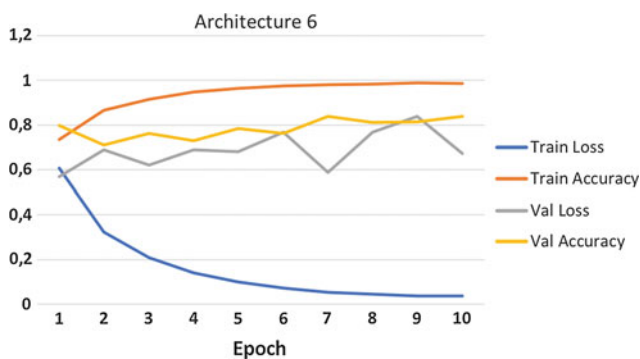


Fig. 8 Accuracy and loss of architecture 6

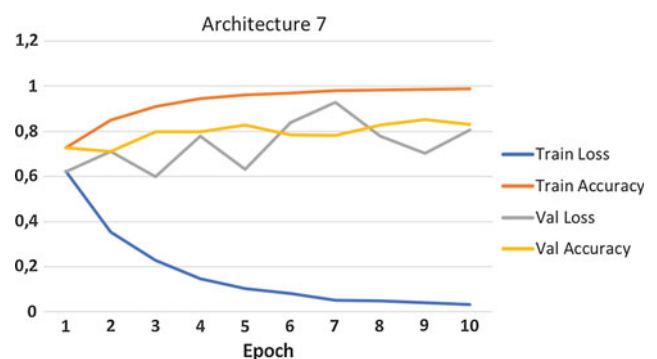


Fig. 9 Accuracy and loss of architecture 7

## 6 Conclusion

In this paper, we introduced CNN to automatically classify the three most common types of brain tumor, i.e. the Glioma, Meningioma, and Pituitary; without requiring region-based pre-processing steps. We identified an optimal CNN architecture (architecture 2) consisting of 2 layers of convolution, activation (ReLU), and maxpool, followed by one hidden layer of 64 neurons. Architecture 2 is the only architecture that show a consistently decreasing pattern in the validation loss as the number of epoch increases, leading to the highest validation accuracy out of all five architectures. The training and validation accuracies of architecture 2 at best is 98.51% and 84.19%, respectively. These figures, although somewhat lower, are still comparable to the accuracies of conventional algorithms with region-based pre-processing, which performed at 71.39–94.68% [1, 2]. For future work, we consider to include color balancing step into our CNN, to improve classification accuracy of textured brain MRI pixels [19]. Our algorithm may be implemented in as a simple supportive tool for medical doctor in classifying brain tumor.

**Disclosure** The authors declare that they have no conflict of interest.

## References

1. Jun Cheng. (2017). *Brain Tumor Dataset* (Version 5). Retrieved from <https://doi.org/10.6084/m9.figshare.1512427.v5>
2. Cheng, J., Huang, W., Cao, S., et al. (2015). Classification via Tumor Region Augmentation and Partition. *PLoS One*, 10(10).
3. Varade, A. A., Ingle, K. S. (2017). Brain MRI Classification Using PNN and Segmentation Using K Means Clustering. *International Journal of Advanced Research in Electrical, Electronics and Instrumentation Engineering*, 6(5), 6181–6188.
4. Cheng, J., Yang, W., Huang, M., et al. (2016). Retrieval of Brain Tumors by Adaptive Spatial Pooling and Fisher Vector Representation. *PLoS One*, 11(6).
5. Lavanyadevi, R., Machakowsalya, M., Nivehitha, J., et al. (2017). Brain tumor classification and segmentation in MRI images using PNN. *IEEE Xplore*.
6. Siegel, R. L., Miller, K. D., Jemal, A. (2016). Cancer statistics, 2016. *CA: A Cancer Journal for Clinicians*, 66(1), 07–30.
7. Quinn, T., Ostrom, M.A., Gittleman, H., et al. (2016). American Brain Tumor Association Adolescent and Young Adult Primary Brain and Central Nervous System Tumors Diagnosed in the United States in 2008–2012. *Neuro-Oncology*, 18(1), i1–i50.
8. Gordillo, N., Montseney, E., Sobrevilla, P. (2013). State of the art survey on MRI brain tumor segmentation. *Magnetic Resonance Imaging*, 31(8), 1426–1438.
9. Kaur, H., Sharma, R. (2016). A Survey on Techniques for Brain Tumor Segmentation from MRI. *IOSR Journal of Electronics and Communication Engineering*, 11(5), 01–05.
10. Hasan, M. H., Meziane, F., et al. (2016). Segmentation of Brain Tumors in MRI Images Using Three-Dimensional Active Contour without Edge. *Symmetry*, 8(11), 132.
11. Wu, J. (2017). Introduction to Convolutional Neural Networks. National Key Lab for Novel Software Technology Nanjing University, China.
12. He, K., Zhang, X., Ren, S., et al. (2015). Deep residual learning for Image Recognition. *CVPR*, 770–778.
13. Brownie, J. (2016, March 21). Overfitting and Underfitting With Machine Learning Algorithms. Retrieved from <https://machinelearningmastery.com/overfitting-and-underfitting-with-machine-learning-algorithms/>.
14. Zacharaki, E. I., Wang, Sumei., Chawla, S., et al. (2009). Classification of Brain Tumor Type and Grade Using MRI Texture and Shape in a Machine Learning Scheme. *Magnetic Resonance in Medicine*, 62(6), 1609–1618.
15. Kingma, D. P., Ba, J. (2014). Adam: A Method for Stochastic Optimization. *arXiv preprint arXiv:1412.6980*.
16. Gawande, S. S., Mendre, V. (2017). Brain Tumor Diagnosis Using Deep Neural Network (DNN). *International Journal of Advanced Research in Electrical, Electronics and Instrumentation Engineering*, 5(5).
17. Simonyan, K., Zisserman, A. (2015). Very Deep Convolution Networks for Large-Scale Image Recognition. *ICLR 2015*.
18. Pereira, S., Pinto, A., Alves, V., et al. (2016). Brain Tumor Segmentation Using Convolutional Neural Networks in MRI Images. *IEEE Transactions on Medical Imaging*, 35(5), 1240–1251.
19. DiPietro, Rob. (2016, May 2). A Friendly Introduction to Cross-Entropy Loss. Retrieved from <https://rdipietro.github.io/friendly-intro-to-cross-entropy-loss/>.

# A Novel Method for 3D Reconstruction of Coronary Bifurcation Using Quantitative Coronary Angiography

Ioannis O. Andrikos, Atonis I. Sakellarios, Panagiotis K. Siogkas, Panagiota I. Tsompou, Vassiliki I. Kigka, Lampros K. Michalis, and Dimitrios I. Fotiadis

## Abstract

Many methods have been proposed for the 3-dimensional (3D) reconstruction of coronaries arteries by combing information from two or more X-ray views of the coronary tree, since the 2D representation of coronary lesion using X-ray coronary angiographies is limited. The aim of this study is to present a new semi-automated method for the accurate 3D reconstruction of coronary arterial bifurcations using X-ray coronary angiographic views (CA). X-ray angiography was acquired from seven patients, both pre and post angioplasty procedure, and their data were used for the 3D reconstruction methodology. The proposed approach consists of 3 steps. Initially, the 2D lumen borders and centerlines are detected. Then the 3D bifurcation path is extracted and the 3D lumen borders are reconstructed around the 3D bifurcation path and finally, the main and side segments are intersected in order to produce the finally model of the bifurcated artery. Considering the X-ray angiography as the gold standard, we validated the proposed method based on the 2D versus the 3D bifurcation segment model. More specifically, in the current dataset our results indicate excellent correlation with the 2D angiography:

$r = 0.98$ ,  $p < 0.001$ ;  $r = 0.97$ ,  $p < 0.001$ ;  $r = 0.94$ ,  $p < 0.001$  and  $r = 0.88$ ,  $p < 0.001$  for the Reference Lumen Diameter (RLD), Minimal Lumen Diameter (MLD), Degree of Stenosis (DS) and Lesion Length (LL), respectively. Moreover the mean values of the Hausdorff Distance and the Dice correlation between the 2D annotated borders and the forwardly projected borders are 0.3031 mm and 91% for the first CA while 0.3103 and 92% for the second one.

## Keywords

X-ray angiography • 3D reconstruction • 3D QCA

## 1 Introduction

### 1.1 A Subsection Sample

Several studies address with the assessment of the Coronary Artery Disease (CAD) both using clinical and imaging data. Invasive X-ray Coronary Angiography (CA) is the one of the most commonly used imaging methods in cardiology and is considered the “gold standard” in clinical therapy treatment [1]. In fact, diagnosis of CAD based on the 2D CA provides various quantitative features of atherosclerosis progression such as the coronary region of the lesion, the degree of stenosis, the lesion length etc. Nevertheless, CA is fundamentally limited in some aspects. Actually, in many clinical cases, the vessels overlapping, the limited visualization of all coronary branches as well as the poor image resolution could lead to overestimation or underestimation of the coronary lesion and wrong decision making for the treatment strategy [2].

Nowadays, several clinical techniques, for the accurate diagnosis of atherosclerosis, are based on the visualization of the coronary tree from multiple angiographic projections. In addition, various studies propose techniques for the 3D reconstruction of the vessels from 2D projections, providing

I. O. Andrikos (✉) · A. I. Sakellarios · P. K. Siogkas  
P. I. Tsompou · V. I. Kigka · D. I. Fotiadis  
Unit of Medical Technology and Intelligent Information Systems,  
Department of Materials Science and Engineering, University  
of Ioannina, 45110 Ioannina, Greece  
e-mail: john.andrikos@gmail.com

D. I. Fotiadis  
e-mail: fotiadis@cc.uoi.gr

I. O. Andrikos · A. I. Sakellarios · P. K. Siogkas  
P. I. Tsompou · V. I. Kigka · D. I. Fotiadis  
Department of Biomedical Research, FORTH-IMBB,  
45110 Ioannina, Greece

L. K. Michalis  
Department of Cardiology, Medical School, University  
of Ioannina, 45110 Ioannina, Greece

thus a quantitative analysis of the coronary arteries silhouette. However, the majority of them focus on the coronary segments, omitting the side branch from the bifurcated artery anatomy [3, 4] or reconstruct coronary bifurcations using hybrid methods [5].

The aim of this study is to propose a novel method for the 3D reconstruction of the coronary bifurcation arteries from CA images (3D Quantitative Coronary Angiography—QCA). Seven coronary bifurcations, both pre and post the Percutaneous Transluminal Coronary Intervention (PTCI) procedure, were reconstructed into the 3D space, while the evaluation of the proposed method was held by comparing the 3D vessels with the accurate 2D silhouette of the arteries on the CA.

## 2 Materials and Methods

The algorithm of the proposed 3D reconstruction method consists of the following three steps: (i) the segmentation of the vessel and the 2D centerline extraction, (ii) the 3D reconstruction of the centerline and lumen borders, (iii) the registration of the main and side branch to produce the final 3D model of the bifurcated coronary artery.

### 2.1 Data Acquisition

Totally seven patients with stenosis close to the region of the bifurcation subjected to invasive X-ray angiography examination and angioplasty treatment therapy. Four CA images of each patient, two before and two after the angioplasty procedure were selected at the R wave of the Electrocardiography (ECG) signal, which corresponds to the end of the heart's diastolic time [6].

Moreover, for each pair of the selected angiographic images, the total angle offset between the first and the second projection view was greater than  $30^\circ$  [7].

### 2.2 Vessel Segmentation and 2D Centerline Extraction

Initially, the user provides a “pseudo-annotation” of the vessels by defining some points around the vessel's silhouette. Obviously, the starting and the ending point of the user annotation must correspond to common vessels landmarks between the angiographic projections. Then, the edged image is computed for each CA, while a minimum cost path-based method [8] is applied to the user-defined points to segment the lumen borders [9]. For each CA view totally four lumen borders are extracted: two for the main and two for the side branch, while the bifurcated centerline is calculated as the middle points of the lumen borders along the coronary vessels.

### 2.3 Centerline and Lumen Borders 3D Reconstruction

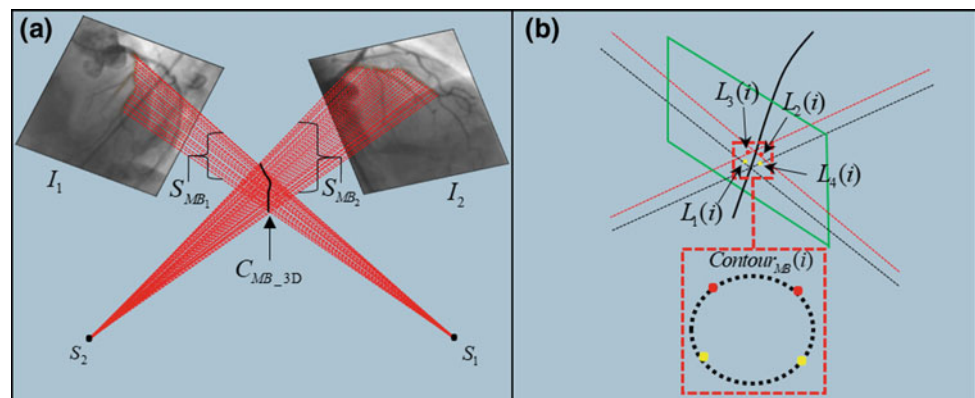
The main idea of this step is to translate the angiographic views from the  $(x, y)$  coordinates to  $(u, v, t)$  coordinates, which correspond to the real dimensions of X-ray image intensifier system and the C-arm gantry rotation angles. In fact, this process consists of the following steps: (i) image calibration based on the Pixel Size, (ii) definition of the X-ray source points to  $(x, y, z)$  coordinates, (iii) translation and rotation of the CA views and source points according to X-ray acquisition settings of the C-arm system. Improving the back-projection method of [10], the bifurcated 3D centerline is computed in Eqs. (1) and (2):

$$S_{MB_1} - S_{MB_2} = 0, \quad (1)$$

$$S_{SB_1} - S_{SB_2} = 0, \quad (2)$$

where  $S_{MB_1}$ ,  $S_{MB_2}$ ,  $S_{SB_1}$  and  $S_{SB_2}$  represent the bifurcated back-projected surfaces of the angiographic views (see Fig. 1a).

**Fig. 1** **a** 3D centerline extraction, **b** reconstruction of the 3D lumen borders



Regarding the lumen borders reconstruction,  $n$  planes perpendicular to the centerline are computed while the intersections of the  $P_i$ ,  $i = 1, \dots, n$  plane with  $i$ -th back-projected lines of the annotated vessel borders are calculated. Totally, the  $i$ -th lumen elliptical contour is reconstructed by interpolating all the calculated 3D borders using a spline method (see Fig. 1b).

## 2.4 Registration of the Main and the Side Branch

The final morphology of the 3D bifurcation artery model was accomplished by removing the points of the side branch which were common with the main branch. Finally, the lumen surfaces of the 3D model were reconstructed using a triangulation method.

## 2.5 Evaluation Methodology

Considering the CA as the “gold standard” the validation of the proposed methodology was accomplished by comparing the 3D reconstructed models with the annotated 2D silhouette of the lumen borders on the angiography. Quantitative coronary analysis both for 2D and 3D vessels were

performed, based on the bifurcation segment model (Proximal Main—PM, Distal Main—DM and Side Branch—SB) (see Fig. 2a). Moreover, each 3D vessel was projected forward onto the angiographic projections to extract the 2D borders of the model (see Fig. 2b, c). Comparisons between the true 2D lumen borders and the recovered 2D model borders were performed, using Spatial distance and overlap based metrics, such as the Hausdorff Distance (HD) and the Dice Coefficient (DC) [11].

## 3 Results

In this work we presented a novel method for the 3D reconstruction of bifurcated arteries utilizing two angiographic projections of the coronary vessels. Seven coronary bifurcations, both pre and post the angioplasty procedure, were reconstructed into the 3D space. Initially, the comparison between the 3D models and the 2D CA were performed based on lumen diameter metrics such as the Reference Vessel Diameter (RVD), the Minimum Lumen Diameter (MLD), the Degree of stenosis (DS) and the Lesion Length (LL) [12].

Considering Table 1, the proposed method presents high accuracy for the reconstruction of the stenosed and the stented coronary vessel. Obviously, expansion of the lumen

**Fig. 2** Forward projection of the 3D models onto: **a** the first CA view, **b** the second CA view

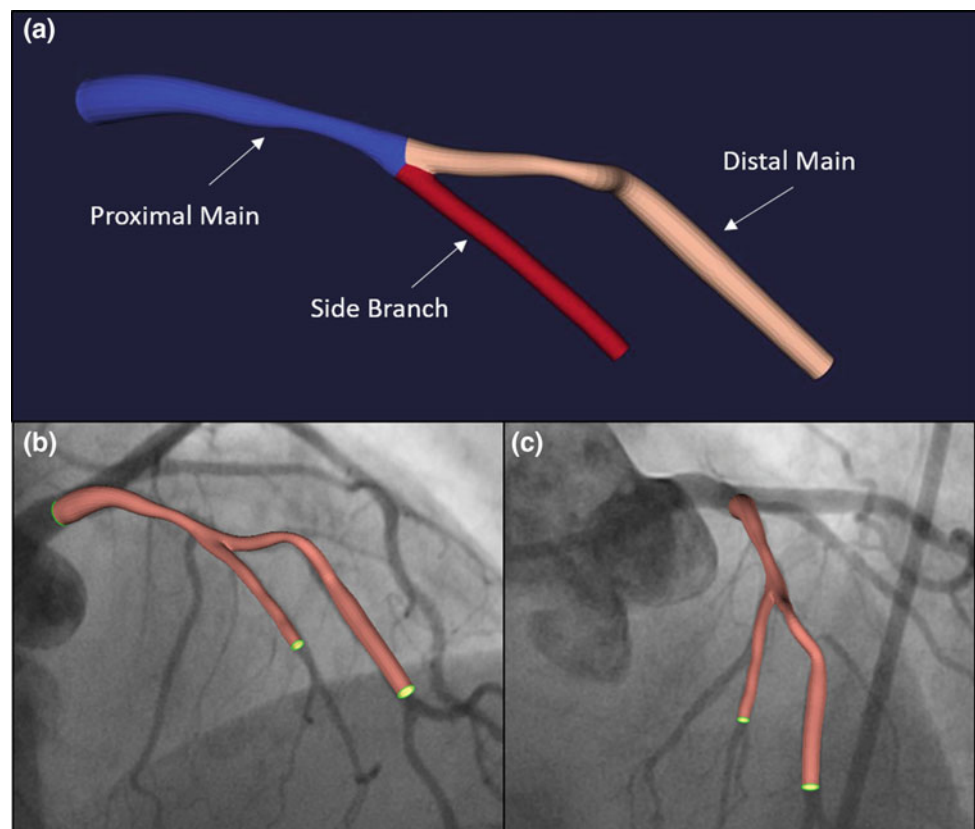




**Table 1** Comparison of the 3D model with the CA using lumen diameter-based measurements

	N = 7							
	Pre-procedure				Post-procedure			
	2D QCA (mm)	3D QCA (mm)	r	p	2D QCA (mm)	3D QCA (mm)	r	p
<i>Proximal main</i>								
RVD (mm)	3.39 ± 0.61	3.40 ± 0.55	0.99	<0.001	3.72 ± 0.64	3.69 ± 0.59	0.99	<0.001
MLD (mm)	2.77 ± 0.61	2.82 ± 0.68	0.98	<0.001	3.21 ± 0.42	3.19 ± 0.31	0.89	0.008
DS (%)	18 ± 14	17 ± 15	0.96	0.001	13 ± 8	13 ± 7	0.83	0.019
LL (mm)	7.45 ± 3.52	8.97 ± 5.59	0.87	0.012	9.59 ± 4.01	11.04 ± 4.87	0.92	0.004
<i>Distal main</i>								
RVD (mm)	2.66 ± 0.34	2.64 ± 0.34	0.99	<0.001	2.74 ± 0.51	2.76 ± 0.54	0.99	<0.001
MLD (mm)	1.36 ± 0.65	1.48 ± 0.63	0.92	0.003	2.04 ± 0.63	2.16 ± 0.62	0.99	<0.001
DS (%)	49 ± 22	44 ± 22	0.86	0.013	27 ± 12	23 ± 11	0.97	<0.001
LL (mm)	11.96 ± 4.29	13.52 ± 4.76	0.76	0.047	13.77 ± 5.02	15.95 ± 4.48	0.83	0.021
<i>Side branch</i>								
RVD (mm)	2.32 ± 0.47	2.39 ± 0.55	0.97	<0.001	2.48 ± 0.43	2.34 ± 0.37	0.97	<0.001
MLD (mm)	1.56 ± 0.64	1.80 ± 0.70	0.95	0.001	1.94 ± 0.53	1.94 ± 0.56	0.96	0.001
DS (%)	34 ± 25	26 ± 24	0.97	<0.001	23 ± 10	20 ± 8	0.82	0.022
LL (mm)	11.63 ± 2.40	12.83 ± 2.06	0.73	0.159	13.42 ± 6.74	15.87 ± 6.91	0.97	<0.001

**Table 2** Comparison of the 2D model borders and the CA

	View 1		View 2	
	HD (mm)	DC (%)	HD (mm)	DC (%)
1	0.0900	97.55	0.3499	87.61
2	0.1896	93.45	0.1263	97.87
3	0.1088	95.15	0.1683	95.57
4	0.1174	97.18	0.0846	98.56
5	0.0709	98.45	0.4752	78.59
6	0.0777	97.91	0.5008	79.85
7	0.4263	94.62	0.2398	91.86
8	0.3853	94.31	0.0931	97.06
9	1.0771	74.72	0.2222	95.34
10	0.3196	95.33	0.1508	97.31
11	0.8788	77.37	0.0787	98.77
12	0.2847	93.98	0.0984	96.24
13	0.0841	98.02	1.2583	80.15
14	0.1325	96.63	0.4972	87.94

diameter is observed in the vessels after the angioplasty procedure, especially the Proximal Main branch.

Furthermore, the comparison between the 2D annotated lumen borders and the retrieved 2D model borders is depicted in Table 2. Taking into account totally 14 coronaries arteries, the Dice Coefficient between the retrieved 2D borders of the models and the annotated lumen borders is 91% for the first angiographic projection and 92% for the second one, while the Hausdorff Distance between them is 0.3031 mm and 0.3103 mm, respectively.

## 4 Discussion

In this study, we proposed a novel methodology for the 3D reconstruction of coronary bifurcated arteries from X-ray Angiographies (3D QCA) while other studies address only with the coronary segments, neglecting the impact of the side branch in the coronary bifurcation anatomy. To provide a proof of concept, we reconstructed seven coronary bifurcation arteries both a priori and a posteriori of the



PTCI procedure while the evaluation of the proposed method was performed considering the X-ray angiography as the “gold standard”. Moreover, the results show that the 3D model can be reconstructed into the 3D space with a decent accuracy.

Regarding the pros and cons of the proposed method, 3D QCA is a quick and accurate method to assess the CAD into the 3D space, but limited visualization of the coronary branches on the CA projections as well as confined angle offset between the angiographic views, potentially leads to failed reconstruction.

## 5 Conclusions

Nowadays, both the accurate diagnosis of the CAD and the prediction of the plaque growth, are based on the representation of the coronary arteries in the 3D space. In this work we proposed a study for the 3D reconstruction of the coronary bifurcated arteries. Nevertheless, in the future the number of the required angiographic views for the reconstruction of the coronary tree must be addressed.

**Acknowledgements** This work is part-funded by the European Commission. SMARTool simulation modelling in coronary artery disease: a tool for clinical decision support. GA 689068

**Conflict of Interest** The authors declare that they have no conflict of interest.

## References

1. D. B. Mark, D. S. Berman, M. J. Budoff, J. J. Carr, T. C. Gerber, H. S. Hecht, *et al.*, “ACCF/ACR/AHA/NASCI/SAIP/SCAI/SCCT 2010 expert consensus document on coronary computed tomographic angiography,” *Catheterization and Cardiovascular Interventions*, vol. 76, 2010.
2. N. E. Green, S. Y. J. Chen, A. R. Hansgen, J. C. Messenger, B. M. Groves, and J. D. Carroll, “Angiographic views used for percutaneous coronary interventions: A three-dimensional analysis of physician-determined vs. computer-generated views,” *Catheterization and Cardiovascular Interventions*, vol. 64, pp. 451–459, 2005.
3. C. V. Bourantas, F. A. Jaffer, F. J. Gijssen, G. Van Soest, S. P. Madden, B. K. Courtney, *et al.*, “Hybrid intravascular imaging: recent advances, technical considerations, and current applications in the study of plaque pathophysiology,” *European heart journal*, vol. 38, pp. 400–412, 2016.
4. K. Toutouzas, Y. S. Chatzizisis, M. Riga, A. Giannopoulos, A. P. Antoniadis, S. Tu, *et al.*, “Accurate and reproducible reconstruction of coronary arteries and endothelial shear stress calculation using 3D OCT: comparative study to 3D IVUS and 3D QCA,” *Atherosclerosis*, vol. 240, pp. 510–519, 2015.
5. I. O. Andrikos, A. I. Sakellarios, P. K. Siogkas, G. Rigas, T. P. Exarchos, L. S. Athanasiou, *et al.*, “A novel hybrid approach for reconstruction of coronary bifurcations using angiography and OCT,” in *Engineering in Medicine and Biology Society (EMBC), 2017 39th Annual International Conference of the IEEE*, 2017, pp. 588–591.
6. L. Husmann, S. Leschka, L. Desbiolles, T. Schepis, O. Gaemperli, B. Seifert, *et al.*, “Coronary artery motion and cardiac phases: dependency on heart rate—implications for CT image reconstruction,” *Radiology*, vol. 245, pp. 567–576, 2007.
7. S. Çimen, A. Gooya, M. Grass, and A. F. Frangi, “Reconstruction of coronary arteries from X-ray angiography: A review,” *Medical image analysis*, vol. 32, pp. 46–68, 2016.
8. J. A. Sethian, “Fast marching methods,” *SIAM review*, vol. 41, pp. 199–235, 1999.
9. M. T. Dehkordi, S. Sadri, and A. Doosthoseini, “A review of coronary vessel segmentation algorithms,” *Journal of medical signals and sensors*, vol. 1, p. 49, 2011.
10. C. V. Bourantas, I. C. Kourtis, M. E. Plissiti, D. I. Fotiadis, C. S. Katsouras, M. I. Papafaklis, *et al.*, “A method for 3D reconstruction of coronary arteries using biplane angiography and intravascular ultrasound images,” *Computerized Medical Imaging and Graphics*, vol. 29, pp. 597–606, 2005.
11. A. A. Taha and A. Hanbury, “Metrics for evaluating 3D medical image segmentation: analysis, selection, and tool,” *BMC medical imaging*, vol. 15, p. 29, 2015.
12. P. Garrone, G. BIONDI-ZOCCAI, I. Salvetti, N. Sina, I. Sheiban, P. R. Stella, *et al.*, “Quantitative coronary angiography in the current era: principles and applications,” *Journal of interventional cardiology*, vol. 22, pp. 527–536, 2009.

# Machine Learning Techniques for Classification of Breast Cancer

Ahmed Osmanović, Sabina Halilović, Layla Abdel Ilah, Adnan Fojnica, and Zehra Gromilić

## Abstract

The major challenge in cancer diagnosis is the number of patients who are incorrectly diagnosed. To address this, we have developed and tested different expert diagnostic systems which differentiate among patients with and without breast cancer based on samples describing characteristics of the cell nuclei present in the digitized image of a fine needle aspirate (FNA). Data was collected from the UCI machine learning respiratory, specifically 699 samples. Our results demonstrate that a Feed Forward Backpropagation single hidden layer neural network with 20 neurons and TANSIG transfer function has the highest classification accuracy (98.9% and 99% accuracy in training and test set, respectively). The accuracy of multilayer architectures was significantly lower, and valued between a range of 74.9–86.3%, where the average was 81.37%. A developed expert system with a proven accuracy can be used in the future in laboratory conditions as a promising method for early classification diagnosis for breast cancer.

## Keywords

Breast cancer • Classification • Machine learning  
Artificial Neural Network

## 1 Introduction

According to the American Cancer Society (ACS), breast cancer makes up 25% of cancer diagnoses in women globally [1]. Breast cancer tumors can be categorized into two main groups: (i) Benign (Noncancerous), whereby the

immune system segregates benign tumors from normal cells, (ii) Malignant (Cancerous), which initiate from abnormal cell growth and invade nearby tissue. Identification of normal, benign, and malignant tissues is crucial for treatment [2, 3].

Innovative techniques have been used in various areas of healthcare [4–11], specifically for classification and detection of disease. Artificial Neural Networks (ANNs) are termed as a ‘hot’ research area in medicine due to increasing diagnostic accuracy, reduced costs and human resources. ANNs are integrate systems inspired by biological neuron networks. In machine learning and cognitive sciences, these networks estimate functions depending on inputs [12]. Researchers are currently using various algorithms to investigate breast images depending on the demand of the disease, the status of the disease, and the quality of the images [2]. Santos-Andre and da Silva [13] choreographed an ANN for the analysis of mammograms for diagnosis of breast cancer. The system uses Kohonen’s self-organizing map and a multilayer perceptron trained with the back-propagation algorithm. In 2005, Revett et al. [14] presented a breast cancer diagnosis system with a probabilistic neural network that performed supervised classification. In a comparative study conducted by Padmavati [15], a supervised feed forward neural network with one hidden layer was implemented using a Radial Basis Function (RBF) neural network. Additionally, the author of this study compared the performance of the RBF neural network with the Multilayer Perceptron network model.

This research was developed to design an ANN with a high level of accuracy to be applied for early breast cancer detection, thus provoking earlier diagnosis, treatment, and survival in cancer diagnosed patients. Differentiating among cytological attributes of the breast mass, medical analysis has been speeded up, while labor intensive data analysis simplified. Developed ANN not just help medical analysis with earlier detection, but also reduces costs and human resources required in diagnostics.

A. Osmanović (✉) · S. Halilović · L. A. Ilah  
International Burch University, Sarajevo, Bosnia and Herzegovina  
e-mail: ahmed\_osmanovic@hotmail.com

A. Fojnica · Z. Gromilić  
Biotechnology, Graz University of Technology, Graz, Austria

## 2 Methods

A data set was obtained from UCI Machine Learning Repository [16] containing 699 samples describing characteristics of the cell nuclei present in a digitized image of a fine needle aspirate (FNA) of a breast mass. Each sample contained nine attributes representing cytological characteristics of breast fine-needle aspirates. Characteristics are represented in Table 1.

The data set was partitioned into two sets: training and testing with a ratio of 70–30, which was assigned according to expert recommendation [17]. The training set contained 490 samples (161 malignant and 329 benign samples), while the test set contained 209 samples (80 malignant and 129 benign samples). The data set divisions are shown in Table 2.

Samples obtained from the dataset, all features were extracted and divided in training and test set. Then the artificial neural network was designed, trained and tested.

Obtained results were compared with the given diagnosis. Finally, accuracy was calculated and discussed.

The ANN within this study was configured with nine input neurons (number of attributes) and one output neuron (benign or malignant). Trial and error was used by changing three parameters: number of layers, number of neurons in hidden layers and transfer functions, to compare the performance of different ANN architectures (as seen in Fig. 1 with the Results section). The number of neurons within the hidden layer was 10, 20, 30, 40 and 50. The number of hidden layers was 1, 2, 3, 4, and 5. The transfer functions were: TANSIG, LOGSIG, and PURELINE. The performance received from these systems were compared and are depicted in Table 3. After changing parameters, the optimal classifiers were identified and employed for network architecture comparison. To investigate optimal ANN architecture for breast cancer classification, morphological data was applied to four types of neural network and their performance was compared. The trained networks were Feed Forward Back propagation network (BPA), Radial Basis Function (RBF), Multilayer perceptron (MLP), and Probabilistic neural network (PNN). Performance obtained was compared in terms of training and test design, and a

**Table 1** Attributes representing cytological characteristics of breast FNAs

S. No	Attribute	Explanation
1	Clump thickness	Cancerous cells (CC) are organised in multilayers
2	Uniformity of cell size	CC have mismatched sizes
3	Uniformity of cell shape	CC are misformed
4	Marginal adhesion	CC lose the ability to attach together
5	Single epithelial cell size	CC affect glandular tissue formation
6	Bare nuclei	Benign tumors have a nuclei that is not surrounded by a cytoplasm
7	Bland chromatin	CC have coarse chromatin
8	Normal nucleoli	CC contain abnormal nucleoli
9	Mitoses	CC have uncontrollable levels of mitoses
	Class	2 for benign, 4 for malignant

**Table 2** Divisions of morphological features of data sets

Total cases = 699		
Data set	Training	Testing
Benign	329	129
Malignant	161	80
Total	490	209

**Table 3** Accuracies of tested parameters in independent experiments. Testing of different number of hidden layers (1, 2, 3, 4, 5), different number of neurons in hidden layer (10, 20, 30, 40, 50) and different types of transfer function (TANSIG, LOGSIG, and PURELINE)

Number of hidden layers	Accuracy %	Number of neurons	Accuracy %	Training algorithm	MSE
1	86.5	10	92.8	TANSIG	0.0002
2	74.9	20	99.5	LOGSIG	0.0121
3	81.3	30	91.6	PURELINE	0.0056
4	86.3	40	93.1		
5	82.98	50	96.2		

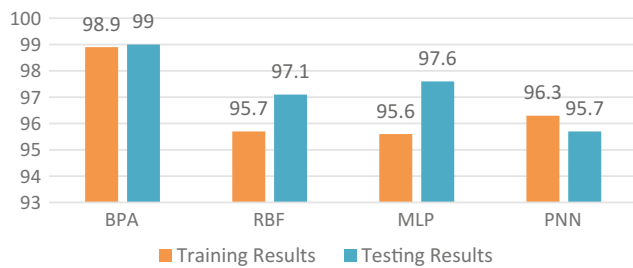


**Fig. 1** Performance comparison of all neural network models for classification of breast cancer

confusion matrix was designed for the highest performing architecture.

### 3 Results and Discussion

It was found that one hidden layer network achieved the highest accuracy (86.5%), whereas a two layers network achieved the lowest accuracy (74.9%). The accuracy of multi-layer architectures was significantly lower and valued across a range of 74.9–86.3%. The average was 81.37%. Single layer architectures performed with a mean accuracy of 86.5%.

According to previous research [18], a multi-layer network has higher accuracy than a single layer network despite data set size. Number of hidden layers and data division are not defined in their research; however, they are defined in our work. It is shown in Table 2 that increasing the number of hidden layers from 1 to 2 or from 4 to 5 decreases the accuracy, while increasing it from 2 to 3 or from 3 to 4 increases the accuracy. It is concluded that increasing or decreasing the hidden layer number by one does not correlate to a higher accuracy.

Accuracy of a network with one hidden layer and 10, 20, 30, 40, and 50 neurons respectively in the hidden layer are presented in Table 3. The 20 neurons network achieves the highest accuracy (99.5%), whereas the 40 neurons network has the lowest accuracy (93.1%). These results indicate a 99.5% chance that by using this artificial neural network, patients will be diagnosed with this condition (Table 3). A poorly defined number of neurons in a hidden layer can

cause over fitting problems, which leads to a poor training performance and an insufficient testing performance. Mean Square Error (MSE) of a network with three different transfer functions: TANSIG, LOGSIG, and PURELINE are presented in Table 3. It was found that the network with TANSIG algorithm achieves the least MSE (0.0002), whereas the network with LOGSIG has the highest MSE (0.0121). Similar results were obtained in previous research [19]. It is evident that the best network architecture is a network with one hidden layer, 20 neurons in the hidden layer, and TANSIG as an activation function. In previous neural network-based cancer examination has been demonstrated that a single hidden layer, usually provides the best compromise in terms of accurate results in a specific context, but also allowing generalization required for classification of cancer [20].

Accuracy of networks are presented in Fig. 1 for both training and test sets. It was found that the Backpropagation network achieves the highest accuracy in both training (98.9%) and test sets (99%). The Radial Basis network has the lowest accuracy in training (95.4%), and the Probabilistic network has the lowest accuracy in the test set (95.7%).

Table 4 represents a confusion matrix designed for the Backpropagation network. These results indicate that there is 99% chance that by using this artificial neural network, a patient will be diagnosed correctly. Percentage of true positive rate or sensitivity demonstrates accuracy in terms that benign breast cancer patients will not be classified as malignant breast cancer patients. Specificity percentage indicates that when benign breast cancer patients are tested with this network, there is a 97.6% chance that they will be negatively classified. In fact, previous research recommends a Feed Forward Backpropagation network as a strong tool for classification purposes [21].

Number of hidden layers, number of neurons in the hidden layers, architecture type, and transfer function type are parameters that effect ANN performance. Other parameters are not discussed here such as training time, adoption learning function, performance function, and training function. Designing an ANN requires considering the parameters discussed above. Concentrating on one parameter, like in [8–10], limits the network accuracy in breast cancer classification.

**Table 4** Confusion matrix of BPN ANN models for testing dataset

Testing sample n = 209	Classified benign breast cancer	Classified malignant breast cancer	Accuracy (AC) 99%
Actual benign breast cancer	80	2	True positive rate (TPR) or sensitivity 100%
Actual malignant breast cancer	0	127	True negative rate (TNR) or specificity 97.6%

## 4 Conclusion

Knowing that there is a lack of generalized neural network system with zero mistakes for any application, an ANN with a high and acceptable level of accuracy can be designed by testing different number of hidden layers, number of neurons in the hidden layer, the type of transfer functions, and the architecture type. The ANN as a tool in diagnosis of breast cancer can further be improved to expand its application. It can be used as a background in developing a device that could help doctors in more rapid diagnostics and monitoring of patient's condition. Additionally, with modification of the network and further development, the system could even provide adequate therapy for breast cancer. For the use of this implemented ANN by the physicians, in the future authors will also develop Graphical User Interface (GUI) [6].

**Declaration of Interest** The authors have no conflict of interest to declare.

## References

- Schneider, A. P., Zainer, C. M., Kubat, C. K., Mullen, N. K., & Windisch, A. K. (2014). The breast cancer epidemic: 10 facts. *The Linacre Quarterly*, 81(3), 244–277.
- Al-Hajj, M., Wicha, M. S., Benito-Hernandez, A., Morrison, S. J., & Clarke, M. F. (2003). Prospective identification of tumorigenic breast cancer cells. *Proceedings of the National Academy of Sciences*, 100(7), 3983–3988.
- Simm, H. P., & Kreipe, H. (2013). A brief overview of the WHO classification of breast tumors. *Breast Care*, 8(2), 149–154.
- Osmanović, A., Abdel-Ilah, L., Hodžić, A., Kevric, J., & Fojnica, A. (2017). Ovary Cancer Detection using Decision Tree Classifiers based on Historical Data of Ovary Cancer Patients. In *CMBEBIH 2017* (pp. 503–510). Springer, Singapore.
- Bušatlić, E., Osmanović, A., Jakupović, A., Nuhic, J., & Hodžić, A. (2017). Using Neural Networks and Ensemble Techniques based on Decision Trees for Skin Permeability Prediction. In *CMBEBIH 2017* (pp. 41–50). Springer, Singapore.
- Fojnica, A., Osmanović, A., & Badnjević, A. (2016, June). Dynamical model of Tuberculosis-Multiple Strain Prediction based on artificial neural network. In *Embedded Computing (MECO), 2016 5th Mediterranean Conference on* (pp. 290–293). IEEE.
- Alić, B., Gurbeta, L., & Badnjević, A. (2017, June). Machine learning techniques for classification of diabetes and cardiovascular diseases. In *Embedded Computing (MECO), 2017 6th Mediterranean Conference on* (pp. 1–4). IEEE.
- Badnjevic A., Cifrek M., Gurbeta L., Feric E., “Classification of Chronic Obstructive Pulmonary Diseases Based on Neuro-Fuzzy Software” in the Book: “Chronic Obstructive Pulmonary Disease (COPD): Clinical Symptoms, Emerging Treatment Strategies and Impact on Quality of Life”, 2016, Nova Science Publisher, ISBN: 978-1-63484-500-7, 2016.
- Alic B, Sejdinovic D, Gurbeta L, Badnjevic A, “Classification of Stress Recognition using Artificial Neural Network”, *IEEE 5th Mediterranean Conference on Embedded Computing (MECO)*, 12–16 June 2016, Bar, Montenegro.
- Halilovic S, Avdihodžić H, Gurbeta L, (2016) Micro cell culture analog Apparatus ( $\mu$ CCA) output prediction using Artificial Neural Network, *5th Mediterranean Conference on Embedded Computing (IEEE MECO 2016)*, Bar, Montenegro;
- Fojnica, A., Osmanović, A., Tarakčija, D., & Demirović, S. (2017). Quantification of protein concentration adsorbed on gold nanoparticles using Artificial Neural Network. In *CMBEBIH 2017* (pp. 142–146). Springer, Singapore.
- Lamamra, K., Vaidyanathan, S., Azar, A. T., & Salah, C. B. (2017). Chaotic System Modelling Using a Neural Network with Optimized Structure. In *Fractional Order Control and Synchronization of Chaotic Systems* (pp. 833–856). *Springer International Publishing*.
- Santos-Andre, T. C., & da Silva, A. C. R. (1999). A neural network made of a Kohonen's SOM coupled to a MLP trained via backpropagation for the diagnosis of malignant breast cancer from digital mammograms. In *Neural Networks, 1999. IJCNN'99. International Joint Conference on* (Vol. 5, pp. 3647–3650). IEEE.
- Revett, K., Gorunescu, F., Gorunescu, M., El-Darzi, E., & Ene, M. (2005, November). A breast cancer diagnosis system: a combined approach using rough sets and probabilistic neural networks. In *Computer as a Tool, 2005. EUROCON 2005. The International Conference on* (Vol. 2, pp. 1124–1127). IEEE.
- Padmavati, J. (2011). A comparative study on breast cancer prediction using RBF and MLP. *International Journal of Scientific & Engineering Research*, 2(1), 1–5.
- Asuncion, A., & Newman, D. (2007). UCI machine learning repository.
- Shahin, M. A., Maier, H. R., & Jaksa, M. B. (2004). Data division for developing neural networks applied to geotechnical engineering. *Journal of Computing in Civil Engineering*, 18(2), 105–114.
- Rani, K. U. (2010). Parallel approach for diagnosis of breast cancer using neural network technique. *International Journal of Computer Applications*, 10(3), 1–5.
- Abdel-Ilah, L., & Šahinbegović, H. (2017). Using machine learning tool in classification of breast cancer. In *CMBEBIH 2017* (pp. 3–8). Springer, Singapore.
- Taktak, A. F., & Fisher, A. C. (Eds.). (2006). *Outcome prediction in cancer*. Elsevier.
- Swathi, S., Rizwana, S., Babu, G. A., Kumar, P. S., & Sarma, P. V. G. K. (2012). Classification of Neural Network Structures for Breast Cancer Diagnosis. *International Journal of Computer Science and Communication*, 3(1), 227–231.



# Segmentation and 3D-Modelling of Single-Rooted Teeth from CBCT Data: An Automatic Strategy Based on Dental Pulp Segmentation and Surface Deformation

Jerome Harrison, Steeve Chantrel, Matthieu Schmittbuhl, and Jacques A. de Guise

## Abstract

Individual three-dimensional (3D) models of the teeth obtained from Cone Beam Computed Tomography (CBCT) images are needed in orthodontics and maxillofacial surgery for treatment planning and simulation purposes. Such models can be obtained with the help of segmentation algorithms. In order to comply with clinical needs, the segmentation process should not rely on human intervention, while providing reliable patient-specific models. In this research, a fully automatic segmentation method based on surface deformation of in situ reconstructed models of dental pulps is proposed. A volume partitioning step defines separating planes between each tooth on both superior and inferior dental arches. A pulp segmentation strategy followed by a hierarchical surface deformation scheme, allows surface evolution until the tooth boundary is reached. Accuracy of the method is assessed by comparison of 26 single-rooted teeth randomly selected in 9 Cone Beam CT scans with ground truths obtained from manual segmentation. Experimental results show a Dice Similarity Coefficient of  $92.19 \pm 2.31\%$ , a Jaccard Similarity Coefficient of  $85.59 \pm 3.89\%$ , an Hausdorff distance of  $1.54 \pm 0.52$  mm, and an average symmetric surface distance of  $0.24 \pm 0.05$  mm.

## Keywords

In situ prior • Tooth segmentation • Dental CBCT

## 1 Introduction

Cone Beam Computed Tomography (CBCT) is a widely used imaging approach in dentomaxillofacial radiology. The success of this modality relies on the production of images of higher spatial resolution while greatly reducing exposure to radiation when compared to medical CT scan [1]. CBCT is thus not only of clinical importance for diagnosis but it facilitates image guided surgery and treatment planning [2]. Individual three-dimensional (3D) models of the teeth obtained from CBCT images could be valuable tools for accurate treatment planning in maxillofacial surgery and orthodontics [3]. Tooth segmentation is an essential step in reconstructing a 3D model but it remains a challenge mainly due to the complex morphology of teeth, the similar intensity of the alveolar bone compared to the dental tissue, and the lack of contrast accuracy of CBCT images [4]. Consequently, borders between touching structures such as adjacent crowns or root and contiguous alveolar bone are often indistinguishable.

Many methods have been proposed in the literature for tooth segmentation. Most of them are active-contour based, and employ level-sets with different custom-made priors and constraints [5–7]. These methods rely on slice-by-slice contour propagation, which is prone to error accumulation. In recent years, other methods have integrated additional 3D models in order to perform a more reliable segmentation. For example, in [8–10], optical scans of dental casts were used for crown segmentation, and merged with 3D models of corresponding roots obtained by segmentation on CT scans. The above works rely on previously collected data that can exacerbate clinical workflow or data processing. Moreover, prior-shape model driven segmentation approaches often lack generalizability and require large databases in order to capture variability.

In this research, a fully automatic strategy for single-rooted tooth segmentation is introduced. The main contribution of this work lies in two aspects: first, a surface

J. Harrison (✉) · J. A. de Guise  
École de Technologie Supérieure, Montréal, QC, Canada  
e-mail: jerome.harrison.1@ens.etsmtl.ca

J. Harrison · S. Chantrel · M. Schmittbuhl · J. A. de Guise  
Imaging and Orthopaedics Research Laboratory, CHUM Research Center, Montréal, QC, Canada

M. Schmittbuhl  
Faculté de Médecine Dentaire, Université de Montréal, Montréal, QC, Canada



deformation algorithm, constrained by the shape of dental pulp models reconstructed in situ, is applied to CBCT images for three-dimensional segmentation; second, a volume partitioning strategy is proposed to achieve a rough delineation of single tooth sub-volumes, while restraining surface evolution around dental contact zones. Segmentation accuracy and efficiency are assessed by quantitative comparison with manually delineated ground truths.

## 2 Methods

The segmentation workflow takes advantage of heuristics derived from knowledge of tooth anatomy. While touching teeth remain a challenging segmentation task, their respective dental pulp can be straightforwardly obtained. On CBCT images, they appear as darker structures enclosed in brighter shells (dentine or enamel). As reported in [11], this inner shape is morphologically similar to the outer tooth structure, while encompassing information such as orientation and localization. Thus, in this study, dental pulps are used as pre-personalized models, and help supervise three-dimensional segmentation. A volume partitioning step, which defines single tooth sub-volumes inside the original DICOM space, is used as means to avoid over-segmentation at crown level. Both steps are described in the following sections.

### 2.1 Volume Partitioning

**Dental arches separation.** A first partition step aims to isolate inferior and superior dental arches. In the scope of this study, it is assumed that CBCT acquisitions were performed with patients' teeth in an open bite position. Therefore, maxillary and mandible teeth do not overlap in any slice.

An empirically determined global threshold is applied on a sagittal Maximal Intensity Projection (MIP) of the original DICOM stack in order to separate crown intensities of lower and upper jawbones. A blob detector applies a different label

to both regions, and the spatial position of these labels is used to train a  $k$  nearest neighbour classifier (see Fig. 1a). The classification algorithm is applied to every point of the region of interest, providing a boundary that can be generalized to the entire three-dimensional volume.

**Teeth separation planes.** A second partition step, applied separately on both arches, is designed to find a set of planes that best describe the boundary between each tooth.

The same empirically determined global threshold is used on an axial MIP, in order to obtain crown intensities from which the shape of both arches are approximated. A second order polynomial curve is interpolated from a sub-sample of these data points. Positions along the curves are encoded as  $i \in (0, \dots, N_i)$ .

Candidate planes are placed along the curve at a uniform distribution rate. An intensity and gradient-based [12] cost function  $C_{plane}$ , that determines optimal positions for each plane, is introduced in Eq. 1. To assess the likelihood of correct positioning, plane configurations are simulated by rotating each candidate plane along the x-axis and y-axis, respectively represented by rotation angles  $\phi_1$  and  $\phi_2$ .

$$C_{plane}(P_{i,\phi_1,\phi_2}) = \alpha \frac{1}{N_p} \sum_{n=0}^{N_p} I(\vec{p}_u) + \beta \sum_{n=0}^{N_p} I(\vec{p}_u) \left| \frac{\nabla I(\vec{p}_u)}{I(\vec{p}_u)} \times \vec{n} \right| \quad (1)$$

where  $P_{i,\phi_1,\phi_2}$  is a solution plane,  $\vec{n}$  is the plane's normal vector,  $\vec{p}_u$ ,  $u \in (0, \dots, N_p)$ , is a sample point located on the plane's surface,  $I(\vec{p}_u)$  and  $\nabla I(\vec{p}_u)$  are the respective grayscale and gradient value interpolated at the sample point. Weighting coefficients  $\alpha$  and  $\beta$  are applied to both terms. The cost function is evaluated for each combination of  $(i, \phi_1, \phi_2)$ .

The minimal cost value at every position  $i$  along the central arch curve is stored as  $C_{plane}(P'_i)$ . Local minima  $i_{loc}$  are identified on the latter curve to reveal potential location of teeth boundaries (Eq. 2). Indeed, these locations have a

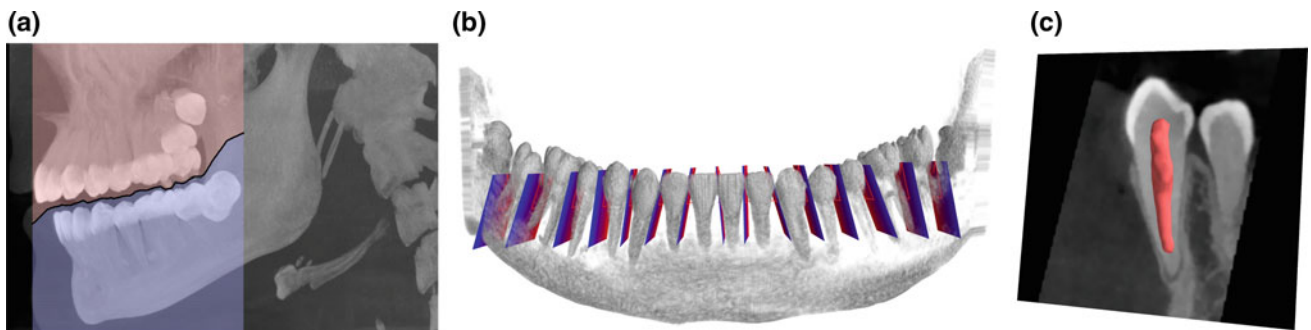


**Fig. 1** Volume partition steps. **a** Superior and inferior dental arches are separated by a boundary line obtained from a  $k$ -nn classification algorithm. **b** A directed graph-based strategy finds a set of separating

planes that best describe the boundary between each tooth. Mandible has been unrolled around its arch central curve for display purposes. **c** Dental pulp segmentation is carried out on single tooth sub-volumes

significantly lower cost than their neighbours, which indicates that they are very unlikely to be cutting through high-density bony structures.

$$\{i_{loc}\} \subseteq i \quad \text{s.t.} \quad C_{plane}(P'_j) \quad \forall \quad P'_j \in D_{i_{loc}} \quad (2)$$

where  $D_{i_{loc}}$  represents the local neighbourhood of  $i_{loc}$ .

In order to avoid identification of false boundaries (e.g. local minima representing a cutting plane that goes through low density dental pulps), each potential local minima is represented by a node  $\mathcal{N}$  in a directed graph  $G = (\mathcal{N}, \Sigma)$ . Possible combinations of local minima are connected by a set of edges  $\Sigma$ , which are then weighted by their associated plane cost. Connections are determined by a distance rule: two consecutive local minima (i.e. planes) must have a relative distance  $d$  that lie within a fixed interval  $d \in [d_{min}, d_{max}]$  which is derived from manual measurements. A legal combination of local minima, thus a legal combination of planes, would link  $P'_0$  to  $P'_{N_i}$ , and provide the lowest cost. A shortest path algorithm is applied on the graph and provides the optimal set of local minima (see Fig. 1b):

$$\{P'_{i_{loc}}\} = \underset{k=0}{\operatorname{argmin}} \sum_{k=0}^M C_{plane}(P'_{i_{loc}}) \quad \text{s.t.} \quad (P'_{i_{loc}}, P'_{i_{loc}+1}) \in \Sigma \quad (3)$$

where  $M$  denotes the number of identified planes (typically 15 for a complete dentition). Single-tooth sub-volumes can be extracted by limiting the information contained in the CBCT sequence to the voxels lying between two consecutive separating planes.

## 2.2 Three-Dimensional Segmentation

**Dental pulp segmentation.** On CBCT images, dental pulps appear as dark cavities enclosed in brighter shells. This phenomenon is employed to automatically isolate dental pulp [11] and proceed to surface reconstruction. The strategy

is based on morphological image reconstruction which consists of sequential morphological dilation operations on a marker  $F$ , based on information included in a mask  $G$ . This operation is notated  $R_G(F)$ . As dental pulps resemble holes in the image, a hole-filling algorithm  $H$  is used on each slice of the sub-volumes [11].

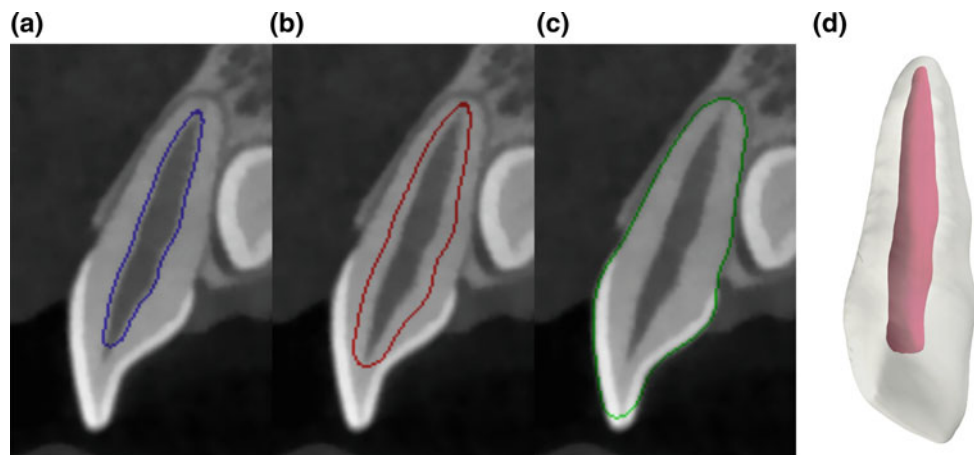
$$I^F = H(I) = [R_{I^c}(F)]^c \quad (4)$$

where  $I$  is the slice and  $I^c$  the complement of image  $I$ . The marker  $F$  consists of an image with pixel values set to 0, except for those on the border which are set to  $1 - I$ . This operation creates an image  $I^F$  on which zones of low-intensity pixels enclosed inside zones of high-intensity pixels, such as dental pulp, appear as filled. A simple voxel-wise subtraction of  $I^F$  with the original slice  $I$  produces an image of the dental pulp alone. A three dimensional application of this algorithm provides a set of voxels that represent the shape of dental pulp (see Fig. 1c).

**Hierarchical surface deformation.** In this step, a mesh representation of each pulp is iteratively deformed with a Hierarchical Surface Deformation (HSD) algorithm [13]. In this scheme, vertices of the input mesh are moved toward a target boundary, which is identified through an intensity profile search. The search is initially conducted in large areas outside the mesh, and is gradually reduced at each iteration. Large search areas increase the risk of false boundary identification. Thus, HSD carries out a rigid-to-flexible process: first iterations are constrained by the general shape of the input mesh, while last iterations allow local deformations to fit teeth boundaries. The HSD process stops after a given number of iterations  $N^{iter}$ . The output mesh of the last iteration provides the final tooth segmentation (see Fig. 2). The following computation steps are carried out iteratively:

**A. Vertex matching.** Every vertex  $v_i$  of the input mesh is matched to the position of a potential characteristic of interest  $g_i$  around the surface. Intensity profiles  $P(u, v)$  are

**Fig. 2** HSD process. From an in situ reconstructed surface model of the dental pulp (a), HSD performs iterative local deformation (b) until the surface matches the boundary of the teeth (c). A 3D surface of the teeth is then obtained (d)



interpolated along the normal  $\vec{n}_v$  of each vertex through a mapping function  $M$ :

$$\begin{aligned} P(u, v) &= \Omega(M_x, M_y, M_z) \\ &= \Omega(n_{v_x} \cdot u^T + v_x, n_{v_y} \cdot u^T + v_y, n_{v_z} \cdot u^T + v_z) \end{aligned} \quad (5)$$

where  $u = [-L^{iter}, \dots, L^{iter}]$  is the profile length at the current iteration, and  $\Omega$  a linear interpolation method. Parameter  $L^{iter}$  is gradually decreased at each iteration to allow coarse-to-fine deformation. In the initial implementation, [13] centers the profile at vertex location. For this specific purpose, profiles are defined from the surface outward for the first iteration, and are moved toward a centered position to ensure that the surface is evolving toward the outer tooth boundary. A gradient and Gaussian-based cost function determines the position of  $g_i$  along the profile.

**B. Weighted average displacement.** Each vertex is matched to a set of neighbours  $S_i$ , according to a distance parameter  $R^{iter}$ . This parameter decreases at every iteration to allow rigid-to-flexible deformation. Neighbouring vertices contribute to the calculation of the final displacement of each vertex:

$$v'_i = v_i + \frac{\sum_{v_k \in S_i} \omega_k (g_i - v_i)}{\sum_{v_k \in S_i} \omega_k} \quad \text{with} \quad \omega_k = \frac{R^{iter} - d(v_i, v_k)}{R^{iter}} \quad (6)$$

where  $d(v_i, v_k)$  is the distance between vertex  $v_i$  and  $v_k$ .

Even though deformation is constrained by the shape of the input mesh, over-segmentation can still take place where adjacent crowns touch. This issue is addressed ad hoc by penalizing the set of points of an intensity profile that cross a separation plane. Such points are considered as invalid for gradient search. This eliminates the risk of a vertex being moved on the other side of a separation plane. The invalid points must satisfy the following criteria to be excluded:

$$a'_{i_{loc}} \cdot M_x + b'_{i_{loc}} \cdot M_y + c'_{i_{loc}} \cdot M_z - d'_{i_{loc}} > 0 \quad (7)$$

where  $a'_{i_{loc}}$ ,  $b'_{i_{loc}}$ ,  $c'_{i_{loc}}$  and  $d'_{i_{loc}}$  are the constants of adjacent plane  $P'_{i_{loc}}$ . The algorithm described above is applied on every dental pulp model independently, providing a surface representation of each tooth.

### 3 Results and Discussion

Following the approval of CHUM Research Center Ethics board, the segmentation method was evaluated using nine Cone Beam CT exams. Acquisitions were done with a Newtom 5G or a Newtom VGI unit (Newtom, Verona Italy) in high resolution scan mode with a field of view of either  $8 \times 8$  or  $12 \times 8$  cm. Images are represented on a voxel grid of sizes  $512\text{-}820 \times 512\text{-}820 \times 498\text{-}656$  with a resolution of  $0.125\text{-}0.150 \times 0.125\text{-}0.150 \times 0.125\text{-}0.150$  mm. The following parameters were used for surface deformation:  $iter = 20$ ,  $L^{iter} \in [25, \dots, 5]$  and  $R^{iter} \in [40, \dots, 10]$ .

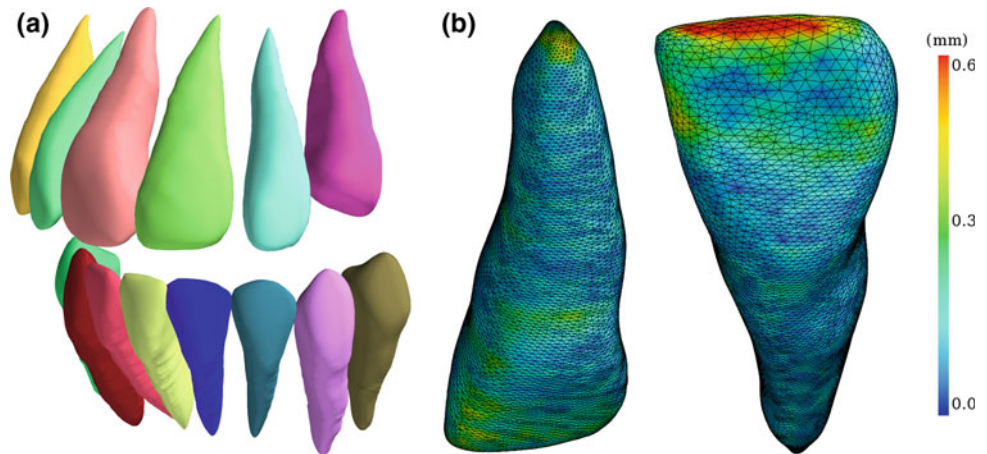
The validation database consists of 26 teeth randomly selected through the available Cone Beam CT scans. Only single-rooted teeth (11 incisors, 9 canines and 6 premolars) were observed in the scope of this study. Ground truths were manually produced by one observer and compared with the automatic segmentation. The accuracy of the segmentation was evaluated with four metrics, described in [14]: Dice Similarity Coefficient (DSC), Jaccard Similarity Coefficient (JSC), Hausdorff distance (Haus) and Average Symetric Distance (ASD). Table 1 presents experimental results on the validation database. A surface reconstruction of single-rooted teeth of one dataset is shown in Fig. 3a. An error map of the upper right central incisor of the same CBCT exam is included in Fig. 3b.

Results show that the method is able to provide the general tooth shape from its dental pulp. The constraints imposed by this in situ reconstructed prior model limit improbable deformation or segmentation overflow to nearby structures. As a case in point, Fig. 2c demonstrates that surface evolution is able to accurately match tooth boundary even in the presence of a touching erupting tooth and alveolar bone. In most cases, largest segmentation errors are located either at the root tip (apex) or at incisal edges and cusp locations. In the first scenario, the boundary information is too poor because the apex is represented by only a few pixels that share similar intensities with the neighbouring alveolar bone. For the second case, it can be noted that cusp boundaries are generally further away from the initial dental pulp model than any other structure in the tooth. Hence, in first iterations, when the search profile length is

**Table 1** Measures of automatic segmentation performance

Type of teeth	DSC (%)	JSC (%)	Haus (mm)	ASD (mm)
Incisor	91.73 ± 2.09	84.79 ± 3.55	1.70 ± 0.53	0.24 ± 0.06
Canine	92.21 ± 2.59	85.64 ± 4.24	1.53 ± 0.53	0.25 ± 0.04
Premolar	93.63 ± 2.30	88.08 ± 4.06	1.09 ± 0.23	0.20 ± 0.03
Average	92.19 ± 2.31	85.59 ± 3.89	1.54 ± 0.52	0.24 ± 0.05

**Fig. 3** Surface reconstruction of single-rooted teeth (a) and symmetric distance error mapping over the surface of the upper right central incisor (b)



large enough to capture cusps boundaries, only rigid deformations are allowed due to the large distance parameter  $R^{iter}$ . This initial constraint limits surface evolution toward distant parts of the tooth such as the cusps. An additional surface deformation could be carried out with the 3D models obtained from this research as inputs, in order to capture detailed features such as the two mentioned above.

#### 4 Conclusion

In this work, a fully automatic tooth segmentation method from Cone Beam CT images was introduced. Experimental results have shown the efficiency and precision of the method on a database of 26 single-rooted teeth. Future steps include generalization of the algorithm on teeth with multiple roots.

**Acknowledgements** This work was supported in part by the Natural Sciences and Research Council of Canada and by Useful Progress Canada Inc. under the Collaborative Research and Development program.

**Conflict of Interest** The authors declare that they have no conflict of interest.

#### References

- Liang, X., Lambrichts, I., Sun, Y., Denis, K., Hassan, B., Li, L., Pauwels, R., Jacobs, R.: A comparative evaluation of Cone beam computed tomography (CBCT) and multi-slice CT (MSCT). Part II: On 3D model accuracy. *European Journal of Radiology* 75(2), 270–274 (2010)
- Rios, H.F., Borgnakke, W.S., Benavides, E.: The Use of Cone-Beam Computed Tomography in Management of Patients Requiring Dental Implants: An American Academy of Periodontology Best Evidence Review. *Journal of Periodontology* 88(10), 946–959 (2017)
- Lee, R.J., Weissheimer, A., Pham, J., Go, L., De Menezes, L.M., Redmond, W.R., Loos, J.F., Sameshima, G.T., Tong, H.: Three-dimensional monitoring of root movement during orthodontic treatment. *American Journal of Orthodontics and Dentofacial Orthopedics* 147(1), 132–142 (2015)
- Pauwels, R., Jacobs, R., Singer, S.R., Mupparapu, M.: CBCT-based bone quality assessment: Are Hounsfield units applicable? *Dentomaxillofacial Radiology* 44(1) (2015)
- Gao, H., Chae, O.: Individual tooth segmentation from CT images using level set method with shape and intensity prior. *Pattern Recognition* 43(7), 2406–2417 (2010)
- Gan, Y., Xia, Z., Xiong, J., Zhao, Q., Hu, Y., Zhang, J.: Toward accurate tooth segmentation from computed tomography images using a hybrid level set model. *Medical physics* 42(1), 14 (2015)
- Xia, Z., Gan, Y., Chang, L., Xiong, J., Zhao, Q.: Individual tooth segmentation from CT images scanned with contacts of maxillary and mandible teeth. *Computer Methods and Programs in Biomedicine* 138, 1–12 (2017)
- Yau, H.t., Yang, T.j., Chen, Y.c.: Tooth model reconstruction based upon data fusion for orthodontic treatment simulation. *Computers in Biology and Medicine* 48, 8–16 (2014)
- Jung, W., Park, S., Shin, H.: Combining volumetric dental CT and optical scan data for teeth modeling. *CAD Computer Aided Design* 67–68, 24–37 (2015)
- Barone, S., Paoli, A., Razonale, A.V.: Creation of 3D multi-body orthodontic models by using independent imaging sensors. *Sensors (Switzerland)* 13(2), 2033–2050 (2013)
- Chantrel, S.: Segmentation des structures céphaliques à topologie complexe. Ph.D. thesis (2016)
- Kim, G., Lee, J., Seo, J., Lee, W., Shin, Y.G., Kim, B.: Automatic teeth axes calculation for well-aligned teeth using cost profile analysis along teeth center arch. *IEEE Transactions on Biomedical Engineering* 59(4), 1145–1154 (2012)
- Chav, R., Cresson, T., Chartrand, G., Kauffmann, C., Soulez, G., Guise, J.A.: Kidney Segmentation from a Single Prior Shape in MRI. *Biomedical Imaging (ISBI), 2014 IEEE 11th International Symposium on*. IEEE pp. 818–821 (2014)
- Taha, A.A., Hanbury, A.: Metrics for evaluating 3D medical image segmentation: analysis, selection, and tool. *BMC Medical Imaging* (2015)



# A Three-Dimensional Quantification of Calcified and Non-calcified Plaque Based on Computed Tomography Coronary Angiography Images: Comparison with Virtual Histology Intravascular Ultrasound

Vassiliki I. Kigka, Antonis Sakellarios, George Rigas, Panagiota Tsobou, Ioannis O. Andrikos, Lampros K. Michalis, and Dimitrios I. Fotiadis

## Abstract

The identification, quantification and characterization of coronary atherosclerotic plaque has a major influence on diagnosis and treatment of coronary artery disease (CAD). Recent studies have reported the ability of Computed Tomography Coronary Angiography (CTCA) to identify non-invasively coronary plaque features. In this study, we present a novel methodology for the identification of the plaque burden of the coronary artery and the volumetric quantification of calcified plaques (CP) and non-calcified plaques (NCP), utilizing CTCA images in comparison with virtual histology intravascular ultrasound (VH-IVUS). The proposed methodology includes seven steps: CTCA images pre-processing, blooming effect removal, vessel centerline extraction using Multistencil Fast Marching Method (MSFM), estimation of membership sigmoidal distribution functions, implementation of an extension of active contour models using prior shapes for the lumen, the outer wall and CP segmentation, detection and quantification of NCP and finally three-dimensional (3D) models

construction. Bland Altman and correlation plot analyses were performed to assess the agreement between the presented methodology and VH-IVUS. Assessment of volume and length of lesion length in 18 lesions indicated good correlation with VH-IVUS. More specifically, the Pearson's correlation ( $r$ ) is ( $r = 0.93$ ,  $p < 0.001$ ) and ( $r = 0.92$ ,  $p < 0.001$ ) for CP and NCP volume, respectively, while the correlation for the length of lesion is ( $r = 0.84$ ,  $p < 0.001$ ) and ( $r = 0.95$ ,  $p < 0.001$ ) for CP and NCP, respectively.

## Keywords

Computed tomography angiography • Coronary artery disease • Coronary arteries • Atherosclerotic plaque  
Calcified plaque • Non-calcified plaque • Level-set segmentation

## 1 Introduction

Atherosclerotic disease, the underlying cause of coronary artery disease (CAD), is one of the leading causes of mortality and morbidity in western societies. Atherosclerosis is characterized by molecular and cellular events, such as the deposition of low-density lipoprotein (LDL) molecules, smooth cell proliferation, calcification and fibrosis, causing compositional and geometric changes in coronary vessels. Several of these changes can be identified by Computed Tomography Coronary Angiography (CTCA), a non-invasive imaging modality, which accurately detects the inner and the outer wall of coronary arteries and also permits the characterization of atherosclerotic plaque composition [1].

V. I. Kigka (✉) · A. Sakellarios · G. Rigas · P. Tsobou  
I. O. Andrikos · D. I. Fotiadis  
Unit of Medical Technology and Intelligent Information Systems,  
Department of Materials Science and Engineering, University of  
Ioannina, 45110 Ioannina, Greece  
e-mail: kigkavaso@gmail.com

V. I. Kigka · A. Sakellarios · I. O. Andrikos · D. I. Fotiadis  
Department of Biomedical Research Institute – FORTH, Institute  
of Molecular Biology and Biotechnology, University Campus of  
Ioannina, 45110 Ioannina, Greece

L. K. Michalis  
Department of Cardiology, Medical School, University  
of Ioannina, 45110 Ioannina, Greece

In the literature, different studies were presented to examine the diagnostic accuracy of CTCA for the detection of coronary plaques. Dey et al. [2] examined the accuracy of CTCA to detect CP and NCP using an automated scan-specific threshold level-based approach. Similarly, in another study, proposed by Brodoefel et al. [3], an automated software was implemented to analyze the atherosclerotic plaque composition based on CT attenuation values. On the other hand, Graaf et al. [4] studied the correlation between the plaque volume derived by CTA automatic software (QAngio CT 1.1, Medis medical imaging systems) and the plaque volume provided by VH IVUS, which was defined as the gold standard. Jawaid et al. [5] implemented a SVM classifier to identify the abnormal coronary segments and further proposed a derivative-based method to localize the position and length of the NCP inside the segment.

The proposed study is dedicated to present a semi-automatic methodology, which permits the 3D models construction of the inner wall and the outer wall, as well as the detection and volumetric quantification of CP and NCP. The VH IVUS is used to validate the proposed study. Except of its semi-automated nature, the innovative aspect of this approach is that both the active contour models and the dynamic thresholding techniques are totally adapted to each CTCA image, and allow accurately 2D segmentation independently of the acquisition dose protocol.

## 2 Materials and Methods

The proposed methodology consists of seven steps: the preprocessing, the blooming effect removal, the vessel centerline extraction, the estimation of membership functions, the inner wall, outer wall and CP segmentation, the NCP segmentation and finally 3D models construction.

### 2.1 Preprocessing

In this step, the Frangi Vesselness filter [6] is applied on the acquired axial DICOM CTCA images to detect the potential vessels regions.

### 2.2 Blooming Effect Removal

In this stage, we aim to improve the visualization of small high-density objects and to limit the blooming effect. The output CTCA image is considered as the convolution result of the input image with the system's point spread function (PSF). Thus, we approximate the system's PSF using a

Gaussian kernel and we apply the Richardson Lucy algorithm on high intensity regions, to acquire the deblurred CTCA image [7].

### 2.3 Centerline Extraction

The implemented vessel centerline extraction approach, proposed by Metz et al. [8], is a minimum cost approach, based on the combination of the vesselness measure ( $w_{\text{vessel}}$ ) and the lumen intensity ( $w_{\text{lumen}}$ ) information. The considered cost function was defined as

$$V = w_{\text{vessel}} * w_{\text{lumen}}, \quad (1)$$

where  $w_{\text{vessel}}$  is calculated in the pre-processing step, whereas the ( $w_{\text{lumen}}$ ) is a generalized bell-shaped function.

### 2.4 Estimation of Memberships Functions

In this step, three membership functions were estimated to compensate three different intensity protocols for the discrimination of the lumen, the outer wall and the CP. More specifically, the selected intensity ranges depend both on the literature and the extracted mean luminal intensity.

### 2.5 Segmentation of the Lumen, the Outer Wall and CP

In this step, an active contour model [9], which incorporates a prior shape [10] is implemented to segment the inner wall, the outer wall and the CP. The 2D segmentation approach includes four different stages: the update of lumen intensities, the approximation of an initial binary image, the calculation of the curve speed function and finally the sparse field algorithm implementation. More specifically, we modify the estimated lumen membership function. Based on the extracted vessel centerline, we consider only the pixels of the CTCA image, whose distance from the centerline is lower than the value obtained by dividing an estimation of lumen radius by the pixel spacing of the CTCA image. Consequently, an initial image-shape  $\phi$  is estimated to implement the active contour models. This image  $\phi$  is a binary image, whose pixels are 1's, when the updated lumen membership function multiplied with a threshold value is larger than 500 HU. Except of the initial binary image  $\phi$ , a shape function  $\psi$  and a labelling function  $L$  are introduced [10, 11]. In this approach, the defined speed function to evolve the curve is defined by:

$$E(\phi, \psi, L) = E_{\text{cv}} + E_{\text{shape}} + E_{\psi}, \quad (2)$$



where  $E_{cv}$  is the Chan-Vese energy,  $E_{shape}$  is the shape comparison term and  $E_{\psi}$  is the labelling term. The sparse field algorithm implementation follows, aiming to extract the minimal representation of  $\varphi$ . The sparse field algorithm is implemented twice, in order to achieve a smooth segmented shape for the inner and the outer wall.

A similar procedure is implemented for both the outer wall and the CP segmentation.

## 2.6 NCP Segmentation

The detection of NCP based on CTCA images remains a challenging problem, since their intensity range values depend on the luminal intensity and the acquisition dose protocol [12]. Furthermore, the segmentation of NCP could not be successfully achieved by implementing a level set based approach, since NCP intensity values are close to the ranges of the outer wall. Thus, in this study a dynamic threshold technique is applied in the region simultaneously outside the inner wall and inside the outer wall, which is considered as the region of interest (ROI). The main idea of the detection of NCP is the extraction of a critical intensity value, the mean lumen intensity ( $ml$ ). This value corresponds to the mean intensity values of the pixels of the 50% of the image intensities. After the definition of  $ml$  value, the intensity value for the NCP segmentation ranges between 100 HU lower than  $ml$  and 100 higher than  $ml$ .

## 2.7 3D Models Construction

The 3D models for the lumen, the outer wall, the CP and the NCP are constructed based on the Marching Cubes approach [13], by applying a triangulation approach.

## 3 CTCA-IVUS Comparison

The presented methodology was compared using the corresponding frames of VH IVUS modality. The accurate registration was achieved based on anatomical landmarks, such as side-branches, ostia and CP. Furthermore, the VH IVUS images were analyzed based on a previously published study, introduced by Bourantas et al. [14], whereas the NCP volume is calculated based on the Simpson-rule method [15].

The accuracy of the presented methodology to detect plaque burden and to quantify the CP and NCP is evaluated using two different metrics for each plaque type, the plaque volume and the length of lesion. The plaque volume corresponds to the volume of plaque between the proximal and

distal ends of the coronary lesion, whereas the length of lesion is the distance between the proximal and distal ends of the coronary lesion.

## 4 Results

In the validation procedure, we used totally 18 coronary arteries, 9 left anterior descending (LAD), 3 left circumflex (LCX) and 6 right coronary (RCA). The Bland Altman analysis and the correlation plots between the proposed CTCA based methodology and VH IVUS images analysis is illustrated in Fig. 1 and Fig. 2 for CP and NCP, respectively.

The evaluation procedure indicates that the CP and NCP extracted volumes and lengths of lesion derived from the proposed methodology correlate well with those derived by VH IVUS images analysis. More specifically, the Pearson's correlation ( $r$ ) is 0.93 and 0.92 for the CP and NCP volume, respectively, whereas the Pearson's correlation ( $r$ ) is 0.84, 0.95 for the CP and NCP length of lesion, respectively.

## 5 Discussion

In this work, a semi-automated methodology for the reconstruction of the lumen, the outer wall and the CP and NCP of coronary arteries is presented. The approach relies primarily on the active contour models, while the NCP detection is achieved by a dynamic threshold based approach. Although, level set based threshold techniques are promising approaches in the field of 2D segmentation, in case of NCP segmentation they are not applicable, due to the lower intensity values of NCP, which are close to the outer wall intensities.

Furthermore, the methodology of the inner and outer wall detection, proposed in this study has already been validated [16] using both manual annotations and IVUS modality. Thus, in this manner an accurate plaque burden region is assumed to be accurately identified and as a result the quantification of CP and NCP is successfully achieved.

Moreover, the basic innovative aspect of the presented methodology is its adaption to each CTCA image. It has been demonstrated that the mean luminal attenuation value differs using different acquisition protocols, as well as it varies between different patients. Contrary to others studies [2, 3], in our approach the selected threshold values are not fixed, but fully dynamic and adapted to different CTCA images.

Another basic innovative aspect of our approach is the incorporation of blooming effect removal. This deconvolution procedure implementation prevents the vessel stenosis overestimation and reduces the volumetric quantification of CP. Additionally, our algorithm allows the 3D reconstruction of the full arterial coronary tree and as result the CP

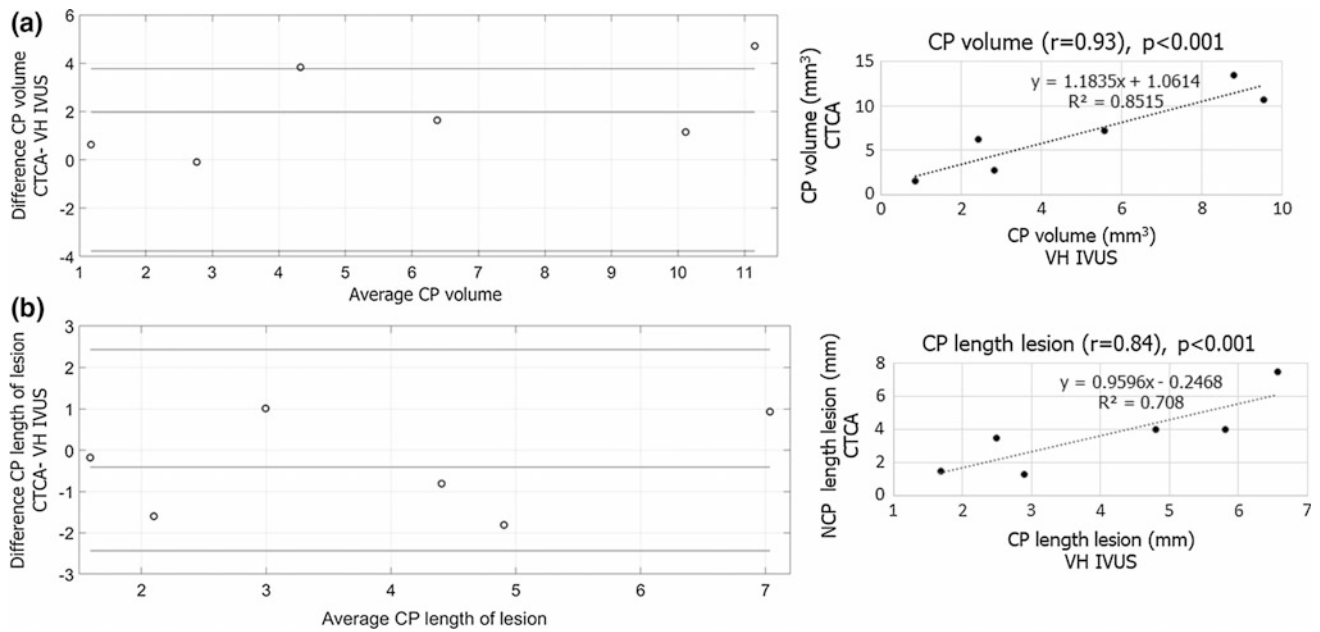


**Fig. 1** Bland Altman and correlation plots for CTCA and VH IVUS for the volume (a) and the length of lesion (b) for CP

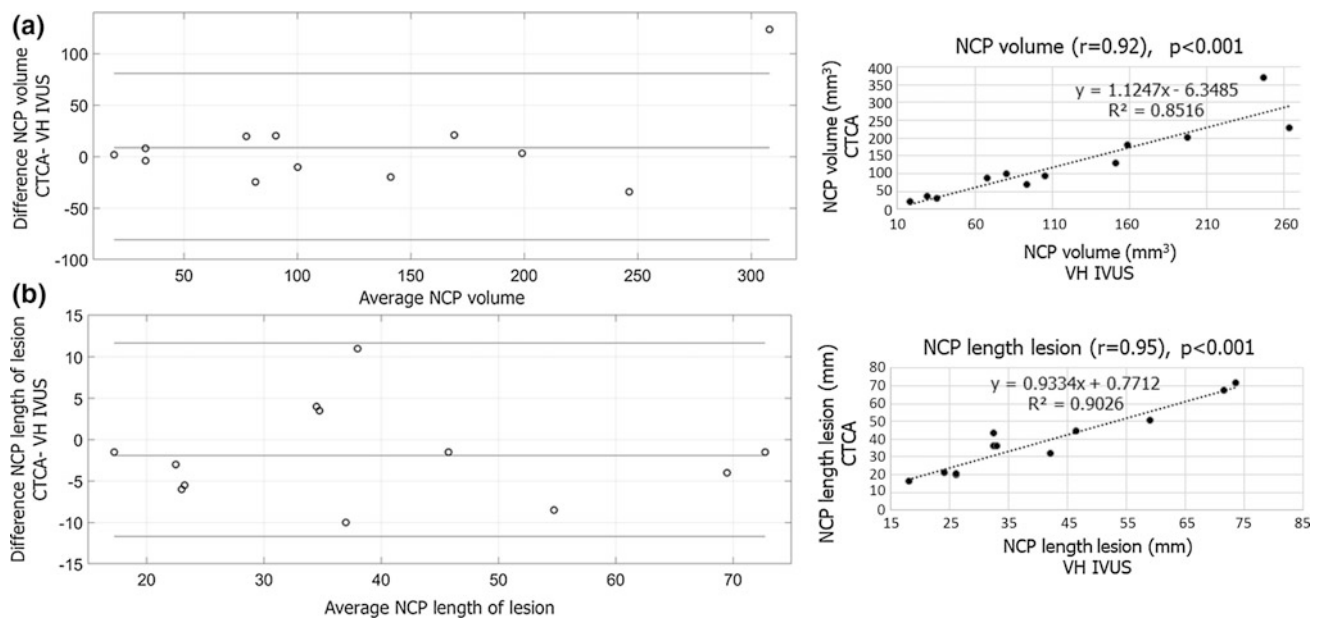


**Fig. 2** Bland Altman and correlation plots for CTCA and VH IVUS for the volume (a) and the length of lesion (b) for NCP

and NCP can be visualized in critical regions, such as the bifurcations.

## 6 Conclusions

The presented methodology provides an accurate segmentation of the lumen, the outer wall, the CP and the NCP of 2D CTCA images, the plaque burden characterization,

reliable coronary reconstruction and 3D representation of coronary anatomy and pathology. The validation procedure indicates that the proposed methodology correlates well with VH IVUS. Thus, its integration into a quantitative software may contribute to the diagnostic and prognostic value of CTCA and may provide a wide clinical and research applicability.

**Acknowledgements** This work is funded by the European Commission: Project SMARTOOL, “Simulation Modeling of coronary ARtery disease: a tool for clinical decision support—SMARTool” GA number: 689068).

## References

1. Voros, S., et al., *Coronary Atherosclerosis Imaging by Coronary CT Angiography: Current Status, Correlation With Intravascular Interrogation and Meta-Analysis*. JACC: Cardiovascular Imaging, 2011. **4**(5): p. 537–548.
2. Dey, D., et al., *Automated Three-dimensional Quantification of Noncalcified Coronary Plaque from Coronary CT Angiography: Comparison with Intravascular US*. Radiology, 2010. **257**(2): p. 516–522.
3. Brodoefel, H., et al., *Accuracy of dual-source CT in the characterisation of non-calcified plaque: use of a colour-coded analysis compared with virtual histology intravascular ultrasound*. The British Journal of Radiology, 2009. **82**(982): p. 805–812.
4. de Graaf, M.A., et al., *Automatic quantification and characterization of coronary atherosclerosis with computed tomography coronary angiography: cross-correlation with intravascular ultrasound virtual histology*. The International Journal of Cardiovascular Imaging, 2013. **29**(5): p. 1177–1190.
5. Jawaid, M., et al., *Framework for detection and localization of coronary non-calcified plaques in cardiac CTA using mean radial profiles*. Vol. 89. 2017.
6. Frangi, A.F., et al., *Multiscale vessel enhancement filtering, in Medical Image Computing and Computer-Assisted Intervention — MICCAI '98: First International Conference Cambridge, MA, USA, October 11–13, 1998 Proceedings*, W.M. Wells, A. Colchester, and S. Delp, Editors. 1998, Springer Berlin Heidelberg: Berlin, Heidelberg. p. 130–137.
7. Castillo-Amor, A.M., et al. *Reduction of blooming artifacts in cardiac CT images by blind deconvolution and anisotropic diffusion filtering, in 11th International Symposium on Medical Information Processing and Analysis*. 2015. International Society for Optics and Photonics.
8. Metz, C., et al., *Coronary centerline extraction from CT coronary angiography images using a minimum cost path approach*. Vol. 36. 2009. 5568–79.
9. Chan, T.F. and L.A. Vese, *Active contours without edges*. IEEE Transactions on Image Processing, 2001. **10**(2): p. 266–277.
10. Chan, T. and Z. Wei. *Level set based shape prior segmentation, in 2005 IEEE Computer Society Conference on Computer Vision and Pattern Recognition (CVPR'05)*. 2005.
11. Cremers, D., N. Sochen, and C. Schnörr, *Towards Recognition-Based Variational Segmentation Using Shape Priors and Dynamic Labeling, in Scale Space Methods in Computer Vision: 4th International Conference, Scale Space 2003 Isle of Skye, UK, June 10–12, 2003 Proceedings*, L.D. Griffin and M. Lillholm, Editors. 2003, Springer Berlin Heidelberg: Berlin, Heidelberg. p. 388–400.
12. Dalager, M.G., et al., *Impact of luminal density on plaque classification by CT coronary angiography*. The International Journal of Cardiovascular Imaging, 2011. **27**(4): p. 593–600.
13. Lorensen, W.E. and H.E. Cline, *Marching cubes: A high resolution 3D surface construction algorithm, in Proceedings of the 14th annual conference on Computer graphics and interactive techniques*. 1987, ACM. p. 163–169.
14. V Bourantas, C., et al., *A new methodology for accurate 3-dimensional coronary artery reconstruction using routine intravascular ultrasound and angiographic data: Implications for widespread assessment of endothelial shear stress in humans*. Vol. 9. 2013.
15. Medina, R., et al., *Three methods for accurate quantification of plaque volume in coronary arteries*. The International Journal of Cardiovascular Imaging, 2003. **19**(4): p. 301–311.
16. Kigka, V.I., et al., *3D reconstruction of coronary arteries and atherosclerotic plaques based on computed tomography angiography images*. Biomedical Signal Processing and Control, 2018. **40**(Supplement C): p. 286–294.

# Creation of Computational Breast Phantoms with Extracted Abnormalities from Real Patient Images

Nikolay Dukov, Zhivko Bliznakov, Ivan Buliev, and Kristina Bliznakova

## Abstract

The current contribution presents an approach for creation of complex computational breast phantoms, with included breast abnormalities. In-house developed and validated software tool, called *BreastSimulator*, is used to create different models of healthy breasts, by varying parameters like shape, size, duct tree features, Cooper ligaments, skin, etc. Separately, different 3D tumour models are constructed from segmented tumour regions on sets of real tomosynthesis images from real patients. A semi-automatic algorithm was developed to segment the abnormalities in the images. The algorithm applies a series of image processing operations and region-growing techniques with minimal interaction from the user to find the areas of the lesions. The flat tumour images are then correctly stacked and stored in a 3D voxel matrix, matching the desired resolution. Relevant information about the lesion (voxel size, matrix size, geometrical centre, etc.) is also saved. Selected tumour models are then inserted at various locations into the computational models of the healthy breasts. Examples of simulated mammographic and tomosynthesis images from such breast phantoms are presented to illustrate the potential of the proposed approach. Combining mathematical breast modelling with segmented real 3D tumour shapes results in the creation of realistic breast phantoms. The approach allows implementation of multiple scenarios and unlimited number of cases, which can be used for further software modelling and investigation of breast imaging techniques.

## Keywords

Breast phantom • Breast simulator • Tumour segmentation

## 1 Introduction

Early diagnosis of breast cancer can significantly increase the probability for successful treatment of the disease. Therefore, many efforts are focused on improvement of the existing imaging techniques or investigations of new ones. Along that, anthropomorphic phantoms, either physical or computational, are widely used in the relevant research studies.

This work presents an approach for creation of complex computational breast phantoms, with included breast abnormalities.

## 2 Materials and Methods

### 2.1 Clinical Data

For the current study we have used sets of tomographic images from real patients with lesions. Twenty image sets are acquired from the University Hospital of Leuven, Leuven, Belgium, using Siemens Mammomat Inspiration, while 15 image sets are acquired from Alexandrovska University Hospital, Sofia, Bulgaria, where a Giotto Tomo IMS is in service. The pixel size of the tomosynthesis images provided by the Siemens machine from the University Hospital of Leuven is  $85 \times 85 \mu\text{m}$ . The tomosynthesis images are obtained from 26 projection images acquired from a compressed breast. The pixel size of the tomosynthesis images provided by the Giotto machine from the Alexandrovska University Hospital is  $90 \times 90 \mu\text{m}$ . The tomograms are reconstructed iteratively from 13 low-dose planar transmission images. The clinical data is priori anonymized and only technical data such as pixel values, voxel size, image dimensions, etc., are kept for the purposes of further processing and for the creation of the computational breast models and subsequent simulations.

N. Dukov (✉) · Z. Bliznakov · I. Buliev · K. Bliznakova  
Technical University of Varna, Varna, Bulgaria  
e-mail: nikolay.dukov@tu-varna.bg

K. Bliznakova  
e-mail: kristina.bliznakova@gmail.com

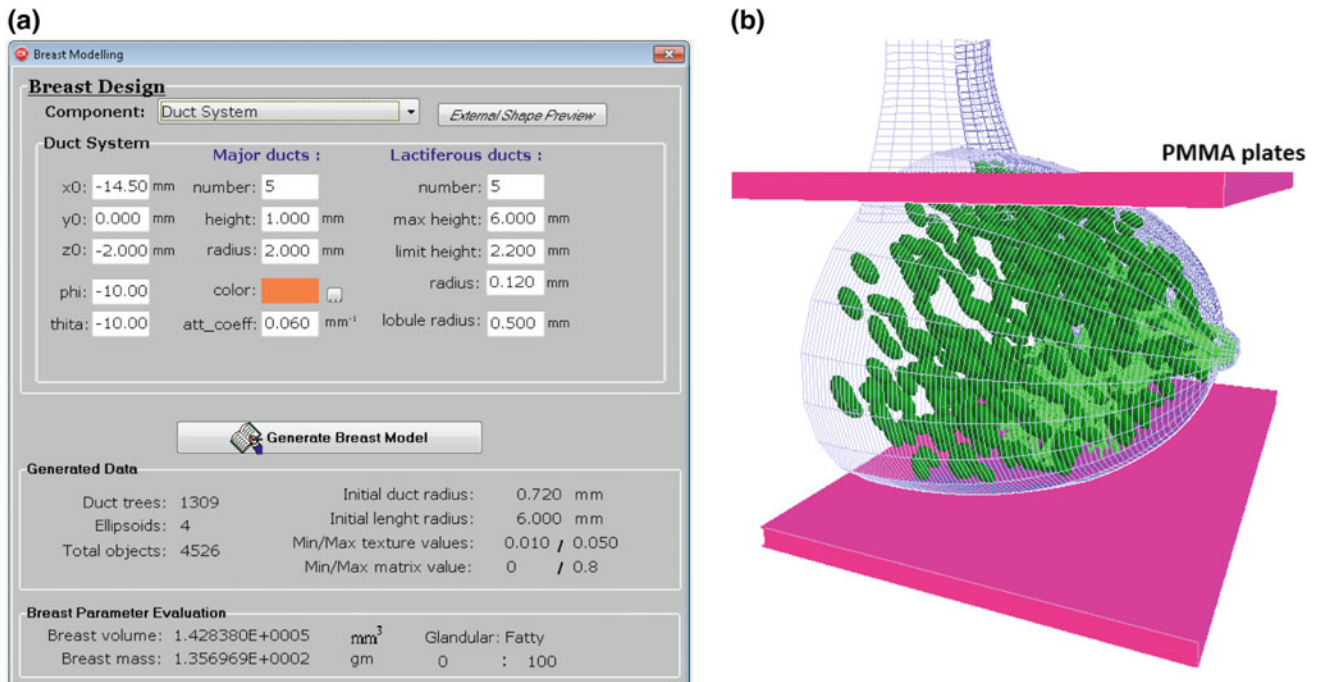


**Fig. 1** A screenshot from the *Breast Simulator* software application, showing **a** the application user interface for modelling the duct tree and **b** the compression of a breast phantom, generated with the this tool

## 2.2 Breast Simulator

For the creation of the breast models we use an in-house developed and validated software tool, called *Breast Simulator* [1, 3–5]. The tool can create models of healthy breasts, by varying parameters like shape, size, duct tree features, Cooper ligaments, skin, etc. A screenshot from the software tool is shown in Fig. 1a. The generated 3D breast phantom is then subjected to a simulation of the compression procedure applied during mammography imaging. This procedure is described in details in Zyganitidis et al. [8], as the basic parameters include the desired breast compressed thickness and the elastic modulus of the breast tissues.

## 2.3 Segmentation Algorithm

The different 3D tumour models are obtained through segmentation of tumour regions on sets of real tomosynthesis images from real patients. For the purpose, an in-house semi-automatic algorithm is used to segment the abnormalities in the images [6, 7].

The algorithm consists of four major steps shown in Fig. 2: (i) loading the clinical data, (ii) pre-processing of the data, (iii) segmentation of the tumour masses, and (iv) creation of a 3D tumour voxel matrix.

The algorithm requires an input from the operator (user) for the initial selection the range of images at which the segmentation algorithm will be performed, as well as, a rough selection of a Region of Interest (first image from the range of images). The region selection is then automatically transferred to the rest of the images.

Results from the different steps of the segmentation procedure are shown in Fig. 3 and present how the procedure extracts the lesion for a given slice. Finally, a 3D volume, containing the segmented shape is created and stored into a MATLAB data file.

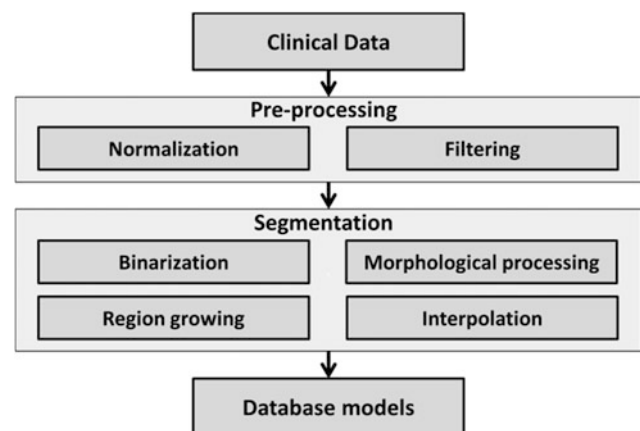


**Fig. 2** Segmentation steps for the in-house developed algorithm



**Fig. 3** Results from the different steps of the segmentation algorithm obtained after: (i) thresholding; (ii) morphological processing; (iii) region growing; (iv) interpolation

## 2.4 Insertion of Extracted Abnormalities into Computational Breast Phantoms

The results of applying the segmentation procedure on patient data are in fact computational models of breast abnormalities, represented as Boolean three-dimensional voxel matrices with voxel values of 1 where the abnormality is present. The user selects the place in the breast volume (phantom) where the breast abnormality will be integrated. Then the properties of the abnormality are changed in such a way that the abnormality is smoothly integrated to the surrounding tissues within the breast volume. The degree of smoothing of each voxel from the abnormality matrix depends on its distance from the centre. The more distant the voxels are, the higher degree of smoothing is achieved.

## 3 Results and Discussions

### 3.1 Phantoms

For this experimentation we generated a medium in size breast phantom with a 25% glandular tissue without skin (33% with skin) as shown in Fig. 4a. The number of Cooper ligaments (presented as ellipsoids) is approximately 1000,

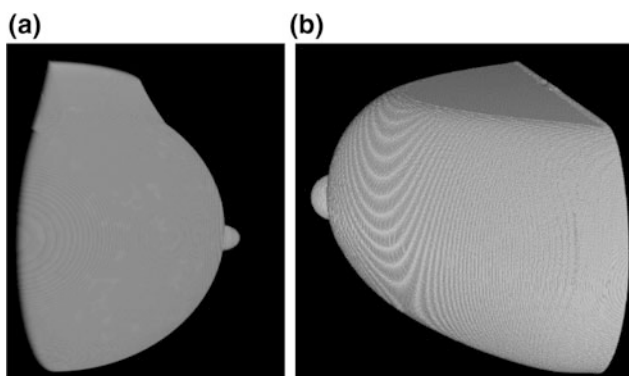


**Fig. 4** Modelled breast phantom of **a** average breast (590 ml), **b** compressed version of the computer breast model

while the glandular duct tree is composed of approximately 8000 cylinders of different sizes. The model is then transformed into a 3D breast voxel matrix, which contained glandular, adipose and skin tissues. Subsequently, this voxel-based breast model is subjected to a compression simulation which resulted in a breast phantom with a thickness of 4 cm, as shown in Fig. 4b.

### 3.2 Segmented Models

An extracted tumour model from the segmentation algorithm is shown in Fig. 5a, b.

The tumour mass shown in Fig. 5 is segmented from 12 slices, each one with a thickness of 1 mm. The size of the segmented tumour is 7.3 mm × 12.3 mm × 12 mm. The size of the 3D matrix containing it is 96 × 155 × 22 voxels. The mass was assessed subjectively by a physician (visual inspection) before introducing it into the computational breast phantom.

### 3.3 Computational Breast Phantoms with Extracted Abnormalities

#### The 3D model

The selected tumour model is then inserted into the computational breast phantom (Fig. 6).

#### Simulations

Breast tomosynthesis images with the composed breast phantom with an introduced abnormality are simulated by using *XRAYImagingSimulator* [1, 3–5]. 26 X-ray projection images of the software phantom are produced with energy of 20 keV for monochromatic X-ray beam. Scatter and detector responses are not simulated. Distances from the source to the breast support table, where the phantom is placed, and to the detector surface, are 600 mm and 650 mm, respectively. The size of the images is 1200 × 1200 pixels with pixel size of 0.085 mm × 0.085 mm. A mammography image obtained





**Fig. 5** An extracted model obtained from the segmentation procedure: **a** 2D segmentation tumour area from a single slice; **b** 3D visualization of the same segmented abnormality, shown from different angle views

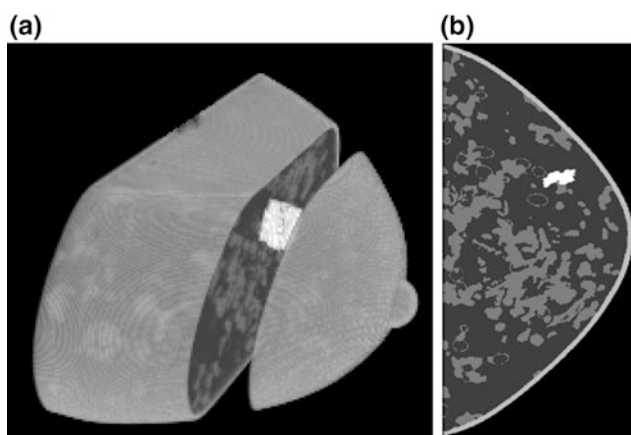


**Fig. 6** Breast phantom with an introduced abnormality: **a** 3D view; **b** 2D view

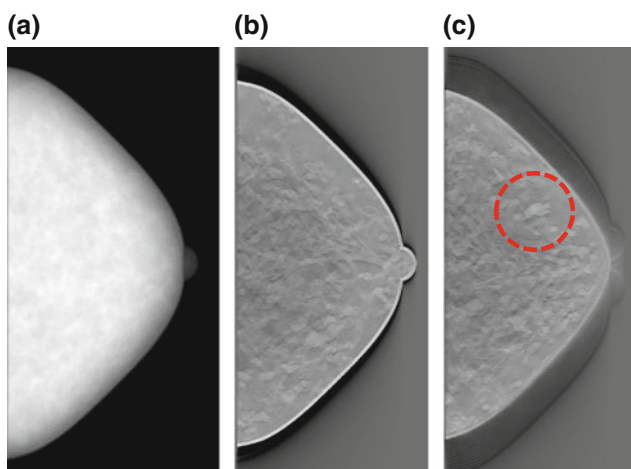


**Fig. 7** Images obtained with the software phantom: **a** craniocaudal projection image, and tomosynthesis images reconstructed at two different phantom heights: **b** at the isocentric plane, **c** at the plane, where the abnormality is located

at craniocaudal view is shown in Fig. 7a. The 26 projection images are then used with the FDKR software application, which is an application for reconstruction of tomosynthesis slices [2]. Figure 7b, c show the reconstructed tomosynthesis images at two different planes of the reconstructed breast phantom.

## 4 Conclusions

Combining mathematical breast modelling with segmented realistic 3D tumour shapes results in the creation of realistic breast phantoms, which can be used to generate realistic simulated X-ray projection images. The approach allows implementation of multiple scenarios and unlimited number of breast tumour cases, which can be used for further software modelling and investigation of breast imaging techniques.

**Acknowledgements** This work is supported by MaXIMA project, which has received funding from the European Union's Horizon 2020 research and innovation programme under grant agreement No. 692097. This work is also supported by the Bulgarian National Science Fund under grant agreement DN17/2.

**Conflict of Interest** The authors declare that they have no conflict of interest.

## References

1. Bliznakova K, et al. (2010) "Experimental validation of a radiographic simulation code using breast phantom for X-ray imaging" *Computers in biology and medicine* **40** 208–214.
2. Bliznakova, K., P. Russo, et al. (2016). "In-line phase-contrast breast tomosynthesis: a phantom feasibility study at a synchrotron radiation facility." *Phys Med Biol* **61**(16): 6243–6263.
3. Bliznakova, K., I. Sechopoulos, et al. (2012). "BreastSimulator: A software platform for breast X-ray imaging research." *Journal of Biomedical Graphics and Computing* **2**(1): 1–14.

4. Bliznakova, K., R. Speller, et al. (2010). "Experimental validation of a radiographic simulation code using breast phantom for X-ray imaging." *Comput Biol Med* 40(2): 208–214.
5. Bliznakova, K., S. Suryanarayanan, et al. (2010). "Evaluation of an improved algorithm for producing realistic 3D breast software phantoms: Application for mammography." *Med Phys* 37(11): 5604–5617.
6. Dukov, N., Feradov, F., Bliznakova, K., Encheva, E., Gluhcheva, Y., Bulyashki, D., et al. (2016). "Computational breast cancer models created from patient specific CT images: Preliminary results." *Series G. Medicine, Pharmacy and Dental Medicine, Vol. XIX*: 106–109. Plovdiv.
7. Dukov, N., Bliznakova, K., Buliev, I., Feradov, F., Bliznakov, Z., Kostova-Lefterova, D., et al. (2017). "Development and implementation of an algorithm for segmentation of irregular lesions in Digital Breast Tomosynthesis and CT images." *Book of Abstracts RAD 2017*: 101. Budva.
8. Zyganitidis, C., K. Bliznakova, et al. (2007). "A novel simulation algorithm for soft tissue compression." *Med Biol Eng Comput* 45 (7): 661–669.

# Metal Artifact Reduction by Morphological Image Filtering for Computed Tomography

Yakdiel Rodríguez-Gallo, Rubén Orozco-Morales,  
and Marlen Pérez-Díaz

## Abstract

When metal implants are present in the field of measurement, artifacts degrade image quality. Metal artifact reduction (MAR) methods produce images with improved quality leading to confident and reliable clinical diagnosis. Currently, there are many methods developed, but no generally accepted solution to this issue has been found. In this work we propose a morphological image filtering approach for metal artifact reduction (MIFMAR) algorithm for image quality improvement. MIFMAR performance was compared with three well-known MAR methods, which are linear interpolation (LI), normalized metal artifact reduction (NMAR) and frequency split metal artifact reduction (FSMAR), using clinical studies. The methods were applied to images acquired from 30 clinical studies of patients with metallic implants. Image quality was evaluated by three experienced radiologists completely blinded to the information about if the image was processed or not to suppress the artifacts. They graded image quality in a five points-scale, where zero is an index of clear artifact presence, and five, a whole artifact suppression. Image quality on images were compared using the non-parametric Friedman-ANOVA test. Inter-observer agreement was evaluated using linear-weighted  $\kappa$  test. MIFMAR ensures efficient reduction of metal artifacts with high image quality, preserving all of tissues and details in CT images. Image quality and diagnostic scores improved significantly ( $p < 0.01$ ) with

good inter-observer agreement. MIFMAR is computationally inexpensive compared with other methods and does not use raw CT data.

## Keywords

Computed tomography • Metal artifact reduction  
Image quality

## 1 Introduction

With the continuing development of new state-of-the-art imaging equipment, the clinical use of computed tomography (CT) is increasing in all fields of radiology [1]. A number of methods to suppress metal artifacts in CT images have been proposed. Most conventional methods developed for MAR can be divided mainly into six classes: Acquisition Improvement, Physics-based Pre-processing, Projection Completion, Iterative Reconstruction, hybrid methods and Image-based Approaches. In order to improve the acquisition process, dual-energy protocols have been proposed [2]. Other MAR techniques have been developed based on the assumption that the projections associated with the metal objects are completely missing or corrupted and are useless for CT image reconstruction. Missing data are replaced by synthetic data, which can be obtained by polynomial, wavelet interpolation or linear interpolation methods. Others algorithms use a normalization step [3, 4] that compares raw sinogram data to a prior image sinogram to improve projection completion processes.

Another strategy for reducing metal artifacts is recover missing information using iterative algorithms [5]. Other methods are hybrid algorithms who combine both analytical and iterative methods in different combinations. On the other hand, a small proportion of methods prefer to handle the artifacts in the image domain [6].

In this paper, a new MAR technique (MIFMAR) is proposed to remove the artifacts caused by data inconsistency.

Y. Rodríguez-Gallo (✉) · R. Orozco-Morales · M. Pérez-Díaz  
Departament of Electronic and Telecommunications, Universidad  
Central “Marta Abreu” de Las Villas (UCLV), Carretera a  
Camajuaní km 5 ½, Santa Clara, Cuba  
e-mail: yrodriguez-gallo@uclv.edu.cu

## 2 Materials and Methods

### 2.1 Metal Artifact Reduction Approaches

In this study, we selected three well-known MAR methods, which are implemented to compare them with MIFMAR. The first algorithm selected was linear interpolation (LI), who was developed by Kalender et al. [7]. Although, this method reduces the artifacts, new ones are induced. NMAR algorithm proposed by Meyer et al. [3] was the second algorithm chosen. To maintain the size and the edges of the metal implant, both methods, LI and NMAR, reinsert the metal image from the originally reconstructed image in the final corrected image. In addition, to improve the edge information of surrounding bone structures the application of a frequency split metal artifact reduction (FSMAR) algorithms was introduced by Meyer et al. [4], being the third algorithm selected in this research.

### 2.2 Morphologically Image Filtering

The proposed method is composed by four steps (Fig. 1): image segmentation, morphological and smoothing filters application, interpolation, and reconstruction process.

First step of the proposed MAR method is the image segmentation. A simple thresholding was applied to find the image metal ( $I^{Metal}$ ) from original image ( $I^{Original}$ ). In this work, 3000 HU is selected as the threshold, which is proper

to extract metal according to the literature [8]. Then, the forward projection (FP) of the obtained  $I^{Metal}$  is performed to obtain metal traces, which specifies the projections affected by metals.

Prior image ( $I^{prior}$ ) (Fig. 1) is obtained using morphological filters (MF) and a L0 Gradient Minimization (LOGM) smoothing algorithm [9]. Firstly, a morphological opening and a morphological closing on the  $I^{Original}$  with a disk structuring element is applied. Next, LOGM is used to reduce low-amplitude structures. This procedure also guarantees to preserve and enhance outgoing edges, even if they are boundaries of very narrow objects, obtaining  $I^{prior}$ . Subsequently, sinogram from  $I^{prior}$  was gotten using forward projection. Following the well-known method developed by Meyer et al. [3], the original sinogram is normalized ( $S^{Norm}$ ). Moreover, all values from the  $I^{Norm}$  that lie within the metal trace are replaced in each row by linear interpolation (See Kalender et al. [7] for further details). Next, the corrected sinogram ( $S^{Corr}$ ) is obtained by denormalization of the interpolated ( $S^{Inter}$ ). Finally, the final image ( $I^{Final}$ ) is obtained using filtered back projection (FBP) with linear interpolation.

### 2.3 Patients

The images used from a kV on-board imaging (OBI) were employed in previous research [10]. Additionally, the other dataset was approved by Institutional Review Board in the

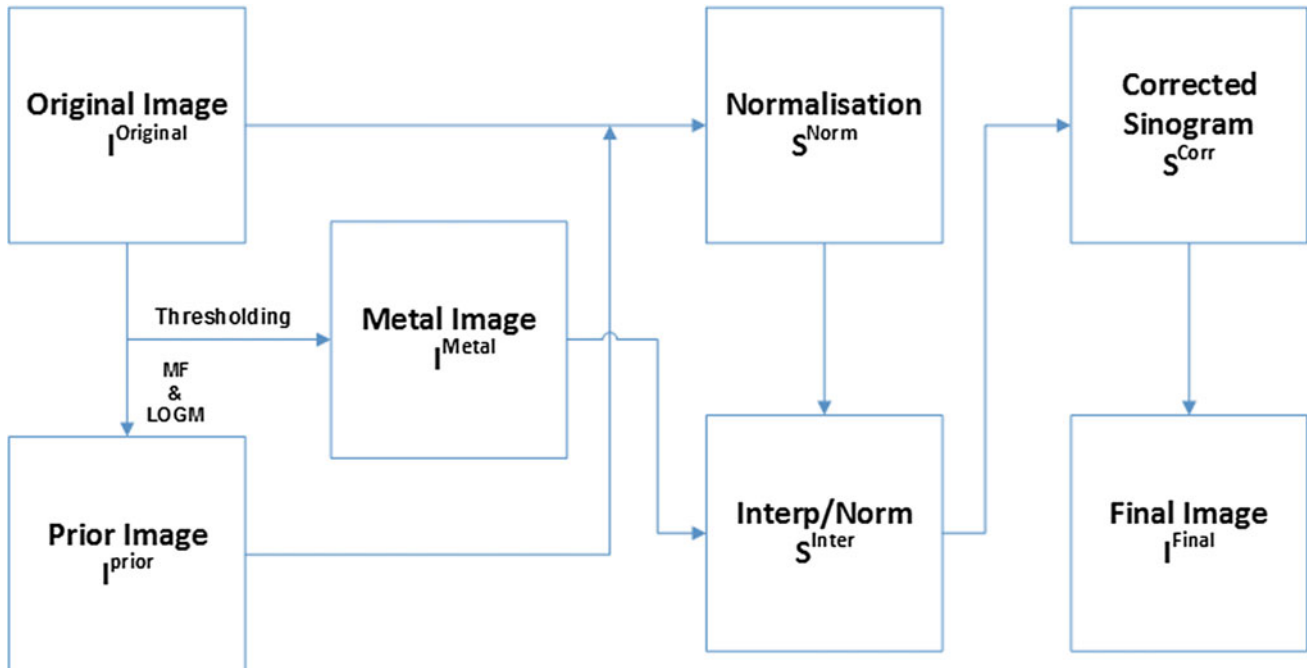


Fig. 1 Flowchart of the proposed method MIFMAR

**Table 1** Study data

Number of patients	Implants
5	Seed implants
5	Hip implants
15	Dental implants
5	Heart valve implants

hospital where it was obtained. Informed consent was obtained from all these patients. The scope of experiments included images from a variety of anatomic regions covering different types of metal implants including dental fillings, heart valve implants, hip implants and seed implants. These are summarized in Table 1.

## 2.4 Evaluation and Statistical Analysis

The diagnostic image quality was scored on CT images on a scale from 1 to 5 (1, severely reduced image quality, non-diagnostic; 2, markedly reduced image quality, with impaired diagnostic interpretability; 3, acceptable image quality and diagnostic interpretability; 4, good image quality, with high diagnostic confidence; 5, excellent image quality, with full diagnostic interpretability). All numeric values were reported as the mean  $\pm$  SD.

In order to compare subjective image quality scores of the datasets, non-parametric Friedman-ANOVA was performed. P-values were adjusted for multiple comparisons using the Bonferroni-Holm method. With the purpose of assessing interobserver agreement Cohen's kappa was used. The  $\kappa$  values of 0.01–0.20 were considered to indicate slight agreement, 0.21–0.40 for fair agreement, 0.41–0.60 for moderate agreement, 0.61–0.80 for substantial agreement and 0.81–1.00 for almost perfect agreement.

## 3 Results

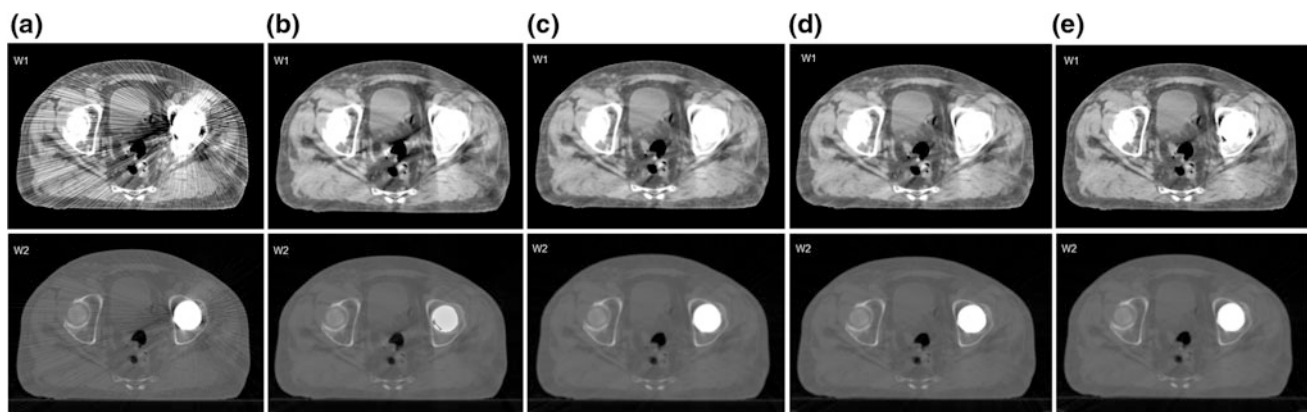
To evaluate the performance of MIFMAR algorithm, the corrected images were compared with original images and images corrected by LI, NMAR and FSMAR. Artifacts were significantly lower in all images corrected compared with the original image. Figure 2 shows the results for patients with a heart valve implant and seed implants.

Image quality scores among MAR algorithms can be seen in Table 2. The MIFMAR algorithm achieved the best results as shown by the positive mean score in every instance. Overall pair-wise comparison showed significant differences among all combinations. The p-values for specific anatomical regions are given in Table 3.

The  $\kappa$  values for the three observers achieved in the inter-observer agreement were from 0.714 to 0.930 for image quality in all the study (all with  $p < 0.001$ ). The worst agreement was between observer 1 and 2 with  $\kappa = 0.714$  ( $p < 0.001$ ) in presence of artifacts caused by permanent seeds.

## 4 Discussion

In this study, it was evaluated a new MAR algorithm by comparison with three well-known algorithms. In the presence of metals the effects of beam hardening, scattered radiation, photon starvation and noise cause that FBP algorithm produces reconstructions characterized by artifacts. Radiologists observed that new streaks were often produced by LI algorithm in some tissue regions. On the other hand, NMAR improved image quality and proved to be better than to LI, being depends on a good prior image with accurate segmentation. The algorithms NMAR and FSMAR had similar performance. Additionally, MIFMAR was able to recover structures around the implants and reduced



**Fig. 2** Influence of the MAR algorithms on image quality. Patient with hip implant. **a** The original artifact CT image (FBP) and the corrected images using the various MAR approaches: **b** LI, **c** NMAR,

**d** FSMAR and **e** MIFMAR. Window 1 level: 10 HU, width: 400 HU; Window 2 level: 300 HU, width: 2500 HU

**Table 2** Image quality scores among MAR algorithms

Implants	FPB	LI	NMAR	FSMAR	MIFMAR
Seed	2.00 ± 0.01	2.50 ± 0.25	3.50 ± 0.25	3.75 ± 0.10	4.00 ± 0.20
Hip	2.00 ± 0.28	3.33 ± 0.20	4.23 ± 0.15	4.00 ± 0.01	4.23 ± 0.15
Dental	1.75 ± 0.14	1.83 ± 0.25	3.13 ± 0.30	3.33 ± 0.26	3.75 ± 0.24
Heart valve	2.75 ± 0.10	3.00 ± 0.01	3.50 ± 0.25	3.50 ± 0.15	4.00 ± 0.12

**Table 3** Differences in image quality among the algorithms. P-values for pair-wise comparison of the different reconstruction techniques using Friedman-ANOVA and adjustment for multiple comparisons with the Bonferroni–Holms method

	LI	NMAR	FSMAR	MIFMAR
FBP	0.057	0.0001	0.0001	0.0001
LI		0.0001	0.0001	0.0001
NMAR			0.895	0.0001
FSMAR				0.0001

significantly the artifacts in all cases, having a good image quality score. The comparison showed significant differences among all algorithms ( $p < 0.0001$ ). Also, MIFMAR was computationally inexpensive and does not use raw CT data.

## 5 Conclusions

In this paper, we presented a new MAR that work on DICOM images. The MIFMAR algorithm significantly reduced artifacts and improve image quality. This performance was the best in most of the study cases used in this work. The effect of MIFMAR was particularly noticeable in the regions most affected by artifacts. Assessing the effect of MIFMAR on different scanning parameters was beyond the scope of this study but could represent an important consideration to reduce the radiation dose while maintaining image quality.

**Acknowledgements** The authors would like to thank Professor Dr. Norbert Pelc from Stanford University and Dr. Samuel Mazin from RefleXion Medical for proving clinical data.

**Conflict of Interest** The authors declare that they have no conflict of interest.

## References

- Fang, J., Zhang, D., Wilcox, C., Heidinger, B., Raptopoulos, V., Brook, A., Brook, O.R.: Metal implants on CT: comparison of iterative reconstruction algorithms for reduction of metal artifacts with single energy and spectral CT scanning in a phantom model. *Abdom. Radiol.* 42, 742–748 (2017).
- Guggenberger, R., Winklhofer, S., Osterhoff, G., Wanner, G.A., Fortunati, M., Andreisek, G., Alkadhi, H., Stolzmann, P.: Metallic artefact reduction with monoenergetic dual-energy CT: systematic ex vivo evaluation of posterior spinal fusion implants from various vendors and different spine levels. *Eur. Radiol.* 22, 2357–2364 (2017).
- Meyer, E., Raupach, R., Lell, M., Schmidt, B., Kachelrieß, M.: Normalized metal artifact reduction (NMAR) in computed tomography. *Med. Phys.* 37, 5482–5493 (2010).
- Meyer, E., Raupach, R., Lell, M., Schmidt, B., Kachelrieß, M.: Frequency split metal artifact reduction (FSMAR) in computed tomography. *Med. Phys.* 39, 1904–1916 (2012).
- Zhang, H., Wang, L., Li, L., Cai, A., Hu, G., Yan, B.: Iterative metal artifact reduction for x-ray computed tomography using unmatched projector/backprojector pairs. *Med. Phys.* 43, 3019–3033 (2016).
- Naranjo, V., Lloréns, R., Alcañiz, M., López-Mir, F.: Metal artifact reduction in dental CT images using polar mathematical morphology. *Comput. Methods Programs Biomed.* 102, 64–74 (2011).
- Kalender, W.A., Hebel, R., Ebersberger, J.: Reduction of CT artifacts caused by metallic implants. *Radiology.* 164, 576–577 (1987).
- Zhang, Y., Yan, H., Jia, X., Yang, J., Jiang, S.B., Mou, X.: A hybrid metal artifact reduction algorithm for x-ray CT. *Med Phys.* 40, 4 (2013).
- Xu, L., Lu, C., Xu, Y., Jia, J.: Image Smoothing via L0 Gradient Minimization. *ACM Trans Graph.* 30, 174:1–174:12 (2011).
- Golden, C., Mazin, S.R., Boas, F.E., Tye, G., Ghanouni, P., Gold, G., Sofilos, M., Pelc, N.J.: A comparison of four algorithms for metal artifact reduction in CT imaging. In: *Proc. SPIE.* p. 79612Y (2011).



# Fully Automatic CAD System for Spine Localisation and Vertebra Segmentation in CT Data

Roman Jakubicek, Jiri Chmelik, Jiri Jan, Petr Ourednicek, Lukas Lambert, and Giampaolo Gavelli

## Abstract

In this paper, we describe a fully automatic CAD system for spine detection in CT data followed by vertebra identification and segmentation. There are several basic problems: spine detection including the determination of spinal axis in spinal CT data, a localisation of individual vertebrae and identification of their types (order in spine) in case of incomplete scans of spine and also the final vertebra segmentation. By a subjective strict expert validation, the algorithm provides 82.6% of fully correct vertebra segmentations. Based on that, it seems to be routinely usable and fully applicable in preparation for the following automatic spine bone lesion analysis.

## Keywords

Spine detection • Vertebra identification and segmentation • CADx • CT data • Oncological patient

## 1 Introduction

Computer-aided diagnosis (CAD) systems are an essential part of the medical decision-making process and the field of spine imaging, particularly, includes many manual steps. Automatic spine analysis cannot be done without previous detection and segmentation of individual vertebrae. The development of the CAD system within the long-term project is targeted at pathological cases that contain severely deformed vertebrae. This turned out to be a complicated task. Nevertheless, the significant progress has been made in development of the presented CAD system.

Even though that CAD systems for spine analysis consist of several basic steps, some publications only deal with a part of the system. The step of spine detection was solved in publications such as [1–3]. Other authors published their algorithms for the localisation [4, 5] and/or identification (determining their type and order) of individual vertebrae or intervertebral discs (IVD) in [5–7].

The semi-automatic systems were designed e.g. in [8–12], which require a user intervention during parts of the analysis. Whereas, in publications [13–19], the authors describe fully automatic algorithms, which enable a spine analysis. The advantage of these algorithms is that they can run autonomously in the background of the system during its routine operation.

The algorithms based on machine learning methods, frequently fully automatic, are published in [6, 7, 14, 19], whereas other authors in [11, 12, 20, 21] use a wide range of advanced methods of image processing that do not use artificial intelligence. Some methods (e.g. [8, 9, 13, 17]) utilise mean or statistical shape models of vertebrae (mesh or intensity), which involve a priori information about anatomic shape of vertebrae or their variabilities. A detailed overview of the algorithms for spinal analysis is presented in our review paper [22].

We present a fully automatic CAD system for the spine detection in CT data followed by vertebra identification and

---

R. Jakubicek (✉) · J. Chmelik · J. Jan  
Faculty of Electrical Engineering and Communication,  
Department of Biomedical Engineering, Brno University  
of Technology, 61600 Brno, Czech Republic  
e-mail: jakubicek@feec.vutbr.cz

P. Ourednicek  
Department of Medical Imaging, St. Anna University Hospital  
Brno and Faculty of Medicine Masaryk University, 65691 Brno,  
Czech Republic

L. Lambert  
First Faculty of Medicine, Department of Radiology, Charles  
University in Prague and General University Hospital in Prague,  
12808 Prague, Czech Republic

G. Gavelli  
Istituto Scientifico Romagnolo Per Lo Studio e La Cura Dei  
Tumori, Istituto Di Ricovero e Cura a Carattere Scientifico,  
Radiologia, 47014 Meldola, Italy

segmentation of heavily deformed vertebrae in oncological patients. Proposed approaches, which are part of the system, exploit sophisticated statistically based methods utilising the database of pathological cases. In comparison with other methods, the proposed algorithm allows analysis credibly scans with multiple metastatic lesions or severe vertebral compressions.

## 2 Methodology

The designed system contains several steps with their continuity outlined on Fig. 1. For evaluation described in Section Result and Discussion, there is added the option of interruption, enabling checking and possibly correcting the detected locations of the intervertebral discs, thus also the disc centroids.

The rough delimitation area of the spine is obtained by the analysis of the global and then local projections in  $z$  direction. The finding of spine ends is based on a matched filtration of mean intensity models; complex of C1-2 vertebrae and sacral bone. Subsequent the tracking of a spinal cord canal is performed by the maximum circle enables determining the spinal axis.

From the linearised-spine, the 1D brightness profiles are obtained, which are subsequently filtered by adaptive IIR filters by the Butterworth filter design. The frequency responses of the second-order filters are derived from statistical models of cut-off frequencies. The analysis of filtered profiles in this way provides intervertebral disc positions thus enabling improved delimitation of the vertebrae.

The vertebra identification of types in the case of an incomplete spine is based on a kernel-PCA approach with global dynamic optimisation. The non-linear statistical models have been determined from the aligned intensity-gradient (by Sobel's operator) derived vertebrae. These models are then compared with each vertebra of the tested spinal segment and its resulting indices are subsequently obtained by the global optimisation utilising a

dynamic programming, which finds the optimal path in the derived score matrix from similarities (Euclidean distances) between tested vertebra and k-PCA models.

In the first phase, the individual spine model for each patient is created. The adaptation of individual vertebra models to their position and inclination in the spine completed by affine pre-registration makes it possible to also respect potential severe distortions. Next, the spine model is deformed by an efficient 2-step flexible registration with a pyramidal approach. The masks of vertebrae thus obtained are refined by a graph-cut based method leading to reliable and precise segmentation.

## 3 Results and Discussion

In our CAD system, there are two possibilities: to either let the programme run fully automatically until the final results, or to interrupt its running after the first phase of spine segmentation in order to check and possibly correct the intermediate results (IVD locations).

### 3.1 Our Database

In the test database, a total of 78 CT image spinal scans were available. 49 CT scans have been acquired using Philips Brilliance iCT scanner with 256 channel multidetector row at the Osteo Oncology Center, Istituto Scientifico Romagnolo per lo Studio e la Cura dei Tumori (I.R.S.T.) S.r.l., Meldola, Italy and the remaining scans have been provided by other institutions (referred as authors' affiliations). It should be emphasised that, different to most published studies working with primarily healthy cases, our database consisted of 88.3% of pathological vertebrae.

Based on medical expert validation by a visual inspection, 71.5% of vertebra segmentations performed by the system utilising manual editing of vertebra locations were evaluated as acceptable, especially for the following automatic spine bone lesion analysis.

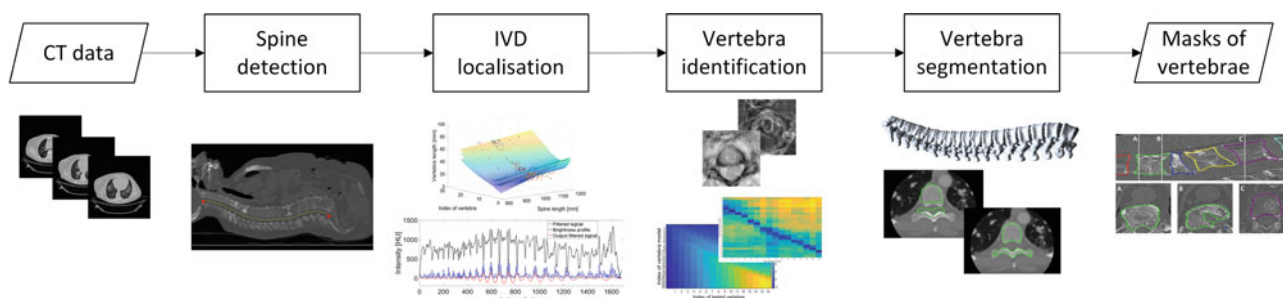


**Fig. 1** Block scheme of proposed CAD system for vertebra segmentation in CT data

**Table 1** Segmentation results for Datasets 2 and 15 (average) and the comparison of the fully automatic run and the approach utilising the option of program interruption

	Vertebral body		Whole vertebra	
	MASD (mm)	Dice (%)	MASD (mm)	Dice (%)
with correction	0.52	93.4	0.80	87.8
Automatic	0.62	92.4	0.98	88.3

For each pair of segmentations (i.e. the binary mask from fully automatic uninterrupted run versus the mask obtained utilising the option of program interruption), the Dice coefficient has been calculated. It has been confirmed by visual inspection that in all cases, when this coefficient was higher than 0.8, the shape differences were negligible. Such a congruity has been found in 82.6% of investigated vertebrae. This leads to the conclusion that the segmentations in both alternatives are practically of the same quality. This is supported by the fact that the fully automatic method provides about 20% of spine segmentations identical to those provided with possible corrections during interruption, while the remaining cases contain on average only 21.7% of differently segmented vertebrae. It seems that, namely for screening purposes, the fully automatic approach might be well acceptable.

### 3.2 Publicly Available Datasets

The same evaluation approach has been used for publicly available Dataset<sup>1</sup> 2 and 15 [23]. The fully automatic method provides coincident segmentations in 86.4% of tested vertebrae. From the perspective of the success of automatic segmentation of entire segments, which do contain different segmented vertebrae, 70% of patient data have been obtained.

Besides that, because the ground truth segmentations in form binary masks are available, we present values of MASD<sup>2</sup> and Dice coefficient listed in Table 1. Although the proposed system segments whole vertebra, our research project is primarily aimed at analysis of vertebral bodies. For this reason, we present the results for whole vertebrae and their bodies separately.

The values of MASD and Dice, shown in Table 1, affirm that the segmentations performed by a fully automatic approach are comparable with the program version with a human editing of detected vertebrae.

<sup>1</sup>Datasets of the spinal CT data on the SpineWeb website is available from: <http://spineweb.digitalimaginggroup.ca>

<sup>2</sup>Mean Absolute surface distance

## 4 Conclusion

Based on the achieved results of the proposed CAD system for the vertebrae segmentation, it seems to be routinely usable and fully applicable in preparation for the following automatic spine bone lesion analysis. Our fully automatic system provides the same results as the semi-automatic approach in 82.6% of cases. This leads to the conclusion that the segmentations in both alternatives are practically of the same quality and besides that, the mean error and Dice coefficient of segmented masks on public available datasets support the fact that the proposed method provides good results and, might be well acceptable, namely for screening purposes.

**Conflict of Interest** These results were obtained through international cooperation between the Brno University of Technology and Philips Healthcare Netherlands. No conflicts of interest were identified.

**Ethical approval** All procedures performed in studies involving human participants were in accordance with the ethical standards of the institutional and/or national research committees and with the 1964 Helsinki declaration and its later amendments or comparable ethical standards.

## References

1. Hanaoka, S., Nomura, Y., Nemoto, M., Masutani, Y., Maeda, E., Yoshikawa, T., Hayashi, N., Yoshioka, N., Ohtomo, K.: Automated segmentation method for spinal column based on a dual elliptic column model and its application for virtual spinal straightening. *Journal of computer assisted tomography* 34(1), 156–162 (2010)
2. Archip, N., Erard, P.J., Egmont-Petersen, M., Haeffliger, J.M., Germond, J.F.: A knowledge-based approach to automatic detection of the spinal cord in ct images. *IEEE Transactions on Medical Imaging* 21(12), 1504–1516 (2002)
3. Burnett, S.S., Starkschall, G., Stevens, C.W., Liao, Z.: A deformable-model approach to semi-automatic segmentation of ct images demonstrated by application to the spinal canal. *Medical physics* 31(2), 251–263 (2004)
4. Forsberg, D.: Atlas-based registration for accurate segmentation of thoracic and lumbar vertebrae in ct data. In: *Recent Advances in Computational Methods and Clinical Applications for Spine Imaging*, pp. 49–59. Springer (2015)
5. Stern, D., Vrtovec, T., Pernus, F., Likar, B.: Automated determination of the centers of vertebral bodies and intervertebral discs in ct and mr lumbar spine images. In: *Medical Imaging: Image Processing*, p. 762350 (2010)
6. Glocker, B., Feulner, J., Criminisi, A., Haynor, D., Konukoglu, E.: Automatic localization and identification of vertebrae in arbitrary field-of-view ct scans. In: *Medical Image Computing and Computer-Assisted Intervention—MICCAI 2012*, pp. 590–598. Springer (2012)
7. Cai, Y., Osman, S., Sharma, M., Landis, M., Li, S.: Multi-modality vertebra recognition in arbitrary views using 3d deformable hierarchical model. *IEEE transactions on medical imaging* 34(8), 1676–1693 (2015)
8. Hardisty, M., Gordon, L., Agarwal, P., Skrinikas, T., Whyne, C.: Quantitative characterization of metastatic disease in the spine. part

- i. semiautomated segmentation using atlas-based deformable registration and the level set method. *Medical physics* 34(8), 3127–3134 (2007)
9. Peter, R., Malinsky, M., Ourednicek, P., Jan, J.: 3d ct spine data segmentation and analysis of vertebrae bone lesions. In: *Engineering in Medicine and Biology Society (EMBC), 2013 35th Annual International Conference of the IEEE*. pp. 2376–2379. IEEE (2013)
  10. Mastmeyer, A., Engelke, K., Fuchs, C., Kalender, W.A.: A hierarchical 3d segmentation method and the definition of vertebral body coordinate systems for qct of the lumbar spine. *Medical image analysis* 10(4), 560–577 (2006)
  11. Courbot, J.B., Rust, E., Monfrini, E., Collet, C.: 2-step robust vertebra segmentation. In: *Image Processing Theory, Tools and Applications (IPTA), 2015 International Conference on*. pp. 157–162. IEEE (2015)
  12. Dai, Y., Niebur, G.L.: A semi-automated method for hexahedral mesh construction of human vertebrae from ct scans. *Computer methods in biomechanics and biomedical engineering* 12(5), 599–606 (2009)
  13. Ibragimov, B., Korez, R., Likar, B., Pernuš, F., Vrtovec, T.: Interpolation-based detection of lumbar vertebrae in ct spine images. In: *Recent Advances in Computational Methods and Clinical Applications for Spine Imaging*, pp. 73–84. Springer (2015)
  14. Chu, C., Belavý, D.L., Armbrecht, G., Bansmann, M., Felsenberg, D., Zheng, G.: Fully automatic localization and segmentation of 3d vertebral bodies from ct/mr images via a learning-based method. *PLoS one* 10(11), e0143327 (2015)
  15. Klinder, T., Ostermann, J., Ehm, M., Franz, A., Kneser, R., Lorenz, C.: Automated model-based vertebra detection, identification, and segmentation in ct images. *Medical image analysis* 13(3), 471–482 (2009)
  16. Kadoury, S., Labelle, H., Paragios, N.: Spine segmentation in medical images using manifold embeddings and higher-order mrfs. *IEEE transactions on medical imaging* 32(7), 1227–1238 (2013)
  17. Hammernik, K., Ebner, T., Stern, D., Urschler, M., Pock, T.: Vertebrae segmentation in 3d ct images based on a variational framework. In: *Recent Advances in Computational Methods and Clinical Applications for Spine Imaging*, pp. 227–233. Springer (2015)
  18. Cheng, E., Liu, Y., Wibowo, H., Rai, L.: Learning-based spine vertebra localization and segmentation in 3d ct image. In: *Biomedical Imaging (ISBI), 2016 IEEE 13th International Symposium on*. pp. 160–163. IEEE (2016)
  19. Chen, H., Shen, C., Qin, J., Ni, D., Shi, L., Cheng, J.C., Heng, P. A.: Automatic localization and identification of vertebrae in spine ct via a joint learning model with deep neural networks. In: *International Conference on Medical Image Computing and Computer-Assisted Intervention*. pp. 515–522. Springer (2015)
  20. Huang, J., Jian, F., Wu, H., Li, H.: An improved level set method for vertebra ct image segmentation. *Biomedical engineering online* 12(1), 48 (2013)
  21. Štern, D., Likar, B., Pernuš, F., Vrtovec, T.: Parametric modelling and segmentation of vertebral bodies in 3d ct and mr spine images. *Physics in medicine and biology* 56(23), 7505 (2011)
  22. Jakubicek, R., Chmelik, J., Jan, J.: Vertebrae segmentation in 3d ct data: A review of methods and evaluation approaches. *Current Medical Imaging Reviews* 13(4), 1–14 (2017), iSSN 1573-4056/1875-6603. [in press]
  23. Yao, J., Burns, J.E., Forsberg, D., Seitel, A., Rasoulian, A., Abolmaesumi, P., Hammernik, K., Urschler, M., Ibragimov, B., Korez, R., et al.: A multi-center milestone study of clinical vertebral ct segmentation. *Computerized Medical Imaging and Graphics* 49, 16–28 (2016)

# Hyperdense Middle Cerebral Artery Segmentation in Non Contrast Computed Tomography

Nelly Gordillo<sup>1</sup>, Alberto Davis<sup>1</sup>, Felipe García<sup>1</sup>, José Mejía<sup>1</sup>, and Xavier Aymerich<sup>2</sup>

## Abstract

The hyperdense middle cerebral artery (MCA) sign refers to focal increased density of the MCA in Non-Contrast Computed Tomography (NCCT) and is the earliest sign of acute ischemic stroke. In this paper, we present the implementation of a method that allows the automatic segmentation of the hyperdense MCA sign in NCCT pathological clinical cases, as a first phase in the development of a tool that will support the early detection of cerebral infarction. A fully automated algorithm was proposed for the delimitation of volumes of interest and the segmentation of the hyperdense MCA. Volumes of interest were defined according to the anatomical location of the suprasellar cistern, and features of the hyperdense MCA were extracted according to the Hounsfield Units and entropy. The segmentation was carried out using a model of region growing and active contours (snakes). The results show an accuracy of 96% (99% per slice) and a mean correlation of automatic versus manual segmentation of 94%.

## Keywords

Hyperdense MCA sign • NCCT • Automated segmentation

## 1 Introduction

According to the World Health Organization, cerebrovascular diseases (CVD) remain the second leading cause of death, and is the leading cause of disability in adults [1].

N. Gordillo (✉) · F. García · J. Mejía  
University of Ciudad Juárez, Juárez, Mexico  
e-mail: nelly.gordillo@uacj.mx

A. Davis · X. Aymerich  
Barcelona TECH, Barcelona, Spain

Ischemic stroke is one of the most common CVD and is characterized by the sudden loss of blood circulation to an area of the brain. Identifying the early presence of an ischemic stroke is of vital importance, since the affected tissue can be rescued within the first hours after the onset of the stroke.

The hyperdense middle cerebral artery (hMCA) is one of the early signs in non-contrast computed tomography images within the first 90 min [2], and is assumed to be a radiological marker of acute intra-arterial occlusion. Despite the clinical relevance of the hyperdense MCA sign, few contributions in the literature have addressed automatic segmentation techniques of this sign [3, 4].

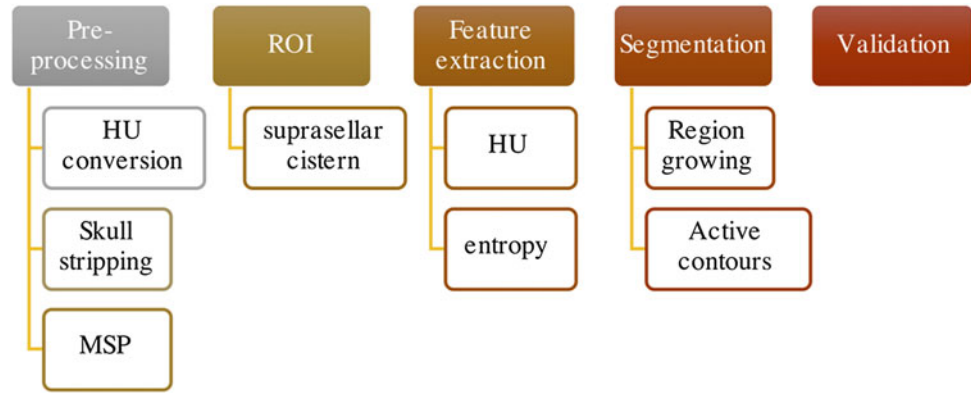
In this paper, we propose the fully automated segmentation of the hMCA sign in NCCT pathological clinical cases. Once the anatomical region of interest was defined, features of the hMCA radiological attenuation index denoted by the Hounsfield Units and the entropy were extracted. The segmentation was based on a model of region growing and active contours.

## 2 Methodology

The methodology was composed of five major steps: pre-processing, anatomical delimitation of the region of interest, feature extraction, segmentation of the hMCA, and validation (Fig. 1).

We used NCCT brain imaging, 44 cases of non-pathological patients (male and female) with thicknesses of 3 mm and mean ages of  $30 \pm 20$  years, and 6 pathological cases presenting the hyperdense MCA sign. Image datasets have a resolution of  $512 \times 512$  pixels (16-bits). The cases were collected from 3 CT scanners from two hospitals located in Juárez, Mexico. Their use in this research was approved by a bioethics committee.

**Fig. 1** Steps involved in the methodology



## 2.1 Preprocessing

Since the Hounsfield Units (HU) are the main characterization feature in clinical practice, we performed the gray scale conversion to HU using (Eq. 1). where  $Y$  is the gray level,  $m$  is the rescale slope and  $a$  is the rescale intercept, these two data can be found in the information contained in the DICOM file

$$HU(i,j) = m * Y(i,j) + a \quad (1)$$

We also implemented two previously developed algorithms for the automatic skull stripping and mid-sagittal plane extraction [5], the algorithm creates an image mask of the brain that limits processing within the mask pixels. Based on the resulting mask, the second algorithm, extracts the MSP by detecting the anterior longitudinal fissure.

## 2.2 Region of Interest

Considering that the suprasellar space contains the cerebrovascular circle of Willis, in order to delimit the region in which the hMCA sign can be found, an algorithm capable of detecting the suprasellar cistern was designed. The suprasellar cistern is located above the sella turcica, under the hypothalamus and between the uncus of the temporal lobes [6]. In the coronal and sagittal planes, it is around 20 mm in length. Due to its anatomical location, for the detection of the cistern, only the slices below the middle part of the brain and above the first quarter were considered. Since the MSP delineation algorithm places the brain in each

slice in the center of the image, the detection could also be limited to the center of the anterior half of the brain.

Considering that the cistern is full of cerebrospinal fluid (CSF), the region was binarized using a threshold in the intensity ranges of the CSF, from 0 to 20 HU. From the binarized image an erosion was carried out using a disc-shaped structural element to eliminate small objects. Then, the objects were labeled and their area was calculated. The object with the largest area was selected and a closing operation to eliminate small holes was applied. Finally, in order to identify the slice that shows more extensively the suprasellar cistern, the roundness and inclination of the segmented object in the previous step was evaluated. The roundness indicates how close an object is to a circle (Eq. 2), where  $A$  is the area and  $p$  the perimeter.

$$r = 4\pi A/p^2 \quad (2)$$

Having the suprasellar cistern a shape similar to a pentagon, it is expected to have a considerable roundness. The inclination of the object with respect to the center of the image was evaluated in order to discard objects with more than  $15^\circ$ , since the suprasellar cistern is very close to the center of the brain. A volume of interest equivalent to the thickness of the cistern (20 mm) was demarcated defining the slice previously identified as the center of the cistern.

## 2.3 Feature Extraction

Subsets of non-pathological brain tissue, white matter (WM), gray matter (GM) and CSF, and samples containing the

**Table 1** Main statistical measurements in HU of NCCT brain tissues in slices of 3 mm

Tissue	min	max	mean
CSF	0	14	5.28
WM	20	35	29.46
GM	33	57	43.8
hMCA	51	80	52.56



**Fig. 2** Six cases that present the hMCA sign and their automatic and manual segmentations

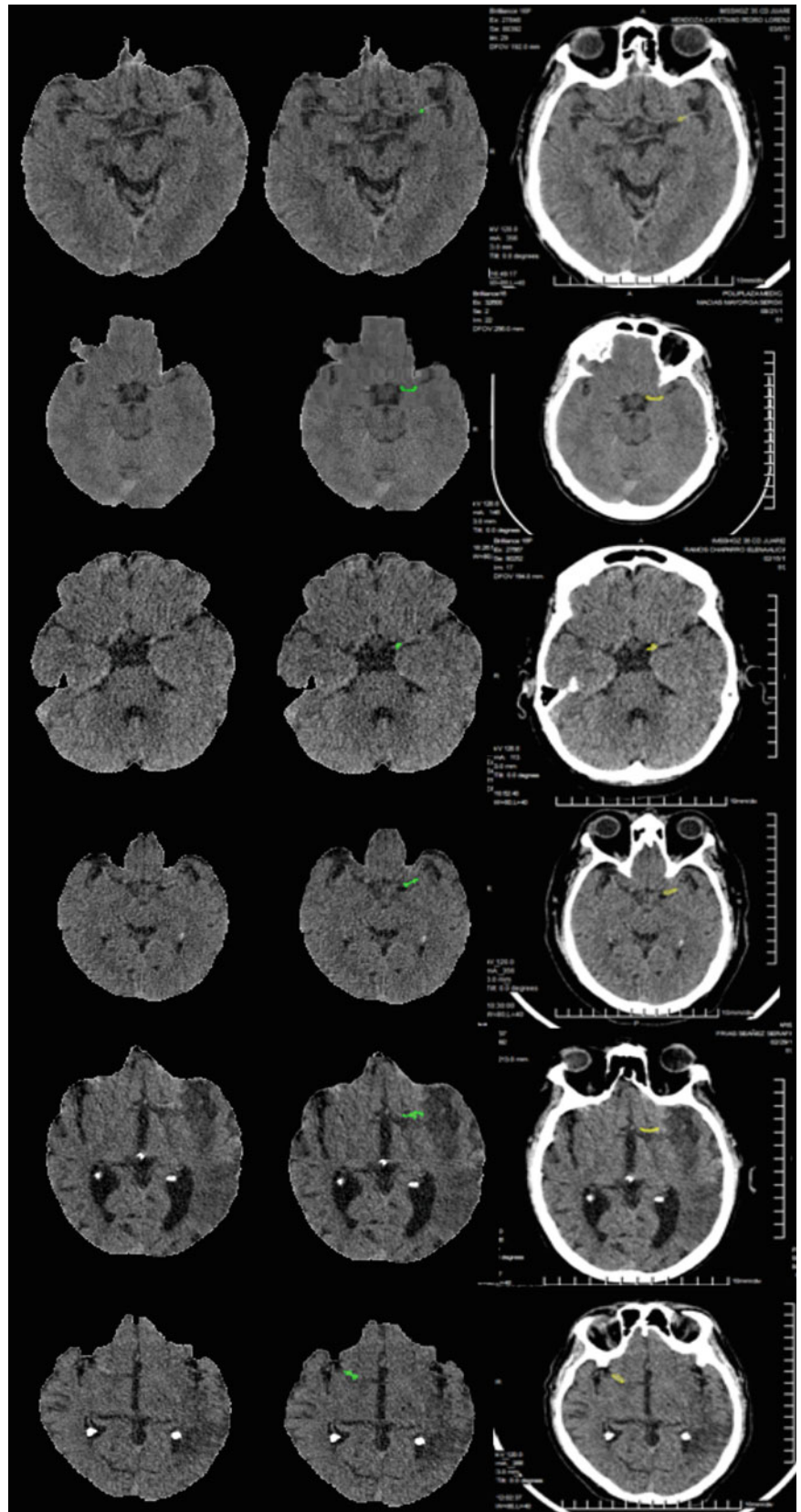


**Table 2** Results of the segmentation of the hMCA sign in pathological cases

Case	Slices	TP	TN	FP	FN	S	E	ACC	corr	len	vol
1	65	1	64	0	0	1	1	1	0.93	9	20.25
2	63	1	62	0	0	1	1	1	0.94	7	25.5
3	61	1	60	0	0	1	1	1	0.95	6	45.75
4	62	1	61	0	0	1	1	1	0.96	3	18
5	60	1	59	0	0	1	1	1	0.94	5	11.25
6	62	1	61	0	0	1	1	1	0.93	3	12.75
7–50	2685	0	2685	2	0	1	0.99	0.99	–	–	–

hyperdense MCA sign were selected with the aim of analyzing their HU characteristics (Table 1). Entropy (Eq. 3) is another characteristic that was considered, it is related to the variety of intensities of a structure, the higher the entropy, the greater is the variety of intensities. The hMCA is a structure whose entropy is low, since most of the pixels that compose the hMCA have similar intensities due to the hyperdensity.

$$e = - \sum_{i=0}^{L-1} p(z_i) \log_2 p(z_i) \quad (3)$$

Using the characteristics of HU and entropy, a threshold was first implemented based on the values of the hyperdense MCA sign. Structures with areas smaller than 10 pixels were discarded. Then, structures whose entropy was medium to high were also excluded.

Inclination and location features of the structures were also considered. The hMCA is located on one side of the upper middle part of the suprasellar cistern. For this reason, structures greater than 30° with respect to the center of the suprasellar cistern were excluded, indicating that these structures were not found on the sides. The hMCA is located in segment M1, the horizontal or sphenoid segment, and part of segment M2, the insular segment, with an inclination not greater than 45°. Structures present in the right hemisphere of the brain whose inclination was greater than 45° and structures with less than -45° inclination in the left hemisphere were excluded. Structures whose maximum value was less than 55 HU were also excluded.

## 2.4 Segmentation

For the hyperdense MCA sign segmentation two techniques were used: region growing and active contours. The objects that fulfilled the characteristics of the previous section were defined as seed points. The neighboring pixels in the range of intensities of the hMCA with maximum distances to 2 pixels were added. From the initial approximation generated by the technique of region growing, an active contour model

(snakes) was applied, minimizing the energy function in Eq. 4.

$$\int_0^1 [E_{int}(v(s)) + E_{im}(v(s)) + E_{ext}(v(s))] ds \quad (4)$$

## 2.5 Validation

In order to validate the segmentation algorithm, the correlation of the automatic segmentations performed by the algorithm against manual segmentations performed by neuroradiological physicians was evaluated. Non-pathological cases were also evaluated.

## 3 Results and Discussion

Figure 2 shows six cases that present the hMCA sign and their corresponding segmentation: automatic and manual. In all the pathological cases, it was possible to successfully segment the hMCA sign, while in the non-pathological cases only 2 false positives were found, they corresponded to hyperdense vascular structures close to the anatomical location of the MCA. Table 2 contains the results of the segmentation showing for each case the number of slices, true positives (TP), true negatives (TN), false positives (FP), false negatives (FN), sensitivity (S), specificity (E), accuracy (ACC), the correlation of automatic versus manual segmentation (corr), and finally the length and volume of the hMCA in mm. The global accuracy of hMCA detection is shown in Table 3.

**Table 3** Global accuracy of hMCA detection

Cases	TP	TN	FP	FN	ACC
50	6	44	2	0	0.96

## 4 Conclusions

The selection of volumes of interest based on the detection of the suprasellar cistern, allowed to adequately delimit the slices where the hMCA segmentation algorithm was implemented, considerably reducing the segmentation time. In all cases, it was possible to locate the suprasellar cistern. The characterization of the hMCA in terms of HU and entropy allowed us to successfully differentiate between a case containing the hyperdense MCA sign and possible false positives in more than 99% of the slices of the 50 cases evaluated (96%). Automatically segmented regions have a 93–96% correlation with manual segmentations. To the best of our knowledge, this is the first contribution for the fully automatic segmentation of the hMCA sign in NCCT images.

## References

1. WHO, “Global Health Estimates 2015: Deaths by Cause, Age, Sex, by Country and by Region, 2000–2015,” Geneva, 2016.
2. T. Nakatsuka, M. Kurotsuchi, H. Morita, T. Inaoka, and H. Terada, “Can 5-mm Axial CT Images Sufficiently Depict the Hyperdense Middle Cerebral Artery Sign in Patients with Acute Brain Ischemia?,” vol. 2013, no. December, pp. 196–200, 2013.
3. E. M. M. Santos *et al.*, “Development and validation of intracranial thrombus segmentation on CT angiography in patients with acute ischemic stroke,” *PLoS One*, vol. 9, no. 7, 2014.
4. C. W. Haddad, K. Drukker, R. Gullett, T. J. Carroll, G. A. Christoforidis, and M. L. Giger, “Fuzzy c-means segmentation of major vessels in angiographic images of stroke,” vol. 5, no., pp. 14501–14511, 2018.
5. A. Davis and N. Gordillo, “Fast algorithms for the automatic skull stripping and mid-sagittal plane extraction in neurologic CT images,” *Mem. del Congr. Nac. Ing. Biomédica*, 2014.
6. M. St-Amant, “Supracellar cistern,” *Radiopaedia*. 2018.

# Joint Adaptive Beamforming to Enhance Noise Suppression for Medical Ultrasound Imaging

Acacio J. Zimbico, Diogo W. Granado, Fabio K. Schneider, Joaquim M. Maia, Amauri A. Assef, Nivaldo S. Junior, and Eduardo T. Costa

## Abstract

In this work we suggest a combination of two beamformers (BFs) to improve the array noise-suppression abilities using the moments of the eigenvalues (EV) of the data covariance matrix (CM). The eigenspace minimum variance (EMV) BF suffers from the input signal with low SNR, while with high SNR, the dominant mode rejection (DMR) BF degrades. Thus, the random matrix theory (RMT) is used based on the principle that the EV of CM allow predicting the actual moments of the EV so that the SNR level of the proper input data is estimated based on a specified threshold. Compared to the threshold, the higher values of the EV function are associated with the input signal with higher SNR level, so that the EMV BF is adopted, otherwise, the DMR BF. The raw data of the multipurpose phantom (84-317) were acquired using the Verasonics ultrasound system with linear array transducer L11-4v. The performance of the proposed BF (EMV + DMR) was evaluated in terms of lateral resolution using the full width at half maximum (FWHM), peak sidelobe level (PSL) and contrast (CR). Furthermore, the resolution and contrast were improved, indicating that the proposed approach can improve the image quality.

## Keywords

Adaptive beamformer • Ultrasound • Noise suppression  
Image quality

## 1 Introduction

Delay and sum (DAS) is the conventional beamforming technique implemented in medical ultrasound imaging. The DAS is a fixed weight beamformer (BF) so that different standard windows (e.g. boxcar, hamming) can be applied providing different tradeoffs between the sidelobe level and the main lobe width, however, the BF output suffers from poor resolution and contrast. Adaptive BFs which are data-dependent by updating the weighting window could improve the image quality [1]. Minimum variance (MV) BF is popularly known to be accurate in signal estimation in areas such as radar and sonar [1] and, recently, the application of this method has gained a special attention to medical ultrasound [2]. Differently to the fixed weight BFs, the MV BF uses the structure of the received signals across the array to estimate the weight which is applied to the data to determine the BF output [1, 2]. The covariance matrix (CM) estimation is a key step of the MV BFs by determining the performance of the algorithm. The MV BF adapts the steering weights in order to suppress signals that do not match the desired response introducing benefits relative to conventional imaging such as narrowing of the main lobe and reducing the effects of interfering sources which can farther darken weak targets [2]. The eigenspace MV (EMV) BF could improve the performance of MV BF [3], however, it performs poorly if data with low source SNR is used while the DMR BF suffers from quality degradation if data with high SNR level is applied [4–6]. The proper input data need to be applied so that the abovementioned BFs do not fail to provide better performance thus, the source SNR need be estimated from data. The random matrix theory (RTM) [4–6] allow predicting the moments of the eigenvalues (EV) of CM so that the source SNR level can be estimated from data based on a predefined threshold. In this context, a synergetic combination of the EMV BF and DMR BF based on RTM could aggregate some benefits. In this work, we aim to use the RTM abilities in estimating the

A. J. Zimbico (✉)

Eduardo Mondlane University (UEM), Maputo, Mozambique  
e-mail: ajzimbico@gmail.com

A. J. Zimbico · D. W. Granado · F. K. Schneider · J. M. Maia  
A. A. Assef · N. S. Junior  
Federal University of Technology Parana (UTFPR), Curitiba,  
PR, Brazil

E. T. Costa  
State University of Campinas (UNICAMP), Campinas, SP, Brazil

source (echo data) SNR level in order to combine the EMV BF and the DMR BF to derive a new joint adaptive BF.

## 2 Beamformers

For an  $M$  element transducer in which  $x_i(k)$  is the sampled output from element  $i$ , the output of a BF can be described as:

$$z(k) = \sum_{i=0}^{M-1} w_i(k)x_i(k - \Delta_i) = w^H(k)x(k) \quad (1)$$

where  $w_i(k)$  is a complex weight,  $\Delta_i$  is a time delay applied to each individual channel  $i$  in order to focus at specific image point,  $w^H(k) = [w_0(k), w_1(k), \dots, w_{M-1}(k)]$  and  $x(k) = [x_0(k - \Delta_0), x_1(k - \Delta_1), \dots, x_{M-1}(k - \Delta_{M-1})]^T$  [2]. For delay and sum (DAS) BF, the weights  $w(k)$  are predetermined. However, in minimum variance (MV) BF, the adaptive weight is found by minimizing the power of the output ( $w^H R w$ ) subject to the constraints as follows:

$$\min_w (w^H R w) \text{ subject to } w^H a = 1 \quad (2)$$

where  $R = \mathbb{E}(xx^H)$  is the covariance matrix (CM),  $\mathbb{E}(\cdot)$  is the expectation operator and,  $(\cdot)^H$  the Hermitian conjugate. The weight of the MV  $w_{MV}$  BF is:

$$w = \frac{R^{-1}a}{a^H R^{-1}a} \quad (3)$$

where  $a$  is the steering vector. The  $a$  will be a vector of ones since the signals in  $x(k)$  have been delayed [2]. The CM must be estimated from the received signal by averaging either in temporal or spatial domain, or a combination of both approaches. Averaging in spatial domain consists of dividing the transducer into overlapping subarrays  $X_i(k)$ , whose length is limited to ( $L \leq M/2$ ) and, averaging the spatial CMs of each subarray. In general, the CM estimate (4) is averaged over  $E = 2T + 1$  time steps, where  $T$  is the number of temporary samples and,  $F = M - L + 1$  is the number of subarrays of length  $L$ . Furthermore, the CM is diagonally loaded in order to get a robust estimate [2] as in (4),

$$\hat{R}(k) = \frac{1}{E} \frac{1}{F} \sum_{k=-K}^K \sum_{l=1}^F X_l(k) X_l(k)^H + \varepsilon I \quad (4)$$

where  $X_l(k) = [x_l(k); x_{l+1}(k); \dots; x_{l+L-1}(k)]^T$ . The diagonal loading (DL) factor expressed as  $\varepsilon = 1/(\Delta_f L) Tr(R)$  was defined in [2]. The factor  $\Delta_f$  is a constant,  $I$  is the identity matrix and,  $Tr$  stands for trace. The BF output is formulated as in (5) [2].

$$z_{MV}(k) = \frac{1}{F} \sum_{l=1}^F w_{MV} X_l(k) \quad (5)$$

In the EMV BF the eigendecomposition of CM is performed (6) as in [3] in order to identify  $L \times r$  matrix  $U_s$  and  $L \times (L - r)$  matrix  $U_n$ , the signal and noise subspace, respectively. In (6), the EVs of CM are sorted in descending order  $\lambda_1 \geq \lambda_2 \geq \dots \geq \lambda_L$  so that the eigenvectors  $U = [v_1, v_2, \dots, v_r]$  corresponding to the largest EVs  $\Lambda = [\lambda_1, \lambda_2, \dots, \lambda_r]$  define the signal subspace while the eigenvectors corresponding to the remaining EVs  $\Lambda = [\lambda_{r+1}, \lambda_{r+2}, \dots, \lambda_L]$  define the noise subspace, respectively [3].

$$\begin{aligned} R &= \sum_{i=1}^L \lambda_i u_i u_i^H = \sum_{i=1}^r \lambda_i u_i u_i^H + \sum_{i=r+1}^L \lambda_i u_i u_i^H \\ &= U_s \Lambda_s U_s^H + U_n \Lambda_n U_n^H \end{aligned} \quad (6)$$

The EMV BF weight is obtained by projecting the MV weight onto the signal sub-space ( $P_s = U_s U_s^H$ ) as follows:  $w_{EMV} = P_s w_{MV} = U_s U_s^H w_{MV}$ . In DMR BF, a version of CM  $R \approx R_{DMR}$  is determined based on (6). The estimate of CM uses the average of the smaller EVs  $\alpha$  as in (7) [4, 5, 7].

$$\begin{aligned} R_{DMR} &= \sum_{i=1}^r \lambda_i u_i u_i^H + \alpha \sum_{i=r+1}^L u_i u_i^H \rightarrow R_{DMR}^{-1} \\ &= \alpha^{-1} \left[ I - \left( \frac{\lambda_i - \alpha}{\alpha} \right) \sum_{i=r+1}^L u_i u_i^H \right] \end{aligned} \quad (7)$$

The DMR BF is obtained by applying the inverted version of CM  $R_{DMR}^{-1}$  (7) in (3).

## 3 Proposed Method

The eigenvalues  $\lambda_i, i = 1, \dots, L$  used in (6)–(7) are ordered in descending order so that they can represent the EV function  $\Phi(i)$  in (8). In (8),  $\mu_j$  represents the real-valued solution to (9) whose elements must be sorted in descending order.

$$\Phi(i) = \begin{cases} 1 + \sum_{i=1}^r \left( \frac{\lambda_i}{\lambda_j - \lambda_i} - \frac{\mu_i}{\lambda_j - \mu_i} \right) & \text{if } j \geq r + 1; \\ - \sum_{i=r+1}^L \left( \frac{\lambda_i}{\lambda_j - \lambda_i} - \frac{\mu_i}{\lambda_j - \mu_i} \right) & \text{otherwise.} \end{cases} \quad (8)$$

$$f(\mu) = \frac{1}{L} \sum_{j=1}^L \left( \frac{\lambda_j}{\lambda_j - \mu} \right) = \frac{E}{L} \quad (9)$$

In (9), the consistency of the estimation procedure is determined by  $E/L$  [4–6], the rate between the temporary samples and the subarray length used in CM estimate in (4). Furthermore, the definition of the required threshold ( $\delta$ ), is



**Table 1** The algorithm of the proposed beamformer

(I)	From input data, compute the CM estimate (4) and, the MV weight (3)
(II)	Perform the eigendecomposition of CM (6) and calculate the EMV weight
(III)	Calculate the DMR CM version in (7) and compute the DMR weight (3)
(IV)	Compute the threshold ( $\delta$ ) value using RMT (8)-(10) and, based on estimated SNR level, chose the BF

performed by solving (9). In accordance with the RMT, the middle hand of (9) has an asymptotic behavior so that  $f(\mu)$  will increase or decrease depending on the variable position  $\mu$  [4, 5]. If  $j = r$ , then  $\Phi(i) = \Phi(r)$  and (8) can be solved as in (10).

$$\Phi(r) = - \sum_{k=r+1}^L \left( \frac{\lambda_j}{\lambda_r - \lambda_j} - \frac{\mu_j}{\lambda_r - \mu_j} \right); \quad (10)$$

Based on (10), we can determine which BF should be adopted so that  $|\Phi(r)| \geq \delta$  the SNR level is low and the DMR BF is applied otherwise, the EMV BF should be adopted. Moreover,  $|\Phi(r)| \in [0, 1]$  and the critical range for

threshold selection is  $|\Phi(r)| \in [0.1, 0.2]$ . For phantom experiments, a  $\delta$  of 0.15 was adopted. The proposed beamforming algorithm can be summarized in Table 1.

### 4 Results and Discussion

The raw data of the multipurpose phantom (84-317) were acquired with a constant f-number of 0.75 using the Verasonics ultrasound system, 128-elements linear array transducer L11-4v, 6.25 MHz central frequency, a pitch of 0.308 mm and for the channel data processing the sampling rate of 40 MHz. In the displayed images, the phantom point marked in the green box, Fig. 1a, presents an improved definition in MV compared to the DAS BF. The EMV BF presents a point with better definition compared to DMR BF and both outperform MV BF. However, the proposed BF outperformed the different BFs. In order to complement the qualitative analysis, Table 2 presents the quantitative results of resolution evaluation using FWHM and PSL. Figure 2a presents the lateral profile of different BFs for the phantom point target. In terms of contrast, the displayed images in Fig. 1 allows observing that the MV has an improved contrast compared to DAS but the MV is outperformed by the

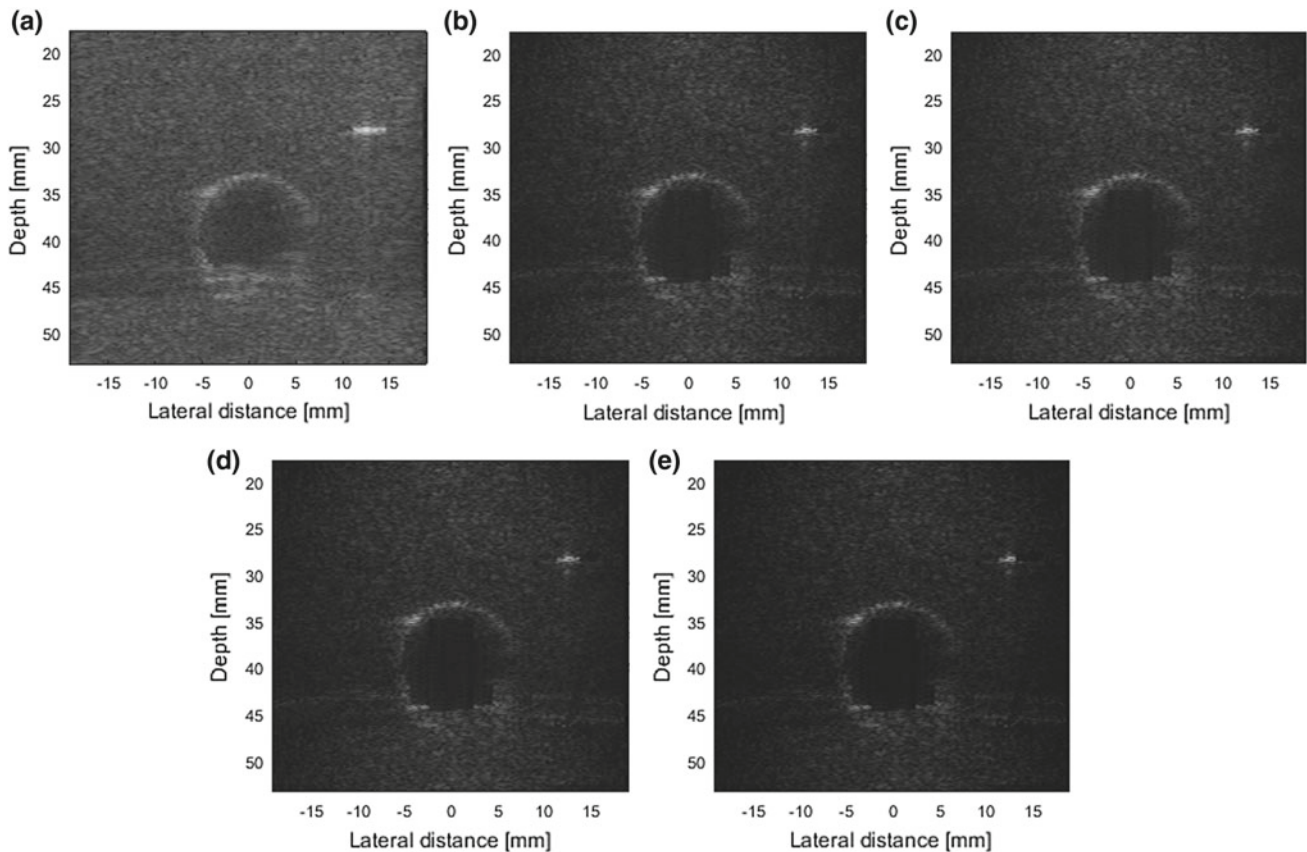


**Fig. 1** Phantom imaging for the anechoic cyst for **a** DAS, **b** MV, **c** EMV, **d** EMV, **e** proposed method



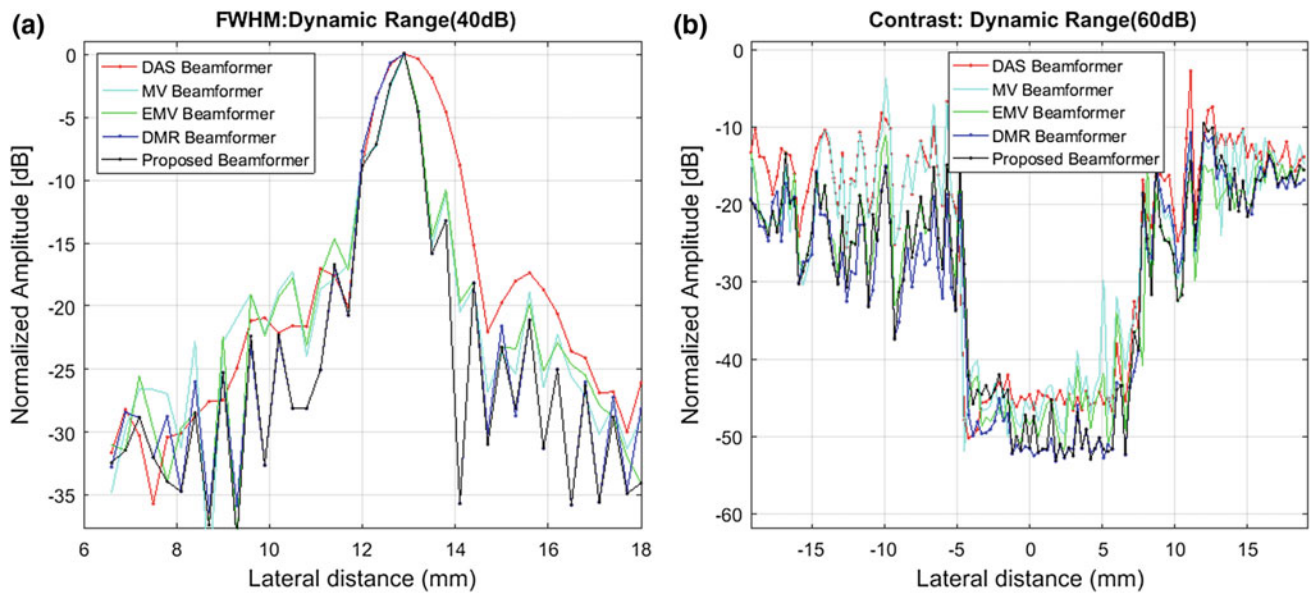


**Fig. 2** Lateral profile for **a** resolution for point target and **b** the contrast for the anechoic cyst for different BFs, respectively

**Table 2** Quantitative results of different beamformers for resolution and contrast

Resolution			Contrast		
BF	FWHM (mm)	PSL (dB)	IIC (dB)	IOC (dB)	CR (dB)
DAS	1.75	-17.15	-55.10	-43.53	11.26
MV	1.26	-17.39	-56.22	-44.56	11.66
EMV	1.06	-17.68	-58.44	-39.04	19.40
DMR	1.14	-18.13	-58.35	-39.01	19.34
Prop.	0.83	-18.36	-56.88	-36.39	20.88

IIC Intensity inside cyst

IOC Intensity outside cyst

EMV and the DMR BFs, respectively, however, the proposed BF presents an improved contrast compared to the different BFs. Table 2 presents the quantitative results of contrast evaluation. Figure 2b presents the lateral profile of different BFs at  $z = 40$  mm for the phantom circular anechoic cyst of 10 mm diameter located at  $(x, z) = (0.40, 40)$  mm. Observing Fig. 2b, it is possible to see that the proposed BF was superior in suppressing a larger part of noise in the interior of the cyst compared to the different BFs while preserving the speckle outside cyst which results in an improved image contrast. Additionally, while solving (8)–(10), the proposed method will need some computational effort compared to EMV and DMR.

## 5 Conclusion

We have successfully demonstrated that the EMV and DMR BFs can be combined using the random matrix theory (RMT) in order to improve the image quality. The RTM based method estimates the SNR level of the input data using the eigenvalues of CM based on a specified threshold. The resolution and contrast were improved, which demonstrates that the suggested method can improve the image quality.

## References

1. Capon, Jack: High-resolution frequency-wavenumber spectrum analysis. Proceedings of the IEEE, 57, 1408–1418 (1969). <https://doi.org/10.1109/proc.1969.7278>
2. Synnevag, JF and Austeng, Andreas and Holm, Sverre, Srinivas: Minimum variance adaptive beamforming applied to medical ultrasound imaging. Proc. IEEE Ultrason. Symp. 2, 1199–1202 (2005). <https://doi.org/10.1109/ultrason.2005.1603066>
3. Asl, Babak Mohammadzadeh and Mahloojifar, Ali: Eigenspace-based minimum variance beamforming applied to medical ultrasound imaging. IEEE transactions on ultrasonics, ferroelectrics, and frequency control, 57, 11 (2010). <https://doi.org/10.1109/ultrason.2008.0258>
4. Mestre, Xavier: Improved estimation of eigenvalues and eigenvectors of covariance matrices using their sample estimates. IEEE Transactions on Information Theory, 54, 5113–5129 (2010). <https://doi.org/10.1109/tit.2008.929938>
5. Wu, Ying and Wang, Yunlong and others: ESB-DMR beamforming under random matrix theory judgment principle. IET, (2015). <https://doi.org/10.1049/cp.2015.1006>

6. Mestre, Xavier and Lagunas, Miguel: Modified subspace algorithms for DoA estimation with large arrays. *IEEE Transactions on Signal Processing*, 56, 598–614 (2008). <https://doi.org/10.1109/tsp.2007.907884>
7. Tracey, Brian and Lee, Nigel and Turaga, Srinivas: Cluster analysis and robust use of full-field models for sonar beamforming. *The Journal of the Acoustical Society of America*. 5, 2635–2647 (2006). <https://doi.org/10.1121/1.2346128>

# Label-Free Nuclear Staining Reconstruction in Quantitative Phase Images Using Deep Learning

Tomas Vicar, Jaromir Gumulec, Jan Balvan, Michal Hracho, and Radim Kolar

## Abstract

Fluorescence microscopy is a golden standard for contemporary biological studies. However, since fluorescent dyes cross-react with biological processes, a label-free approach is more desirable. The aim of this study is to create artificial, fluorescence-like nuclei labeling from label-free images using Convolution Neural Network (CNN), where training data are easy to obtain if simultaneous label-free and fluorescence acquisition is available. This approach was tested on holographic microscopic image set of prostate non-tumor tissue (PNT1A) and metastatic tumor tissue (DU145) cells. SegNet and U-Net were tested and provide “synthetic” fluorescence staining, which are qualitatively sufficient for further analysis. Improvement was achieved with addition of bright-field image (by-product of holographic quantitative phase imaging) into analysis and two step learning approach, without and with augmentation, were introduced. Reconstructed staining was used for nucleus segmentation where 0.784 and 0.781 dice coefficient (for DU145 and PNT1A) were achieved.

## Keywords

Deep learning • Quantitative phase imaging  
Cell analysis • Cell nuclei segmentation

T. Vicar (✉) · M. Hracho · R. Kolar  
Department of Biomedical Engineering, Brno University of  
Technology, Brno, Czech Republic  
e-mail: vicar@feec.vutbr.cz

T. Vicar · J. Gumulec  
Department of Pathological Physiology, Masaryk University,  
Brno, Czech Republic

J. Gumulec · J. Balvan  
Department of Physiology, Masaryk University, Brno, Czech  
Republic

J. Gumulec  
Central European Institute of Technology, Masaryk University,  
Brno, Czech Republic

## 1 Introduction

Fluorescence microscopy is a golden standard for contemporary biological studies. Regardless of the staining probe used, the purpose of such approach is to (1) identify individual cells, (2) localize processes to cytoplasm/nucleus or to (3) facilitate cell tracking in image analysis. Nevertheless, the usage of any fluorescent probes, e.g. transfection-based ones (see [1]) affect the cellular physiology due to unavoidable photo-toxicity. This include changes in cellular morphology, migration, division and various others. With this in regard, a label-free approach is an promising alternative. While most of the other label-free microscopic techniques (DIC, PC, etc.) suffer from artifacts like a halo in phase contrast, a quantitative phase imaging lacks those. Thus the image processing is dramatically easier.

Convolution neural networks (CNNs) has proved to be efficient tool for both classification and segmentation tasks, including applications on biological data like microscopic cell images [2]. Major disadvantage of such process is high demands for training data, where creation of labeled database is highly time consuming and biological tasks often require an expert. Our approach to deal with this task for cell nuclei segmentation, is to use fluorescence staining from simultaneous acquisition of fluorescence and label-free modality. If we train a model on such data, this model then can be used for nuclei segmentation on data without fluorescence. This approach therefore enables a creation of a training set with tens of thousands of cells without the need of manual annotations.

## 2 Materials and Methods

### 2.1 Experimental Data

Adherent cell lines from prostate non-tumor tissue (PNT1A) and metastatic tumor tissues (DU145) were used in the experiment. All cell lines were cultured in RPMI-1640

medium supplemented with antibiotics (penicillin 100 U/ml and streptomycin 0.1 mg/ml) with 10% fetal bovine serum (FBS). Prior microscopy acquisition, the cells were maintained at 37 °C in a humidified (60%) incubator with 5% CO<sub>2</sub> (Sanyo, Japan). For acquisition purposes, the cells were cultivated in Flow chambers  $\mu$ -Slide I Lauer Family (Ibidi, Martinsried, Germany).

Objective Nikon Plan 10/0.3 was used for hologram acquisition with a CCD camera (XIMEA MR4021MC). For the fluorescence mode a solid state light source (Lumencor Aura II) was used and images were captured by sCMOS camera (Andor Zyla 5.5, 2560 × 2160 px). Holographic data were numerically reconstructed with Fourier transform method (described in [3]) and phase unwrapping was used on phase image. As a result we obtain Quantitative phase image (QPI) and amplitude image, which is practically a Bright-field (BF). Both QPI and BF images are spatially registered on fluorescence images. Ordinarily, only QPI image is used for image analysis, thanks to its contrast and desirable properties, but we decided to test addition of BF image (by-product of holographic QPI) to improve our model.

## 2.2 Used Models

There are plenty of CNN’s pixel-to-pixel models, where the most popular are the encoder-decoder type. First, SegNet [4] network (its SegNet-Basic version) was employed, because of its ease of training, but afterwards U-net [2], which is widely used for biological tasks, has shown to have better results. Both of these networks are encoder-decoder type, where SegNet uses unpooling and U-net uses transposed convolution with concatenation of decoder data with encoder data of same degree. This block concatenation allow a better combination of high and low level features. For both networks, the original topologies from those papers were used and both networks were optimized identically as described below.

## 2.3 Preprocessing

One of the main problem in fluorescence data analysis is the fluctuation of intensities of the fluorescence between different cells, moreover between experiments. CNN has no chance to recognize how much fluorescence staining was captured by each cell, thus we must somehow locally normalize. Similar problem is in QPI image, where highly adhered cells have much less contrast than mitotic/apoptic cells, which are less adhered and round-shape. This issue was tested to solve with local histogram equalization using CLAHE method [5], applied on both source (QPI/BF) and desired (fluorescence) images. CLAHE is widely used as a preprocessing of CNNs (e.g. [6]), but we even use it on the

fluorescence (label) images. The disadvantage of this approach is that resulting “synthetic” fluorescence is equalized-like and the original fluorescence can not be reconstructed. Both QPI and BF pixel intensities were z-scored with mean and standard deviation computed from whole training database (QPI has exactly quantified values, thus single image z-score would lead to loss of information).

## 2.4 Network Implementation

For training we constructed image triples of QPI, BF and fluorescence images—where 10/14 fields of view (FOVs) were used for training and 4/14 FOVs were used for testing and evaluation (each FOV contains 30 time-lapse images—1.5 h of recording, all FOVs and time points were mixed together). Network were trained with Adam optimizer [7] (learning rate 0.001,  $\beta_1 = 0.9$  and  $\beta_2 = 0.99$ —which is all the default settings from the paper) and Mean Squared Error (MSE) loss (L2 loss) was used as an optimization criteria. Small 320 × 320 px randomly selected patches were used for training, which were cropped from original 600 × 600 px images. PyTorch 0.3.0 was used for network implementation and training.

Many test with a dropout and data augmentation with rotation, shearing and scaling were done, but neither leads to good convergence of the network. However, these techniques can significantly improve network generalization. For this reason, a modified two step learning was employed—learning without data augmentation (only random choosing of patches were employed) for pre-training of the network and re-training with the data augmentation (flipping, scaling, shearing and rotation before patch selection). The typical progress of MSE during learning is shown on Fig. 1, where test data MSE was 0.304 and 0.364 for the two step learning and learning without the augmentation, respectively. Moreover we tested L1 and Huber (L2 for small and L1 for large values) loss instead of L2 (MSE), but both lead to visually less sufficient results.

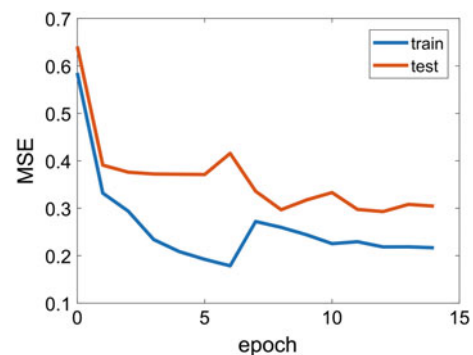


**Fig. 1** Example of model MSE on training and testing datasets for U-Net, QPI + BF images and PNT1A cells

**Table 1** MSE and Dice between original and reconstructed nuclear staining images (with U-net unless otherwise stated), \* value is not comparable with others

Value	Cell line	QPI	BF	QPI + BF	QPI + BF SegNet	QPI + BF CLAHE
MSE	DU145	0.311	0.451	0.285	0.336	0.0028*
	PNT1A	0.335	0.590	0.304	0.381	0.0024*
Dice	DU145	0.758	0.622	0.784	0.767	0.752
	PNT1A	0.712	0.542	0.764	0.758	0.781

## 2.5 Nucleus Segmentation

From the “synthetic” staining, a final nucleus segmentation was obtained by thresholding with an automatic threshold method based on Poisson distribution of the histogram [8] (better for cell images than Otsu), followed by morphol-

ogical operations—morphological closing and elimination of small objects and holes (<50 px). Original staining was segmented similarly. This segmentation step has been performed for both, the comparison of the reconstruction results and proving the segmentability of the “synthetic” fluorescence data.

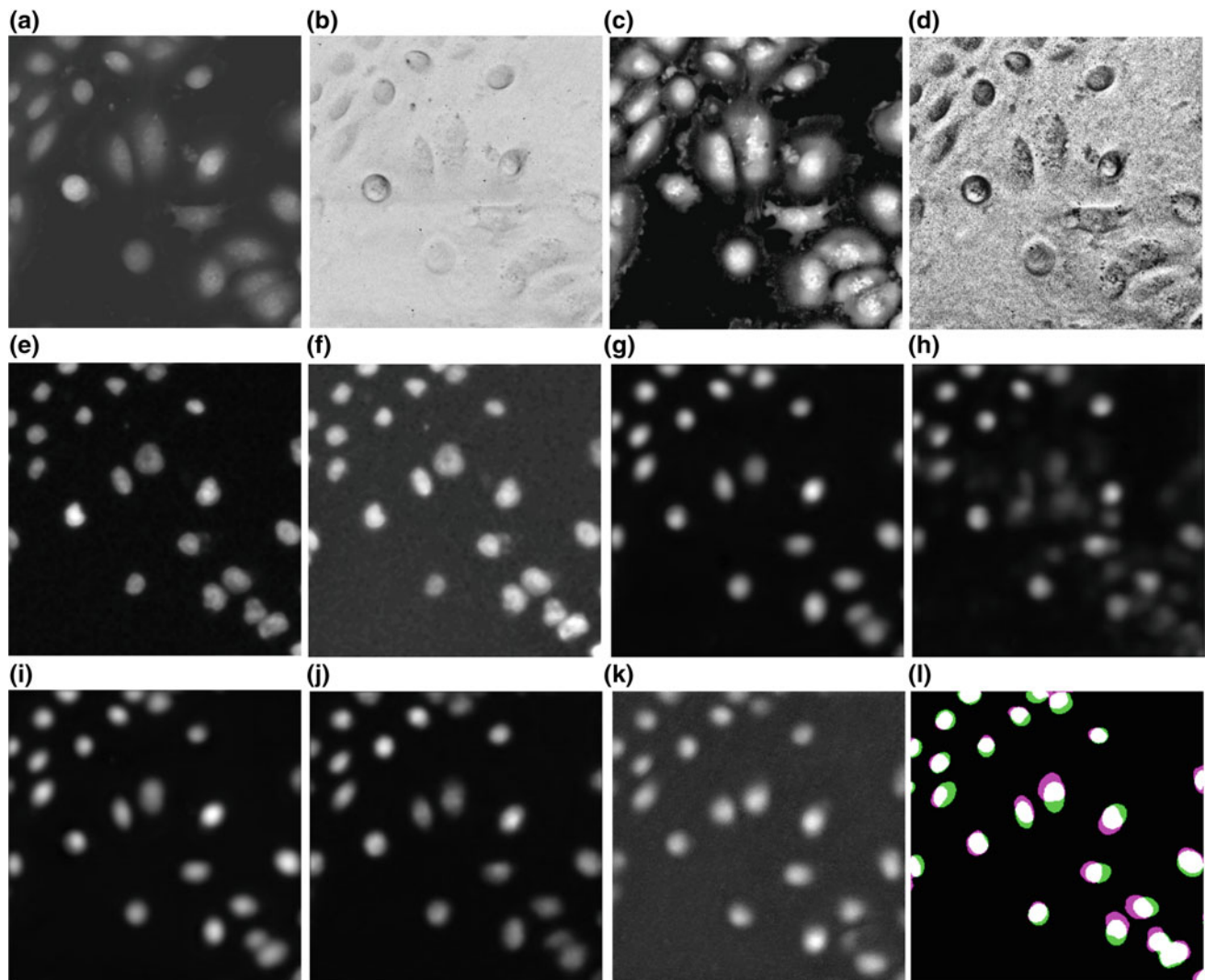


**Fig. 2** Example of results for a patch of DU145 cells reconstructed with U-net unless otherwise stated. **a** QPI, **b** BF, **c** equalized QPI, **d** equalized BF, **e** fluorescence, **f** equalized fluorescence, **g–k** “synthetic” fluorescence for QPI, BF, QPI + BF, QPI + BF SegNet,

QPI + BF CLAHE, **(L)** segmentation results from original (purple) and synthetic fluorescence (green) (dice 0.752 and for QPI + BF data used), 10 × magnification and image width 200 μm (color figure online)



### 3 Results

The aim of this study was to (1) create artificial masks for nuclei for further segmentation and (2) to reconstruct the structure of the nuclei. With this regard, first the accuracy of different networks can be well evaluated in term of MSE, which can be well compared between different settings. Disadvantage of MSE is data dependency and as such different cell lines or data with equalization are not comparable. As shown in Table 1, addition of BF image leads to improvement 0.026 and 0.031 for DU145 and PNT1A, respectively. U-net performed better for this task as expected. The results of non-equalized images are incomparable with equalized images, because MSE is image value-dependent, however without using of an equalization the convergence of the network was slower during the training and results were worse in images with both distinctive cells and less visible cells.

One of the main motivations for nuclear staining reconstruction is nucleus segmentation. Segmentation was evaluated in term of dice coefficient (see e.g. [9]), which is also much less data dependent and as such, thus is also better for comparison of different data sets than original MSE. As shown in Table 1, very similar results for both cell lines were achieved. Despite the fact that the images reconstructed with CLAHE are visually better, so CLAHE leads to better results for PNT1A (by 0.018 of dice), but worse results for DU145 (by 0.032 of dice). Maximal achieved dice (0.784 for DU145 and 0.781 for PNT1A) can be considered sufficient for further analysis, moreover if we consider lack of clarity of nuclei in QPI images. As you can see in Fig. 2, the main inaccuracy arises at the point of nearby nuclei, where they will be interconnected in “synthetic” fluorescence image.

### 4 Discussion

Overall, reconstructed “synthetic” fluorescence leads to blurry images, which may be used for localization of cell nuclei and nuclei segmentation, but their usability for precise nuclei segmentation is limited. However it is possible to consider using higher magnification. Another improvement might be done with enlargement of training database, which was relatively limited for such easy to obtain data. Using a more precise nuclei segmentation method must also be considered.

Another possible use of “synthetic” fluorescence could be found in cell detection (cell counting). Further analysis should be done for another staining for segmentation of other cell organelles. Other possibility is to use similar approach with staining signaling phases of cell cycle or ongoing apoptosis for detection of such states.

### 5 Conclusions

The proposed method can provide an easy-to-obtain annotated dataset for CNN training, which is then able to produce fluorescence-like images usable for numerous biological applications. Application of CLAHE on both source and desirable images shown to be usable approach for fluorescence image contrast normalization. The data augmentation prevents the network convergence, but two step learning approach was presented to enable the use of data augmentation. Reconstructed staining has proven to be useful for the nuclei segmentation.

**Acknowledgements** This work has been supported by the Czech Science Foundation, grant number 18-24089S.

**Conflict of Interest** The authors declare that they have no conflict of interest.

### References

1. Wang, Z., Millet, L., Chan, V., Ding, H., Gillette, M.U., Bashir, R., Popescu, G.: Label-free intracellular transport measured by spatial light interference microscopy. *Journal of Biomedical Optics* 16(2), 026019–026019–9 (2011), <http://dx.doi.org/10.1117/1.3549204>
2. Ronneberger, O., Fischer, P., Brox, T.: U-net: Convolutional networks for biomedical image segmentation. In: *International Conference on Medical image computing and computer-assisted intervention*. pp. 234–241. Springer (2015)
3. Slaby, T., Kolman, P., Dostal, Z., Antos, M., Lostak, M., Chmelik, R.: Off-axis setup taking full advantage of incoherent illumination in coherence-controlled holographic microscope. *Optics Express* 21(12), 14747–14762 (2013)
4. Badrinarayanan, V., Kendall, A., Cipolla, R.: Segnet: A deep convolutional encoder-decoder architecture for image segmentation. *IEEE transactions on pattern analysis and machine intelligence* 39(12), 2481–2495 (2017)
5. Reza, A.M.: Realization of the contrast limited adaptive histogram equalization (clahe) for real-time image enhancement. *Journal of VLSI signal processing systems for signal, image and video technology* 38(1), 35–44 (2004)
6. Cireşan, D., Meier, U., Masci, J., Schmidhuber, J.: A committee of neural networks for traffic sign classification. In: *Neural Networks (IJCNN), The 2011 International Joint Conference on*. pp. 1918–1921. IEEE (2011)
7. Kingma, D.P., Ba, J.: Adam: A method for stochastic optimization. *arXiv preprint arXiv:1412.6980* (2014)
8. Al-Kofahi, Y., Lassoued, W., Lee, W., Roysam, B.: Improved automatic detection and segmentation of cell nuclei in histopathology images. *IEEE Transactions on Biomedical Engineering* 57(4), 841–852 (2010)
9. Zou, K.H., Warfield, S.K., Bharatha, A., Tempany, C.M., Kaus, M.R., Haker, S.J., Wells, W.M., Jolesz, F.A., Kikinis, R.: Statistical validation of image segmentation quality based on a spatial overlap index1: scientific reports. *Academic radiology* 11(2), 178–189 (2004)



# Performance Comparison of Segmentation Algorithms for Image Quality Degraded MR Images

Galip Ozdemir, Huseyin Nasifoglu, and Osman Eroglu

## Abstract

Medical image segmentation is one of the most important research areas of clinical diagnosis. Especially, brain is the most critical organ that is tracked, investigated and analyzed mostly by using Magnetic Resonance Imaging (MRI). Developing a highly accurate automated segmentation of brain region is a very difficult task due to involving noise and deviation. In recent years, various image segmentation techniques have been developed in the literature such as clustering, thresholding (intensity-based), active contours (surface-based), expectation maximization (probability-based). In this study, these commonly used algorithms are handled in order to see the performance of the segmentation while degrading the image quality and saving from memory for brain MR images. For this purpose, the level of acceptable degradation is obtained by compressing MR slice images with different quality factors by using JPEG algorithm. Peak signal to noise ratio (PSNR), bits per pixel (BPP), mean, variance parameters of the MR images are used to characterize the corresponding compressed image degradation quality. On the other hand, segmented intracranial area, white matter (WM), gray matter (GM) regions are compared with the non-compressed MR images for various compression ratios. Then, the area overlap ratio for these regions is obtained in order to get segmentation performance results. It is believed that detected optimum parameters can be used as prior indicators to determine which segmentation algorithm (or which group, i.e. intensity or surface-based) should be chosen. Besides, it

will be able to occupy less space in memory by compressing image for appropriate parameters.

## Keywords

Segmentation • Compression • Brain • MRI

## 1 Introduction

Nowadays, many imaging modalities are utilized for the diagnosis of diseases. Magnetic resonance imaging (MRI) is a popular of these modalities, in the sense of high image quality. MRI provides better results on diagnosis in soft tissues compared to other modalities such as computer tomography (CT), ultrasonography (US), computed radiography (CR). Various techniques have been developed with the use of MR images especially for segmentation of brain regions: possible tumor tissue, intracranial area (IA), white matter (WM) and gray matter (GM).

Kasban H. et al. proposed a fully automatic algorithm to segment the region of interest in gamma radiographs by thresholding method [1]. Hue T.T.M., Kim J.Y. and Fahriddin M., emphasized that high noise levels in radiographic images, low contrast and complex intensity distributions are the factors that challenge medical image analysis [2]. Ertas G., Demirgunes D.D. and Eroglu E., segmented the chest region in MR images using cellular neural networks [3]. Karhikeyan B. et al. have investigated the segmentation success of medical images where watershed segmentation, thresholding and K-means clustering methods are used [4]. While the K-means is faster than the other methods, it has been shown that the thresholding method yields the desired part in the foreground by detecting the imperfections in the image with high success.

In terms of storage, the downside of MRI is that it occupies high memory space in PACS (Picture Archiving and Communication System) due to having many image slices for single imaging. Additionally medical images are

---

G. Ozdemir · H. Nasifoglu (✉) · O. Eroglu  
Department of Biomedical Engineering, TOBB University  
of Economics and Technology, Ankara, Turkey  
e-mail: hnasifoglu@etu.edu.tr; hnasifoglu@gmail.com

G. Ozdemir  
e-mail: g.ozdemir@etu.edu.tr

O. Eroglu  
e-mail: erogul@etu.edu.tr

generally stored in DICOM 3 format which involves no compression and requires much space in database in this manner. Therefore, reducing the image size while preserving diagnostic data has become a need in recent years. It is possible to find many studies on medical image compression. Sophia P. and Anitha J. have investigated the physician's region of interest (ROI) in compression of MR images [5]. ROI has been compressed lossless while the region outside ROI compressed lossy. Researchers indicated that higher compression rates were achieved when the ROI was small, resulted in an average compression ratio of 4.2 times and a PSNR of 20.76 dB. Yulianti L. and Mengko T. R. proposed a hybrid method in which the fractal properties of the image are compressed by Huffman coding [6]. In another research on brain images, a method is proposed in which the interest area is compressed by the contextual tree method, while the remaining part is compressed by fractal image compression [7]. In one study, researchers proposed a new quantization table for angiocardigram images [8]. The table was generated from the transfer function of the angiocardigraphic system. As a result of the objective evaluation, it was determined that the new quantization table could be applied on angiocardigram images.

In this paper, brain MR images are compressed by JPEG algorithm using several quality factors. Followingly, several segmentation techniques are applied to both compressed and non-compressed images to detect intracranial area, WM and GM regions. Then the overlap ratio has been examined for these images in order to investigate the effects of compression (degradation) on segmented brain region areas as a new approach. Compression (degradation) effects are evaluated by PSNR, BPP, compression ratio (CR) and variance of error as objective criteria.

## 2 Methodology

There are two main methodologies in this study. One is the compression of MR images by JPEG algorithm with several quality factors as lossy approach. Second methodology is the segmentation of intracranial area, WM and GM for brain MR images with different techniques. The segmentation techniques are also applied to the compressed images and the overlap ratio (overlapping of segmented non-compressed and compressed images) has been examined in order to observe the level of degradation and performance of compression algorithm on segmented regions. In Fig. 1, general block diagram of the methodology used in this study is shown. To investigate the success of the segmentation algorithms, *BrainWeb* database has been used as reference images for discrete model, WM and GM. These images are anatomical models of human brains and models available in the database are completely synthetic. IA images are obtained from interior of skull region (is the remaining area, after the skull is stripped).

### 2.1 JPEG Compression Algorithm

Having less computational complexity and being fast for computational processes, JPEG is one of the most commonly preferred compression algorithms [9]. Besides, being compatible with DICOM standard, JPEG allows compression of medical images by lossy and lossless approach. In this paper, lossy compression algorithm is implemented in order to observe the loss of data in image content while segmenting brain regions. It is possible to scale quantization by using quality factor (QF) between 1 and 100 so that it will be able

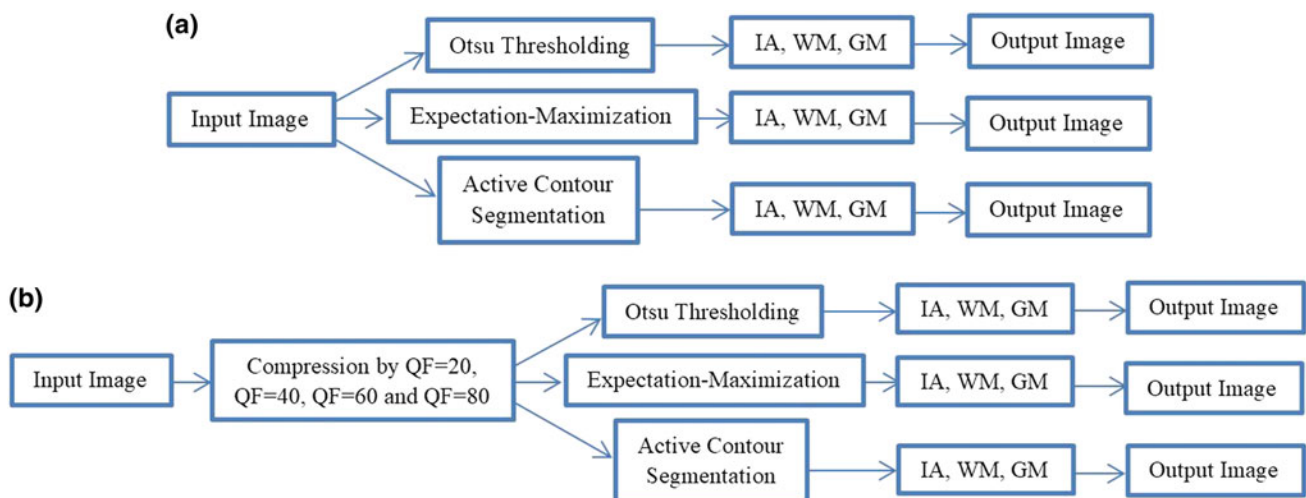


**Fig. 1** a Block diagram of methodology for non-compressed images. b Block diagram of methodology for compressed images

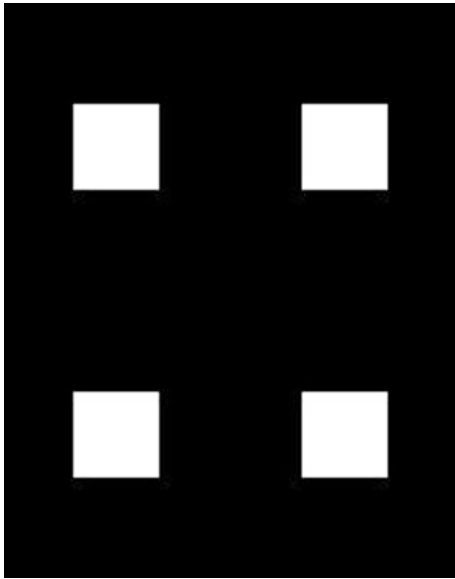


**Fig. 2** Initial seed regions used for AC segmentation

to control the loss of data (degradation level) by setting appropriate QF parameter. Lastly, Huffman encoding is used for compression of quantized data.

## 2.2 Intracranial Area, White Matter and Gray Matter Segmentation

### Otsu Thresholding

Otsu's method aims to find the threshold value at the minimum to segment regions by iterating all possible thresholds in an image [10]. For this purpose, Within Class Variance is measured for all thresholds applied to the image. Here, the

lowest sum of weighted variance represents final threshold value to segment image into two distinct regions. In this study, Otsu threshold value is obtained for the image and then binarization is applied with appropriate thresholds to obtain IA, WM and GM.

### Expectation-Maximization Algorithm

Expectation-Maximization (EM) algorithm is an iterative method used for many signal and image processing implementations. It basically searches the maximum likelihood of the clusters of an image with the help of Gaussian mixture model. Using these probabilistic estimates, image is segmented into different clusters (regions). Implementation of EM algorithm is done in 2 steps: First we considered the input image having 3 main regions which are background, skull and IA and EM is implemented in this manner. In the following step, IA is further segmented into multiple regions and WM and GM regions are analyzed in results section.

### Active Contour Segmentation

Active Contour (AC) algorithm is an iterative method [11] generally used for foreground background segmentation by deforming an initial boundary corresponding to energy minimization around this spline. The output is critically dependent on the initial spline. Due to this dependence, 4 square regions have been initialized located at the center of each quadrant of the image (Fig. 2). Since AC is able to segment the image in 2 regions, an approach of recursive AC implementation has been used. Regions in an order as first background elimination are extracted. Remaining input is segmented as IA and skull at the 2nd implementation. WM detection and GM segmentation are next steps.

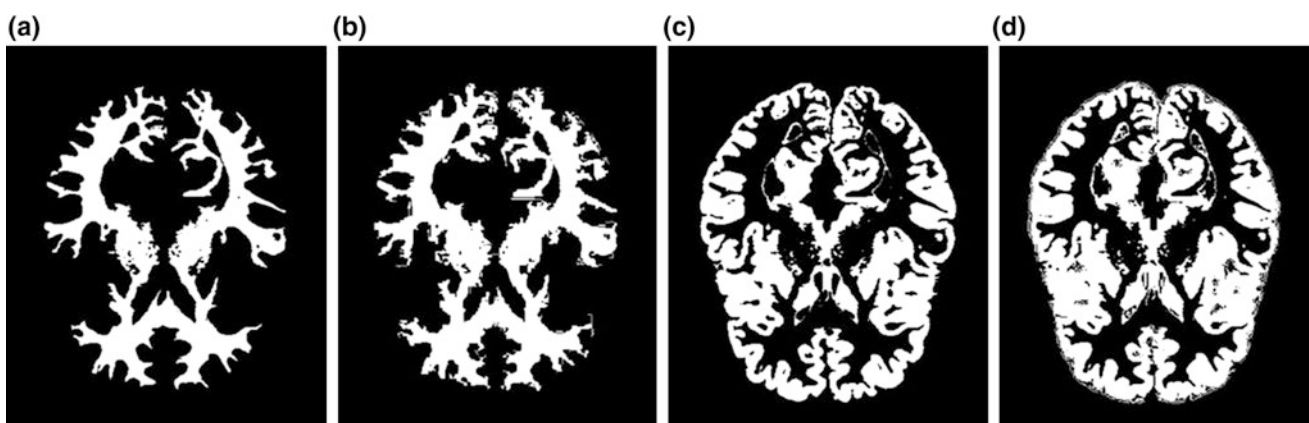


**Fig. 3** a Segmented WM (Otsu), b Segmented WM for QF = 20 (Otsu), c Segmented GM (Otsu), d Segmented GM for QF = 20 (Otsu)

### 3 Results

8 brain MR images have been used to segment related regions. Each image is compressed by four different quality factors  $QF = 20$ ,  $QF = 40$ ,  $QF = 60$  and  $QF = 80$  in MATLAB environment. In total, 4 datasets (4 different compressed images for each input) are obtained in order to investigate the effects of compression on each segmented region. Sample output images for Otsu Thresholding, Expectation-Maximization Algorithm and Active Contour Segmentation are given in Figs. 3, 4 and 5.

Segmentation results are given in Tables 1, 2 and 3. These results are the mean values of overlapping regions for 8 MR images.

It is clear and expected that best overlap ratio is obtained for  $QF = 80$  among the compressed image datasets. Each dataset is evaluated by objective criteria of CR, PSNR, BPP, error variance and the mean results for all  $QF$  datasets are given in Table 4. These parameters represent the degradation level of MR image quality. Since all degraded images have exactly the same total pixel number ( $362 \times 434$  pixels) as the original image, segmentation process requires same amount of time in all datasets.



**Fig. 4** a Segmented GM (EM), b Segmented GM for  $QF = 80$  (EM), c Segmented IA (EM), d Segmented IA for  $QF = 40$  (EM)

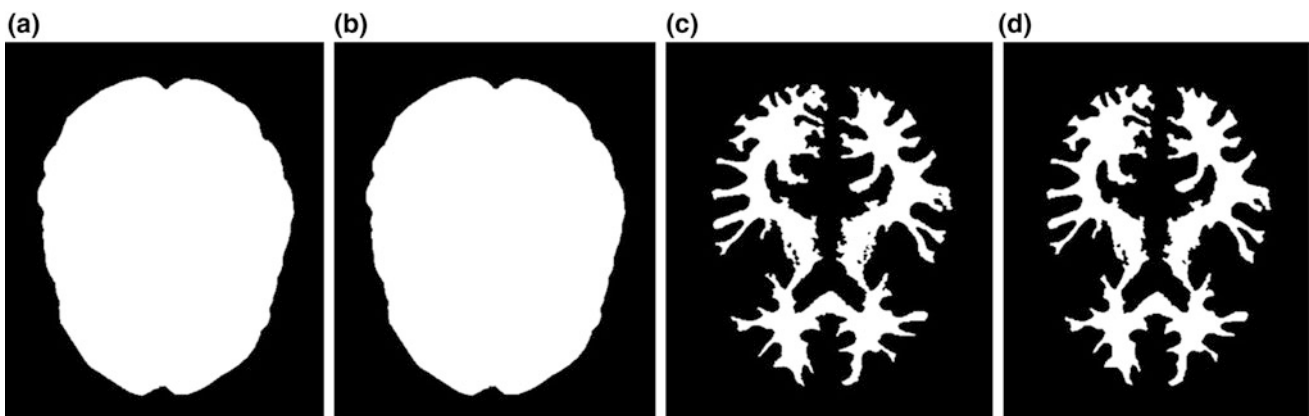


**Fig. 5** a Segmented IA (AC), b Segmented IA for  $QF = 60$  (AC), c Segmented WM (AC), d Segmented WM for  $QF = 80$  (AC)

**Table 1** Segmentation results of intracranial area

IA area-overlap ratio	$QF = 20$	$QF = 40$	$QF = 60$	$QF = 80$	Non-compressed
Otsu	0.9283	0.396	0.9440	0.9525	0.9834
EM	0.9808	0.9818	0.9840	0.9846	0.9846
AC	0.9249	0.9252	0.9258	0.9265	0.9289

**Table 2** Segmentation results of white matter

WM area-overlap ratio	QF = 20	QF = 40	QF = 60	QF = 80	Non-compressed
Otsu	0.8107	0.8465	0.8598	0.8806	0.9665
EM	0.7406	0.8205	0.8778	0.9140	0.9947
AC	0.9131	0.9188	0.9335	0.9548	0.9717

**Table 3** Segmentation results of gray matter

GM area-overlap ratio	QF = 20	QF = 40	QF = 60	QF = 80	Non-compressed
Otsu	0.8657	0.8812	0.8870	0.8987	0.9695
EM	0.6640	0.7294	0.7858	0.8602	0.9935
AC	0.8174	0.8204	0.8271	0.8368	0.8453

**Table 4** Compression evaluation results for compressed MR images

QF dataset	CR	PSNR (dB)	BPP	Error variance
QF = 20	17.31	27.67	0.46	111.27
QF = 40	11.24	29.90	0.71	66.39
QF = 60	8.60	31.93	0.93	41.82
QF = 80	5.90	35.99	1.36	16.43

## 4 Conclusion

In this study, 8 images have been compressed with several QFs and 4 datasets been formed for performance comparison. Three segmentation techniques have been applied on non-compressed and compressed images in order to detect intracranial area, white matter and gray matter. Results show that EM has the best performance for IA, Otsu's algorithm for GM segmentation, where AC is better for WM area detection. These findings suggest that a hybrid segmentation model which implements EM, Otsu's method and AC for segmentation of IA, GM and WM respectively provide a superior modality. More interestingly, it appears that AC is almost not susceptible to image quality degradation. Overlapping region ratios for AC do not significantly change when image quality is altered. Additionally, EM algorithm has best segmentation accuracy for the IA segmentation and this performance remains fairly constant within different level of degraded images. Therefore, if the memory-gain is taken into account, this dataset can be preferable for clinical applications with acceptable degradation limits. In this way, it is possible to segment IA and WM regions having an accuracy of larger than 90% (implementing EM for IA and AC for WM regions) even for compressed images with QF = 20. However, it is suggested for GM areas that Otsu's algorithm can be applied with a minimum QF = 40, where 88% accuracy for overlapping regions is obtained. These findings show that compressed images will contribute to

PACS management by occupying less storage space and transmission simplicity while providing sufficient segmentation accuracy.

**Conflict of Interest** The authors declare that they have no conflict of interest.

## References

1. Kasban, H., Arafa, H., Elaraby, S.M., Zahran, O., El-Kordy, M.: Automatic Segmentation of Industrial Radiographic Images. International Conference on Computer Engineering & Systems (ICCES), 213–218 (2011).
2. Hue, T.T.M, Kim, J.Y., Fahriddin, M.: Hand Bone Radiograph Image Segmentation with ROI Merging. Recent Researches in Mathematical Methods in Electrical Engineering and Computer Science, 147–154 (2011).
3. Ertas, G., Demirgunes, D.D., Erogul, O.: Conventional and Multi-State Cellular Neural Networks in Segmenting Breast Region From MR Images: Performance Comparison. International Symposium on Innovations in Intelligent Systems and Applications (INISTA), 1–5 (2012).
4. Karthikeyan, B., Vaithyanathan, V., Venkatraman, B., Menaka, M.: Analysis of Image Segmentation for Radiographic Images. Indian Journal of Science and Technology 5 (11), 3660–3664 (2012).
5. Sophia, P., Anitha, J.: Implementation of Region Based Medical Image Compression for Telemedicine Application. International Conference on Computational Intelligence and Computing Research (ICCIC), 1–4 (2014).
6. Yulianti, L., Mengko, T.R.: Application of Hybrid Fractal Image Compression Method for Aerial Photographs. MVA2000 IAPR Workshop on Machine Vision Applications, 574–577 (2000).

7. Kaur, M., Wasson, V.: ROI Based Medical Image Compression for Telemedicine Application. 4th International Conference on Eco-friendly Computing and Communication Systems (ICECCS 2015), 579–585 (2015).
8. Onnasch, D.G.W, Prause, G.P.M, Ploger, A.: Quantization table design for JPEG compression of angiocardiographic images. *Computers in Cardiology*, 265–268 (1994).
9. Gonzalez, R.C., Woods, R.E.: *Digital Image Processing*. 2<sup>nd</sup> edn. Prentice Hall, Upper Saddle River, NJ (2002).
10. Vertan, C., Florea, C., Florea, L., Badea, M.S.: Reusing the Otsu Threshold Beyond Segmentation. *International Symposium on Signals, Circuits and Systems*, 1–4 (2017).
11. Chan, T.F.: Active Contours Without Edges. *IEEE Transactions on Image Processing*, vol. 10, no. 2, 266–277 (2001).



# Application of Low-Cost 3D Printing for Production of CT-Based Individual Surgery Supplies

Filip Górski, Radosław Wichniarek, Wiesław Kuczko, Jacek Banaszewski, and Maciej Pabiszczak

## Abstract

The main problem addressed in this paper is the use and evaluation of low-cost additive manufacturing (3D printing) techniques and CT images as tools for manufacture of usable and individualized, anatomically correct models, assisting surgeons in their daily work. The authors formulate own methodology of design and additive manufacturing of medical products on the basis of medical imaging data. A specific case was selected—a surgical lower jaw template for use in the middle of operation. Two Fused Deposition Modeling machines—professional and low-cost—were used to manufacture the same product, which was later evaluated, inspected for accuracy (by 3D scanning) and used during the surgery. By two 3D printing processes comparison it was found that the low cost comes at a price of lower accuracy and increased demand for process supervision. The authors obtained a fully usable medical product used during an actual reconstruction surgery. Partial clinical results are presented—use of 3D printed templates helped reduce surgery time and generally improved the patient recovery process.

## Keywords

Mid-surgery supplies • 3D printing • Computed tomography

## 1 Introduction

Additive manufacturing (widely known as 3D printing) and rapid prototyping have found many applications in medicine [1, 2]. They are in use everywhere there is a need of an individualized solution, as they allow fast obtainment of a demanded shape with no tooling [3]. One of the main barriers of widespread production of professional 3D printing is the price of both the machines and materials [4, 5], as well as the required qualifications and time consumption to both prepare data and launch and supervise the additive manufacturing processes [4]. In recent years, 3D printing has gained wide popularity thanks to so-called low-cost additive manufacturing processes, which are mostly inexpensive variations of the long-known fused deposition modeling technology. However, they have certain limitations. Another problem is lack of standard methodologies of designing medical products on the basis of medical imaging data.

The mid-surgery supplies are an important aid for a surgeon during the stage of planning and scheduling a detailed course of operation, as well as during the operation itself, for example as a template for bone cutting [6, 7]. The main area in which the authors focus their work is surgery, especially in terms of reconstruction and implanting after resection. The use of 3D printed metal implants is nowadays a known technique [1], although limited in use. Use of low-cost 3D printing to produce mid-surgery supplies is uncommon, mostly due to lack of low-cost metal-processing techniques and process stability and product quality problems.

All of the above-mentioned problems are premises of research undertaken by the authors of this paper. The general and long-term aim of the research is to establish a reliable set of methods of building medical products of certain categories in order to make it more available for both doctors and patients.

F. Górski (✉) · R. Wichniarek · W. Kuczko  
Chair of Management and Production Engineering, Faculty of  
Mechanical Engineering and Management, Poznan University of  
Technology, 60-965 Poznań, Poland  
e-mail: filip.gorski@put.poznan.pl

J. Banaszewski · M. Pabiszczak  
Department of Otolaryngology, Poznan University of Medical  
Sciences, 60-355 Poznań, Poland

## 2 Introduction

### 2.1 Research Problem

The main problem of this paper is a proper utilization of low-cost additive manufacturing and Rapid Prototyping techniques as tools of effective manufacturing of usable, individualized medical products, for use both by doctors and patients on various stages of treatment. This paper addresses issues of design and low-cost 3D printing on the basis of CT (computed tomography) data. The considerations are based on examples of specific cases of medical products used by doctors in real-world scenarios. As the main case, a mandibular reconstruction template was selected.

### 2.2 Methodology of Design and Rapid Manufacturing of Medical Products

The proposed methodology is based on other available general methodologies [2, 8]. However, the authors have expanded the existing methodologies with the aspects of clear indication of required skills and involved people and indication of proposed software at each stage, mostly aiming at freeware or open-source software.

The best and most suitable tools, as tested by the authors, are indicated in the full methodology, which is not included here due to limited space. The methodology scheme is presented in Fig. 1.

The authors have distinguished eight consecutive stages that require at least three separate competence areas: medical technician (stages 1 and 8), biomedical engineer (stages 2–4) and 3D printing technician (stages 5–7). The most demanding stage in terms of skills and time is Stage 4, where

a surface and/or solid model must be created. Stage 4 can be especially demanding when Stage 2 is conducted improperly [9]. Stage 3 also requires a large amount of skills of manual processing of 3D mesh.

### 2.3 The Fused Deposition Modelling Technology

The fused deposition modeling (FDM) process is currently the most widespread additive manufacturing technology [10]. The consistent problem of the FDM process is that produced parts have weak interlayer bonds, which decrease overall strength of the part [11]. Furthermore, part orientation greatly influences the obtained technical characteristics [12]. The problems of selecting optimal parameters of the FDM process and obtaining good properties of products has been widely described in literature [13].

For the studies, two machines were used—a Stratasys Dimension BST 1200 (a professional machine) and a MakerBot Replicator 2X (a low-cost machine). To provide a valid comparison for later evaluation, in the conducted studies similar parameters and materials were selected for both machines.

### 2.4 Mandibular Reconstruction Template—Case Description

The main case is mandibular reconstruction using fibular free flaps in patients after resections. Proper planning of the reconstruction surgery using 3D data of the lower jaw, obtained by medical imaging, has been widely described in literature [14]. Application of rapid prototyping methods in

**Fig. 1** Schematic course of proposed methodology to design and manufacture medical products using 3D printing techniques

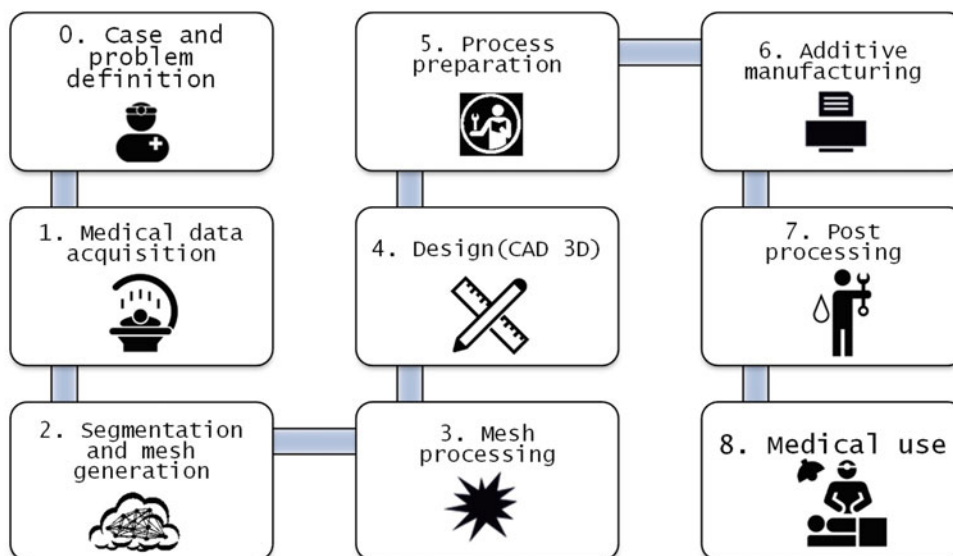




**Fig. 2** Example of fitting of titanium plates on a lower jaw template, before the surgery

such a procedure is evaluated as effective and helpful, especially in terms of reduction of operation time and better geometrical fitting of the reconstructed jaw [15]. However, the costs of such an approach are high.

The case presented in this paper involves a patient subjected to partial lower jaw resection. The patient was male and aged 47. The side part of the jaw body had to be removed due to cancer and the resulting defect was reconstructed. It was aimed at obtaining full jaw functionality, including junction stability, mobility and cosmetic effect. The FDM process was used to manufacture a template of the reconstructed jaw out of ABS material, to use before and in the middle of the surgery, to shape stabilizing titanium plates

(Fig. 2) and to be used as a template to cut the desired shape from patient's fibula in shorter time. The approach was tested earlier by the authors in clinical tests, using solely the professional BST 1200 machine, with full success.

## 2.5 Course of Studies

The studies were divided into two main parts. The first part focused on using the defined methodology to manufacture the jaw templates using both low-cost and professional FDM processes out of ABS material, starting from medical data processing, through design, 3D printing process preparation and post-processing. The second part of the studies focused on evaluation of the obtained products.

Firstly, medical imaging data was obtained, in form of DICOM file with CT data (Stage 1). The computed tomography images of lower jaws were converted to digital 3D models (Stage 2). The created models were exported to the STL format. In further stages, the raw models were processed in the GOM Inspect software, until final shape was obtained (Stage 3). In a similar way, a digital model of the fibula was obtained. Models prepared in such a way were imported to a computer-aided design system. A piece of damaged bone was removed from the lower jaw model. Then, a missing piece was digitally recreated (Stage 4). In the next stage (Stage 5), the FDM process was prepared. Similar manufacturing parameters and materials were used

**Table 1** Comparison of basic information about manufacturing on two FDM machines

Parameters	BST 1200 (professional)	Replicator 2X (low-cost)
Product mass (g)	62,98	65,01
Production time	5 h 18 min	6 h 5 min
Model mat. usage	71,63 g	100,83 g (+purge walls)
Support mat. usage	14,24 g	29,81 g (as above)
Layer thickness (mm)	0,254	0,25

**Fig. 3** 3D printed jaw templates, Replicator 2X (left), Dimension BST 1200 (right)



(see Table 1). In stages 6 and 7, the jaw templates were manufactured and post processed. The post-processing was the same in both cases and consisted solely in mechanical support removal.

At this point, both products were optically measured using Atos Compact Scan 5M 3D scanner. Measurement field was set to  $130 \times 150$  mm. Both scans were superimposed on the original, final STL export (nominal geometry), using the GOM Inspect software and the best-fit algorithm. Inspection points locations were consulted with the surgeons.

### 3 Results

The manufactured reconstructed mandible templates are shown in Fig. 3. Basic information regarding the manufacturing processes and obtained economical characteristics are presented in Table 1.

The 3D scanning and inspection results are presented in Fig. 4. The average scan fitting error was 0.05 mm for the BST 1200 machine and 0.27 mm for the Replicator 2X machine. In terms of fitting of the selected 11 points—for the BST 1200 machine all points are within tolerance of  $\pm 0.05$  mm, while for the Replicator 2X all points are outside this tolerance, with maximal deviation  $-0.56$  mm in point no. 5.

Both products were sterilized in plasma at  $55^\circ\text{C}$  for 45 min. No geometrical changes were observed. Both products were then evaluated and compared by a team of surgeons. No visible quality defects were observed and the surgeons marked both products as acceptable for use during the surgery. The surgery was performed and it ended with full success and patient recovery.

### 4 Discussion

In terms of product design issues, it was found that it is required to use at most three different software tools in order to generate the mesh out of medical data, process the mesh and create a design. The most labor-consuming process is the work done by a biomedical engineer, i.e. time spent in-between raw DICOM data and a final computer-aided model. In the presented case, the time of work was 12 h. This is, in authors' opinion, a rather short time, with a standard time of 3–6 days. The paper describes a single case, but the methodology was applied to several other cases as well, with similar results. Still, more clinical tests would be required, but this type of surgery is rather rare, so it will probably take a few more years.

Out of the medical product classes available nowadays on low-cost 3D printers, the mid-surgery supplies production using low-cost 3D printing is the most viable option in terms of usefulness and cost efficiency, in authors' opinion. Its effectiveness has been confirmed by clinical tests.

A low-cost FDM process allows the possibility to reduce product costs by more than two times, but at the cost of greatly limited dimensional accuracy. Fortunately, in terms of products that resemble the shape of the human body, the accuracy ensured by low-cost FDM is enough, as proven by the positive results of the performed surgery (contrary to findings by other researchers, such as in [9]). Unfortunately, low-cost FDM processes require a considerably high level of supervision. Examples of errors are clogging of extruders, miscalibrated building plate, filament entanglement and self-unsticking of the model. Each error requires operator to perform manual actions. It is, in authors' opinion, a large barrier in making the 3D printing widespread in healthcare.

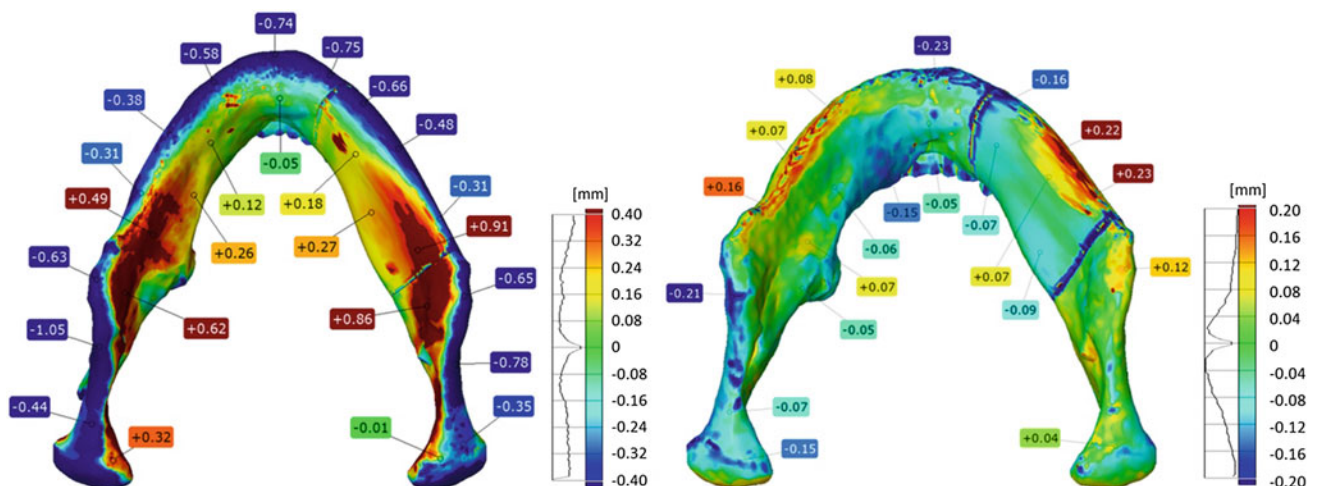


**Fig. 4** Results of accuracy inspection—colorful deviation map, Replicator 2X model (left) and Dimension BST 1200 model (right)



## 5 Conclusions

Based upon the presented studies, the following final conclusions may be drawn:

1. It is effectively possible to use a low-cost 3D printer to manufacture a medical product usable by surgeons during an operation, on the basis of computed tomography data.
2. Use of a defined methodology shortens time spent on searching for appropriate tools and ways of conduct, thus reducing time of preparation of a medical product, which is often a crucial factor in life-saving surgery.
3. Obtaining usable medical products by methods of 3D printing requires cooperation between at least 4 specialists: a doctor, a medical imaging technician, a biomedical engineer (computer-aided design specialist) and a 3D printing technician.

Future work will focus on more clinical tests of different medical products, such as prostheses, orthoses and mid-surgery aids, as well as developing communication standards between engineers and doctors.

**Conflict of Interest** The authors declare that they have no conflict of interest.

## References

1. Syam, W. P., Mannan, M. A., Al-Ahmari, A. M. (2011), "Rapid prototyping and rapid manufacturing in medicine and dentistry", *Virtual and Physical Prototyping*, 6:2, 79–109, <https://doi.org/10.1080/17452759.2011.590388>
2. Marro, A., Bandukwala, T., Mak, W. (2016), "Three-Dimensional Printing and Medical Imaging: A Review of the Methods and Applications", *Current Problems in Diagnostic Radiology*, 45, 2–9, DOI: <https://doi.org/10.1067/j.cpradiol.2015.07.00>
3. Chua, C. K., Leong, K. F., and Lim, C. S., (2010), *Rapid Prototyping: Principles and Applications*, World Scientific Publishing Co. Pte. Ltd., Singapore, 25–35
4. Thompson, M.K., Moroni, G., Vaneker, T., Fadel, G., Campbell, R.I., Gibson, I., Bernard, A., Schulz, J., Graf, P., Ahuja, B., Martina, F. (2016), *Design for Additive Manufacturing: Trends, opportunities, considerations, and constraints*, *CIRP Annals – Manufacturing Technology*, <https://doi.org/10.1016/j.cirp.2016.05.004>
5. Fasel, J. H. D., Aguiar, D., Kiss-Bodolay, D., Montet, X., Kalangos, A., Stimec, B. V., Ratib, O. (2016), "Adapting anatomy teaching to surgical trends: a combination of classical dissection, medical imaging, and 3D-printing technologies", *Surgical and Radiologic Anatomy*, 38, 361–367, <https://doi.org/10.1007/s00276-015-1588-3>
6. Bibb, R. (2006), *Medical modelling: the application of advanced design and development techniques in medicine*, Woodhead Publishing
7. Tukuru, N., Gowda, S.K.P., Ahmed, S.M., Badami, S. (2008), "Rapid prototype technique in medical field", *International Journal of PharmTech Research*, 1(4), 341–344
8. Nasr, E.S.A., Al-Ahmari, A., Moiduddin, K. (2014), "CAD Issues in Additive Manufacturing. Comprehensive Material Processing", in Hashmi, S., *Comprehensive Materials Processing Vol. 10: Advances in Additive Manufacturing and Tooling*, Springer, 375–399, <https://doi.org/10.1016/b978-0-08-096532-1.01015-3>
9. Huutilainen, E., Jaanimets, R., Valasek, J., Marcian, P., Salmi, M., Tuomi, J., Makitie, A., Wolff, J. (2014), "Inaccuracies in additive manufactured medical skull models caused by the DICOM to STL conversion process", *Journal of Cranio-Maxillo-Facial Surgery*, 42, e259–e265, <https://doi.org/10.1016/j.jcms.2013.10.001>
10. Caffrey, T. and Wohlers, T. (2015). *Wohlers Report 2015 – Additive Manufacturing and 3D Printing State of the Industry – Annual Worldwide Progress Report*. Fort Collins: Wohlers Associates, Inc.
11. Górski, F., Wichniarek, R., Kuczko, W., Zawadzki, P., Buń, P. (2015). "Strength of ABS parts produced by fused deposition Modeling technology - a critical orientation problem", *Advances in Science and Technology-Research Journal*, 9, 12–19. <https://doi.org/10.12913/22998624/2359>
12. Górski, F., Wichniarek, R., Zawadzki, P., Hamrol, A. (2015). "Computation of Mechanical Properties of Parts Manufactured by Fused Deposition Modeling using Finite Element Method", in *Advances in Intelligent Systems and Computing*, Springer, 368, 403–413, [https://doi.org/10.1007/978-3-319-19719-7\\_35](https://doi.org/10.1007/978-3-319-19719-7_35)
13. Byun, H. S., Lee, K.H. (2005), "Determination of the optimal part orientation In layered manufacturing using genetic algorithm", *International Journal of Production Research*, 43, 2709–2724, <https://doi.org/10.1080/00207540500031857>
14. Eckardt, A. and Swennen, G.R. (2005): "Virtual planning of composite mandibular reconstruction with free fibula bone graft", *The Journal of Craniofacial Surgery*, 16(6), 1137–40
15. Liu, Y., Xu, L., Zhu, H., Liu, S.S.Y. (2014), "Technical procedures for template-guided surgery for mandibular reconstruction based on digital design and manufacturing", *BioMedical Engineering*, 13:63, <https://doi.org/10.1186/1475-925x-13-63>

# Examination of the Spatial Structure of Pigs' Melanoma in Tissue Sections Based on Histology and Mass Spectrometry

Jiri Anyz, Lenka Vyslouzilova, Vratislav Horak, Olga Stepankova, Tomas Vaculovic, and Vojtech Adam

## Abstract

We examine the spatial structure of the melanoma in tissue sections. The pigs melanoma was examined in 10 tissue samples obtained from animals of age between 4 and 22 weeks. The tissue sections were measured by light microscopy and Laser Ablation Ion Inductively Coupled Plasma Mass Spectrometry to obtain spatial metal (Cu, Zn) distribution. The exploratory analysis of the tissue sections indicates there is clearly a pattern in the spatial structure. Different projections of the spatial structure of the melanoma are obtained by the different measurement methods. The spectral clustering on the data was utilized to describe the structure in the data. According to the clustering results, there are distinct clusters of observations in the histological data. The spatial elemental distribution of the metals Cu and Zn cannot be clustered—the data form one compact cluster. The clustering of the histological images produces clusters which are related to the annotation of the biological samples in broader terms—the differences between fibrous and cancerous tissue.

## Keywords

Clustering • Image processing • MeLiM • Melanoma  
2D maximum overlap wavelet transform

## 1 Introduction

The development in laboratory measurement techniques provides us with new means to examine biological samples. The DNA sequencing started a new research field of genomics which allowed us to study the genetic traits observed in organisms, especially humans [1]. With the advances in measurement equipment, the genomics was followed by transcriptomics, proteomics [2] and metabolomics [3], which study the RNA, proteins and metabolites respectively. These new methods produce a type of data, which stimulate the development of new methods for dealing with their unusual features. An example of such a data is the mapping of distribution of elements in tissue samples by Laser Ablation Ion Inductively Coupled Plasma Mass Spectrometry (LA-ICP-MS). The LA-ICP-MS technique allows us to study the distribution of biologically active metals (zinc Zn, copper Cu) in tissue samples [4, 5]. The analysis of the biologically active compounds measured by LA-ICP-MS may be performed manually [5], however, we are able to substitute several of the manual steps with an algorithm which can provide better, more reliable and easily reproducible results [4]. The process of semi-automated analysis of the distribution of biologically active metals in tumor tissue samples integrates various sources of information (LA-ICP-MS measurement, histological image, histological annotation), but the data still has to be prepared manually [4]. We believe that the process may be improved in such way that any manual preparation of the data except for the obvious tasks such as the histological annotation, where the expert knowledge cannot be replaced, would be needed. In order to enhance the data integration procedures, first, we have to understand the data. A good start is to perform

J. Anyz (✉) · O. Stepankova  
Faculty of Electrical Engineering, Department of Cybernetics,  
Czech Technical University, Prague, Czech Republic  
e-mail: anyzjiri@fel.cvut.cz

L. Vyslouzilova · O. Stepankova  
Czech Institute of Informatics, Robotics, and Cybernetics, Czech  
Technical University, Prague, Czech Republic

V. Horak  
Laboratory of Tumour Biology, Institute of Animal Physiology  
and Genetics, Czech Academy of Sciences, Libechov, Czech  
Republic

T. Vaculovic  
Faculty of Science, Department of Chemistry, Masaryk  
University, Brno, Czech Republic

V. Adam  
Department of Chemistry and Biochemistry, Mendel University,  
Brno, Czech Republic



exploratory unsupervised analyses on the input data and assess whether there are any relationships among the data without prior knowledge.

## 2 Methods

### 2.1 Data Collection

The data were obtained by examination of tissue samples from ten MeLiM animals with multiple skin melanomas. The animals varied in age (range 4–22 weeks), there are clear age-dependent changes in the development of melanoma. One melanoma sample was taken from each animal. This experimental treatment was performed in accordance with the Project of Experiment approved by the Animal Science Committee of the IAPG AS CR, v.v.i. (Libechov, Czech Republic), following the rules of the European Convention for the Care and Use of Laboratory Animals. For the detailed description of the tissue sample treatment refer to [4]. The tissue samples were sliced in order to provide tissue section of two types—thinner section suitable for histological analysis and thicker sections for analysis by LA-ICP-MS.

### Histology

The tissue sections for histological analysis were stained to observe tissue structure. The cryosections were scanned by the VS120 Olympus microscope with OlyVIA software (Olympus, Japan). An expert identified histologically different zones. Three to eight rectangular areas of each zone (growing melanoma tissue, early and late spontaneous regression, fibrous tissue) per cryosection were chosen for comparison with Zn and Cu map to detect their local concentration [4]. A simplified annotation of the tissue sample histology is shown in Fig. 1.

### Elemental Mapping Procedure with LA-ICP-MS

Imaging experiments were performed using LA-ICP-MS setup consisting of laser ablation system UP213 (NewWave, USA) operated at wavelength of 213 nm. The ablated material is washed away by helium. This mixture is transferred into quadrupole ICP-MS spectrometer Agilent 7500CE (Agilent, Japan) equipped with collision-reaction cell (CRC) for suppressing possible polyatomic interferences. Elemental mapping was performed using line scan mode so that each line starts on glass substrate outside of the tumour tissue. The laser beam moved on the sample surface

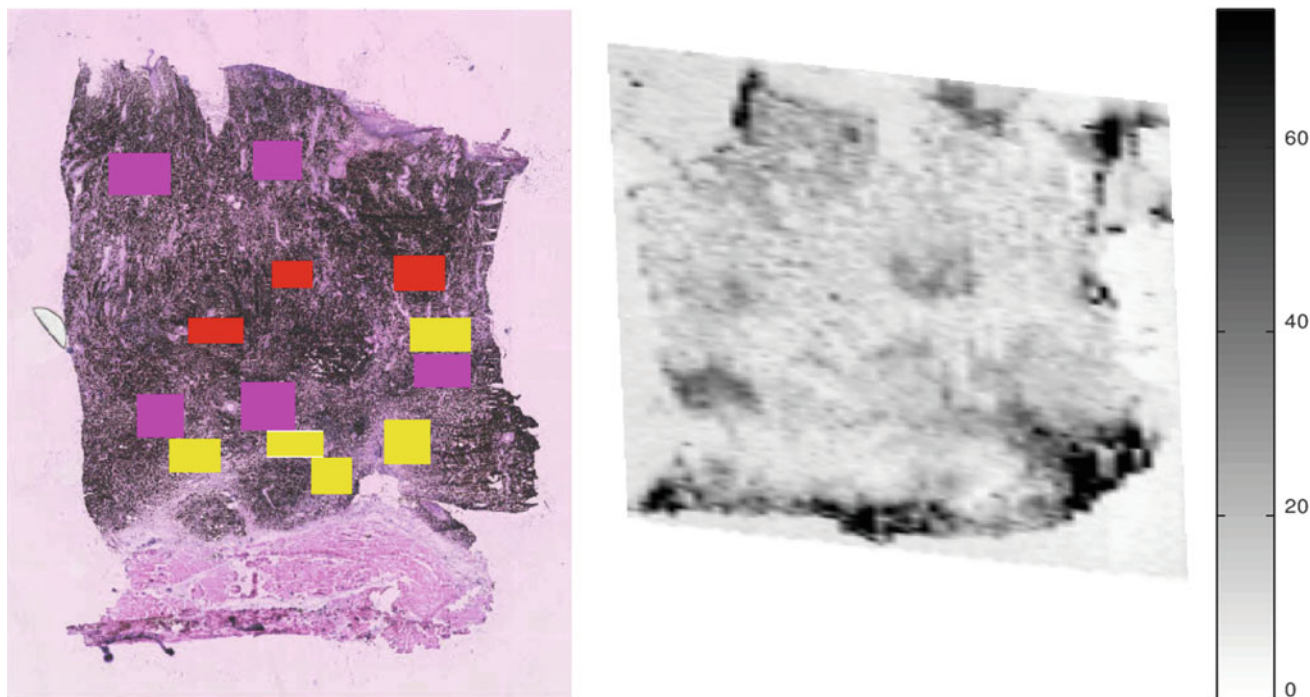


**Fig. 1 Left:** N115—an example of histological image. The coloured rectangles correspond to histologically differing zones identified in haematoxylin-eosin stained slices—red—growing melanoma tissue, pink—early spontaneous regression, yellow—late spontaneous

regression, green—fibrous tissue. The actual dimension of the sample is approximately  $8 \times 5$  mm. **Right:** N115—elemental map of copper  $^{63}\text{Cu}$ , the colorbar indicates the values of metal signal intensity normalized on  $^{12}\text{C}$  content

continuously along straight line with constant scan rate of 200 m/s. Laser beam diameter and distance between individual straight lines were 100  $\mu$ m for both. The laser fluence was 8 J/cm<sup>2</sup> [4]. An example of a distribution of metal in tissue sample is in Fig. 1.

## 2.2 Data Integration

To integrate the data and create a dataset we utilized the image registration procedure. The image registration creates a reference frame for indexing among different types of data. The integration procedure relies on extraction of a silhouette from the studied images and finding such a transformation which minimizes the sum of squared differences between the silhouettes. The algorithm for sequential approximation on image pyramid was used [4]. The image registration was performed in the Octave software [6].

## 2.3 Clustering

To examine the structure of the tissue section we decided to use standard clustering algorithms used in image processing. We performed clustering with the state-of-the-art clustering algorithm the spectral clustering [7]. The clustering was carried out using the R software [8] and the package Kernlab was used [9]. We applied the clustering algorithm to the histological images, to the elemental matrices and to the combination of the histological images and the elemental matrices. We used the 2D maximum overlap wavelet transform (2D MODWT) [10] to extract local features of the image. The spectral clustering was performed with kernel distance matrix. The radial basis function was used, the parameter  $\sigma$  of the kernel was first optimized by the heuristic function supplied by the Kernlab package [9]. The number of clusters was chosen as the drop in values of the distance matrix eigenvalues.

## 2.4 Statistical Analysis

The results of the clustering were compared by tables of the coincidence between cluster assignment and the histological annotation. The tables were tested by  $\chi^2$  test to assess any relationships between the different clustering experiments and the histological zones. Consequently, the logistic regression model was used to test each category of histological zone and each cluster. The relationship was considered significant if the p value was lower than a threshold value of 0.05 corrected for the actual number of all test by Bonferroni correction.

## 3 Results

### 3.1 Data Integration

The data integration process provided us with 10 integrated data sets—each consisting from a histological image, histological image silhouette, elemental map for Zn and Cu, and annotation of histological zones. The data integration process ensures that we are able to index all the images for corresponding locations. The histological image and the elemental maps were decomposed by the 2D MODWT, level of decomposition 2, and the coefficients were used alongside the original features for the clustering.

### 3.2 Clustering

#### Clustering of Elemental Maps

The clustering of the elemental maps showed that there are no distinctive clusters in the elemental maps. In all the samples, the clustering is dominated by one cluster, which contains the majority of the observations, and the remaining clusters represent only small fraction of the data. Only one sample (N113) indicated possible relationship between the clustering and the histological annotation, however none of the consequent tests by the logistic regression showed any significant result. Therefore, we may assume there is no simple relationship between the elemental maps and the histological annotation.

#### Clustering of Histology

The histological images contain areas which may be divided into clusters easily. Based on the original histological image and local features the clustering is able to assign correctly the pixel into these categories. The clustering seems to be consistent with the histological areas (except samples L619, N129). In the majority of samples we are able detect a relationship and identify the clusters which correspond to the histological zones. Unfortunately the results don't allow to distinguish all the histological zones, but only the zones in broader categories of melanoma tissue or fibrous tissue. The visualization of the result of clustering is in Fig. 2.

#### Clustering of Combination of Histology and Elemental Maps

The combination of the features was performed by combining the original histological data and the elemental maps into one data set. The results of the clustering were similar to those of clustering elemental maps. The addition of the elemental maps features to the promising results on histological data did not result in better clustering results. Only

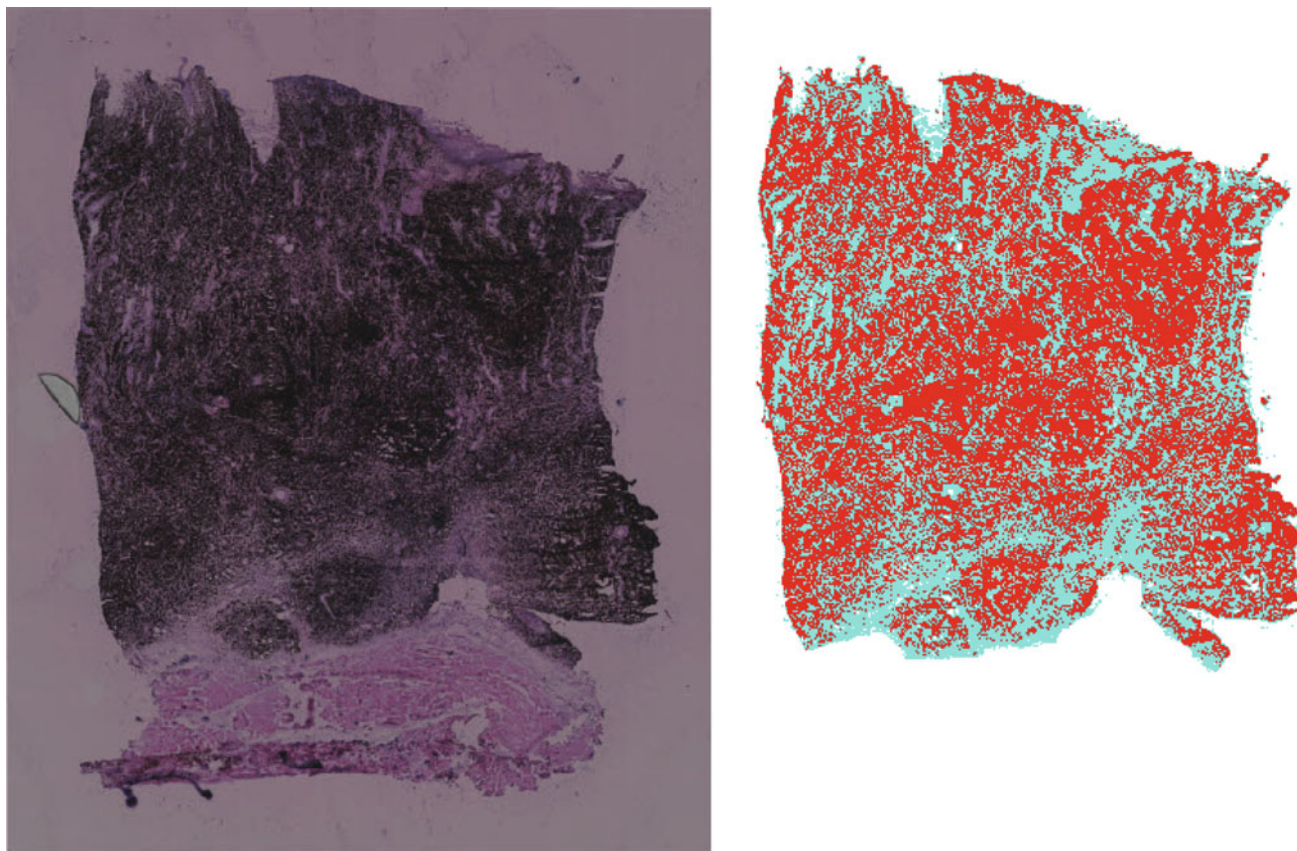


**Fig. 2** Left: N115—histology image. Right: N115—the clustering based on the histological data into two clusters

two samples passed the  $\chi^2$  test (L619, N129). And in the case of these two samples the consequent test by logistic regression model did not show any specific relationships among the histological zones and the clustering.

## 4 Conclusion

In conclusion by the application of the spectral clustering algorithm on data from pigs melanoma samples, we were able to detect structure in the histological images, but not in the distribution of metals (Cu, Zn) or the combination of the histology and distribution of metals. By using the histological annotations we were able to test the relationship between individual histological zones and clusters obtained from histological data. The procedure which consisted from testing by  $\chi^2$  test for any relationship and follow up test by logistic regression in case of positive result from  $\chi^2$  test to test histological zones against clusters. This procedure showed that the clusters in the histological data may be related to the histological zones in broader terms—melanoma cells and other types of tissue. The exploratory analyses presented in this paper show us, that there is definitely a structure in the

data, but even though we used the state-of-the-art methods for image processing we were not able relate the clusters and histological information completely.

**Acknowledgements** This work was supported by the Grant Agency of the Czech Technical University in Prague, grant No. SGS16/231/OHK3/3T/13.

## References

1. Lockhart, David J., and Elizabeth A. Winzeler. "Genomics, gene expression and DNA arrays." *Nature* 405.6788 (2000): 827.
2. Gupta, Archana P., Zbynek Bozdech, and Peter R. Preiser. "Transcriptomics and proteomics." *Advances in Malaria Research* (2016): 197.
3. German, J. Bruce, Bruce D. Hammock, and Steven M. Watkins. "Metabolomics: building on a century of biochemistry to guide human health." *Metabolomics* 1.1 (2005): 3–9.
4. Anyz, Jiri, et al. "Spatial mapping of metals in tissue-sections using combination of mass-spectrometry and histology through image registration." *Scientific reports* 7 (2017): 40169.
5. Riesop, David, et al. "Zinc distribution within breast cancer tissue: A possible marker for histological grading?." *Journal of cancer research and clinical oncology* 141.7 (2015): 1321–1331.
6. Kovesi, Peter D. "MATLAB and Octave functions for computer vision and image processing. School of Computer Science &

- Software Engineering, The University of Western Australia.” (2000).
7. Ng, Andrew Y., Michael I. Jordan, and Yair Weiss. “On spectral clustering: Analysis and an algorithm.” *Advances in neural information processing systems*. 2002.
  8. R Core Team (2017). R: A language and environment for statistical computing. R Foundation for Statistical Computing, Vienna, Austria. URL <https://www.R-project.org/>.
  9. Alexandros Karatzoglou, Alex Smola, Kurt Hornik, Achim Zeileis (2004). kernlab - An S4 Package for Kernel Methods in R. *Journal of Statistical Software* 11(9), 1–20. URL <http://www.jstatsoft.org/v11/i09/>
  10. Lee, Tai Sing. “Image representation using 2D Gabor wavelets.” *IEEE Transactions on pattern analysis and machine intelligence* 18.10 (1996): 959–971.
  11. Brandon Whitcher (2015). waveslim: Basic wavelet routines for one-, two- and three-dimensional signal processing. R package version 1.7.5. <https://CRAN.R-project.org/package=waveslim>



# Automatic Characterization of Plaques and Tissue in IVOCT Images Using a Multi-step Convolutional Neural Network Framework

G. A. Cheimariotis, M. Riga, K. Toutouzas, D. Tousoulis, A. Katsaggelos, and N. Maglaveras

## Abstract

Intravascular optical coherence tomography (IVOCT) is a light-based imaging modality of great interest because it can contribute in diagnosing and preventing atherosclerosis due to its ability to provide in vivo insight of coronary arteries' morphology. The substantial number of slices which are obtained per artery, makes it laborious for medical experts to classify image regions of interest. We propose a framework based on Convolutional Neural Networks (CNN) for classification of regions of intravascular OCT images into 4 categories: fibrous tissue, mixed plaque, lipid plaque and calcified plaque. The framework consists of 2 main parts. In the first part, square patches ( $8 \times 8$  pixels) of OCT images are classified as fibrous tissue or plaque using a CNN which was designed for texture classification. In the second part, larger regions consisting of adjacent patches which are classified as plaque in the first part, are classified in 3 categories: lipid, calcium, mixed. Region classification is implemented by an AlexNet version re-trained on images artificially constructed to depict only the core of the plaque region which is considered as its blueprint. Various simple steps like thresholding and morphological operations are used through the framework, mainly to exclude background from analysis and to merge patches into regions. The first

results are promising since the classification accuracy of the two networks is high (95% and 89% respectively).

## Keywords

Segmentation • Intravascular OCT • Convolutional neural networks • Deep learning

## 1 Introduction

Intravascular optical coherence tomography (IVOCT) is a high-resolution ( $\sim 10 \mu\text{m}$ ) imaging technique of great interest since it helps in diagnosing and preventing atherosclerosis due to its ability to provide in vivo insight of the artery anatomy. The clinical interest focuses on detecting the morphological characteristics of atherosclerotic plaques, evaluating the stent strut placement and extracting the 3D geometry of the vascular artery. The catheter that enters the artery gives routinely multiple cross-sectional images (100–300 per artery). An example of a slice containing mixed plaque (green contour) and a calcified plaque (white contour) is depicted in Fig. 1. The substantial number of slices makes it laborious for medical experts to classify image regions of interest.

For this reason, various automatic methods have been proposed recently to make lumen segmentation and tissue characterization automatic and faster. Athanasiou et al. [1] proposed several machine learning techniques to classify 4 kinds of tissue. Shalev et al. [2] proposed SVM to classify plaques based mainly on statistical properties of the images Xu et al. [3] proposed Support Vector Machine to classify tissue using as feature among other Fisher vector, histogram of oriented gradients and local binary pattern.

Abdolmanafi et al. [4] proposed to extract features from OCT images using Alexnet [5]. These features are then used to classify media and intima using AlexNet or other machine learning classifiers. Alexnet is a specific convolutional neural network (CNN), very successful to classify images of

G. A. Cheimariotis (✉) · N. Maglaveras  
Lab of Computing, Medical Informatics and Biomedical Imaging Technologies, Aristotle University, Thessaloniki, Greece  
e-mail: ncheimar@gmail.com

M. Riga · K. Toutouzas · D. Tousoulis  
1st Department of Cardiology, Athens University, Hippokraton Hospital, Athens, Greece

A. Katsaggelos · N. Maglaveras  
Department of Electrical Engineering & Computer Science, Northwestern University, Evanston, IL, USA

N. Maglaveras  
Department of Industrial Engineering & Management Sciences, Northwestern University, Evanston, IL, USA

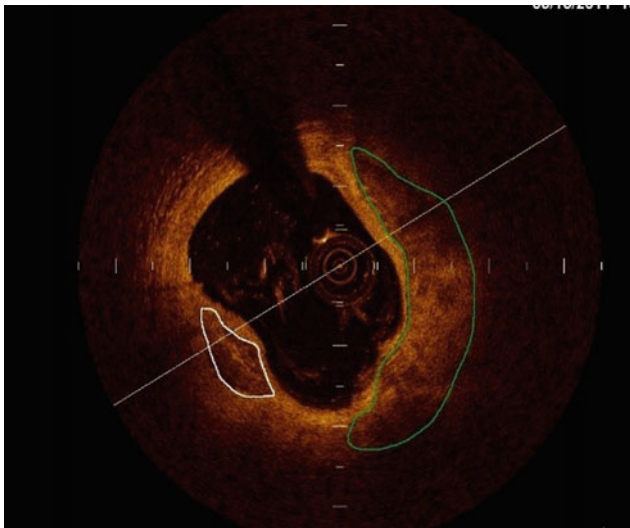


**Fig. 1** Manually segmented OCT image. White contour encloses a calcified plaque and green contour encloses a mixed plaque

the large database ImageNet which is used to compare computer vision algorithms performance. In general, CNNs are neural networks that have commonly convolutional layers along with the fully connected layers that neural networks have and they outperform other algorithms in computer vision tasks. AlexNet consists of five convolutional layers with rectified linear unit (ReLU) activations, some of which are followed by max-pooling layers, and three dense layers. The network was trained with stochastic gradient descent.

However, usually they are not trained to classify medical images. Transfer learning is adjusting parameters of a pre-trained CNN by retraining it with images that belong to different classes of those used in initial training. This can be applied to medical images.

A common task in medical image analysis, is to discriminate image regions based on texture of the image. Texture classification uses normally smaller parts of the image that are dealt as different images with more particular properties residing compared to full-scale images. This could lead to a different CNN architecture in addition to adjusting only the parameters of a state-of-art CNN.

In order, to classify texture of lung CT images Anthimopoulos et al. [6] proposed a prototype CNN that is specialized in classifying small segments of the image that were referred as patches in this paper. The main characteristics of this network are: 5 convolutional layers, 3 dense layers, input size  $32 \times 32$ , very small convolutional kernels  $2 \times 2$ , no pooling layers between convolutional layers.

In this paper, we propose a multi-step framework to detect fibrous tissue and the potential presence of plaque and to characterize plaque regions if they are present. Its first key step is texture classification of the part of the lumen wall of

the image in 2 categories: fibrous tissue and plaque. It is based on Anthimopoulos et al. implementation. Its second key step is the classification of regions that consist of parts of the image characterized as plaques in the previous step, into 3 categories (lipid, calcified, mixed). This classification is implemented by an AlexNet version re-trained on bigger patches of images artificially constructed to depict the core of the plaque region.

## 2 Methods

### 2.1 Materials

The dataset consisted of IVOCT cross-sectional images where a medical expert delineated fibrous tissue and plaques according to the published expert consensus [7, 8].

For the non-overlapping patches analysis that included splitting the image to square patches, calcium plaques provided the smaller dataset because calcium plaques are usually smaller. Therefore, we randomly selected equal patches from the other categories. The ratio of training versus testing patches was 5:1.

For larger scale overlapping patches analysis, we had only 7 images with mixed plaque and so equal number of the other 3 categories were selected to train and test AlexNet. Therefore, we had in total 28 images. Having a small dataset, the ratio between train and test set was 6:1.

### 2.2 Patches Analysis

The aim of this work was to segment fibrous tissue, lipid plaque, calcified plaque or/and mixed plaque in an IVOCT image. Initially, it was attempted to train first level CNN to classify square patches with ranging size from  $7 \times 7$  to  $15 \times 15$  pixels. The patches were extracted by splitting the image without overlap between them. If 95% of one patch fell inside a region delineated by the medical expert, it got its corresponding plaque label. In Fig. 2 there is an example of two patches. The first level CNN is specialized in classifying texture on medical images. Therefore, it was considered that it would have potential to recognize differences in texture between the 4 classes. However, it performed well only classifying fibrous tissue against all the other plaques with average accuracy 95%, while it did not work to discriminate the 3 plaque patches from each other (accuracy 65%).

AlexNet was also tried, having similar performance (90% accuracy for the first task, 62% for the second task). This is because plaques did not present significant texture differences on the small patches level, for the dataset tested. Larger patches may be more distinct but then there would be plaques with less size than the patch and they would not be



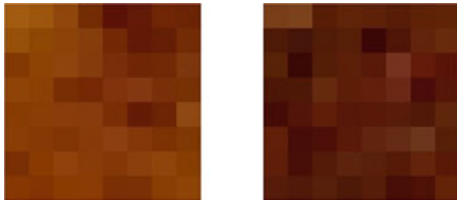


**Fig. 2** Patches from mixed plaque and calcified plaque

identified. Consequently, we use the first level network only to segment fibrous tissue and the segmentation of plaques is tried with images that include bigger bounded patches of potential plaque regions.

### 2.3 Classification of Plaques—Transfer Learning

We retrained AlexNet's 3 fully-connected layers, using stochastic gradient descent with momentum and having as input larger scale patches to characterize plaque. These images were constructed as follows: We kept the manually segmented plaques from the images as they were in the original image. The rest of the image was set to background level 0. This was accomplished by applying a dilated binary mask which corresponds to the handmade contour to the original image. The intuition of using dilated mask, was to include also close surroundings of the manually segmented parts because plaque borders' is sometimes more distinctive than its texture. Finally, we selected the biggest bounding boxes that included the masks' region to be inputs to retrain AlexNet's 3 fully connected layers with stochastic gradient descent with momentum.

Having, only 4 bounding boxes to test the accuracy in each of the 10-fold random permutations of the train set resulted in an accuracy ranging from 50 to 100%. The 50% was the most common case when mixed plaque was confused for calcified plaque and vice versa. However, this was

observed on clearly delineated test set from medical experts and to a small dataset.

We also examined the potential of classifying plaques using as blueprint the bigger bounded patches inside their region. We extracted from each slice, overlapping square patches with size close to the bounded boxes observed. This augmented both the training and the test set. Experiments were carried out with varying size of patches and overlap between them. One of the best results was 89% accuracy for patches of  $32 \times 32$  pixels with  $8 \times 8$  pixels overlap between them. Consequently, this trained network was found more suitable for plaque classification.

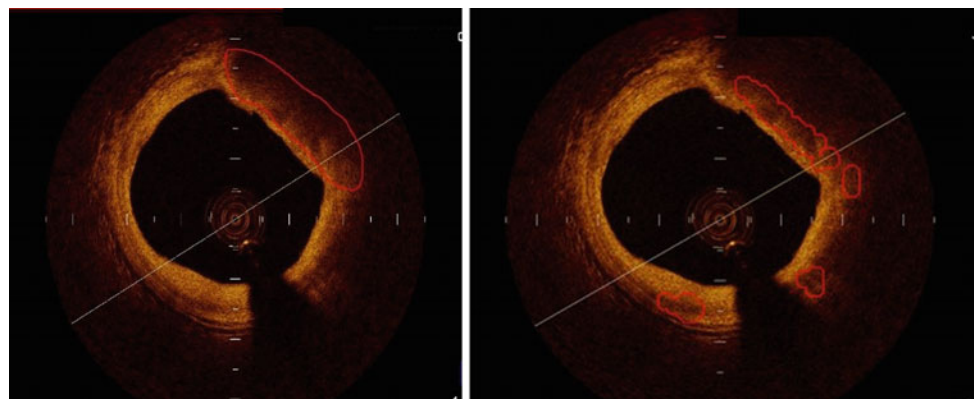
### 2.4 Multi-step Processing

The training procedure described above, is preparative work that must be done to have pipeline steps to process a new image to segment fibrous tissue and plaques. This process is described below.

Given the fact that fibrous tissue is normally the most reflective part of an IVOCT image, the highest pixel intensities are inside its region. However, guide wire artifacts and other artifacts may present also high intensities and sometimes fibrous tissue is under the shadow of an artifact that may lower the intensity of its part. Thresholding was essential before patches analysis because sometimes, fibrous tissue is so thin that cannot characterize a whole patch. Therefore, we propose one high threshold which will discriminate potential fibrous tissue, plaques, guide wire artifact and other artifacts from the background.

Fibrous tissue is detected by applying the first level CNN on the outcome of thresholding. The rest is classified as plaque. Morphological closing is applied to the binary mask which represents plaque to make its parts coherent. Then morphological opening is applied to remove artifacts. These operations are also performed to discriminate plaque regions

**Fig. 3** Results of the automatic characterization of plaque (right figure) versus the manually segmented lipid plaque (left figure)



that are close to each other and they are potentially different plaques and to shape them like the ones used for training.

If the outcome of the above, are multiple potential plaques in a slice, equal number of specially constructed boxes are generated to be classified. Afterwards, we extract the bigger bounded patches ( $32 \times 32$ ) of the same form as the ones used for the training set which were input to the already trained AlexNet. The final decision for characterization of each examined plaque is the maximum number of classifications of patches inside each plaque. An example result is presented in Fig. 3.

### 3 Results

We already referred to the results of the training procedure which indicate that this method has good potential to characterize plaques in IVOCT.

Namely, the first level CNN presented high average accuracy 95% in classifying patches of fibrous tissue and of plaque. Many patches can be extracted from a small dataset but there was not much diversity of samples, to reach a safe conclusion about the performance on a different dataset. On the other hand, having more images for training would possibly enhance the performance.

AlexNet presented 89% accuracy, in classifying  $32 \times 32$  overlapping patches. However, the test set was produced with the same manner with the training set. As the visual result show, it is not an easy task to extract the potential plaques in the steps between the CNNs classifications.

To determine the overall accuracy of this framework, we should test it against another dataset that it would be input to the framework. Few images were excluded from the training set of CNNs (images of lipid plaque) and were available to for further evaluation. Besides, as it is observed in Fig. 3, a plaque can be characterized correctly but its borders would not coincide with manual segmentation and accuracy metrics like dice for the overall evaluation would underestimate the potential of this method. One minor reason is the subjective manner of manual segmentation but the main reason is the post-processing of what is potential plaque after the first level CNN classification, which included morphological operations. Instead of these operations, k-means classification, watershed segmentation or other techniques could be more efficient in splitting and determining the borders of regions of interest getting information not only from binary masks but also from pixel intensities inside the plaques. This will be one of the main aspects the for further research.

### 4 Discussion

Other steps of this framework can be altered to enhance overall performance. To begin with, we can process the images in the polar coordinate as it is common for IVOCT processing. We can also process 3D images, if consecutive slices of the same artery are available. Furthermore, the patches can be the outcome of superpixels algorithm instead of square. The input to AlexNet can also be constructed in other ways e.g. getting more information of the potential plaque surroundings. Other CNN architectures or modified versions of the ones used, can also enhance performance.

### 5 Conclusion

In this paper, we are proposing a framework to characterize plaques in two levels: texture and region, using suitable CNNs in each level. While the overall performance of the framework was only evaluated by visual inspection, the two networks demonstrated high accuracy in classifying patches and specially constructed input (95% and 89% respectively). There are several improvements proposed for further research such as the use of 3D or/and images expressed in polar coordinates, altering patches and regions extraction, and using different CNN architectures.

**Funding Sources** This research is funded by the Greek State Scholarships Foundation and European Social Fund.

**Conflict of interest** The authors declare that they have no conflict of interest.

### References

1. Athanasiou L, Bourantas C, Rigas G et al (2014) Methodology for fully automated segmentation and plaque characterization in intracoronary optical coherence tomography images. *Journal of Biomedical Optics* <https://doi.org/10.1117/1.jbo.19.2.026009>
2. Shalev R, Nakamura D, Nishino S et al (2016) Automated Volumetric Intravascular Plaque Classification using Optical Coherence Tomography (OCT) Twenty-Eighth IAAI Conference
3. Xu M, Cheng J, and Wong D W K (2016) Automatic Image Classification in Intravascular Region. 10 Conference (TENCON), 2016 IEEE <https://doi.org/10.1109/tencon.2016.7848275>
4. Abdolmanafi A, Duong L, Dahdah M et al Deep feature learning for automatic tissue classification of coronary artery using optical coherence tomography. *Biomed Opt Express*. 2017 Jan 30; 8 (2):1203–1220. <https://doi.org/10.1364/boe.8.001203>

5. A. Krizhevsky, I. Sutskever, and G. Hinton, ImageNet Classification with Deep Convolutional Neural Networks. *Adv. Neural Inf. Process. Syst.*, p. 9, 2012
6. Anthimopoulos, Ebner L, Christe A et al (2016) Lung Pattern Classification for Interstitial Lung Diseases Using a Deep Convolutional Neural Network. *IEEE Transactions on Medical Imaging* <https://doi.org/10.1109/tmi.2016.2535865>
7. Toutouzas K, Chatzizisis YS, Riga M et al (2015) 'Accurate and reproducible reconstruction of coronary arteries and endothelial shear stress calculation using 3D OCT: Comparative study to 3D IVUS and 3D QCA.,' *Atherosclerosis*. 240(2):510–9. 2015
8. Tearney G J, Regar E, Akasaka T et al (2012) "Consensus standards for acquisition, measurement, and reporting of intravascular optical coherence tomography studies: a report from the international working group for intravascular optical coherence tomography standardization and validation," *J. Am. Coll. Cardiol*, 59(12), 1058–1072

# Iterative Methods for Fast Reconstruction of Undersampled Dynamic Contrast-Enhanced MRI Data

Hynek Walner, Michal Bartoš, Marie Mangová, Olivier Keunen, Rolf Bjerkvig, Radovan Jiřík, and Michal Šorel

## Abstract

This paper introduces new variational formulation for reconstruction from subsampled dynamic contrast-enhanced DCE-MRI data, that combines a data-driven approach using estimated temporal basis and total variation regularization (PCA TV). We also experimentally compares the performance of such model with two other state-of-the-art formulations. One models the shape of perfusion curves in time as a sum of a curve belonging to a low-dimensional space and a function sparse in a suitable domain (L + S model). The other possibility is to regularize both spatial and time domains (ICTGV). We are dealing with the specific situation of the DCE-MRI acquisition with a 9.4T small animal scanner, working with noisier signals than human scanners and with a smaller number of coil elements that can be used for parallel acquisition and small voxels. Evaluation of the selected methods is done through subsampled reconstruction of radially-sampled DCE-MRI

data. Our analysis shows that compressed sensed MRI in the form of regularization can be used to increase the temporal resolution of acquisition while keeping a sufficient signal-to-noise ratio. DCE-MRI, iterative reconstruction techniques, compressed sensing.

## Keywords

DCE-MRI • Iterative reconstruction techniques  
Compressed sensing

## 1 Introduction

Dynamic contrast-enhanced magnetic resonance imaging (DCE-MRI) is a method for quantification of parameters describing tissue perfusion. It is based on data capturing spatiotemporal distribution of a contrast agent. Reconstruction of DCE-MRI data in general aims to reconstruct an image sequence from the raw k-space data. The result is subsequently used for pharmacokinetic modeling and perfusion-parameter estimation for each reconstructed-image voxel. In more recent years it is benefiting from both parallel imaging [1] and compressed sensing (CS) [2] due to their abilities to significantly reduce the number of acquired k-space data. The latter technique relies on adding sparsifying transformations to the acquired image sequence, such as the Fourier or the Wavelet transform [3], spatiotemporal finite differences [4], or combinations of these [5] and exploiting underlying temporal dynamics by employing principal component analysis (PCA) [6]. These data-driven sparsifying transforms assume that the image sequence can be represented by a matrix of low-rank or as a combination of low-rank and sparse components. Namely, this is the case of L + S model applied in [7, 8], however, these models presume global separability of the dynamic data and the background and such a separation is not generally applicable. A current improvement of this approach employs a patch-based decomposition [9] or applies PCA to obtain

H. Walner (✉) · M. Bartoš · M. Šorel  
Image Processing, Institute of Information Theory and  
Automation, The Czech Academy of Sciences, Prague,  
Czech Republic  
e-mail: walner@utia.cas.cz  
URL: <http://www.utia.cz/people/walner>

M. Mangová  
Department of Telecommunications, Brno University  
of Technology, Brno, Czech Republic

O. Keunen · R. Bjerkvig  
Norlux Neuro-Oncology Laboratory, Department of Oncology,  
Luxembourg Institute of Health, Luxembourg, Luxembourg

R. Bjerkvig  
Department of Biomedicine, University of Bergen, Bergen,  
Norway

R. Bjerkvig  
KG Jebsen Brain Tumor Research Center, University of Bergen,  
Bergen, Norway

R. Jiřík  
Magnetic Resonance and Cryogenics, Institute of Scientific  
Instruments, The Czech Academy of Sciences, Brno, Czech  
Republic

temporal basis functions from low-resolution data [6]. These are used as L1-penalized model-consistency constraints rather than imposing strict low-rank assumptions, while the model order needs to be determined heuristically. Generalizing CS approaches, variational models for image reconstruction allow to introduce different assumptions on an unknown object which weights regularization against data fidelity. A possible extension of the well-known total variation (TV) is the total generalized variation (TGV) functional [10], which balances between different orders of differentiation, enforcing linear or polynomial smoothness while still allowing sharp discontinuities [11]. Such a model was shown to be useful for still images [12] and highly parallelized CINE cardiac data [13]. This paper aims to assess selected approaches to reconstruct DCE-MRI image sequences from signal attained at small animal scanners, that have usually small parallelization (fewer elements of array coils) than clinical scanners and can have a smaller signal-to-noise ratio (SNR).

## 2 Models

### 2.1 TV Regularization with Pre-estimated Temporal Basis

Proposed variational formulation using total variation as a spatial image prior [14] combining temporal regularization using a PCA basis of the given data [6] (PCA TV) can be written as

$$\min_u \left\{ \sum_{t,i} \frac{1}{2} \|y_{t,i} - F_t S_i B_t u\|_2^2 + \lambda \|\nabla B_t u\|_1 \right\}, \quad (1)$$

where index  $t$  enumerates time frames,  $i$  receiver coils. In our study, non-Cartesian golden angle k-space sampling is assumed as one of the most popular compressed-sensing MRI acquisition method. Therefore, the Fourier transform for the time-frame  $t$ , denoted by  $F_t$ , is automatically assumed in its non-uniform variant [15]. All coil sensitivity maps  $S_i$ ,  $i$  being a coil index, were estimated using the ESPIRiT algorithm proposed in [16]. Temporal basis functions at time frame  $t$  are denoted by  $B_t$  and are estimated using the PCA method from low-resolution data. Order of the basis is given to the model as an input parameter,  $\|\cdot\|_1$  is the sparsity enforcing L1 norm and Frobenius norm  $\|\cdot\|_2$  measured closeness to the measured k-space data  $y_{t,i}$ ,  $t$  for time-frame  $t$  and coil  $i$ . Solution  $x_t^* = B_t u$  for each time-frame  $t$  can be achieved using iterative technique Alternating Direction Method of Multipliers (ADMM) [17].

### 2.2 Low-Rank Plus Sparse (L + S)

The L + S decomposition method [8] assumes that each time-frame  $x_t$  can be decomposed into a sum of two matrices,  $x_t = l_t + s_t$ , where matrix  $l_t$  represents the low-rank part of the signal and matrix  $s_t$  is assumed sparse in the sense of a linear transformation  $T$  (in this case temporal Fourier transformation). The overall formulation is

$$\min_{l,s} \left\{ \sum_{t,i} \frac{1}{2} \|y_{t,i} - F_t S_i (l_t + s_t)\|_2^2 + \lambda_l \|l\|_* + \lambda_s \|Ts\|_1 \right\}, \quad (2)$$

where  $\|\cdot\|_*$  stands for the nuclear norm giving the sum of singular values and enforcing low rank. Contrasting with the previous model the temporal basis functions are estimated automatically.

### 2.3 ICTGV Model

A possible extension of the TV regularization is employed in the ICTGV model proposed in [13]. This formulation regularizes data by weighting two TGV by infimal convolution

$$\min_x \left\{ \sum_{t,i} \frac{1}{2} \|y_{t,i} - F_t S_i x_t\|_2^2 + \lambda \text{ICTGV}_{\beta_1, \beta_2, \gamma}^2(x) \right\}, \quad (3)$$

The ICTGV model itself was not implemented, but the reconstruction software AVIONIC written by its authors [13] was rather used for comparison with other methods.

## 3 Data Acquisition and Evaluation Methods

Synthetic data were generated from a real DCE-MRI dataset (rat with brain tumor) [18]. 42 manually segmented regions of interests (ROIs) were assigned its reference perfusion parameters based on the values estimated from the real dataset as described in [18]. The concentration curves were constructed using the same pharmacokinetic model as the one used in [18]. 2D golden-angle radial-sampling k-space data were then constructed assuming a 2D SPGR acquisition with TR = 15 ms, flip angle = 20° and acquisition time = 15 min, 128 samples per echo signal, a 4-element surface coil (sensitivities derived from the real recording), with additive corruption by Gaussian noise to average SNR = 26.7 dB (calculated as  $\text{SNR} = 10 \log_{10}(P_{\text{signal}}/P_{\text{noise}})$ , where  $P_{\text{signal}}$  is the mean power of the echo signals and  $P_{\text{noise}}$  the power of noise) to match the real data.

Real data originate from an in vivo experiment with a normal Sprague-Dawley rat on a 9.4T Bruker BioSpin small animal scanner, 2D golden-angle SPGR acquisition with



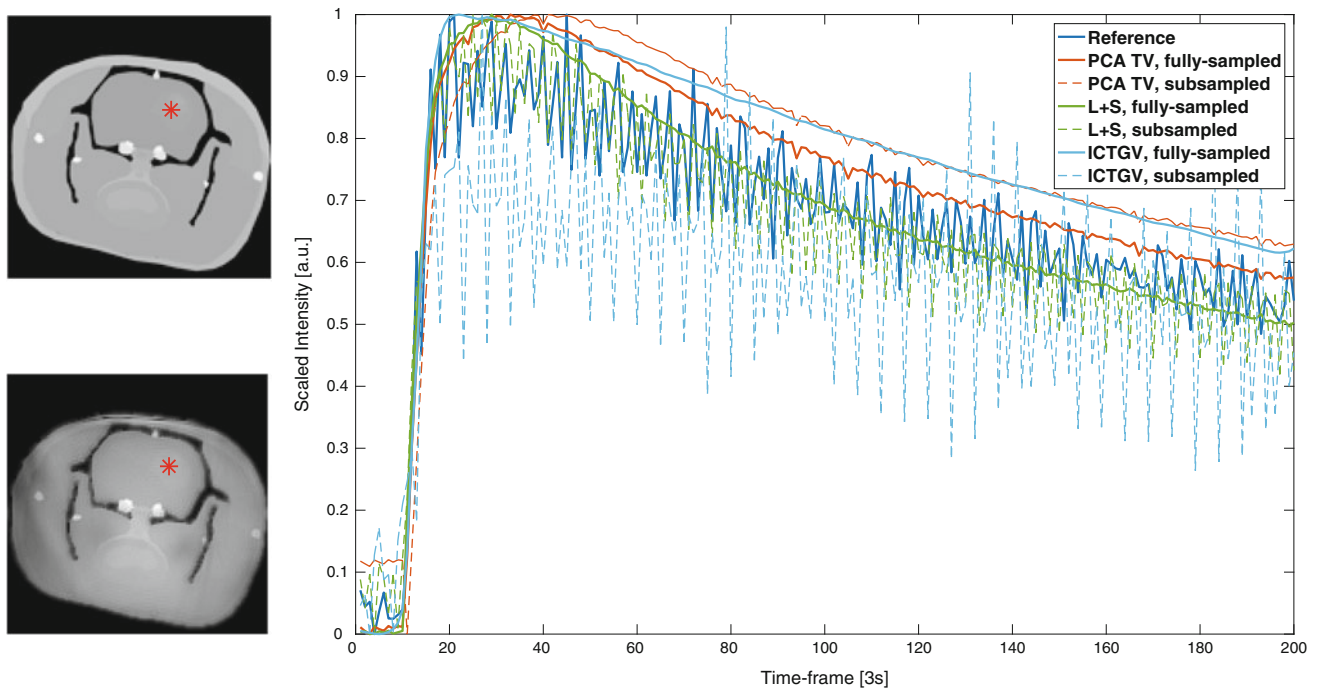


**Fig. 1** One time-frame of the reference phantom image sequence (upper left) and the corresponding reconstructed time-frame (lower left) with output intensity curves for the marked pixel (tumour).

TR = 17 ms, flip angle = 25°, acquisition time = 14 min, 128 samples per echo signal, 4-element surface coil.

For both datasets, different levels of subsampling (skipping projections in the measured signal) were tested to explore the abilities of the models to reconstruct comparable intensity curves with higher temporal resolution. As a reference for evaluation of the algorithms, gridding [15] of fully-sampled data (i.e. 200 projections per time-frame) was used. In order to provide comparability between different models with various parameter settings, output curves were scaled to the  $[0, 1]$  interval.

## 4 Results and Discussion

Firstly, the selected models (L + S, PCA TV and ICTGV) were evaluated on a synthetic dataset. Image sequences were computed using various settings of parameters, levels of subsampling and ranks of temporal basis. Fidelity of reconstruction for a typical benchmark voxel (corresponding to a simulated tumour) can be found in Fig. 1. It can be seen, that the nearest solution (in the sense of mean squared error, see Table 1) was achieved by the L + S model and the PCA TV reconstruction with a priori estimated basis functions of rank 3. The ICTGV method was not resulting in good fits to the reference curves, but it was the best at localising the position of the intensity peak.

Fully-sampled data use 200 radial projections per time-frame, subsampled reconstructions take 28 projections (i.e.  $7 \times$  subsampling)

**Table 1** Mean squared error of reconstruction methods for synthetic data ( $MSE_s$ ) and real data ( $MSE_r$ ) and selected ROI

Method	$MSE_s$	$MSE_r$
PCA TV, fully-sampled	0.0083	0.0136
PCA TV, subsampled	0.0162	0.0126
L + S, fully-sampled	0.0052	0.0272
L + S, subsampled	0.0071	0.0447
ICTGV, fully-sampled	0.0134	0.0148
ICTGV, subsampled	0.0365	0.0184

Overall, it can be stated, that both L + S and PCA TV proved to be the best and the most robust (in terms of subsampling stability) models for synthetic data.

However, comparison on the real data showed a different situation. In order to avoid over-fitting of the models to the one specific experiment, rank 3 was assumed for both the PCA TV and the L + S model. Temporal basis functions were exploited from the regridded data and are shown in Fig. 2.

The PCA TV model with estimation of the temporal basis of rank 3 led to a stable solution (in terms of mean square error). It seems to allow to downsample (and thus increase the temporal resolution) up to the factor of 7 (see Fig. 3). Surprisingly, the L + S model did not achieve as good results as for the synthetic data and the output intensity curves notably differed from the reference. The ICTGV model resulted in



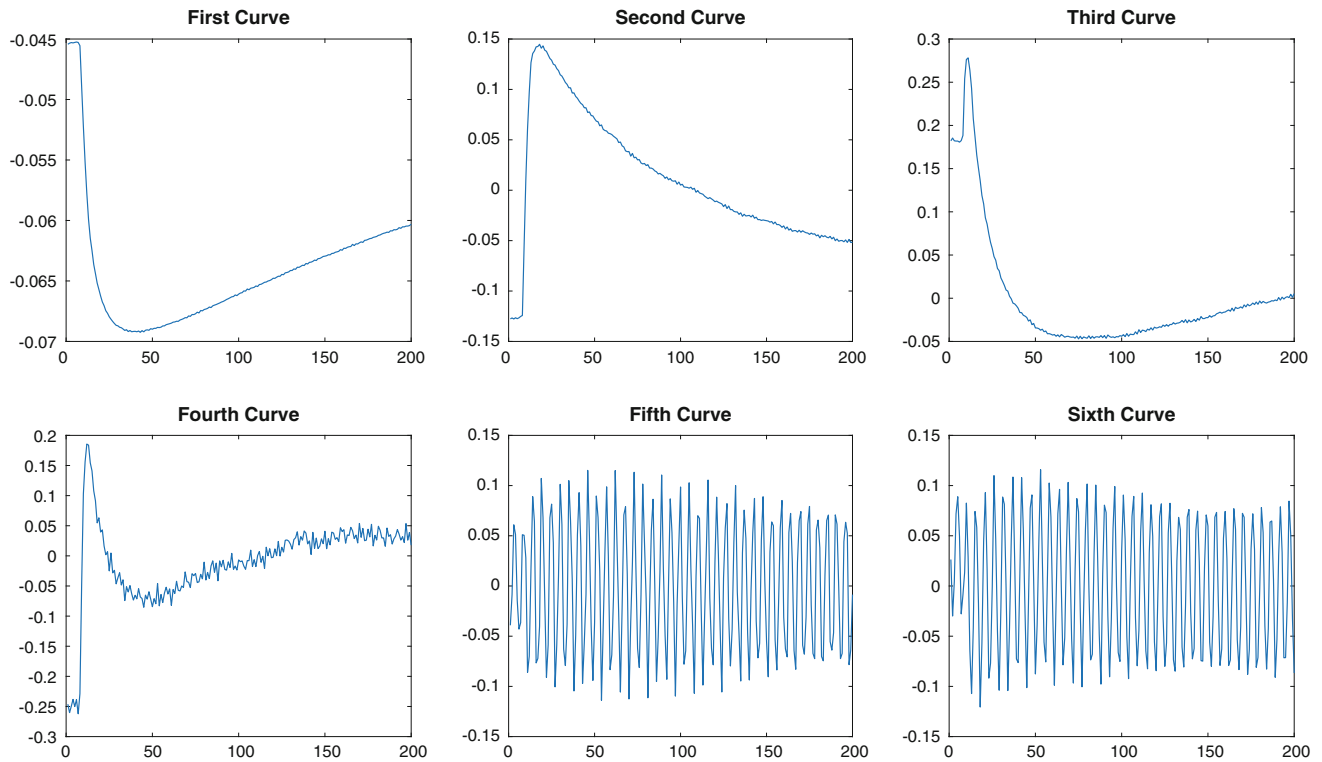


**Fig. 2** Temporal basis functions of the real data ordered by significance

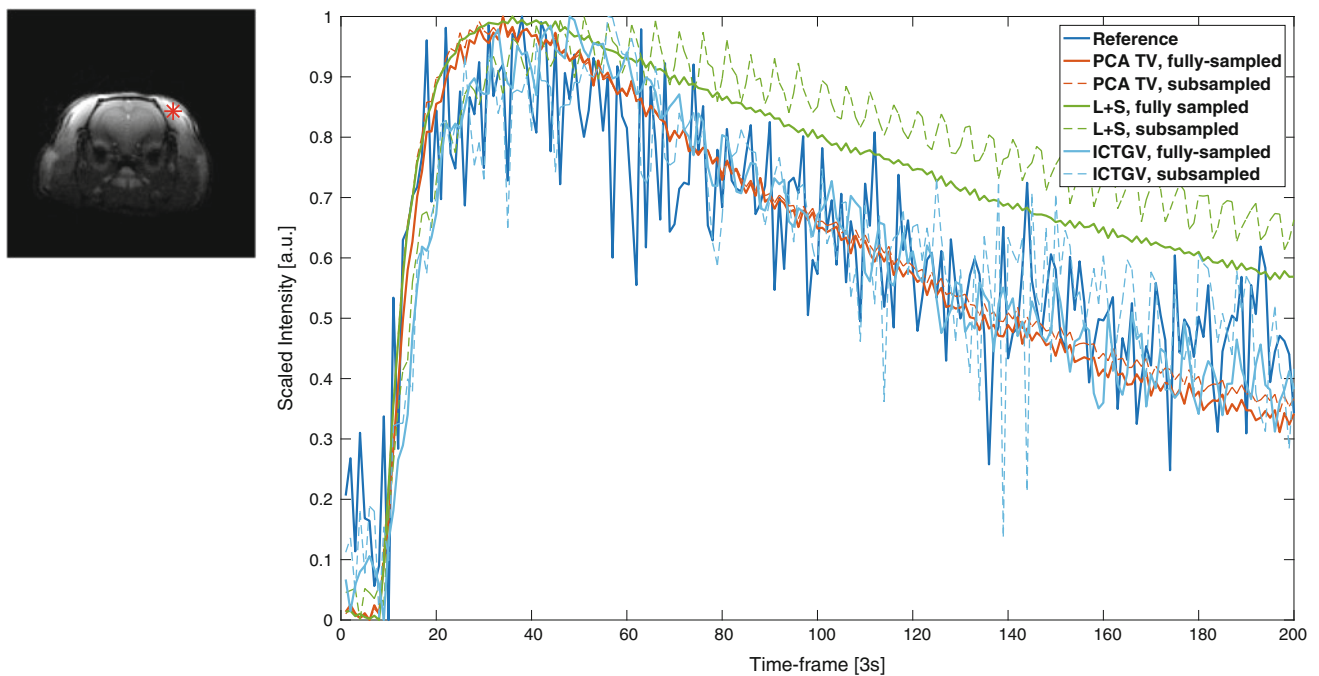


**Fig. 3** Image reconstruction of real data with signal intensity curves of different methods in marked pixel (temporalis muscle)

quite noisy, but with overall good fit to the reference. It is possible, that this behaviour can be improved by fine-tuning the reconstruction parameters. In selected regions, given the

information about the temporal basis, the PCA TV model gave the best results for the measured data (see Table 1).

## 5 Conclusions

We have evaluated three different iterative methods for reconstruction of DCE-MRI data. The evaluation was done on both generated and real data, where it showed quite different results. It can be stated that models assuming a low-rank temporal basis (smaller than 3) were outperformed by those without this presumption or with the PCA-TV model working with a priori information about the character of the temporal dynamics. This can be due to the inability of a small basis to correctly describe the dynamics of the data or due to a lower SNR and fewer array-coil elements of a small-animal NMR scanner compared to clinical NMR scanners. In our experiments, PCA TV was the best reconstruction method in terms of image quality and computational speed (enabling increasing time resolution up to the factor of 10). To draw stronger conclusions, the evaluation will be extended to include both comparison of the reference and reconstructed data on the level of estimated perfusion parameters for various pharmacokinetic models and datasets of mouse tumours where higher levels of SNR (and consequently more precise results) are expected.

**Acknowledgements** This work was funded by the Czech Science Foundation Fund “GA16-13830S” (2016–2018).

**Conflict of Interest** The authors declare that they have no conflict of interest.

## References

- Pruessmann, K.P., Weiger, M., Scheidegger, M.B., Boesiger, P.: SENSE: sensitivity encoding for fast MRI. *Magn Reson Med* 42, 952–962 (1999).
- Donoho, D.L. Compressed sensing. *IEEE Trans Inf Theory* 52, 1289–1306 (2006).
- Jung, H., Sung, K., Nayak K.S., Kim E.Y., Ye J.C.: k-t FOCUSS: a general compressed sensing framework for high resolution dynamic MRI. *Magn Reson Med* 61, 103–116 (2009).
- Adluru, G., Awate, S.P., Tasdizen, T., Whitaker, R.T., DiBella, E. V.: Temporally constrained reconstruction of dynamic cardiac perfusion MRI. *Magn Reson Med* 57, 1027–1036 (2007).
- Lustig, M., Santos, J.M., Donoho, D.L., Pauly, J.M.: k-t SPARSE: high frame rate dynamic MRI exploiting spatio-temporal sparsity. In *Proceedings of the 14th Annual Meeting of ISMRM*, Seattle, Washington, USA. p. 24–20 (2006).
- Velikina, J.V., Samsonov, A.A.: Reconstruction of dynamic image series from undersampled MRI data using data-driven model consistency condition (MOCCO). *Magn Reson Med* 74, 1279–1290 (2015).
- Gao, H., Rapacchi, S., Wang, D., Moriarty, J., Meehan, C., Sayre, J., Laub, G., Finn, P., Hu, P.: Compressed sensing using prior rank, intensity and sparsity model (PRISM): applications in cardiac cine MRI. In *Proceedings of the 20th Annual Meeting of ISMRM*, Melbourne, Australia. p 22–42 (2012).
- Otazo, R., Candes, E., Sodickson, D.K.: Low-rank plus sparse matrix decomposition for accelerated dynamic MRI with separation of background and dynamic components. *Magn Reson Med* 73, 1125–1136 (2015).
- Ong, F., Zhang, T., Cheng, J., Uecker, M., Lustig, M. Beyond low rank—sparse: multi-scale low rank reconstruction for dynamic contrast enhanced imaging. In *Proceedings of the 23th Annual Meeting of ISMRM*, Toronto, Canada, p 05–75 (2015).
- Holler, K., Holler, M.: Regularization of linear inverse problems with total generalized variation. *J Inverse and Ill-Posed Problems* 22, 871–913 (2014).
- Knoll, F., Bredies, K., Pock, T., Stollberger, R.: Second order total generalized variation (TGV) for MRI. *Magn Reson Med* 65, 480–491 (2011).
- Holler, M., Kunisch, K.: On infimal convolution of TV type functionals and applications to video and image reconstruction. *SIAM J Imaging Sci* 7, 2258–2300 (2014).
- Schloegl, M., Holler, M., Schwarzl, A., Bredies, K., Stollberger, R.: Infimal convolution of total generalized variation functionals for dynamic MRI. *Magn Reson Med* 78(1), 142–155 (2017).
- Rudin, L., Osher S.J., Fatemi, E.: Nonlinear total variation based noise removal algorithms. *Physica D.*, 60, 259–268 (1992).
- Fessler, J.A., Sutton, B.P.: Nonuniform fast fourier transforms using min-max interpolation. *IEEE Transactions on Signal Processing* 51(2), 560–574 (2003).
- Uecker, M., Lai, P., M, M.J., Virtue, P., Elad, M., Pauly, J.M., Vasanawala, S.S., Lustig, M.: ESPIRiT An Eigenvalue Approach to Autocalibrating Parallel MRI: Where SENSE meets GRAPPA. *Magn Reson Med* 71(3), 990–1001 (2014).
- Boyd, S., Parikh, N., Chu, E., Peleato, B., Eckstein, J.: *Distributed Optimization and Statistical Learning via the Alternating Direction Method of Multipliers* Foundations and Trends in Machine Learning, Vol. 3, No. 1 11–22 (2010).
- Obad, N., Espedal, H., Jirik, R., Sakariassen, P.O., Rygh, C.B., Lund-Johansen, M., Taxt, T., Niclou, S.P., Bjerkvig, R., Keune, O.: Lack of functional normalisation of tumour vessels following anti-angiogenic therapy in glioblastoma. *Journal of Cerebral Blood Flow & Metabolism*, 1–13 (2017).

# Multimodality Image Fusion of the Liver Using Structure-Guided Deformable Image Registration in Velocity AI—What Is the Preferred Approach?

S. Kuznetsova, P. Grendarova, N. Ploquin, and K. Thind

## Abstract

This study looked at the impact of using different volume segmentation in deformable image registration (DIR) for multimodality imaging, specifically planning computed tomography (CT) and post stereotactic body radiation therapy (SBRT) magnetic resonance imaging (MRI), where liver was the target of the registration. Planning CT and post-SBRT MRI scans for 9 previously treated patients were used in this study. The MRI scan was deformed on to the planning CT using structure-guided DIR using the commercial software Velocity AI. Three different deformation methods were employed based on different contoured regions of the liver and liver itself. The Dice similarity coefficient (DSC) was quantified for all of the structures within the liver along with the average voxel displacement. The registration method that was based only on the liver contours had the largest DSC for some of the internal liver structures, which suggests a preferred approach when using structure-guided DIR for the liver.

## Keywords

Deformable image registration • Stereotactic body radiation therapy • Liver MRI

## 1 Introduction

The deformable image registration (DIR) is a common tool in both the clinical and research setting for the registration of image volumes each containing particular information central to the user in radiation therapy. As more DIR algorithms become available, commercially and on open source [1], it becomes essential to determine the best approach to register a set of multimodality images to reach the highest accuracy in the registration. Unlike rigid registration which is limited by rotational and translation motion, DIR is able to account for the volumetric changes of structures by shifting each voxel individually within the image volume. This becomes especially useful in radiation therapy where internal anatomical structures can undergo volumetric changes throughout patient's treatment timeline [2].

The liver is one of the examples of anatomical sites that can undergo volumetric changes [3]. Past study that looked at rigid registration associated with liver for 4D-CT and respiratory gated MRI (obtained on the same day) found the distance between manually chosen points to be more than 5 mm [4]. Higher rigid registration error can be expected for planning CT and post-SBRT MRI, where image volumes are acquired prior to treatment (planning CT) and after treatment (MRI). The purpose of this study is to look at structure-guided DIR which is a commercial DIR solution provided by Velocity AI 3.2 (Velocity Medical Systems, Atlanta, GA) for multiple volume segmentation image registration of planning CT and post-SBRT MRI.

Structure-guided DIR is a B-spline [5] hybrid registration method which consists of rigid registration followed by DIR [6]. In addition, this registration method uses corresponding structure pairs to minimize the distance between points on the surfaces of the structures and puts an emphasis on voxels within the outlines [6]. Velocity AI implements intensity based DIR method [7] using mutual information similarity metric [8], while structure-guided DIR includes a feature-based component based on the sum of squared

S. Kuznetsova (✉) · N. Ploquin · K. Thind  
Department of Physics and Astronomy, University of Calgary,  
Calgary, AB, Canada  
e-mail: skuznets@ucalgary.ca; lncs@springer.com

P. Grendarova · N. Ploquin · K. Thind  
Department of Oncology, University of Calgary, Calgary, AB,  
Canada

N. Ploquin · K. Thind  
Department of Medical Physics, Tom Baker Cancer Centre,  
Calgary, AB, Canada

differences as part of the registration. The approach to DIR that includes structure component can result in better registration of structures undergoing volumetric changes [9].

In this study, we employ three different methods for structure-guided DIR on the liver to find the best approach that will maximize the conformality between image objects.

## 2 Materials and Methods

### 2.1 Structure Segmentation

Non-contrast enhanced planning CT along with post-SBRT MRI were obtained for nine patients with liver tumors (hepatocellular carcinoma, cholangiocarcinoma or liver metastasis). The mean age of the patient cohort was 73 years old (range: 62–82), where seven out of nine patients were male. Patients in the study underwent liver SBRT treatment where the prescription dose of 40 Gy to 50 Gy was delivered in five fractions in seven out of nine patients; in two out of nine patients, the prescription dose was 30 Gy delivered in 5 fractions. The liver, along with the following three structures within the liver were contoured and approved by Radiation Oncologist: left lobe (LL) which included segments 2 and 3, portal region (PR), and inferior vena cava with caudate lobe (IVC-L). In order to assess the performance of DIR for entire liver volume, the three minor liver volumes were subtracted from the liver contour, thus resulting in the *major liver volume* (MLV). Contoured structures were chosen based on the visibility of specific liver regions on both the MRI and the CT.

### 2.2 Deformable Image Registration

Structure-guided DIR in Velocity AI consists of the establishment of the region of interest (ROI) followed by the rigid registration, followed by the selection of structure pairs, and finally followed by the DIR. The three methods used for the structure-guided DIR were:

- (1) Using the entire liver contour only; one registration per patient
- (2) Using internal liver structures (LL, PR, IVC-L, MLV); Four registration per patient, where each internal structure corresponded to one registration
- (3) Using individual internal liver structures along with the entire liver contour; four registrations per patient where the internal liver structure along with the liver contour contributed to one registration.

In all of the cases mentioned above, MRI scans were deformed on to the planning CT. Following the DIR, the

displacement vector field generated within the software allowed for the transfer of structures from the planning CT on to the MRI or vice versa. Using structures in the same image volume, Dice Similarity Coefficient (DSC) was calculated for each interior liver structure. The DSC is defined as the volume of the overlapping region between structures  $A$  and  $B$ , multiplied by two and divided by the sum of volumes; it has the following form:

$$DSC(A, B) = \frac{2|A \cap B|}{|A| + |B|}.$$

If the DSC is equal to one, then that implies that the structures have perfect overlap and high conformality; If DSC is equal to zero, then that indicates that structures have no overlap. In addition to DSC, the average voxel displacement was measured for the corresponding structure for each registration method.

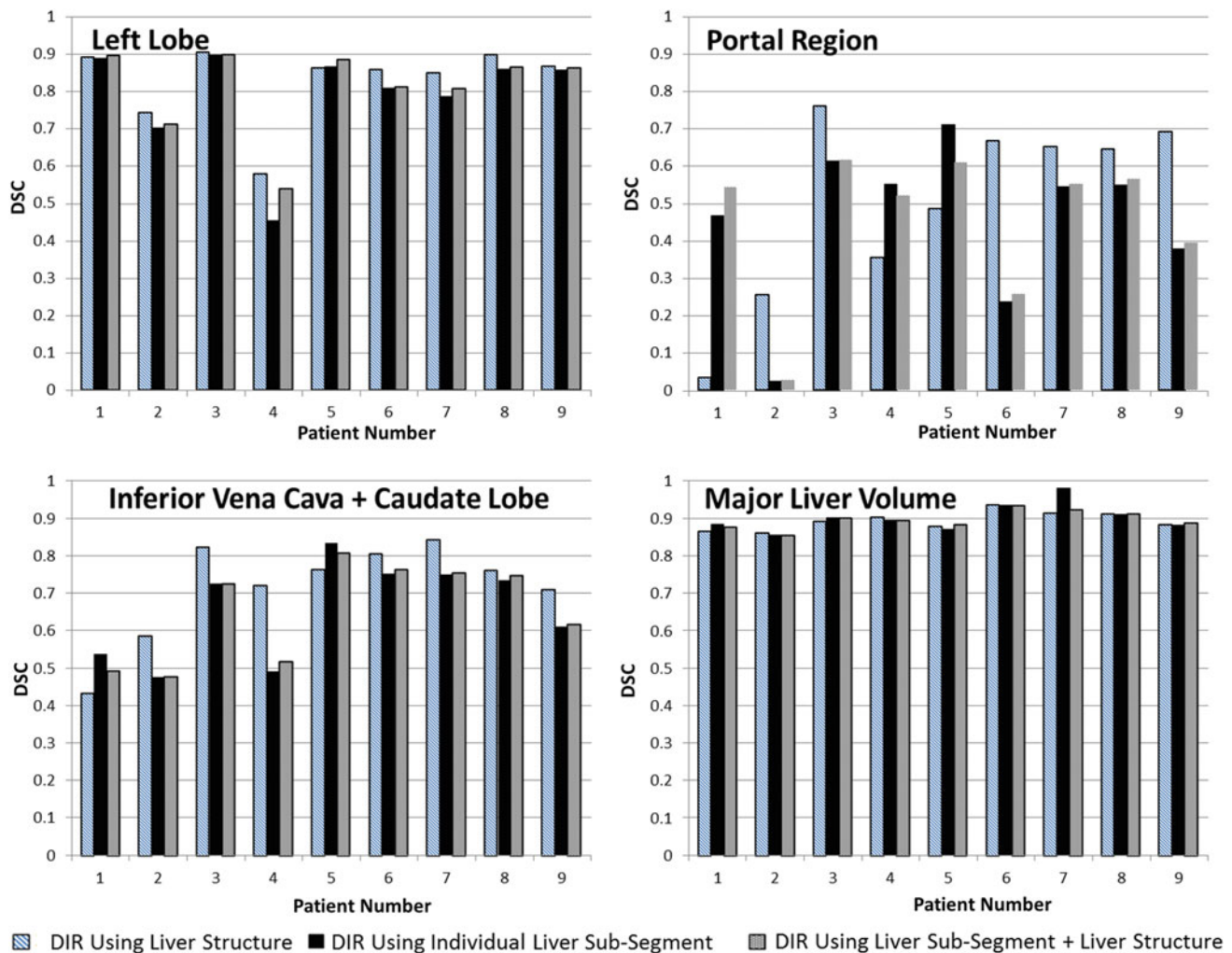
## 3 Results

Figure 1, displays DSC results for the three registration methods on an entire patient cohort for the four liver sub-segments. The first method of registration resulted in higher DSC for LL, PR, and IVC-L structures for the majority of patient cases. Specifically for LL and IVC-L, the DSC was higher using the first registration method in 7 out of 9 patients (78%); for PR, this was the case in 6 out of 9 patients (67%). For the MLV, the DSC for all of the three registration methods did not vary by more than 2% for each patient in 8 out of 9 cases, the only exception being patient-7 where DSC for registration methods 1 and 2 varied by 7%.

Table 1, contains the summary of the median and range corresponding to three registration methods and four contoured structures. The portal region has the lowest median DSC (0.54–0.64) compared to other structures and varies the most among the patient group. The MLV, on the other hand, varies the least and has the highest median DSC (0.89, 0.9). The LL has the second highest DSC (0.86), while IVC-L has the second lowest median DSC (0.72, 0.76) for all registration methods.

Figure 2, displays average voxel displacement throughout the structure volume, which was measured to assess the magnitude of the voxel shift during DIR. Highest average voxel displacements were observed for the PR structure, specifically for patient-1 and patient-2 where average voxel displacement was as high as 41 mm.

The percentage of Planning treatment volume (PTV) in each of the four interior liver segments was briefly assessed. In seven out of nine patients, the PTV primarily resides in the major liver volume (~62–86%).



**Fig. 1** DSC calculated for the four sub-segments of the liver for the patient cohort using three different registration methods. For each plot, the horizontal axis corresponds to the patient number, and the vertical axis corresponds to the calculated DSC

**Table 1** Median DSC and corresponding range for the nine patient group

Liver sub-segments	DIR method 1	DIR method 2	DIR method 3
LL	0.86 (0.58–0.90)	0.86 (0.46–0.90)	0.86 (0.54–0.90)
PR	0.64 (0.03–0.76)	0.55 (0.03–0.71)	0.54 (0.03–0.61)
IVC-L	0.76 (0.43–0.84)	0.72 (0.48–0.84)	0.72 (0.48–0.81)
MLV	0.89 (0.86–0.94)	0.90 (0.86–0.98)	0.90 (0.86–0.94)

## 4 Discussion

The PR volume had the lowest DSC, suggesting that structure-guided DIR struggles with deformation of this specific region within the liver. Since MRI was registered to non-contrast CT, the lack of contrast in CT resulted in a more homogeneous intensity distribution throughout the liver which could have impacted the DIR. For PR structure,

the DSC for the first registration method for patient-1 was 0.03; This was also the case for patient-2 for the second and third registration method. In these three low DSC instances, the average voxel displacement was as high as 3.5–4.1 cm. This shows a correlation between the high displacement of voxels (above 3 cm) and low DSC. Recording the average voxel displacement could be used as a flagging metric in order to alert the user of possible discrepancies in the DIR.



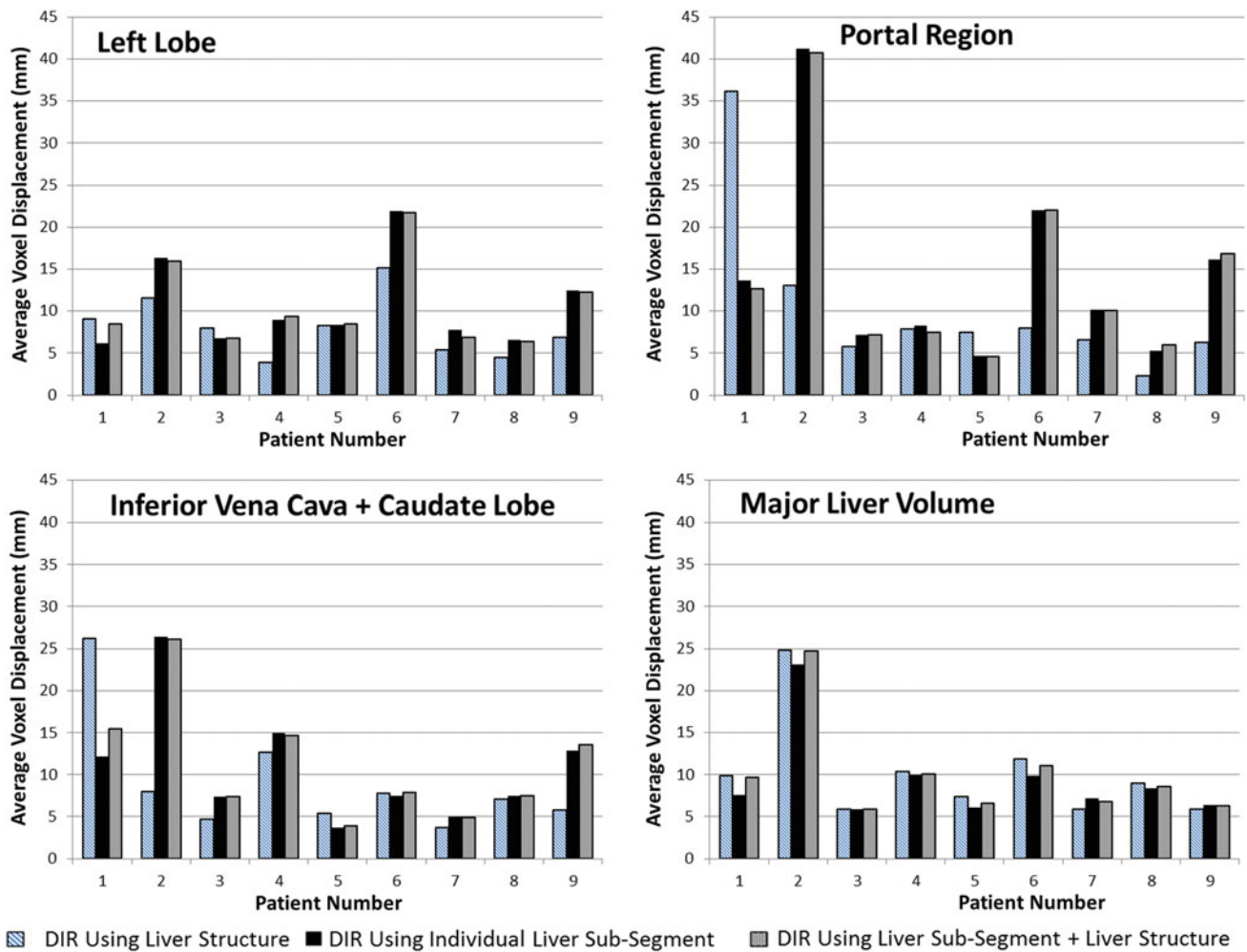


**Fig. 2** Average voxel displacement measured for the four sub-segments of the liver for the patient cohort using three different registration methods. For each plot, the horizontal axis corresponds to the patient number, and the vertical axis corresponds to the average voxel displacement

The correlation between DSC and voxel displacement was observed for the IVC-L structure, where with the decrease in DSC with respect to other registration methods had an increase in the voxel displacement relative to the same registration methods. This relationship was observed for 8 out of 9 patients.

The MLV had the largest DSC out of all of the structures, and in majority of cases, it had the largest PTV encompassed within its contours ( $\sim 60\%$ ). The conformality of this region is high ( $\geq 0.86$ ) regardless of the registration method suggesting that if PTV is primarily contained within MLV, using liver contours in structure-guided DIR will yield similar registration results as other methods. The median DSC for the liver structures after undergoing the first registration method was 0.90 (0.86–0.98) and average mean voxel displacement for nine patients was 9.7 mm which is similar to MLV with average voxel displacement of 9.6 mm. These results suggest that all three registration methods will yield similar result specifically for MLV region of the liver.

## 5 Conclusion

Structure-guided DIR allows the focussing of the registration on the specific organ(s). The results shown in the study demonstrate that the first registration method which utilized only liver contour pairs, either had a higher median DSC specifically for PR and IVC-L structures (median DSC 0.64 and 0.76); or it was equivalent to other registration methods with respect to LL and MLV structures where median DSC did not vary by more than 0.01.

It was also shown that average voxel displacement of the structure volume can serve as a flagging metric. In this study, average voxel displacement above 3 cm was correlated with DSC as low as 0.03 for PR structure. Further research will concentrate on using the structure-guided DIR on contrast-enhanced CT scans and post-SBRT MRI where additional metrics such as the Jacobian, mean surface distance, and target registration error will be assessed.



**Acknowledgement** Acknowledge Alberta Cancer Foundation.

**Conflict of Interest** Authors have no conflict of interest to declare.

---

## References

1. Kodaya, N. et al, Evaluation of various deformable image registration algorithms. *Journal of Radiation Research* 55, 175–182 (2014).
2. J. Lawson et al: Quantitative evaluation of a cone-beam computed tomography-planning computed tomography deformable image registration method for adaptive radiation therapy. *Journal of Applied Clinical Medical Physics* 8(4), 96–113 (2007).
3. Polan, D. F. et al: Implementing Radiation Dose-Volume Liver Response in Biomechanical Deformable Image Registration. *International Journal of Radiation Oncology Biology Physics* 99(4), 1004–1012 (2017).
4. Yu, J I: Evaluation of anatomical landmark position differences between respiration-gated MRI and four-dimensional CT for radiation therapy in patients with hepatocellular carcinoma. *British Journal of Radiology* 86(1021), 1–7 (2014).
5. Wognum S. and Heethuis S.E. et al: Validation of deformable image registration algorithms on CT images of ex vivo porcine bladders with fiducial markers. *Medical Physics* 41(7), (2014).
6. Velocity User Manual. Velocity User Manual Velocity 3.2.0. Atlanta, GA, USA (2016).
7. Chapman C.H., et al: Deformable image registration-based contour propagation yields clinically acceptable plans for MRI-based cervical cancer brachytherapy planning. *Brachytherapy*, <https://doi.org/10.1016/j.brachy.2017.11.019> (2018).
8. Gianfranco. et al.: Performance of commercially available deformable image registration platforms for contour propagation using patient-based computational phantoms: A multi-institutional study. *Medical Physics*, <https://doi.org/10.1002/mp.12737>.
9. Heerden L.E. et al: Structure-based deformable image registration: Added value for dose accumulation of external beam radiotherapy and brachytherapy in cervical cancer. *Radiotherapy and Oncology*, 123(2), 319–324 (2017).

# First Validation of Semi-automatic Liver Segmentation Algorithm

Philipp Matthies, Jan Wuestemann, Francisco A. Pinto,  
and Julius C. Neba

## Abstract

Selective internal radiotherapy (SIRT) is a treatment modality in advanced liver cancer. A careful treatment planning including an angiographic evaluation of the hepatic blood supply and determination of liver and tumor volume by imaging (e.g. contrast-enhanced MRI) is part of the pre-therapeutic workflow. Treatment is performed by an intra-arterial angiographic application of  $^{90}\text{Y}$ -labeled microspheres. Particularly, the segmentation of the liver and calculation of tumor burden are time-consuming activities, but they are a prerequisite of state-of-the-art dosimetry models. In this study, we validated an interactive software tool, which provides a semi-automatic segmentation of co-registered image data (e.g. contrast-enhanced abdominal CT, SPECT/CT, and MRI). A reader experienced in manual liver segmentation for SIRT work-up employed dosimetry software to segment abdominal CT and MRI scans and documented the completion time. A first database contains ten cases (contrast-enhanced CT data) from the Liver Tumor Segmentation (LiTS) Challenge. Results from software-guided semi-automatic segmentation were compared to the published ground truth using Sørensen-Dice coefficient (mean score =  $92.9 \pm 1.5\%$ ). The average time for semi-automatic liver segmentation was 3.8 times faster compared to the manual slice-by-slice delineation. Main deviations between both approaches were observed in the areas of the gall bladder, vena cava inferior and hepatic vascular network. Furthermore, a second analyzed database consists of SPECT/CT and MRI datasets (or CT

in case of contraindication for MRI) from pre-therapeutic imaging in 20 patients scheduled for SIRT. All 20 datasets were segmented manually and by using the semi-automatic algorithm of the analyzed software. The examination of the second database does not show any significant difference between both applied methodologies. Using the present tool, segmentations of the liver can be achieved with high accuracy while speeding up the physician's workflow.

## Keywords

SIRT • Radioembolization • Liver segmentation  
Hepatic tumor burden

## 1 Introduction

Selective internal radiotherapy (SIRT) is an effective and safe treatment in patients with advanced primary and secondary liver malignancies. Under angiographic monitoring, resin or glass microspheres labeled with the beta-emitting radionuclide  $^{90}\text{Y}$  are administrated into the tumor supplying arterial vessels. However, the pre-therapeutic evaluation requires an immense working process [1] of the individual patient including angiographic exploration of hepatic arterial branches, administration of  $^{99\text{m}}\text{Tc}$ -labeled macroaggregate albumin ( $^{99\text{m}}\text{Tc}$ -MAA), and detection of extrahepatic shunts. The latter can be seen in a post-interventional SPECT/CT measuring the  $^{99\text{m}}\text{Tc}$ -MAA distribution. Beyond that, the physician must carefully determine the liver volume and tumor burden. This elaborate and time-consuming process step is usually done in a T1-weighted MRI series performed with liver-specific contrast agent. Otherwise, e.g. in presence of contraindication for MRI, the segmentation must be performed in a contrast-enhanced CT dataset. The determination of liver and tumor volume ( $V_{\text{liver}}$  and  $V_{\text{tumor}}$ , respectively) is essential to calculate the treatment activity

P. Matthies · F. A. Pinto  
SurgicEye GmbH, Munich, Germany

J. Wuestemann (✉)  
Department of Radiology and Nuclear Medicine, University  
Hospital Magdeburg, Magdeburg, Germany  
e-mail: jan.wuestemann@med.ovgu.de

J. C. Neba  
Department of Nuclear Medicine, University Hospital Würzburg,  
Würzburg, Germany

according to the body surface area (BSA) model, where  $A$  is the activity of  $^{90}\text{Y}$  microspheres to be injected:

$$A[\text{GBq}] = \text{BSA} - 0.2 + V_{\text{tumor}} / (V_{\text{liver}} + V_{\text{tumor}}) \quad (1)$$

A promising approach to optimize the current workflow is to shorten the preparation effort. Several solutions for whole liver segmentation in CT and MRI datasets are available [2–5], among them dedicated ones for SIRT planning [3]. In this work, we validated an interactive software tool, which provides a semi-automatic segmentation of the liver and the intrahepatic lesions in anatomical three-dimensional datasets as well as dividing the liver into left and right lobe. Moreover, this dedicated tool promises to cover almost the entire workflow of an individual SIRT preparation. Object of this study is to create first evidence that the present software reproduces results from conventional manual segmentations of the liver and intrahepatic malicious lesions.

## 2 Methods

A physician with experience in manual liver segmentation for SIRT dosimetry used the dedicated software (DosePlan [6], SurgicEye GmbH, Germany, see Fig. 1) on two different databases. The first one comprises ten randomly selected CT datasets out of the 130 public available datasets from the Liver Tumor Segmentation (LiTS) Challenge [7] including the provided ground truth segmentations of the liver, which

were acquired by a board-certified radiologist and verified by another expert. While no timings are provided for these datasets, published timing data based on 35 manual liver segmentations yielded  $32:48 \pm 6:54$  min [8].

The software provides an interactive segmentation based on user-defined initial seeds of the foreground and background regions of several slices in orthogonal views. The segmented region is then computed based on these seeds by employing a graph-based segmentation algorithm. We performed this procedure for contrast-enhanced CT datasets of these ten patients and documented the completion time. Segmentation quality versus the ground truth was evaluated using the Sørensen-Dice coefficient.

Moreover, we used a second database comprising of a cohort of 20 patients (male/female 15/5, age  $69.2 \pm 10.9$  years) with hepatocellular carcinoma (HCC,  $N = 9$ ) or metastatic colorectal cancer (mCRC,  $N = 11$ ) scheduled for SIRT. Except for two patients having contrast-enhanced CT of the abdomen instead of a liver MRI because of contraindications, all other patients underwent complete imaging of T1-weighted liver MRI and post-angiographic SPECT/CT after  $^{99\text{m}}\text{Tc}$ -MAA application. Apart from that, general preconditions for SIRT applied to all individuals. Patient characteristics including liver volume, tumor burden, number of individual lesions, and lung shunt fraction (LSF) have been determined using conventional software (OsiriX, version 5.9, Pixmeo SARL, Switzerland), which is utilized in clinical routine and allows

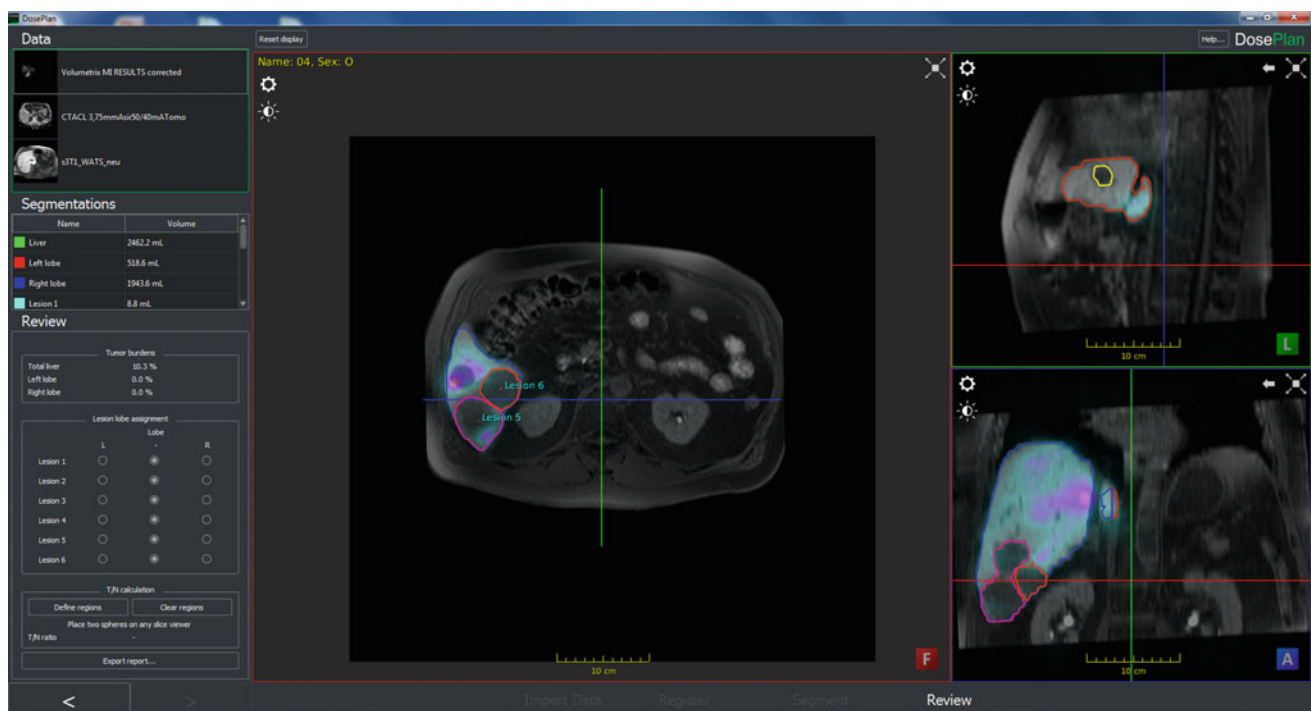


**Fig. 1** User interface for semi-automatic segmentation of (co-registered) MRI and CT abdominal datasets for SIRT planning

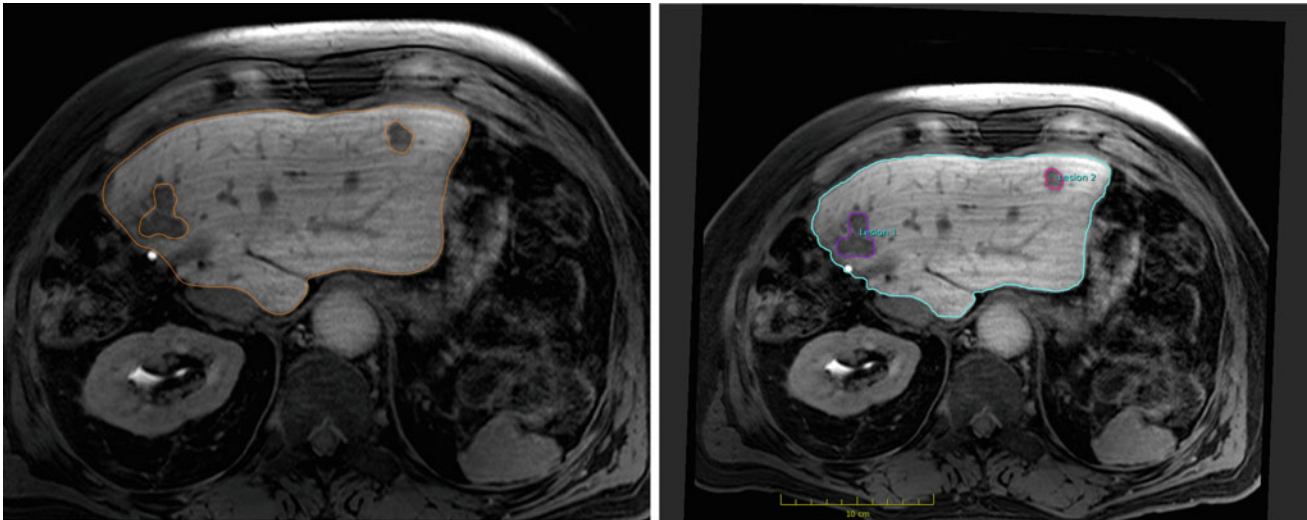


**Fig. 2** Direct comparison of manual (left) and automatic (right) segmentation of liver and two intrahepatic lesions contoured in the same slice

manual segmentation of volumes in three-dimensional scans. Although time for the conventional segmentation method was not explicitly measured, a careful liver segmentation can take over 30 min, a similar time requirement as published in [8].

Utilizing the available software tool, MRI and low-dose CT for anatomical mapping of SPECT are automatically co-registered in a first step. The next step is similar to the one in the first cohort; segmentation of the liver and visible individual malicious lesions (see Fig. 2) was performed. After finishing liver segmentation, the user has the option to divide the liver into left and right lobe by drawing a plane.

In addition, the user can assign each metastasis to a liver lobe before the results are exported as a PDF report. Procedure time was measured for each examination. Differences between the segmentation variables (liver volume, tumor volume, number of metastases, and tumor burden) were assessed by the Wilcoxon signed-rank test. Time differences referring to different cohorts were compared to each other using the Wilcoxon rank sum test. Values were expressed as mean  $\pm$  standard deviation. We assumed statistical significance at  $p < 0.05$ .

### 3 Results

The first examination of ten contrast-enhanced abdominal CT scans (database one) served to verify concordance between semi-automatically and manually contoured liver shape. The corresponding average Sørensen–Dice score for the reader was  $92.9 \pm 1.5\%$ . The average time to segment the entire liver using the interactive algorithm was  $8:45 \pm 1:13$  min, a factor of 3.8 times faster compared to the manual slice-by-slice delineation published in [8].

The analysis of the second available database of 20 SIRT patients yielded no significant difference between

semi-automatic and conventional manual segmentation in all considered quantities (see Fig. 3).

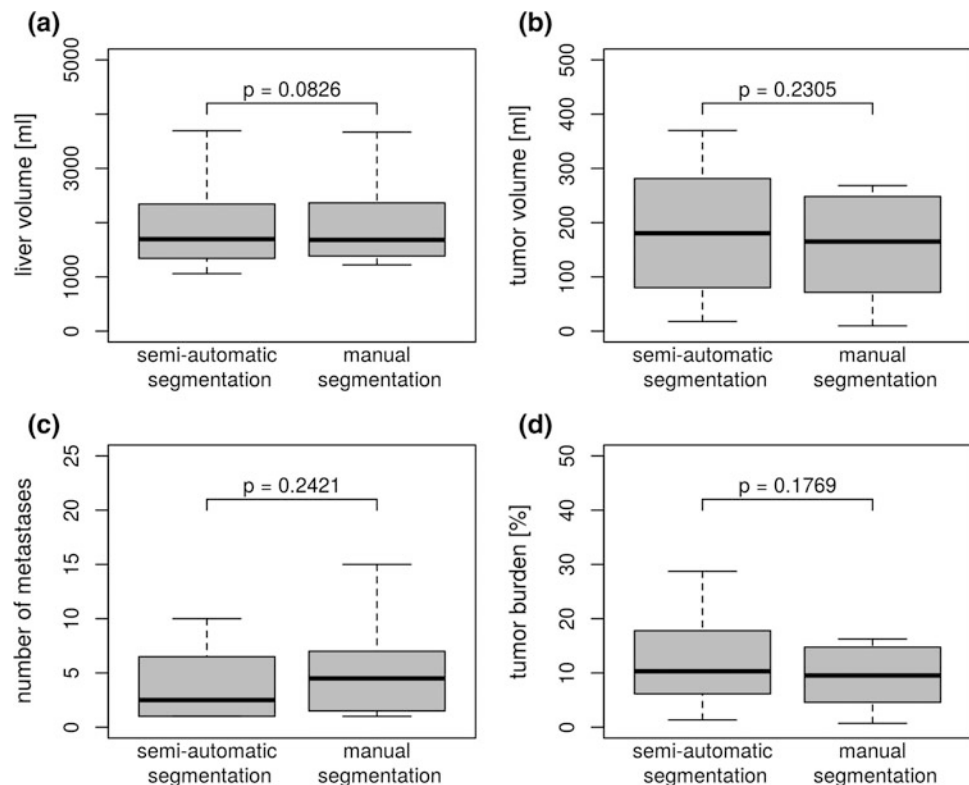
The expenditure of time averaged to  $6:03 \pm 5:12$  min, whereas a closer observation indicated differences depending on the underlying cancer entity. In 9 patients with HCC, the time requirement yielded  $03:54 \pm 1:50$  min; in 11 patients with mCRC the procedure took  $07:48 \pm 6:25$  min. The time dependency on the considered type of cancer was significant ( $p = 0.0248$ ).

### 4 Discussion

We examined a software tool providing a user interface dedicated to cover laborious pre-therapeutic procedures during SIRT planning. We tested the software on two existing databases, analyzing validity compared to conventional methods or given standard of truth. The results were promising and showed no significant differences to previous data. Based on published data and own experience, the time effort was significantly reduced.

While our results statistically reproduce the physicians' findings, we must discuss and hypothesize several points that need clarification with further research. First, small discrepancies in absolute metastatic volume can reflect a more precise determination of what recognizable malignant tissue is and what is not. The main deviations in the segmentations occurred patently in those areas where the liver tissue adjoins the gall bladder, near the lower vena cava, and around the visible hepatic vascular network. Sometimes a manual redefinition of the volume border was necessary to exclude extrahepatic structures. In the utilized version, a missing step is the calculation of the LSF, which is a determinant factor for the activity to be administered. Therefore, a tool suitable for clinical routine must have LSF determination capabilities. Segmentation on liver MRI

**Fig. 3** Comparison of segmentation values of main variables that have been obtained by both DosePlan and OsiriX as boxplots: **a** liver volume, **b** tumor volume, **c** number of metastases, and **d** fractional tumor burden. The depicted p-values refer to the performed Wilcoxon signed-rank test without indicating any significant differences between each examined distribution pairs



datasets was much faster than the same procedure in contrast-enhanced CT scans. The whole preparation workflow that has been already integrated was investigated using the second database where segmentations were predominantly performed on MRI datasets. Because of higher contrast in MRI, the liver contour produced more accurate results on the first run. Corrections of obvious segmentation errors were less frequently necessary.

However, retrospective imaging data with known segmentations of the liver and corresponding intrahepatic lesions were used to test the success of the implemented semi-automatic segmentation algorithm. Hard evidence of benefit in clinical usage can only be obtained in a prospective trial with SIRT patients of different cancer primaries. Furthermore, the inter-reader reliability has still to be proven.

## 5 Conclusion

Using the semi-automatic segmentation algorithm in DosePlan, segmentations of the liver can be achieved with a clinically acceptable accuracy of >92% in under 9 min, greatly speeding up the physician's workflow when compared to manual slice-by-slice segmentation.

**Acknowledgements** The German Federal Ministry of Education and Research funded the work (grant number ZF4276201TS6).

**Conflict of Interest** Philipp Matthies and Francisco Pinto are employees of SurgicEye GmbH and were involved in the development of examined DosePlan tool. All other authors declare no conflict of interest.

## References

1. Lau, W.-Y., Kennedy, A.S., Kim, Y.H., et al.: Patient selection and activity planning guide for selective internal radiotherapy with yttrium-90 resin microspheres. *International Journal of Radiation Oncology• Biology• Physics* 82(1), 401–407 (2012).
2. Masoumi, H., Behrad, A., Pourmina, M.A., et al.: Automatic liver segmentation in MRI images using an iterative watershed algorithm and artificial neural network. *Biomedical Signal Processing and Control* 7(5), 429–437 (2012).
3. Goryawala, M., Gulec, S., Bhatt, R., et al.: A low-interaction automatic 3D Liver segmentation method using computed tomography for selective internal radiation therapy. *BioMed Research International* 2014 (2014).
4. Huang, L., Weng, M., Shuai, H., et al.: Automatic liver segmentation from CT images using single-block linear detection. *BioMed Research International* 2016 (2016).
5. Yang, D., Xu, D., Zhou, S.K., et al.: Automatic liver segmentation using an adversarial image-to-image network. *International Conference on Medical Image Computing and Computer-Assisted Intervention*. Springer, Cham. 507–515 (2017).
6. DosePlan Community, <http://www.dose-plan.com>, last accessed 2018/01/31.
7. LiTS – Liver Tumor Segmentation Challenge, <http://www.lits-challenge.com>, last accessed 2018/01/31.
8. Nakayama, Y., Li, Q., Katsurawaga, S., et al.: Automated hepatic volumetry for living related liver transplantation at multisection CT. *Radiology* 240(3), 743–748 (2006).



# Image Quality Optimization and Soft Tissue Visualization in Cone-Beam CT Imaging

Aude Castonguay-Henri, Dmitri Matenine, Matthieu Schmittbuhl, and Jacques A. de Guise

## Abstract

Cone Beam CT is a well-established diagnostic tool for numerous applications. While providing better spatial resolution and exposing the patient to lower radiation doses than conventional CT, it is also subject to spatially dependent bias due to the beam energy spectrum, resulting in a very limited capacity for soft-tissue and quantitative imaging. The goal of this work is to improve image contrast resolution and density quantification, to reinforce diagnosis efficiency and accuracy. An iterative polyenergetic approach is adapted to CBCT in order to reduce the artifacts caused by the beam hardening phenomenon and monoenergetic approximations at reconstruction level. It integrates the X-ray spectrum of the source and the cone-beam geometry, and is based on the Iterative Maximum-likelihood Algorithm for CT (IMPACT), which defines the energy-dependent attenuation coefficient as a linear combination of photoelectric and Compton effects. Our preliminary results demonstrate reduction of cupping and successful quantitative reconstruction of simple phantoms using simulated and experimental CBCT data.

## Keywords

Cone beam CT • Iterative reconstruction • Spectral reconstruction • Soft tissue imaging

A. Castonguay-Henri (✉) · D. Matenine · M. Schmittbuhl · J. A. de Guise

Laboratoire de Recherche en Imagerie et Orthopédie, Centre de Recherche du Centre Hospitalier de L'Université de Montréal, Montréal, QC, Canada  
e-mail: Aude.castonguay@gmail.com

A. Castonguay-Henri · D. Matenine · J. A. de Guise  
Département de Génie de La Production Automatisée, École de Technologie Supérieure, Montréal, QC, Canada

M. Schmittbuhl  
Faculté de Médecine Dentaire, Université de Montréal, Montréal, QC, Canada

## 1 Introduction

Cone beam computed tomography (CBCT) has recently become a leading technology in medical imaging and is gaining new applications such as ear, nose and throat imaging or osteoarticular exploration of extremities. It has proven its value in comparison with multidetector CT (MDCT) by offering radiologists high-resolution images of bony structures, while using less ionizing radiation for the patient. However, even with a better resolution than the MDCT, CBCT of dental and bony structures is subject to various artifacts arising from beam hardening, with many of the structures being composed of compact bone, and also due to routine presence of metallic dental restorations. In addition to this, CBCT suffers from artifacts due to scattered radiation, due to its large cone opening. The combination of beam hardening and scattering limits the diagnostic use for soft tissue. Therefore, improving contrast in soft tissue would lead to a low-dose and high-resolution imaging systems for a broader range of diagnostic applications.

Computed tomography imaging estimates a 3D map of *radiodensity* or radiation attenuation coefficients of the subject. The methods currently used for clinical CBCT reconstructions are usually based on filtered backprojection, like the Feldkamp, Davis and Cress (FDK) approach [1]. They have the advantage of requiring low computational resources, but rely on empirical corrections for sources of artifacts. In order to allow for accurate CBCT imaging of soft tissue, the most promising approaches are model-based iterative reconstruction algorithms [2]. Such iterative methods have the advantage over analytical ones to allow for the incorporation of prior information on the system and the imaged object. The prior information we aim to use is the emission spectrum of the source, while the attenuation model is largely based on Alvarez-Macovski decomposition [3], in order to reduce the spectral artifacts typically encountered with analytical reconstruction methods. Moreover, a quantitative imaging algorithm is desirable, so that a



low bias in radiodensity estimation is ensured in the whole 3D volume. Therefore, it may become possible to visualize and eventually segment soft tissues based on their linear attenuation coefficient, and to evaluate the feasibility of accurate quantitative cone-beam imaging. The approach adapted to CBCT in this paper is the Iterative Maximum-likelihood Polychromatic Algorithm for CT (IMPACT) by De Man et al. [4]. It is to note that the goal of this paper is not to attain the high spatial resolution typically expected from CBCT systems nor to propose a fast numerical implementation, but mostly to propose a proof of concept of enhanced soft tissue imaging in CBCT.

## 2 Materials and Methods

### 2.1 Attenuation Physics

In the IMPACT algorithm selected for image reconstruction, the attenuation coefficient of each voxel is estimated iteratively by interpreting the intensity measured by the detector and comparing it with the expected intensity given the tissues and materials encountered by the photons. It therefore needs a model of attenuation adapted to the radiation source, the detector and the expected attenuating behaviour of different tissues. The selected direct model is the polychromatic Beer-Lambert attenuation law discretized over space and photon energy spectrum:

$$\hat{y}_i = \sum_k I_k E_k S_k \exp\left(-\sum_j x_{ij} \mu_j(E_k)\right), \quad (1)$$

where  $\hat{y}_i$  is the expected intensity at detector bin  $i$ ,  $I_k$  is the normalized intensity emitted at energy  $k$ ,  $E_k$  is the energy in keV,  $S_k$  is the detector's sensitivity at energy  $k$ ,  $x_i$  is the distance travelled by ray  $i$  inside voxel  $j$  in cm and  $\mu_j(E)$  is the attenuation coefficient of voxel  $j$  in  $\text{cm}^{-1}$ . In this model, the emitted spectrum and the detector sensitivity may be estimated once and used as sets of constants. However,  $\mu_j(E)$  depends on the subject composition, which is heterogeneous.

The definition for  $\mu$  arises from modelization of the physical phenomena encountered by the x photons [2, 4, 5], as we aim to represent the CBCT system and its associated phenomena with enhanced accuracy. Three main interactions take place in kV x-ray imaging: Rayleigh scattering, Compton scattering and photoelectric absorption [6]. The first one can be omitted, as photons are scattered at low angles and do not lose energy in the process, and the interaction cross-section strongly decreases with higher energies. Compton scattering is an interaction where a photon loses energy and changes direction via an inelastic

collision with an electron essentially considered free, and is prevalent in soft tissues. The photoelectric effect is the absorption of photons by ejection of bound electrons of atoms, prevalent in bones and metallic restorations [6]. The energy dependence of the photoelectric cross-section is approximated by  $\Phi(E) = 1/E^3$ , while Compton scattering cross-section is modelled by the Klein-Nishina function  $\Theta(E) = f_{KN}(E)$  [3]. These relationships allow for estimation of relative occurrence rates of both phenomena, where photon energy is the independent variable. A second set of weighting factors is determined by the equivalent atomic number of the tissue or material. This leads to the following definition of  $\mu$ :

$$\mu = \phi \cdot \Phi(E) + \theta \cdot \Theta(E), \quad (2)$$

where  $\phi$  and  $\theta$  are respectively the photoelectric effect and the Compton effect coefficients of the tissue based on a limited number of base materials. Equations (1) and (2) define the attenuation model that will be used for the reconstruction, while geometrical modelling follows Siddon's ray-tracing method, which considers a space of square voxels and infinitely thin linear x-ray attenuation paths [7].

As most iterative methods, an initial image is assumed and then modified after each iteration. We used a uniform image with  $\mu = 0.1$  as initialization. The attenuation coefficient of each voxel in then associated with its Compton and photoelectric components by interpolating on the  $\phi(\mu)$  and  $\theta(\mu)$  curves drawn with the values shown in Table 1, proposed by De Man [4].

Projections of the estimated image are calculated based on Eqs. (1) and (2), and are then used to determine the correction  $\Delta\mu_j^n$  needed for voxel  $j$  at iteration  $n$ . The objective function to maximize is the log-likelihood  $L$ :

$$L = \sum_{i=1}^I (y_i \cdot \ln(\hat{y}_i^n) - \hat{y}_i^n), \quad (3)$$

where  $y_i$  is the measured intensity at detector bin  $i$ . The maximum-likelihood algorithm for transmission tomography (ML-TR) [8] was employed to maximize Eq. (3). We applied a  $3 \times 3$  median filter on the image every 10 iterations to reduce aliasing artifacts.

**Table 1** Attenuation coefficients at 70 keV and associated Compton and photoelectric coefficient for common substances

Substances	$\theta$ (1/cm)	$\phi$ (1/cm)	$\mu$ (1/cm)
Air	0.0002	1.7e-05	0.0002
Soft tissue	0.1777	0.0148	0.1935
Water	0.1783	0.0144	0.1946
Aluminium	0.4274	0.2125	0.6523
Iron	1.3904	5.32734	7.0748

## 2.2 Experiments

Our main hypothesis states that the reduction of beam hardening artifacts will enhance the contrast in CBCT imaging. We therefore tested our algorithm on numerical and physical phantoms in order to observe the impact of polychromatic iterative reconstruction on the cupping artifact. Those images were compared with a monochromatic iterative method, the ordered subsets convex algorithm with total variation regularization (OSC-TV) proposed by Mateine et al. [9], as well as with FDK. The latter was implemented using the OpenRTK library [10] and OSC-TV was implemented in-house using C++. IMPACT was implemented using Matlab<sup>®</sup>. Two types of input sets of projections or *sinograms* were used: simulated and real.

Two different phantoms were reconstructed using experimental projection data. The water phantom was a thin-walled plastic cylinder filled with tap water and a diameter of 8 cm. It was used to observe the algorithm's effect on the cupping artifact. The polytetrafluoroethylene (PTFE) wedge phantom was similar in construction to the water phantom, with a water cylinder of 11 cm in diameter and a quarter-disk PTFE insert held in place by a thin polymethyl methacrylate (PMMA) plate. It was used to analyse the capacity for quantitative imaging of highly attenuating objects. The expected profiles were estimated with data from the *XCOM* database [11].

A simulated sinogram of the wedge phantom was acquired via Siddon's ray-tracing in a voxelized numerical phantom of equal dimensions, using attenuation coefficients for photon energies from 1 to 110 keV with increments of 1 keV, retrieved from the *XCOM* database for the materials of interest. Matlab was used for the numerical implementation. This allowed us to compare reconstructed images based on simulated projections with the physical phantom reconstructions and in turn compare quantification accuracy. It is important to notice that simulated sinograms did not include scatter readings, while real sinograms were affected by scatter. Comparison of reconstructions of simulated and real sinograms permitted to quantify bias due to scattered radiation. Real projections were acquired with the NewTom 5G (Verona, Italy) cone beam CT scanner, see Table 2 for acquisition parameters.

The x-ray source spectrum used for simulated scans was generated at 1 keV increments using the SRS-78 application [12], which uses the scanner tube anode angle, filtration and peak voltage (kVp) as inputs. The same estimated spectrum was used in the IMPACT reconstruction algorithm, with a more coarse discretization over 20 energy bins. The detector sensitivity profile was considered uniform with respect to photon energy for the simulated and real data studies.

**Table 2** Real sinogram CBCT acquisition protocols and corresponding image pixel sizes for reconstructed slices. The slice thickness is equal to the pixel side

Experiment	FOV: diameter (cm) × axial coverage (cm)	Reconstructed pixel size (mm × mm)
Water phantom	8 × 8	1.5 × 1.5
Wedge phantom	15 × 5	0.6 × 0.6

The central slice was reconstructed using FDK, OSC-TV and IMPACT. Still, the cone beam collimation was that of clinical CBCT protocols and scattered radiation contributed to the central slice sinogram. Line profiles of the reconstructed slice were acquired on the central sagittal axis in order to evaluate cupping. For the water phantom, cupping was quantified by computing a polynomial fit on the part of the profile which represents water only, using the model below:

$$\mu(x) = a(x - b)^2 + c, \quad (4)$$

where  $a$  is the coefficient which increases with increasing cupping and  $b, c$  are translation parameters. The bias on  $\mu$  was quantified on a circular region of interest (ROI), centered on a uniform region of the phantom and excluding borders. Mean value and standard deviation of  $\mu$  over the ROI were calculated. The  $\mu$  values were compared for a reference energy of 70 keV, which, in a clinical setting, ensures a good contrast between soft and bony tissues.

## 3 Results

### 3.1 Water Phantom

Figure 1 shows profiles and images for a real water cylinder reconstruction with IMPACT, OSC-TV and FDK. The polynomial fit led to  $a = (1.31 \pm 0.16) \times 10^{-5}$  for IMPACT,  $a = (2.28 \pm 0.10) \times 10^{-5}$  for OSC-TV and  $a = (3.2 \pm 1.0) \times 10^{-5}$  for FDK. This indicates that the monochromatic approaches suffer from more severe cupping than IMPACT.

The mean and standard deviation in the circular ROI inform us on the bias in the image. Higher values of standard deviation indicate that the attenuation coefficients are held within a larger range of values, which includes noise and spatially-dependent bias. Figure 2 shows the analysis of all the water voxels of the water cylinder phantom, excluding borders, for each method. On a relative scale, we observe a  $(2.5 \pm 0.9)\%$   $\mu$  bias for IMPACT,  $(12 \pm 2)\%$  for OSC-TV

**Fig. 1** Reconstruction of the central slice of the real water phantom and  $\mu$  for each voxel along the central line of the image. Some cupping is present in the IMPACT reconstruction, likely due to scattered radiation, but more accurate attenuation coefficients are obtained

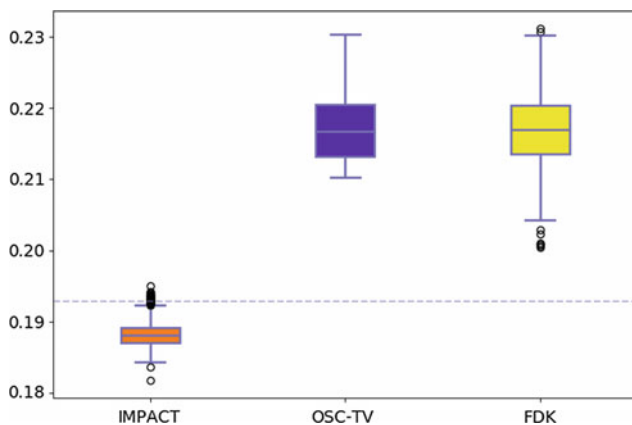
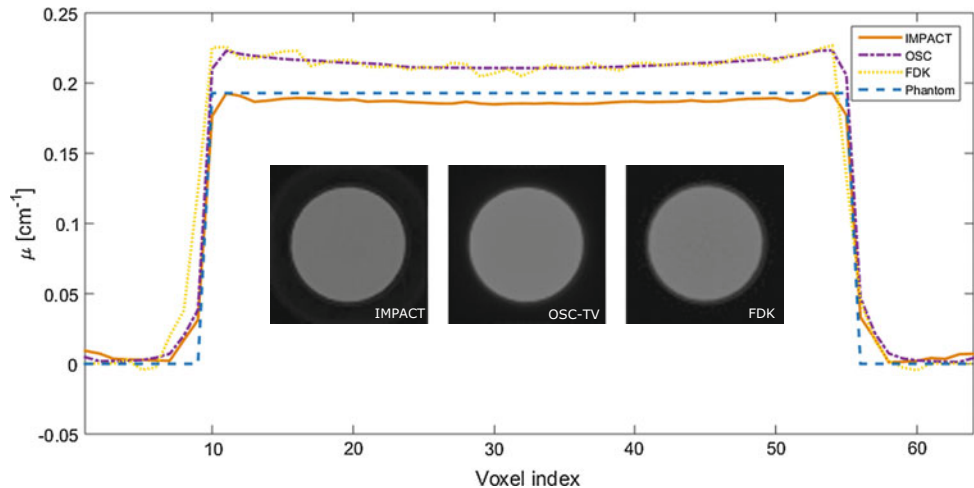


**Fig. 2** Analysis of reconstructed water phantom attenuation coefficient for each method. IMPACT leads to more accurate and more precise values. The dashed line represents the ground truth

and  $(12 \pm 2)\%$  for FDK, when compared to the ground truth. In general, we observe that monochromatic approaches yield a systematically higher  $\mu$  estimate and suffer from severe cupping, while IMPACT yields a more uniform profile closer to the expected value. The remaining cupping for IMPACT is likely due to scattered radiation, which also causes cupping.

### 3.2 Wedge Phantom

Figure 3 shows the reconstructions of the wedge phantom. While OSC-TV and FDK seem to lead to very similar images, IMPACT reconstructions show lower contrast between the water and the PTFE. This is explained by the lower  $\mu$  calculated with IMPACT for PTFE, as shown by the profiles in Fig. 4a, b. The bias values were also calculated in circular regions of interest excluding borders for PTFE.

For the simulated phantom, a  $(0.6 \pm 1.0)\%$   $\mu$  bias was observed for IMPACT,  $(32 \pm 3)\%$  for OSC-TV and

$(32 \pm 3)\%$  for FDK in the wedge region. The lower standard deviation for IMPACT still indicates a reduction in cupping, in addition to the visual aspect of the profiles. Moreover, we observe an important reduction of streak artifacts with IMPACT, compared to FDK.

For the real wedge phantom, the  $\mu$  bias in the wedge region was of  $(11 \pm 1)\%$  for IMPACT,  $(3 \pm 3)\%$  for OSC-TV and  $(3 \pm 4)\%$  for FDK. The reconstructed  $\mu$  are closer to the phantom's values with OSC-TV and FDK for the central region, but cupping is prominent on the edge of the phantom. IMPACT yields a systematic under-estimation of the profile, but a successful cupping correction.

## 4 Discussion and Conclusions

IMPACT shows definitive potential for both quantitative reconstruction and cupping reduction. The latter was reduced in all cases, simulated and real. Discrepancies between reconstruction of simulated and real projections give us indications as to how well the system is modelled. The main difference is that scattered radiation was not considered, but only beam hardening artifacts were. In consequence, IMPACT seems to interpret scatter signal as beam hardening, so the reconstructed profiles are relatively flat, but are somewhat biased. Another source of bias is the detector sensitivity profile. It is currently approximated as a constant for lack of an experimentally obtained sensitivity profile. An additional source of bias is the emission spectrum, which was estimated instead of being measured for the individual x ray tube. Having the individual emission spectrum could lead to a better estimation of polychromatic phenomena, and therefore more accurate values of linear attenuation coefficients. It should be noted that even though the simulations were performed in 2D, experimental projection data were affected by substantial

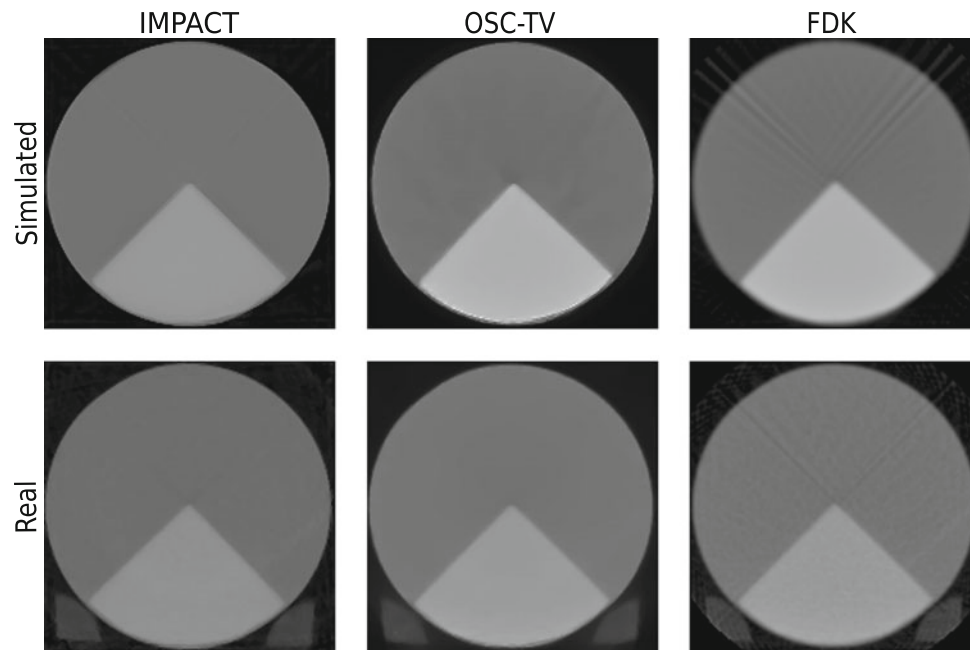


**Fig. 3** Comparison of both simulated and real wedge phantoms, reconstructed using IMPACT, OSC-TV and FDK. Reduced streaking was observed for IMPACT

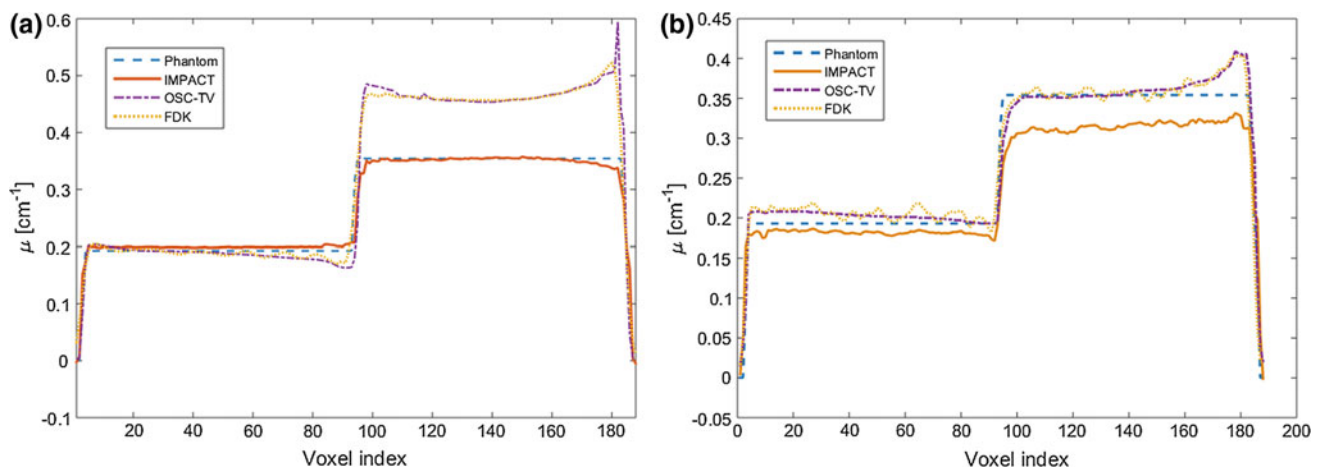


**Fig. 4** Profiles of the reconstructed wedge phantoms. An important difference regarding cupping between the monochromatic and polychromatic methods was observed with both **a** simulated and **b** experimental sinograms

scatter and the final results are representative of accuracy attainable by IMPACT in CBCT.

The next step will be to evaluate the behaviour of IMPACT with respect to more complex objects, including anatomical phantoms, and implement a practical scatter correction. In order to handle larger amounts of data, a parallel implementation of IMPACT is envisioned.

**Acknowledgements** This work was partly financially supported by Mitacs through the Mitacs Accelerate program and by Canada Research Chairs. The authors would like to thank Useful Progress Service Inc. (Montreal, QC) and its founder Francis Siguenza for financially supporting the Mitacs Program.

**Conflicts of Interest** Dmitri Matenine is an employee of Useful Progress Services Inc. (Montreal, QC). Other authors declare that they have no conflict of interest.

## References

1. Feldkamp, L.A., Davis, L.C., Kress, J.W. (1984). Practical cone-beam algorithm. *J. Opt. Soc. Am. A*, 1(6). doi:<https://doi.org/10.1364/josaa.1.000612>.
2. Nuyts, J., De Man, B., Fessler, J.A., Zbijewski, W., Beekman, F. J. (2013). Modelling the physics in the iterative reconstruction for transmission computed tomography. *Physics in Medicine and Biology*, 58(12). doi:<https://doi.org/10.1088/0031-9155/58/12/r63>.
3. Alvarez, R.E., Macovski, A. (1976). Energy-selective reconstructions in X-ray computerized tomography. *Physics in Medicine and Biology*, 21(5). doi:<https://doi.org/10.1088/0031-9155/21/5/002>.
4. De Man, B. et al. (2001). An Iterative Maximum-Likelihood Polychromatic Algorithm for CT. *IEEE Transactions on Medical Imaging*, 20(10), 999-1008. doi:<https://doi.org/10.1109/42.959297>.
5. Beister, M., Kolditz, D., Kalender, W.A. (2012). Iterative reconstruction methods in X-ray CT. *Physica Medica*, 28(2). doi:<https://doi.org/10.1016/j.ejmp.2012.01.003>.
6. Bushberg, J.T., Seibert, J.A., Leidholdt, E.M., Boone, J.M. (2012). *The Essential Physics of Medical Imaging*, 3rd edition. Lippincott Williams & Wilkins, Philadelphia, USA. isbn: 978-0-7817-8057-5.
7. Siddon, R. (1985). Fast calculation of the exact radiological path for 3-D CT. *Medical Physics*, 12(2). doi:<https://doi.org/10.1118/1.595715>
8. J. Nuyts, B. De Man, P. Dupont, M. Defrise, P. Suetens, and L. Mortelmans. (1998). Iterative reconstruction for helical CT: A simulation study. *Phys. Med. Biol.*, vol. 43, pp. 729737.
9. Matenine, D., Mascolo-Fortin, J., Goussard, Y. & Després, P. (2015). Evaluation of the OSCTV iterative reconstruction algorithm for cone-beam optical CT. *Medical Physics*, 42(6376). doi:<https://doi.org/10.1118/1.4931604>.
10. S. Rit, M.V. Oliva, S. Brousmiche, R. Labarbe, D. Sarrut, and G. C. Sharp. (2014). The Reconstruction Toolkit (RTK), an open-source cone-beam CT reconstruction toolkit based on the Insight Toolkit (ITK). *Journal of Physics: Conference Series*, 489 (1).
11. Berger, M.J., Hubbell, J.H., Seltzer, S.M., Chang, J., Coursey, J.S., Sukumar, R., Zucker, D.S., and Olsen, K. (2010), XCOM: Photon Cross Section Database (version 1.5). [Online] Available: <http://physics.nist.gov/xcom> [2018, January 25]. National Institute of Standards and Technology, Gaithersburg, MD.
12. K. Carney, B. J. Gilmore, G. W. A. Fogarty and L. Desponds. (1997). *Catalogue of Diagnostic X-ray Spectra and Other Data: Report No 78*, Institute of Physics and Engineering in Medicine.
13. Hsieh, J. (2009). *Computed Tomography: Principles, Design, Artifacts, and Recent Advances* (2e dition). SPIE Press.



# A Method to Detect Potentially Malignant Skin Lesions Through Image Segmentation

Carlos A. Wilches, Óscar J. Perdomo, and César A. Perdomo

## Abstract

Melanoma is a form of skin cancer responsible for most cancer deaths. The detection of melanoma in an early stage is still a challenge with high importance. The aim of this paper was the design of a system to analyse the mole's characteristics, based on the ABCDE criteria, for identifying potentially malignant skin lesions. The segmentation was based on Otsu thresholding, chain code and skeletonization methods were used to compute the main features: asymmetry, border, color and texture, for a future classification of skin lesions as normal or potentially malignant melanoma. The system was evaluated successfully using 92 images with 27 benign and 65 malignant melanomas from Dermatology Information System (DermIS).

## Keywords

Asymmetry • Border • Color • Melanoma Segmentation • Vector of features

## 1 Introduction

The skin is the largest organ in mammals with the important function of protecting the body from multiple environmental factors. One of the factors that generates health problems in the skin is ultraviolet radiation exposure, mainly UVA and UVB, from sunlight and artificial sources. The skin has cells called *melanocytes* that produce melanin, a pigment that

dissipates 99.9% UV radiation. As a consequence of over-exposure to UV radiation, benign or malignant skin lesions are generated [1].

Melanoma is a type of skin cancer accounts for less than 5% of all types of skin cancer, but it is the most dangerous and responsible for most number of deaths [1]. The detection in an early stage is vital for an accurate diagnosis and effective treatment. Medical personnel is trained to observe and detect possible signs for making a diagnosis, but this task depends of experience and in some subjects produce diagnosis can be subjective. In a study at the University of Illinois with 190 fourth-year medical students, only 29% correctly diagnosed a melanoma [2].

Early signs of a potentially malignant melanoma are based on the ABCDE criteria: **A**symmetry, **B**order, **C**olor, **D**iameter and **E**volution [3]. A characteristic that also identifies a possible malignant lesion is texture, being generally rougher in a potentially malignant than in a benign lesion [4]. For this reason, it has sought to develop systems to support the physician in the early detection of melanoma using image processing and classification [5–11].

The main objective of this work is to segment images of skin lesions and extract their main features, for allowing their identification as benign or potentially malignant. The remainder of this paper is organized as follows: an overview of the methods implemented and data is presented in Sect. 2. The results are reported in Sect. 3. Finally, Sect. 4 draws discussion and conclusions.

## 2 Materials and Methods

The image database was obtained from *DermIS—Dermatology Information System* [12], and pictures of skin lesions minimum size:  $100 \times 100$  pixels were selected. These images have neither a size reference for the diameter of the lesion, nor time evolution required for monitoring subjects. Due to these reasons, the only extracted features were *asymmetry, border, color, and texture*.

C. A. Wilches

Pontificia Universidad Javeriana, Bogotá, Colombia  
e-mail: c.wilches@javeriana.edu.co

Ó.J. Perdomo

Universidad Nacional de Colombia, Bogotá, Colombia  
e-mail: ojperdomoc@unal.edu.co

C. A. Perdomo (✉)

Universidad Distrital Francisco José de Caldas, Bogotá, Colombia  
e-mail: cperdomo@udistrital.edu.co



## 2.1 Region of Interest

The images consisted on two regions: The background is usually clear, and it is related to healthy skin; and the foreground or Region of Interest (RoI) than contains the darker skin lesion. The Otsu thresholding method is applied to the raw images to binarize images and to highlight the RoI from the background. Additionally, several gaps are eliminated on the RoI, and then object with the largest area is cropped for next step, avoiding that small gaps affect the feature extraction. A circular averaging filter is applied in order to remove segmentation noise without losing the shape of the lesion (Fig. 1b).

## 2.2 Asymmetry Criterion from ABCDE Rule for Melanoma Detection

According to ABCDE criteria, the first criterion for identifying potentially malignant skin lesions is the assessment of asymmetry [3]. Furthermore, a benign lesion is defined through a bilateral symmetry, while the malignant lesion is asymmetric with a non-common definite shape as shown in Fig. 2.

Symmetry assessment is performed by dividing the image in half by its axis of symmetry, and counting the number of pixels in common. This method was simple but not robust. Otherwise, if the axis of symmetry of the image is not the vertical axis, the image will be considered asymmetrical and misidentified as potentially malignant.

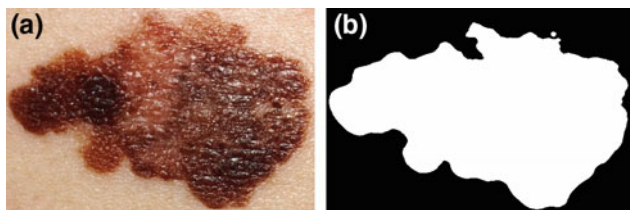


**Fig. 1** a Raw image with melanoma from DermIS database; b Binary mask with RoI detection obtained using the thresholding Otsu method

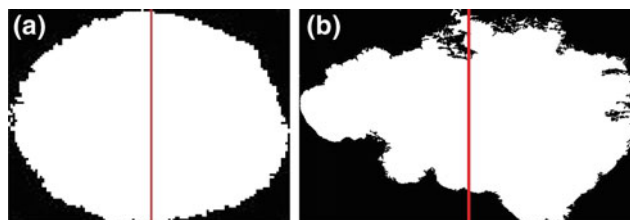


**Fig. 2** a Symmetric lesion from a subject without melanoma; b Asymmetric lesion from a subject with melanoma

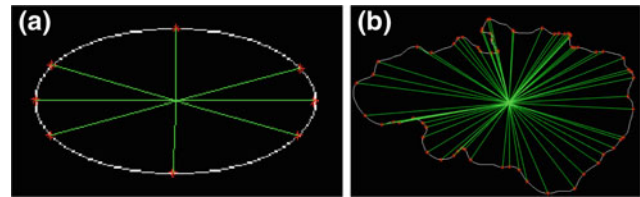


**Fig. 3** a Ellipse shape with four axes and eight intersection points; b asymmetric skin lesion with possible axes and intersection points. red: corners. green: axes

To avoid asymmetrical misidentification, a method to find the axis of symmetry of the object was assessed. Different simple objects, such as squares and ellipses, have axes of symmetry which are mainly in the corners, so this method searches these corners to find all possible axes of symmetry. Then, the object is rotated so that every axis of symmetry is vertical and the quantification method of the symmetry explained above is applied as reported in Fig. 3. The symmetry calculated as the highest symmetry value measured from all possible values found with each axis.

## 2.3 Border Criterion from ABCDE Rule for Melanoma Detection

The second criterion used in ABCDE rule is border smoothness [3]. A benign lesion has a roughly elliptical shape defined with a smooth border. A malignant lesion has an irregular border, with protrusions. Two methods were assessed: chain code and skeletonization.

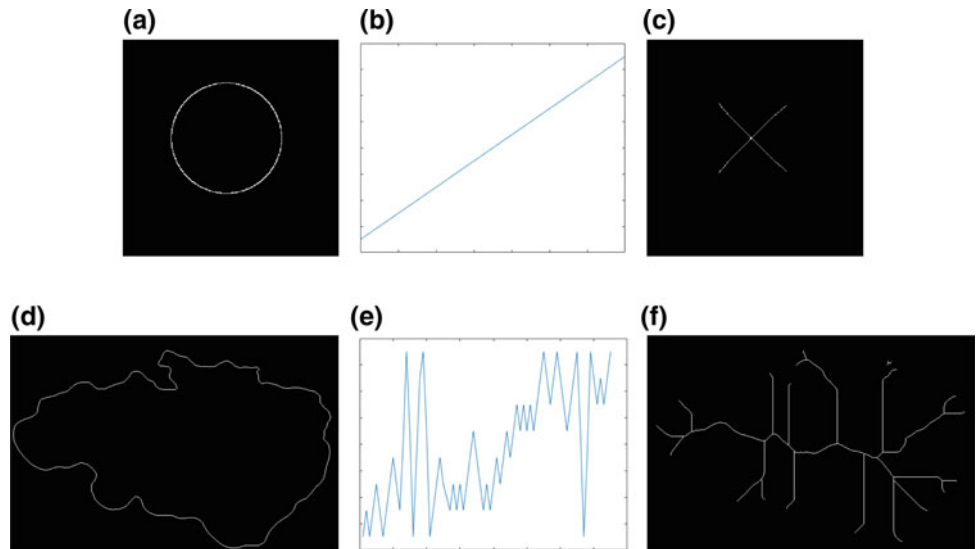
The chain code method consisted on coding the contour of an object through a code representing the way the pixels are connected. The coded contour is processed to eliminate consecutive numbers and to identify abrupt changes. An elliptical contour contains no abrupt changes (Fig. 4b), while an irregular contour contains multiple abrupt changes (Fig. 4e).

The method of skeletonization consisted on obtaining the contour skeleton, a thin representation of the object, preserving the original geometric and topological properties of the object. The number of branches of the skeleton is proportional to the number of irregularities of the contour. The skeleton of a circle, like in lesions with regular borders, has four branches (Fig. 4c), while a lesion with irregular borders has more branches (Fig. 4f).

## 2.4 Colour Variation Criterion from ABCDE Rule for Melanoma Detection

The colour variation is defined as the third criterion to assess in ABCDE criteria [3]. The background is removed and only the grayscale histogram of the skin lesion is obtained to

**Fig. 4** **a** Circle contour; **b** circle contour using Chain code method; **c** circle contour using skeleton method; **d** skin lesion; **e** skin lesion contour using chain code method; **f** skin lesion contour using skeleton method



observe the colour variability. The variance of the histogram is related to the variability of color of the lesion, being a high value when the color of the lesion is variable (Fig. 5).

### 2.5 Texture Parameter for Melanoma Diagnosis

The proposed method assess the texture in the images as a complement of ABCDE criteria for classifying potentially malignant skin lesions [4]. A benign lesion has a smooth texture, while a potentially malignant skin lesion has a rough texture. The method determines the roughness of the skin lesions by extracting the borders of the grayscale image (Fig. 6a, b). The elevations or protrusions on the surface are highlighted by edge detection, using canny operator. Smooth surfaces contains no open edges, so obtaining the extreme

points of the edges is a measure of texture roughness, as shown in Fig. 6.

### 3 Results

The experimental results for border, symmetry, colour and texture assessment in malign and benign lesions are presented in Fig. 7. Benign lesions have symmetry values close to 100%, while malignant lesions have lower percentages of symmetry, as shown in Fig. 7a. The chain code method to assess border irregularity found that lesions with smoother contours have less abrupt changes (1–17), compared to rough contours (5–108). The results from skeletonization method shown that smoother contours have less branches than irregular borders, presented in Fig. 7b. Color variability

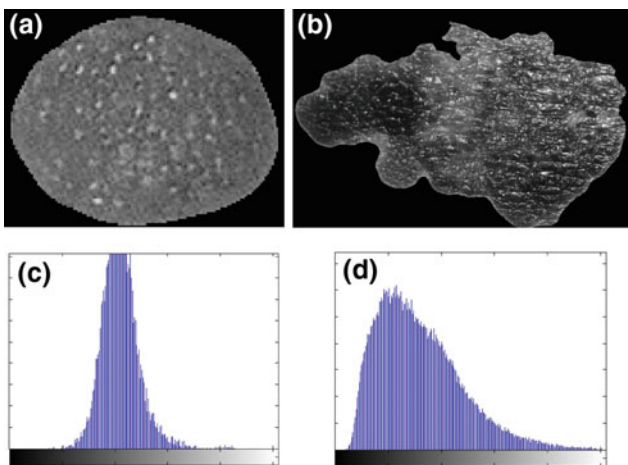


**Fig. 5** **a** Grayscale image with a normal skin mole; **b** Grayscale image with melanoma lesion; **c** grayscale image histogram of normal skin mole; **d** grayscale image histogram of melanoma lesion

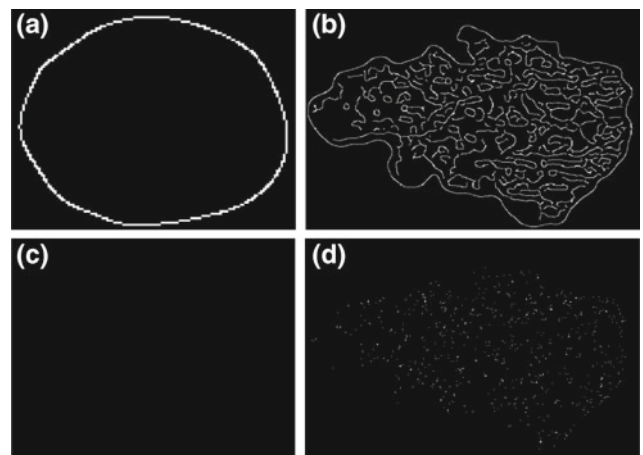
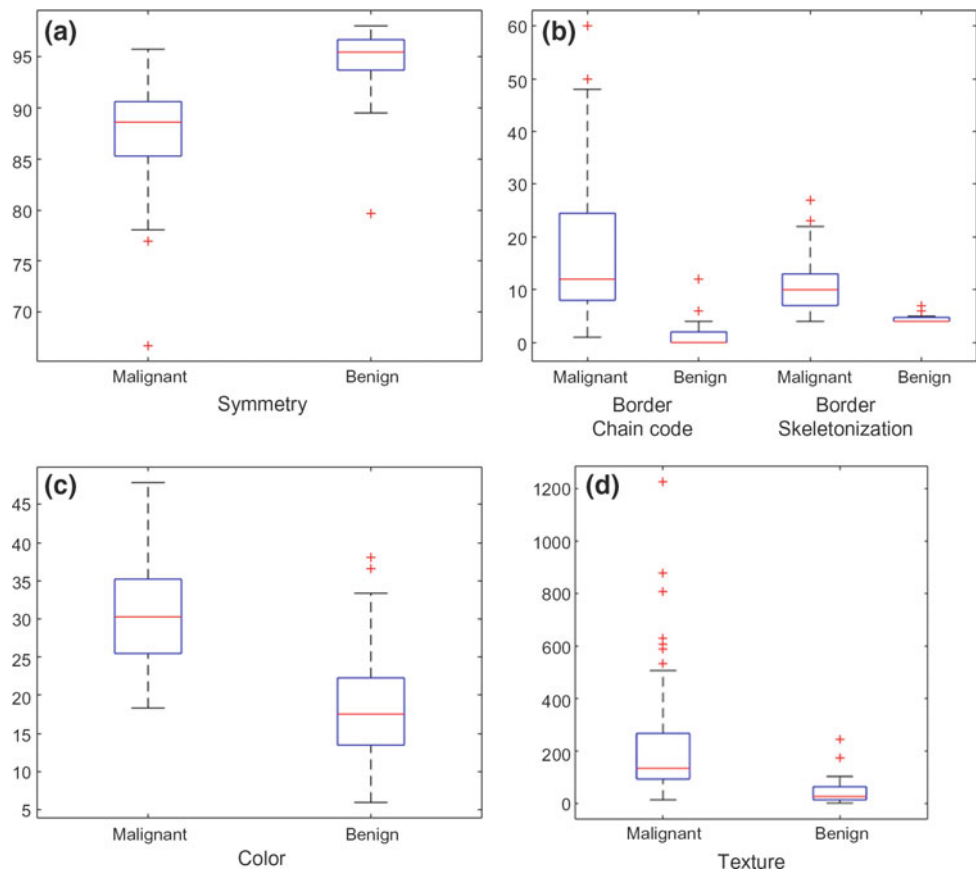


**Fig. 6** **a** Border detection in a normal mole; **b** border detection in a melanoma lesion; **c** texture detection using dots in a normal mole; **d** texture detection using dots in a melanoma lesion

**Fig. 7** Experimental results from DermIS dataset. **a** Symmetry lesion for benign and malignant lesions; **b** Border criteria in malignant and benign lesion using chain code and skeletonization methods; **c** Colour variation in malignant an benign lesions; **d** Texture proposed parameter for malignant and bening lesions



was assessed by calculating the *variance* of the grayscale histogram, which is higher in images with high color variation, corresponding to malignant lesions, as shown in Fig. 7c. The texture was calculated by counting the extreme points of open edge detected. The results shown that rougher textures from malignant lesions presented a higher number of points, compared to benign lesions, as shown in Fig. 7d.

## 4 Discussion and Conclusion

The methods presented in this project to extract relevant features of the images of skin lesions satisfactorily. Thresholding is enough for extracting the region of interest, although can be improved by controlling the brightness during acquisition.

The extraction of features is appropriate to classify skin lesions between benign and potentially malignant. The methods used to extract symmetry, border irregularity using chain code and skeletonization, color variability, and texture roughness, proved to be effective.

While the texture analysis conducted in this project is not a formal analysis of this feature, this method shows clear trends in both groups, which could be used as an indicator of roughness.

**Conflict of Interest** The authors declare that they have no conflict of interest.

## References

1. D'Orazio, J., Jarrett, S., Amaro-Ortiz, A., Scott, T.: UV Radiation and the Skin. *International Journal of Molecular Sciences*. 14(6), pp. 12222–12248, 2013. <https://doi.org/10.3390/ijms140612222>.
2. Lowry F.: Los doctores jóvenes reconocerán el melanoma? 2011. <http://www.publico.es/actualidad/doctores-jovenes-reconoceran-melanoma.html> Accessed: 2015-07-28.
3. American Academy of Dermatology Ad Hoc Task Force for the ABCDEs of Melanoma, Tsao, H., Olazagasti, J.M., Cordero, K. M., Brewer, J.D., Taylor, S.C., Bordeaux, J.S., Chren, M.M., Sober, A.J., Tegel, C., Bhushan, R., Begolka, W.S.: Early detection of melanoma: reviewing the ABCDEs. *J Am Acad Dermatol*. 72(4), pp. 717–723, 2015. <https://doi.org/10.1016/j.jaad.2015.01.025>.
4. Goodson, A.G., Grossman, D.: Strategies for early melanoma detection: approaches to the patient with nevi. *Journal of the American Academy of Dermatology*, 60(5), pp. 719–738, 2009.
5. Shivangi Jain, Vandana jagtap, Nitin Pise, Computer Aided Melanoma Skin Cancer Detection Using Image Processing. *Procedia Computer Science*. 48, pp. 735–740, 2015. <https://doi.org/10.1016/j.procs.2015.04.209>.
6. Roberta B. Oliveira, Mercedes E. Filho, Zhen Ma, João P. Papa, Aledir S. Pereira, João Manuel R.S. Tavares. Computational methods for the image segmentation of pigmented skin lesions: A

- review. *Computer Methods and Programs in Biomedicine*. 131, pp. 127–141, 2016. <https://doi.org/10.1016/j.cmpb.2016.03.032>.
7. Pennisi, A., Bloisi, D., Nardi, D., Giampetruzzi, A., Mondino, C., Facchiano A.: Skin lesion image segmentation using Delaunay Triangulation for melanoma detection. *Computerized Medical Imaging and Graphics*. 52, pp. 89–103, 2016. <https://doi.org/10.1016/j.compmedimag.2016.05.002>.
  8. O. Abuzagheh, B. D. Barkana and M. Faezipour.: SKINcure: A real time image analysis system to aid in the malignant melanoma prevention and early detection. 2014 Southwest Symposium on Image Analysis and Interpretation, San Diego, CA, pp. 85–88, 2014. <https://doi.org/10.1109/ssiai.2014.6806035>.
  9. O. Abuzagheh, B. D. Barkana and M. Faezipour.: Noninvasive Real-Time Automated Skin Lesion Analysis System for Melanoma Early Detection and Prevention. *IEEE Journal of Translational Engineering in Health and Medicine*, 3, pp. 1–12, 2015. <https://doi.org/10.1109/jtehm.2015.2419612>.
  10. S. B. Sathiya, S. S. Kumar and A. Prabin.: A survey on recent computer-aided diagnosis of Melanoma. 2014 International Conference on Control, Instrumentation, Communication and Computational Technologies (ICCICCT), Kanyakumari, pp. 1387–1392, 2014. <https://doi.org/10.1109/iccicct.2014.6993179>.
  11. Z. Ma and J. M. R. S. Tavares.: A Novel Approach to Segment Skin Lesions in Dermoscopic Images Based on a Deformable Model. *IEEE Journal of Biomedical and Health Informatics*, 20, 2, pp. 615–623, 2016. <https://doi.org/10.1109/jbhi.2015.2390032>.
  12. DermIS - Dermatology Information System. Superficial Spreading Melanoma (SSM). 2015. <http://dermis.net/dermisroot/en/17570/diagnose.htm> Accessed: 2015-07-31.

---

**Part III**

**Information Technology in Healthcare**

# A Gait Character Analyzing System for Osteoarthritis Pre-diagnosis Using RGB-D Camera and Supervised Classifier

Xiwen Cui, Zhe Zhao, Cong Ma, Fang Chen, and Hongen Liao

## Abstract

The gait-related disease, such as osteoarthritis (OA) is a crippling disease which is the most prevalent form of arthritis in the elderly with an incidence rate of more than 50%. In today's clinical diagnosing, the physicians always judge and record the gait of a patient qualitatively. Therefore, a cheap, easy-to-use gait analyzing system is important to achieve a quantified description and recording for both newly diagnosed patients and the follow-up patients. This study proposed an accurate gait analysis method by using RGB-D camera and supervised classifier. Firstly, we set up a gait assessment framework for OA patients using the RGB-D camera; design a joint data acquisition software to build a clinical setting. Secondly, the joint data of both patients and healthy controls from the sensor are analyzed to acquire fourteen quantitative gait parameters. Finally, a supervised SVM classifier is trained on the gait parameters of OA patients to help automatically diagnosis the gait anomalies. Experimental results demonstrated that gait parameters between OA patient and healthy controls shows significant different according to unpaired t-test. The average accuracy of the gait classification could reach 97%. Therefore, our study offers a scientific approach for quantitative, non-interactive and low-cost analysis of the gait, which can facilitate the diagnosis and treatment of the gait-related disease.

## Keywords

Gait analysis • RGB-D camera • Osteoarthritis

X. Cui · C. Ma · F. Chen · H. Liao (✉)  
Department of Biomedical Engineering, School of Medicine,  
Tsinghua University, Beijing, 100084, China  
e-mail: liao@tsinghua.edu.cn

X. Cui  
e-mail: cuixw16@mails.tsinghua.edu.cn

Z. Zhao  
Department of Orthopaedics, Beijing Tsinghua Changgung  
Hospital, Beijing, 102218, China

## 1 Introduction

Gait analysis is important for judging the status of a patient with osteoarthritis (OA), which is the most prevalent form of arthritis in the elderly with symptoms of pain, stiffness and decreased range of motion of the joints. However, gait analysis is always simply performed by physicians or therapists through observing a patient's gait and documenting subjective assessments. Motion analysis devices such as high-speed infrared cameras [1], force plates and electromyography (EMG) system [2] are restricted to laboratory settings, for they are expensive and require expert operation, involving an intrusive and cumbersome marker setup procedure. Compared with these methods, depth camera provides the best solution for clinical gait assessment, for it is low-cost, easy-to-use and has eligible tracking speed.

As one kind of the most commonly used depth cameras, Kinect has been clinically validated by a number of researchers [3, 4]. Clark et al. [3] adopted Vicon system as gold standard, which has an acquisition rate of 120 Hz, results show that the acquired gait parameters such as step length, velocity etc. match well on the two systems. Baldewijns et al. [4] took a GAITRite Electronic Walkway as gold standard, and the two systems also show excellent agreement.

Several researchers study the abnormal gait based on Kinect while most are focusing on neuro-degenerative diseases and neurological disorder, such as Parkinson, Hemiplegia [5], which could be classified into neurological gait disorders, without focusing on OA gait measurement. Higa et al. [6] studied the gait pattern of hip OA with Kinect sensor and force plates, however this study lacks certification test on real patients.

In this study, we use a single Kinect setting in the clinic, develop a program to gather data. Gait parameters are calculated to train a machine-learning model which can classify knee OA patient and healthy controls. Experimental results validate the gait character analyzing system using RGB-D



camera and supervised classifier is feasible for clinical knee OA pre-diagnosis and quantitatively recording rehabilitation status.

## 2 Materials and Methods

### 2.1 Gait Data Acquisition and Analysis

The data is acquired from a single Kinect with a laptop connected to it. The depth camera is approximately 1.20 m high, which is slightly changed according to the height of the volunteer, and the depth camera remains horizontal.

Data of 25 joints from a single person is recorded in a time sequence. The sequence is cut into unidirectional sequence, and each sequence becomes a test unit. During the acquisition process, the center and the skeleton size slightly changed, so the normalization procedure is essential.

The noise reduction procedure could delete the unrelated people who happen to be caught in the view zone and also, apply a low-pass filter to the skeleton data to delete the outlier. Then the data is linear interpolated to achieve the same length. The overall procedure is described in Fig. 1, including the data acquisition and analysis procedure and classification procedure.

### 2.2 Gait Features and Classifier

Fourteen gait features are calculated based on a gait cycle. The gait cycle consists of two phase, swing phase and stance phase, the phase could be defined by the periodically changed distance between the two ankles. The stride length is the moving distance of the same side foot during a gait cycle, and step length is the distance between two feet during a gait cycle [7], as seen in Fig. 2.

Dynamic time warping (DTW) is a useful method for comparing the difference between time series, such as knee angle [8]. It defines a cost function and uses a nonlinear transformation to warp the two sequences in order to minimize the cost function: the optimal value of the cost function could be regarded as a “distance measure” between the two series. The DTW is computed for each patient gait cycle with all the healthy gait samples and get a mean value for it. We denoted the healthy group size to be  $N_h$ , for patient  $k$ , the mean DTW distance for knee and hip angle could be defined as:

$$D_k = \frac{1}{N_h} \left( \sum_{j=1}^{N_h} DTW(\theta_k, \varphi_j) \right) \quad (1)$$

Gait features which could reflect the clinical differences between OA patients and healthy people are selected according to the t-test value. The selected features of OA patients and healthy people are input into a classifier of support vector machine (SVM), which can solve the binary classification problem by formulating the learning problem as a quadratic optimization [9].

## 3 Results

### 3.1 Experimental Set up

The experiment is performed in the clinic room of Beijing Tsinghua Changgung Hospital. The gait-capture system consists of a single Microsoft Kinect V2, a tripod and a computer with windows 10 (i7-7700HQ CPU @ 2.80 GHz). The Kinect SDK could extract 25 joints from a person. The sketch and real scene is shown in Fig. 3.

The acquisition software is developed using C++, which could save both color picture and depth picture and

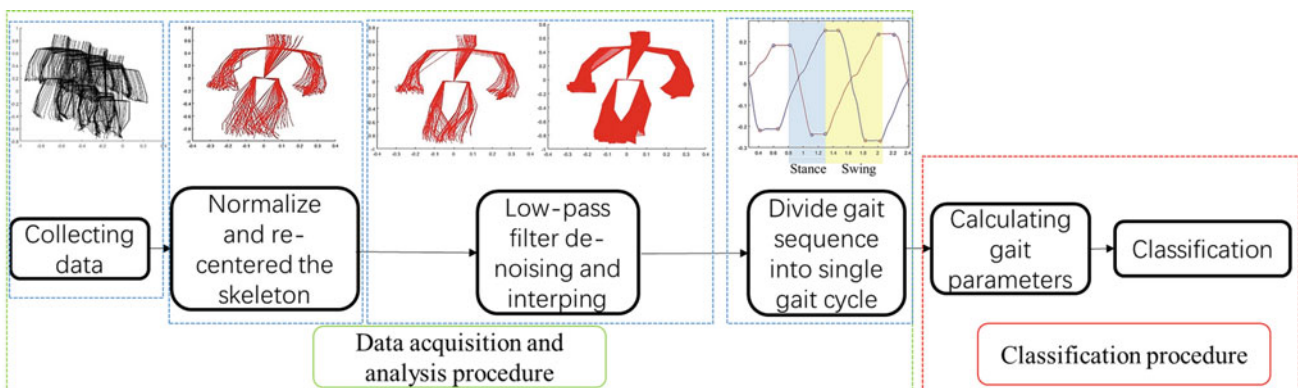
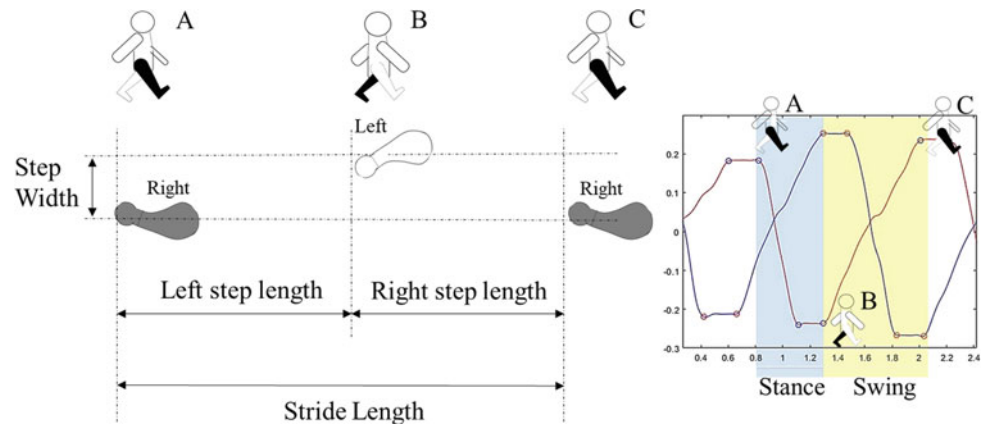
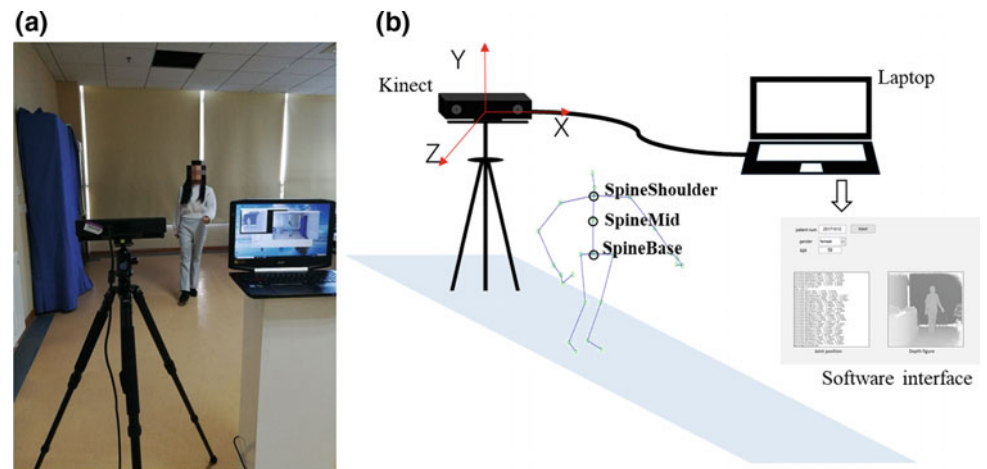


Fig. 1 The flow chart of gait analysis system

**Fig. 2** Definition for step length and stride length



**Fig. 3** **a** The scene photo of the system. **b** The schematic of the system. A Kinect camera is connected to laptop, the definition of coordinate is shown in **(b)**, after inputting the patient’s information to the program, both joints’ position and figures are recorded at the same time



recording the joint information at a framerate of approximately 30 fps. There are 65 walking sequences in experiment group from 19 patients, and 56 walking sequences in control group from 19 healthy volunteers. The detail information for the subjects is presented in Table 1.

According to imaging diagnosis, 7 patients have OA in both knees, 3 are infected in left knee, and 9 in right knee.

### 3.2 Calculating Parameters

Unpaired t-tests are applied for both groups to reveal the statistical differences. All the parameters and their p-value are illustrated in Table 2. The parameters with t-test’s p-value less than 0.05 are chosen to be the characters used in supervised classifier.

**Table 1** The information of subjects in different group

	Number of sequences	Average age	Female/male
Experiment group	65	50.6	10/9
Control group	56	51.0	11/8

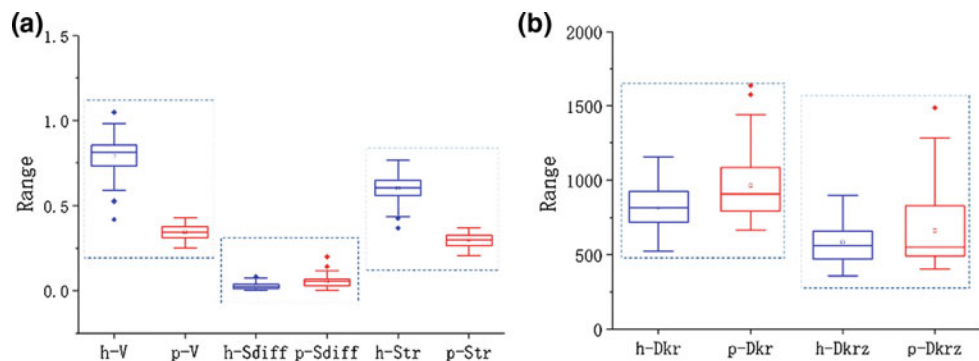
The static parameters such as velocity, stride length have significant difference, which is in accordance with the clinical features of osteoarthritis [10], that OA patients walk slower than normal people and shorter stride length. The DTW value for right knee angle varies from patients to healthy controls, the value for both space angle and abduction-adduction angle could be put into classifier, for most patients in the data set have right knee OA. Box plots for important static and dynamic parameters between healthy volunteers and patients are illustrated in Fig. 4.

### 3.3 Classification for OA Patients

The selected features of OA patients and healthy people are input into a classifier of SVM. The size of training data set is 58/50 (patient/healthy), and test set is 7/6 (patient/healthy). We adopt 10-fold cross validation to test the classification result, and promise each gait sequence to be in test group once. The average accuracy of SVM with different kernel function is shown in Table 3. The best accuracy could achieve 99% for classifying the OA patients out from healthy adults.

**Table 2** Gait parameters and definition

Parameter (unit)	Definition	Parameter abbreviation (patient/healthy)	t-test p-value
velocity ( $s^{-1}$ )	Walking velocity	p-V/h-V	4.07846e-55
Step length (m)	Step length of both side	p-Lsl/h-Lsl (left) p-Rsl/h-Rsl (Right)	0.0039 (left) 0.752 (right)
Stride length (m)	Length of a single stride	p-Str/h-Str	3.19696e-55
Step difference (m)	The difference between left and right step	p-Sdiff/h-Sdiff	1.03609e-06
Step width (m)	Distance between the two ankles in double support phase	p-sw/h-sw	0.0053
Knee angle range (deg)	The range of knee angle in a gait cycle on both side	p-klr/h-klr (Left) p-krr/h-krr (Right)	0.2205 (left) 0.9788 (right)
DTW for knee angle (deg)	DTW distance for knee angle sequence on both side	pD-kl/hD-kl (Left) pD-kr/hD-kr (Right)	0.1052 (left) 9.4845e-5 (right)
DTW for knee angle in yz plane/xy plane (deg)	DTW value for abduction-adduction (x-y plane), extension-flexion angle (y-z plane)	pD-klz/Hd-klz (Left) pD-krz/hD-krz (Right) pD-klx/Hd-klx (Left) pD-krx/hD-krx (Right)	0.2269 (left) 0.0415 (right) 0.9097 (left) 0.1686 (right)

**Fig. 4** **a** Difference in static parameters; **b** Difference for dynamic parameters

## 4 Discussion and Conclusion

We establish a gait analyzing system based on RGB-D camera. Data from patients with knee OA and healthy adults are collected. Gait features are selected for the supervised SVM classifier. The average accuracy of the classification is 97%, and the best accuracy is 99%. Results show that our easy-to-operate gait analyzing system could record the skeleton position at a pretty high speed and thus we could generate gait features which have clinical meanings. The proposed system would be beneficial for the pre-diagnosis of

knee OA patients, and also for the recording of follow-up procedure.

**Acknowledgements** The authors thank the support of Beijing Municipal Science & Technology Commission (Z151100003915079), National Key Technology R&D Program of China (2015BAI01B03), Beijing Municipal Natural Science Foundation (7172122, L172003), National Natural Science Foundation of China (81427803, 81771940) and Soochow-Tsinghua Innovation Project (2016SZ0206).

**Conflict of Interest** The authors declare that they have no conflict of interest.

**Table 3** The average accuracy of SVM classifier with different kernel function

Kernel function	Linear	Gaussian	Polynomial
Accuracy (%)	98	95	99
Average accuracy (%)	97		

## References

1. Sutherland D, The evolution of clinical gait analysis part III—Kinetics and energy assessment. *Gait Posture*, 21(4), 447–461 (2005).
2. Chen S, Lach J, Lo B, et al. Toward Pervasive Gait Analysis with Wearable Sensors: A Systematic Review. *IEEE J Biomed Health Inform*, 20(6), 1521–1537(2016).
3. Clark R A, Bower K J, Mentiplay B F, et al. Concurrent validity of the Microsoft Kinect for assessment of spatiotemporal gait variables. *Journal of Biomechanics*, 46(15), 2722–5(2013).
4. Baldewijns G, Verheyden G, Vanrumste B, et al. Validation of the kinect for gait analysis using the GAITRite walkway Engineering in Medicine and Biology Society. *IEEE*, 5920–5923(2014).
5. Li Q, Wang Y, Sharf A, et al. Classification of gait anomalies from kinect. *Visual Computer*, 1–13(2016).
6. Higa M, Kawabata F, Kobayashi Y, et al. Impact of gait modifications on hip joint loads during level walking. *World Congress on Medical Physics and Biomedical Engineering*, pp. 346–349. Springer International Publishing, Toronto (2015)
7. Levine, David, Richards, Jim, Whittle, Michael W. *Whittle's Gait Analysis*. 5<sup>th</sup> edn Whittle's Gait Analysis. Elsevier LTD, Oxford, (2012).
8. Veeraraghavan A, Roychowdhury A K, Chellappa R. Matching shape sequences in video with applications in human movement analysis. *IEEE Trans Pattern Anal Mach Intell*, 27(12):1896–1909 (2005).
9. Kecman V. *Learning and Soft Computing: Support Vector Machines, Neural Networks, and Fuzzy Logic Models*. MIT Press (2001).
10. Kaufman K R, Hughes C, Morrey B F, et al. Gait characteristics of patients with knee osteoarthritis. *Journal of Biomechanics*, 34 (7):907–915(2001).

# Architecture and Organization of a Computational System for the Management of Data from Individuals with Parkinson's Disease

João Paulo Folador<sup>✉</sup>, Luciene Chagas<sup>✉</sup>, Marcus Fraga Vieira<sup>✉</sup>, and Adriano O. Andrade<sup>✉</sup>

## Abstract

The volume of data for monitoring wellbeing and health of individuals, and the number of devices used to perform tests in patients remotely, have grown substantially. Following this trend, over the past years we have seen an increase in the number of studies reporting the monitoring of the cardinal signs (e.g., tremor, stiffness and bradykinesia) of Parkinson's disease (PD) during prolonged activities for hours or days. A major challenge in the area is to monitor the progress of the disorder objectively so that treatments can be customized. In addition, patients suffer from the lack of predictive information regarding their health condition in the future. In this context, customized systems, i.e., database, that can group information from the motor symptoms of PD are of paramount relevance. By using such systems, one can track the progress of the disorder and more importantly can use data mining for seeking hidden patterns in the data. To contribute for the organization and management of

information obtained from patients with PD this research proposed the architecture and organization of a multi-platform system with customized user control, modules and permissions to manipulate information on each screen. This system has three modules, being the first for storing and organizing information from data collection with distinct types of data; the second for the management of information from the application of the Unified Parkinson's Disease Rating Scale (UPDRS); and the third for promoting technological innovation in the area. These three modules in a single system can be part of the clinical routine of hospitals and research centers dedicated to the understanding, treatment and research in PD.

## Keywords

Parkinson's disease • Computational system  
Biomedical data

---

J. P. Folador · L. Chagas · A. O. Andrade (✉)  
Centre for Innovation and Technology Assessment in Health,  
Postgraduate Program in Electrical and Biomedical Engineering,  
Faculty of Electrical Engineering, Federal University of  
Uberlândia, Uberlândia, Brazil  
e-mail: adriano@ufu.br

J. P. Folador  
e-mail: jpfolador@gmail.com

L. Chagas  
e-mail: lchagasoliveira@gmail.com

M. F. Vieira  
Bioengineering and Biomechanics Laboratory, Federal University  
of Goiás, Goiânia, Brazil  
e-mail: marcus@ufg.br

## 1 Introduction

Parkinson's disease (PD) is a progressive disease of the central nervous system that affects the individual's movement. Despite scientific advances, the disease remains incurable, but should be treated by controlling the symptoms as well as slowing its progress [5]. In this context, the cure of PD remains one of the greatest challenges, in which multimodal information collected from individuals and its understanding play a fundamental role in the diagnosis and monitoring of the progress of the disorder [10].

The amount of information in the world is growing very fast. In 2020, the projection to this scenario is 7.6 billion of people against 50 billion of devices, an average of 6.58 devices per person [2]. Healthcare data are part of this context, representing, in 2013, the amount of 153 Exabytes against a projection of 2,314 Exabytes in 2020 [4]. It means the data in health care is growing 48% per year [2].

The use of computational systems, such as Electronic Health Record (EHR) are increasing the volume of data in healthcare. EHRs can provide different ways to obtain information from patients. These systems allow the user to include or get data from radiology, medicines, patient documentation and others [11].

Following this trend, we have seen an increase in the number of studies reporting the monitoring of the cardinal signs (tremor, stiffness and bradykinesia) of PD for hours or days [3, 10]. A major challenge is to objectively monitor the progress of the disorder to customize treatments. In addition, patients suffer from the lack of predictive information regarding their health condition in the future. Thus, customized systems that can group information from motor symptoms of PD are of paramount relevance.

PD does not have good biomarkers that can confirm its diagnosis. Thus, the expertise of a clinical specialist in PD is necessary to do the assessments. Over the years, different approaches have been proposed to aid diagnosing PD, by means of analyzing information from the brain, tremor, speech, gait, handwriting and others. This generates a lot of information with different structures that must be secured for future analysis [3].

Based on the studies of the Centre for Innovation and Technology Assessment in Health (NIATS) (Uberlândia, Brazil), focused on multimodal data collection from PD patients (e.g., Electrocardiogram—ECG, Electroencephalogram—EEG, Electromyography—EMG, Inertial Sensors and Images), it became necessary to organize all these data in a structured way, to be easily managed and shared among researchers.

Data organization allows for the management of data input and growth, prevention of data loss (the process of data acquisition from individuals with PD is expensive), understanding the progress of the disorder, and for data mining to seek hidden patterns. There is a lack of specific system architectures for PD management, integrating health management systems and data organization of different types of exams (such as subjective rating scales, EEG, ECG and EMG) performed in individuals with PD [1, 9, 10].

EHR and pervasive healthcare systems provide an effective solution for monitoring the wellbeing of patient recovery and monitoring the progression of neurodegenerative diseases, such as PD. For this challenge, in this research it is proposed an architecture of an EHR system for the management and organization of data from individuals with PD. A proof of concept application, so-called SIDABI (Integrated Biomedical Data System), was developed. It is a multiplatform-based software and it has been built to include different software modules in a common place. The main features of SIDABI and the modules that have been implemented so far are discussed in the next sections.

## 2 Materials and Methods

### 2.1 Model-View-Controller Architecture and Development Environment

To standardize and modularize the implementation of SIDABI the Model-View-Controller (MVC) pattern, which proposes software implementation based in layers, was employed. This approach make access to reliable database while providing a clean, organized, reusable, scalable and efficient code. MVC is the most acceptable and used pattern in different languages to develop customized web applications [6].

The MVC adopted in this project is illustrated in Fig. 1. It considers the interaction of system user and the response of the system to the user. The View component shows the layout of the application in HTML (the language used to build pages on the web), the Cascading Style Sheets (CSS), which is the mechanism to give style on the pages, and JS, which is the program language used on client-side to make possible the interaction between the user and the system [6].

When the user interacts with the system, e.g. click on a save button, the request made is passed through JS that sends it to a controller. The controller uses Hypertext Preprocessor (PHP) to code the server-side system. The View controller assembles the results brought by the model controller or a simple page requested and shows it in the browser. The Model controller interacts with the Model component and brings information from the database and apply the rules. The Model have a Class that manages the application data and allows database connections [6, 7].

Rapid Application Development (RAD) was adopted in the process of development. This methodology is incremental, emphasizing fast and reusable coding for the development of application modules [8].

The hardware used to test the software was a computer with Windows 7 Pro 64 bits, Processor Intel Core i5-2500 k (3.30 GHz, 1 CPU, 4 cores), 32 GB RAM DDR3 memory,

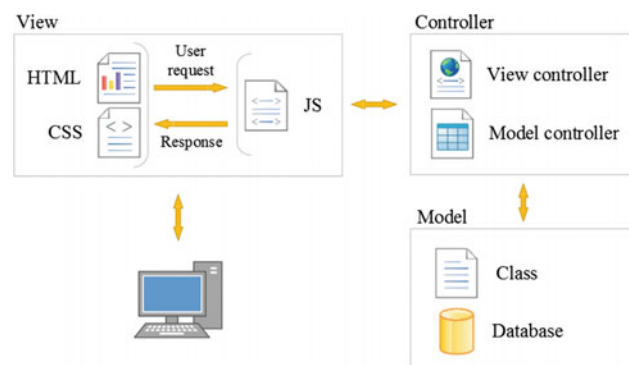


**Fig. 1** The MVC pattern applied to the development of SIDABI



Hard Drive with 3.5 Terabytes, video card NVIDIA GeForce GT 630 and network card Intel 82579 V 7 Giga-bit. On this server it was installed the Apache HTTP web server 2.4, PHP program language 5.6.31 and the database PostgreSQL 9.5.2.

The web application was built by using libraries and plugins that provide faster development and facilitate the software use in different devices. The concept of Responsive Web Design (RWD) [12] was employed for designing views with optimum experience, good ergonomics and usability while navigating through the pages.

For software development it was employed jQuery 3.1, which is a library of functions made in JavaScript (JS) language that interacts with Hypertext Markup Language (HTML) in the web browser; Bootstrap 3.3.7, which is a framework front-end component to build responsive pages and cross-browser applications; AjaxFileUpload, which is a class to help the management of uploading files. All libraries used are Open Source. The pgAdmin III was used to manage and build the database, and the Netbeans program was used to codify the project.

### 3 Results

Figure 2 depicts the web application diagram, which represents the architecture of the implemented software. The user accesses SIDABI by an authentication with a user name and password. The user is registered with personal information (name, password, e-mail and user profile) to get access to the system. The password is informed by the user and a Message-Digest algorithm 5 (MD5) is applied to securely store it. After the user gets access to the system, he can visualize all the modules that he has permission to access. Currently, SIDABI has three modules named: BIODATA, INOVA and UPDRS, which are briefly described in Table 1.

The tables of each module are created in the same database but separated by schemas (logical groups that makes the database more manageable). All the common tables in

different modules are stored in the same schema named public.

The BIODATA module has a report screen to show all the file collection inserted by the user and it is possible to download the selected files in a compact way. Similarly, the UPDRS module permits the user to export data from the assessments to be used in another program.

### 4 Discussion and Conclusion

With an increasing amount of data in the health area over the last years, there is a lack of integrated technologies emphasizing the possibilities of research [2–4]. To meet the identified needs, it was proposed an architecture for data management with the integration of software modules for organizing, seeking and finding information from people with PD, comprising two specific modules for managing data collected from individuals with PD: UPDRS and BIODATA.

To be easily accessed on the internet from a personal computer, tablet or smartphone the proposed platform, SIDABI, is a web-based and responsive application, whose information flow is presented in Fig. 2.

The module BIODATA contains all data collected from different equipment and experimental protocols. In the future, all data will be assessed through additional modules integrated in the platform, to seek patterns for grouping and classification. This will be a valuable tool for the diagnosis and management of PD.

Furthermore, SIDABI will integrate new modules capable of monitoring and implementing data acquisition from wearable sensors, as shown in [1, 9, 10], using the integration capability proposed in this paper. This integration facilitates different applications to share information, reuse of data, increase the efficiency for managing the information of patients, enabling the automation of processes to find hidden information for objective PD diagnosis and follow-up.

**Fig. 2** Web application diagram of SIDABI

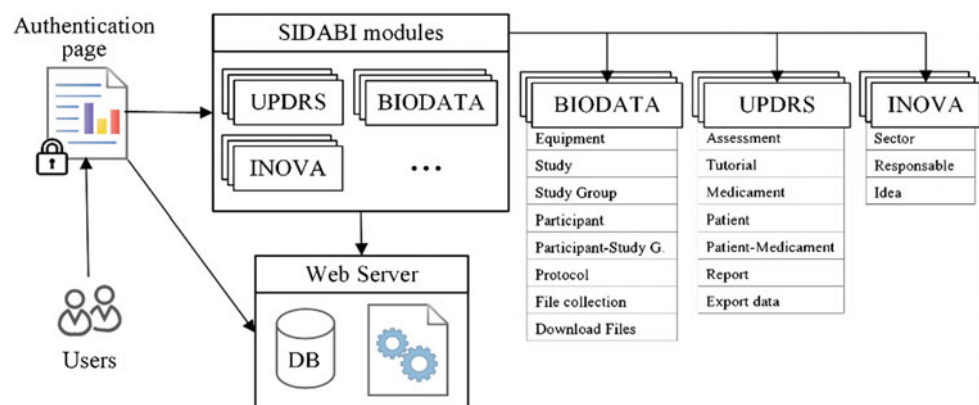


**Table 1** Description of the modules of SIDABI

Module	Description
SIDABI Setup	This module allows the system administrator register new users, control permissions to create and access modules, screens and user actions
BIODATA	Through this module the user can upload and manage files resulting from data collections (e.g., ECG, EEG, EMG). It allows for the recording of information such as type of equipment, description of the study, group of study and its participants, assignment of participants to a group and experimental protocols
UPDRS	This module allows the management of UPDRS (Unified Parkinson's Disease Rating Scale) assessments, patients and medicines. The user can learn how to apply the UPDRS in individuals with PD by a video prepared by a specialist and available in the tutorial area
INOVA	This application is used to promote technological innovation in the area. The user register ideas or problems faced by individuals with PD. These ideas/problems are analyzed and considered in research proposals and technological development

**Acknowledgements** The present work has the support of National Council for Scientific and Technological Development (CNPq), Coordination of Improvement of Higher Level Personnel (CAPES), and Foundation for Research Support of the State of Minas Gerais (FAPEMIG—Project TEC—APQ-00942-17). A. O. Andrade is a Fellow of CNPq, Brazil (305223/2014-3).

**Conflicts of Interest** The authors declare no conflict of interest.

## References

1. ElHelw, M. et al.: An integrated multi-sensing framework for pervasive healthcare monitoring. In: Proceedings of the 3d International ICST Conference on Pervasive Computing Technologies for Healthcare. ICST (2009).
2. EMC, C., IDC: Vertical Industry Brief: Digital Universe Driving Data Growth in Healthcare. 16 (2015).
3. Espay, A.J. et al.: Technology in Parkinson's disease: Challenges and opportunities. *Mov. Disord.* April, (2016).
4. Evans, D.: The Internet of Things - How the Next Evolution of the Internet is Changing Everything. CISCO white Pap. April, 1–11 (2011).
5. Fabbrini, G. et al.: Levodopa-induced dyskinesias. *Mov. Disord.* 22, 10, 1379–1389 (2007).
6. Jailia, M. et al.: Behavior of MVC (Model View Controller) based Web Application developed in PHP and .NET framework. In: 2016 International Conference on ICT in Business Industry & Government (ICTBIG). pp. 1–5 IEEE (2016).
7. Komara, H. et al.: Dynamic generic web pattern for multi platform. In: 2016 International Conference on Data and Software Engineering (ICoDSE). pp. 1–5 IEEE (2016).
8. Mihai Liviu DESPA: Comparative study on software development methodologies. *Database Syst. J.* 5, 3, 37–56 (2014).
9. Pepa, L. et al.: An architecture to manage motor disorders in Parkinson's disease. In: 2015 IEEE 2nd World Forum on Internet of Things (WF-IoT). pp. 615–620 IEEE (2015).
10. Ramji, V. et al.: Parkinson's disease medication state management using data fusion of wearable sensors. In: 2017 IEEE EMBS International Conference on Biomedical & Health Informatics (BHI). pp. 193–196 IEEE (2017).
11. Sarkar, I.N.: Biomedical informatics and translational medicine. *J. Transl. Med.* 8, 1, 22 (2010).
12. Technology, I., Burka, B.A.: Responsive Web Development. 2, X, 272–277 (2015).

# Developing an Automated Clinical Trending Tool for the Neonatal Intensive Care Unit (NICU)

M. Frize, A. Esty, J. Gilchrist, J. Harrold, and E. Bariciak

## Abstract

The purpose of this work was to develop a clinical trending tool which tracks patient vital signs and generates alerts for deviations from a defined baseline. This work analyzes four types of patients: a stable patient, a patient who left the Neonatal Intensive Care Unit for an extended period, and two patients who experienced a clinical deterioration. By displaying visual tools which are more intuitive and user friendly for physicians and alerting for short term vital sign deviations of these different patients, we aim to identify trends which may precede clinical deterioration in patients.

## Keywords

Trending physiological parameters • Heart rate  
Oxygen saturation • Warnings and alerts • Visualization tools

## 1 Introduction

The primary objective of this work was to develop algorithms to display heart rate (HR) and oxygen saturation (SpO<sub>2</sub>) data in a useful manner for clinicians; additionally, the tool should issue alerts for major changes according to ranges set by our physician partners. Current ICU monitors can display physiologic parameters such as: heart rate, blood pressure, oxygen saturation, and respiratory rate. But nurses

and physicians have to integrate several rapidly changing physiologic parameters with clinical signs to understand a patient's current condition. In the case of an unexpected and potentially life-threatening deterioration, the clinician needs to interpret the changes in patient data to intervene quickly. By providing the clinical team with vital sign trending information and alerts for pre-defined deviations, in an efficient and easy to interpret manner, a reduction in the time needed to detect changes in clinical status may be achieved. Currently, monitors are not designed as cognitive aids for the rapid detection of changes in patient status [1].

De Giorgia et al. state: "Most devices have data output ports for data acquisition but there is no universally adopted standard that facilitates multimodal data acquisition and synchronization in a clinical setting; each device often has a unique communication protocol for data transfer and often the time base for each device is independently set rather than determined from a standard source. Commercial products do not support high-resolution physiologic data acquisition, archiving, or annotation with bedside observations for clinical applications. Such systems have been developed in academic settings, mainly for clinical research" [2]. Because they are not open source, most of these systems are not readily accessible.

In 2009, our research group developed a Clinical Data Repository (CDR) which allows for the real time collection of data from infants admitted to the 20 bed Neonatal Intensive Care Unit (NICU) at the Children's Hospital of Eastern Ontario (CHEO). The CDR stores data in a manner which is secure and easily retrievable. It uses open-source tools and collects data from the cardiac monitor, ventilator, pulse oximeter, test results from the laboratory, admissions and discharge information, and discharge diagnoses. The CDR integrates patient data into a single location, facilitating the implementation of clinical decision support tools. Our design allows for the use of multiple data types in a single table. By using NULL values in the columns that are not used less space is wasted as a NULL value requires little

M. Frize (✉) · A. Esty · J. Gilchrist · E. Bariciak  
Systems and Computer Engineering Department, Carleton  
University, Ottawa, Canada  
e-mail: mfrize@gmail.com

M. Frize  
School of Electrical Engineering and Computer Science,  
University of Ottawa, Ottawa, Canada

J. Harrold · E. Bariciak  
Division of Neonatology, Children's Hospital of Eastern Ontario,  
Ottawa, Canada

memory. Our design includes time. Since 2010, tens of millions of data points have been collected [3, 4].

## 2 Methodology

### 2.1 Displaying the Heart Rate Data

Four widely different cases of patients admitted to the NICU were used to develop the trending tool: (i) a patient who deteriorated after undergoing surgery; (ii) a patient who deteriorated due to a complex infection; (iii) a patient who had surgery; (iv) a clinically stable patient. The purpose of looking at these different cases was to examine which of our analytic approaches performed optimally and would best meet physicians' needs. These four cases were representative of various patient scenarios seen in the usual population in the NICU. Different case types were chosen to explore how their HR data differed. Predictions are only useful if there is some way to detect abnormalities that are beyond background variation. The data of a stable patient can be used to determine the level of normal background variation. Two sick patients were selected to assess their degree of variability compared to that of a stable patient. Another question investigated was: could data trends be found in the hours before the patient became obviously clinically unwell, providing an early warning (alert) to physicians and nurses about the patient's deterioration?

The data were divided into 24-h periods (1440 min) and a baseline HR was obtained by averaging the data over the full 24-h for a given day. Trends and alerts were tracked by comparing 4-h trendlines, which were obtained by averaging the HR data over a 4-h period, to a 24-h baseline which occurred 2 calendar days prior. Two calendar days was chosen to ensure that a stable baseline is used for comparison and gradual changes of HR that are part of clinical deterioration do not affect the baseline and mask the trend. This guarantees a stable background as the physician knows that the patient did not clinically deteriorate in the interval.

For instance, if physicians were looking at patient data on Wednesday, they would see a 24-h baseline from Monday overlaid against Wednesday's HR data (see Fig. 1). Six trendlines representing 4-h of averaged HR data can be displayed daily. An alert is triggered when there is a 10% increase in HR data for a given trendline when compared to the 24-h baseline which was derived from 2 calendar days prior.

Variable length windows were explored in order to determine the window that best eliminates background fluctuations due to nursing or parent care (diaper changes, feeding, x-rays) and patient movement and different sleep states. The time of clinically noted deterioration was known for the patients having surgery or developing infection. The

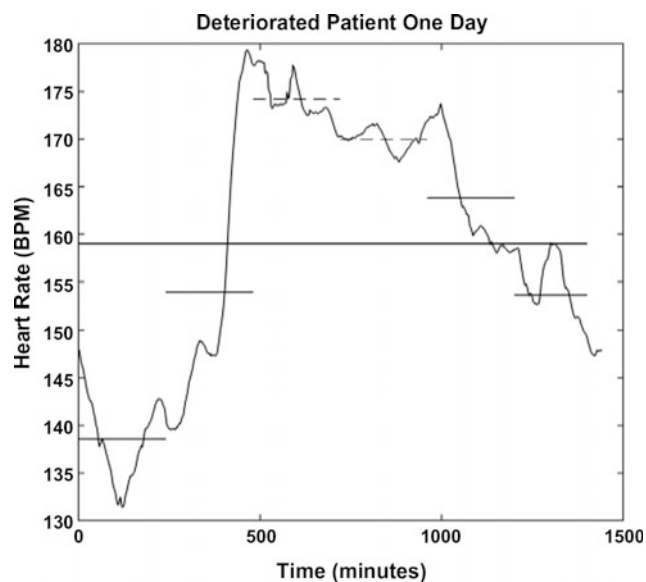


**Fig. 1** 24-h period (1440 min) heart rate data with six, 4-h averaged trendlines for a deteriorated patient. The x-axis is time (minutes) and the y-axis is heart rate (BPM). The alerts are represented by the dashed lines

24-h period prior to the clinical deterioration was examined in detail to determine the duration of the change in HR trend and the best averaging window to pick up this difference from the baseline.

We found that multiple 4-h trendline periods allowed for capture of differences in patient status in comparison to an 8-h trendline periods when looking at HR trending. Figure 1 shows HR data from a patient who showed signs of deterioration over a 24-h period. Alerts are displayed (dashed lines) as the trendlines exceeded the 24-h baseline value which was obtained from two calendar days prior by more than 10%. The figure shows six, 4-h averaged trendlines superimposed onto the 24-h HR filtered data. Figure 2 shows HR data from a stable patient over the same 24-h period, where no alert was triggered.

### 2.2 Using a Filter

To reduce the noisy raw heart rate data and obtain a smoother tracing, we needed to average HR data points. HR data was obtained every minute for each patient. One approach was to query the database and only obtain data points every 5 or 10 min; however, this resulted in a loss of clinically important information, especially when looking over a 24-h period. We decided to use a moving average filter with a window size of 60 min. For each 24-h time period we averaged the first 60 HR data points, then frame shifted this 60 point average over by 1 min to average the next 60 HR data points, then shifted the window over again

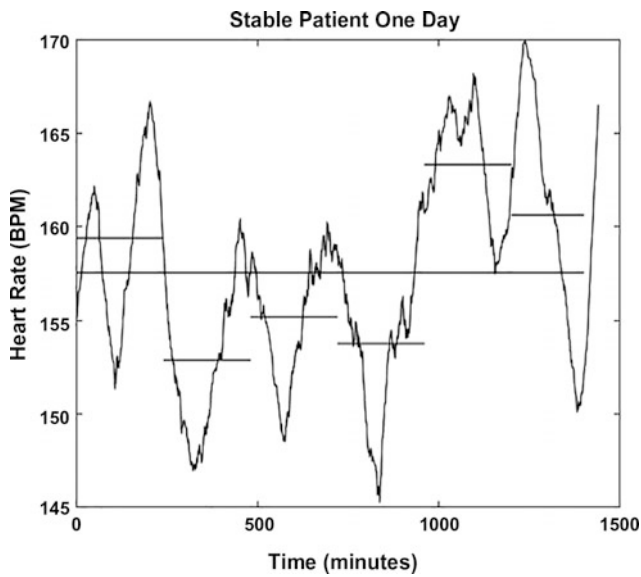


**Fig. 2** 24-h period heart rate data with six, 4-h averaged trendlines for a stable patient. The x-axis is time (minutes) and the y-axis is heart rate (BPM)

by a minute and continued this averaging successively to achieve a smoother plot. For the moving average filter, several different window sizes were tested; but a window size of 60 was a good balance between reducing the fluctuations and not losing too much information from the HR data. The filter was applied to all the raw HR data graphs. The purpose of applying the moving average filter was so that visually the graph was understandable for clinicians by removing large amounts of noise from the raw HR graph. However, the moving average filter was not applied to the baseline or trendline data; only the raw HR data was used for these calculations.

### 2.3 Displaying the Oxygen Saturation Data

For optimum patient care, clinicians target a narrow range of oxygen saturations. It would be clinically useful to have a system to alert them when patients are spending too much time outside of this target range. This was implemented by tracking how much time within a day (1440 min) each patient spent at a certain SpO2 level. The ideal saturation ranges are from 92 to 95% SpO2 (we aim for at least 70% of the time in this range). For the SpO2 variables, this data was obtained each minute by the CDR. Our clinical partner wanted to track and generate alerts for the following information over each 24-h period:

- (1) Was the patient’s SpO2 level less than 92%, more than 288 times (20% of the day)?

- (2) Was the patient’s SpO2 level greater than 95%, more than 144 times (10% of the day)?

The most appropriate method for visualizing these parameters for the clinician was a histogram. The data was ordered in Excel, to stratify the saturation ranges for the 4 types of patients used in our tool design. Through analysis using Excel, it was found that the deteriorated patients spent most of the time in the lower levels of the SpO2 region (<92%) and the stable patient spent most of the time in the high level of the SpO2 region (>96%), and the patient who left the unit to undergo surgery spent most of the time within the 92–96% region. Once the data was displayed in a histogram, the next step was to display visual alerts. We used conditional logic to count the number of times the SpO2 value was less than 92% or greater than 95%; once this count value exceeded 288 or 144 min (20% and 10%) of the day respectively, an alert was triggered. This alert was communicated by displaying the text readout for a histogram (see Fig. 3). The alerts are as follows: red text when the SpO2 level is less than 92% more than 288 times and yellow text when the SpO2 level drops to 92%. This same alert pattern is repeated with the 95% SpO2 level more than 144 times and will display green when the SpO2 levels are within the target range. This will be displayed in colour on the screens at the hospital. Figure 4 shows this visual display in black and white.

### 2.4 Visualization Tools

Most of the analysis was done in either MATLAB or Excel, and although each program has visualization tools, we wanted to use a program which could easily connect to a database so that we can use the algorithms developed in this research work with real time data streaming. We decided to use RStudio (<https://www.rstudio.com/>) in R because this program contains many packages which make graphs easily accessible, are user-interactive, and can connect to databases using the RMySQL (<https://cran.r-project.org/web/packages/RMySQL/index.html>) package. For instance, R has a package called ShinyR (<https://shiny.rstudio.com>) which is used for app development. This allowed us to create a heart rate

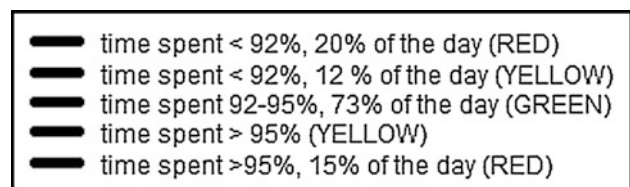


**Fig. 3** Example text readout for a histogram based on clinical alerts



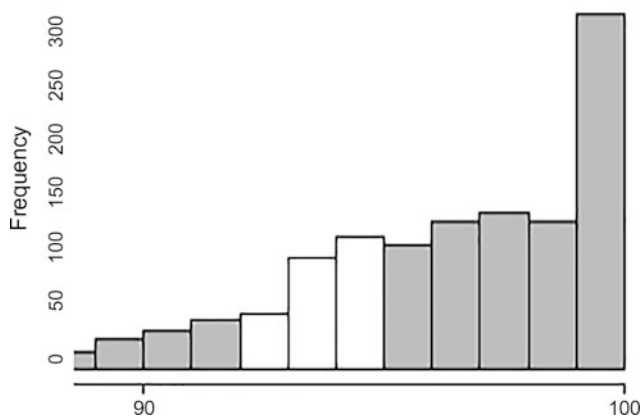


**Fig. 4** Zoomed-in portion of a histogram displaying the Oxygen Saturation Level (SpO<sub>2</sub>) over one day for a stable patient. The x-axis defines the SpO<sub>2</sub> levels (%SpO<sub>2</sub>) and the y-axis is the frequency (count) at these specific SpO<sub>2</sub> levels

graph which the user could manipulate with a zoom-in, zoom-out feature, using a slider, to allow the clinician to focus on various time frames. ShinyR allowed for conditional fill to colour in the histogram based on the parameters provided to us by the clinician for app development.

### 3 Results and Discussions

Initially we looked at 4-h and 8-h averaged baselines, but since HR fluctuations naturally occur, especially during feedings and handling of the patients, which influences the overall heart rate baseline, we chose a 24-h baseline to compensate for these consistent recurrences of HR deviations. These 24-h baselines were used to trigger alerts when comparing subsequent days' averaged 4-h trendlines. In addition, another visual element was to add 4-h trendlines for a 24-h period which were then compared to a 24-h baseline derived from 2 calendar days prior, and overlaid within the 24-h period (see Fig. 1) being monitored to see the general trend.

One important step when displaying HR data was to reduce the noise from the raw HR data before displaying the graphs seen in Figs. 1 and 2 by applying a moving average filter. This type of filter was chosen against other filters, such as Gaussian methods, because of its superior performance using time domain signals whereas other filters perform better with signals in the frequency domain [5].

For the oxygen saturation data, specific parameters were outlined for alerts. When the target saturation level was

within the ideal SpO<sub>2</sub> range (92–95%) the histogram text readout was colored green, and when the target saturation level was out of range the histogram text readout was colored yellow or red depending on the amount of time this deviation from the target range occurred over. This alert system was applied by using conditional logic to count the number of times the SpO<sub>2</sub> value was less than 92% and or greater than 95% and if this value surpassed 288 or 144 which represented 20 and 10% of the day, then the histogram text readout can be shown in colour based on the alert conditions.

### 4 Conclusions

This research was done in collaboration with our physician partners, with suggestions from other care providers in the NICU at CHEO. The physician involved found the visual tool most helpful and looks forward to its implementation in the NICU, in the near future, following a usability study planned for next summer.

Future developments of this work include connecting to the hospital system and applying these algorithms to real-time data instead of the pre-loaded data which was analyzed in this project. In addition, we plan to integrate this tool to our Physician-Parent Decision Support tool (PPADS) which includes a module for physicians and a module for parents of infants in the NICU [4].

**Acknowledgements** This research was made possible through a grant from the Natural Sciences and Engineering research Council.

### References

- Henriksen, K., et al.: Peer Reviewers—Volume 3—Advances in Patient Safety: New Directions and Alternative Approaches: Performance and Tools. Rockville, Maryland (2008).
- Georgia M.A.D., et al.: Information technology in critical care: review of monitoring and data acquisition systems for patient care and research. *The Scientific World Journal* 2015:1–9 <https://doi.org/10.1155/2015/727694> (2015).
- Gilchrist, J.: Performance evaluation of various storage formats for clinical data repositories. *IEEE Trans. Instrum. Meas.*, vol. 60, no. 10, pp. 3244–3252 (2011).
- Frize, M., Bariciak, E., and Gilchrist, J.: PPADS Physician-Parent Decision-Support for Neonatal Intensive Care MedInfo Proceedings of the 14th World Congress on Med. & Health Inform. Copenhagen, Denmark, pp 23–27 (2013).
- Smith, S.W.: *The scientist and engineer's guide to digital signal processing* (1997).



# Data Analytics for Metabolic Syndrome Diagnostics

Ľudmila Pusztová, František Babič, and Ján Paralič

## Abstract

Metabolic syndrome (MS) represents an important risk factor for the development of cardiovascular diseases, as well as type 2 diabetes mellitus, which as one of a few clinical syndromes affects more than 25% of the world population. The diagnosis is often associated with various negative activities like little physical exercise, poor diet, stress, genetic predisposition, and excessive alcohol consumption. The aim of this paper is to provide a literature review of the current state of the art in the area of MS diagnosis by means of data mining methods. We structure our literature review by means of the CRISP-DM methodology, which is typically used to organize the analytical process. The reviewed problem was most often approached as a binary classification problem and frequently used methods have been decision trees, neural networks and logistic regression. Some of the authors applied also suitable statistical methods like Welch's t-test, Pearson's chi-squared test. Mostly, the size of analyzed data samples was more than one thousand patients.

## Keywords

Metabolic syndrome • Prevalence • OR • Regression methods

## 1 Introduction

The Metabolic syndrome (MS), otherwise called the syndrome of insulin resistance, belongs to the set of significant risk factors of some cardiovascular diseases (CVD) and type 2 diabetes mellitus [1]. A serious problem in MS diagnostics is a selection of common criteria for identifying patients suffering from this disease. In the past, various expert groups like WHO [2], AACE [3], and NCEP [4] attempted to specify common diagnostic criteria, that in general consist of: insulin resistance, abdominal obesity, atherogenic dyslipidemia (increased triacylglycerol [5], high LDL cholesterol and low HDL cholesterol levels [5] and raised blood pressure. These factors belong to the most widespread factors of the MS [6]. The overall prevalence of MS is rapidly increasing [5, 7–11], which supports the importance of its prevention, diagnostics, and treatment throughout the population.

We focused on papers describing applications of suitable data analytics methods on different data samples related to the MS. We identified the following crucial challenges related to the analyzed problem: integration of heterogeneous data; inconsistent data representation; original large number of variables; missing or incomplete data; a relatively large number of results; validation of the knowledge extracted from the data; privacy and ethical aspects. We organized our paper according to the CRISP-DM methodology, typically used for data analytics tasks [12]. This approach enables us to consider different aspects of the machine learning-based diagnostic process. CRISP-DM represents an iterative and interactive process containing six main phases: business understanding, data understanding, data preparation, modelling, evaluation, and deployment.

Ľ. Pusztová (✉) · F. Babič · J. Paralič  
Department of Cybernetic and Artificial Intelligence, Faculty of  
Electrical Engineering and Informatics, Technical University of  
Košice, Letná 9, 042 00 Košice, Slovak Republic  
e-mail: ludmila.pusztova.2@tuke.sk

F. Babič  
e-mail: frantisek.babic@tuke.sk

J. Paralič  
e-mail: jan.paralic@tuke.sk

## 2 CRISP-DM

### 2.1 Business Understanding

The first phase is to understand what the customer wants to accomplish from a business point of view. Customer in our case can be not only a doctor but also hospitals or health insurance companies. Their business perspectives can cover cost containment in diagnostic and treatment phase, improved quality of life or quality of the healthcare services. Data analytics can support these objectives with reliable inputs to the relevant decision processes. But, MS diagnosis is not a simple task. The doctors have to consider various symptoms, patient's history and other necessary factors. Data analytics can help to identify the most significant symptoms, and relations between them. The obtained findings are further used in the modeling phase to improve the model accuracy or to extract most helpful rules for MS diagnostics.

We identified two main directions appearing in the most of the existing works. The first group of authors approaches the problem as a typical predictive modelling task, usually a binary classification [13–16]. The second group of authors focused on an investigation which input variables are the most important for the target diagnosis. For this purpose, they used suitable regression methods, especially binary logistic regression [17–22].

### 2.2 Data Understanding

Authors used different data samples representing various target groups of patients around the world like USA [23, 24]; Africa [5, 25]; Asia [8, 9, 14, 21] or Europe [25–27]. We observed two possible approaches how to obtain data suitable for this task. The first covers free available data from appropriate surveys like the National Health and Nutrition Examination Survey NHANES [7, 17, 23, 28, 29]; and the second is a data collected from clinical practice from blood tests and/or selected questionnaires. A sample size varied from several hundred samples [5, 18], through a few thousands [9] to almost 40 thousand participants [8].

The patients are typically described by socio-demographic characteristics, lifestyle behaviors (e.g. alcohol consumption or smoking status), personal medical and family history, biochemical measurements (e.g. glycemia, triglyceridemia, total cholesterol, and HDL cholesterol) or obesity indicators like BMI and waist circumference. Some of the studies involved patients older than 50–60 years [9, 13, 30, 31]; and the second group analyzed a larger group of patients aged 19 years and older [5, 8, 18, 20]. Some authors considered also non-traditional factors like resistance exercise RE [17],

leptin-to-adiponectin ratio or insulin resistance [18], myocardial infarction and brain stroke [29].

In our case [13], we extended conventional combination of variables determining the MS with new potentially influential variables easily available in the everyday physician's practice. We have experience with a smaller sample (100–200 records) containing anonymized medical information about elderly patients collected within a family practice located in an urban area of the town of Osijek in Croatia [13, 32]. Currently, we've been working on an investigation of a relation between menopause and MS diagnosis.

### 2.3 Data Preparation

Data preparation is focused mainly on data cleaning and feature selection. In [29] authors excluded e.g. patients older than 89 years, pregnant or breast-feeding women and patients with fasting times less than 7 h based on analyses indicating no difference in the prevalence of hypertriglyceridemia and insulin resistance. Patients who had serious chronic illness, ongoing or recent acute illness, or were currently taking any medication were also removed [18, 33]. Some authors removed the missing or incomplete data [28, 33, 34], or data about the patients who had already died. Other authors focused on the differences between male and female or various modifications of the age structure [35]. Most studies work only with a single data sample (training set), in contrast with the study [36], where authors divided the input data into three datasets: training, validation and a dataset for external validation.

In one of our experiments we dealt with a data sample representing anonymized medical information about elderly patients extracted from their health records. This data sample contained almost 100 records described by more than 60 variables. It affected expected results from various points of view like statistical significance or reliability. We tried several feature selection methods to identify only those really important variables for predictive modeling.

### 2.4 Modelling

In general, we divide the modelling phase into several directions: descriptive, predictive and prescriptive modelling. The first one is typically represented by exploratory data analysis to summarize the main data characteristics through suitable visualization methods. The second one covers tasks like classification, regression, and clustering or association rules. Both approaches provide the basis for medical data analytics.

The investigation of possible relations between input variables or between them and the target diagnosis uses typically regression methods like multiple [7] or binary logistic regression [18, 21]. The outputs are evaluated by odds ratios (ORs) and 95% confidence intervals (CIs). Some authors used the statistical tests like Welch's t-test or Pearson's chi-squared test to investigate an association between input attributes (continuous or categorical) and target binary MS diagnosis [5, 8, 9, 28]. Authors in [8] reported for continuous attributes the mean  $\pm$  standard deviation and compared them using ANOVA test. Spearman's analysis was used in [18] to calculate the correlations between continuous attributes. Predictive modelling is represented by classification methods like Decision trees, Support Vector Machine or k-Nearest Neighbors used in [1, 14–16]. Hierarchical clustering was applied to the standardized prevalence ratio of MS in [35].

In our experiments, we analyzed several directions. First one covered an application of various algorithms like CART [32] or C4.5 [37] to generate as accurately as possible decision tree models. The second one [25, 32] dealt with a searching of optimal cut-off values for the most important attributes by Youden's index [38]. The final one covered statistical tests like Pearson's chi-squared test, logistic regression and some methods for attributes reduction like LASSO [39], forward or backward stepwise selection [40]. In this case we used Mallows's  $C_p$  [41] and Bayesian information criterion [42] to evaluate the generated regression models.

## 2.5 Evaluation

In this section, we present briefly some interesting results and findings from referenced works. The prevalence of MS was higher in rural than urban residents (39.9% vs. 32.8%), among both men (39.7% vs. 33.3%) and women (40.2% vs. 32.3%, respectively) [7]. Smoking was an independent risk factor for MS in women, and female smokers who smoked more than 10 cigarettes per day or over 25 years were associated with 96% or 74% increased MS risk, compared with non-smokers [8]. The abdominal obesity was present in 70.41% of women aged 50–59 years, where the prevalence of MS was 53.57% [5]. Patients with high triglyceride were 71 times more likely to develop MS than patients with normal triglyceride [21]. Our initial results show an important role of the level of Folic acid (for males) and an average level of blood glucose over the previous 3 months, monocytes % in White Blood Cell differential and Thyroid-stimulating hormone (for females). New results are in progress.

## 3 Conclusion

This paper represents a literature review of current state of the art in the diagnosis of Metabolic syndrome using the data analytics. We have highlighted some of the important challenges for the data analysts. Relatively large number of results and their validation requires a tight interaction with end-users to utilize the expert and domain knowledge. Missing or incomplete data problem can be solved with clustering or k-Nearest Neighbor algorithm based on patient's similarities. The original set of input variables can be reduced through features selection methods like Principal Component Analysis, LASSO or stepwise regression. From a business point of view, it is important to consider security, privacy (GDPR), ethical aspects and a relative lack of local clinical studies which means that it is hard to consider an applicability of medications.

**Acknowledgements** This work was supported by the Slovak Research and Development Agency under the contract No. APVV-16-0213, the Slovak Grant Agency of the Ministry of Education and Academy of Science of the Slovak Republic under grant No. 1/0493/16 and by the COST Action CA TD1405.

**Conflicts of Interest** We declare that we have no conflict of interest.

## References

1. Reaven, G.M.: Role of Insulin Resistance in Human Disease. *Diabetes* 37, 1595–1607 (1988)
2. Alberti, K.G., Zimmet, P.Z.: Definition, diagnosis and classification of diabetes mellitus and its complications. Part 1: diagnosis and classification of diabetes mellitus: provisional report of a WHO consultation. *Diabetic Medicine* 15, 539–553 (1998)
3. Einhorn, D., Reaven, G.M., Cobin, R.H.: American College of Endocrinology position statement on the insulin resistance syndrome. *Endocrine Practice*, 237–252 (2003)
4. Third report of the National Cholesterol Education Program (NCEP) expert panel on detection, evaluation, and treatment of high blood cholesterol in adults (Adult Treatment Panel III). Final report. *Circulation*. 2002; 106: 3143–3421
5. Brini El O. et al.: Prevalence of metabolic syndrome and its components based on a harmonious definition among adults in Morocco. *Diabetes, Metabolic Syndrome and Obesity: Targets and Therapy* 7, 341–346 (2014)
6. Grundy, S.M., Brewer, H.B., Cleeman, J.I., Smith, S.C., Lenfant, C.: Definition of Metabolic Syndrome. *Circulation* 109, 433–438 (2004)
7. Trivedi, T., Liu, J., Probst, J.C., Martin, A.B.: The metabolic syndrome: are rural residents at increased risk? *The Journal of rural health* 29(2), 188–197 (2013)
8. Xiao, J. et al.: Prevalence of metabolic syndrome and its risk factors among rural adults in Nantong, China. *Scientific reports* 6 (2016)
9. Liu, M. et al.: Increasing Prevalence of Metabolic Syndrome in a Chinese Elderly Population: 2001–2010. *PLoS One* 8(6), 1–6 (2013)

10. Ranasinghe, P., Mathangasinghe, Y., Jayawardena, R., Hills, A. P., Misra, A.: Prevalence and trends of metabolic syndrome among adults in the asia-pacific region: a systematic review. *BMC Public Health* 17(101), 1–9 (2017)
11. Srikanthan, K., Feyh, A., Visweshwar, H., Shapiro, J. I., Sodhi, K.: Systematic Review of Metabolic Syndrome Biomarkers: A Panel for Early Detection, Management, and Risk Stratification in the West Virginian Population. *International Journal of Medical Sciences* 13(1), 25–38 (2016)
12. Chapman, P., Clinton, J., Kerber, R., Khabaza, T., Reinartz, T., Shearer, C., Wirth, R.: CRISP-DM 1.0 Step-by-Step Data Mining Guide (2000)
13. Babič, F., Majnarić, L., Lukáčová, A., Paralič, J., Holzinger, A.: On Patient's Characteristics Extraction for Metabolic Syndrome Diagnosis: Predictive Modelling Based on Machine Learning. *International Conference on Information Technology in Bio- and Medical Informatics*, Springer, 118–132 (2014)
14. Kavakiotis, I., Tsave, O., Salifoglou, A., Maglaveras, N., Vlahavas, I., Chouvarda, I.: Machine Learning and Data Mining Methods in Diabetes Research. *Computational and Structural Biotechnology Journal*, 104–116 (2017)
15. Behadada, O., Abi-Ayad, M., Kontonatsios, G., Trovati, M.: Automatic Diagnosis Metabolic Syndrome via a k–k–Nearest Neighbour Classifier. *International Conference on Green, Pervasive, and Cloud Computing, Lecture Notes in Computer Science* 10232, 627–637 (2017)
16. Miller, B., Fridline, M.: Development and Validation of Metabolic Syndrome Prediction and Classification-Pathways using Decision Trees. *Metabolic Syndrome* 4(1), 1–9 (2015)
17. Churilla, J.R., Johnson, T.M., Magyari, P.M., Crouter, S.E.: Descriptive analysis of resistance exercise and metabolic syndrome. *Diabetes & Metabolic syndrome* 6(1), 42–47 (2012)
18. Ayina, C. N.A. et al.: Association of the leptin-to-adiponectin ratio with metabolic syndrome in a sub-Saharan African population. *Diabetology & Metabolic Syndrome* 9(66), 1–6 (2017)
19. Edwardson, C.L., et al.: Association of Sedentary Behaviour with Metabolic Syndrome: A Meta-Analysis. *PLoS One* 7(4), 1–5 (2012)
20. Preuss, H.G., Mrvichin, N., Clouatre, D., Bagchi, D., Preuss, J.M., Perricone, N.V., Swaroop, A., Kaats, G.R.: General Lack of Correlations between Age and Signs of the Metabolic Syndrome in Subjects with Non-diabetic Fasting Glucose Values. *The Journal of the American College of Nutrition* 36(7), 556–564 (2017)
21. Albayati, A.H., Alhusuny, A.: Assessment of Metabolic Syndrome and Its Risk Factors among Patients with Type 2 DM at Merjan Teaching Hospital, Al-Hilla City. *IOSR Journal of Dental and Medical Sciences* 13(9), 69–75 (2014)
22. Bhandari, R., Kelley, G.A., Hartley, T.A., Rockett, I.R.H.: Metabolic Syndrome Is Associated with Increased Breast Cancer Risk: A Systematic Review with Meta-Analysis. *International Journal of Breast Cancer* 2014, 1–13 (2014)
23. Ford, E.S., Giles, W.H., Dietz, W.H.: Prevalence of the Metabolic Syndrome Among US Adults Findings From the Third National Health and Nutrition Examination Survey. *JAMA* 287(3), 356–359 (2002)
24. Aguilar, M., Bhuket, T., Torres, S., Liu, B., Wong, R.J.: Prevalence of the Metabolic Syndrome in the United States, 2003–2012. *JAMA* 313(19), 1973–1974 (2015)
25. Babič, F., Paralič, J., Vadovský, M., Muchová, M., Lukáčová, A., Vantová, Z.: What is a Relation between Data Analytics and Medical Diagnostics? *International Journal on Biomedicine and Healthcare* 5(1), 8–12 (2017)
26. Scuteri, A., et al.: Metabolic syndrome across Europe: Different clusters of risk factors. *European Journal of Preventive Cardiology* 22(4), 486–491 (2015)
27. Vliet-Ostaptchouk, J.V., et al.: The prevalence of metabolic syndrome and metabolically healthy obesity in Europe: a collaborative analysis of ten large cohort studies. *BMC Endocrine Disorders* 14(9), 1–13 (2014)
28. Jung, C.H. et al.: Association of meal frequency with metabolic syndrome in Korean adults: from the Korea National Health and Nutrition Examination Survey (KNHANES). *Diabetology & Metabolic Syndrome* 9(77), 1–9 (2017)
29. Ninomiya, J.K., L'Italien, G., Criqui, M.H., Whyte, J.L., Gamst, A., Chen, R.S.: Association of the metabolic syndrome with history of myocardial infarction and stroke in the Third National Health and Nutrition Examination Survey. *Circulation* 109(1), 42–46 (2003)
30. Liu, M. et al.: Association between Metabolic syndrome and Mild Cognitive Impairment and its Age Difference in a Chinese Community Elderly Population. *Clinical Endocrinology* 82(6), 844–853 (2015)
31. Lee, S., Ko, Y., Kwak, Ch., Yim, E.: Gender differences in metabolic syndrome components among the Korean 66-year-old population with metabolic syndrome. *BMC Geriatric* 16(27), 1–8 (2016)
32. Babič, F., Vadovský, M., Muchová, M., Paralič, J., Majnarić, L.: Simple Understandable Analysis of Medical Data to Support the Diagnostic Process. *IEEE 15th International Symposium on Applied Machine Intelligence and Informatics*, 153–158 (2017)
33. Stern, M.P., Williams, K., González-Villalpando, C., Hunt, K.J., Haffner, S.M.: Does the metabolic syndrome improve identification of individuals at risk of type 2 diabetes and/or cardiovascular disease?. *Diabetes care* 27(11), 2676–2681 (2004)
34. Yates, K.F., Sweat, V., Yau, P.L., Turchiano, M.M., Convit, A.: Impact of metabolic syndrome on cognition and brain: a selected review of the literature. *Arteriosclerosis, Thrombosis, and Vascular Biology* 32(9), 2060–2067 (2012)
35. Hikada, T., Hayakawa, T., Kakamu, T., Kumagai, T., Hiruta, Y., Hata, J., Tsuji, M., Fukushi-ma, T.: Prevalence of Metabolic Syndrome and Its Components among Japanese Workers by Clustered Business Category. *PLoS ONE* 11(4), 1–11 (2016)
36. Worachartcheewan, A., Nantasenamat, Ch., Isarankura-Na-Ayudhya, Ch., Pidetcha, P., Prachayasittiku, V.: Identification of metabolic syndrome using decision tree analysis: *Diabetes research and Clinical practice* 90 (2010)
37. Salzberg, S. L.: C4.5: Programs for Machine Learning by J. Ross Quinlan. *Machine Learning* 16(3), 235–40 (1994)
38. Youden, W.J. Index for rating diagnostic tests. *Cancer* 3, 32–35 (1950)
39. Tibshirani, R.: Regression Shrinkage and Selection via the lasso. *Journal of the Royal Statistical Society* 58(1), 267–288 (1996)
40. Efronson, M. A.: Multiple Regression Analysis. *Mathematical Methods for Digital Computers*, John Wiley (1960)
41. Gilmour, S. G.: The interpretation of Mallows's Cp-statistic. *Journal of the Royal Statistical Society* 45 (1), 49–56 (1996)
42. Schwarz, G.: Estimating the dimension of a model. *Annals of Statistics* 6(2), 461–464 (1978)
43. Breiman, L.: Classification and Regression Trees. Repr. Boca Raton: Chapman & Hall (1998)
44. Seo, J.-Y., Kim, J.H.: Validation of surrogate markers for metabolic syndrome and cardiometabolic risk factor clustering in children and adolescents: A nationwide population-based study. *PLoS one* 12, e0186050. <https://doi.org/10.1371/journal.pone.0186050> (2017)



# Medical Expert System with the Properties of Artificial Intelligence

Sergo Dadunashvili

## Abstract

Elaboration of synergetic-sinarchic concepts of structural harmonization of systems. Creation of the ideological and methodological instrument of structural research and design based on the theory of structures-attractors. Introduction of objective invariants of evolution and self-organizing. Efficiency of developed based on the discussed principles expert system determined by the fact that it can be “embedded” into the environment of potential users, adapting to their requests. Due to this, the expert system provides a new information technology that approaches intellectual activity in those areas where there is accumulated experience of experts based on understanding the structure and purpose of specific knowledge. Support for the intellectual activity of the user of the expert system with a synarchy algorithm in generating new knowledge is the rapid implementation of the cycle of building models, their analysis and evaluation.

## Keywords

Structural harmonization • Artificial intelligence  
Expert system

## 1 Introduction

Monitoring of functioning of social, biological and technical systems shows a set of objective features, pointing out that existing ways of research and description of these systems have already exhausted themselves. It is necessary to transit to the following, essentially new level that will allow identifying the phenomena invisible until now. These data will promote deeper understanding of reality and new reflection on scientific achievements about nature and society.

Today, there is a broad spectrum describing the system dynamics. The commonality of these theories is that their complex systems always form in self-development, in the unity of macro and micro scales of their features, movement and extent. Under self-development of the real system, we understand the process of inducing necessary internal diversity, thus creating excessive structures used as a reserve, orienting the system towards stereotype of optimal organization [1–3].

The leading role in this mechanism is played by the principle of saving and regulating definite number of levels of freedom. Based on this, the unity of internal orders, proportions and compositions, relations and connections, that guaranty the livelihood of the system in the conditions of increased aggressive environment, is being realized.

In parallel, the new jet of ideas has flown into the theory of self-organizing, related to understanding of coherent interaction of distributed sources of activity, to the “order parameters”. Each feature of the system, certain way of action, was attributed with order of integral parameter of the system. Self-organizing has stratified into “homogeneity zones”. In the same self-organizing process, we can identify merging conditions with substantial differences in the course of time, differences in intentionality of neighboring “tempo-worlds”.

Study of the concepts described above has shown that they lack the understanding of *tolerance* as a landmark of the system evolution and invariants of this evolution. The issue of *tolerance*, as a defining criterion of optimality, even for the cases of stationary condition has in fact not been raised. With elimination of the time factor, this representation still reflected static proportionality of its wholeness, harmonious orderliness. Everything was evaluated from the position of “here” and “now” and thus was a ready-made material for measurement, comparison and harmonization.

S. Dadunashvili (✉)  
Georgian Technical University, Tbilisi, Georgia  
e-mail: dadu@gtu.ge

## 2 Integrality and Meta Logic

In the hierarchical system, the correlation between two factors could directly take place only based on the two laws: by *analogy*, if they lay in different layers of hierarchy, but at the same time are connected by identity of essence, and by *opposites of antinomies*, if they lay in the same section of hierarchy. All other more complex correlations are only the combination of the above two main types.

The bifurcate unity and identity of opposites, as a fundamental principle and a starting point in building the basic theory of self-organizing allows to investigate the process of self-organizing in its most general terms and draw the relevant invariants—centers of “*tolerance zones*” on knotted line of measures.

Determination of regularities of self-organizing as self-organization, finding invariants, forming the knotted line of measures, opens up the basis of the law of harmony of *tolerance* in the framework of the bifurcate unity. Thus, bifurcate unity in the process of self-organizing and structural development of systems determines the law of conservation of diversity together with the measure of the structural organization of systems.

Within the *tolerance-genesis*, we are talking about the measure of correlation of the members of the relationship forming the bifurcate unity, and about its result—harmony of measures. The analysis is based on a separate consideration of elementary variant of “space”, in which the correlation—binary opposition with certain weight characteristics of its elements (members of relationship)—takes place.

The dimension of space of the “chosen” conditions is expressed through integer values, rational parameters, in the same way as their metric. These conditions exactly are realized by the nature in the process of system genesis, using modularity and self-similarity. The transition from one dimension to another quantifies the measure of organization.

Any binary opposition is the change space for the members of relationship that is mutually oriented, lacking any other standards, measures of comparison, except for those that they present for themselves, or those that one bears for another. In other words, any binary opposition is a self-contained world, the simplest out of those, where the “gravity” of sides are spread throughout the space, aspiring towards each other in a self-search of measures of their harmonious connection.

Naturally, because such movement is localized and is free from entry influences, reason for establishing a measure, rules of measure-genesis, mechanisms of realization of principle of identification of extremes and establishing their harmonious unity should be searched only in the framework of this limited space, having attributes of the elements—members of the binary opposition as a unified attitude.

In the synarchy, a transition made from the imperative (ideal) of completeness, to the imperative (ideal) of wholeness. The laws of the change of the whole determine the movement of each part of it, thus, the program actions of the parts take place.

If we understand everything as consisting of simple components, because of the formation of complex ensembles, the problem arises: knowing the measure of each component as a member of the ensemble, to find the integral measure of the ensemble as a whole. Having reduced the individual measures of the individual components to one general measure, we shall have an integral measure of the ensemble (of the whole system as a whole). In addition, as such, it is equivalent (identical) to the harmony of simple measures of its structural subunits. A measure, one and the same for parts and for the whole, is able to tie together everything that is projected, what appears in the plans and what is then embodied in the material.

The metaphysical adjustment matrix concentrates the basic codes of such large systems as space, society, economics, culture, etc., codes governing their schemes of perception, exchange, their forms of expression and reproduction, values, hierarchy of their practices. Thus, this matrix acts as a source of “pre-established harmony.”

Self-organizing systems as ensembles, cooperative formations of various subject specificities and profiles, compound mixes, statistical distributions, alliances of different agents of action, and aggregates of structural subunits that form organic integrity are just some of the natural arenas of the effective operation of the law of synarchy.

There are the original system matrices. They necessity and value lies in the fact that they is a condition for the possibility of simultaneous communication between actors and their freedom from each other. Systemic qualities of the Universe do not contain any opposites; they are an expression of its harmony. Moreover, they are so necessary for its existence that even local conflicts and the disintegration of elements within the Universe are possible only under the condition of preserving at least a minimum of their harmony, unity and organic structure.

As part of the universe, the most visible is the real being, i.e. Space-time or temporal processes (physical and mental). The spatial and temporal extrapolation of parts of real being is capable of forming a systematic unity and meaningfulness of the sphere of reality only insofar as it based on an ideal being. The cause gives rise to temporal and spatial processes. Wherever there is an action, where is a time process, the source of it is a substantial actor.

On the real plane, there are objects whose unity is determined from the ideal plan, and life—by a real being. Objects of reality are embedded as an organic whole, which is not composed externally from its parts. The whole exists



in the field of the ideal plane, and the parts are able to arise and exist only in the system and under the guidance of the whole. Parts are derived and relative; their multiplicity generated from a single whole. Within the real being, the primacy of the rational, systemic aspects of the Universe acts.

The notion of an expedient connection applies not only to a series of processes that are consistent in time, but also to a multitude of coexisting things or parts of the whole. Expediency of the body corresponds the fact that parts of the organism exist not only because of each other, but also for the sake of each other, and also for the sake of the whole.

Let us single out those possible original principles, thanks to which the plurality on the real plane, firstly, has the character of the system and, secondly, preserves the side of integrity. The system is possible only where there is a relationship between the elements. Each side of reality consists of the similarity and difference to all other aspects of reality. All sides of reality, to which the concept of magnitude applies, contain countless quantitative relations. Add here the relationship in time, in space, etc., and then it becomes clear that the network of relationships is something all-pervading and all entangling.

Relationships are not independent, they cannot exist on their own, without members of the relationship. Consequently, relations are only an expression of the organization of real being, but they are not the primary source of it, explaining how it was created. But how does the attitude itself relate to these members? Members and their relation to each other are represented as one whole, in which each side exists together with the rest based overall. Spatiality and temporality belong to specific whole objects and events, as for relations, even spatial and temporal, they are moments of a concrete whole, not spatial and not temporary.

The presence of relations is a condition of the possibility of every order, of any systems nature and all that gives the nature of the Universe, and not chaos, to a multitude of beings and events, the character of a reasonable sense.

The spatial form of a thing exists only in the relationship with the environment. The relativity of spatial forms manifested in the fact that they are many-sided objects. Multifacetedness is inherent in the subject not in one and the same, but in different respects to the environment. In the relative multiformity of a thing, the organic character of the structure of the world, the existence of an object not in itself, but only in the system of the whole, is particularly striking.

Non-locality not seen as Unity, which includes the world's multitude, but as the creator of the Universe. Non-locality creates an ideal plan filled with perfect unity and harmony. All his members, living the life of the One, live not only in him and for him, but also in each other and for each other. This is not an abstract, but a real unity, a

sphere of harmony. The multiplicity in this world is due only to the ideal differences of one member from the other; individualized opposites, without any participation of opposites. The unity of the sphere of harmony is not the functional dependence of abstract ideas, but the communication of beings living in an infinite life. Life in such a world does not tire and does not satiate because there is no one-sidedness in it.

Non-locality does not destroy the empirical character of a man with his creative omnipotence, but at every moment of his life gives countless reasons to perceive and experience the intrinsic absolute value of non-locality. Man is created as the bearer of a creative meta-logical force and released to freedom for free creative activity, which illuminated by the guiding star of an individual idea as an individual norm, but not a law that restricts freedom. Hence the opportunity to rise up into the realm of super-temporal rest and supra-spatial integrity.

As a super-temporal and supra-spatial existent, non-locality can enter into relation to any time and space, but this is not enough, because of its infinite power, its connection with every time and place is topical, in other words, non-locality is omnipresent in space and time. Being in unity with non-locality, all members of the ideal plan are in unity with each other directly. All relations in this communication have an internal character and there is no opposition between form and content, not because, in the ideal plan of forms, there was not, on the contrary, a comprehensive, infinite interpenetration of the fullness of individual and, at the same time, harmoniously combined contents.

---

### 3 Tolerance and Harmonization

The new concept of self-organizing based on its natural basis—the theory of *tolerance* and theory of harmony and is presented through especially informative, with all the commonalities and involvement in the subject specificity of the most diverse areas of knowledge.

This independent direction of the research of the mechanism of self-organization, self-organizing processes, self-organizing systems, in which, on the first place there is a measure that serves as a logical-organizational configurant—that eternal existence, which in objective world defines the optimum; and characterizes evolutionary maturity and quality of a self-developing system whole.

The concept of self-organizing, in which the central role is played by the notion of tolerance and tolerance-genesis, harmony and harmonization, obtaining in the given process the form of self-organization, having as a source the intrasystem mechanisms of coordination of changes in subsystems and other system components.

In the framework of the binary opposition there is a synthesis of its constituent parts, the identity manifested, connection in proportion to their qualitative and quantitative characteristics takes place. In relation to the more complex areas of the universe that are structurally dissected, having certain internal diversity, and are able to process to the evolutionary mature condition of whole objects, then, we are able to talk about the phenomenon of harmonization.

The nature of a structural harmony of self-organizing systems is defined by the mechanisms of the tolerance development process. The structural harmonization of the complex whole carried out in a self-organizing manner and thus receiving the form of the self-organization, directly connected to its restructuring—redistribution of specific weights of structural elements. In order to carry out such transformations and to secure the newly obtained condition—maintenance of a stationary mode of self-reproduction of integral quality of a whole, it is necessary to have additional flow of a resource, material and informational costs, intensification of the energy exchange.

Disharmony is associated with the incommensurability of intrasystem interactions and therefore—increased waste of resources, energy costs. The inability of the system to overcome such state of duality, the coexistence of unconjugated extreme positions and therefore it being doomed to carry the opposites within, which cannot reach the phase of synthesis, and exist separately. Each of them influences it in their own way, and serves as a source of every kind of anomalies and misbalances, leading to its accelerated extinction.

Harmonization, on the contrary, means the self-consistency of the inhomogeneous, correlation of grounds and norms, commensurability and co-operability of actions and processes of self-realization of the subsystem potential, alien to any double installations, with a nature of intrasystem relationship. This creates preconditions to the operation of universal law, turning subunits of whole, structural elements of the system, from mutually indifferent members to the aggregate of subjects of the same exchange process. Thus, the “collective subject” is being formed, centered in its own, already unified action.

Harmony is an inner connection of things, without which the universe could not exist. Harmony is objective, it exists independently of our consciousness and is expressed in the harmonious arrangement of everything that exists, beginning with the Universe and ending with the micro world. Harmony reigns throughout the world, it is the ordering and creative beginning of all nature and the Universe.

The invariant aspect of any system is its structure, which always has a certain level of diversity. By its means, the

system harmonization receives a nonequilibrium state, which is necessary for its effective life activity. The system becomes open and flowing with the exchange processes on which life is based. Thus, the system acquires an optimal mode of existence, distinguished by a new functional quality.

---

## 4 Conclusions

An experimental verification of the considered synarchic regularities will allow creating a new instrument for probing and controlling systems of various nature.

In general, the whole has a definite “net” scale for streamlining its parts. The “net” of knots are symmetrically and non-linearly situated between the poles of a unity thus are the products of the geometry of a whole, and it exists independently from presence or absence in it of a substrate, which only discovers it, through being distributed in a whole, in one way or another.

Leaving the space for individual freedoms, mechanism of coordination of self-reproduction of system quality, in which the “mystery of organism” is contained, is “anchored” on a solid, all-penetrating attitude, playing the role of structural invariant, which keeps the mode of functioning of the system in the given parameters of stationarity.

Synergetic—synarchic concept of structural harmonization of systems in nature and society served as the basis for creating an original expert system [3–5]. Efficiency, developed based on the discussed principles, the expert system determined by the fact that it can be “embedded” into the environment of potential users, adapting to their requests. Due to this, the expert system provides a new information technology that approaches intellectual activity in those areas where there is accumulated experience of experts based on understanding the structure and purpose of specific knowledge.

Support for the intellectual activity of the user of the expert system with a synarchy algorithm in generating new knowledge is the rapid implementation of the cycle of building models, their analysis and evaluation. At the same time, the processing of partial, fragmentary knowledge accompanied by an increase in the level of its systematic and integrated.

Real differences in the ways of thinking people of different professions not found. The interactive participation of the expert system using various interfaces in a real thought process will lead to leveling out the difference between the system and the user and may be evidence of the emergence of hybrid intelligence.

## References

1. Dadunashvili S. Biosignals Processing in the Structural Levels of Body - World Congress on Medical Physics and Biomedical Engineering, Beijing. Springer, IFMBE Proceedings Vol. 39, p. 581–584. (2012).
2. Dadunashvili S. System Pattern of Consciousness Functioning - Springer, Heidelberg, Germany. IFMBE Proceedings 38, p. 5–10. (2012).
3. Dadunashvili S. Multilevel Signal Processing for Biomedical Nanodevices. Springer, IFMBE Proceedings Vol. 55, 329–331. (2016).
4. Pourabbas E., Shoshani A. The Composite Data Model: A Unified Approach for Combining and Querying Multiple Data Models, *IEEE Transactions on Knowledge and Data Engineering*, 27 (5):1424–1437, <https://doi.org/10.1109/tkde.2014.2365815>. (2015).
5. B. Schmidt, C. Villarraga, T. Fehmel, J. Bormann, M. Wedler, M. Nguyen, D. Stoffel, W. Kunz: “A New Formal Verification Approach for Hardware-dependent Embedded System Software” *IPSJ Transactions on System LSI Design Methodology* Vol. 6 (2013).

# A Simple Room Localization Method to Find Technology in a Big Trauma Center

J. Regolini, F. Frosini, E. Ciagli, A. Benassi, D. Cocchi, R. Miniati, P. Tortoli, and A. Belardinelli

## Abstract

Trauma Center is a big operating theatre of over 4000 m<sup>2</sup> on two floors and 14 operating rooms. In this context, the share of the equipment is fundamental to reduce expedition but may cause an excessive loss of time by medical staff that needs devices for the clinical therapy. Therefore, knowing localization is useful for health monitoring of important electromedical devices. In recent years, a lot of technologies have been developed for the indoor localization, like the Bluetooth wireless standard technology. In particular, Beacon technology is very interesting, which uses the Bluetooth low energy (BLE) technology. However, due to the complexity of internal ambiances, the development of an indoor localization method is always associated with various problems, mainly for the presence of obstacles among the direction of propagation of signals. Application of BLE for the localization of medical equipment could help to save time during an emergency. With this preliminary study, using Beacon devices like tag, three mathematical average methods for reducing variability in indoor localization techniques are performed. Although mathematic average methods can reduce variability, it is very difficult to eliminate the calculation error of the tag-reader distance. Nevertheless, in this preliminary analysis the mathematical method using the average of RSSI measures present a constant error pattern, along distances, ranged between 0 and 8 m not too big for a room localization method.

## Keywords

Indoor localization • Medical emergency • Bluetooth low energy

## 1 Introduction

In recent years, overcrowding at hospital emergency departments is a common problem in many countries in the world. Because of limited resources, both human and technological, the medical staff often could lose a lot of time to look in the various rooms of the ward for devices that are necessary for therapies [1, 2]. This situation can lead to reduce efficiency in the Emergency Room, especially when physicians have to look for important devices, like defibrillators and ventilators. Therefore, knowing the exact position of devices is useful for health monitoring, in particular, during emergency situations.

In recent years, many technologies have been developed for internal tracking, mainly based on infrared (IR), radio frequency (RF) or ultrasound (US) [3, 4]. Among this, RF systems are especially attractive for actual widespread availability of wireless network infrastructure existing and their facility of positioning and implementation. In particular, the Bluetooth technology is a wireless technology very popular, because most of mobile devices have already an integrated Bluetooth module. Advantages of this technology are high security, low cost, low power required and small size [5, 6]. Between most recent proposals, it is very interesting iBeacon technology. This system uses Bluetooth Low Energy (BLE) technology implemented by Apple that acts as an emitter for transmitting continuously Bluetooth signals.

In general, the localization systems based on RF, as Bluetooth, is composed of two main components: a tag and a reader [7, 8]. Readers receive data transmitted by tags through a defined radio frequency using a precise protocol to transmit and receive information. Tags are assigned to objects to be monitored, while readers are installed in the

---

J. Regolini · F. Frosini · E. Ciagli (✉) · A. Benassi · D. Cocchi  
R. Miniati · P. Tortoli  
Department of Information Engineering, University of Florence,  
Florence, Italy  
e-mail: elena.ciagli@unifi.it

A. Belardinelli  
Department of Innovation, Quality and Control, Careggi Teaching  
Hospital, Florence, Italy

area where it requires the recognition. Through tags, close readers, whose positions are known and fixed, perceive objects involved. In this way, it is possible to determine positions of objects through different methods.

However, due to the complexity of the interior environments, the development of a localization method is always accompanied by a series of problems, like the presence of obstacles—such as walls, equipment and people—along the direction of propagation of signals. For this reason, many researchers have spent energies for the development of robust algorithms to improve the location accuracy.

In the present study, it is decided to use Beacon devices such as tags, to search a hypothetical electro-medical device, while Raspberry Pi implemented with appropriate Bluetooth 4.0 modules are used as readers for tag detection.

To increase efficiency in the Emergency Room, the goal of this research is to lay the groundwork for a future implementation of a tracking system. Specifically, in this study it is evaluated three mathematical average methods to assess the reduction of variability suffered by indoor localization systems. In particular, tags positions can be achieved through two steps [9]:

- To select and detect some parameters of signals between tags and readers for measuring of distances;
- to assess the position of objects using appropriate computational algorithms.

The three main methods used are based on timing, angles or intensity of received signals (RSSI) [10]. Regarding parameters involved in the first phase of location process the following method have been used [11–13].

In Time Of Arrival method (TOA), the distance  $D$  between tag and reader is calculated by the time of transmission  $T$ , note  $C$  the speed of the signal.

One of the disadvantages of TOA technique is that require a precise time synchronization of all devices. Therefore, measurements need the presence of additional server, which increases the cost of the system.

Time Difference-of-Arrival (TDOA) uses two different types of transmission signals that differ in speed ( $C1$  and  $C2$ ). The difference between  $T1$  and  $T2$  of the transmission timing of the two signals is used to assess the distance  $D$  of the tag. In TDOA method, only readers require time synchronization. This approach is quite suitable in environments where the number of sensors is reduced.

Round Trip Time (RTT) method has been developed with the aim to eliminate the need of readers synchronization of the TOA method. In the RTT method, the distance is calculated using  $T_{rt}$ , that indicates the amount of time required for a signal to be transmitted from one node to another and vice versa,  $\Delta T$ , that is the known time delay necessary for

the receiving node for retransmitting the signal, and  $C$ , the speed of the signal. In this way, the measurement uses only a node to record transmission and arrival times, eliminating the need of synchronization. However, this method increases the complexity of the system. Furthermore, in RTT technology other uncertainty factors, such as noise, co-exist during the time of the measurement process.

The main method employing angular measurements is Angle-of-Arrival technique (AOA). This method is based on the fact that the tag or the reader is able to measure the angle of arrival of the transmission, for example with directional antennas or array of antennas. This method does not require any synchronization between schedules of various nodes. The principle behind the measurement AOA via antenna arrays following this: from the differences in arrival times of a signal input to the different antenna elements is possible to deduce the angulation of the transmission, given the geometry of the array of antennas. The main limitation of the AOA method is associated to its high sensitivity to environmental interference. This aspect that can make the internal localization process very difficult, especially when distances increase. Furthermore, antenna systems increase complexity and cost of the system.

In techniques based on the Received Signal Strength Index (RSSI), the distance is measured on the basis of the attenuation introduced by the propagation of the signal from the tag to the reader.

On the basis of this RSSI, several methods have been proposed to estimate the position of tag, and can be classified as parametric or non-parametric. Parametric methods are based on propagation models that link detected RSSI values with tag-reader distances. These models introduce a certain degree of simplification, which leads to a corresponding approximation. The most widely used mathematical model is the following:

$$\text{RSSI} = A - 10 * N * \log_{10}(D) \quad (1)$$

where  $A$  represents the value of the RSSI detected at 1 m, and  $N$  is the index of the signal attenuation due to the environment.

## 1.1 Methods for Position Calculation

On the basis of parameters measured in the first phase and known coordinates of readers, then it is possible to proceed to the second phase of the location and calculate the physical location of tags [14]. To proceed with this calculation, several algorithms have been developed, although those most commonly used are triangulation and trilateration techniques.

Triangulation algorithm could be selected when there was take AOA measurements. Unlike trilateration, in the triangulation technique the position of tags can be determined by the intersection of different pairs of lines, requiring only two-reference reader.

Trilateration algorithm uses three reference readers to calculate the physical location of tag. This method creates circles centred in the three readers whose radius is determined by the single reader-tag distance based on the signal parameters. On the basis of the coordinates of three reference nodes and the produced circumferences, it is possible to trace the coordinates of the tag by taking the centre of gravity of the triangle formed by the cords between the points of intersection of the three circles.

## 1.2 Methods for Reducing the Variability of Signals

Considering that RSSI measures present value fluctuations, it becomes impossible to determine a two-way relationship between RSSI and distance. This aspect makes difficult the direct use of the data recorded in triangulation and trilateration algorithms [15]. To improve the accuracy of localization is necessary to reduce the variability of the data, through the use of filters. The filters are mathematical methods used for the prediction of an unknown variable from some surveys carried out from the system. From this point of view, the most widely used method is mathematical average of the data.

## 2 Methods

### 2.1 Selected Methods for Study

In reference of analysis conducted on the literature and considering that the level of precision required can be hire as satisfactory if method is able to show us the room, or the corridor region, in which is positioned the device, it is selected an approach based on the evaluation of RSSI, detecting 45 measures each reader and using the model previously shown in Eq. (1) for the calculation of the distance between tag and reader, where the parameters  $A$  and  $N$  were obtained by autoregressive model based on measurements between 1 and 7 m between tags and readers.

It is initially made an analysis of performances of readers to understand the variability of measures taken. In particular, accuracy is defined as the mean of localization errors (difference between real distances and estimated distances with RSSI), while precision is evaluated by the standard deviation of localization errors.

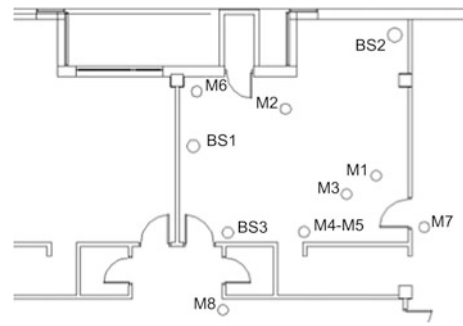


**Fig. 1** Map of readers (BS1, BS2, BS3) and 8 tag (M) positions

In result, it is passed to the application of three different types of media, to evaluate the reduction of variability:

- Average distance  $D_d$ , calculated from single distances  $D_{m-i}$  obtained by the  $RSSI_i$  of every measurement;
- Average distance  $D_R$ , calculated with  $RSSI_m$  that is equal to the average of the single  $RSSI_i$ ;
- Average distance  $D_{RC}$ , calculated with  $RSSI_{m-cmax}$  that is equal to the average of the three  $RSSI_{i-cmax}$  appearing several times during the detection (count max).

Performances of these models have been evaluated with relative error between real and estimated position, defined as error index (EI). Regarding analysis of Beacon tags, there are selected 8 different random positions of the tag (M), while holding the positions of the three Bluetooth readers (BS). The Fig. 1 shows the design of the experiment.

## 3 Results and Discussion

It exposes the results for the calibration phase of readers. For example, in Fig. 2 it is presented only one of the three devices. The calibration phase of the other devices is similar to this one.

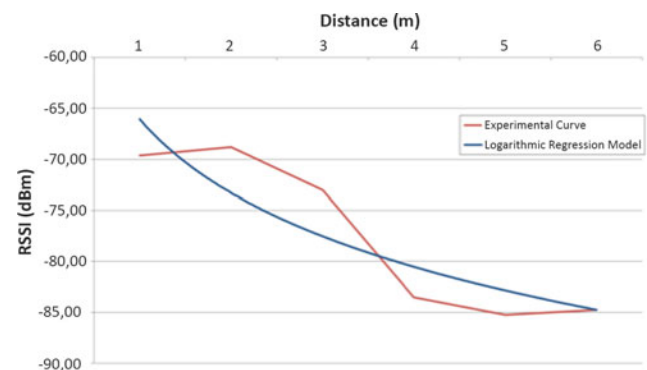


**Fig. 2** Calibration process of reader RS1, with the curve experimentally obtained (in red) and the curve extrapolated from the logarithmic regression model (in blue)



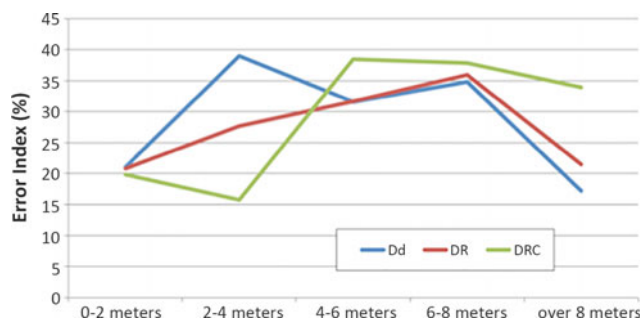


**Fig. 3** Performances of error index of readers referred with different distances from Beacon tag

From the curve obtained by logarithmic regression model, it is possible to get values of  $A$  and  $N$ , amounting to  $-59.01$  dBm and 2.23.

The effect of variability of the signal can be observed by analyzing the result of precision and accuracy for each player in each of the 8 measurements. The result is that each test is affected by low precision and accuracy, and this data became significantly worse with increasing of distance tag-reader distance and in presence of walls between tag and reader (M7–M8). Therefore, it is proven the absolute necessity of methods to counter this excessive uncertainty.

Turning to the application of the selected mathematical average methods, it can be observed that all methods present considerable error indices. Therefore, from EI it is difficult to establish the true superiority of one method over the others.

Going to group the measurements obtained according to the actual distance tag-reader (up to 2, 2.4, 4.6, 8.6 and over 8 m) and achieving the average of the errors obtained is presented in Fig. 3.

From this graph, it is possible to note that the method of calculation of the distance based on the average RSSI (proves to be the one with the most constant EI into the range in analysis ( $D_R$  mean value at 27.6 Vs. 28.8% of  $D_d$  and 29% with  $D_{RC}$ ).

## 4 Conclusions

The aim of this study is to find a localization method able to detect a technology with the precision of a room. This study shows the high variability of indoor localization system based on RSSI signal emitted from Beacon tags. To fix this problem, we study the effect of three mathematical averaged methods. From this analysis, it is emerged that method based on the calculation of the distance with the average RSSI present the more constant behavior of the error index. This

conclusion has a considerable importance, since it constitutes a factor of greater solidity of this method. Certainly, in the future, it is expected to also use other methods and more complex filters already used in localization systems, such as Kalman, Monte Carlo and Gaussian filters.

**Conflict of Interest** The authors declare that they have no conflict of interest.

## References

1. A. Redondi, M. Chirico, L. Borsani, M. Cesana, and M. Tagliasacchi, "An integrated system based on wireless sensor network for patient monitoring, localization and tracking", *Ad Hoc Networks*, vol. 11, 2013, pp. 39–53.
2. J. Wyffels, J.P. Goemaere, P. Verhoeve, P. Crombez, B. Nauwelaers, and L. De Strycker, "A novel indoor localization system for healthcare environments", *Computer-Based Medical Systems (CBMS), 25th International Symposium on*, 2012.
3. Z. Farid, R. Nordin, and M. Ismail, "Recent advances in wireless indoor localization techniques and system", *Journal of Computer Networks and Communications*, 2013.
4. E. Iadanza, F. Dori, R. Miniati, R. Bonaiuti, Patients tracking and identifying inside hospital: a multilayer method to plan an RFID solution. (2008) *Conference proceedings: Annual International Conference of the IEEE Engineering in Medicine and Biology Society. IEEE Engineering in Medicine and Biology Society. Conference*, pp. 1462–1465.
5. X. Lin, T. Ho, C. Fang, Z. Yen, B. Yang, and F. Lai, "A mobile indoor positioning system based on iBeacon technology", *Engineering in Medicine and Biology Society (EMBC), 37th Annual International Conference of the IEEE*, 2015.
6. S. Chai, R. An, and Z. Du, "An indoor positioning algorithm using Bluetooth Low Energy RSSI", *Advanced Material Science and Environmental Engineering, AMSEE International Conference on*, 2016.
7. W. Chen, H.H. Chang, T.H. Lin, P.C. Coen, L.K. Chen, S. J. Hwang, D.H.J. Yen, H.S. Yuan, and W.C. Chu, "Dynamic indoor localization based on active rfid for healthcare applications: a shape constraint approach", *Biomedical Engineering and Informatics, BMEI'09 2nd International Conference on*, 2009.
8. K. Kaemarungsi, R. Ranron, and P. Pongsoon, "Study of received signal strength indication in ZigBee location cluster for indoor localization", *Electrical Engineering/Electronics, Computer, Telecommunications and Information Technology (ECTI-CON), 10th International Conference on*, 2013.
9. D. Zhang, F. Xia, Z. Yang, L. Yao, and W. Zhao, "Localization technologies for indoor human tracking", *Future Information Technology (FutureTech), 5th International Conference on*, 2010.
10. S. Kajioaka, T. Mori, T. Uchiya, I. Takumi, and H. Matsuo, "Experiment of indoor position presumption based on RSSI of Bluetooth LE beacon", *Consumer Electronics (GCCE), IEEE 3rd Global Conference on*, 2014.
11. F. Gustafsson and F. Gunnarsson, "Positioning using time-difference of arrival measurements," in *2003 IEEE International Conference on Acoustics, Speech, and Signal Processing*, 2003. *Proceedings. (ICASSP '03)*, 2003, vol. 6, p. VI-553-6 vol. 6.

12. R. B. Ertel and J. H. Reed, "Angle and time of arrival statistics for circular and elliptical scattering models," *IEEE Journal on Selected Areas in Communications*, vol. 17, no. 11, pp. 1829–1840, Nov. 1999.
13. M. Svecova, D. Kocur, and R. Zetik, "Object localization using round trip propagation time measurements," in *2008 18th International Conference Radioelektronika*, 2008, pp. 1–4.
14. Y. Wang, X. Yang, Y. Zhao, Y. Liu, and L. Cuthbert, "Bluetooth positioning using RSSI and triangulation methods", *Consumer Communications and Networking Conference (CCNC)*, 2013.
15. E. Dahlgren, and H. Mahmood, "Evaluation of indoor positioning based on Bluetooth Smart technology", *Master of Science Thesis*, Chalmers University of Technology, Goteborg, Sweden, 2014.

# The Influence of the Voice Acquisition Method to the Mental Health State Estimation Based on Vocal Analysis

Yasuhiro Omiya, Naoki Hagiwara, Shuji Shinohara, Mitsuteru Nakamura, Masakazu Higuchi, Shunji Mitsuyoshi, Eiji Takayama, and Shinichi Tokuno

## Abstract

Mental health disorders have become a social problem, and countermeasures are thus required. Previously, the authors developed the MIMOSYS (Mind Monitoring System) algorithm to evaluate an individual's mental health state using their voice. An individual's mental health state is detected using aspects of emotions that are present in their voice; however, since emotions change subtly, influence to emotions will be concerned owing to voice acquisition methods such as a natural conversation with someone else or reading fixed phrases. The aim of this research was to evaluate the influence of the type of voice acquisition method on the estimation of emotion and mental health state using the vocal analysis in MIMOSYS. In the experiments, we collected emotions and MIMOSYS analysis results from voice recordings during calls and during readings of fixed phrases from the application for over two weeks. In addition, the Beck's Depression Inventory (BDI) test was used to evaluate participants' subjective depression levels at the beginning of the experiment. In the evaluation, we analyzed recordings of calls and readings of fixed phrases for the participants in the normal range of the BDI test. Results indicated that the expression of emotions was suppressed in the recordings of readings of fixed phrases when

compared to the recordings of calls, and the analysis result by MIMOSYS tended to be lower. Consequently, when measuring an individual's mental health state from their voice, it may be necessary to match the type of voice acquisition methods or correct the estimations according to acquisition method.

## Keywords

Vocal analysis • Voice • Mental health care

## 1 Introduction

Mental health disorders have become a worldwide social problem. To deal with this issue, we need screening methods that can detect depression and stress. Self-administered psychological tests [1, 2] have been used as traditional methods to do so, and biomarkers [3, 4] have been used as experimental methods. However, these methods are associated with various problems, including reporting bias, inspection costs, analysis time, high-cost burdens, and requirements of dedicated devices on the examinees.

The authors have been engaged in the development of a method that estimates stress and depression using vocal data [5]. In doing so, we developed a core technology, MIMOSYS (Mind Monitoring System) [6], which measures an individual's mental health state from their voice. We also implemented MIMOSYS on the Android OS smartphone. An individual's mental health state is detected from aspects of their emotions that are present in their voice; however, emotions can change subtly, and influencing emotions will be an issue owing to voice acquisition methods such as having a natural conversation with someone or reading a fixed phrase without having someone with whom to talk. In this paper, our aim was to evaluate the influence of the type of voice acquisition method on the ability of MIMOSYS to estimate an individual's emotion and mental health state using their voice.

Y. Omiya (✉) · N. Hagiwara  
PST Inc., Kanagawa, Japan  
e-mail: omiya@medical-pst.com

Y. Omiya · S. Shinohara · M. Nakamura · M. Higuchi  
S. Mitsuyoshi · S. Tokuno  
The University of Tokyo, Tokyo, Japan

E. Takayama  
Asahi University, Gifu, Japan

## 2 Materials and Methods

### 2.1 Vocal Analysis

We used the Sensibility Technology (ST) software (AGI Inc., Tokyo, Japan) [7–9], which measures a variety of emotions, including “calmness,” “anger,” “joy,” and “sorrow.” The amplitude of each emotion detected in the input voice is an output value that is rated as an integer value from zero to ten. The intensity of “excitement” is also an output value that is calculated and rated as an integer value from one to ten.

In addition, we used the MIMOSYS software, which estimates mental health status using emotions present in the voice. Based on the aspects of emotions present in the voice, MIMOSYS calculates “vitality,” which is a short-term mental health indicator. Vitality is an output value that is rated as a real number value from zero to one. The recording format was a linear pulse-code modulation, the sampling frequency was 11,025 Hz, and the quantization bit rate was set to 16 bits. MIMOSYS is an application that operates on a smartphone, and it automatically records and analyzes voices during telephone call recordings and displays the results. It is also possible to analyze voice recordings manually. In addition to “vitality,” MIMOSYS calculates “mental activity,” which is a medium- and long-term mental health indicator, as an index of mental health. These indices are output as real values from zero to one. The vocal analysis flow is shown in Fig. 1.

### 2.2 Beck’s Depression Inventory

The Beck’s Depression Inventory (BDI) test is widely used for screening depression and consists of 21 questions about how the participant has been feeling over the last few days, including the current day. Each question has four possible sets of answers. When the test is scored, a value from zero to

**Table 1** Categories for the BDI scores

BDI score	Level of depression
0–9	Minimal depression
10–18	Mild depression
19–29	Moderate depression
30–63	Severe depression

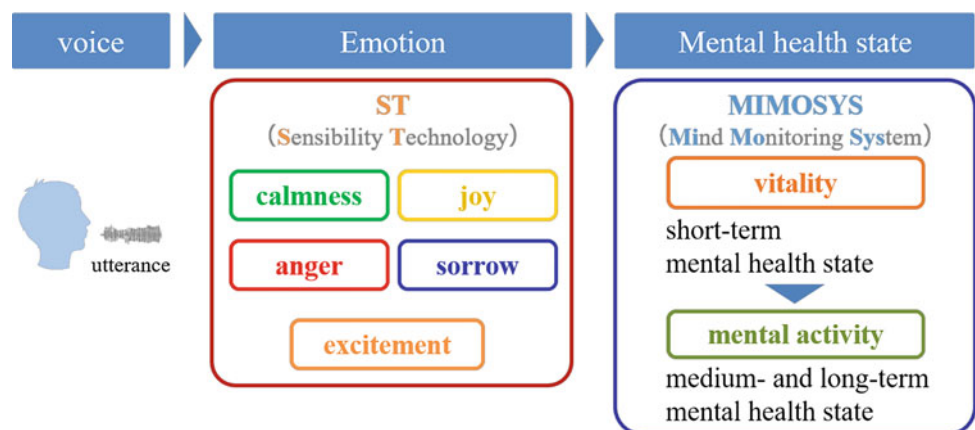
three is assigned for each answer, after which the total score is compared with the key to determine the severity of depression. The standard cut-off scores according to the Ref. [10] are shown in Table 1. In this research, participants who had a score of 9 or less were considered mentally healthy and were used in the study.

### 2.3 Experiment

Prior to this current research, we conducted a pilot examination that found a difference based on the type of voice acquisition method [11]. In this study, our goal was to verify that difference by using data from a larger sample of participants.

In the experiment, we collected BDI scores and vocal analysis results using the application installed on an Android smartphone. The BDI test was incorporated into the MIMOSYS application and was completed when the application was first launched at the start of the experiment. Moreover, we implemented two ways to obtain the participants’ voices over the smartphone: the user’s voice reading a variety of sentences (hereinafter referred to as fixed phrase recordings) and their voice while talking on the phone (hereinafter referred to as call recordings). The fixed phrases that the participants read included 17 phrases. Additionally, to verify differences in the voice between the fixed phrase recordings and call recordings, information about which method was used to obtain the recordings was included. The application erased the recorded voice file after the analysis,

**Fig. 1** Vocal analysis flow by ST and MIMOSYS



but the analysis results and user information were sent over a network to be collected and stored in a database. All the analysis results were obtained via this database.

The experiment was conducted with the cooperation of various companies, organizations, and volunteers. Participants were assigned to one of three groups and completed either one or both of the voice acquisition methods, including the call recordings or fixed phrase recordings. This research was approved by the Research Ethics Review Committee and carried out with the participants' consent.

## 2.4 Analysis of Data

The results, including the emotions, vitality, and mental activity obtained by the MIMOSYS application, were exported into a csv file via the database. We then excluded participants who had abnormal BDI scores or a low recording count (less than six recordings). In the analysis, we first calculated the mean values of the five emotional indices and vitality for each participant for each recording method. We then calculated the overall mean values for each recording method. We used Microsoft Excel functions and analysis tools to analyze the data.

## 3 Results

Participants' voices were recorded and obtained in the experiment via two different voice acquisition methods. Group A conducted only call recordings, group B conducted only fixed phrase recordings, and group C conducted both. In addition, there was no duplication of participants between groups. The number of participants with valid data used in the analysis from each group is shown in Table 2.

**Table 2** The number of participants with valid data

Group	Call recordings	Group	Fixed phrase recordings
A	294	A	–
B	–	B	843
C	29	C	29

## 3.1 Effect of the Recording Method

We analyzed and compared the mean values of the five emotional indices and vitality for each participant for each recording method. The mean values for calmness, anger, joy, sorrow, excitement, and vitality are shown in Table 3.

The t-test results revealed that there were significant differences between the mean values in all of the indices for call recordings and fixed phrase recordings for participants in group C. Moreover, as shown in Fig. 2, the t-test results revealed that there were significant differences in all of the indices between the mean values for call recordings and fixed phrase recordings all together.

## 4 Discussion

As a result of comparing the emotional indices and vitality obtained by analyzing the fixed phrase and the call respectively, the fixed phrase tended to have a lower value. Past research found that although the execution rate declines with fixed phrase recording with the passage of time, on the other hand, the frequency of telephone use has declined [12]. Therefore, for useful monitoring, it is necessary to use both in combination, but it is necessary to correct both results. In fixed phrase recordings, it is necessary to compare differences between the phrases and to search for more effective phrases. On the other hand, in call recordings, natural

**Table 3** The mean values of the emotional indices and vitality

	Calmness	Anger	Joy	Sorrow	Excitement	Vitality
<i>Call recordings</i>						
A	4.58 ± 0.74	1.56 ± 0.37	2.18 ± 0.58	1.68 ± 0.45	3.78 ± 1.00	0.49 ± 0.10
B	–	–	–	–	–	–
C	4.76 ± 0.89	1.48 ± 0.39	2.00 ± 0.68	1.76 ± 0.34	3.48 ± 1.07	0.47 ± 0.08
Total (A + C)	4.60 ± 0.75	1.56 ± 0.37	2.16 ± 0.59	1.68 ± 0.44	3.75 ± 1.01	0.49 ± 0.10
<i>Fixed phrase recordings</i>						
A	–	–	–	–	–	–
B	5.09 ± 0.94	1.49 ± 0.44	1.08 ± 0.59	2.34 ± 0.53	2.54 ± 0.63	0.31 ± 0.09
C	5.52 ± 1.02	1.25 ± 0.41	1.16 ± 0.69	2.07 ± 0.67	2.77 ± 1.12	0.36 ± 0.12
Total (B + C)	5.10 ± 0.94	1.49 ± 0.44	1.08 ± 0.60	2.33 ± 0.54	2.55 ± 0.65	0.31 ± 0.09

Note Mean ± standard deviation

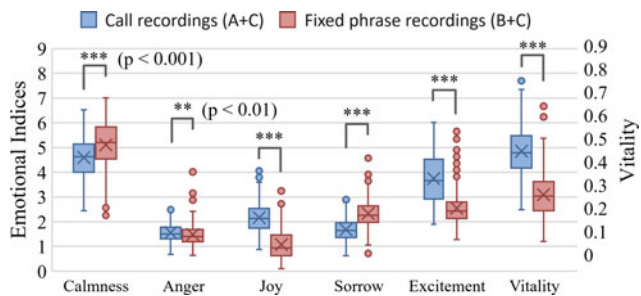


**Fig. 2** Comparison of the results of emotional indices and vitality

conversation depends on the communication content and partner. Thus, this research is limited. We are currently working on a project that directly measures an individual's mental state from voice characteristics other than emotions [13]. Combined with these indicators, it may be possible to adjust the results between a reading voice and conversation voice.

## 5 Conclusion

In this paper, we evaluated the influence of the type of voice acquisition method on the estimation of an individual's emotions and mental health state by MIMOSYS. We analyzed recordings of participants' call voice and recordings of participants' reading voice for the participants in the normal range, as measured by the BDI test. The results indicated that the expression of emotions was suppressed in the fixed phrase reading recordings when compared to the call recordings, and the analysis result by MIMOSYS tended to be lower. Consequently, when measuring an individual's mental health state using their voice, it is suggested that it was necessary to take measures such as matching voice acquisition methods or correcting estimated result by recording method.

**Conflict of Interest** Department of Voice Analysis of Pathophysiology, Graduate School of Medicine, The University of Tokyo was the University-Community Relations Projects funded by PST Inc.

## References

- Goldberg, D., Hillier, V.: A scaled version of the General Health Questionnaire. *Psychological Medicine* 9(1), 139–145 (1979).
- Beck, A.T., Ward, C.H., Mendelson, M., Mock, J., Erbaugh, J.: An Inventory for Measuring Depression. *Arch Gen Psychiatry* 4, 561–571 (1961).
- Ito, Y., Iida, T., Yamamura, Y., Teramura, M., Nakagami, Y., Kawai, K., Nagamura, Y., Teradaira, R.: Relationships between Salivary Melatonin Levels, Quality of Sleep, and Stress in Young Japanese Females. *International Journal of Tryptophan Research* 6 (Suppl 1), 75–85 (2013).
- Kawamura, N., Shinoda, K., Ohashi, Y., Ishikawa, T., Sato, H.: Biomarker for depression, method for measuring a biomarker for depression, computer program, and recording medium., U. S. Patent, US2015126623 (2015).
- Shinohara, S., Mitsuyoshi, S., Nakamura, M., Omiya, Y., Tsumatori, G., Tokuno, S.: Validity of a voice-based evaluation method for effectiveness of behavioral therapy. *Pervasive Computing Paradigms for Mental Health*, Springer International Publishing, 43–51 (2015).
- Shinohara, S., Nakamura, M., Omiya, Y., Hagiwara, N., Mitsuyoshi, S., Tokuno, S.: A mental health assessment method based on emotional level derived from voice, in preparation.
- Mitsuyoshi, S., Ren, F., Tanaka, Y., Kuroiwa, S.: Non-verbal voice emotion analysis system. *International Journal of Innovative Computing, Information and Control*. 2(4), 819–830 (2006).
- Mitsuyoshi, S., Tanaka, Y., Shibasaki K., Kato M., Minami T., Murata T.: Emotion voice analysis system connected to the human brain. In: *International Conference on Natural Language Processing and Knowledge Engineering*, 476–484 (2007).
- Mitsuyoshi, S.: Emotion recognizing method, sensibility creating method, device, and software. U. S. Patent, US20030182123 (2003).
- Beck, AT, Steer RA, Garbin MG J.: Psychometric properties of the Beck Depression Inventory Twenty-five years of evaluation. *Clinical Psychology Review* 8(1), 77–100 (1988).
- Hagiwara N., Omiya Y., Shinohara S., Nakamura M., Higuchi M., Mitsuyoshi S., Yasunaga H., Tokuno S.: Validity of Mind Monitoring System as a Mental Health Indicator using Voice. *Advances in Science, Technology and Engineering Systems Journal* 2(3), 338–344 (2017).
- Omiya Y., Hagiwara N., Takano T., Kirita T., Shinohara S., Nakamura M., Higuchi M., Mitsuyoshi S., Tokuno S.: Evaluation by difference of recording method in Mind Monitoring System using Voice. In: *Japanese Society for Medical and Biological Engineering Symposium 2017, Nagano* (2017). (in Japanese).
- Shinohara S., Omiya Y., Nakamura M., Hagiwara N., Higuchi M., Mitsuyoshi S., Tokuno S.: Multilingual evaluation of voice disability index using pitch rate. *Advances in Science, Technology and Engineering Systems Journal* 2(3), 765–772 (2017).



# Using Artificial Neural Network to Predict Functional Recovery of Patients Treated by Intravenous Thrombolysis in Acute Ischemic Stroke

Hung-Wen Chiu, Yu-Ting Huang, and Chun-An Cheng

## Abstract

In general, cerebrovascular diseases are composed of approximately 80% ischemic strokes. They are both expensive and time consuming while physicians take care of the acute ischemic stroke (AIS) patients. It is well-known that thrombolysis treatment in AIS patients can reduce disability and increase survival rate, however only one-half of patients have good outcomes. Therefore, we designed a functional recovery prediction model by artificial neural network (ANN) for AIS patients after intravenous thrombolysis to help make better clinical decisions. In this study, we retrospectively collected 157 AIS patients who received intravenous thrombolysis at a medical center in north Taiwan. The outcome defined Modified Rankin Scale  $\leq 2$  after three-months follow-up as favorable recovery. 80% data were selected for training this predictive ANN model and 20% data were used for validation. The performance of models is evaluated by Receiver Operating Characteristic (ROC) Curve Analysis. An ANN with 5 inputs and 6 neurons in hidden layer was obtained. The performance of this model was with accuracy 83.87% and the area under ROC curve 0.87. This results showed that this ANN model could achieve a high prediction accuracy for functional recovery evaluation. It is an important issue to predict prognosis of treatment for personalized medicine. Risk and benefit should always be balanced before any treatment is to be applied. The developed prediction models may help physicians to individually discuss and explain the likely recovery probability to patients and their families within short therapeutic time before thrombolysis treatment in the emergency room.

## Keywords

Ischemic stroke • Artificial Neural Network  
Decision support

## 1 Introduction

In general, approximately 80% of all cerebrovascular disease cases are ischemic strokes. The management of acute ischemic stroke (AIS) is both expensive and time consuming. Intravenous thrombolysis can increase the survival rate and reduce disability or length of hospital stay in patients with AIS [1–3]. Since some patients may have unfavorable outcomes, patients and families are concerned with the recovery probability before electing to undergo intravenous thrombolysis treatment. Hence, the intravenous thrombolysis rate is low in previous researches [4, 5]. To increase the thrombolysis rate and reducing the in-hospital delay, a useful tool is required to help for early treatment decision-making and as the bridge between the doctor and patient for communication. The majority of previous studies classify only well or poor recovery situations without quantifying the degree of recovery, and thus, physicians are not able to use recovery probability data to persuade AIS patients and relatives to consider intravenous thrombolysis during short therapeutic windows.

Younger age and lower National Institute of Health Stroke Scale (NIHSS) score are associated with a better level of recovery [2]. The DRAGON score [6] is a functional prediction system based on immediate pretreatment parameters that was established to predict good (modified Rankin Scale [mRS]: 0–2) or poor recovery (mRS: 5–6) with acceptable sensitivity and specificity for acute ischemia stroke patients; however, the patients with an mRS of 3 and 4 were missing from the evaluation [6]. The Stroke Prognostication using Age and NIH Stroke Scale (SPAN)-100 index evaluates age and the NIHSS score of neurological impairment to predict the clinical response and risk of

H.-W. Chiu (✉) · Y.-T. Huang  
Graduate Institute of Biomedical Informatics, Taipei Medical University, Taipei, Taiwan  
e-mail: hwchiu@tmu.edu.tw

C.-A. Cheng  
Department of Neurology, Tri-Service General Hospital, National Defense Medical Center, Taipei, Taiwan

haemorrhagic complications after thrombolysis in AIS patients, but it has limited efficacy for recovery prediction [7]. Hence, we need to develop a tool for functional recovery probability assessment so that stroke treatment physicians may be able to estimate the likelihood of functional recovery before recommending intravenous thrombolysis during the early stage of AIS.

Artificial Neural Networks (ANN) are widely used for prediction of disease prognosis and support medical decision making [8, 9]. ANN uses machine learning algorithms to get the relations between features (independent variables) and outputs (dependent outcomes) and forms a model for further prediction. ANN outperforms the traditional statistical model in some aspects especially in nonlinear problem and multiple output system. In this study, we attempted applying ANN to create a model to predict the functional recovery of patients treated by intravenous thrombolysis in acute ischemic stroke.

## 2 Materials and Methods

### 2.1 Data Collection

In this study, we collected the retrospective data of 157 AIS patients who received intravenous thrombolysis treatment without contraindications within 3 h of stroke symptom onset from January 1, 2011 to December 31, 2016 in the Tri-service General Hospital according to the Taiwan Stroke Association guidelines. The Tri-service General Hospital is a tertiary medical center and the Armed Taoyuan Hospital is a

community hospital in northern Taiwan. The study was approved by the Institutional Review Board of the Tri-Service General Hospital.

The input feature variables of ANN model including age, NIHSS score measured at the emergency room within 3 h, gender, onset of treatment time (OTT), estimated glomerular filtration rate (estimated GFR), internal carotid artery occlusion, hypertension (blood pressure more than 140/90 mmHg or was previously receiving antihypertensive therapy), diabetes mellitus (fasting blood sugar more than 126 mg/dl at two readings or was previously taking anti-hyperglycaemic agents), previous stroke, coronary artery disease, atrial fibrillation, anaemia (haemoglobin <13 mg/dl in males and <12 mg/dl in females) were collected. In outcome of ANN model, mRS was adopted to evaluate the stroke recovery situation; an mRS  $\leq 2$  within 3 months after thrombolysis treatment was defined as functional recovery (recovery group). The others were grouped as poor.

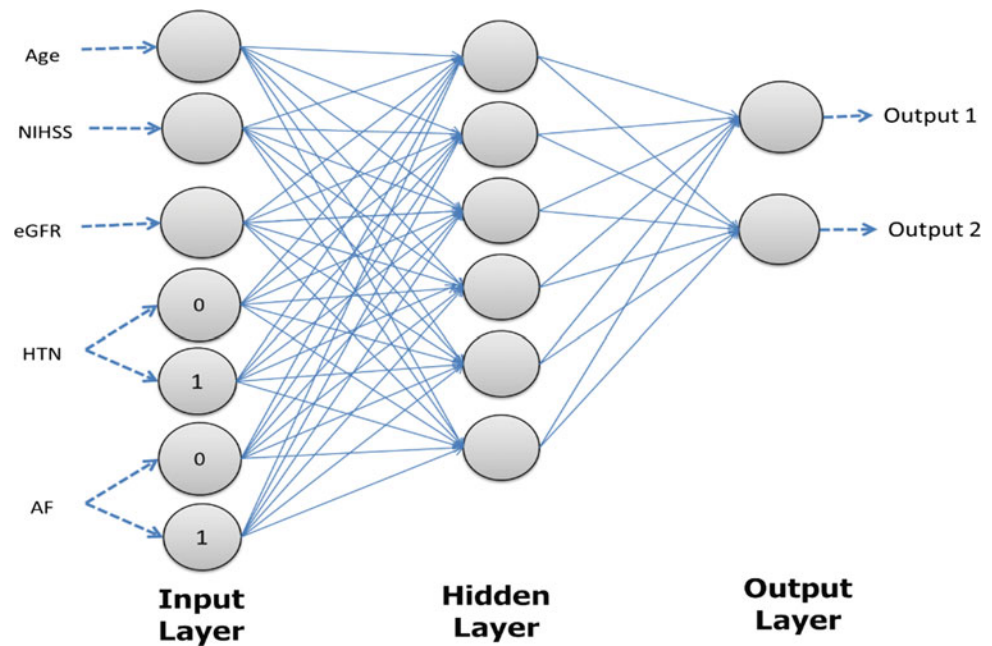
### 2.2 ANN Model Construction and Evaluation

The ANN model was constructed by Statistica Academic13 with 80% patients (125 cases) selected randomly as training set and remained 20% patients (32 cases) for validation. The structure of ANN is multiple layer perceptron (MLP) with one hidden layer. The number of neurons and activation function of hidden layer was selected by a trial-and-error procedure embedded in software to get acceptable models. Five input features (age, NIHSS score, estimated GFR,

**Table 1** Patient characteristics between two groups. Continuous values (mean  $\pm$  std) were tested for significance ( $p < 0.05$  marked with \*) with t-test and the categorical variables were tested by Chi-squared test

	Poor (75)	Recovery (82)	<i>p</i> -value
Age	66.6 $\pm$ 10.3	59.7 $\pm$ 13.0	<0.0001*
NIHSS score	17.7 $\pm$ 4.5	13.3 $\pm$ 5.3	<0.0001*
Hemoglobin	14.0 $\pm$ 1.7	14.0 $\pm$ 1.8	0.98
Onset of treatment time	132.1 $\pm$ 34.3	124.8 $\pm$ 43.6	0.25
Estimated GFR	79.6 $\pm$ 26.4	87.2 $\pm$ 31.8	0.09
Gender (Male)	45 (60.0%)	52 (63.4%)	0.66
ICA occlusion	11 (14.7%)	8 (9.8%)	0.79
Hypertension	57 (76.0%)	48 (58.5%)	0.02*
Diabetes mellitus	18 (10.7%)	12 (14.6%)	0.14
Previous stroke	10 (13.3%)	16 (19.5%)	0.29
Hyperlipidemia	47 (62.7%)	61 (81.7%)	0.11
Coronary artery disease	18 (24.0%)	14 (17.1%)	0.28
Atrial fibrillation	37 (49.3%)	23 (28.0%)	0.006*
Anemia	7 (9.3%)	8 (9.8%)	0.93

**Fig. 1** The structure of the ANN created in this study (MLP 7-6-2) with 6 neurons in hidden layer. NIHSS = National Institute of Health Stroke Scale, eGFR = estimated GFR, HTN = hypertension, AF = atrial fibrillation



hypertension, atrial fibrillation) were selected by logistic regression method. Total accuracy and area under receiver operating characteristic (ROC) curve are used to present the performance of the constructed model.

### 3 Results

Table 1 showed the statistic test results of features candidates applied to create the predictive model. The results revealed that there were significant different in age, NIHSS score, hypertension and atrial fibrillation between the poor and recovery groups.

The ANN models were trained with different structures, among them a model with better performance was chosen as the predictive model for functional recovery treated by intravenous thrombolysis. Figure 1 showed the structure of this ANN model (MLP 7-6-2) with input features. The input eGFR is estimated GFR, HTN is hypertension and AF is atrial fibrillation. The categorical data HTN and AF are coded as dummy variables with 2 neurons. The prediction outcome data is recovery or poor also coded as dummy variable with 2 neurons in output layer. The accuracy of this model is 83.87% with validation set test. When setting recovery as positive condition, the sensitivity is 90.9% and the specificity 80.0% in validation. The arear under ROC curve is 0.869.

### 4 Conclusions and Discussion

The present study aimed to demonstrate the possibility of applying ANN predicting the outcome of recombinant tissue plasminogen activator (rt-PA) treatment in ischemic stroke patient. Our result revealed that this ANN model can achieve above 80% accuracy such that it can help physicians in informing and discussing treatment options with patients and their families. We hope this tool can efficiently shorten the time in communication between the medical members and patient's family. Therefore, a more confidence and quality of medical care can be expected. Because of our limited sample size, these results need to be further verified with a larger prospective study.

### References

1. Wardlaw, J.M., Murray, V., Berge, E., et al.: Recombinant tissue plasminogen activator for acute ischaemic stroke: an updated systematic review and meta-analysis. *Lancet* 379 (9834), 2364–2372 (2012).
2. Ifejika-Jones, N.L., Harun, N., Mohammed-Rajput, N.A., et al.: Thrombolysis with intravenous tissue plasminogen activator predicts a favorable discharge disposition in patients with acute ischemic stroke. *Stroke* 42(3), 700–704 (2011).
3. Hung, L.C., Hu, Y.H., Sung, S.F. Exploring the impact of intravenous thrombolysis on length of stay for acute ischemic

- stroke: a retrospective cohort study. *BMC health serv res* 15, 404 (2015).
4. Hsieh, C.Y., Chen, C.H., Chen, Y.C., et al. National survey of thrombolytic therapy for acute ischemic stroke in Taiwan 2003–2010. *J Stroke Cerebrovasc Dis* 22(8), e620–627 (2013).
  5. Alshekhlee, A., Mohammadi, A., Mehta, S., et al. Is thrombolysis safe in the elderly? Analysis of a national database. *Stroke* 41(10), 2259–2264 (2010).
  6. Strbian, D., Meretoja, A., Ahlhelm, F., et al. Predicting outcome of IV thrombolysis-treated ischemic stroke patients The DRAGON score. *Neurology* 78(6), 427–432 (2012).
  7. Saposnik, G., Guzik, A.K., Reeves, M., et al. Stroke Prognostication using Age and NIH Stroke Scale SPAN-100. *Neurology* 80(1), 21–28 (2013).
  8. Çelik, G., Baykan, Ö.K., Kara, Y., et al. Predicting 10-day mortality in patients with strokes using neural networks and multivariate statistical methods. *J Stroke Cerebrovasc Dis* 23(6), 1506–1512 (2014).
  9. Wu, C.F., Wu, Y.J., Liang, P.C., et al. Disease-free survival assessment by artificial neural networks for hepatocellular carcinoma patients after radiofrequency ablation. *J Formos Med Assoc* 116(10), 765–773 (2017).

# Estimation of the Heart Rate Variability Features via Recurrent Neural Networks

Mihaela Porumb<sup>✉</sup>, Rossana Castaldo<sup>✉</sup>, and Leandro Pecchia<sup>✉</sup>

## Abstract

Heart rate variability (HRV) analysis has increasingly become a promising marker for the assessment of the autonomic nervous system. The easy derivation of the HRV has determined its popularity, being successfully used in many research and clinical studies. However, the conventional HRV analysis is performed on 5 min ECG recordings which in e-health monitoring might be unsuitable, due to real-time requirements. Thus, the aim of this study is to evaluate the association between the raw ECG heartbeats and the HRV features to further reduce the number of heart beats required for the HRV estimation enabling real time monitoring. We propose a deep learning based system, specifically a recurrent neural network for the inference of two time domain HRV features: AVNN (the average of all the NN intervals) and IHR (instantaneous heart rate). The obtained results suggest that both AVNN and IHR can be accurately inferred from a shorter ECG interval of about 1 min, with a mean error of  $<5\%$  of the computed HRV features.

## Keywords

Heart rate variability • Long short-term memory (LSTM)

## 1 Introduction

Over the last decades heart rate variability (HRV) analysis has become a popular method for the assessment of the autonomous nervous system in diverse fields of research.

M. Porumb (✉) · R. Castaldo · L. Pecchia  
University of Warwick, Coventry, CV4 7AL, UK  
e-mail: m.porumb@warwick.ac.uk

R. Castaldo  
e-mail: r.castaldo@warwick.ac.uk

L. Pecchia  
e-mail: l.pecchia@warwick.ac.uk

Depressed HRV has been proven to be an independent predictor for several clinical outcomes, such as death in chronic congestive heart failure [1], myocardial infarction, mental stress detection [2], risk of accidental falls in hypertensive patients [3] and many other. HRV analysis attempts to assess cardiac autonomic regulation by quantifying the sinus rhythm variability [4], which is usually derived from the consecutive QRS intervals (RR) of the electrocardiogram (ECG).

The HRV features are usually divided into two categories: time-domain and frequency-domain measures [1]. Time-domain measures treat the normal sinus to normal sinus (NN) interval as an unordered set of intervals and employ different statistical methods to express the variance of such data. The frequency-domain measures perform a power spectral analysis of the ordered NN intervals and show how these NN intervals distributes as a function of frequency. Commonly, both time-domain and frequency features are computed using a long term (24-h) ECG recording, however recent studies have shown that some of these features can be reliably computed and used from shorter ECG recordings (less than 5 min). The HRV features computed from an ECG segment that is less than 15 and 5 min are often referred to as short-term and ultra-short HRV features, respectively [1]. The need for reducing the ECG monitoring period is crucial, especially for real-time applications where decisions are usually taken from the analysis of the most recent ECG beats. Shorter ECG recordings can be easily recorded without significant increase in healthcare costs using wearable devices and they can be easily translated in the out-patient clinical life. Thus, being able to reduce the ECG recording interval without compromising the analysis results represents an important step towards using the HRV analysis in real-time applications.

The aim of this study is to evaluate the association between the time and space representation of the heartbeats and some of the HRV features to further reduce the number of beats required for the HRV estimation. Recent studies

**Table 1** Some SHHS 5 min HRV features

Time-domain features	Frequency-domain features
AVNN (the average of all the NN intervals)	TOTPWR (total NN interval spectral power up to 0.4 Hz)
IHR (Mean value of instantaneous heart rate. For a given NN interval, the IHR is calculated as $60/NN$ )	HF (high frequency power: the NN interval spectral power between 0.15 and 0.4 Hz)
SDNN (the standard deviation of all NN intervals)	LF/HF ratio (the ratio of low to high frequency power).

[3, 5] performed both short and ultra-short term HRV analysis for the comparison of their prediction capability on different clinical outcomes. Instead, we are interested to find out whether the HRV features computed on a 5 min ECG can be inferred using a shorter ECG interval. In order to achieve this, we developed a framework based on deep learning methodologies that proved to be appropriate for learning time series representations in recent studies [6, 7].

## 1.1 Related Work

Deep learning methods have been successfully employed for different time series analysis tasks, for problems such as classification and time series forecasting. Recurrent neural networks (RNN) are capable of large scale learning as showed in recent studies, being used for speech recognition [8], language translation models [9], or mental stress classification based on ECG data [10], thus proved to be successful in learning temporal dependencies between the inputs.

However, a significant limitation of the simple RNN models which integrate state information over time is known as the vanishing or exploding gradient effects, both referring to the ability of RNNs to backpropagate an error signal through a long-range temporal interval. The RNN version, known as Long Short-Term Memory (LSTM), first proposed in [11], are recurrent modules which enable long-range learning. LSTM units consist of hidden states augmented with nonlinear mechanisms to allow a state to propagate without modification, be updated, or be reset, using simple learned gating functions. Thus, in this study we propose a LSTM based model for the HRV features inference.

## 2 Methods

### 2.1 Dataset Description

This study was carried out using the publicly available dataset from the Sleep Heart Health Study (SHHS) [12]. The SHHS is a multi-center cohort study implemented by the National Heart, Lung and Blood Institute (United States of America) to determine the cardiovascular problems of sleep-disordered breathing. Out of the total 6441 subjects

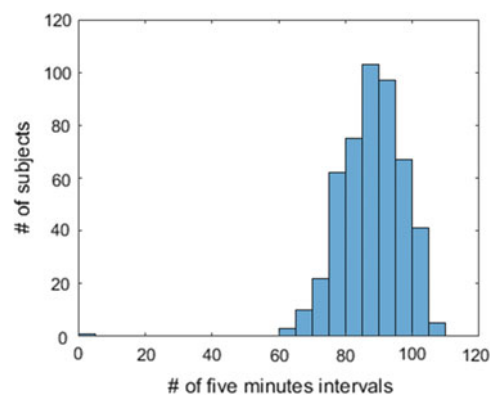
enrolled in the study, a subset of 500 subjects with high-quality ECG recordings (125-Hz sampling frequency) were selected for a sub-study to quantify the HRV by sleep stage. The computed 5-min HRV features for the 500 subjects together with the original ECG recordings were made available. Some of the available HRV features are summarize in Table 1.

The available data for each subject comprises a mean of 7 h of ECG recordings, which represent around 70 intervals of consecutive 5-min ECG segments together with the corresponding HRV features for each segment. A histogram presenting the distribution of the 5-min segments for the 500 subjects is presented in Fig. 1.

It has been previously shown that some of the HRV features are highly correlated with each other, and so for short term data only the time-domain measures of AVNN, SDNN, rMSSD, pNN10–pNN50 and the frequency-domain measures of total power, VLF power, LF power, HF power and LF/HF ratio can be reliably computed [4]. Considering all these observations, this study focuses only on prediction of 4 HRV features: AVNN, SDNN, HF and IHR.

### 2.2 ECG Preprocessing

The ECG recordings were segmented into consecutive 5-min excerpts with no overlap, followed by a QRS-complex detection algorithm similar to the one proposed in [13]. In order to filter the noisy segments from the actual beats an additional check was performed for each extracted beat.

**Fig. 1** Distribution of the 5 min ECG intervals for the 500 subjects



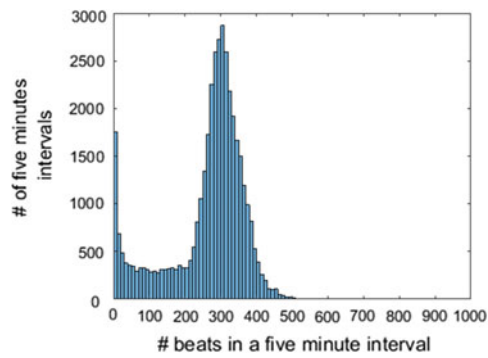


**Fig. 2** Distribution of the selected beats in the 5 min intervals

Specifically, it was checked that the minimum and the maximum values of each detected heartbeat lie close to the annotated R peak. In case this condition was violated, the beat was discarded from the list of beats that correspond to the 5-min interval. In addition to restricting the analysis to RR intervals  $<1.5$  and  $>0.75$  s, only the 5-min excerpts with at least 200 heart beats but no more than 400 were analyzed. The distribution of the beats in the 5-min intervals is presented in Fig. 2. The final number of filtered 5 min intervals used in the study is 29945, that were split into three different datasets for training (21945), validation (2718) and testing (2282) of the proposed model. The number of samples for each dataset were obtained by randomly splitting the subjects into these three different groups (400 subjects for training, 100 for validation and testing) then performing the above filtering. Thus, the proposed system was trained and tested on different subjects.

### 2.3 LSTM Architecture for the ECG Analysis

For the HRV features inference problem, the input is sequential consisting of consecutive heartbeats in a 5-min window. Thus, the aim in this work is to investigate whether LSTM-based networks are able to learn a sequence of ECG beats for inferring the ultra-short term HRV features. The intuition behind employing an LSTM-based model is that the time-varying beat dynamics are explained by the HRV features and in the same time RNNs are specialized in learning temporal dependencies.

The LSTM model employed in this study is shown in Fig. 3. The architecture consists of three parts: (1) data preprocessing, (2) aggregation of beats across time, sequence-learning, and (3) single/multiple stacked linear layers for performing a linear regression. Different number of beats extracted from each segment were considered as inputs to the LSTM cells, the tested values were: 250, 200 and 100, 50. The number of units in the LSTM cell was set to 60, the dense layer size was set to 100.

### 2.4 Training and Evaluation

For training the network, we used the mean squared error (MSE) as optimization objective, the learning rate was set to 0.01 and the used optimizer was the Adam optimizer [14]. The batch size was set to 100. Furthermore, we used dropout with probability 0.5 for all cells and an early stopping criterion based on the minimum MSE obtained on the

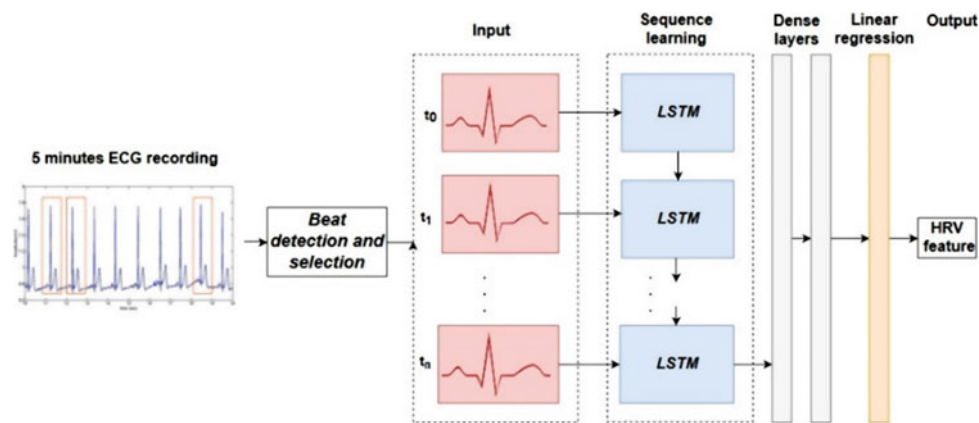


**Fig. 3** The LSTM architecture used for HRV feature regression

validation dataset. We trained the model for a maximum number of 15,000 steps that correspond to about 68 epochs.

We evaluated the regression performance of the proposed LSTM model on the SHHS dataset. The regression performance was assessed using multiple measures: the MSE, median absolute error (MedAE), mean absolute error (MAE), the Pearson correlation coefficient (R) between the predictions and the correct HRV values and for measuring the agreement we used the Bland-Altman plot [15].

### 3 Results

The regression results obtained by employing the proposed LSTM architecture, using a maximum number of 250 time steps, for the selected four HRV features are presented in Table 2. Table 3 shows the regression results for the AVNN and IHR variables that could be predicted with a satisfactory error, as shown in Table 2, but using less time steps: 200, 100 and 50. The results were obtained on the test dataset, after training the model for the maximum number of epochs. The results for the early stopping criteria are not shown here as they are very similar to the presented ones.

The number of samples that are predicted correctly on the test dataset within an error range of 5% of 10% of the correct value are presented in Table 4.

### 4 Discussion

The results presented in Sect. 3 indicate that the aggregation of beats across time using and LSTM network is effective for the HRV features estimation that are AVNN and IHR. The prediction errors for the AVNN are between 5 and 6% when using 250 down to 50 beats for a 5 min ECG segment, which for AVNN is less than the known measurement error <10% [4]. This implies that the AVNN can be predicted with an average error of 5% and if this satisfactory for the study then the proposed method can be used to infer the AVNN value by using around 50 ECG beats (<1 min ECG), in contrast to a 5 min segment. The IHR was predicted with less than 5% mean error even when using only 50 time steps. Figures 4 and 5 present the errors distribution between the computed HRV feature and the predicted one. It can be observed that for IHR the variance of the errors distribution is smaller than for AVNN and the peak of the distribution lies very close to 0, which represent a perfect prediction. Figures 6 and 7 present another view on the agreement between the measurement and the prediction, revealing that the majority of the points lie within  $\pm 1.96$  std of the mean difference for both of the variables.

We developed and evaluated a deep learning model employing an LSTM network for the HRV features inference based on the raw ECG signal. We investigated the

**Table 2** Test dataset LSTM regression results corresponding to four HRV features: AVNN, SDNN, HF and IHR for 250 time steps (250 input beats)

Variable	MSE	MedAE	Correlation (R)	MAE/Mean value (%)
AVNN	3951	37.58 ms	0.843	48.27 ms/953.42 ms (5%)
SDNN	615.5	13 ms	0.603	17.55 ms/52.1 ms (33.6%)
HF	163.3	311 ms <sup>2</sup>	0.04	552.9 ms <sup>2</sup> /593.5 ms <sup>2</sup> (93.2%)
IHR	13.4	2.09 bpm	0.89	2.71 bpm/63.86 bpm (4.2%)

**Table 3** Test dataset—LSTM results obtained for AVNN and IHR features considering different number of time steps

# beat	AVNN				IHR			
	MSE	MedAE (ms)	R	MAE (ms) (% of mean)	MSE	MedAE (bpm)	R	MAE [bpm] (% of mean)
200	4743	39.69	0.79	51.8 (5.4%)	15.4	2.268	0.87	2.95 (4.6%)
100	4728	41.43	0.8	52.3 (5.48%)	22.61	2.51	0.80	3.34 (5.2%)
50	5437	46.55	0.78	57.04 (5.9%)	21.4	2.76	0.81	3.49 (5.4%)

**Table 4** # of correct predictions for AVNN and IHR using of 5 and 10% error threshold

Variable	# of correct predictions out of a total of 2718	
	5% error	10% error
AVNN	1624 (59.7%)	2387 (87.82%)
IHR	1866 (68.6%)	2493 (91.72%)

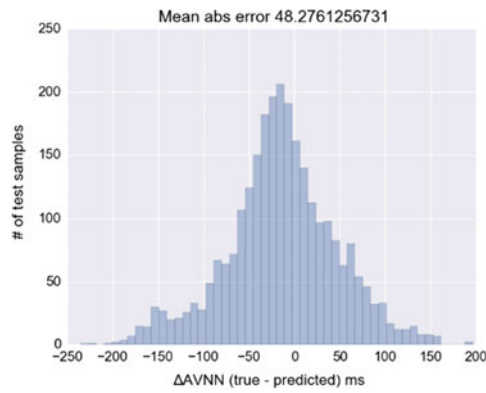


**Fig. 4** Distribution plot of the error between computed and predicted AVNN

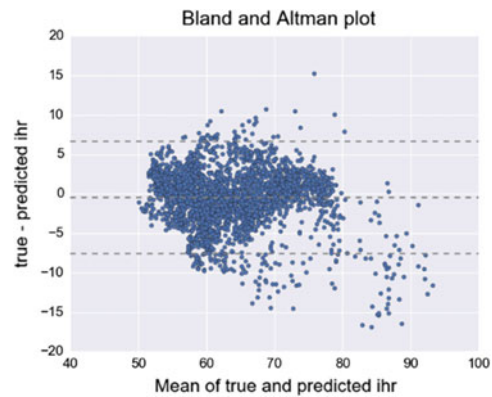


**Fig. 7** Bland Altman plot for the IHR on the test dataset

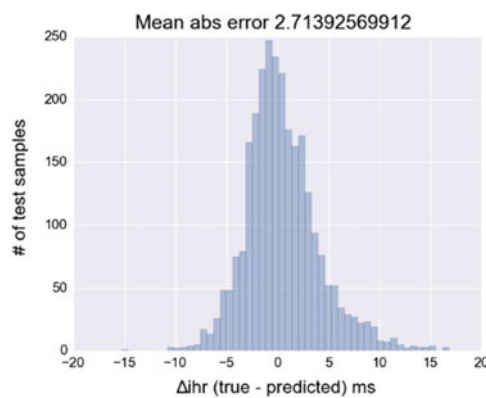


**Fig. 5** Distribution plot of the error between computed and predicted IHR

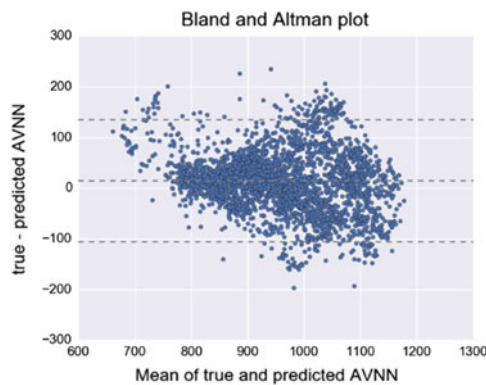


**Fig. 6** Bland Altman plot for the AVNN on the test dataset

number of beats that are necessary to predict some of the time domain features with a satisfactory mean absolute error, and we showed that 50 beats are appropriate. However, changing the network architecture and cascading a CNN with the LSTM are interesting directions to be explored in the future.


**Conflict of Interest** The authors declare that they have no conflict of interest.

## References

1. T. F. of the E. S. of C. the N. A. S. of P. Electrophysiology, "Heart Rate Variability: Standards of Measurement, Physiological Interpretation, and Clinical Use," *Circulation*, vol. 93, no. 5, pp. 1043–1065, Mar. 1996.
2. R. Castaldo, W. Xu, P. Melillo, L. Pecchia, L. Santamaria, and C. James, "Detection of mental stress due to oral academic examination via ultra-short-term HRV analysis," *Conf. Proc. Annu. Int. Conf. IEEE Eng. Med. Biol. Soc. IEEE Eng. Med. Biol. Soc. Annu. Conf.*, vol. 2016, pp. 3805–3808, 2016.
3. R. Castaldo, P. Melillo, R. Izzo, N. D. Luca, and L. Pecchia, "Fall Prediction in Hypertensive Patients via Short-Term HRV Analysis," *IEEE J. Biomed. Health Inform.*, vol. 21, no. 2, pp. 399–406, Mar. 2017.
4. J.-P. Niskanen, M. P. Tarvainen, P. O. Ranta-aho, and P. A. Karjalainen, "Software for advanced HRV analysis," *Comput. Methods Programs Biomed.*, pp. 73–81, Oct. 2004.
5. R. Castaldo, P. Melillo, and L. Pecchia, "Acute Mental Stress Detection via Ultra-short term HRV Analysis," in *World Congress on Medical Physics and Biomedical Engineering, June 7–12, 2015, Toronto, Canada*, 2015, pp. 1068–1071.
6. Z. C. Lipton, D. C. Kale, C. Elkan, and R. Wetzell, "Learning to diagnose with LSTM recurrent neural networks," *ArXiv Prepr. ArXiv151103677*, 2015.
7. S. Kiranyaz, T. Ince, and M. Gabbouj, "Real-Time Patient-Specific ECG Classification by 1-D Convolutional Neural Networks," *IEEE Trans. Biomed. Eng.*, pp. 664–675, Mar. 2016.
8. A. Graves, A. Mohamed, and G. Hinton, "Speech recognition with deep recurrent neural networks," 2013, pp. 6645–6649.
9. I. Sutskever, O. Vinyals, and Q. V. Le, "Sequence to sequence learning with neural networks," in *Advances in neural information processing systems*, 2014, pp. 3104–3112.
10. P. Bashivan, I. Rish, M. Yeasin, and N. Codella, "Learning Representations from EEG with Deep Recurrent-Convolutional Neural Networks," *ArXiv151106448 Cs*, Nov. 2015.
11. S. Hochreiter and J. Schmidhuber, "Long Short-Term Memory," *Neural Comput.*, vol. 9, no. 8, pp. 1735–1780, Nov. 1997.

12. D. A. Dean *et al.*, “Scaling Up Scientific Discovery in Sleep Medicine: The National Sleep Research Resource,” *Sleep*, vol. 39, no. 5, pp. 1151–1164, May 2016.
13. S. Yazdani, S. Fallet, and J.-M. Vesin, “A Novel Short-term Event Extraction Algorithm for Biomedical Signals,” *IEEE Trans. Biomed. Eng.*, Jun. 2017.
14. D. P. Kingma and J. Ba, “Adam: A Method for Stochastic Optimization,” *ArXiv14126980 Cs*, Dec. 2014.
15. J. M. Bland and D. G. Altman, “Statistical methods for assessing agreement between two methods of clinical measurement,” *Lancet Lond. Engl.*, pp. 307–310, Feb. 1986.

# Study on Non-contact Heart Beat Measurement Method by Using Depth Sensor

Hirooki Aoki , Atsushi Suzuki, and Tsuyoshi Shiga

## Abstract

For the purpose of simple observation of the mechanical phenomenon of the heart, we propose a new non-contact heartbeat measurement using a depth sensor. The depth sensor is an image sensor applying infrared light projection, and by using this sensor it is possible to calculate the three dimensional shape of the chest. In addition, it is possible to measure minute displacement appearing on the body surface by heartbeat. By visualizing the distribution of shape change using computer graphics, visualization of the heart beat is realized. Since the method is non-contact measurement, it does not prevent simultaneous measurement with the electrocardiogram. Therefore, it can be expected to be used as a means for simultaneously observing mechanical and electric phenomena of the heart. Simultaneous measurement using the method and electrocardiogram was performed. As a result of the measurement of three subjects (two males in 20 s and one male in 40 s), it was confirmed that the peak interval of the waveforms obtained by the two methods shows high consistency. The difference between the two peak intervals was less than 0.04 s. In the measurement, subjects stopped respiration, by applying the filtering process, it is also possible to detect the heartbeat waveform during breathing. During respiration, fluctuations are included in the measured waveform. In the simultaneous measurement of the two methods, the difference in the peak intervals is less than 0.05 s. This value is slightly larger than when breathing is stopped. In addition, as a result of the visualization of heart beat, the phase of vibrations by the heartbeat is different at each position on the chest surface. Specifically, a phase lag occurred upward direction from the abdominal, and it is

visible by animation. This result suggests that the observation of the mechanical phenomenon of the heart may be realized by the method.

## Keywords

Heartbeat measurement • Non-contact measurement  
Depth sensor

## 1 Introduction

Conventionally, the time series analysis of the heartbeat was performed only on the electric phenomenon of the heart by the electrocardiogram. It is considered clinically difficult to treat the mechanical phenomena (contraction/expansion mode) of the heart as clinical information.

For example, the actual condition has not been sufficiently clarified about the contraction/expansion style of the heart in which Excitation-Contraction Coupling (EC coupling) in the heart failure or ischemic heart is impaired. Although CT scan can be used as a method to know the mechanical phenomenon of the heart, frequent implementation is difficult due to the problem of damage from radiation.

We have clarified that cardiac pulsation can be detected without contact by measurement of shape change of the chest wall applying 3-dimensional image measurement by the active stereo method [1]. In addition, visualization of cardiac beat is performed by outputting minute changes in body surface shape caused by heartbeat as color images.

In our previous research, a commercially available LCD projector was used as the pattern light projecting means in the active stereo method. To reduce the size and weight of the system, we have studied replacing this LCD projector with a dot matrix pattern projector using a combination of a transmission type diffraction grating and an infrared laser light source. So far, we have applied this dot matrix pattern projector to non-contact respiration measurement [2].

H. Aoki (✉)  
Chitose Institute of Science and Technology, Chitose, 0668655,  
Japan  
e-mail: h-aoki@photon.chitose.ac.jp

A. Suzuki · T. Shiga  
Tokyo Women's Medical University, Tokyo, 1628666, Japan

As a result of applying it to the measurement of the prototype system, the following two problems to be solved were mentioned.

1. In the near-infrared image of the dot matrix pattern, since only the dot matrix pattern is imaged, it is difficult to confirm the state of the pattern projection by the monitor, and positioning is troublesome.
2. The dot matrix pattern has periodicity, so it is not a unique pattern. In order to restore the three-dimensional shape of the chest using the active stereo method, it is necessary to acquire the approximate distance between the sensor and the chest in advance.

Therefore, in recent years, inexpensive three-dimensional image sensors have been marketed since Microsoft's Kinect (1st generation), which was released in 2010. Intel's RealSense launched in 2015 is one of them and it is small and inexpensive because it is developed on the premise of incorporation into a PC.

Since Kinect and RealSense use the active stereo method as the 3-dimensional measurement principle, there was a possibility that it could be applied to the non-contact heartbeat measurement proposed by us. However, since the baseline length between the imaging device and the patterned light projection device is short, it has been confirmed that they do not have sufficient distance measurement sensitivity to detect the displacement of the body surface due to the heartbeat.

In this paper, we will use a green laser as a light source to solve the above first problem and the RealSense as an imaging device to cope with the second problem. We construct a prototype system based on the proposed method and examine the feasibility of non-contact heart rate measurement.

## 2 Method

### 2.1 System Configuration

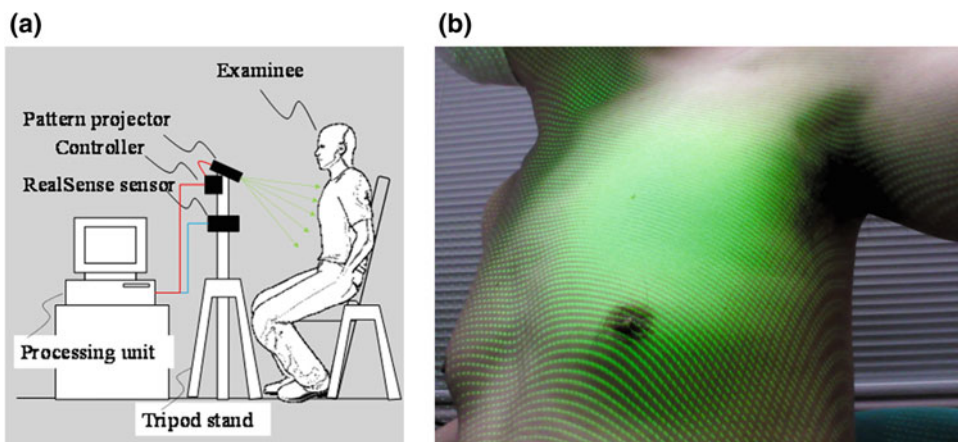
In the proposed method, Intel RealSense F200 is used as an imaging device for active stereo measurement. The RealSense sensor was developed by Intel as a device installed to PC for performing PC operation by gesture recognition, voice recognition, and facial expression recognition. The RealSense sensor has a function of photographing a depth image based on the active stereo method. In the proposed method, this function is used to acquire the three-dimensional shape of the chest.

The RealSense sensor carries a color camera separately from the infrared camera for depth image acquisition, and it is possible to acquire a VGA color image at a frame rate of 60 fps. The frame rate of Kinect's VGA color image is 30 fps. The depth measurement range of RealSense is from 20 cm, and compared with Kinect, it has the feature that measurement of a short distant object is possible. This feature seemed to work advantageously to capture the variation of minute body surface of heartbeat.

Figure 1a shows the system configuration for implementing the proposed method. The sensor section of the system is composed of a RealSense sensor and a dot matrix pattern projector.

The dot matrix pattern projector is formed by combining a green laser and a transmission type diffraction grating. In the transmission type diffraction grating, a sheet in which two optical fibers are arranged in a reed like shape is fixed so that the directions of the optical fibers are orthogonal [3]. When a laser-beam is incident on the transmission type diffraction grating, a dot matrix pattern is projected. The dot matrix pattern projected on the chest and abdomen of the subject is imaged by the RealSense color camera as shown in Fig. 1b and the cardiac mechanical phenomenon is

**Fig. 1** a System configuration and b dot-matrix pattern projected on chest





monitored by calculating minute motion of the chest surface with the heartbeat by image analysis.

As a laser light source of the dot matrix pattern projector, it is also possible to use a laser (red, blue) having a color different from that of green. However, although a red laser is inexpensive, it penetrates into human skin and diffuses more easily than green or blue. Blue lasers are more expensive than green lasers. For this reason, we decided to adopt green laser in the proposed method.

## 2.2 Detection of Heart Beat

From the color image of the dot matrix pattern projected on the chest, the green region corresponding to the dot light is extracted.

Specifically, a region corresponding to the dot matrix pattern is extracted by converting the color image from the RGB color space to the HSV color space and setting threshold values in the hue, saturation, and lightness range corresponding to the green laser. The binary image of the region extracted as the dot matrix pattern is shown in Fig. 2a.

As a result of the above-described green region extraction processing, a hole-like defective region is generated inside the extracted dots, so that filling is performed by morphological processing. Figure 2b shows an image after the filling process.

The dots constituting the dot matrix pattern move in the image due to the change in the body surface shape. The

**Fig. 2** **a** Binary image of the region extracted as the dot matrix pattern and **b** image after the filling process

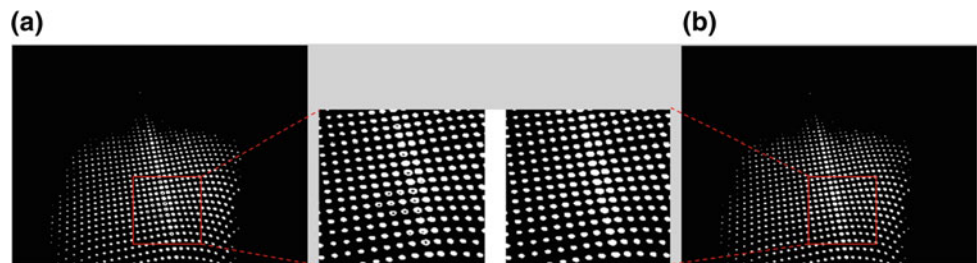
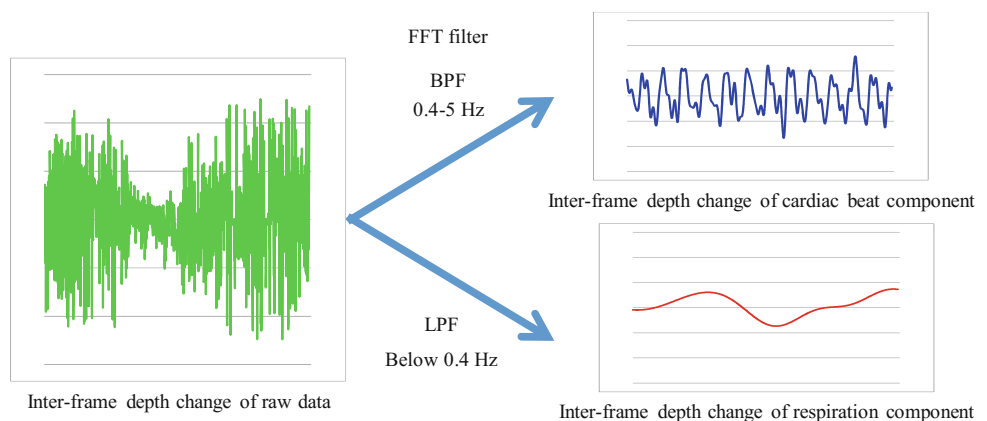


**Fig. 3** Separate extraction of heartbeat and respiration



barycentric coordinates of each dot are obtained for each frame, and each dot is tracked by associating dots between frames based on the barycentric coordinates of the dots.

Then, time series data of the interframe movement amount of dots is obtained. Changes in the body surface shape causing the movement of the dots are caused by respiratory motion, convulsive tremor and heart beat when the subject is in a rest state. The cause of the appearance as the movement amount of dots includes not only the shape change of the body surface, but also the electronic noise in the moving image and speckle noise of the laser. Therefore, the time series waveform of the movement amount of the dot shows a waveform dominated by the high frequency component like the waveform shown in green in the upper part of Fig. 3.

This waveform contains biological signals such as respiratory motion and heartbeat. A respiratory component waveform is extracted from this waveform by performing Low-Pass Filtering (LPF) processing that passes through a frequency band of less than 0.4 Hz. By performing Band-Pass Filtering (BPF) processing that passes through the frequency band of 0.4–5 Hz, the heart beat component waveform is extracted.

## 3 Experiment and Result

A prototype system was constructed to conduct fundamental studies on the validity of the proposed method. The sensor section consists of Intel RealSense, a green TTL laser

manufactured by Laser Create Co., Ltd. Image data acquired by RealSense is captured by a PC (Panasonic CF-SX 3). We use the microcontroller (Arduino UNO R3) connected to the PC to control emission and supply power of the laser.

Two men in their twenties and one male in their forties are measured. For the measurement, explanation concerning measurement was orally and written to the subjects, and consent form from the subjects was obtained.

Three examples of measurement results are shown in Fig. 4. Subjects stopped respiration for about 12 s from the start of measurement. In the waveform extracted by the LPF process, a flat waveform was shown for about 12 s at the start of measurement, and then the large fluctuation associated with respiration was observed. In the waveform extracted by the BPF process, a periodic vibration waveform was obtained.

Simultaneous measurement by electrocardiogram was carried out to confirm that this vibration waveform was due

to extraction of heart beat. The electrocardiogram used to be a compact wireless ECG logger manufactured by LOGICAL PRODUCT.

As a result of comparing the peak interval of the vibration waveform extracted by the proposed method and the peak interval of the ECG waveform, the difference was 0.04 s or less in either subject. During respiration, fluctuations are included in the measured waveform. In the simultaneous measurement of the two methods, the difference in the peak intervals is less than 0.05 s. The value is larger than when the breath was stopped, but the interval of the vibration coincided with the peak interval of the ECG waveform. Therefore, it was considered that the displacement of the body surface caused by the heartbeat could be extracted by the proposed method.

The heartbeat component and the respiratory component of the dot velocity were calculated, and the distribution was presented as a color map (Fig. 5). By outputting the time change of

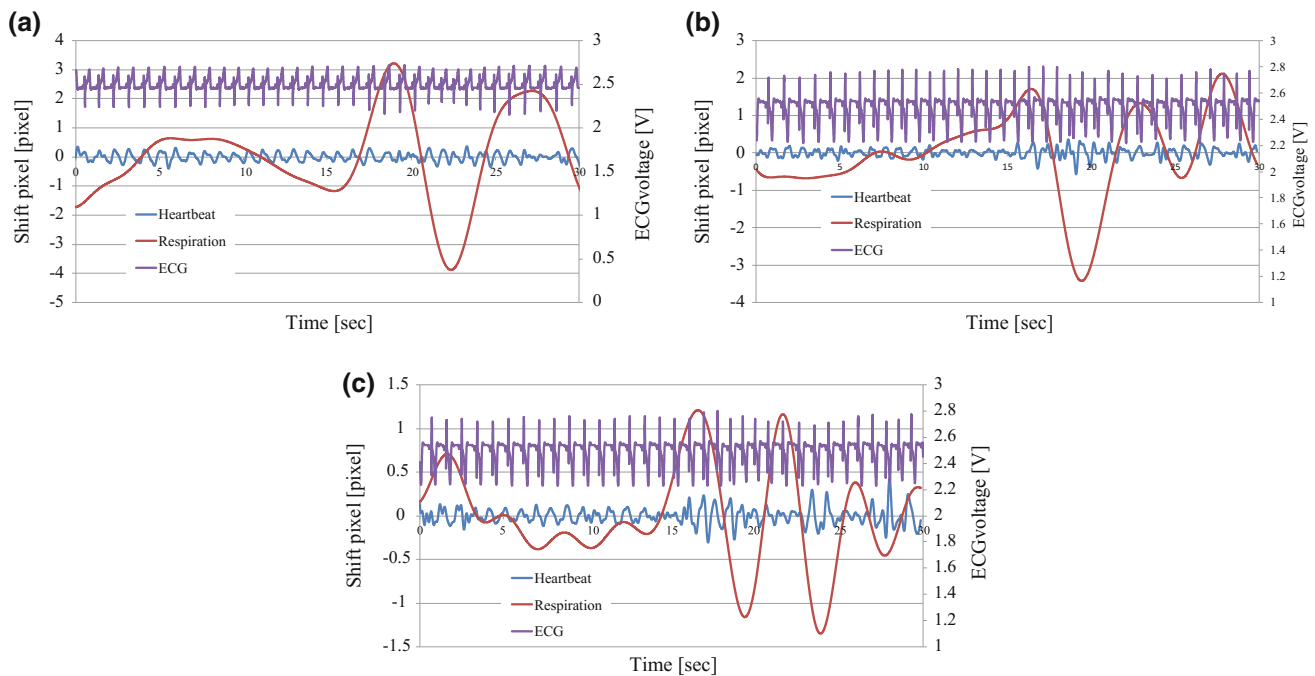
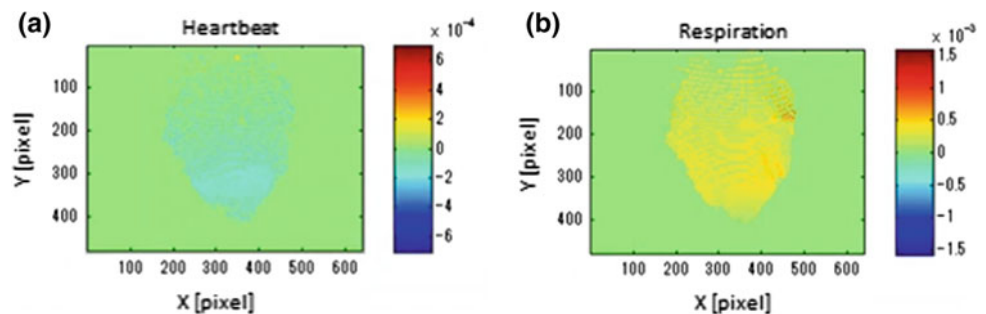


**Fig. 4** Measurement results (a subject I, b subject II and c subject III.)

**Fig. 5** Color map animation of velocity (a heartbeat component, b respiratory component)



the color map as an animation, we could visualize respiratory motion or heartbeat motion on the chest wall. By presenting it as a moving image, it can be visually recognized that there is a phase difference in the surface movement at each part on the chest surface. It can be confirmed that the phase lag increases as it goes upward from the abdomen. This result suggests that the proposed method may be useful for grasping mechanical phenomena of the heart (expansion/contraction mode).

---

## 4 Conclusion

By combining a green laser light source and a RealSense sensor, we proposed a new heartbeat measurement method based on active stereo measurement system. As a result of fundamental examination by the prototype system, it is

suggested that the proposed method can visualize chest surface vibration accompanying heartbeat.

**Acknowledgements** This work was supported by JSPS KAKENHI Grant Number JP16K08977.

---

## References

1. Aoki, H., et al. "Extraction and Visualization of Cardiac Beat by Grid-Based Active Stereo," *Advances in Depth Images Analysis and Applications*, LNCS7854, pp. 147–157, Springer (2013)
2. Machida, H., et al.: "High Efficiency Fiber Grating for Producing Multiple Beams of Uniform Intensity," *Appl. Opt.*, 23(2), pp. 330–332 (1984)
3. AOKI, H, et al.: "Calculation of Ventilation Threshold Using Noncontact Respirometry," In: *Proceedings of 30th IEEE EMBC*, pp. 2273–2276 (2008)

# Design Reflection on Mobile Electronic Data Capturing Forms in African Rural Settings

Ole Andreas Krumsvik<sup>1</sup>, Ankica Babic<sup>2</sup>, and Alice Mugisha<sup>3</sup>

## Abstract

This paper presents a literature review of the existing tools for data capture in African rural settings. The objective has been to investigate and understand design approaches, usability, user satisfaction, as well as feasibility of capturing data using mobile device forms. Existing open source solutions are most commonly used in a variety of applications such as maternal care, newborn child health, and routine health care monitoring. The common design issues involve customizing forms for the intended purpose and for semi- or non-literate user groups. User evaluation is also not often reported, however some of the studies suggest a high satisfaction as compared to the traditional paper-based approach. Typical barriers include: cost, user input, user motivation, limited graphical user interface, and availability of technology in rural areas. Some of these barriers could be addressed by practicing User-Centered Design. We suggest including all future user groups in the development of mobile electronic data capturing forms to increase usability, data accuracy, and the user satisfaction.

## Keywords

User-centered design • HCI • Mobile electronic data capturing forms • Rural Africa • Pregnancy

## 1 Introduction

In recent years, there has been a shift regarding forms that are used for data collection in African rural areas. The traditional paper-based approach has gradually been replaced

by mobile Electronic Data Capturing (EDC) tools. These have become cheaper and easily obtainable, and at the end of 2015 there were more than half a billion unique subscribers to mobile services in Africa [1]. Moreover, such tools provide automated support for data collection, reporting, query resolution, randomization, validation, and other features depending on the context of use.

The data collection forms are used to collect data from user groups in vulnerable situations, e.g. pregnant and recently delivered women. The maternal mortality rate in developing countries is 239 per 100 000 live births versus 12 per 100 000 in live births in developed countries, reported by the World Health Organization [2].

The most commonly used tools in rural areas for mobile EDC are open-source applications such as ODK (Open Data Kit), REDcap (Research Electronic Data Capture), OpenClinica, and EpiCollect [3–6]. In addition, lightweight mobile EDC solutions facilitated by short message services are also utilized [7]. With the introduction/implementation of these tools several challenges arise. These challenges include implementation cost, user participation, availability of technology or lack of it, constraints to the graphical user interface, software installation, user communication, and technical support [8]. Therefore, it is imperative that the tools emphasize usability and a user experience which could aid high quality data collection.

In this paper, we reflect on the existing form solutions for mobile EDC tools that are used to collect pregnancy related data in rural areas in Africa, as well as the most viable design approach for enabling efficient mobile EDC.

## 2 Method

A literature review was conducted using PRISMA [9]. Inclusion criteria for the paper retrieval was pregnancy-related articles published during the 2006–2017 period which included peer-reviewed articles, open source mobile electronic data capturing forms, and usability

O. A. Krumsvik (✉) · A. Babic · A. Mugisha  
University of Bergen, 5007 Bergen, Norway  
e-mail: lncs@springer.com; oa.krumsvik@gmail.com

A. Babic  
Linköping University, 581 83 Linköping, Sweden

evaluation as topics. Exclusion criteria were projects not located in Africa and non-handheld devices. The literature review was carried out in August and September of 2017 by two authors (Krumsvik and Babic). Search engines used were Google Scholar, PubMed, and ScienceDirect. 778 records were identified through PubMed and ScienceDirect, whereas 1942 records were identified in Google Scholar. Duplicate articles were automatically removed using Mendeley and resulted in a total of 2652 records [10]. 2652 records were screened, which led to an exclusion of 2625 records. 27 full-text articles were assessed for eligibility, and 24 of these were excluded in accordance with our criteria. All study designs were included if they had elements of the User-Centered Design (UCD) approach, which is a part of the Human-Computer Interaction domain.

UCD is an iterative development approach and consists of four primary stages: analysis, design, evaluation, and implementation [11]. Additionally, UCD is recommended when designing for health care [12]. Usability is defined as a quality attribute that assesses how straightforward user interfaces are to use. It consists of 5 components: learnability, efficiency, memorability, errors, and satisfaction according to Nielsen [13].

### 3 Results

The typical tools used for mobile EDC by default are very simple in terms of graphical outlay [3–6]. All of them offer vertical scrolling in the forms, something which should be kept to a minimum for mobile device forms, since the objective should be to reduce the inputs required from users. Furthermore, user data input in forms, e.g. free-text typing, is usually avoided as it is error prone and time-consuming. It is also recommended to include hint text above free-text labels, to reduce the likelihood of user error [14, 15]. The forms, in addition, are highly customizable and it should therefore not be an issue to follow recommended form design principles to increase their usability.

According to Rothstein et al., a high degree of usability and user acceptance is of importance in mobile EDC. This could increase the accuracy of gathered data and enhance the delivery in this context of maternal, neonatal, and child health services, leading to improved health outcomes [16]. Additionally, Rothstein et al. conducted an evaluation assessing the feasibility, usability, and acceptability of MOTECH's mobile Client Data App which gathers data through mobile EDC forms to improve care regarding maternal, neonatal, and child health in rural Ghana. 23 community health nurses, 2 midwives, 2 district health directors, and 2 district health information officers were interviewed to evaluate the application. 2 were below 26 years of age, 20 were between 26 and 29 years of age,

and 7 were 30 years or above; 24 females and 5 males [16]. The evaluation's key findings impacting the usability were: improved productivity due to simplified data gathering, technical errors leading to incomplete tasks, lacking interoperability with the national health information system, and interruptions in network connectivity [16].

A study carried out by Velez et al., assessed the usability of an mHealth EDC application for rural Ghanaian midwives named mClinic [17]. Seven midwives previously trained as nurses with 2–42 years of clinical practice experience participated in the evaluation. mClinic captured patient data such as encounter date, weight, blood pressure, gestational age, fundal height, and iron folic acid tablets given. The usability problems of mClinic were attributed to the touch screen while capturing data, no application-level password was required, and there were issues with modifying patient data. The participants believed that the application would be helpful to them, however, as it could reduce the time spent on creating monthly reports [17].

Diversity of the user groups involved in mobile EDC concerning pregnancy in rural Africa ought to be taken into consideration when designing for usability. In Munro et al.'s research, the data collectors were 63 Traditional Birth Attendants (TBA) [7]. The TBA were semi- or non-literate: 60.3% had no formal schooling, 7.9% had attended 2nd to 6th grade, and 6.4% of them 7th to 12th grade in school. Their age ranged from 38 to 60 years, however 39.7% did not know their exact age. The training that the TBA had to undergo involved elementary mobile phone skills, such as turning on the mobile phone, make calls, create text messages, and send text messages [7]. The participants transmitted real-time pregnancy case data on the number of women who had become pregnant within each geographic region, serviced by a rural primary health facility and encouraged these women to seek antenatal care at the closest facility. The data transmitted contained a personal ID code, health facility ID code under which the woman lives, her age, and if the TBA referred the pregnant woman to antenatal care [7].

### 4 Discussion

Mobile EDC forms could either be designed for technically low-skilled users [16], involve technically competent users [17], or have the users undergo extensive training [7]. It is crucial that the collected data is of high quality, as it involves vulnerable user groups with a high maternal mortality rate [2].

We recommend utilizing mobile UCD for improving the usability and user experience of mobile EDC forms. There are similar successful experiences with applying UCD in the context of maternal, newborn, and child health services in

**Table 1** Mobile UCD feature overview and our recommendations

Main features of mobile UCD	Practical recommendations
1. Assess the current situation	Collect data from form users about the tools they currently use
2. Understand the users	Assess the form user's technical skills and user needs
3. Mobile user experience	Emphasize usability goals
4. Mobile design considerations	Create several design alternatives. Have form users evaluate them
5. Review and refine	Collect and implement user feedback on low-, mid-, and high-fidelity prototypes

**Table 2** Usability quality components and our recommendations

Usability quality components	Practical recommendations
Learnability	Ensure that one is not overstepping the users' level of education, making it a difficult learning experience: involving users in the development process could increase simplicity and learnability
Efficiency	Involve users into carrying out tasks in order to measure the efficiency after they have learned how to use the system. This should be sequential and logical
Memorability	Users should agree with the features used in the design and these should be recognizable to them: icons, colors, work flow, navigation, list pickers etc.
Errors	Limit the possibility of user errors. Minimize the user workload when correcting errors by implementing real-time validation, use of informative labels, and tracking of user errors when testing
Satisfaction	Include users in selecting the final design. An easy to use and pleasant design is of importance

rural areas of India [18]. Implementation of the UCD approach when creating such forms could result in more usable systems, increased user satisfaction, improved performance, long-term cost efficiency, improved credibility, and a more enjoyable user experience [11]. Furthermore, UCD requires involvement of stakeholders, domain experts, and the intended users through every stage of the design process [11]. While this could be more time-consuming than other approaches, the long-term consequences could be constructed forms that are of high usability, increased data accuracy, cost-effective over time, and lead to a pleasant user experience. As stated by Waugaman, UCD is also recognized as the best practice for development technology [19]. An overview of the main features of mobile UCD can be viewed in Table 1 [20].

Features of the Table 1 are common for mobile devices but could be applied to the mobile EDC forms. The differences in context and user groups could be modifying factors for tailoring design to suit specific needs. For example, if low educated staff is expected to collect data, the design must accommodate such user group needs.

Although the UCD approach could be highly beneficial in improving mobile EDC forms, one should reflect on limitations related to the devices that are available, as well as the infrastructure in rural Africa. Several studies in this literature review address the constraints concerning the accessibility of mobile devices [7, 16, 17]. All the devices are low-cost, and some of the devices that have been used for mobile EDC could be technically restricted. As previously mentioned,

much as the number of mobile subscriptions are increasing, with the decrease in the prices of mobile phones, rural Africa is still resource-limited. Additionally, infrastructure limitations are present. Poor internet connectivity, high patient volumes, and staff shortages negatively impacts the usefulness of mobile EDC [17]. Recent research carried out by Cunningham et al. address similar issues concerning mobile EDC in rural Africa, as well as suggesting UCD principles for improving healthcare services [21]. The goal of UCD is to generate products that have a high degree of usability, and the aforementioned components ought to be taken into consideration as displayed in Table 2 [22].

## 5 Conclusion

Our strong final recommendation would be to encourage mobile EDC designers and developers to adapt the mobile UCD approach, as it could have a positive impact on the applications directed towards mobile EDC. In addition, proper training must be given to data collectors to facilitate an accurate, timely, and agile data collection. That in turn could lead to improved user-satisfaction and better data capture, both essential for securing patient care. Limitations are not solely constrained to technology and infrastructure. There is a clear need to improve the design, and UCD is also recommended for developing countries, as well as health-care. This is based on the potential of UCD to involve users and suggest design close to the user needs.



**Acknowledgements** The authors would like to thank the Norwegian Agency for Development Cooperation (NORAD) for supporting the research through the HI-TRAIN project.

**Conflict of Interest** The authors declare that they have no conflict of interest.

## References

1. GSMA (2016) The Mobile Economy - Africa 2016. <https://www.gsma.com/mobileeconomy/africa/>, last accessed 2017/9/10.
2. WHO (2016) Maternal Mortality. <http://www.who.int/mediacentre/factsheets/fs348/en>, last accessed 2017/8/9.
3. Brunette W, Sudar S, Sundt M, et al (2013) Open Data Kit 2.0. HotMobile '13 Proc 14th Work Mob Comput Syst Appl.
4. Harris PA, Taylor R, Thielke R, et al (2009) Research electronic data capture (REDCap)-A metadata-driven methodology and workflow process for providing translational research informatics support. *J Biomed Inform* 42:377–381.
5. Cavelaars, M, Rousseau, J, Parlayan, C, et al (2015) OpenClinica. *Journal of Clinical Bioinformatics* 5 (2015).
6. Aanensen DM, Huntley DM, Feil EJ, et al (2009) EpiCollect: Linking smartphones to web applications for epidemiology, ecology and community data collection. *PLoS One* 4.
7. Munro ML, Lori JR, Boyd CJ, Andreatta P (2014) Knowledge and skill retention of a mobile phone data collection protocol in rural Liberia. *J Midwifery Women's Heal* 59:176–183.
8. Welker JA (2007) Implementation of electronic data capture systems: Barriers and solutions. *Contemp Clin Trials* 28:329–336.
9. Liberati A, Altman DG, Tetzlaff J, et al (2009) The PRISMA statement for reporting systematic reviews and meta-analyses of studies that evaluate health care interventions: Explanation and elaboration. *PLoS Med* 6.
10. Mendeley (2017) Mendeley - Reference Management Software & Researcher Network. [www.mendeley.com](http://www.mendeley.com), last accessed 2017/8/9.
11. IDF (2017) What is User Centered Design? <https://www.interaction-design.org/literature/topics/user-centered-design>, last accessed 2017/9/1.
12. Fricker SA, Thummler C, Gavras A (2015) Requirements Engineering for Digital Health. Springer International Publishing.
13. Nielsen J (2012) Usability 101: Introduction to Usability. <https://www.nngroup.com/articles/usability-101-introduction-to-usability>, last accessed 2017/9/9.
14. IDF (2017) Designing for the Mobile Environment – Some Simple Guidelines. <http://www.interaction-design.org/literature/article/designing-for-the-mobile-environment-some-simple-guidelines>, last accessed 2017/9/10.
15. LAPDP (2017) Online Survey Design Guide. [http://lap.umd.edu/survey\\_design/theory.html](http://lap.umd.edu/survey_design/theory.html), last accessed 2017/9/9.
16. Rothstein JD, Jennings L, Moorthy A, et al (2016) Qualitative Assessment of the Feasibility, Usability, and Acceptability of a Mobile Client Data App for Community-Based Maternal, Neonatal, and Child Care in Rural Ghana. *Int J Telemed Appl* 2016.
17. Vêlez O, Okyere PB, Kanter AS, Bakken S (2014) A usability study of a mobile health application for rural Ghanaian midwives. *J Midwifery Women's Heal* 59:184–191.
18. Modi D, Gopalan R, Shah S, et al (2015) Development and formative evaluation of an innovative mHealth intervention for improving coverage of community-based maternal, newborn and child health services in rural areas of India. *Glob Health Action* 8.
19. Waugaman, A, (2016) From principle to practice: implementing the principles for digital development. Proceedings of the Principles for Digital Development Working Group.
20. IDF (2017) A User-Centred Approach to Mobile Design and a 5 Stage Process for You to Use. <https://www.interaction-design.org/literature/article/a-user-centred-approach-to-mobile-design-and-a-5-stage-process-for-you-to-use>, last accessed 2017/8/10.
21. Cunningham PM, Cunningham M, Van Greunen D, et al (2016) Implications of baseline study findings from rural and deep rural clinics in Ethiopia, Kenya, Malawi and South Africa for the co-design of mHealth4Afrika. *GHTC 2016 - IEEE Glob Humanit Technol Conf Technol Benefit Humanit Conf Proc* 666–674.
22. WAI (2008) Notes on User Centered Design Process. <https://www.w3.org/WAI/redesign/ucd>, last accessed 2017/8/8.

# Evaluation Methodology and Measurement of Physiological Data to Determine Operational Preparedness of Air Defense Staff: Preliminary Results

Vaclav Krivanek, Patrik Kutilek, Radek Duskocil, Jan Farlik, Josef Casar, Jan Hejda, Slavka Viteckova, Petr Volf, and Pavel Smrcka

## Abstract

The aim of the article is to introduce new evaluation methodology to determine operational preparedness of air defense staff based on measurement of physiological data. The individuals working with air defense systems are under very high level of stress and long-term monotone air picture observation workload during the mission. We designed an experiment and a method of measuring the biomedical signals for monitoring the actual operator condition during long-term work on air picture simulator that shows real-time aircraft flight information. Long-term monitoring and recording of potential airborne targets in the area of interest to which operators are subjected is accompanied by monitoring the physiological data such as heart rate, body temperature, movement activity and perspiration intensity of operators. The proposed methodology and measurements were tested on four air defense

system operators of the Army of the Czech Republic. Operators took part in a 4-h intensive measurement without any break and their training was evaluated. Designed methods could help to monitor, on the base of physiological data and data from simulators, the stress load level and operational preparedness.

## Keywords

Operational preparedness • Tiredness • Physiological data • Air defense • Simulator

V. Krivanek (✉) · R. Duskocil · J. Farlik · J. Casar  
Faculty of Military Technology, University of Defence,  
Kounicova 65, Brno, Czech Republic  
e-mail: vaclav.krivanek@unob.cz

R. Duskocil  
e-mail: radek.duskocil@unob.cz

J. Farlik  
e-mail: jan.farlik@unob.cz

J. Casar  
e-mail: Josef.casear@unob.cz

P. Kutilek · J. Hejda · S. Viteckova · P. Volf · P. Smrcka  
Faculty of Biomedical Engineering, Czech Technical University in  
Prague, Sitna sq. 3105, Kladno, Czech Republic  
e-mail: kutilek@fbmi.cvut.cz

J. Hejda  
e-mail: jan.hejda@fbmi.cvut.cz

S. Viteckova  
e-mail: slavka.viteckova@fbmi.cvut.cz

P. Volf  
e-mail: petr.volf@fbmi.cvut.cz

P. Smrcka  
e-mail: smrcka@fbmi.cvut.cz

## 1 Introduction

The requirement for the selection and participation of complex system operators in practice is to identify their preparedness. Intensive research is currently underway on the development of for monitoring the health condition, i.e. physical and psychological readiness, of employees in army [1]. The objective of health condition measurement is to use this information to increase safety, i.e. to exclude the less-prepared operators of complex systems from the control or decision-making process [2, 3]. However, in the development of prospective systems, monitoring of anti-aircraft missile system operator has never been presented or mentioned. Nevertheless, the health state monitoring of other personnel in army such as pilots or soldiers of ground troops of special units, is given high attention.

The aim of the article is to describe our contribution to development of evaluation method of physical and psychological readiness, training simulators and systems for measurement of the physiological data of ground based air defense missile system operators. The reason for physiological data monitoring is to test the possibility of usage them to estimate the physical and psychological readiness and for identification of dangerous situations in the staffing. The assumption is that, for example, heart rate and

perspiration level are related to stress level and this is related to the subject's readiness.

For the evaluation of data, it is possible to use standard evaluation methods. The parameters determined by the evaluation methods include the average values and maximum of the measured data, but also the correlation coefficient determined for the measured data.

## 2 Methods

Based on the above mentioned drawbacks, measurement methodology and measurement and evaluation methods of physical and psychological readiness of the anti-aircraft missile system operators can be designed. Methods assume a direct measurement of the performance indicators by the simulators of air situation and physiological indicators of the health condition of operators. In our case, operators are members of air defense and monitoring should allow headquarters and identification of dangerous situations in the condition of operators during training or military mission.

### 2.1 Participants

Four soldiers (aged 24) were recruited for measurement. Soldiers were cadets of University of Defence which is the only military institution of higher education of the Czech Armed Forces. Students were future members of air defense staff preparing for the profession of anti-aircraft missile system operator. Cadets were subjected to diagnostic evaluation focused on detailed disease history, a neurologic examination, and routine laboratory testing. The study was performed in accordance with the Helsinki Declaration. The study protocol was approved by the local Ethics Committee

of the Faculty of Biomedical Engineering of the Czech Technical University (CTU) in Prague. The subjects were measured on same days.

### 2.2 Measurement Equipment

Measurement systems can be divided into two groups: simulators of air situation for training and system for physiological data monitoring.

The base for the design of physiological data monitoring was the FlexiGuard system, originally developed at the Faculty of Biomedical Engineering, Czech Technical University in Prague [4]. The FlexiGuard system is modular biotelemetric system for real-time monitoring of soldiers of the ground troops of special military units, see [4, 5]. The system consists of a set of sensors for monitoring body temperature, heart rate, acceleration and humidity [4, 5], see Fig. 1b. The modular sensing units records the measured data and send them wireless to the visualization unit [1].

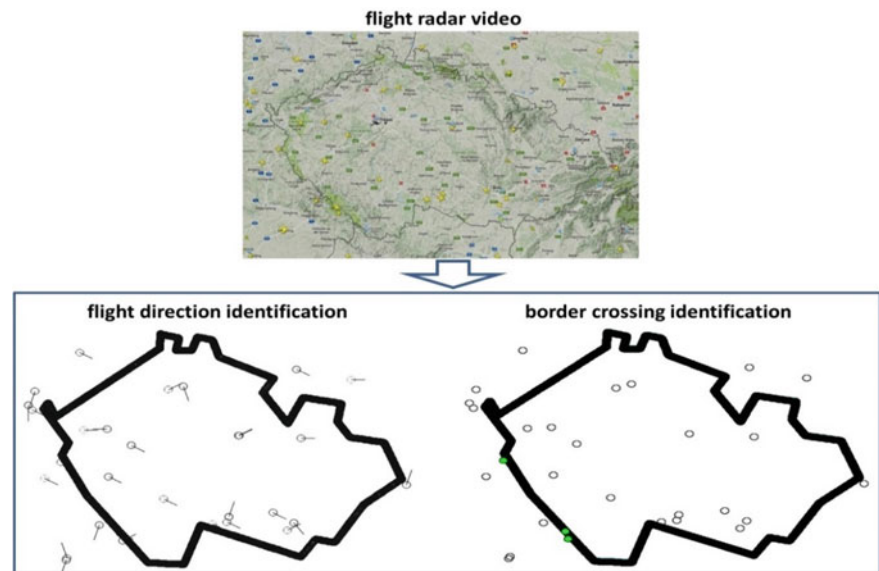
Simulators for training of anti-aircraft missile system operators is based on Flightradar24 web site (Flightradar24 AB company), see Fig. 1a. It includes flight tracks numbers, origins and destinations, flight numbers, aircraft types, positions, altitudes, headings and speeds [6]. Subjects only monitor the airspace and record the air situation over a defined area, it was also necessary to create software for the automated monitoring of the air situation. Software is designed to count the number of airplanes flying in and out of the area of interest (i.e. the Czech Republic). It is created in MatLab software (MatLab R2010b, Mathworks, Inc., Natick, MA, USA) [7]. The general concept is presented in Fig. 2.

The software for video processing and definition of the boundary of the area of interest is created in MatLab

**Fig. 1** Simulators of air situation during training of operators (a) and application of modular sensing unit (b) for measurement of physiological data



**Fig. 2** Concept of the identification of the flight directions and the number of airplanes above the border of the Czech Republic which is area of interest



software. The coordinates of each airplane are calculated and compared with the predefined zone along the boundary. The coordinates of each airplane in each video frame are detected in the pictures automatically using the contrast between the yellow color of airplane (the yellow mark for aircraft is defined by the Flightradar24) and the color of background. If the detected airplane coordinates are in a defined zone along the boundary, they are further considered in the calculation. The sum of all the airplanes in the zone along the boundary is counted. The velocity vectors of airplanes in the zone along the boundary is determined, i.e. the flight direction of the each airplane is determined from coordinates in two consecutive video frames. After that, it is determined in which direction each plane is moving in the border zone. If the velocity vector is pointing towards the predefined area, it is an airplane passing through the area, if the velocity vector directs the opposite, it is an airplane flying out of the area. Then custom-written program divides the total number of airplanes in the border zone into number of airplanes flying in and out of predefined area.

### 2.3 Test Procedure

The proposed systems are used for simultaneous measurement of the working performance and physiological data of the four operators during their training. Before each measurement, four portable systems for the monitoring physiological data were placed on the trunk of each cadet in accordance with [3, 4], see Fig. 1b. Then, four simulators of air situation were used for training of four operators. Four subjects conducted real-time air tracking and manually enrolled potential targets flying in or out of the Czech Republic's airspace. The measurement was carried out

continuously for 4 h. After the measurement, simulators determined the numbers of airplanes flying in and out of the monitored area. The data obtained from the simulators are then compared with the biomedical data monitoring system.

### 2.4 Data Processing

Four-hour long recordings of physiological data, the number of the airplanes in the border zone and the number of manually enrolled potential targets are synchronized. Due to synchronization of data, better interpretation and faster processing, all recordings were resampled to 1 Hz. This process was done using a custom-designed MatLab program based on the functions of the MatLab software.

## 3 Results

In preliminary research of performance and physiological data to determine operational preparedness of air defense staff, authors present, how the monitoring system, simulator, methodology of measurement and data processing were designed and selected. Preliminary results showed that the number of the airplanes in the border zone and the number of manually enrolled potential targets by operators did not change significantly, i.e. is approximately constant, during a 4-h measurement. Thus flight identification results (e.g. border crossings) are constant during measurement.

If we focus on the behavior of biomedical data during a 4-h measurement, data show some trends, see Figs. 3 and 4.

The most interesting results came from a preliminary assessment of heart rate and humidity. At the beginning of the measurement, the dispersion of heart rate values of four



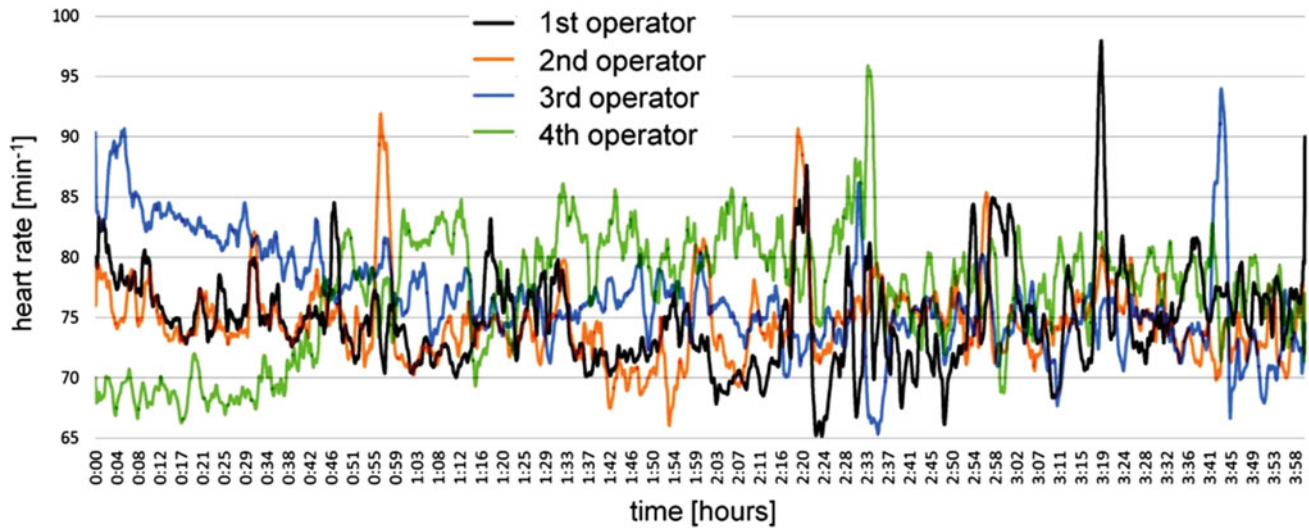


**Fig. 3** Example of the output from user sw: real-time heart rate graphs of four operators during training

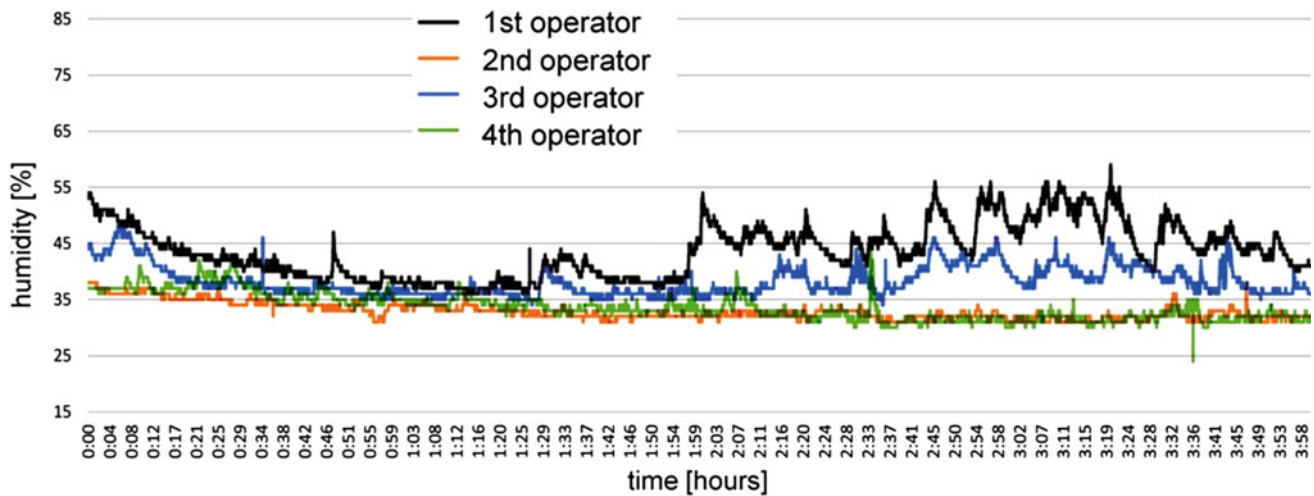


**Fig. 4** Example of the output from user sw: real-time graphs of the humidity of the body surface under the suits of four operators during training

operators was greater. For some operators, the maximum and or minimum values were measured immediately at the start of the measurement. However, within 1 h of measurement, the heart rate value of all operators is approximately 76. Between the first and the third hour of the measurement, the heart rate is oscillating around the above-mentioned value. After the third hour of the measurement, the dispersion of the heart rate values of the operators decreases. In the case of humidity of the body surface under the suits, group of operators can be divided into two, at first the humidity changes and the other does not change. Interesting is the drop of humidity (i.e. sweating) during the first hour of measurement and subsequent increase of humidity after 2 h, which persists until the end of the measurement. Preliminary results showed higher correlations among the subjects above.

## 4 Discussion

Authors present, how the monitoring system was selected and designed, training simulator designed, and measurement and tests were performed. Testing of the functionality of the methodology took place in laboratory environment. In the case of carrying out the measurements on four air-defense operators, the performance is evaluated based on number of recordings, and biomedical data monitoring. Preliminary results show different results in biomedical data of operators during measurement. From the results, we can assume that the monitoring system and training simulators are suitable to determine operational preparedness. We can say that low sweating and heart rate with the same work performance show better preparedness

[3]. Thus, the systems and technique can offer information, which may help to monitor the stress load level.

There are limitations to our study. The most important one is that the sample of the subjects was small and probably not representative of the larger population. However, to test the basic attributes of the method proposed for the study of operational preparedness in this preliminary study, a sample of subjects is sufficient.

## 5 Conclusion

The proposed systems, methodology and measurements were tested on the four operators. Described preliminary findings demonstrate the ability of the proposed systems and technique to identify differences in the states of air-defense operators. Next goal is to verify the method on more subjects measured over a longer time period, and integration into practice.

**Acknowledgements** This work was done in the framework of research project SGS17/108/OHK4/1T/17 sponsored by Czech Technical University in Prague as well as by the Czech Republic Ministry of Defence (University of Defence development program “Research of sensor and control systems to achieve battlefield information superiority”).

**Conflict of Interest** The authors declare that they have no conflict of interest.

## References

1. Kutilek, P., Volf, P., Viteckova, S., Smrcka, P., Lhotska, L., Hana, K., Krivanek, V., Dosekocil, R., Navratil, L., Hon, Z., Stefek, A.: Wearable Systems and Methods for Monitoring Psychological and Physical Condition of Soldiers. *Advances in Military Technology* 12(2), pp. 259–280 (2017).
2. Fraga-Lamas, P., Fernández-Caramés, T.M., Suárez-Albela, M., Castedo, L., González-López, M.: A Review on Internet of Things for Defense and Public Safety. *Sensors* 16(10), 1–44 (2016).
3. Kutilek, P., Volf, P., Viteckova, S., Smrcka, P., Krivanek, V., Lhotska, L., Hana, K., Dosekocil, R., Navratil, L., Hon, Z., Stefek, A.: Wearable Systems for Monitoring the Health Condition of Soldiers: Review and Application. In: *ICMT 2017 – 6<sup>th</sup> International Conference on Military Technologies*, University of Defence, Brno (2017).
4. Schlenker, J., Socha, V., Smrčka, P., Hána, K., Begera, V., Kutilek, P., Hon, Z., Kašpar, J., Kučera, L., Mužik, J., Veselý, T., Vítězník, M.: FlexiGuard: Modular Biotelemetry System for Military Applications. In: *Proceedings of the 5<sup>th</sup> International Conference on Military Technologies – ICMT ’15*, University of Defence, Brno (2015).
5. Hon, Z., Smrcka, P., Hana, K., Kaspar, J., Muzik, J., Fiala, R., Vitezniak, M., Vesely, T., Kucera, L., Kuttler, T., Kliment, R., Navratil, V.: A surveillance system for enhancing the safety of rescue teams; *Communications – Scientific Letters of the University of Zilina* 17(1), 81–86 (2015).
6. Xhafa, F., Naranjo, V., Barolli, L., Takizawa, M.: On streaming consistency of big data stream processing in heterogenous clusters. In: *18<sup>th</sup> International Conference on Network-Based Information Systems, NBIS 2015*, pp. 476–482, Tamkang University Taipei, Taiwan (2015).
7. Gonzalez, R.C., Woods, R.E. Eddins, S.L.: *Digital Image Processing Using MATLAB*, (2003).



# A Multiple Criteria Decision Making System for Setting Priorities

Sergio Miranda Freire, Aline Nascimento, and Rosimary Terezinha de Almeida

## Abstract

The demand for improvement in the quality and cost control in health care stimulates the utilization of the Multiple Criteria Decision Making (MCDM) approach, which is a sub-discipline of operations research that explicitly evaluates multiple conflicting criteria in decision making. The aim of this paper was to develop a user-friendly multiple criteria decision making support system in order to facilitate the application of an MCDM method by decision-makers. The system was developed in Java and compares alternatives (i.e., technologies or projects) by a single or a group of individuals with a set of criteria evaluated by means of an ordinal or numeric scale. An ordinal scale is used to set the weights for each criterion. Then an MCDM method, known as TODIM (Tomada de Decisão Interativa Multicritério, in Portuguese), aggregates the values attributed to each alternative for each criterion in order to obtain a ranking of the alternatives for each individual. Finally, some fuzzy aggregation methods are applied in order to reach a group decision. The preferences of eleven decision-makers, members of a graduate course in Health Technology Assessment at Rio de Janeiro, based on seven criteria, was obtained for three oncological medicine alternatives. Besides allowing the decision-makers to set the scenario of the priority setting process (specification of alternatives, criteria, evaluators and criteria scales), the system shows all the intermediate steps of the decision process, and how individual preferences are formed. Through its output, it is possible to identify patterns in the individual preferences, the most influential criteria, and to perform a sensitivity analysis in order to show how the outcome is sensitive to changes in the alternatives' evaluations. In

this way the system brings transparency to the decision making process.

## Keywords

Multiple criteria decision making • Priority setting  
Group decision

## 1 Introduction

Decision making in healthcare is usually characterized by a low degree of transparency due to the lack of a systematic evaluation framework [1]. In addition, such decisions rarely have simple solutions because of several factors, such as limited resources, patient group pressures for the “new” treatment, an increasing number of technologies in the market, and often information that is not available or with weak evidence about these technologies [2]. The use of economic evaluations such as cost-effectiveness analysis may not be sufficient for decision making [1, 3].

In this context, Multiple Criteria Decision Making (MCDM) methods have emerged as a technical approach of interest for Health Technology Assessment [2, 4]. MCDM can be conceptualized as a set of methods in which two or more criteria are used to explore the relevance of individual or group decisions. Thus, these methods have the capacity to aggregate, in a comprehensive manner, all the characteristics considered important, including non-quantitative ones, allowing for the transparency and systematization of the decision process [4, 5].

There are different MCDM methods which are usually classified into three types [2, 4]: value measurement models; reference-level models; and outranking methods.

The value measurement approach is the most used and has the objective of constructing a global value for each alternative in order to compare them and to define those with more preference. Two such methods are the Hierarchical Process Analysis (HPA) [6], and MACBETH (Measuring

S. M. Freire  
Universidade do Estado do Rio de Janeiro, Rio de Janeiro, RJ,  
Brazil

A. Nascimento · R. T. de Almeida (✉)  
Universidade Federal do Rio de Janeiro, Rio de Janeiro, Brazil  
e-mail: rosal@ufrj.br

Attractiveness by a Categorical Based Evaluation Technique) [7]. In the reference level models there is a search for the alternative that most closely matches the predefined minimum standards of performance in each criterion. The Technique for Order of Preference for Similarity to Ideal Solution (TOPSIS), Goal Programming and Data Envelopment Analysis (DEA) [2, 8] are such examples. In the outranking methods, paired comparisons of the alternatives are made that generate a measure of dominance among the alternatives for each criterion. From this measure, an ordering between the alternatives is defined [4]. Two such systems are: the ELECTRE (Élimination et Choix Traduisant la Réalité) and the PROMETHEE families (Preference Ranking Organization Methodology for Enrichment Evaluations) [9]. Finally the so-called hybrid methods have technical elements of more than one of the approaches quoted above. An example of this is the TODIM (Tomada de Decisão Interativa Multicritério, in Portuguese) method [5].

This paper presents a prototype computer system, AOGruPO (Agregando Opinião em Grupo, in Portuguese), designed to allow decision-makers to apply a multiple criteria method through a graphic user interface.

## 2 Materials and Methods

The details of the multiple criteria method implemented in AOGruPO are presented elsewhere [10]. Here only a brief summary of it will be presented, in order to give a context on how the system works.

A decision problem is based on a set of finite alternatives  $A: \{a, b, c, \dots\}$  and a set of judgement criteria  $C: \{1, \dots, k, \dots, p\}$ . Given the alternatives and criteria, a matrix  $V: \{V_k(a)\}$  is obtained, reflecting the viewpoint of the decision maker (DM), where  $V_k(a)$  corresponds to the evaluation of alternative  $a$  ( $a \in A$ ). Value judgement for each criterion can be expressed on either a cardinal or an ordinal scale. These scales are employed for ordering alternatives with respect to criteria and to weight the criteria. By directly using ordinal scales, judgmental statements are converted into numerical values read on the cardinal scale.

In prospect theory, the key element is a value function, obtained for each criterion reflecting the gain and losses of the alternative as compared to a selected reference criterion [11]. Based on the prospect theory, an interactive multiple criteria decision making method (TODIM) has been proposed by Gomes [5]. In this method, the matrix  $V$ , representing the value judgement of the DM, is normalized across alternatives obtaining a matrix of  $p$  criteria  $\times$   $n$  alternatives  $W: \{w_c(a)\}$ , which is called the position matrix of the DM. From matrix  $V$ , a position matrix  $W$ , representing the normalized value judgement of the DM, is obtained using a normalized set of weights,  $G(g_c)$ . The transformation is

based on expressing the scores of each alternative as positive or negative deviations (gains or losses) from all other alternatives. For each DM and criterion, an  $n \times n$  matrix,  $\Phi_c$ , called partial dominance is generated. The elements  $\Phi_c(i, j)$  are obtained using a function that closely describes the shape of the prospect value function.

TODIM can be used either for a single DM or for some group of decision agents. In both cases, the analyst constructs an  $n \times n$  dominance matrix  $D: \{\delta(i, j)\}$ .  $\delta(i, j)$  are obtained using a function expressing the sum of the partial dominance for the criteria. If  $\delta(i, j) > 0$ , then alternative  $i$  is said to dominate alternative  $j$ , that is, alternative  $i$  is preferable to alternative  $j$ ; if  $\delta(i, j) = 0$ , alternatives  $i$  and  $j$  are equivalent. The overall values of the various alternatives are combined to produce a rank ordering.

When more than one agent is involved in the decision process, the viewpoint of all DMs must be considered in the final result. One alternative to aggregate different opinions is through fuzzy aggregation [9]. This allows us to deal with uncertainty and imprecision that are always present in decision-makers' mind. As originally proposed by Znotinas and Hipel [12], the set of criteria can be viewed as a fuzzy set  $F$ , and the DM is required to provide a value reflecting the degree of membership directly, using some qualitative scale. Here, the degree of membership is derived from each partial dominance matrix  $\Phi_c$  to obtain what is termed the net benefit evaluation matrix for position  $P$  of the DMs. Four of the aggregation methods proposed by Znotinas and Hipel [12] were implemented in AOGruPO: pessimistic aggregation, mean aggregation, optimistic aggregation, and modified pessimistic aggregation. The pessimistic aggregation considers the worst viewpoints in an attempt to minimize risk. The mean aggregation is simply an averaging calculation. The optimistic aggregation considers the best viewpoints. Finally, the modified pessimistic aggregation is obtained by averaging the mean aggregation with the pessimistic aggregation. The method tries to nullify the effects of extreme responses while maintaining the risk minimization characteristic of the pessimistic aggregation.

## 3 Results

### 3.1 AOGruPO

This is a system that can compute all the steps necessary for the MCDM process described above. The system was developed in Java 1.8, through the Netbeans Integrated Development Environment 8.2, and the JFreeChart 1.0.13 was used as the graphics library. Data, either the problem structure or the results, are stored in a relational schema in a MySQL database, version 5.5. The system is available through a contact with the first author.

The screenshot displays a software interface for configuring a decision-making problem. It is divided into several sections:

- Projects:** A list box containing 'Demo Project', 'Project1', and 'Project2'. 'Demo Project' is selected.
- Title:** A text input field containing 'Demo Project'. Below it are 'new', 'Save', and 'delete' buttons.
- Criteria Weight Scale:** A dropdown menu set to 'importance'. Below it is a list of scale values: 'very low importance = 1', 'little importance = 2', 'high importance = 4', 'very high importance = 5', and 'medium importance = 3'. A 'close' button is at the bottom.
- Evaluators:** Two list boxes. 'Available Evaluators' contains A1 through B4. 'Selected Evaluators' contains AL-D10 through AL-D7. Arrows between the boxes allow moving items between them.
- Alternatives:** Two list boxes. 'Available Alternatives' contains 'Citizen Check', 'Community Center for the Def', 'Family Health', 'Generate Lives', 'Hospitable Rio', and 'Integrated Family Assistance'. 'Selected Alternatives' contains 'Carfilzomib', 'Nivolumab', and 'Palbociclib'. Arrows between the boxes allow moving items between them.
- Criteria:** Two list boxes. 'Available Criteria' contains 'Impact on child mortality rate', 'Impact on families with >2 per...', 'Impact on insufficient income', 'Impact on life expectancy', 'Impact on people out of school', 'Impact on students with >1 ye', and 'Impact on the educational lev...'. 'Selected Criteria' contains 'Epidemiological relevance', 'Impact on healthcare budget', 'Impact on safety', 'Impact on the healthcare unit cost', 'Impact on the reduction of mortality', 'Relevance to the current treatment', and 'Relevance to the healthcare policies'. Arrows between the boxes allow moving items between them.

**Fig. 1** Problem setting screen. Users select the list of alternatives, decision-makers involved, criteria and the corresponding scale of measurement

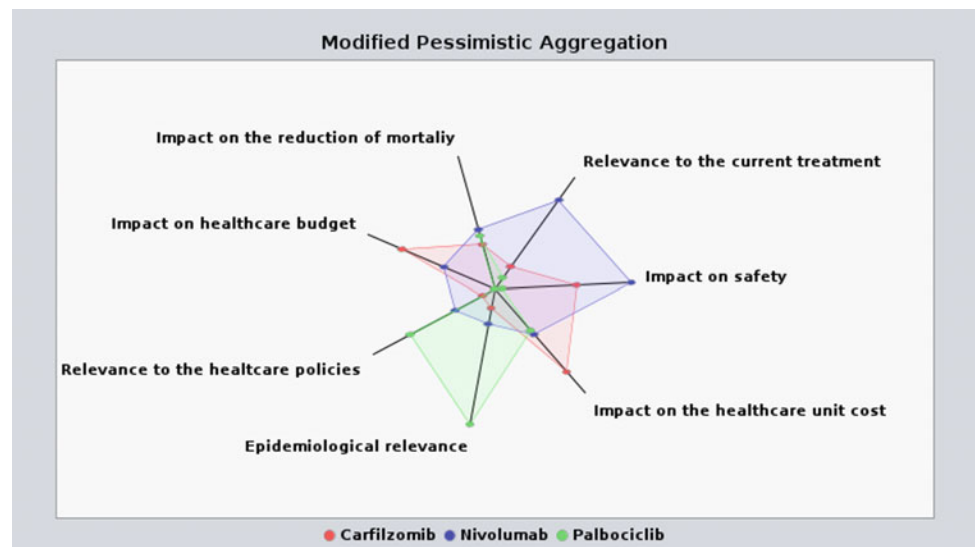
Through a menu, the user can configure the problem scenario: alternatives, evaluators, criteria, and scales for each criterion (Fig. 1). Configurations from previous problems may be reused. After the configuration phase, the DM must attribute weights/values to each alternative with respect to each criterion, according to the criterion scale. The system does not allow values outside each scale range. Results are not computed until all data are entered.

The results are shown for all the phases of the priority process, either through a series of tables or charts, so that users can follow all the steps from data entry to the final aggregation. By going to the configuration screens and changing values in the evaluation matrix, the user may remove or add criteria, DMs, alternatives, and change scales. The change in the results can be seen with the new configuration.

### 3.2 An Application of AOGruPO in a Real Scenario

A pilot study was performed with 11 members of a graduate course in Health Technology Assessment with the objective of prioritizing three drugs for the treatment of cancer: Carfilzomib, Nivolumab, and Palbociclib. The decision problem was evaluated by means of 7 criteria: (a) Epidemiologic relevance; (b) Relevance to health polices; (c) Impact on the reduction of mortality; (d) Relevance to the current treatment; (e) Impact on the Brazilian Unified Health System budget; (f) Impact on the healthcare unit cost; and (g) Safety. All the criteria scales were ordinal. The weight for each criterion is given by the following scale: 1—very low importance, 2—low importance, 3—medium importance, 4—high importance, 5—very high importance.

**Fig. 2** Preferences of the evaluators for the 3 drugs in each criterion



The individual preferences of each DM were calculated by means of the TODIM method. The final order set, according to the modified pessimistic approach, was: 1—Nivolumab, 2—Palbociclib, 3—Carfilzomib. Figure 2 shows the spider web chart for the group preferences for each drug and each criterion, where it can be seen that the area under Nivolumab is the greatest of the three drugs.

## 4 Discussion

In the health sector, MCDM methods have been applied relatively recently. According to Marsh et al. [13], the first MCDM study in the health area dates back to 1990, with more than half of the studies published since 2011. One challenge to a more widespread use of MCDM methods in healthcare is the lack of familiarity of healthcare DM with the diversity of MCDM methods and their theoretical underpinnings [1].

The proposed system offers a user-friendly interface that enables users to apply a hybrid MCDM method in order to support the priority setting process. It also shows decision-makers how the preferences are formed, transformed, and supported. An important aspect in the application of MCDM methods is the need of a sensibility analysis of the decision process because it can validate the final result. A review of the literature has shown that this aspect is little emphasized [14].

This system may not only support the decision making process, but also help the diffusion of the MCDM methods to the appropriate audience. The process of deciding which technologies should be prioritized gains greater transparency and efficiency, as recommended by health technology assessment prioritization guidelines [15].

**Conflicts of Interest** The authors declare that they have no conflict of interest.

## References

- Mühlbacher, A.C., Kaczynski, A.: Making Good Decisions in Healthcare with Multi-Criteria Decision Analysis: The Use, Current Research and Future Development of MCDA. *Appl Health Econ Health Policy* 14, 29–40 (2016).
- Thokala, P., Devlin, N., Marsh, K., Baltussen, R., Boysen, M., et al.: Multiple Criteria Decision Analysis for Health Care Decision Making – An Introduction: Report 1 of the ISPOR MCDA Emerging Good Practices Task Force. *Value in Health* 19, 1–13 (2016).
- Devlin, N. J., Sussex, J. Incorporating Multiple Criteria in HTA: Methods and Processes. Available: [https://healthpolicy.fsi.stanford.edu/sites/default/files/ohe\\_hta\\_methods.pdf](https://healthpolicy.fsi.stanford.edu/sites/default/files/ohe_hta_methods.pdf), last accessed 2018/01/23.
- Angelis, A., Kanavos, P.: Value-Based Assessment of New Medical Technologies: Towards a Robust Methodological Framework for the Application of Multiple Criteria Decision Analysis in the Context of Health Technology Assessment. *Pharmacoeconomics* 34, 435–446 (2016).
- Gomes, L.F.A.M., Araya, M.C.G., Carignano, C.: Tomada de Decisões em Cenários Complexos: Introdução aos Métodos Discretos do Apoio Multicritério à Decisão. *Pioneira Thomson Learning*, São Paulo (2004).
- Saaty, T.L.: Decision making with the analytic hierarchy process. *Int. J. Services Sciences*, 1(1), 2008. Available: [http://www.colorado.edu/geography/leyk/geog\\_5113/readings/saaty\\_2008.pdf](http://www.colorado.edu/geography/leyk/geog_5113/readings/saaty_2008.pdf), last accessed 2016/08/17.
- Bana e Costa, C.A., de Corte, J.M., Vansnick, J.C.: MACBETH. *International Journal of Information Technology & Decision Making* 11(2), 359–87 (2012).
- Mobinizadeh, M., Raeissl, P., Nasiripour, A. A., Olyaeemanesh, A., Tabibi, S. J.: A Model for Priority Setting of Health Technology Assessment: the Experience of AHP-TOPSIS Combination Approach, *DARU Journal of Pharmaceutical Sciences*, 24 (10), <https://doi.org/10.1186/s40199-016-0148-7> (2016).

9. Roy, B., Vanderpooten, D.: The European School of MCDA: Emergence, Basic Features and Current Works. *Journal of Multi-Criteria Decision Analysis* 5, 22–38 (1996).
10. Nobre, F.F., Trotta, L.T.F., Gomes, L.F.A.M.: Multi-Criteria Decision Making - An Approach to Setting Priorities in Health Care, *Statistics in Medicine* 18, 3345–3354 (1999).
11. Kahneman D, Tversky A. Prospect theory: an analysis of decision under risk. *Econometrica* 47, 263–291 (1979).
12. Znotinas, N.M., Hipel, K.W.: Comparison of Alternative Engineering designs. *Water Resources Bulletin* 15, 44–58 (1979).
13. Marsh, K., Lanitis, T., Neasham, D., Oreas, P., Caro, J.: Assessing the Value of Healthcare Interventions Using Multi-Criteria Decision Analysis: A Review of the Literature. *Pharmacoeconomics*, 32, 345–365 (2014).
14. Broekhuizen, H., Groothuis-Oudshoorn, C.G., van Til, J.A., Hummel, J.M., Ijzerman, M.J.: A Review and Classification of Approaches for Dealing with Uncertainty in Multi-Criteria Decision Analysis for Healthcare Decisions, *Pharmacoeconomics* 33 (5), 445–55 (2015).
15. Husereau, D., Boucher, M., Noorani, H.: Priority setting for health technology assessment at CADTH, *International Journal of Technology Assessment in Health Care* 26(3), 341–347 (2010).

# Towards Computer Supported Search for Semiological Features in Epilepsy Seizure Classification

Michaela Nova, Lenka Vyslouzilova<sup>✉</sup>, Zdenek Vojtech, and Olga Stepankova<sup>✉</sup>

## Abstract

Seizure semiology has always been an important part of seizure classification. Value of the most common ictal signs for localization and lateralization of a seizure focus, as well as their sensitivity and specificity for certain focal epilepsies, is well known. All over it, there still remain many signs and poorly described patient behaviours during a seizure whose relation to a seizure focus have yet to be specified and confirmed. Some new signs have been introduced recently but all of them have been based on data provided from just a few dozens of patients. This is no surprise since checking for presence of a specific ictal sign in a patient requires lengthy manual review of video records documenting his/her seizures. We suggest a novel approach toward identification/verification of new ictal signs based on computer supported systematic review of unique extensive dataset of Na Homolce Hospital containing approximately 1.000 seizures (representing data of 400 patients with up to 5 seizures annotated). This requires transforming the original set of patient records into a database consisting of annotated ictal video-EEG recordings in a structured form suitable for statistical analysis as well as for analysis of sequence patterns. This contribution describes our SW tool ASTEP designed and developed for this purpose and demonstrates some properties of ASTEP database, namely advantages of the used seizure description as a sequence of considered

ictal signs complemented by detailed information on timing, duration, repetition and mode of appearance of these signs. Finally, some preliminary results are reported.

## Keywords

Epilepsy • Seizure semiology • Video-EEG analysis

## 1 Introduction

The epilepsies are one of the most common neurological disorders. In some cases treatment with antiepileptic drugs does not render the patient seizure-free. In a subgroup of focal epilepsies the proportion of intractable patients is about 30%. Important part of them will be epilepsy surgery candidates [2].

The aim of presurgical evaluation is to ascertain the localization and extent of epileptogenic zone (i.e. the cortical region in which seizures are arising and after resection of which they are abolished). Symptomatogenic zone is defined as a region of cerebral cortex responsible for the initial seizure semiology. Apart from meticulous seizure history the most accurate method for its diagnosis is video-EEG analysis. Ictal signs may not provide unequivocal evidence of localization of the epileptic focus but often they help to direct subsequent investigations leading to the ultimate localization [11]. Their topical relation to the epileptogenic zone is variable [7], because each of the used methods has its shortcomings (e.g. surface recordings have problems to identify seizure onsets occurring in cortical regions located relatively deep with respect to the scalp surface).

There are many ictal signs that are recognized for their sensitivity and specificity when used for localization and lateralization of a seizure focus of certain focal epilepsies [13]. There has been developed a widely used semiological seizure classification [6] and a classification of seizures and epilepsies [1] that are both based on seizure semiology.

M. Nova · L. Vyslouzilova (✉) · Z. Vojtech  
Nemocnice Na Homolce, Roentgenova 37/2, 150 30 Praha 5,  
Czech Republic  
e-mail: lenka.vyslouzilova@cvut.cz

L. Vyslouzilova · O. Stepankova  
Czech Institute of Informatics, Robotics, and Cybernetics, Czech  
Technical University, Jugoslávských partyzánů 1580/3, 160 00  
Prague 6, Czech Republic

O. Stepankova  
Department of Cybernetics, Faculty of Electrical Engineering,  
Czech Technical University, Technicka 2, 166 27 Prague 6, Czech  
Republic



Current ILAE classification deals even with ictal signs that have been described by witnesses of the seizure or patients themselves, only—such description is often unclear [4]. A video-EEG record of a seizure allows more detailed analysis of seizure semiology and ictal signs. Some ictal signs and patient behaviours during a seizure are still poorly described and their relation to the focus has to be found, yet:

1. Some new ictal signs are described only in case reports, especially if they are conspicuous or bizarre [10]. Less conspicuous signs could be missed, although their value for the localization or lateralization could be crucial.
2. In some ictal signs (e.g. automatisms, convulsions), additional subtle features, beyond their general character, are important (timing, duration, repetition, mode of appearance) [3]. **These features are described only in small cohorts of patients and their sensitivity and specificity is unknown.** Careful inspection of activities occurring during seizures of much bigger groups of patients will probably result in identification of new ictal signs. We expect further clinical use of these additional subtle characteristics that could significantly contribute to accuracy and reliability of the presurgical evaluation.
3. With respect to the rapid spread of epileptic discharge, several ictal signs may coexist during the same seizure. Sequence of their appearance [9] could be correlated with results of other diagnostic methods (i.e. neuroimaging) and epilepsy surgery. This knowledge could contribute to improved diagnostics of focal epilepsies [8].

In 2016, our PubMed search for papers dealing with seizure semiology brought 767 results and only minority of them was devoted to description of seizure semiology. Nevertheless, the analysis of seizure semiology remains still a “hot topic” [5] where new attempts to integrate semiological and other clinical data in the diagnostic process start to appear [12].

All over general agreement on importance of ictal signs or their sequences for epilepsy diagnostics there are no modern articles about semiological characteristics of both epileptic and non-epileptic seizures performed on a large group of unselected patients. This is a surprising finding because lot of relevant data is collected in epilepsy centres all over the world. For example, our home institution Na Homolce Hospital as a comprehensive tertiary epilepsy centre functioning since 1993 succeeded to collect **a unique dataset of approximately 1.000 video recorded seizures** most of which can be further complemented by information from the hospital archive about future development of the patient and his/her disease. Unfortunately, this format of data makes it far from ready to be subjected to thorough analysis. The mayor problem of such a plan is that the revision of such

a large material would have to be done manually and this represents an extremely laborious and time-consuming activity. To face the curse of this complexity we have decided to extract all relevant information contained in the video-EEG recordings into a structured database that will store information implicitly present in the videos in a digital format that will contain information about the seizures and its ictal signs with respect to its timing, duration, repetition and mode of appearance. Transition to this new representation of considered observations will make them ready for detailed statistical and data mining analysis.

The Sect. 2 of this paper describes basic features of an original software tool ASTEP we have designed and developed and indicates its advantages by explaining few preliminary findings based on current content of the created database. The Sect. 3 reviews our user experience with this tool during the process of seizure annotations and identifies some novel aspects of the used data representation and highlights benefits of the suggested approach for analysis of video-EEG. In the concluding Sect. 4 we review our further plans how to work with the content of our database and what additional features we would like to implement into ASTEP.

---

## 2 ASTEP: Annotation and Statistical Tool for EPilepsy

The SW tool **ASTEP** has been designed to support a physician who annotates the video-EEG recordings with intention to store all relevant information in a structural database consisting of annotated ictal video-EEG recordings performed in patients with (epileptic and non-epileptic) seizure disorders. Figure 1a shows the main window of ASTEP tool which helps the neurologist in doing following three activities.

First, he/she inputs the patient’s anamnesis (process analogous to working with the hospital info system). Second, the EEG part of the video-EEG recording is used to determine the exact time of the beginning and end of the electrographic ictal activity. Now, the third and core ASTEP activity starts. At this moment the neurologist can fully focus on the video record annotation: he/she follows the time-stamped record in the right part of the screen. The video can be frozen whenever the neurologist identifies something worthy of recording. He/she selects from the drop-down menu (offering all formerly used elementary signs) the observed sign and registers it in the patient record together with its start and end time. If a new (not yet used) sign appears, it is given its correct name according to [6] and it is added to the drop-down menu.

ASTEP offers a graphical summary of all signs identified in a seizure—a picture showing not only the list of occurring signs but also their sequence in time and their duration; see the central part of Fig. 1a. This is useful e.g. for visual

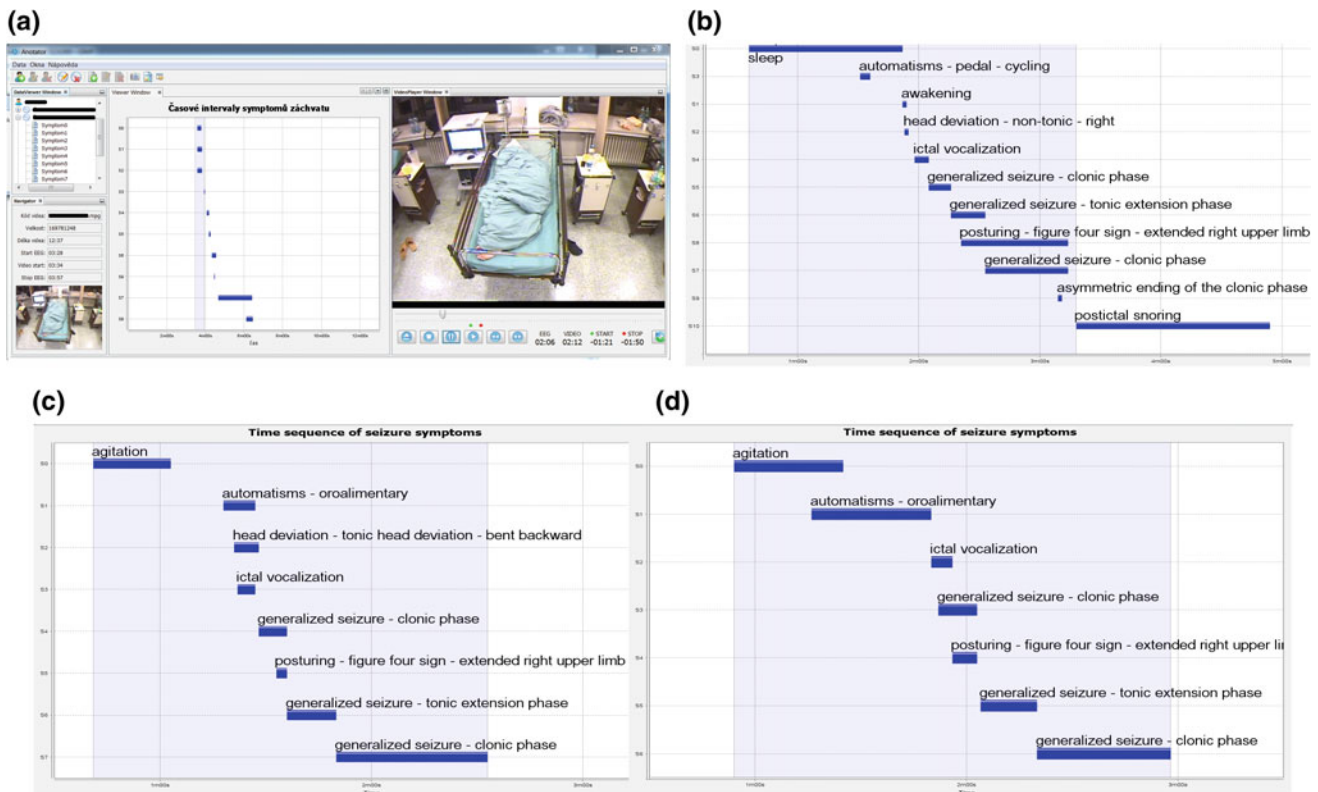


**Fig. 1** **a** The screenshot of ASTEP interface for video annotation. The image was edited to anonymize the patient. **b** Graphical summary of a seizure. **c** and **d** are graphical summaries of two different seizures of a patient with left mesial temporal sclerosis

comparison of the course of several seizures of a single patient (see the graphical summaries on Fig. 1b–d complemented by the comments given in the last paragraphs of this section).

Figure 1c, d allow comparing two different seizures present in one patient whose final diagnosis is left mesial temporal sclerosis. It is clearly visible that the variability of seizure semiology in the considered patient is very small. This is typical for epileptic seizures, while in psychogenic non-epileptic seizures their ictal semiology can vary a lot). Both depicted seizures begin with an *agitation* of the patient, continue with *oroalimentary automatisms* and via *vocalization* to *secondary generalization with tonic phase* including *asymmetric limb posturing (figure four sign)* and end by *clonic phase of generalized seizure*. The *tonic head deviation* seen in first seizure (indicated by an arrow) was not present in the second one. Only little differences in the semiology like this were found in so far annotated seizures of a single patient. This is why we decided to annotate 5 seizures for each patient maximally. On this patient we can also show the localization/lateralization value of several signs. For example the *oroalimentary automatisms* are typical sign for temporal lobe epilepsy as well as the *figure four sign with extended right upper limb* implies the epileptogenic zone is in contralateral (i.e. left) hemisphere.

Patient whose seizure is depicted on Fig. 1b suffered from epilepsy due to a cavernoma in left frontal lobe. It is already known that seizures coming from frontal lobe have various semiology (but stereotypical in one patient as it was already mentioned). In this patient the seizure begins from *sleep*, at the beginning the *non-tonic head deviation* and *pedal automatisms* are present (frequently seen in frontal lobe epilepsy) and rapid *secondary generalization* introduced by *vocalization*. As well as in the previous patient *figure four sign* is seen—the *extended upper limb (right)* again corresponds to the origin of seizure in contralateral (left) hemisphere. And last but not least another typical sign with high lateralization value is shown—*asymmetric ending of clonic phase* of secondarily generalized tonic clonic seizure.

### 3 User Experience and Preliminary Results

Up to now, the ASTEP tool has been utilized for annotation of approximately 60 seizures selected from the video-EEG recordings archive of Na Homolce Hospital. The average length of such video-EEG records is approximately 10 min. The traditional manual annotation of seizures is very demanding—it requires full attention of a medical expert and according to our experience it takes 1–2 h. All over this

demanding procedure has to be ensured for all EEG-video recordings most of its results are never reused and they remain finally hidden in the verbal description of the neurologist's assessment of a single patient. ASTEP does not speed up the annotation—it brings another benefit: all the observed signs remain safely recorded in a searchable database and thus they are ever ready for further detailed analysis. The resulting database can be gradually complemented by additional recent cases. It is simple to query the newly created database on statistical relevance of individual ictal signs e.g. seizure focus or on specific features of all the patients with specified symptoms.

Very friendly user interface offered by ASTEP is highly appreciated by the neurologist responsible for video annotation, because it significantly simplifies systematic annotation of seizures, storage of unique data as well as their interpretation. The current content of ASTEP database is expected to grow during the coming years. But already now it is ready to answer questions on existence of additional novel complex patterns characterized by sequences of ictal signs and check for their occurrence in all our annotated data. This transition from the separate ictal signs towards their sequences can bring richer possibilities for diagnosis of epilepsies and non-epileptic seizures and assess their occurrence in respect to timing, duration, clustering, repetition etc., as well as study their value for definitive diagnosis. For example, it is commonly assumed that closed eyes during a seizure point to non-epileptic nature of the attack. Nevertheless, timing, context (whether it is found during automatisms or generalized convulsions is early/late ictal sign etc.) and sensitivity of this sign are unknown.

Such problems cannot be tackled with the other current relevant databases, e.g. ACTIVE database (<http://www.active-fp7.eu>) storing information about a seizure in the form of a bag of signs expressed or present in the seizure. Such a representation can neither provide any claims about duration of the signs nor distinguish between the seizures where sign A precedes the sign B and the seizures where B occurs before A.

## 4 Conclusions

Storing annotations of seizures in the structured database makes it possible to perform statistical and sequence analysis repeatedly over ever larger datasets and consequently obtain more accurate results on elementary signs that can improve semiological seizure classification. This is very helpful in searching for already described or newly found semiological signs and their relation to chosen patients' characteristic (mainly the diagnosis/localization of the epileptogenic lesion) which is useful in planning the epilepsy surgery. Moreover, the identified sequences will be

offered for extension of newly created epilepsy and seizure ontology (EpSO) using a four-dimensional epilepsy classification system that integrates the latest International League Against Epilepsy terminology recommendations and National Institute of Neurological Disorders and Stroke common data elements [12]. Special attention will be given to analysis of groups of ictal signs during a seizure and appropriate machine learning methods will be made available for that purpose in ASTEP tool.

**Acknowledgements** The research has been partially supported by the Internal Grant of the Nemocnice Na Homolce, Internal Grant of the Czech Institute of Informatics, Robotics, and Cybernetics, CTU in Prague and CTU grant SGS16/231/OHK3/3T/13.

## References

1. BERG, Anne T., et al. Revised terminology and concepts for organization of seizures and epilepsies: report of the ILAE Commission on Classification and Terminology, 2005–2009. *Epilepsia*, 2010, 51.4: 676–685.
2. ENGEL, Jerome. Another good reason to consider surgical treatment for epilepsy more often and sooner. *Archives of neurology*, 2011, 68.6: 707–708.
3. FRANCA, Sara, et al. Side-to-side axial movements. Adding a new sign to the asymmetry of the clonic phase and asymmetric seizure termination in differentiating primary and secondarily generalised tonic-clonic seizures. *Epileptic Disorders*, 2014, 16.1: 1–4.
4. FISHER, R. S., et al. Operational classification of seizure types by the International League Against Epilepsy: Position Paper of the ILAE Commission for Classification and Terminology. *Epilepsia*, 2017, 58: 522–530.
5. JIN B, et al. Analysing reliability of seizure diagnosis based on semiology. *Epilepsy Behaviour*, 2014 Dec; 41: 197–220.
6. LÜDERS, H., et al. Semiological Seizure Classification\*. *Epilepsia*, 1998, 39.9: 1006–1013.
7. LÜDERS, Hans O., et al. The epileptogenic zone: general principles. *Epileptic disorders*, 2006, 8: S1.
8. MAILLARD, Louis, et al. Semiologic and electrophysiologic correlations in temporal lobe seizure subtypes. *Epilepsia*, 2004, 45.12: 1590–1599.
9. NOACHTAR, S.; ARNOLD, S. Simple motor seizures: localizing and lateralizing value. Textbook of epilepsy surgery. London/Boca Raton, FL: Informa Healthcare, Taylor & Francis distributor, 2008, 450–461.
10. OZKARA, C., et al. Ictal kissing and religious speech in a patient with right temporal lobe epilepsy. *Epileptic disorders: international epilepsy journal with videotape*, 2004, 6.4: 241–245.
11. ROSSETTI, Andrea O.; KAPLAN, Peter W. Seizure semiology: an overview of the 'inverse problem'. *European neurology*, 2009, 63.1: 3–10.
12. SAHOO, Satya S., et al. Epilepsy and seizure ontology: towards an epilepsy informatics infrastructure for clinical research and patient care. *Journal of the American Medical Informatics Association*, 2014, 21.1: 82–89.
13. TUFENKJIAN, Krikor; LÜDERS, Hans O. Seizure semiology: its value and limitations in localizing the epileptogenic zone. *Journal of Clinical Neurology*, 2012, 8.4: 243–250.

# Scoring System for the One-Year Mortality Prediction of Sepsis Patients in Intensive Care Units

Javier E. García-Gallo, Nelson J. Fonseca-Ruiz,  
and John F. Duitama-Muñoz

## Abstract

Sepsis is a life-threatening organ dysfunction induced by a dysregulated host response to infection and carries a high mortality and morbidity, therefore, after patients are admitted in an ICU it is necessary to synthesize the large volume of information that is collected in a value that represents their condition. Traditional severity of illness scores seek to be applicable to all patient populations, and usually assess in-hospital mortality. However, people who survive sepsis may have permanent organ damage and eventually suffer from a sepsis-related death. This study presents the development of a score for the one-year mortality prediction of the patients that are admitted in an ICU with a sepsis diagnosis. 5650 ICU admissions extracted from MIMICIII database were evaluated and divided into two groups (70% development, 30% validation). LASSO and SGB variable importance methodologies were used over the training subset to select the set of predictors that make up the score. Cut-off points that divided the cohort into two groups with different risks were found for each of these variables, and the numeric data were converted into binary. These predictors were used in a LR model, and its coefficients were rounded to the nearest integer, resulting in the point values that make up the score when multiplied with each binary variable and summed. Then, the one-year mortality probability was estimated using the score as the only variable in a LR model. The score, was evaluated using the validation subset, obtaining an AUROC of 0.73, which outperforms

the results obtained with three commonly used severity of illness scores on the same subset.

## Keywords

Intensive care unit (ICU) • Least absolute shrinkage and selection operator (LASSO) • Logistic regression (LR) Mortality prediction • Sepsis • Severity of illness Stochastic gradient boosting (SGB)

## 1 Introduction

More than twenty years ago, sepsis was defined as a systemic inflammatory process in response to an infection; and from that moment the systemic inflammatory response syndrome (SIRS) was used together with the presence of infection to diagnose sepsis [1]. However, advances into the pathobiology, management, and epidemiology of sepsis led to the reexamination of the definitions. The most recent consensus, held in 2016, suggests that Sepsis should be defined as life-threatening organ dysfunction caused by a dysregulated host response to infection. Organ dysfunction can be represented by an increase in the Sequential Organ Failure Assessment (SOFA) score of 2 points or more [2]. The consensus also evaluated which clinical criteria best identified infected patients most likely to have sepsis. The evaluated criteria were: SOFA, Logistic Organ Dysfunction System (LODS) and SIRS; In Intensive Care Unit (ICU) patients with suspected infection, discrimination for in-hospital mortality with LODS and SOFA were not statistically different but were statistically greater than that of SIRS, and since SOFA is better known and simpler than the LODS, the consensus recommends using SOFA to represent organ dysfunction [2, 3]. The Consensus also introduced a new clinical score termed quick Sequential Organ Failure Assessment (qSOFA) for identification of patients at risk of sepsis outside the ICU, however, its performance within the ICU has also been evaluated, and it has been concluded that

---

J. E. García-Gallo (✉) · J. F. Duitama-Muñoz  
Engineering and Software Investigation Group, Universidad de  
Antioquia UdeA, Medellín, Colombia  
e-mail: jesteban.garcia@udea.edu.co

N. J. Fonseca-Ruiz  
Critical and Intensive Care, Medellín Clinic, Medellín, Colombia

N. J. Fonseca-Ruiz  
Critical and Intensive Care Program, CES University, Medellín,  
Colombia



was statistically greater than SIRS [3, 4] criteria but significantly less than SOFA [3].

Despite advances in care, recent studies suggest that sepsis remains a major cause of mortality [5], with a high in-hospital mortality rate ranging from 25 to 30%, besides, epidemiologic data for sepsis are scarce for low- and middle-income countries [6], therefore the mortality rate could be even higher. Moreover, sepsis survivors suffer from additional morbidities such as higher risk of readmissions, cardiovascular disease, cognitive impairment and death (one in six sepsis survivors die in the first year following the sepsis episode) [7]. For these reason this work presents the development of a score for the one-year mortality prediction of the patients that are admitted in an ICU with a sepsis diagnosis, which could help to identify risk factors during an ICU stay and lead to a better understanding of the long-term consequences and events occurring after hospital discharge.

## 2 Methods

### 2.1 Data Description

MIMIC-III (Medical Information Mart for Intensive Care) is a large, single-center database comprising information relating to patients admitted at the ICUs of Boston's Beth Israel Deaconess Medical Center between 2001 and 2012 [8]. MIMIC-III contains data associated with 53,423 distinct hospital admissions for patients aged 16 years or above; of which 14,105 admissions with a diagnosis of sepsis according to the Angus criteria [9] were extracted; of those admissions 269 admissions were discarded because the ICU stays were shorter than 24 h, then 4,456 admissions were discarded because they had less than 70% of the laboratory measurements listed in Table 1, and 3,730 were disposed of since they had Less than 70% of routine charted data

**Table 1** Laboratory measurements variable included in the study

Laboratory measurements	Unit
Platelet count	$10^9/L$
Bilirubin	mg/dL
Creatinine	mg/dL
White Blood Cell (WBC) count	$10^3/mm^3$
Potassium	mEq/L
Sodium	mEq/L
Bicarbonate	mEq/L
Lactate	mg/dL
Arterial pH	pH
Hematocrit	%
Hemoglobin	mg/dL

presented in Table 2; resulting in a study cohort of 5650 admissions, which was randomly divided into two groups: a training subset with 70% of the admissions and a validation subset of 30% of the admissions. The maximum and the minimum values of the data listed in Tables 1 and 2 during first 24 h of each ICU stay were calculated as possible items in the scoring system, beside those candidate predictors, the following data, related to patient and his stay in the ICU, were extracted and evaluated:

- i. Data taken at the time of ICU admission: Gender, Age.
- ii. Comorbidities: Immunosuppressive diseases, Malignancy, Hematologic malignancy, Metastatic cancer, Heart failure, Pulmonary diseases, Hypothyroidism.
- iii. Organ dysfunction: Cardiovascular, Hepatic, Hematologic, Renal, Mechanical Ventilation.

### 2.2 Score Development

The laboratory measurements and routine charted data described in the previous section were converted into 40 predictors (maximum and minimum values of each variable), then two methodologies were implemented over the training subset, in order to select the set of predictors used to develop the score; the first one is Least Absolute Shrinkage and Selection Operator (LASSO), a method that performs both variable selection and regularization [10]; the second one is variable importance using Stochastic Gradient Boosting (SGB), a procedure that indicates the contributions of each of the predictors to the predictive ability of a SGB model [11]. SGB is an ensemble methodology based on decision trees, and the relative contribution of each predictor is based on the number of times a variable is selected for splitting, weighted by the squared improvement to the model as a result of each split, and averaged over all trees [12, 13]. The impact of each variable is scaled so that the relative importance of all predictors amounts to 100, higher numbers represent a greater influence on the output [12]. R software were used to implement the models; the R-packages used were caret [14], gbm [15] and glmnet [16]. Unlike LASSO, the SGB variable importance methodology does not automatically select the predictors, however it indicates which have a stronger influence on the response; Therefore, it is possible to select a set of predictors that allow developing a model that presents a performance similar to the model with all the predictors. A cutoff point (CP) for the age, and each of the variables that were selected with both methodologies (the intersection of LASSO and SGB variable importance predictors), were obtained; for this a set of values were used to divide the dataset into two groups, those below the CP and those above, afterwards the mortality rate of each group were

**Table 2** Routine charted data variables included in the study

Routine charted data	Unit
Temperature	°C
Heart rate	bpm
Arterial blood pressure systolic	mmHg
Arterial blood pressure diastolic	mmHg
Arterial blood pressure mean	mmHg
Urine output	mL
Base excess	mEq/L
Glucose	mg/dL
Peripheral capillary oxygen saturation (SpO <sub>2</sub> )	%

calculated and the number of admissions in each group were assessed. Thus, the CP was selected taking into account the following criteria:

- i. The smallest group contains at least 30% of admissions.
- ii. The biggest difference between the mortality rates between the groups.

After the selection of the CP, all predictors were binarized, for this, a one is assigned to each predictor, if its value is within the population with a higher mortality rate. Then the binary data were used in conjunction with the data taken at the time of ICU admission, the comorbidities and the organ dysfunction information to develop a logistic regression (LR) model, the coefficients of that model were rounded to the nearest integer and used as the point values of the scoring system, when this point values are multiplied with each binary variable and summed generate the final score; then, the one-year mortality probability was estimated using the final score as the only variable in a LR model. Model discrimination was examined using the Area under Receiver Operating Characteristic (AUROC) of the LR model with the final score.

The admissions of the validation subset were divided into ten equal size groups according to the increasing estimated probabilities of one-year mortality given by the model, so that in the first group are those admissions that have the lowest probabilities of dying, and in the last group are those admissions with the highest probabilities of dying. For each group the observed and the estimated number of deaths were calculated and compared graphically.

### 3 Results

According to the methodology described in the previous section, a score was developed using the rounded coefficients of a LR model that used the binary form of the predictors of the LASSO and SGB variable importance intersection, the data taken at the time of ICU admission and the comorbidities and

**Table 3** Scoring system

Parameter	Value	Score
Gender	Male	2
Age	>66	12
Heart rate Max	>117	2
Systolic ABP Min	<80	3
Systolic ABP Max	<142	2
Temperature Min	<36.2	1
Temperature Max	>37.6	4
Urine output	<1041.8	10
Blood urea nitrogen Max	>23	4
White Blood Cell Count Min	>11.9	3
Potassium Min	>3.9	1
Bilirubin Max	>0.7	2
Glucose Min	<90	5
Hemoglobin Max	<10.9	5
Lactate Min	>1.4	2
Platelet Count Max	<171.4	3
<i>Comorbidities</i>		
Hematologic malignancy		4
Metastatic cancer		8
Immunosuppressive diseases		1
Malignancy		4
Heart failure		4
Pulmonary diseases		1
Hypothyroidism		1
<i>Organ dysfunction</i>		
Cardiovascular		2
Hematologic		1
Hepatic		2
Renal		2
Mechanical Ventilation		8

organ dysfunction to estimate the one-year mortality. The scoring system is presented in Table 3.

The final score is a number between 0 and 99 (however no patient gets the maximum score in our study). Figure 1, presents the relation between the final score and the predicted probability of one-year mortality. Observed versus predicted numbers of deaths were compared graphically (Fig. 2) within the ten different groups of increasing probability of one-year mortality. The probability of one-year mortality on the validation subset was estimated using the final score as the sole variable in a logistic regression model, the obtained AUROC was 0.73. To benchmark the scoring system, the AUROC of SOFA, qSOFA and Oxford Acute Severity of Illness Score (OASIS) [17] on the validation subset were calculated. The AUROC values for qSOFA,



**Fig. 1** Relation between the final score and the probability of one-year mortality

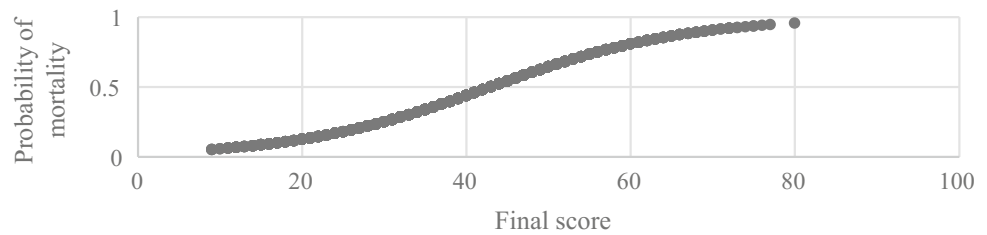


**Fig. 2** Comparison of observed versus predicted number of deaths by groups of increasing probability of one-year mortality



SOFA and OASIS scores on the validation subset were 0.5565, 0.5885 and 0.6317 respectively.

## 4 Conclusions

The developed score accurately estimated the probability of one-year mortality in sepsis diagnosed patients. AUROC analysis shows that the presented score outperforms other scoring systems, even more, the predictive capacity of the score is better, in this study, than the SOFA and qSOFA, that are the scoring systems used for the most recent sepsis and septic shock consensus [2, 3]. The objective of this score is to early alert of a worse prognostic, however it is possible to use the values of the variables listed in Table 3 to develop a non-linear model for the one-year mortality prediction of ICU patients diagnosed with sepsis.

**Acknowledgements** This work was supported by COLCIENCIAS-Departamento Administrativo de Ciencia, Tecnología e Innovación de la República de Colombia through the Doctorados nacionales program.

**Conflicts of Interest** The authors declare that they have no conflict of interest.

## References

- Bone RC, Balk RA, Cerra FB, et al (1992) Definitions for sepsis and organ failure and guidelines for the use of innovative therapies in sepsis. *Chest* 101:1644–1655
- Opal SM, Rubenfeld GD, Poll T Van Der, et al (2016) The Third International Consensus Definitions for Sepsis and Septic Shock (Sepsis-3). *JAMA J Am Med Assoc* 315:801–810. <https://doi.org/10.1001/jama.2016.0287>
- Seymour CW, Liu VX, Iwashyna TJ, et al (2016) Assessment of Clinical Criteria for Sepsis. *Jama* 315:762. <https://doi.org/10.1001/jama.2016.0288>
- Finkelsztein EJ, Jones DS, Ma KC, et al (2017) Comparison of qSOFA and SIRS for predicting adverse outcomes of patients with suspicion of sepsis outside the intensive care unit. *Crit Care* 21:1–10. <https://doi.org/10.1186/s13054-017-1658-5>
- Bennett SR (2015) Sepsis in the intensive care unit. *Surg* 33:565–571
- Fleischmann C, Scherag A, Adhikari NKJ, et al (2016) Assessment of Global Incidence and Mortality of Hospital-treated Sepsis. 193:259–272. <https://doi.org/10.1164/rccm.201504-0781oc>
- Shankar-Hari M, Rubenfeld GD (2016) Understanding long-term outcomes following sepsis: Implications and challenges. *Curr Infect Dis Rep* 18:37
- Johnson AEW, Pollard TJ, Shen L, et al (2016) MIMIC-III, a freely accessible critical care database. *Sci data* 3. <https://doi.org/10.1038/sdata.2016.35>
- Angus DC, Linde-Zwirble WT, Lidicker J, et al (2001) Epidemiology of severe sepsis in the United States: analysis of incidence, outcome, and associated costs of care. *Crit Care Med* 29:1303–1310. <https://doi.org/10.1097/00003246-200107000-00002>
- Tibshirani R (1996) Regression shrinkage and selection via the lasso. *J R Stat Soc Ser B* 267–288
- Friedman JH (2002) Stochastic gradient boosting. *Comput Stat Data Anal* 38:367–378
- Elith J, Leathwick JR, Hastie T (2008) A working guide to boosted regression trees. *J Anim Ecol* 77:802–813
- Friedman JH, Meulman JJ (2003) Multiple additive regression trees with application in epidemiology. *Stat Med* 22:1365–1381
- Kuhn AM, Wing J, Weston S, Williams A (2007) The caret Package. *Gene Expr*
- Ridgeway G (2007) Generalized Boosted Models: A guide to the gbm package. *Compute* 1:1–12. <https://doi.org/10.1111/j.1467-9752.1996.tb00390.x>
- Jerome A, Hastie T, Simon N, Tibshirani R (2017) Package “glmnet”
- Johnson AEW, Kramer AA, Clifford GD (2013) A new severity of illness scale using a subset of acute physiology and chronic health evaluation data elements shows comparable predictive accuracy. *Crit Care Med* 41:1711–1718

# Computerized Cognitive Assessment System for Dementia Screening Application

Jia-Yun Wu, Sheei-Meei Wang, Kuo-Sheng Cheng, and Pei-Fang Chien

## Abstract

The occurrence of dementia is increasing in an aging, even aged society. According to the previous research reports, early diagnosis and treatment of dementia may slow down the progression of illness and reduce the cost of care-giving. There are several assessment measures currently applied in clinics, such as Mini-Mental State Examination (MMSE), Clinical Dementia Rating (CDR), Cognitive Abilities Screening Instrument (CASI), Montreal Cognitive Assessment (MoCA), etc. However, their common feature is the need of instructors to guide one patient at a time. In addition, most of the tests are based on western culture. In Taiwan area, the hospital visiting rate of dementia patients is very low. This points out the problem that the clinical assessments are not often used for screening. In this study, a game based computerized measure for assisting the assessment of the suspected subjects is developed and its efficacy is discussed. The proposed system is developed and embedded in an interactive game based on Taiwanese culture theme. This system can work on Android and Windows platform, and it includes obtaining the user background and testing different cognitive domains, including attention, language, memory, visuospatial abilities, executive function and orientation.

## Keywords

Dementia screening • Computerized • Cognitive assessment • Game

## 1 Introduction

### 1.1 Background

Dementia is shown to be an age-related disease and becomes an important issue among elderly population. According to the world Alzheimer report in 2015, it is revealed that the rapid growing of population with dementia is about 46.8 million, and in average, there will be one more dementia case every 3 s [1].

In 2015, the global cost of care for dementia is about 818 billion dollars [1]. This is due to the increases in numbers of people with dementia and in per person cost [2]. From a statistical estimation of previous study, the costs for moderate dementia patients were 1.4 times compared to the cost for mild dementia. Furthermore, for severe dementia, it is doubled [3]. This implies that the total cost increases significantly by the disease severity. Early detection and diagnosis of dementia offers a number of benefits that health care providers can deliver better care to help affected cases and their family, further more improve those reversible cognitive impairment condition.

However, according to the population report provided by National Development Council, Taiwan [4], about 73% of dementia patients are not diagnosed and treated. It shows the early detection of dementia among people with an easy assessment measure is needed and important.

### 1.2 Cognitive Assessments

General clinical assessments such as Mini-Mental State Examination (MMSE) [5], Cognitive Abilities Screening Instrument (CASI) [6] and Montreal Cognitive Assessment (MoCA) [7] and so on, have been often used.

MMSE and MoCA have different criteria to set cut-off points for different years or education and age. CASI even concerns the sex as scoring criteria, for example, cut-off

J.-Y. Wu (✉) · S.-M. Wang · K.-S. Cheng  
Department of Biomedical Engineering, National Cheng Kung University, Tainan, Taiwan  
e-mail: hotajia@gmail.com

S.-M. Wang · P.-F. Chien  
Department of Psychiatry, Tainan Hospital of Ministry of Health and Welfare, Tainan, Taiwan

point is 63 for male who is under 79 years old and didn't receive education, but for female, it is 49. They are usually applied with paper format and administrated by professional psychologists.

A comparison for these assessments is listed in Table 1. Although these tests are validated clinically, they are not easily employed for general use without appropriate knowledge.

### 1.3 Computerization

Personal computer and mobile device applications have been developed for psychology evaluation recently. They are able to enhance clinical judgment, reduce testing time, improve ecological validity, optimize models for treatment planning, and incorporate new assessment theories [8]. Computerized assessment is likely to enhance efficiency through rapid scoring, and novel presentation [9]. According to Finger et al., computer-administered results also have been found to have negligible differences in scores compared to paper-pencil method [10].

Though there are many advantages, computerization report should not replace the judgement from clinicians [9]. The proper application of computerized assessment will be the assistant tool for clinicians to judge or interpret [8].

### 1.4 Serious Game

Tong et al. compared the differences between the traditional paper-and-pencil cognitive assessments and serious games, the serious game can be administrate by non-clinicians and has the advantages of repeatability and more entertainment to motivate subjects to perform the test [11]. Sea Hero Quest is a mobile serious game designed to help early diagnosis for dementia [12]. However, to finish whole game needs much time. In addition, it focuses on memory and orientation measures, but not other domains.

As mentioned above, in this study we try to develop a mobile game which covers general cognitive domains, and design it with a friendly user interface. We hope it can be

applied as an assistive tool for clinical assessment, or help general people for self-assessment.

## 2 Materials and Methods

### 2.1 Computerized Cognitive Assessment System

The computerized cognitive assessment system (CCAS) is proposed and developed according to the general clinical cognitive assessments as previous mentioned. It includes obtaining the user basic information, and testing the orientation, attention, calculation, naming, language, memory, executive function and visuospatial abilities, as the main domains of the diagnosis criteria.

The game elements in the CCAS are based on Taiwanese culture. The user interface is designed with big pictures and buttons, and displays instructions with live leading speaking [13], to make it more friendly and easier for elder users and the subjects with illiterate to operate. As shown in Fig. 1, the form of CCAS is in mobile game, which is played on 13-in. touch screen in a well illuminated environment for the experiments.

In CCAS, we set the total score as 100 points. User will get a score and a corresponding suggestion in the end of the game. The points are divided into 3 levels: 80–100 describes that users' cognitive abilities are normal, 60–79 means users' cognitive abilities are not bad but they should try to exercise brain often, and under 59 is for those whose cognitive abilities probably have impairment or degradation and should receive treatment.

### 2.2 Subject Information

The ages of enrolled participants range from 50 to 95 years old. They are recruited from Tainan Hospital, Ministry of Health and Welfare with the written informed consent and IRB approved. Clinical Dementia Rating (CDR) [14] score is used to classify the participants into 3 groups. Normal Control (NC) includes the participants whose CDR score is

**Table 1** Comparison of different clinical assessment

Test	Time	Administrator	Form	
MMSE	10–15 min	Yes	Paper-and-pencil	Health insurance payment condition in Taiwan; less sensitive to high educated patients
MoCA	10–25 min	Yes	Paper-and-pencil	More sensitive to MCI and interesting
CDR	15–20 min	Yes	Paper-and-pencil	Detailed for staging dementia severity
CASI	20–30 min	Yes	Paper-and-pencil	More assessment details on different domains
Sea Hero Quest	75 levels	No	Mobile game	An interesting game with vivid story; Need time to finish all levels

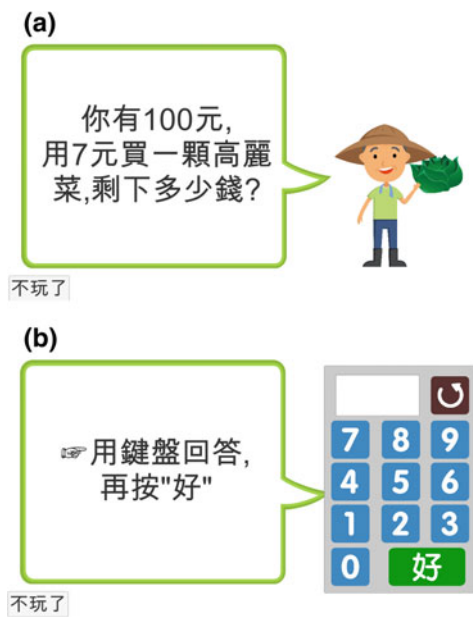


**Fig. 1** An example of the game interface for testing attention and calculation ability. **a** Display the question with text and live speaking, and **b** guide the user to answer

0; Mild Cognitive Impairment (MCI) is CDR score is 0.5; Dementia is whose CDR score is 1–2. Exclusion criteria is the patient who has (1) significant listening or visual disability, (2) significant hand dysfunction, (3) the diagnosed mental illness, (4) the addiction to alcohol or medicine, and (5) CDR score equal to 3 or higher, those who obviously are unable to understand or follow the instructions.

All the 3 groups are asked to perform the standard cognitive assessment, including Mini-Mental State Examination (MMSE), Cognitive Abilities Screening Instrument (CASI), Montreal Cognitive Assessment (MoCA), Activity of Daily Living Inventory(ADL-I), and also to play the computerized cognitive assessment system (CCAS) that proposed and implemented in this study.

### 2.3 Experimental Design

The flowchart of experimental protocol is designed and depicted in Fig. 2. The pilot test is set to check the system primarily. Some part of interface design has been modified by the users’ feedbacks. Then we conduct clinical trial including different assessment tools and a questionnaire about the system, to get at least 50 normal controls and 50 dementia cases, and all of them have to be confirmed by doctors. For the results we will calculate the cut-off score, reliability, validity, sensitivity of the system, and do correlation between the system and other tests. Finally, the statistical results are analyzed and discussed about its performance.

### 2.4 Questionnaire

In this study, a brief questionnaire is used to figure out whether the CCAS is acceptable to be applied for cognitive assessment. It includes questions about user background (sex, age, education etc.), whether it is easy for user to use tablet, how users feel interesting and familiarity to the game story, user experience of the interface design (typesetting, color, instruction etc.), and compared to other assessments whether the CCAS is more interesting, more clear to understand, and easier to operate on their own. The scale of each question is 5-point, the more points means the more user agrees with the statements.

## 3 Results and Discussion

### 3.1 Results

The pilot test results are shown in Table 2. We recruited 5 normal cases and 5 dementia cases whose age is ranged from 53 to 89 years old. The value under each cognitive abilities

**Fig. 2** Flowchart of experiment

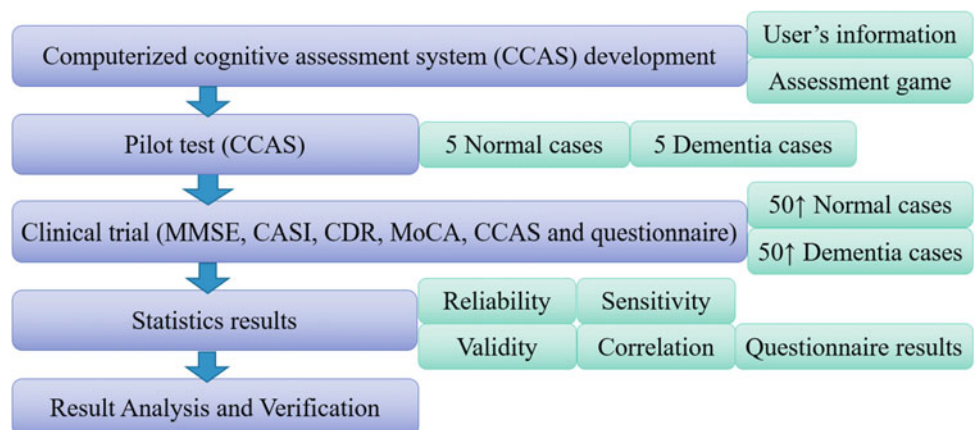


**Table 2** Pilot test results

No.	Group	Age	Orientation	Attention	Calculation	Naming	Language	Verbal fluency	Visuospatial abilities	Memory
A	Normal	53	1	1	1	1	1	1	1	0.4
B	Normal	68	0.8	1	1	0.8	1	1	1	0.2
C	Normal	70	1	1	0.8	0.8	1	1	1	0.2
C	Normal	78	1	1	0.4	0.8	0.8	0.9	1	0.2
D	Normal	85	0.6	0	0.4	0.6	0.2	0.8	1	0
F	Dementia	68	0.6	1	1	0.7	1	1	1	0
G	Dementia	80	0.8	1	1	0.8	1	0.9	1	0.4
H	Dementia	83	0.2	0	0.6	0.6	0	0.8	0	0
I	Dementia	84	0	0	0	0.5	0.4	0.8	0	0
J	Dementia	89	0.2	0	0	0.6	0.2	0.7	0	0

is the correct rate, which is the ratio of the numbers of correct answers and total questions. More data will be reported during conference.

### 3.2 Discussion

The pilot test results are shown to have good correlation. The correct rate in dementia group is approximately lower than in normal group, and it is also age-relative. Case F and G show the noticed performance, it's probably because they are diagnosed as slight Alzheimer's disease, they may still keep cognitive ability. As to memory domain, the result seems not so significant, so we would modify the question and instruction. The current small data helps us to improve this system, and we expect the results from clinical trial would be more complete and reliable.

From subjects' experience feedback, it showed that they like this game and think it is interesting, the play-time is acceptable, and family of some patients even want to obtain the CCAS that they can play it at home. Generally, the CCAS is potential.

## 4 Conclusion

Due to the aging problem of our society, it is an important issue to deal with the dementia. If the patients can be diagnosed and treated earlier, not only can slow down the disease degradation, but also can save more labors and cost on caregiving. Nowadays, smart phones and tablet are easily available, so the App-based game assessment is proposed and developed in this paper for early detection. Based on the comparison analysis, the proposed system is demonstrated to be a potential tool for dementia screening.

## References

1. M. J. Prince, A. Wimo, M. M. Guerchet, G. C. Ali, Y.-T. Wu, and M. Prina, "World Alzheimer Report 2015 - The Global Impact of Dementia: An analysis of prevalence, incidence, cost and trends," Aug. 2015.
2. A. Wimo *et al.*, "The worldwide costs of dementia 2015 and comparisons with 2010," *Alzheimers Dement.*, vol. 13, no. 1, pp. 1–7, Jan. 2017.
3. L.-J. E. Ku, M.-C. Pai, and P.-Y. Shih, "Economic Impact of Dementia by Disease Severity: Exploring the Relationship between Stage of Dementia and Cost of Care in Taiwan," *PLOS ONE*, vol. 11, no. 2, p. e0148779, Feb. 2016.
4. "Taiwan Statistical Data Book." National Development Council (ROC), 2016.
5. 郭乃文, 劉秀枝, 王珮芳, and 徐道昌, "中文版 [簡短式智能評估](MMSE) 之簡介," *臨床醫學*, vol. 23, pp. 39–42, 1989.
6. K.-N. Lin, P.-N. Wang, C.-Y. Liu, W.-T. Chen, Y.-C. Lee, and H.-C. Liu, "Cutoff Scores of the Cognitive Abilities Screening Instrument, Chinese Version in Screening of Dementia," *Dement. Geriatr. Cogn. Disord.*, vol. 14, no. 4, pp. 176–182, 2002.
7. Z. S. Nasreddine *et al.*, "The Montreal Cognitive Assessment, MoCA: a brief screening tool for mild cognitive impairment," *J. Am. Geriatr. Soc.*, vol. 53, no. 4, pp. 695–699, Apr. 2005.
8. G. Groth-Marnat, "Visions of clinical assessment: then, now, and a brief history of the future," *J. Clin. Psychol.*, vol. 56, no. 3, pp. 349–365, Mar. 2000.
9. G. Groth-Marnat, *Handbook of Psychological Assessment*. John Wiley & Sons, 2003.
10. M. S. Finger and D. S. Ones, "Psychometric equivalence of the computer and booklet forms of the MMPI: A meta-analysis," *Psychol. Assess.*, vol. 11, no. 1, pp. 58–66, 1999.
11. T. Tong, M. Chignell, M. C. Tierney, and J. Lee, "A Serious Game for Clinical Assessment of Cognitive Status: Validation Study," *JMIR Serious Games*, vol. 4, no. 1, May 2016.
12. "Sea Hero Quest - Gaming to Help Study Dementia." [Online]. Available: <http://www.seaheroquest.com/site/en>. [Accessed: 27-Jan-2018].
13. J. M. Morris, "User interface design for older adults," *Interact. Comput.*, vol. 6, no. 4, pp. 373–393, Dec. 1994.
14. "Stability of the Clinical Dementia Rating: 1979–2007." [Online]. Available: <https://www.ncbi.nlm.nih.gov/pmc/articles/PMC2779108/>. [Accessed: 15-Mar-2018].



# Modeling Biological Data Through Dynamic Bayesian Networks for Oral Squamous Cell Carcinoma Classification

Konstantina Kourou, Costas Papaloukas, and Dimitrios I. Fotiadis

## Abstract

We propose a computational approach for modeling the progression of Oral Squamous Cell Carcinoma (OSCC) through Dynamic Bayesian Network (DBN) models. RNA-Seq transcriptomics data, available from public functional genomics data repositories, are exploited to find genes related to disease progression (i.e. recurrence or no recurrence). Our primary aim is to perform a computational analysis based on the differentially expressed genes identified. More specifically, a search for putative transcription factor binding sites (TFBSs), in the promoters of the input gene set, as well as an analysis of the pathways of the suggested transcription factors is conducted. Activities of transcription factors which are regulated by upstream signaling cascades are further discovered. These activities converge in certain nodes, representing molecules which are potential regulators of OSCC progression. The resulting gene list is further exploited for the inference of their causal relationships and for disease classification in terms of DBN models. The structure and the parameters of the models are defined subsequently, revealing the changes in gene-gene interactions with reference to disease recurrence after surgery. The objectives of the proposed methodology are to: (i) accurately estimate OSCC progression, and (ii) provide better insights into the regulatory mechanisms of the disease. Moreover, we can conjecture about the

interactions among genes based on the inferred network models. The proposed approach implies that the resulting regulatory molecules along with the differentially expressed genes extracted, can be considered as new targets, and are candidates for further experimental and in silico validation.

## Keywords

Biological data • Classification • Dynamic Bayesian Networks • Transcription factors

## 1 Introduction

One of the most complex and heterogeneous disease with different subtypes is cancer [1]. The different subtypes of this multi-parametric disease are characterized by body cells that proliferate uncontrolled within tissue. The most common type of Head and Neck Squamous Cell Carcinoma (HNSCC) is Oral Squamous Cell Carcinoma (OSCC). It mainly occurs in any part of the oral cavity or oropharynx [2]. Because of the high mortality rates of the disease, the clinical significance of an early detection of a disease recurrence and/or diagnosis has impelled the researchers to improve the classification of OSCC samples through the utilization of gene expression profiles. Gene expression profiling, through high throughput technologies, enables the simultaneous monitoring of the activity of thousands of genes, i.e. their expression as it changes during the disease progression [3]. The huge amount of experimental data produced by high-throughput technologies, reveal the importance of identifying and discovering these genes that may be co-expressed and may participate in important regulatory mechanisms. Gene selection from expression profiling results has been studied widely aiming to identify molecules that are expressed differentially under certain experimental conditions [4, 5]. These approaches state the problem of gene identification which plays a crucial role in disease

K. Kourou (✉) · C. Papaloukas  
Department of Biological Applications and Technology,  
University of Ioannina, 45110 Ioannina, Greece  
e-mail: konstadina.kourou@gmail.com

K. Kourou · D. I. Fotiadis  
Unit of Medical Technology and Intelligent Information Systems,  
Department of Materials Science and Engineering, University of  
Ioannina, 45110 Ioannina, Greece

D. I. Fotiadis  
Institute of Molecular Biology and Biotechnology (IMBB),  
Foundation for Research and Technology Hellas (FORTH), 45110  
Ioannina, Greece



progression, while encompass statistical methods for more accurate feature identification. Hence, the classification of cancer samples into distinct subgroups for disease prediction is related to the detection of highly differential gene expression profiles. In addition, the amount of such experimental data can be utilized subsequently to provide an overview of how genes interact with each other, thus forming a gene network. Analyzing and modeling transcriptomic data in order to identify significant genes and their structure of the underlying causal network is very appealing. Moreover, the extraction of transitions between nodes in biological networks may provide additional insights for the molecular processes in cancer.

Towards this, several studies in the literature have presented computational methods for the inference of gene network models by utilizing different sources of biological data. Specifically, in [6] a network model has been proposed for the reconstruction of gene regulatory networks in ovarian cancer. Different topologies in the resulting networks have been identified with reference to the regulatory mechanisms associated with the different types of the disease. Moreover, similar approaches have been published which employ Dynamic Bayesian Networks (DBNs) for the inference of gene regulatory networks [6, 7]. These methods integrate data from genome wide association studies and implement DBN algorithms for learning the structure accurately. A slightly different algorithm has been presented recently in the literature that scores regulatory interactions between genes through the use of DBNs [7]. The authors validated their method in mRNA time series data extracted from breast cancer samples and identified significant co-expressed genes.

The proposed approach provides a way to systematically discover and examine the predictive power of genes and their transcription factors for classifying patients into disease groups through DBN modeling. Moreover, the presented workflow is an exemplar of integrating biological information with reference to the regulatory mechanisms underlying the disease progression; hence, new targets for validating experimental and in silico models can be considered in the disease management and therapeutic protocols. In comparison with other studies from the literature, the proposed approach exhibits quite promising results with reference to

the transcription factors of differentially expressed genes among different phenotypes.

## 2 Materials and Methods

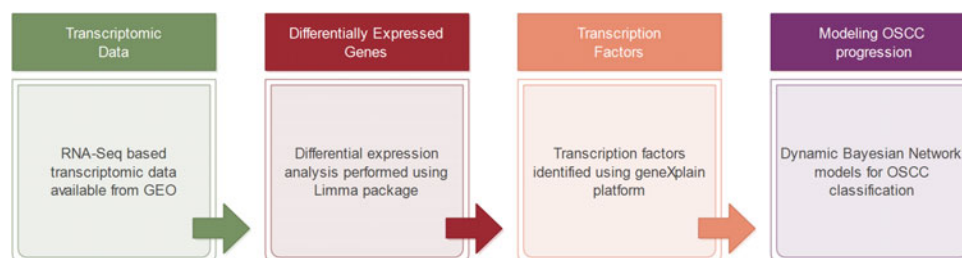
Figure 1 illustrates the steps followed in the proposed work aiming to identify an indicative gene set that contributes to the OSCC progression in terms of disease recurrence. Transcription factors are discovered based on the identified differentially expressed genes between patients that have suffered a disease relapse and those who have not. The overall proposed gene list is further utilized by a DBN technique, as presented below, for classifying the disease progression.

### 2.1 Transcriptomic Dataset

RNA-Seq-based transcriptomics data available from the Gene Expression Omnibus (GEO) public functional genomics data repository [8] were utilized. A search query was applied containing the keywords “gene expression profiling of OSCC” AND “Homo sapiens”. A total of 33 GEO datasets in the database were found. These results were sorted based on the number of samples in each study and the year of publication. It should be noted that datasets that are referred to: (i) metastasis, or (ii) treatment or (iii) other than microarray data (i.e. Single Nucleotide Polymorphism data) were excluded. Additionally, GEO projects with less than 50 samples in their datasets were also omitted. The sample size cut-off was explicitly determined concerning the predictive classification in terms of the selected algorithms [9]. The final representative dataset selected for further analysis in the current study was derived based on a thorough user selection. More specifically, we searched and found this dataset that had the largest number of samples analyzed in order to achieve more accurate results. In addition, it should be noted that only datasets that have been uploaded to GEO with representative citations were considered during our search.

To this end, GSE85446 series was selected which contains the expression profiling of primary oral cavity

**Fig. 1** Workflow of the proposed computational approach



squamous cell carcinoma (OSCC) samples. More specifically, in this project gene expression profiling of 66 HPV-negative OSCC primary tumor was performed to identify gene expression that is related to disease recurrence and poor prognosis. This dataset contains the expression values of 37,662 probes. 13 out of 66 patients were suffered a disease relapse after surgery, while the remaining ones are disease free. It should be mentioned that the expression profiles of 84 OSCC primary tumors from another study that were combined with the GSE85446 series by the contributors were removed. Moreover, the expression values of all samples were transformed in a log base 10 scale and the processed data were further considered in the proposed computational workflow.

## 2.2 Differentially Expressed Genes

Differential expression analysis was performed in the R Bioconductor environment with the utilization of the Limma package [10]. Limma has the ability to fit gene-wise linear models to microarray or RNA-seq data, aiming at performing differential analysis for gene expression data. Towards this, two matrices are specified, namely the design and the contrast matrix. The design matrix provides a representation of the different samples within the experiment of interest, while in the contrast matrix all the pair-wise comparisons among the groups of interest are specified. In our work, we examine which genes has responded differently at the follow-up period after surgery in the patients that have suffered a disease relapse with reference to those who have not. Limma package provides function, namely `topTable()`, which summarizes the results of the linear model. Hence, only the most statistical significant genes are extracted in terms of calculated p-values and adjusted p-values.

## 2.3 Transcription Factors

The upstream analysis of the resulting differentially expressed genes was performed by employing the geneXplain [11] comprehensive bioinformatics platform. The geneXplain platform is a commercial online workbench that comprises a number of bioinformatics and systems biology modules. It also facilitates a number of standard analyses through pre-composed workflows. Upstream analysis is an approach to analyze gene expression data and indicates the reason why a certain set of genes has been up- (or down-) regulated in the disease under study.

In the current work, potential transcription factor binding sites (TFBSs) were identified in all promoters of the differentially expressed genes identified previously. This was implemented with the TRANSFAC library [11] of positional

weight matrices (PWMs). Activities of transcription factors are regulated by upstream signaling cascades. Hence, a complete upstream analysis was performed including a search for putative TFBSs in the promoters of the input gene set. As mentioned above, the input gene table is the list of the most differentially expressed genes among patients that had suffered a disease relapse after surgery and those that had not. Subsequently, the top differentially expressed genes, which exhibited the lowest p-value, along with the identified transcription factors are further considered for assessing their predictive value in OSCC.

## 2.4 Dynamic Bayesian Network Modeling

The approach of Dynamic Bayesian Networks has been widely used for the inference of gene regulatory networks from transcriptomic data; thus, they constitute an appealing choice for modeling the progression of OSCC by utilizing gene expression profiling measurements. DBNs are an extension of Bayesian Networks (BNs) which encode the joint probability distributions over a set of random variables. They are defined by a graphical structure and a set of parameters. Therefore, in order to construct a DBN we need to specify the intra-slice topology (connections within a slice), the inter-slice topology (connections between two slices) and the parameters for the first two slices. Our models were implemented using MATLAB and the Bayes Net Toolbox [12]. Figure 2 illustrates a simple structure of a DBN with two time slices ( $t = 0$  and  $t = 1$ ). Intra and inter-slice topology can be observed between the variables.

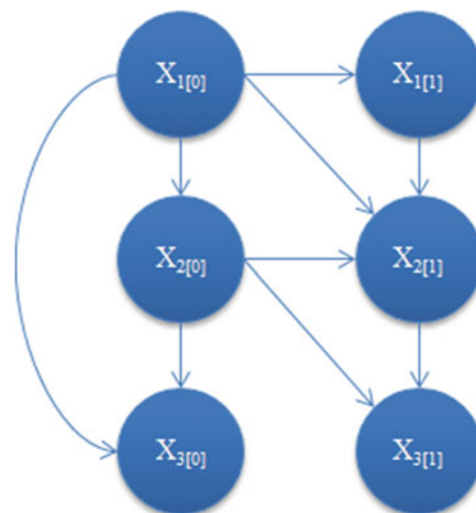


**Fig. 2** A simple example of a DBN structure

### 3 Results and Discussion

Our primary aim was to detect a limited set of representative genes and transcription factors that contribute to the OSCC patient classification.

#### 3.1 Differentially Expressed Genes

A total of 71 genes were identified with a p-value  $< 0.005$ . Small p-value indicates the strong evidence regarding the null hypothesis (no differential expression between genes). In order to select the most representative ones, we further picked the top ten genes (those with a p-value  $< 0.005$ ), that showed significant changes in their expressions between relapsers and no-relapsers. These genes exhibited also the lowest calculated adjusted p-values.

#### 3.2 Transcription Factors

Site search was performed using the TRANSFAC library of PWMs. The output of this step is a list of PWMs (i.e. transcription factors) the hits of which are overrepresented in the submitted gene list (i.e. differentially expressed genes). For each potential regulatory molecule, the Score [11], and Z-score [11] were calculated and the results were filtered by Z-Score  $> 1.0$  and Score  $> 0.2$  to select the statistically significant transcription factors. Table 1 presents the top

three transcription factors with Z-score  $> 2.0$ , as provided by the platform among the total number of identified transcription factors, along with an indicative description.

#### 3.3 Modeling OSCC Through DBNs

In order to estimate the performance of our predictive methodology, the leave-one-out cross validation technique was employed. Based on the fact that our dataset is characterized by a limited number of samples, this technique is well suited for the assessment of our predictive models. As cross validation does not exploit all the data in order to build a model, it is a widely used method to prevent overfitting during the training phase [9]. The overall accuracy reported by our methodology towards the prediction of oral cancer recurrence is 66.7% and the area under the curve (AUC) is 0.43, which constitutes an accurate result for further investigation by the medical experts. However, thorough investigation and biological interpretation by the medical experts is needed to extract more adequate knowledge, with reference to the prediction of a possible relapse for a specific patient. The inferred interactions through the DBN models were further explored through the NCBI database [13]. From all the detected interactions, it is worth to note that interactions between the REPS2 gene and the transcription factors E2F1 and HTm4 should be validated computationally and experimentally as well.

**Table 1** The top three transcription factors that found to regulate the differentially expressed genes along with a brief description

Name	Description
MS4A3 (HTm4)	A hematopoietic cell cycle regulator that interacts with CDKN3 and regulates dephosphorylation of CDK2
CDKN3	Cyclin-dependent kinase inhibitor 3, plays a role in G1-S transition of mitosis, cell proliferation, and cell migration, upregulated in hepatocellular and breast cancers
E2F1	Binds to DNA, regulates neurogenesis, aberrant expression is associated with Alzheimer disease associated with Down syndrome, breast and several neoplasms

## 4 Conclusions

Concerning the steps followed in the proposed methodology, the structure and parameters between the differentially expressed genes and their transcription factors within the first time slice and across the first and the second time slice were inferred, in terms of DBN models. Subsequently, we were able to conjecture about the causal relationships among genes within the same time-slice and between consecutive time-slices. Moreover, the mapping of these interactions to known and verified pathways that have been found in the literature to be associated with the disease progression could provide better insights into its underlying molecular processes. In a future work, the enrichment of our dataset with more experimental data, either from GEO or other published studies, would lead to more reliable predictions.

**Acknowledgements** This work is funded by the General Secretariat for Research and Technology (GSRT) and the Hellenic Foundation for Research and Innovation (HFRI).

**Conflicts of Interest** The authors declare that they have no conflict of interest.

## References

1. D. Hanahan and R. A. Weinberg, "Hallmarks of cancer: the next generation," *cell*, vol. 144, pp. 646–674, 2011.
2. Y. Safdari, M. Khalili, S. Farajnia, M. Asgharzadeh, Y. Yazdani, and M. Sadeghi, "Recent advances in head and neck squamous cell carcinoma—A review," *Clinical biochemistry*, vol. 47, pp. 1195–1202, 2014.
3. L. Fahmideh, H. Kord, and Y. Shiri, "Importance of Microarray Technology and its Applications," *Journal of Current Research in Science*, vol. 4, p. 25, 2016.
4. A. Sharma and K. K. Paliwal, "A gene selection algorithm using Bayesian classification approach," *American Journal of Applied Sciences*, vol. 9, pp. 127–131, 2012.
5. K. Glass, J. Quackenbush, D. Spentzos, B. Haibe-Kains, and G.-C. Yuan, "A network model for angiogenesis in ovarian cancer," *BMC bioinformatics*, vol. 16, p. 115, 2015.
6. Y. Kim, S. Han, S. Choi, and D. Hwang, "Inference of dynamic networks using time-course data," *Briefings in bioinformatics*, vol. 15, pp. 212–228, 2014.
7. B. Baur and S. Bozdog, "A Canonical Correlation Analysis-Based Dynamic Bayesian Network Prior to Infer Gene Regulatory Networks from Multiple Types of Biological Data," *Journal of Computational Biology*, vol. 22, pp. 289–299, 2015.
8. T. Barrett, D. B. Troup, S. E. Wilhite, P. Ledoux, D. Rudnev, C. Evangelista, I. F. Kim, A. Soboleva, M. Tomashevsky, and R. Edgar, "NCBI GEO: mining tens of millions of expression profiles—database and tools update," *Nucleic acids research*, vol. 35, pp. D760–D765, 2007.
9. S. Arlot and A. Celisse, "A survey of cross-validation procedures for model selection," *Statistics surveys*, vol. 4, pp. 40–79, 2010.
10. M. E. Ritchie, B. Phipson, D. Wu, Y. Hu, C. W. Law, W. Shi, and G. K. Smyth, "limma powers differential expression analyses for RNA-sequencing and microarray studies," *Nucleic acids research*, p. gkv007, 2015.
11. F. Kolpakov, V. Poroikov, G. Selivanova, and A. Kel, "GeneXplain—Identification of Causal Biomarkers and Drug Targets in Personalized Cancer Pathways," *Journal of biomolecular techniques: JBT*, vol. 22, p. S16, 2011.
12. K. Murphy, "The bayes net toolbox for matlab," *Computing science and statistics*, vol. 33, pp. 1024–1034, 2001.
13. R. C. NCBI, "Database resources of the National Center for Biotechnology Information," *Nucleic acids research*, vol. 41, p. D8, 2013.

# A Process Modelling and Analytic Hierarchy Process Approach to Investigate the Potential of the IoT in Health Services

K. Tsiounia, N. G. Dimitrioglou, D. Kardaras, and S. G. Barbounaki

## Abstract

E-health's ultimate vision is to empower stakeholders, such as patients, families and societies to engage in the decision-making and management of their own health status. The proliferation of the Internet of Things (IoT) is expected to change the way that health services are designed, implemented and delivered. However, little research has been done to investigate the IoT potential in the health sector. The IoT represents a significant technological field with enormous implications for both patients and health organizations. This paper combines process modelling and the Analytic Hierarchy Process (AHP) multicriteria analysis method in order to investigate and assess the potential of the IoT in health services quality. First, this paper, utilizes process modelling in order to capture the workflow of delivering health services to patients. It suggests that workflow modelling provides the conceptual foundation for the systematic consideration of the opportunities stemming from the IoT deployment. Further, this paper utilizes the AHP, in order to measure the potential of the IoT opportunities that can be identified along the workflow, in terms of its contribution to health services quality. An AHP questionnaire was structured and data were collected and analyzed from a group of health care experts. The results advocate the wide use of IoT in health services and argue for the applicability of the suggested approach as a means for medical organizations to design and deliver quality health services.

## Keywords

Internet of Things • Multicriteria analysis  
Process modeling • E-health • Health service

## 1 Introduction

It is widely cited that the healthcare industry is under-going fundamental changes. Health care companies took steps to prove their integrity, high quality of care, and cost-effectiveness of their methods. E-health has played a significant role in this transformation. However, it should not focus merely on these aspects. Currently, patients are concerned more often with their personal well-being decisions, which indicate a shift from curing medical problems to preventing health problems. E-health can empower stakeholders, such as patients, families and societies to engage in the decision-making and management of their own health status. Therefore, it is urgent for the healthcare industry to develop advanced and practical health-related technologies and services. To this end, the proliferation of the Internet of Things (hereinafter IoT) is expected to change the way that health services are designed, implemented and delivered.

As a promising paradigm, IoT has gained vital attention during the past decade. IoT realization of the IoT concept is possible through integration of several enabling technologies, such as Radio Frequency Identification (RFID) systems, Wireless Sensor Networks (WSN), middle-ware, cloud computing and IoT application software [1]. Currently, the IoT is penetrating a wide range of industries including manufacturing, logistics, transportation, maritime and healthcare [2, 3]. The benefits of the IoT implementation in the healthcare domain can be grouped in three categories: (i) tracking of objects and people (medical team, staff, and patients), (ii) identification and authentication of people and (iii) automatic data collection and sensing [3]. However, the use of IoT in the healthcare domain involves extra data

---

K. Tsiounia · D. Kardaras  
School of Business, Athens University of Economics and  
Business, Athens, Greece

N. G. Dimitrioglou (✉)  
School of Chemical Engineering, National Technical University of  
Athens, Athens, Greece  
e-mail: nikosdimitri@mail.ntua.gr

S. G. Barbounaki  
Merchant Marine Academy of Aspropyrgos, Aspropyrgos, Greece

transfer cost, and thus, novel metrics and methods have to be introduced maximizing the capabilities [4]. The rapid development of modern information and communication technologies can contribute in IoT application in a more widespread and efficient way by resolving significant challenges. In particular, specific issues to be considered are the interoperability among interconnected device, the degree of smartness, as well as the security and privacy of the users' data [5].

The potential of IoT in hospital industry is expected to be of paramount importance for both the patients and the health service providers. In particular, the implementation of IoT in such asset-intensive and extremely information-intensive environments, emerges plentiful possibilities and potential outcomes. For instance, the medical equipment and related health care objects can be connected and monitored in order to achieve numerous benefits. However, little research has been done to investigate the IoT potential in a hospital environment until now. This paper aims to propose an evaluation model by combining process modelling and the Analytic Hierarchy Process (AHP) multicriteria analysis method. It is suggested that workflow modelling provides the conceptual foundation for the systematic consideration of the opportunities stemming from the IoT deployment. By identifying these opportunities along the workflow, the AHP is utilized, in order to measure the potential in terms of its contribution to health services quality.

## 2 Method

Figure 1 shows the steps of the methodology adopted for the evaluation the IoT potential in health services. A process modeling is firstly performed in order to identify tasks and information flow. Key Performance Indicators (KPIs) are identified to evaluate the process. By monitoring and improving the KPIs, an organization can improve its total performance and finally achieve goals. The KPIs are defined so that they firstly reflect the health services quality and subsequently they are refined at the process level so that they reflect the process performance. The definition and standardization of KPIs regarding a process is not an easy task, and thus, in depth knowledge of the industry particularity is necessary.

Based on the KPIs, the AHP model is constructed. The AHP model is used to compare and contrast the current process with an IoT based process. Both criteria and alternatives are used to establish the AHP hierarchy. Experts with many years of experience in healthcare are eligible to evaluate the relevant importance of the criteria and relevant preference of the alternatives. The data are collected and analyzed in order to draw conclusions. Particularly, the AS-IS and the IoT based processes are compared according

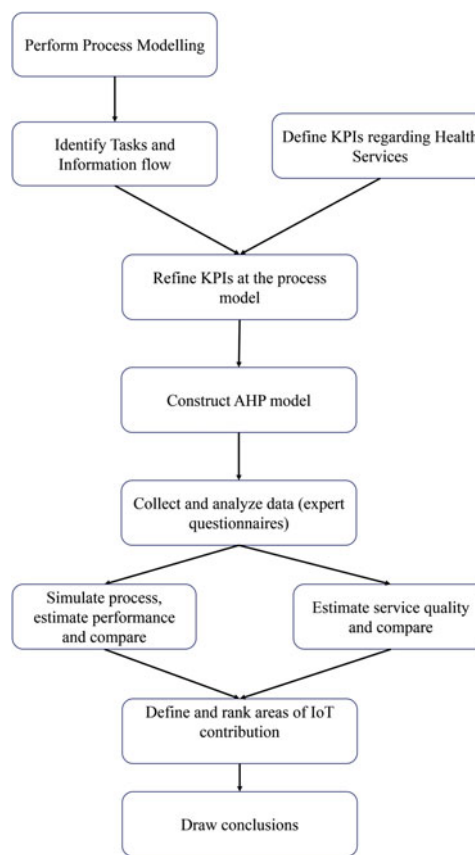


**Fig. 1** The proposed methodology for the evaluation the IoT potential in health services

to the AHP model considered in this study. The final rankings reveal the potential of the IoT, in terms of its contribution to the health services quality. Furthermore, the AHP model analysis is utilized to measure the contribution of the IoT to the process performance. “Time to complete admittance” and “Diagnosis accuracy” are chosen as two important performance indicators. To estimate the KPIs' values, simulations were conducted for five scenarios using ADO-NIS. The Time to complete admittance is the summation of times of each task that are estimated through observations. Due to great dependence on the surgery type [6], a mean surgical time of 2.7 h was taken granted for every scenario. The values of diagnosis accuracy are drilled through hospital data. The geometric mean of the results is calculated and used for the AS-IS process' performance respectively. The IoT based process performance is measured by quantifying experts' judgments.

For the purposes of this study, a service to admit patient, operate a surgery and provide medical treatment is chosen as a case of study. The steps for initiating a patient's operating procedure with potential problems are represented in Table 1. The five dimensions of health service quality, aiming to measure patient's satisfaction [7] are: tangibility,



**Table 1** Steps of a surgery procedure with potential problems

Procedure steps	Potential problems
Patient pre-admission	Delay to fill in documents. Lack of data in medical records and health insurance information
Patient transfer to the operating room	Unavailability of operating rooms. Late delivery of the required pre-operational medical check-ups from the appropriate departments
Patient transfer into the surgical room	Late update to complete the previous process, Delay of a cleaning team to sanitize the operating room from previous procedures
Anesthesia	Anesthesiologist's unavailability, Malfunctions in the anesthetic gas supply system
Performing surgical procedure	Unavailability of surgical rooms, Insufficient number and proper specialization of staff, Lack of resources, medical tools, equipment
Transfer patient to recuperate	Lack of coordination between surgery and recuperation, Lack of stretcher bearer
Stay on recuperation until full recovery	Post-operative complications requiring re-introduction of the patient, Problems of patient's recovery that prolong their time in the room
Patient transfer to a room or ICU if required	Inadequate bed allocation for patient hospitalization, Delay of transfer

reliability, responsiveness, assurance and, empathy. In particular, an excellent health services hospital has up-to-date facilities (buildings, equipment, X-ray department, laboratories, etc.). It is reliable by acting proactively, providing its services on time and being precise regarding the schedule of operations, treatment etc. Moreover, the personnel in an excellent hospital gives prompt service to patients (appointments, advice, etc.) and is always willing to help patients.

For a surgery process, tangibility, reliability, responsiveness, time to complete admittance and diagnosis accuracy are chosen as criteria. Tangibility is an important dimension, since IoT concept is based on the idea where objects store, process and communicate information. For instance, the surgery equipment can be monitored and the availability of any room (operating, surgery, recovery, ICU) can be checked.

Responsiveness and reliability can be accomplished by tracking the hospital personnel (staff, medical team, anesthesiologist, surgical team), as well as the patient. Customized services, on time operations and treatments can be achieved by these actions. Furthermore, lack of data in medical records could be crucial in diagnosis accuracy. Delay to fill in documents or errors could be prevented by transmitting personal medical data from a smart watch or a mobile application. The criteria reliability and responsiveness are expanded to drill down to a lower level of details. The sub-criteria are validated by in-depth interviews with two experienced hospital managers.

## 2.1 Process Modeling

Figure 2 illustrates the flowchart of a surgery procedure. Depending on the added value, the tasks can be grouped in

three categories: (i) tasks that create value for the client-patient (ii) tasks that are necessary for the service delivery, although value is not created, and (iii) tasks that do not create any value and should be removed from the process. IoT can assist in removing of unnecessary tasks or improving the necessary and added-value tasks. For instance, sanitation of the surgical room is a necessary procedure, however, it does not create value for the patient. In this case, IoT implementation can potentially contribute to the process performance and health service quality. Furthermore, the patient's medical file filling procedure can negatively impact the time to complete admittance or the diagnosis accuracy due to delay or incorrect filling respectively.

## 2.2 Analytical Hierarchy Process

The AHP is utilized to capture medical experts' opinions and to quantify the relevant importance of IoT implementation in a surgery procedure. Saaty's nine point scale is used and preferences between alternatives are given as equally, moderately, strongly, very strongly, or extremely preferred. The pairwise comparisons can be represented as:

$$A = [a_{ij}] = \begin{bmatrix} 1 & a_{12} & \dots & a_{1n} \\ 1/a_{12} & 1 & \dots & a_{2n} \\ \vdots & \vdots & \ddots & \vdots \\ 1/a_{1n} & 1/a_{2n} & \dots & 1 \end{bmatrix}, \quad (1)$$

where  $a_{ij}$  represents the value that experts compare the criterion  $i$  with the criterion  $j$ . The relative weights of the criteria in this matrix are estimated by comparing the priority of the criteria. Therefore, the eigenvalues and eigenvectors are estimated using the following equation:

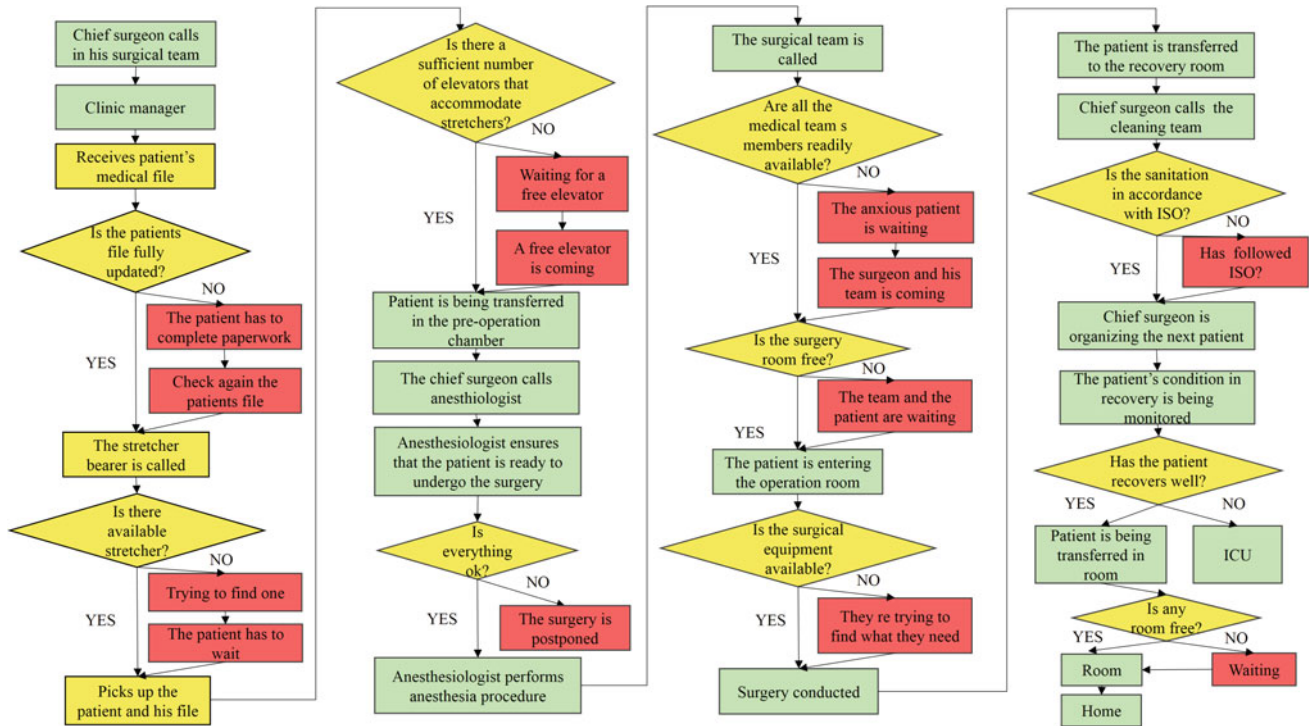


Fig. 2 Flowchart of a surgery procedure

$$A \cdot w = \lambda_{\max} \cdot w, \tag{2}$$

where  $w$  is the eigenvector of the matrix  $A$ , and  $\lambda_{\max}$  is the largest eigenvalue of the matrix  $A$ .

The reliability of judgments is tested by calculating the Consistency Index ( $CI$ ) and the Consistency Ratio ( $CR$ ) that are respectively defined as:

$$CI = \frac{\lambda_{\max} - n}{n - 1}, \tag{3}$$

$$CR = \frac{CI}{RI}, \tag{4}$$

where  $n$  is the number of criteria being compared in this matrix, and  $RI$  is the Random Index.

### 3 Results

One-to-one interviews were conducted for the purposes of this research during December, 2017. Each interviewer was informed beforehand of the research object and the interview duration. Six medical experts were invited to evaluate the potential of IoT in healthcare. The reliability of the judgments was examined by calculating the  $CR$  of each matrix. The total number of questionnaires submitted was eight. However, the final results were extracted from five

questionnaires, as these only fulfilled the requirement of consistency ( $CR < 0,1$ ).

Figure 3 illustrates the AHP model and the related weights. With respect to the hierarchy, the weights of each criterion and sub-criterion are represented in Table 2. Diagnosis accuracy is by far the most important criterion, in terms of its contribution to the health services quality. Reliability and Time to complete admittance ranked second and third respectively. From reliability perspective, customization is the most crucial factor, while helping patients is the most important criterion from responsiveness perspective.

The rankings per criterion and final ranking of the alternatives are represented in Table 3. The results reveal that IoT based process is the most preferable by far in terms of its contribution to the health services quality. Moreover, IoT based process is much better in respect to each criterion compare to the current process.

Simulations were conducted for five different scenarios. The geometric mean of Time to complete admittance ( $T$ ) was estimated 4.2 h for AS-IS process, while the geometric mean of Diagnosis Accuracy ( $DA$ ) was estimated 89%. The range used to quantify experts' judgments was  $3.4 \text{ h} \leq T \leq 5.0 \text{ h}$ . Process performance regarding the KPIs are represented in Table 4. One can observe that the IoT based process' performance in respect to  $T$  and  $DA$  is

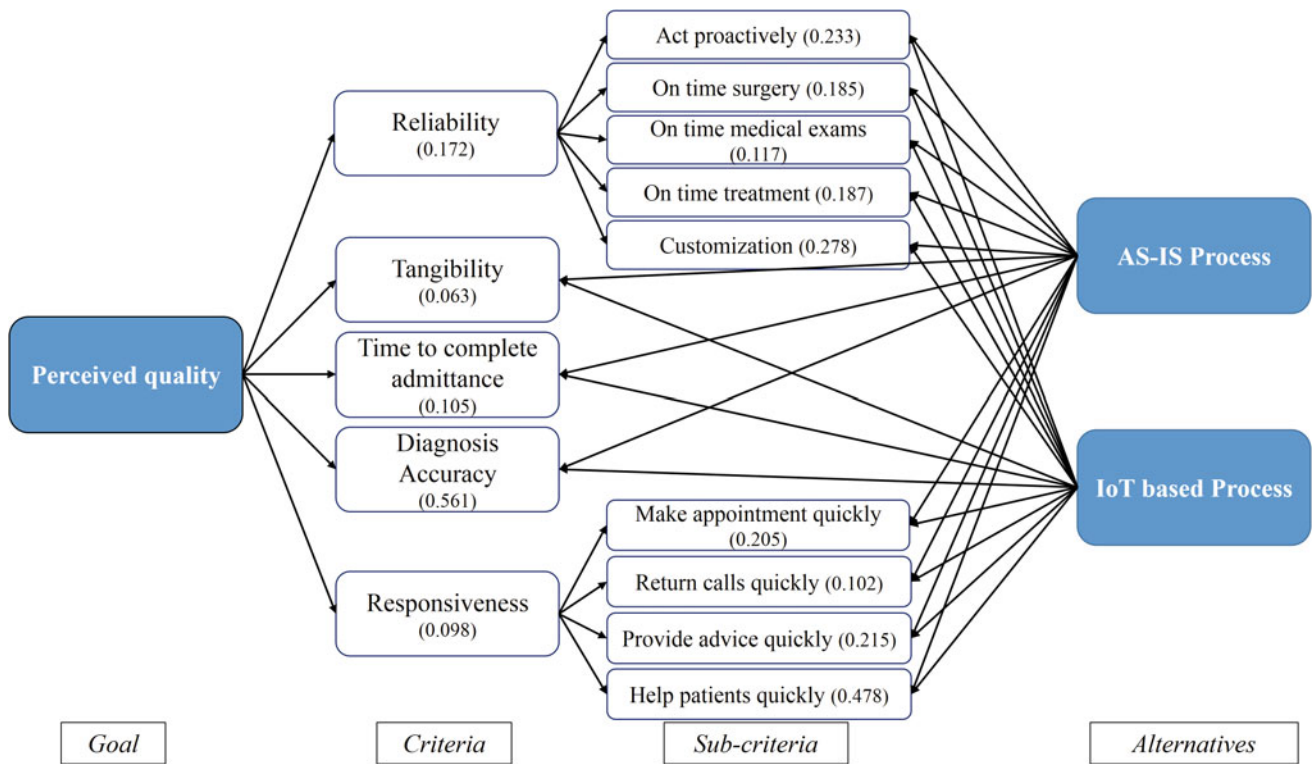


**Fig. 3** Analytical hierarchy model

**Table 2** Weights of criteria and sub-criteria

Criteria	Weight	Rank	Sub-criteria	Weight	Rank
Reliability	0.172	2			
			Act proactively	0.040	3
			Surgery	0.032	5
			Medical exams	0.020	7
			Treatment	0.032	4
			Customization	0.048	1
Tangibility	0.063	5			
Time Adm	0.105	3			
DA	0.561	1			
Responsiveness	0.098	4			
			Appointments	0.020	8
			Return calls	0.010	9
			Advice	0.021	6
			Help	0.047	2

**Table 3** Ranking per criterion and final ranking

Criterion	AS-IS		IoT	
	Score	Weighted score	Score	Weighted score
Reliability	0.349	0.060	0.651	0.112
Tangibility	0.151	0.010	0.849	0.054
Time Adm	0.192	0.020	0.808	0.085
DA	0.205	0.115	0.795	0.446
Responsiveness	0.273	0.027	0.727	0.071
Qof Service		0.232		0.768

**Table 4** Process performance regarding T and DA

Expert	T (h)	Difference	DA (%)	Difference (%)
1	3.6	-0.6	91	+2
2	4.0	-0.2	89	+0
3	4.0	-0.2	92	+3
4	4.0	-0.2	91	+2
5	3.6	-0.6	91	+2
Average	3.84	-0.36	91	+2

higher in both cases. The results reveal that the use of IoT decreases the T by 0.36 h and increases the DA by 2%.

**Conflicts of Interest** The authors declare that they have no conflict of interest.

## 4 Conclusions

This paper combines process modelling and the AHP multicriteria analysis method in order to investigate and assess the potential of the IoT in health services quality. The aim of this study was to propose a methodology to evaluate the potential of IoT application in health service procedure in respect to perceived quality and at the same time quantify the process performance. The KPIs were defined regarding service quality and were refined at the process level.

The results advocate the wide use of IoT in health services and argue for the applicability of the suggested approach as a means for medical organizations to design and deliver quality health services. IoT based process is the most preferable in terms of its contribution to the health services quality. Furthermore, IoT implementation has the potential to improve service's quality by enhancing the reliability, the responsiveness and the tangibility of the delivered service, as well as, by ameliorating the diagnosis accuracy and time to complete admittance. Furthermore, the results reveal that the use of IoT have a positive impact on the performance of the process in respect of two KPIs, e.g. Diagnosis accuracy and Time to complete admittance. It is proposed that the comprehensiveness of KPIs have to be validated in other processes (checkup, hospitalization, etc.).

## References

- Lee BM, Ouyang J (2014) Intelligent Healthcare Service by using Collaborations between IoT Personal Health Devices. *Int J Bio-Science Bio-Technology* 6(1):155–164 <https://doi.org/10.14257/ijbsbt.2014.6.1.17>.
- Gubbi J, Buyya R, Marusic S, Palaniswami M (2013) Internet of Things (IoT): A Vision, Architectural Elements, and Future Directions. *Futur Gener Comput Syst* 29(7):1645–1660 <https://doi.org/10.1016/j.future.2013.01.010>.
- Atzori L, Iera A, Morabito G (2010) The Internet of Things: A Survey. *Comput networks* 54(15):2787–2805 <https://doi.org/10.1016/j.comnet.2010.05.010>.
- Paschou M, Sakkopoulos E, Sourla E, Tsakalidis A (2013) Simulation Modelling Practice and Theory Health Internet of Things: Metrics and methods for efficient data transfer. *Simul Model Pract Theory* 34:186–199 <https://doi.org/10.1016/j.simpat.2012.08.002>.
- Wortmann F, Flüchter K (2015) Internet of Things Internet of Things. *Bus Inf Syst Eng* 57(3):221–224 <https://doi.org/10.1007/s12599-015-0383-3>.
- Stepaniak PS, Heij C et al (2009) Modeling Procedure and Surgical Times for Current Procedural Terminology-Anesthesia-Surgeon Combinations and Evaluation in Terms of Case-Duration Prediction and Operating Room Efficiency: A Multicenter Study. *Anesth Analg* 109(4):1232–1245 <https://doi.org/10.1213/ane.0b013e3181b5de07>.
- Scholefield H (2007) Embedding quality improvement and patient safety at Liverpool Women's NHS Foundation Trust. *Best Pract Res Clin Obstet Gynaecol* 21(4):593–607 <https://doi.org/10.1016/j.bpobgyn.2007.02.005>.

# A Virtual CPR (Cardio-Pulmonary Resuscitation) Learning System Using Motion Capture Device

Yasushi Yamauchi and Tae Hayashida

## Abstract

The general content of CPR (Cardio-Pulmonary Resuscitation) includes chest compression and electrical shock by an AED (Automated External Defibrillator). In order to disperse CPR, we have developed a virtual CPR learning system that includes patient, an AED and chest compression simulation. Our virtual CPR is implemented using Unity 5.4.1 game engine and a Leap Motion motion capture device. The trainee can move ‘virtual’ hand to operate ‘virtual’ AED and compress chest. Our CPR scenarios include the phases of booting the AED, pasting electrode pads on appropriate position of the virtual patient’s chest, waiting for ECG analysis, electrical shock and chest compression. In the phase of chest compression, Leap Motion detect the position of trainee’s hand while he/she repeatedly compresses chest of virtual patient. Then the system evaluates the position, depth and tempo of the compression. If the compression is insufficient, the system visually alerts it to the trainee. Our evaluation revealed that we have succeeded to implement three scenarios of CPR, and that the mismatch of hand-eye coordinate may affect the performance of learning CPR.

## Keywords

Cardio-Pulmonary Resuscitation • AED • Motion capture

AED (Automated External Defibrillator) is a medical device that treats ventricular fibrillation (VF) using electrical shocks. In 2014, cumulative shipments of AED in Japan have exceeded half-million. Japan and other countries have permitted non-medical persons to use AEDs in emergency. Besides, earlier use of CPR is important to save patient’s life. However, only 31.7% of adults answered that they could use AED when they see persons of sudden illness or injury [1]. One-in-four (27.3%) answered that they could chest compression in the same situation. In contrast, this survey revealed that 65.8% want to learn how to CPR that includes AED.

Life-saving course is an official and common opportunity of learning CPR for non-medical persons in Japan. The trainees must visit fire departments, and at least spend 3 h to learn. The trainers (mostly emergency lifeguards) use an AED trainer, combined with a patient simulator equipped with several sensors and actuators. The high price of training equipment (e.g. 1,000USD for an AED trainer and 4,000USD for a patient simulator) and limited professional trainers are the main cause of insufficient learning opportunity of CPR.

To fill the needs of learning CPR of non-medical persons, we have decided to develop a low-cost virtual CPR learning system that includes AED and chest compression simulation. This system can be used for *self-learning* at home, school and office using their own computers.

## 1 CPR Training for Non-medical Persons

CPR (Cardio-Pulmonary Resuscitation) is a medical procedure to rescue patients who have cardiopulmonary arrest. It includes consciousness confirmation, chest compression, artificial respiration and electrical shock by an AED.

Y. Yamauchi (✉) · T. Hayashida  
Toyo University, 2100 Kujirai, Kawagoe, 3508585, Japan  
e-mail: yamauchi@toyo.jp

## 2 Hand Motion Capture Device for Simulator

The key points for successful CPR are proper ‘actions’ as well as ‘decision making’ of rescuers. Most of the CPR operations, including chest compression, are performed with fingers and palms. For example, according to the American Heart Association (AHA) Guideline 2015 [2], untrained lay rescuers “should continue compression-only CPR” and the characteristics of chest compression include position, rate



and depth. In use of an AED, two electrode pads should be pasted on appropriate positions on the patient's chest.

We chose Leap Motion (Leap Motion, Inc.) as a motion capture device specialized in fingers and hands motion capturing. The Leap Motion can acquire the movement of the user's palm and fingers by holding the user's hand over Leap Motion. Its field of view is approximately 135° with 8 cubic feet of 3D space, and sufficient for hand motion in CPR. The cost of Leap Motion is lower (\$69) than existing AED trainer.

### 3 CPR Training Scenarios

#### 3.1 Reference AED Trainer

To determine training scenarios of our system, we investigated an existing AED trainer (TRN-2100, Nihon Kohden Corporation) as a reference (Fig. 1). TRN-2100 is equivalent to the real AED (AED-2100, Nihon Kohden Corporation), except that it has no defibrillation function.

As real AEDs, TRN-2100 has function of artificial voice announcement to urge rescuers to perform the next action. Although the AED trainer is widely used for CPR training courses, the AED trainer itself is intended for use with healthcare provider, not for self-education.

#### 3.2 CPR Scenarios

The TRN-2100 has five scenarios (No. 1–5) of CPR including AED operation. Among them, we have selected and implemented three scenarios (No. 1, 4 and 5), that are more common than the others are. To start the system, trainee touches the start button by virtual hand. Then, one of the three scenarios is selected randomly.



**Fig. 1** The reference of our learning system: A CPR patient simulator (Little Anne® CPR Training Manikin, Laerdal, left) and an AED trainer (TRN-2100, Nihon Kohden, right)

## 4 Implementation of Virtual CPR Learning System

### 4.1 System Development Environment

We develop virtual CPR learning system using Unity 5.4.1f1 as implementation software of virtual CPR behaviors and Leap Motion Orion 3.1.3+41910 as the operation device. The computer specifications are as follows: Windows 8.1 Pro 64-bit as the operating software, Intel(R) Core(TM) i7-4790 CPU @ 3.60 GHz (8 CPUs) as the CPU, NVIDIA GeForce GTX 750 Ti as the GPU. A text-to-speech software VOICEROID + Tamiyasu Tomoe EX is used to generate voice announcements.

Figure 2 shows a scene of use of our learning system. A trainee moves his/her hand over the Leap Motion. A 'virtual' hand, shown as a skeleton hand, appears in the simulator and moves as the real hand moves. The trainee hears the announcements of usage by a headphone.

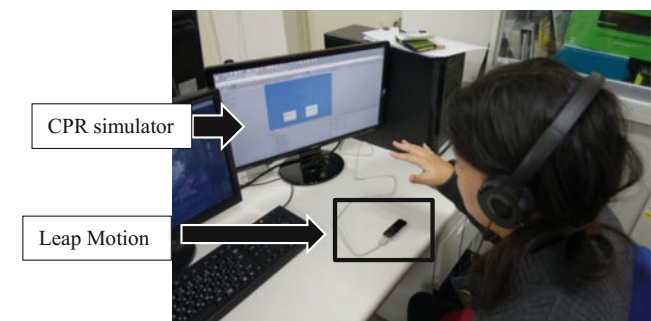
### 4.2 Simulated Procedure of AED Usage

Figure 3 shows a simulated procedure of AED usage, as #1 to 4, 6 and 7 in Table 1.

Figure 3a is the initial situation. The trainee activates the AED, and 'undress' the patient by touching the AED and the clothes (Fig. 3b). The trainee removes the electrode pads from the AED and pastes them on the patient (Fig. 3c). After the ECG analysis, the trainee presses the button to do electronic shock, if necessary.

### 4.3 Tutorials

In actual life-saving course, professional trainers make practical guidance for trainee. The tutorials of our system are equal to the scenarios shown in Table 1, but give additional guidance for trainees by voice, text and visual emphasis to



**Fig. 2** A scene of use of the CPR learning system



**Fig. 3** A simulated procedure AED usage by the learning system

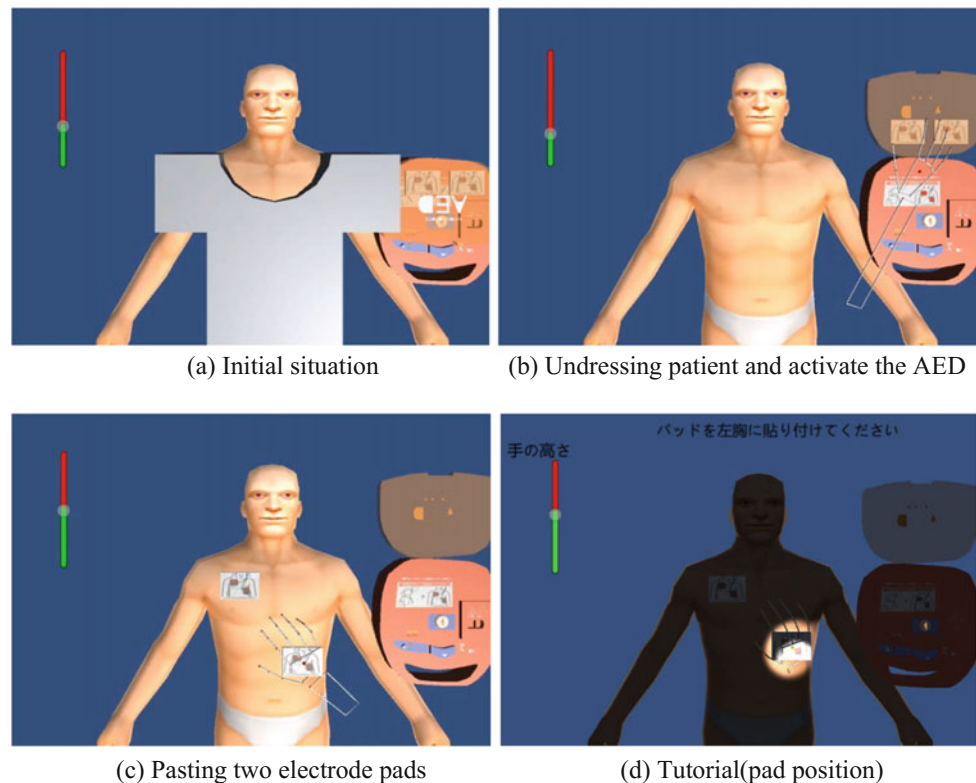


**Table 1** Three scenarios for virtual CPR learning system

Phase #	Scenario No. 1	Scenario No. 4	Scenario No. 5
1.	Turn on AED object by virtual hand, start announcement of the way to use AED		
2.	Following the announcement, touch the clothes of human model to remove it. After, paste electrode pads by virtual hand		
3.	First ECG analysis		
4.	Shock is not necessary	Press the button to do electronic shock.	
5.	Chest compression (2 min)		
6.	Second ECG analysis		
7.	Shock is not necessary		ECG analysis is failed
8.	Chest compression (2 min)		

help self-learning. Figure 3d shows an example of tutorials in pasting left electrode. A correct position of the pad is spotlighted, and an explanatory text is shown above the objects.

#### 4.4 Simulated Procedure of Chest Compression

We implemented chest compression simulation with the aid of 3D motion capture of the Leap Motion (Fig. 4). Adequate conditions for chest compression for adult, recommended by the AHA guideline, are as follows:

1. Compression rate: 100–120/min
2. Compression depth: at least 5 cm, but not greater than 6 cm
3. Hand placement: two hands on the lower half of the breastbone.

The trainee adjusts the virtual hand on the lower half of the breastbone and moves the hand up and down. The hand depth from the surface of the patient is shown as the length of a red bar. When the hand placement and motion do not fulfill the above recommendation, the system alerts the trainee to it by a text.

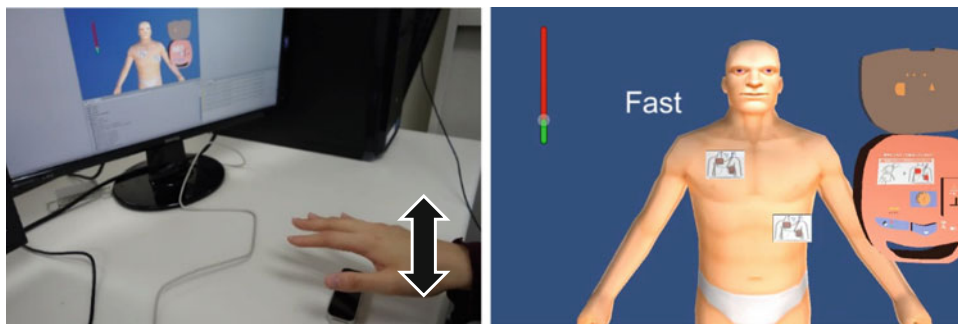
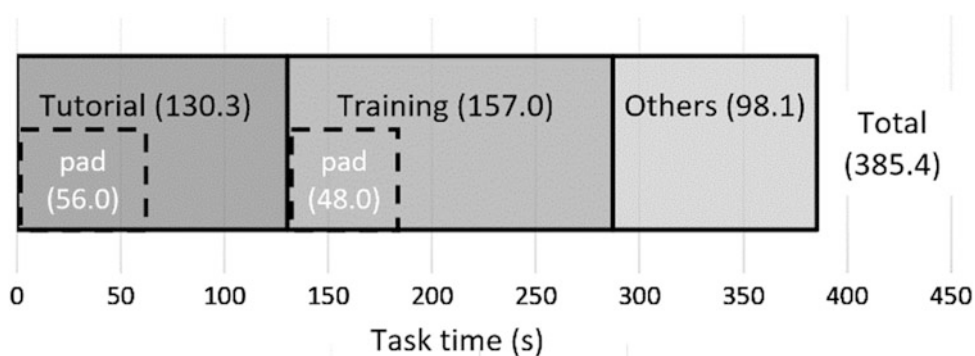


**Fig. 4** Chest compression simulation. Left: the trainee adjusts the hand position and move it up and down. Right: system alerts by the text ‘Fast’, as the compression rate exceeds 120/min

**Fig. 5** Result of task time analysis. Pad placement times are shown by dashed squares



## 5 Usability Evaluation

To confirm the functionality of our CPR learning system and clarify the issues to be solved, we performed usability evaluation test. Ten non-medical subjects of 20 s have involved the evaluation. All subjects have already experienced an AED training once, as a part of driving license education in Japan. Subjects are asked to perform the scenario no. 4 and its tutorial, excluding chest compression. Behavioral analysis has been done by measuring time for each task. Subjects are also asked to fill a questionnaire.

Figure 5 shows the average task time for tutorial and training task. The average total time exceeded 6 min. The average time of training was longer than that of tutorial, but the difference was not statistically significant (paired *t*-test,  $p > 0.05$ ).

Results of questionnaire (Table 2) suggested that the subjects had favorable response for our CPR learning system but felt difficult to manipulate Leap Motion.

**Table 2** Results of questionnaire for difficulty level (# of subjects)

Difficulty	Very hard	Hard	Moderate	Easy	Very easy
CPR learning system	0	0	3	6	0
Leap motion	1	8	0	0	0

## 6 Discussion

We have succeeded to implement three scenarios of CPR, including AED manipulation and chest compression. We also prepared tutorials to help self-learning instead of professional trainers. Task time analysis showed no difference of completion time between the tutorial and the following training. We assume that the trainee properly learnt by the tutorial and performed training correctly without additional guidance.

The most likely cause of the difficult manipulation of the Leap Motion is the mismatch of hand-eye coordinates. The Leap Motion is laid horizontally on the table, and when the subject moves his/her hand up and down, the virtual hand moves back and forth. Rearranging the setup of the Leap Motion and the monitor, using HMD, or additional tutorial will help solving this problem.

Some CPR professionals argue that the force feedback is strong in chest compression. It is important that the trainee knows about it. However, in the AHA guideline, there is no quantitative recommendation for its force. The rate, depth and hand placement, all that we have implemented, have higher priority in the CPR.

**Conflicts of Interest** The authors declare that they have no conflict of interest.

## References

1. Tokyo Fire Department: Opinion survey about rescue and disasters, <http://www.tfd.metro.tokyo.jp/> [Japanese], last accessed 2017/1/20.
2. American Heart Association: Guidelines for CPR & Emergency Cardiovascular Care, <https://eccguidelines.heart.org/>, last accessed 2018/1/31.

# Usability of Electronic Patient Records for Assessment and Care Planning in Nursing Homes

Kate Shiells<sup>✉</sup>, Iva Holmerová<sup>✉</sup>, and Olga Štěpánková<sup>✉</sup>

## Abstract

Nursing homes are more frequently turning to the electronic patient record (EPR) to manage documentation. Potential benefits associated with EPR include the storage of longitudinal information, interoperability, and improved documentation quality. However, the uptake of EPR in nursing homes has varied considerably across countries, which has been associated with the incompatibility of some EPR systems with this environment. Furthermore, the suitability of EPR for planning dementia care is largely unknown. This study aims to produce recommendations for the future development of EPR systems for use in the assessment and care planning for people with dementia in nursing homes. Case studies of four nursing homes using EPR in Belgium, Czech Republic, Spain and the UK will be conducted. There are two elements to the study: (i) the contextual inquiry method will be employed to explore usability issues with different types of end users. Data will be analysed using qualitative content analysis; (ii) the electronic care plan used in each of the homes will be compared with best practice guidelines for dementia care planning in order to explore the extent to which they include aspects of care that are relevant for people with dementia. Primary data collection will be ongoing throughout 2018, and results will form the basis of recommendations for future EPR development. It is expected that results will lead to improved design of EPR for use in nursing homes, specifically in the assessment and care planning for people with dementia.

## Keywords

Dementia care • Electronic patient record  
Nursing home

## 1 Background

It is estimated that there are currently 47 million people living with dementia worldwide [1]. Despite a growing awareness of the ‘physical environment as a component of care’ [2], the progressive nature of dementia, worsening of co-morbidities, and carer-breakdown [3] have meant that people with dementia are still likely to spend time in a nursing home as they pass through the continuum of care [4].

Alzheimer’s Disease International describe four main ‘apparatus’ of long-term care, the first of which being the, ‘assessment and evaluation of social and health care status, resulting in explicit care plans’ [5]. However, although documentation plays an important role in the care of people with dementia in nursing homes [6], increased regulatory pressures [7] have meant completing documentation has become one of the most time-consuming activities for staff [8]. As a result, nursing homes are more frequently turning to electronic solutions, such as the electronic patient record (EPR), to manage the process of documentation.

Despite the envisaged benefits of EPR as a health information technology (HIT), several systematic reviews exploring the impact of electronic documentation systems have found numerous incompatibilities with the nursing home environment [9–11]. These incompatibilities have been linked with a lack of research investigating the usability of electronic documentation systems from the end-user’s perspective [12], with clinicians reporting a lack of involvement in the design of systems [13]. An understanding of the ways in which EPR systems facilitate or create barriers for end users to carry out their work in nursing homes is thus crucial in order for developers to modify and improve EPR technology for this specific environment [14].

K. Shiells (✉) · I. Holmerová  
Faculty of Humanities, Centre of Expertise in Longevity  
and Long-Term Care, Charles University, Prague, Czech Republic  
e-mail: kate.shiells@fhs.cuni.cz

O. Štěpánková  
FEE, Department of Cybernetics, Czech Technical University  
in Prague, Prague, Czech Republic

This paper describes the protocol for a study exploring usability issues associated with EPR systems for use in the assessment and care planning for people with dementia in nursing homes. The study is part of a broader European project entitled ‘Interdisciplinary Network for Dementia using Current Technology’ (INDUCT). We begin by introducing the research objective and research questions, and subsequently suggest a methodology for addressing these questions.

## 2 Research Objectives

The overarching aim of this study is to produce recommendations for the future development of electronic documentation systems for use in the assessment and care planning of people with dementia living in nursing homes.

The following research questions will be addressed as part of this study:

- Which types of devices and software are used by nursing homes for assessment and care planning in Belgium, Czech Republic, Spain and the United Kingdom? Which types of information do the systems capture?
- What are the usability issues associated with the electronic patient record system for assessment and care planning for people with dementia in nursing homes? What are the suggested modifications?
- What are the contextual conditions of the nursing home in which the electronic patient record system has been introduced? What is the impact of these contextual conditions on usability?
- What are the best practice guidelines for care planning for people with dementia that should be captured by the care plan? To what extent are the electronic patient records used by nursing homes capturing this information?

## 3 Study Design and Methods of Data Collection and Analysis

### 3.1 Study Design

This study uses an exploratory, qualitative research design with a case study approach in order to examine usability issues associated with EPR from the staff perspective, as well as the contextual conditions of the nursing home in which the EPR has been implemented.

### 3.2 Data Collection

For the purposes of this study, the contextual inquiry (CI) method will be employed. CI is based on the premise that understanding exactly who users are and how they work is implicit in effective design [15]. Therefore, the CI method frequently involves combining interviews and observations of users within their natural environments [16].

An initial interview will be carried out in order for the researcher to grasp an understanding of contextual factors, such as number of hours of training with the EPR system, and availability of technology. This will be followed by an observational interview with a defined task, and a follow-up interview to allow the participant to expand on any issues discussed during the task. During observations, each participant will be observed recording assessment and care planning documentation for one resident with dementia and asked to use the ‘think aloud’ method to describe components of the EPR system that are facilitating or hindering the task.

A list of problem statements developed prior to data collection will be referred to during the observations and follow-up interviews [17]. These problem statements have been developed from evidence collated from an earlier literature review carried out by the lead researcher exploring the ways in which EPR systems are facilitating or hindering assessment and care planning in nursing homes, and from a scoping review of the literature on best practice for care planning for dementia. An example of a problem statement is: ‘do forms use standardised nursing terminology?’. Each problem statement also corresponds to a ‘structural quality component’ (organizational support, hardware, software, functionality) as listed in the Health Information Technology Research-based Evaluation Framework (HITREF) [18].

### 3.3 Sampling and Inclusion Criteria

According to research carried out by Nielsen and Landauer [19], the testing of 8–10 participants will identify at least 80% of usability issues. However, they recommend that with distinct groups of users, 3–4 participants from each group is sufficient. There are three foreseen groups of participants within the nursing home (managers, nurses and care assistants). Therefore, observations and interviews will be carried out with a minimum of 9–12 staff members from the nursing home. Transcripts will also be analysed for data saturation (i.e. until new codes are no longer emerging), and if not reached, the sample size will be increased and additional interviews will be conducted.

Individuals will be selected if they: (i) are a permanent member of staff who manages or provides care to residents; (ii) are involved in completing assessment and care planning documentation; (iii) have worked in the nursing home for at least 6 months; (iv) have been trained in how to use the electronic documentation system, and; (v) have been using the electronic documentation system for at least 6 months.

### 3.4 Data Analysis

Recorded interviews will be transcribed and translated by an external transcriber and translator. Transcripts will be de-identified and coded by the lead researcher using NVivo. Contextual data (e.g. length of time working with the system) will be grouped into categories and displayed quantitatively.

Qualitative content analysis will be employed to analyse qualitative data. More specifically, empirical post hoc coding will be used. This refers to the creation of codes that are not predefined, and rather 'emerge through the exploration of data' [20]. Commonalities across the data will be explored, and codes will then be grouped into overarching, a priori themes, which correspond to the structural quality components specified by the HITREF [18].

## 4 Ethical Issues

### 4.1 Assessment and Management of Risk

Any risks of harm involved in participation for this group are low. However, before data collection begins, participants will be informed that they can withdraw from the study at any time. There are ethical considerations in relation to ensuring anonymity of participants who could potentially be identified due to the small sample size. This may mean some participants may be reluctant to discuss any negative aspects during the interviews. In order to reduce this risk, demographic data will not be collected, except for in relation to: (i) role (ii) length of time using the electronic documentation system.

Furthermore, there are ethical considerations in relation to the confidentiality of patient documentation. As a result, no data will be collected that could lead to the identification of residents. Ethical approval will be obtained in all four countries before data collection commences. At the time of writing, ethical approval has already been received in the Czech Republic and Belgium.

Data confidentiality will be maintained through the following measures: (i) all participant data will be de-identified

and participants will be assigned pseudonyms; (ii) no identifying information (such as role) will be assigned to any quotes in the write-up; (iii) the number of individuals accessing data (for reasons of transcription, translation, and analysis) will be limited; (iv) interview recordings will be destroyed following transcription; (v) field notes from observations will be immediately written up and stored electronically in NVivo, with password protection. Original notes will be destroyed; (vi) transcripts will be uploaded to NVivo for data analysis, which will be password protected.

### 4.2 Consent

After initially expressing interest in participating, the staff member will be provided with an information sheet describing the purpose of the study and their involvement. They will then have the opportunity to ask questions about the study, as well as be provided with a written consent form and asked to confirm that they have: (i) read the information sheet; (ii) received sufficient information about the project and the implications of participating; (iii) had the opportunity to ask further questions about the research; (iv) understood that they are able to withdraw from the study at any time, without giving a reason; (v) agreed to their anonymised data being used in the write-up.

## 5 Impact of Results

Data collection will be ongoing throughout 2018. It is anticipated that the results of the study will lead to a reduction in usability issues associated with EPR for assessment and care planning for dementia, and subsequently, increased adoption and more successful implementation of EPR, as well as improved care for people with dementia in nursing homes. Results will also form part of the broader European project 'Interdisciplinary Network for Dementia using Current Technology' (INDUCT), which aims to produce guidelines on human interaction with technology and dementia.

### Compliance with Ethical Standards

**Funding** The research presented in this paper was carried out as part of the Marie Curie Initial Training Network (ITN) action, H2020-MSCA-ITN-2015, under grant agreement number 676265, CVUT grant SGS16/231/OHK3/3T/13, and DEMDATA: The Czech Austrian Long-Term Care Project No. GF16-34873L funded by the Grant Agency of the Czech Republic.

**Conflicts of Interest** The authors declare that they have no conflict of interest.



## References

1. Alzheimer's Disease International. World Alzheimer Report 2016: Improving healthcare for people living with dementia- Coverage, quality, and costs now and in the future. ADI, London (2016).
2. Calkins, MP. Evidence-based long term care design. *Neurorehabilitation* 25(3), 145–54 (2009).
3. Alzheimer's Australia NSW. The Most Difficult Decisions: Dementia and the Move into Residential Aged Care. Discussion Paper 5. Alzheimer's Australia NSW, North Ryde (2012).
4. OECD. Dementia Care in 9 OECD Countries: A Comparative Analysis. OECD, Paris (2004).
5. Alzheimer's Disease International. World Alzheimer Report 2013: Journey of Caring- An analysis of long-term care for dementia. ADI, London (2013).
6. Omelan, C. Approach to managing behavioural disturbances in dementia. *Canadian Family Physician* 52(2), 191–199 (2006).
7. Fournier, D., Gosselin, D., and Rioux, N. The challenges of implementing an electronic medical record system in a long-term care facility. *Geriatric Nursing* 27(1), 28–30 (2006).
8. Martin, A., Hinds, C., and Felix, M. Documentation practices of nurses in long-term care. *Journal of Clinical Nursing* 8(4), 345–352 (1999).
9. Kruse, CS., Mileski, M., Vijaykumar, AG., et al. Impact of Electronic Health Records on Long-Term Care Facilities: Systematic Review. *JMIR Medical Informatics* 5(3), (2017).
10. Meißner, A., and Schnepf, W. Staff experiences within the implementation of computer-based nursing records in residential aged care facilities: a systematic review and synthesis of qualitative research. *BMC Medical Informatics and Decision Making* 14(54), (2014).
11. Phillips, K., Wheeler, C., Campbell, J., and Coustasse, A. Electronic Medical Records in Long-Term Care. *Journal of Hospital Marketing & Public Relations* 20(2), 131–142 (2010).
12. Zhang, J., and Walji, MF. TURF: Towards a unified framework of EHR usability. *Journal of Biomedical Informatics* 44(6), 1056–1067 (2011).
13. Sockolow, PS., Bowles, KH., and Rogers, M. Health Information Technology Evaluation Framework (HITREF) Comprehensive-ness as Assessed in Electronic Point-of-Care Documentation Systems Evaluations. *Studies in Health Technology and Informatics* 216, 406–409 (2015).
14. Meehan, R. Electronic Health Records in Long-Term Care: Staff Perspectives. *Journal of Applied Gerontology* 36(10), 1175–1196 (2015).
15. Holtzblatt, K., and Meyer, HR. Contextual Design. In: Soegaard, M., and Dam, RF. (eds.) *The Encyclopaedia of Human-Computer Interaction*. 2nd edn. The Interaction Design Foundation, Aarhus (2013).
16. Martin, JL., and Crowe, JA. Contextual inquiry for medical device development: A case study. In: Duffy, V. (ed.) *Advances in Human Factors and Ergonomics in Healthcare*. CRC Press, Florida (2010).
17. Rubin, J. *Usability Testing: How to Plan, Design and Conduct Effective Tests*. John Wiley & Sons, New York (1994).
18. Sockolow, PS., Crawford, PR., and Lehmann, HP. Broadening a general framework for evaluating health information technology through health services research evaluation principles. *Methods of Medical Information* 51(2), 122–130 (2012).
19. Nielsen, J., and Landauer, TK. A mathematical model of the finding of usability problems. In: *Proceedings of the INTERCHI '93 Conference on Human Factors in Computing Systems*, pp. 206–213. IOS Press, Amsterdam (1993).
20. Gibson, W., and Brown, A. *Working with Qualitative Data*. Sage Publications, London (2009).



# Data Security and Raw Data Access of Contemporary Mobile Sensor Devices

Till Handel, Max Schreiber, Katrin Rothmaler, and Galina Ivanova

## Abstract

Mobile sensor devices have made a great leap in terms of popularity and proliferation amongst the public in recent years, being used for a wide variety of lifestyle, fitness and health applications. This makes them very attractive for scientists and users who are interested in the actual bio and environmental data these devices measure, what they are capable of and their limitations. However manufacturers like to limit access to such data, storing it on their own private servers, only giving customers access to the results of their often very specific and limited analyses. The underlying filtering methods, algorithms and training sets are virtually never disclosed. Mobile sensor devices use various Bluetooth-protocols like RFCOMM and GATT to transfer data onto a smartphone or tablet. And there is the crux of the matter: Hardly any of the manufacturers encrypt their connection, because that would take precious processing and battery power as well as more resources in development. This paper describes how to access raw bio-data on a selection of wearable and stationary sensor devices using nothing but a contemporary Android-smartphone and a PC. A detailed example of how to access such a device is given. In empirical tests three out of four devices showed a total lack of effective security measures. From the combined experience of accessing several mobile sensor devices a generalized approach was formulated. Finally a shortlist of simple methods that should prevent abusive exploits is given in the hope that future devices will show improved data security in particular for health-relevant applications that deal with sensitive information.

## Keywords

mHealth • Wearable • Security • Bluetooth  
Bio-sensor • Mobile

## 1 Introduction

In recent years, mobile sensor devices like smartwatches, sleep sensors or fitness trackers have entered the consumer market and become very popular amongst the public. They are used in a variety of applications including lifestyle, fitness, health and medical applications [1]. This trend is a very significant one for some members of the scientific community, medical personnel and ambitious users, because it allows them for the first time to collect biological and environmental data of decent quality, continuously, under real-life conditions. Unfortunately, manufacturers tend to limit access to such data. They store it on their own private servers, and provide customers with highly pre-processed data without disclosing any information about the applied preprocessing methods. At the same time, they usually neglect to encrypt their connection in order to save processing and battery power as well as resources in development.

This paper aims to demonstrate that a contemporary Android-smartphone and a PC are sufficient to gain direct access to the raw biological data, collected using such mobile sensor devices. Based on experience with several wearable and stationary sensor devices, this paper formulates a generalized approach of how to access such devices and provides a shortlist of simple methods that could prevent abusive exploits and improve data security.

## 2 Materials

The devices required for the subsequently described approach are a recent Bluetooth (BT) and Bluetooth Low Energy (BT LE) capable smartphone and a PC. The

T. Handel (✉) · M. Schreiber · K. Rothmaler · G. Ivanova  
Institute for Applied Informatics, Goerdelerring 9, 04109 Leipzig,  
Germany  
e-mail: handel@infai.org  
URL: <https://www.biomedical-data-science.org>

smartphone used in this demonstration was a Samsung Galaxy S7 SM-G930 running Android 7.0. The PC was a Dell Precision T7500 with Windows 10 as operating system.

The exploit was written in Java with Android Studio 3.0.1 as IDE. Wireshark was used as package-analyzer and Notepad++ for quick Hex-to-ASCII conversions and data pattern searches. Optionally BinWalk could be used for data entropy analysis.

Subject to this investigation were four wearable or stationary bio-sensor devices that were obtainable on the open consumer market in 2016/2017. These particular devices were selected as samples among the large number of possible candidates, because they met several important criteria. First they were developed by major vendors in the field for health or fitness applications. Second they used some form of Bluetooth for data-transfer onto an Android smartphone. Third they contained several different qualitatively good bio-sensors and were in the price-range below 250 Euro. Fourth, all four sensors were CE-certified.

### 3 Methods

#### 3.1 Data Access

The general method employed to gain access to raw data was similar for each bio-sensor device as illustrated in Fig. 1.

First the manufacturer-app was downloaded and installed on the phone. Enabling the developer options in the Android settings makes the HCI-snoop log function available to users. When enabled it logs all Bluetooth communication on the lowest software-level of the BT-stack—the Host Controller Interface (HCI). This log can be read into a package-analyzer like Wireshark. Wireshark shows all sent and received data-packets, detects the employed BT-protocol, and gives information about protocol-specific flags, addresses and where the payload is situated in each packet. When running the HCI-snoop log while the manufacturer-app connects and communicates with the device, one can gain all the insight needed to reverse-engineer the communication protocol. For the correct identification of the communication protocol it is important to capture the packets sent during device coupling and channel negotiation. Hence it is recommended to turn off Bluetooth, then turn on the HCI-snoop log, turn on Bluetooth again and to finally start the manufacturer-app.

All the wearable (or stationary) bio-sensor devices we tested used either the RFCOMM or the GATT protocol to exchange data via a Bluetooth-transmitter. There exist many other BT-protocols but they are either derivatives of the above two or are hardly ever implemented in BT-chips that can be bought on the market. Hence a wearable biosensor will most likely employ one of the two above.

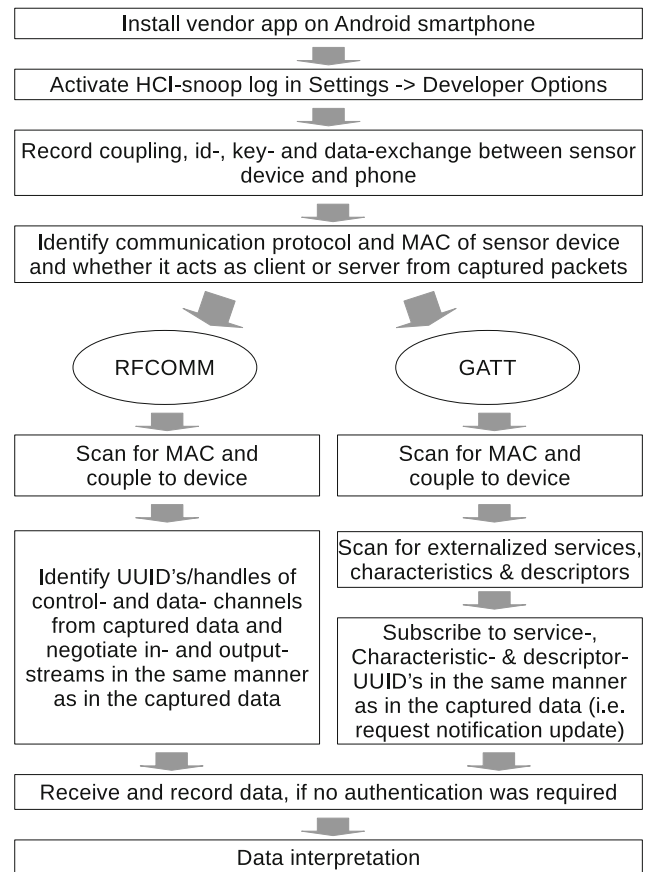


**Fig. 1** Generalized approach to access and interpretation of mobile sensor data

The RFCOMM-protocol emulates one or several serial connections. After negotiating the connection the manufacturer app on the smartphone usually sends some configuration- and control-data. The sensor device typically answers by sending information about its state and if so configured, streaming sensor-data (usually on a separate serial channel) until the connection is broken or de-authenticated [2].

The Generic ATtribute (GATT) profile is a common Bluetooth protocol that is used primarily in newer BT sensor devices. It typically operates at lower data rates than RFCOMM. Hardware layer encryption and coupling between devices is not required, although supported. It allows for parallel communication of many devices, the number depending on hard- and software-implementation of the BT-radio. Communication between devices takes place in a question and answer scheme or in form of notifications signaling that new data is available. In the between-time virtually no data is sent which makes this protocol so power efficient [3, 4].

Finally a proof-of-principle-app was written in Java for Android that attempted to emulate the manufacturer-app and thus was able to control the bio-sensor device as well as receiving and interpreting data from it.

### 3.2 Data Interpretation

After obtaining access to the device-data in the previously described fashion it was still not clear what the data meant. One could now calculate the entropy over binned data (i.e. with BinWalk). If a white noise-like entropy distribution arises, this means that the data is encrypted. However in three of four cases the data showed an obvious structure which meant this was indeed raw or slightly obscured data.

A few sensible assumptions could be made about the data:

1. If there were several different sensor-types in the sensor-device, their values will probably be written in a fixed position in each packet if they are all sampled at equal intervals. If not there will probably be a sensor-id followed by one or several values according to sensor-type.
2. Sensor-ids will probably be integers of 1 or 2 byte length.
3. Sensor values will most likely be integers or floats of 1, 2, 4 or 8 byte length.
4. There might be time-stamps, most likely 4, 8 or 16 byte integers in some form of unix-time, or cpu-clock-time.

Thus a sample from a 3-axis accelerometer will probably look like this:

```
sensor-id [int8/16], (timestamp [int32/64/128]),
x-acceleration [float16/32], y-acceleration
[float16/32],
z-acceleration [float16/32]
```

By simply converting the data to Hex, and opening it in Notepad++ one could identify repeating patterns in three of the four data-sets (i.e. identical packet lengths or identical prefixes). By inserting newlines so that identical features match up across each line one could derive how many bytes of values belong to each sensor-id. Endedness could be derived from whether the 0s were on the leading or the trailing edge of a number.

Association of each sensor-id with its sensor-type could be done in two ways: Either by selecting each sensor-type individually in the vendor-app and snooping the data each time. Or if this approach was not possible by manipulating one sensor-type after another and observing changes in the data-set. (i.e. move accelerometer linearly, then rotate gyrometer, then flash light at the light sensor, etc.).

Finally a parser was written for each data-set. The sensor-data was plotted and calibrated by experiment or with information from the sensor-datasheets if available.

### 3.3 Results

Table 1 shows that sensible data could be extracted with the above method from 3 of the 4 investigated sensor-devices (A, C, D). The method was shown to work for both the RFCOMM- and the GATT-protocol. Whether permanent coupling of the BT-devices is required did not affect the method. All 4 communication protocols were proprietary, non-standard, based on standard BT-protocols. None of them was publicly documented and thus they all were somewhat obscure. However it could be shown that data-extraction and data-interpretation was still possible, demonstrating that obscurity is not a safety feature.

Device B seemed to use some form of encryption. A non-static handshake could be observed but time did not allow determining which encryption method, key-length and possible check-sums were used. Thus interpretable data could not be extracted from this device. That does not mean however, that one could not in principle reverse engineer the decryption process, but it does add a sensible layer of security.

In device A where control over the device was sufficient to configure sensor-types and sample rates ourselves, it was found that using many sensor-types with high sample-rates in parallel did lead to jumbled BT-packets. This would indicate that either the bandwidth or the computation limit of the device was reached. Further this mode of operation led to a battery life of about  $\frac{1}{8}$  of the vendor-specified typical battery life.

**Table 1** Overview of the data access schemes of 4 exemplary bio-sensors

Device	Protocol	Permanent coupling required	Encryption	Sensible data extracted	Comments
A	RFCOMM	Yes	No	Yes	Full control acquired, equivalent to vendor API
B	GATT	Yes	Yes	No	Deauthentication when encryption handshake failed
C	GATT	Yes	No	Yes	Real-time data and data in memory could both be extracted
D	GATT	No	No	Partially	Proprietary data pre-conditioning on device makes data difficult to interpret

## 4 Conclusion

Based on the results explained it can be concluded that in three of the four investigated bio-sensor devices, sensible data could be accessed with a fairly simple, generic approach. This is great news for researchers and interested members of the public who would like to access the actual raw-data on their device. On the down-side this almost total lack of security measures leaves a gaping hole of possible entry vectors for unauthorized listeners. Possible attack scenarios are most prominently:

- Interception in the smartphone BT-stack similar to what the HCI-snoop log does.
- Capturing the device-coupling, deauthenticating a connection, faking addresses, taking over the connection or staging a man-in-the-middle-attack
- A whole range of packet-injection methods.

Device B showed that the implementation of some basic security-features can add immensely to the barrier unauthorized listeners would have to overcome. One could theorize that major contributors to the bad safety of these devices are:

- The tight margins of power and computational resources developers have to deal with in mobile sensor devices. This is supported by the massive dip in performance, device A experienced when the sensor-configuration was altered. Encryption would put an extra drain on the performance.
- The relative novelty of the technology; particularly the BT LE standard and its accompanying safety features.
- Short development periods in the mobile technology sector.

We believe that the aforementioned anti-patterns in software and hardware development should be addressed as soon as possible. This is not only because people become increasingly aware of the importance of data-security in their daily lives and companies will lose the trust of their customers if they don't act soon. Much more importantly these devices often claim to give accurate information about the fitness and health-state of a person. However with the current degree of carelessness in the development of fringe application on the intersection of the strongly regulated health-sector to the virtually unregulated lifestyle sector, standards have been slipping for some time while legislation has been lagging behind.

## 5 Outlook

Possible safety-features vendors should try to include in their future mobile sensor-devices are:

- A proper handshake key exchange in a secure environment.
- A certificate-based asymmetric encryption.
- Untrustworthiness and plausibility-checks for the BT-connection. Immediate termination of the connection in case they fail.
- Using openly developed standardized transmission and encryption protocols. As demonstrated obfuscation through proprietary development practices is not a safety feature. On the contrary custom cryptography implementations tend to be under-tested and thus more vulnerable. Finally, true raw-data export features would reduce the motivation for ambitious users to break the system, would greatly widen the application spectrum for such hardware and thus encourage development and innovation in the field.

Provided these insights come to fruit, mobile sensor devices open up the possibility for anybody interested to take their research from a controlled laboratory setting into a real life environment. If the apparent data security issues are addressed, these devices might even make the jump from predominantly fitness- and health-centered to medically certified applications in the near future.

**Conflict of Interest** The authors declare that they have no conflict of interest.

## References

1. Adams, Z.W., McClure, E.A., Gray, K.M., Danielson, C.K., Treiber, F.A., Ruggiero, K.J.: Mobile devices for the remote acquisition of physiological and behavioral biomarkers in psychiatric clinical research. *Journal of psychiatric research* (2017)
2. RFCOMM Specification: RFCOMM WITH TS 07.10, Serial Port Emulation [https://www.bluetooth.org/docman/handlers/DownloadDoc.ashx?doc\\_id=263754](https://www.bluetooth.org/docman/handlers/DownloadDoc.ashx?doc_id=263754) 2018.31.01
3. GATT Specification <https://www.bluetooth.com/specifications/gatt/> 2018.31.01
4. Tosi, J., Taffoni, F., Santacatterina, M., Sannino, R., Formica, D.: Performance Evaluation of Bluetooth Low Energy: A Systematic Review. *Sensors* (2017)

# Security Mechanism for Medical Record Exchange Using Hippocratic Protocol

Jose Pirrone and Monica Huerta

## Abstract

The use of new technologies in healthcare sector is growing and, as a consequence, the security problems using these technologies are increasing. So a communication protocol based on Hippocratic principles and its standardization was proposed to increase data security when these technologies were used. To evaluate this proposal from a practical point of view, a system based on an application for mobile terminals with the Android operating system and WiFi, as the connection platform to exchange medical records between health personnel and information database of a medical center, was developed. For this system it was assumed that the patient controls the relationship between doctors and patient and this relationship needs to be established personally, using a terminal with NFC technology, but may be dissolved by the patient remotely, without interaction with the doctor. Some operative problems were found but the conclusion is that this is a viable solution and that applying the Hippocratic principles is possible to have two levels of security, being the more secure the use of the Hippocratic protocol.

## Keywords

Hippocratic protocol • Medical record

## 1 Introduction

These days, the development of electronics and telecommunications have generated the possibility of mobile terminals of relatively low cost, which has led to mass use by the population, not only to communicate but to exchange data. The use of informatics applications for mobile terminals: smartphones and tablets, is changing the way of doing things in all professional fields. One of the most important features of this phenomenon is the fact that companies incorporate wireless networks in their environment so that their employees use their own terminals as a tool to improve their productivity, which creates an important corporate security problem, since the data stored in one of these devices would be available to unauthorized persons if the personal device is stolen or hacked, or if the owner of the device shows this information to a third party during a conversation, off the premises.

In the health sector, new technologies have allowed a greater and better monitoring of patients, which improves their treatment, however, this monitoring generates an additional amount of information that must be handled by health personnel, doctors and nurses, and which is highly sensitive, so if they use their own devices, a security problem is generated that is much more important than what could be generated in any other sector.

One of the most important element containing information in the health sector is the medical record. Traditionally, it has been a folder full of papers written by the doctor collecting his observations about the patient in different moments that have been treated. In some countries, like United States, a law motivated his physicians to adopt a digital format [1]. Medical data is collected from the patient when he is treated and his consent to collect this information was assumed [2].

In [3], a Hippocratic characteristics applicable to databases (DB) had defined, these are: 1. Specification of purposes: there is an associated purpose for data registration,

---

J. Pirrone (✉)  
Universidad Catolica Andres Bello, Caracas, 1020, DC,  
Venezuela  
e-mail: JPIRRONE@UCAB.EDU.VE  
URL: <https://w2.ucab.edu.ve/escueladeingenieratelecomunicaciones.html>

M. Huerta  
Universidad Politecnica Salesiana, Grupo de Investigacion en  
Telecomunicaciones y Telematica, Cuenca, Ecuador



2. Consent: purpose defined for data must have authorization from the owner, 3. Limited collection: Collect only data necessary to fulfill the purpose, 4. Limited use. All DB queries must be consistent with the purpose, 5. Limitation of the disclosure: data obtained from DB must have the consent of the owner, 6. Limitation of the retention: data will be stored only during specified time, 7. Accuracy: owner's information must be legitimate and up-to-date, 8. Security: user's information must be protected, 9. Opening: user will be able to modify and consult his information, 10. Compliance. owner of data can verify compliance with all the above points. These Characteristics are implemented in some legal framework like Health Information Technology for Economic and Clinical Health (HITECH) act in USA and General Data Protection Regulation (GDPR) in European Union.

Applying these characteristics to the transmission and reception of data, a standard protocol that has these characteristics, called Hippocratic Protocol, was proposed in [4] and an implementation model was presented in [5] for evaluate the protocol performance. The methodology used was based on an investigation about the clinical histories and medical records, then a system with security mechanisms based on the Hippocratic protocol was developed, and, some tests to evaluate this mechanisms was done.

The purpose of this paper is to present the results of the development of a security mechanism for exchange medical data that can be used in medical records using Hippocratic protocol and assuming that the patient is responsible of the control of his data.

## 2 Test Model Elements

### 2.1 Hardware

To simulate a clinical center with WiFi network, we use a computer with an i5 CPU, 4 Gbytes on RAM and a WiFi interface. The WiFi network used an access point 802.11 n. We use two tablets NEXUS 7 with ANDROID 4.4 operating system with NFC. These tablets do not have access to mobile providers; they only work like data terminals in a WiFi network. The connection between computer and Access point was wireless. In Fig. 1 a scheme is shown.

### 2.2 Server Software

The server was implemented with an open source packet called WAMPSEVER64 on a 64 bits CPU. Two roles were defined: Doctors and patients, the system assigns a code number that is unique to each doctor, or each patient, that is registered. The database of the system has three tables, one

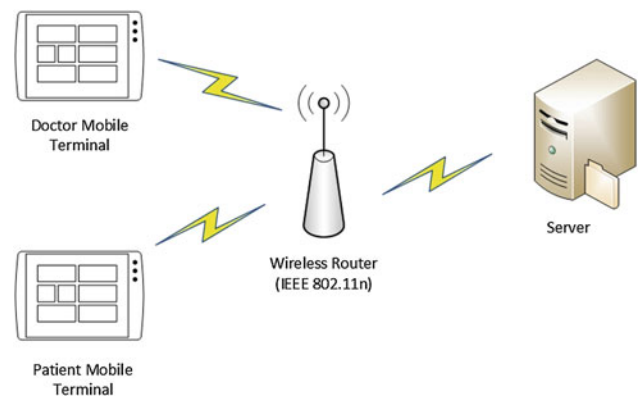


Fig. 1 Scheme connection

for Doctors, one for patient and one to register the relation between them and the code that represents the information of the Medical Record of the patient that the Doctor can access and consult.

The interaction with server software is done with a group of subprograms, written in PHP, which allow the ANDROID application of the tablets to read or write the data to which the Doctor is authorized to access.

### 2.3 Terminal Software

The Medical Record used for test was a group of 17 question normally used when a patient begins a medical relationship with a Doctor. Each answer was stored in a 100 character variable. All the answers to this questionnaire can be restricted by the patient so that the Doctor can only have access to those that the patient considers. The structure of this software consists of five screens: one for access (like patient or doctor), one for register patient and his information, one to register Doctor and his information, one to consult information in the role of Doctor and one to consult information in the role of patient.

## 3 Test Performed

### 3.1 Hippocratic Characteristics

The first test involved the use of the NFC connection to create the relationship between patients and doctors, which is what allows doctor to access patient information when the patient sends to the doctor the corresponding authorization code. These tests turned out well, since the terminals used required up to 4 cm of separation to transfer the information from one terminal to another, which is indicated by the NFC standard. The data used was enciphered using 128-bit AES encryption with a symmetric key. The application was based

on the use of the Hippocratic protocol, which only allowed doctors view the information for which the patient authorized them. During the tests to verify the speed of response of the application, it was observed that is possible adapt the graphic interface of the application to have Hippocratic Characteristics. This observation means that it is possible to have applications that seems to have Hippocratic characteristics but this does not mean that Hippocratic protocol is used and the security is apparent.

### 3.2 Time Response

A second test performed was the measuring of time response from server to terminal. Since the exchange of data may depend of the authorization code, the time exchange is variable and delays too, then tests were performed to verify if the delays incurred were perceptible by the users. Table 1 shows the results of the measurements made. As the information to access are the answers given by the patient when registering, access tests were made for reading and writing by the Doctor to verify the delay in loading or writing the information to and from the tablets. Reading and writing accesses were made of 2 answers, 3 answers and all the answers.

The times were measured using WIRESHARK from the beginning of the request to the final acknowledgment by the terminal. The time differences between the case “Hippocratic presentation, all the answers” and the case “Hippocratic protocol, all the answers” lies in the fact that in the second case if the Hippocratic protocol is used to guarantee security, an attacker only could have partial access to the information while in the first case, he can intercept all data and access them.

### 3.3 Persistence of Data in the Terminal

As you can see in the Fig. 2, before leaving the ANDROID application using the finish () routine, all the variables are initialized, with which, its previous value is cleaned and lost.

This result is similar for each of the modules that correspond to the program, mainly due to how the exit button was implemented. On the other hand, it was verified that the only

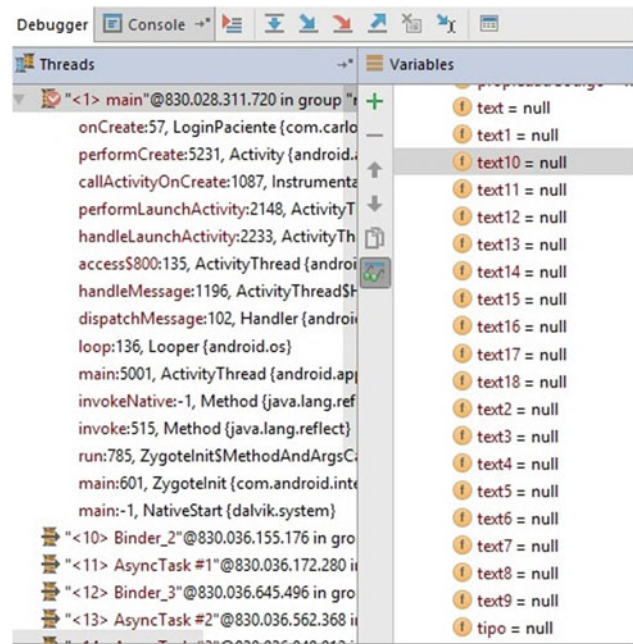


Fig. 2 Value of the test application variables before concluding

information that remains in the device is what is required to be able to execute the application.

## 4 Discussion

The tests carried out with terminals showed that it is possible to develop applications that comply with Hippocratic principles using the Hippocratic Protocol. The use of this protocol assumes that the exchanges between the doctors and the system, that stores them, only is allowed if the information is authorized, and only the information to which they have access, and this represents an increase in the security of the patients information, because only a part of the information could be affected if the system is attacked. This increase in security translated into greater reading and writing access times for doctor roles than for patient roles. During the test an issue on authentication was found. The authentication tests allowed visualizing the potential problem that a doctor or a patient lose their terminal and have no possibility of accessing the registered information. This point should be studied in depth to create a procedure that allows the user to authenticate again in the system. The other characteristics of the Hippocratic protocol were not affected by this issue. A point to test in the application, and considered in the Hippocratic protocol, is the analysis of the purpose, prior to the reading of the information by the doctors. The medical record test application has a single purpose; however, the way the database was organized would allow each user to create relationships with different purposes, for example. scientific research and audit.

Table 1 Time for interaction with database

Case	Read (s)	Write (s)
Hippocratic presentation all answer	2,67	5,20
Hippocratic protocol 2 answer	5,06	5,11
Hippocratic protocol 3 answer	5,23	5,16
Hippocratic protocol all answer	5,81	6,60

## 5 Conclusion

The use of the Hippocratic protocol is a mechanism to improve security in electronic medical records and guarantees consent of patient to grant the doctor the access to his information at the time of the consultation, and provide a tool to fulfill legal requirements, but some operative problems need more study, for example, what happens with an emergency in which the patient is unconscious? The doctor must have access to all the information or only one part? Will there be a third party that will grant these permits and how?, What happens with the diagnoses that the doctor has already issued if a patient cancels the relationship?. The generation of categorization of medical information in a simple way, which is indispensable access for all specialties, is an important area of research, since complexity can generate disadvantages that discourage application and also its use by the sector's personnel. Improvements in authentication mechanisms and work with digital certificates are also open for further development.

**Conflict of Interest** The authors declare that they have no conflict of interest.

---

## References

1. Tang, P.C., Lee, T.H.: Your Doctor's Office or the Internet Two Paths to Personal Health Records. *N Engl J Med* 2009; 360:1276–1278. <https://doi.org/10.1056/nejmp0810264>.
2. M. Bromwich and R. Bromwich: "Privacy risks when using mobile devices in health care," *CMAJ: Canadian Medical Association Journal*, vol. 12, pp. 855–856, 06 09 2016.
3. Agrawal, R., Kiernan, J., Srikant, R., Xu, Y.: "Hippocratic Databases", in *Proceedings 28th VLDB Conference*, Hong Kong, China, 2002.
4. J. Pirrone and M. Huerta: "Hippocratic Protocol Design to Improve Security and Privacy in Healthcare Applications for NFC Smartphone," in *IUPESM World Conference*, Toronto, Canada, 2015.
5. C. Kowalewicz, J. Pirrone and M. Huerta: "Implementation model using a Hippocratic protocol in mobile terminals with NFC technology," in *2017 International Caribbean Conference on Devices, Circuits and Systems (ICDCS)*, Cozumel, 2017.

# An Engineering Module to Identify Potential Diabetes Patients and Preventive Measures for Diabetes in Developing Countries like Bangladesh

Md. Ashrafuzaman, Mohammad Tareq Alam,  
and Md. Abdullah-Al-Harun

## Abstract

Diabetes has demonstrated as the main chronic disease and crucial problem in Bangladesh. According to a data of International Diabetes Federation (IDF) Bangladesh is the 10th in terms of diabetes patients in the world and diabetes prevalence in Bangladesh would reach from present 7 to 12 million by 2035 posing a colossal challenge to the health care system. People of all ages are being affected with diabetes, which has become a silent killer. Objective of this study is to develop a module with assistance of doctors and CE/BME which will be used to identify the actual number of diabetes patients and measure the potential risk on health index. The goal of this study is to bring as much people as possible within survey and find the potential diabetic patients together with the peoples who might not have diabetes now but possess the credible risk factors. We will be able to provide preventive information to these populations and motivate and suggest for more care on individual health to avoid diabetes. An optimized software and database is designed for performing several tasks to analyze the patients' data collected from various hospitals' of Bangladesh. The numerical statistic will represent the overall patients' health index for diseases and assessment will allow us to determine the actual patients' number with appropriate threat in categories of diabetes diseases. Findings can confirm both individuals with diabetes and the control group with possible diabetes threat. Proper Diagnosis and treatment then can be assured for these

individuals and national precautionary action will accomplish through regulatory control. Future assessment and intervention can be further explored from the perspectives of patients and diabetes information processing which can improve the patients' indexing, safety and health care management in many developing countries.

## Keywords

Diabetes • Health index • Patients risk • Social challenges

## 1 Background

Bangladesh is densely populated country and the diabetes patients are increasing considerably in this country. A recent study showed that T2D is emerging as a problem in children and adolescents in Bangladesh [1]. According to Zafar et al. approximately 78.3 million (8.5%) of the adult population living in South East Asia (SEA) region suffer from type 2 diabetes mellitus (T2DM) in the year of 2015 [2]. Besides, SEA region also witnessed 24.2% of all live births affected by high blood glucose during pregnancy in this region at the same time. In another study we have found that the prevalence of diabetes for all age-groups worldwide will reach to 4.4% in 2030 and the total number of diabetes patients is expected to rise from 171 million in 2000 to 366 million in 2030 [3]. These studies showed the prevalence of diabetes is higher in men than women, but in reality there are more women with diabetes than men. It also revealed that significant demographic change for diabetes prevalence across the world seems to be increased in the proportion of people over 65 years of age. These findings indicate that the “diabetes epidemic” will remain even more in future and it is likely that these figures provide an underestimate of future diabetes prevalence if initiative not taken to calculate actual potential population for diabetes.

Md. Ashrafuzaman (✉) · M. T. Alam  
Department of Biomedical Engineering, Military Institute of  
Science & Technology, Dhaka, 1216, Bangladesh  
e-mail: ashezaman@gmail.com

M. T. Alam  
e-mail: tareq.mist@gmail.com

Md. Abdullah-Al-Harun  
Bangabandhu Sheikh Mujib Medical University, Shahabag,  
Dhaka, 1000, Bangladesh  
e-mail: dhbsmmu@gmail.com

**Table 1** South Asian diabetes estimates for 2011 by country

Country	Diabetes cases	National prevalence of diabetes
Bangladesh	8,406,000	9.6
Bhutan	21,000	4.9
India	61,258,000	8.31
Maldives	15,000	7.6
Nepal	488,000	3
Sri Lanka	1,078,000	7.8

## 2 Current Status of Diabetes in Southeast Asia

Type 2 diabetes mellitus (T2DM) currently affects approximately 366 million people worldwide [4]. This includes individuals in developed countries, but also those living in urban and rural areas of developing countries. 2–4 South Asians (those who live in or have their roots in India, Pakistan, Sri Lanka, Bangladesh, Nepal, Bhutan, or the Maldives) seem to be at especially high risk for developing T2DM. While the overall prevalence of T2DM in South Asia is high and increasing, there is considerable heterogeneity across South Asian countries much of this heterogeneity can be attributed for differing the states of socioeconomic development, variations in lifestyle factors, and differences in prevalence of undiagnosed versus diagnosed diabetes among countries like Bangladesh. The majority of T2DM data from South Asia have come from India, the South Asian country with the largest diabetes burden, and where the prevalence has increased steadily over the past 40 years. For an example, the most recent national prevalence study collected data from three states and one union territory covering a population of over 200 million people. The overall weighted prevalence was 10.4% in Tamilnadu, 8.4% in Maharashtra, 5.3% in Jharkhand, and 13.6% in Chandigarh. If extrapolated nationwide, these estimates translate to 62.4 million individuals in India currently living with T2DM [5<sup>1</sup>] (Table 1).

## 3 Diabetes Related Software Apps Survey

### 3.1 POWER2DM

The main objective of POWER2DM [6] is to develop and validate a personalized self-management support system for Type 1 and Type 2 diabetes patients that combines and integrates: A decision support system based on leading

European predictive personalized models for diabetes inter-linked with predictive computer models, An automated e-coaching functionalities based on behavioral Change Theories, and Real-time Personal Data processing and interpretation.

### 3.2 MISSION-T2D

This aims at developing and validating an integrated, multilevel patient-specific model for the simulation and prediction of metabolic and inflammatory processes in the onset and progress of the type 2 diabetes (T2D) [6].

### 3.3 ProEmpower

Improving detection of type II diabetes and improving treatment through person-centered and personalized care. Addressing the problems of patient; improve knowledge of diabetes; support patients in communicating their treatment preference to physicians and support them in aiming for a healthy lifestyle [7]. Finally we are striving to stop the onsets of diabetes and through that avoid complications.

## 4 Objectives

Diabetes has become a national health concern in Bangladesh. However, treatment and control are quite low. Improving detection, awareness, and treatment strategies is urgently needed to prevent the growing burden associated with diabetes. In Bangladesh, which had a population of 149.8 million in 2011 a recent meta-analysis showed that the prevalence of diabetes among adults had increased substantially, from 4% in 1995 to 2000 and 5% in 2001 to 2005 to 9% in 2006 to 2010 [8]. According to the International Diabetes Federation, the prevalence will be 13% by 2030. Nevertheless, no nationally representative, epidemiological study of the prevalence of diabetes mellitus and its risk factors has been carried out in the country. The aims of this study, therefore, are to identify potential diabetic patient who

<sup>1</sup>Annals of the New York Academy of Sciences 1299 (98): 51–63 (2013).



are not aware of their diabetes. Many patients already have type 2 diabetes which they do not know. Our goal is to make an application that will bring out actual statistics of the potential diabetic patients. This project is also is just a designed project at now; actual data will be collected soon through the online survey in hospitals and among the population. Thus, we will be able to estimate the current status of diabetes in Bangladesh once the project implemented nationwide. For that we are reviewing journals related to diabetes published in our country and set of questionnaires has been developed to run in the application during survey.

### 5 Methods and Related Works

The total number of Internet Subscribers has reached 80.483 million at the end of December, 2017 [9]. So almost 50% of the total population is now using internet. So it has become very easy to reach millions of people through the internet. Web application and mobile applications are widely used

now. This is why in our methodology we are using internet of things for reaching mass people. We have developed apps using some internet protocols (Fig. 1) where user will login with their basic data. Then user will be presented with some Health Assessment Questionnaires (HAQ) related to diabetes and quality of life to measure potential population having diabetes or in threat for diabetes in near future. The terminology in below flowchart is described here.

A set of questionnaires was prepared with help of renowned local diabetes specialist and international collaborators [10]. Once the user answers the questionnaires from the web application or mobile APP, system will store the information in server along with patient identification and demographic data. These data will be then analyzed for finding out whether the user has potential risk of having diabetes. The system will also ask information of current medications etc. in order to find out whether any physician already suggesting any medicine related to diabetes or not. The flowchart of the application has started with the questionnaires and test reports and answers to lead towards the

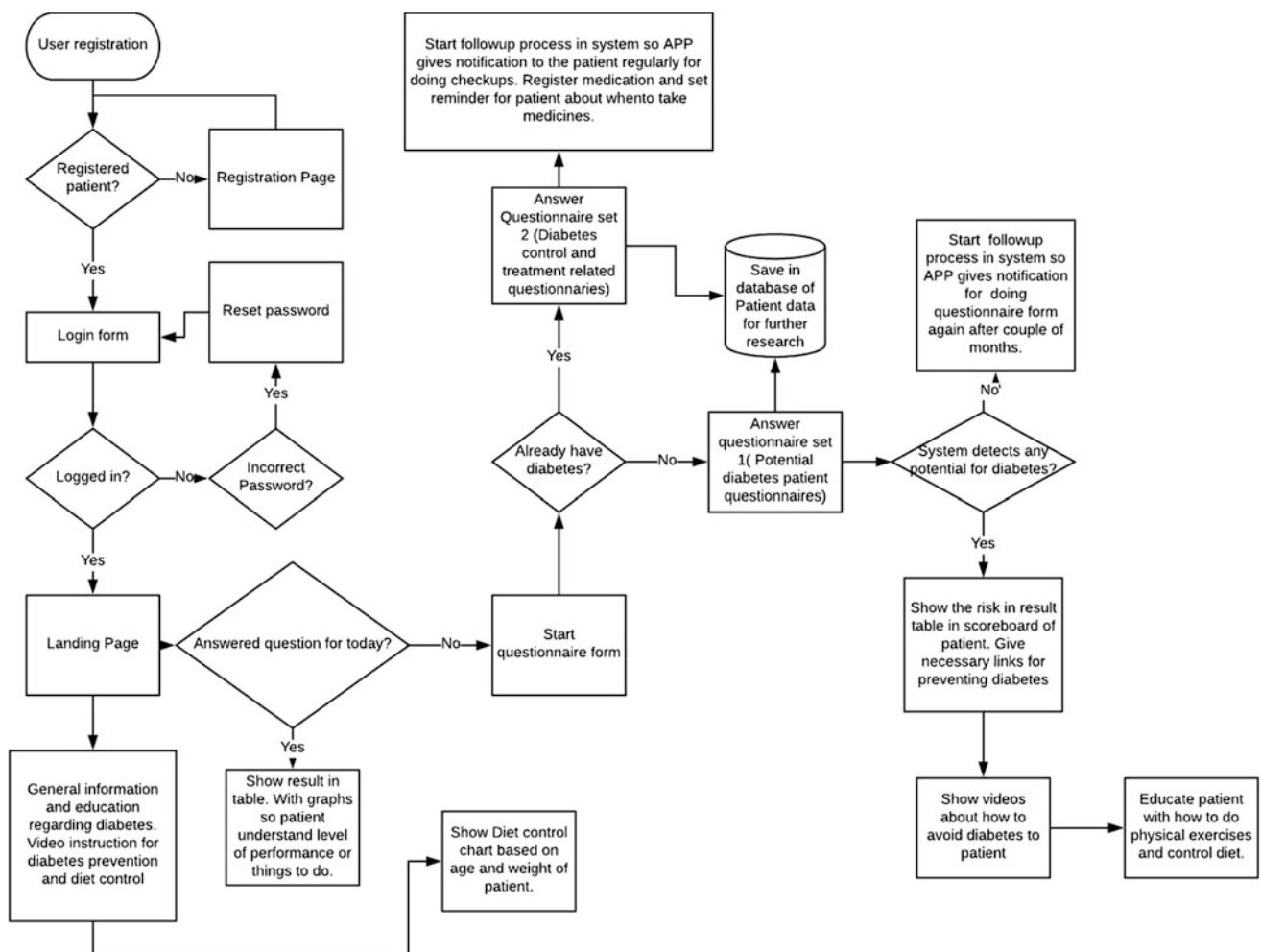


Fig. 1 Flowchart for the development application



The figure displays eight sequential screens of a diabetes questionnaire application. Each screen has a dark green header with the text 'DIABETES QUESTIONNAIRE'. The screens are as follows:

- Screen 1 (Introduction):** Titled 'INTRODUCTION', it states 'You will get some questions regarding your health now. Please read carefully and choose answers accordingly.' and features a 'START ANSWER' button.
- Screen 2 (Question 1):** Titled 'QUESTION 1 OF 10', it asks 'Do you have diabetes already?' with 'YES' and 'NO' options.
- Screen 3 (Question 2):** Titled 'QUESTION 2 OF 10', it asks 'Are you...?' with 'MALE' and 'FEMALE' options.
- Screen 4 (Question 3):** Titled 'QUESTION 3 OF 10', it asks 'How old are you?' with options: 'UNDER 25', '25-40', '41-50', '51-60', and 'OVER 75'.
- Screen 5 (Question 6):** Titled 'QUESTION 6 OF 10', it asks 'Do you usually do some physical activity such as brisk walking for at least 30 minutes each day?' with 'YES' and 'NO' options.
- Screen 6 (Question 8):** Titled 'QUESTION 8 OF 10', it asks 'Have you ever been told by a doctor or nurse that you have high blood pressure?' with 'YES' and 'NO' options.
- Screen 7 (Question 10):** Titled 'QUESTION 10 OF 10', it asks 'Have any of your blood relatives ever been diagnosed with diabetes?' with 'YES' and 'NO' options.
- Screen 8 (Result):** Titled 'RESULT', it states 'This is the place to show the results of the quick survey. Scores are divided into dimensions accordingly.' and shows two dimensions: 'Dimension 1: Already have diabetes?' and 'Dimension 2: Potential risk of diabetes?'.

**Fig. 2** Set of questionnaires for the target population

decision regarding what type of diabetes that patient possess potentially at that certain time (Fig. 2). We are designing the application questionnaire interface and gathering more question to lead the system for making more precise decision for a person whether he/she has diabetes or not.

In future we will focus more precisely on the diagnostic results and knowledge about the diabetes profile which includes;

**C-peptide:** A C-peptide test is used to assess how much insulin your pancreas is producing, **Auto-antibodies:** Auto-antibodies refers to immune cells which target and kill the insulin producing cells in the pancreas, a **GAD test** is used to detect the presence of specific auto-antibodies in the blood, **Type 2:** Type 2 diabetes, the most common in adults, **IM Type 1:** Immune mediated type 1 diabetes, the most

common form of type 1 diabetes, **Idiopathic Type 1:** A rare form of type 1 diabetes with no known cause, **MODY:** Maturity onset diabetes of the young, a rarer form of diabetes caused by specific genetic mutations.

The application will not only detect what is the most probable type of diabetes patient can have, it will also suggest prevention plan customized for the potential diabetes patient. System will suggest different exercises, diet plans, and calorie calculations for the patient to more easily keep track of his/her food habit and how to minimize risk of having diabetes on the long run. It will keep historical data in a personalized way so only the patient can see these data. Collected data can be used for research purpose to present real time information to other organization related with diabetes patients' care.

## 6 Expected Outcomes

Proposed designed project can give expected outcome to one about his/her health. Patients those are not aware of diabetes after answering few questions will find out potential risk of diabetes. Patient can take necessary measure to control the risk of having diabetes and this way prevent the diabetes. Patient can be helped by the system and with its constant reminder patient will become more health conscious. The researchers can understand the potential number of patient that can be affected by diabetes soon. This can give overall status for a country about how the actual number of diabetes patient is changing. Government can also be benefited by the indicators coming from the system. In future this project can be used globally to find out where is the potential number of diabetes patient is increasing. If the internet connections and app usability is a blocker for users then this can also be installed inside the diabetes test center where patient can go and sit in front of a touch screen and complete the questionnaire before visiting the doctor. This will also help doctor by seeing the PROM (Patient reported outcome) data along with the medication data to understand the improvement of the patient. Mostly this tool is aimed for people who still have a chance for not having diabetes.

## 7 Conclusion

The proposed designed project is aimed to solve the problem of finding potential diabetes patients in Bangladesh. Also this will be an engineering module which will run on any platform like webpage, mobile app and as desktop software. But the data collected from this module will be saved in a central database for further research. We have aim also to collaborate with IT organizations worldwide who are expert in this field of study. We believe at some point this will become a registry of diabetes patient where researchers can do research with collected data from South East Asia especially Bangladesh. And we also think this will be a platform for running medical trial under applied legislations with collaboration with renowned medical companies who are already in the business of diabetes related drug in Bangladesh. If this project starts collecting data from mass people in Bangladesh soon it will become national registry for diabetes in Bangladesh. This then will open many doors for doing more research in similar aspect in other Southeast

Asian countries. And then it is also possible to compare the situation of diabetes patients across borders and also researchers will understand more the geographical, lifestyle, economic and demographic impact on Diabetes patient or potential diabetes patients.

**Acknowledgements** Authors would like to acknowledge the support from the Biomedical Engineering Department, Military Institute of Science and Technology (MIST), Bangladesh.

**Conflict of interest** The Authors declare that they have no conflict of interest.

## References

1. Bedowra Zabeen, Jebun Nahar, Samin Tayyeb, Fauzia Mohsin, Nazmun Nahar, Kishwar Azad: Characteristics of children and adolescents at onset of type 2 diabetes in a Tertiary Hospital in Bangladesh. *Indian Journal of Endocrinology and Metabolism* 20 (5), 638–642 (2016).
2. Zafar Ahmed Latif, SM Ashrafuzzaman, Mohammad Feroz Amin, Arvind Vilas Gadekar, Md Javed Sobhan, Tanvir Haider: A Cross-sectional Study to Evaluate Diabetes Management, Control and Complications in Patients with type 2 Diabetes in Bangladesh. *BIRDEM Medical Journal* 7(1), 17–27 (2017).
3. Sarah Wild, Gojka Roglic, Anders Green, Richard Sicree, Hilary King: Global Prevalence of Diabetes: Estimates for the year 2000 and projections for 2030. *American Diabetes Association, Diabetes Care* 27(5): 1047–1053 (2004).
4. Abdulfatai B. Olokoba, Olusegun A. Obateru, Lateefat B. Olokoba: Type 2 Diabetes Mellitus: A Review of Current Trends. *Oman Medical Journal* 27(4): 269–273 (2012).
5. Unjali P. Gujral, R. Pradeepa, Mary Beth Weber, K.M. Venkat Narayan, V. Mohan: Type 2 diabetes in South Asians: similarities and differences with white Caucasian and other populations. *Annals of the New York Academy of Sciences* 1299 (98): 51–63 (2013).
6. European Commission: EU-funded Research & Innovation in the field of ICT for Health, Wellbeing & Ageing - an overview. *Online Brochure* (2017).
7. Haugvik S, Beran D, Klassen P, Hussain A, Haaland A.: “My heart burns”—A qualitative study of perceptions and experiences of type 1 diabetes among children and youths in Tajikistan. *Chronic Illness* 13: 128–139 (2017).
8. Shamima Akter, M. Mizanur Rahman, Sarah Krull Abe, Papia Sultana: Prevalence of diabetes and prediabetes and their risk factors among Bangladeshi adults: a nationwide survey. *Bulletin of the World Health Organization* 92: 204–213 (2014).
9. Bangladesh Telecommunication Regulatory Commission. <http://www.btrc.gov.bd/content/internet-subscribers-bangladesh-december-2017>.
10. Diabetes Canada. <http://www.diabetes.ca/>.

# MULTISAB: A Web Platform for Analysis of Multivariate Heterogeneous Biomedical Time-Series

A. Jovic, D. Kukolja, K. Friganovic, K. Jozic, and M. Cifrek

## Abstract

There is a growing need for efficient and accurate biomedical software in healthcare community. In this paper, we present MULTISAB, a web platform whose goal is to provide users with detailed analysis capabilities for heterogeneous biomedical time series. We describe the system architecture, including its subprojects: frontend, backend and processing. Emphasis is placed on the processing subproject, implemented in Java, which incorporates data analysis methods. The subproject is divided into several frameworks: record input handling, preprocessing, signal visualization, general time series features extraction, specific (domain) time series features extraction, expert system recommendations, data mining, and reporting. Common signal features extraction framework includes a great number of features in time (both linear and nonlinear), frequency and time-frequency domain. Currently, domain specific frameworks for heart rate variability, ECG and EEG feature extraction are supported, which also include preprocessing techniques for noise reduction and detection methods for characteristic waveforms (like QRS complexes, P and T waves in ECG). Parallelization is implemented for feature extraction to increase performance. It is realized using multi-threading on several levels: for multiple records, traces, and segments. Expert system is implemented, which provides automatic recommendation of the set of significant expert features that should be extracted from the

analyzed signals, depending on the analysis scenario. The expert system, apart from the role in recommending features, can also participate in automatic diagnosis, after the features are extracted. Current expert system prototype contains diagnostic rules for acute myocardial ischemia, based on medical guidelines. Data mining framework contains dimensionality reduction methods and machine learning classifiers used to construct accurate and interpretable disorder models. A report is produced at the end of the process using openly available libraries. The platform includes best practices from medicine, biomedical engineering, and computer science in order to deliver detailed biomedical time series analysis services to its users.

## Keywords

Biomedical time series • Web platform • Analysis

## 1 Introduction

In the era of expanding big data, the need for healthcare community to develop tools for analysis and inspection of their data is inevitable. Clinicians and researchers are mainly restricted to use off-line solutions, like MATLAB (or Octave) based scripts or frameworks [1], or other specialized software, e.g. for heart rate variability (HRV) analysis [2].

In this paper, we present a web-based platform for analysis of biomedical time series, developed under the ongoing MULTISAB (MULTivariate TIME Series Analysis in Biomedicine) project ([http://www.zemris.fer.hr/~ajovic/hrzz\\_multisab/platform.html](http://www.zemris.fer.hr/~ajovic/hrzz_multisab/platform.html)). The platform is intended for researchers and clinicians to perform detailed analysis and set diagnosis based on imported biomedical time series data, as well as to visualize and inspect signals data. The access to MULTISAB can be achieved through web browsers, and is therefore available from any computer, without requisite installations. A major benefit of using the platform is that a

A. Jovic · D. Kukolja · K. Friganovic (✉) · M. Cifrek  
Faculty of Electrical Engineering and Computing, University of Zagreb, Unska 3, 10000 Zagreb, Croatia  
e-mail: kresimir.friganovic@fer.hr

A. Jovic  
e-mail: alan.jovic@fer.hr

D. Kukolja  
e-mail: davor.kukolja@fer.hr

K. Jozic  
INA – Industrija Nafta d.d., Avenija Veceslava Holjevca 10,  
P.P. 555, 10002 Zagreb, Croatia

user doesn't need excessive computing power to do the analysis, as the computations are done remotely. The project is currently in the process of module integration and extensive testing. We plan to provide access in a few months.

The MULTISAB project is divided into three subprojects: *backend*, *frontend*, and *processing*. Detailed description of the architectural overview of the platform can be found in [3]. Due to lack of space, in continuation of this paper, we inspect in some detail only the *processing* subproject, which covers the majority of platform's functionality. Architecture and frameworks implemented in the subproject are described in Sect. 2, while in Sect. 3 we introduce an example of analysis in MULTISAB platform from a user's perspective. Conclusion is given in Sect. 4.

## 2 The Processing Subproject Architecture

The *processing* subproject, located on the server side, is responsible for data analysis. Within it, key frameworks for processing and analysis of biomedical time series are implemented, namely: record input handling, preprocessing, signal visualization, general time series features extraction, specific (domain) time series features extraction, expert system recommendations, data mining, and reporting frameworks.

To reduce computation time needed to perform an analysis, multithreaded parallelization is implemented under the *analysis* package for feature extraction. We plan to add it also for data mining methods. The details about parallelization will be presented in another forthcoming paper. All the *processing* frameworks are written in Java 9 and run on a host computer. They are described in the following subsection.

## 2.1 Implemented Frameworks

Record input handling framework supports a majority of data formats used for biomedical time series storage: *.ann*, *.csv*, *.edf/edf+c* and *.txt* file formats. Additionally, metadata and signal parameter data are supported. Signal visualization is entirely done through the web browser. Signals are uploaded and, based on the selected record data, the image of a record or its segment is generated. The images are generated in the *processing* subproject and sent to the *backend* subproject in order to be delivered to the user on *frontend*.

In the preprocessing framework, functions for noise filtering and morphological mathematical operations (erosion, dilation, opening and closing) are implemented. Commonly used features in signal processing, with emphasis on biomedical applications, are extracted under the general time series features framework. In Table 1, a list of those features is given. EEG, ECG and HRV specific time series features extraction are implemented under *eegAnalysis*, *ecgAnalysis* and *hrvAnalysis* packages, respectively, and are also shown in Table 1.

Two phases of an expert system are implemented under the MULTISAB platform. The first phase is designed to recommend a list of specific features intended for feature extraction (some cardiac diagnoses are currently supported), based on medical knowledge (guidelines and other scientific sources) about a disease. A user can add or remove the features from the list, which enables flexibility in particular cases. The second phase consists of a set of rules for reaching a specific diagnosis, for example for acute heart ischemia, which is done after the features are extracted. For feature selection, we currently support ReliefF, Symmetrical Uncertainty (SU) and Chi Square Score (Chi2) [4]. Multi-layer Perceptron (MLP), RBF, NEAT and PNN neural

**Table 1** General time series features implemented in the framework

Domain	Features
Time	Auto correlation coefficient, Fano factor, mean, standard deviation, variance, minimum, maximum, PCA
Frequency	Fast Fourier transform PSD estimate, Burg autoregressive PSD estimate, Lomb-Scargle PSD estimate
Nonlinear	Correlation dimension, space fill index (SFI), central tendency measure (CTM), largest Lyapunov exponent, recurrence plot, nonlinear forecasting, DFA, Higuchi dimension, Hurst exponent, 1/f power law alpha exponent, corrected conditional Shannon entropy, alphabet entropy, approximal entropy (ApEn), one dimensional Carnap entropy, correlation entropy, Renyi entropy, fuzzy ApEn, Sample entropy, Shannon entropy, cross recurrence, mutual dimension, synchronization likelihood, Allan factor, Lempel-Ziv complexity
ECG specific	R wave amplitude, QRS complex duration, P wave amplitude, P wave absence, P wave duration, T wave amplitude, T wave duration, ST segment duration, ST segment slope, QT interval duration, PR interval duration, J point amplitude, R/S ratio, Q wave amplitude, R wave duration, S wave duration, atrial fibrillatory rate
EEG specific	Mean of first differences, mean of second differences, mean of first differences normalized, mean of second differences normalized, total PWR, delta band power, theta band power, alpha band power, beta band power, gamma band power, spectral entropy
HRV specific	AVNN, SDNN, RMSSD, pNNX, NNX, SDDSD, SDANN, HRV triangular index, TINN, total PWR, ULF, VLF, LF, HF, LF/HF ratio, spectral entropy, standard deviation ratio

networks classification methods are supported via Encog library [5], while SVM classification method is supported via LIBSVM library [6]. Class-Attribute Contingency Coefficient is used for discretization of numerical features. Additional methods are planned for implementation (e.g. random forest, RIPPER). For evaluation,  $k$ -fold cross-validation and train:test:validation dataset separation are supported.

### 3 Analysis Scenario

In this chapter, we will introduce the MULTISAB platform with one analysis scenario, from user's perspective. For the use case, we have selected cardiac rhythm classification based on MIT-BIH Arrhythmia Database records [7]. After starting a new analysis, the user can select a predefined scenario for cardiac rhythm classification (for more detail,

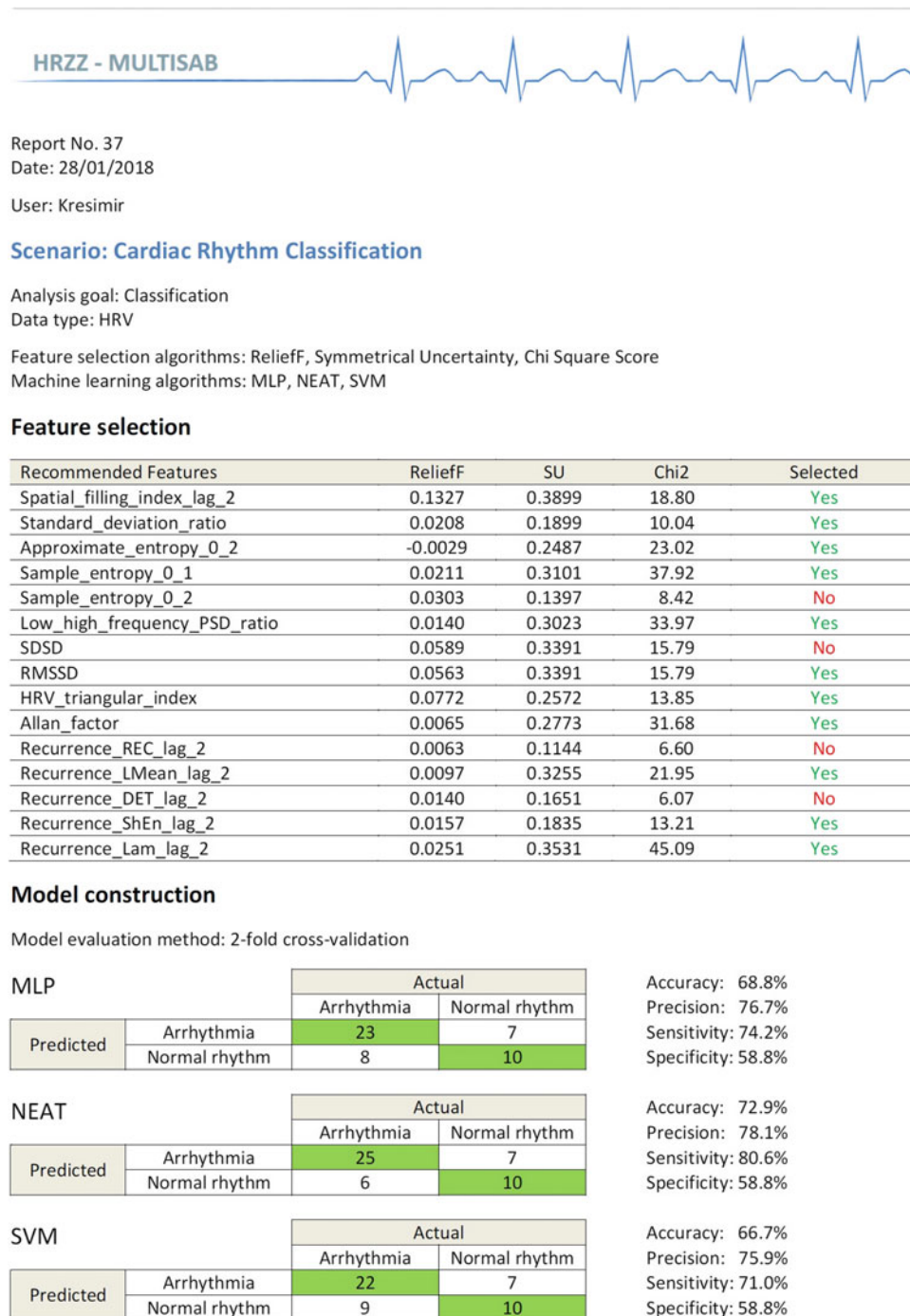


**Fig. 1** The report created for cardiac rhythm classification on MIT Arrhythmia Database



see [8]). This predefined scenario contains all the necessary preprocessing steps and recommended expert features that need to be extracted from the signals. The cardiac rhythm classification scenario is based on the authors previous research [9] and on consultations with cardiologists. The goal type of the analysis in this scenario is classification. The data type is HRV. To complete the specification of the scenario, the user has selected: 30 s segment length; ReliefF, SU and Chi2 feature selection algorithms; MLP, NEAT, and SVM classifiers. After the specification of the scenario, the user needs to upload the data for analysis.

In this use case, the 48 .ann records from MIT-Arrhythmia are uploaded into the platform. In the next step, the user can inspect and visualize the uploaded data. In the following preprocessing step, the user can select various procedures for signal filtering, characteristic waveform detection, and data transformations. In the case of HRV analysis for cardiac rhythm classification, the user needs to select the appropriate transform to obtain spectrum for frequency domain feature extraction. The expert system by default selects Lomb Scargle [10]. Feature extraction is the central step in the analysis of biomedical time series. In this use case, the user will already be provided with a set of recommended expert features. The list of expert features is not fixed, it depends on the chosen segment length and preprocessing procedures. Regardless of the scenario, the user can modify the list of features in the feature extraction phase. The user can also specify parameters for calculation of a particular feature.

In this use case, the user has selected one segment length of 30 s, starting at 0 s. This gives one sample (feature vector) per record. In the feature extraction analysis tab, the user defines classification label/disease for each segment or record. Although .ann files from MIT database have reference annotations, in this use case, the user has manually annotated each record with arrhythmia or normal rhythm. Alternatively, the user could select automatically the definition based on segment annotations, but here, that would result in detection of 12 disorders plus normal rhythm, with too few examples for each class for classifiers to learn from. After feature extraction, the user can download the extracted features in .arff or .csv file format and continue independent analysis locally. In feature selection step, the user can see the results for feature selection measures. Based on these results, the user can omit certain features from further analysis. To complete the analysis, the user has to, in model construction step, select the model evaluation method(s). At the end of the analysis, the user can see the generated report, based on JasperReports library [11]. In Fig. 1, we can see the report created for this scenario. At the beginning of the report, we can see the report number, analysis end date and the user who conducted the analysis. In the feature selection part, the list of all extracted feature is given, together with the information about feature selection measures. We also see

which features were used for model construction (green “Yes” in the “Selected” column). In model construction part, we see the results for arrhythmia classification for each machine learning method. In this scenario, model evaluation method was twofold cross-validation. The results are given in the form of confusion matrix and related accuracy, precision, sensitivity and specificity values. For the final version of MULTISAB platform, we plan to develop a more detailed report, which will contain the information about all the analysis steps.

---

## 4 Conclusion

In this work, we have provided a brief view into the currently developing MULTISAB platform, with the focus on data analysis (*processing*) part. The progress made will soon enable on-the-web analysis of multiple biomedical time series for interested medical and biomedical engineering professionals. For near future work, we plan to add more support for heterogeneous biomedical time series analysis and expand the selection of currently implemented data mining methods.

**Acknowledgements** This work has been fully supported by the Croatian Science Foundation under the project number UIP-2014-09-6889.

**Conflict of interest** The Authors declare that they have no conflict of interest.

---

## References

1. Robbins, K.A.: EEGVIS: A MATLAB Toolbox for Browsing, Exploring, and Viewing Large Datasets. *Front Neuroinform.* 6, 17 (2012).
2. Tarvainen, M.P., Niskanen, J.P., Lipponen, J.K., Ranta-aho, P.O., Karjalainen, P.A.: Kubios HRV – Heart rate variability analysis software. *Comput Methods Programs Biomed* 113(1), 210–220 (2014).
3. Friganovic, K., Jovic, A., Jozic, K., Kukolja, D., Cifrek, M.: MULTISAB project: a web platform based on specialized frameworks for heterogeneous biomedical time series analysis - an architectural overview. In: *Proc. Int. Conf. on Med & Biol Eng (CMBEBiH 2017)*, pp. 9–15. Springer Nature, Sarajevo, Bosnia and Herzegovina (2017).
4. Tang, J., Alelyani, S., Liu, H.: Feature Selection for Classification: A Review. In: Aggarwal, C. (ed.). *Data Classification: Algorithms and Applications*. CRC Press (2014).
5. Heaton, J.: Encog: Library of Interchangeable Machine Learning Models for Java and C#. *JMLR* 16, 1243–1247 (2015).
6. Chang, C.-C., Lin, C.-J.: LIBSVM: a library for support vector machines. *ACM TIST* 2(27), 1–27 (2011).
7. Moody, G.B., Mark, R.G.: The impact of the MIT-BIH Arrhythmia Database. *IEEE Engineering in Medicine and Biology Magazine* 20(3), 45–50 (2001).



8. Jovic, A., Kukulja, D., Friganovic, K., Jozic, K., Car, S.: Biomedical Time Series Preprocessing and Expert-System Based Feature Extraction in MULTISAB Platform. In: *Proc. Int. Conf. MIPRO 2017*, pp. 349–354. IEEE, Opatija, Croatia (2017).
9. Jovic, A., Jovic, F.: Classification of cardiac arrhythmias based on alphabet entropy of heart rate variability time series. *Biomedical Signal Processing and Control* 31(2017), 217–230 (2017).
10. Narin, A., Isler, Y., Ozer, M.: Investigating the Performance Improvement of HRV Indices in CHF using Feature Selection Methods based on Backward Elimination and Statistical Significance. *Computers in Biology and Medicine* 45, 72–79 (2014).
11. Tibco Software, Inc. 2018. JasperReports® Library, Open Source Java Reporting Library. <https://community.jaspersoft.com/project/jasperreports-library> (last accessed: 2018/01/21).

# Technologies Catalog to Support the Identification of User Behavior During Usability Tests

Thâmmara Lariane Henriques Tito, Andrei Guilherme Lopes, and Daniel Scherer

## Abstract

IEC ISO 60601-1-6:2015 is the regulatory standard for Medical Device (MD) and directs to ISO IEC 62366:2015 as a technical standard. However, due to the general nature of this standard, it does not provide details about criteria to guide usability testing of MD. In this way, the manufacturer deals with the unpredictability of the user according to the subjective convenience that he deems necessary to the type and class of the device. Objectives: To present a Catalog indicating technologies that can be used to detect the ergonomic or biomechanical behavior of the user. So that the test team has support for the follow-up of the experiment and for assistance in interpreting the test results. Method: A bibliographical review on technologies used to detect human behavior, and a technical survey of the market for products capable of capturing such behavior, were carried out in 2017 to establish and create the Catalog. Results: Findings allowed to list technologies that can be used to analyze the behavior of the user, assisting the execution of usability tests (UT) of the MD, being effective to detect the behavior and generate data to support the analysis and generation of reports. Conclusion: The Catalog classified technologies that can generate information about the usability of the MD, considering the analysis of the user's behavior. The Catalog contains the association between the technology and behavioral possibilities that can be identified, serving as support to choose the technology most appropriate to the UT.

## Keywords

User behavior • Usability test • Medical device

## 1 Introduction

The requirements for regulatory systems for medical device (MD) vary across the world; however, in accordance with the principles of good governance and good regulatory practice, regulatory authorities should consider national health plans, current legislation, resources available, manufacturing and import practices [21, 22]. Guidance for national regulatory authorities to adopt a uniform regulatory process is provided by the World Health Organization, which further provides indications of procedures and requirements for Health Technology Assessment for benefit analysis and efficacy, clinical and technical safety, and of the cost-effectiveness, in addition to directing the manufacturer requirements considered in the registration process [22].

The diversity of regulatory requirements across jurisdictions infers that manufacturers' efforts to meet MD registration requirements are complex and time-consuming. The manufacturer invests in additional drafts, mainly for the compilation of test documents, without harmonized requirements to assess the safety, efficacy or performance of MD [21].

In the case of medical equipment, which involves a real need for user testing, regulatory authorities require the registration of IEC 60601 to comply with safety and risk management requirements, including the standard collateral IEC 60601-1-6:2013 [7] to meet the usability criteria (influential on basic security requirements and essential performance), which mentions IEC 62366:2015—specific of usability engineering for devices [6]. Because they are generalist standards, IEC 60601-1-6 and IEC 62366 do not determine criteria for accepting or directing UT, leaving it to the responsible team to handle the user's unpredictability [6, 7].

The targeting for usability testing of MD cited by such standards is the performance of the test by specialists of the manufacturer company. If it guarantees the safety of the product from the documentation that certifies the risk management, safety and usability, or that meets the requirements

T. L. H. Tito (✉) · A. G. Lopes · D. Scherer  
Nucleus of Strategic Technologies in Health, State University  
of Paraíba, Campina Grande, PB 58429-500, Brazil  
e-mail: nutes@uepb.edu.br

of ISO 14971:2009 [6, 7, 9, 19] and UE 2017/745 [1]. It should be noted that usability test (UT) deal with the user's impassibility, and validated techniques are not yet known to predict the possibility of a person making a mistake during risk management [6, 19].

It should also be understood that inspecting the usability of a device through a UT differs from an analysis of user behavior (UB), which is broader and involves the interaction of the individual with the device (thoughts, feelings and perceptions during the interface), also non-verbal communication can transmit information that in an interview or questionnaire that would be omitted or forgotten [17].

Considering that IEC 62366:2015 has the user-centered Usability Engineering process and is driven by its needs, being the critical element of the system, research involving MD should direct the focus to the interface of the health professional operating device in a laboratory or field environment, thus involving intentional and unintentional actions and errors of use (slips and lapses); involve memory failures that do not necessarily manifest as actual behavior and may be evident only to the individual in the condition of life, and may be a shortcoming in the manufacture of MD [19].

The emphasis the test phase of usability of MD, focusing on the behavior of the user, in which the operator who deals with the unpredictability of the user during the interface may be based on patterns of behavior that technological resources capture, among facial and body expressions, being a way to support a UT process directed to the type of reaction that the usability of the product causes in the user.

For the adoption of standardized technical, it is considered that the general application of these standards will not be affected since, even if they are tests of different MD or the technology used to evaluate the user's behavior, the phenomenon evaluated and measured does not changes [17].

## 2 Method

The research was based on personal knowledge of the authors and of the international literature [5, 6, 11, 14, 17, 20] relative to the concepts of human behavior and technologies with potential uses in usability testing, as well as on studies available from past experiences published in the Science Direct and Google Scholar databases, using the descriptors: User, behavior, physical, interaction, facial, expression, emotions, capture.

A filter was adopted for articles published between 2015 and 2017 in newspapers dealing with human behavior, neuroscience and computer science, and selected journals with impact factor  $\geq 1,300$ , selecting those that used technologies to capture data on human behavior. The filtering resulted articles [2–5, 10, 12, 13, 15, 18, 23, 24] which show which technologies cited by authors in the international

literature have been used in the last 2 years and with which purpose of analyzing UB. And, the study cites the technologies currently available in the world market.

## 3 Study of Behavioral Categories

Based on previous study [16], this study have a focus on the detection of UB (stress, fatigue and attention/vigilance/interest). However, these are psychophysiological and can be associated in correlation when they present themselves in the behavior of the user [11, 20].

“Careful behavior” implies a degree of continuous attention with maintaining a focus over a relatively long period of time in critical environments, such as where health professionals work in emergency and emergency monitoring. At present, there is evidence of the influence of mental fatigue on physiological efficiency in vigilance, readiness, that is, the duration of the task is not always responsible for reducing the degree of attention, but the complexity of the task and the requirement of high and constant levels of cognition [11].

To understand the sensory evidence that reaches the central nervous system, the “noises” must be decoded to generate information that will guide a decision process, in this case a cognitive process. Likewise, technologies that capture such signals should consider noise identification and exclusion, so system calibration for reliable data to be usable, and recognize what each peak or frequency [11, 17, 20]. The real indication is that technologies that identify very specific behaviors are associated with others that may help to confirm information or identify what causes UB, and this will avoid false positive data analysis [6, 11, 14, 17].

Complex tasks that require a high degree of concentration have high levels of overall mental workload and may increase when the work strategy changes, such as simultaneous tasks for successive tasks, affecting the performance of the degree of attention. Similar effects are found in fatigue studies in which performance effects usually appear to be related to strategy rather than loss of resource availability—a metaphorical reservoir of energy or fuel for processing [11].

As described, complex tasks developed in critical health environments, possibly associated with physical stressors of the environment, may imply reduced performance required of health professionals who work for several hours at a time, with sleep deprivation and fatigue, which may influence various functions of information processing of alert operations, and consequently increase risks, errors and accidents [11, 17].

Fatigue refers to the feeling of tiredness related to prolonged activities, and an example of the potential complexity of fatigue states is evidenced by burnout syndrome, caused by fatigue and occupational stress, a common diagnosis in

the hospital emergency and emergency work environment. Tiredness can be accompanied by feelings of anger, anxiety and tension, and is an example of ergonomic behavior that can be detected by the technologies cited in this study, for laboratory or field usability testing [11].

But the stress has a strong connection with emotions and can be experienced in negative ways including acute stress, chronic, illness and absenteeism, or positively, benefiting the individual proactive in the work environment, relevant to a boom performance [11]. Extinctive behaviors, such as sleep and wakefulness, or subjective as emotion and alertness, or the pattern of waveform change evident in the electroencephalogram as the state of behavior changes and indicators of Sympathetic Nervous System (SNS) activity such as heart rate and conductance of the skin, are evidence of conditions in which stress can be measured [11, 17].

The sensitivity of the team of experts and the knowledge about metrics to transform the data provided by the technologies and correct and accurate information is necessary, as well as the study on the human behavior and the definitions of physiological and subjective components, thus being able to conclude an effective report [11, 14, 17].

#### 4 Technologies That Detect User Behavior

The technologies used for analysis of UB mentioned in this study, and exemplified in Table 1, are non-invasive procedures that can be used in UT, consisting of Stress, Fatigue and Attention inspections [11, 17].

The observation is clear in the scientific literature and research with tests that these technologies have more

**Table 1** Technologies used to analyze UB during interface design of products that use metrics for behavioral and physiological experiences

Technology	Description	Detection UB
Ocular screening—pupillary response [14, 17]	Measure types of emotions by the amount of mental concentration or emotional arousal—using a baseline to quantify changes in pupil diameter (contraction and relaxation of respective muscles) while capturing images	Stress; degree of attention
Ocular screening—infrared light source [10, 14, 17] or WebCam [12, 14, 17]	The ocular tracing can identify, through corneal reflex via infrared light source. The course and fixation time in the areas of interest with the measurement of pupil size as baseline. Can also be traced by eye movement located through WebCam	Degree of attention
Electrocardiogram [5]	Electrodes positioned near eyes, capture signals of electrical activity generated from the eye movement—muscle contractions	Stress; degree of attention
Sensor/device to identify electrodermal activity [4, 17, 18]	Sensor positioned in contact with the skin and the user wrist, which measures the electrical conductance of the skin. The data allow the measurement of the activity of the SNS, identifying activation or emotional excitation	Stress
Electromyography [3, 5]	Positioning of electrodes to detect electrical response of muscle activity, during a contraction movement. It detects positive or negative results	Physical fatigue
Electroencephalography [2, 5, 13, 15, 17]	Analyzes emotional engagement by a user's behavior by capturing brain wave data using evoked potential studies	Stress; degree of attention; mental fatigue
Electrocardiogram [2, 5, 13, 15, 17]	An examination that records the variation of electrical potentials that occur during myocardial activity. They indicate increase of the SNS, for example	Stress; physical fatigue
Heart rate monitor [17]	Measures changes in heart rate per minute, inferring experiences that may change user stress levels during the use	Stress
Sensor for identification of respiratory activity [4, 5, 18]	Identifies chest movement to capture respiratory rate data per minute. It can identify anxiety, tension, or intense physical activity, and it is appropriate to associate it with other technologies in cases of UT	Stress; physical fatigue
Sensor for recognition of pressure [17]	Sensors capture pressure intensity data that the user applies on something they hold while examining the design of a product, for example, or the intensity of pressure applied to a chair while sitting, allowing the analysis of adopted postures	Stress; degree of attention/interest
System of recognition of facial expressions [23, 24]	Software that can consider video transmission—via the user's computer—as input to predict the presence of facial expressions in approximate time	Stress
Thermographic camera	An apparatus that uses infrared thermography for real-time high resolution shooting (averaging 307,200 megapixels), detecting areas with higher thermal activity during video recording. Available from medium to high thermal sensitivity (>2 to >0.3 °C). They help detect the possibility of muscle fatigue during repetitive movements, for example, and for analysis there is usually a dedicated Software	Physical fatigue
Capture of movements [12, 13]	Sensitive points should be placed strategically on the user's body, sometimes there is a proper clothing, adapted to the sensor of the camera. The image is captured and the sensor captures data, sent to the software that will reproduce information about body movements, and musculature used	Physical fatigue; stress

reliability in a UT when associated and correlated their data [11, 17]. The highlight was observed in the recent study [5] that associated technologies for the analysis of physiological conditions and activities of the SNS, being identified as a gold standard.

Thus, the findings allowed to list technologies that can be used to analyze UB, assisting the execution of UT of the MD, being effective to detect the behavior and generate of the ones to support the analysis and generation of reports.

## 5 Conclusion

The Catalog classified technologies that can generate information about the usability of the MD, considering the analysis of the user's behavior. There is an association between the technology and the behavioral possibilities that can be identified, serving as support to the specialist team to choose the technology best suited to the specific UT that one wishes to perform.

The suggestion is that the Catalog of Technologies presented may support the support teams of manufacturers of MD and Compliance Assessment Laboratories accredited as Certification Body of Products that provide regulatory services and certification of these products.

## References

1. AGENCIA ESPAÑOLA DE MEDICAMENTOS Y PRODUCTOS SANITARIOS (AEMPS). Regulation (EU) 2017/745 of the European Parliament and of the Council of 5 April 2017 on medical devices, amending Directive 2001/83/EC, Regulation (EC) No 178/2002 and Regulation (EC) No 1223/2009 and repealing Council Directives 90/385/EEC and 93/42/EEC. Diario Oficial de la Unión Europea. L 117, de 5 de mayo de 2017.
2. ATKINSON, J.; CAMPOS, D. Improving BCI-based emotion recognition by combining EEG feature selection and kernel classifiers. *Expert Systems With Applications*. v. 47, pp. 35–41, 2016.
3. BHANDARI, U., et al. Effects of interface design factors on affective responses and quality evaluations in mobile applications. *Computers in Human Behavior*. v. 72, pp. 525–534, 2017.
4. CHEN, et al. Detecting driving stress in physiological signals based on multimodal feature analysis and kernel classifiers. *Expert Systems With Applications*. v. 85, pp. 279–291, 2017.
5. CIPRESSO, P. et al. Psychometric modeling of the pervasive use of Facebook through psychophysiological measures: Stress or optimal experience? *Computers in Human Behavior*. v. 49, pp. 576–587, 2015.
6. GOODMAN, E.; KUNIAVSKY, M.; MOED, A. Observing the user experience – A practitioner's guide to user research. Morgan Kaufmann Publishers. San Francisco, USA. p. 560, 2003.
7. INTERNATIONAL ORGANIZATION FOR STANDARDIZATION - International Electrotechnical Commission IEC 60601 Medical electrical equipment - Part 1-6: General requirements for basic safety and essential performance - Collateral standard: Usability. Geneva, p. 121, 2013.
8. INTERNATIONAL ORGANIZATION FOR STANDARDIZATION - International Electrotechnical Commission IEC 62366 Medical devices - Application of usability engineering to medical devices. Geneva, p. 114, 2015.
9. INTERNATIONAL ORGANIZATION FOR STANDARDIZATION ISO 14971 Medical devices - Application of risk management to medical devices. Geneva. p. 82, 2007.
10. KASPAR, K.; GAMEIRO, R. R.; KÖNIG, P. Feeling good, searching the bad: Positive priming increases attention and memory for negative stimuli on webpages. *Computers in Human Behavior*. v. 53, pp. 332–343, 2015.
11. MATTHEWS, G.; DAVIES, D. R.; WESTERMAN, S. J.; STAMMERS, R. B. *Human Performance – Cognition, stress and individual differences*. 1<sup>a</sup> ed. Psychology Press. USA. p. 398, 2000.
12. MCCALL, C. et al. Introducing the Wunderkammer as a tool for emotion research: Unconstrained gaze and movement patterns in three emotionally evocative virtual worlds. *Computers in Human Behavior*. v. 59, pp. 93–107, 2016.
13. MORGAN, E.; GUNES, H.; BRYAN-KINNS, N. Using affective and behavioural sensors to explore aspects of collaborative music making. *International Journal of Human – Computer Studies*. v. 82, pp. 31–47, 2015.
14. NIELSEN, J.; PERNICE, K. *Eyetracking Web Usability*. New Riders. California, USA. p. 437, 2009.
15. RODRÍGUEZ, A. et al. Assessing brain activations associated with emotional regulation during virtual reality mood induction procedures. *Expert Systems with Applications*. v. 42, pp. 1699–1709, 2015.
16. SCHERER, D.; NETTO, A. V. S.; VIEIRA, M. F. Q.; AGUIAR, Y. P. C. Programming a User Model with Data Gathered from a User Profile. *Cognitively Informed Intelligent Interfaces: Systems Design and Development*. Pennsylvania: IGI Global, pp. 235–257, 2012.
17. TULLIS, T.; ALBERT, B. *Measuring the User Experience – Collecting Analyzing, and Presenting Usability Metrics*. 2<sup>nd</sup> ed. Morgan Kaufmann Publishers. Waltham, USA. pp. 295, 2013.
18. VERPLAETSE, J.; SMET, D. D. Mental beliefs about blood, and not its smell, affect presence in a violent computer game. *Computers in Human Behavior*. v. 63, pp. 928–937, 2016.
19. VINCENT, C. J.; LI, Y.; BLANDFORD, A. Integration of human factors and ergonomics during medical device design and development: It's all about communication. *Applied Ergonomics*. v. 45, n. 3, pp. 413–419, 2014.
20. WEIGER, M. B.; WIKLUND, M. E.; GARDNER-BONNEAU, D. J. *Handbook of human factors in medical device design*. CRC Press. New York. p. 821, 2011.
21. WORLD HEALTH ORGANIZATION. Regulation of medical devices: a step-by-step guide. WHO Regional Office for the Eastern Mediterranean, Cairo, Egypt. p. 62, 2016.
22. WORLD HEALTH ORGANIZATION. WHO Global Model Regulatory Framework for Medical Devices including in vitro diagnostic medical devices - WHO Medical device technical series. WHO Document Production Services, Geneva, Switzerland. p. 74, 2017. Licence: CC BY-NC-SA 3.0 IGO.
23. ZHANG, et al. Adaptive facial point detection and emotion recognition for a humanoid robot. *Computer Vision and Image Understanding*. v. 140, pp. 93–114, 2015.
24. ZHANG, Y.; ZHANG, Z.; HOSSAIN, M. A. Adaptive 3D facial action intensity estimation and emotion recognition. *Expert Systems with Application*. v. 42, pp. 1446–1464, 2015.



# t-SNE Applied to Discriminate Healthy Individuals from Those with Parkinson's Disease Executing Motor Tasks Detected by Non-contact Capacitive Sensors

Fábio Henrique M. Oliveira<sup>✉</sup>, Thaila Ferreira Zaruz<sup>✉</sup>,  
 Marcus Fraga Vieira<sup>✉</sup>, and Adriano O. Andrade<sup>✉</sup>

## Abstract

The diagnosis and evaluation of Parkinson's disease (PD) is a task that has been performed through clinical evaluation and subjective scales. Over the years several studies have reported results and technologies with the purpose of making the follow-up of PD more objective. Usually, in the objective evaluation, inertial and electromyographic sensors are employed for recording movement and muscular activation. A major challenge that exists in the area is related to the monitoring of the technological horizon, to identify and incorporate new technologies and methods that can be used for the evaluation of PD. In this perspective, it was proposed in this research the use of non-contact capacitive sensors to record four motor activities of the hand and wrist (i.e., radial deviation, ulnar deviation, flexion and extension). Another identified challenge is related to the correct classification of individuals with PD. To accomplish this, it makes necessary the use of tools for signal processing and machine learning. In this study, features related to amplitude and time of the signal were estimated and then combined by means of t-Distributed Stochastic Neighbor Embedding (t-sne), which is an innovative tool for dimensionality reduction and visualization of information.

Experimental data were collected from a neurologically healthy individual and one with PD. The use of t-sne allowed for the visualization of data on a two-dimensional. The use of non-contact capacitive sensors introduces an innovative way to measure information from people with PD. Furthermore, the application of t-SNE showed to be a successful tool for the discrimination between a healthy individual from that with PD.

## Keywords

Parkinson's disease • Non-contact sensor • T-Distributed stochastic neighbor embedding

## 1 Introduction

Parkinson's disease (PD) is a neurodegenerative disease that leads to progressive loss of dopaminergic neurons from the substantia nigra. Dopamine deficiency produces a severe extrapyramidal system effect, resulting in decreased muscular strength. These pathophysiological changes generate typical neurological symptoms found in patients with PD such as bradykinesia, rest and postural tremor, postural instability, and muscular stiffness [2].

A research area that can contribute to individuals with PD is related to measurement technologies capable of generating quantitative information that can be used for the diagnosis and follow up of the disorder. Over the years distinct types of sensors have been employed for the assessment of the motor signs of PD, being the inertial sensor the most common type of technology employed in the field [4].

In this study, we present the use of a recent technology, based on non-contact capacitive sensors for the assessment of motor tasks executed by a healthy person and one suffering from PD. Amplitude and time-dependent features extracted from the collected signals are estimated and projected on a 2-dimensional lower space by using the t-distributed stochastic neighbor embedding (t-sne) [5]. The

F. H. M. Oliveira (✉) · T. F. Zaruz · A. O. Andrade  
 Centre for Innovation and Technology Assessment in Health,  
 Federal University of Uberlândia, Uberlândia, Brazil  
 e-mail: oliveirafhm@gmail.com

T. F. Zaruz  
 e-mail: tzaruz@gmail.com

A. O. Andrade  
 e-mail: adriano@ufu.br

F. H. M. Oliveira  
 Federal Institute of Science and Technology, Campus Brasília,  
 Brasília, Brazil

M. F. Vieira  
 Bioengineering and Biomechanics Laboratory, Federal University  
 of Goiás, Goiânia, Brazil  
 e-mail: marcus.fraga.vieira@gmail.com



found results suggest that the proposed measuring technology can be used as an alternative to those which employ contact sensors.

## 2 Methods

### 2.1 Experimental Setup

This is an ongoing research that has been approved by the National Committee for Ethics in Research (CAAE: 65165416.4.0000.5152). Two subjects, being one healthy and the other suffering from PD participated in this study.

The experiments were carried in an electrically and acoustically isolated cabin (Fig. 1). A three-axial gyroscope (L3GD20H, STMicroelectronics, Switzerland) was positioned on the dorsal region of the hand together with a laser pointer for aiding the subject to execute a set of motor tasks (Fig. 1). A pair of non-contact capacitive sensors (PS25454, Plessey semiconductors, UK) was attached to a custom-made structure (Fig. 1) that included a squared board used for guiding the participant.

The subjects were instructed to start the motor task with the visual laser point at the central region of the board (highlighted with a crossed circle). The white circles on the board were set as targets considering each type of experimental task (Fig. 1). For tasks T1 to T4 the subjects were asked to execute the hand movements 5 times in 10 s, whereas for tasks T5 to T8 they were asked to execute the same type of tasks 15 times in 10 s. For the execution of tasks T5 to T8 the hand was rotated and positioned at  $90^\circ$  to the horizontal line defined by the pair of capacitive sensors.

In terms of physiology, the chosen motor tasks are close related to motor tasks performed by patients during the evaluation using the Unified Parkinson's Disease Rating Scale (UPDRS) [3], which is a common instrument used by physiotherapists to assess the PD state. Also, the selected movements are suitable for the use of gyroscope, because they normally have enough amplitude, which facilitates the signal analysis.

Signals collected from the gyroscope were sampled at 50 Hz and from the capacitive sensors at 3 kHz; they were synchronized by an external trigger. Considering the directions of the executed movements, only the y and z coordinates of the gyroscope are considered.

### 2.2 Signal Preprocessing

The signal obtained from the gyroscope was pre-processed by using a moving average filter and a nonlinear detrending technique described in [1]. For the signals detected from the capacitive sensors the following sequence of steps were employed: (i) the signal lower envelope of the peaks of the 60 Hz component was estimated; (ii) the same sequence of steps applied for the gyroscope [1] was applied on the lower envelope.

### 2.3 Feature Extraction

Three features were estimated from the collected signals and used for data analysis and visualization. The first was the median between peak time intervals (mpi); the second was

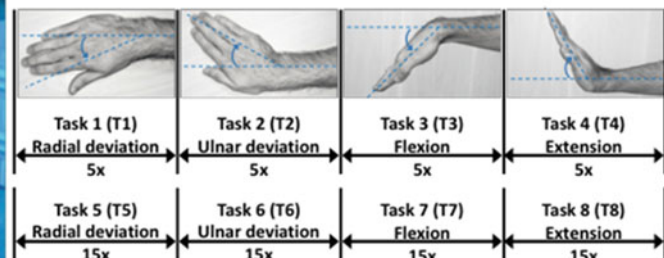
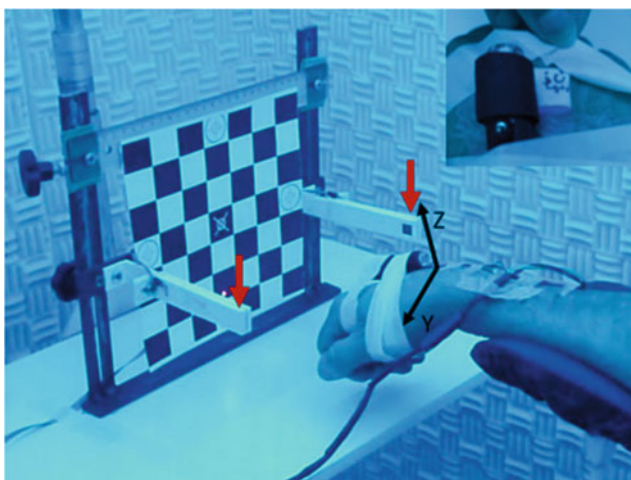


**Fig. 1** (left) Experimental setup. The 3-axial gyroscope is positioned on the dorsal part of the hand (the inset shows the sensor and laser pointer). The y and z axes are indicated. The forearm is on the support. The red arrows show the location of the pair of non-contact capacitive

sensors. The squared board is used for guiding the participant during the experiment. (right) Set of tasks executed. The number of repetitions for each task is shown

the time difference between the first and last peak (tfl); and the third was the median of the amplitude of the peaks. The peaks were identified by using predefined thresholds considering the peak amplitude and allowed time distance between peaks.

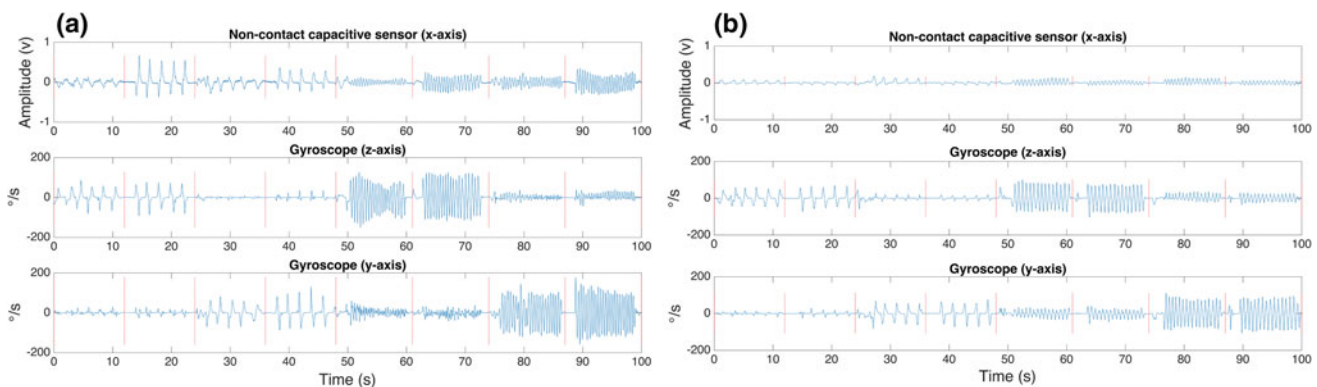
## 2.4 Data Visualization

The set of three-dimensional features were projected on a two-dimensional space for easing data visualization. The methods t-sne, Sammon's mapping and Principal Component Analysis (PCA) were employed for generating distinct visualizations of the data. Prior to data projection the data were standardized.

## 3 Results

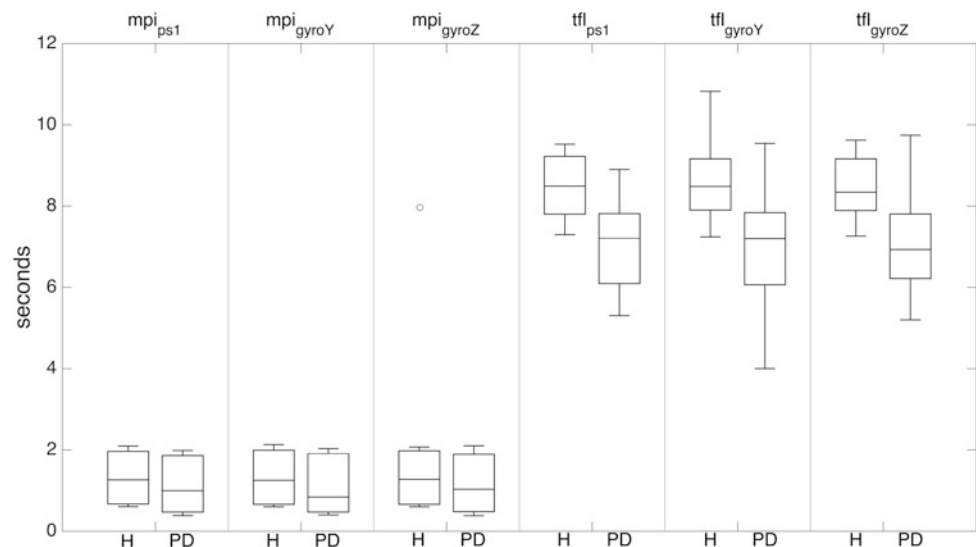
### 3.1 Typical Waveforms

Figure 2 depicts typical waveforms obtained for each subject executing the tasks shown in Fig. 1.



**Fig. 2** Typical signals collected for the healthy subject (a) and for the person with PD (b)

**Fig. 3** Boxplot of the set of the time-dependent features including all tasks. The identification of each feature is indicated at the top whereas the identification of the subject is at the bottom. The sensors are labeled as ps1 (capacitive sensor) and gyro (gyroscope) at the top. The label H represents data of the healthy person whereas PD for the person with Parkinson's disease



## 3.2 Feature Analysis

Figure 3 shows boxplots of the time-dependent features for each sensor and individual, considering all tasks. Figure 4 shows boxplots for the median time between peak intervals considering the dissociation of data obtained from tasks T1, T2, T3 and T4 from T5, T6, T7 and T8.

The mean of the peak amplitude for the healthy subject and the person with PD is presented in Table 1.

## 3.3 Data Visualization

All features were employed for dimensional reduction and data visualization. In Fig. 5 the estimated projections are provided considering PCA, Sammons' mapping and t-sne.

## 4 Discussion and Conclusion

In this study, it was presented a method for the evaluation of motor tasks of the hand based on the use of a non-contact capacitive sensor. The use of non-contact sensors can be

**Fig. 4** (left) Boxplot of the set of time-dependent features estimated from tasks executed five times in 10 s. (right) Boxplot of the set of time-dependent features estimated from tasks executed fifteen times in 10 s

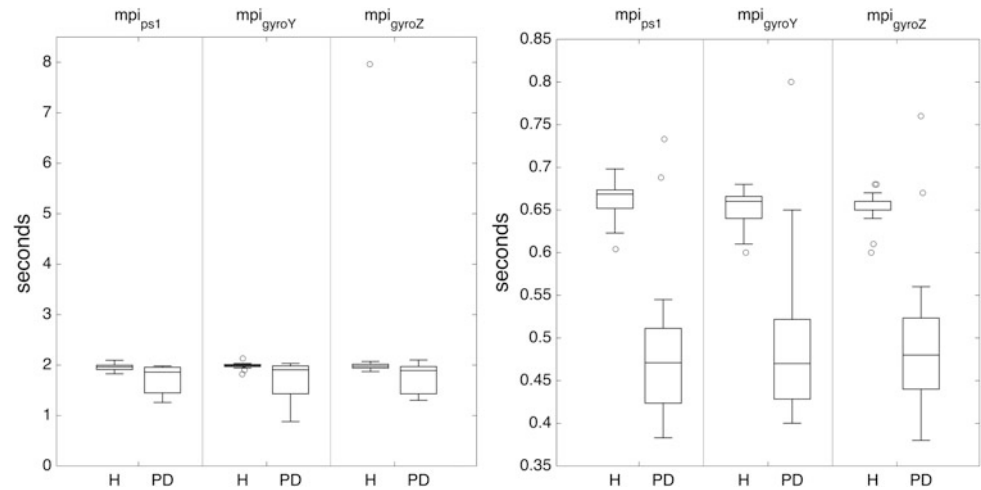


**Table 1** Mean and standard deviation for the amplitude of the peaks considering all tasks

Sensor	Mean $\pm$ Std (Healthy)	Mean $\pm$ Std (PD)
ps1	0.053 $\pm$ 0.025	0.245 $\pm$ 0.192
gyroY	36.272 $\pm$ 27.078	50.014 $\pm$ 35.005
gyroZ	35.430 $\pm$ 25.683	48.221 $\pm$ 28.656

beneficial for people who have sensitive skin such as the elderly, being this most people suffering from PD.

The lower amplitude of the time-dependent features found for the person with PD is justified by the fact that the person suffered from muscular rigidity (a typical symptom of PD), making it difficult for him to execute the tasks with the full amplitude of movement. As he could not execute the movements completely, considering the full range of extension and deviation of the hand, he typically finished the movements earlier than the healthy person.

The peak amplitude was larger for the person with PD. This could be detected by both types of sensors, and it can be

explained by the fact that the person with PD has difficulty in executing fine movements, thus after the movement starts it continues abruptly resulting in increment of the angular speed and large variation of the electric field in a short time window.

The evaluation of data projections showed that t-sne was capable of grouping features considering the similarity of tasks and the condition of the person. This could also be observed by PCA and Sammon's mapping. The actual advantages of t-sne should be assessed quantitatively and with additional data set.

The main limitation of this research is the number of subjects. However, based on the results of the pilot study presented here we are increasing it so that all the methods can be further evaluated.

**Acknowledgements** The present work has the support of Brazilian government (FAPDF, CNPq, CAPES, FAPEMIG- APQ-00942-17). A. O. Andrade is a Fellow of CNPq, Brazil (305223 /2014-3). The authors thank the volunteers who participated in the study and the researcher Luiza Maire for helping during data collection.

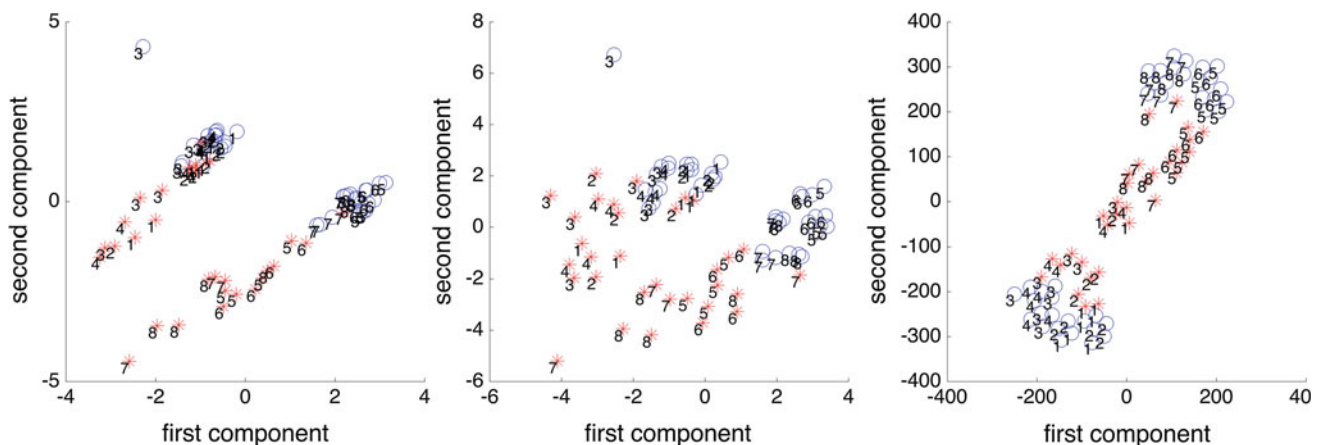


**Fig. 5** Two-dimensional projection by using PCA (left), Sammon's mapping (center) and t-sne (right). The blue circles indicate the healthy subject and the red asterisks indicate the PD subject. Labels from 1 to 8 represent the tasks

**Conflicts of Interest** The authors declare no conflict of interest.

---

## References

1. Andrade AO, Ferreira LCV, Rabelo AG, Vieira MF, Campos AR, Gonçalves BF, Pereira AA (2017) Pelvic movement variability of healthy and unilateral hip joint involvement individuals. *Biomed Signal Process Control* 32:10–19. <https://doi.org/10.1016/j.bspc.2016.10.008>
2. Dickson JM, Grünewald RA (2004) Somatic symptom progression in idiopathic Parkinson's disease. *Parkinsonism Relat Disord* 10:487–492. <https://doi.org/10.1016/j.parkreldis.2004.05.005>
3. Goetz CG, Tilley BC, Shaftman SR, Stebbins GT, Fahn S, Martinez-Martin P, Poewe W, Sampaio C, Stern MB, Dodel R, Dubois B, Holloway R, Jankovic J, Kulisevsky J, Lang AE, Lees A, Leurgans S, LeWitt PA, Nyenhuis D, Olanow CW, Rascol O, Schrag A, Teresi JA, van Hilten JJ, LaPelle N, Agarwal P, Athar S, Bordelan Y, Bronte-Stewart HM, Camicioli R, Chou K, Cole W, Dalvi A, Delgado H, Diamond A, Dick JP, Duda J, Elble RJ, Evans C, Evidente VG, Fernandez HH, Fox S, Friedman JH, Fross RD, Gallagher D, Goetz CG, Hall D, Hermanowicz N, Hinson V, Horn S, Hurtig H, Kang UJ, Kleiner-Fisman G, Klepitskaya O, Kompoliti K, Lai EC, Leehey ML, Leroi I, Lyons KE, McClain T, Metzger SW, Miyasaki J, Morgan JC, Nance M, Nemeth J, Pahwa R, Parashos SA, Schneider JSJS, Schrag A, Sethi K, Shulman LM, Siderowf A, Silverdale M, Simuni T, Stacy M, Stern MB, Stewart RM, Sullivan K, Swope DM, Wadia PM, Walker RRRW, Walker RRRW, Weiner WJ, Wiener J, Wilkinson J, Wojcieszek JM, Wolfrath S, Wooten F, Wu A, Zesiewicz TA, Zweig RM (2008) Movement Disorder Society-Sponsored Revision of the Unified Parkinson's Disease Rating Scale (MDS-UPDRS): Scale presentation and clinimetric testing results. *Mov Disord* 23:2129–2170. <https://doi.org/10.1002/mds.22340>
4. Lieber B, Taylor BES, Appelboom G, McKhann G, Connolly ES (2015) Motion Sensors to Assess and Monitor Medical and Surgical Management of Parkinson Disease. *World Neurosurg* 84:561–566. <https://doi.org/10.1016/j.wneu.2015.03.024>
5. Van Der Maaten L, Hinton G (2008) Visualizing Data using t-SNE. *J Mach Learn Res* 9:2579–2605

# Electronic Delivery Book: Structured Database Enables Analysis of Perinatal Risk Factors

Michal Huptych, Václav Chudáček, Ibrahim Abou Khashabh, Jiří Spilka, Miroslav Burša, Lukáš Hruban, and Petr Janků

## Abstract

The Electronic Delivery Book (EDB), an electronic information system, was developed in cooperation with obstetricians, midwives, and neonatologists from the University Hospital in Brno. The main aim was to create structured electronic documentation of selected delivery-related parameters based on the existing paper-based documentation. The system contains information from the different stages of delivery: parameters of the pregnancy, medications/interventions during the birth, outcome measures for the newborn(s), and primary attributes from neonatology. The EDB also allows creating overviews and basic statistics for everyday clinical needs and offers structured data for retrospective as well as prospective studies. One of the first results based on data collected using the EDB was the analysis aimed at identification of potential risk factors for low umbilical cord artery pH in term, singleton pregnancies. The data selected from EDB represents a basis for the retrospective case-control study. Cases were deliveries characterized by umbilical cord artery pH  $\leq 7.05$ , controls were with no sign of hypoxia. In the database of 10637 deliveries, collected between 2014 and 2015 at the University Hospital in Brno, we identified 99 cases. Univariate analysis of clinical features was performed. The following risk factors were associated with low pH: the length of the first stage (odds ratio (OR) 1.40; 95% CI 1.04–1.89) and the length of the second stage of labor (OR 2.86; 1.70–4.81), primipara

(OR 2.99; 1.90–4.71) and meconium stained fluid (OR 1.60; 1.07–2.38).

## Keywords

Obstetrics • Electronic medical documentation  
Medical data analysis • Statistical analysis

## 1 Introduction

One of the most important focuses in the obstetrics field is on early detection of fetal hypoxia during delivery. An evaluation of cardiotocogram (CTG) is a common way how to reveal possible presence of fetal hypoxia during delivery. However, obstetricians evaluate the CTG in relation to all information about a state of a mother and all antepartum information about a fetus. If there are some critical factors linked with hypoxia present, the evaluation of the CTG can be substantially different. For purpose of this study, we assume a relation of fetus hypoxia and low pH outcomes in the newborn cord artery blood. Thus, the goal of this study is to find clinical factors which are associated with low pH of newborn cord artery blood. And, we use the fact that we developed our system for collection of the clinical information around a delivery that is used in the University Hospital in Brno already last 4 years (more in Chap. 2).

There are many articles aimed at an identification of clinical factors which increased the risk for mother and child during delivery. Several studies (e.g. [1–3]) dealt with the relation of clinical factors and Caesarean section. The work [1] tested the association between maternal age and Caesarean section, in [2] is published a study (on over 12,000 deliveries) of various risk factors and Caesarean section and [3] investigated clinical factors leading to Caesarean section in multiparous women. The Caesarean section can be among other indications related to the hypoxia but it does not appropriate to use it instead of the pH. In other words, the aim of our study is different.

M. Huptych (✉) · V. Chudáček · J. Spilka · M. Burša  
Czech Institute of Informatics, Robotics, and Cybernetics,  
Czech Technical University in Prague, Prague, Czech Republic  
e-mail: Michal.Huptych@cvut.cz

I. A. Khashabh  
Department of Cybernetics, FEE Czech Technical University  
in Prague, Prague, Czech Republic

L. Hruban · P. Janků  
Obstetrics and Gynaecology Clinic, The University Hospital Brno,  
Brno, Czech Republic



Risk factors influencing birth outcomes are also investigated e.g. in the studies [4, 5] that are aimed to pre-term delivery risk factors for various degrees of prematurity, and on an assessment of factors contributing to a prolonged labor. The most relevant works are articles [6–9] (characterized by the phrase “risk factors for birth asphyxia”). All these studies take the asphyxia in relation to the Apgar score, which is a subjective observation and it cannot be considered as reliable indicator of asphyxia [10]. Retrospective study [6] presents finding that primiparous women and those with pre-eclampsia had a significantly ( $p < 0.01$ ) greater risk of a low Apgar score. The study [7] was focused as for antepartum risk factors as well as intrapartum risk factors. The found antepartum risk are place of the antenatal visit, malaria during pregnancy, and preeclampsia. Intrapartum risks included prolonged labor, stationary labor, and term prolonged rupture of membranes. Same as the previous study, the study [8] is aimed at antenatal and intrapartum risks and indicated anemia, pre-eclampsia, meconium stained fluid and low birth weight among the most significant risks with respect to outcome assessed by the Apgar score. In the work [9], meconium was highlighted together with several CTG-related parameters as the factors increasing the risk of asphyxia (again assessed based on Apgar score) the most.

## 2 Electronic Delivery Book

The Electronic Delivery Book (EDB) is an electronic form of the medical documentation for collection of a clinical information about/from admission at the obstetrician ward, delivery period, newborn(s), and neonatology. The reason for collection of a clinical information in the electronic form stemmed from our work on a computer analysis of the cardiotocogram (CTG), together with obstetrics department of the University Hospital in Brno, e.g. [11, 12], where the clinical information seemed to be potentially useful. Lots of information is stored in the hospital information system. Unfortunately, the clinical information from the hospital information system is not (in our case) reliably available in a format usable for further computerized processing. Moreover, many clinical data regarding a delivery were also collected in a paper-based documentation which was already existing at the obstetrics department before onset of our project. The forms of this paper-based documentation were pre-printed and this fact led to many flexible changes to adapt documentation as was necessary for a given situation and requests. For simple instance, if there was necessary to collect information about the presence of a father during a labor, there was necessary to write this information somewhere to some prepared column (e.g. information about mother surname) and mark this information separately beside the proper information of the column. Even more,

these ad-hoc adjustments were not placed always in the same columns and marked by the same way. This complication led us to the result that it is not possible to use some methods of the Optical Character Recognition (OCR) for an acquisition of the information. Therefore, the paper-based documentation became a pattern for the EDB design.

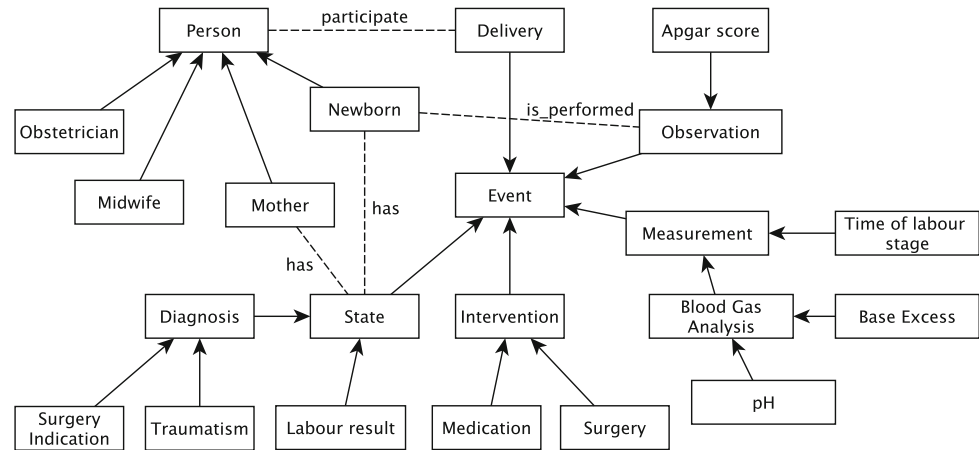
We started to develop a standalone application, which had clearly defined several features. The first step was to create structured electronic documentation [13]. The structure of the record is characterized by a model of the domain, by a model of the database as well as by an environment for the entry of values. The domain model represents a list of concepts and their relationships. It is not on so strong formal level that we can call it an ontology, but it is a lower form of the conceptualization [14]. The reason that we did not define the domain model on high formal (ontology) level was the time-consuming process of such formal conceptualization and a need of the real usable prototype of the application in relatively short time. The basic part of the domain model is depicted on Fig. 1.

The domain model in Fig. 1 contains only crucial classes, for example, the pH is further divided to arterial and venous pH, Apgar score is determined in the 1st, 5th and the 10 min after birth, and so on. Also, there are not presented all relationships between classes in Fig. 1, but just basic taxonomy and a few examples of others relationships. In total, there are 67 parameters gathered within the EDB. Based on the domain model, we derived database schema which was used as the basis of the application. Within the database schema was defined all used attributes of the domain. The database model was several-times changed and adjusted since the first design, however, the basic idea is still same. Here it is worth mentioning that it was crucial to keep many attributes from the paper-based documentation (including those added during the course of time), which strongly defined the elementary form of the electronic version of the documentation. The database schema is too large for publication in this paper and its informative contribution is not so crucial in this case. For implementation, we used the MS SQL database, which was provided by the hospital.

The EDB is implemented in programming language Java. This selection was reasoned by request of a implementation without installation and with a possibility to delivery updates of the application during everyday work. This request is fulfilled by Java itself and by Java Web Start service. The reason why we did not develop web application was a complications with providing of application/web server within the hospital in the started years. The application has many restrictions for filled values like format definitions (number, string, date), variables range definition (e.g. Apgar score is defined between values 1 and 10) and strictly range of values definition (vocabularies and classifications like [15] and/or proprietary code-books are used for e.g. diagnoses,



**Fig. 1** The main part of the domain model for the Electronic Delivery Book



interventions, medications, etc.). These restrictions are defined in order to keep the record in clear form for the next potential export and further processing of the data as well as for the potential communication and data exchange. The export of records for further processing is anonymized. The EDB allows also to define study and its branches and to assign particular newborns to the selected study branch. This feature can be useful especially in a prospective study.

In the EDB, the basic two features for an everyday clinical data use are possibilities to filter relevant records based on conditions combination (selectable from all collected parameters) and creation of overviews and basic statistics for particular months in given year as well as for comparison of particular months in different years. The EDB contents over 24,000 deliveries from years 2014 up to 2017 and the data collection still continues. The collection and use of the data was approved by the ethics committee at the University Hospital in Brno.

### 3 Critical Factor Analysis

#### 3.1 Data and Features

Electronic Delivery Book provided the data for retrospective study in this case. We used collected data at the delivery ward of the University Hospital in Brno from January 2014 to December 2015. All data are fully anonymized. We extracted from the records 107 clinical parameters describing the state of a mother, process of a delivery, and state of a newborn, respectively. The database consists of 12274 recordings between years 2014 and 2015. Since we would like to ensure the most possible clearest interpretation, we have applied the following homogenizing conditions for the final dataset: arterial pH is available; gestational age  $\leq 37$  weeks; singleton pregnancy; no known congenital diseases. By this way, we obtained final 10637 deliveries for our study.

How is mentioned above, we extracted 107 clinical features which can be divided into following three categories according to a moment of the care when the features are determined: (a) before delivery (e.g. gravidity, parity, sex of the fetus, induction of labor, diagnoses related to mother and pregnancy) (b) during delivery (e.g. diagnoses related to delivery, interventions, length of delivery stages, medications) (c) after delivery (e.g. the weight of a newborn, Apgar score, admittance to the NICU, seizures or intubation).

#### 3.2 Statistic Evaluation

The odds ratios (OR), their 95% confidence intervals (CI), and two-sided p-values were used for evaluation of a relation between each feature and the pH outcome. All three statistics indicators (OR, 95 The odds ratio (OR) represents an association between an observed factor and an outcome. In other words, OR expresses how strong impact has the presence of the factor on chances of getting the disease [16]. Thus, the OR is very useful in case-control studies as well as cross-sectional and cohort studies [17]. The comparison of a use of the OR and/or relative risk (RR) estimation can be found in [18] as well as more additional information about OR. In our case, the difference between OR and RR is negligible, because the event rate of pathological cases is very low, so  $OR \simeq RR$  [16]. All computations were done in Matlab 2015a.

#### 3.3 Results

Results of the analysis are depicted in Table 1. The umbilical artery pH with cutoff in 7.05 defines two groups (cases and controls) of newborns. The pH cutoff point in 7.05 is a common set-up value in the studies using pH, e.g. [19, 20].

**Table 1** A collection of the most interesting results from a univariate analysis of the features. pH, Apgar and SC are outcome measures, while all the other features represent knowledge or an action known prior to delivery. Entonox and epidural analgesia are medications given during the labor

	Cases—pH $\leq 7.05$		Controls—pH $>7.05$		OR (95% CI)	p-value
	#	Mean (std)	#	Mean (std)		
pH	99	6.99 (0.09)	10523	7.29 (0.08)	–	–
Apgar score 5 min	203	6.50 (0.88)	10400	9.65 (0.59)	24.68 (15.49–39.31)	<0.001
Sectio Caesarea	2110	1.00 (–)	8285	0.00 (–)	1.58 (1.02–2.45)	<0.001
Induced delivery	2198	1.00 (–)	8424	0.00 (–)	1.44 (0.92–2.25)	<0.001
Entonox	144	1.00 (–)	10478	0.00 (–)	2.30 (0.72–7.35)	<0.001
Epidural analgesia	1915	1.00 (–)	8707	0.00 (–)	1.01 (0.60–1.69)	1.000
Ist stage (>360 min)	1807	440.15 (64.77)	8015	226.22 (73.79)	1.36 (0.84–2.20)	<0.001
IIInd stage (>30 min)	884	54.12 (20.60)	7862	11.04 (7.18)	2.86 (1.70–4.81)	<0.001
Parity (<2)	5299	1.00 (0.00)	5302	2.34 (0.78)	2.99 (1.90–4.71)	<0.001
Sex (Male)	5468	1.00 (–)	5143	2.00 (–)	0.69 (0.46–1.03)	0.001
O100—hypertension	533	–	10089	–	1.45 (0.67–3.13)	<0.001
O140—preeclampsia	114	–	10508	–	1.92 (0.47–7.87)	0.008
O365—IUGR	375	–	10247	–	1.78 (0.77–4.08)	<0.001
O681—meconium	784	–	9838	–	2.09 (1.18–3.69)	<0.001
D650—defibrination syndrome	258	–	10364	–	2.63 (1.14–6.06)	<0.001
D695—secondary thrombocytopenia	36	–	10586	–	6.36 (1.51–26.85)	<0.001

## 4 Conclusion

In this paper, we presented the analysis of clinical data as factors in relation to low pH value as well as the information system which was used for collection of this clinical data and thus made this analysis enable.

The Electronic Delivery Book (EDB) is electronic information system designed for the collection of the clinical information from admission to the obstetrics ward, through delivery and newborn, up to the selected neonatology information. The EDB collects important information in the structured form, which is ensured by the clear definition of the domain model and propagation of this model down to the database schema and application itself. Then, the filled database provides a quality basis for the data analysis. The ultimate goal in utilizing data available from the EDB database is to provide the clinical data analysis together with CTG/FHR analysis in order to prepare comprehensive decision support during delivery. The presented study is just an initial investigation with the use of the EDB database. According to the literature review, there are no studies associating the clinical factors known before and during delivery with the outcome represented by pH value. There are studies, e.g. [21], suggest the relation between low pH and an adverse outcome is only weak. On the other side, there are other studies, e.g. [22], showing the significantly

increased risk of neurological impairment associated with pH  $\leq 7.1$ . Thus, irrespective of the controversy of the pH as a proof of the hypoxia during labor, the contribution of the effort to avoid a low pH value is indisputable.

From the perspective of our analysis, there was identified several risk factors related to low umbilical cord artery pH like parity, sex of the fetus, induced labour, and also those related to specific diagnosis in association with the delivery, e.g. meconium staining (O681) and defibrination syndrome (D650). However, some uncertainties on the side of the interpretation of the results would have to be clarified before we move on to the multivariate analysis.

The size of the database is very promising, but the size of several subsets representing individual features is limited. Especially for diagnostic factors can be ICD-10 coding to the lowest level too detailed and thus many subsets contain only tens of cases. It is insufficient to allow conclusions to be drawn with high confidence.

Although all features, except the epidural analgesia, have significant ( $p < 0.01$ ) result, it is necessary to interpret very carefully the clinical relevance of all factors, which odds ratios point to the hypoxia risk ( $OR > 1$ ).

**Acknowledgements** This work was supported by Czech Science Foundation Agency project 14-28462P Statistical methods of intrapartum CTG signal processing in the context of clinical information. In addition, we would like to express our thanks to the team at the University Hospital in Brno, in particular to Dr. Janků and Dr. Hruban.

**Conflict of Interest** The authors declare that they have no conflict of interest.

**Statement of Informed Consent**

The collection and use of the data and patient informed consent have been approved by the ethics committee at the University Hospital in Brno.

## References

1. Ilana F Gareen, Hal Morgenstern, Sander Greenland, and Deirdre Spelliscy Gifford. Explaining the association of maternal age with cesarean delivery for nulliparous and parous women. *Journal of clinical epidemiology*, 56(11):1100–1110, 2003.
2. Roshni R Patel, Tim J Peters, Deirdre J Murphy, ALSPAC Study Team, et al. Prenatal risk factors for caesarean section. analyses of the alspac cohort of 12 944 women in england. *International journal of epidemiology*, 34(2):353–367, 2005.
3. Corine J Verhoeven, Cedric T van Uytrecht, Martina M Porath, and Ben Willem J Mol. Risk factors for cesarean delivery following labor induction in multiparous women. *Journal of pregnancy*, 2013, 2013.
4. Joachim A Martius, Thomas Steck, Martin K Oehler, and Karl-H Wulf. Risk factors associated with preterm (<37+0 weeks) and early preterm birth (<32+0 weeks): univariate and multivariate analysis of 106 345 singleton births from the 1994 statewide perinatal survey of bavaria. *European Journal of Obstetrics & Gynecology and Reproductive Biology*, 80(2):183–189, 1998.
5. Sara E Szal, Mary S Croughan-Minihane, and Sarah J Kilpatrick. Effect of magnesium prophylaxis and preeclampsia on the duration of labor. *American journal of obstetrics and gynecology*, 180(6):1475–1479, 1999.
6. Hafiz Muhammad Aslam, Shafaq Saleem, Rafia Afzal, Umair Iqbal, Sehrish Muhammad Saleem, Muhammad Waqas Abid Shaikh, and Nazish Shahid. Risk factors of birth asphyxia. *Italian journal of pediatrics*, 40(1):1–9, 2014.
7. Andreas Chiabi, Seraphin Nguetack, Mah Evelyne, Sostenne Nodem, Lawrence Mbuagbaw, Elie Mbonda, Pierre-Fernand Tchokoteu, and Doh Anderson. Risk factors for birth asphyxia in an urban health facility in cameroon. *Iranian Journal of Child Neurology*, 7(3):46–54, 2013.
8. D Kaye. Antenatal and intrapartum risk factors for birth asphyxia among emergency obstetric referrals in mulago hospital, kampala, uganda. *East African medical journal*, 80(3):140–143, 2004.
9. Lars Ladfors, Klara Thiringer, Aimon Niklasson, Anders Odeback, and Eva Thornberg. Influence of maternal, obstetric and fetal risk factors on the prevalence of birth asphyxia at term in a swedish urban population. *Acta obstetrica et gynecologica Scandinavica*, 81(10):909–917, 2002.
10. Steven R Leuthner et al. Low apgar scores and the definition of birth asphyxia. *Pediatric clinics of north america*, 51(3):737–745, 2004.
11. V. Chudáček, J. Spilka, M. Huptych, G. Georgoulas, L. Lhotská, M. Stylios, C. Koucký, and P. Janků. Linear and non-linear features for intrapartum cardiotocography evaluation. In *Computers in Cardiology*, volume 35, 2010.
12. V. Chudáček, J. Spilka, Miroslav Burša, P. Janků, L. Hruban, M. Huptych, and L. Lhotská. Open access intrapartum ctg database. *BMC Pregnancy Childbirth*, 14(1):16, 2014.
13. K. Häyrinen, K. Saranto, P. Nykänen. Definition, structure, content, use and impacts of electronic health records: A review of the research literature *International Journal of Medical Informatics*, Volume 77, Issue 5, May 2008, Pages 291–304.
14. Uschold M., Gruninger M. Ontologies: principles, methods, and applications. *Knowledge Engineering Review*, 11 (2), 1996, pp. 93–155.
15. The Data Standard (DASTA) of Ministry of Health of the Czech Republic Available: <http://ciselniky.dasta.mzcr.cz>. [Accessed 31. 1. 2018].
16. Carsten Oliver Schmidt and Thomas Kohlmann. When to use the odds ratio or the relative risk? *International journal of public health*, 53(3):165–167, 2008.
17. Magdalena Szumilas. Explaining odds ratios. *J Can Acad Child Adolesc Psychiatry*, 19:227, 2010.
18. J Martin Bland and Douglas G Altman. The odds ratio. *Bmj*, 320(7247):1468, 2000.
19. M. Doret, J. Spilka, V. Chudáček, P. Gonçalves, and P. Abry. Fractal Analysis and Hurst Parameter for intrapartum fetal heart rate variability analysis: A versatile alternative to Frequency bands and LF/HF ratio. *PLoS ONE*, 10(8), Aug 2015.
20. P. Karvelis, J. Spilka, G. Georgoulas, V. Chudáček, C. D. Stylios, and L. Lhotská. Combining latent class analysis labeling with multiclass approach for fetal heart rate categorization. *Physiol Meas*, 36(5):1001–1024, May 2015.
21. C. Dani, C. Bresci, E. Berti, S. Lori, Maria Di Tommaso, and S. Pratesi. Short term outcome of term newborns with unexpected umbilical cord arterial ph between 7.000 and 7.100. *Early Hum Dev*, 89(12):1037–1040, Dec 2013.
22. P. Yeh, K. Emary, and L. Impey. The relationship between umbilical cord arterial ph and serious adverse neonatal outcome: analysis of 51,519 consecutive validated samples. *BJOG*, 119(7):824–831, Jun 2012.

# Wearable Cardiorespiratory Monitoring System for Unobtrusive Free-Living Energy Expenditure Tracking

Ke Lu<sup>1</sup>, Liyun Yang<sup>1</sup>, Farhad Abtahi<sup>2</sup>, Kaj Lindecrantz<sup>3</sup>, Kristian Rödbby, and Fernando Seoane<sup>4</sup>

## Abstract

In this work, we want to introduce combined heart rate and respiration monitoring for more accurate energy expenditure tracking on free-living subjects. We have developed a wearable cardiorespiratory monitoring system with unobtrusive heart rate measurement and ventilation estimation function for this purpose. The system is based on a garment with integrated textile electrodes for one-lead electrocardiogram and impedance pneumography measurements. A pilot experiment has been performed to prove the concept and to evaluate the characteristics of heart rate and ventilation estimated by our system in relation to energy expenditure. In the experiment, ventilation shows a better linearity in relation to the energy expenditure at the low intensity region than heart rate. Based on these characteristics, a model combining heart rate and ventilation for energy expenditure estimation is proposed which shows a significantly lower estimation error than the heart rate only model.

## Keywords

Wearable devices • Energy expenditure • Impedance pneumography

K. Lu (✉) · L. Yang · K. Lindecrantz  
School of Engineering Sciences in Chemistry, Biotechnology and Health, KTH Royal Institute of Technology, Hälsovägen 11C, 141 57 Huddinge, Sweden  
e-mail: kelu@kth.se

F. Abtahi  
Institute of Environmental Medicine, Karolinska Institutet, Solnavägen 1, 171 77 Solna, Sweden

K. Lindecrantz · F. Seoane  
Department of Clinical Science, Intervention and Technology, Karolinska Institutet, Hälsovägen 7, 141 57 Huddinge, Sweden

K. Lindecrantz · K. Rödbby · F. Seoane  
Swedish School of Textiles, University of Borås, Allégatan 1, 501 90 Borås, Sweden

F. Seoane  
Department of Biomedical Engineering, Karolinska University Hospital, 1, 171 76 Solna, Sweden

## 1 Introduction

The real-time energy expenditure (EE) tracking provides valuable information of the metabolic state and physical activity level. This information will help people in the management of their daily life and exercise, and even in prevention and treatment of many life-style-related health problem such as obesity and diabetes [1].

Heart rate (HR) monitoring is often used to estimate the free-living EE [2]. However, the relationship between HR and EE is poor in low intensity activities and sedentary condition [3], and it can be influenced by several other factors that are not related to physical activity, such as food intake or mental stress [4]. Another potential approach is to use respiration variables [5, 6]. Several studies have demonstrated that EE can be estimated using pulmonary ventilation ( $V_E$ ) only or together with other variables and that  $V_E$  shows higher linearity with EE compared to the HR [7]. Accurate measurement of  $V_E$  requires devices with facemasks or mouthpieces which limits its use in free-living conditions. Recent developments in wearable technologies, such as impedance pneumography (IP) integrated in smart clothing [8, 9], give new opportunities to use respiration measurements for EE estimation in a free-living setting. However, those wearable solutions also have their limitations. For example, the IP is sensitive to the subject's posture, change in breathing mechanics, and movements that lead to the change of ribcage shape and skin-electrode impedance [10, 11].

Hence, combining the information from HR and respiration can be a good approach to improve the accuracy of EE tracking for the free-living subjects. For this purpose, we have developed a wearable cardiorespiratory monitoring system with functionality of unobtrusive HR measurement and  $V_E$  estimation. The system is based on a garment with integrated textile electrodes for electrocardiography (ECG) and impedance pneumography measurements. To prove the concept and to explore the characteristics of HR

and  $V_E$  estimated by our system in relation to EE, a pilot experiment has been executed. Based on the experiment, a potential model to combine HR and  $V_E$  for EE estimation was created.

## 2 System Architecture

The system consists of a vest integrated with removable textile electrodes and conductive textile wiring, a wireless compact ECG and IP measurement device, and software on Android and PC for data logging, pre-processing and visualization.

**The Garment and Textile Electrodes.** The vest was manufactured in the Swedish School of Textiles at the University of Borås. Figure 1a shows the overall design of the vest. One pair of textile electrode pads are placed on the left and right axillary midline to achieve good linearity between change of volume and the change of impedance [12, 13]. Each electrode pad has two electrodes, where the outer one is for impedance current injection and the inner one for potential measuring for both impedance and ECG (Fig. 1b). The textile electrode pads are knitted using conductive fabric Shieldex® P130+B (STATEX GmbH., Bremen, Germany) with terry towel structure. The electrode pads are attached to the vest with snap bottoms. Intarsia knitting with conductive yarn, which has been introduced in our previous study [14], is used to integrate conductive segments on the vest to make connection between electrodes and the measurement device. The vest is knitted with two levels of elasticity where extra tightness is introduced at the chest region to ensure good skin-electrode contact during activities without compromising the comfort.

**Measurement Device.** A compact wireless recorder (Fig. 1c), ECGZ2 (Z-Health Technologies AB, Borås, Sweden) [15], is connected to the vest through snap buttons to record the ECG and IP signals. The unit features a one-lead ECG and impedance pneumography with 50 kHz injection current. The sampling rate of the ECG and IP are 250 Hz and 100 Hz respectively. Data is transmitted to PC or Android device through Bluetooth.

**Signal Processing.** HR is extracted from the ECG signal using a modified online R-peak detector and abnormal beats were removed. The raw IP signal is first down sampled to 20 Hz and then reconstructed by the first 5 levels of its wavelet (db5) decompositions with a threshold of 5  $\Omega$ . Peaks and valleys are then detected, hence the relative measure of the tidal volumes ( $V_{T-rel}$ ) are acquired by having the differences between each pair of peaks and valleys. The relative measure of the  $V_E$  ( $V_{E-rel}$ ) in a certain window is calculated by summing of  $V_{T-rel}$  in that window.

## 3 Experiment

The experiment covered a variety of living, sporting and working scenarios with different postures, activity intensities, and muscle groups to simulate complex free-living environments. An indirect calorimeter (Jaeger Oxycon Pro, Germany) was used simultaneously with the wearable system during the experiment as the reference measurement of EE. The real-time oxygen uptake was used since the dynamics of EE, instead of the steady state, was of interest in this study.

**Fig. 1** a The outside (left) and inside (right) of the vest. b The textile electrode pad. c ECGZ2, a compact ECG and electrical bioimpedance measurement device





Ethical approval for the study was obtained from the Regional Ethics Committee in Stockholm (Dnr 2016/724-31/5).

**Experiment Protocol.** The experiment protocol consisted of three categories of activities: resting, simulated working tasks, and submaximal tests. After each task, the subject had a rest for 5–25 min until the HR returned to within 10% of the resting HR. The timeline of the detailed tasks and their corresponding physical activity levels are shown in Fig. 2. The participant was asked to avoid intense physical activity for 1 day before the experiment and eating, smoking, drinking tea, coffee or alcohol for at least 2 h before.

The experiment started with the resting tests that included resting in three postures: 20 min in lying, 5 min in sitting and 5 min in standing. The resting metabolic rate and resting HR of the subject was obtained during the lying test.

The submaximal tests session included 3 different submaximal tests. The first one was the Chester step test with an increasing pace by each 2-min stage [16]. The second test was a walking pace treadmill test as described in [17]. Each stage of the treadmill test lasted 3 min, where the speed was increased after the first and the second stage and subsequently the grade was raised by 2% between each stage. The third test was an arm ergometer test with a constant cadence but an increased resistance [17]. All the submaximal tests were terminated when the HR of the subject reached the 80% of the age-predicted maximal HR ( $220 - \text{age}$ ).

Five different tasks (i.e. office work, painting, cycling, simulated meat cutting, and box lifting) were performed with varying intensities, postures, and muscle groups. Each of the tasks lasted 8–10 min.

**Data Processing and Statistics.** As the measurement from Oxycon Pro has a time resolution of one sample per 15 s, the

beat-by-beat HR was averaged by a 15-s moving window and the  $V_{E\text{-rel}}$  was also set with the same window size.

Data from the submaximal treadmill test was used to obtain personalized calibration of HR-EE and  $V_{E\text{-rel}}$ -EE. The slopes and intercepts were obtained through linear regression for HR-EE and  $V_{E\text{-rel}}$ -EE respectively. Thus, the estimated EE using HR ( $EE_{HR}$ ) and  $V_{E\text{-rel}}$  ( $EE_{VE}$ ) were calculated with the personal calibrated linear model.

The root-mean-square errors (RMSE) and the Person correlation coefficients ( $r$ ) were calculated for the realtime data to compare estimated  $V_E$  and EE from our system to the reference system.

## 4 Results and Discussion

**Relative ventilation ( $V_{E\text{-rel}}$ ) measurement from the system.** The  $V_{E\text{-rel}}$  extracted from the impedance pneumography measurement of our system had a good linear relationship with the reference measure of pulmonary ventilation ( $r = 0.80$ ). The accuracy of the measurement was compromised by some non-linearity in change of impedance and lung volume using current the electrode configuration [12], posture change [11], and motion artifacts [10].

**HR-EE and  $V_{E\text{-rel}}$ -EE relationships.** The HR-EE and  $V_{E\text{-rel}}$ -EE relationships are demonstrated in Fig. 3 with scatter plots. The  $V_{E\text{-rel}}$  had a better linearity in the low intensity region than the HR, but the linearity reduced when the intensity increased. The EE estimations by the  $V_{E\text{-rel}}$  model ( $EE_{VE}$ ) (RMSE = 3.00 ml/kg/min) are more accurate than the ones by the HR model ( $EE_{HR}$ ) (RMSE = 5.05 ml/kg/min).

**Combined model of HR and  $V_{E\text{-rel}}$ .** Based on the characteristics that were observed in the experiment a model to

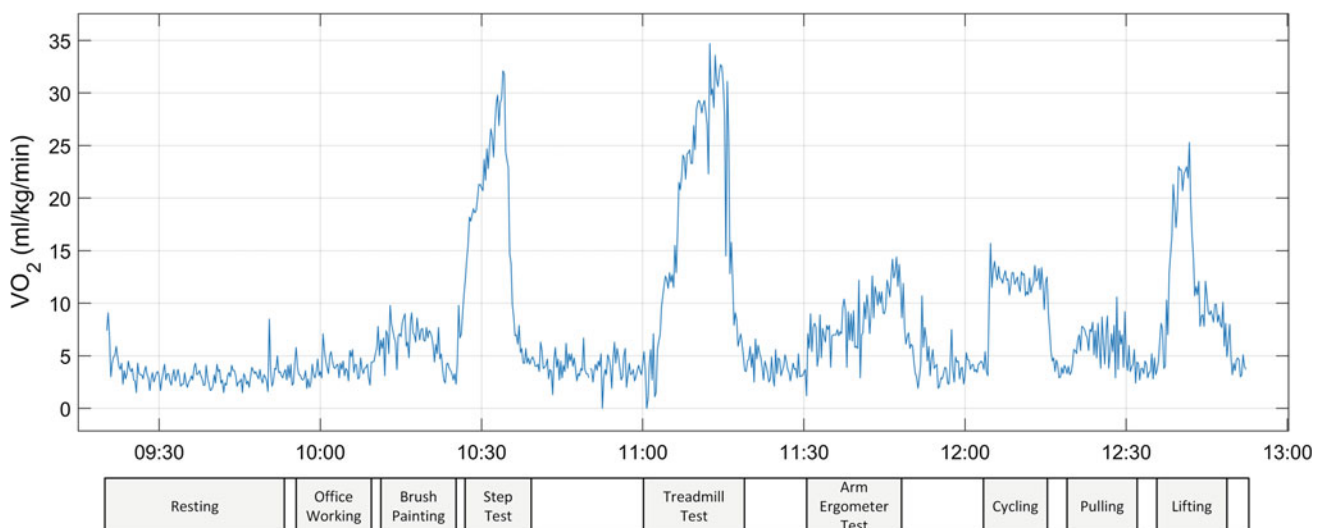


**Fig. 2** The timeline of the tasks of the experiment with the corresponding  $VO_2$  level of the test subject



**Fig. 3** The scatter plots of HR-EE (left) and  $V_{E-rel}$ -EE (right) relation. The blue line on each plot shows the linear model established by the personalized calibration during the submaximal treadmill test

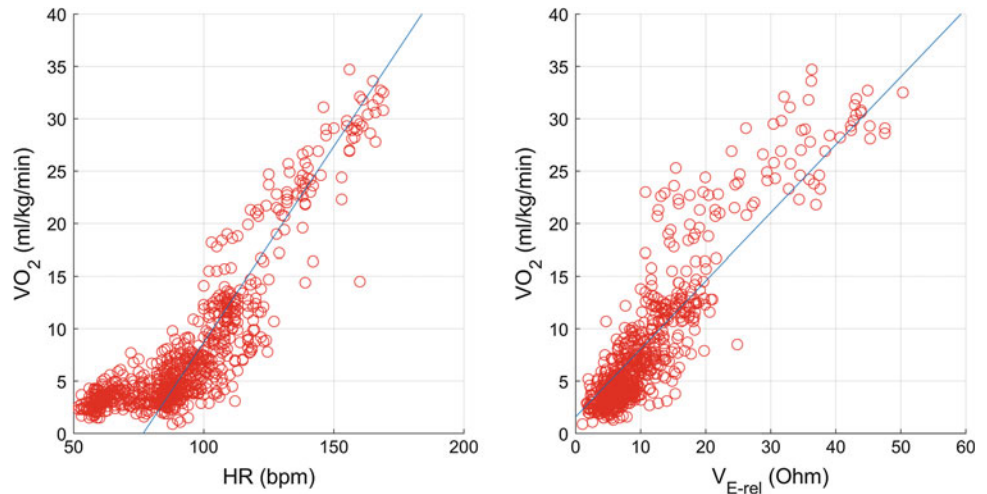


**Table 1** Comparison of EE estimated by using HR,  $V_{E-rel}$  and the combined model of HR and  $V_{E-rel}$

Estimation method	$VO_2$ (ml/kg/min)			
	Mean	Standard deviation	Root mean square error	Person's correlation coefficient
Reference ( $EE_{ref}$ )	7.62	6.71	–	–
HR ( $EE_{HR}$ )	5.84	9.06	5.05	0.69
$V_{E-rel}$ ( $EE_{VE}$ )	8.26	5.18	3.00	0.67
HR and $V_{E-rel}$ ( $EE_{Com}$ )	8.46	5.61	2.53	0.80

combine the HR and  $V_{E-rel}$  for realtime EE estimation was proposed ( $EE_{Com}$ ). When both  $EE_{VE}$  and  $EE_{HR}$  are below 25% of the maximum  $VO_2$  predicted by the age-predicted maximal HR, only the  $EE_{VE}$  is used for estimation ( $EE_{Com} = EE_{VE}$ ). Otherwise, the average of  $EE_{VE}$  and  $EE_{HR}$  will be used ( $EE_{Com} = (EE_{VE} + EE_{HR})/2$ ). The combined model had a better accuracy for estimating the EE (RMSE = 2.53 ml/kg/min,  $r = 0.80$ ) compared to the other two models, as shown in Table 1. The combined model need to be further validated and refined through experiment with more subjects in the future.

## 5 Conclusion

In this work, we have presented a wearable cardiorespiratory monitoring system for the purpose of tracking EE in free-living conditions. The pilot experiment showed the functionality of the system and the potential of using combined HR and  $V_E$  information to improve EE estimation. The validity of the system and proposed model will be examined with larger number of subjects in the future studies.

**Acknowledgements and Conflict of Interest** This work was supported by Vinnova, Sweden's Innovation Agency, through the Challenge Driven Innovation program, project 'Smart textiles for a sustainable work life', dnr: 2016-03782, and EIT Health, through project no. 17102, 'Wellbeing, Health and Safety @ Work'. Kaj

Lindcrantz and Fernando Seoane are owners of Z-Health Technologies AB, Borås, Sweden.

## References

- Colberg, S.R., Sigal, R.J., Yardley, J.E., Riddell, M.C., Dunstan, D.W., Dempsey, P.C., Horton, E.S., Castorino, K., Tate, D.F.: Physical activity/exercise and diabetes: a position statement of the American Diabetes Association. *Diabetes Care* 39, 2065–2079 (2016)
- Eston, R.G., Rowlands, A.V., Ingledew, D.K.: Validity of heart rate, pedometry, and accelerometry for predicting the energy cost of children's activities. *Journal of applied physiology* 84, 362–371 (1998)
- Luke, A., Maki, K.C., Barkey, N., Cooper, R., McGEE, D.: Simultaneous monitoring of heart rate and motion to assess energy expenditure. *Medicine and science in sports and exercise* 29, 144–148 (1997)
- Hiilloskorpi, H., Fogelholm, M., Laukkanen, R., Pasanen, M., Oja, P., Mänttari, A., Natri, A.: Factors affecting the relation between heart rate and energy expenditure during exercise. *International journal of sports medicine* 20, 438–443 (1999)
- Gastingier, S., Nicolas, G., Sorel, A., Sefati, H., Prioux, J.: Energy expenditure estimate by heart-rate monitor and a portable electromagnetic-coil system. *International journal of sport nutrition and exercise metabolism* 22, 117–130 (2012)
- Gastingier, S., Donnelly, A., Dumond, R., Prioux, J.: A review of the evidence for the use of ventilation as a surrogate measure of energy expenditure. *Journal of Parenteral and Enteral Nutrition* 38, 926–938 (2014)

7. Gilgen-Ammann, R., Koller, M., Huber, C., Ahola, R., Korhonen, T., Wyss, T.: Energy expenditure estimation from respiration variables. *Scientific reports* 7, 15995 (2017)
8. Loriga, G., Taccini, N., De Rossi, D., Paradiso, R.: Textile sensing interfaces for cardiopulmonary signs monitoring. In: *Engineering in Medicine and Biology Society, 2005. IEEE-EMBS 2005. 27th Annual International Conference of the*, pp. 7349–7352. IEEE, (2006)
9. Seoane, F., Ferreira, J., Alvarez, L., Buendia, R., Ayllón, D., Llerena, C., Gil-Pita, R.: Sensorized garments and textrode-enabled measurement instrumentation for ambulatory assessment of the autonomic nervous system response in the atrec project. *Sensors* 13, 8997–9015 (2013)
10. Rosell, J., Cohen, K.P., Webster, J.G.: Reduction of motion artifacts using a two-frequency impedance plethysmograph and adaptive filtering. *IEEE transactions on biomedical engineering* 42, 1044–1048 (1995)
11. Seppä, V.-P., Viik, J., Hyttinen, J.: Assessment of pulmonary flow using impedance pneumography. *IEEE Transactions on Biomedical Engineering* 57, 2277–2285 (2010)
12. Seppä, V.-P., Hyttinen, J., Uitto, M., Chrapek, W., Viik, J.: Novel electrode configuration for highly linear impedance pneumography. *Biomedizinische Technik/Biomedical Engineering* 58, 35–38 (2013)
13. Wang, H.-b., Yen, C.-w., Liang, J.-t., Wang, Q., Liu, G.-z., Song, R.: A robust electrode configuration for bioimpedance measurement of respiration. *Journal of healthcare engineering* 5, 313–328 (2014)
14. Abtahi, F., Ji, G., Lu, K., Rodby, K., Seoane, F.: A knitted garment using intarsia technique for Heart Rate Variability biofeedback: Evaluation of initial prototype. In: *Engineering in Medicine and Biology Society (EMBC), 2015 37th Annual International Conference of the IEEE*, pp. 3121–3124. IEEE, (2015)
15. Seoane, F., Mohino-Herranz, I., Ferreira, J., Alvarez, L., Buendia, R., Ayllón, D., Llerena, C., Gil-Pita, R.: Wearable biomedical measurement systems for assessment of mental stress of combatants in real time. *Sensors* 14, 7120–7141 (2014)
16. Sykes, K., Roberts, A.: The Chester step test—a simple yet effective tool for the prediction of aerobic capacity. *Physiotherapy* 90, 183–188 (2004)
17. Strath, S.J., Brage, S., Ekelund, U.: Integration of physiological and accelerometer data to improve physical activity assessment. *Medicine and science in sports and exercise* 37, S563–S571 (2005)

# Design Variations for Improved Usability of Mobile Data Capture in Rural Uganda

Ole Andreas Krumsvik<sup>1</sup>, Ankica Babic<sup>2</sup>, and Alice Mugisha<sup>3</sup>

## Abstract

Several form design alternatives were created as a starting point for a usability evaluation in a project dedicated to maternal and child care in the rural Northern Ugandan area. The project is concerned with ensuring that pregnant mothers deliver from the hospitals and that their babies receive the necessary care after delivery, despite the limited resources. Health care workers are collecting data to document current resources using their hand-held devices, mainly phones. The basic requirements are that the application design should be simple, easily understandable by a broad user group, and supported by Android mobile platforms. We have created four design alternatives, all simple, straightforward, and suitable for low cost Android mobile devices. The major differences are concerned with the overall layout and color usage. There are variations in the radio buttons, check boxes, date formatting, progress visualization, font, labeling, data input validation, tables, and navigation buttons. The software, Axure RP 8, was used for designing alternatives based on the currently used mobile electronic data capture form “SurvPlus\_FirstVisit\_4” which is made in ODK Collect and has many usability issues. By coming up with these four mid-fidelity prototypes we expect to address variations in design that the current software allows. Suggested designs are common for many other applications, the majority of which mobile device users are familiar with. User preference testing was carried out to explore user preferences regarding the holistic design and particular design features.

## Keywords

Usability • Mobile EDC • Rural Uganda  
Maternal care • Child care • Redesign

## 1 Introduction

Usability, according to the ISO 9241-11 standard, is defined as the extent to which a product can be used by specified users to achieve specified goals with effectiveness, efficiency, and satisfaction in a specified context of use [1]. It has become a key factor when designing and developing mobile applications and can thus determine the success or failure of the application [2]. If usability is ignored, this can present issues of varying magnitude. As reported by Nielsen [3], it could cost companies large amounts of money in sales and labor costs. A major computer company that emphasized on increasing usability of a security application, resulted in saving 41,700\$ on the first day of implementation [3]. Deep and complicated navigation, oversimplified navigation, lack of auto-fill, unresponsive gestures, insufficient user testing, demanding too many steps, and confusing or vague content are some of the most common usability issues in mobile applications [4, 5].

In previous research, findings related to usability in the context of mobile electronic data capturing in resource-limited countries are absent. In this paper we present and discuss several design variations to improve the usability of mobile electronic data capturing forms in rural Uganda. The forms are used to gather data about pregnant and recently delivered women, and they have many usability problems.

In total, we designed, and user preference tested four different mid-fidelity prototypes that could serve as an alternative for the SurvPlus forms or as design guidelines for a refined version [6]. We could not alter the textual content in SurvPlus as it belonged to the Survival Pluss project, and therefore the research was focused on the form design.

O. A. Krumsvik (✉) · A. Babic · A. Mugisha  
University of Bergen, 5007 Bergen, Norway  
e-mail: lncs@springer.com; oa.krumsvik@gmail.com

A. Babic  
Linköping University, 581 83 Linköping, Sweden

Furthermore, we believe that to enable efficient and accurate mobile electronic data capturing, usability must be prioritized.

The currently used forms were created in the free and open-source suite of tools named Open Data Kit (ODK) Collect for the Android mobile operating system. ODK Collect supersedes paper forms used in survey-based data gathering and is intended for countries in developing regions. It renders complex applicational logic and allows manipulation of data types that involve text, location, images, audio, video, and barcodes [7]. Advantages include easy installation, deliverance, and collection of the aforementioned data types. Disadvantages are concerned with auto-fill issues, slower software due to data checks, and inability to edit forms after they have been sent to a server. Research conducted by Mugisha, Babic, Wakholi, Nankabirwa, and Tylleskär [8] investigated the form developers' views on usability and discovered several issues. The results suggest that form developers had a limited understanding of usability, time-constraining deadlines, no standard procedure of measuring usability, software limitations, and unclear user needs. Moreover, the end-users typically do not participate in the form development, which could be a contributing factor to the usability issues.

## 2 Methods

To refine the existing solution of the *SurvPlus\_FirstVisit\_4* forms, several methods were applied in the research. Firstly, a literature review was carried out followed by the creation of personas. The latter is a User-Centered Design (UCD) technique to design for the end-user [9]. UCD is a term used to describe design processes in which end users impact how a design takes shape [10]. A variant of UCD was applied to the research. We chose this approach, based on the assumption that users will have an easier time to choose one of the designs. Secondly, an individual expert review was carried out by one author (Krumsvik) to discover the usability problems of the current forms [11]. Thirdly, four mid-fidelity prototypes of the forms were created in Axure RP 8 to streamline the data capturing for mobile devices [12]. Material Design guidelines were used to aid the design process [13], and some of Don Norman's interaction design principles [14]. The primary objective was to explore ways of simplifying the data input for the user, however, the mid-fidelity prototypes do not have back-end functionality. Consequently, we chose to focus on the principles regarding visibility, consistency, feedback, and affordance. We argue that this combination of methods could result in a great user experience. Lastly, the design alternatives were tested for user preferences with intention to obtain feedback and

guidance on how to make the best design for the users [15]. The studies have shown that user preferences and performance were positively correlated [15].

## 3 Results

### 3.1 Individual Expert Review

Several usability issues were discovered in the individual expert review, some of which are:

1. No progress indicator was available.
2. No navigation buttons. Navigations between screens are solely limited to swiping.
3. Incomplete error checking, e.g. the telephone number "222" is accepted.
4. Input fields with poor or no labeling.
5. The user must fill in numbers manually for a response such as "Don't know", which must be filled in as "99".
6. One question per screen regardless of the question and the alternatives.
7. Inconsistent use of vertical scrolling.
8. Some error messages are not consistent with labeling. "Participant Id no" is referred to as "PID" if the number is incorrect.
9. Particular error messages appear when trying to advance to the next page. E.g. after filling in 10 fields, there could be an error in field 2.
10. Some input fields that require a numerical response allow letters, as well.

Figure 1 displays a screenshot of selected pages from the mobile electronic forms that are currently used to gather data from recently delivered women in Uganda. The user interface design has not been prioritized by the developers, and one can also see the use of numerical responses for an alphabetical answer in the current forms.

### 3.2 Mid-Fidelity Prototypes

As depicted in Fig. 2a, design alternative 1 informs the user about percentage of progress while filling out the form. Additionally, radio buttons have been implemented to ease the user input effort when selecting a response that previously demanded a numerical input. Navigation buttons have been added, and labels that inform about e.g. the currency. In addition, there are several questions per page if the interface allowed it.

Figure 2b displays design alternative 2 which includes a progression bar that displays for example step 4 of 6, and a

SI-3. What mode of transport have you used to get to this place of delivery?

- Private car
- Bus
- Taxi
- Ambulance
- Bicycle
- motorcycle
- On foot
- Other.....

SI-5. How much did it cost you to buy materials to go with to the place of delivery?  
Nothing=00 and -99 for Don't Know/Don't Remember  
For those on insurance you put the lumpsum in other

Clothes  
Enter -99 if Doesn't know  
-99

Cotton  
Enter -99 if Doesn't know  
0

Gauze  
Enter -99 if Doesn't know  
0

Plastic sheet  
Enter -99 if Doesn't know  
0

SI-7. How much did it cost you to pay the health care provider during this delivery?  
Nothing=00  
Paid in kind=86  
DK=99  
0

1 2 3 -  
4 5 6 -  
7 8 9 -  
, 0 .

Fig. 1 SurvPlus\_FirstVisit\_4 (Screenshot), as used in the Survival Pluss project

(a) SI-6. How much have you spent during this delivery?  
\_\_\_\_\_ UGX  Don't know

SI-7. How much did it cost you to pay the health care provider during this delivery?  
\_\_\_\_\_ UGX  Don't know  Paid in kind

SI-8. How far is the place of birth from your home (kilometres)? 1 mile = 1.6 KM.  
\_\_\_\_\_ KM  Don't know

SI-9. Did your husband/someone else escort you to the place of delivery?  
 Yes, husband  
 Yes, someone  
 No  
 Do not know

(b) SI-4. What mode of transport did you use to get from the place of delivery to your home?

- Private car
- Bus
- Taxi
- Ambulance
- Bicycle
- Motorcycle
- On foot
- Other

(c) SI-6. How much have you spent during this delivery?  
Price in UGX \_\_\_\_\_  Don't know

SI-7. How much did it cost you to pay the health care provider during this delivery?  
Price in UGX \_\_\_\_\_  Don't know  Paid in kind

SI-8. How far is the place of birth from your home (kilometres)? 1 mile = 1.6 KM.  
Distance in KM \_\_\_\_\_  Don't know

SI-9. Did your husband/someone else escort you to the place of delivery?  
 Yes, husband  
 Yes, someone  
 No  
 Do not know

(d) SI-10. Who in this home decides on where the baby should be delivered from?

- Mother of baby
- Father of baby
- Mother in law
- Sister
- Grandmother
- Friend
- Health professional
- Other (specify)

Fig. 2 a Design alternative 1. b Design alternative 2. c Design alternative 3. d Design alternative 4

placeholder label for the fields that require free text input. Additionally, there are customized radio buttons and check lists. The design alternative provides several questions per page, material design buttons, and a blue and white design theme. The layout is similar to design alternative 1.

Design alternative 3, as shown in Fig. 2c, has a progress bar with rounded corners, custom navigation buttons with arrows, and horizontal lines to frame the questions in the forms. Moreover, it contains two labels, e.g. type of item and

currency in the free text questions to aid the user. The design has customized list pickers, a red and white color theme, and several questions per page.

The final design alternative, presented in Fig. 2d, contains one question per page. The content is center aligned, with question alternatives separated by horizontal lines, and includes larger list pickers as compared to the other design alternatives, as well as customized navigation buttons. In addition, a hint text label is placed in the free text fields. The



progress indicator is filled with white color and rounded, and the color theme in this design alternative is mainly blue with white text.

All four design alternatives fulfil the Web Content Accessibility Guidelines AA criteria created by the Web Accessibility Initiative [16].

Google's default Android font, Roboto, was applied to all the prototypes. As for font-weight, three variants were used: bold, medium, and regular. The font size ranged from 12 points to 16 points, in accordance with Material Design guidelines [13].

### 3.3 User Preference Testing

The participants included 48 research assistants who had been collecting data using ODK for a period ranging between 3 months to 1 year on the Survival Puss projects, BCG and Chlorhexidine projects in Uganda. Each of the research assistants were able to access the prototype on their phones, from where they were able to view the different design features, after consenting. They later filled a questionnaire indicating their user preferences for the different design features. The design feature options with the highest frequencies were considered to be the preferred features and can be viewed in Table 1.

## 4 Discussion

Four mid-fidelity prototypes were created to help enhance usability of the open source solution ODK for data capture. Our motivation for coming up with completely different designs was to enable the potential evaluators to decide on preferences for specific colors as well, not merely limiting the evaluation to just displaying the new and distinct navigation buttons, progress bars, list pickers etc. with a grey and white color scheme. Furthermore, the purpose of the development was to introduce designs that are typically seen in newer types of applications.

From our perspective, the mid-fidelity prototypes were found to be time saving, and enough detail-oriented to

highlight the differences between the different designs and give the user a feeling of a finalized data capture solution. In addition, these designs provide more functionality such as the implementation of list pickers, since the data collector previously had to fill in numbers that indicated the response "don't know". We believe that this could increase the data accuracy as it can make it harder to commit an error, and at the same time reduce the user input effort. Since it is easier to fill in data in the prototypes, one can also assume that the actual data collection will be more productive compared to the current forms.

The mid-fidelity prototypes have simple interactions regarding the buttons, list pickers, examples of data input validation, and free text input. These interactions are very similar to the original SurvPlus forms.

The standard ODK Collect forms spare a lot of development efforts, however we believe that both design and interaction ought to be emphasized to increase usability and the user experience. The best practice for designing an interface is to know the intended user. A good design involves understanding user goals, skills, preferences, and habits [17].

Applying UCD in a healthcare setting is recommended by Fricker et al. [18]. In fact, in healthcare, the implementation of UCD when developing mobile health applications has been proven successful [19]. This is, however, not the most established practice as healthcare software developers commonly overlook relevant user characteristics, user tasks, and usability issues. In addition, basic design principles are not prioritized [20]. Thus, by further using UCD in this development we aim to increase user satisfaction, productivity, user acceptance, decrease user errors, and user training time.

Research conducted by Nielsen [21], highlights the value of usability. The average return of investment when prioritizing usability is 83%. This shows that it is imperative to increase usability. Although these forms are not about revenue, it could lead to a cost-benefit for the Ugandan government as they can be usable and transferable to other settings. Furthermore, it is imperative to note that good quality data especially in the health discipline leads to accuracy in decision making both at the clinical and policy levels, short of which the results could be disastrous. Ultimately, the improved accuracy resulting from better usability is expected to lead to more efficient and improved healthcare services.

The usability review and user preference testing has shown to be valuable in addressing many of the existing usability issues in SurvPlus4\_FirstVisit, as well as aiding the design process. The cause of SurvPlus4's current usability issues could be attributed to both the creators of ODK Collect and the form developers.

There are several other issues related to the usability of open source projects identified by Twidale and Nichols [22].

**Table 1** Preferred design features results from the user preference testing (n = 48)

Navigation button	Blue and white (Fig. 2d)
Progress bar	Black and white (Fig. 2a)
Radio button	Red and white (Fig. 2c)
Checkbox	White and blue (Fig. 2b)
Layout	Black and white (Fig. 2a)
Color layout	Black and white (Fig. 2a)



In particular, they address the impact of user interface on usability in terms of the mechanisms, techniques and technology used to design and refine the interfaces. We have focused on application complete design as whole to offer the complete user experience instead of going into the technical details of development and programming. In that way we wanted to secure input of potential users. However, many improvements could be reached by addressing programming, organizational and issues of the standards, as suggested by Twidale and Nichols [22].

## 5 Conclusion

Several mid-fidelity prototypes were created, and user preference tested for the *SurvPlus\_FirstVisit\_4* since they illustrate the end-product in sufficient detail, but do not require full development effort. We found this to be time-saving, as well as cost-beneficial. Moreover, we argue that UCD is the most viable design approach in this context. It is not often that end-users are asked about their input with respect to the forms. This research has shown that there is a place for them to provide their input in order to substantially improve the user experience.

**Acknowledgements** The authors would like to thank the Norwegian Agency for Development Cooperation (NORAD) for supporting the research through the HI-TRAIN project.

**Conflict of Interest** The authors declare that they have no conflict of interest.

## References

- ISO/IEC (1998). 9241-14 Ergonomic requirements for office work with visual display terminals (VDT)s - Part 14 Menu dialogues, ISO/IEC 9241-14: 1998 (E).
- Harrison R, Flood D, Duce D (2013) Usability of Mobile Applications: Literature Review and Rationale for a New Usability Model. *J Interact Sci* 1:1–16. <https://doi.org/10.1186/2194-0827-1-1>.
- Nielsen, J.: Usability engineering. Elsevier (1994).
- Evanhaim D (2017) 9 Usability Issues that Plague Today's Mobile Apps. <https://blog.appsee.com/9-usability-issues-that-plague-mobile-apps>, last accessed 2017/11/16.
- Gerber S (2016) The 8 most overlooked mobile app usability issues. <http://mashable.com/2016/05/26/mobile-app-usability-issues>, last accessed 2017/11/30.
- Engelberg D, Seffah A (2002) A framework for rapid mid-fidelity prototyping of web sites. *Usability Gaining a Compet Edge* 99:203–215. [https://doi.org/10.1007/978-0-387-35610-5\\_14](https://doi.org/10.1007/978-0-387-35610-5_14).
- Hartung C, Anokwa Y, Brunette W, et al (2010) Open Data Kit: Tools to Build Information Services for Developing Regions. *Proc Int Conf Inf Commun Technol Dev* 1–11. <https://doi.org/10.1145/2369220.2369236>.
- Mugisha A, Babic A, Wakholi P, et al (2017) Usability in Mobile Electronic Data Collection Tools: Form Developers' Views. *Stud Health Technol Inform* 238:72–75.
- Blomkvist S (2002) Persona – an overview. 1–8.
- Abras C, Maloney-Krichmar D, Preece J (2010) User-Centered Design. *Work* 37:445–456. <https://doi.org/10.3233/wor-2010-1109>.
- Wilson, C.: User Interface Inspection Methods, 1st edn. Morgan Kaufmann (2013).
- Axure (2017) Prototypes, Specifications, and Diagrams in One Tool. <https://www.axure.com>, last accessed 2017/11/30.
- Google (2017) Introduction - Material Design. <https://material.io/guidelines>, last accessed 2017/11/13.
- Norman, D.: The Design of Everyday Things. Basic Books (2013).
- Nielsen J, Levy J (1994) Measuring usability: preference vs. performance. *Commun. ACM* 37:66–75.
- W3C (2017) Web Content Accessibility Guidelines (WCAG) Overview. <https://www.w3.org/WAI/intro/wcag>, last accessed 2017/11/12.
- Shneiderman B, Plaisant C (2010) Designing the User Interface: Strategies for Effective Human-Computer Interaction. Pearson 5th:639.
- Fricker SA, Thummler C, Gavras A (2015) Requirements Engineering for Digital Health. Springer International Publishing.
- McCurdie T, Taneva S, Casselman M, et al (2012) mHealth Consumer Apps: The Case for User-Centered Design. *Biomed Instrum Technol Mob Heal* 46:49–56.
- Johnson CM, Johnson TR, Zhang J (2005) A user-centered framework for redesigning health care interfaces. *J Biomed Inform* 38:75–87. <https://doi.org/10.1016/j.jbi.2004.11.005>.
- Nielsen J (2008) Usability ROI Declining, But Still Strong. <https://www.nngroup.com/articles/usability-roi-declining-but-still-strong>, last accessed 2017/11/12.
- Twidale MB, Nichols DM (2005) Exploring usability discussions in open source development. In: System Sciences, 2005. HICSS'05. Proceedings of the 38th Annual Hawaii International Conference on. IEEE.

# Advancing Medical Practice Through Computer Expert Systems

K. I. Nkuma-Udah, G. Chukwudebe, and E. Ekwonwune

## Abstract

This research is designed to enable the clinicians to identify certain diseases and describe methods of treatment to be carried out. The Java programming language is the tool for use to design the system. In the system, a number of patient cases are selected as prototypes and stored in a separate database. The knowledge is acquired from literature review and human experts of the specific domain and is used as a base for analysis, diagnosis and treatment recommendations. Different rules exist for diagnosis based on three groups of determining factors of Sr (Sign/Symptom/Investigating report is Strongly Required for Diagnosis), Rn (Sign/Symptom/Investigating report is Relevant but Not necessarily required) and Nr (Sign/Symptom/Investigating report is Not Related/Relevant). The system provides a simple, interactive, graphical user interface. The employment of a low cost software such as Java makes the system affordable to the medical doctors, who are the end users. It is expected that the use of the system will enhance the diagnosis of certain diseases and so reduce the problems that come with mis-diagnosis including their mortality. This in turn reduces healthcare cost and improves the quality and outcomes of healthcare especially in the developing African countries where malaria is endemic and every aspect of health resources manpower, technology, finances, etc.—is in short supply.

## Keywords

Expert system • Medical diagnosis • Artificial intelligence • Java • Healthcare informatics  
Decision support system

## 1 Introduction

Medical diagnosis is a complicated cognitive clinical process requiring high level of expertise. A clinician uses several sources of data through a series of algorithms to make a diagnostic impression. The whole aim of medical diagnosis is to arrive at an appropriate treatment decision, which in turn leads to a good prognosis for the particular ailment or disease. Therefore, any mis-diagnosis will lead to a wrong treatment and by extension an addition to the cost of medical or healthcare.

In the developing countries, malaria is known to have a major negative effect on economic development [1]. This socioeconomic implication of malaria makes it an important issue in its diagnosis.

In situations such as above, confirming the diagnosis of malaria [3] becomes a difficult task for the physician. This is because the diagnostic procedures of gathering the requisite data, as in signs, symptoms and investigations to narrow the differential diagnosis and arrive for instance at the correct diagnosis of malaria rather than of typhoid fever, is a complex process. However, employing intelligent health informatics into the process drastically simplifies it and ensures that mis-diagnosis or missing data is eliminated from the medical care system.

This work specifically deals with the use of an affordable and available expert system (in this case the Java Programming language) to exactly diagnose malaria, enteric or dengue fever in the developing countries using Nigeria as a case study. In the system, a number of patient cases are selected as prototypes and stored in a separate database, known as the knowledge base. The knowledge is acquired from literature review and human experts of the specific

---

K. I. Nkuma-Udah (✉)  
Biomedical Technology, Federal University of Technology,  
Owerri, Nigeria  
e-mail: drkinkumaudah@gmail.com

G. Chukwudebe  
Electrical/Electronic Engineering, Federal University of  
Technology, Owerri, Nigeria

E. Ekwonwune  
Computer Science, Imo State University, Owerri, Nigeria

domain (malaria experts) and is used as a base for analysis, diagnosis and treatment recommendations.

## 2 Literature Review

An expert system represents an expertise as data or rule within the computer. These rules and data can be called upon when needed to solve problems. Expert System is a major aspect of artificial intelligence. The field of artificial intelligence came to be, when attempts were made to look at the behavior/reasoning of intelligent entities such as humans, and developed algorithms based on that behavior.

Expert system as an application area of artificial intelligence is a computer system that emulates the decision-making ability of a human expert [4]. It is designed to solve complex problems by reasoning about knowledge, like an expert, and not by following the procedure of a developer as is the case in conventional programming [5].

### 2.1 Components of Expert Systems

When conclusions are drawn (inferences) by computer-based systems, they are contained in the inference engine. These inferences are derived from information (knowledge) supplied to or stored in the computer system as knowledge-base. Therefore expert systems usually consist of two core parts in its kernel: a knowledge base and an inference engine [6].

For a user to interact with the expert system, there has to be an additional part other than the knowledge base and the inference engine. This is the user interface. Therefore, the entire expert system shell (architecture) in the most simplified version consists of three parts: a knowledge base, an inference engine and a user interface (Fig. 1).

### 2.2 Applications of Expert Systems

The spectrum of applications of expert systems technology to solve problems in industrial, commercial and other areas

is so wide as to defy easy categorization. However, about seven categories of applications have been delineated for expert systems technologies [7]. These include: Diagnosis and Troubleshooting of Devices and Systems of All Kinds; Planning and Scheduling; Configuration of Manufactured Objects from Subassemblies; Financial Decision Making; Knowledge Publishing; Process Monitoring and Control; and Design and Manufacturing.

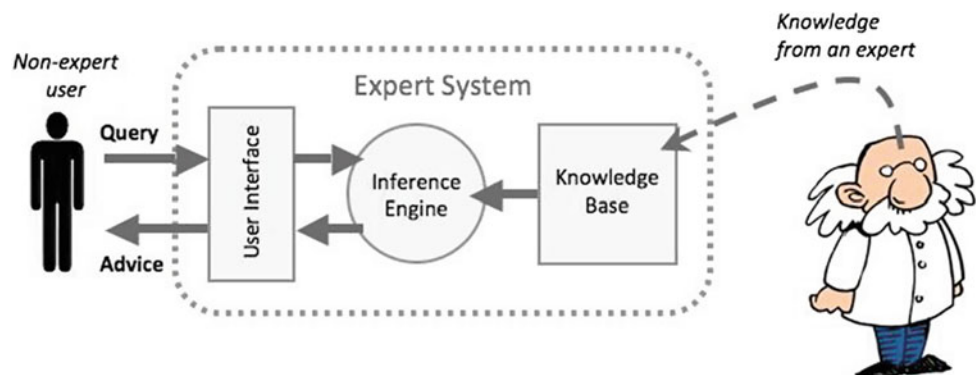
Expert systems currently play important roles in medicine, medical practice or medical care. About nine areas of the medical practice have been identified to employ the use of computer expert systems. These are: Prediction of Disease, Prevention of Disease, Diagnosis of Disease, Staging of Disease, Therapy of Patient, Rehabilitation of Patient, Health Status of the Patient, Counselling of the Patient, Advocacy for the Patient [8].

Categorically, expert systems can be applied in the following tasks in the medical practice [9]: Generating alerts and reminders, Diagnostic assistance, Therapy critiquing and planning, Agents for information retrieval. In the task of diagnostic assistance, an expert system can help suggest likely diagnoses based on patient data, when a patient's case is complex, rare or the clinician making the diagnosis is quite inexperienced in the given specialty.

### 2.3 Medical Practice, Malaria, Developing Countries and Expert Systems

Medical practice is the art of diagnosis and treatment of human diseases or ailments. One group of human diseases that is of concern in the developing countries are infectious diseases. Yet these are mainly curable. Many of them are endemic in these countries. Among the curable infectious diseases that are endemic in the developing countries are malaria and some of its differentials. These are so important, that the Goal 6 of the World Health Organisation, WHO Millennium Development Goals, MDG 2000–2015 (*Combat HIV/AIDS, Malaria and Other Diseases*) was specifically dedicated to malaria and the other infectious diseases. And when in 2015 the goal was not totally achieved, although the

**Fig. 1** The concept of expert system (Retrieved from [www.Bandicam.com](http://www.Bandicam.com))



global malaria incidence rate has fallen by an estimated 37% and the mortality rate of malaria reduced by 58% [10], another set of development goals were pronounced by the WHO.

The Sustainable Development Goals (SDG), eighteen in number, were developed to replace the MDGs. The SDG with timeline between 2016 and 2030, has its Goal 3 as Good Health and Well-being, with one of targets *To end by 2030, the epidemics of malaria and other neglected tropical diseases* [11].

Malaria is one disease that is commonly associated with poverty and known to have a major negative effect on economic development is malaria. [12]. This is why every development goal has retained it for emphasis. In Nigeria, malaria as well as some of its differentials like enteric fever and dengue fever, is among the common infectious diseases that are endemic [13, 14]. This makes all three—malaria, enteric and dengue fever—diseases of a very important public health concern.

**Examples of Medical Expert System:** A classical medical diagnosis expert system is the MYCIN. It was developed to capture the knowledge of medical experts in infectious blood diseases [15]. Aside from MYCIN, another expert system, Diagnosis Pro provides differential diagnosis in the field of general internal medicine, family practice, paediatrics, geriatrics and gynaecology [16]. Another expert system used in medical diagnosis is the Global Infectious Diseases & Epidemiology Network, GIDEON. In addition to diagnosis, GIDEON is used for simulation and informatics in the fields of geographic medicine and infectious diseases, and Clinical Microbiology. Then, Post-Operative Expert Medical System, POEMS provides decision support system for post-operative care.

### 3 Methodology

In the Expert System designed using Java programming language, the knowledge base was built by accumulating factual knowledge from medical experts of the specific medical domain of malaria. In this case the consultants (medical experts) in internal medicine, community medicine, general medical practice and paediatrics in Abia State University Teaching Hospital, Aba, Abia State, Nigeria were used. This was done by the use of a specialized questionnaire given to the medical experts to gather the experts' knowledge on malaria and its related diseases' conditions, namely their symptoms, signs, possible clinical investigations and treatment options.

The data accumulated from the specialized questionnaire above were analyzed by establishing possible associations between the signs and symptoms of patients with given clinical investigations. These were the determining factors

for diagnosis of the three diseases provided for diagnosis in the designed system: malaria, dengue fever, enteric fever. The possible signs, symptoms and investigation reports of these diseases were organized in groups, which helps in diagnosis. Each disease entity or unit is provided with three groups of signs/symptoms/investigation results used as determining factors in the diagnosis as follows:

- (a) *Sr = Sign/Symptom/Investigating report is Strongly Required for Diagnosis;*
- (b) *Rn = Sign/Symptom/Investigating report is Relevant but Not necessary for diagnosis;*
- (c) *Nr = Sign/Symptom/Investigating report is Not Related/Relevant for diagnosis*

Further knowledge was acquired from literature review of books and journals in the domain of malaria and its related diseases and then from the internet. These were used as a base for analysis, diagnosis and recommendations. Knowledge in the design was represented via a production rule.

### 4 Results and Discussion

The proposed expert system is a rule based medical expert system for the diagnosis of malaria, enteric and dengue fever using Java as the programming language. Forward chaining inference mechanism is employed in the system. This is a graphical user interface based interactive system where systems communicate with user in common understandable language. The system consists of multiple sub-system options or platforms as: log in, Patient's Information, Diagnosis system, Treatment system, Prognosis and log out. The system works on the Java environment. And as the system uses plain English language to interact with user no special knowledge is required for individual to use it.

To use the expert system, a 64-bit Windows web development environment, the WampServer 2.4, will first be switched on. Once WampServer is on, user clicks on the MDES folder to open into the MDES software. Double clicking on the software icon (Expert System for Malaria\_Enteric\_Dengue) runs the program. A booting display first announces the MDES. This is followed by a log in window. This is to give the expert system a form of security. So the user enters the user name and password to access the system. The log in window is displayed in Fig. 2.

When the system is accessed, a menu window containing the sub-system options—Patient information, Diagnostic System, Treatment System and Log out—pops out. The Patient information option is default and forms the Welcome screen. Figure 3 shows the Welcome screen of the MDES. The Patient Information enables the user to key in new patients' biodata or retrieve old patients' information by

**Fig. 2** Log in window of the expert system

**Fig. 3** Welcome screen (Homepage) of the expert system

supplying their phone number and clicking the search button.

The Diagnosis system option enables the user to decide on which disease the patient has. When the diagnosis is confirmed from the Diagnosis system, the Treatment system is used to recommend therapeutic regimens based on the diagnosis. The user clicks on the Ailment already diagnosed and then on Proceed to get the treatment options available. The user, who is a human expert (medical doctor), now uses his/her initiative to choose the best treatment option he/she thinks best fit. At the end of each patient's session, the user logs out.

## 5 Conclusion

It is important to note that the Expert System designed here, like other expert systems, is not intended to replace clinician-experts activities but only to be a complementary tool. The humans can elaborate decisions using their knowledge and intuition. The intuition allows the elaboration of the decisions without the use of all the necessary knowledge, this way sometimes problems, for which does not exist elaborated solving methods, can be solved. The artificial thinking prompted by expert systems allows the problems solving based on existent problem solving methods sometimes verifying many conditions. This way, the

artificial agents can solve many times the problems precisely, verifying conditions that can be ignored by the humans.

**Conflict of Interest** The authors declare no conflict of interest.

## References

1. Chandra R., "Social, Health, and Environmental Infrastructures for Economic Growth", IGI Global, Hershey, USA, 2017
2. Viraj P. et al., "Chemical and Biochemical History of Antimalarials: A Podium of Plasmodium Unicellular Unit", British Biomedical Bulletin, UK, 2014
3. Rees P. J., J. Pattison and C. Kosky, "100 Cases in Clinical Medicine, 3rd Ed", Taylor & Francis Group, LLC, Boca Raton, USA, 2014
4. Peter J., (1998), Introduction To Expert Systems (3 ed.), Addison Wesley, p. 2, ISBN 978-0-201-87686-4
5. Barzilay R., McCullough D., Rambow O, DeCristofaro J., Korelsky T. and Lavoie B. (1998) "A new approach to expert system explanations", CoGenTex, Inc
6. Galliers R.D. and D.E. Leidner, "Strategic Information Management: Challenges and Strategies in Managing Information Systems 4th Ed", Routledge, London, UK, 2009Author, F.: Article title. Journal 2(5), 99–110 (2016)
7. Yet B., A. Constantinou; N. Fenton, Norman; Neil, Martin; Luedeling, E.; Shepherd, K., (2016) "A Bayesian Network Framework for Project Cost, Benefit and Risk Analysis with an Agricultural Development Case Study". Expert Systems with Applications. 60: 141–155

8. Feldman S and Sherman C., (2001), The High Cost of Not Finding Information, An IDC White Paper
9. World Health Organisation WHO, (2017). Malaria. Retrieved on 24/12/2017 @ [www.who.int/ith/2017-ith-chapter7.pdf](http://www.who.int/ith/2017-ith-chapter7.pdf)
10. WHO. (2015). Global technical strategy for malaria 2016–2030, World Health Organization, Geneva, Switzerland
11. Gallup JL and Sachs JD (2001) The Economic Burden of Malaria, American Journal of Tropical Medicine and Hygiene. 64, 1
12. Enabulele S. and Awunorl S.N. (2016), Typhoid fever in a Tertiary Hospital in Nigeria: Another look at the Widal agglutination test as a preferred option for diagnosis, Niger Med J., May–Jun; 57(3): 145–149



# Propose a Model of Multimedia Electronic Patient Record System for Sri Lankan Public Health Sector

A. L. Pallewela and V. Parameshwaran

## Abstract

Multimedia electronic patient record systems are not a new idea in the world, but in Sri Lankan health sector it is a new idea. Multimedia electronic patient record systems is complete online patient data, including traditional medical chart information and clinical images, are essential to providing good health care. A complete multimedia electronic patient record system can improve patient care, promote safe practice, and enhance communication between patients and multiple providers, reducing the risk of error. Currently there is no available any multimedia electronic patient record system in Sri Lankan health sector. It is possible to analyze current requirement of Sri Lankan health sector and propose a model of multimedia electronic patient record system for Sri Lankan health sector. A questionnaire survey, mathematical and statistical analysis method is used in this investigation to analyze an appropriate model of multimedia electronic patient record system. 30 hospitals were responded for this survey and out of 30 hospitals 21 were government and 9 were private hospitals. Using statistical methods, it is possible to propose a model of multimedia electronic patient record system for health sector of Sri Lanka and this survey reveals major barriers and suggestions which have to be implemented in order to achieve an efficient electronic patient record system for Sri Lankan health sector.

## Keywords

Electronic patient record • Telemedicine • Implementation • Questionnaire survey

A. L. Pallewela (✉)  
Sri Jayawardenapura General Hospital, Colombo, Sri Lanka  
e-mail: lakmalasela88@gmail.com

V. Parameshwaran  
General Sir John Kotelawala Defence University, Ratmalana, Sri Lanka

## 1 Introduction

Multimedia electronic patient record system is complete online patient data, including traditional medical chart information and clinical images, are essential to providing good health care. Information must be available at any location and any time that the patient needs care [1, 2]. A complete multimedia patient record allows health care networks to provide care seamlessly, without repeating studies and delaying treatment. An electronic patient record (EPR) is a repository of electronically maintained information about an individual's lifetime health status and health care, stored such that it can serve the multiple legitimate users of the record. Clinicians can access their patient's medical information automatically from any facility where care has been provided and they can navigate between cloud information and the associated images using the graphical user interface [3, 4]. An endoscopic database network system uses intranet technology being developed for electronically managing integrated medical records of patients in a special procedures clinic such as an endoscopy center. Features such as image capture and voice activation are incorporated into the system to facilitate real-time operation during clinical procedures [5]. Distributed medical information systems are prone to security flaws at three main different levels: storage, processing and transmission. Among implemented security mechanisms, few concern intrinsic patient records multimedia content protection. There are Secured Specialized Electronic Patient Record (SSEPR) based on a JPEG2000-XML structure designed to provide interaction with the Medical Information System (MIS) security mechanisms and policies [6].

A Web-Based Medical Multimedia Visualization Interface for Personal Health Records, presented the healthcare industry has begun to utilize web based systems and cloud computing infrastructure to develop an increasing array of online personal health record (PHR) systems. Although these systems provide the technical capacity to store and

retrieve medical data in various multimedia formats, including images, videos, voice, and text, individual patient use remains limited by the lack of intuitive data representation and visualization techniques [7, 8].

The Electronic Multimedia Health Fascicle (EMHF), a truly new software system for the very large number of available electronic health records. It allows the physician to see at a glance the patient's clinical biometric measurements and biologic parameters, so as to be able to link any alarming physical status to his recent medical history. Web based, accessible from any mobile device, and easy to use by both physicians' and patients, the system facilitates patient-medical interaction. Using the system can also promote better adherence to medical guidelines by the physicians and to medical prescriptions and advice by the patients [9–11].

## 2 Materials and Methods

A questionnaire was designed based on the requirement of a multimedia electronic patient record system for Sri Lankan public health sector and this questionnaire was used to collect the quantitative data [12, 13]. The quantitative analysis methods used to analyze an appropriate model of multimedia electronic patient record system. According to the literature review and the statistical analysis, sample size of this project was 30 hospitals where 21 were government teaching and 9 private hospitals [14]. The survey data of different hospitals was analyzed using the Minitab 17 software with  $\alpha = 0.05$  normal distribution.

## 3 Results and Discussion

In this investigation, responses had been received from 30 hospitals including 21 government teaching hospitals and 9 Private hospitals to represent Sri Lankan public health sector. Some selected electronic functionalities and their level of implementation in Sri Lanka shows below table.

### 1. Analysis of clinical documentation implementation in electronic Format

It has found a vast variety in the implementation of key electronic clinical documentation across Sri Lankan health sector. 63.33% of hospitals are familiar with patient demographics across all clinical units. A lot of important patient information can be found in the patient demographic page. It is important to having a complete electronic format in patient demographics in Sri Lankan health sector. 90% of hospitals do not have resources but considering implement electronic

in physician notes. Only 10% of hospitals have been using electronic in physician notes. Even though majority of hospitals do not have facility to use physician notes, physicians are not quiet interested using this, as they are too much familiar with paper based systems.

Only 6.67% of hospitals are currently using nursing assessment in their multimedia electronic patient record system and 90% of hospitals do not have any resources to implement. In present scenario the need of implementation of nursing assessment is not well identified. Nursing assessment is the first part of the nursing process, and thus forms the basis of the care plan which helps to perform a well-balanced patient care. 13.33% of hospitals had institute problem lists across all clinical units and 86.67% of hospitals do not have resources but considering implementing in future. 70% of hospitals are not familiar with the discharge summaries in electronic format. Even though it has not implemented discharge summaries one of the key factors in the electronic functionalities in any health sector as paper based in patient discharge summaries are slow and fraught with problems, not least from illegible e hand writing. An electronic discharge summary system provides a fast, accurate, secure and simple to use alternative (Table 1).

### 2. Analysis of result viewing implementation in electronic format

46.67% of hospitals are already familiar with electronic lab reporting. 50% of do not have required resources to implementing the system. Electronic lab reporting is a secure, automated mechanism for the reporting of laboratory and patient information by hospitals and commercial laboratories. In present scenario 33.33% of hospitals are using radiology reports via an electronic record system. The Sri Lankan ministry of health is now considering implementation of radiology information system (RIS) in twenty public hospitals around Sri Lankan public health sector which shows the need of implementation of radiology report in an electronic patient record system.

3.33% of hospitals have implanted electronics in consultant reports across all clinical units in Sri Lankan health sector. Can clearly identified most of the hospitals do not have required resources, but they are considering to implement in future. Health sector consultant reports are important for identified real situation of a patient, compare with the paper based reports electronic consultant reports are well structure, clear and can keep long time of period in the database so it's possible to access consultant reports any time (Table 1).

### 3. Analysis of computerized provider order entry (CPOR) implementation in electronic format

**Table 1** Electronic functionalities and their level of implementation in Sri Lanka

Electronic functionality	Fully implemented across all units	Fully implemented in at least one unit	Beginning to implement in at least one unit	Have resources to implement in the next year	Do not have resources but considering implementing	Not in place and not considering implementing
Clinical documentation	Percent of hospitals (number of hospitals)					
Patient demographics	63.33 (19)	–	3.33 (1)	–	33.33 (10)	–
Physician notes	10 (3)	–	–	–	90 (27)	–
Nursing assessments	6.67 (2)	–	–	–	90 (27)	3.33 (1)
Problem lists	13.33 (4)	–	–	–	86.67 (26)	–
Medication lists	13.33 (4)	–	–	–	86.67 (26)	–
Discharge summaries	23.33 (7)	–	3.33 (1)	3.33 (1)	70 (21)	–
<i>Results viewing</i>						
Lab reports	46.67 (14)	–	–	3.33 (1)	50 (15)	–
Radiology reports	33.33 (10)	3.33 (1)	–	3.33 (1)	56.67 (17)	3.33 (1)
Radiology images	33.33 (10)	3.33 (1)	–	3.33 (1)	56.67 (17)	3.33 (1)
Diagnostic test results	20 (6)	–	–	3.33 (1)	73.33 (22)	3.33 (1)
Diagnostic test images	3.33 (1)	–	–	3.33 (1)	90 (27)	3.33 (1)
Consultant reports	3.33 (1)	–	–	–	90 (27)	6.67 (2)
<i>Computerized provider order entry</i>						
Laboratory test	36.67 (11)	–	–	–	60 (18)	3.33 (1)
Radiology test	16.67 (5)	–	–	6.67 (2)	73.33 (22)	3.33 (1)
Medication	20 (6)	–	–	10 (3)	70 (21)	–
Consultation request	10 (3)	–	–	10 (3)	70 (21)	10 (3)
Nursing orders	6.67 (2)	–	–	6.67 (2)	73.33 (22)	13.33 (4)
<i>Decision support</i>						
Clinical guidelines	3.33 (1)	–	–	–	–	80 (24)
Clinical reminders	–	–	–	–	–	76.67 (23)
Drug allergy alerts	–	–	–	–	–	76.67 (23)
Drug-drug interaction alerts	–	–	–	–	–	76.67 (23)
<i>Other functionalities</i>						
Telemedicine images	–	–	–	–	93.33 (28)	6.67 (2)
Radio frequency ID	3.33 (1)	–	–	–	93.33 (28)	3.33 (1)

Computerized provider order entry (CPOE) is paramount important for a multimedia electronic patient record system. It is the process of medical professional entering orders electronically instead of on paper charts. The primary advantage of computerized provider order entry is that it can help reduce errors related to the poor hand writing or transcription of orders. According to the results obtain from the survey 36.67% hospitals have fully implemented electronic

format in laboratory tests across all clinical units. Medication is a major part of CPOE, if its anything goes wrong while ordering medication, patient will get wrong medication so reduce this kind of human error best solution is using electronic in medication (Table 1).

4. Analysis of decision support and other functionalities implementation in electronic format

Decision support in health care sector includes clinical guidelines (e.g., Beta blockers post-MI), clinical reminders (e.g. pneumovax), drug allergy alerts and drug-drug interaction alerts. The implementation of electronic in decision supports also one of the important parts of a multimedia electronic patient record system. Its major advantage is assist the nurses and doctors to take quick, easy and correct decision at correct time. 23.33% of hospitals do not have resources, but they are considering implement electronic in clinical reminders, drug-allergy alerts and drug-drug interaction alerts and 76.67% of hospitals do not considering implementing electronics in clinical reminders, drug-allergy alerts and drug-drug interaction alerts. Can clearly identified most of the hospitals were not interested to implementing electronic in decision support, the reason behind that the deficiency of human knowledge about the electronic decision support system (Table 1).

Mainly telemedicine and radio frequency ID are the considerable other functionality in multimedia electronic

patient record system. According to the results obtain from the survey 93.33% of hospitals do not have required resources, but they are considering implement electronic in telemedicine and 6.67% of hospitals do not considering implementing electronic in telemedicine. 93.33% of hospitals do not have required resources, but considering implement electronic in radio frequency ID (Table 1).

#### 5. Analysis of barriers and suspected barriers to implementing a MEPRS

In order to implement a multimedia electronic patient record system, need to encounter many barriers. Same survey has been used to analyze these data as questionnaire was consisted with different parts to respond. Important barriers, suspected barriers and their level of impact in Sri Lanka show in Tables 2 and 3.

Among the hospitals most commonly cited major barriers were the amount of capital needed to purchase and

**Table 2** Important barriers and their impact level

Barriers	Major barrier	Minor barrier	Not a barrier
	% of hospitals (number of hospitals)		
The amount of capital needed to purchase and implement an MEPRS	76.67 (23)	20 (6)	3.33 (1)
Uncertainty about the return on investment from an MEPRS	23.33 (7)	36.67 (11)	40 (12)
Concerns about the ongoing cost of maintaining MEPRS	3.33 (1)	53.33 (16)	43.33 (13)
Resistance to implementation from physician	3.33 (1)	40 (12)	56.67 (17)
Lack of capacity to select, contract for and implement an MEPR system	6.67 (2)	53.33 (16)	40 (12)
Disruption in clinical care during implementation	3.33 (1)	10 (3)	86.67 (26)
Lack of adequate IT staff	3.33 (1)	10 (3)	86.67 (26)
Concerns about inappropriate disclosure of patient information	3.33 (1)	86.67 (26)	10 (3)
Concerns about illegal record tampering or "hacking"	3.33 (1)	86.67 (26)	10 (3)
Finding an MEPR system that meets your organization's needs	–	70 (21)	30 (9)
Lack of interoperable IT systems in the market place	–	26.67 (8)	73.33 (22)
Concerns about a lack of future support from vendors for upgrading and maintaining the system	–	43.33 (13)	56.67 (17)

**Table 3** The suspected barriers and their impact level

Suspected barriers	Major positive impact	Minor positive impact	No impact	Minor negative impact
	% of hospitals (number of hospitals)			
Change the law to protect EPR or for privacy and security	83.33 (25)	10 (3)	6.67 (2)	–
Objective evaluations of MEPRS capabilities and implementation experience ('consumer reports' for MEPRS)	33.33 (10)	63.33 (19)	3.33 (1)	
Technical assistance for implementation and process change	13.33 (4)	26.67 (8)	60 (18)	
Incentives for the purchase and implementation of an MEPRS (e.g. tax credits, low interests, loans, grants)	40 (12)	26.67 (8)	30 (9)	3.33 (1)
Additional reimbursement for the use of an MEPRS	–	10 (3)	90 (27)	

implement MEPRS (76.67%) and uncertainty about the return on investment (ROI) from an EPR (23.33%). Clearly identified minor barriers were concerns about the ongoing cost of maintaining an MEPR system (53.33%), resistance to implementation from physicians (40%), lack of capacity to select, contract for, and implement an MEPR system (53.33%) concerns about inappropriate disclosure of patient information (86.67%), concerns about illegal record tampering or “hacking” (86.67%) and finding a MEPR system that meets organization’s needs (70%). Some other factors were identified as not a barrier including disruption in clinical care during implementation (86.67%), lack of adequate IT staff (86.67%), lack of interoperable IT systems in the market place (73.33%) and concerns about a lack of future support from vendors for upgrading and maintaining the system (Table 2).

According to the survey, respondents have identified financial issues as the predominant barriers to adaption of multimedia electronic patient record system for Sri Lankan health sector. The costs of implementing MEPRS may include purchase price, coordination costs, and monitoring costs, negotiating costs, upgrading costs and governance costs. These costs remain biggest barriers to implementation. The high up-front financial costs of implementing MEPRS are a major barrier to their adaption. Health care sectors were far more worried about finding a system that met their needs or future obsolescence of their MEPR systems.

Lack of interoperable IT systems in the market place also considering has a barrier to the implementation of MEPR system. Interoperability as a determinant factor for adapting this system that interoperability could reduce rework by care providers. Interoperability is important because it decreases the cost of electronic health records and makes it feasible for an individual. Security and privacy also identified as a barrier. Despite of evidence to contrary, nonusers believe that there are more security and confidentiality risks involved with EPRs than paper records. There is added concern for privacy, confidentiality, and security for computerized patient information. However a communication standard like ISO 27799 can be recommended as it defines guidelines to support the interpretation and implementation in health informatics.

Insufficient incentives for implementing MEPR system also considering has a barrier. The EPRs use could be increased through financial rewards for quality improvement and for public reporting of multiple measures of quality performance. Technical support facilitated use both in the initial days and weeks of EPR and afterward. Support staff was generally perceived as knowledgeable and helpful, although some hospital noted support staff was unavailable sometimes (off hours, holidays).

Lack of technical training and support from vendors has been reported as a barrier to the adaption of MEPR system.

Therefore, the quality of vendors of MEPR systems is crucial for the acceptance of MEPR system. Inappropriate disclosure of patient information and record tampering or “hacking” also considering has a major barrier to the implementation of MEPR system.

According to the survey it reveals that security and privacy of a MEPR and purchasing the same have major positive impacts while evaluation of a MEPR has minor positive impact (Table 3).

There are some limitations during the study, when considering the Sri Lankan public health sector, the knowledge about the Multimedia electronic patient record system is very low. The people responsible for EPR systems, they don’t have clear cut idea about the EPR system and also, they don’t like to answer the questionnaire survey.

**Table 4** Questionnaire model and proposed model

Electronic functionality	Questionnaire model	Proposed model
<i>Clinical documentation</i>		
Patient demographics	✓	✓
Physician notes	✓	✓
Nursing assessments	✓	✓
Problem lists	✓	✗
Medication lists	✓	✓
Discharge summaries	✓	✓
<i>Resulting viewing</i>		
Lab reports	✓	✓
Radiology reports	✓	✓
Diagnostic test results	✓	✓
Diagnostic image results	✓	✓
Consultant reports	✓	✓
<i>Computerized provider order entry</i>		
Laboratory tests	✓	✓
Radiology tests	✓	✓
Medication	✓	✓
Consultation requests	✓	✓
Nursing orders	✓	✓
<i>Decision support</i>		
Clinical guidelines	✓	✗
Clinical reminders	✓	✗
Drug allergy alerts	✓	✗
Drug-Drug interaction alters	✓	✗
<i>Other functionalities</i>		
Telemedicine	✓	✓
Radio frequency ID	✓	✓

## 6. Proposed model of MEPRS for Sri Lankan health sector

In this questionnaire a model had been proposed and the results of the survey were analyzed according to the interest which was given by the respondents in each section to make an appropriate model for Sri Lankan public health sector (Table 4). Following propose model has been proposed by analyzing the interest of each hospital within Sri Lankan environment and statistical results which were obtained in Table 1.

## 4 Conclusion

This research has become to highlight major components of an electronic patient record system for Sri Lankan health sector. The very low level of adaption of electronic patient records in Sri Lanka was identified and majority of hospitals suggest that the law to protect EPR or for privacy has to be changed as security was a major positive impact to the implementation of MEPR system. A policy strategy based of financial assistance, interoperability, and training of technical support staff may be necessary to increase implementation of MEPR system in Sri Lanka.

## References

1. R. I. Kitney, C.F Dewey (1997). "The electronic medical record and object relational databases", *TEKRA* 97, pp. 208–214.
2. Ruth E. Dayhaff, MD, Peter M. Kuzmak and Stuart A. Frank (2003). "The Multimedia Electronic Patient Record: Current Issues", *AMIA annual symposium*, pp. 1063.
3. Dr. Ruth, E. Daahaff, Mr Peter, M. Kuzmak, and Mr. Kevin Meldrum, "Integrated multimedia patient record system", pp. 343–357.
4. Uslu, A.M., Stausberg, J. (2008). Value of the electronic patient record: An analysis of the literature. *Journal of Biomedical Informatics*, pp. 675–682.
5. Shankar M. Krishnan & Goh P.M.Y and Ye Datian (1997). "A multimedia-based medical database network system for special clinical procedures in healthcare delivery", 19<sup>th</sup> Annual International Conference on Engineering in Medicine & Biology. Institute of Electrical & Electronics Engineer.
6. G. Coatrieux, J. Puentes, L. Lecornq C. Chere Le Rest and C. Rou (2006). "Compliant Secured Specialized Electronic Patient Record Platform", *Transdisciplinary Conference on distributed Diagnostic and home healthcare*, pp. 156–159.
7. Ying Han, Jun Wei Wang, Yan Li, and Yong Xia Chen (2012). "Information Security of EHRs", *Multimedia Information Networking and Security*, pp. 896–899.
8. Michael de Ridder, Liviu Constantinescu, Lei Bi, Youn Hyun Jung, Ashnil Kumar, Jinman Kim, David Dagan Feng and Michael Fulham (2013). "A Web - based medical Multimedia Visualization interface for personal records", *Computer - Based Medical System*, pp. 191–196.
9. William B. Hanlon, Ethan F. Fener (1995). "Data Storage and Management Requirements for the Multimedia Computer-Based Patient Medical Record", pp. 11–16.
10. Mee Young Sung, Moon Suck Kim and Muung-Whun Sung, "CoMed: A Real-time Collaborative Medicine System" (2000). *Computer - Based Medical System Journal*, pp. 215–220.
11. Giovanni Dimauro, Danilo Caivano, Francesco Girardi and Marco Matteo Ciccone (2014). "The Patient Centered Electronic Multimedia Health Fascicle - EMHF", *IEEE work shop on Biometric Measurements and Systems for Security and Medical Applications (BIONS) proceedings*, pp. 61–66.
12. McNabb, David E (2008). "Research Methods in Public Administration and Nonprofit Management".
13. Singh, Kultar (2007). "Quantitative Social Research Methods", Los Angeles. CA: Sage.
14. R.I. Kitney, S. Bickram, and S. Claesen (1998). "Clinical Trials of an Electronic Medical Record System", vol. 50, pp. 201–205.



# Multiple Sclerosis Application Design with Medical Expert Evaluation

Aleksander Nygård Tonheim<sup>✉</sup> and Ankica Babic<sup>✉</sup>

## Abstract

This paper presents a high-fidelity prototype of a mobile application for patient self-management within the field of Multiple Sclerosis (MS). **Method.** Development included mixed and high-fidelity prototypes which were based on the information needs inquired from the potential user groups and their reflection on publicly available applications. The aim was to design an application to suit Norwegian user groups. It is evident from the results that the application has four selected modules: *Diary module*, *Physical activity module*, *Summary module*, and a *To-do list*. Two medical experts were interviewed at two different times at the Haukeland University hospital in Bergen, Norway, to evaluate two design iterations. The semi-structured interview consisted of two parts; one with questions on which the experts could elaborate, and one with evaluation of the prototype *msHealth* using System Usability Scale (SUS). **Results.** The results have suggested that healthcare personnel would be interested in patient data from a mobile diary, and how a patient should plan a day if suffering from symptoms. These are the two most prominent functionalities. **Conclusions.** Feedback from medical staff using SUS was promising. Several suggestions were given, as how to personalise the prototype to encourage the user to plan desired activities

and learn how to live with the disease. All these new functionalities are being implemented to reduce stress, and include the prototype application as a decision support during a patient–physician consultation.

## Keywords

Application design • Multiple sclerosis • Mobile diary  
Expert evaluation • Disease management

## 1 Introduction

MS is a chronic condition and affects the central nervous system [1]. The condition needs management through monitoring of symptoms, organising daily activities, exercise, taking daily medication and when pain and when symptoms are present. The treatment is symptomatic, and all affected by it are organising their lives according to their symptoms [2]. IT technology has been employed to deliver solutions in terms of monitoring symptoms, planning activities and general well-being. This is especially helpful during longer periods where no additional treatment is included, as it gives insight into the disease dynamics. It is important to sufferers to understand what leads them to attacks, how to prevent them and how to keep up with the healthy routines [3]. The prototype consists of four modules: *Diary module*, *Physical activity module*, *Summary module* and a *To-do list*. The main components are the *Diary module* and the *Summary module*. The user can register mood, symptoms and activities in the *Diary module*. Data registered via the *Diary module* is then represented in graphs in the *Summary module*. Data collected by users can have an important role during a patient–physician consultation as a part of the disease monitoring [4]. The prototype aims to be a tool for persons with MS to follow the disease development and provide knowledge about the disease to the users. Lastly, we will explore at how IT technology can support the disease treatment and consultations.

A. N. Tonheim (✉) · A. Babic  
Department of Information Science and Media Studies, University  
of Bergen, Bergen, Norway  
e-mail: aleksander.tonheim@gmail.com

A. N. Tonheim · A. Babic  
Department of Biomedical Engineering, Linköping University,  
Linköping, Sweden

## 2 Method

Two medical experts at Haukeland University Hospital Bergen Norway, were interviewed following two design iterations. The medical experts were MS-specialist nurse Anne Britt Skår, and neurologist chief consultant Lars Bø at the Norwegian competence centre of MS. They were selected and visited during autumn 2017 and early winter 2018 as the representatives at Haukeland when four semi-structured interviews were conducted in natural settings at the Hospital.

The first design iteration consisted of two semi-structured interviews with two parts; one with questions on which the experts could elaborate, and one with evaluation of the mixed-fidelity prototype, as presented in The Fig. 1. The evaluation of the prototype entitled *msHealth* was assessed using SUS [5], which provided quick and efficient feedback on the applications' perceived usability. However, SUS does not give feedback on specific functionalities in a system

alone. The mixed-fidelity prototype was shown on a computer simulating a mobile device via a Xcode simulator, as well as on a mobile device. The experts were able to explore the prototype during the interview.

After the second design iteration, two more semi-structured interviews with two parts were conducted. The first part was to show main functionalities of the high-fidelity prototype, presented in the Fig. 2 which was followed by a SUS evaluation. Then, specific questions were asked regarding each functionality.

## 3 Results

Feedback from medical staff was promising in both design iterations. The first design iteration provided feedback on how to modify the prototype (Fig. 1) to personalise it by encouraging the user to plan desired activities and learn to live with the disease. The second design iteration suggested

**Fig. 1** Four wireframes of the mixed-fidelity prototype used in the first design iteration

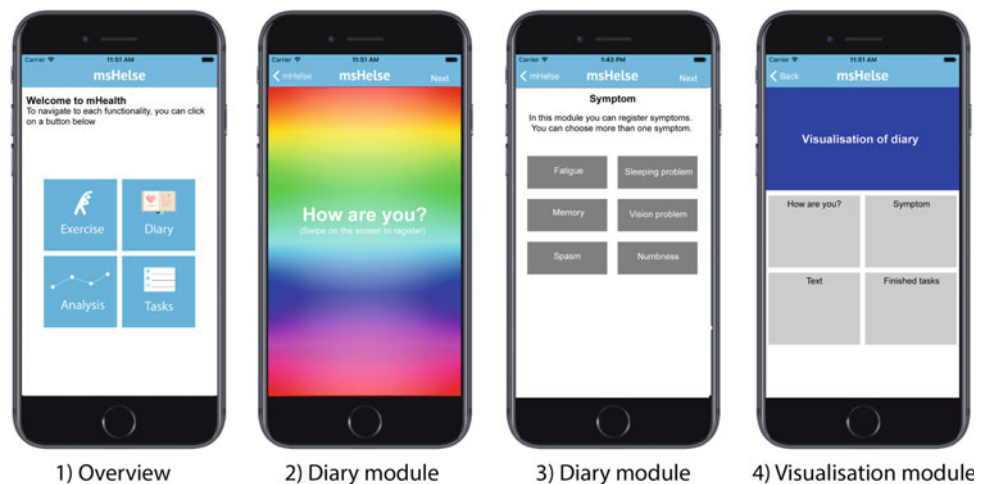
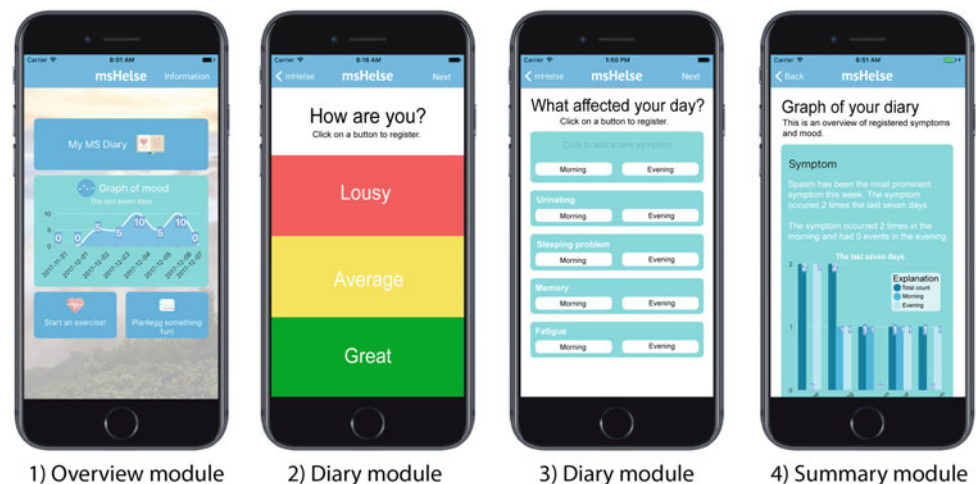


**Fig. 2** A selection of four wireframes from the high-fidelity prototype



adjustments of data collected in the *Summary module* (Fig. 2), and how to speed up the diary registration process. The feedback also focused on how the application could support in a patient–physician consultation.

### 3.1 First Design Iteration

Both experts found exercise to be generally favorable, but needs to be adjusted to symptoms. However, it could be problematic to exercise when suffering from fatigue since fatigue drains energy. The MS-specialist nurse said that exercise could also be a learning process of understanding one's own limits. Furthermore, it was important to shift the focus from managing symptoms to preventing them. Another issue is to address poor sleep, i.e. if a person sleeps poorly it is important to identify the underlying causes.

Among all the data captured by the diary, the health personnel are generally interested in the patient's symptoms and the time they occurred (i.e. morning, mid-day, night) provided in graphs. The question has been discussed whether the focus on symptoms could be beneficial for users. The neurologist advised to register symptoms in a straightforward and effective way. He would also appreciate information on preventive medicine, medication reminders, and questions of interest prior to the consultation. That in turn helps answering the question; *how has the patient been since the last consultation?*

The experts found it important that persons are living as normally as possible, but pay attention to the symptoms. In case of relapsing-remitting MS, persons must be aware of the risk of developing a possible MS-attack.

When asked if they would recommended applications to monitor the disease, only MS-specialist nurse recalled advising one patient to use SymTrac [6]. She was open minded about the effects of using such applications in managing the disease, but she had reservations about inquiring about sexual activity. In contrast, the neurologist did not recommend any applications. However, he mentioned My MS Manager [7] as a starting point for building a new Norwegian MS application.

The experts wishes were to create a mobile application containing a diary module with information about symptoms, visualisation and development of the disease since last the consultation. The MS-specialist nurse said that the application should support the patient, either before or during a patient–physician consultation. The neurologist would expect the data to be systematically summarized prior to the consultation. He would validate such information with patients' medical journals.

In the second part of the interview, both the experts provided feedback on the prototype (Fig. 1). The MS-specialist nurse said that the *Diary module 2* could use

three classifications (good, medium and poorly) answering the question *how are you?* The neurologist said that the *Diary module 2* could also consider anxiety, depression and how this is affecting symptoms. Both said that the *Diary module 3* should provide grading of symptoms, i.e. if a patient is experiencing symptoms in the morning, mid-day or evening. Moreover, the neurologist suggested to provide additional information about the disease, insurance and about living with MS.

The MS-specialist nurse rated the SUS score to be 82.5 and the neurologist gave 85 in SUS score.

### 3.2 Second Design Iteration

In the second design iteration, the medical experts provided feedback on all functionalities, specifically the *Diary module* and *Summary module* (Fig. 2).

The symptom registration in the *Diary module 1* (Fig. 2) should prompt specific questions to the user to identify the severity of the symptom. The MS-specialist nurse suggested that the symptom urinating is a general symptom and does not highlight what the actual problem is. The system should be specific and ask; *Did you feel that you needed to use the toilet, but when you came to the toilet you did not manage to urinate?* or *Did you urinate yourself and did not feel the need to use the toilet?* The neurologist also mentioned the need for the system asking specific questions to the user in addition to adding the specific time the symptom occurred. The information about the symptom with specific questions and time could support the patient during a patient–physician consultation.

The *Summary module* (Fig. 2) should be flexible enough to select and present variables that are of interest for a patient or physician. For example, by allowing users to display a specific time-period would help select interesting data the user wants to see. Another example concerns medication, if the patient received new medicine at the last appointment, then the physician could at the next consultation look at the effect the medicine had on symptoms. The neurologist said that the *Summary module* would benefit from displaying the data as a range of data, since he was more interested in the variation of symptoms rather than the total count of each symptom. Furthermore, the MS-specialist nurse suggested to move additional information about the symptom to a layer below, for example, if the user tapped on one bar in the graph, it should display the symptoms' attributes i.e. total count, occurrence at time of day and what specific problem the patient had with the symptom.

The *To-do list* should support prioritising tasks for the user and to add reminders. For example, if the user has five tasks to do one week, then the user should be able to prioritise the most important task in order to learn to plan a day

if the disease is active. Additionally, the neurologist suggested separate topics lists with different focus, such as having one list of topics the user would like to talk about with their physician at the next appointment.

The *Exercise module* should have the ability to register hikes in addition to the implemented stress-management module with the breathing exercise. The MS-specialist nurse expected the breathing exercise would have a calming effect.

For this design iteration, the MS-specialist nurse SUS score was 92.5 and the neurologist SUS score was 87.5.

---

## 4 Discussion

Both the experts were selected as the representatives of the medical specialists as highly relevant for this study. They provided consistent comments and suggestions in both design iterations to secure a detailed and relevant feedback.

Their feedback in design iteration one focused on changing the mind-set of the user, as well as on improvement on functionalities in the mixed-fidelity prototype (Fig. 1). Surprisingly enough, they reported that they generally did not recommend MS specific applications to their patients. One reason could be the lack of such applications available in the Norwegian language, and that the existing ones do not fit into the Norwegian healthcare system. There is no guideline based on application data that is acting accordingly to the Norwegian care guidelines, and how to react in an event of a possible MS-attack. Hence, a national guideline regarding IT technology is needed to define and suggest actions to the user.

The first mixed-fidelity version of the prototype did not include graphs representing data stored through the *Diary module* (Fig. 1). The neurologist said that data entries of symptoms must be represented in a good way to get a quick and effective overview, and that they should support a patient-physician consultation. Based on feedback from MS-specialist nurse, the *Diary module 1* (Fig. 1) could classify answers into three categories. This could help users to register their mood in a quick and efficient way.

In the design iteration two, the medical experts provided feedback mainly on the *Diary module* and the *Summary module* (Fig. 2). One suggested improvement concerned prompting a specific question regarding general symptoms, which could lead to describing the specific problem, rather than the general situation. By adding more specific attributes would provide another layer of information that will document the development of the disease. Graphically, this would be implemented in the *Summary module* (Fig. 2) in which a bar could be double-clicked to reveal detailed information. Such insight would be of help to the user to better understand their own situation.

The variation of symptoms was more important than displaying the count of each symptom. The neurologist found that displaying the variation of symptoms as more informative than displaying them in great detail. This is especially useful when a new medication is given to reduce or remove a symptom.

The presentation of symptoms, shown in the *Diary module 2* (Fig. 2) includes the functionality to register when a symptom occurred. There is a variation of symptoms related to MS, but not all of them might be relevant for all persons. That is why the application is not listing a long list of symptoms, so we included a functionality to enter the symptoms based on user preferences.

Overall, the medical experts suggested small changes to present information in a better way and provided solutions to make the implemented functionalities even better. One example was to allow users to prioritise tasks in the *To-do list*, and to create additional lists with topics where one could contain information the user would like to discuss with their physician. The other one was to have reminders of everyday tasks. Additionally, the *Exercise module* could be coordinated with a physiotherapist to recommend exercises to the user. This would help the users to economise the personal energy and be rational about the priorities. The exercise should not be too demanding on the body, and the right level of activity is crucial to determine the well-being of the users.

The evaluation of the system using SUS provided quick and efficient feedback on how the applications' usability was perceived. We also used a semi-structured interview to collect feedback on specific functionalities. The high SUS scores achieved in these evaluations reflect a satisfaction that the medical experts felt towards the designed outlines, which is encouraging. User input was assessed in a separate study [8]. However, the potential users would have the possibility to add their own preferences. This way, both groups could influence the design of the prototype.

---

## 5 Conclusions

All these new functionalities are being implemented to reduce stress and include the prototype application as a decision support during a patient-physician consultation. This is something that is not currently being practiced in Norway, so the future research will attempt to address the potential of the application in the patient routine care. The development will continue through one more design evaluation, taking into account the feedback from this study. Finally, intended users will have one more opportunity to evaluate the application prototype.

**Acknowledgements** The authors are thankful for neurologist Lars Bø, MD, Ph.D., and MS specialist nurse Anne Britt Rundhovde Skår, M.Sc., for sharing their expertise.

**Compliance with Ethical Standards** The authors declare that they have no conflict of interest. The study has been approved by the Norwegian data protection official (NSD). All participants signed an informed consent form.

---

## References

1. Ljøstad, U., Mygland, Å., (2016). Diagnostikk av MS og Behandling av MS. Retrieved January 17, 2018, <http://nevro.legehandboka.no/handboken/sykdommer/demyeliniserende-sykdommer/>
2. Trumbic, B. et al., (2017). Is the Choosing Wisely® campaign model applicable to the management of multiple sclerosis in France? Retrieved January 30, 2018, <http://www.ncbi.nlm.nih.gov/pubmed/29128151>
3. Tacchino, A. et al., (2015). A New App for At-Home Cognitive Training: Description and Pilot Testing on Patients with Multiple Sclerosis. JMIR mHealth and uHealth. Retrieved May 28, 2017, <http://www.ncbi.nlm.nih.gov/pubmed/26323749>
4. Engelhard, M.M. et al., (2017). Remotely engaged: Lessons from remote monitoring in multiple sclerosis. International Journal of Medical Informatics. Retrieved January 31, 2018, <http://www.ncbi.nlm.nih.gov/pubmed/28241935>
5. Brooke, J. (2013). SUS: A Retrospective, 8(2), 29–40. Retrieved December 2, 2017, <http://www.usabilityprofessionals.org>
6. Novartis UK, (2015). SymTrac MS. Retrieved January 30, 2018, <http://www.symtrac.com/ms/>
7. Multiple Sclerosis Association of America, (2017). Retrieved January 30, 2018, <http://mysaa.org/msaa-community/mobile/>
8. Tonheim, A., Babic, A., (2018). Assessing Information Needs for a Personal Multiple Sclerosis Application. MIE, Medical Informatics Europe. Gothenburg, Sweden. 24–26 April 2018 Accepted for publication.



# Design Features for Usable Mobile Electronic Data Capturing Forms: The Form Developers' Perspective

Alice Mugisha<sup>1</sup>, Peter Wakholi<sup>2</sup>, and Ankica Babic<sup>3</sup>

## Abstract

Mobile Electronic Data Capturing Forms (MEDCFs) are electronic form applications that are primarily used for data capture using mobile devices in the place of paper-based routines. Translating paper-based forms to MEDCFs presents several usability challenges due to the design limitations of using mobile devices. The main objective of this study therefore was to define the most important design features that need to be considered when developing MEDCFs. Fifteen mobile form developers each received a semi-structured questionnaire via Email. The questions were derived from sub heuristics for mobile applications and were based on features that are common to forms such as form content, form layout, input type, error handling and form submission. The study identified the eighteen most important design features that all MEDCFs should have in order to provide a usable tool. These include feedback, logic implementation, form navigation, data input format requirements, unique identification, language translation and error handling among others. With a shorter design feature checklist specific to MEDCFs, and collaboration efforts amongst the various stakeholders, it will be possible to develop usable mobile electronic data collection forms.

## Keywords

Mobile Electronic Data Capturing Forms • Usability Design features • Form developers

## 1 Introduction

Mobile Electronic Data Capturing Forms (MEDCFs) are being used to collect health data in rural settings during health surveys, surveillance and patient monitoring. These forms are created using customizable electronic data collection (EDC) tools and are usually a representation of hard copy questionnaires designed by form developers, based on the array of functionalities or features provided by the EDC tools [1]. Form developers are responsible for creating mobile forms through the customization of EDC tools, and therefore experience the design limitations in some of these tools. In addition, they are responsible for addressing the usability challenges as reported by the data collectors or field users on a day to day basis or during the piloting and training phases. Electronic forms used to collect health data if poorly designed may result in data entry challenges which in turn may contribute to medical errors [2]. This can seriously impact the level of data quality and thus affect the care provided.

These electronic forms are used by field staff or users who are usually members of rural populations with very little experience in the use of computer or mobile technology [3] and are therefore likely to have usability challenges. These challenges, stemming from interface design or by factors related to the type of data being collected such as a number's length, type, magnitude or font appearance, etc. affect the accuracy, usefulness and applicability of data collected [4]. Thus, designing forms for mobile devices needs to address the limitation of display size/screen, which can have an impact on users' performance for tasks like browsing, information retrieval, readability or even target selection, which emphasize the risk of error increase during data entry [5]. This leads to incorrect choice selection and wastage of time in additional scrolling activities which is also common with smaller interfaces [6, 7]. Additionally, the keyboard size or character setting are limited irrespective of the users' finger size [6, 8], and the content.

A. Mugisha (✉) · A. Babic  
University of Bergen, 5007 Bergen, Norway  
e-mail: lncs@springer.com; mugishaalice@gmail.com

A. Mugisha · P. Wakholi  
Makerere University, Makerere hill road, Kampala, Uganda

A. Babic  
Linköping University, 581 83 Linköping, Sweden



Various studies have shown that electronic data collection using is mainly hinged on five different constructs namely form content, form layout, the input type, error handling and form submission [9–11]. Form content is usually questions and labels or fields of text entry [11]. The form layout shows how the form is presented on the mobile user interface, and this influences the way a user interacts with it. Designs, positions and lengths of the labels and input fields, the date format, number of columns and buttons among others all define the layout of the form [11]. The input type refers to the way data is captured or entered into the form and therefore which input type is most appropriate for a given case for example check boxes, radio buttons etc. Care should always be taken not to confuse users by using many different input types in one form [12]. During error handling, users need to be guided as quickly and as error free as possible during the process of filling forms from the start by explaining the restrictions in advance [11]. This includes formatting and content rules such as minimum length of numbers or words, entry formats, putting help instructions, etc. being communicated well in advance. Sometimes errors are unavoidable, and therefore users need to be helped to recover from them as quickly and as easily as possible by clearly stating what the error is and how it can be corrected in a familiar language [13, 14]. Form submission is more concerned with what happens after the user has pressed the submission button in order to avoid multiple submissions in cases of system response delays [14].

This study therefore seeks to determine the minimum viable design features that can support the development of Mobile Electronic Data Capturing Forms. This is because of the big sizes of checklists that exist for mobile application development such that the form developers are torn in between what to include in the mobile forms. Further still, there is a need to improve on the user experience using these design features as guidelines during data collection so as to improve on the quality of data.

## 2 Methods

The study sought to determine the most important design features that must be considered when developing mobile electronic data collection forms. An electronic semi-structured questionnaire was created using Survey Monkey, an online data collection tool and was distributed using Email to fifteen ( $n = 15$ ) mobile form developers between November 2016 and January 2017. The questionnaire comprised of 55 semi structured questions, which were derived from literature on mobile application heuristics

[15–17] and some from best practices [18]. The questions were categorized under Nielsen's 10 usability heuristics [19].

The form developers in this study included a research associate, an epidemiologist, a systems analyst, a monitoring and evaluation specialist, a software developer, a database manager, a designer, programmer, a design consultant, health informaticians ( $n = 2$ ), an IT professional and software engineers ( $n = 2$ ). These form developers were all involved in developing mobile forms for collection of health data using various software like Open Data Kit (ODK) ( $n = 9$ ), District Health Information Software (DHIS2) ( $n = 6$ ), Open Medical Records System (OpenMRS) ( $n = 5$ ). Other applications included mUzima ( $n = 2$ ), Medic Mobile Toolkit, CSpro, Survey CTO, koBo Toolbox, Survey Monkey and OpenXData. The form developers had developed mobile forms for collection of health data for varying periods of time, ranging from 1 year to 8 years.

We received responses from fourteen ( $n = 14$ ) form developers, after 1 opted out. We put our findings in an excel sheet, categorized the frequencies and determined the number of design features for each category.

## 3 Results

Several design features had a high frequency of agreement from the form developers. In particular, eighteen design features had maximum frequency score of 80–100% and were thus referred to as the most important features to consider during form development. Fifteen design features scored between 60–79%, 18 design features scored between 40–59% and only 3 scored 40%.

The results (refer to Table 1) indicate the eighteen most important design features in their order of ranking starting from the one with the highest frequency of agreement to the least. *Feedback* was considered to be the most important feature especially when a user completes filling the form, and it was equally important to immediately inform the user in case an error is committed.

It is important for the *error message* to be clear and visible enough, therefore where it is positioned, the content and color matter. Having a *unique identifier* was very important, but it does not have to be automatically generated *language translation* was also considered to be very important however access of the translation anywhere in the form was not necessary. It was also found to be very important for the user to be shown how to enter the data by including the *data input requirements* just below the text box in order to reduce on the error rates. *Skip logic implementation* was also found to be

**Table 1** Form developers' most important design features

Construct	Design feature
Feedback	Feedback is any kind of message a user receives after completing an activity or task in the form. The user should be able to receive feedback after saving, completing or submitting the form
Error handling	Error handling is concerned with handling errors when they occur. The user should be informed immediately in case an error is committed using an error message. This should be visible, should clearly indicate that an error has occurred, what the mistake is and how it can be corrected in the shortest possible time
Logic implementation	Logic implementation is meant to ensure that users only access what is relevant for them to answer based on the previous answer. Skip and filter logic should be automatically implemented
Colour	The background colour on the screen should not interfere with the visibility of the questions in the form. Care must be taken to understand whether the data collection will happen indoors or outdoors
Form navigation	Navigation is the ability to move through the form in a forward and backward manner. Swiping is the most preferred way of navigating the mobile form
Question presentation	Question presentation is concerned with the way questions are presented in the form. The number of questions on the screen should be limited, with big text size, must be logically arranged and consistently numbered
Unique Identification	A unique identifier is a special number that is assigned to a person e.g. a patient and is not shared with any other person. There should be a unique identifier to differentiate between the different entities in the form
Presentation of tables	Tables may be used in the form when there is a need to capture data about an event in a repeated manner. Thus the fields in the tables should be clearly labelled
Terminologies	There is need for consistent use of terminologies throughout the form. This will help the users not to misinterpret questions during data collection
Language translation	In cases where the questions in the form have to be translated into a language the user understands, the translated language should be a true representation of the original language of the form
Data input format requirements	Data input requirements are meant to ensure that the user enters the data in the appropriate format with ease, thus the requirements must be visible to the user. There should also be recognition of specific data input types and automatic adjustment of input modes where applicable before the user attempts to enter data

very important as it helps reduce on the crowding of the screen by presenting only what the user needs to see at the time.

## 4 Discussion

This study produced the 18 most important design features as agreed upon by the form developers that need to be considered in order to design a minimum viable mobile data collection form. These include; the time in which *feedback* is received by the user, the way *error messages* are presented and the *implementation of logic*. *Colour* contrasts and the way *questions are presented* on the screen are equally important to the form developers. These mentioned features solely depend on the discretion of the form developers to implement. For example the text in the error message may not be very clear to the user, or the skip logic in some of the questions may be omitted during form development. Thus in this case the onus is on the form developer to implement the features appropriately. Swiping as a *form of navigation*, assigning *unique identification*, *tables* and including *data input format requirements* in the form was also considered to be very important. However, these are dependent on the EDC tool. Consistent use of *terminologies* and appropriate *language translation* were also considered to be very

important during form development, but it is the implementers' responsibility to ensure that these are functional. These design features are however quite novel to the developers, implementers and users in the rural parts of Uganda and Africa, and are thus not often considered during form development.

It is also important to note that the effect of these design features on the usability of the forms may not be known or is not often obvious and thus considered by the developers. This is because the major role of the form developers is to create forms, and they are seldom in position to use the forms they have created to collect data. Therefore this list of design features can be a very good support to pay attention to the usefulness of the forms. Some of the design features are already existent in some but not in all EDC software. An example is the use of unique identifiers to differentiate between entities and the language translation ability by the mobile forms. Open Data Kit software has the ability to handle language translation, which is not possible with some EDC tools like mUzima. However, unique identification of entities is still a challenge in ODK because the system cannot derive its own unique identification but relies on those that are entered by the users, which creates a risk for errors.

Generally, the functionalities and design capabilities vary across EDC tools, some of which the form developers that

participated in this study have not used to develop forms. These design capabilities affect the way the forms are created and presented. Thus it may have been a challenge to put a preference on a feature the form developers had never implemented. For example the table presentation had some of the lower scores possibly because not many EDCs have provisions for including tables in the data collection forms. In addition, some of the features like the questions are given by the implementers and therefore the form developers have no control over that for example, the length of the form, the type of questions, language translation, etc. This can be considered as one of the limitations to this study. However, fourteen developers is a significant number of evaluators and the resulting findings could have some bearing on the form development.

This study has thus identified design features that the surveyed form developers found most important based on their experience and judgment. A different set of developers may have suggested a somewhat different list of most important features to consider for developing the forms. The implementation of these basic interaction features during form development could improve the users' experience and accuracy of data input. For example controlling the scrolls provides a sense of control and a manageable amount of data to enter.

## 5 Conclusion and Recommendation

Out of the 55 possible design features suggested by the literature, 18 were found to be most relevant by the fourteen form developers that participated in the study. Findings from the study suggest that usability of MEDCFs cannot be addressed by form developers alone. Other stakeholders like the software developers who develop the EDC software and the project implementers who are in charge of the content in the questionnaire need to come on board. In addition, it is still important to know what the actual users or data collectors would prefer, besides the various stakeholders in order to improve their data collection experience.

We therefore recommend that data collectors' preferences are collected and addressed. More so, there needs to be collaboration between the different stakeholders in order to develop usable mobile data capturing forms. This is because some of the usability challenges are due to design limitations in the features and functionalities of the EDC tools while others are caused by the content in the questionnaires which form developers cannot address during development of the MEDCFs.

**Ethics** The authors declare that they have no conflict of interest.

## References

1. Pakhare A, Bali S, Kalra G. Use of mobile phones as research instrument for data collection. *Indian Journal of Community Health*. 2013;25(2):95–8.
2. Kushniruk AW, Triola MM, Borycki EM, Stein B, Kannry JL. Technology induced error and usability: the relationship between usability problems and prescription errors when using a handheld application. *International journal of medical informatics*. 2005;74(7):519–26.
3. King C, Hall J, Banda M, Beard J, Bird J, Kazembe P, et al. Electronic data capture in a rural African setting: evaluating experiences with different systems in Malawi. *Global health action*. 2014;7(1):25878.
4. Tu H, Oladimeji P, Li Y, Thimbleby H, Vincent C, editors. The effects of number-related factors on entry performance. *Proceedings of the 28th International BCS Human Computer Interaction Conference on HCI 2014-Sand, Sea and Sky-Holiday HCI; 2014: BCS*.
5. Haller G, Haller DM, Courvoisier DS, Lovis C. Handheld vs. laptop computers for electronic data collection in clinical research: a crossover randomized trial. *Journal of the American Medical Informatics Association*. 2009;16(5):651–9.
6. Jones M, Marsden G, Mohd-Nasir N, Boone K, Buchanan G. Improving Web interaction on small displays. *Computer Networks*. 1999;31(11):1129–37.
7. Jones S, Jones M, Marsden G, Patel D, Cockburn A. An evaluation of integrated zooming and scrolling on small screens. *International Journal of Human-Computer Studies*. 2005;63(3):271–303.
8. Ehrler F, Haller G, Sarrey E, Walea M, Wipfli R, Lovis C. Assessing the usability of six data entry mobile interfaces for caregivers: a randomized trial. *JMIR human factors*. 2015;2(2).
9. Bargas-Avila JA, Brenzikofer O, Tuch AN, Roth SP, Opwis K. Working towards usable forms on the worldwide web: optimizing multiple selection interface elements. *Advances in Human-Computer Interaction*. 2011;2011:1–5.
10. Bargas-Avila JA, Brenzikofer O, Tuch AN, Roth SP, Opwis K. Working towards usable forms on the world wide web: optimizing date entry input fields. *Advances in Human-Computer Interaction*. 2011;2011:1–8.
11. JA B-A, Brenzikofer O. Simple but crucial user interfaces in the world wide web: introducing 20 guidelines for usable web form design. *Croatia: InTech*; 2011.
12. Miller S, Jarrett C. Should I use a drop-down? Four steps for choosing form elements on the web. *Effortmark Limited*. 2001;30.
13. Nielsen J. Error message guidelines. *Nielsen Norman Group*. 2001:06–24.
14. Linderman M, Fried J. *Defensive Design for the Web: How to improve error messages, help, forms, and other crisis points*. Carmel, IN: New Riders Publishing; 2004.
15. Pierotti D. *Heuristic evaluation-a system checklist*. Xerox Corporation. 1995.
16. Thitichaimongkhol K, Senivongse T, editors. *Enhancing Usability Heuristics for Android Applications on Mobile Devices*. WCECS'16; 2016, October 19–21; San Francisco, USA: Springer.
17. Yáñez Gómez R, Cascado Caballero D, Sevillano J-L. Heuristic evaluation on mobile interfaces: A new checklist. *The Scientific World Journal*. 2014;2014:1–19.
18. Tan CC. *Mobile form design strategies 2011* [updated March 15. Available from: <http://www.uxbooth.com/articles/mobile-form-design-strategies/>.
19. Nielsen J. *Usability engineering*. San Francisco, CA: Morgan Kaufmann; 1994.

# Task-Based Approach Recommendations to Enhance Data Visualization in the Kenya National Health Data Warehouse

Milka Gesicho<sup>✉</sup> and Ankica Babic<sup>✉</sup>

## Abstract

The health sector still lags behind in development of data visualization tools due to the complex nature of health data. Furthermore, due to the volume, velocity and veracity of health data consolidated from various sources, re-presenting them in a way that promotes decision-making while supporting various aspects of human interaction becomes even more challenging. With the plethora of research on improving visualization of integrated health data, focus is shifting from simple charts to novel ways of data re-presentation. Literature also suggests the need for an in-depth exploration on aligning visualizations to tasks, context, and appropriate cognition aspects. We conducted a field study at the Kenya National Health Data Warehouse (KNHDW) in the month of July 2017 to identify the techniques and practices used to visualize data. Two salient tasks performed in the KNHDW were identified in order to explore possibilities of visualizing the data. We then adopted a task-based approach in developing recommendations based on categorical data. These recommendations include (1) use of visualization approaches that promote proper space utilization, and (2) use of leverage points that influence aspects of human cognition process. In addition, the proposed visualizations enable potential users to get a new experience with the data and explore possibilities for visualization. Nevertheless, these recommendations are by no means exhaustive but aim at encouraging best practice in health data visualization in the KNHDW.

## Keywords

Data visualization • Health data warehousing  
Recommendations

## 1 Introduction

Health data is complex due to its high volume, low veracity, great variety, and high velocity [1]. Data visualization plays a key role in deriving meaning from health data. Nevertheless, the health sector still lags behind in development of data visualization tools [1]. Numerous tools to visualize data exist. However, most of these tools use simple charts such as bar graphs, scatter plots, and pie charts, that only represent few facets of data [1]. It is important that various facets of data are included and more so ensuring that the elements of interaction design such as cognition are critically considered. This will further assist in promoting understanding of health data, and decision-making. Currently, the Kenya National Health Data Warehouse (KNHDW) relies on off-the-shelf data visualization tools to perform various visual analysis tasks [2]. Simple visualizations such as choropleth maps, bar charts, and scatter plots, are provided by majority of off the shelf tools [3, 4]. Nevertheless, the use of simple visualizations enable only representation of few facets of data, hence less effective for complex tasks [1]. Thus, researchers are now proposing for more innovative approaches [5–10]. Furthermore, in Low- and Middle-Income Countries (LMICs) where resources are limited and health system interventions are based on funding, innovative approaches that are to be considered ought to be cost effective.

An attempt by the KNHDW to perform visual analysis on various facets of data simultaneously, in some cases leads to crowding of the dashboard. Hence, this can result to information overload which limits the chances of using the data effectively for decision-making [11]. With the plethora of research on optimal approaches, techniques, frameworks and designs to improve information visualization for integrated

M. Gesicho (✉) · A. Babic  
University of Bergen, Fosswinckels Gate 6, 5020 Bergen, Norway  
e-mail: milcagesicho@gmail.com; lncs@springer.com

A. Babic  
Linköping University, 58183 Linköping, Sweden

health records [1, 5, 10], [12–15], focus should also be directed to ensure that cognitive aspects are considered. This paper provides recommendations on approaches to leverage cost effective visualizations while considering cognitive aspects. The scope of this paper is limited to representation of categorical data from integrated health records and does not involve approaches based on diagnostic visualizations that use genomic data, in-depth aspects of visual analytics nor technical aspects of visualization. This is because the latter does not apply in the objectives for this paper.

## 2 Methods

The study was conducted in the KNHDW in order to identify the techniques and practices used to visualize data. This was done in July 2017 through shadowing during work routines and interviews with the officials in charge. In addition, to develop the recommendations, we adopted a task-based approach. This was based on the concept of task abstraction, which is considered a possible solution in dealing with challenges that accompany visualization of large volumes of data [15], as is the case with data warehouses. Furthermore, development of the visualizations was informed by a pattern-based framework proposed by Sedig and Persons [16]. The framework promotes the use of novel-design approaches [1]. Given that our focus was on categorical data, our aim was to ensure that the various relations in the data can be viewed in parallel at a glance. Further still, the human cognition framework was used to inform the recommendations in order to promote consideration of human factors in visualization [17].

## 3 Results

The field study identified two most frequent tasks performed in the KNHDW: visualization of patient aggregated data and county distribution of EMRs by implementing partners. The recommendations are thus based on visualization of these tasks.

### 3.1 Tasks: Distribution of EMRs and Patient Health Outcomes

A data warehouse entails consolidation of data from disparate sources. The sources of data for the KNHDW are EMRs that are distributed across 650 public health facilities and this number keeps increasing with implementation [18]. It is important that stakeholders who are also users of the KNHDW know the number of EMRs implemented and the supporting implementation partners. This information is

stored in the KNHDW. Hence, the visual analysis tasks performed include but are not limited to; identifying geographic location of EMRs, implementing partners supporting various EMRs and performance of the implemented EMRs. For each of these tasks, the number of EMRs are also identified. The other salient task includes visual analysis of the distribution of HIV-patients and their health outcomes.

### 3.2 Recommendations

#### (a) Use of visualization approaches that promote proper space utilization

A task that involves visualizing the distribution of EMRs and the respective implementing partners or patient categorical data such as age, CD4 count, and viral suppression may result to crowded dashboards when attempting to display various facets of the data. Currently, 2D choropleth maps, bar charts, pie charts, and filter parameters used simultaneously to re-present this information often leads to crowded dashboards and mental overload. Figure 1 demonstrates exploration of a proposed approach that utilizes space and promotes high level cognitive functioning and decision-making. Users are able to view at a glance the main EMRs (A to D) in relation to the supporting implementing partners and the distribution of EMRs. For instance, partner 7 supports EMR E and F, distributed in different counties in Kenya. Figure 2 on the other hand reveals ages 24–49 as having majority of people living with HIV (PLHV). In addition, we are able to view at a glance that CD4 count was not recorded for majority of the patients and suppression rate was low. Moreover, we are able to view at a glance the number of patients that are alive, dead, left-to-follow-up (LTFU) or those defaulted from treatment (default). The use of open source tools [19] to develop these visualizations makes it cost effective.

#### (b) Identify and use leverage points that influence aspects of human cognitive process

The current approach used in the KNHDW requires that users compare results from a bar or pie chart to a choropleth map. This approach uses color as a stimulus feature, within the change-detection flicker paradigm. The flicker paradigm entails having users detect the original image alternating with the modified image [17]. Areas on the map that represent the same color on the pie chart or bar chart are likely to interpret a relation. Failure to blend the colors such that same color is coded on related visualizations increases the chances of change blindness, which is the inability to see the difference in change [17]. To mitigate the challenges on this



**Fig. 1** County distribution of EMRs supported by implementing partners

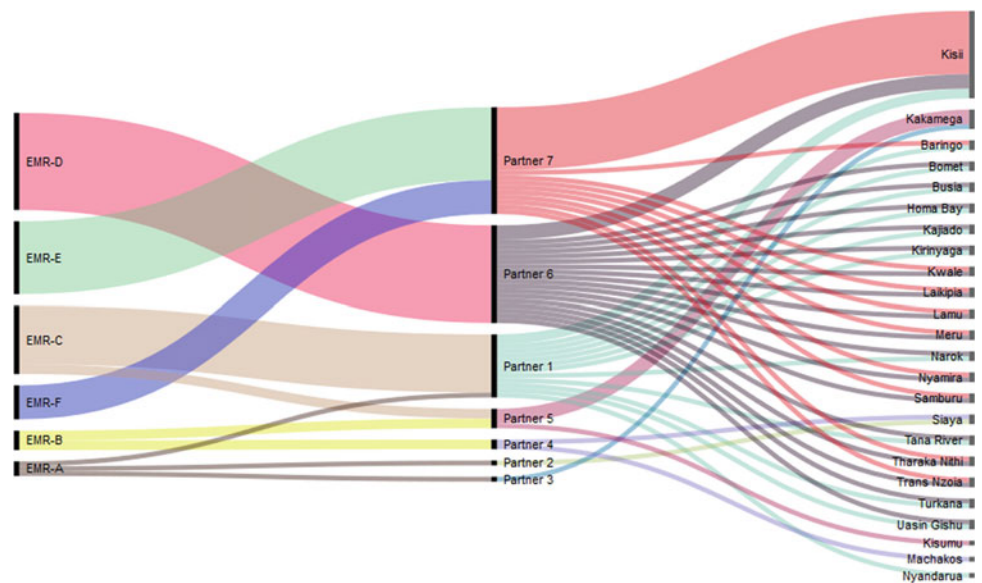
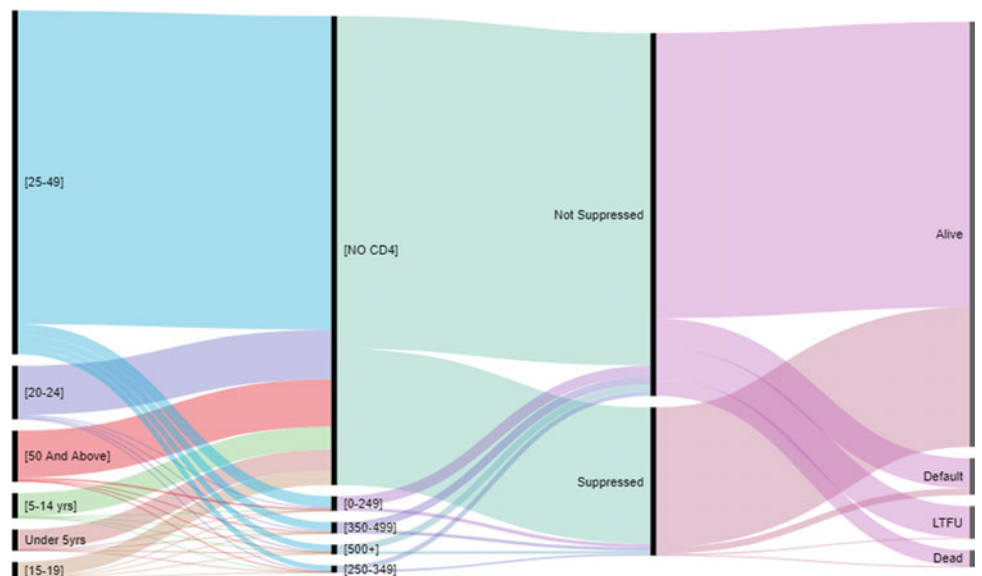


**Fig. 2** Patient outcomes in terms of disease suppression and survival rate



task, we propose use of aspects of human cognition influenced by using leverage points such as facilitating chunking and aiding reasoning with mental models as illustrated in Fig. 1 and Fig. 2 respectively.

Elements are grouped by color, and continuity, which is a gestalt principle of grouping, in order to promote chunking. This aims at providing retrieval cues for long term memory [17].

#### 4 Discussion

Effectiveness of a data visualization used for a particular task, context, and paired with appropriate cognitive aspects promote better understanding of the data, knowledge

extraction, and better decision-making [13]. Nevertheless, this has been given minimal emphasis especially due to the fact that one shoe does not fit all. In this paper, we employ a task-based approach by selecting two routine tasks performed in the KNHDW. We then illustrate the use of cost effective sophisticated data visualization approaches and highlight cognitive aspects that we think are salient in order to promote efficacy of identified tasks. In addition, complex health data can be re-presented using a similar approach. Nevertheless, in some cases background knowledge is necessary to interpret the visualizations.

In addition, the discrete nature of categorical data make it a challenge in visualization hence providing a good case for our recommendations [20]. Methods such as parallel coordinates work well with continuous data and might be less



efficient when applied to categorical dimensions [20]. Hence, we chose alluvial diagrams (inclined to the branch pattern) [16] due to their suitability in re-presenting relations in categorical data [21]. Alluvial diagrams adopt the layout of parallel coordinates but use bins instead of axes, which have ranges of values. In addition, they are suitable for re-presenting relations in categorical data and provide a high-level summary and quick overview of the data. Furthermore, they enable potential users to get a new experience with the data and explore possibilities for visualization. Nevertheless, the proposed recommendations are by no means exhaustive but aim at encouraging best practice in health data visualization in the KNHDW.

## 5 Conclusion

As LMICs begin to consolidate and represent health data from multiple sources, recommendations that promote the use of sophisticated data visualization approaches that are cost effective and promote decision-making play an important role. We have demonstrated how visualization could be applied to tasks that are performed routinely and might be of interest to the users of the KNHDW.

**Acknowledgements** This work was supported in part by the NORHED program (Norad: Project QZA-0484). The content is solely the responsibility of the authors and does not necessarily represent the official views of the Norwegian Agency for Development Cooperation. All authors report no conflicts of interest.

## References

- O. Ola and K. Sedig, "Beyond simple charts: Design of visualizations for big health data.," *Online J. Public Health Inform.*, vol. 8, no. 3, p. e195, 2016.
- MeSH Consortium, "Kenya-HIV-CBS-SWOT-Case-Study\_MeSH-Consortium (3)," 2016.
- L. N. Carroll, A. P. Au, L. T. Detwiler, T. chieh Fu, I. S. Painter, and N. F. Abernethy, "Visualization and analytics tools for infectious disease epidemiology: A systematic review," vol. 51. Academic Press, 2014, pp. 287–298.
- L. Zhang and S. Mittelst, "Visual Analytics for the Big Data Era – A Comparative Review of State-of-the-Art Commercial Systems," in *Visual Analytics Science and Technology (VAST), 2012 IEEE Conference on*, 2012, pp. 173–182.
- A. Rind, "Interactive Information Visualization to Explore and Query Electronic Health Records," *Found. Trends® Human-Computer Interact.*, vol. 5, no. 3, pp. 207–298, 2013.
- R. Kosara and S. Miksch, "Visualization methods for data analysis and planning in medical applications.," *Int. J. Med. Inform.*, vol. 68, no. 1–3, pp. 141–53, Dec. 2002.
- O. E. Sheta and A. N. Eldeen, "The Technology of Using a Data Warehouse to Support Decision-Making in Health Care," *Int. J. Database Manag. Syst.*, vol. 5, no. 3, pp. 75–86, Jun. 2013.
- S. Faisal, A. Blandford, and H. W. Potts, "Making sense of personal health information: Challenges for information visualization," *Health Informatics J.*, vol. 19, no. 3, pp. 198–217, Sep. 2013.
- V. L. West, D. Borland, and W. E. E. Hammond, "Innovative information visualization of electronic health record data: a systematic review," *J. Am. Med. Informatics Assoc.*, vol. 22, no. 2, pp. 330–9, 2014.
- E. Y. Gorodov, V. V. Gubarev, V. V. Gubarev, and evich, "Analytical Review of Data Visualization Methods in Application to Big Data," *J. Electr. Comput. Eng.*, vol. 2013, pp. 1–7, Nov. 2013.
- M. Q. Wang Baldonado, A. Woodruff, and A. Kuchinsky, "Guidelines for using multiple views in information visualization," in *Proceedings of the working conference on Advanced visual interfaces - AVI '00*, 2000, pp. 110–119.
- B. Shneiderman, C. Plaisant, and B. W. Hesse, "Improving healthcare with interactive visualization," *Computer (Long Beach Calif.)*, vol. 46, no. 5, pp. 58–66, May 2013.
- M. Blevins, F. H. Wehbe, P. F. Rebeiro, Y. Caro-Vega, C. C. McGowan, and B. E. Shepherd, "Interactive data visualization for HIV cohorts: Leveraging data exchange standards to share and reuse research tools," *PLoS One*, vol. 11, no. 3, p. e0151201, Mar. 2016.
- Measure Evaluation, "Data Visualization That Works Facilitating HIV Program Targeting : Case Examples and Considerations Data Visualization That Works Targeting : Case Examples and," *Meas. Eval.*, no. April, 2016.
- H. Helwig, "The Future of Big Data," in *The Future of Big Data Visualization*, 2017, no. February.
- K. Sedig and P. Parsons, *Design of Visualizations for Human-Information Interaction: A Pattern-Based Framework*, vol. 4, no. 1. 2016.
- R. E. Patterson et al., "A human cognition framework for information visualization," *Comput. Graph.*, vol. 42, pp. 42–58, Aug. 2014.
- Centres for disease control and prevention Kenya, "Annual Report 2015," 2015.
- M. Mauri, T. Elli, G. Caviglia, G. Uboldi, and M. Azzi, "RAWGraphs: A Visualisation Platform to Create Open Outputs," in *Proceedings of the 12th Biannual Conference on Italian SIGCHI Chapter*, 2017, p. 28:1–28:5.
- F. Bendix, R. Kosara, and H. Hauser, "Parallel sets: visual analysis of categorical data," in *IEEE Symposium on Information Visualization*, 2005. INFOVIS 2005., pp. 133–140.
- M. Rosvall and C. T. Bergstrom, "Mapping Change in Large Networks," *PLoS One*, vol. 5, no. 1, p. e8694, Jan. 2010.

# Design of a Smart Multimodal Earthquake Response Mobile Application

Allya Paramita Koesoema, Yoke Saadia Swito, Annisa Riyani, Masyithah Nur Aulia, Dody Qori Utama, and Tauhid Nur Azhar

## Abstract

Indonesia is located in the Pacific Ring of fire, putting it under constant risk of natural disasters such as volcanic eruptions, earthquakes, and tsunamis. Earthquakes are one of the biggest threat of natural disasters in Indonesia and can strike anytime in any area. A key example is the 2004 Aceh earthquake, which caused a large tsunami, killing more than 160,000 people and destroyed more than 200 shops and homes. While Indonesia has significantly improved its disaster mitigation systems in the past decade, problems remain. Seismological stations are still relatively few and in between, community readiness and resilience for earthquakes remains low, and response activities are often hampered by lack of equipment, such as for finding potential survivors trapped in rubble. In order to help alleviate these issues, this paper describes the design of a smart multimodal earthquake response mobile application. The proposed system has four main functionalities, namely (1) broadcast of earthquake alert to mobile phones from the local earthquake measurement centre, (2) smart voice activated interactive guide to guide community members on how to react to an earthquake event and arrive to a safe place based on their current situation, (3) A system to search for trapped survivors based on Bluetooth and wifi hotspot emitted by survivors, and (4) recording of earthquake waves based on mobile phone accelerators to be used to build a more granular geospatial database on earthquake features. The system implements machine learning algorithm, utilizes voice,

picture and text activated interface to match any situation's need, and basic augmented reality to help guide users to a safe place.

## Keywords

First keyword • Second keyword • Third keyword

## 1 Introduction

Indonesia is an archipelago situated in the Pacific Ring of fire, which makes it especially prone to natural disasters such as volcanic eruptions, earthquakes, and tsunamis. A major example was the 2004 Aceh earthquake, which caused a large tsunami, killing more than 160,000 people and destroyed more than 200 shops and homes. Given this high potential and risk of natural disasters, Indonesia has significantly improved its disaster mitigation systems in the past decade. This include infrastructure improvements, such as national tsunami detection systems, as well as education and socialization for the community. However, problems remain. In terms of detection, seismological stations are still relatively few and in between when compared to the breadth of area of Indonesia. Moreover, community readiness and resilience for earthquakes and other disaster events are still low. In the event of disaster, a significant number of the community is not exposed enough to the education and training effort to respond accordingly. Finally disaster response actions are often still hampered by insufficient infrastructure, organization, and equipment, such as for finding potential survivors trapped in rubble. For example, quick evacuation of quake survivors trapped under buildings are difficult, due to obstacles in finding and excavating the site. To conclude, Indonesia still have significant limitations in managing the readiness, early detection, risk mitigation, response and rehabilitation from disasters.

In order to help alleviate these issues, this paper describes the design of a smart multimodal earthquake response.

A. P. Koesoema (✉) · Y. S. Swito  
Indonesian EHealth and Telemedicine Society,  
Bandung, Indonesia  
e-mail: apkoesoema@gmail.com

A. P. Koesoema · Y. S. Swito · A. Riyani · M. N. Aulia  
D. Q. Utama  
Biomedical Engineering, Institut Teknologi Bandung,  
Bandung, Indonesia

T. N. Azhar  
UNISBA, Bandung, Indonesia

It uses an integrated mobile based system that integrates input from the national bureau of meteorology (BMKG) and other data sources, and includes both communities and responder teams as their users. This system is also multi-modal, utilizing input from different communication channels (cellular signals, wifi and Bluetooth), as well as mediums (text, visual and audio) to provide user service. The proposed system has several intended functions, including an alert system for communities, an adaptive voice activated interactive guide to help people respond to earthquakes, a system to help search for trapped survivors, and a crowd-based geospatial database on earthquake features using data from users' mobile phone accelerometers in quake situations.

This system is aimed to increase the community resilience and reduce the impact of earthquake disasters in Indonesia, including increasing general community knowledge and responsiveness, increasing disaster respondent capacity as well as the distribution of earthquake data through outsourcing methods.

---

## 2 Existing Research and Practice

There is a rich research and empirical literature on earthquake detection and risk mitigation systems. These include, among others, earthquake detection systems, community resilience studies, as well as response/risk mitigation systems. In this section, we highlight some recent developments in aspects relevant to our design.

In general, most public earthquake detection system in developing countries, including Indonesia, still rely on a limited number of specifically located seismograph stations, although there has been recent development of crowd-sourcing and other alternative methods of earthquake detection systems [7, 8]. With regards to increasing community knowledge to improve Resilience to Earthquakes and other disasters, most countries still focuses on face-to-face training, with some related development with mobile app or web based knowledge sources. However, existing applications generally are limited to textual or some non interactive instructional video that are not adaptive to the situation. These resources are difficult and unwieldy to access in a real time emergency/disaster situation. To address this issue, in this design, we plan to build a voice activated adaptive system that would be comparatively practical and simple to use in cases of emergency.

On the other hand, in terms of finding earthquake victims trapped in rubble, there has been several streams of research, including the use of robots, radar technology, microwave, as well as several other technologies. Bloch et al. [3], Hao et al. [10] Chen et al. (2016). Most of these technologies focus on the search team, with some of them relying on physiological

signals from the trapped victims [10]. In the proposed design, we take another approach where the potential victim can emit a mobile hotspot or Bluetooth signal to alert searchers to their location, combining both searcher-centric and victim-centric approach.

---

## 3 Proposed System

The proposed design is aimed for application on smartphones with features that include a basic accelerometer, GPS and Bluetooth/mobile hotspot. It is aimed to be an integrated and multimodal system, using different input modalities, integrating data from several sources for the integrated use between different users. The system implements machine learning algorithm, utilizes voice, picture and text activated interface to match any situation's need, and basic augmented reality to help guide users to a safe place.

The proposed system has four main functions, namely (1) broadcast of earthquake alert to mobile phones from the local earthquake measurement centre, (2) smart voice activated interactive guide to guide community members on how to react to an earthquake event and arrive to a safe place based on their current situation, (3) A system to search for trapped survivors based on Bluetooth and wifi hotspot emitted by survivors, and (4) recording of earthquake waves based on mobile phone accelerators to be used to build a more granular geospatial database on earthquake features. This next part of this section will elaborate on each of these functionalities in turn.

### 3.1 Earthquake Alert

In the event of an earthquake, sensors from seismographs and other resources of the Indonesian National Bureau of Meteorology (BMKG) will announce the event on its website. However, this website may have limited exposure to potential affected communities. To complement this mechanism, our proposed system will continuously read the data by consuming BMKG's API and cross-referencing them with location data. If a user is within potential impact area, alerts are sent, and the interactive voice activated disaster guide is activated. Figure 1 illustrates the usecase of the earthquake alert system.

### 3.2 Voice Activated Interactive Guide

If a user is in the risk zone of an earthquake, after giving the local alert, the system automatically activates the voice interactive guide, which will start by offering assistance/ asking for the status of the user. The feature can also be

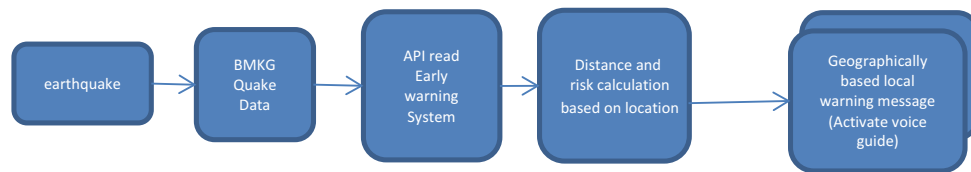


**Fig. 1** Earthquake alert system use case

activated upon user's request. The system would provide personalized help for the user to go to the nearest safe place/evacuation point based on their geographical coordinates. In addition, the user can use the system to handle specific emergencies by stating its nature. The key utility of this function is to provide a personalized, voice activated guide for disaster response. Existing systems and applications are generally not personalized (e.g. giving general evacuation guidelines for everyone regardless of their position and condition), and often are text based, which may be difficult to use in emergency situations.

To realize these functions, the system utilizes a combination of existing general guides for disaster response and machine learning. Personalized evacuation process would be done through connections to existing map applications (the system can periodically save local map and disaster response instruction data for offline use in case of communication infrastructure breakdown). In previously mapped places (e.g. office or school buildings), the system may also use Augmented Reality overlays to help guide users to a safe place.

### 3.3 Active Earthquake Victims Search Tool

As highlighted in the previous section, in the event of a major earthquake, the system will predict which users are potentially affected based on their geographical location and determine if they are in a safe location. In the case that the user states that they are not in a safe space and require assistance, the system will automatically activate the FindMe feature, which is an active earthquake victim search tool.

This feature will automatically send a position broadcast and distress signal using one of the following three options, sending out GPS coordinates, activating the trapped victim's

Bluetooth, or WiFi hotspot tethering function and set the WiFi/Bluetooth SSID into the name of the victim and an SOS signal. Any SAR personnel that are in the vicinity and using the application or having a wifi enabled mobile phone can detect the distress signal (GPS, Wifi or Bluetooth) from the trapped victim and know that there is a person needing help in their area. The system would also help determine the location by using the signal strength to roughly determine distance from the SAR personnel, giving a rough indication of whether they are getting closer or farther from the target. The choice of signal used depends on the condition of the event. If the affected area's communication network was not down, the mobile phone will use the network to send the person's GPS coordinate based on their smartphone to the FindMe server. While this has the highest accuracy, it requires the existence of an internet connection. In the absence of internet connectivity, the second option is using periodic wifi tether, which has a better detection sensitivity compared to Bluetooth. The system will periodically turn on and off the wifi to conserve power. Finally, the third option when battery is comparatively low is a low power Bluetooth signal with a 50 m radius. The three options also differ in terms of battery usage. Due to the short life of the phone battery, the system will use the bluetooth mode as battery drains, and use wifi tether when the phone has more power. Figure 2 illustrates the use case of the FindMe feature.

### 3.4 Distributed Earthquake Wave Recording

The final feature of this system is the recording of earthquake waves based on user mobile phone accelerators. This feature records data from affected users and transmits them to the system server once the user is marked as being in a

**Fig. 2** Use case for the FindMe feature



safe place. While it is not yet directly impactful to real time response, the resulting data can be used to build a more granular geospatial database on earthquake features. To et al. [7, 8, 13], for example, uses data from multiple mobile phones as an early warning system for earthquakes. To distinguish regular movement with earthquake waves, the system combines data from multiple phones, and is only activated when the phone is being charged or stationary. The proposed feature is aimed to function similarly as a crowd-based detection for earthquakes, with signal processing implemented to help distinguish regular movement from earthquake waves.

#### 4 Discussion and Next Steps

The aim of this design is to increase community response capacity to earthquakes as well as mitigate some of the impacts of earthquakes in Indonesia. At this stage, the project is in the design stage. We are currently consulting with relevant stakeholders and experts, including academics, relevant government institutions, earthquake response organizations and other stakeholders to fine tune the design according to available resources and needs. We will then proceed to the realization of a prototype with the finalized specifications, which will undergo laboratory based functional testing. Finally, we will conduct pilot testing in use cases of controlled disaster response drill. To analyze effectiveness of our design, we will evaluate its performance against traditional training and response methods.

In addition to its direct function in mitigating disaster impact, it is hoped that the data from the application users can be used to build a more accurate and granular spatial database of earthquakes. Combined with the geographical scale and diversity of Indonesia, and its location in the “ring of fire”, we hope that this can contribute as a unique resource to the field of research and development for disaster early detection and mitigation in Indonesia, and eventually the world.

#### References

1. Agrafiotis, Panagiotis, et al. “Real Time Earthquake’s Survivor Detection using a Miniaturized LWIR Camera.” Proceedings of the 9th ACM International Conference on Pervasive Technologies Related to Assistive Environments. ACM, 2016.
2. Aydin, Can, et al. “Improving disaster resilience using mobile based disaster management system.” *Procedia Technology* 22 (2016): 382–390.
3. Bloch, Tanya, Rafael Sacks, and Oded Rabinovitch. “Interior models of earthquake damaged buildings for search and rescue.” *Advanced Engineering Informatics* 30.1 (2016): 65–76.
4. Chen, Kun-Mu, et al. “Microwave life-detection systems for searching human subjects under earthquake rubble or behind barrier.” *IEEE Transactions on Biomedical Engineering* 47.1 (2000): 105–114.
5. Doulamis, Nikolaos, et al. “Human Object Detection using Very Low Resolution Thermal Cameras for Urban Search and Rescue.” Proceedings of the 10th International Conference on Pervasive Technologies Related to Assistive Environments. ACM, 2017.
6. Fajardo, Jovilyn Therese B., and Carlos M. Oppus. “A mobile disaster management system using the android technology.” *WSEAS Transactions on Communications* 9.6 (2010): 343–353.
7. Kong, Qingkai, et al. “MyShake: A smartphone seismic network for earthquake early warning and beyond.” *Science advances* 2.2 (2016): e1501055.
8. Kong, Qingkai, et al. “Smartphone-based networks for earthquake detection.” *Innovations for Community Services (I4CS)*, 2015 15th International Conference on. IEEE, 2015.
9. Li, Changzhi, et al. “Radar remote monitoring of vital signs.” *IEEE Microwave Magazine* 10.1 (2009): 47–56.
10. Lv, Hao, et al. “Characterization and identification of IR-UWB respiratory-motion response of trapped victims.” *IEEE Transactions on Geoscience and Remote Sensing* 52.11 (2014): 7195–7204.
11. Ray, Sayan Kumar, Ruopak Sinha, and Swapan Kumar Ray. “A smartphone-based post-disaster management mechanism using WiFi tethering.” *Industrial Electronics and Applications (ICIEA)*, 2015 IEEE 10th Conference on. IEEE, 2015.
12. Sachs, Jürgen, et al. “Remote vital sign detection for rescue, security, and medical care by ultra-wideband pseudo-noise radar.” *Ad Hoc Networks* 13 (2014): 42–53.
13. To, Hien, Seon Ho Kim, and Cyrus Shahabi. “Effectively crowdsourcing the acquisition and analysis of visual data for disaster response.” *Big Data (Big Data)*, 2015 IEEE International Conference on. IEEE, 2015.



# A Mobile App for the Self-management of Type 1 Diabetes as Tool for Preventing of Exercise-Associated Glycemic Imbalances

Miloš Ajčević, Federica De Dea, Giovanni Barbieri, and Agostino Accardo

## Abstract

mHealth is a growing field of research, concerning the great potentialities of mobile technology as a tool for self-management of chronic conditions. Physical activity greatly influences blood glucose levels, therefore for type 1 diabetes patients is important to adapt their diet and therapy in order to avoid exercise-induced hyperglycemia and hypoglycemia. The latter represents one of the major barriers to physical activity and it limits volitional exercise in type 1 diabetes patients. However, there is lack of stand-alone mobile tool that provides the support to the patient in order to perform physical activity and exercise under safe glycaemia levels. Recently, Exercise Carbohydrate Requirement Estimating Software (ECRES) algorithm was proposed to calculate patient-exercise tailored glucose supplement required to maintain safe blood glucose levels during physical activity. The objective of this study was to develop a mobile App which implements an individualized predictive system for blood glucose in type 1 diabetes, depending on exercise strength. Its usability and accuracy were compared to original ECRES estimating software in 15 volunteer subjects. The developed application provides relevant feedback to patients on carbohydrate intake needed to carry out a planned physical activity, in a safe manner. Furthermore, application provides other important features, for self-management of this chronicity, reported in recent literature: entry of blood glucose values, display of diabetes-related data, such as blood glucose readings and their analysis, carbohydrate intake, insulin doses, and easy data export. The application also incorporates food atlas in order to facilitate carbohydrates calculation. The results of the test showed that developed application accurately implements ECRES algorithm and the self-management features.

In conclusion, proposed App could be a useful support tool to diabetes type 1 patents. The results should be confirmed in larger clinical study.

## Keywords

mHealth • Type 1 diabetes • Decision support system  
Glycaemia • Exercise

## 1 Introduction

Patients with chronic diseases, in their everyday lives, deal with a range of conditions that require self-management and relevant decision-making. mHealth technologies may act as a complementary tool to provide support and motivation to regular patient's self-monitoring of health parameters [1]. Success of mHealth solutions depends also on their ability to address and meet users' needs [2]. In general, patients are not usually interested in single data, rather in trend and overall scenarios [2]. Therefore, the development of an intelligent system for data analysis and Decision Support Systems is essential for helping patients in self-management of their condition [3]. The resulting empowerment may help patients to achieve personal health objectives, modify lifestyle patterns and/or diminishing high risk behaviors for an optimal management of their chronic condition.

Type 1 diabetes mellitus is an autoimmune disease, which is preventing the body from being able to produce enough insulin to adequately regulate blood glucose concentration. Despite decades of improved insulin therapy and significant advancements in blood glucose monitoring, large excursions in blood glucose levels remain a major challenge for the active person with type 1 diabetes [4]. Regular moderate-intensity physical activity, which can include structured exercise in a variety of forms, offers a net benefit for most individuals with diabetes. It enhances insulin sensitivity, increases cardiorespiratory fitness, improves glycemic control, reduces the risk of cardiovascular mortality, and

M. Ajčević (✉) · F. De Dea · G. Barbieri · A. Accardo  
Department of Engineering and Architecture, University of  
Trieste, Trieste, Italy  
e-mail: majcevic@units.it

enhances psychosocial well-being [5]. On the other side, exercise-associated hypoglycemia represents one of the major barriers to physical activity and it limits volitional exercise in type 1 diabetes patients. To overcome this problem, recently, Exercise Carbohydrate Requirement Estimating Software (ECRES) decision support system was proposed to estimate patient-exercise tailored glucose supplement required to maintain safe blood glucose levels during physical activity [5].

Different mHealth solutions for self-management of diabetes type 1 are available on the market. However, there is lack of stand-alone mobile tool that provides the support to the patient in order to perform physical activity and exercise under safe glycaemia levels.

The objective of this study was to develop a mobile App which implements an individualized predictive system for management of exercise associated blood glucose imbalances in type 1 diabetes, together with other important features for self-management of this chronicity reported in recent literature.

## 2 Requirements

The main goal of mobile apps in self-management of diabetes is to improve control and glycemic support, helping the diabetic to avoid dangerous situations of hypo or hyperglycemia as well as to facilitate patients' everyday life. A recent study, reported that among patient, who use mobile apps for type 1 diabetes self-management, the most appreciated features regarded: carbohydrates counting, recording blood glucose levels, tracking my physical activity, tracking my weight and insulin dose calculation [6]. However, the same study highlights that only 24% of patients if their study population used mobile apps, mainly because they think that app could not help them in self-management or they have not found any good yet. In general, current applications are limited in their features, in fact about 60% of them do not include the four "keys" for an optimal diabetes self-management, such as: blood glucose control, adherence to drug therapy, diet monitoring and physical activity [7]. In addition, in order to enlarge the use of these usable tools, it is very important to include other features like [8–10]:

- electronic diary (therapy, carbohydrates intake, physical activity, possible malaise, stress, sleep time, blood sugar values)
- sharing of data to third parties (doctors, educators or family members) in order to monitor the patient's health status and provide adequate support.
- food database, in order to simplify the decision on food intake and comply to prescribed diet, with particular focus on calculation of carbohydrates

- carbohydrates calculator and to user friendly input of the dish consumed
- record of specific events through a pre-existing list
- backup of personal settings and diary in a web-storage
- variation of insulin dose based on duration and intensity of physical activity
- tracking of active insulin to avoid overlap dosages keeping track of the doses already taken and considering the insulin that still has to act, thus reducing the risk of hypoglycemia
- friendly, intuitive, and stimulating interface.

The clinical guidelines emphasize the role of education on self-management of the disease as an integral part of diabetes care, however most applications do not provide any support in this regard [9]. The inclusion of suggestions, educational content and guides within the applications could, even partially, help the user to become aware of what he is doing.

In order to assess the presence of above mentioned features and functionalities in the market, we analyzed their availability in some of most downloaded Android and iOS apps for diabetes type 1 management. The summary of features and functionalities of the analyzed apps available in the Google play store and Apple iTunes is reported in Table 1. However, there is lack of stand-alone mobile tool that provides the support to the patient in order to perform physical activity and exercise under safe glycaemia levels.

Taking in account previous requirements, following features and functionalities were chosen to be implemented in our work: Carbohydrates calculator, Possibility to change units of measure; Insulin dose calculator; Electronic diaries (therapy diary, glycemic diary, food diary, activity diary); Graphs and statistics relating to blood glucose values; Possibility of exporting data; Food database; Intuitive and user friendly interface, tool for preventing of exercise-associated glycemic imbalances (ECRES algorithm). This user friendly tool requires following information to be inserted in the ECRES algorithm:

1. patient usual therapy (i.e. insulin types, doses and time scheduling, together with the dietary carbohydrates)
2. the time of day and duration of the physical activity
3. the capillary blood glucose level measured just before the start of the activity
4. predicted average HR based on specific physical activity.

In brief, this algorithm calculates the amount of carbohydrates required to avoid glycemic imbalances as a fraction of the overall amount of carbohydrates burned during the exercise and further corrects it by subtracting (or adding) the excess (or lack) of glucose contained in the extracellular compartment. ECRES algorithm was previously described in detail in the previous work [5].

**Table 1** Summary of features and functionalities in apps for self-management of type 1 diabetes patients

Name	Diary	Graph	Statistics	Data export	Sync..	Other
Diabete-Glucose diary	Yes	Yes	Intervals 7, 14, 28, 90 dd	E-mail SD (CSV, XML)	No	Editable theme, reminder
Diabetes diary MySugr	Yes	Yes	Intervals 1, 14, 30, 90 dd	E-mail (PDF, CSV, XLS) Facebook	FreeStyle Libre, Google Fit	Personal account, unlockable goals, food database
Diabetes:M	Yes	Yes	Intervals 7, 14, 30, 90 dd	Dropbox o GoogleDrive. Backup. (CSV, XLS)	Google Fit, android wear	Personal account, Insulin calculator, active insulin, CHO and glycaemia, Reminder
La mia glicemia: diabete Libro	Yes	Yes	Yes	E-mail (PDF, CSV, XLS)	No	Reminder, editable theme
Diabete Ufficiale	Yes	Yes	Intervals 7, 14, 30, 60, 90 dd	SD Backup (CSV, PDF)	No	Personal account, Reminder, unit of measure conversion
Social diabetes	Yes	Yes	Intervals yesterday, today, 7, 30 dd	E-mail Backup (CSV, PDF) Dropbox	iHealth Android Wear	Personal account CHO calculator
Diabetes connect	Yes	Yes	Intervals 2, 4, 6, 8 weeks	E-mail bluetooth messages (PDF, CSV) Dropbox GoogleDrive	No	Personal account
SiDiary	Yes	Yes	Intervals 1, 7, 14, 28, 60, 90, 120 dd	SD SMS	Beurer Cygnus Fora	Editable theme, blind modality
SugarSense	Yes	Yes	Intervals 1, 7, 14, 30, 90 dd	E-mail, messages bluetooth, Dropbox, GoogleDrive (PDF)	Fitbit, Jawbone Misfit, ecc	Personal account reminder, tips, community forum

### 3 Results

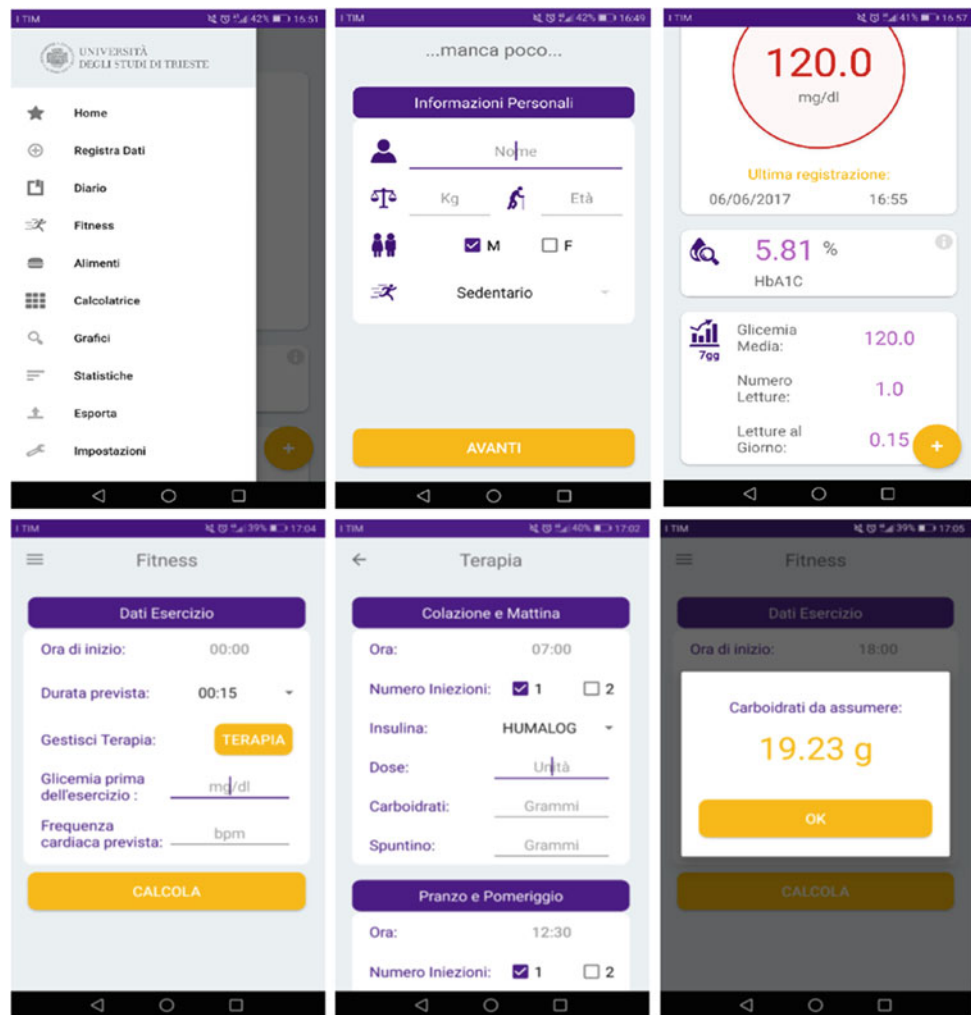
The app was developed in Java by means the IDE platform that includes the java development kit (JDK) and the Software development kit (SDK) dedicated for Android apps. The graphic structure was defined by XML language.

The following features were implemented in the developed app (Fig. 1).

- possibility to choose whether mg/dL or mmol/L, as regards glycaemia, % or mmol/mol for glycated hemoglobin;
- data input/reading in/from the electronic diary: therapy, glycemic measurements data such as day, time, glycaemia, insulin, time of day, carbohydrates intake, health status, systolic and diastolic pressure, heart rate, free text and photo;
- graphs and statistics (number of measurements, daily measurements, maximum glycemic level, minimum glycemic level, average glycaemia, number of hyperglycemia events, number of hyperglycemia events) related to a well-defined period (today, yesterday, one week, two weeks, one month, three months, six months, nine months, one year);
- food database, with the possibility to see the nutritional data of each product;
- carbohydrates calculator
- carbohydrates intake calculation, using the ECRES algorithm, to prevent hypoglycemia during physical activity;
- possibility to export the database table containing the storage saving in the smartphone, or by sending an e-mail as an attachment in the CSV format;
- possibility to modify personal information and preferences.

The app prototype was tested in 15 volunteer subjects. The implemented ECRES algorithm was compared to the original ECRES software. The feedback from the volunteer subjects was gathered after 10-day test. The developed application provided accurately relevant feedback to subjects on carbohydrate intake needed to carry out a planned physical activity, in a safe manner. Moreover, the test showed that the features were implemented properly and that the app is simple to use. In addition, the most appreciated features, beside ECRES and Carbohydrates calculator, was the implemented food database. The features like synchronization with a smart-band and device for Continuous Glucose Monitoring will be implemented in a future study.

**Fig. 1** Mobile app for self-management of diabetes type 1 with implemented ECRES algorithm



## 4 Conclusions

In conclusion, this study proposed a mobile App for the self-management of type 1 diabetes with a user friendly tool for preventing of exercise-associated glycemical imbalances. The developed App could be a useful support tool to overcome the barriers to physical activity in type 1 diabetes patients related to exercise-induced hypoglycemia. The results should be confirmed in larger clinical study.

**Acknowledgment** The study was funded by University of Trieste research funds—FRA2015.

**Conflict of Interest** The authors declare that they have no conflict of interest.

### Compliance with Ethical Requirements

The study was conducted according to the Declaration of Helsinki.

## References

1. Marcegaglia, S., Bonacina, S., Zaccaria, V., Pagliari, C., Pincirolì F.: How might the iPad change healthcare? *Journal of the Royal Society of Medicine* 105(6), 233-241 (2012).
2. Lasorsa, I., D'Antrassi, P., Ajčević, M., Stellato, K., Di Lenarda, A., Marcegaglia, S., Accardo, A.: Personalized support for chronic conditions. *Applied clinical informatics* 7(03), 633-645 (2016).
3. Kawamoto, K., Houlihan, C. A., Balas, E. A., Lobach, D. F.: Improving clinical practice using clinical decision support systems: a systematic review of trials to identify features critical to success. *Bmj* 330(7494), 765 (2005).
4. Riddell, M.C., Perkins, B.A.: Type 1 diabetes and vigorous exercise: applications of exercise physiology to patient management. *Canadian Journal of Diabetes* 30(1), 63-71 (2006).
5. Francescato, M.P., Geat, M., Accardo, A., Blokar, M., Cattin, L., Noacco, C.: Exercise and glycemical imbalances: a situation-specific estimate of glucose supplement. *Med Sci Sports Exerc* 43(1), 2-11 (2011).

6. Trawley, S., Baptista, S., Browne, J. L., Pouwer, F., Speight, J. The Use of Mobile Applications Among Adults with Type 1 and Type 2 Diabetes: Results from the Second MILES—Australia (MILES-2) Study. *Diabetes technology & therapeutics* 19(12), 730-738 (2017).
7. Klasnja, P., Kendall, L., Pratt, W., & Blondon, K.: Long-term engagement with health-management technology: a dynamic process in diabetes. In: *AMIA Annual Symposium Proceedings* Vol. 2015, p. 756. American Medical Informatics Association, San Francisco, USA (2015).
8. Knight, B. A., McIntyre, H. D., Hickman, I. J., Noud, M.: Qualitative assessment of user experiences of a novel smart phone application designed to support flexible intensive insulin therapy in type 1 diabetes. *BMC medical informatics and decision making* 16 (1), 119 (2016).
9. El-Gayar, O., Timsina, P., Nawar, N., & Eid, W. Mobile applications for diabetes self-management: status and potential. *Journal of diabetes science and technology* 7(1), 247-262 (2013).
10. LKirwan, M., Vandelanotte, C., Fenning, A., Duncan, M. J.: Diabetes self-management smartphone application for adults with type 1 diabetes: randomized controlled trial. *Journal of medical Internet research* 15(11), e235 (2013).



# An Online Service for Topics and Trends Analysis in Medical Literature

Spyridon Kavvadias<sup>✉</sup>, George Drosatos<sup>✉</sup>, and Eleni Kaldoudi<sup>✉</sup>

## Abstract

Topic modeling refers to a suite of probabilistic algorithms for extracting word patterns from a collection of documents aiming for data clustering and detection of research trends. We developed an online service that implements different variations of Latent Dirichlet Allocation (LDA) algorithm. Scientific literature origin from targeted search queries in PubMed, works as input while output files are available for every step of the process. Researchers can compare the results of different corpora, preprocessing texts and topic modeling parameters in a quick and organized way. Information regarding topics help users assign labels and group them to categories. Visualization of data is a contribution of our service with graphs generated on the fly providing information about the corpora, the topics, groups of topics and categories as well. We rely in modern technologies and follow the principles of agile software development to achieve scalability and discreet design.

## Keywords

Topic modeling • Content analysis • Trend analysis  
Visualization

## 1 Introduction

Our era is characterized by continuous advances in biomedical sciences and a corresponding large amount of scientific publications each year. Literature topics and trends

S. Kavvadias (✉) · G. Drosatos · E. Kaldoudi  
School of Medicine, Democritus University of Thrace,  
Alexandroupoli, Greece  
e-mail: skavvadi@med.duth.gr

G. Drosatos  
e-mail: gdrosato@ee.duth.gr

E. Kaldoudi  
e-mail: kaldoudi@med.duth.gr

analysis is increasingly employed to give insights on past and future research directions. Several statistical algorithms have been applied to model topics in scientific literature [1–5]. As such methods require considerable mathematical and programming background, recent research proposes user friendly integrated tools to enable researchers of various backgrounds to explore topics analysis [6–8]. However, currently available tools do not cover the entire topics and trends analysis workflow and require custom set up. In this paper, we propose an open source and platform independent service to support topic modeling and trends analysis for the biomedical expert. The service allows creation and description of biomedical literature corpora, supports the entire workflow of topic modeling and trends analysis and provides visual navigation of the results.

## 2 Topic Modeling

Topic modeling [9] refers to a suite of algorithms that aim to analyze the hidden structure of a collection of documents. Each document is characterized by a variation of topics, each topic consists of a collection of words and each word has its own statistical weight. Several topic modeling approaches are available [3–5, 10], Latent Dirichlet Allocation (LDA) being one of the most popular. The algorithm starts by randomly assigning each word of a document in one of  $K$  topics. Then, it calculates conditional probabilities for each topic in each document ( $(t|d)$  where  $t$  denotes the topic and  $d$  denotes the document) and for each word in every topic ( $(w|t)$  where  $w$  denotes word). Through an iterative process, it reassigns words and topics until they reach a steady state. The algorithm requires setting the initial number  $K$  of assumed topics and the parameters that define the Dirichlet prior for the per document topic distribution (parameter  $\alpha$ ) and for the per topic word distribution (parameter  $\beta$ ).

Topic modeling has been successfully applied in many other research areas, for example to analyze and classify genomic sequences [11], classify images based on visual

words topic modeling [12], detect discussion themes in social networks [13] and analyze source code [14]. Additionally, there are several implementations of topic modeling (and especially of LDA) in different programming languages [15–18]. In this paper, we integrate some of the existing implementations in an online service which provides added value functionalities, including user-friendly interface to visualize and label topics and tools to support trend analysis. The service also allows for generation of rich metadata for each step of the workflow, to fully document the topic modeling experiments.

### 3 Topic Modeling and Trends Analysis Service

An overview of literature topic modeling and trends analysis workflow is presented in Fig. 1. The process starts with the generation of the initial literature corpus, as a collection of relevant published papers; most often the collection is limited to paper titles and abstracts due to access restrictions. Following a rudimentary text preprocessing, the topic modeling algorithm is parametrized and applied to identify topics that are essentially word collections. Human intervention is required to label topics so that they are meaningful for human interpretation. Finally, popularity of topics over time is assessed for trends analysis.

We have developed a user-friendly web-based environment to encapsulate this entire workflow of topic modeling and trends analysis and provide this as a service for the non-expert biomedical scientist. The input of the service is a corpus of research abstracts retrieved from PubMed as a result from a specific query. The system allows the user to describe each corpus via relevant metadata, including corpus generation date, initial database query, study aim and user details. Basic corpus statistics are also calculated, e.g. number of publications per year (given as a graph), total number of articles, number of articles with an abstract and minimum–maximum year of articles.

Text preprocessing is routinely used to clean the corpus via: (1) removal of all the punctuation and escape codes; (2) exclusion of stop-words; (3) conversion of all words to their lemmas by applying the stemming procedure; and (4) exclusion of articles with no words in their abstracts or less than 3 letters in their titles. Current service implementation uses the most commonly used Krovetz stemmer [19] as a default option for the stemming process. However, the service allows importing of additional stemming algorithms [10]. The service provides basic preprocessing statistics and allows the user to generate metadata to richly describe preprocessed corpora for future reference.

The processed corpus can be archived and used as input to the topic modeling procedure along with the necessary execution parameters. Currently, we support two different

**Fig. 1** The basic workflow, inputs and outputs of the platform

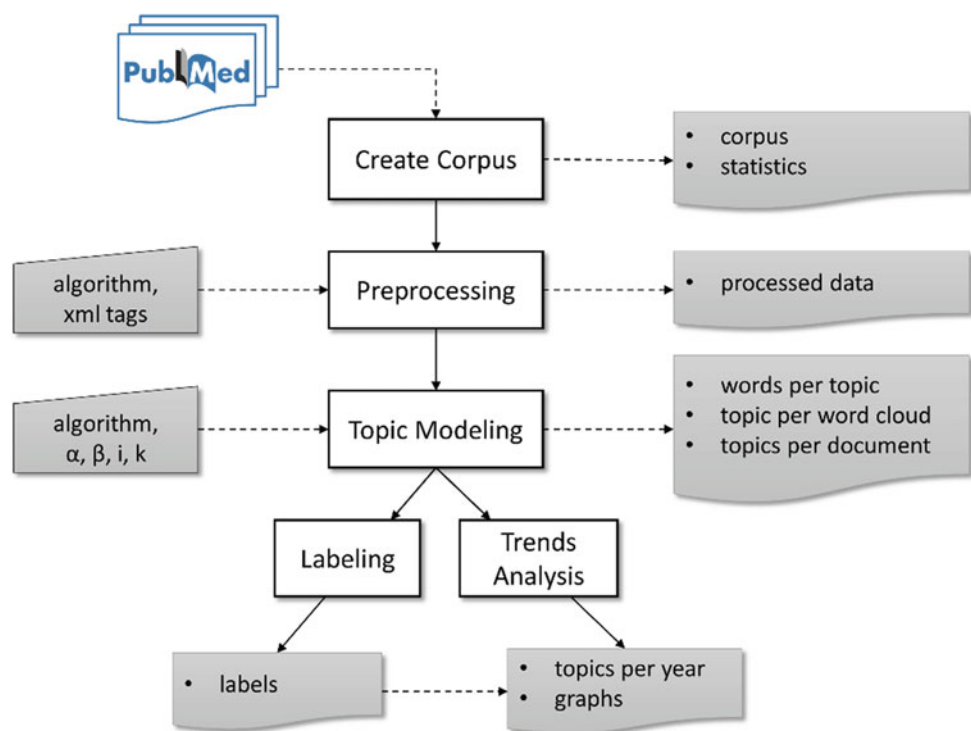


**Fig. 2** Metadata table for topic modeling

Topic Modeling							Download		
Title	Algorithm	alpha	beta	topics	iterations				
very_small_pr_0.1_0.01_20_2000	jLDADMM	0.1	0.01	20	2000				finished
normal_pr_0.1_0.01_20_2000	jLDADMM	0.1	0.01	20	2000			started	
normal_pr_0.1_0.01_20_2000	MalletParallel	0.1	0.01	20	2000			started	
normal_pr_0.1_0.01_10_1000	jLDADMM	0.1	0.01	10	1000			started	
normal_pr_0.1_0.01_40_100	MalletParallel	0.1	0.01	40	100			pending	
med3_pr_0.1_0.01_100_500	jLDADMM	0.1	0.01	100	500			pending	
med2_pr_0.1_0.01_200_1000	jLDADMM	0.1	0.01	200	1000			pending	

implementations of LDA based on the Java libraries Mallet ParallelTopicModel [17] and jLDADMM [18] with input/output performance enhancements. Service architecture supports easy integration of other LDA implementations based on predefined public interface descriptions.

Topic modeling experiments are resource and time consuming while they often be repeated with different initialization parameters. The proposed service displays a current status of scheduled topic modeling experiments and supports a powerful experimental lab-bookkeeping. As shown in Fig. 2, the user is guided to insert relevant metadata that describe in detail each topic modeling experiment. Metadata can be edited and updated, while they automatically inform saved experimental results and trends analysis and visualizations produced in the following steps of the workflow.

Another important service feature of added value is the ability for the user to label each topic. The procedure of assigning labels to topics is shown in Fig. 3. For every topic that has been generated by the execution of the algorithm, the top most words (number indicated by the user) that describe the topic are ranked by statistical weight and displayed for the user in tabular form or as word clouds. The

user can then assign a title to each topic and create nested categories to organize various topics.

The final step in the workflow involves trends analysis on the identified topics. The popularity ( $t, y$ ) of the topic ( $t$ ) for each year ( $y$ ) is calculated as the mean of the weight of this topic for all documents published this year ( $D_y$ ):

$$P(t, y) = \frac{1}{|D_y|} \sum_{d \in D_y} \frac{|\{w \in d : \text{topic}(w) = t\}|}{|d|} \quad (1)$$

where  $t$  represents a topic and  $w$  is a word in document  $d$  of the documents' collection  $D_y$  for year  $y$  [20]. Calculated trends are then displayed as graphs. The service supports for rich visualizations which allows comparative displays of different topics and categories and corpora, while preserving metadata information describing the different experiments whose results are compared. An example is shown in Fig. 4. The user can generate graphs on the fly for any group of selected topics or categories and compare trends for a chosen time range.

The system is implemented in NodeJS with LoopBack framework (<http://loopback.io>) and is accessible at <https://>

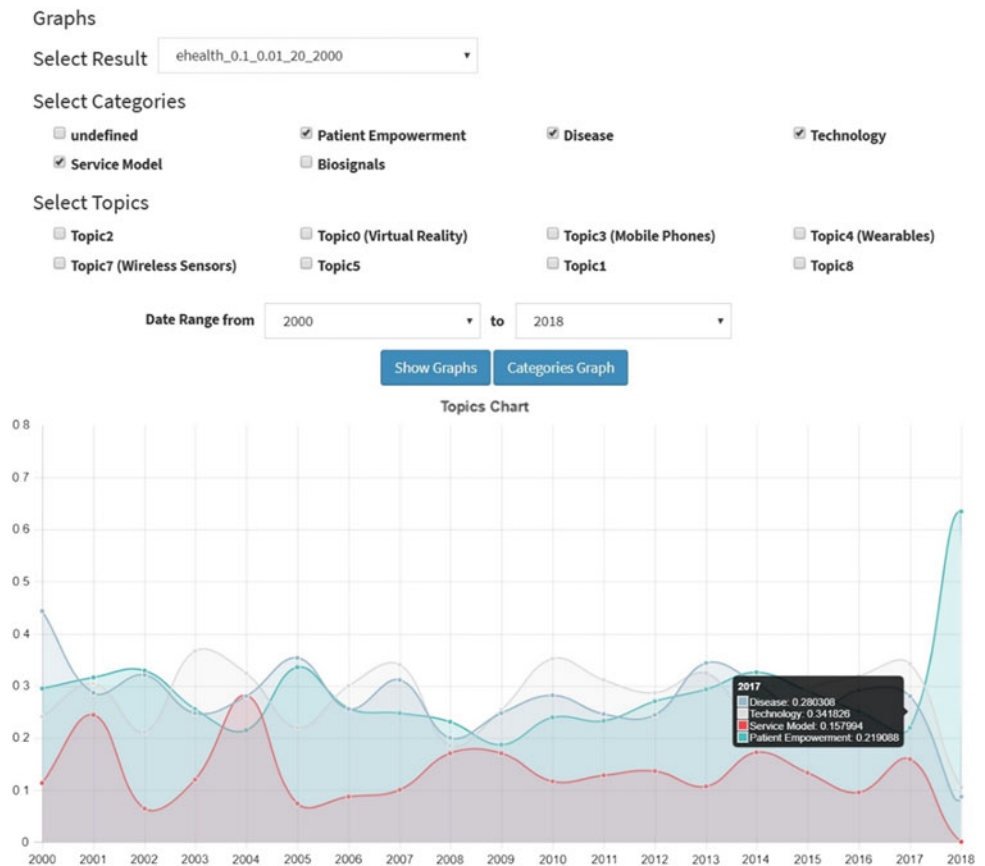
**Fig. 3** Assigning labels and categories to topics

Viewing: ehealth\_0.1\_0.01\_20\_2000

Topics	Top Words	Labeling	Category	Edit
Topic0	<ul style="list-style-type: none"> <li>physical: 0.043727</li> <li>activity: 0.037</li> <li>weight: 0.022826</li> <li>condition: 0.022586</li> <li>body: 0.019462</li> </ul>	Physical Activity	Treatment	
Topic1	<ul style="list-style-type: none"> <li>health: 0.054492</li> <li>care: 0.047859</li> <li>intervention: 0.02211</li> <li>social: 0.017298</li> <li>service: 0.014047</li> </ul>	Social	Intervention	

First Previous 1 2 3 4 Next Last

**Fig. 4** Categories Graph. The user selects the result and the categories that wants to compare. The topics of each category appear after the user check them



[trends.duth.carre-project.eu/](https://trends.duth.carre-project.eu/). Data storage is based on the MongoDB (<https://www.mongodb.org>). The frontend is powered by AngularJS framework (<https://angularjs.org>) and the graph visualizations are implemented using Chart.js (<http://www.chartjs.org/>) and Vis.js library (<http://visjs.org>). In the backend, we developed a mechanism for the management of parallel processes that are possible to be requested by the same user or not. For this purpose, we used a FIFO philosophy (first-in, first-out) for the execution of processes and limitations on the number of processes (e.g. three) that are possible to be executed simultaneously. This is required because our system has limited computing resources and the topic modeling algorithms require high computational cost.

## 4 Discussion

This paper proposes a web-based service that allows biomedical researchers with no experience in data modelling and programming to execute topic modeling and trends analysis experiments of biomedical literature corpora, keep experimental details and visualize the results. Work in progress includes to make our web service free of bugs, support more topic modeling algorithms with an easy mechanism to

add new implementations of them, and to develop a mechanism that would add a batch of processes with different parameters with goal to select the appropriate ones (e.g. the number of topics). Additionally, we plan to perform an evaluation of our system regarding the system's performance and the users' satisfaction.

**Acknowledgements** This work was supported by the FP7-ICT project CARRE (Grant No. 611140), funded in part by the European Commission and Greek National Matching funds (DUTH KE81442).

**Conflict of Interest** The authors declare that they have no conflict of interest.

## References

1. Paul, M., Girju, R.: Topic modeling of research fields: An interdisciplinary perspective. In: International Conference Recent Advances in Natural Language Processing (RANLP 2009), pp. 337–342 (2009).
2. Liu, L., Tang, L., Dong, W., Yao, S., Zhou, W: An overview of topic modeling and its current applications in bioinformatics. *SpringerPlus*, 5(1), 1608 (2016).
3. Blei, M., D., Andrew, Y., J., Jordan, I., M.: Latent dirichlet allocation. *Journal of Machine Learning Research*, Vol. 3, pp. 993–1022 (2003).

4. Deerwester, S., Dumais, S. T., Furnas, G. W., Landauer, T. K., Harshman, R.: Indexing by latent semantic analysis. *Journal of the American society for information science*, 41(6), 391 (1990).
5. Hofmann, T.: Probabilistic latent semantic analysis. In: 15th Conference on Uncertainty in Artificial Intelligence. Morgan Kaufmann Publishers Inc. pp. 289–296 (1999).
6. Scriver, O., Davis, J.: Topic modeling of scholarly articles: Interactive text mining suite. In: Computational Linguistics and Intellectual Technologies: Proceedings of the International Conference “Dialogue 2016” (2016).
7. Kim, D., Swanson, B. F., Hughes, M. C., Sudderth, E. B.: Refinery: An open source topic modeling web platform. *Journal of Machine Learning Research*, 18(12), 1–5 (2017).
8. Gardner, M. J., Lutes, J., Lund, J., Hansen, J., Walker, D., Ringger, E., Seppi, K.: The topic browser: An interactive tool for browsing topic models. In: NIPS Workshop on Challenges of Data Visualization (Vol. 2) (2010).
9. Blei, M.: Probabilistic topic models. *Communications of the ACM*, 55(4):77–84, (2012).
10. Jurafsky, D., Martin, J. H: *Speech and language processing*. 3rd edn. Pearson, London (2017).
11. La Rosa, M., Fiannaca, A., Rizzo, R., Urso, A.: Probabilistic topic modeling for the analysis and classification of genomic sequences. *BMC Bioinformatics*, 16(6), S2 (2015).
12. Rasiwasia, N., Vasconcelos, N.: Latent dirichlet allocation models for image classification. *IEEE Transactions on Pattern Analysis and Machine Intelligence*, 35(11), 2665–2679 (2013).
13. Lau, J. H., Collier, N., Baldwin, T.: On-line trend analysis with topic models: #twitter trends detection topic model online. In: 24th International Conference on Computational Linguistics, pp. 1519–1534 (2012).
14. Binkley, D., Heinz, D., Lawrie, D., Overfelt, J.: Understanding LDA in source code analysis. In: 22nd International Conference on Program Comprehension, pp. 26–36, ACM, New York, NY, USA (2014).
15. Topic Modeling Software, [http://www.cs.columbia.edu/~blei/topicmodeling\\_software.html](http://www.cs.columbia.edu/~blei/topicmodeling_software.html), last accessed 2018/02/05.
16. Grün, B., Hornik, K.: topicmodels: An R package for fitting topic models. *Journal of Statistical Software*, 40(13), 1–30 (2011).
17. MALLET: A machine learning for language toolkit, <http://mallet.cs.umass.edu>, last accessed 2018/02/05.
18. jLDADMM: A Java package for the LDA and DMM topic models, <http://jldadmm.sourceforge.net>, last accessed 2018/02/05.
19. Krovetz, R.: Viewing morphology as an inference process. In: 16th Annual International ACM SIGIR Conference on Research and Development in Information Retrieval, pp. 191–202, ACM, New York, NY, USA (1993).
20. Priva, U. C., Austerweil, J. L.: Analyzing the history of Cognition using topic models. *Cognition*, 135, 4–9 (2015).



---

**Part IV**  
**Modelling and Simulation**

# Paced Electrical Field Modeling Within Ischemic Myocardium

D. Korpas and P. Barta

## Abstract

Cardiac pacing in an ischemic area is very disadvantageous because of higher pacing thresholds and lower sensed intrinsic signal. An irregular propagation of myocardial activation in the ventricles is also a clinical problem of ischemia. The aim of this paper is to model the theoretical electrical depolarization propagation within the paced ventricular myocardium, using mathematical and computation methods. For numerical simulation of different biological or physiological systems, models utilizing the differential equation are appropriate. The basic model is Hodgkin-Huxley, describing the action potentials on the basis of varying channel permeability for different ions. Our characteristics of modeled tissues are described according to the FitzHugh-Nagumo model which is a simplification of Hodgkin-Huxley. The computation was performed using the Comsol Multiphysics software. The results are composed of several models of paced ventricles: a physiological one, one with apical ischemia, and one with left lateral ischemia as well as a combination of all three with low or high energy right ventricular or biventricular pacing. The results of the simulations of right ventricular pacing are consistent with the clinical experience. They confirm an increase in ischemic dyssynchrony because of different activation times in the right ventricle in comparison with the left ventricle. Apical pacing in the ischemic area shows the latest activation times in comparison with the physiological reference. In this case, lead reposition would be recommended in the practice. The location of an ischemic lesion within the model is adjustable and can also be used for the assessment and planning of pacing effectiveness.

## Keywords

Cardiac modeling • Pacing • Ischemic tissue  
FitzHugh-Nagumo model

## 1 Introduction

Cardiac pacing in an ischemic area is very disadvantageous because of higher pacing thresholds and lower sensed intrinsic signal. An irregular propagation of myocardial activation in the ventricles is an additional clinical problem of ischemia. The aim of this paper is to model the theoretical electrical depolarization propagation within an ischemic ventricular myocardium, using mathematical and computation methods. The novelty is in the incorporation of right ventricular (RV) and biventricular pacing. This can be useful in the clinical practice for the estimation of left ventricular (LV) pacing vector selection and for timing optimization.

There are several approaches for modeling and, subsequently, simulating ventricular depolarization. In one approach, each element of the heart model acts as a separate generator and influences the surrounding elements. Another approach is modeling of the heart tissue at the scale of cellular ion fluxes. These models attempt to describe chemical-electrical processes within the myocardium as closely as possible, and then to apply the summation patterns to the entire volume of the heart ventricles. The approach that appears to be most useful is the one describing the system using differential equations. An example of such an approach is the FitzHugh-Nagumo equation for excitable environments to describe the propagation of, e.g., excitation in the tissue.

In most studies, excitation is spread according to the Huygen's principle. The activation of the element is dependent on the activation threshold voltage, the refractory phase, and the activation time. In practice, it means that excitation in the physiological tissue cannot be spread in the retrograde direction as these depolarized cells are in a refractory phase during which no new depolarization can be

D. Korpas (✉)  
Faculty of Public Policies, Institute of Nursing, Silesian  
University, Opava, Czech Republic  
e-mail: david.korpas@fvp.slu.cz

P. Barta  
Rhythm Management Department, Boston Scientific CR s.r.o.,  
Prague, Czech Republic

started. The algorithms for subsequent simulations are based on the finite element method [1, 2].

## 2 Methods

As mentioned above, for numerical simulation of different biological systems, models utilizing the differential equations are appropriate. The basic model is Hodgkin-Huxley describing the action potentials on the basis of varying channel permeability for different ions. The Hodgkin-Huxley model is very complex and, therefore, very difficult for analysis and modeling. For this reason, the FitzHugh-Nagumo model was used in this study. This model reduces the four unknowns from the Hodgkin-Huxley model to two. One is the rapid variable  $u_1(t)$  causing depolarization, and the other variable  $u_2(t)$  is responsible for repolarization, i.e. recovery of the depolarized area. The FitzHugh-Nagumo model is described by the following differential equations [3, 4]:

$$\frac{\partial u_1}{\partial t} = (\alpha - u_1)(u_1 - 1)u_1 - u_2$$

describes the dynamics of sodium ions, and

$$\frac{\partial u_2}{\partial t} = \varepsilon(\beta u_1 - \gamma u_2 - \delta)$$

describes the dynamics of potassium ions [3]. A disadvantage of this model is the fact that its simplification results in the loss of quantitative information about the action potential. However, this model is sufficient to describe the activation maps or the occurrence of circulatory excitation in an environment [3, 4]. A major advantage is its relatively simpler analyzability and interpretation compared with the basic Hodgkin-Huxley model [5–7].

The main dimensions of the ventricular model are shown in Fig. 1.

A key task for applying the FitzHugh-Nagumo model was the optimization of differential equation parameters. Ischemic

tissue was simulated by empirically determined parameters of the FitzHugh-Nagumo equation in which the course of action potential corresponds to the ischemic area in the heart. Analogously, the equation parameters for the bundle branch were determined. The specific parameters of each type of tissue were established using the Matlab-Simulink block modeling program. Ischemic tissues were empirically placed on the left and right bottom walls and, in some models, on the left lateral wall of the left ventricle. The pacing energy was approximated as the spherical volume of the directly activated part of the myocardium, i.e. lower-level energy directly activates fewer cells than higher-level energy.

In all models, ten points were uniquely determined by their coordinates, which did not change within the models. The sites are shown graphically in Table 1. Point positions were empirically selected in the most appropriate areas for comparison [8]. Five points are located in the basal region of the LV, septum, and RV. These are the most suitable locations for comparing the ventricles activated later. The other four points are located in the medial plane on the free RV and LV walls. The last point is chosen at the most remote point of the apex. It can be used to determine the difference between a physiological and ischemic apex and activation times when conducting an excitation or pacing at the apex of the RV.

## 3 Results

The results are several models of the ventricles: a physiological one, the ones with apical or left lateral ischemia, and all three with low or high energy RV or biventricular pacing. Activation times of the ten chosen points in our geometry are compared mutually as well as with the reference physiological model. The results confirm an increase in ischemic dyssynchrony because of different activation times in the RV in comparison with the LV. Apical pacing in the ischemic area shows the latest activation times in comparison with the physiological reference. Below can be found the graphics for nine models. The cyan color corresponds to inactivated cells

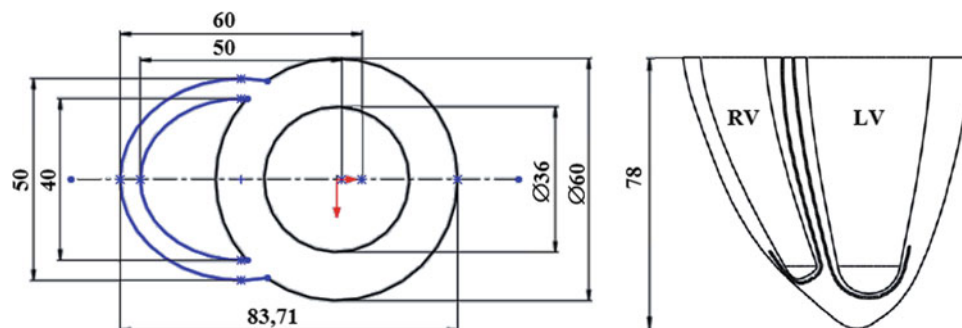
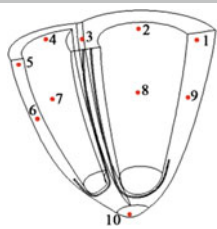


**Fig. 1** The main dimensions in the basal transversal section of the 3D ventricular model (left). Model height and frontal section. Bundle branches are represented here by a 1-mm thick fiber of circular cross-section drawn along a curve copying the inside of the ventricles (right)

**Table 1** Comparison of the differences in activation at the points of the models [time steps]

Point number/Model	1	2	3	4	5	6	7	8	9	10
FOSL	>180	320	>630	>370	>140	230	210	140	230	140
IASL	>180	170	>630	>370	>140	270	280	270	230	250
ILSL	>180	>370	>630	>370	>140	230	200	230	340	130
FOSH	50	160	470	260	80	60	60	-10	70	70
IASH	130	220	540	320	130	60	110	30	180	80
ILSH	>180	230	460	270	110	60	60	70	230	10
FOSBIV	-370	-100	370	270	>140	190	190	-140	-440	120
IASBIV	-380	-110	390	270	>140	260	250	-160	-440	210
ILSBIV	-370	90	580	>370	>140	190	200	20	-300	120



and the red color to the depolarized cell. The dark blue shows repolarized cells. From the left, the time steps are 0; 500; and 800.

**Physiological tissue model with low voltage RV-only pacing (FOSL).** By overtaking the intrinsic conducted signal of pacing in the RV, the onset of excitation is concentrated only in the vicinity of the pacing electrodes. As expected, there is a considerable delay in the spreading process. In practice, this situation occurs when the pacing energy is so low that no capture occurs. Such pacing is therefore inappropriate (Fig. 2).

**Apical ischemia model with low voltage RV-only pacing (IASL).** An even longer delay occurs in the case of pacing delivered to an ischemic apex. This phenomenon is common in cardiac pacing practice. When ischemic tissue is paced, the heart tissue only responds to higher pacing energies which are often inadequate due to irritation of the vagus nerve or diaphragm (Fig. 3).

**Lateral wall ischemia model with low voltage RV-only pacing (ILSL).** Unlike ischemia at the apex, the ischemic area in the LV lateral wall exhibits smaller activation time differences than the FOSL model. The apex and RV are activated with a delay comparable to that of a physiological condition; more basal LV regions show delays due to an ischemic obstruction in the propagation of the depolarization wave. Delays can be observed naturally even in the ischemic area (Fig. 4).

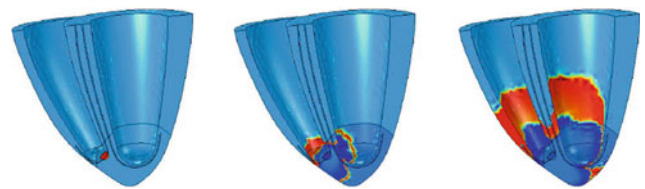


**Fig. 3** Spreading of excitation in the IASL model

**Physiological tissue model with high voltage RV-only pacing (FOSH).** What is different in comparison with the previous three models is a higher pacing energy. Depending on the values of activation times, there is a significant improvement where a considerable delay only occurs in the areas of the septum and LV. This improvement corresponds to the response of the heart to higher pacing amplitudes, and the efficacy of such therapy is higher. However, there are still risks associated with dyssynchrony, due to long-term overtaking of the complete activation of the RV before the LV (Fig. 5).

**Apical ischemia model with high voltage RV-only pacing (IASH).** In the case of pacing to the ischemic apex with higher energy, the area with considerable delay increased. This is again due to the attenuating properties of ischemic tissue in the apex, which slows the spreading of the initial activation. In this model, an effect of increasing pacing effectiveness with a higher pacing energy compared with the AISL model can be observed (Fig. 6).

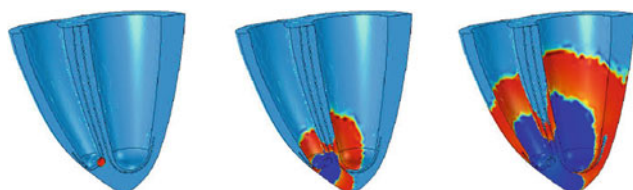


**Fig. 2** Spreading of excitation in the FOSL model

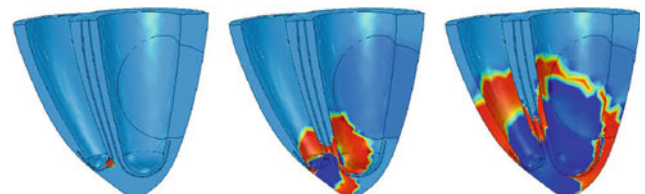


**Fig. 4** Spreading of excitation in the ILSL model

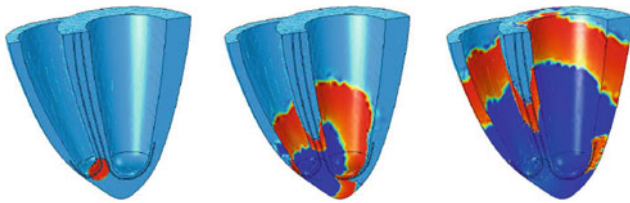


**Fig. 5** Spreading of excitation in the FOSH model

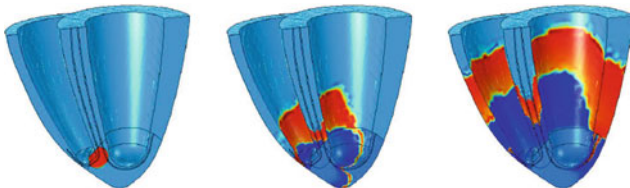


**Fig. 6** Spreading of excitation in the IASH model

**Lateral wall ischemia model with high voltage RV-only pacing (ILSH).** A model with higher energy pacing for ischemia in the LV lateral wall indicates improvements in the activation times of the apex and RV. The left ventricular basal areas remain largely delayed. This case is associated with a high risk of developing muscle dilation. This is because an adequate response of the heart muscle has already arisen, but with large temporal differences between contraction of the RV and LV (Fig. 7).

**Physiological tissue model with low voltage BIV pacing (F0SBIV).** Models with biventricular pacing show enormous improvements in the activation times in the LV, with some of the delays even reaching negative values. However, this rapid depolarization of the LV precedes the depolarization of the RV, and again there would be a risk of ventricular dyssynchrony. In fact, biventricular pacing is a very effective therapy the long-term administration of which can lead to reverse remodeling of dilated cardiac tissue. It depends on the exact location of pacing, pacing vector, pacing energy, and individual anatomy of the bundle branch and Purkinje fibers (Fig. 8).

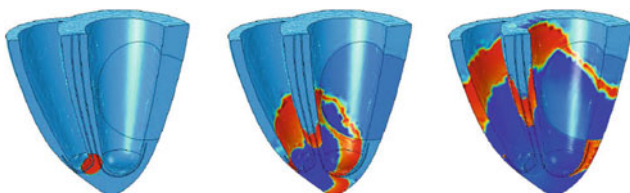


**Fig. 7** Spreading of excitation in the ILSH model

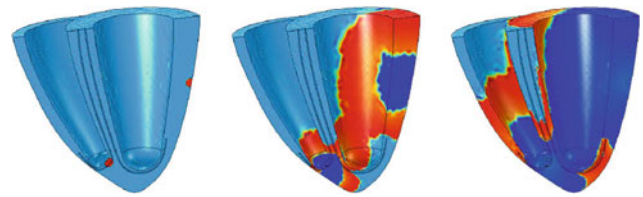


**Fig. 8** Spreading of excitation in the F0SBIV model

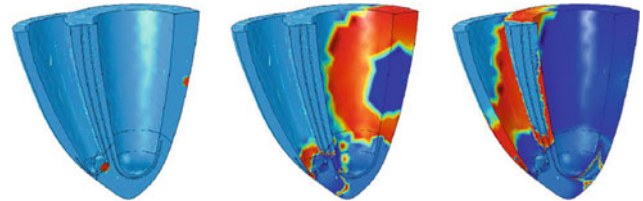


**Fig. 9** Spreading of excitation in the IASBIV model

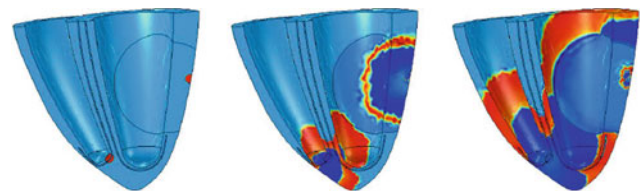


**Fig. 10** Spreading of excitation in the ILSBIV model

**Apical ischemia model with BIV pacing (IASBIV).**

See Fig. 9.

**Lateral wall ischemia model with BIV pacing (ILSBIV).**

See Fig. 10.

The results support the thesis of the advantageousness of intrinsic RV and paced LV fusion. A fusion of RV intrinsic activation and LV pacing would reduce dyssynchrony.

Table 1 describes the differences in activation times at each point of the ischemic models in comparison with the physiological model without ischemic areas. The bold values indicate differences of 20–100 time-steps. The bold underlined values indicate differences of more than 100 time-steps.

## 4 Discussion

Based on the comparison of the activation times of each model, the models with low pacing energy are the least suitable. First and foremost, this trend is confirmed in the



model with an apical ischemic area with pacing delivered directly to this affected site. Increasing pacing energy at the same location of ischemia leads to a more physiological reference. This confirms the hypothesis that the placement of pacing electrodes in ischemic sites is associated with higher pacing thresholds and the need for lead repositioning. The problem of uneven right and left ventricular activation during RV pacing at the apex is confirmed by simulations in models with lower and higher RV pacing energies. Due to this fact, concerns have been raised in the clinical practice regarding the potential risk of dilation of the muscle during chronic long-term right ventricular pacing.

The presented model is adjustable and allows changing both the location of ischemic areas and the mechanical parameters of pacing electrodes, their output, and their site according to the needs of particular centers.

**Conflict of Interests** The authors declare that they have no conflict of interest.

## References

1. Tysler M., Tinová M.: Representation of myocardium depolarization by simple models, In: Proceedings of Computers in Cardiology Conference, pp. 703–706, IEEE, London (1993)
2. Adam DR.: Propagation of depolarization and repolarization processes in the myocardium-an anisotropic model, *IEEE Trans Biomed Eng.* 38(2), 133–41 (1991)
3. Keener J., Sneyd J.: *Mathematical physiology*. 2nd ed. Springer, New York (2009)
4. Pullan AJ., Cheng LK. Buist LM.: *Mathematically modelling the electrical activity of the heart: from cell to body surface and back again*. World Scientific, New Jersey (2005)
5. Goktepe S., Kuhl E.: Computational modeling of cardiac electrophysiology: A novel finite element approach. *International Journal for Numerical Methods in Engineering.* 79(2), 156–178 (2009)
6. Rodríguez B., Tice BM., Eason JC., Aguel F., Ferrero JM., Trayanova N.: Effect of acute global ischemia on the upper limit of vulnerability: a simulation study. *Am J Physiol Heart Circ Physiol.* 286(6), 2078–88 (2004)
7. Kogan BY: *Introduction to computational cardiology: mathematical modeling and computer simulation*. Springer, New York (2010)
8. Despopoulos A., Silbernagl S.: *Color Atlas of Physiology*, 6th ed. Georg Thieme Verlag KG (2009)

# Mathematical Modeling of Ocular Pulse Blood Filling in Rheophthalmography

D. M. Shamaev, P. V. Luzhnov, and E. N. Iomdina

## Abstract

Blood flow in the anterior segment of the eye is examined. In rheographic studies, the volume/resistance ratio is used to calculate the increase in blood volume. The coefficient of proportionality depends on the shape of the biological object, its spatial heterogeneity, and other factors. In ophthalmology, the coefficient of proportionality has not been calculated so far. We show that this coefficient can be calculated using a parameterized model, described in the paper: we use the increment of pulse volume and the total volume of the orbit. The model follows eyeball morphology and involves three components of the vascular layer: the iris, the ciliary body, and the choroid. It is a figure of rotation with an axis that coincides with the antero-posterior axis of the eye. The rheophthalmic signals were taken from a group of patients with an anophthalmos: in total, three two-minutes long records were analyzed. The model disregarded the eyeball but took account of all surrounding tissues. In the simulation, a spherical element was introduced as a glass prosthesis. By simulation, we determined the ratio of the changes in eyeball volume and the rheophthalmic signal. This ratio takes into account the eyeball, the surrounding tissues and pulse fluctuations of both.

## Keywords

Transpalpebral rheophthalmography • Mathematical modeling • Eye • Blood filling

## 1 Introduction

The normal functioning of the eye, like that of any other human body organ, requires an adequate level of trophicity of its tissues, which is detected by the relevant blood flow parameters during diagnostic procedures. In eye pathologies like myopia, diabetic retinopathy, glaucoma, or retinal vascular occlusion, hemodynamic tests of the eye provide the ophthalmologist with additional data on the pathogenesis of the disease, ensure prospects of early diagnosis, and enable the evaluation of treatment efficiency.

Impedance methods of diagnostics are known in ophthalmologic practice [1–3]. Rheophthalmography is used to test eye hemodynamics in physiological conditions [4]. Our method of diagnostics, called transpalpebral rheophthalmography (TP ROG), could be used in the diseases listed above [3, 5, 6].

When analyzing TP ROG signals, we need to determine the contribution of ocular blood flow. TP ROG involves the examination of the anterior segment, namely the vascular structures: the ciliary body and the iris [7]. We also need to assess the contribution of eye blood supply into the amplitude of the registered signals [6, 8].

The paper examines the flow of the anterior segment of the eye. Changes in the volume of the choroid are not considered. The anterior segment accounts for more than two thirds of the volume of circulation. In rheographic studies, the volume/resistance ratio is used to calculate the increment in blood volume. The coefficient of proportionality depends on the shape of the biological object, its spatial heterogeneity, and other factors. In ophthalmology, the proportionality coefficient has not previously been calculated. We show that this coefficient can be calculated using a parameterized model. We use the increment of pulse volume and the total volume of the orbit. Changes in the model parameters are determined using geometric formulas in solving the inverse problem.

D. M. Shamaev (✉) · P. V. Luzhnov  
Bauman Moscow State Technical University, 2-nd Baumanskaya  
5, 105005 Moscow, Russia  
e-mail: shamaev.dmitry@yandex.ru

E. N. Iomdina  
Moscow Helmholtz Research Institute of Eye Diseases,  
Sadovaya-Chernogryazskaya 14/19, 105062 Moscow, Russia

## 2 Materials and Methods

Following the morphology of the eyeball [9, 10], the vascular layer can be divided into three components (see Fig. 1):

- (1) the iris;
- (2) the ciliary body;
- (3) the choroid.

The iris is a thin and movable diaphragm with a pupil in the center. The average thickness is 0.4 mm, the horizontal diameter is 12.5 mm, the vertical diameter is 12 mm. For calculations, it is assumed that the iris has the shape of a circle with a diameter of 12 mm. The pupil diameter in the relaxed state averages 3.5 mm. The cross-section of the iris can be approximated by an ellipse. The dimensions of the ellipse (see Fig. 2) are determined by the semi-minor axis  $a = 0.2$  mm and the semi-major axis  $b = 2.125$  mm.

The iris is a figure of rotation with an axis that coincides with the antero-posterior axis of the eye. The axis of rotation does not pass through the anterior segment. Therefore, the second theorem of Gulden is used to calculate the volume. The center of mass of the ellipse is located at the intersection of its axes. Its distance to the axis of rotation is 3.875 mm. The estimated volume of the iris is  $32.50 \text{ mm}^3$ . The value of the small semi-axis varies in order to take account of the pulse oscillations. It does not change the position of the center of mass in the simulation. Then, as the blood volume increases, the thickness of the iris changes, and the diameter remains constant.

The ciliary body is represented in the section as a triangle (see Fig. 3). The first vertex is at point T1. This point is a contact between the iris and the ciliary body. It is located at a distance of 6 mm from the axis of rotation. The second vertex is at point T2. It is determined by a distance equal to the diameter of the relaxed lens 4.75 mm (with an average lens diameter of 9.5 mm). The point T3 is determined from the data of the anatomical atlas [9]. The axis of rotation

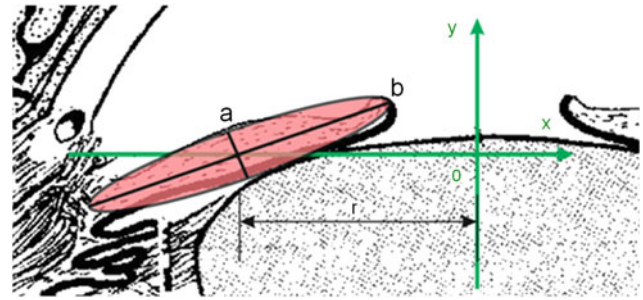


**Fig. 2** Modeling components parameters of the iris

passes through the antero-posterior axis of the eye. Three points determine the rotation figure of the ciliary body in the chosen coordinate system. The radius of rotation of the ciliary body is 6.92 mm.

During pulsations in the ciliary body, the position of the point T1 changes along the cross-section of the frontal plane. The points T2 and T3 remain fixed in the anatomical structures of the eye. This will change the position of the center of mass of the triangular section. The calculated volume of the ciliary body yields  $88.275 \text{ mm}^3$ .

It is known that the thickness of the choroid is normally 0.3 mm on average (see Fig. 4). Its thickness is reduced to 0.12 mm on the distal part. The diameter of the eyeball is 23 mm in the equatorial region. It is possible to specify the inner area of the choroid with a sphere of a smaller radius than that of the outer one. The center of the inner sphere is shifted relative to the center of the outer sphere in the direction of the pupil. The radius of the inner sphere is determined by means of geometric constructions. The center offset is 0.09 mm. The volume of the choroid is  $233 \text{ mm}^3$ .

At the next stage of the simulation, it is necessary to take into account the pulse oscillations of the surrounding eye tissues. For this purpose, the pulse volume of the orbit is calculated. Using the data of the method gamma-resonance ophthalmovelocitysymmetry is possible. Measurements of the oscillation of the anterior segment of the eye in the antero-posterior direction are described. According to the

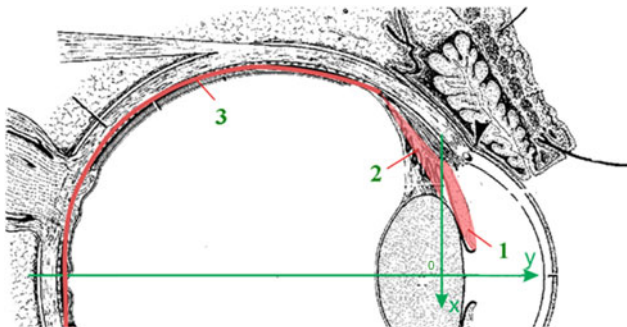


**Fig. 1** The vascular layer of the eye and the components of the model

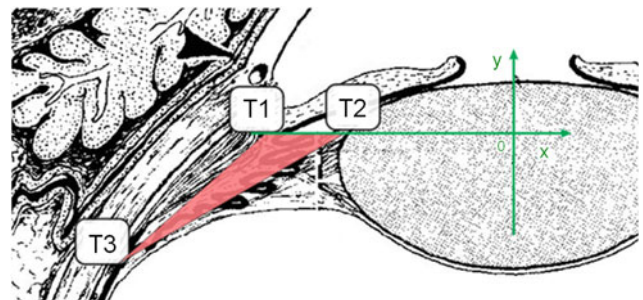


**Fig. 3** Modeling components parameters of the ciliary body

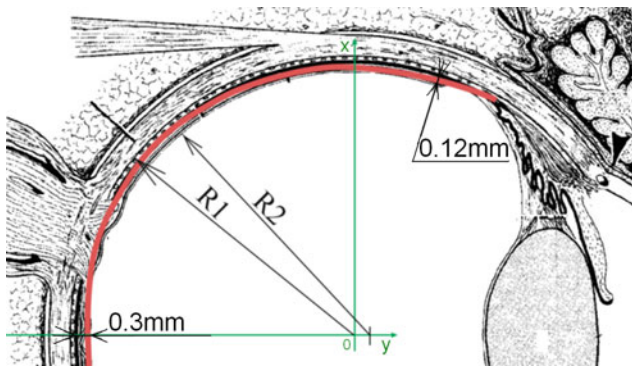


**Fig. 4** Modeling components parameters of the choroid

gamma-resonance ophthalmovelsymmetry method and [11], the oscillation is about 22  $\mu\text{m}$ .

Pulse oscillations are possible only in one axial direction. All other directions are not considered because of the anatomical structure of the orbit. In the calculation, it is assumed that the entire volume of the orbit is an ellipsoid. The volume variations of such ellipsoid can be determined by varying the length of one half-axis. It is the longitudinal axis, which coincides with the anterior-posterior axis of the eye. The volume of the orbit is about 30 ml. It was determined that the pulse volume of all orbital tissues was

17.2  $\text{mm}^3$  using the formulas obtained. Pulse volume is 15.2  $\text{mm}^3$  for surrounding tissues, based on the fact that the pulse volume of the eyeball is 2  $\text{mm}^3$ .

The simulation used the finite element method. The mathematical apparatus of the model is described by means of electromagnetic interaction equations taking into account the boundary conditions. To solve such problems, Maxwell's equations are used in combination with other fundamental equations. In particular, the equation of continuity, Ohm's law in a differential form with allowance for external current sources, as well as the equation of the relationship between the electric potential and the electric field strength.

The results of the simulation were tested experimentally. At the stage of modeling the eye and orbit, the data of previous studies [3] on a group of patients without ophthalmopathy were used. To verify the results of the simulation of pulse oscillations of the eye's orbit (without the eyeball), the results of studies conducted on three patients with an anophthalmos were used.

### 3 Compliance with Ethical Requirements

This study was performed in accordance with the Declaration of Helsinki and was approved by the Local Committee of Biomedical Ethics of the Moscow Helmholtz Research

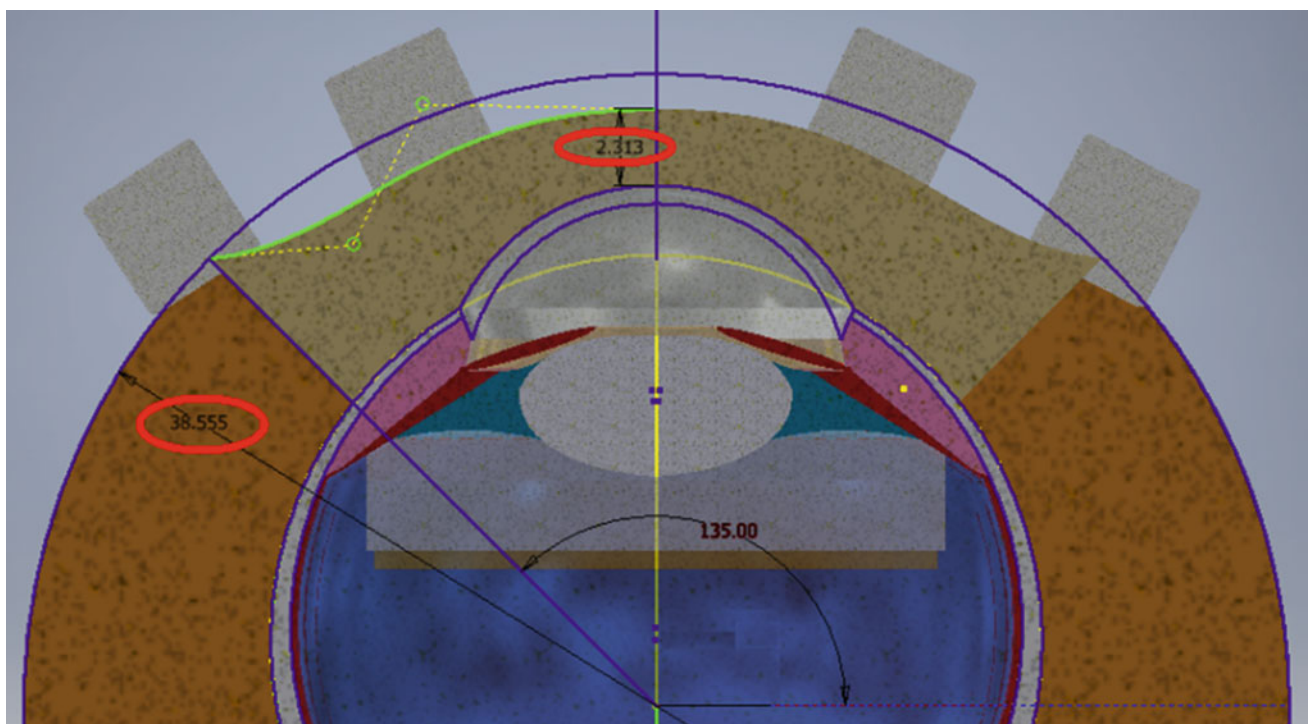


**Fig. 5** Modeling TP ROG parameters by pulse oscillations



**Table 1** Modeling parameters during pulse oscillations

Modeling steps	Eyelid thickness (mm)	Orbit inner radius (mm)
Step 1	2.300	38.5500
Step 2 with pulse	2.313	38.5552

Institute of Eye Diseases. A written informed consent was obtained from all participants.

## 4 Results

TP ROG signals were taken from a group of patients with an anophthalmos. The model disregarded the eyeball but took account of all surrounding tissues. Glass or plastic eye prostheses are usually used. In the simulation, a spherical element was introduced as a glass prosthesis. As a result, all the tissues of the eye are represented by a glass prosthesis, which was surrounded by the fat layer and the eyelid.

It was proposed to change the values of the thickness of the eyelid and the inner radius of the orbit to simulate pulse oscillations (see Fig. 5).

Modeling parameters are presented in Table 1.

Results of modeling have shown that the resistance increment to an impedance makes:

$$dR/R = 0.78 \times 10^{-3}.$$

TP ROG signals of six patients with eye prostheses have been analyzed, yielding the following results:

$$dR/R = (0.72 \pm 0.10) \times 10^{-3}.$$

The difference between modeling and experimental results amounted to 7%.

Thus, taking into account the modeling data, we can formulate the following ratio:

$$dR/R = 7.12 \times dV/V.$$

Finally, for TP ROG, the proportionality taking account of eye's pulse oscillations can be considered as  $K_{\text{ROG}} = 7.12$ .

## 5 Conclusions

Our simulation was used to determine the ratio of changes in the blood flow volume of the eyeball and the signal. This ratio takes into account not only the surrounding tissues but also their pulse fluctuations.

**Acknowledgements** The paper was supported by a grant from RFBR (No.18-08-01192).


**Conflict of Interest** The authors declare that they have no conflict of interest.

## References

1. Avetisov, E.S., Katsnel'son, L.A., Savitskaia, N.F. Rheocyclographic examinations in myopia. *Vestnik Oftal'mologii* 80(3), 3–7 (1967).
2. Lazarenko, V.I., Kornilovsky, I.M., Il'enkov, S.S. et al. Our method of functional rheography of eye. *VestnikOftal'mologii* 115 (4), 33–37 (1999).
3. Luzhnov, P.V., Shamaev, D.M., Iomdina, E.N. et al. Transpalpebral tetrapolar reoophthalmography in the assessment of parameters of the eye blood circulatory system. *Vestn Ross Akad Med Nauk* 70(3), 372–377 (2015).
4. Lazarenko, V.I., Komarovskikh, E.N. Results of the examination of hemodynamics of the eye and brain in patients with primary open-angle glaucoma. *Vestnik Oftal'mologii* 120(1), 32–36 (2004).
5. Shamaev, D.M., Luzhnov, P.V., Pika, T.O. et al. Applying Transpalpebral rheophthalmography to monitor effectiveness of the treatment of patients with glaucoma. *Int J Biomed* 6(4), 287–289 (2016).
6. Luzhnov, P.V., Shamaev, D.M., Iomdina, E.N. et al. Using quantitative parameters of ocular blood filling with transpalpebral rheophthalmography. *IFMBE Proceedings* 65: 37–40 (2017).
7. Standring, S. *Gray's Anatomy: The Anatomical Basis of Clinical Practice*, 39 edition. Elsevier (2005).
8. Shamaev, D.M., Luzhnov, P.V., Iomdina, E.N. Modeling of ocular and eyelid pulse blood filling in diagnosing using transpalpebral rheophthalmography. *IFMBE Proceedings* 65:1000–1003 (2017).
9. Krstic, R.V. *Human Microscopic Anatomy*. Springer-Verlag (1991).
10. Roebuck, J. *Anatomy 360: The Ultimate Visual Guide to the Human Body*. Thunder Bay Press (2015).
11. Schmetterer, L., Kiel, J. *Ocular Blood Flow*. Springer (2012).



# Velocity Measurement at Carotid Siphon: Quantitative Comparison of Phase Contrast MRI and Computational Fluid Dynamics

Chi Zhang , Jinfeng Yang, Ning Ding, Feiyan Chang, Sheng Xie, Deyu Li, and Xiaoxu Hou

## Abstract

Phase contrast magnetic resonance imaging (PC MRI) and the computational fluid dynamics (CFD) are two of the most important technologies in the investigation on the velocity field in blood vessels *in vivo*. In order to quantitatively compare the differences between the two methods, the blood flow velocity measurements based on PC MRI and patient-specific CFD were conducted at internal carotid artery from 9 healthy volunteers. The 3D velocity field calculated from PC MRI data were compared with CFD simulation in 5 planes covering the carotid siphon. Then the resistance index (RI), and errors in the magnitude and direction of velocity were calculated between the two methods. The results showed that the flow patterns of PC MRI and CFD were similar, and the velocity distribution and RI was in good agreement. But there were significant differences in the velocity magnitude near the posterior knee and vessel wall, while the directional error was larger at the center of the artery. These comparison between PC MRI and CFD may guide the development of CFD technology and improve its accuracy.

## Keywords

Carotid siphon • Phase contrast magnetic resonance imaging • Computational fluid dynamics • Blood flow Velocity field

C. Zhang (✉) · J. Yang · N. Ding  
Beihang University, Beijing, 100083, China  
e-mail: chizhang@buaa.edu.cn

F. Chang · S. Xie  
China-Japan Friendship Hospital, Beijing, 100029, China

D. Li  
State Key Laboratory of Virtual Reality Technology and Systems,  
Beihang University, Beijing, 100083, China

X. Hou  
National Institutes for Food and Drug Control, Beijing,  
102629, China

## 1 Introduction

Phase contrast magnetic resonance imaging (PC MRI) is a technique that uses changing phases to enhance blood flow signals [1]. This technique is widely used in the studies on cardiovascular diseases related to abnormal blood flow, such as the diagnosis of aortic stenosis [2]. Especially, PC MRI is one of the best methods in the noninvasive measurement of intracranial blood flow [3–7]. Harloff [8] found that PC MRI performed better in the measurement of blood flow in small cerebral arteries, when comparing with ultrasound. On the other hand, computational fluid dynamics (CFD) is a calculation method based on mathematics, hydrodynamics and computing, which is widely used to simulate blood flow under physiological and pathological conditions [9]. However, CFD has some limitations. The results of CFD depend on the model which should be physically reasonable, mathematically applicable and suitable for computing. In addition, the preparation of the model depends largely on the experience and skills, and the calculation is based on some simplified hypotheses.

As the two important methods are applied to the hemodynamic analysis *in vivo*, the comparison between PC MRI and CFD is of great significance. Leuprecht [10] studied the blood flow of two subjects' ascending aortas by PC MRI and CFD, and found the blood velocity derived from the two methods had good consistency. However, the main focus of previous comparative studies was usually on the aorta, while the studies on more tortuous blood vessels are rare, such as internal carotid artery (ICA). ICA is a common site of vascular stenosis and aneurysms. Studies have shown that the occurrence of stenosis and aneurysms at this place is associated with its tortuous geometry and the hemodynamic factors [11, 12]. Therefore, the study on the blood flow here is of great significance to reveal the mechanism of stenosis and other diseases at ICA.

In this paper, the velocity fields in ICA of 9 healthy volunteers were measured by PC MRI. The velocity fields were then visualized and compared with those calculated

from CFD. The correlation of the RI calculated from CFD and PC MRI was analyzed. Relative errors in the magnitude and direction of velocity were calculated to quantitatively compare velocity fields obtained from CFD and PC MRI.

## 2 Subjects and Methods

### 2.1 PC MRI Scan

The scan was performed on a 3T MRI system (Philips Ingenia, Philips Medical Systems, Holland) in China-Japan Friendship Hospital, Beijing. 9 healthy volunteers participated in the MRI examination at carotid siphon, which included anterior and knee. The examination was a phase-contrast 3D flow MRI to obtain velocity field of blood flow. Further imaging parameters were as follows: velocity encoding parameter (VENC) 100 cm/s, spatial resolution  $0.625 \text{ mm} \times 0.625 \text{ mm} \times 2.4 \text{ mm}$  for 30 layers, flip angle  $15^\circ$ , TE 3.1 ms, TR 6.42 ms, and 18 frames per cardiac cycle. The experiment protocol was approved by the ethics committee of Beihang University.

### 2.2 Image-Based CFD Modeling

The 3D geometric models of the carotid artery were derived from PC MRI scan and produced in MIMICS software (Materialise Inc., Belgium). The inlet plane was selected at the straight part of ICA (upstream of the posterior knee), which was perpendicular to the blood vessel. The outlet plane was selected at the downstream of the anterior knee. The models were then imported into Gambit (ANSYS, US) for meshing to tetrahedrons and hexahedrons. The blood was considered as incompressible fluid with the density  $\rho = 1056 \text{ kg/m}^3$ . Newtonian fluid was assumed in this CFD simulation, with the dynamic viscosity  $\mu = 4 \times 10^{-3} \text{ kg/m} \cdot \text{s}$ . The motion of blood was assumed as unsteady laminar flow in the study according to the  $Re$  number. The vascular wall was assumed as rigid wall with a non-slip boundary condition in this paper. The fluid computing was conducted in Fluent (ANSYS, US) and then the converged consequence was used to compare with the data from 3D PC MRI.

The inlet condition of the CFD model was derived from PC MRI measurement. With the sampling rate of 18 frames per cardiac cycle, the flow waveform at each point in the inlet plane was fitted by Fourier fitting method:

$$f(x) = a_0 + \sum_{n=1}^3 (a_n \cos n\omega t + b_n \sin n\omega t)$$

where  $\omega$  was calculated by patient-specific frequency of arterial pulse. Because the velocity data from PC MRI was sparser than the mesh nodes used in CFD, cubic interpolation was carried out to PC MRI data to obtain the velocity profile in the inlet plane, which was used as the boundary condition for the inlet. A free outflow was set as the boundary condition for the outlet.

### 2.3 Comparison and Statistical Analysis

In order to compare the velocity vectors measured from CFD and PC MRI quantitatively, 5 horizontal planes were chosen evenly distributed from the upstream of the posterior knee to the downstream of the anterior knee (Fig. 1). Resistance index (RI) calculated from CFD and PC MRI results was compared in Z1 and Z5 plane for all the subjects. The RI was calculated from the velocity by the following formula:

$$RI = (SV - DV) / SV \quad (1)$$

where SV was peak systolic velocity, DV was end-diastolic velocity.

The difference of velocity field obtained from PC MRI and CFD were assessed by the magnitude and direction errors. The magnitude error was calculated as the relative error of the velocity magnitude between the PC MRI (V1) and CFD (V2) as  $|(V2 - V1) / V1|$ . For the direction error, we proposed a method that can quantitatively describe direction difference between the two velocity vectors. Firstly, the two velocity vectors were normalized respectively. Then the subtraction of the two normalized vectors was obtained, the magnitude of which was used to assess the directional difference between the two velocity vectors.

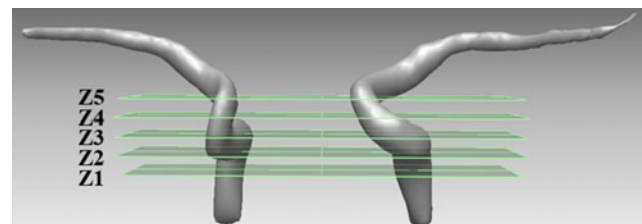


Fig. 1 The 5 planes perpendicular to the z axis

### 3 Results

The velocity field obtained from CFD and PC MRI were visualized and compared between 9 subjects (Fig. 2). The flow pattern was generally the same (Fig. 3). However, some differences were found regionally. The velocity calculated from CFD method was generally larger than that measured by PC MRI. More turbulence was found near the bend, such as the posterior knee, in CFD results; while in PC MRI results, the flow pattern was closer to laminar flow.

RI is a quantitative indicator commonly used to reflect the magnitude of blood flow resistance, which is also considered as an indirect diagnosis index of vascular stenosis [24]. Figure 4 presented the correlation of RI between the two methods in Z1 and Z5 plane from all the subjects. It was observed that the RI results from PC MRI and CFD were in

linear correlation to each other, and the results in Z1 and Z5 were similar. But the slope in the figure was not close to 1, indicating that the RI values obtained from CFD method cannot be used directly for clinical diagnosis.

The magnitude difference of velocity obtained from CFD and PC MRI highly depended on the position within and between planes. In each plane, the relative error was smaller at the center of blood vessel, but bigger near the wall. Moreover, it showed that the errors in the planes near the anterior and posterior knee were higher than those far away from them. However, errors of velocity direction showed a different distribution from the magnitude (Fig. 5). It was observed that near the vessel wall, the direction error was lower; but it was higher at the center of the vessel. This rule was found in all the planes, no matter they were near or far from the siphon bends.

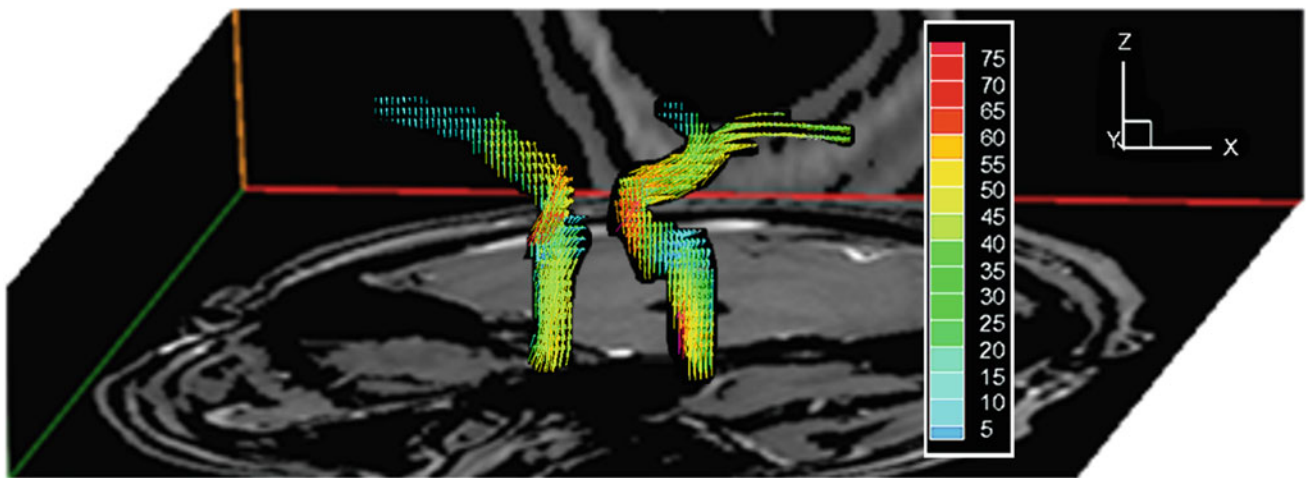


**Fig. 2** Velocity vector field reconstructed using PC MRI data from a subject. Different colors of vectors represented the blood flow speed. The unit was cm/s

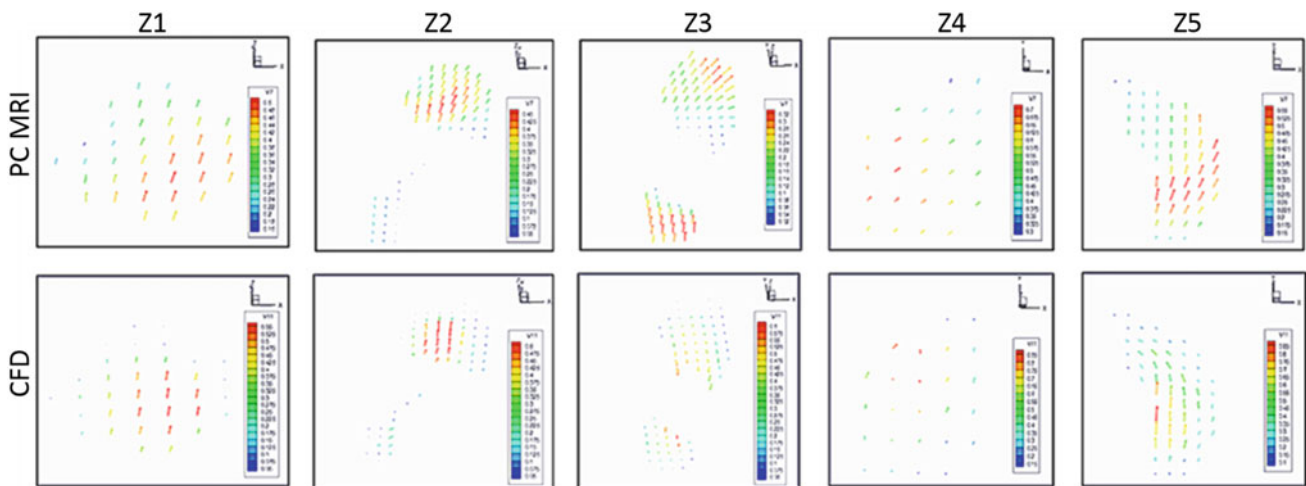


**Fig. 3** Distribution of vectors from PC MRI and CFD

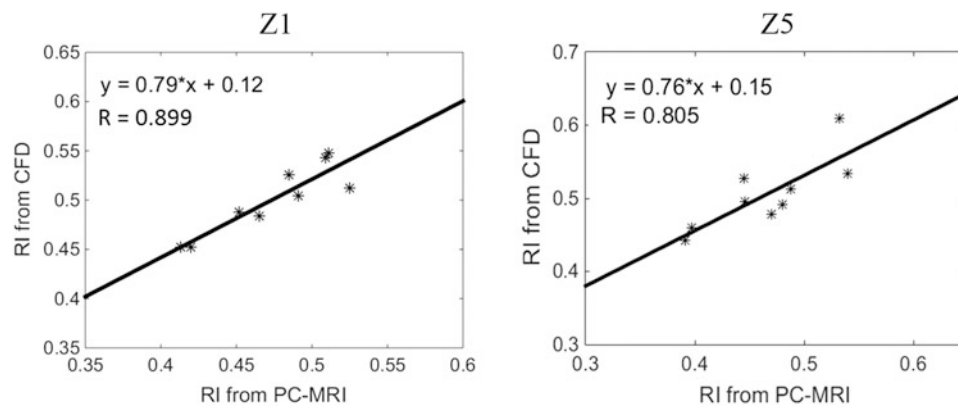


**Fig. 4** The correlation of RI in plane Z1 and Z5 calculated by PC MRI and CFD

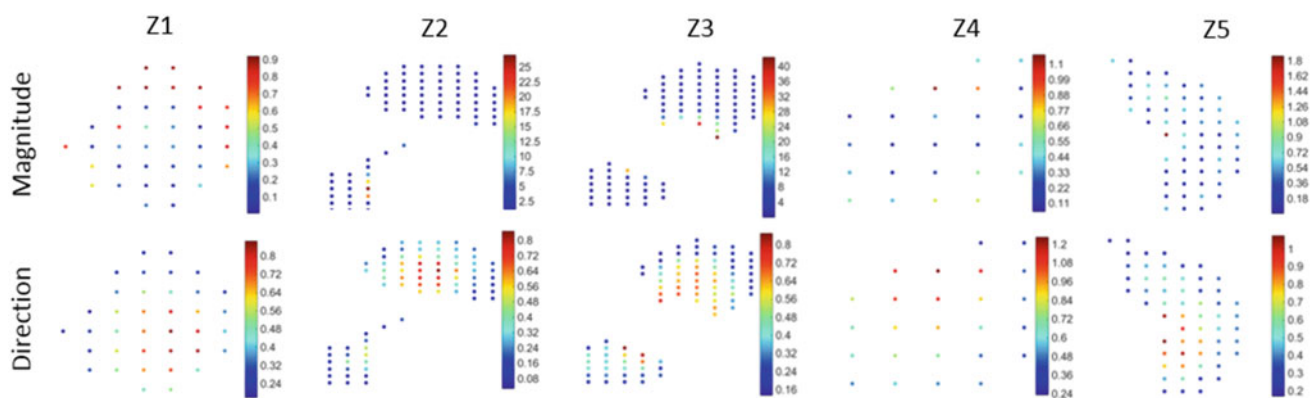


**Fig. 5** Quantitative comparison between PC MRI and CFD

## 4 Discussion and Conclusion

The diagnosis of cerebrovascular diseases is increasingly dependent on hemodynamic information which can be obtained by CFD method. CFD can achieve very high spatial and temporal resolution, but its boundary conditions need to be set carefully. The boundary conditions usually depend on the image technology and the measurement of flow rate and pressure. Moreover, there are some idealized assumptions in the simulation process, which are also the sources of CFD errors. This study compared the PC MRI results with the CFD simulation at ICA siphon among 9 healthy volunteers. The quantitative comparison of the two methods can give more comprehensive hemodynamic analysis for ICA, which helps to establish a reliable and accurate method to evaluate the hemodynamic factors in cerebral arteries.

Inlet boundary conditions of CFD directly affect the simulation results of flow field. Ali SF [13] used PC MRI

measurements to produce patient-specific flow-time waveform and assigned it as inlet boundary condition for blood velocity calculation at the carotid bifurcation on a 30-year old normal male subject. The inlet boundary conditions used in above study concerned the blood flow rate of cross section, rather than the velocity profile, which may result in inaccurate results. In this study, the inlet velocity, varied not only temporally but also spatially, were used as boundary conditions during CFD calculation. Therefore, the result was closer to the physiological condition, which could reduce the error due to the inaccuracy of boundary conditions.

Previous studies have focused on quantitative comparison of the magnitude errors between the two methods. For example, Ali SF [13] and Harloff A [14] quantitatively compared the velocity magnitude of PC MRI and CFD in the carotid bifurcation. However, the comparison of the velocity direction was limited to qualitative studies. This paper transforms the direction difference into a vector obtained from the subtraction of two normalized vectors. It provides a



novel approach to quantitatively compare the vector directions between PC MRI and CFD.

Taking the advantages above, the results of this study shows that, though the velocity derived from the two methods shows a similar pattern, there are still some differences in local and detail, which is similar to the previous studies. Van OP [15] and Cebra JR [16] measured the blood flow of the carotid bifurcation and the normal cerebral arteries with CFD and PC MRI, and compared the results of the two methods. They found that the results of the two techniques have a good consistency, and show a greater difference at the bifurcation. The difference between the two technologies found in our paper mainly reflected in the relative errors of the velocity at the tortuous part of ICA. It showed that the error near the bend is relatively large, which may be related to the complicated flow pattern at the bend. It was also found that magnitude errors were bigger near the vessel wall than at the center. But for the error of velocity direction, the distribution was opposite; the error was larger at the center of the vessel, probably because of the restriction of the vessel wall.

There are still some limitations in this paper. The blood vessel was simplified as a rigid wall, and blood was assumed as Newton fluid, which may lowered the accuracy of the simulation. On the other hand, the results showed larger errors at the bend, implying that the turbulence model may help to improve the accuracy at the bend. In addition, the samples used in this paper were all from healthy individuals. As ICA stenosis is a common intracranial arterial disease, the study on the blood velocity in the stenosed ICA is of great significance for the diagnosis and treatment. Therefore, the subjects with ICA stenosis should be included for the hemodynamics analysis in the future.

In conclusion, the measurement of blood flow at ICA is important for understanding the mechanism of ICA stenosis. In this paper, the blood flow in ICA siphon was obtained by CFD and PC MRI, and the results were compared quantitatively. Patient-specific inlet conditions obtained from PC MRI were used to as boundary condition of CFD. Although the two methods show consistency in the distribution of velocity, a larger difference has been found at the siphon bend. In each plane, the relative error of the velocity magnitude was larger near the vessel wall; while the directional error was larger at the center. Comparison of the two methods may help us to establish a more reliable and accurate measurement of blood flow in ICA.

**Acknowledgements** This work was supported by National Natural Science Foundation (No. 11672026 and No. 11302019), and State Key Laboratory of Virtual Reality Technology and Systems.

**Conflict of Interest** The authors declare that they have no conflict of interest.

**Statement of Informed Consent** Informed consent was obtained from all individual participants included in the study.

**Protection of Human Subjects and Animals in Research** All procedures performed in studies involving human participants were in accordance with the ethical standards of the institutional and/or national research committee and with the 1964 Helsinki declaration and its later amendments or comparable ethical standards.

## References

1. Macdonald, M.E.: Cerebrovascular MRI: a review of state-of-the-art approaches, methods and techniques. *Nmr in Biomedicine* 28(7), 767–791 (2015).
2. Goubergrits, L.: MRI-based computational fluid dynamics for diagnosis and treatment prediction: Clinical validation study in patients with coarctation of aorta. *Journal of Magnetic Resonance Imaging* 41(4), 909–16 (2015).
3. Lotz, J.: Cardiovascular Flow Measurement with Phase-Contrast MR Imaging: Basic Facts and Implementation. *Radiographics A Review Publication of the Radiological Society of North America Inc* 22(22), 651–671 (2002).
4. Hofman, M.B.M.: In Vivo Validation of Magnetic Resonance Blood Volume Flow Measurements with Limited Spatial Resolution in Small Vessels. *Magnetic Resonance in Medicine* 33(6), 778–784 (1995).
5. Alperin, N.: Hemodynamically independent analysis of cerebrospinal fluid and brain motion observed with dynamic phase contrast MRI. *Magnetic Resonance in Medicine* 35(35), 741–754 (1996).
6. Spilt A.: Reproducibility of total cerebral blood flow measurements using phase contrast magnetic resonance imaging. *Journal of Magnetic Resonance Imaging* 16(1), 1–5 (2010).
7. Bardan, G.: Simple patient-based transmante pressure and shear estimate from cine phase-contrast MRI in cerebral aqueduct. *IEEE Transactions on Biomedical Engineering* 59(10), 2874–2883 (2012).
8. Harloff, A.: Comparison of blood flow velocity quantification by 4D flow MR imaging with ultrasound at the carotid bifurcation. *American Journal of Neuroradiology* 34(7), 1407–1413 (2013).
9. Pekkan, K.: In Vitro Hemodynamic Investigation of the Embryonic Aortic Arch at Late Gestation. *Journal of Biomechanics* 41(8), 1697–1706 (2008).
10. Leuprecht, A.: Blood flow in the human ascending aorta: a combined MRI and CFD study. *Journal of Engineering Mathematics* 47(3), 387–404 (2003).
11. Zhang, C.: Flow patterns and wall shear stress distribution in human internal carotid arteries: the geometric effect on the risk for stenoses. *Journal of Biomechanics* 45(1), 83–89 (2012).
12. Zhang, C.: Geometric classification of the carotid siphon: association between geometry and stenoses. *Surgical and Radiologic Anatomy* 35(5), 385–394 (2013).
13. Ali, S.F.: Velocity Measurement in Carotid Artery: Quantitative Comparison of Time-Resolved 3D Phase-Contrast MRI and Image-based Computational Fluid Dynamics. *Iranian Journal of Radiology* 12(3), e18286 (2015).



14. Harloff, A.: 3D blood flow characteristics in the carotid artery bifurcation assessed by flow-sensitive 4D MRI at 3T. *Magnetic Resonance in Medicine* 61(1), 65–74 (2009).
15. Van, O.P.: 3D cine phase-contrast MRI at 3T in intracranial aneurysms compared with patient-specific computational fluid dynamics. *American Journal of Neuroradiology* 34(9), 1785–1791 (2013).
16. Cebal, J.R.: Hemodynamics in Normal Cerebral Arteries: Qualitative Comparison of 4D Phase-Contrast Magnetic Resonance and Image-Based Computational Fluid Dynamics. *Journal of Engineering Mathematics* 64(4), 367–378 (2009).

# Proposal of Physical Model of Cardiovascular System; Improvement of Mock Circulatory Loop

Lukas Peter, Norbert Noury, and Martin Cerny

## Abstract

Each heart ejection gives the blood a pressure force and it creates a pulse wave which travels from the heart to peripheral blood vessels (blood vessel in fingers, toes, ...). This pulse wave travels during arterial tree and it depends on arterial properties as elasticity, stiffness or thickness of the artery wall. It will be very useful to describe the relationship between blood pressure, pulse wave propagation and hemodynamics parameters in real or very similar conditions as are in real cardiovascular system. The whole cardiovascular system can be described as an electrical circuit with resistors (resistivity of blood vessels  $R$ ), capacitors (compliance of blood vessels  $C$ ) and inductors (inertance of blood vessels  $L$ ). It is possible to evaluate all of parameters of arteries and developed physical model of cardiovascular system. Physical model has to simulate real conditions which are in human cardiovascular system. It would bring a better knowledge about the behaviour of cardiovascular system and improve its treatment. In this paper are describe possibilities how to model cardiovascular system and developing of physical model of cardiovascular system.

## Keywords

Cardiovascular system • Mock circulatory loop  
Physical model • Model of hemodynamics

L. Peter (✉) · M. Cerny  
Department of Cybernetics and Biomedical Engineering,  
VSB-Technical University of Ostrava, Ostrava, 70800, Czech  
Republic  
e-mail: lukas.peter@vsb.cz

N. Noury · M. Cerny  
University of Lyon, Lab. INL, UMR 5270 CNRS-INSA Lyon,  
Villeurbanne, France

## 1 Introduction

Cardiovascular system is a very important system which is responsible for transport nutrient and oxygen to tissues. As a consequence, the CV system involves complex relationships between various systems in a living body. Therefore it is difficult to run experiments with control of the different parameters and thus, it is interesting to work with a model.

The Cardiovascular system is affected by many factors which makes it very difficult to describe the relationships between hemodynamic and others parameters or pathologies which affected function of cardiovascular system without invasive entrance [1]. Some of these relationships aren't possible to describe by mathematic models because there isn't possible to make experiments in real conditions in real time A multiphysics simulation of the CV system is not accessible. For this kind of purpose would be interesting to have some tool which be able to make this experiments without invasive entrance into the human body [2].

It would be interesting to have some model where would be possible to adjust independently the hemodynamic parameters or to make some pathology and watch their effects to function of cardiovascular system in real time. Some model which will be able to reproduce physiology signal as output with real flow and pressure. It could be also use for education purpose.

## 2 Problem Definition

Nowadays there are exist some cardiovascular models which are used as extravascular blood circuit or as tools for testing of artificial heart's valve or implantable devices. Unfortunately, none of them is possible to use for looking relationships between hemodynamics parameters and propagation of pulse wave and blood pressure value.

## 2.1 Mathematical Models

The mathematical modelling of the cardiovascular system is extremely complex and at the present time no model exists that is able to describe all the parameters of cardiovascular system [3].

It isn't possible to build whole physical model of cardiovascular system with all of its parts (due to quantity and length of all of blood vessels). Based on the equivalence between hydraulic and electrical circuits, it is possible to connect the numerical model to an electrical circuit which is based on a merging of lumped parameter method into a numerical model.

## 2.2 Mock Circulatory Loop Method

Multiple mechanical circulatory support devices (MCSDs) have been developed in recent decades, including total artificial hearts (TAHs) and ventricular assist devices (VADs). Under long-term support circumstances, a physiological control algorithm is necessary for an MCSD to meet various physiological demands. It isn't possible to test it directly in human body so it is necessary to use some system which will be similar to cardiovascular system. For testing such kind of devices was established Mock circulatory loop (MCL) as an in vitro platform for evaluation of cardiac assistance technologies and can provide valuable insights to physiological control development prior to animal and clinical trials [4].

For design of MCL elements, firstly it is necessary to use lumped method for mathematical evaluation of properties of elements afterwards it is possible to developed MCL which will produce similar conditions as human cardiovascular system. Thanks to MCL is possible to measure pressure and flow changes but without effects of modulus of elasticity and other properties of artery segments. It isn't possible to watch relationship between propagation of pulse wave, blood pressure and blood flow. Also it isn't possible to test pressure, flow and other sensor for monitoring of cardiovascular system in real conditions [5] (Fig. 1).

It will be useful to develop some loop which will connected all of nowadays method for simulation of cardiovascular system.

## 3 Implementation of New Solution

Nowadays doesn't exist physical mode of cardiovascular system which has possibility to change all of hemodynamics parameters. Such kind of model would be beneficent for monitoring changes of pulse wave propagation and blood pressure based on hemodynamic parameters.

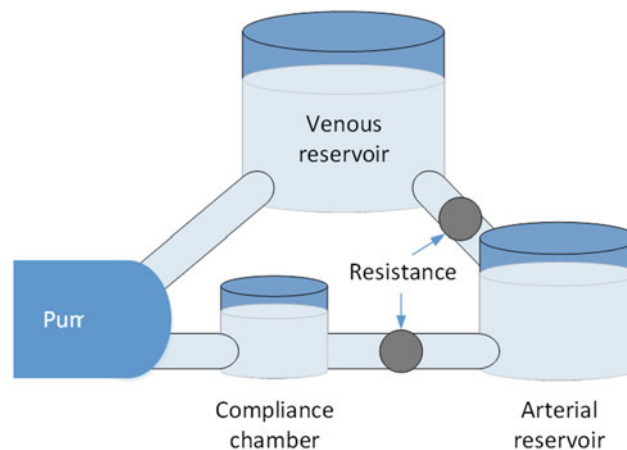


**Fig. 1** Design of MCL consist from arterial and venous reservoirs to simulate compliance and resistance of whole human body, from compliance chamber to simulate compliance of aortic segment and to set offset of pressure and from adjustable valves to change resistance for blood flow

It isn't possible to make model of cardiovascular system which includes all of blood vessels with their parameters. In human body there are thousand kilometres of blood vessels. It is necessary to make some approximation of some parts of cardiovascular system.

It is necessary to produce pulsatile flow, same as in human body. For this purpose was used pulsatile pump (Harvard Apparatus) which is clinically used as external heart. It was used type of pump which is able to simulate the heart of bigger animal with the possibility to change basic hemodynamic parameters. It is possible to set stroke volume in range 5–30 ml, heart rate in range 0–200 bpm and ratio of systole to diastole.

For model of blood vessel segments was needed to use tubes and tubules with define properties as inner diameter, width of artery wall and modulus of elasticity. As the closest material of real blood vessel tissue was choose silicone. For simulation of pathology of arterial segments and for monitoring of pulse wave properties based on changing in arterial tree were also used PVC and Teflon material (Fig. 2).

It was model aortic segment as separate part for measurement of pulse wave propagation. Rest of arterial tree was model as reservoir produces its resistivity and compliance. The venous tree was model simply as reservoir. It was build close circulation loop which was based on adjustment of Mock circulatory loop. It is possible to change some hemodynamics parameters and monitor changes of pulse wave propagation. For such experiment was needed to have a possibility to change blood flow, range of pressure value of systolic, diastolic and pulsatile pressure just with changing of resistivity, compliance of artery segments or heart rate or stroke volume of pulsatile pump.

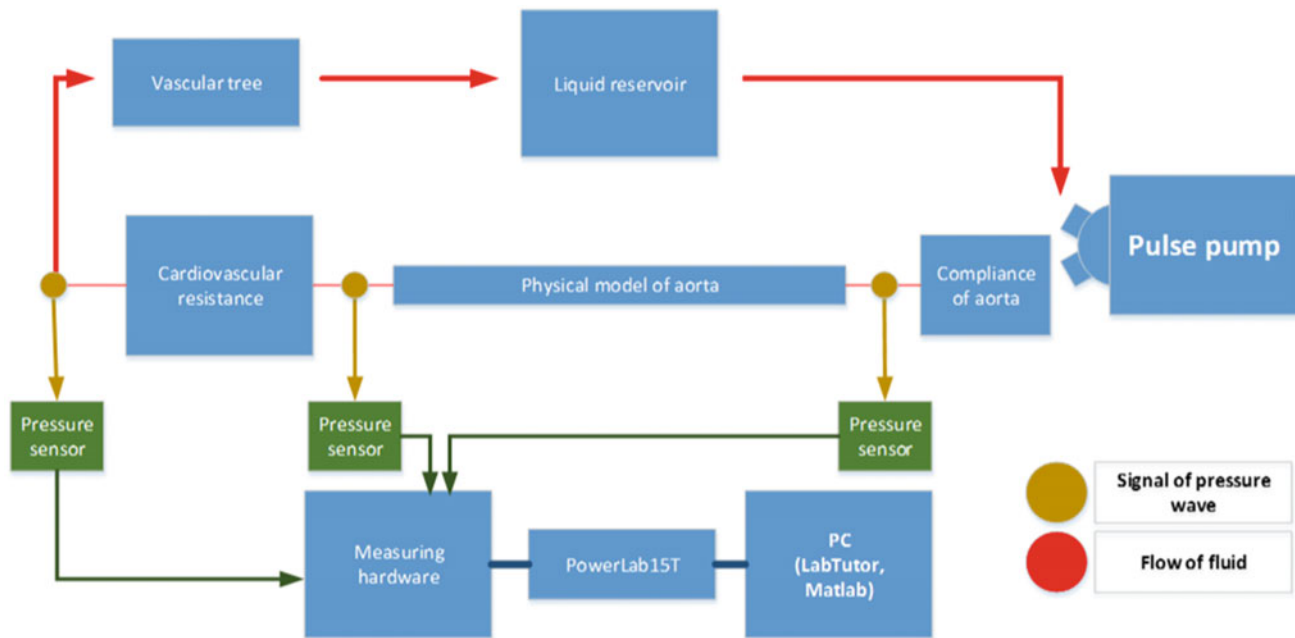


**Fig. 2** Reduced model of cardiovascular system. Pulsatile pump produces liquid flow which continues through first compliance chamber, aortic segment and second compliance chamber to reservoir. It is close loop

### 3.1 First Approach

For the first experiment was developed model of cardiovascular system which contains segment of aorta, one reservoir for simulate compliance of artery tree, one reservoir for simulate compliance and volume of venous tree and one valve to change of resistance of artery. It was necessary to add one chamber on the beginning of aorta for simulation of aortic arch which is the biggest store of energy of each systole of the heart. Without this chamber was measured negative blood pressure.

For aortic segment was used silicone tube with properties. Inner diameter 1.23 cm (inner diameter of aortic part is in range from 2.8 to 1 cm). Width of wall 1 mm width of artery wall is in range from 1.6 to 0.7 mm). Modulus of the elasticity 1.79 MPa (modulus of aortic part is approximately 0.4 MPa. Length 30 cm (length of aortic part is approximately 45 cm).

In the human body the first part of aorta absorbs a lot of kinetic energy of ejected blood. It was needed to add compliance chamber which simulate this kind of effect. Chamber was developed as hermetically closed box where was monitor height of surface of water. On the end of aortic segment was added first bifurcation of arteries to iliac artery. Each of this artery has controllable valve to change resistivity of artery part. Iliac arteries led to reservoir which simulate venous system. This reservoir was open reservoir for store liquid. For first measurement was used water with viscosity 1. Thanks this setting it was measured blood pressure wave close to reality but without physiological

properties (shape affected by bifurcations of artery tree, dicrotic notch, and pulsatile pressure). Pressure wave was measured on the beginning and on the end of aortic segment. With changing hemodynamic parameters was possible to recognize changes in systolic and diastolic blood pressure value and it was possible to detect their time delay (Fig. 3).

## 4 Measured Signal

Pulse wave was measured in several places. With the change of hemodynamics parameters via a pulsatile pump, as HR, stroke volume or positivity (ratio between systole and



**Fig. 3** Preparation for developing of physical model of aorta for the second approach

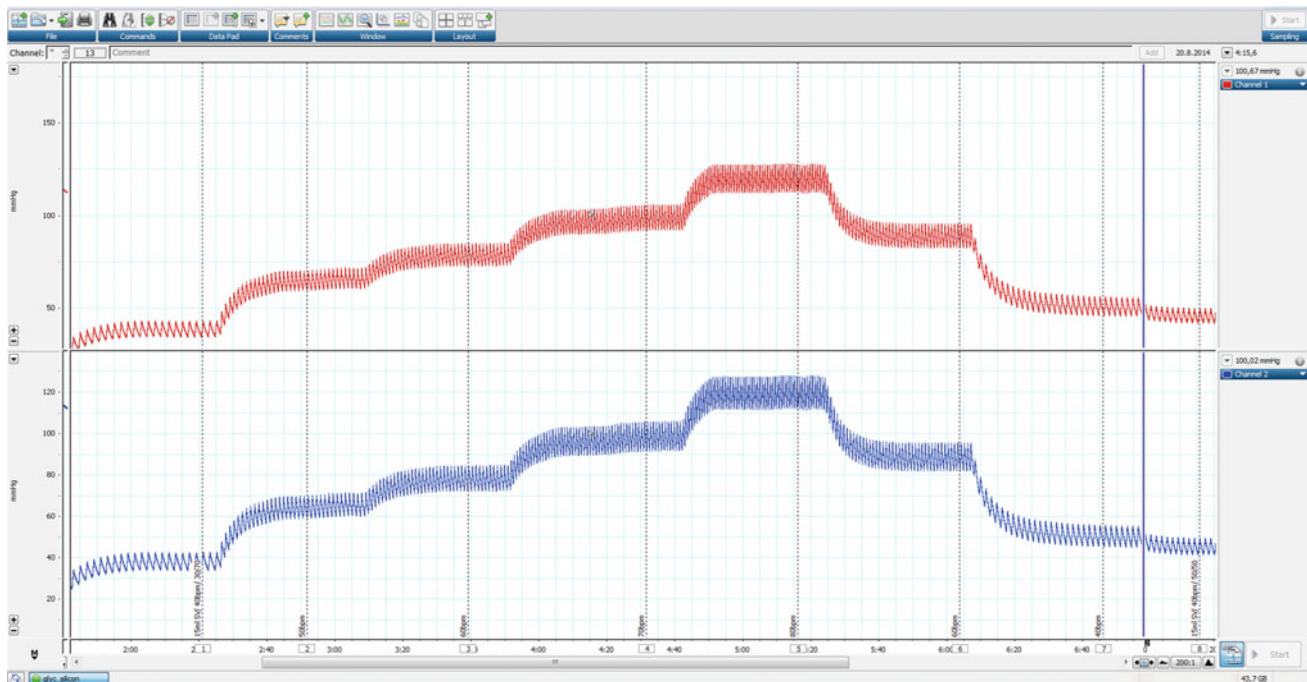


**Fig. 4** The change in blood pressure value for different HR

diastole), it is possible to see change in pulse wave velocity and blood pressure value.

The main goal was to improve Mock circulatory loop to be close to real cardiovascular conditions. It was important to develop physical models of cardiovascular system where will be possible to measure pulse wave and blood pressure with the same properties as in real cardiovascular system as in the human body.

Measured signal was compared with physiologic signal which was measured invasively via catheter. It is possible to see that signal measured thanks to model is very close to real signal.

## 5 Conclusion

It is very important to monitor the state of the cardiovascular system. There are many parameters which can bring significant information about its condition. The best indicator is value of blood pressure. This value gives global information about state of cardiovascular system, but many times it is more useful to know information about each part of the cardiovascular system. Possibility how to evaluate the parameters of each part is to measure pulse wave which gives information about state of blood vessel which reflects the state of the cardiovascular system (Fig. 4).

For precise evaluation based on propagation of pulse wave is necessary to know relationships between

hemodynamics parameters and state of cardiovascular system. This kind of research is very complicated because it is needed invasive measurement. Our model brings a new possibility how to evaluate and describe relationships in cardiovascular system without any risk for patient.

**Acknowledgements** The work and the contributions were supported by the project SV4506631/2101 'Biomedicínské inženýrské systémy XII'.

## References

1. VAN DE VOSSE, Frans N.; STERGIOPULOS, Nikos. Pulse wave propagation in the arterial tree. *Annual Review of Fluid Mechanics*, 2011, 43: 467–499.
2. JERNSTEDT, G. C.; NEWCOMER, Jeffrey P. Blood pressure and pulse wave velocity measurement for operant conditioning of autonomic responding. *Behavior Research Methods & Instrumentation*, 1974, 6.4: 393–397.
3. LIU, Yingjie, et al. Design and initial testing of a mock human circulatory loop for left ventricular assist device performance testing. *Artificial organs*, 2005, 29.4: 341–345.
4. GARRISON, Laura A., et al. A new mock circulatory loop and its application to the study of chemical additive and aortic pressure effects on hemolysis in the Penn State electric ventricular assist device. *Artificial organs*, 1994, 18.5: 397–407.
5. PATEL, S., et al. Design and construction of a mock human circulatory system. In: *Summer Bioengineering Conference*, Sonesta Beach Resort, Florida. 2003.



# Numerical Study on the Effects of Segmental Aqueous Humour Outflow on Ocular Drug Delivery

Ean Hin Ooi, Chai Yee Loke, Norlina Ramli, and Amir Samsudin

## Abstract

The present study develops a 3D model of the human eye to investigate the effects of segmental aqueous humour outflow on ocular drug delivery. Segmental outflow is modelled by prescribing the permeability of the trabecular meshwork (TM) as a spatially-varying heterogeneous function that follows a rectangular profile. The choice of the rectangular profile is decided based on a recent experimental study on segmental outflow. Results from the numerical simulations showed that segmental outflow causes the majority of the drugs to egress through the active part of the TM. In the context of glaucoma treatment, this can be detrimental to the treatment efficacy, since it is the non-active region is the primary target site of the drugs.

## Keywords

Drug delivery • Aqueous humour • Glaucoma

existence of segmental outflow can potentially affect the delivery of ophthalmic drugs to the TM by promoting greater flow of drugs through the active regions, while minimizing drugs exposure of the non-active regions. Since it is the non-active regions of the TM that are targeted by anti-glaucoma drugs, the different drug exposure of the active and non-active regions can potentially cause scenarios of ‘over-treatment’ and ‘under-treatment’ of the disease.

In this paper, a computational model of the human eye is developed to investigate the effects of segmental AH outflow on the delivery of ophthalmic drugs. A 3D eye model is developed and simulations are carried out using the commercial software COMSOL Multiphysics 5.3®. Segmental AH outflow is modelled by prescribing the permeability of the TM as a spatially-varying heterogeneous function. Zones of the TM that mimic active regions are prescribed with a baseline permeability, while zones mimicking non-active regions are assigned with a near-zero permeability.

## 1 Introduction

In a recent study [1], it was found that the outflow of aqueous humour (AH) through the trabecular meshwork (TM) is segmental and heterogeneous, where some parts of the pathway are filtration-active, while the others are not. Filtration active regions generally have a lower flow resistance, while non-active regions are more hydraulically resistant to AH flow. This morphologic variation has been suggested to be the result of a heterogeneous hydraulic resistance across the TM. According to Chang et al. [1], the

## 2 Materials and Methods

### 2.1 The Eye Model

The 3D eye model is developed based on the dimensions reported by Ooi and Ng [2]. A ring-like domain is added into the model around the circumferential edge of the anterior chamber to represent the TM. A gap of 25  $\mu\text{m}$  is created between the iris and the lens to allow the flow of AH from the posterior to the anterior chamber. The model developed is illustrated in Fig. 1a.

### 2.2 The Flow, Thermal and Transport Models

The flow and thermal models used to describe the hydrodynamics of AH are similar to those used by Ooi and Ng [2]. For brevity, these equations (Navier-Stokes equations and

E. H. Ooi (✉) · C. Y. Loke  
School of Engineering, Monash University Malaysia,  
47500 Bandar Sunway, Selangor, Malaysia  
e-mail: ooi.ean.hin@monash.edu

N. Ramli · A. Samsudin  
Faculty of Medicine, Department of Ophthalmology,  
University of Malaya, 50603 Kuala Lumpur, Malaysia

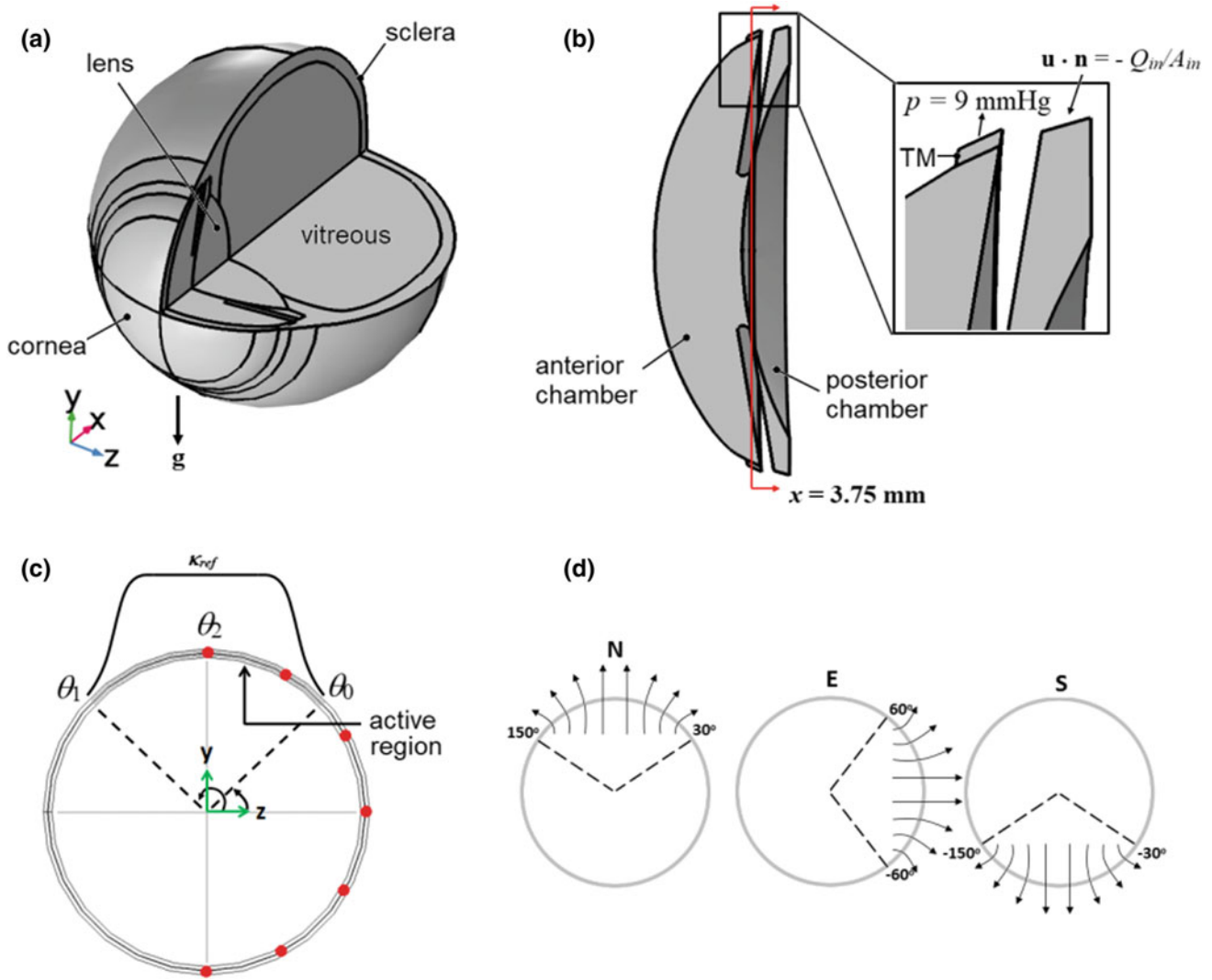


**Fig. 1** **a** The 3D model of the human eye with a cut-view of the interior; **b** the boundary conditions prescribed across the anterior chamber, the posterior chamber and the TM; **c** an illustration of the

profile of the rectangle function; **d** locations of the active outflow for the north (N), east (E) and south (S) positions

bioheat equation) are not presented here and readers may refer to the aforementioned paper for more details. Flow through the TM, which is a porous structure, is described using the Stokes-Brinkmann equation:

$$-\nabla p = -\frac{\mu}{\kappa} \mathbf{u} + \frac{\mu}{\varepsilon} \nabla^2 \mathbf{u} \quad (1)$$

where  $\mu$  is viscosity,  $p$  is pressure,  $\kappa$  is the permeability,  $\varepsilon$  is the porosity and  $\mathbf{u}$  is the velocity vector.

The model describing the delivery of drugs is active only in the cornea, the anterior and posterior chambers and the TM. Only the delivery of ophthalmic drugs via topical eye drops is considered. From the corneal surface, the drugs are

assumed to diffuse into the cornea before entering the AH circulation inside the anterior chamber. The drugs will then egress through both the filtration-active and non-active regions of the TM. The rate of change of the eye drop concentration upon administration onto the corneal surface is given by [3]:

$$\frac{dc}{dt} = -\frac{S}{V_L + V_i \exp(-k_d t)} c \quad (2)$$

where  $c$  is the drug concentration normalized against its initial concentration,  $S$  is the lacrimal secretion rate,  $k_d$  is the tear drainage constant,  $V_L$  is the normal lacrimal volume and  $V_i$  is the initial tear volume after eye drop administration.

Inside the cornea, the anterior and posterior chambers, and the TM, the following equations are prescribed:

$$\frac{dc}{dt} = D_c \nabla^2 c - K_c c \quad (3)$$

$$\frac{dc}{dt} + \mathbf{u} \cdot \nabla c = D_a \nabla^2 c - \frac{C_l}{V_a} c \quad (4)$$

$$\frac{dc}{dt} + \mathbf{u} \cdot \nabla c = D_m \nabla^2 c \quad (5)$$

where  $D_c$ ,  $D_a$  and  $D_m$  are the diffusion coefficients of the cornea, the anterior and posterior chambers, and the TM, respectively,  $K_c$  is the metabolic rate of drugs within the cornea,  $C_l$  is the drug clearance inside the anterior and posterior chambers and  $V_a$  is the volume of the anterior and posterior chambers. The model describing the transport of drugs is adapted from the work of Zhang et al. [4].

### 2.3 Boundary Conditions

The boundary conditions for the flow field are illustrated in Fig. 1b. The boundary conditions for the thermal field are identical to those used by Ooi and Ng [2] and will not be presented here. The boundary condition assigned to the corneal surface for the transport field merits some discussion. When the eye drop is administered onto the corneal surface, it mixes with the surrounding tear film. Since the tear film is not part of the solution domain, the time evolution of drug concentration on the corneal surface is obtained by solving Eq. 5. This gives:

$$c(t) = \left( \frac{V_L \exp(k_d t) + V_i}{V_L + V_i} \right)^{-\frac{S}{k_d V_L}} \quad (6)$$

where  $c$  is the drug concentration,  $V_L$  is the normal lacrimal volume,  $V_i$  is the initial tear volume after eye drop administration,  $k_d$  is the tear drainage constant and  $S$  is the lacrimal secretion rate. Equation 6 represents the boundary condition on the corneal surface.

Table 1 summarizes the values of the parameters used in the present work with regards to Eqs. 2–6.

**Table 1** Values of the parameters used to describe the ocular drug delivery model

Parameters	Value	Parameters	Value
$D_c$ (m <sup>2</sup> /s)	$5.74 \times 10^{-9}$	$V_{-L}$ ( $\mu$ l)	7
$D_a$ (m <sup>2</sup> /s)	$5 \times 10^{-11}$	$V_i$ ( $\mu$ l)	10
$D_m$ (m <sup>2</sup> /s)	$1.62 \times 10^{-11}$	$K_c$ (1/min)	$1.07 \times 10^{-5}$
$S$ ( $\mu$ l/min)	1.2	$C_l$ ( $\mu$ l/min)	30
$k_d$ (1/min)	1.45		

### 2.4 Segmental Outflow

As stated in Sect. 1, segmental outflow is modelled by prescribing the permeability of the TM in Eq. 1 as a spatially-varying function along the circumferential direction of the TM. Using the results from the fluorescent tracer distribution study of Chang et al. [1] as a guide, the chosen rectangular function is expressed mathematically as:

$$\kappa(\theta) = \begin{cases} \kappa_{ref} & \text{for } \theta_1 < \theta < \theta_2 \\ 0.0001\kappa_{ref} & \text{otherwise} \end{cases} \quad (7)$$

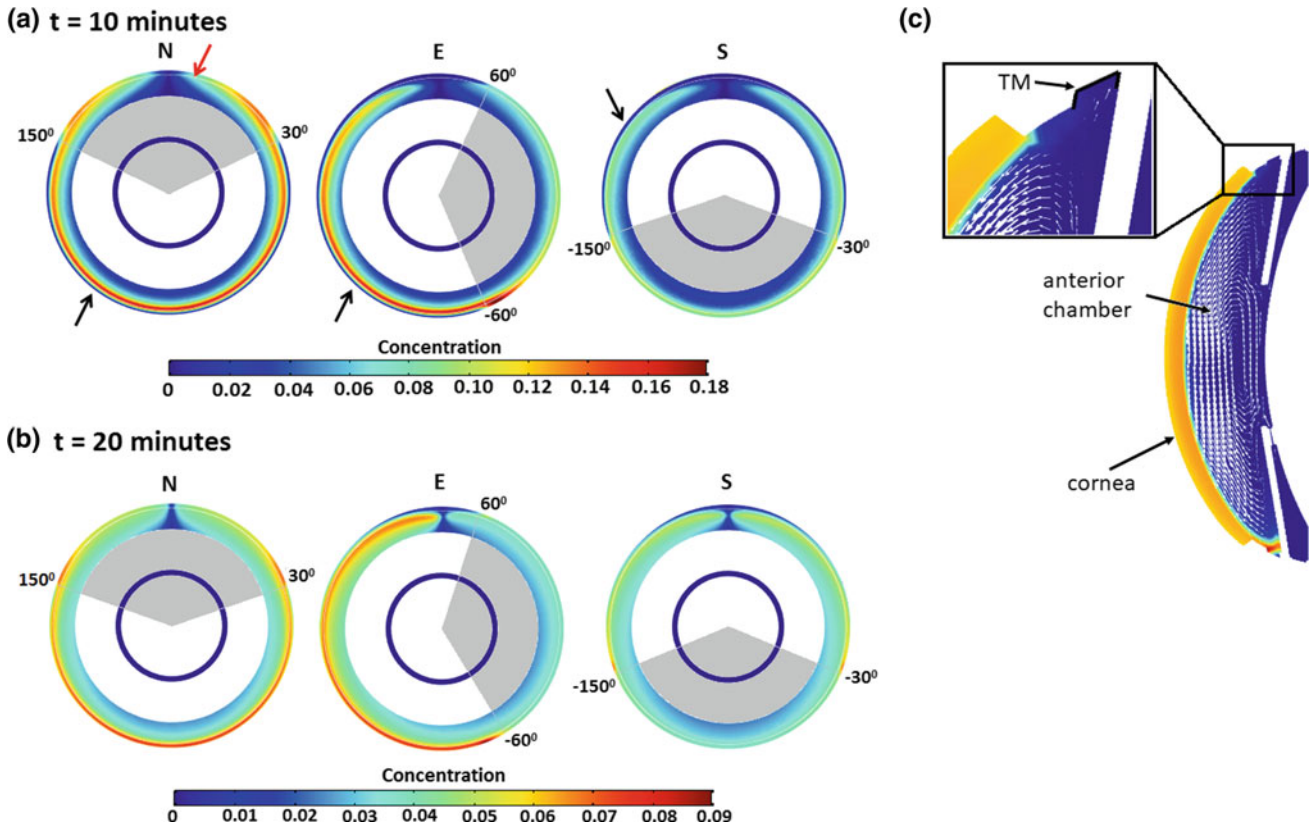
where  $\kappa_{ref}$  is the baseline permeability value of the TM,  $\theta$  is the angular coordinate that represents the circumferential position along the TM, and  $\theta_1$  and  $\theta_2$  are respectively, the lower and upper limits of the function. This is depicted in Fig. 1c.

## 3 Results

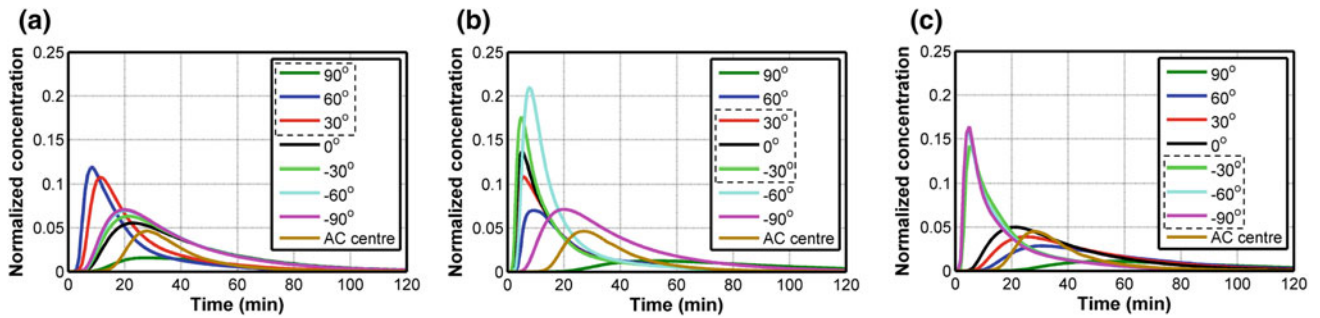
Simulations were carried out for three different active outflow locations defined by N ( $(\theta \leftarrow_{-1}, \theta \leftarrow_{-2}) = [30^\circ, 150^\circ]$ ), E ( $(\theta \leftarrow_{-1}, \theta \leftarrow_{-2}) = [-60^\circ, 60^\circ]$ ) and S ( $(\theta \leftarrow_{-1}, \theta \leftarrow_{-2}) = [-150^\circ, -30^\circ]$ ). These are shown in Fig. 1d. The eye is assumed to be in the standing position such that gravity is acting in the  $-y$  direction (see Fig. 1a). The values of the material properties used in the present study are obtained from the literature and they represent typical values for the human eye. Figure 2 illustrates the contours of the drug concentration distribution across the  $x = 3.75$  mm plane (see Fig. 1b) 10 and 20 min after eye drop administration. At 10 min, large drug concentration is seen across the active regions (see grey region), while the drug concentration across the non-active regions remains low (see black arrows). At 20 min, the non-active regions show a higher drug concentration than the active regions.

Figure 3 tracks the drug concentration at seven points around the TM over 120 min. The selected seven points are defined by  $\theta = -90^\circ, 30^\circ, 90^\circ$ . Peak drug concentration is observed across the points within the active region during the first 10 min. After 10 min, the drug concentration across the active region decreases, while those across the non-active region increases. The results in Figs. 2 and 3 may be explained by the dominant drug transport mechanism across the TM at different times. Convection dominates the egression of drugs through the active region; hence, most drugs egress through this region during the first 10 min due to its shorter timescale. The non-active region is dominated by diffusion, which has a longer time scale. As such, significant drug activity is only observed 20 min after the administration of eye drop.

From Fig. 3, one may observe that the point  $\theta = 90^\circ$  has the lowest concentration regardless of the location of active



**Fig. 2** Contours of the drug concentration distribution across the  $x = 3.75$  mm plane at **a** 10 min and **b** 20 min after the administration of eye drops. Grey region represents the zones of active outflow. **c** velocity vectors superimposed on the contours of drug concentration across the sagittal plane of the eye



**Fig. 3** Plots of the drug concentration at seven points across the TM against time for the model with outflow in the **a** N, **b** E and **c** S positions. The dashed box in the legend indicates the points that fall within the active region

outflow (see red arrow). This is also depicted in Fig. 2 by the dark blue region indicating low drug concentration at the 12 o'clock position. The low drug concentration at  $\theta = 90^\circ$  is a consequence of the AH hydrodynamics, which cause minimal drug flow through the top region of the TM. For the eye in the standing position, gravity, which is directed downwards, causes the flow of AH to change direction in the vicinity of the point  $\theta = 90^\circ$ . Consequently, the majority of the drugs would be directed downwards leaving only a very

tiny amount to egress through the top portion of the TM. This is shown in Fig. 2c.

To determine the amount of drugs that have been delivered to the active and non-active regions, the following integral is evaluated:

$$M_{total} = \int_0^{t_a} \iint_{\Gamma} \left( -D \frac{\partial c}{\partial n} + uc \right) dS dt \quad (8)$$

**Table 2** Total amount of drugs delivered across the active and non-active regions of the TM

	$M_{total} (\times 10^{-8})$					
	10 min			15 min		
	N	E	S	N	E	S
Active	0.071	1.505	1.912	1.876	2.471	2.881
Non-active	0.141	0.130	0.116	0.296	0.252	0.203

where  $M_{total}$  is the total amount of drugs delivered,  $t_A$  is the duration of drug exposure, which is taken at 10 and 15 min and  $\Gamma$  represents the interface between the anterior chamber and the TM across either the active or non-active regions. The values of  $M_{total}$  are tabulated in Table 1. It is apparent from Table 1 that the majority of the drugs egress through the active region compared to the non-active region, regardless of the position of the active outflow. Overall, the total amount of drugs flowing through the active region is two orders higher than those flowing through the non-active regions (Table 2).

#### 4 Conclusion

When Chang et al. [1] demonstrated the existence of segmental AH outflow across the TM, they postulated that this phenomenon may cause the non-active regions, i.e. the regions of the TM that are targeted by anti-glaucoma drugs, to be severely under-treated. Results from the numerical simulations of this study support this hypothesis. With segmental outflow, the amount of drugs that flow through the non-active regions was found to be two orders smaller than those that flow through the active-regions. These findings suggest that there is a need to take into consideration the

effects of segmental outflow when planning for the treatment protocol involving topical eye drop administration. This is especially true for diseases such as glaucoma, where the primary target site of the drugs is the TM.

**Acknowledgements** This project is supported by the Ministry of Education Malaysia through the Fundamental Research Grant Scheme under the project FRGS/2/2014/SG02/MUSM/02/1.

**Conflict of Interest** None declared

#### References

1. Chang, J.Y.H., Folz, S.J., Laryea S.N., Overby D.R.: Multi-scale analysis of segmental outflow patterns in human trabecular meshwork in changing intraocular pressure. *Journal of Ocular Pharmacology and Therapeutics* 30(2–3), 213–223 (2014).
2. Ooi, E.H., Ng, E.Y.K.: Simulation of aqueous humor hydrodynamics in human eye heat transfer. *Computers in Biology and Medicine* 38(2), 252–262 (2008).
3. Ferreira, J.A., de Oliveira, P., da Silva, P.A., Murta, J.N.: Numerical simulation of aqueous humor flow: from healthy to pathologic situations. *Applied Mathematics and Computation* 226(1) 777–792 (2014).
4. Zhang, W., Prausnitz, M.R.: Model of transient drug diffusion across cornea. *Journal of Controlled Release* 99(2) 241–258 (2004).



# Numerical Simulation of Fluid-Structure Interaction Under the Condition of Pulsatile Blood Flow of Renal Artery with Radiofrequency Electrode

Qun Nan, Yanyan Cheng, Zhen Tian, Tong Dong, and Xiang Gao

## Abstract

To investigate the effect of Fluid-Structure interaction of the renal artery with radiofrequency electrode under the situation of pulsatile blood flow, the ideal renal artery model that contains electrode was constructed by Solid Works. The renal arterial bifurcation vessel model with electrode and non-containing electrode was selected for comparison. Comsol software was applied to mimic the pulsatile blood flow. Six key points was selected for the analysis of hemodynamic parameters. The distribution of velocity, pressure, the equivalent stress and the deformation of the vascular wall were obtained. Compared to the pure arterial model, the speed is reduced and the pressure and equivalent stress are increased at point F When containing electrode. However, the deformation of vessel walls caused by this is very small and can be neglected. And the velocity pressure, equivalent stress and deformation of point B are relatively small at the same time. which to some extent protects the blood vessels. In combination, the insertion of RF electrode does little harm to the arterial blood vessels.

## Keywords

Fluid-solid interaction • Numerical simulation  
Pulsating blood flow • Hemodynamics • Radiofrequency electrode

## 1 Introduction

The arterial disease and hemodynamics are closely related. The flow-solid coupling of blood vessels is a hot and difficult point in the study of hemodynamics. Studying and observing

the hemodynamic characteristics (such as velocity distribution, pressure distribution, and stress) are important for explaining arterial pathogenesis diseases.

With the development of computer technology and finite element analysis, numerical simulation has been widely applied to the study of cardiovascular and cerebrovascular. In recent years, fluid-solid interaction (FSI) plays a key role in studying the flow of blood in elastic blood vessels, the causes of aneurysm and atherosclerotic plaque rupture [1–3].

At present, catheter radiofrequency ablation (RFA) of the renal sympathetic nerve is a new method of treatment of resistant hypertension. Its principle is the catheter electrode puncture through the femoral artery into the renal artery and produce radio frequency energy to achieve renal sympathetic damage. However, when electrode is inserted into the renal artery, it is bound to cause changes in the hemodynamic parameters. There is a possibility of complications such as perforation, dissection and atherosclerosis. It is essential to observe the changes of hemodynamic parameters when RF electrodes are inserted into the renal artery. Di Martino et al. [3] performed a fluid-structure interaction analysis of abdominal aortic aneurysm under pulsatile flow conditions and determined whether the abdominal aortic aneurysm ruptured by von Mises stress. Yang et al. [4] mimicked the normal aortic arch elastic vessel wall and rigid vessel wall and obtained the normal aortic arch hemodynamic parameters through FSI analysis. To date, there have been few studies on the hemodynamics after radiofrequency ablation of the renal artery.

The aim of the present study is to investigate the hemodynamic changes of blood at pulsatile velocities with regard to the coupling effects of fluid-solid by numerical simulation when arteries inserted electrode. 3D arteries and electrode models were reconstructed, and finite element models were performed.

Q. Nan (✉) · Y. Cheng · Z. Tian · T. Dong · X. Gao  
College of Life Science and Bioengineering, Beijing University of  
Technology, Beijing, China  
e-mail: nanqun@bjut.edu.cn

## 2 Methods

According to the anatomic features, solid Works software was used to establish the idealized three-dimensional model of renal artery. The diameter of the renal artery was 5 mm, the outer diameter was 7 mm, the bifurcated inner diameter was 3.5 mm, the outer diameter was 5.5 mm, and the bifurcation angle was  $50^\circ$ . Radiofrequency ablation electrodes were built according to the actual size in clinical applications. A model of artery with electrode were reconstructed and its six key point (A–F) is shown in Fig. 1.

Vessel wall and the electrode are all of linear elastic property. The arterial wall is incompressible, isotropic property [5]. Blood is incompressible viscous Newtonian fluid. The blood flow is set to pulsatile flow and the velocity changes periodically with time. The surfaces of blood are contacted with the inner surfaces of vessel, and they are the interface of FSI where the no-slip condition is satisfied.

The initial values of each vector such as blood velocity, pressure, displacement and stress are set to zero. For elastomers, blood vessels are subject to certain restrictions in the human body, we completely limit the freedom of access and exit of the artery. The outer wall of the blood vessel gives a free wall condition without limitation; the inner wall surface of the blood vessel is defined as the coupling interface condition. For fluid, given its inlet velocity conditions [6, 7]. The typical human heart beat frequency is 75 beats/min (the heart beat cycle  $T = 0.8$  s). During the entire 0.8 s of Systolic accounted for 0.35 s, cardiac systolic was 0.45 s. The inlet pulsation velocity curve shown in Fig. 2. The arterial outlet boundary conditions were set to zero pressure.

In numerical simulations of blood flow that does not consider heat transfer, it can be considered that the energy conservation equation is not established. The equations used to control the fluid here are only the continuity equation and the momentum conservation equation. The Fluid continuity equation is shown in Eq. 1.

$$\frac{\partial U_i}{\partial t} = 0 (i = 1, 2, 3) \quad (1)$$

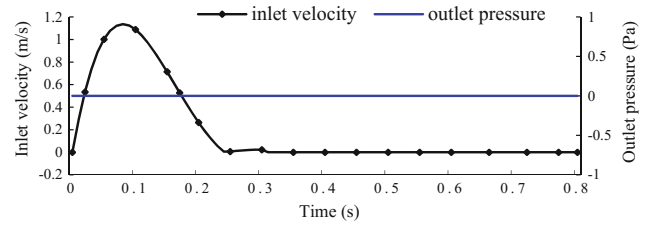
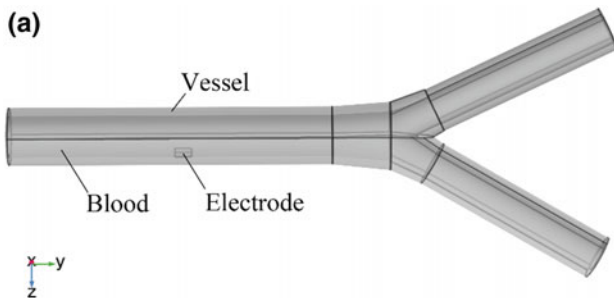


Fig. 2 Boundary conditions of inlet and outlet

where,  $U_i$  is the speed vector. The above equation states that the density of the fluid particles remains constant along the trace. The Fluid motion equation is shown in Eq. 2.

$$\rho_f \left( \frac{\partial U_i}{\partial t} + U_j \frac{\partial U_i}{\partial X_j} \right) - \frac{\partial \delta_{ij}}{\partial X_j} = \rho_f f_i (i, j = 1, 2, 3) \quad (2)$$

where,  $\delta_{ij}$  is the stress tensor component,  $\rho_f$  is fluid density,  $f_i$  is the component of physical strength.

$$\rho_s \left( \frac{\partial^2 d_i}{\partial t^2} \right) - \frac{\partial \delta_{ij}}{\partial X_j} = \rho_s F_i (i, j = 1, 2, 3) \quad (3)$$

where,  $d_i$  and  $\delta_{ij}$  respectively are the components of displacement vector and stress tensor of solid parts, and  $\rho_s$  is the density of solid part, and  $F_i$  is the component of physical strength of the solid part.

$$\begin{cases} \delta_{ij}^B \cdot n_j|_{FSI} = \delta_{ij}^W \cdot n_j|_{FSI} \\ d_{ij}^B \cdot n_j|_{FSI} = d_{ij}^W \cdot n_j|_{FSI} \end{cases} \quad (4)$$

In the formula,  $\delta^B$  represents the stress tensor of blood,  $\delta^W$  denotes the stress tensor of the vessel wall, and the inside of the blood vessel wall, and the inner surface of the vascular wall is expressed as FSI.

According to the Refs. [8, 9], the material properties of each domain are listed in Table 1. Comsol software was applied to mimic the blood flow under the fluid-solid interaction.

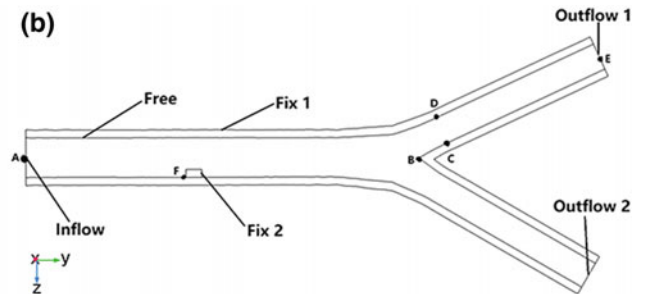
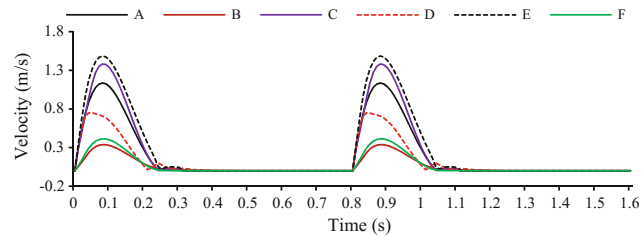


Fig. 1 Illustrating geometry model (a), boundary conditions and six key point (A–F) (b)

**Table 1** Material properties in different domains

Parameter	E (MPa)	$\nu$	$\rho$ (g m <sup>3</sup> )	$\mu$ (kg m s <sup>-1</sup> )
Blood	—	—	1050	0.0035
Vessel	0.6	0.495	1150	—
Electrode	$110 \times 10^3$	0.34	8700	—

Note E—Young’s modulus,  $\nu$ —Poisson’s ratio,  $\rho$ —density,  $\mu$ —viscosity



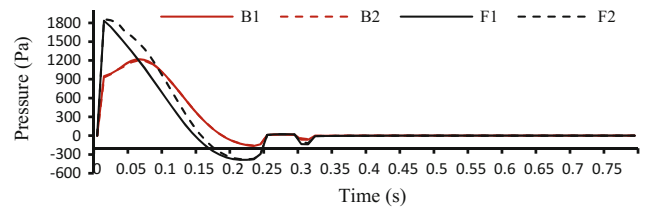
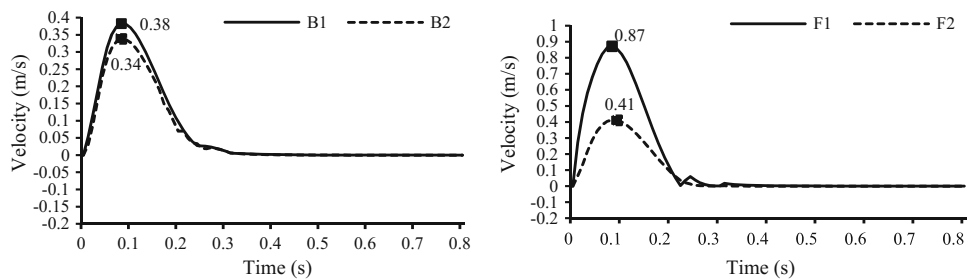
**Fig. 3** Velocity variations at six typical nodes in model with electrode

### 3 Results

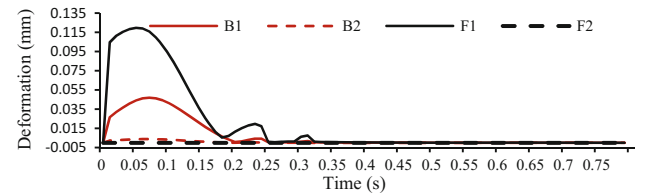
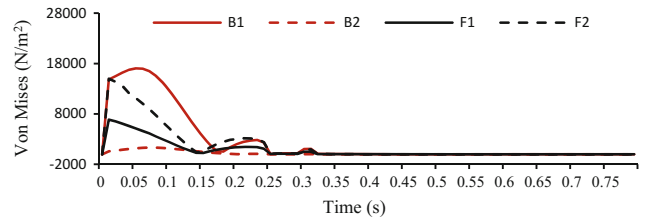
Figure 3 depicts the variation of velocity field with time in two cycle in artery model with electrode. The variation rule of velocity is in agreement with that of pressure difference, but the variation magnitudes are different. In the case of pulsatile flow, the speed of the six key points also shows a fluctuating trend. It can be found that the speed at the point B changes slowest during systole.

Figure 4 illustrates the comparison of velocity at node B and F between artery with electrode (B2, F2) and artery without electrode (B1, F1). As can be seen in Fig. 4, there is no significance change in B1 and B2, and the speed reached the maximum in 0.1 s, but the speed of B2 is less than B1. It means that the electrode does not have much effect on the velocity of point B. And the velocity F2 point changed significantly slower than F1 during 0–0.2 s. This is because the presence of the electrodes blocks the flow of blood.

**Fig. 4** Comparison of the velocity at point B and F



**Fig. 5** Comparison of pressure at point B and F



**Fig. 6** Comparison of Von Mises and deformation at point B and F

Figure 5 shows that during one cardiac cycle, the pressure difference between points B1 and B2 are almost unchanged. This implies that the presence of electrode has little effect on arterial bifurcation pressure at the node B. The pressure curve at point F2 changes faster than F1 in the range 0.01–0.2 s.

Figure 6 demonstrates the contrast of equivalent stress and displacement at point B and F between artery with electrode (B2, F2) and it without electrode (B1, F1). Due to the electrode is inserted, the equivalent stress at point F2 changes relatively faster, while the deformation is slower in the range about 0.1–0.18 s. The equivalent stress and

deformation at point B2 are relatively smaller than B1 at critical time 0–0.2 s.

#### 4 Conclusion

The distributions of velocity, pressure, displacement and stress etc. were investigated in this paper by numerical simulation under pulsatile blood flow. By selecting the key points, the results of the intravascular containing and non-containing electrodes are compared. The study found that the electrode does not have much effect on the velocity and pressure make the equivalent stress and deformation are smaller in the bifurcation. From the deformation of the wall of vessel wall, the deformation of the vessel wall is reduced after the electrode adhered to the wall. There is a possibility that the blood vessel pulsation rate may decrease, but it has little effect on the whole blood vessel. However, the model belongs to the idealized model. The future work will take personalized renal artery model for fluid-structure interaction numerical simulation.

**Acknowledgements** The research is supported by National Science Foundation of China (31771021) and Beijing Natural Science Foundation (3162006).

#### References

1. LIU Y, YIN Y, ZHANG D, et al. Analysis of Non-Newtonian Blood Flow in Stenotic Carotid Artery under Fluid-Structure Interaction [J]. *Applied Mathematics and Mechanics*, 2015, Vol. 36, No. 10, pp. 1058–1066. (in Chinese).
2. YANG J, YU H, LIU J, et al. Layered abdominal aortic aneurysm model based on fluid-structure interaction [J]. *BME & Clin Med*, July 2014, Vol. 18, No. 4, pp. 310–314. (in Chinese).
3. Nixon A M, Gunel M, Sumpio B E. The critical role of hemodynamics in the development of cerebral vascular disease: a review [J]. *Journal of Neurosurgery*, 2010, Vol. 112, No. 6, pp. 1240–1253.
4. Di M E, Guadagni G, Fumero A, et al. Fluid-structure interaction within realistic three-dimensional models of the aneurysmatic aorta as a guidance to assess the risk of rupture of the aneurysm [J]. *Medical Engineering & Physics*, 2001, Vol. 23, No. 9, pp. 647–655.
5. YANG J, XU Y, YU H, et al. Analysis of blood flow in human aortic arch by fluid-structure interaction coupled computational fluid dynamics simulation. *Chinese Journal of Medical Physics*, 2013, Vol. 17, No. 1, pp. 1–5. (in Chinese).
6. Kelly S, O'Rourke M. Fluid, solid and fluid-structure interaction simulations on patient-based abdominal aortic aneurysm models [J]. *Proc Inst Mech Eng H*, 2012, Vol. 226, No. 4, pp. 288–304.
7. YANG J, YU H, LIU J, et al. Comparison of blood flow dynamics in thoracic aortic dissection and normal based on CT images [J]. *Biomedical Engineering and Clinical Medicine*, 2010, 14(5): 390–396. (in Chinese).
8. Shahcheraghi N, Dwyer HA, Cheer AY, et al. Unsteady and three-dimensional simulation of blood flow in the human aortic arch [J]. *J Biomech Eng*, 2002, Vol. 124, No. 4, pp. 378–387.
9. DI MARTINO ES, GUADAGNI G, FUMERO A, et al. Fluid-structure interaction within realistic three-dimensional models of the aneurysmatic aorta as a guidance to assess the risk of rupture of the aneurysm [J]. *Med Eng Phys*, 2001, Vol. 23, No. 9, pp. 647–655.
10. MOLONY DS, CALLANAN A, MORRIS LG, et al. Geometrical enhancements for abdominal aortic stent-grafts [J]. *J Endovasc Ther*, 2008, 15 (5): 518–529.

# In Vitro Evaluation of Hemodynamic Performance for Right Ventricular Outflow Tract Reconstruction with Trileaflet ePTFE Valved Conduit

Wei-Ling Chen, Chiu-Chin Wu, and Chung-Dann Kan

## Abstract

Right ventricle to pulmonary artery (RV-PA) continuity reconstruction traditionally is treated by open repair with pulmonary valve implantation or replacement. Percutaneous pulmonary valve implantation (PPVI) has evolved as most exciting development surgical strategy with dysfunctional right ventricle-pulmonary artery conduits. However, size restrictions of the currently available valves for PPVI application prevents development in a larger pool of patients. We propose a formula for designing handmade trileaflet-valved conduits with different diameters. The formula is derived from a trigonometric function and can be used to estimate the optimal parameters for ePTFE-valved conduits for young adults and children. The purpose of this study is to investigate the hemodynamic and functional consequences of the new design using a mock circulation system. We recorded the diastolic valve leakage and calculated pulmonary regurgitation, regurgitation fraction, and ejection efficiency in pulsatile setting. Additionally, the prosthetic leaflet behavior was assessed with an endoscope camera and the pressure drops through valves were measured. All the in vitro parameters indicated that the ePTFE-valved conduits did not have an inferior outcome compared with

commercial mechanical or tissue valve conduits and could decrease the regurgitation volume and increase the efficiency. Compatible early clinical outcomes were also found among ePTFE-valved conduits and other valved conduits used for RVOT reconstruction, and ePTFE-valved conduits could be implanted in patients of a significantly smaller size. In vitro experimental study provided evidence that a handmade ePTFE-valved conduit could be an attractive alternative to other commercialized valved conduits used for surgical Right ventricle to pulmonary artery (RV-PA) continuity reconstruction.

## Keywords

ROVT reconstruction • EPTFE-valved conduits  
Hemodynamic • Mock circulation loop

## 1 Introduction

Right ventricle to pulmonary artery (RV-PA) continuity reconstruction is one of the important and distinctive procedures for the complex congenital heart surgery. Reconstruction of Right Ventricular Outflow Tract (RVOT) may necessitate placing a conduit that establishes the continuity between the Right Ventricle (RV) and the Pulmonary Artery (PA) [1]. These prosthetic conduits are composed of non-viable homograft or xenograft tissue which cannot grow with patients. In order to minimize the number of surgical procedures, surgeons desire to delay the reintervention intervals as long as possible. However, chronic pulmonary valve regurgitation might result in right ventricular volume overload and with potential subsequent right and left ventricular dysfunction [2]. Pulmonary valve replacement (PVR) sometimes became inevitable. This clinically challenging task prompts the need to develop the minimally invasive valve therapies. Percutaneous pulmonary valve implantation (PPVI) evolves as a valuable treatment option for patients with dysfunctional right ventricle-pulmonary

W.-L. Chen  
KSVGH Originals & Enterprises, Kaohsiung Veterans General Hospital, Kaohsiung, Taiwan  
e-mail: lynnchen.k@gmail.com

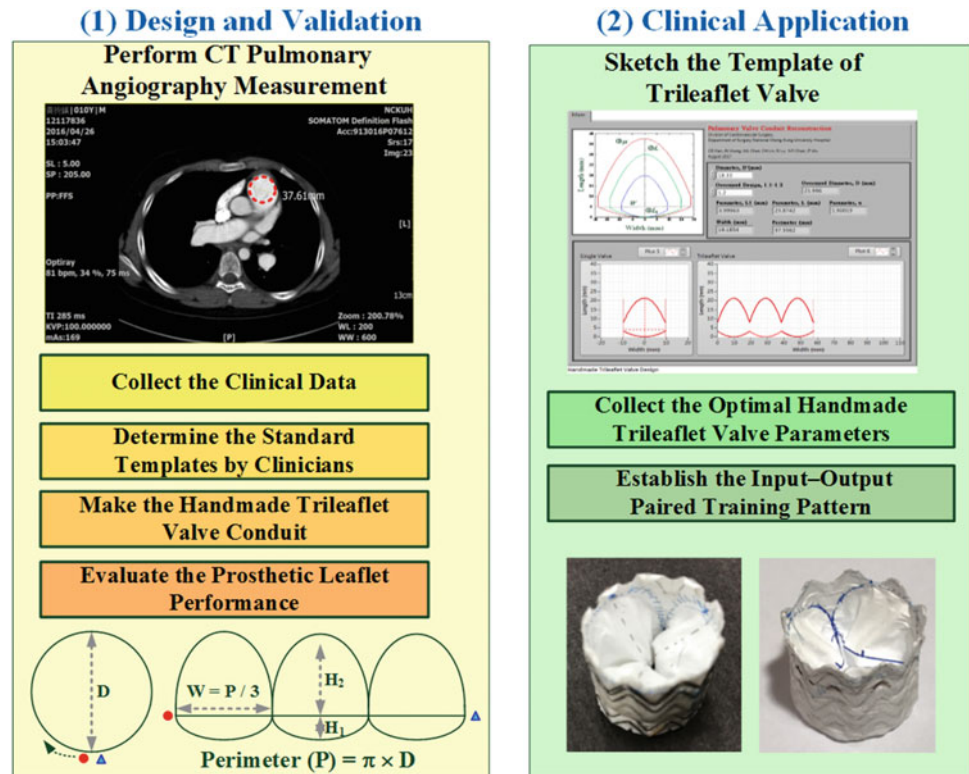
W.-L. Chen  
Department of Engineering and Maintenance, Kaohsiung Veterans General Hospital, Kaohsiung, Taiwan

C.-C. Wu  
Department of Mechanical Engineering, Chienkuo Technology University, Changhua, Taiwan  
e-mail: wcj@ctu.edu.tw

C.-D. Kan (✉)  
Division of Cardiovascular Surgery, Department of Surgery, National Cheng Kung University Hospital, College of Medicine, National Cheng Kung University Tainan, Tainan, Taiwan  
e-mail: kcd56@mail.ncku.edu.tw



**Fig. 1** Handmade trileaflet valve design and clinical application



artery conduits [3]. This procedure might reduce the number of operation need over the lifespan with RVOT and avoid ROVT revision in the majority of patients.

Since 2000, Dr. Bonhoeffer et al. reported the first successful PPVI and this technology led to significant improvement in both valve design and procedural approach [4]. Patient has significant improvement and no complications after long term investigation. Melody® transcatheter pulmonary valve replacement (TPVR) technique [5] is an approach used to treat narrowed pulmonary valves or leaky valves without the need for pen-heart surgery. Its technique can reduce surgical risk, and improves patient care by achieving fast recovery times and short hospital stays. In addition, previous studies [6–9] have shown that handmade expanded polytetrafluoroethylene (ePTFE) trileaflet conduits provide a large range of customized diameters for right ventricular outflow tract (RVOT) reconstruction in children and adult patients. The expanded polytetrafluoroethylene (ePTFE) products have good biocompatibility and low antigenicity properties, and the good outcomes of handmade ePTFE-valved conduits for open RVOT reconstruction surgery have been reported [2].

In our previous study [6–9], we thus, in a previous study, we designed a cost-effective, handmade trileaflet stent graft by suturing a bisemilunar tricuspid-shaped expanded ePTFE pericardial membrane (W. L. Gore & Associates, Inc, Flagstaff, Ariz) onto a commercial transcatheter stent graft.

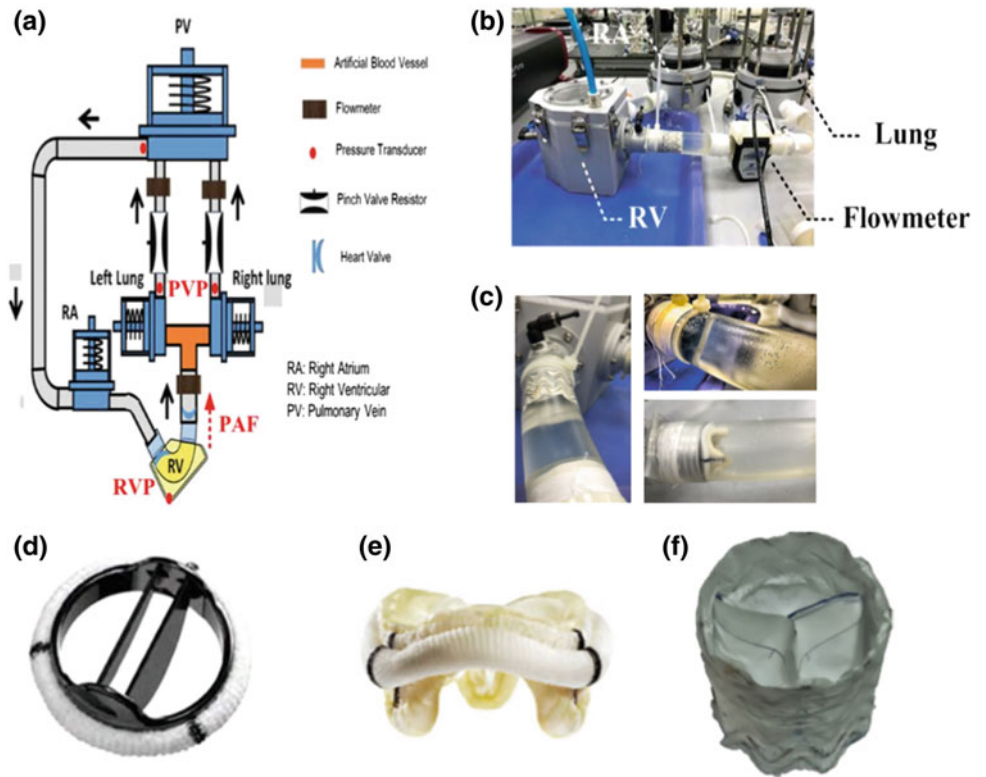
Moreover, we also developed the optimal design algorithm for clinical application of handmade ePTFE trileaflet-valved conduits, as Fig. 1 shown. Using these formule, the ePTFE membrane can be trimmed into a semilunar tricuspid-shaped leaflet, which can then be mounted in the stent conduit via hand suturing. Nerveless, the hemodynamic and functional exams of ePTFE-valved conduits compared with mechanical valves and tissue valves have not been studied. This study was to examine the hemodynamic and flow conditions of different pulmonary valves in a bio-physical circulation system. Through valve competency tests, the regurgitation fraction (RF) and efficiency of valve were employed to validate that ePTFE-valved conduits had not inferior outcome compared with commercial mechanical or tissue valve conduits. The ePTFE-valved conduits could decrease the regurgitation volume and increase the efficiency of valve as compared with valveless condition.

## 2 Materials and Methods

### 2.1 Mock Circulation System

An experimental circulation system is established to mimic the cardiopulmonary circulation loop system, consisting of an artificial right ventricle (ARV), an artificial pulmonary artery (APA) with the right and left pulmonary arterial

**Fig. 2** The configuration of pulmonary circulation. **a** The schematic diagram of biophysical pulmonary circulation loop system; **b** Artificial right ventricle; **c** Artificial pulmonary artery and pulmonary valve; **d** Mechanical valve; **e** Tissue valve (Epic™); **f** Handmade trileaflet valve



branches, right and left pinch valve resistors (artificial lung, AL), a pulmonary vein, and an artificial right atrium (ARA) [9–12], as shown in Fig. 2a. Two compliance chambers and pinch valve resistors at the end of right and left pulmonary arterial branches are designed to mimic the compliance characteristics of the distal vasculature. Blood pressures and flows are driven by a digitally controlled hydraulic piston pump (ViViTro Labs Inc., Super Pump System, Victor, BC) to produce pulsatile waves with heart rates of 60 and 80 beats/min from ARV to ARA. The APA is made of 2.0 mm-thick silicone rubbers with a T-shaped geometry connecting to the right and left ALs, and allowed blood flow volumes of 40, 50, and 60 mL through the artificial pulmonary valve, as handmade pulmonary valved conduit and Epic valve stent in Fig. 2b, c. The blood-mimicking fluid is made from water and glycerin (water: glycerin = 1.688: 1.000; kinematic viscosity: 2.8–3.8 m<sup>2</sup>/s; density: 1.05–1.06 kg/m<sup>3</sup>) at 37 ± 2 °C. The metering system consisting of a transonic clamp-on flow sensor (ME16PXL, Transonic Systems, Ithaca, NY, USA; resolution, 10 Hz; ±5 mL/min, bidirectional flow) and three pressure transducers (81A 006G Sensormate, Chang Hau, Taiwan) is employed to acquire the ARV pressure, APA pressure, and APA flow via a data acquisition (DAQ) card (National Instruments™, PCI-6259 Austin, TX, USA) connecting to a laptop PC for further signal analysis. A transonic clamp-on flow sensor (ME16PXL, Transonic

Systems, Ithaca, NY) monitor pulmonary artery flow (FPA) and transducers (81A 006G Sensormate, Chang Hau, Taiwan) were employed to obtain the pressures before (right ventricular pressure, PRV) and after (pulmonary artery pressure, PPA) the prostheses valves. An endoscope inspection camera with 7 mm waterproof diameter and 6 pcs LED light positioned above the prostheses valves captures all valve leaflet motion at 30 frames per second.

## 2.2 Handmade Trileaflet Valve Design Method

According to the templates of trileaflet pulmonary leaflets (Fig. 1), lower and upper curved geometric lines and two vertical lines can be presented as follows [9, 12], two curved lines,  $C_1$  and  $C_2$ :

$$C_1(x) = \frac{x^2}{8 \times (D/20) \times L_1}, \quad x \in [-W_1, +W_1] \quad (1)$$

$$C_2(x) = \frac{x^2}{-\mu \times (D/20) \times L_1} + L, \quad x \in [-W_1, +W_1] \quad (2)$$

$$L = \left| \frac{x^2}{-\mu \times (D/20) \times L_1} \right| + 2 \times L_1 \quad (3)$$

Two vertical lines,  $C_3$  and  $C_4$ :

$$x = -W_1, C_3(x) \in [L_1, 2L_1] \quad (4)$$

$$x = +W_1, C_4(x) \in [L_1, 2L_1] \quad (5)$$

where  $D$  (mm) is the diameter of the pulmonary trileaflet valved conduit; length,  $L_1 = 3.0\text{--}5.0$  mm (experience valves), is the connecting junction at the lower curved structure [9];  $W = 2 \times |\pm W_1|$  is the horizontal width (mm) of each leaflet and its valve is one-third of perimeter,  $P = (\pi \times D)/3$  (mm); and  $L$  is the vertical length (mm) of each leaflet. Based on the 20 mm diameter commonly observed in children, two terms,  $[8 \times (D/20) \times L_1]$  and  $[-\mu \times (D/20) \times L_1]$ , are used to modify the curved lines,  $C_1$  and  $C_2$ , and can obtain different valve diameters.

### 2.3 Hemodynamic Evaluation

Four valvar conditions were tested: Valveless, Mechanical valve—Masters HPTM and Epic stented tissue valve (St. Jude, St. Paul, MN), Handmade ePTFE-valved conduits, as Fig. 2d–f shown. Each condition was also tested at three separate stroke volumes (40, 50, and 60 mL) and two heart rates (60 and 80 beat/min) to mimic six separate cardiac outputs ranging from 2.4 to 4.8 L/min.

Valve stent performance index were obtained by stroke volume and regurgitation volume. Valve stent efficacy was evaluated using the regurgitation fraction (RF) which was calculated as the ratio between backward and forward flow through the pulmonary valve in each heartbeat. Pulmonary regurgitation (PR) was incompetency of the pulmonic valve causing blood flow from pulmonary artery into the right ventricle during diastole. A leaky pulmonary valve allows blood to flow back into the heart chamber, due to insufficiency of the pulmonic semilunar valve. Pulmonary insufficiency is evaluated on the basis of the regurgitation fraction, which is defined as the percentage of PAF that regurgitates through the pulmonic valve to the right ventricle. The pulmonary arterial flow volumes can be obtained using the on-line flow metering. For each heartbeat, the end-systolic and end-diastolic volumes are computed by integral operations, as

$$SV = \int_{t_1}^{t_2} PAF_{fw} dt \quad (1)$$

$$RV = \int_{t_1}^{t_2} PAF_{rv} dt \quad (2)$$

where  $SV$  is the forward stroke volume (mL);  $PAF_{fw}$  is the forward PAF rate during systolic period,  $[t_1, t_2]$ ;  $RV$  is the

regurgitation volume (mL); and  $PAF_{rv}$  is the regurgitation flow rate during diastolic period,  $[t_2, t_3]$ . The RF can be represented as:

$$RF\% = \frac{RV'}{SV'} \times 100\% \quad (3)$$

where index,  $RF\%$ , offers a quantitative measurement of the severity of the valvular lesion, as normal condition means no blood regurgitates, then  $RF\% \approx 0$ . In cases with severe valvular lesions,  $RF\%$  can approach 50–80%.

Ejection Efficiency (EE) index is also related the quantity of blood delivered to the right and left lungs as:

$$EE\% = \frac{\text{Outflow Volume}}{\text{Inflow Volume}} \times 100\% = \frac{SV'}{SV' + RV'} \times 100\% \quad (4)$$

where  $EE\% > 80\%$  indicates the good valve stent efficacy. We can quantify the relationship between  $EE\%$  and  $RF\%$  using the linear regressions.

## 3 Results and Discussion

In our previous study, we designed a trileaflet stent graft by suturing a bi-semilunar tricuspid-shaped expanded ePTFE Preclude® pericardial membrane (WL Gore & Associates Inc, Flagstaff, AZ) onto a commercial transcatheter stent graft. However, ePTFE-valved conduit's function and hemodynamic status were suboptimal. Thus, we designed an experimental model mimicking the human pulmonary circulation system. Moreover, four conditions of pulmonary valve were used to estimate the hemodynamic determinant of pulmonary valve motion, the valveless group had quite distinction presentations to the various valved groups (mechanical valve, Epic™ tissue valve, and ePTFE-valved conduits), as Fig. 3a shown. Due to no cusps to prevent backflow during diastolic phase, the variation of pressure (−4.9 to 17.7 mmHg) was distinctive vibrated in valveless group. It was the baseline condition compared with the other groups. In contrast to the valveless group, the porcine bio-prosthetic valve and mechanical valve were gold standard and the pressure changed limited in 16.7–23.8 mmHg and 12.4–23.9 mmHg, respectively. Hence, the handmade ePTFE-valved conduit was determined to effective increase pulmonary pressure to 13.9–23.8 mmHg, as well as gold standard valve.

Analysis of pulmonary valve function by pressure-flow loops is attractive because it quantifies various determinants of valvular function. The phase diagram of PA pressure and PA flow and the conventional indexes such as forward stroke volume (SV) and backward stroke volume (regurgitation

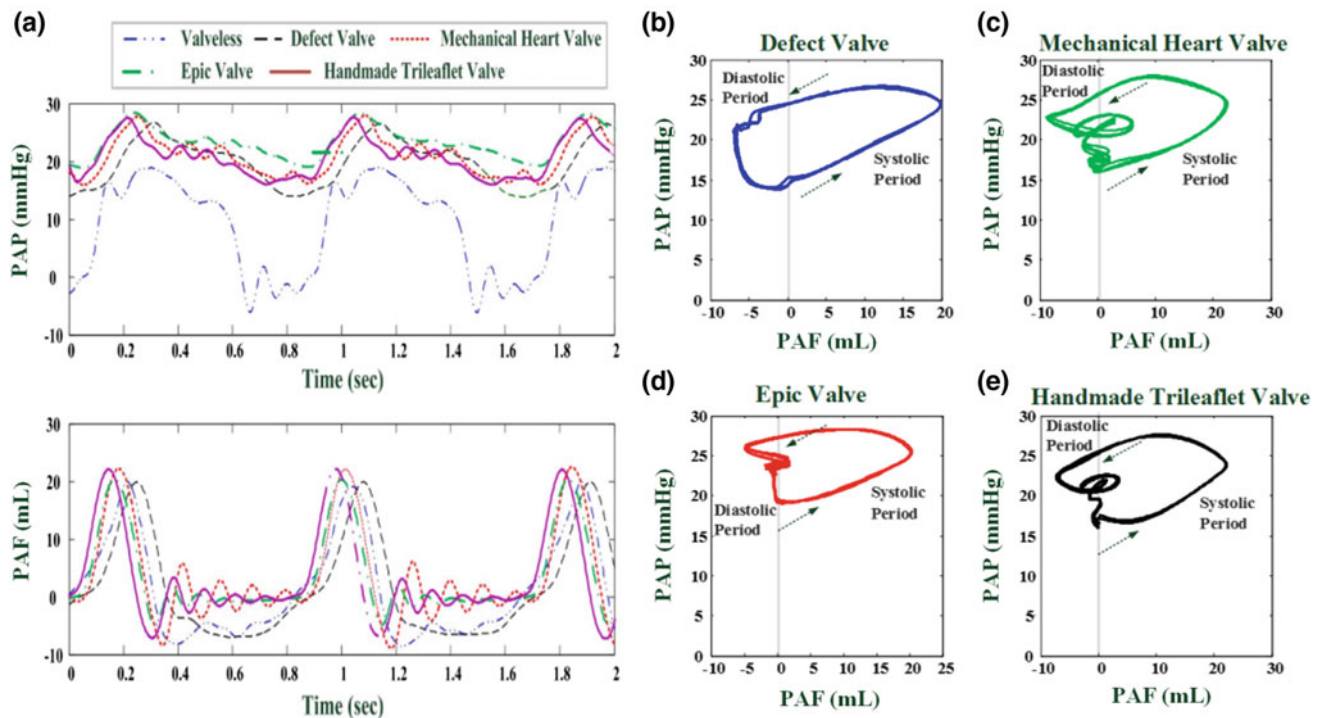


**Fig. 3** Pulmonary artery pressure waveform and pulmonary artery flow waveform at HR = 60 beat/min and PAF = 50 mL

volume; RV), PA pressure, and PA flow can be directly derived from the loop. In the first quadrant, the area of PAP-PAF loop indicated the positive stroke work, and the second quadrant demonstrated the negative stroke work. Figure 3b is the valves PAP-PAF loop appeared that the areas of SV fairly equaled RV, and Table 2 demonstrated RF% is very high. Figure 3b–e have similar PAP-PAF loop.

Hand-made ePTFE-valved conduit seems to be a feasible and reproducible method used for RVOT reconstruction, especially for earlier children, and our early clinical outcomes were impressive. Previous studies have demonstrated that ePTFE has good durability and biocompatibility. The microporous structure of ultrathin ePTFE membrane impedes host cellular infiltration, which prevents further development of calcification. The negatively charged surface that prohibits platelet adherence makes ePTFE membrane less thrombogenic. Furthermore, explanted ePTFE grafts also showed very minimal inflammatory responses. These properties promote the leaflets made from ultrathin ePTFE membrane being free from, if any, attachment of cellular or extra-cellular component and having sustained flexibility. When used for RVOT reconstruction, previous studies have demonstrated that both patches with ePTFE monocusp and ePTFE-valved conduits could exhibit long-term freedom from re-operation or significant valvular dysfunction.

Our in vitro experimental study also showed clear evidences of adequate hemodynamic function of the ePTFE-valved conduits, which was at least not inferior to

those commercially available prosthetic valves and valved conduits. By using the mock circulation system, long-term quality of the ePTFE-valved conduits should be stimulated and analyzed, and further suitable modifications of the hand-made valved conduits could be made.

## References

1. Hussam S. Suradi, et al., Percutaneous pulmonary valve implantation. *Glob Cardiol Sci Pract*, 2015. 2015(2): 23.
2. McElhinney DB, et al., Short- and medium-term outcomes after transcatheter pulmonary valve placement in the expanded multi-center US melody valve trial. *Circulation*. 010; 122(5):507–16, Epub 2010/07/21.
3. Yamashita, E., et al., Smaller-Sized Expanded Polytetrafluoroethylene Conduits With a Fan-Shaped Valve and Bulging Sinuses for Right Ventricular Outflow Tract Reconstruction. *Ann Thorac Surg*, 2016. 102(4): p. 1336–44.
4. Bonhoeffer P, et al., Percutaneous replacement of pulmonary valve in a right-ventricle to pulmonary-artery prosthetic conduit with valve dysfunction. *Kachaner J Lancet.*, 2000. 356(9239): p. 1403–5.
5. Lurz P, et al., Percutaneous pulmonary valve implantation: impact of evolving technology and learning curve on clinical outcome. *Circulation*. 2008;117(15):1964–72, Epub 2008/04/09.
6. Ting-Wei Lin, Jieh-Neng Wang, Chung-Dann Kan, and Yu-Jen Yang, “Handmade trileaflet valved stent graft for pulmonary valve implantation,” *The Journal of Thoracic and Cardio-vascular Surgery*, vol. 148, no. 4, 2014, pp. 1753–1755.
7. Ming-Tai Lin, Jou-Kou Wang, Pei-Yuan Wu, Chun-Wei Lu, Te-I Chang, and Yih-Sharn Chen, “Successful transcatheter



- handmade-valved graft stent for branch pulmonary regurgitation: novel approach in a special event," *The Society of Thoracic Surgeons*, vol. 12, 2016, pp. E541–543.
8. Pranav Loyalka, Michael Schechter, Angelo Nascimbene, Ajay Sundara Raman, Cezar A Ilieascu, Igor D Gregoric, and Biswajit Kar, "Transcatheter pulmonary valve replacement in a carcinoid heart," *Texas Heart Institute Journal*, vol. 43, no. 4, 2016, pp. 341–344.
  9. Chung-Dann Kan, Jieh-Neng Wang, Wei-ling Chen, Pong-Jeu Lu, Ming-Yao Chan, Chia-Hung Lin, and Wan-Chin Hsieh, "Applicability of the handmade ePTFE trileaflet-valved conduits for pulmonary valve reconstruction: an ex vivo and in vivo study," *The Journal of Thoracic and Cardiovascular Surgery*, Article in Press, September 2017, <http://dx.doi.org/10.1016/j.jtcvs.2017.09.049>.
  10. E. Yamashita, M. Yamagishi, T. Miyazaki, Y. Maeda, Y. Yamamoto, N. Kato, H. Hongu, and H. Yaku, "Smaller-sized expanded polytetrafluoroethylene conduits with a fan-shaped valve and bulging sinuses for right ventricular outflow tract reconstruction," *Ann Thorac Surg*, vol. 102, no. 4, 2016, pp. 1336–44.
  11. Cheng-Hsien Chiang, Ming-Long Yeh, Wei-Ling Chen, and Chung-Dann Kan, "Apparatus for comparison of pullout forces for various thoracic stent grafts at varying neck angulations and oversizes," *Annals of Vascular Surgery*, vol. 31, 2016, pp. 196–204.
  12. Chung-Dann Kan, Wei-Ling Chen, Chia-Hung Lin, Jieh-Neng Wang, Pong-Jeu Lu, Ming-Yao Chan, and Jui-Te Wu, "Handmade trileaflet valve design and validation for pulmonary valved conduit reconstruction using taguchi method and cascade correlation machine learning model," *IEEE Access*, Article in Press, December 2017, <https://doi.org/10.1109/access.2017.2782686>.



# Real-Time Monitoring of Yeasts Growth Based on Bioimpedance Spectroscopy

Marcos Antonio Salvino da Silva, Elizabeth Gomes Sanches, Alexandre Visintainer Pino, and Marcio Nogueira de Souza

## Abstract

Industrial bioprocesses usually occur in bioreactors, where the stages of a microorganism growth must be monitored to optimize the whole process. *Off-line* analytical methods are considered gold standard for such monitoring, but they are time consuming and may postpone important decisions making. Thus, there is always demand for the development of real time (*on-line*) monitoring methods for bioprocesses. Despite the existence of some real time methods used to measure the concentration of biomass in real time, such as optical density or turbidimetry, many of them are not able to distinguish living microorganisms from other materials, including dead microorganisms. This work proposes an *on-line* method for monitoring of total biomass, as well as the amount of viable cells, using a bioimpedance spectroscopy based on the current response to a step voltage excitation. To evaluate the proposed method, we performed an experiment of growth with yeast strain *Saccharomyces cerevisiae* species with initial inoculum of 0.1 and 0.5 g/L. The total amount of microorganism (using Neubauer chamber), the number of viable ones (using dyeing with methylene blue), and bioimpedance data were collected every hour during a period of 12 h. For each initial inoculum, series of data were collected. The results indicate the proposed technique presents good prediction of the total amount of microorganism ( $r = 0.918$ ) and of the number of viable ones ( $r = 0.858$ ).

## Keywords

Bioprocess • Bioimpedance spectroscopy • Monitoring yeast growth

## 1 Introduction

Industrial bioprocess are normally developed in bioreactors and must be monitored, preferably in real time (*on-line*). Despite of this, many are still accompanied by *off-line* analytical methods, because they are considered gold standard. Examples of such methods are: counting the total number of cells by Neubauer chamber; the staining of live/dead cells; the spectrophotometry, among others. More over, these analytical methods usually require a lot of laboratory work and are time consuming [1–3].

Electrical techniques, bioimpedance spectroscopy among them, have been proposed to monitor some bioprocesses in real time have also been used in an attempt to monitor bioprocesses in real time [4–7]. Despite this, no *on-line* monitoring work was that aimed to distinguish the percentage of live microorganisms, besides the total result of the biomass, performing the total measurement time in less than 100 s. Thus, this work proposes an alternative monitoring of biomass by bioimpedance spectroscopy based on the current response to the voltage step [8], hereinafter referred to as *BIS-STEP*, which also to provide the percentage of live microorganisms in the indicated amount of biomass.

## 2 Materials and Methods

For the evaluation of the proposed method, a yeast growth experiments were carried out in three Erlenmeyers, one of which was adapted with electrodes for bioimpedance measurement and two for aliquot removal and to be analyzed by traditional *off-line* methods (Fig. 1a).

M. A. Salvino da Silva (✉) · E. G. Sanches  
Oswaldo Cruz Foundation – FIOCRUZ/Farmanguinhos,  
22775-903 Rio de Janeiro, Brazil  
e-mail: marcosalvino@peb.ufrj.br  
URL: <http://www.peb.ufrj.br>

M. A. Salvino da Silva · A. V. Pino · M. N. de Souza  
Biomedical Engineering Program – COPPE/UFRJ, PO Box 68510  
21945-970 Rio de Janeiro, Brazil

M. N. de Souza  
Electronics and Computer Engineering Department – EE/UFRJ,  
21945-970 Rio de Janeiro, Brazil

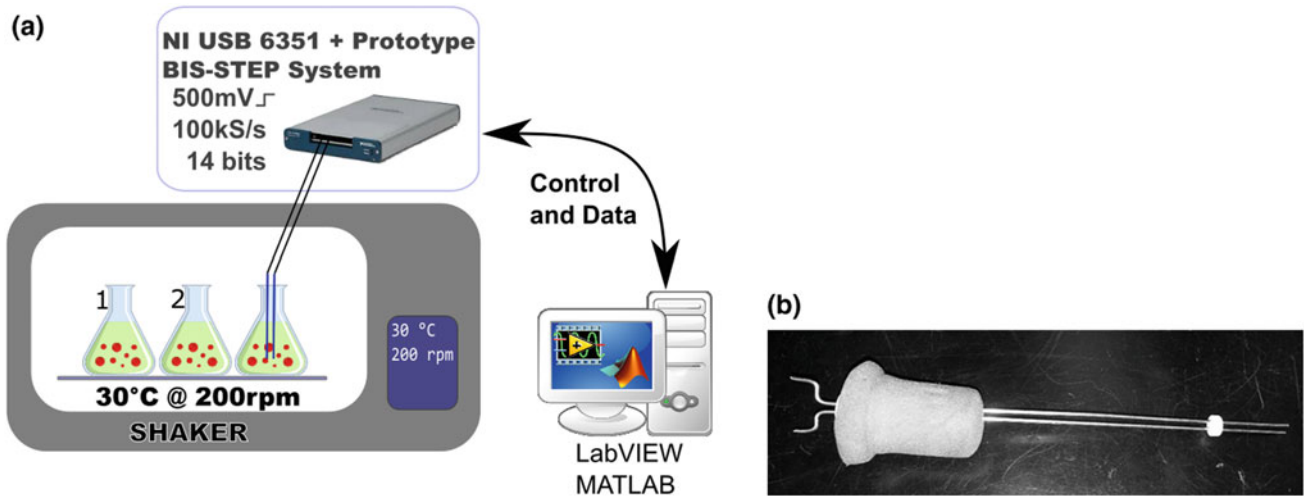


**Fig. 1** a Set-up of the experiment. b Electrodes with spacers and insulating foam stopper

## 2.1 Yeast and Culture Media

The microorganism used in this study was a yeast strain, *Saccharomyces cerevisiae* species, found in the form of instant dry yeast (Fleischmann, AB Brasil Ind. e Com. Ltda). Two initial inoculum concentrations were used in the experiments, 0.1 and 0.5 g/L. The adapted culture medium containing: Anhydrous glucose ( $C_6H_{12}O_6$ ) – 10 g/L; Potassium phosphate monobasic ( $KH_2PO_4$ ) – 1.5 g/L; Ammonium sulfate ( $(NH_4)_2SO_4$ ) – 2.0 g/L; Magnesium sulfate heptahydrated ( $MgSO_4 \cdot 7H_2O$ ) – 1.0 g/L and Yeast extract – 1.0 g/L.

**Culture Conditions:** Three 250 mL culture medium were prepared within 500 mL Erlenmeyer flasks, autoclaved at 121 °C for 20 min. At room temperature the flasks were inoculated with the yeast concentration of 0.1 g/L or 0.5 g/L. From the two Erlenmeyer analyzed by traditional *off-line* methods, two aliquots of 2 mL were alternately withdrawn every hour. The third Erlenmeyer was connected to the bioimpedance measurement hardware and placed on a shaker at 200 rpm @ 30 °C (Fig. 1a).

## 2.2 Bioimpedance Spectroscopy System

A hardware prototype implementing the bipolar bioimpedance spectroscopy based on the current response to a voltage step [8] was specifically designed for this application (Fig. 2a), which was controlled by a program developed in LabVIEW (National Instruments, USA). The current response signals were acquired at 14-bit resolution at a rate of 100 kS/s by a data acquisition board (National Instruments, USA–USB model 6351). Each final current signal

was coherent average of 20 readings, requiring a total time of 20 s.

The electrodes (stainless steel with 1.54 mm diameter, spaced 2 mm each other) used to perform the bioimpedance measurement were fixed in the Erlenmeyer by means of an insulating foam stopper (Fig. 1b).

**Analysis of the current response to the voltage step excitation:** Experimental conditions (illustrated in Fig. 2a) was modeled by the equivalent electrical circuit presented in Fig. 2c, in what concerns the analysis of the current signal (Fig. 2b) observed during the experiments. Such equivalent circuit has been used elsewhere [9]. In such circuit  $C_m$  indicates the capacitance of associated to the cellular membrane;  $C_{dl}$  states the electrodes capacitance;  $R_{cy}$  represents the resistance modeling the intracellular medium; and  $R_s$  the resistance associated to the extracellular or culture solution medium. It can be demonstrated that for the circuit of Fig. 1 the current response  $I(s)$  in the Laplace domain is expressed by Eq. (1):

$$I(s) = I_p \frac{s+A}{(s^2 + Bs + C)} = I_p \left\{ \frac{K_1}{(s-s_1)} + \frac{K_2}{(s-s_2)} \right\} \quad (1)$$

where:

$$I_p = v_d \left( \frac{R_s + R_{cy}}{R_s \cdot R_{cy}} \right); \quad A = \frac{1}{(R_s + R_{cy})C_m} \quad (2)$$

$$B = \left( \frac{R_s \cdot C_{dl}}{C_m} + R_s + R_{cy} \right) \frac{1}{R_s \cdot R_{cy} \cdot C_{dl}}; \quad (3)$$

$$C = \frac{1}{R_s \cdot R_{cy} \cdot C_{dl} \cdot C_m}$$

The inverse Laplace transform of Eq. (1) gives the current response in the time domain  $i(t)$ .

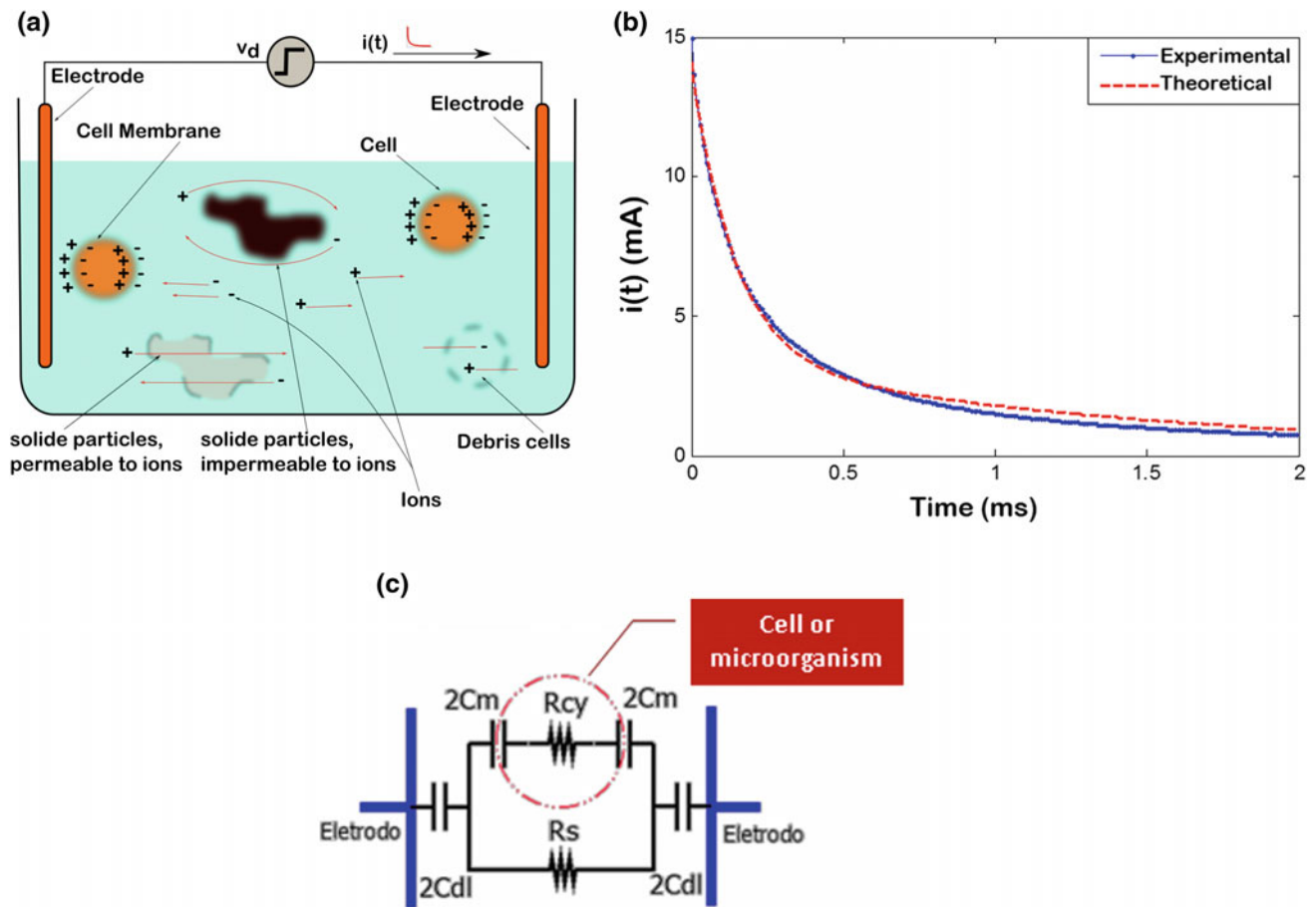


**Fig. 2** BIS-STEP: **a** Culture medium (suspension) of the microorganism. **b** Typical experimental curve of the current response for a voltage step excitation and adjustment of the theoretical equation. **c** Its equivalent electrical model, where  $V_d$  is the magnitude of the voltage

step,  $i(t)$  is the current in the time domain,  $C_{dl}$  is the total capacitance of the electrodes,  $R_s$  is the resistance of the culture medium (suspension),  $R_{cy}$  is the intracellular resistance and  $C_m$  is cell membrane capacitance

$$i(t) = I_p(K_1 \cdot e^{s_1 t} + K_2 \cdot e^{s_2 t}) \quad (4)$$

whose parameters  $K_1$ ,  $s_1$ ,  $K_2$  and  $s_2$  are obtained from the electrical parameters ( $C_{dl}$ ,  $R_s$ ,  $R_{cy}$  and  $C_m$ ).

An optimization routine was implemented in MATLAB to obtain the values of electrical parameters that minimized the mean square error between each experimental measure (Fig. 2b) and the theoretical (Eq. 4) expectation of the current response.

**Multivariate Linear Regression Model:** The estimated electrical parameters ( $C_{dl}$ ,  $R_s$ ,  $R_{cy}$  and  $C_m$ ) were used to derive a multivariate linear regression model to estimate the number of the total and viable cells. All regressions were made by *R Software* (*R Foundation for Statistical Computing*), using data associated to the inoculum of 0.1 and 0.5 g/L.

**Growth Yeast Monitoring:** For each inoculum (0.1 g/L or 0.5 g/L) the yeast growth experiment was monitored each hour during a 12 h period by two *off-line* methods, considered gold standard (Neubauer chamber to count the total

cells and dyeing with methylene blue to differentiate living and dead microorganisms) and by the proposed *on-line* bioimpedance method. Two experiments (duplicate) were performed using the inoculum of 0.1 g/L and three experiments (triplicate) using 0.5 g/L.

### 3 Results and Conclusions

The Fig. 3 shows the results of the multivariate linear regression for the number of total cells and for the viable cells, ( $r = 0.918$  and  $r = 0.858$ , respectively). Graphical representations of experimental and estimated number of total cells, as well as of the viable cells, can be seen in the Fig. 4, where the thin red line represents the identity function and the thick black line represents the regression.

A time of approximately 40 s was elapsed from the beginning of the data acquisition, estimating the electrical parameters, and deriving the number of total cells and of the viable ones.

<p><b>(a)</b></p> <p>call: lm(formula = CelulasTotais ~ delta_Cm + delta_cd1 + delta_Rcy + delta_Rs)</p> <p>Residuals: Min 1Q Median 3Q Max -8487092 -1750924 -148196 1490238 10743667</p> <p>Coefficients: Estimate Std. Error t value Pr(&gt; t ) (Intercept) 919055 757690 1.213 0.229 delta_Cm 1089499 99815 10.915 &lt; 2e-16 *** delta_cd1 -1208346 104291 -11.586 &lt; 2e-16 *** delta_Rcy 888462 92907 9.563 1.65e-14 *** delta_Rs -512740 67409 -7.606 7.71e-11 ***</p> <p>--- Signif. codes: 0 '***' 0.001 '**' 0.01 '*' 0.05 '.' 0.1 ' ' 1</p> <p>Residual standard error: 3476000 on 73 degrees of freedom Multiple R-squared: 0.8422, Adjusted R-squared: 0.8336 F-statistic: 97.43 on 4 and 73 DF, p-value: &lt; 2.2e-16</p>	<p><b>(b)</b></p> <p>call: lm(formula = CelulasViaveis ~ delta_Cm + delta_cd1 + delta_Rcy + delta_Rs)</p> <p>Residuals: Min 1Q Median 3Q Max -6063310 -1257440 -156543 926812 11985851</p> <p>Coefficients: Estimate Std. Error t value Pr(&gt; t ) (Intercept) 1318048 655122 2.012 0.0479 * delta_Cm 670174 86304 7.765 3.88e-11 *** delta_cd1 -769861 90173 -8.538 1.37e-12 *** delta_Rcy 492001 80331 6.125 4.17e-08 *** delta_Rs -370340 58284 -6.354 1.60e-08 ***</p> <p>--- Signif. codes: 0 '***' 0.001 '**' 0.01 '*' 0.05 '.' 0.1 ' ' 1</p> <p>Residual standard error: 3006000 on 73 degrees of freedom Multiple R-squared: 0.7367, Adjusted R-squared: 0.7223 F-statistic: 51.07 on 4 and 73 DF, p-value: &lt; 2.2e-16</p>
--	---

**Fig. 3** Results from multivariate linear regression. **a** Total cells. **b** Viable cells

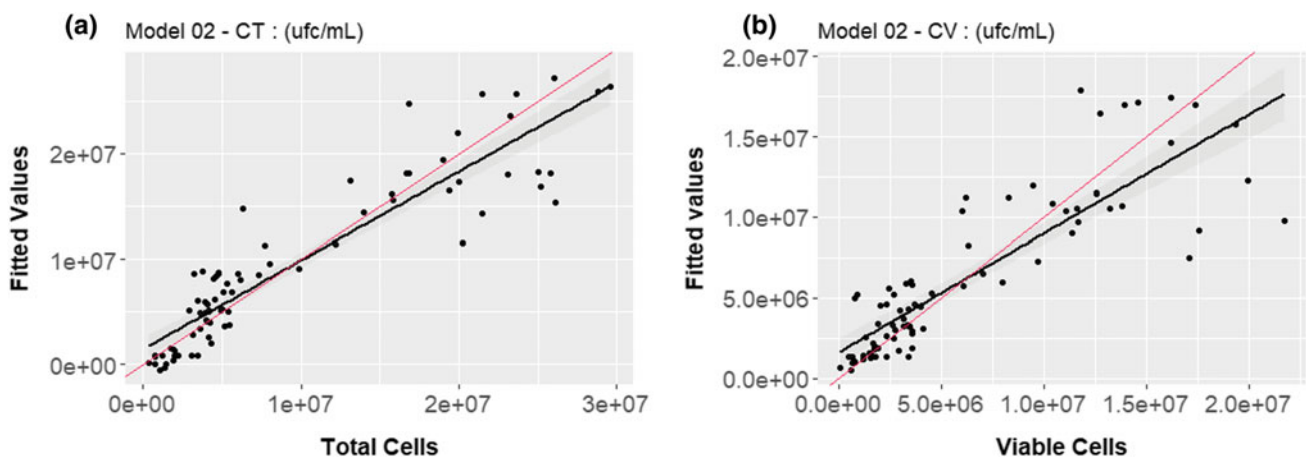


**Fig. 4** Graphical representation of the multivariate linear regression. **a** Total cells. **b** Viable cells

In conclusion, despite the present work has shown good results in using bioimpedance technique to estimate the total number of microorganisms and the number of viable ones in a yeast growth experiment, more studies with different microorganisms are necessary to state the method can be applied for monitoring of industrial bioprocesses.

**Acknowledgements** To the Brazilian governmental agencies CNPq, CAPES and FINEP, for financial support. To the Laboratory of Bioprocess Development (LADEBIO) of School of Chemistry of UFRJ for the support in the accomplishment of the analytical tests.

**Conflict of Interest** The authors declare that they have no conflict of interest.

## References

- Dabros, M., Dennewald, D., Currie, D. J., Lee, M. H., Todd, Marison, I. W., von Stockar, U.: Cole–Cole, linear and multivariate modeling of capacitance data for on-line monitoring of biomass. *Bioprocess and Biosystems Engineering*, Vol. 32, p. 161, Springer (2009)
- Kim, Y. Hu., Park, J. S., Jung, H. I.: An impedimetric biosensor for real-time monitoring of bacterial growth in a microbial fermentor. *Sensors and Actuators B: Chemical*, Vol. 138, pp. 270–277, Elsevier (2009)
- Lei, K. F.: Review on impedance detection of cellular responses in micro/nano environment. *Micromachines*, Vol. 5, pp. 1–12, Multidisciplinary Digital Publishing Institute (2014)
- Sarró, E., Lecina, M., Fontova, A., Gódiá, F., Bragós, R., Cairó, J. J.: Real-time and on-line monitoring of morphological cell parameters using electrical impedance spectroscopy measurements. *Journal of Chemical Technology and Biotechnology*, Wiley Online Library (2015)
- Martinez-Teruel, J., García Sánchez, T., Fontova, A., Bragós, R.: Electrical Impedance Spectroscopy cell monitoring in a miniaturized bioreactor. 19th IMEKO TC 4 Symposium Measurements of Electrical Quantities, 17th TC 4 Workshop IWADC on ADC and DAC Modeling and Testing, pp. 446–450, 2013
- Dinorín-Télez-Girón, J., Delgado-Macuil, R. J., Corona, C. P. L., Montes, F. J. M., de la Torre Martínérez, M., López-Y-López, V. E.: Reactance and resistance: main properties to follow the cell differentiation process in *Bacillus thuringiensis* by dielectric

- spectroscopy in real time. *Applied Microbiology and Biotechnology*, Vol. 99, pp. 5439–5450, Springer (2015)
7. Ruiz, G. A., Zamora, M. L., Felice, C. J.: Isoconductivity method to study adhesion of yeast cells to gold electrode. *Journal of Electrical Bioimpedance*, Vol. 5, pp. 40–47, 2014
  8. Neves, C. E. B., Souza, M. N.: A method for bio-electrical impedance analysis based on a step-voltage response. *Physiological Measurement*, Vol. 21, p. 395, IOP Publishing (2000)
  9. Pliquet, U.: Bioimpedance: a review for food processing. *Food Engineering Reviews*, Vol. 2, pp. 74–94, Springer (2010)



# Agent-Based Model of the Budding Yeast Cell Cycle Regulatory Network

Carlos Castro<sup>✉</sup>, Dora-Luz Flores<sup>✉</sup>, Eunice Vargas<sup>✉</sup>,  
David Cervantes<sup>✉</sup>, and Efren Delgado<sup>✉</sup>

## Abstract

Kinetic parameters are a crucial aspect when studying reactions involving proteins. Unfortunately, these are often unknown or hard to measure in the laboratory. Therefore, modeling phenomena involving protein reactions without using kinetic parameters can be a significant advantage. In this work, an agent-based model of the budding yeast (*Saccharomyces cerevisiae*) cell cycle was created based on a cell cycle regulatory network, to obtain the correct sequence of states of the regulatory proteins. Comparing the results to a Boolean network model, having similar results, following the correct sequence of phases and reaching in 71% of the cases the biological G1 stationary state of the cell. Yeast cell cycle is highly conserved among other eukaryotes, meaning that its regulators works similar than the ones in humans; knowing that, yeast cells can be mutated to have behavior related to a specific tumor and then treated with different drugs to check which is better to kill that particular tumor. This model could be a starting point for being used in the development of cancer drugs adding cell cycle mutations that match a specific type of tumor cell cycle and an agent representing the medication or treatment.

## Keywords

Agent-based model • Budding yeast • Cancer Cell cycle

## 1 Introduction

### 1.1 Yeast as a Model for Research

Yeast had been a powerful organism for the study and development of anticancer drugs [1, 2]. The primary characteristics that make yeast a complete model usable as a tool in cancer research are its less complexity compare to human tumors, significant similitude between yeast and mammalian cellular processes, and easy genetic transformation [3, 4].

*Saccharomyces cerevisiae* commonly called budding yeast is a single-celled organism that carries out a rapid cell division in the ideal environment. During its reproduction, the cell produces a bud (from his colloquial name, budding yeast) that grows throughout the cell cycle giving precise morphological information of the progress. It is important to highlight that the cell structure, synthesis, and chromosome replication are highly homologous to greater eukaryotes like plants, animals and also humans [5]. Due to the above, the budding yeast has been a robust model to study cell cycle regulations, Deoxyribonucleic Acid (DNA) repair, growth and cellular pathways of human diseases. In addition, there is an approximate from 25 to 30% homolog genes associated with diseases between yeast and humans [3, 4].

Genetic defects in cells can lead to genetic problems that affect the cell cycle machinery, DNA, or cell cycle checkpoints, thus, transforming it into a cancer cell. These defects can create vulnerability for the cancer cell making it able to be targeted for therapeutic purposes. The way to do it is transforming yeast cells in a way that match the characteristics of specific tumors like mismatch of repair, cyclins, etc. Then the normal and transformed cells are tested with drugs to identify which kill the mutated cell faster [2].

C. Castro · D.-L. Flores (✉) · E. Vargas  
Autonomous University of Baja California, Ensenada, Mexico  
e-mail: dflores@uabc.edu.mx

D. Cervantes · E. Delgado  
New Mexico State University, Las Cruces, NM, USA

## 1.2 Cell Cycle Regulators Network

The cell cycle is a vital process where the cell divides itself into two daughters. Budding yeast cell cycle is well known having around 800 genes that are involved in some way in its cell cycle regulation, but the key regulation of the cycle is made by just a little amount of proteins [6].

The regulatory network for the budding yeast is summarized in Fig. 1, was simplified by Li et al. [6]. The simplify regulatory network was chosen in order to make a direct comparison from the results of Li et al. Green arrows represent a positive regulation or activation. meaning that a protein affects to another protein, (by expression of a gene, changing molecular concentration, doing phosphorylation, etc.) making it able to fullfil its role in the cell cycle regulatory network. Red arrows are a process of deactivation or inhibition/degradation, it happens when a protein affects other protein (by dephosphorylating, changing the concentration negatively or denying gene expression of that protein) making it unable to do its role in the regulation. Yellow arrows are a self-degradation process added to proteins that are not deactivated by others. Also, a checkpoint of cell size is incorporated to represent when the cell reaches the necessary size to commit division.

## 1.3 Agent-Based Modeling

Agent-Based Modeling (ABM) is a modeling technique used to make a representation of a real phenomenon, created by using autonomous agents representing the entities or parts of the model. The agents have a set of rules that define its behavior to reproduce the real entity. Agents also have interactions with other agents and with the environment. The quality of this rules and interactions will determine if the model represents the real phenomenon [7]. ABM is a technique widely used in the modeling of biological systems thanks to its facility to integrate qualitative and quantitative

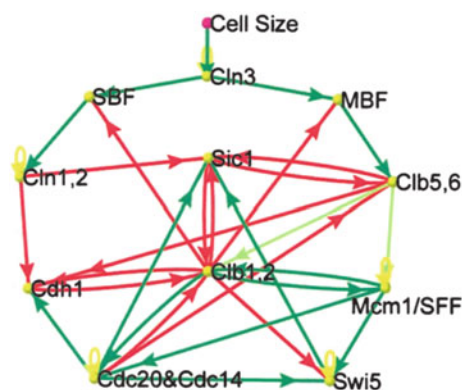


Fig. 1 Budding yeast cell cycle regulatory network from Li et al.

information [8]. Some examples of the application of ABM in biological studies can be found in previous research [9–12].

ABM works on the premise that everything can be modeled if it can be represented as agent, an environment and interactions agent to agent, and agent to environment [13]. Regarding the cell cycle, the proteins will be set as agents and the cell as the environment and arrows in the regulatory network are the interactions. Therefore, the ABM of the budding yeast cell cycle can be achieved.

In this paper the Cell Cycle Agent-Based Model (CCABM) of the budding yeast was created based on the regulatory network from [6] to reproduce the correct sequence of the cell cycle phases, reaching the expected stationary G1 state. The model was made without taking neither kinetic parameters nor concentrations of the proteins into consideration, reducing the complexity of the model and the facility of creation due to the often lack of information about cellular parameters. NetLogo [14] was used to create the CCABM because is the most widely used to program ABM [13].

## 2 Methodology

The steps described in [13] for the creation of an ABM are designed, built and analyzed.

### 2.1 Designing the Model

This step consists in setting up how the phenomenon will be modeled, depending on the type of physical problem to study, how much information has been recollected and personal preferences for coding in NetLogo. The model will be under the category of phenomena-based modeling, where the design starts knowing the desired target phenomenon, in this case, the G1 stationary state of the budding yeast cell cycle. Then a set of agents have to be defined and loaded with a set of rules that will generate the target. Eleven agents were chosen, one for each of the proteins for the regulatory network in Fig. 1 (Cln3, MBF, SBF, Cln1,2, Cdh1, Swi5, Cdc20&Cdc14, Clb5,6, Sic1, Clb1,2, and Mcm1/SFF). Each agent having the set of rules that act as the activation and deactivation arrows from the network fully represented by adding a binary value to each agent, having a value of 0 when it is deactivated and 1 when it is activated. This property will help to know in what phase of the cycle is the cell and if the desired output was obtained. Also, the design was made under the top-down approach, meaning that all the definition of the conceptual model (which agents, the environment and the rules of behavior) was made before writing the code in the software.

## 2.2 Building the Model

The coding of the model was made in NetLogo version 6.1 [14]. Each protein in the regulatory network was programmed as a breed on the model; proteins react when they are on the same physical space with other proteins which they can react (green and red arrows on the regulatory network), changing the activity value of the protein in the process.

## 2.3 Analyzing the Model

Whenever a model has stochastic properties, like this one, it is necessary to run the model several times to properly identify the behavior of the model. Having anomalous response in the model is possible, if the model is only run once it will be difficult to know if the result of that run is the expected behavior of the model or if it is just an atypical case.

Checking the times' percentage the model reached G1 stationary state 100 runs were performed, under the same exact initial conditions. The initial state for each protein were set as mentioned in [6], being  $Cln3 = 1$ ,  $MBF = 0$ ,  $SBF = 0$ ,  $Cln1,2 = 0$ ,  $Cdh1 = 1$ ,  $Swi5 = 0$ ,  $Cdc20 \& Cdc14 = 0$ ,  $Clb5,6 = 0$ ,  $Sic1 = 1$ ,  $Clb1,2 = 0$ , and  $Mcm1/SFF = 0$ , the exact same way as in biological conditions, the moment that cell size signal activate  $Cln3$  and starts the cycle.

Additionally, the model was run  $2^{11} = 2048$  times by varying the initial state of each protein to cover all the possible configurations, to determine whereas the cell is fixing towards the G1 stationary state.

## 3 Results and Discussion

When running the model 100 times under biological initial conditions the cell followed the cycle by starting at the G1 phase, going to the S phase, the G2 phase, the M phase and finishing in the G1 stationary state, that is the biological pathway of the regulatory network. The cell reached the G1 stationary 71% of the cases, meaning that the model is correctly obtaining the target phenomenon. It is important to notice the fact that the model did not reached 100% of the times the G1 stationary state, meaning that the model is stochastic and therefore it is not lineal, thus, not following an exact same sequence over and over again, negating any type of complexity in the model.

Table 1 shows the sequence obtained by the model the 71% of the cases when the cell reached its biological stationary state. The sequence of events shows the start of the cycle leading towards G1, S, G2, M and finally the G1 stationary state.

In Table 2 are the stationary states obtained and the number of times each state was reached, with the G1 stationary state predominating over the others 67% of the cases confirming cell stability to fix towards the target state. In this model an emergent behavior was found, having an extra stationary state in contrast with Li et al, the state where all proteins are set on 0, this is a variation of the state when only  $Cdh1$  is active and can be attributed to the stochastic movement of the proteins.

These results give enough information to say that the CCABM of the budding yeast can be used to study the biological cell cycle of this yeast. Primarily using it as a base model for being used in cancer research, applying the experimentation process described above, adding some

**Table 1** Sequence of events of the budding yeast cell cycle

Step	Cln3	MBF	SBF	Cln12	Cdh1	Swi5	Cdc20	Clb56	Sic1	Clb12	Mcm1	Phase
1	1	0	0	0	1	0	0	0	1	0	0	Start
2	0	1	1	0	1	0	0	0	1	0	0	G1
3	0	1	1	1	1	0	0	0	1	0	0	G1
4	0	1	1	1	0	0	0	0	0	0	0	G1
5	0	1	1	1	0	0	0	1	0	0	0	S
6	0	1	1	1	0	0	0	1	0	1	1	G2
7	0	0	0	1	0	0	1	1	0	1	1	M
8	0	0	0	0	0	1	1	0	0	1	1	M
9	0	0	0	0	0	1	1	0	1	1	1	M
10	0	0	0	0	0	1	1	0	1	0	1	M
11	0	0	0	0	1	1	1	0	1	0	0	M
12	0	0	0	0	1	1	0	0	1	0	0	M
13	0	0	0	0	1	0	0	0	1	0	0	G1

**Table 2** Stationary states of the cell cycle network modeled

Cln3	MBF	SBF	Cln12	Cdh1	Swi5	Cdc20	Clb56	Sic1	Clb12	Mcm1	Times
0	0	0	0	1	0	0	0	1	0	0	1367
0	0	1	0	0	0	0	0	0	0	0	367
0	1	0	0	1	0	0	0	1	0	0	202
0	0	0	0	0	0	0	0	0	0	0	94
0	0	0	0	0	0	0	0	1	0	0	11
0	1	0	0	0	0	0	0	1	0	0	5
0	0	1	1	0	0	0	0	0	0	0	1
0	0	0	0	1	0	0	0	0	0	0	1

modification to match the behavior of a tumor cell and then adding an agent representing the drug that wants to be tested.

## 4 Conclusions

An agent-based model for the budding yeast cell cycle was obtained, using a regulatory cell cycle network to define agents, agent properties, and rules of behavior. The model showed the G1, S, G2 and M phases as the biological phenomenon similar to the results from Li et al.; both models use the same regulatory network of the cell cycle to simulate the sequence of protein states in each phase without using any quantitative data as molecule concentrations, kinetic parameters, etc. but adding an stochastic movement to the proteins of the CCABM. The major difference between those models is the computational technique used where ABM was not used before to model the budding yeast cell cycle, therefore, being prove that ABM can be addressed when studying cell cycle regulation based on regulatory interactions of proteins.


This model is a base for the study of the cell cycle saving economic and time resources. Computational biology proves to be of significant help for research and analyze biological phenomena that can be hard or impossible to realize in the laboratory. Therefore it is a field to be considered in further investigations alongside the agent-based modeling approach, especially in hard topics as cancer drug development and cancer research in general.

**Conflict of interest** The authors declare no conflict of interest regarding the publication of this paper.

## References

1. Nitiss, J. L. & Heitman, J. *Yeast as tool in cancer research*. (2007).
2. Hartwell, L. H. Yeast and cancer. *Biosci. Rep.* **24**, 525–544 (2005).
3. Matuo, R. *et al.* Saccharomyces cerevisiae as a model system to study the response to anticancer agents. *Cancer Chemother. Pharmacol.* **70**, 491–502 (2012).
4. Kalia, V. C. & Saini, A. K. *Metabolic Engineering for Bioactive Compounds*. (2017). <https://doi.org/10.1007/978-981-10-5511-9>.
5. Hartwell, L. H. Saccharomyces cerevisiae cell cycle. *Bacteriol. Rev.* **38**, 164–198 (1974).
6. Li, F., Long, T., Lu, Y., Ouyang, Q. & Tang, C. The yeast cell-cycle network is robustly designed. *Proc. Natl. Acad. Sci.* **101**, 4781–4786 (2004).
7. Bonabeau, E. Agent-based modeling: methods and techniques for simulating human systems. *Proc. Natl. Acad. Sci.* **99**, 7280–7287 (2002).
8. Bayrak, E. S. *et al.* In Silico Cell Cycle Predictor for Mammalian Cell Culture Bioreactor Using Agent-Based Modeling Approach. *IFAC-PapersOnLine* **49**, 200–205 (2016).
9. Bauer, A. L., Beauchemin, C. A. A. & Perelson, A. S. Agent-based modeling of host-pathogen systems: The successes and challenges. *Inf. Sci. (Ny)*. **179**, 1379–1389 (2009).
10. Khataee, H. R., Aris, T. N. M. & Sulaiman, M. N. An agent-based model of muscle contraction process as a bio-robotic process. *2011 5th Malaysian Conf. Softw. Eng. MySEC 2011* 55–60 (2011). <https://doi.org/10.1109/mysec.2011.6140643>.
11. Manzanarez-ozuna, E. *et al.* Computational modeling of the MAPK pathway using NetLogo. 1–4 (2015). doi:<https://doi.org/10.13140/rg.2.1.4179.6244>.
12. Zhang, L., Wang, Z., Sagotsky, J. A. & Deisboeck, T. S. Multiscale agent-based cancer modeling. *J. Math. Biol.* **58**, 545–559 (2009).
13. Wilensky, U. & Rand, W. *An Introduction to Agent-Based Modeling*. (2015).
14. Wilensky, U. NetLogo. *Center for Connected Learning and Computer-Based Modeling, Northwestern University, Evanston, IL* (1999). Available at: <http://ccl.northwestern.edu/netlogo/>.

# Basic Concepts of Sensing Respiratory Sounds at the Surface of Human Chest

Vladimir Korenbaum , Alexandr Tagiltcev, Sergei Gorovoy, Anatoly Kostiv, Anton Shiryayev, and Oksana Kabancova

## Abstract

Acoustic sensors for recording lung sounds at the chest surface should meet some basic requirements—(a) achievement the acceptable sensitivity or sensitivity threshold to the useful signal, (b) a linearity of frequency response, and (c) sufficient noise immunity. Specific condition of recording acoustic wave propagating through human thorax is its registering on the border of the body with air medium which can be regarded as an acoustically soft one. Existing types of acoustic sensors usually used may be divided into contact and non-contact receivers. Non-contact receivers are still exotic to some extent. Currently, three types of acoustic receivers mounted in contact with the chest surface are used. They are accelerometer sensor, stethoscope sensor with microphone, and so called “contact” sensor. Any acoustic sensor having a mass when placed on a layer of soft tissues having hardness should inevitably have an eigenfrequency of suspending. According to ratio of working frequency range and the frequency of suspending all mentioned sensors are modeled as the receivers of oscillatory acceleration, velocity, displacement or dynamic force. Experimental study and theoretical estimates indicate that there is no one optimal sensor meeting all basic requirements for all scenarios of acoustic study of lungs. Hence a passive recording of lung sounds is more frequently performed with a stethoscope or with “contact” sensor, whereas active transmission sounding is performed with an accelerometer or “contact” sensor. However even these sensors are frequently used in non-optimal modes. New studies are welcome to design more optimal sensors.

## Keywords

Acoustic sensor • Chest surface • Lung sounds

## 1 Introduction

Acoustic sensors for recording lung sounds at the chest surface should meet some basic requirements: (a) achievement the acceptable sensitivity or sensitivity threshold to the useful signal, (b) a linearity of frequency response and (c) sufficient noise immunity. Specific condition of recording acoustic wave propagating through human thorax is its registering on the border of the body with air medium.

The objective is a study of the characteristics of various types of acoustic sensors in recording lung sounds at the chest surface.

## 2 Theory

The border of the chest with air medium, where an acoustic sensor is placed to receive approximately flat wave (long wave approximation) generated by lung sounds sources inside thorax, can be regarded as an acoustically soft one.

Existing types of acoustic sensors usually used may be divided into contact and non-contact receivers.

A non-contact pick up of kinematic parameters (oscillatory acceleration, velocity, displacement) of wave motion should be ideal for any measurement at acoustically soft border. There are now laser interferometer oscillatory displacement receivers or the Doppler oscillatory velocity receivers having even the scanning versions making possible serial pick up of signals in various part of chest [1]. However the non-contact receivers are still exotic and highly expensive.

Currently, three types of acoustic receivers mounted in contact with the chest surface are used to record respiratory sounds. They are accelerometer sensor, stethoscope sensor with microphone, and so called “contact” sensor, in which

V. Korenbaum (✉) · A. Tagiltcev · S. Gorovoy · A. Kostiv  
A. Shiryayev · O. Kabancova  
Pacific Oceanological Institute, Russian Academy of Sciences,  
Baltiiskaya str. 43, 690041 Vladivostok, Russia  
e-mail: v-kor@poi.dvo.ru



the sensitive piezotransducer is situated between the surface of the chest and the sensor housing [2].

Any acoustic sensor having a mass  $M$  when placed on a layer of soft tissues (skin and adipose layer) having a hardness  $K$  should inevitably have an eigenfrequency of suspending, which in the long wave approximation of a rubber vibration damper, as well as with consideration on a small viscosity of biological tissues may be found as

$$f_0 \approx (K/M)^{0.5}/2\pi. \quad (1)$$

With  $M \approx 7\text{--}8$  g, and sensor diameter of about 30 mm the  $f_0$  is assessed for the lower chest surface being about 200 Hz according to Eq. 1.

When operating at frequencies 1.5–2 times lower than  $f_0$ , the sensor will make common vibrations with the surface of the chest. On the contrary, when operating at frequencies substantially higher than  $f_0$ , the sensor can be considered isolated from vibrations of the medium. Note that the linear vibration isolation (V.I.) effect, according to the known law

$$\text{V.I.} = 20 \log(f/f_0), \quad (2)$$

begins to manifest itself from frequencies of about  $(1.5\text{--}2)f_0$  and increases approximately linearly with elevating frequency.

Let's consider approximate frequency characteristics of sensors at the chest surface being essentially below or above the suspending resonance frequency, because in vicinity of this resonance sensors their behavior is more complicated.

### 3 Results and Discussion

#### 3.1 Frequency Response and Sensitivity

The idealized frequency responses of sensors with assumption of equal masses and diameters are presented in Fig. 1.

As for characteristic of an accelerometer sensor (Fig. 1—1), such acoustic sensor if the resonance of its sensitive element is higher than the analyzed range, during operation at frequencies lower than  $f_0/(1.5\text{--}2)$ , will make common vibrations with the surface of the chest and, thus, should be a classic oscillatory acceleration receiver. During operation above  $f_0$ , such sensor will be an oscillatory velocity receiver, owing to compensation of the accelerometer's natural frequency response, by an almost linear drop in the transfer characteristic due to vibration isolation effect (Eq. 2), beginning from approximately  $(1.5\text{--}2)f_0$ . However at very high frequencies (more  $10 f_0$ ) the sensor is transformed to oscillatory acceleration receiver ones more sensing vibrations of the co-oscillating mass of the medium (tissues) [3].

The stethoscopic sensor with electret microphone built into the bell at frequencies above  $(1.5\text{--}2)f_0$  works as an

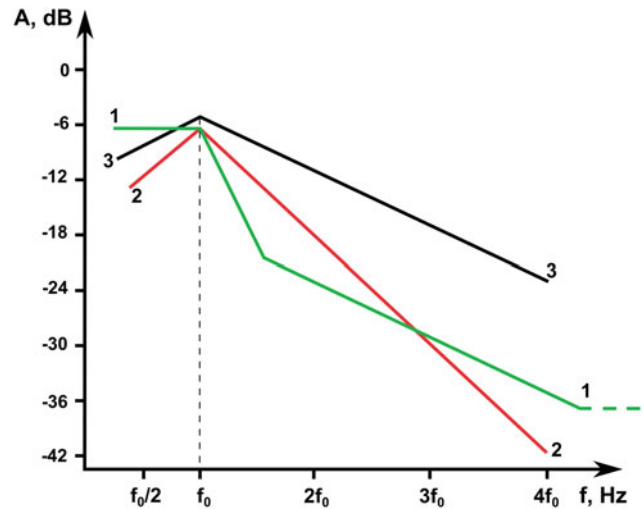


**Fig. 1** Idealized frequency responses of sensors of three types: 1—accelerometer sensor (green), 2—stethoscopic sensor with the microphone (red), 3—“contact” sensor (black)

oscillatory displacement receiver, while below  $f_0/(1.5\text{--}2)$  it has very low sensitivity due to very high vibrational immunity of the microphone (Fig. 1—2) [4].

The “contact” acoustic sensor below  $f_0/(1.5\text{--}2)$  works as an accelerometer (oscillatory acceleration receiver) while above  $(1.5\text{--}2)f_0$  it has a characteristic of dynamic force (contact pressure) receiver, which in locally flat wave in the first approximation is identical to the response of an oscillatory velocity receiver (Fig. 1—3) [4].

Thus the best characteristics for recording respiratory sounds on the chest surface in terms of sensitivity and the absence of frequency response distortions in the range of about 100–700 Hz belong to the heavy stethoscopic sensor with a microphone and the heavy “contact” sensor with a piezotransducer, the own resonance frequency of which lies substantially higher than the studied frequency range. There is a difference in the frequency slope of these sensors, making “contact” sensors more pertinent for recording high frequency sounds than stethoscopic one (Fig. 1).

The light accelerometers as well as the light “contact” sensors with flexural sensitive piezotransducer [2] have substantial distortions of the frequency response in the range of 100–700 Hz. The only possibility to increase  $f_0$  up to 400 Hz is an application of MEMS accelerometers (mass less than 4 g) unfortunately they still have very bad sensitivity threshold (high level of self-noise). However it is interesting that the light accelerometer with high enough frequency of own resonance is the only sensor suitable now to record sounds of high frequency range of 10–20 kHz [3].

The non-contact sensor like laser interferometer Doppler oscillatory velocity receiver should be ideal for linearity of frequency response since only light reflecting film should be

mounted at chest surface making  $f_0 \rightarrow 0$ . However the features of its frequency response slope (Fig. 1—3) in combination with bad sensitivity threshold still limit its high frequency range by approximately 300 Hz [1].

### 3.2 Noise Immunity

It should be noted that all mentioned types of sensors are exposed to noises and their noise immunity is different.

The most frequent noises are external sound signals, propagated through air medium; vibrations involved by oscillations of the chest surface or operator's hand, holding sensor; and so named pseudo sound, caused by oscillatory compression-expansion of elastic volume, adjacent to sensitive element. The last kind of noise is connected with mechanical vibrations too.

The stethoscopic sensor with a microphone has low immunity to external sound signals, as well as pseudo sound, while its immunity to vibrations is high. The accelerometer sensor is highly sensitive to vibrations, whereas its immunity to external sound signals and pseudo sound seems remarkable. The "contact" sensor has acceptable noise immunity to external sound signals; however it is prone to vibrations/pseudo sound.

The combined acoustic receiver containing a heavy "contact" sensor and a stethoscopic sensor with an electret microphone developed [4], which responses are intensimetry (orthogonally) processed, seems a promising solution in terms of noise immunity [5].

Another problem is a multichannel recording. When sensors are placed "back to back" at chest surface a cross interference on their responses could be essential through damping chest wall oscillations and exiting surface waves. The best performance in the case is achievable by light accelerometers, while heavy "contact" sensors are the worst.

The non-contact sensors like laser interferometer Doppler oscillatory velocity receivers should be ideal for multichannel recording below approximately 300 Hz [1]. Though the sensors are non-sensitive to pseudo sound, the problem of their immunity to vibrations of chest as well as of own

apparatus, and external sound signals still remains poorly understood.

## 4 Conclusions

There is no an optimal sensor for all scenarios of acoustic study of lungs. Therefore a passive recording of lung sounds at chest is more frequently performed by a stethoscopic sensor with microphone (especially at low frequencies) or by a "contact" sensor. Whereas under transmission sounding of lungs a recording is performed better with an accelerometer [6] or a "contact" sensor. However even these sensors are frequently used by researchers in non-optimal modes as related to non-distorted frequency response and/or sufficient noise immunity. New studies are welcome to design more optimal sensors as well as their modes of application.

**Acknowledgements** The study was supported by the Russian Foundation for Basic Research grant 16-08-00075-a.

**Conflict of Interest** The authors declare that they have no conflict of interest.

## References

1. Peng, Y., Dai, Z., Mansy, H., Sandler, R., Balk, A., Royston, T.: Sound Transmission in the Chest under Surface Excitation: an Experimental and Computational Study with Diagnostic Applications. *Med Biol Eng Comput* 52(8), 695–706 (2014).
2. Korenbaum, V., Tagil'tsev, A., D'yachenko, A., Kostiv, A.: Comparison of the Characteristics of Different Types of Acoustic Sensors when Recording Respiratory Noises on the Surface of the Human Chest. *Acoustical Physics* 59(4), 474–481 (2013).
3. Korenbaum, V., Shiriaev, A., Kostiv, A., Safronova, M.: Low- and high-speed arrivals decomposition in 10–19 kHz transmission sounding of human lungs. *In this book* (2018).
4. Korenbaum, V., Tagiltcev, A., Shiryaev, A., Kostiv, A., Gorovoy, S.: On localization of wheezing respiratory sounds in human lungs by means of intensimetric processing of signals detected on the chest surface. *Acoustical physics* 62(5), 600–607 (2016).
5. RU Patent No. 2496421 (2013).
6. Korenbaum, V., Nuzhdenko, A., Tagiltsev, A., Kostiv, A.: Investigation into transmission of complex sound signals in the human respiratory system. *Acoustical physics* 56(4), 568–575 (2010).

# Computational Modeling of Drug Delivery for Treatment of Age-Related Macular Degeneration

N. G. Dimitrioglou, M. E. Kavousanakis, and D. T. Hatzivramidis

## Abstract

Age-related macular degeneration (AMD) is a progressive, neurodegenerative ocular disease. It involves cell proliferation and uncontrolled growth in blood vessels leading to leaking of blood and proteins, scarring of the macula region, and, eventually, irreversible loss of vision. Neovascular AMD results from uncontrolled expression of the vascular endothelial growth factor (VEGF) and is treated primarily with the anti-VEGF macromolecular drugs, administered by intravitreal (IVT) injection. A less invasive, less risky system of delivery involves delivery from thermally responsive hydrogels of poly-(N-isopropylacrylamide) (pNIPAm), placed episclerally. In this case, most of the drug load is released by convection, and the remaining, close to 30% by weight, is released by diffusion. It was recently indicated that the chronic exposure to oxidative stress and a decline in lysosomal activity of retinal pigment epithelium (RPE) cells is a possible cause for RPE degeneration. An exogenous delivery of recombinant hHsp70 chaperone protein can protect RPE cells from oxidative stress and thus has the potential to be a therapeutic option against AMD. In this study, delivery of rhHsp70 from an episcleral hydrogel implant has been simulated with an anatomically and physiologically correct model of the human eye. The average drug concentration in sclera, choroid, retina and vitreous is compared, when the rhHsp70 is released at the limbus and the posterior of the eye. The results indicate that drug delivery from thermally responsive hydrogels, placed episclerally, is more effective than the currently practiced delivery through IVT injection.

## Keywords

Age-related macular degeneration • Heat shock protein  
Drug delivery • Gel implant • Posterior eye

## 1 Introduction

Age related macular degeneration (AMD) is a posterior eye disease and the leading cause of central vision loss in the elderly in the developed world [1]. AMD is a complex progressive, neurodegenerative ocular disease occurring at its advanced stage in two major forms: non-exudative (“dry”) and exudative (“wet”). In non-exudative AMD, also known as geographic atrophy, progressive atrophy and massive loss of retinal pigment epithelium (RPE) cells, photoreceptors, and choriocapillaries occurs. In exudative AMD, also known as neovascular AMD, RPE produces significant amounts of growth factor (VEGF) causing choroidal neovascularization that breaks through the blood retina barrier (BRB), and results in fluid, lipids and blood leaking and fibrous scarring. Unfortunately, there is no effective treatment targeting both AMD forms.

The exact mechanism of AMD’s pathogenesis is currently not known, however, there is evidence that chronic oxidative stress and autophagy decline are factors implicated in this pathology. Constant oxidative stress impairs autophagy and heterophagy, increases protein missfolding and aggregation and causes inflammatory activation [2]. The chronic oxidative stress is mainly caused by: (i) high levels of oxygen consumption, (ii) exposure to lipid peroxidation products, and (iii) exposure to constant light stimuli [3]. Increased levels of heat shock proteins (Hsp) have been observed in retina cells of AMD patients [4] highlighting their important role in repairing the missfolding damage. In this context, a new therapeutic strategy was proposed by

N. G. Dimitrioglou (✉) · M. E. Kavousanakis  
D. T. Hatzivramidis  
School of Chemical Engineering, National Technical University  
of Athens, Zografou, Athens, Greece  
e-mail: nikosdimitri@mail.ntua.gr

D. T. Hatzivramidis  
e-mail: dhatz@chemeng.ntua.gr

exogenous delivery of recombinant human Hsp70 chaperone protein (72 kDa) that can protect RPE cells from oxidative stress [3]. In almost all cellular compartments a set of abundant cellular machines that assist a large variety of protein folding processes is compromised by Hsp70 chaperones [5].

Currently, neovascular AMD is treated primarily with anti-VEGF macromolecular drugs, administered by intravitreal (IVT) injection. The best known anti-VEGF drugs contain pegylated aptamers of IgG1 Fab fragment. Delivery of ocular drugs through IVT injections poses a challenge because of the presence of physiological and anatomic barriers, e.g., BRB. Given the presence of many distinct tissues targeted drug delivery is a necessity. Moreover, ophthalmic delivery of macromolecules is difficult because of the large size of the active pharmaceutical ingredient (API) that limits the rate of diffusion [6]. A less invasive, less risky system of delivery involves transcleral delivery from thermally responsive hydrogels of poly-(N-isopropyl acrylamide) (pNIPAm) [7]. A certain time after implantation in the sclera close to the optical nerve, the hydrogel undergoes de-swelling when it reaches the body temperature. Ninawe et al. [8] developed a model that describes the de-swelling of the gel implant and the release of IgG1 Fab fragment. The simulation results revealed that most of the drug load is released by convection, and the remaining, close to 30% by weight, is released by diffusion [8]. Drug release is influenced by many factors, such as the type of polymer, the drug load, the implant morphology, and the hydrogel permeability [9].

Ninawe et al. [8] proposed a model that utilizes compartments for various eye tissues, with individual compartments considered to be completely mixed. In a compartmental model the drug transport between compartments occurs by one-dimensional diffusion. Although simulations with their model produced results comparable to those of clinical trials, the idealization of the eye tissues as continuously stirred tanks is not realistic. In Kavousanakis et al. [10] research, the compartmental model was replaced by an anatomically and physiologically correct model which was more realistic than the former. Based on in silico results, delivery of IgG1 Fab from an episcleral gel implant is as effective as the currently practiced delivery of IgG1 Fab through IVT. The aim of this study, is to utilize the anatomically and physiologically correct model to simulate the delivery of Hsp70 chaperones, as a potentially new drug for the prevention of AMD. IVT injection and episcleral hydro-gel implant at the posterior of the eye are tested as two different routes of administration.

## 2 Method

A cross-sectional view of the three-dimensional geometric model is shown in Fig. 1. The human posterior eye model consists of spherical shells. The sclera, choroid, and retina thicknesses are 0.6 cm, 0.32 cm and 0.22 cm, on the average, respectively [11]. The lens is excluded from the model, as it is almost impermeable to drugs due to highly compacted cellular material. In particular, the spacing between the fiber cells remain smaller than the wavelength of visible light [12]. The hyaloid membrane, forms a boundary between the stagnant vitreous and the flowing aqueous humor. Once drugs pass through the hyaloid membrane, they are eliminated by the flowing aqueous humor [13]. The vitreous humor is treated as a static, incompressible porous medium.

The Darcy flow equation is applied to describe the flow of the aqueous through the vitreous humor:

$$\frac{K}{\mu} \nabla^2 P = 0 \quad (1)$$

The flow of the aqueous humor is assumed to remain unaffected by the drug transport in the vitreous humor. The aqueous humor is incompressible and cannot permeate the lens. Values for the pressure at the outer surface of the Choroid-Sclera (CS) interface and at the hyaloid are equal to the intraocular pressure (IOP) which together with the hydraulic conductivity for the various tissues and other properties take the same values as in Kavousanakis et al. [10].

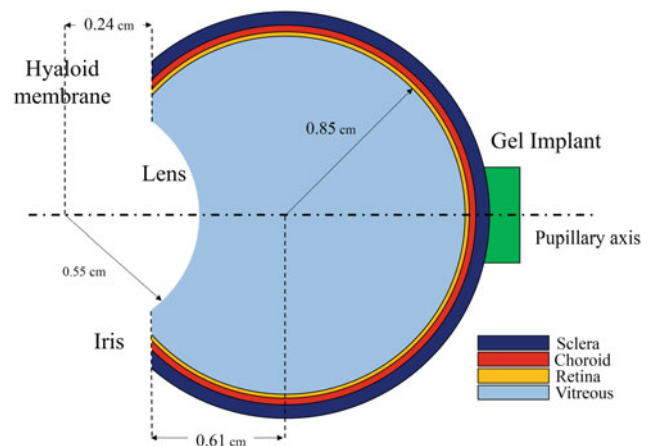


**Fig. 1** Schematic geometry of the posterior eye with an episcleral gel implant

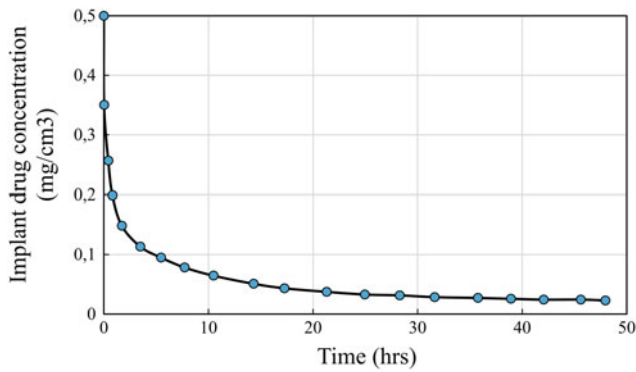


**Fig. 2** Decay of drug concentration at the gel implant when  $C_{drug}(t = 0) = 0.5 \text{ mg/cm}^3$

The drug is released by convection and molecular diffusion to the eye through two different routes of administration: (i) IVT injection and (ii) episcleral hydrogel implant at the posterior of the eye. A 30-gauge needle is commonly used for IVT injection [14], and thus, the nominal inner diameter of the needle is taken equal to 0.15 mm. The cylindrically shaped hydrogel implant is shown in Fig. 1. and the radius of hydrogel,  $R_h$ , is equal with 0.25 cm [8]. Separate mass balance equations are used for the tissues of the posterior eye,

$$\frac{\partial c}{\partial t} - D_s \nabla^2 c + \mathbf{v} \cdot \nabla c = 0 \quad (2)$$

$$\frac{\partial c}{\partial t} - D_c \nabla^2 c + k_{ec} c + \mathbf{v} \cdot \nabla c = 0 \quad (3)$$

$$\frac{\partial c}{\partial t} - D_r \nabla^2 c + k_{er} c + \mathbf{v} \cdot \nabla c = 0 \quad (4)$$

where,  $\mathbf{v}$  is the velocity field,  $D_s$ ,  $D_c$ ,  $D_r$  are the drug diffusivities in the sclera, choroid and retina, and  $k_{ec}$  and  $k_{er}$  rate constants of drug elimination in the choroid and retina,

respectively. Drug elimination follows first-order kinetics. At the outer surface and in contact with the sclera, a cylindrical hydrogel implant releases drug at a concentration,  $c(t)$ . The drug concentration decays exponentially as in Fig. 2. At the rest of the outer surface of sclera, elimination due to loss to conjunctival, lymphatics and episcleral veins as well as other possible mechanisms occurs. Values for the drug elimination coefficients in choroid and sclera and for the mass transfer coefficient are the ones used for IgG1 Fab fragment delivery [10].

Transport of macromolecules like Hsp70 through the hyaloid and the tissues of the posterior eye is insignificant. At the vitreous-retina interface, the drug is transferred solely by convection. Knowing the molecular weights and equivalent molecular radii of IgG and Hsp70, and the effective diffusivity of IgG in the sclera, the effective diffusivity of the Hsp70 in the sclera can be estimated. The diffusivity coefficients in the choroid and retina for the Hsp70 are estimated accordingly. The vitreous diffusivity of the Hsp70 was calculated using the fluorescein radius. The values of parameters used in the simulations for the transport of Hsp70 are shown in Table 1.

The Galerkin finite element method (GFEM) is used to solve the equations for pressure and drug concentration. Details about the implementation of the algorithm and the validation of the computational model can be found in Kavousanakis et al. [10].

### 3 Results

Simulations are made with an anatomically and physiologically correct model to determine the correct time of sustained delivery. For the purposes of this study the monthly dose is chosen to be equal with 0.5 mg. First, 0.5 mg/l of Hsp70 are injected at the vicinity of the limbus for 60 s. The spatial distribution of the drug on the  $z = 0$  plane 1 h, 8 h and 24 h after injection is plotted in Fig. 3.

**Table 1** Values of simulation parameters

Parameter	Value	Source
Hsp70 Stokes' Radius, $a_{Hsp}$	4.1 nm	[15]
IgG Stokes' Radius, $a_{IgG}$	5.23 nm	[16]
Fluorescein Stokes' Radius, $a_f$	0.5 nm	[16]
Vitreous Diffusivity, $D_v$	$7.317 \times 10^{-7} \text{ cm}^2/\text{s}$	[17]
Sclera Diffusivity, $D_s$	$3.272 \times 10^{-7} \text{ cm}^2/\text{s}$	[8]
Choroid Diffusivity, $D_c$	$2.572 \times 10^{-8} \text{ cm}^2/\text{s}$	[8]
Retina Diffusivity, $D_r$	$1.739 \times 10^{-7} \text{ cm}^2/\text{s}$	[8]



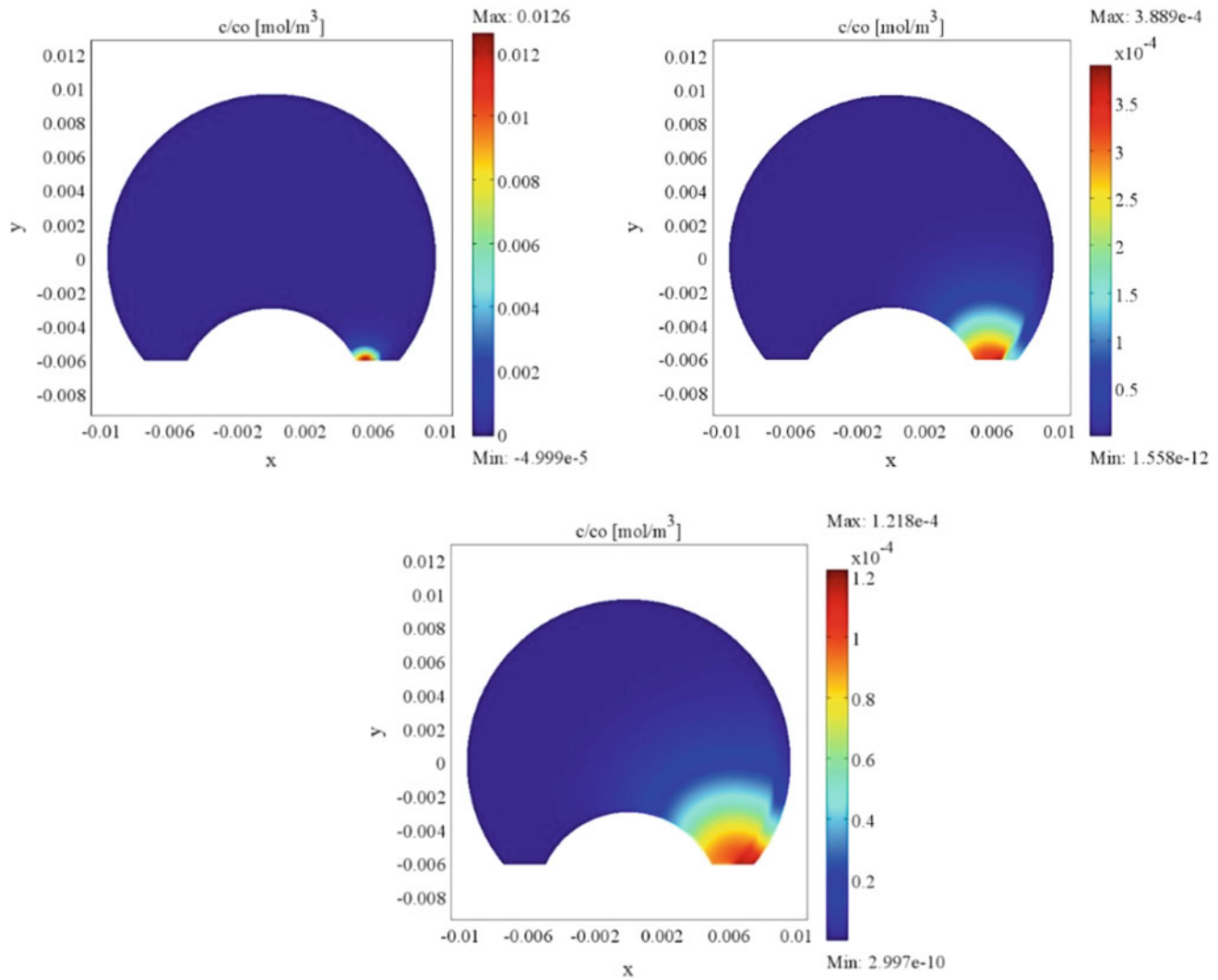
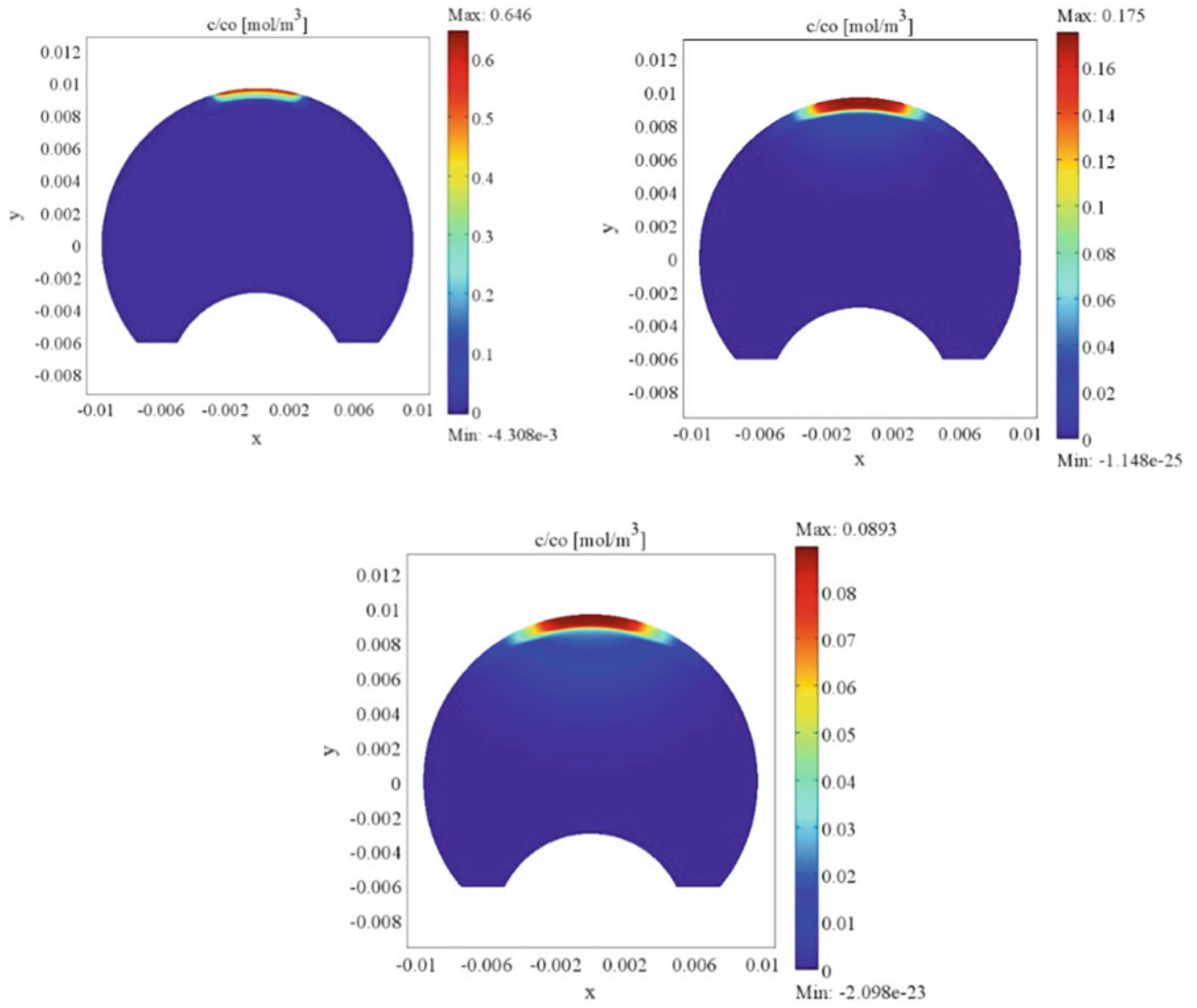


**Fig. 3** Spatial distribution of the drug on the  $z = 0$  plane 1 h, 12 h and 24 h after injection

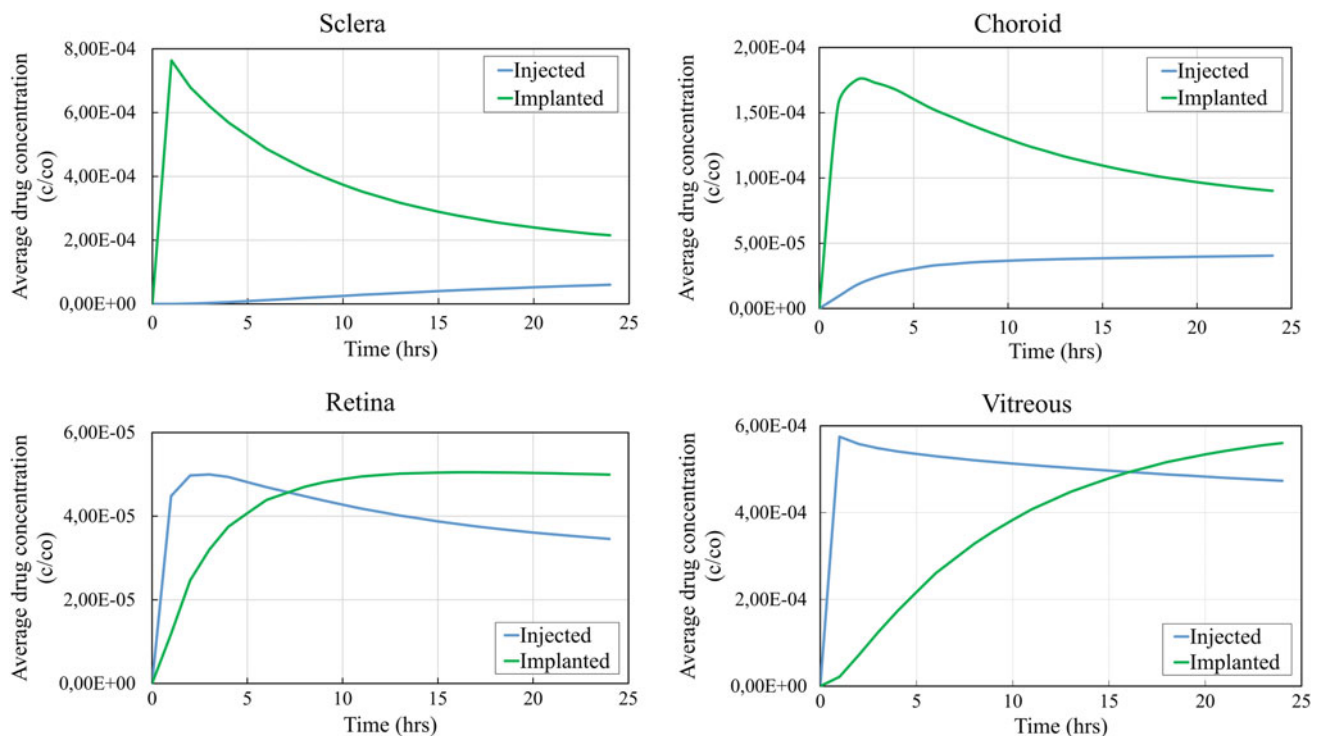
The drug is released to the posterior eye from a cylindrically shaped hydrogel implant. At the contact of the implant with the sclera the initial drug concentration  $C_{drug}(t = 0)$  is equal to  $0.5 \text{ mg/cm}^3$ . Figure 4 shows the average drug concentration in the sclera, choroid, retina and vitreous humor during the first day after implantation.

Figure 5 illustrates the comparison of the average drug concentration in sclera, choroid, retina and vitreous humor

when injected at the limbus and released to the posterior eye from a gel implant. One can see that the average drug concentration in the sclera and choroid are constantly higher when the drug is administered at the posterior eye. The average drug concentration on retina and vitreous is lower for 7 and 16 h after administration, respectively.



**Fig. 4** Spatial distribution of the drug released to the posterior eye on the  $z = 0$  plane 1 h, 12 h and 24 h



**Fig. 5** Average concentration in the sclera, choroid, retina, vitreous tissues, during the first day

## 4 Conclusions

The aim of this study was to evaluate the effectiveness of Hsp70 delivery for treatment of AMD through simulations with an anatomically and physiologically correct model of the eye. Hsp70 suppresses the development of AMD by keeping lysosomal enzymes functionally active and preventing inflammatory signalling in RPE cells. Therefore, the administration route of Hsp70 should ensure that the drug concentration in choroid and RPE cells remains at therapeutic levels. An episcleral hydrogel implant at the posterior eye was chosen as a less risky delivery system and was compared with IVT injection. The primary results of this study revealed the advantage of the Hsp70 delivery through an episcleral implant compared to conventional administration routes. The average drug concentration in the choroid, the area of interest, are constantly higher when the drug is administered to the posterior eye.

Hsp70 has the potential to be used as the API of a new drug for the prevention of AMD. The evaluation of effectiveness through simulations with an anatomically and physiologically correct model of the eye could play a significant role in the drug design and development process. Furthermore, this model can assist significantly in the design of the hydrogel implant material contributing to a more efficient drug release profile.

**Conflict of Interest** The authors declare that they have no conflict of interest.

## References

- Jager RD, Mieler WF, Miller JW (2008) Age-Related Macular Degeneration. *N Engl J Med* 358(24):2606–2617 <https://doi.org/10.1056/nejmra0801537>.
- Kaarniranta K, Tokarz P, Koskela A. (2017) Autophagy regulates death of retinal pigment epithelium cells in age-related macular degeneration. *Cell Biol Toxicol* 33:113–128 <https://doi.org/10.1007/s10565-016-9371-8>.
- Kivinen N, Hyttinen JMT, Viiri J, et al (2014) Hsp70 binds reversibly to proteasome inhibitor induced protein aggregates and evades autophagic clearance in ARPE-19 cells. *J Biochem Pharmacol Res* 2(1):1–7.
- Decanini A, Nordgaard CL, Feng X, et al (2008) Changes in Select Redox Proteins of the Retinal Pigment Epithelium in Age-related Macular Degeneration. *Am J Ophthalmol* 143(4):607–615 <https://doi.org/10.1016/j.ajo.2006.12.006>.
- Bukau B, Horwich AL (1998) The Hsp70 and Hsp60 Chaperone Machines. *Cell* 92(3):351–366 [https://doi.org/10.1016/s0092-8674\(00\)80928-9](https://doi.org/10.1016/s0092-8674(00)80928-9).
- Kim CY, Chiang B, Wu X, Prausnitz MR. (2014) Ocular delivery of macromolecules. *J Control Release* 190:172–181 <https://doi.org/10.1016/j.jconrel.2014.06.043>.
- Fanger C, Wack H, Ulbricht M (2006) Macroporous Poly (N-isopropylacrylamide) Hydrogels with Adjustable Size “Cut-off” for the Efficient and Reversible Immobilization of Biomacromolecules. *Macromol Biosci* 6(6):393–402 <https://doi.org/10.1002/mabi.200600027>.

8. Ninawe PR, Hatzivramidis D, Parulekar SJ (2010) Delivery of drug macromolecules from thermally responsive gel implants to the posterior eye. *Chem Eng Sci* 65(18):5170–5177 <https://doi.org/10.1016/j.ces.2010.06.014>.
9. Lee SS, Hughes P, Ross AD, Robinson MR (2010) Biodegradable Implants for Sustained Drug Release in the Eye. *Pharm Res* 27(10):2043–2053 <https://doi.org/10.1007/s11095-010-0159-x>.
10. Kavousanakis ME, Kalogeropoulos NG, Hatzivramidis DT. (2014) Computational modeling of drug delivery to the posterior eye. *Chem Eng Sci* 108:203–212 <https://doi.org/10.1016/j.ces.2014.01.005>.
11. Missel PJ. (2012) Simulating Intravitreal Injections in Anatomically Accurate Models for Rabbit, Monkey, and Human Eyes. *Pharm Res* 29(12):3251–3272 <https://doi.org/10.1007/s11095-012-0721-9>.
12. Jensen MØ, Dror RO, Xu H, et al (2008) Dynamic control of slow water transport by aquaporin 0: Implications for hydration and junction stability in the eye lens. *Proc Natl Acad Sci USA* 105(38):14430–14435 <https://doi.org/10.1073/pnas.0802401105>.
13. Xu J, Heys JJ, Barocas VH, Randolph TW (2000) Permeability and Diffusion in Vitreous Humor: Implications for Drug Delivery. *Pharm Res* 17(6):664–669 <https://doi.org/10.1007/s11095-012-0721-9>.
14. Kim JE, Mantravadi AV, Hur EY, Covert DJ (2008) Short-term Intraocular Pressure Changes Immediately After Intravitreal Injections of Anti-Vascular Endothelial Growth Factor Agents. *Am J Ophthalmol* 146(6):930–934 <https://doi.org/10.1016/j.ajo.2008.07.007>.
15. Palleros DR, Shi L, Reid KL, Fink L (1994) hsp70-Protein Complexes. *J Biol Chem* 269(18):13107–13114.
16. Ambati J, Canakis CS, Miller JW, et al (2000) Diffusion of High Molecular Weight Compounds through Sclera. *Invest Ophthalmol Vis Sci* 41(5):1181–1185.
17. Balachandran RK, Barocas VH (2008) Computer Modeling of Drug Delivery to the Posterior Eye: Effect of Active Transport and Loss to Choroidal Blood Flow. *Pharm Res* 25(11):2685–2696 <https://doi.org/10.1007/s11095-008-9691-3>.



# Numerical Simulation of Selective Withdrawal Pertinent to Efficient Cell Encapsulation

N. G. Dimitrioglou and D. T. Hatzivramidis

## Abstract

Cell encapsulation represents a growing technology of dealing with immunogenicity of cells transplanted for disease treatment and regenerative medicine. The development and standardization of an efficient encapsulation method will render cell transplantation the therapeutic modality of choice, significantly contributing to treatment of severe chronic diseases, e.g., diabetes mellitus type 1, and repair of damaged tissue. Complete, uniform-thickness coating of differently-sized cells or cell clusters, e.g., pancreatic cell islets, is necessary for preservation of graft integrity and function. We propose a method of cell en-capsulation based on selective withdrawal from the lower of two immiscible-fluid layers. Optimal encapsulation occurs, when the perturbed fluid-fluid interface is kept stable and transition to viscous entrainment is prevented. The physical model consists of a finite-size tank containing the two immiscible-fluid layers and two equal-dimension cylindrical tubes located on either side of and at equal distance from the fluid-fluid interface. Numerical simulations are carried out using the commercial software COMSOL Multiphysics™. An Arbitrary Lagrangian–Eulerian (ALE) method is utilized to track the motion and deformation of the fluid-fluid interface, and critical conditions for selective withdrawal are established. The results of the simulations indicate that the mean curvature at the hump tip of the interface depends on the withdrawal flow rate and the distance of the tube inflow tip from the unperturbed interface. The simulations reveal that the phenomenon of selective withdrawal occurs into two stages, (a) the movement of the interface hump and (b) the steepening of the hump tip.

## Keywords

Cell encapsulation • Fluid-fluid interface • Selective withdrawal • Micro-encapsulation

## 1 Introduction

Micro-encapsulation is a versatile technology and has already been applied to numerous food and biotechnology processes. Possible micro-encapsulation techniques include droplet generation, emulsion formation, polyelectrolyte multilayering, and direct polymerization from a surface-adsorbed initiator [1]. When applied to cell micro-encapsulation, many of these methods become limited by specifications and constraints on chemical composition, uniformity and thickness of the membrane, polymerization schemes, and maximum allowable shear stress [2]. The methods for fabrication of encapsulated cells are widely varied, and some of them are electrified coaxial liquid jets [3], electrospinning [4], inkjet printing [5], hydrodynamic focusing [6] and vibrating technology [7]. Despite the good outcomes, some of them do not take into consideration the stochastic cell or tissue loading, and others fail to encapsulate in a reasonable time the amount of live biomaterial which is necessitated by the requirements of each treatment. Hence, the primary issue in micro-encapsulation is the design and development of a high-rate, high-efficiency encapsulation apparatus.

Hatzivramidis [8] designed a high-rate, high efficiency pancreatic islet encapsulation device combining hydrodynamic focusing and selective withdrawal. A two-nozzle feeder of islets together with an aqueous polymer solution ensures separate encapsulation of individual islets. The separated islets enter a chamber containing a two layer water–oil system in which are encapsulated by selective withdrawal. The entrained spout of the above fluid breaks both above and below the particle because of stretching, when the radius particle is significantly large, otherwise

N. G. Dimitrioglou (✉) · D. T. Hatzivramidis  
School of Chemical Engineering, National Technical University  
of Athens, Zografou, Athens, Greece  
e-mail: nikosdimitri@mail.ntua.gr

D. T. Hatzivramidis  
e-mail: dhatz@chemeng.ntua.gr



because of Rayleigh capillary instability. The polymer in the aqueous coat is subsequently cross-linked by being exposed to laser light to produce semipermeable capsules. Care is taken to keep the fluid-fluid interface stable by returning to the encapsulation chamber equal amounts of removed fluids.

The main advantage of this approach is that enables uniform coats of controllable thickness onto particles with diverse size and shape, like pancreatic  $\beta$ -cell islets. Firstly, Cohen et al. proposed this technique to encapsulate micro-particles [1]. Selective withdrawal is the draining of one immiscible fluids from two stratified layers through a tube placed close to their interface [9]. When fluid is withdrawn through the tube at low flow rates, only the upper fluid is withdrawn. As the flow rate is increased, the flow undergoes a transition where the lower fluid becomes entrained in a spout along with the upper fluid [10]. Lister [11] considered the case of selective withdrawal from the upper layer of two stratified layers of immiscible fluids with the same viscosity with the simplest geometry possible. Case and Nagel [12] explored the nature of selective withdrawal, proceeding via a discontinuous jump and resembling first-order hysteretic transitions.

Hatzivramidis and Pozrikidis [13] investigated the selective withdrawal process modeled as a physical system consisting of a point source and a point sink of equal strength located on either side of a fluid interface. The boundary element simulations reveal that the interface deforms in accordance with the withdrawal flow rate. In case of sufficiently small flow rate the interface reaches a steady shape, while in case of large flow rate, the interface continues to evolve into a nearly cusped conical shape whose tip eventually arrives at the point sink. In all cases the distance of the source and the sink from the undisturbed interface was fixed.

The aim of this study is the simulation of the selective withdrawal pertinent to efficient cell encapsulation taking into account the polydispersity in size and the different shape of the cells or islets. The system feeds the cells the same way as in the apparatus previously described [8], ensuring separation and dealing with stochastic loading. The cells enter the encapsulation chamber and move towards the cusp tip (Fig. 1) causing extra disturbance due to it. At that point the disturbed cusp collapses creating drops that encapsulate the cell or the cell aggregate.

For a floating particle, the force due to weight and buoyancy is counterbalanced by the vertically resolved surface tension force, acting per unit length of the three-phase contact line [14]. The horizontal force is equal to zero, as there is symmetry. In the event of a moving particle, an extra force is applied and can be calculated if the terminal velocity of the particle is known. The contact angle is exclusively determined from the size of the cell and the

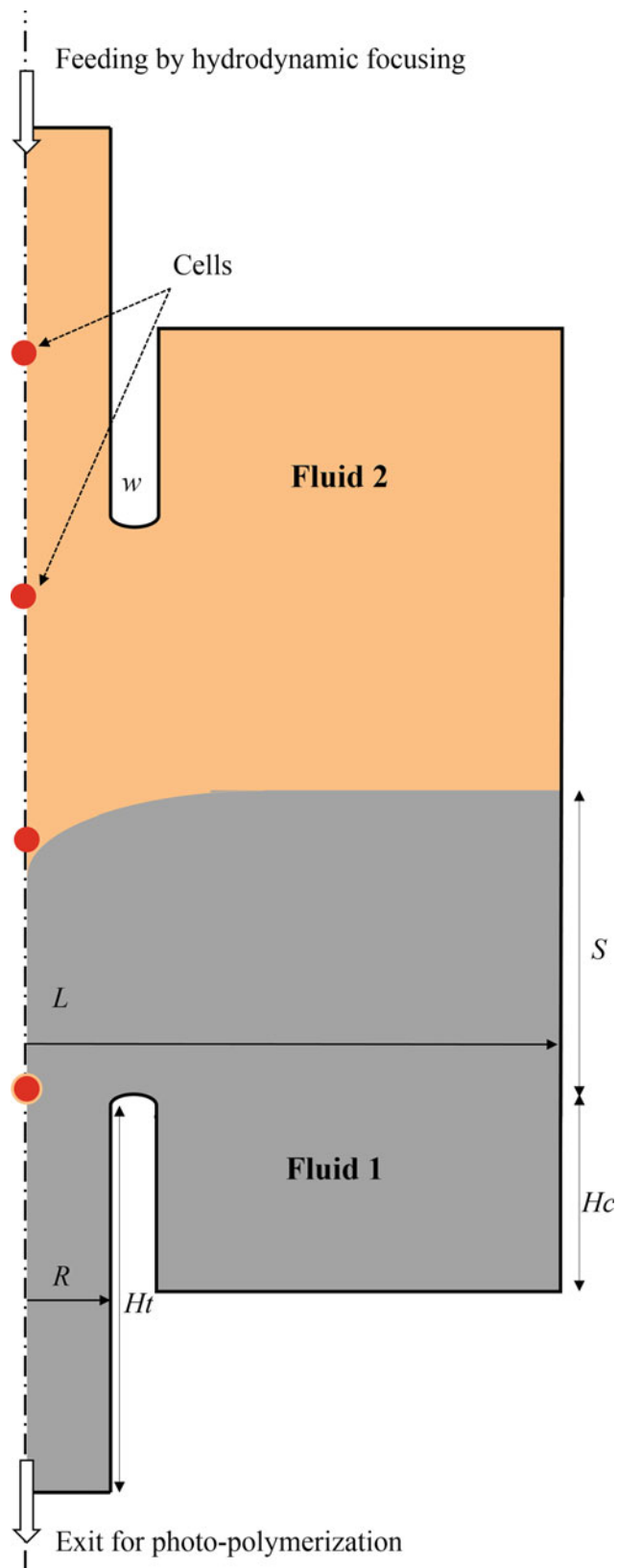


**Fig. 1** Meridian plane of the axisymmetric geometry used to model selective withdrawal in a cell encapsulation chamber

interface shape. In this paper, we simulate the case of an axisymmetric flow generated by two cylindrical tubes located on either side of the horizontal interface between two immiscible viscous liquids in a circular tank to determine the critical conditions for stable and unstable disturbance of the interface. The dependence of the curvature and the hump height on the geometry and the flow rate is investigated.

## 2 Method

### 2.1 Physical Model

We consider the case of a finite-size circular tank containing two immiscible-fluid layers and two equal-dimension cylindrical tubes located on either side of and at equal distance from the fluid-fluid interface. The lower and heavier fluid, fluid 1, drains out through the lower tube, and the upper and lighter fluid, fluid 2, charges in through the upper tube. Figure 1 shows half of the physical domain for the axisymmetric flow of interest and the geometry parameters are presented in Table 1.

### 2.2 Mathematical Model

The flow, being laminar, is governed by the Navier-Stokes equations and the equation of mass conservation for incompressible fluids. On the liquid-liquid interface, the kinematic and the stress boundary conditions are

$$\left. \begin{aligned} \mathbf{u}_1 &= \mathbf{u}_2 \\ \mathbf{n}_1 \cdot \mathbf{T}_1 - \mathbf{n}_2 \cdot \mathbf{T}_2 &= \gamma(\nabla_t \cdot \mathbf{n}_1)\mathbf{n}_1 - \nabla_t \gamma \end{aligned} \right\} \quad (1)$$

where  $\mathbf{n}$  is the outward unit normal vector and  $\gamma$  the surface tension.

The no-slip boundary condition applies on the side walls. At the upper surface boundary, the pressure is zero ( $p_0 = 0$  Pa)

and at the bottom, the pressure is  $p = p_0 + (\rho_1 g + \rho_2 g) \cdot (S + H_c)$ . This specification is necessary to keep the unperturbed interface at a fixed height,  $S$ .

Following Zhou and Feng [15], we introduce a capillary number, and following Hatzivramidis and Pozrikidis [13] we introduce the Bond number, respectively, as:

$$Ca \equiv \frac{\mu_1 g}{\gamma R^2}, \quad Bo \equiv \frac{\Delta \rho g R^2}{\gamma} \quad (2)$$

where  $\mu_1$  is the viscosity of the lower fluid,  $g$  the gravity acceleration and  $\Delta \rho$  the density difference of the two liquids,  $\rho_2 - \rho_1$ .

The axisymmetric interface can be approximated by an equation of the form  $z = f(r)$  and the mean curvature at any of its points can be calculated from the equation

$$2\xi = \frac{f''(r)}{[1 + (f'(r))^2]} + \frac{f'(r)}{r \cdot [1 + (f'(r))^2]^{1/2}} \quad (3)$$

where  $f'(r) = df/dr$  and  $f''(r) = d^2f/dr^2$ .

### 2.3 Computational Model

Numerical simulations are carried out using the commercial software COMSOL Multiphysics™. The governing equations are solved numerically using the Galerkin-Finite Element method to resolve the flow and an Arbitrary Lagrangian–Eulerian (ALE) method to track the movement and deformation of the liquid-liquid interface is employed. Mesh-size independence of the numerical solution is checked using the traditional way of decreasing the mesh size until the solutions with two consecutive mesh sizes show no considerably difference. The smallest grid size is typically around  $10^{-3}R$ , while the mesh is refined near the interface. For convergence reasons, the number of elements of the unstructured triangular mesh depends on the container size.

**Table 1** List of geometry parameters

Symbol	Explanation	Value
$R$	Inner tube radius	0.08 cm
$L$	Chamber radius	3.2 cm
$w$	Tube wall thickness	0.04 cm
$H_t$	Tube height	2.0 cm
$H_c$	Distance of each tube inlet from the chamber bottom	0.4 cm
$S$	Distance of each tube from the unperturbed interface	$0.55 \text{ cm} \leq S \leq 0.8 \text{ cm}$

### 3 Results

The validation of the numerical model is firstly presented. The computational model was validated with experimental data from Cohen and Nagel's study [10]. Simulations are made with the same geometry and parameters and for  $S = 0.508$  cm. To calculate the mean curvature, the locations of the mesh nodes on the interface are fitted to a parabola around the tip. The validation results indicate that the thickness of the tube wall influences the mean curvature,  $\kappa$ . Figure 2 shows that, for  $w/R = 7.5$ , the simulations of this study agree well with the experimental results for different values of  $S$ , while for  $w/R = 1$ , agreement is only observed at the lowest values of  $q$ . It must be noted that no explicit description of the tube geometry is given in Cohen and Nagel's research [10]. For the present study,  $w/R = 0.5$  is used in all cases.

In the simulations of this study, the Bond number is kept constant and equal to 0.044, thus, the effect of surface tension is dominant compared to gravity forces. The density ratio  $a = \rho_1/\rho_2$  is equal to 1.2, while the viscosity ratio  $\lambda = \mu_2/\mu_1$  is kept equal to 10. Moreover, the capillary number,  $Ca$ , takes values between 3.65 and 34.71, signifying the importance of viscous forces. The values of physical parameters that are used in the current simulations are shown in Table 2.

The interface at steady state is shown in Fig. 3. Simulations are made for: (a)  $S$  held constant and equal to 0.8 cm while  $q$  -increases consecutively from 0.2 to 0.952 ml/s ( $7.29 \leq Ca \leq 34.71$ ), and (b)  $q$  held constant and equal to

0.4 ml/s while  $S$  decreases consecutively from 0.8 to 0.55 cm ( $Ca = 14.58$ ). For all values of  $q$  and for all values of  $S$  the interface is unperturbed for  $R \gtrsim 2$  cm. In Fig. 3a, as  $S$  decreases from 0.8 to 0.55 cm, the tip of the free surface moves closer to the inlet of the withdrawal tube and the tip of the free surface transitions to a cusp, very close to the tube inlet at  $S = 0.55$  cm. Specifically, the  $h_{max}$  increases from 0.099 to 0.259 cm as  $S$  decreases, while the curvature increases from 0.653 to  $14.39 \text{ cm}^{-1}$ . In Fig. 3b, as  $q$  increases from 0.2 to 0.952 ml/s, the tip of the hump moves closer to the inlet of the withdrawal tube and the tip of the interface transitions to a cusp, very close to the tube inlet. In particular, the  $h_{max}$  ranges from 0.022 to 0.464 cm for varying flow rates, while the curvature increases from 0.118 to  $43.668 \text{ cm}^{-1}$ . Similar results were obtained by Hatzivramidis and Pozrikidis for fixed  $S$  [13].

Figure 4 shows four snapshots of the hump interface for different periods. In all cases  $Ca = 25.52$  and the initial distance of the withdrawal tube inlet from the unperturbed interface,  $S$ , is equal to 0.7 cm. Numerical simulations are carried out for times up to  $t = 2$  s. For times  $0 \text{ s} \leq t < 0.5$  s, the whole hump profile moves downward rapidly, while for time  $t > 0.5$  s only the hump tip moves downward. As the hump tip approaches the withdrawal tube inlet, it becomes sharper and the curvature increases rapidly. Note that there is no noticeable change for  $t \geq 1$  s, and the hump stays stable. Figure 5 illustrates the evolution of the height,  $h$ , for hump tip ( $0, h(0)$ ) and two reference points ( $0.3, h$

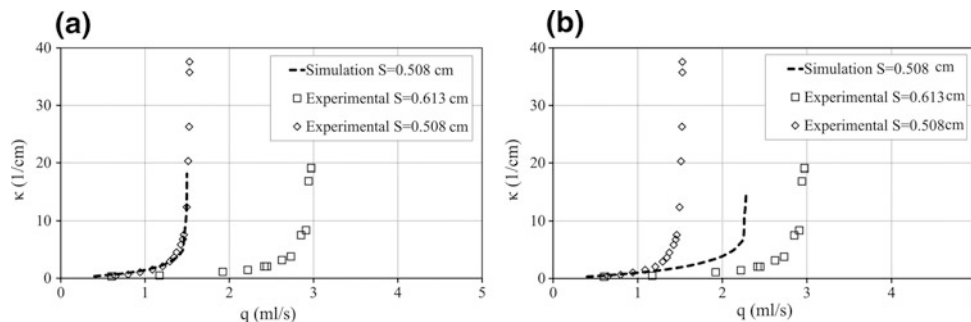


**Fig. 2** Mean curvature at the hump tip,  $\kappa$ , as a function of withdrawal flow rate,  $q$ . **a**  $w/R = 7.5$ , **b**  $w/R = 1$

**Table 2** List of physical parameters

Symbol	Value and unit
$\gamma$	0.03 N/m
$\rho_1$	$1260 \text{ kg/m}^3$
$\mu_1$	0.7 Pa s
$\rho_2$	$1050 \text{ kg/m}^3$
$\mu_2$	0.07 Pa s

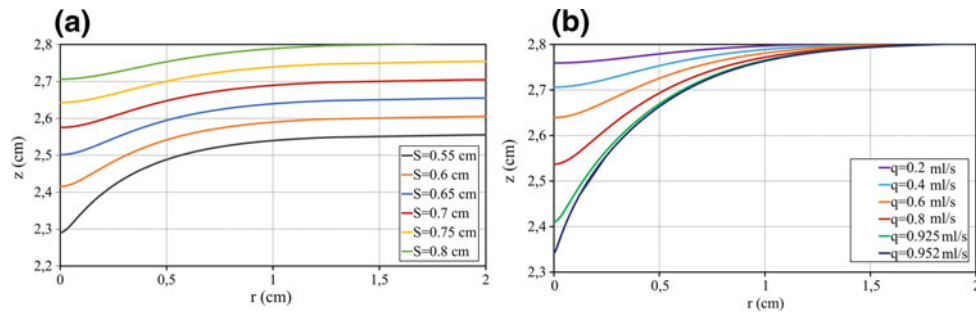


**Fig. 3** Shape of the interface. The outlet of the withdrawal tube is located at  $z = 0$ . In all cases  $w/R = 0.5$ . **a** Varying  $S$ ,  $q = 0.4$  ml/s in all cases, **b** Varying  $q$ ,  $S = 0.8$  cm in all cases

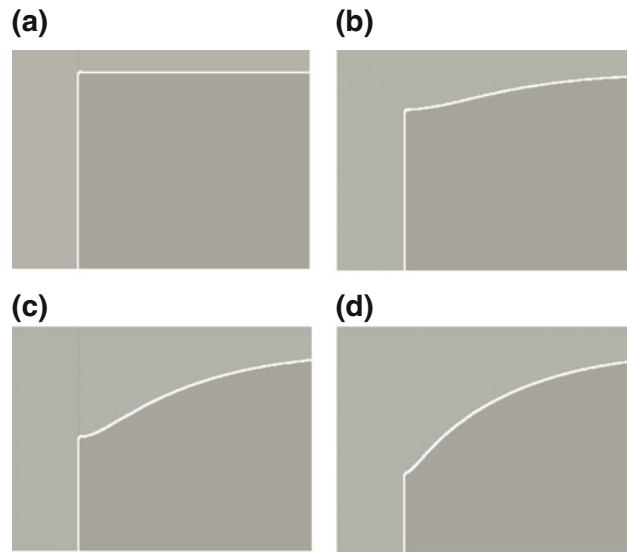


**Fig. 4** Interface snapshots at different times **a**  $t = 0$  s, **b**  $t = 0.2$  s, **c**  $t = 0.5$  s, **d**  $t = 2$  s

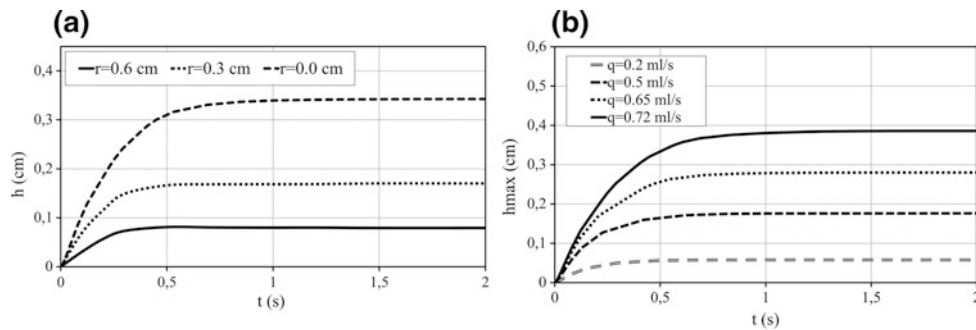


**Fig. 5** In all cases  $S = 0.7$  cm. **a** Height,  $h$ , for hump tip ( $0, h(0)$ ) and two reference points ( $0.3, h(0.3)$ ) and ( $0.6, h(0.6)$ ) as a function of time,  $t$  and  $Ca = 25.52$ , **b** Height,  $h_{max}$ , of the tip as a function of time for varying  $q$

(0.3)) and (0.6,  $h(0.6)$ ) as a function of time,  $t$ . One can observe that the hump tip is moving faster and longer than the two reference points. Furthermore, the viscosity ratio,  $\lambda$ , which is used in the present simulations does not cause hysteresis which has been observed in Cohen and Nagel's study [10].

## 4 Conclusions

The standardization of an efficient encapsulation method will render cell transplantation the therapeutic modality of choice, significantly contributing to treatment of chronic diseases. To this end, an encapsulation method is proposed utilizing hydrodynamic focusing and selective withdrawal. Optimal encapsulation occurs, when the perturbed fluid-fluid interface is kept stable and transition to viscous entrainment is prevented. In this study, we simulate the problem of a finite-size tank with two immiscible-fluid layers and two cylindrical tubes located on either side of and at equal distance from the interface. Numerical simulations are carried out using COMSOL Multiphysics™ and an ALE method is utilized to track the fluid-fluid interface.

The simulations reveal that the mean curvature at the hump tip of the interface depends on the withdrawal flow rate and the distance of the tube inflow tip from the unperturbed interface. As  $S$  decreases, the tip of the interface moves closer to the inlet of the withdrawal tube and the tip of the interface transitions to a cusp, very close to the tube inlet at  $S = 0.55$  cm. As  $q$  increases, the tip of the hump moves closer to the inlet of the withdrawal tube and the tip of the interface transitions to a cusp, very close to the tube inlet. Lastly, the phenomenon of selective withdrawal is accomplished into two stages, (a) the movement of the interface hump and (b) the steepening of the hump tip. In particular, for 25% of the simulation time ( $0 \text{ s} \leq t \leq 0.5 \text{ s}$ ), the whole hump profile moves rapidly, while for the rest ( $t > 0.5 \text{ s}$ ) of the simulation the hump tip moves down and the curvature increases.

**Acknowledgements** The author Nikos Dimitrioglou would like to thank the State Scholarship Foundation of Greece (IKY) for the funding of his research, through the implementation of the Project "Human Resources Development through doctoral research" in the framework of the Operational Program "Human Resources Development, Education and Life Long Learning" (2014–2020), co-funded by the European Social Fund and the Greek State.

**Conflict of Interest** The authors declare that they have no conflict of interest.

## References

1. Cohen I, Li H, Hougland JL, Mrksich M, Nagel SR (2001) Using selective withdrawal to coat microparticles. *Science* 292 (5515):265–267 <https://doi.org/10.1126/science.1059175>.
2. Hatzivramidis DT, Karatzas TM, Chrousos GP (2013) Pancreatic islet cell transplantation: An update. *Ann Biomed Eng* 41(3):469–476 <https://doi.org/10.1007/s10439-012-0676-3>.
3. Loscertales IG, Barrero A, Guerrero I, et al (2002) Micro/nano Encapsulation via Electrified Coaxial Liquid Jets. *Science* 295 (5560):1695–1698 <https://doi.org/10.1126/science.1067595>.
4. Townsend-Nicholson A, Jayasinghe SN (2006) Cell Electrospinning: A Unique Biotechnique for Encapsulating Living Organisms for Generating Active Biological Microthreads/Scaffolds. *Biomacromolecules* 7(12):3364–3369 <https://doi.org/10.1021/bm060649h>.
5. Xu T, Kincaid H, Atala A, Yoo JJ (2008) High-Throughput Production of Single-Cell Microparticles Using an Inkjet Printing Technology. *J Manuf Sci Eng* 130(2):021017 <https://doi.org/10.1115/1.2903064>.
6. Edd JF, Di Carlo D, Humphry KJ et al (2008) Controlled encapsulation of single-cells into monodisperse picolitre drops. *Lab Chip* 8(8):1262–1264 <https://doi.org/10.1039/b805456h>.
7. Whelehan M, Marison IW (2011) Microencapsulation using vibrating technology. *J Microencapsul* 28(8):669–688 <https://doi.org/10.3109/02652048.2011.586068>.
8. Hatzivramidis DT Apparatus and Method for Encapsulating Pancreatic Cells 2012:5.
9. Psihogios J, Benekis V, Hatzivramidis D (2015) Selective withdrawal and draining of a viscous liquid under air from a cylindrical tank through a tube imbedded in the liquid. *Chem Eng Sci* 138:516–523 <https://doi.org/10.1016/j.ces.2015.08.038>.
10. Cohen I, Nagel SR (2002) Scaling at the Selective Withdrawal Transition through a Tube Suspended above the Fluid Surface. *Phys Rev Lett* 88(7):074501 <https://doi.org/10.1103/physrevlett.88.074501>.
11. Lister JR (1989) Selective withdrawal from a viscous two-layer system. *J Fluid Mech* 198:231–254 <https://doi.org/10.1017/s002211208900011x>.
12. Case SC, Nagel SR (2007) Spout States in the Selective Withdrawal of Immiscible Fluids through a Nozzle Suspended above a Two-Fluid Interface. *Phys Rev Lett* 98(11):114501 <https://doi.org/10.1103/physrevlett.98.114501>.
13. Hatzivramidis D, Pozrikidis C (2008) Hydrodynamic analysis of pancreatic islet micro-encapsulation by selective withdrawal. *Eng Anal Bound Elem* 32(1):11–20 <https://doi.org/10.1016/j.enganabound.2007.07.001>.
14. Kralchevsky P, Nagayama K (2001) *Particles at Fluid Interfaces and Membranes*. New York, NY, USA, Elsevier Science.
15. Zhou D, Feng JJ (2010) Journal of Non-Newtonian Fluid Mechanics Selective withdrawal of polymer solutions: Computations. *J Nonnewton Fluid Mech* 165(15–16):839–851 <https://doi.org/10.1016/j.jnnfm.2010.04.004>.



# Simulation of Respiratory Impedance Variations During Normal Breathing Using a Morphometric Model of the Lung

Adam G. Polak<sup>1</sup> and Zoltán Hantos<sup>2</sup>

## Abstract

The forced oscillations technique (FOT) enables a non-invasive monitoring of respiratory mechanics, returning the impedance of the respiratory system ( $Z_{rs}$ ) at chosen frequencies. Recently it has been shown that the intrabreath variations of  $Z_{rs}$  are correlated with respiratory diseases, mainly due to the sensitivity of  $Z_{rs}$  to morphological changes in the respiratory system. The aim of this study was to develop a morphology-based computational model able to simulate the variations of airway dimensions during normal breathing and the resulting temporal changes in  $Z_{rs}$ . The model counts the symmetric structure of the bronchial tree, lung and thorax wall viscoelasticity, and properties of the upper airways. It takes into account the distributed character of pressure loss along the airways and flow-limiting mechanisms. Quasi-dynamic simulations are performed, and for each time instant the distributed properties of airways are recalculated to a lumped parameter net corresponding to the momentary  $Z_{rs}$ . The implemented model enabled simulations of primary signals characterising quiet breathing and the intrabreath variations in  $Z_{rs}$  for both the normal case and small airways constriction. The simulation results recovered the flow- and volume-dependent variations of  $Z_{rs}$  observed in healthy subjects and their alterations associated with uniform bronchial obstruction. However, testing specific hypotheses about the manifestation of inhomogeneous lung diseases in the intrabreath FOT data involves future incorporation of structural heterogeneity into the model.

## Keywords

Respiratory impedance • Forced oscillations technique  
Morphometric model

A. G. Polak (✉)  
Wrocław University of Science and Technology, Wrocław, Poland  
e-mail: adam.polak@pwr.edu.pl

Z. Hantos  
University of Szeged, Szeged, Hungary

## 1 Introduction

The forced oscillation technique (FOT) has established a significant amount of data characterising the mechanical behaviour of the respiratory system and it is becoming one of the main functional assessment techniques in the respiratory clinical field [1]. The FOT has provided fundamental information for sophisticated modelling studies focusing mainly on the impedance of the respiratory system ( $Z_{rs}$ ) as a function of the frequency of the imposed oscillations, with special regard to the structural heterogeneity of the lungs [2]. The frequency domain approach to linear systems has become dominant and the early seminal work on the non-linear phenomena in respiratory mechanics, which are significant even during normal breathing [3, 4] was neglected. Recent studies addressing the temporal changes in  $Z_{rs}$  within the breathing cycle [5–7] have revealed marked nonlinearities combined with spatial inhomogeneity in pulmonary diseases, and this underlines the importance of simulation tools in the interpretation of the intrabreath dynamics of  $Z_{rs}$  data.

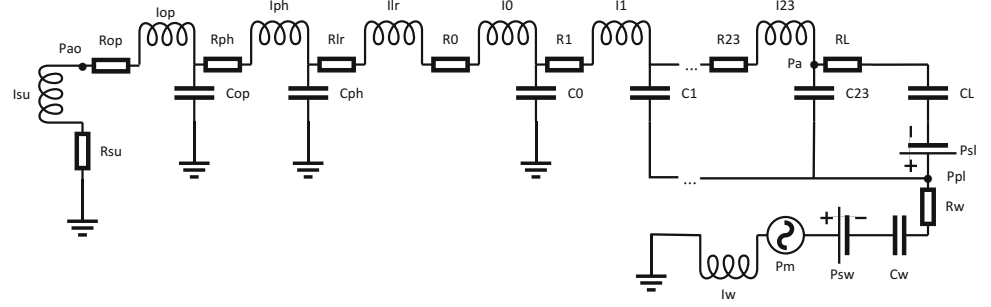
The aim of this study was to develop a morphology-based computational model able to simulate the variations of airway dimensions during normal breathing and the resulting temporal changes in  $Z_{rs}$ .

## 2 Computational Model

### 2.1 Model Structure

The electrical equivalent of the computational model consists of a few segments (Fig. 1): the measurement setup (resistance  $R_{su}$  and inertance  $I_{su}$  in series); upper airways divided into the oral pathway ( $R_{op}$ - $I_{op}$ - $C_{op}$ ), pharynx

**Fig. 1** Electrical scheme of the model structure



( $R_{ph}$ - $I_{ph}$ - $C_{ph}$ ) and larynx ( $R_{lr}$ - $I_{lr}$ ) parts; extrapulmonary trachea ( $R_0$ - $I_0$ - $C_0$ ); intrapulmonary airways ( $R_g$ - $I_g$ - $C_g$ ) controlled by pleural pressure  $P_{pl}$  (generations 1–23); lung tissue ( $R_L$ - $C_L$ ), and thorax wall segment ( $R_w$ - $C_w$ - $I_w$ ). A symmetrical structure of the bronchial tree is assumed [8], thus the lumped parameters represent the properties of generation airways connected in parallel. Additional polarizing sources  $P_{sl}$  and  $P_{sw}$  are added to obtain physiological values of pressures produced by nonlinear lung and thorax wall recoils at functional residual capacity (FRC). Respiration is generated by a time-varying muscle pressure source  $P_m$ .

## 2.2 Computational Scheme for Normal Breathing Simulation

The general scheme of breathing simulation is based on the previous model for forced expiration [9], completed by its counterpart for inspiration. Specifically, the pressure drop along an airway (and thus along an airway generation in the symmetric bronchial tree) is computed for a given flow by solving the nonlinear differential equation, taking into account airway dimensions and mechanical properties (the tube law), viscous pressure loss, Reynolds number, and wave speed [10]. Upper airways are included as three segments: nonlinear viscoelastic oral pathway and pharynx, and a stiff larynx, with mechanical properties deduced from [11–13].

Normal breathing driven by muscle pressure  $P_m$  is simulated at intervals of 10 ms with tidal volume  $V_t \approx 0.5$  L. Instantaneous pressure drops are calculated for a steady flow; however, dynamic effects are evaluated by difference equations using data from two successive time instants, thus the model is quasi-dynamic.

Actual airway dimensions result directly from their morphological and mechanical features, and they change in time with flow and pleural pressure  $P_{pl}$  controlled by the elastic recoil of lung tissue and thorax wall. The lung pressure-volume characteristics is nonlinear [14], and other parameter values are set according to [15].

## 2.3 Calculation of Instantaneous Respiratory Impedance $Z_{rs}$

The numerical procedure (Runge-Kutta 4–5 order method) for solving the differential equation describing the tube law [9] returns not only the drop of lateral pressure, but also transmural pressures at a few points along the airway. This information is further used to calculate airway areas  $A$  (decreasing in flow direction) and elementary compliances ( $dA/dP_m$ ) at these points, and finally to assess the resistance  $R_a$ , inertance  $I_a$  and compliance  $C_a$  of that airway, and of the whole airway generation  $g$ :

$$R_a = \sum_i \frac{a8\pi\mu\Delta l_i}{A_i^2}, \quad R_g = R_a/2^g, \quad (1)$$

$$I_a = \sum_i \frac{\rho\Delta l_i}{A_i}, \quad I_g = I_a/2^g, \quad (2)$$

$$C_a = \sum_i \left( \frac{dA}{dP_m} \right)_i \Delta l_i, \quad C_g = 2^g C_a, \quad (3)$$

where:  $a$ —empirical constant,  $\mu$ —air viscosity,  $\rho$ —air density,  $\Delta l$ —distance increment returned by the procedure. Values of these parameters are flow-independent as is assumed for ‘ideal’ FOT with insignificantly small amplitudes of pressure/flow oscillations and negligible nonlinear effects. As an example, the impedance of one airway generation at frequency  $f$  is calculated as follows:

$$Z_g = R_g + j\omega I_g - j/(\omega C_g), \quad j = \sqrt{-1}, \quad \omega = 2\pi f. \quad (4)$$

In contrast, flow-dependent resistances  $R_f$  are calculated taking into account energy dissipation resulting in total pressure head decrease and the Bernoulli effect:

$$R_f = \frac{\Delta P_{lt}}{Q} + \frac{\rho Q}{2} \left( \frac{1}{A_0^2} - \frac{1}{A_L^2} \right), \quad (5)$$

where  $A_0$  and  $A_L$  are the cross-sectional areas at the airway’s beginning and end [15].

The detailed structure of the model (Fig. 1) and calculated temporary parameter values enable finally the calculation of input respiratory impedance  $Z_{rs}(t)$  at a single tracking frequency of 10 Hz at every time instant.

### 3 Results of Simulations

Simulations of three respiratory cycles were performed for the normal state of the respiratory system and for small airways (generations from 8 to 19) obstruction case, mimicking airway wall smooth muscle constriction effects [16] (see Fig. 2).

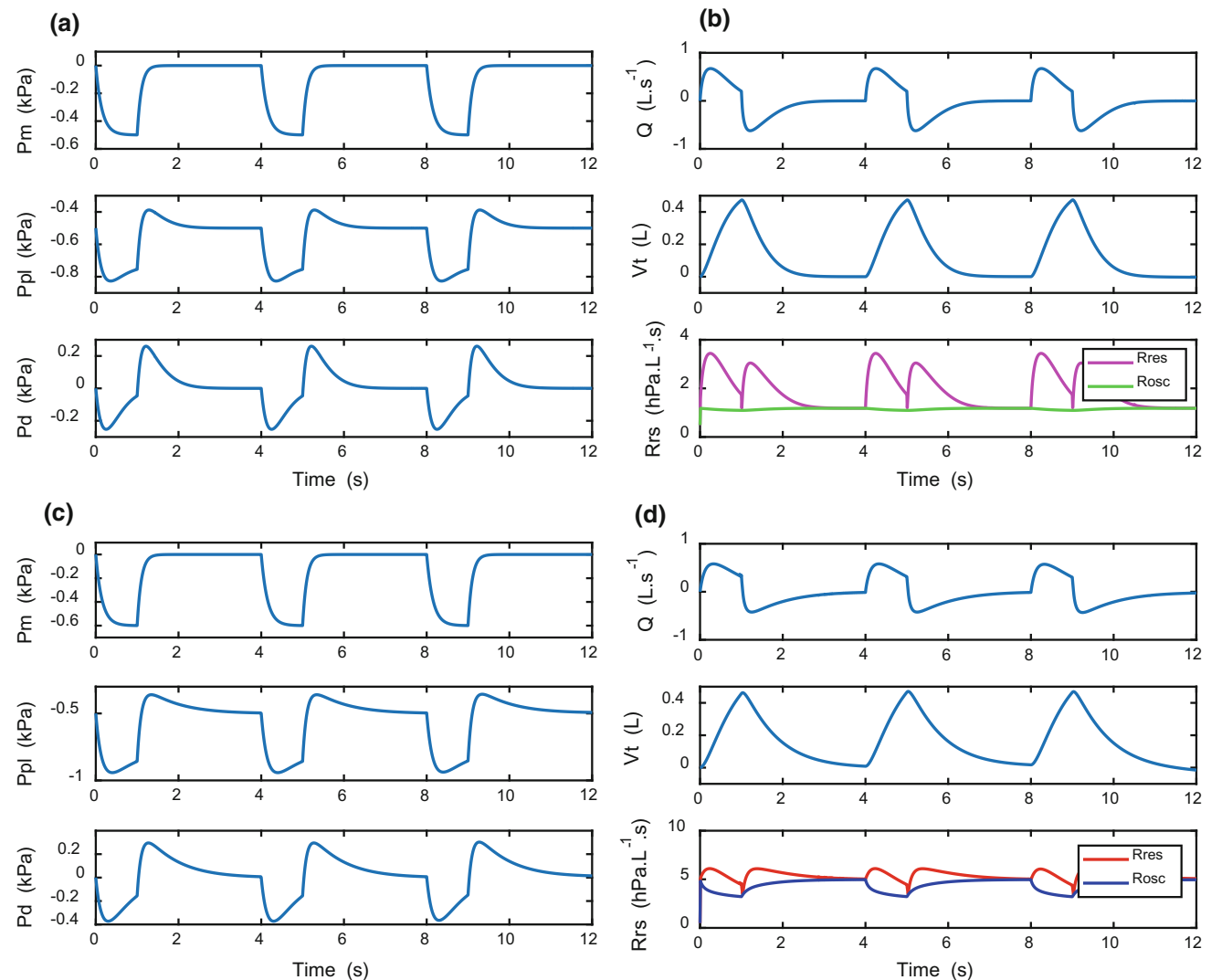


**Fig. 2** Signals simulated for the normal respiratory system state (a) and (b), and small airways constriction (c) and (d): muscle  $P_m$ , pleural  $P_{pl}$  and driving (alveolar)  $P_d$  pressures, flow  $Q$ , lung tidal volume  $V_t$  and respiratory resistances ( $R_{res}$ —resistance to airflow including flow-dependent components,  $R_{osc}$ —flow-independent resistance)

Because the first two cycles are auxiliary and just the third one is proper, impedance trajectories for this 3rd cycle are presented in Fig. 3.

### 4 Discussion and Conclusion

The aim of this study was to investigate temporal changes in  $Z_{rs}$  caused by variations of airway dimensions during normal breathing. All signals representing normal breathing in the time domain (pressures, flow, volume, respiratory resistance) were generated in physiological ranges and resemble the signals recorded in actual measurements. The marked

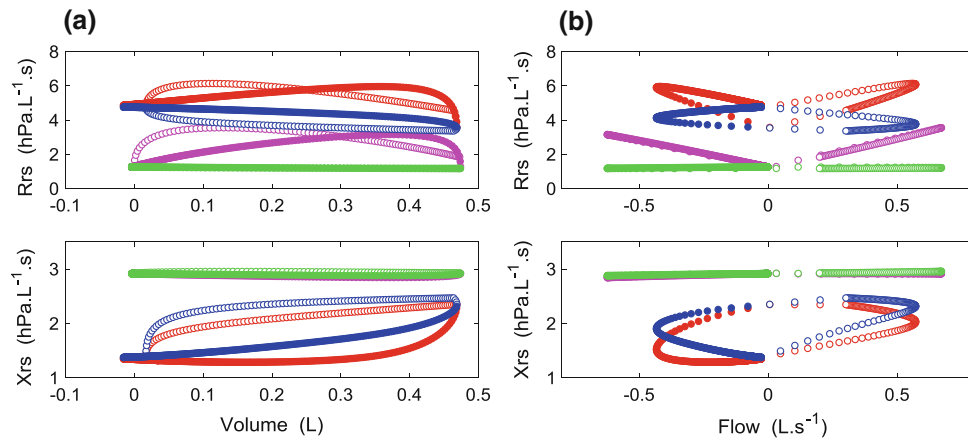


**Fig. 3** **a** Dependences of the oscillatory input resistance  $R_{rs}$  and reactance  $X_{rs}$  on lung volume, **b** Dependences of  $R_{rs}$  and  $X_{rs}$  on flow (magenta—flow-dependent for normal lungs, green—flow-independent for normal lungs, red—flow-dependent for constricted airways, blue—flow-independent for constricted airways, open circles—inspiration, closed circles—expiration) (Colour figure in online)

flow-dependent changes in  $R_{rs}$  are in accordance with intrabreath fluctuations observed in healthy subjects [3, 4, 7] not accompanied by significant changes in  $X_{rs}$  (Fig. 3b), whereas the changes in volume alone cause only minor alterations in both  $R_{rs}$  and  $X_{rs}$ . In contrast, constriction of small airways enhances the changes in  $R_{rs}$  with volume, while invoking significant looping in the  $X_{rs}$  versus volume plots (Fig. 3a). The latter changes mimic the looping patterns of expiratory flow limitation observed in COPD [7]. All these changes are qualitatively independent of the oscillation frequency within the medium-frequency (5–20 Hz) range (data not shown).

While some basic features of the intrabreath changes in  $Z_{rs}$  are reproduced by this model, there are obvious limitations in this preliminary simulation study. First, there is an assumption that the small-amplitude oscillatory flows do not interact with the respiratory signals. Second, departures from the ideal laminar flow conditions, such as the inertial distortion of the parabolic oscillatory flow profile, turbulences of airflow and other nonlinear phenomena that take place during rapid phasic changes in airflow are not accounted for. Finally, common respiratory diseases, such as asthma or COPD, are characterized by spatial inhomogeneity in lung structure and function, so testing specific hypotheses about the manifestation of heterogeneous lung diseases in the intrabreath FOT data requires the incorporation of structural heterogeneity into the model.

**Acknowledgements** This work was supported in part by the grant no. 2016/21/B/ST7/02233 from the National Science Centre, Poland, and grant no. 105403 from the Hungarian Scientific Research Fund.

## References

- Bates, J.H.T., Irvin, C.G., Farré, R., Hantos, Z.: Oscillation mechanics of the respiratory system. *Compr. Physiol.* 1(3), 1233–1272 (2011).
- Kaczka, D.W., Lutchen, K.R., Hantos Z.: Emergent behavior of regional heterogeneity in the lung and its effects on respiratory impedance. *J. Appl. Physiol.* 110(5), 1473–1481 (2011).
- Davidson, R.N., Greig, C.A., Hussain, A., et al.: Within-breath changes of airway calibre in patients with airflow obstruction by continuous measurement of respiratory impedance. *Br. J. Dis. Chest* 80, 335–352 (1986).
- Peslin, R., Ying, Y., Gallina, C., et al.: Within-breath variations of forced oscillation resistance in healthy subjects. *Eur. Respir. J.* 5 (1), 86–92 (1992).
- Dellacà, R.L., Santus, P., Aliverti, A., et al.: Detection of expiratory flow limitation in COPD using the forced oscillation technique. *Eur. Respir. J.* 23(2), 232–240 (2004).
- Czövek, D., Shackleton, C., Hantos, Z., Taylor, K., Kumar, A., Chacko, A., Ware, R.S., Mekan, G., Radics, B., Gingl, Z., Sly, P. D.: Tidal changes in respiratory resistance are sensitive indicators of airway obstruction in children. *Thorax* 71(10), 907–915 (2016).
- Lorx, A., Czövek, D., Gingl, Z., et al.: Airway dynamics in COPD patients by within-breath impedance tracking: effects of continuous positive airway pressure. *Eur. Respir. J.* 2017 Feb 15; 49(2). pii: 1601270. <https://doi.org/10.1183/13993003.01270-2016>. (2017).
- Weibel, E. R.: *Morphometry of the Human Lung*, Springer, Berlin (1963).
- Polak, A.G.: A forward model for maximum expiration. *Comp. Biol. Med.* 28(6), 613–625 (1998).
- Lambert, R.K., Wilson, T.A., Hyatt, R.E., Rodarte, J.R.: A computational model for expiratory flow. *J. Appl. Physiol.: Respirat. Environ. Exercise Physiol.* 52(1), 44–56 (1982).
- Eckel, H.E., Sittel, C., Zorowka, P., Jerke, A.: Dimensions of the laryngeal framework in adults. *Surg Radiol Anat.* 16(1), 31–36. (1994).

12. Mohsenin, V.: Gender differences in the expression of sleep-disordered breathing: role of upper airway dimensions. *Chest* 120(5), 1442–1447 (2001).
13. Persak, S.C., Sin, S., McDonough, J.M., Arens, R. Wootton, D.M.: Noninvasive estimation of pharyngeal airway resistance and compliance in children based on volume-gated dynamic MRI and computational fluid dynamics. *J. Appl. Physiol.* 111(6), 819–1827 (2011).
14. Polak, A.G., Lutchen, K.R.: Computational model for forced expiration from asymmetric normal lungs. *Ann. Biomed. Eng.* 31(8), 891–907 (2003).
15. Polak, A.G., Mroczka, J.: Nonlinear model for mechanical ventilation of human lungs. *Compt. Biol. Med.* 36(1), 41–58 (2006).
16. Morlion, B., Polak, A.G.: Simulation of lung function evolution after heart-lung transplantation using a numerical model. *IEEE Trans. Biomed. Eng.* 52(7), 1180–1187 (2005).



# Discrete Event Simulation Model for the Analysis of Centralized Front Office Service in a Regional Hub Hospital

D. Cocchi, F. Frosini, E. Ciagli, P. Tortoli, C. Carpinì, D. Cirone,  
and A. Belardinelli

## Abstract

Today, hospital rankings are based primarily on basic clinical indicators. The aim of the project shown in this article is to develop a methodology able to improve non-clinical front office operation for the patients (like booking exams, delivering medical reports etc.), keeping the costs under control. The service center serves 600 users every day and it is the core of a great reorganization process, focused on centralization of office activities of the Careggi University Hospital of Florence, to ensure the best services to patients. For this reason, Discrete Event Simulation model (DES) have been used. The project of the model was made according to the real process observed during the confrontation with staff, document verification, field observation stage and study of data stored in hospital's databases. These researches provided parameters necessary for model running, such as number of accesses, service time, available resources and patient's waiting time. Validation confirmed that model is formally correct, and shown that waiting time of patients is substantially equal between real data and simulated outputs. The mean waiting time of all patients calculated by the model (7 min and 9 s) is only 2.6% lesser than real one (7 min and 20 s). Weekly workload of the model (3048 patients) is equal to reality, proving that the schedules of patient's accesses are correct. We used a statistic test to confirm the results. This paper shows that DES is a valuable tool that can be used to save money and improve clinical processes. In the future this model will

be used to evaluate the reorganization of the Service Center with the aim to allow everyone (not only technical staff) to use it, through a web-based support, a predictive machine and a user interface.

## Keywords

Discrete event simulation • Healthcare • Optimization  
Front office service

## 1 Introduction

The organization of front office activity is a problem that every business that provide a public service must deal with great attention. It's necessary to balance the necessity to use resources strictly necessary, with the aim to provide adequate service to customers. These problems are much more important in a critic working environment like public healthcare, which the need of save money became increasingly high in the past years, but also the impressions of patients are very important. The use of simulation models to study and optimize clinic processes is a core part of Lean Thinking approach, which importance is growing during time [1, 2]. A service center, even inside a hospital, can be studied and analyzed like a classic service to the public [3, 4], where the customers go to desks because they need the provision of a service [5, 6]. Often, if the management want to start or change this kind of process [7, 8], they choose to implement immediately the changes and act eventually in a second time if there are some organizational problems (lack of resources, high waiting time, etc.) [9, 10]. Instead, is more efficient and economical to analyze in advance the results of a modification, to optimize the process before working [11]. In literature there are many examples of this kind that uses simulation models [12, 13]. The first step is a deep process analysis, to find information about accesses, available resources, waiting times and duration of services, as well as the internal organization of process itself. The analysis

D. Cocchi · F. Frosini · E. Ciagli (✉) · P. Tortoli  
Department of Information Engineering, University of Florence,  
Florence, Italy  
e-mail: elena.ciagli@unifi.it

C. Carpinì · D. Cirone  
Public Relations Office, Azienda Ospedaliero-Universitaria  
Careggi, Florence, Italy

A. Belardinelli  
Department of Innovation, Quality and Control, Azienda  
Ospedaliero-Universitaria Careggi, Florence, Italy

consists in interviews with workers, use of database and direct observations. The second step is building the simulation model, and finally validation. This is one of the highly complex steps, because the perfect match between real data and outputs of the model are almost impossible [14]. A scope in which is possible to use simulation with great results is public administration. Often, these services have organizational shortcomings that can be studied and corrected with a careful process analysis and a correct use of simulation models [15]. Fundamental data needed to implement a simulation are workload, time of arrival, service times and available resources [16]. The software used for this analysis is Arena, developed by Rockwell Automation, the globally most used product for discrete event simulation [17, 18]. The object of this study is the Service Center of Careggi University Hospital of Florence, which provides several administrative services to the users. The management plans to add more services so, to avoid an overload that lead to a worsening of the quality of the process, we realized a simulation model to evaluate the modifications, to change the process in case of need and maximize the utilization of resources [19]. This article explains the characteristics of the model and its validation.

## 2 Methods

The first step to develop a simulation model is to understand profoundly the process, through a long and deep analysis [20]. Through interviews with the staff and direct observations was possible to understand the needs of users according to the service. Especially, is very important to know the necessity of make a payment during the service at the desks, a fact that leads to an increase of the service time. The Service Center is open from 7:30 to 18:30 every day from Monday to Friday, and from 7:30 to 13:30 on Saturday, there are 13 desks available. There is no priority or dedicated

desk, except for urgencies. The other activities provided now are delivery of diagnostic reports, booking visits and exams, delivery of laboratory exams, request and delivery of medical records. Once understand how the process work, we need to study the historical data, to set workload, service time and available resources inside the model and to calculate waiting time of patients. For this purpose, we used hospital's database, interviews with staff and direct observations. The records of database start from 1/2/2016 to 24/11/2016, in this period there are 126,850 users. Thanks to this data is possible to find the time of arrival of users, the type of service requested and the waiting time. Service time is another core parameter of the process, unfortunately it is impossible to use historical data to estimate it, because the system does not register finish time of service. In this case we needed a direct observation by the staff to know the correct numbers.

During the morning there is a spike of accesses between 9:30 and 11:30 (Fig. 1). So, we calculated the mean value of accesses for every hour, to evaluate the opportunity to develop a time schedule. The trend is the same every day, so the best approach to handle the queues and maximize utilization of resources is to change the number of operators during the day, with a higher number when there are more accesses and a smaller one when the accesses decrease. Considering the extremely discontinuous trend of accesses, the waiting time was calculated based on user's time of arrival (Table 1). The mean waiting time does not change significantly based on service, except for urgencies, but they have a higher priority. In the moment of greater influx (between 10:00 and 12:00), waiting time is sensibly higher compared to the daily mean. Analyzing the trend of waiting time and accesses jointly, there is a direct correlation between the two parameters (Fig. 1). The highest value is 12 min and 43 s between 10:30 and 11:30, and the smallest one is 3 min between 17:30 and 18:30.

**Fig. 1** Number of accesses and waiting time during the day

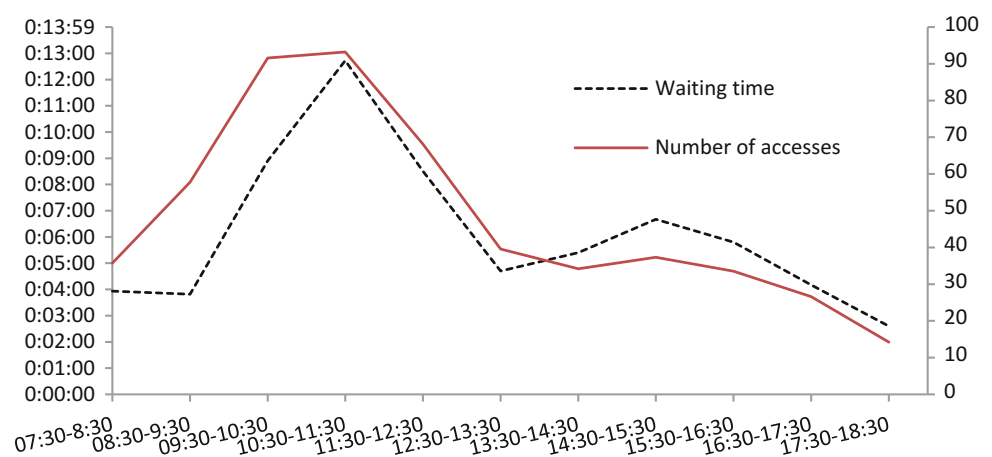


**Table 1** Waiting time of patients

Service	Waiting time (daily)	Waiting time (10:00–12:00)
Documents delivery	7'41"	11'17"
Diagnostic exams	7'18"	11'35"
Laboratory exams	7'18"	11'33"
Documents request	8'00"	11'50"
Urgencies	1'11"	1'07"
Booking	7'32"	11'35"
All services	7'20"	11'30"

The service time cannot be calculated through historical data. Consequently, we used staff's experience and direct observations to find this parameter using a survey with all the information needed. The sampling was made so that the results were statistically significant, with 1510 samples. We used the results of interviews and observations to set the service time inside the simulation model. The historical data of payment time are unavailable as well, so we used interviews and direct observation. After process analysis, we developed a simulation model using Arena software. This activity is strictly connected with process and data analysis and go on parallelly with them.

The number of accesses are variable over the course of the day, so it is impossible to set a fixed time between an arrival and the next one, therefore we used a "schedule". Using this approach, we made a program of accesses that changes hour by hour for every service available. To set the path of the patient we used specific attributes based on process analysis information. Every service shares the same resources and has the same priority, except for urgencies. The number of available desks in every time slot has been set in base of historical data, like the accesses. After creation, the entity enters in a sub-model that simulates the duration of every operational procedure according to the type of request. To simulate the service time, we used an exponential distribution, with mean value based on observations. This kind of distribution is currently used in case of public services, where service time is extremely variable, just like this situation. After completion of request, the entity pass through a module that release the resource, and then the path is over. In case of payment the user follows a parallel path, basically identic to the previous one, but with the creation of a duplicated entity. The aim of duplication is to simulate the duration of payment, while the original entity holds the desk. When the payment is over, the original entity continues its path, finish the procedure, release the resource and exit from the system.

This tool is meant to be used to evaluate the performances of the process changing some parameters.

Especially, it is very important to set the correct number of resources in every time slot, to deal with the number of accesses during day, minimize the costs and improve the KPI of the process. The number of accesses is based on historical data, and, after validation, the model will be used to test how the output of the simulation changes in case of a reorganization of the Service Center. To do this we will analyze some scenarios modifying the number of desks for time slot, to find the best way to face the minimum and maximum number of accesses during day. The selected solution will be the one with the best performances.

### 3 Results

The model needs to be assessed with help of specialists, to be sure that it is formally correct, and needs a validation, that is to compare simulation's outputs with historical data, using statistic tests and numerical confrontation. ACT Operation Research, partner of the project and specialized in discrete event simulation application, made an evaluation of the model and stated that is working properly, after that we started the confrontation with historical data.

The results show that the estimated values are substantially equal to the real ones, with a difference that is less of 5%. The outputs are the mean of 200 replications, each one of them has a length of a week. Weekly workload of the model is equal to reality, this proves that the schedules are correct. Waiting times are like real ones, with a difference that is less than 5% in the worst case, except for urgencies. However, this service has special characteristics, and is so poor in number to be irrelevant for the process. The mean waiting time value of all users calculated by the model is only 2.6% lesser than real one (Table 2). This value is acceptable, especially considering that there are some

**Table 2** Confrontation between historical data and model outputs

KPI	Historical data	Model outputs	Difference (%)
Weekly number of accesses	3048	3048	0
Waiting time for documents delivery	7'41"	7'48"	1.5
Waiting time for diagnostic exams	7'18"	7'01"	4
Waiting time for laboratory exams	7'18"	7'00"	4.2
Waiting time for documents request	8'00"	8'18"	3.7
Waiting time for urgencies	1'11"	35"	50.6
Waiting time for booking	7'32"	7'42"	2.3
Waiting time of all services	7'20"	7'09"	2.6

parameters estimated poorly because of the lack of historical data. To confirm this result, we used a statistic test to compare the waiting time estimated by the model with the real one. The result of Student's test shows that there is no statistic difference between historical data and model outputs, with a significance level of 95%.

## 4 Conclusions

This article proves that discrete event simulation is an instrument that can be used as a decision support tool in healthcare, especially regarding front office activities. This model is formally correct, and validation proves that its outputs are statistically equal to real ones, so the next step will be utilization of model to evaluate the reorganization of Service Center. This goal will be achieved testing a series of scenarios with a different use of the resources, set to manage the different workload during the day, and the one with the best performance between costs and benefits will be chosen. Later the model will be updated to allow everyone to use it, through a web-based support, a predictive machine and a user interface.

**Conflict of interest** The authors declare that they have not conflict of interest.

## References

1. M. Kagioglou, S. Sapountzis: Application of lean thinking a briefing document, Health and Care Infrastructure Research and Innovation Centre (HaCIRIC), University of Salford (2007).
2. A. Kalbasi, D. Krishnamurthy, J. Rolia, S. Singhal: Simulation by example for complex systems, A. Tolk, S. Y. Diallo, I. O. Ryzhov, L. Yilmaz, S. Buckley, and J. A. Miller (eds.), Proceedings of the 2014 Winter Simulation Conference, pp. 974–985 (2014).
3. G. Guizzi, T. Murino, E. Romano: A Discrete Event Simulation to model Passenger Flow in the Airport Terminal, Mathematical methods and applied computing, pp. 427–434 (2008).
4. Tan Chai Xian, Chai Weng Hong, and Nurul Nazihah Hawari: Modeling and Simulation of Queuing System for Customer Service Improvement: A Case Study, Proceedings of the 4th International Conference on Quantitative Sciences and Its Applications (2016).
5. M. A. Ghaleb, U. S. Suryahatmajab and I. M. Alharkan: Modeling and Simulation of Queuing Systems Using Arena Software: A Case Study, Proceedings of the 2015 International Conference on Industrial Engineering and Operations Management (2015).
6. L. Destin, Machfud, Y. Arkeman: Queue System Improvement of Certificate Checking For Increasing Public Service in Bogor District Land Registry Office, International Journal of Scientific and Research Publications, Volume 5, Issue 10, pp. 1–7 (2015).
7. G. Converso: Dualità delle logiche lean-agile nel Dimensionamento delle risorse per l'erogazione dei Servizi ospedalieri ad alto contenuto tecnologico, PhD thesis, Department of Chemical Engineering of Materials and Industrial Processes, University of Naples Federico II (2015).
8. A. Torri: Utilizzo della simulazione ad eventi discreti come strumento per l'analisi ed il re-engineering dei processi sanitari, PhD thesis in Economics and Management of Companies and Health Organizations, University of Naples Federico II (2015).
9. P. Chen, R. Aurelius C. Robielos, P. Kate V. C. Palañ, P. Lorenzo L. Valencia, G. Y. Chen: Scheduling Patients' Appointments: Allocation of Healthcare Service Using Simulation Optimization, Journal of Healthcare Engineering, Vol. 6 No. 2 pp. 259–280 (2015).
10. B. Mocarzel, D. Shelton, B. Uyan, E. Pérez, J. A. Jimenez, L. DePater: Modeling and simulation of patient admission services in a multi-specialty outpatient clinic, R. Pasupathy, S.-H. Kim, A. Tolk, R. Hill, and M. E. Kuhl (eds.), Proceedings of the 2013 Winter Simulation Conference, pp. 2309–2319 (2013).
11. K. Šteins: Discrete-Event Simulation for Hospital Resource Planning – Possibilities and Requirements, Department of Science and Technology, Linköping University, SE-601 74 Norrköping, Sweden (2010).
12. C. Duguay, F. Chetouane: Modeling and Improving Emergency Department Systems using Discrete Event Simulation, Faculty of Engineering, University of Moncton, Moncton, NB, Canada (2007).
13. A. P. Vijayan: Effect of appointment schedules on the operational performance of a university medical clinic, Department of Mechanical and Industrial Engineering, Louisiana State University (2015).
14. R. Harpring, G. W. Evans, R. Barber, S. M. Deck: Improving efficiency in social services with discrete event simulation, Computers & Industrial Engineering, pp. 159–167 (2014).
15. M. Rinaldi, R. Montanari, E. Bottani: Improving the efficiency of public administrations through business process reengineering and simulation, Business Process Management Journal, Vol. 21 Iss 2 pp. 419–462 (2015).
16. R. Al-Aomar: Simulating Service Systems, Discrete Event Simulations, Aitor Goti (Ed.), ISBN: 978-953-307-115-2, InTech, (2010).
17. S. Deb, N. F. A. Chowdhury, D. Claudio: Service Quality Improvement in an IT Center: A Simulation Study, Proceedings of the 2014 Industrial and Systems Engineering Research Conference (2014).
18. P. P. Borthakur, R. Deka: Simulation of Service Industry: An Effective Approach to Improve Service quality under Dynamic Demand Scenario, International Journal of Engineering Research & Technology (IJERT) Vol. 2 Issue 8, pp. 1329–1336 (2013).
19. O. Bataineh, R. Al-Aomar, A. Abu-Shakra: Simulation-based optimization for performance enhancement of public departments, Jordan Journal of Mechanical and Industrial Engineering, pp. 346–351 (2010).
20. S. D. Roberts: Tutorial on the simulation of healthcare systems, S. Jain, R.R. Creasey, J. Himmelspach, K.P. White, and M. Fu (eds.), Proceedings of the 2011 Winter Simulation Conference, pp. 1408–1419 (2011).

# Numerical Study for Lung Microwave Ablation in Different Thermal and Electrical Properties

Zhen Tian, Yanyan Cheng, Tong Dong, Xiang Gao, and Qun Nan

## Abstract

Microwave ablation (MWA) is a minimal invasive operation for treating lung cancer, and it has been widely used in clinic. Lung contain tracheas and bronchus, and the properties of thermal conductivity, electrical conductivity and density change by variations in the lung's internal air volume. Thus, it is difficult to control the precise formation of coagulation zones. In this paper, we propose to use finite element method (FEM) to simulate the microwave ablation for lung cancer in a simple lung model. We set the power as 10 watts for 10 s at 2.45 GHz. We built the lung model and a small bronchus was placed close to the opened-tip coaxial antenna with airflow at the rate of 3 L/min. We operated eight patterns including the collapsed and aerated lung in different thermal conductivity, electrical conductivity and density to simulate. The results preliminarily showed that the electrical conductivity had the greatest influence on the microwave ablation temperature field of lung.

## Keywords

Microwave ablation • Lung • Thermal conductivity  
Electrical conductivity • Simulation

## 1 Introduction

Lung cancer seriously affects human health. Because of smoking and the deterioration of living environment, a number of patient from the disease is never decrease [1]. The surgical approach to lung malignancies represents the first therapeutic choice [2]. However, only 20% of all diagnosed lung tumors are resectable [2, 3]. Microwave ablation (MWA) is a way of thermal therapies. Because of its

minimally invasive and highly thermal efficiency, MWA has been widely used in clinical, and it has become an important means of treating lung tumor. When the tissue around the electrode reaches a temperature of around 60 °C, tissue coagulation occurs as a result of protein denaturation.

Lungs contain abundant air and it greatly affects the thermal distribution. Since the presence of trachea and bronchus inside the lung, the properties of thermal conductivity, electrical conductivity and density change by variations in the lung's internal air volume [4].

The objective of this study is to simulate the microwave ablation for lung cancer in different patterns under a simple lung model. The physical structure of the lungs is complex, including the trachea, bronchus and capillaries. In order to simplify the calculation, we built the lung model and a small bronchus was placed. And we set the airflow at the rate of 3.0 L/min which is the same rate of human breath motion. We operated eight patterns including the collapsed and aerated lung in different thermal conductivity, electrical conductivity and density to simulate.

## 2 Methods

### 2.1 Geometric Model

We used the finite element method software Comsol Multiphysics to solve partial differential equations of single field and multi-field in order to achieve the numerical results. The idealized 3D symmetric simplified model of lung microwave ablation was shown in Fig. 1 [1]. The antenna is consisted by inner and outer conductor and dielectric. As to the coaxial antenna, we set the power input at the inner catheter between the inner and outer conductor [5]. The antenna structure and the size was shown in Fig. 2 and Table 1.

Z. Tian (✉) · Y. Cheng · T. Dong · X. Gao · Q. Nan  
College of Life Science and Bioengineering, Beijing University  
of Technology, Beijing, China  
e-mail: 521071750@qq.com



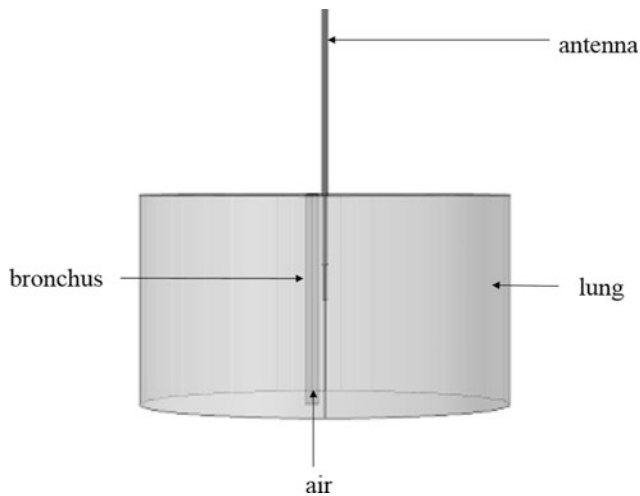


**Fig. 1** Lung model

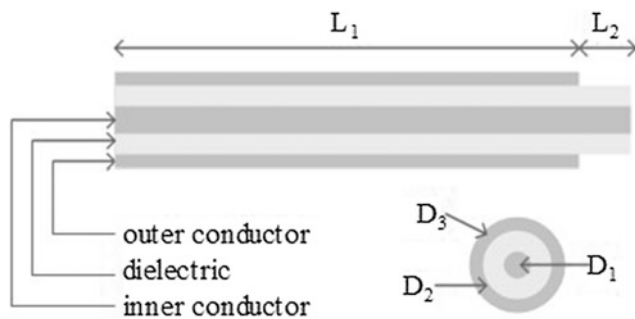


**Fig. 2** Antenna structure

## 2.2 Bio-heat Equation

Microwave energy converted into heat when microwave ablation instrument was turned on, meanwhile, the temperature of tissue was increasing. When temperature approached or exceed 60 °C, the tumor cells produce irreversible necrosis to achieve the purpose of killing tumor. The Pennes

**Table 1** Size of the antenna

Dimension	Size/(mm)
Diameter of inner conductor— $D_1$	0.27
Diameter of dielectric— $D_2$	0.67
Diameter of outer conductor— $D_3$	0.92
Length of outer ( $L_1$ )	45
Length of opened tip ( $L_2$ )	5

bio-heat equation (Eq. (1)) governs heating transfer during the thermal ablation [6, 7].

$$\rho c \frac{\partial T}{\partial t} = k \nabla^2 T + Q_r - \rho_{b1} c_{b1} \omega_{b1} (T - T_{b1}) \quad (1)$$

where:  $\rho$  and  $\rho_{b1}$  is the density of the tissue and the blood ( $\text{kg/m}^3$ ),  $c$  and  $c_{b1}$  is the specific heat capacity of the tissue and the blood ( $\text{J/(kg K)}$ ),  $k$  is the thermal conductivity ( $\text{W/(m K)}$ ),  $T$  and  $T_{b1}$  is the temperature of the tissue and the blood (K),  $\omega_{b1}$  is the blood perfusion (1/s),  $Q_r$  is the heat source ( $\text{W/m}^3$ ). In this simulation we didn't take the blood perfusion into account.

## 2.3 Numerical Setting

In this study, some parameters and boundary conditions were set as follows:

- (1) The duration time was 10 s and the microwave frequency was 2.45 GHz.
- (2) The microwave power was set at 10 W.
- (3) Lung boundary temperature was set at 37 °C, and the outer surface was truncated by a scattering boundary condition.
- (4) We set the airflow at the rate of 3.0 L/min which is the same rate of human breath motion.

**Table 2** The properties of lung [8]

Pattern	Thermal conductivity/(W/(m K))	Density/( $\text{kg/m}^3$ )	Electrical conductivity/(S/m)
a	0.200	480	0.423
b	0.125	480	0.423
c	0.200	240	0.423
d	0.125	240	0.423
e	0.200	480	0.100
f	0.125	480	0.100
g	0.200	240	0.100
h	0.125	240	0.100

**Table 3** Temperature field data

Pattern	Highest temperature/(°C)	Ablation lesion/(mm <sup>3</sup> )
a	267.5	73.9
b	380.6	86.1
c	279.4	168.1
d	401.4	182.3
e	93.8	8.2
f	122.1	10.8
g	98.6	9.5
h	126.4	14.9

From previous research, the lung’s thermal conductivity and electrical conductivity decreased non-linearly with increasing internal air volume in lung [4]. So we set eight patterns to simulate. The properties of lung was shown in Table 2.

Since the mass of the lung can be considered constant (air is less affected), the change of density can lead to the change of the volume [4]. We set the lung model as a cylindrical shape, and the 20 × 30 mm in radius and height respectively when the density was 480 kg/m<sup>3</sup>, and the 28 × 30 mm in radius and height respectively when the density was 240 kg/m<sup>3</sup>.

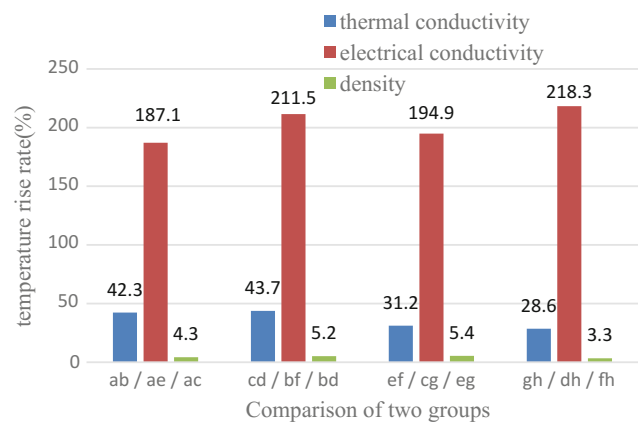
### 3 Results and Discussion

Table 3 shows the related temperature distribution field data. The “a” to “h” in Table 3 correspond to the eight states of Table 2, respectively.

From Table 3 we can see that the temperature was lower when the thermal conductivity was high. Temperature in the high thermal conductivity becomes low because the heat input into the area quickly diffuses into surrounding areas and does not accumulate. Thus when the lung was in the low thermal conductivity the temperature was higher since the heat spread slowly.

Figure 3 shows the increase rate of the highest temperature after ablation in 8 states. When the electrical conductivity increased, temperatures of the a/b/c/d groups were increased than e/f/g/h groups. The rise rate was from 187.1% to 128.3%. And the rate of the parameters of thermal conductivity and density was from 28.6% to 48.7%, and 3.3% to 5.4%, respectively. Thus under the same condition, the effect of electrical conductivity on microwave ablation is greater than that of density and thermal conductivity.

For density, the change of temperature field is the smallest. The temperature of pattern a/b/e/f were higher than parameter pattern c/d/g/h in this simulation. Compared with the previous research [8], when the density changed and the electrical conductivity and thermal conductivity were constant, the change of temperature trend was the same.



**Fig. 3** The increase rate of the highest temperature after ablation in 8 states. In this figure, “ab/ad/ef/gh” represents the comparison of two groups with different thermal conductivity. “ae/bf/cg/dh” represents the comparison of two groups with different electrical conductivity. “ac/bd/eg/fh” represents the comparison of two groups with different density

Figure 4 shows the temperature distribution field after microwave ablation. Refer to the previous research [9] that there was air flow in the bronchus at the rate of 3 L/min, so in the process of heat transfer, the air flow take away the heat. So it formed the temperature field shown in Fig. 4.

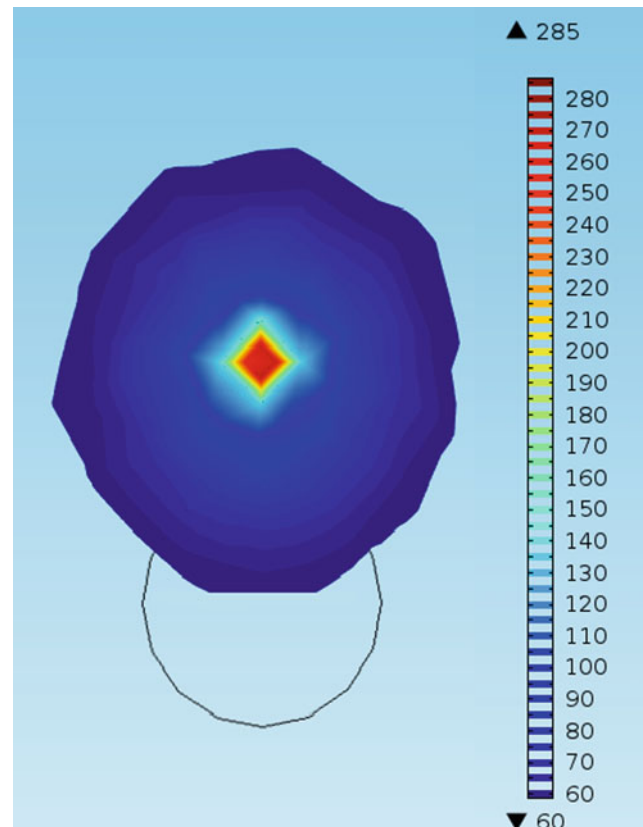


**Fig. 4** Temperature distribution

## 4 Conclusion

This study simulated the microwave ablation for lung cancer in different patterns under a simple lung model. Through the results, it was suggested that the electrical conductivity and thermal conductivity and density had an effect on lung MWA, and by comparing the results the electrical conductivity had a greater effect.

There are still some limits in this research, such as lack of an accurate electrical conductivity data in microwave frequency and the ablative time was short. In future, we'll take these condition into account and to get more accuracy data to compare the results.

**Acknowledgements** This research is supported by National Science Foundation of China (31771021) and Beijing Natural Science Foundation (3162006).

**Ethics Approval and Consent to Participate** Not applicable.

**Competing Interests** The authors declare that they have no conflict of interest.

---

## References

- Phairoh C, Sanpanich A, Kajornpredanon Y, et al.: Airflow effect on microwave ablation in lung model. Biomedical Engineering International Conference 2016, pp. 1–4.
- Carrafiello G, Mangini M, Bernardi I D, et al.: Microwave ablation therapy for treating primary and secondary lung tumours: technical note. *La Radiologia Medica* 115(6), 962(2010).
- Shugarman L R, Mack K, Sorbero M E S, et al.: Race and Sex Differences in the Receipt of Timely and Appropriate Lung Cancer Treatment. *Medical Care* 47(7), 774–781(2009).
- Yamazaki N, Watanabe H, Seki M, et al.: Modeling the internal pressure dependence of thermal conductivity and in vitro temperature measurement for lung RFA. Annual International Conference of the IEEE Engineering in Medicine and Biology Society 2011, pp. 5753–5757.
- Nan Q, Zhai F, Guo X M.: Study on the temperature field of the endocardial point-by-point microwave ablation of atrial fibrillation. *Journal of Beijing University of Technology* 40(10), 1579–1585 (2014).
- H.H. Pennes.: Analysis of tissue and arterial blood temperatures in the resting human forearm. *Journal of Applied Physiology*, 1, 93 (1948).
- Zhai F, Nan Q, Zhang H J, et al.: The Comparison of Two Simulation Methods on the Thermal Ablation with Large Blood Vessel, *Applied Mechanics & Materials*, 444–445 (444-445), 1177–1181(2013).
- Yamazaki N, Watanabe H, Lu X, et al.: Development of a temperature distribution simulator for lung RFA based on air dependence of thermal and electrical properties. *Engineering in Medicine and Biology Society. IEEE*, 2012, pp. 5699–5702.
- Sanpanich A, Khongkhanon C, Kajornpredanon Y, et al.: Thermal ablation for cancer treatment by using microwave energy in a simple lung model. Biomedical Engineering International Conference. IEEE, 2015, pp. 1–4.

# Use of Modelling Simulation to Monitor the Performance of a Pediatric Emergency Department

Giuliana Faiella, Marco Simonetti, Antonio D'Uffizi, Vincenzo Tipo, Mario Cesarelli, and Fabrizio Clemente

## Abstract

Hospitals are complex systems in which different departments interact with each other. Systemic analytical models use systematic representations to facilitate the understanding of a complex process. The models are simulated with an imitation of the operations of a system and its internal processes, usually over time, and in appropriate detail. Simulation is used to study the performance of new systems as well as predict the effect of changes. Since Emergency Departments (ED) are unpredictable and frontline of healthcare service delivery, their detailed description and analysis are highly needed in order to design improvement actions. In this study, we will present the simulation of the ED a pediatric hospital which admits more than 100 k/year patients. The simulation tool is SIMIO®.

## Keywords

Simulation modelling framework • Emergency department • SIMIO®

## 1 Introduction

Healthcare is a very vast and complex system in which different departments interact dynamically with each other. Individuals and teams contribute to serving patients' demand in a dynamic environment [1, 2].

The Discrete Event Simulation (DES) is used like '*the imitation of real operation of a real-world process or system over time*' [3]. DES is a stochastic approach used to create processes and systems, where the state changes instantaneously. It is used for tactical-operational analysis with the objective to study the functional specifications of a system and improve its performance. The process is modelled as a discrete sequence of activities and entities distributed over time, interspersed with queues. Each entity has specific characteristics, which determine the functioning of the model. The durations of the activities are distinct for each single entity and depend on probability distributions. Every event happens in a specific moment of time and the behavior of the system is determined by every single event. This approach is used also to analyse and improve processes concerning not only the manufacturing fields but also human security and Emergency Logistics study [4, 5].

Many hospital emergency departments are critically overcrowded and unable to respond to daily emergencies [1, 6]. The stochastic nature of arrival times and of pathological conditions can have a strong impact on workload and consequently on patient waiting times and quality of care [7].

This work describes the simulation model of a complex healthcare process, such as ED of Santobono Pediatric Hospital in Naples performed with SIMIO®. The model has been designed with a preliminary requirement analysis and validated with real data extracted from the Hospital Information System database.

G. Faiella · F. Clemente (✉)  
Fondazione Santobono Pausilipon, Naples, Italy  
e-mail: fabrizio.clemente@ibb.cnr.it

G. Faiella  
e-mail: giuliana.faiella@gmail.com

M. Simonetti · F. Clemente  
CNR-Istituto di Cristallografia, Rome, Italy

A. D'Uffizi  
CNR-Istituto di Analisi dei Sistemi ed Informatica IASI,  
Rome, Italy

V. Tipo  
AORN Santobono Pausilipon, Naples, Italy

M. Cesarelli  
DIETI, School of Engineering, University of Naples Federico II,  
Naples, Italy

## 2 Materials and Methods

### 2.1 The Emergency Department of Santobono Pausilipon Pediatric Hospital

The type of patients arriving in ED is heterogeneous and the admission of patients is regulated by a priority-based policy. The triage consists in a set of procedures that ensure that patients with critical conditions are admitted before the others. The priority level is usually represented by a color code (white, green, yellow and red) that defines the increasing need of care [8].

Santobono-Pausilipon pediatric hospital is the oldest and the largest pediatric hospital in the South of Italy. The rate of ED's accesses is steadily growing (estimated at 5% per year). Specifically, Santobono-Pausilipon recorded 102.000 accesses in 2016, i.e., about 280 per day. This is the highest rate recorded in Italy by a pediatric emergency department and, to the best of our knowledge, the 2nd highest in Europe.

### 2.2 SIMIO<sup>®</sup> and Simulation Modelling

SIMIO<sup>®</sup> is a widely used simulation software of new generation. It is not built on an outdated 2D technology that limits the ability to visualise and understand the analysed process, but it provides a true object-based 3D modelling environment.

The user simply drags and places the 3D objects from an Object Library into the facility view of the model. All SIMIO<sup>®</sup> model-building products directly integrate with Google Warehouse adding realism to designed models. It is also possible to create a self-made symbol. Moreover, it is possible to use a 3D graphical background with the representation of the physical ambient in which the stakeholders operate [9]. Thus, SIMIO<sup>®</sup> is very useful to create a simple representation that can be shared with no-technical personnel as medical staff and nurses. For this reason, SIMIO<sup>®</sup>, with its branch SIMIO Healthcare, is gaining much confidence in healthcare management since it is designing a new office, outpatient clinic or evaluating new surgical planning strategies, predicting variables such as changing the number of employees who work at any time [10].

## 3 Results

The dynamic simulation of Santobono ED process followed the standard steps of modeling [11, 12]: (i) requirement analysis and identification of the inputs of the model, (ii) model development and (iii) output analysis.

### 3.1 Requirement Analysis and Inputs Identification

The requirement analysis is a fundamental activity to depict a process [13, 14] with a detailed description of the flow. The analysis was carried out by a team composed by the manager of ED and two biomedical engineers and it was performed investigating the locations, the activities (type and duration), the involved resources and their workload. The result of the requirement analysis is the flowchart in Fig. 1.

After the arrival, the patient is registered and assessed by a dedicated nurse in the triage area. After the assessment, the triage nurse assigns a color tag and guides the patient into a specific treatment area.

The treatment areas are distinct in Specialist Departments of Fast Track (i.e., dermatology, ophthalmology departments), placed outside the area of the ED and reserved for care of low acuity patients, and five emergency rooms inside the ED reserved for care of moderate to high acuity patients. The Emergency rooms are divided into one surgical, one orthopedic and three pediatric. They are staffed by five physicians from 8:00 am to 12:00 midnight and by one pediatrician less during the night. Some patients are required to prolong their stay for treatment or observation, and they are admitted for 24/48 h into a treatment area called Short Intensive Care that is staffed by two nurses. According to this description, the simulation required four types of input data:

- Number of patients accesses.
- Percentages of the patients classified into each triage tag;
- Percentages of the accesses in the specialist departments and emergency rooms.
- Percentages of the discharges from the emergency department.

### 3.2 Model Development

After the requirement analysis, the ED process was modelled using SIMIO<sup>®</sup>. The model was tested using 24 h data of a high-intensity working day. The main process was modelled separated in two sub-processes. The first sub-process is an administrative process, which manages the patient registration and the assignment of the triage code (see Fig. 2). The sub-process is composed by three activities (i.e. servers in SIMIO<sup>®</sup>).

In the first sub-process, a source (PatientArrival) generates the generic entity patient according to a Rate Table that shows the number of patients' accesses divided in hourly time slots (see Fig. 3).

Then, the patient is registered at FrontDesk and categorised into the triage classes defined according to the level



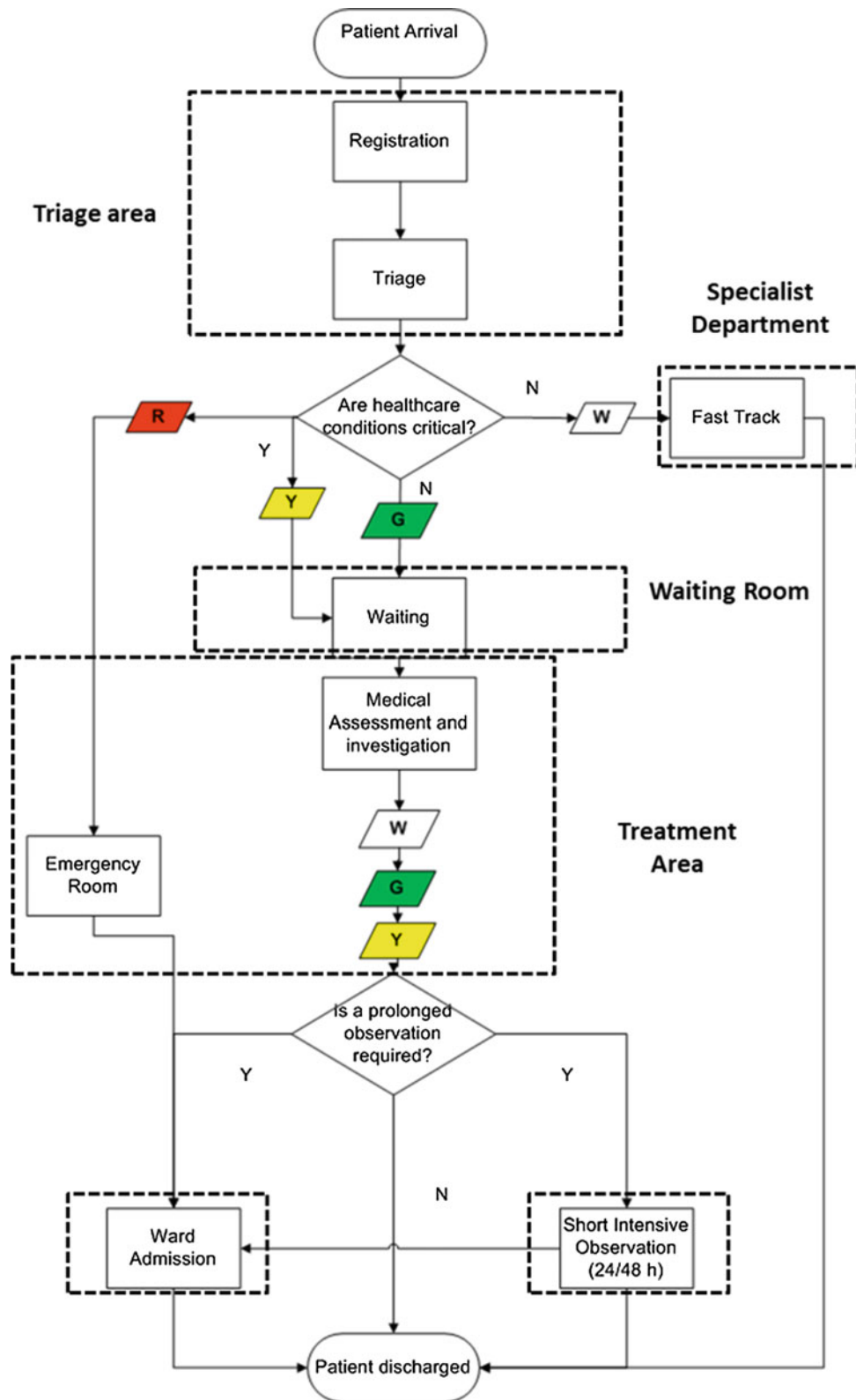


**Fig. 1** Overview of the Santobono Emergency Department flow. The colored parallelograms represent the color tag assigned to patients after the triage

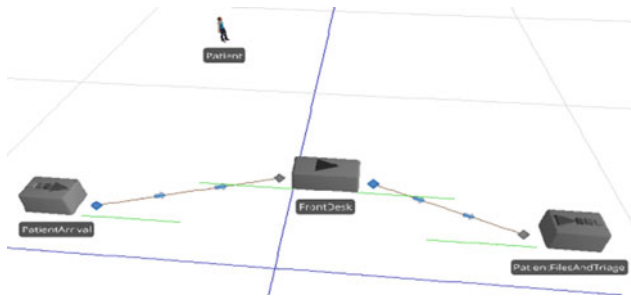


**Fig. 2** Modelling of the administrative sub-process: patient registration and triage

▼ Rate Tables			
ArrivalRate			
	Starting Offset	Ending Offset	Rate (events per hour)
▶	Day 1, 00:00:00	Day 1, 01:00:00	8
	Day 1, 01:00:00	Day 1, 02:00:00	9
	Day 1, 02:00:00	Day 1, 03:00:00	6
	Day 1, 03:00:00	Day 1, 04:00:00	7
	Day 1, 04:00:00	Day 1, 05:00:00	19
	Day 1, 05:00:00	Day 1, 06:00:00	19
	Day 1, 06:00:00	Day 1, 07:00:00	5
	Day 1, 07:00:00	Day 1, 08:00:00	5
	Day 1, 08:00:00	Day 1, 09:00:00	9
	Day 1, 09:00:00	Day 1, 10:00:00	9
	Day 1, 10:00:00	Day 1, 11:00:00	18
	Day 1, 11:00:00	Day 1, 12:00:00	18
	Day 1, 12:00:00	Day 1, 13:00:00	19
	Day 1, 13:00:00	Day 1, 14:00:00	20
	Day 1, 14:00:00	Day 1, 15:00:00	17
	Day 1, 15:00:00	Day 1, 16:00:00	18
	Day 1, 16:00:00	Day 1, 17:00:00	19
	Day 1, 17:00:00	Day 1, 18:00:00	19
	Day 1, 18:00:00	Day 1, 19:00:00	16
	Day 1, 19:00:00	Day 1, 20:00:00	17
	Day 1, 20:00:00	Day 1, 21:00:00	19
	Day 1, 21:00:00	Day 1, 22:00:00	20
	Day 1, 22:00:00	Day 1, 23:00:00	19
	Day 1, 23:00:00	Day 2, 00:00:00	20

**Fig. 3** Rate Table of patient arrivals

of assistance required (i.e., red, yellow, green and white tag). The classified patients will be the inputs of the second sub-process.

Patient Table			
	Patient Tag	Percentage	Type
▶ 1	RedTag	0	1
2	YellowTag	0,05	2
3	GreenTag	0,67	3
4	WhiteTag	0,23	4
5	FastTrack	0,05	5
*			

**Fig. 4** Data Table with the percentages of patients for each triage code

The FrontDesk is modelled as a server that performs the triage operation according to a processing time that follows a normal distribution with a mean of 5 min and a standard deviation of 0.2 min. The assignment of the triage tags is modelled using a Data Table (see Fig. 4) with the percentages of patients in each triage class. The data were extracted from the ED information system. The data table assigns to each entity patient a label that will be used to identify and correctly direct each type of patient.

The second sub-process is a clinical process (see Fig. 5) related to the clinical path of the patient across the treatment areas (modelled as servers in SIMIO® and called Emergency \* Rooms where the \* indicates the name of a generic Emergency Department). The Emergency \* Room processing times follow normal distributions with a mean of 20 min and a standard deviation of 0.2 min.

Depending on triage tag and simulation clock (internal simulation time), the patients follow different paths (see Fig. 1):

- RED TAG patients: they proceed exclusively towards the RedTagBox server;
- FAST TRACK patients: they proceed towards the SpecialisticEmergencyRoom server, which is open only in a defined time slot (8:00 am to 5:00 pm). When the service is not available, the patients are addressed to the WaitingRoom server;
- YELLOW, GREEN and WHITE TAGS patients: they proceed towards the Waiting-Room.

After the WaitingRoom, the patient follows the path that is open according to the time slots, in fact a pediatric emergency room (EmergencyPaediatricRoom3 server) is activated only from 8 am to 12 am. This option has been modelled using a TransferNode, which allows or inhibits the access to the arcs exiting the node. The access to the different EmergencyRoom depends on percentages (see Table 1) and on the room availability (server free). This has been modelled setting the routing and selection logic of the path defined according to percentages provided by the ED information system.

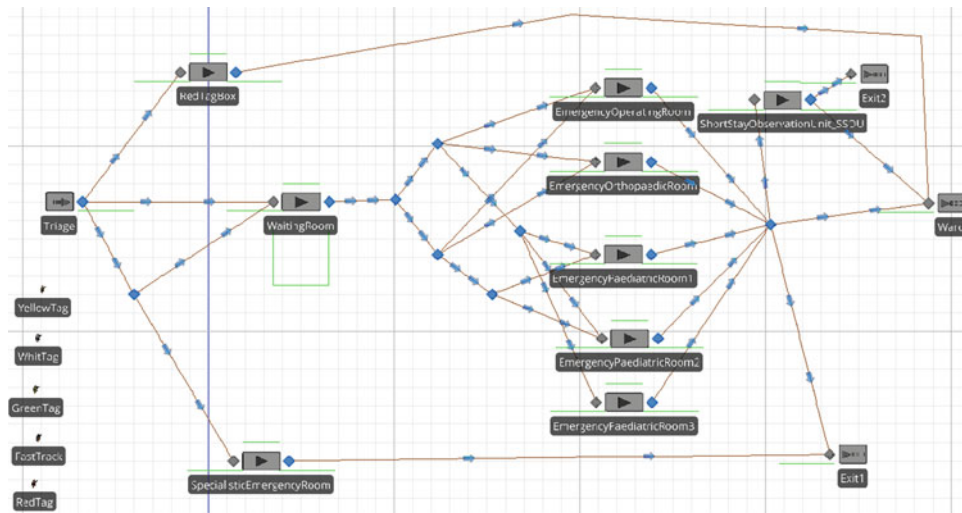


**Fig. 5** Modelling of the clinical sub-process: medical assessment and treatment

**Table 1** Patients’ percentages from the WaitingRoom to the EmergencyOperating Rooms

From WaitingRoom to [*]	Percentage (%)
EmergencyOperatingRoom	20
EmergencyOrthopaedicRoom	16
EmergencyPaediatricRoom (1, 2, 3)	64

**Table 2** Patients’ percentages from the EmergencyOperatingRooms to exit, ward or SSOU

From EmergencyRoom to [*]	Percentage (%)
Exit	90.8
Ward	5.8
Short stay observation unit	3.4

Once the patient leaves the specific emergency room, he/she can follow 3 paths: Exit, Ward and Short Stay Observation Unit (SSOU) server, in relation to the doctor’s prognosis. This has been modelled setting the routing and

selection logic of the path defined according to percentages provided by the ED information system (see Table 2).

#### 4 Tests and Conclusions

The model has been simulated with a dual purpose to evaluate the functionality of Santobono Emergency Department process and check the model’s ability to highlight criticalities using real data. In order to achieve these purposes, the model was tested using real data related to a 24 h high-intensity working day (pre-holiday and wintry day in which there were numerous accesses because of seasonal typical pediatric age illnesses).

In order to simulate the Front Desk (i.e., Patient Registration Desk) and triage management according to the number of patients approaching the ED, two simulation tests were performed. The first (#1) considers the presence of one triage nurse, the second (#2) considers the presence of two triage nurses. Tables 3 and 4 report the time in system and the Front Desk queues. These results show that considering simulation

**Table 3** Results of simulation #1

Simulation #1: n.1 Triage nurse			
Triage tag	Timing system (h:mm)	Max (h:mm)	Min (h:mm)
White	0:31	2:00	0:20
Green	0:27	1:52	0:20
Yellow	0:31	1:42	0:20
Fast track	0:22	0:30	0:20
Front desk queues			
Final output	113 people		
Average	31 people		

**Table 4** Results of simulation #2

Simulation #2: n.2 Triage nurses			
Triage tag	Timing system (h:mm)	Max (h:mm)	Min (h:mm)
White	1:10	3:48	0:20
Green	1:13	4:00	0:20
Yellow	1:00	2:36	0:20
Fast track	1:07	3:32	0:20
<i>Front desk queues</i>			
Final output	0 people		
Average	1 person		

#1 there will be a queue of 113 people at the end of the day. Whereas, considering simulation #2 all patients are treated into 24 h even if the average time in the system is higher.

This suggests that in healthcare, particularly in ED, a robust requirement analysis should be performed by a valuable multidisciplinary team [15, 16] in order to identify the correct model and its real implementation [17].

## References

- Oueida, S., Char, P. A., Kadry, S., & Ionescu, S.: Simulation Models for Enhancing the Health Care Systems. *FAIMA Business & Management Journal*, 4(4), 5 (2016).
- Marshall, D. A., Burgos-Liz, L., IJerman, M. J., Osgood, N. D., Padula, W. V., Higashi, M. K., & Crown, W.: Applying dynamic simulation modeling methods in health care delivery research—the simulate checklist: report of the ispor simulation modeling emerging good practices task force. *Value in health*, 18(1), 5–16 (2015).
- Banks, J., Carson, J.S., Nelson, B.L., Nicol, D.M.: *Discrete-Event System Simulation*, fourth ed. Prentice Hall, Upper Saddle River, NJ (2005).
- Robinson, S., Radnor, Z. J., Burgess, N., & Worthington, C.: SimLean: Utilising simulation in the implementation of lean in healthcare. *European Journal of Operational Research*, 219(1), 188–197 (2012).
- D’Uffizi, A., Simonetti, M., Stecca, G., & Confessore, G.: A simulation study of logistics for disaster relief operations. In: *Procedia CIRP*, 33, 157–162 (2015).
- McHugh, M., VanDyke, K., McClelland, M., & Moss, D: Improving patient flow and reducing emergency department crowding: a guide for hospitals (2012).
- Marshall, D. A., Burgos-Liz, L., IJerman, M. J., Osgood, N. D., Padula, W. V., Higashi, M. K., & Crown, W: Applying dynamic simulation modeling methods in health care delivery research—the SIMULATE checklist: report of the ISPOR Simulation Modeling Emerging Good Practices Task Force. *Value in health*, 18(1), 5–16 (2015).
- Leo, G., Lodi, A., Tubertini, P., & Di Martino, M.: Emergency department management in Lazio, Italy. *Omega*, 58, 128–138 (2016).
- SIMIO Homepage, <https://www.simio.com/applications/healthcare-simulation-software/>.
- Yuen, A., & Wu, H. E: Hospital Patient Flow Capacity Planning Simulation Model at Vancouver Coastal Health. In: *IIE Annual Conference. Proceedings* (pp. 770–775). Institute of Industrial and Systems Engineers (IISE) (2017).
- Kelton, W. D., Smith, J. S., & Sturrock, D. T.: *Simio & simulation: Modeling, analysis, applications*. Learning Solutions (2011).
- Clemente, F., D’Arco, M., & D’Avino, E.: The Use of a Conceptual Model and Related Indicators to Evaluate Quality of Health Care in Intensive Care Units. *Quality Engineering*, 26(2), 196–205 (2014).
- Clemente, F., Stecca, G., Bifulco, P., Cesarelli, M., Faiella, G., & Romano, M.: Process modeling of devices management in home care. In: *E-Health and Bioengineering Conference Proceedings (EHB)*, (pp. 1–4). IEEE 2013.
- Stecca, G., Baffo, I., Galiano, G., & Clemente, F.: Design of a holonic remote monitoring and diagnosis system for fleet management. *Measurement*, 46(6), 1947–1956 (2013).
- Parand, A., Faiella, G., Franklin, B. D., Johnston, M., Clemente, F., Stanton, N. A., & Sevdalis, N.: A prospective risk assessment of informal carers’ medication administration errors within the domiciliary setting. *Ergonomics*, 61(1), 104–121 (2018).
- Faiella, G., Parand, A., Franklin, B. D., Chana, P., Cesarelli, M., Stanton, N. A., & Sevdalis, N.: Expanding healthcare failure mode and effect analysis: A composite proactive risk analysis approach. *Reliability Engineering & System Safety*, 169, 117–126 (2018).
- Clemente, F., Papi, M., Pontecorvi, L., & Menichetti, A.: Evaluation of indices for the measurement of quality in health systems. *International Journal of Metrology and Quality Engineering*, 7(4), 405 (2016).

# Validation of SIMIND Monte Carlo Simulation Software for Modelling a Siemens Symbia T SPECT Scintillation Camera

John E. Ejeh, Johan A. van Staden, and Hanlie du Raan

## Abstract

The use of Monte Carlo (MC) simulations in nuclear medicine is on the rise due to its usefulness in modelling many physical phenomena which are difficult or impossible to measure. To use MC for gamma camera image simulations, it is important to validate the simulated data with the measured data to ensure that what is simulated is a true representation of the physical system being modelled. Therefore, in this study, the SIMIND MC code for modelling a Siemens Symbia T dual head SPECT/CT gamma camera fitted with high energy all-purpose collimators (HEAP) was validated. The validation was done by acquiring and simulating certain NEMA stipulated performance measurements for  $^{131}\text{I}$ . These measured and simulated performance data were processed and the results compared. The FWHM and FWTM for the gamma camera for measured and simulated system spatial resolution were 14.4, 29.7 mm versus 13.9, 25.9 mm. System sensitivity performance measurements and simulation produced results of 49 cps/MBq and 48 cps/MBq respectively. The corresponding measured and simulated values for the septal penetration were 3.8 and 4.2%. From this study it is evident that the SIMIND MC Code can be used with confidence to mimic  $^{131}\text{I}$  studies acquired with a Siemens Symbia T SPECT/CT gamma camera fitted with HEAP collimators.

## Keywords

Computer simulation • Code validation • SIMIND  
Septal penetration fraction • Monte Carlo

J. E. Ejeh (✉) · J. A. van Staden · H. du Raan  
Department of Medical Physics, University of Free State,  
Bloemfontein, South Africa  
e-mail: jenyiejeh@gmail.com

J. E. Ejeh  
Department of Nuclear Medicine, University College Hospital  
Ibadan, Ibadan, Nigeria

## 1 Introduction

Monte Carlo (MC) simulations are used to model real life systems. MC has the advantage of creating a controlled environment to evaluate many phenomena which are difficult or impossible to measure physically. In nuclear medicine it provides the opportunity to study the physics of factors responsible for degradation of images [1]. The optimization of image acquisition and processing in nuclear medicine is one of the reasons why the use of MC simulation is on the rise [2].

Simulation of Imaging Nuclear Devices (SIMIND) [3] is one of the dedicated MC codes for simulating nuclear medicine images acquired with gamma cameras. In SIMIND a standard clinical gamma camera can be defined which can be used to simulate planar and SPECT data [4].

It is necessary to validate all computer models before using them to simulate real world systems. To validate a MC code, results of simulated experiments are benchmarked against results obtained from experimental measurements on the physical system [5]. The validation ensures that the simulated system truly represents the physical system.

Validating nuclear medicine MC codes to simulate imaging systems can be done by performing certain National Electrical Manufacturers Association (NEMA) stipulated performance measurements [6]. Commonly used measurements for gamma cameras are the energy resolution, system spatial resolution, and system sensitivity [7–11]. For this study, the extrinsic planar spatial resolution, system planar sensitivity and collimator septal penetration performance tests were done to validate the MC Code.

The aim of this study was to validate the SIMIND MC code for modelling a Siemens Symbia T SPECT/CT dual head gamma camera fitted with HEAP collimators using  $^{131}\text{I}$ . The validation of SIMIND MC for the aforementioned gamma camera with  $^{131}\text{I}$  was done due to our interest in  $^{131}\text{I}$  dosimetry using simulated SPECT images.



## 2 Materials and Methods

The radionuclide ( $^{131}\text{I}$ ) necessary for the study was measured in a dose calibrator (Biodex Atomlab 500, Biodex Medical Systems New York, NY, USA). Validation measurements were obtained with a dual-head gamma camera (Symbia T, Siemens Medical Solutions, Inc. Hoffman Estates, IL., USA) fitted with HEAP collimators.

A model of the Symbia T gamma camera was created in SIMIND version 5.0 which simulated all planar images required for the validation tests.

All measured and simulated images were processed with the public domain software, ImageJ (version 1.50i) [12].

### 2.1 Gamma Camera Measurement

Only one of the Symbia T dual-head SPECT/CT gamma camera's detector was used to acquire data because acceptance tests showed little difference between the two detectors. The gamma camera data were acquired with a 15% energy window centred at the 364 keV, photopeak of  $^{131}\text{I}$  and all measurements were repeated three times. The matrix size was selected as indicated for each specific test.

**Extrinsic spatial resolution:** Two capillary tubes with an inner diameter of 1 mm were used to determine the system spatial resolution. The capillary tubes were filled with  $9.4 \pm 0.4$  MBq of  $^{131}\text{I}$  and were placed  $10.0 \pm 0.5$  cm apart and  $10.0 \pm 0.5$  cm away from the detector of the gamma camera. Gamma camera images of 4 000 000 counts were acquired in an image matrix of  $512 \times 512$  with a pixel size of 0.12 cm.

The spatial resolution was calculated by drawing a profile across the image of the capillary tubes. The line profile was fitted with a Gaussian function and from this, the full width at half maximum (FWHM) and the full width at tenth maximum (FWTM) were calculated.

**System sensitivity:** A petri dish with an inner diameter of 6.4 cm was filled with water to completely cover the bottom of the dish. Activity of 135.7 MBq of liquid  $^{131}\text{I}$  was dispersed into the petri dish. The petri dish was placed at the centre of the gamma camera detector and  $10.0 \pm 0.5$  cm from the face of the detector. A static image of the set up was acquired for 600 s using a matrix size of  $256 \times 256$  with a pixel size of 0.24 cm.

The system sensitivity was calculated in units of 'counts per second per Mega becquerel (cps/MBq)' using Eq. 1

$$\text{System Sensitivity} \left( \frac{\text{cps}}{\text{MBq}} \right) = \frac{\text{total counts in image}}{\text{time(s)} \times \text{activity(MBq)}} \quad (1)$$

**Septal penetration fraction:** The activity-filled petri dish with which system sensitivity was measured was also used to measure the collimator septal penetration fraction. The same acquisition parameters were implemented in acquiring the petri dish at distances of 5, 10, 15, 20, 25, 30, 35, and 40 cm from the detector of the gamma camera. The decay corrected count rates and the variable distance from the source to collimator were fitted to the function in Eq. 2.

$$R_i = c_0 + c_1 \exp(-c_2 D_i) \quad (2)$$

where  $c_0$ ,  $c_1$ , and  $c_2$  are fitting parameters,  $R_i$  is the decay corrected count rate and  $D_i$  is the distance from the detector to the bottom of the petri dish. The collimator penetration fraction ( $PF$ ) was calculated at  $D_N$ , where  $D_N = 10$  cm, using Eq. 3

$$PF = \frac{c_1 \exp(-c_2 D_N)}{c_0 + c_1 \exp(-c_2 D_N)} \quad (3)$$

### 2.2 Monte Carlo Simulation

#### SIMIND Monte Carlo code

The SIMIND MC code, written in FORTRAN-90 consists of two main programs, SIMIND and CHANGE (which provides a menu in which the system and the study to be modelled is defined). After defining the system in CHANGE, SIMIND executes this system.

All detector and intrinsic characteristics of the gamma camera were defined according to the Siemens Symbia T specification sheet [13]. The thickness of the cover of the scintillation crystal made of aluminium was defined in CHANGE as 0.1 cm. Acceptance test results for energy resolution and intrinsic spatial resolution of the camera were also defined in the CHANGE program to ensure that the characteristics of the physical camera and the digital camera matches.

The CT scanner of the hybrid gamma camera was used to acquire high resolution CT images of each experimental setup. The CT acquisition was carried out in a  $512 \times 512$  image matrix with a pixel size of  $0.127 \times 0.127$  cm<sup>2</sup> and a slice thickness of 0.5 cm. These CT images were segmented using ITK-SNAP version 3.6.0 [14]. Each segmented region of the CT images were assigned a unique value. These unique assigned segmentation values along with the density and radioactivity concentration values were saved in a text file (Zubal file) [4]. In-house software was used to convert

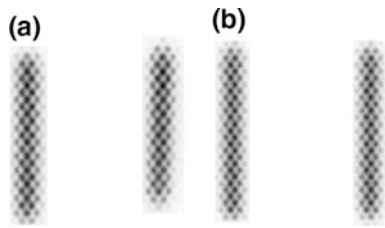


**Fig. 1** a Image of the measured capillary tubes for system spatial resolution b Simulated capillary tubes for system spatial resolution

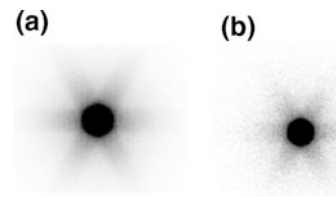


**Fig. 2** a Planar image of the measured sensitivity b Planar image of the simulated sensitivity

**Table 1** Results for the measured and simulated validation tests

Test	Measured	Simulated	Difference	%-difference
<i>Spatial resolution</i>				
FWHM (mm)	14.4 ± 0.72	13.9	0.5	-3.5%
FWTM (mm)	29.7 ± 1.20	25.9	3.8	-12.8%
<i>System sensitivity</i>				
(cps/MBq)	49.0 ± 0.26	48.0	1.0	-2.0%
<i>Septal penetration fraction</i>				
(%)	3.8 ± 0.01	4.2	0.4	10.5%

the Hounsfield values of the CT images to density values. These CT density images along with the text file and the segmented CT images served as input for the SIMIND MC code. The SIMIND MC code, with which the model of the Symbia T gamma camera, was created, was used to simulate the above mentioned experiments. The stop condition for each simulation was based on the same duration used to acquire the corresponding physical gamma camera measurements.

### 3 Results

Figures 1 and 2 show the images obtained for the extrinsic spatial resolution and system sensitivity validation tests. Figures 1a and 2a show the images obtained through measurement, while Figs. 1b and 2b show the simulated images.

Table 1 shows the results for both measured and simulated data for the validation tests. The measured data are shown as the mean value ± SD of the three repeated measurements.

### 4 Discussion and Conclusion

The results for the system spatial resolution shows good agreement between the measured and the simulated data. The differences between the measured and simulated FWHM and FWTM are 3.5% and 12.8% respectively. The difference between the measured and simulated FWTM can be attributed to the absence of the glass tube in the simulated

setup (which cause scatter in the physical measurement). The measured and simulated FWHM of the gamma camera were in good agreement with the specified value given by the manufacturer (13.4 mm).

The measured and simulated system sensitivity agree well as shown in Table 1. The percentage difference between the measured and simulated sensitivity values is 2.0%.

The collimator penetration fraction for the HEAP collimator with  $^{131}\text{I}$  was calculated to be 3.8% and 4.2% for the measured and simulated data respectively. The measured and simulated values compare favourably to the value specified by the manufacturer for the gamma camera fitted with HEAP collimators (3.5%).

The good agreement between the measured and simulated data implies that the SIMIND MC Code is suitable for modelling the Siemens Symbia T SPECT/CT dual head gamma camera fitted with HEAP collimators. This study was aimed at validating SIMIND for simulation of  $^{131}\text{I}$  images. The validation was performed to provide the confidence that the simulated images are true representations of the gamma camera images. The results obtained are comparable to those obtained for similar SIMIND validation tests for different gamma camera models and different isotopes as reported by other researchers [9, 15–18]. Thus SIMIND was accurately validated.

**Acknowledgements** We acknowledge Professor Michael Ljungberg (University of Lund, Sweden) for making SIMIND and technical support freely available. Funding support was received from the NRF/STINT grant, the Post Graduate School and Faculty of Health Sciences, University of Free State, Bloemfontein, South Africa respectively.

**Conflict of Interest** The authors declare that they have no conflict of interest.

## References

- Ljungberg M, Strand S-E, King MA. *Monte Carlo Calculations in Nuclear Medicine Applications in Diagnostic Imaging*. 1st ed. (Ljungberg M, Strand S-E, King MA, eds.). Bristow and Philadelphia: IOP Publishing; (1995).
- Braad PEN, Andersen T, Hansen SB, Hollund-Carlsen PF. Strategies for CT tissue segmentation for Monte Carlo calculations in nuclear medicine dosimetry. *Med Phys*. 43(12):6507–6516 (2016).
- Ljungberg M, Strand SE. A Monte Carlo program for the simulation of scintillation camera characteristics. *Comput Methods Programs Biomed*. 29(4):257–272 (1989).
- Ljungberg M. The SIMIND Monte Carlo program version 6.0. *SIMIND Man version 6*. pp. 1–54 (2017).
- Bostani M, Mueller JW, Mcmillan K, et al. Accuracy of Monte Carlo simulations compared to in-vivo MDCT dosimetry. *Med Phys*. 42(2):1060–1086 (2015).
- National Electrical, Manufacturers Association. NEMA Standards Publication NU 1–2007 Performance Measurements of Gamma Cameras. pp. 1–37 (2007).
- Lazaro D, Buvat I, Loudos G, et al. Validation of the GATE Monte Carlo simulation platform for modelling a CsI(Tl) scintillation camera dedicated to small-animal imaging. *Phys Med Biol*. 49(2):271–285 (2004).
- Momennezhad M, Sadeghi R, Naseri S. Development of GATE Monte Carlo simulation for a dual-head gamma camera. *Radiol Phys Technol*. 5:222–228 (2012).
- Gustafsson J, Brolin G, Cox M, Ljungberg M, Johansson L, Gleisner KS. Uncertainty propagation for SPECT/CT-based renal dosimetry in  $^{177}\text{Lu}$  peptide receptor radionuclide therapy. *Phys Med Biol*. 60(21):8329–8346 (2015).
- Gustafsson A, Arlig Å, Jacobsson L, Ljungberg M, Wikkelso C. Dual-window scatter correction and energy window setting in cerebral blood flow SPECT : a Monte Carlo study. *Phys Med Biol*. 45:3431–3440 (2000).
- Dewaraja YK, Ljungberg M, Koral KF. Characterization of Scatter and Penetration Using Monte Carlo Simulation in  $^{131}\text{I}$  Imaging. *J Nucl Med*. 41:123–131 (2000).
- Ferreira T, Rasband W. ImageJ User Guide. *Image J user Guid*. 1.46r (2012).
- Siemens AG. Symbia S and T System Specifications. 2010: pp. 1–12. <http://www.siemens.com/healthcare> last accessed 2016/11/10.
- Yushkevich PA, Piven J, Hazlett HC, et al. User-guided 3D active contour segmentation of anatomical structures: Significantly improved efficiency and reliability. *Neuroimage*. 1(3):1116–1128 (2006).
- Toossi BMT, Islamian PJ, Momennezhad M, Ljungberg M, Naseri SH. SIMIND Monte Carlo simulation of a single photon emission CT. *J Med Phy*. 35(1):42–47 (2010).
- Rong X, Du Y, Ljungberg M, Rault E, Vandenberghe S, Frey EC. Development and evaluation of an improved quantitative  $^{90}\text{Y}$  bremsstrahlung SPECT method. *Med Phys*. 39(5):2346–2358 (2012).
- Azarm A, Islamian JP, Mahmoudian B, Gharepapagh E. The Effect of Parallel-hole Collimator Material on Image and Functional Parameters in SPECT Imaging : A SIMIND Monte Carlo Study. *World J Nucl Med*. 14(3):160–164 (2015).
- Vicente EM, Lodge MA, Rowe SP, Wahl RL, Frey EC. Simplifying volumes-of-interest (VOIs) definition in quantitative SPECT : Beyond manual definition of 3D whole-organ VOIs. *Med Phys*. 44(5):1707–1717 (2017).

# A Model Describing the Multiphasic Dynamics of Mixed Meal Glucose Responses in Healthy Subjects

Manuel Eichenlaub, Natasha Khovanova, and John Hattersley

## Abstract

Modelling of the glucose metabolism for the purpose of improving the diagnosis and therapy of diabetes mellitus has been the subject of research for decades. Despite this effort, conventional models describing postprandial glucose profiles of healthy subjects fail to include the phenomenon of biphasic glucose responses. Continuous glucose monitoring data recorded from five healthy subjects show that mono- and biphasic glucose responses from regular meals are equally common. We therefore developed a suitable parametric model, capable of producing mono- as well as biphasic meal responses. It is expressed by linear second order differential equation with a dual Gaussian input function. Additionally, a simple method for classifying meal responses into mono- or biphasic profiles was developed. Model inversion was performed using a fully Bayesian method.  $R^2$  values of model output compared to CGM data was  $91.6 \pm 8.3\%$ , indicating the models ability of accurately describing a wide range of mixed meal glucose responses. Parameters were found to be associated with characteristics of individual meals. We suggest that the model could be used to objectively assess postprandial hyperglycemia, one of the main measures for glycemic control.

## Keywords

Healthy subjects • Input function • Postprandial glucose dynamics • System identification

## 1 Introduction

Diabetes mellitus is one of the most common metabolic disorders and manifests itself by a failure of the body to regulate the concentration of glucose in the blood in a healthy range. In this context, various diagnostic and therapeutic methods rely on knowledge of the underlying mechanisms of glucose regulation. For that reason, mathematical modelling of the glucose metabolism in the healthy as well as the diabetic state has gained much attention in research over the past decades. Hereby, one of the main focus points has been the metabolism in a postprandial state, modelled with the help of corresponding profiles glucose and other substances, e.g. insulin. The level of biomedical detail incorporated into those models is thereby strongly dependent on the experimental data available for model identification [1].

By analyzing postprandial glucose profiles from healthy subjects consuming mixed meals, i.e. meals containing carbohydrates as well as fat and protein, the occurrence of two distinct peaks rather than only one single peak in the profiles has been reported [2]. A similar effect has also been described with a pure glucose meal during an oral glucose tolerance test (OGTT) [3]. At present day, the occurrence of biphasic glucose responses has not been incorporated into models describing the postprandial glucose metabolism from mixed meals. Conventional models are only capable of producing monophasic (single peak) responses, including the well-established and highly influential simulation model by Dalla-Man et al. [4]. In those models it is common to use various types of input functions to model the impact of food on the glucose concentration. These input functions can be an impulse (e.g. [5]), of trapezoidal/triangular shape [6] or be described by the general functional form  $f(t) = t \exp(-t)$  or  $f(t) = t \exp(-t^2)$  [7, 8].

In this paper we present a model capable of describing monophasic as well as biphasic responses from mixed meals by introducing a type of input function, often used in the

M. Eichenlaub (✉) · N. Khovanova · J. Hattersley  
School of Engineering, University of Warwick, Coventry, CV4  
7AL, UK  
e-mail: m.eichenlaub@warwick.ac.uk

M. Eichenlaub · N. Khovanova · J. Hattersley  
Human Metabolism Research Unit, University Hospitals Coventry  
and Warwickshire, Coventry, CV2 2DX, UK

modelling of hormone secretion patterns [9]. The model was designed to be identified using only data from continuous, subcutaneous glucose monitoring (CGM). We demonstrate that the model possess enough flexibility to describe responses of greatly varying shape from different meals and that parameters of the model are related to the characteristics of the meal. Secondly we introduce a simple method for classifying meal responses as mono— or biphasic, based on similar process developed for sparsely sampled glucose data during an OGTT [3].

In doing so, we want to establish a method for objectively characterizing the postprandial glucose exposure under realistic conditions. Such a tool could be used to improve the assessment of the overall state of glycemic control in individuals affected by diabetes mellitus.

## 2 Methods

### 2.1 Data Collection

CGM data was collected from five healthy male subjects (Age: 26–47, BMI: 25.2–30.2 kg/m<sup>2</sup>) undergoing inpatient monitoring at the Human Metabolism Research Unit at the University Hospitals Coventry and Warwickshire, UK. For that, the Freestyle Navigator 2 CGM system (Abbot Diabetes Care Inc., 1360 South Loop Road, Alameda CA, USA) providing a 10-min sampling period was utilized. After a sufficient sensor “warm up” period, 18 h of consecutive glucose data, collected between 09:00 and 03:00 the following day was recorded. During this time, subjects consumed a total of four meals and performed two 30 min periods of light stepping exercise at 12:30 and 16:30. The meals consisted of standard western menu items and were identical for all subjects, with only the amounts adapted to ensure an isocaloric diet. In detail, the share of calories from carbohydrates and the overall share of the total daily calorie intake in percent for each meal were as follows: breakfast (52/25), lunch (44/34), dinner (47/26) and snack (74/15).

Prior to the study, appropriate ethical approval including the compliance with the Ethical Principles for Medical Research on Human Subjects set by Declaration of Helsinki was granted (REC Reference: 13/WM/0327).

### 2.2 Model Formulation

The basis for the model formulation is formed by the fact that the metabolism of a healthy person attempts to maintain glucose homeostasis, meaning that an inflow of glucose to the blood from a meal and the subsequent rise in concentration is rapidly compensated by the endocrine system. The model itself was adapted from previous publications [10, 11]

and consists of a linear second-order differential equation with a novel, nonlinear input function:

$$\ddot{x}(t) + \theta_1 \dot{x}(t) + \theta_2 x(t) = f(t, \theta) \quad (1)$$

$$x(0) = x_{01} \quad \dot{x}(0) = x_{02} \quad (2)$$

$$y(t) = x(t) + \varepsilon \quad \varepsilon \sim N(0, \lambda^2) \quad (3)$$

$$f(t, \theta) = \frac{\theta_4}{\sqrt{10\pi}} \exp\left(-\frac{(t-\theta_3)^2}{10}\right) + \frac{\theta_6}{\sqrt{100\pi}} \exp\left(-\frac{(t-\theta_5)^2}{100}\right). \quad (4)$$

The new external input function  $f(t, \theta)$  acts on the system describing the glucose concentration  $x(t)$ . In (3), the process of observing the CGM data  $y(t)$  is described as having a Gaussian distributed measurement error  $\varepsilon$  with zero mean and standard deviation  $\lambda$ . In (1) the linear system behavior is governed by the evolution parameters  $\theta_1$  and  $\theta_2$  with the initial conditions  $x_{01}$  and  $x_{02}$  being described in (2).

The input  $f(t, \theta)$  is defined through the summation of two Gaussian distributions and introduces additional evolution parameters  $\theta_3$  to  $\theta_6$ . By adapting these parameters, it is possible to induce both mono- and biphasic glucose responses from the model. It was designed to represent the biphasic process of glucose absorption. The first component of (4) models an initial inflow of glucose from carbohydrates, whereas the second component describes mixed and delayed effects of carbohydrates, fat and protein in the food. The widths of the two components (corresponding to the standard deviation of a Gaussian) were chosen to produce sharp or flat responses, associated with carbohydrates or fat/protein, respectively [12]. This gives the model the ability to produce a wide variety of responses to different meals as can be seen in Fig. 1.

### 2.3 Parameter Estimation

Equations (1)–(4) specify a total of nine parameters that have to be estimated from the CGM data only. The two initial conditions in expression (2) were fixed, because the dynamics of the model are mainly driven by the input function and therefore have little effect on the model output. This leaves a total of seven unknown parameters, i.e. the evolution parameters  $\theta_1$  to  $\theta_6$  and the measurement error  $\lambda$ , to be identified during model inversion. For that, a variational Bayesian numerical method was employed. It is a fully Bayesian method, allowing the identification of nonlinear models formulated with ordinary as well as stochastic differential equations [13]. By using Bayesian approach, all unknown parameters are characterized by probability distributions rather than fixed values. Furthermore, any existing



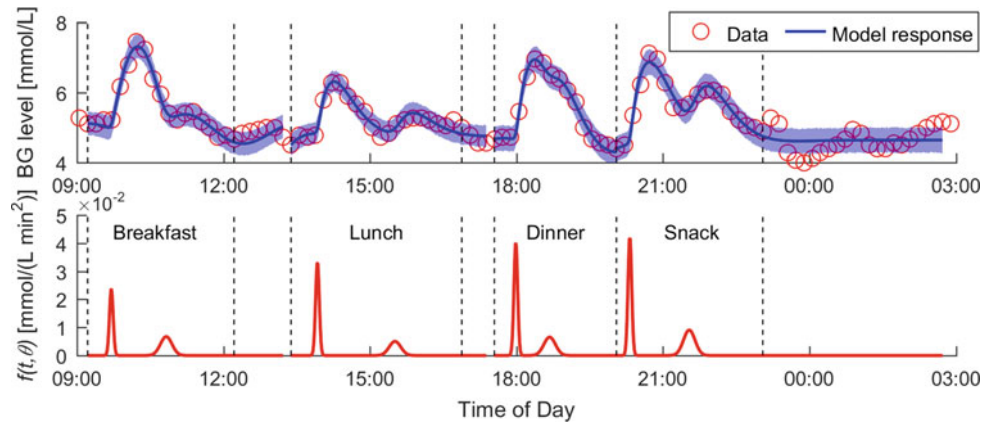


**Fig. 1** Top: example of model outputs with uncertainty. Bottom: plots of the respective input functions  $f(t, \theta)$ . The dashed vertical lines mark beginning and end of every meal period. Here breakfast and dinner

were classified as monophasic responses, whereas lunch and the snack were classified as biphasic

information about the parameters can be included into prior distributions. The particular inference method has been proven to be useful and robust by past research [10, 14].

Based on findings from a previous study [12] and the experimental schedule, the sections of CGM data under meal influence were extracted for each of the 20 recorded meals (see dashed vertical lines in Fig. 1). From that, the value of  $x_{01}$  was set to the first CGM value of the respective meal and  $x_{02}$  to the difference of the second and first measurement point. Additionally the offset of the CGM data was corrected by subtracting a basal glucose concentration value estimated as average between the first and last measurement point of each meal. This is justified by the fact that baseline levels on the timescale of one peak can be considered constant. After that, all seven model parameters were estimated for each individual meal.

All prior distributions utilized existing information to a varying extend. The prior for the measurement error  $\lambda$  was set to in accordance with the experimentally derived value of  $0.9 \pm 0.8$  mmol/L for the used CGM device [15]. The priors for the normally distributed evolution parameters ( $\theta_1$  to  $\theta_6$ ) were chosen to reflect physiologically sensible ranges or based on previous findings with a similar model structure [10].

All derivations were done in MATLAB 2015b (The MathWorks, Inc., 1 Apple Hill Drive, Natick MA, USA). An implementation of the inference method is published as an open-source library of MATLAB functions [16].

## 2.4 Classification of Meal Responses

The meal responses were classified according to the number of significant peaks within the response into the categories

“monophasic” for one and “biphasic” for two peaks. Based on the previously mentioned publication by Tschritter et al. [3], the following criteria for detecting peaks were developed: a continuous rise in BG level by at least 0.5 mmol/L or duration of 30 min and a subsequent continuous drop in BG level by at least 0.5 mmol/L or duration of 30 min. An automated algorithm applying these criteria to the meal responses was implemented.

## 3 Results

The quality of the model fit was evaluated using the coefficient of determination ( $R^2$ ). The overall mean and standard deviation for  $R^2$  are 91.6 and 8.3%, respectively. An example of model output is given in Fig. 1. The classification of the meal responses yielded an exact 50% split between monophasic and biphasic.

In order to increase the understanding in the inferred evolution parameters  $\theta_1$  to  $\theta_6$ , they were transformed into the following, more meaningful quantities:

$$\tau = \frac{2\pi}{\sqrt{\theta_2}} \quad \zeta = \frac{\theta_1}{2\sqrt{\theta_2}} \quad \Delta_T = \theta_5 - \theta_3 \quad \Phi_F = \frac{\theta_4}{\theta_6}. \quad (5)$$

In (5),  $\tau$  is the period of natural oscillation of the system in minutes and  $\zeta$  the damping factor (dimensionless).  $\Delta_T$  describes the time difference between the two peaks of the input function in minutes and  $\Phi_F$  the ratio between the intensities associated with the peaks (dimensionless).

Median values and interquartile ranges of all parameters grouped by meals are displayed in Table 1. The mean and standard deviation of  $\lambda$  over all responses are 0.32 and 0.04 mmol/L, respectively.

**Table 1** Parameters grouped according to meals. Values are given as median [IQR]

Meal	$\tau$ [min]	$\zeta$	$\Delta_T$ [min]	$\Phi_F$	$\lambda$ [mmol/L]
Breakfast	136 [116–146]	0.61 [0.37–0.67]	67.6 [62.4–81.2]	1.55 [1.02–1.80]	0.37 [0.30–0.39]
Lunch	193 [124–205]	1.09 [0.81–1.93]	94.2 [86.9–97.2]	2.11 [1.44–2.36]	0.29 [0.28–0.34]
Dinner	126 [94–135]	0.46 [0.41–0.55]	50 [39.7–2.9]	1.3 [1.11–2.38]	0.32 [0.32–0.33]
Snack	138 [121–179]	0.79 [0.36–1.15]	72.2 [66.2–78.3]	1.47 [1.33–1.56]	0.32 [0.31–0.34]

## 4 Discussion

Our experiments confirm previous findings, regarding the biphasic nature of mixed meal glucose responses [2]. The classification results show that biphasic responses are as common as monophasic responses, justifying the premise of this work and the need to include this phenomenon in realistic models. Apart from that, the main contribution of this work is the addition of an input function to an otherwise established model, allowing the description of a wide range of mono- and biphasic glucose responses. The functional form of two overlapping Gaussians is novel in the context of describing glucose dynamics and enables a high degree of flexibility by allowing the adjustment of the intensity and the timing of the peaks.

In Fig. 1 the capability of the model to accurately describe different degrees of biphasic and monophasic responses is exemplified. The results from the analysis of  $R^2$  values confirm this impression and show the model's ability to fit the data well.

Due to the small number of responses recorded per meal, the use of statistical testing in the analysis of parameters was intentionally forgone. Nevertheless, it is possible to infer information about the explanatory power of the model upon inspection of the parameters (Table 1). In comparison with other meals, the parameters  $\tau$  and  $\Delta_T$  are increased during lunch. This implies that the high overall calorie (34% of total daily carbohydrate intake) and especially fat/protein content (56% of calories) could cause prolonged hyperglycemia. The same argument can be made for the damping parameter  $\zeta$ , also being increased during lunch, compared to other meals. This suggests that these parameters are related to the food characteristics. On the other hand, the results of parameter  $\Phi_F$  do not clearly support the physiological interpretation of the input function as being related to the carbohydrate and fat/protein content of the food. Here, no similarities between ratios of macronutrients in the food and  $\Phi_F$  were found.

In terms of the measurement error  $\lambda$ , the inferred values ( $0.32 \pm 0.04$  mmol/L) lie well within the uncertainty limits

reported in literature ( $0.9 \pm 0.8$  mmol/L) [15]. Additionally, the small standard deviation of  $\lambda$  is a sign of consistent model fitting.

In terms of experimental design, the time difference between meals as well as the time difference between exercise and meal was short. This could have been a limiting factor in the modelling process due to overlapping effects of meals or meals and physical exertion. Additionally, the homogeneity and limited size of the study population hindered the explanatory power of results as well as the ability to relate the model parameters to physiological characteristics.

Based on previous findings in our group [10], this work can be considered as a further step towards our goal of improving the evaluation of glycemic control in people affected by diabetes mellitus. In particular, the model could be used to objectively assess postprandial hyperglycemia, one of the main measures for glycemic control [17]. Future experiments will focus on isolating the effects of different macronutrients and include subjects with different stages of impaired glucose tolerance and DM type 2.

**Conflict of Interest** The authors declare that they have no conflict of interest.

## References

1. C. Cobelli, C. D. Man, G. Sparacino, *et al.*, "Diabetes: Models, Signals, and Control," *IEEE Rev Biomed Eng*, vol. 2, pp. 54–96, Jan 1 2009.
2. D. C. Robbins, J. Jaspan, B. Vasquez, *et al.*, "Biphasic patterns of peripheral insulin and glucose levels after lunch in normal subjects," *Diabetes Care*, vol. 10, pp. 293–9, May–Jun 1987.
3. O. Tschritter, A. Fritsche, F. Shirkavand, *et al.*, "Assessing the shape of the glucose curve during an oral glucose tolerance test," *Diabetes Care*, vol. 26, pp. 1026–33, Apr 2003.
4. C. Dalla Man, R. A. Rizza, and C. Cobelli, "Meal simulation model of the glucose-insulin system," *IEEE Trans Biomed Eng*, vol. 54, pp. 1740–9, Oct 2007.
5. H. Kirchsteiger, R. Johansson, E. Renard, *et al.*, "Continuous-time interval model identification of blood glucose dynamics for type 1 diabetes," *Int J Control*, vol. 87, pp. 1454–1466, 2014.

6. E. D. Lehmann and T. Deutsch, "A physiological model of glucose-insulin interaction in type 1 diabetes mellitus," *J Biomed Eng*, vol. 14, pp. 235–42, May 1992.
7. R. Hovorka, V. Canonico, L. J. Chassin, *et al.*, "Nonlinear model predictive control of glucose concentration in subjects with type 1 diabetes," *Physiol Meas*, vol. 25, pp. 905–20, Aug 2004.
8. T. Pearson, J. A. Wattis, J. R. King, *et al.*, "A mathematical model of the human metabolic system and metabolic flexibility," *Bull Math Biol*, vol. 76, pp. 2091–121, Sep 2014.
9. M. L. Johnson, L. Pipes, P. P. Veldhuis, *et al.*, "AutoDecon: a robust numerical method for the quantification of pulsatile events," *Methods Enzymol*, vol. 454, pp. 367–404, 2009.
10. Y. Zhang, T. A. Holt, and N. Khovanova, "A data driven nonlinear stochastic model for blood glucose dynamics," *Comput Methods Programs Biomed*, vol. 125, pp. 18–25, Mar 2016.
11. H.-i. Wu, "A case study of type 2 diabetes self-management," *Biomed Eng Online*, vol. 4, pp. 1–9, 2005.
12. G. Freckmann, S. Hagenlocher, A. Baumstark, *et al.*, "Continuous glucose profiles in healthy subjects under everyday life conditions and after different meals," *J Diabetes Sci Technol*, vol. 1, pp. 695–703, Sep 2007.
13. J. Daunizeau, K. J. Friston, and S. J. Kiebel, "Variational Bayesian identification and prediction of stochastic nonlinear dynamic causal models," *Physica D: Nonlinear Phenomena*, vol. 238, pp. 2089–2118, 11/1/ 2009.
14. Y. Zhang, D. Briggs, D. Lowe, *et al.*, "A new data-driven model for post-transplant antibody dynamics in high risk kidney transplantation," *Math Biosci*, vol. 284, pp. 3–11, Feb 2017.
15. H. Thabit, L. Leelarathna, M. E. Wilinska, *et al.*, "Accuracy of Continuous Glucose Monitoring During Three Closed-Loop Home Studies Under Free-Living Conditions," *Diabetes Technol Ther*, vol. 17, pp. 801–807, 2015/11/01 2015.
16. J. Daunizeau, V. Adam, and L. Rigoux, "VBA: A Probabilistic Treatment of Nonlinear Models for Neurobiological and Behavioural Data," *PLoS Comput Biol*, vol. 10, p. e1003441, 2014.
17. American Diabetes Association, "Postprandial Blood Glucose," *Diabetes Care*, vol. 24, pp. 775–778, 2001.

# Geant4 Simulation for Commissioning of Proton Therapy Centre

Hong Qi Tan, Jun Hao Phua, Lloyd Tan, Khong Wei Ang, James Lee, and Andrew Anthony Bettiol

## Abstract

In anticipation of the new Proton Therapy Centre in Singapore at 2020, the medical physicists and physicists in NCCS and NUS have come together to do several preparation/preliminary works. Of which, one of the most important programme is to develop the Monte Carlo simulation capability using GEANT4 toolkit. We simulated the entire beam delivery and nozzle based on specifications given by Hitachi. The results of the Energy-Range curves in water phantom together with spot size in air agrees well with measurement data provided by Hitachi. We will show the complete methodology of simulation leading up to the comparison with measurement data. There were 3 main aspects we focused on—(1) The choice of physics models, (2) The determination of initial proton phase space based on Twiss parameters from beam profile measurement and (3) The choice of cut-off energy and step size. This simulation is important for the commissioning of the Proton Therapy System and the methodology presented will be helpful for other upcoming centers who are interested in doing the same.

## Keywords

Proton therapy • Monte Carlo • Beamline simulation

## 1 Introduction

The National Cancer Centre Singapore (NCCS) aims to start its first Proton Therapy treatment in 2021. This is a huge time gap before a physical Proton Therapy Beamline will be available for data collection, measurements, and clinical evaluations. There are available commercial Treatment Planning Systems (TPS) that allow clinicians, physicists and dosimetrists to prepare for the eventual operation of the Proton Therapy Centre. However, most of these analytical model-based TPS have limitations in their modeling of the proton dose distributions [1, 2].

Monte Carlo Simulation is a great tool for simulating radiation transport accurately and can potentially be used to simulate the entire Proton Therapy system [3–5]. Thus, there is a strong motivation to develop an in-house Monte Carlo-based Proton Therapy clinical system capable of producing fast and accurate results using highly parallelised code and GPUs. Furthermore, Monte Carlo simulated beam data can be used as input data to the clinical commercial TPS, thereby reducing the number of measurements during commissioning [6]. This can greatly improve efficiency of the Proton Therapy system commissioning.

In this paper, we will present the methodology of constructing such a Monte Carlo simulation using GEANT4 toolkit [7, 8] version 4.10.02.p02. GEANT4 toolkit is highly configurable and has proven to be invaluable in high energy physics, space technology and medical application. However, this toolkit can be daunting for first time user [2] due to the wide variety of settings available. Thus, our aim is to explain how the settings are chosen for the simulation of Depth-Dose curves (IDD) and in-air spot size at the isocenter for a PT (Proton Therapy) system. Based on our understanding, three important settings are crucial for successful simulation of a PT system—(1) Physics model, (2) Twiss parameters and (3) cut-off energy and stepsize. This simulation will model a Pencil Beam Scanning Proton Therapy

H. Q. Tan (✉) · A. A. Bettiol  
Department of Physics, Centre for Ion Beam Application, National University of Singapore, Singapore, Singapore  
e-mail: hqtan1988@gmail.com

J. H. Phua (✉) · L. Tan (✉) · K. W. Ang · J. Lee  
National Cancer Centre of Singapore, Singapore, Singapore  
e-mail: phua.jun.hao@nccs.com.sg

system which follows the specifications of NCCS's Proton Therapy system (Hitachi, Ltd. Healthcare Business Unit).

## 2 Method of Simulation

The entire geometry and material of the Proton Therapy nozzle is constructed in GEANT4 inheriting the G4VUserDetectorConstruction class. For the Scanning Proton Therapy system, the relevant components are Range Shifter, Main and Sub Dose Monitor, beam spot position monitor and the Kapton window. They will introduce longitudinal and lateral straggling which will affect the beam profile. The X and Y Scanning magnet can be included to deflect the beam in the lateral position by using the G4UniformMagField class and including a suitable integrator class such as G4SimpleRunge, G4HelixImplicitEuler or G4ImplicitEuler etc. The exact integrator class to be used depends on the accuracy, speed and magnetic field profile. However, this consideration is not relevant for the purpose of this paper, thus no magnetic field was applied to the scanner. The final geometry of the nozzle used in the simulation is shown in Fig. 1. The beam is set to start at the Beam Profile Monitor (BPM) as the phase space parameters for the beam is given at this component by the manufacturer. A  $30 \times 30 \times 30$  cm water phantom is placed at the isocenter with a user-defined sensitive detector (shown in Fig. 1 as a blue box) placed within for dose scoring. The geometrical configuration of the detector depends on both the physical quantity that we are interested in and the time required for the simulation. A 1-dimensional slice of resolution 0.1 mm was used along the beam direction for calculating the IDD curve whereas a 3-dimensional voxels of resolution 0.2 mm were used for calculating the beam spot size. The choice of resolution is decided based on the data given by the manufacturer and time required for simulation. The entire water phantom was used for scoring of IDD due to the long range of high energy proton, but only a thin slice

of water phantom at the isocenter is used for scoring of beam spot size as the longitudinal information is not required.

### 2.1 Physics Model

The choice of physics model is undisputedly the most important input for Monte Carlo Simulation and it often involves a trade-off between computation speed and accuracy. It has an impact on the spatial dose distribution which affects the IDD curve and beamspot size. The three main interactions of Proton (considering only energy of relevance to PT, <250 MeV) with biological material are inelastic coulomb scattering, elastic coulomb scattering and non-elastic nuclear reactions [9]. The first interaction contributes the most to defining the dose distribution in the longitudinal direction and the range of the particle, thus having the most impact on the shape of the IDD curve. The non-elastic nuclear reaction serves to reduce the fluence of the incident primary proton beam towards the Bragg Peak which in principle could affect the longitudinal dose distribution as well. However, this is less significant than the other interaction due to its lower cross section. Finally, the elastic coulomb scattering introduces lateral straggling to the proton beam and has a direct impact on the beamspot size.

Due to the significance of the Electromagnetic Process in defining dosimetric characteristic of the proton beam, this preliminary work will focus on investigating how different Electromagnetic (EM) Physics Model affects the IDD curve in water and beamspot size in air. The nuclear model QGSP\_BIC is recommended for medical application [10] and was used for our simulation. The list of models to be examined are:

1. emstandard\_opt1
2. emstandard\_opt2
3. emstandard\_opt3
4. emstandard\_opt4

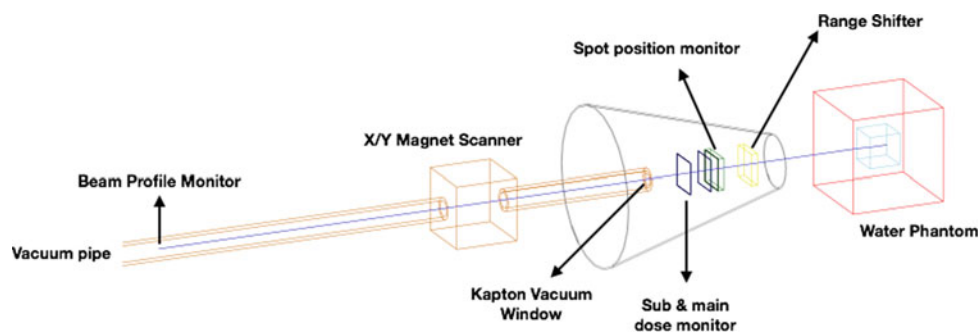


**Fig. 1** A schematic of the geometry used for simulation. The beam is set to start at the Beam Profile Monitor (BPM) and will traverse through the Kapton window, Sub and main dose Monitor, spot position monitor

and finally range shifter before hitting the water phantom centered at the isocenter. The blue cube in the water phantom is the sensitive detector for dose scoring



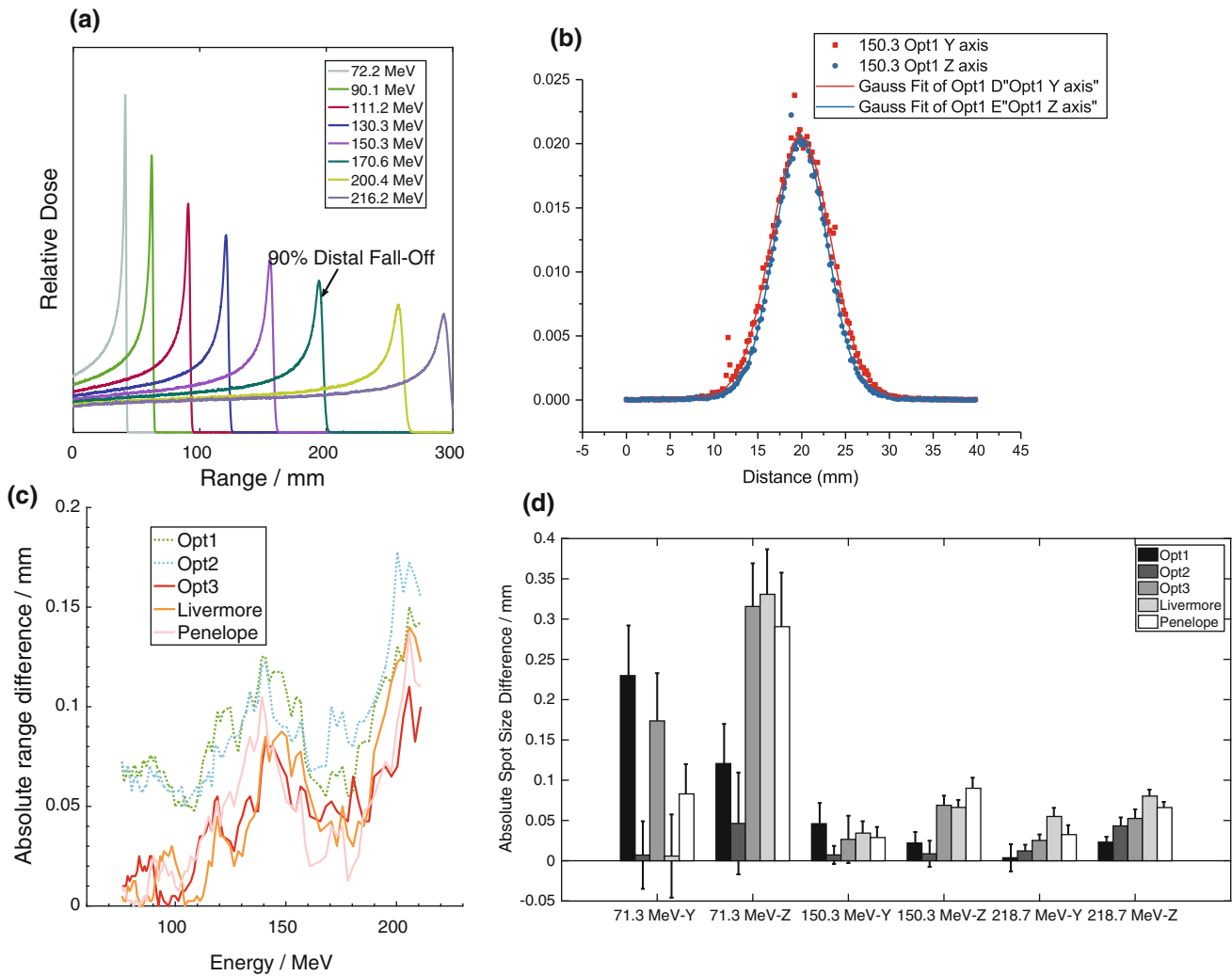


**Fig. 2** **a** Depth-dose curve for different proton’s energy and the definition of the range of proton as the 90% distal fall-off is shown in the figure. **b** Beamspot profile in both horizontal and vertical direction together with their Gaussian fits for 150.3 MeV proton beam. **c** Absolute range difference between the various physics models and

emstandard\_opt4. The dashed lines represent physics models that deviate the most from emstandard\_opt4 and the models represented by solid lines deviate the least. **d** Absolute difference in beamspot sizes for different physics models with respect to emstandard\_opt4

- 5. Livermore
- 6. Penelope.

The results of varying the physics models are shown in Fig. 2 using 20 millions proton in the simulation. Figure 2a shows the comparison of a IDD curves for different energy proton using “emstandard\_opt4” physics model. The definition of the range of proton as the 90% distal fall-off edge is also shown in Fig. 2a. Figure 2b shows the y-z beamspot distribution at the isocenter for a 150.3 MeV proton beam. The spot size is determined from the Gaussian fit of the beamspot distribution in Fig. 2b. Figure 2c shows the absolute range difference of proton under various physics models. This range difference is with respect to “emstandard\_opt4” as this is deemed to be the most accurate Electromagnetic physics model. It can be observed that the

choice of physics model has a greater impact on higher energy incident protons with range difference up to 0.2 mm. Also, emstandard\_opt3, Livermore and Penelope gives the same level of accuracy as emstandard\_opt4, whereas emstandard\_opt1 and emstandard\_opt2 differ the most from emstandard\_opt4. Hence, depending on the range tolerance and computational resources, users can settle for less accurate EM model such as emstandard\_opt2. Figure 2d shows the comparison of spot sizes under different Physics Models. The spot size are again computed with reference to emstandard\_opt4. There are no clear trends between different physics models in determining the spot size. This could be possibly due to the use of 0.2 mm voxel size in the simulation and differences might arise if a smaller voxel size is used. However, it is interesting to note that the impact of physics models seem to be less significant as the energy of

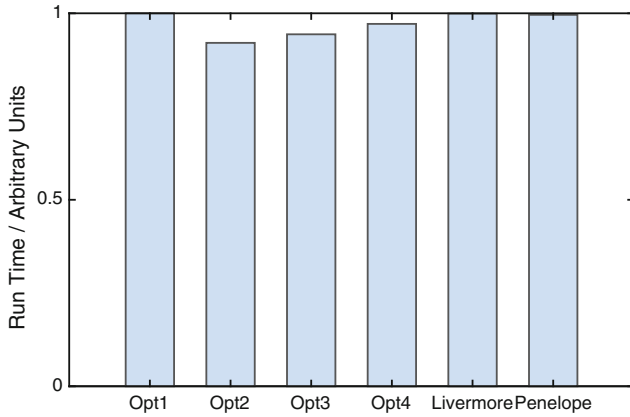


**Fig. 3** Comparison of the run time between different physics models

incident proton increases. The run time comparison of the different physics model is shown in Fig. 3 and is calculated using a single core intel xeon E5620 CPU. emstandard\_opt2 offers the fastest computation time and interestingly emstandard\_opt1 has similar run-time as Livermore, Penelope and emstandard\_opt4 models. This run time trend is for calculation in a homogeneous water medium and could vary substantially when the medium is composed of many different materials and complex geometry. Thus, results in Fig. 3 should be used with caution.

## 2.2 Twiss Parameters

This section focused on the modelling of the phase space in the simulation. The phase space description of the initial beam profile is crucial in calculating the final beamspot size at the isocenter. The phase space ellipse are characterized by 4 parameters— $\alpha$ ,  $\beta$  and  $\gamma$  known as the Twiss parameters and the emittance,  $\epsilon$  which is proportional to the area of the

phase space [11]. Using the Twiss parameters and emittance, the equation defining the ellipse is given by Eq. (1).

$$\gamma x^2 + 2\alpha x x' + \beta x'^2 = \epsilon \quad (1)$$

$$\beta\gamma - \alpha^2 = 1 \quad (2)$$

$x$  is the position and  $x'$  is related to the transverse momenta via  $p_x = p_0 \tan x'$ . For completeness, the maximal  $x$  for the ellipse is  $\sqrt{\epsilon\beta}$  and that of  $x'$  is  $\sqrt{\epsilon\gamma}$ . The three Twiss parameters are not independent and relate to each other through Eq. (2).

In this work, two of the Twiss parameters  $\alpha$  and  $\beta$ , and the Emittance are given by the manufacturer at the BPM for both the vertical and horizontal beam profiles (total of 6 parameters). The  $\gamma$  parameter can be calculated from Eq. (2). In order to sample the  $x - x'$  values from the phase space ellipse, we assumed a bivariate gaussian distribution [11] with covariance matrix given by Eq. (3)

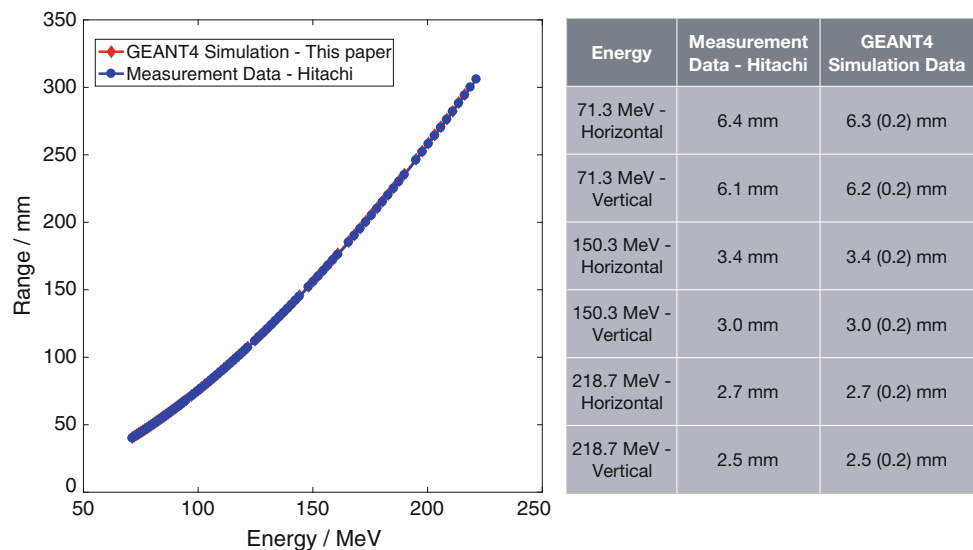
$$\begin{pmatrix} \text{Var}(x) & \text{Cov}(x, x') \\ \text{Cov}(x, x') & \text{Var}(x') \end{pmatrix} = \begin{pmatrix} \epsilon\beta & \epsilon\alpha \\ \epsilon\alpha & \epsilon\gamma \end{pmatrix} \quad (3)$$

Lastly, using Cholesky decomposition technique on the covariance matrix [12], any bivariate gaussian distribution can be sampled from standard normal distribution where the latter is included in GEANT4 G4RandGauss class. This concludes the modelling of the initial phase space distribution of the beam given the Twiss parameters and Emittance.

## 2.3 Cut-Off Energy and Step Size

The cut-off energy and step size are input parameters that are necessary for Monte Carlo simulation [13]. Ideally, a smaller cut-off energy and step size will yield a more accurate result, but this is at the expense of computation speed. Furthermore, there is a practical voxel size resolution of the sensitive

**Fig. 4** Left: Comparison of Hitachi measurement data (blue circle solid line) and GEANT4 simulation data (red diamond solid line). Right: Comparison of transverse 2D beam spot size between Manufacturer's data and simulation for 3 representative energies



detector. If the cut-off range or step size is much smaller than the voxel resolution, the accuracy of the result will not improve. However, it is not clear from literature what is the best recommended cut-off energy (or range) and step size without compromising the computation speed. In this study, we varied both the step size and cut-off from 0.02 to 0.5 mm, but did not observe any clear difference in range and spot size beyond the voxel resolution.

### 3 Comparison with Provided Data

The comparison between the measurement data from the manufacturer and our simulation is shown in Fig. 4. The final setting used in the simulation is emstandard\_opt4 physics model together with manufacturer input of  $\alpha$ ,  $\beta$ ,  $\epsilon$  parameters and step size and cut-off of 0.1 mm each. The left figure in Fig. 4 shows the range comparison and the deviation from data is generally less than 0.5 mm for most energy. However, deviation up to 0.8 mm can be observed for energy more than 200 MeV. The right figure in Fig. 4 shows the spot size comparison and there is excellent agreement between manufacturer's data and simulation data.

### 4 Conclusion

We have validated our configuration of the Geant4 Monte Carlo simulation toolkit based on the specifications of our Proton Therapy beamline from the manufacturer. Further work includes building a customizable treatment planning and clinical evaluation system for Proton Therapy. We aim to extend this development for various studies, including, (1) radiobiological effects, (2) 4D robust optimizations, (3) 4D dose distributions evaluations, (4) commercial treatment planning system validations, and eventually (5) as a commissioning tool during clinical commissioning of our Proton Therapy system.

**Disclosures** No conflicts of interest, financial or otherwise, are declared by the authors.

### References

1. Saini, J., Cao, N., Bowen, S.R., Herrera, Mi., Nicewonger, D., Wong, T., Bloch, C.D.: Clinical Commissioning of a Pencil Beam Scanning Treatment Planning System for Proton Therapy. *International Journal of Particle Therapy* 3(1), pp 51–60 (2016). <https://doi.org/10.14338/IJPT-16-0000.1>.
2. Taylor, P.A., Kry, S.F., Followill, D.S.: Pencil Beam Algorithms Are Unsuitable for Proton Dose Calculations in Lung. *Int. J. Radiat. Oncol. Biol. Phys.* 99(3), pp 750–756 (2017). <https://doi.org/10.1016/j.ijrobp.2017.06.003>.
3. Paganetti, H., Jiang, H., Lee, S.Y., Kooy, H.M.: Accurate Monte Carlo simulations for nozzle design, commissioning and quality assurance for a proton radiation therapy facility. *Med. Phys.* 31, pp 2107–2118 (2004). <https://doi.org/10.1118/1.1762792>.
4. van Goethem, M.J., van der Meer, R., Reist, H.W., Schippers, J. M.: Geant4 simulations of proton beam transport through a carbon or beryllium degrader and following a beam line. *Phys. Med. Biol.* 54, pp 5831–5846 (2009). <https://doi.org/10.1088/0031-9155/54/19/011>.
5. Aso, T., Kimura, A., Tanaka, S., Yoshida, H., Kanematsu, N., Sasaki, T., Akagi, T.: Verification of the Dose Distributions With GEANT4 Simulation for Proton Therapy. *IEEE Transactions on Nuclear Science* 52(4), pp. 896–901 (2005). <https://doi.org/10.1109/tns.2005.852697>.
6. Clasié, B., Depauw, N., Fransen, M., Gom, C., Panahandeh, H.R., Seco J., et al.: Golden beam data for proton pencil-beam scanning. *Phys. Med. Biol.* 57(5), pp 1147 (2012). <https://doi.org/10.1088/0031-9155/57/5/1147>.
7. Agostinelli, S., Allison, J., et. al.: Geant4 - a simulation toolkit. *Nucl. Instr. Meth. Phys. A.* 506, pp 250 (2003). <https://doi.org/10.2172/799992>.
8. Allison, J., Amako, K., et. al.: Recent developments in Geant4. *Nucl. Instr. Meth. Phys. A.* 835, pp 186 (2016). <https://doi.org/10.1016/j.nima.2016.06.125>.
9. Newhauser, W.D., Zhang, R.: The physics of proton therapy. *Phys. Med. Biol.* 60, pp R155 (2015). <https://doi.org/10.1088/0031-9155/60/8/r155>.
10. Cirrone, G.A.P., Cuttone, G., Guatelli, S., Lo Nigro, S., et. al.: Implementation of a new Monte Carlo simulation tool for the development of a proton therapy beam line and verification of the related dose distributions. *IEEE Transactions on Nuclear Science*, 52, pp 1756–1758 (2005). <https://doi.org/10.1109/nssmic.2003.1352218>.
11. Wiedemann, H.: *Particle Accelerator Physics*, Springer (2015).
12. Horn, R.A., Johnson, C.R.: *Matrix Analysis*. Cambridge University Press (1985).
13. Vassiliev, O.N.: *Monte Carlo Methods for Radiation Transport*. Springer (2017).

# 3D Quantification of Biological Damage for a 160 MeV Proton Beam

Hong Qi Tan, Khong Wei Ang, and Andrew Anthony Bettioli

## Abstract

Current Treatment Planning System uses advanced optimization algorithm with Dose Calculation Engine to optimize the dose delivered to the tumor to maximize the tumor-killing potential while limiting the side-effects to the normal tissues. Working in parallel, there are various radiobiology simulation programs being developed by different research groups to quantify biological endpoints such as Double Strand Breaks (DSBs) yield and Chromosome Aberration (CA) induced by different radiation types. In this paper, we conduct a novel preliminary work to combine these two areas to determine DSB yields in a 3D CT geometry. Our preliminary result shows that the position of the Bragg Peak determined from dose deposition differs from the position of maximal DSB yields. The difference can range from 0 to 1 mm, hence showing that dose is not entirely indicative of biological damage in tissue.

## Keywords

Proton therapy • Monte Carlo • Radiobiology simulation

## 1 Introduction

Proton radiobiology has received increasing attention due to evidence that for some endpoints it can trigger a different biological response compared to conventional X-rays [1]. As a result, a proper understanding of proton radiobiology could allow us to optimize the treatment delivered using Proton Therapy (PT), yielding greater positive clinical outcomes.

H. Q. Tan (✉) · A. A. Bettioli  
Department of Physics, Centre for Ion Beam Application, National University of Singapore, Singapore, Singapore  
e-mail: hqtan1988@gmail.com

K. W. Ang  
National Cancer Centre of Singapore, Singapore, Singapore  
e-mail: ang.khong.wei@nccs.com.sg

Currently there are both experimental and computational approaches towards achieving this goal. The latter approach focus on using mathematical model with biological inputs consistent with experiment to quantify biological endpoints such as DSBs, CAs or clonogenic cell survival. There are several groups working on establishing a computational model for this purpose [2–6]. Even though the goal is the same, the approaches and method of implementations differ between the various models. Due to the fact that most of these models are still in development phase, our group in Centre of Ion Beam Application (CIBA) decided to develop our own radiobiology software titled Integrated Radiobiology Simulation with Geant4 and System biology (IRSGS; pronounced as eye-ris) for this purpose. In this paper, we develop a novel methodology to combine the DSBs quantification from IRSGS into a 3D CT geometry and compare it to the dose deposition in this similar geometry. This preliminary study shows that the maximal DSBs spatial location does not coincide with the Bragg's peak, with the maximal DSBs being about 1 mm further. Hence, showing that dose is not entirely indicative of biological damage. This simulation result agrees with experimental observation in Refs. [7, 8]. It is important to note that DSB is not entirely indicative of the cell-killing potential but the initial DNA damage. Chromosome Aberration will be a more suitable endpoint for this purpose but has yet to be included in our IRSGS software. We will first cover the mathematical framework for integrating DSBs quantification in any geometry follow by the results and discussion, and finally the conclusion.

## 2 Mathematical Framework

This section will present the mathematical framework that is used for quantifying the DSB yields in a 3D geometry. The output of IRSGS and other simulation softwares is DSB yield per Giga-basepairs (Gbps) and per Gray,  $Y_{dsb}$  whereas a more appropriate measure of biological damage is DSBs

per GBps,  $Y_{dsb}^D$ . The relation between these two quantities is given in Eq. (1).

$$Y_{dsb}^D(\mathbf{r}) = \int Y_{dsb}(E)D(\mathbf{r}, E)dE \quad (1)$$

$E$  is the energy of the proton particle and  $Y_{dsb}(E)$  is dependent on the energy of the particle.  $D(\mathbf{r}, E)$  is the dose deposited by a proton of energy  $E$  at position  $\mathbf{r}$ . By running the simulation several times for different values of the initial incident proton energy, we obtained a relation between the Linear Energy Transfer (LET) of the particle and  $Y_{dsb}$ . In general, we can express the relationship as a power series as shown in Eq. (2).

$$Y_{dsb}(E) = \sum_i a_i LET(E)^i \quad (2)$$

$a_i$  is the fitting constants for the  $i$ -th term of the power series. However, for proton radiation, our simulation together with other works show that the relation between  $Y_{dsb}$  and LET is approximately linear [2, 4, 9] which is not the case for heavy ion radiation such as carbon ions, alpha particle or oxygen ions or even neutrons. It is important to note that the overkill effect will introduce maximum peak and nonlinearity in the  $Y_{dsb}$  and LET relation which exists only for high LET greater 100 keV/ $\mu\text{m}$ . This range of LET is not achievable by proton ions which is regarded as a low LET radiation. Thus, retaining only the first two terms of Eq. (2), we obtained Eq. (3).

$$Y_{dsb}(E) = a_0 + a_1 LET(E) \quad (3)$$

Substituting Eq. (3) into Eq. (1) and using the relation  $\int D(\mathbf{r}, E)dE = D(\mathbf{r})$  and the definition of dose-averaged LET,  $LET_D(\mathbf{r}) = \int LET(E) \times D(\mathbf{r}, E)dE / \int D(\mathbf{r}, E)dE$ , we obtain Eq. (5)

$$Y_{dsb}^D(\mathbf{r}) = a_0 \int D(\mathbf{r}, E)dE + a_1 \int LET(E)D(\mathbf{r}, E)dE \quad (4)$$

$$= [a_0 + a_1 LET_D(\mathbf{r})]D(\mathbf{r}) \quad (5)$$

Equation (5) gives the crucial mathematical relation in evaluating 3D distribution of DSBs yield,  $Y_{dsb}^D(\mathbf{r})$ . It only requires information of the 3D dose and  $LET_D$  distribution in the geometry as well as the fitting parameters  $a_0$  and  $a_1$  (determined from radiobiology simulation). The dose and  $LET_D$  in 3D geometry of defined materials can be calculated by various methods [12, 13] and  $a_0$ ,  $a_1$  are determined from radiobiology simulations. The simple form of Eq. (3) is due to the linear  $Y_{dsb}$ -LET relationship. Under different irradiation condition used in the simulations (such as different particle or DNA geometry etc.), higher order terms in the power series might be required and  $Y_{dsb}^D$  will depend on higher moments of LET.

### 3 Results and Discussions

As mentioned in the previous section, the first step in quantifying 3D DSB yield distribution  $Y_{dsb}^D(\mathbf{r})$  is calculating the fitting constants  $a_0$  and  $a_1$ . The plot of  $Y_{dsb}$  against LET for IRSGS and other simulations [2, 4] are shown in Fig. 1. The DSB scoring in IRSGS is based on DBSCAN algorithm and the criteria that two SSBs on opposite DSB strand must occur within 10 basepairs from each other. If multiple SSBs exists within 10 basepairs, DBSCAN algorithm will classify them as a single DSB. In general, even though the details of implementation differ between simulations, the DSB yields agree with each other. The difference in range of the LET values between simulations is due difference in physics models between GEANT4 and PARTRAC [2, 5] which results in different LET value for the same incident proton energy. The estimated fitting parameters from all the simulation data are  $a_0 = 7.977$  and  $a_1 = 0.172$ .

Next, the 3D  $LET_D$  and Dose distribution is calculated in the geometry. For this preliminary studies, we used a real CT data of a lung irradiated by a monoenergetic 160 MeV proton beam and calculated the dose and  $LET_D$  using our in-house GEANT4-based Monte Carlo code (the physics models in GEANT4 have been well-validated [14, 15]) which has been validated with commercial Eclipse TPS by Varian Medical System. The conversion of Hounsfield units in CT image to atomic composition for Monte Carlo calculation is achieved using the method by [16]. This study does not include dose uncertainty due to HU conversion or motion as this is a preliminary study to present a methodology of determining 3D DSB yields in a CT image. Such considerations will be included in further work. Figure 2a, b

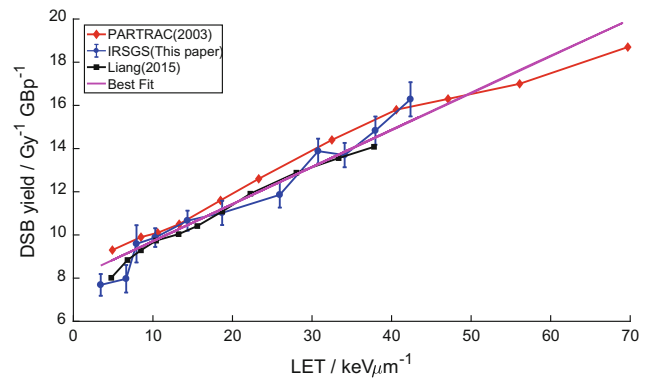


**Fig. 1** This figure compares the DSB yields across different simulation programs. The red diamond data are from PARTRAC [2]. The black square data are from [4]. The blue circle data with error bars are produced from our own software, IRSGS. The magenta solid line is the best fit line obtained from performing linear regression on all the simulation data. The error bars from IRSGS originated the statistical fluctuation in Monte Carlo simulation. The best fit line equation is  $Y_{dsb} = 7.977 + 0.172 \times LET$



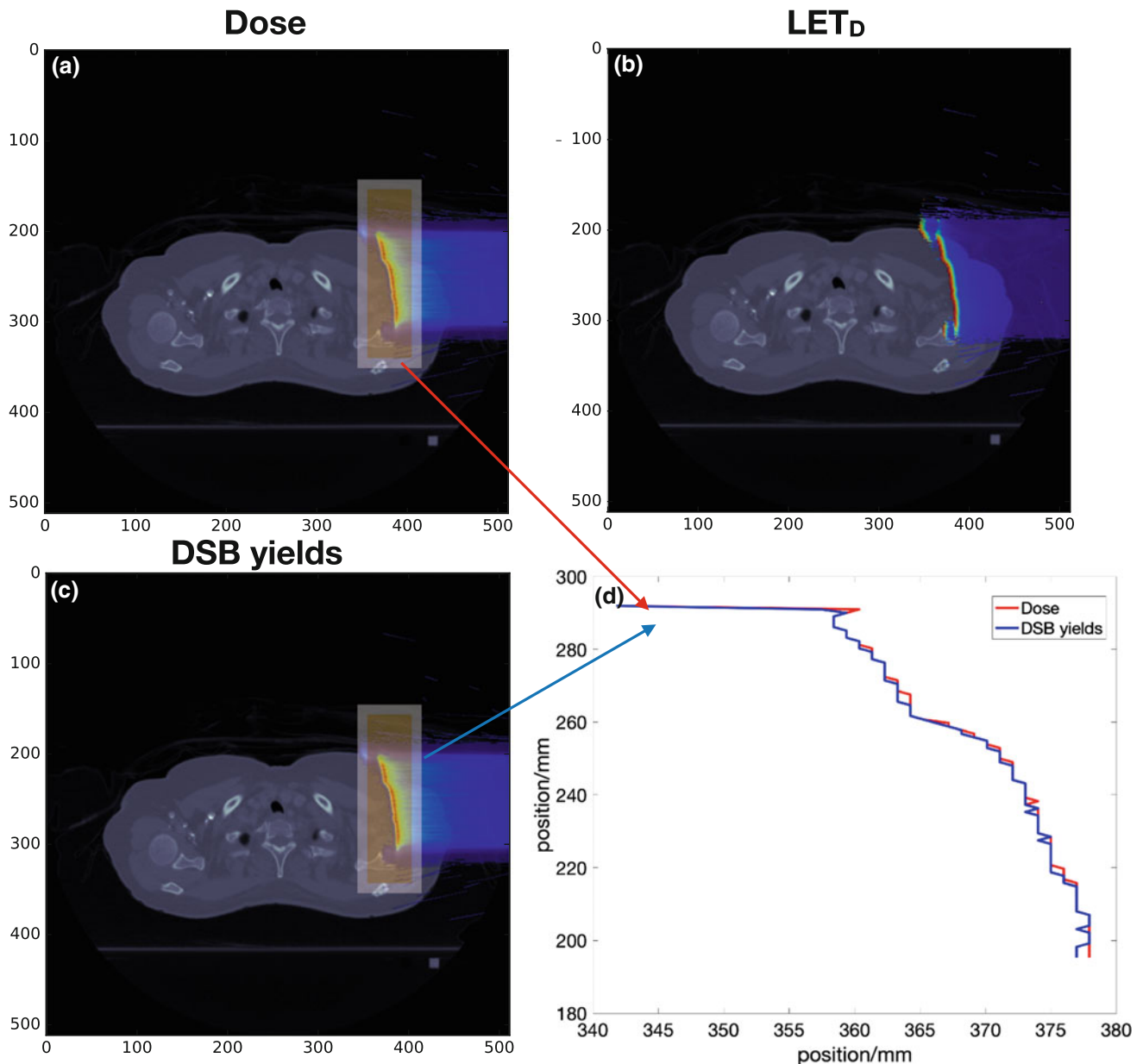


**Fig. 2** **a** Shows the dose deposited in the lung from a 160 MeV proton beam calculated using our in-house GEANT4-based Monte Carlo dose calculation engine. **b** Shows the  $LET_D$  distribution in the lung using the same Monte Carlo code. The secondary neutrons are omitted in this

calculation. **c** 3D distribution of  $Y_{dsb}^D$ . The horizontal and vertical axis for Fig. 2a, b and c are in millimeter. **d** The comparison of the position of the maximal  $Y_{dsb}^D$  (in blue solid line) and the Bragg peak (in red solid line) along the region highlighted in Fig. 2a, c

and c show the dose,  $LET_D$  and  $Y_{dsb}^D$  for a slice of the CT data respectively. The calculation of  $LET_D$  in Monte Carlo simulations follows the approach by [10, 11] and omits the contribution of secondary neutron particles. A visual inspection between Fig. 2a and c seems to suggest they are largely similar. However, a close analysis of the regions highlighted in both figures shows a difference in the spatial positions between their maximal values. Figure 2d shows the comparison between the spatial position of the *maximal*

*DSB yield* and the *Bragg's peak position* along the highlighted regions in Fig. 2c, a respectively. 21% of the data in Fig. 2d shows a 0–1 mm difference between their maximal position with the  $Y_{dsb}^D$  being deeper in the target. This distance discrepancy is non-negligible from a clinical viewpoint. The percentage of data having the discrepancy depends significantly on the geometry and heterogeneity of the target and cannot be estimated prior to performing this calculation. More importantly, this result shows that

maximal dose does not necessarily imply maximal  $Y_{dsb}^D$  and dose is not entirely indicative of biological damage.

## 4 Conclusion

In this paper, we introduced a novel method to determine the DSB yield in a 3D heterogeneous geometry based on Eq. (5) and applied this to a simple test scenario of irradiating a Lung geometry with a monoenergetic 160 MeV proton beam. In doing so, we found that the maximal biological damage could extend up to 1 mm beyond the Bragg peak. This result resembles the concept of RBE weighted dose [9, 17], but offers a different perspective (more radiobiology-oriented) and does not require the knowledge of  $\alpha/\beta$  parameter. Further work includes extension to other biological endpoints (such as to yield a 3D distribution of CA) and running the simulations with realistic clinical proton beam configurations.

**Disclosures** No conflicts of interest, financial or otherwise, are declared by the authors.

## References

- Girdhani, S., Sachs, R., Hlatky, L.: Biological Effects of Proton Radiation: What We Know and Don't Know. *Radiat. Res.* 179(3), 257–272 (2013). <https://doi.org/10.1667/RR2839.1>.
- Friedland, W., Jacob, P., Bernhardt, Ph., Paretzke, H.G., Dingfelder, M.: Simulation of DNA damage after proton irradiation. *Radiat. Res.* 159, 401–410 (2003). [https://doi.org/10.1667/0033-7587\(2003\)159\[0401:SODDAP\]2.0.CO;2](https://doi.org/10.1667/0033-7587(2003)159[0401:SODDAP]2.0.CO;2).
- Friedland, W., Jacob, P., Kundrat, P.: Mechanistic simulation of radiation damage to DNA and its repair: On the track towards systems radiation biology modelling. *Radiat. Prot. Dosimetry* 143, 542–548 (2011). <https://doi.org/10.1093/rpd/ncq383>.
- Liang, Y., Yang, G., Liu F., Wang, Y.: Monte Carlo simulation of ionizing radiation induced DNA strand breaks utilizing coarse grained high-order chromatin structure. *Phys. Med. Biol.* 61, 445–460 (2016). <https://doi.org/10.1088/0031-9155/61/1/445>.
- Meylan, S., Incerti, S., Karamitros, M., Tang, N., Bueno, M., Clairand, I. and Villagrasa, C.: Simulation of early DNA damage after the irradiation of a fibroblast cell nucleus using Geant4-DNA. *Sci. Rep.* 7:11923 (2017). <https://doi.org/10.1038/s41598-017-11851-4>.
- Semenenko, V. A., Stewart, R. D.: A fast Monte Carlo algorithm to simulate the spectrum of DNA damages formed by ionizing radiation. *Radiat. Res.* 161(4), 451–457 (2004). <https://doi.org/10.1667/rr3140>.
- Chauhary, P., Marshall, T. I., Periziello, F. M., Manti, L., et al.: Relative Biological Effectiveness Variation Along Monoenergetic and Modulated Bragg Peaks of a 62-MeV Therapeutic Proton Beam: A Preclinical Assessment. *Int. J. Radiat. Oncol. Biol. Phys.* 90, 27–35 (2014). <https://doi.org/10.1016/j.ijrobp.2014.05.010>.
- Wouters., B. G., Lam, G. K. Y., Oelfke, U., Gardey, K., Durand, K. E. and Skarsgard, L. D.: Measurements of Relative Biological Effectiveness of the 70 MeV Proton Beam at TRIUMF Using Chinese Hamster V79 Cells and the High-Precision Cell Sorter Assay. *Radiat. Res.* 146, 169–170 (1996) <https://doi.org/10.2307/3579588>.
- Paganetti, H.: Relative biological effectiveness (RBE) values for proton beam therapy. Variations as a function of biological endpoint, dose, and linear energy transfer. *Phys. Med. Biol.* 59(22), R419–72 (2014). <https://doi.org/10.1088/0031-9155/59/22/r419>.
- Guan, F., Peeler, C., Bronk, L., Geng, C., Taleei, R., Randeniya, S.: Analysis of the track- and dose-averaged LET and LET spectra in proton therapy using the GEANT4 Monte Carlo Code. *Med. Phys.* 42(11) (2015) <https://doi.org/10.1118/1.4932217>.
- Grassberger, C., Paganetti, H.: Elevated LET components in clinical proton beams. *Phys. Med. Biol.* 56, 6677–6691 (2011). <https://doi.org/10.1088/0031-9155/56/20/011>.
- Wilkens, J.J., Oelfke, U.: Analytical linear energy transfer calculations for proton therapy. *Med. Phys.* 30, 806–815 (2013). <https://doi.org/10.1118/1.1567852>.
- Cortes-Giraldo, M., Carabe, A.: A critical study of different Monte Carlo scoring methods of dose average linear-energy-transfer maps calculated in voxelized geometries irradiated with clinical proton beams. *Phys. Med. Biol.* 60, 2645–2669 (2015). <https://doi.org/10.1088/0031-9155/60/7/2645>.
- Agostinelli, S., et al.: Geant4 - A Simulation Toolkit. *Nucl. Instr. Meth. A* 506, 250–303 (2003). <https://doi.org/10.2172/799992>.
- Allison, J., et al.: Recent Developments in Geant4. *Nucl. Instr. Meth. A* 835, 186–225 (2016). <https://doi.org/10.1016/j.nima.2016.06.125>.
- Schneider, W., Bortfield, T., Schlegal, W.: Correlation between CT numbers and tissue parameters needed for Monte Carlo simulations of clinical dose distributions. *Phys. Med. Biol.* 45(2), 459–478 (2000).
- Wambersie, A., Gahbauer, R.A., Menzel, H.G.: RBE and weighting of absorbed dose in ion-beam therapy. *Radiother. Oncol.* 73 Suppl 2, S176–82 (2004). [https://doi.org/10.1016/s0167-8140\(04\)80044-6](https://doi.org/10.1016/s0167-8140(04)80044-6).

# Dynamic Effects of Obstructed Airways Mechanics on the Forced Expiratory Curve

Adam G. Polak , Dariusz Wysoczański , and Janusz Mrocza 

## Abstract

Spirometry is the most popular test of lung function. Its status arises from the effort-independence of the maximal expiratory flow-volume (MEFV) curve, its reproducibility for a given subject and simultaneous sensitivity to respiratory disorders. Previous trials have shown that the morphology-based, quasi-static models cannot reproduce characteristic swings in the MEFV curve, sometimes visible in the case of obstructive diseases. The aim of this work was to test the hypothesis that the aforementioned details in the MEFV curve are caused by dynamic phenomena occurring during forced expiration, and that they manifest particularly in obstructive diseases. To this end, the computational model for forced expiration including the fundamental physical phenomena in quasi-static conditions was further developed by including the dynamic phenomena: additional flows from narrowing airways, and gas compressibility and inertia. The MEFV curves simulated using the quasi-dynamic and quasi-static models were then compared for a variety of respiratory system states. For most simulated cases, the differences between forced expiratory curves computed with the models were negligible. Only implementing some specific conditions causing flow limitation in small airways yielded a visible alteration and the characteristic swing after the peak expiratory flow (PEF). Concluding, the dynamic effects of airway narrowing and gas compressibility and inertia modify the MEFV curve near the PEF slightly and only in specific cases. This finding justifies the general use of the quasi-static models as an adequate tool for forced expiration simulations.

## Keywords

Forced expiration • Quasi-dynamic model  
Small airways obstruction

## 1 Introduction

Spirometry is the most widely used test of lung function, characterised by high sensitivity and specificity. Its status arises from the effort-independence (thus objectivity) of the registered maximal expiratory flow-volume (MEFV) curve, its reproducibility for a given subject and simultaneous sensitivity to respiratory disorders, such as chronic obstructive pulmonary disease (COPD) or asthma [1].

A few methodologies to model and simulate forced expiration have been proposed for the last decades. They can be grouped into two general approaches: simplified dynamic models built with electrical analogue elements as resistances, capacitors, inductive coils or transistors [2–4]; and morphology-based complex models assuming a quasi-static flow of incompressible air through a symmetric [5–7] or asymmetric bronchial tree [8, 9]. Previous trials have shown that the complex quasi-static models cannot reproduce some specific swings in the MEFV curve, sometimes visible in the case of obstructive diseases.

The aim of this work was to test the hypothesis that the aforementioned specific details in the MEFV curve are caused by dynamic phenomena occurring during forced expiration, and that they manifest particularly in obstructive diseases.

## 2 Methods

### 2.1 Quasi-static Model for Forced Expiration

The quasi-static computational model for maximum expiration through the symmetrical bronchial tree of a healthy

A. G. Polak (✉) · D. Wysoczański · J. Mrocza  
Wrocław University of Science and Technology, Wrocław, Poland  
e-mail: adam.polak@pwr.edu.pl

subject has been described elsewhere [6, 7]. Briefly, it includes Weibel's bronchial structure [10], lung tissue and airway (the so-called tube law) nonlinear mechanical properties, and fundamental physical phenomena as wave-speed and dissipative flow limitation.

The model assumes a static flow through the airways for a given lung volume to calculate pressure losses along the bronchial tree and upper airways, and takes into account the change of lung elastic recoil with its volume modifying the driving pressure, and thus the maximal flow at this lung volume. The used procedure checks pressure drops for tested expiratory flows and finds the flow satisfying the driving pressure excitation (see [6] for details). Finally, the whole MEFV curve is simulated at quasi-static flow conditions.

## 2.2 Quasi-dynamic Model for Forced Expiration

The quasi-static model described above, predicting expiratory flows for succeeding lung volumes, was further developed by including the dynamic phenomena: additional flows from airways narrowing during expiration and produced by gas compressibility, as well as intra-airway pressure modifications caused by gas inertia. All these effects were implemented in a discrete manner, i.e. using the respiratory states at the current and previous lung volumes.

The time between two simulated flow-volume points is assessed using the known expired volume increment  $\Delta V$  (the domain of simulations) and the current flow from the alveoli  $Q_{alv}$ :

$$\Delta t = \Delta V / Q_{alv}. \quad (1)$$

The numerical procedure used for solving the differential equation of the 'tube law' returns the drops of lateral pressure  $\Delta P_{lt}$  and thus transmural pressures  $P_{tm}$  at a few points along the airway. This information is further used to calculate airway areas  $A$  (decreasing in flow direction) and elementary compliances ( $dA/dP_{tm}$ ) at these points, and finally to assess the volume  $V_a$ , inertance  $I_a$  and compliance  $C_a$  of that airway, and of the whole airway generation  $g$ :

$$V_a = \sum_i A_i \Delta l_i, \quad V_g = 2^g V_a, \quad (2)$$

$$I_a = \sum_i \frac{\rho \Delta l_i}{A_i}, \quad I_g = I_a / 2^g, \quad (3)$$

$$C_a = \sum_i \left( \frac{dA}{dP_{tm}} \right)_i \Delta l_i, \quad C_g = 2^g C_a, \quad (4)$$

where:  $\rho$ —air density,  $\Delta l$ —distances along the airway returned by the procedure.

The flexible airways narrow during expiration because of the decrease of lung elastic recoil and the resulting decrease

of transmural pressure [5]. In effect, there is an additional flow  $\Delta Q_v$  coming to a given airway generation from the previous one:

$$\Delta Q_v(g) = \frac{\Delta V_g(g+1)}{\Delta t}. \quad (5)$$

Another flow component  $\Delta Q_p$  is produced by gas compressibility, and (from Boyle's law) it depends on the rate of pressure change:

$$\Delta Q_p(g) = -\frac{V_g(g+1) \Delta P_g}{P_g(g+1) \Delta t}, \quad (6)$$

where  $P_g$  is the absolute pressure in a given generation. Finally, the total flow coming from airway generation  $g+1$  into generation  $g$  is:

$$Q(g) = Q(g+1) + \Delta Q_v + \Delta Q_p. \quad (7)$$

Similarly, the additional modification of pressure drop along an airway stems from gas inertia:

$$\Delta P_i(g) = I_g \frac{\Delta Q(g)}{\Delta t}, \quad (8)$$

so the total pressure loss  $\Delta P_t$  along an airway generation amounts to:

$$\Delta P_t(g) = \Delta P_{lt}(g) + \Delta P_i(g). \quad (9)$$

In a sitting position, there is a gravity-dependent pleural pressure gradient [11] modifying transmural pressure of intrapulmonary airways, and thus their dimensions and dynamic behaviour. Assuming in simplification a vertical airway arrangement from the alveoli at the bottom to the trachea at the top, and taking into account that in a real bronchial tree there is also a vertical distribution of alveoli and small airways, the pleural pressure gradient of 0.3 hPa  $\text{cm}^{-1}$  ( $\sim 0.3 \text{ cmH}_2\text{O}/\text{cm}$ ) was included in this quasi-dynamic model.

## 2.3 Numerical Simulations

Simulations of forced expiration (500 flow-volume points in the range of vital capacity, VC) from the respiratory system of the same structure and parameter values were run using the standard quasi-static and the new quasi-dynamic models, and then compared for two cases: a normal respiratory system state and for the obstructed small airways. Simulation of airway obstruction mimicked airway wall smooth muscle constriction effects [7]. A several patterns of homogeneous airway narrowing were tested to enhance the difference between the results yielded by the two models.

### 3 Results

The MEFV curves simulated using the both models were virtually the same in the case of normal lungs (Fig. 1a), with only minor differences in the folds related to flow limitation movement from one airway generation to another [12]. In the case of obstructed airways, these changes were also negligible in most of tested constriction patterns. Only specific modifications in airway mechanical properties

returned moderate effects. An example outcome, for enlarged central airway areas (generations 2–6) and constricted small airways (generations 10–20) is shown in Fig. 1b.

The physical phenomena implemented in the quasi-dynamic model, according to Eqs. (5, 6, 8), depend on airway volumes and pressure changes during forced expiration. Expiratory traces of these quantities are presented in Fig. 2.

**Fig. 1** MEFV curves simulated for normal lungs (a) and obstructed airways (b)

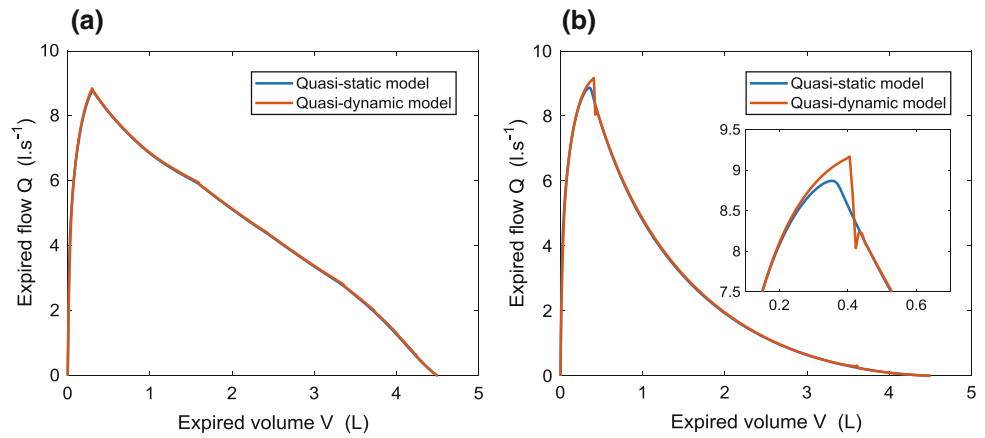
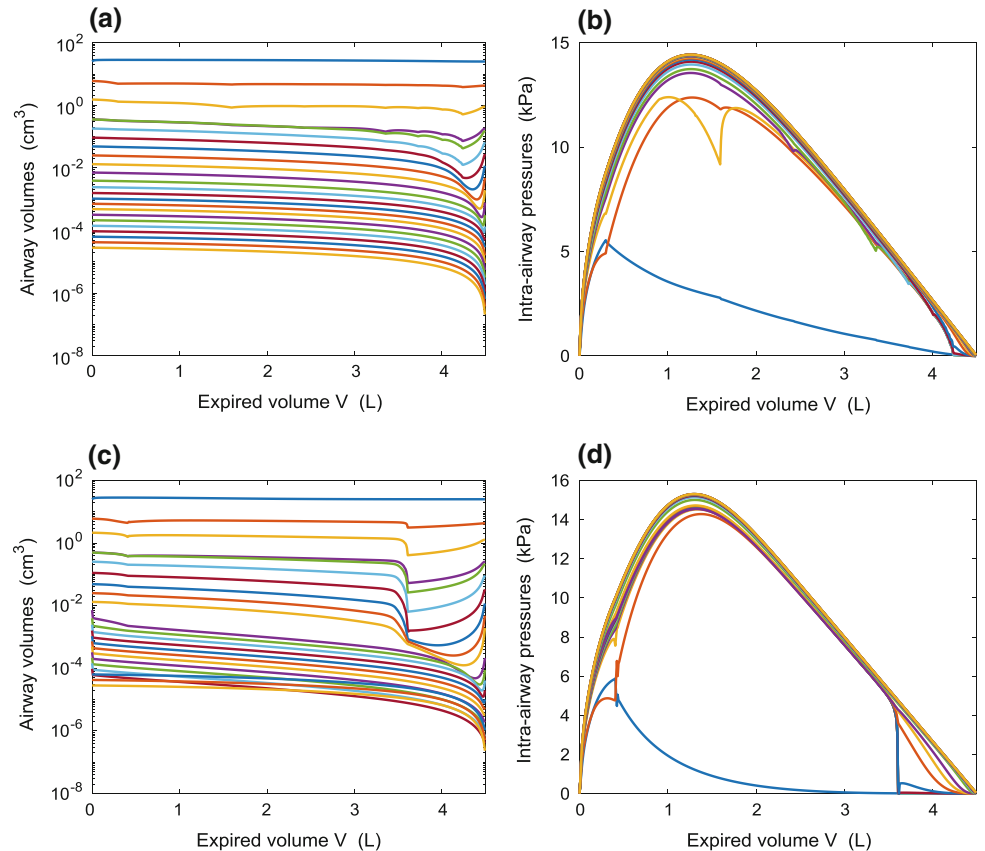


**Fig. 2** Volumes of single airways (a and c, from the trachea at the top to alveolar sacs at the bottom) and intra-airway pressures (b and d, from the trachea at the bottom to alveolar sacs at the top) changes during forced expiration for the normal lungs (a and b) and obstructed small airways (c and d)





## 4 Discussion and Conclusion

The aim of this work was to investigate the effects of dynamic phenomena occurring in the flexible airways during forced expiration on the MEFV curve.

The developed quasi-dynamic model enabled simulation of intra-airway volume and pressure changes responsible for these dynamic processes. The symmetrical structure of the model applied here results in a much simpler computational scheme than using a model with the heterogeneous bronchial tree (compare [6] and [8]), and simultaneously it is quite sufficient for such investigations.

Figure 2a, c prove that airways reduce their volumes for most of expiration time, producing additional flows to the downstream segments, however the central airways recover at the end, when the pressure losses in the upstream segments come to zero and the transmural pressure becomes higher. Intra-tracheal pressure course is very similar to the MEFV curve (compare Fig. 1 with Fig. 2b, d) because it depends mainly on upper airway resistance. The trajectories of pressures in intra-pulmonary airways correspond well to experimental results [3, 13, 14].

The main finding of this work is that only some specific conditions, causing that flow limitation exists right in small airways, yields a visible difference and the characteristic swing after the peak expiratory flow (PEF), reported in the literature [15]. This is in agreement with results presented in [4] and implies that the ‘classic’ quasi-static model is an adequate tool for forced expiration investigations until one needs to analyse heterogeneous diseases.

**Acknowledgements** This work was supported by the grant no. 2016/21/B/ST7/02233 from the National Science Centre, Poland.

## References

- Hyatt, R.E., Schilder, D.P., Fry, D.L.: Relationship between maximum expiratory flow and degree of lung inflation. *J. Appl. Physiol.* 13(3), 331–336 (1958).
- Olender, M.F., Clark, J.W., Stevens, P.M.: Analog computer simulation of maximum expiratory flow limitation. *IEEE Trans. Biomed. Eng.* 23(6), 445–452 (1976).
- Solway, J., Fredberg, J.J., Ingram, R.H., Jr., Pedersen, O.F., Drazen J.M.: Interdependent regional lung emptying during forced expiration: a transistor model. *J. Appl. Physiol.* 62(5), 1013–1025 (1987).
- Gólczewski, T., Darowski, M.: Virtual respiratory system for education and research: simulation of expiratory flow limitation for spirometry. *Int. J. Artif. Organs* 29(10), 961–972 (2006).
- Lambert, R.K., Wilson, T.A., Hyatt, R.E., Rodarte J.R.: A computational model for expiratory flow. *J. Appl. Physiol.* 52(1), 44–56 (1982).
- Polak, A.G.: A forward model for maximum expiration. *Comput. Biol. Med.* 28(6), 613–625 (1998).
- Morlion, B., Polak A.G.: Simulation of lung function evolution after heart-lung transplantation using a numerical model. *IEEE Trans. Biomed. Eng.* 52(7), 1180–1187 (2005).
- Polak, A.G., Lutchen, K.R.: Computational model for forced expiration from asymmetric normal lungs. *Ann. Biomed. Eng.* 31(8), 891–907 (2003).
- Hedges, K.L., Tawhai, M.H.: Simulation of forced expiration in a biophysical model, with homogeneous and clustered bronchoconstriction. *J. Biomech. Eng.* 138(6), 061008 (2016).
- Weibel, E. R., *Morphometry of the Human Lung*, Springer, Berlin (1963).
- Mayo, J.R., MacKay, A.L., Whittall, K.P., Baile, E.M., Paré, P.D.: Measurement of lung water content and pleural pressure gradient with magnetic resonance imaging. *J. Thorac. Imaging* 10(1), 73–81 (1995).
- Polak A.G.: A model-based method for flow limitation analysis in the heterogeneous human lung. *Comput. Methods Programs Biomed.* 89(2), 123–131 (2008).
- McNamara, J.J., Castile, R.G., Glass, G.M., Fredberg, J.J.: Heterogeneous lung emptying during forced expiration. *J. Appl. Physiol.* 63(4), 1648–1657 (1987).
- Warner, D.O., Hyatt, R.E., Rehder, K.: Inhomogeneity during deflation of excised canine lungs. I. Alveolar pressures. *J. Appl. Physiol.* 65(4), 1757–1765 (1988).
- Miller, M.R., Hankinson, J.A.T.S., Brusasco, V., et al.: Standardisation of spirometry. *Eur. Respir. J.* 26(2), 319–338 (2005).

# Electronic-Based Model of the Sensitive Type of Mycobacterium Tuberculosis

R. U. K. Raja Mohd Radzi<sup>✉</sup>, W. Mansor<sup>✉</sup>, and J. Johari<sup>✉</sup>

## Abstract

Early diagnosis of Tuberculosis disease is important to prevent complicated issues from arising. The conventional techniques used to diagnose the Mycobacterium Tuberculosis have limitations such as time-consuming, invasive, tiring, labour intensive and microbiologist expert dependence. There is no electrical instrument to detect Tuberculosis automatically and no electronic circuit model for evaluating the device. This paper describes the development of an electronic circuit model of the sensitive type of Mycobacterium Tuberculosis. The model was developed by first converting the real data to gain, deriving the model equations using Regression model analysis and performing one-way ANOVA to confirm the results. Three types of model were investigated; the first order, second order and third order LC passive low pass filter circuits. It was found that the second order of LC circuit is the best model of the sensitive type of Mycobacterium Tuberculosis as it provides less than 10% discrepancy. The simulation results show that the logarithmic regression model is the best equation that demonstrates the sensitive type of Mycobacterium Tuberculosis.

## Keywords

Tuberculosis • Mycobacterium tuberculosis  
Low pass filter • Regression model analysis  
LC circuits

R. U. K. Raja Mohd Radzi · W. Mansor (✉) · J. Johari  
Faculty of Electrical Engineering, Universiti Teknologi MARA,  
40450 Shah Alam, Selangor, Malaysia  
e-mail: wahidah231@salam.uitm.edu.my

W. Mansor  
Computational Intelligence Detection RIG, Pharmaceutical Life  
Sciences CORE, Universiti Teknologi MARA, 40450 Shah Alam,  
Selangor, Malaysia

## 1 Introduction

The number of tuberculosis cases is increasing every year. Tuberculosis is a disease that is caused by bacteria called Mycobacterium Tuberculosis and has been considered as a global emergency by the World Health Organization (WHO) [1, 2]. Mycobacterium Tuberculosis falls into two categories; Resistant type and Sensitive type [3]. The resistant type of Mycobacterium Tuberculosis does not influence by the medicine. Even though the patients take medications as prescribed, the resistant type of bacteria still alive and the patient will not be cured. Unlike the resistant type, the sensitive type of Mycobacterium Tuberculosis will react to the medicine, and the disease will be cured after taking medicine.

It was reported that techniques such as tuberculin skin test based on purified protein derivative also known as Mantoux Test, X-ray, positive smear for acid-fast bacilli (AFB) and the microscopy are used to detect the bacterium [4–8]. Even though these techniques could identify the bacterium, it takes time to diagnose the disease. Some of the methods are also expensive and need the more skilled person to perform the diagnosis or handle the equipment [9].

Conventional Mycobacterium Tuberculosis detection techniques are invasive. The blood of the patient is taken through injection to detect the bacteria. In some cases, the tissue of the infected organ is removed. The process of removing the tissue is very painful which is not suitable for old people and debilitated patients since this process may be harmful. Therefore, the non-invasive technique is more preferred to replace the invasive method. A model that mimics the sensitive type of Mycobacterium Tuberculosis has to be created before the non-invasive diagnosis system can be used. The reason for this is that the model can act as a tester to examine the functionality of the diagnosis system.

Currently, the model that serves this purpose has not been investigated, and the use of the electronic circuit to model the bacteria has not been reported. In our previous work, we

have studied the performance of three types of an electronic circuit; resistor-capacitor, resistor-inductor and resistor-inductor-capacitor circuits in modelling the sensitive type of *Mycobacterium Tuberculosis* [10, 11]. However, the study only focused on the first order of the electronic circuit.

In this study, the ability of the second order and third order of the electronic circuits to mimic the sensitive type of *Mycobacterium* is investigated. This paper describes the performance of the three types of inductor-capacitor (LC) circuit; the first, the second and the third orders in modelling the sensitive type of *Mycobacterium Tuberculosis*.

## 2 Methodology

The circuit model of the sensitive type of *Mycobacterium tuberculosis* was developed from the real data collected by the Johari et al. [3]. The real data is the number of bacteria

**Table 1** The Transformation from collection rate of bacteria to gain

Frequency (MHz)	Collection rate	Real data gain
1.0	11	1
1.6	9	0.82
2.5	8	0.73
4.0	7	0.64
10	5	0.45
16	3	0.27

remained when electricity is supplied to the sample in the frequency range of 1–16 MHz. The sample used by [3] was their own cultured bacteria that is staphylococci epidermidis strains JD140 (streptomycin sensitive) which was grown in nutrient broth for 16 h at 37 °C, with or without the addition of streptomycin and passed through incubation, centrifugation and resuspension.

The whole process of developing the model encompasses four stages. The first stage was the conversion of the collection rate to gain which was followed by the model design and simulation, model derivation and finally statistical analysis.

### 2.1 Model Development

In the model development, the collection rate was first converted to gain versus frequency and then normalised. This conversion was carried out since the graph of the collection rate poses the characteristics of frequency response. Table 1 shows the collection rate and the gain resulted from the conversion. The electronic circuits were then designed based on the data extracted from the gain versus frequency graph. Since the LC circuit was found to be the best model in our previous work [11], this study continues to look at the performance of the LC circuit, but this time, it extends to the higher order circuit; the second and third order of LC circuits.

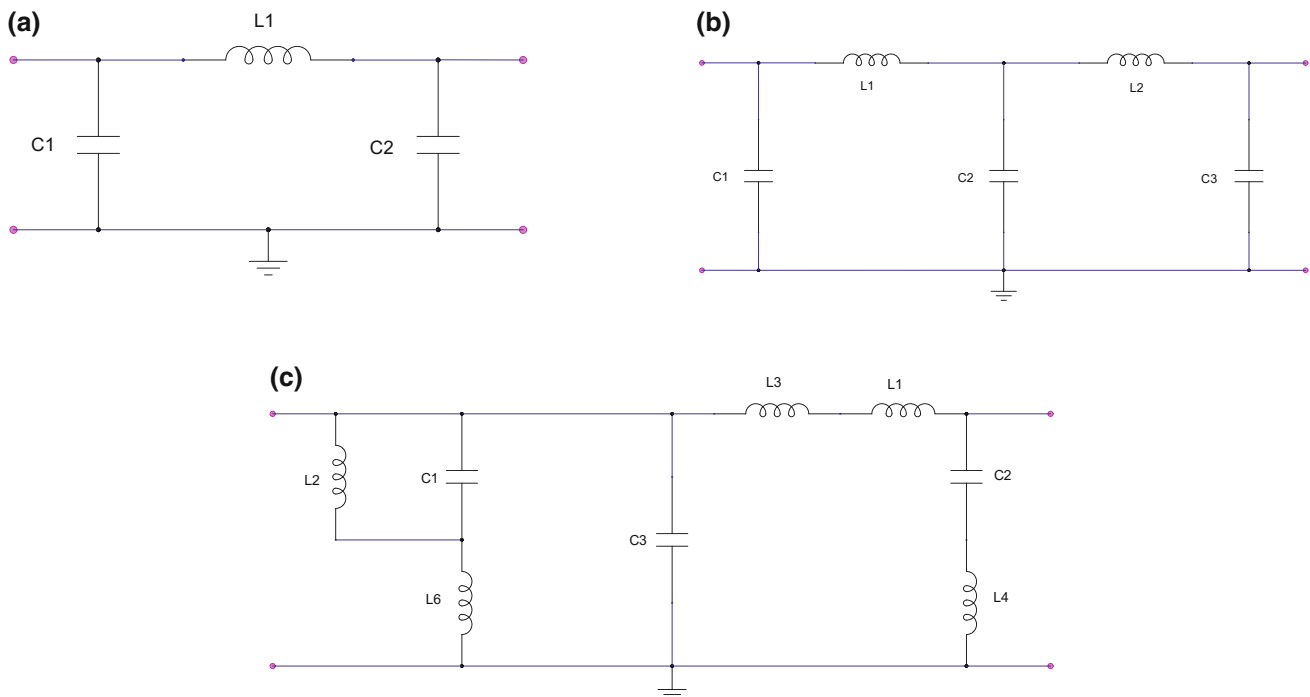


**Fig. 1** Schematic diagram of **a** the first-order LC circuit, **b** the second-order LC circuit and **c** the third-order LC circuit

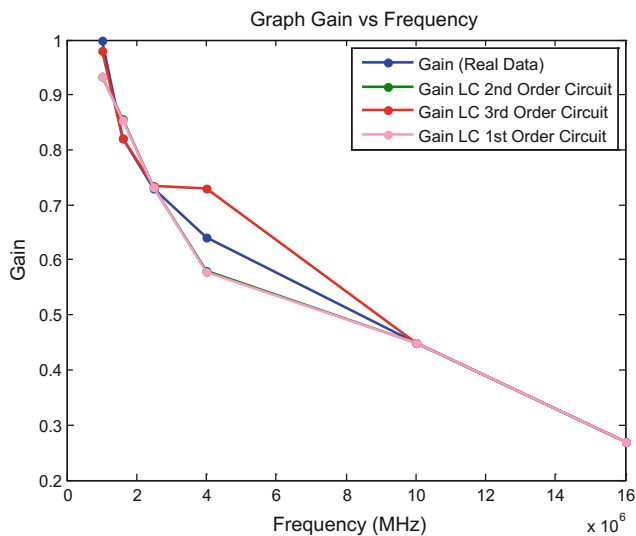


Fig. 2 Frequency response of the LC circuits

Table 2 One-way ANOVA for the optimum LC simulation circuits

Groups	Count	Sum	Average	Variance
P <sub>d</sub> of LC-1st order	6	20.64	3.44	17.09
P <sub>d</sub> of LC-2nd order	6	20.94	3.49	16.17
P <sub>d</sub> of LC-3rd order	6	16.77	2.8	31.18

## 2.2 Simulation and Analysis

The LC circuit models consist of lumped elements, which are a capacitor, C and an inductor, L as shown in Fig. 1. The schematic diagrams of the circuits were drawn using Genesys software and simulated to obtain the expected output gain.

The regression model analysis was used to derive the model equations. Here, four types of regression model analysis were employed; Exponential Regression Model, Linear Regression Model, Logarithmic Regression Model and Power Regression Model. The percentage of discrepancy, P<sub>d</sub> between the values of gain from the equations and the real data gain was then calculated using Eq. (1).

$$P_d = \left| \frac{x - y}{x} \right| \times 100\% \quad (1)$$

where x is the gain from the real data, and y is the gain taken from the equation. The values of discrepancies were analyzed using one-way analysis of variance (ANOVA) to obtain the best equation that fits the real data.

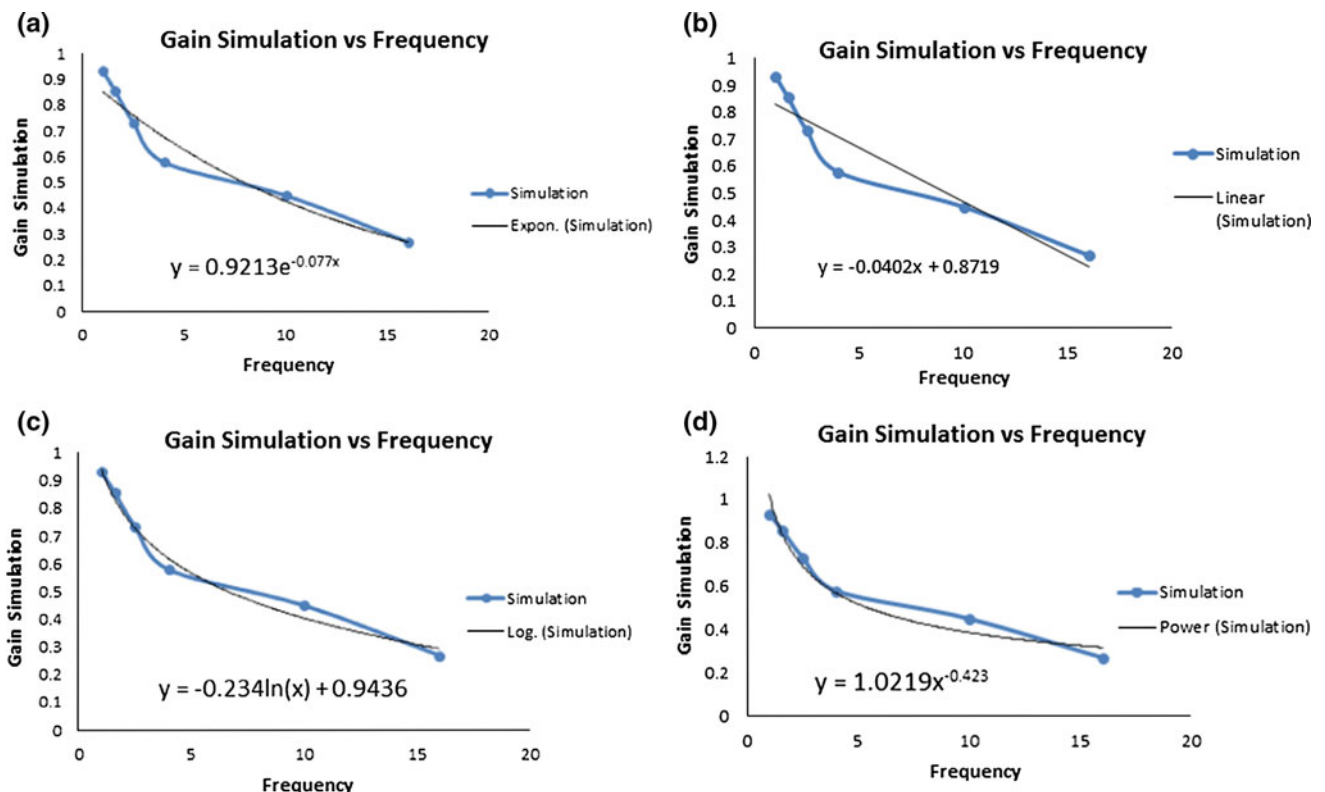


Fig. 3 Graph of a Exponential regression model, b Linear regression model, c Logarithmic regression model, and d Power regression model which represent the simulation circuit

**Table 3** One-way ANOVA of the regression model analysis that represents simulation data

Groups	Count	Sum	Average	Variance
Exponential	6	39.81	6.635	32.49
Linear	6	64.39	10.73167	52.55
Logarithmic	6	30.34	5.056667	17.67
Power	6	50.14	8.356667	40.69

### 3 Results and Discussions

Figure 2 shows the frequency response of the first order, second order and the third order of LC simulation circuits and real data gain. From observation, all graphs of the LC simulation circuits have the similar trend to the graph of actual data gain. The percentage of discrepancies obtained from all LC circuit is between 0.27 and 0.98%. The first order and the second order LC circuit model have the same strength where it follows the real data closely except at 1, 1.6, and 4 MHz. The third order of LC circuit model produces the largest discrepancy at 4 MHz.

Table 2 shows the one-way ANOVA for the optimum LC simulation circuits. The count is sample size or numbers of data collected. Here, the six counts represent the six frequency samples (1–16 MHz). The sum is the total gain in each group while the average is the amount of sum over the count. The result shows that the second-order LC simulation circuit is the optimum model since it has the smallest variance which is 16.17 compared to others.

Figure 3 shows the graphs and the equations derived from the regression model analysis. The lowest percentage of the discrepancy is produced by the logarithmic regression model which is between 0.52 and 10.05%, and the largest difference is given by the linear regression model (4.42–22.82%). Table 3 shows the one-way ANOVA for the four types of the regression model. The largest variance is 52.55, that is produced by the Linear Regression Model whereas the smallest variance is obtained from the Logarithmic Regression Model which is 17.67. Therefore, the Logarithmic Regression Model is the best model compared to others. These results show that the biological data (real data) can be transformed into electrical data to develop an electronic-based model that predicts the sensitive type of Mycobacterium Tuberculosis.

### 4 Conclusion

The simulation circuit models were successfully designed to demonstrate the sensitive type of Mycobacterium Tuberculosis. The second order of LC simulation circuit is the

optimum model since it produces the acceptable percentage of gain discrepancy with the lowest variance compared to the first and the third other LC circuits. The Logarithmic Regression Model that represents the second order LC circuit is the best model of the sensitive type of Mycobacterium Tuberculosis.

**Acknowledgements** This work was supported by Fundamental Research Grant Scheme (FRGS), Malaysia (600-RMI/ST/FRGS 5/3/Fst) and Dana Kecermelangan, UiTM. The authors would like to express their gratitude to Ministry of Higher Education, Malaysia and Universiti Teknologi MARA, Malaysia, for financial support and providing equipment for this research.

**Conflict of Interest** The authors declare that they have no conflict of interest.

### References

- Chen G., Wu Y., Xiao S., and Li C.: Bioinformatics Analysis of Mycobacterium Tuberculosis Gene *rspL* and Its Mutation, International Conference on Biomedical Engineering and Computer Science (ICBECS), pp 1–4, (2010).
- Rui S., Cheng I., and Basu A.: A Hybrid Knowledge-Guided Detection Technique for Screening of Infectious Pulmonary Tuberculosis From Chest Radiographs, IEEE Transactions on Biomedical Engineering, vol. 57, pp 2646–2656, (2010).
- Johari J., Hübner Y., Hull J. C., Dale J. W., and Hughes M. P.: Dielectrophoretic assay of bacterial resistance to antibiotics Physics in Medicine and Biology, vol. 48, pp N193, (2003).
- Tomono K.: The causes of death of pulmonary tuberculosis: late sequelae of pulmonary tuberculosis, Kekkaku:[Tuberculosis], vol. 73, pp 751–754, (1998).
- Yaacob I. and Ahmad Z.: Clinical significance of Mantoux test in Malaysian patients, Med J Malaysia, vol. 45, pp 231–4, (1990).
- Liam C., Lim K., Srinivas P., and Poi P.: Hypercalcaemia in patients with newly diagnosed tuberculosis in Malaysia, The International Journal of Tuberculosis and Lung Disease, vol. 2, pp 818–823, (1998).
- Ismail Y.: Pulmonary tuberculosis-a review of clinical features and diagnosis in 232 cases, Med J Malaysia, vol. 59, pp 56–64, (2004).
- Loh K.: Role of Mantoux test in the diagnosis of tuberculosis, Malaysian Family Physician, vol. 6, pp 2, (2010).
- Das M., Sumana G., Nagarajan R., and Malhotra B. D.: Zirconia based nucleic acid sensor for Mycobacterium tuberculosis detection, Applied Physics Letters, vol. 96, pp 133703–133703-3, (2010).
- Raja Mohd Radzi R. U. K., Mansor W., Johari, J.: Computer Modeling of the sensitive type of Mycobacterium tuberculosis, IEEE Conference on Biomedical Engineering & Sciences, pp 660–663, (2016).
- Raja Mohd Radzi R. U. K., Mansor W., Johari, J.: Optimised Electronic Circuit Model of Sensitive Type of Mycobacterium Tuberculosis, Advanced Science Letters, accepted for publication.



# RF Ultrasound Based Estimation of Pulsatile Flow Induced Microdisplacements in Phantom

Monika Zambacevičienė, Rytis Jurkonis, Sigita Gelman, and Andrius Sakalauskas

## Abstract

Mechanical stimulus is key component to estimate tissue stiffness. Few techniques have been developed to induce external mechanical stimulus into tissues. We hypothesize that the natural tissue motion due to cardiovascular activity could be employed for this purpose and with decrease of tissue stiffness increase their motion amplitude. The assessment of elastic sub-millimeter tissue displacements is one of the leading developments for ultrasonic characterization of tissue stiffness. The objective of this study was to investigate the feasibility to parametrize the phantom material response to pulsatile flow. The displacements were evaluated in tissue-mimicking phantoms with known stiffness. The two agar phantoms, having vessel imitating channel with controlled pulsatile flow inside, were manufactured (agar concentrations 6 and 3 g/l in distilled water, predicted Young modulus was 10 and 7 kPa respectively). The pulse water flow in channel was produced by centrifugal pump MultiFlow (Gampt) with period of 1 s. The length of channel was 19 cm embedded in the tissue mimicking agarose gel. Linear array transducer L14-5 (5–14 MHz) driven by scanner SonixTouch (Ultrasonix) was used for the echoscopy of phantom and ultrasound (US) radiofrequency (RF) data acquisition. The collected beam formed B-mode RF data (120 fps) were used for the displacements estimation applying phase-correlation and sub-sample techniques. The pulsation of channel diameter and displacements of material were estimated at a few distances from channel border in all phantoms. The pulsation of diameter and displacements of material were parametrized extracting double amplitudes. Amplitudes

of displacements of material were normalized respective to pulsation amplitude of channel diameter. The relation of amplitude parameters with concentration of agar was evaluated. It was determined that displacement is correlated with stiffness: with decrease of tissue stiffness the motion amplitude is increasing. The method may provide the technological background for future studies characterizing in vivo tissue stiffness from vascular pulsations generated displacements.

## Keywords

Stiffness • Tissue-mimicking phantom  
Microdisplacement • Radiofrequency signals  
Phase correlation

## 1 Introduction

Mechanical stimulus is key component to estimate tissue stiffness. Few techniques have been developed to induce external and artificial mechanical stimulus into tissues. External force induces shear waves or mechanical strain in the tissue. The technologies are designed to track shear wave propagation and estimate their speed, which correlates with tissue stiffness. On the other hand, so-called endogenous motion in the body can be considered [1] as the excitation for elasticity imaging. The pumping action of the heart provides an excitation that can be used within the vascular system. Physiological motion artifacts arising from breathing and cardiac pulsations cause translational motion and/or mechanical strain components in the liver [2]. Schenk et al. used [3] the pulsing of the aorta to cause tissue distortion as input for real time elastography. They [3] showed the reproducibility of the cardiac-induced distortion. Olsen et al. [4] used naturally occurring transient mechanical waveforms imparted on the liver by the beating heart. They concluded that intrinsic transient magnetic resonance elastography

M. Zambacevičienė (✉) · R. Jurkonis · A. Sakalauskas  
Biomedical Engineering Institute, Kaunas University of  
Technology, Kaunas, Lithuania  
e-mail: monika.zambaceviciene@ktu.edu

S. Gelman  
Department of Gastroenterology, Lithuanian University of Health  
Sciences, Kaunas, Lithuania

might allow for the eventual screening and monitoring of patients with liver disease using standard MRI equipment [4].

We hypothesize that the natural tissue motion due to cardiovascular activity could be employed for the tissue characterization purpose: detection of decreased motion amplitude is predicting about increase of tissue stiffness. The assessment of elastic sub-millimeter tissue displacements is one of the leading developments for ultrasonic characterization of tissue stiffness. The objective of this study was to investigate the feasibility to parametrize the phantom tissue response to pulsatile flow. The induced displacements were evaluated in a tissue mimicking phantoms with known stiffness.

## 2 Materials and Methods

### 2.1 Data Acquisition

RF US signal sequences were acquired using a research-dedicated scanner Ultrasonix SonixTouch (Analogic Ultrasound, Canada), equipped with a 5–14 MHz linear array probe. RF US signals sequences were acquired at a frame rate—120 fps, a sample size in radial direction was

19.25  $\mu\text{m}$ . Microdisplacements were assessed in two tissue-mimicking phantoms.

### 2.2 Tissue-Mimicking Phantom

The two agar phantoms, having embedded thin-wall rubber vessel with controlled pulsatile flow inside, were manufactured (agar concentrations 6 and 3 g/l in distilled water, predicted [5] Young modulus was 10 and 7 kPa in Phantom 2 and Phantom 1 respectively). To obtain scattering we dispersed 0.3 g of graphite powder in 800 ml of agar mixture. The mixture was prepared in water boiling temperature and was slowly mixed manually to cool down. At start of gelation, the mixture was poured into the prepared container with vessel. Container was kept still to solidify at room temperature for 1 h. The structure of phantom is presented in Fig. 1a1. Vessel was made from straight long rubber balloon, which is used in decorations. Diameter of vessel-mimicking balloon was 9 mm. The length of rubber vessel was 27 cm (19 cm embedded in the agar gel). Vessel ends were fixed to tube ports, which were glued in walls of container. These ports were connected to external tubing. Phantom with external tubing compose loop into which

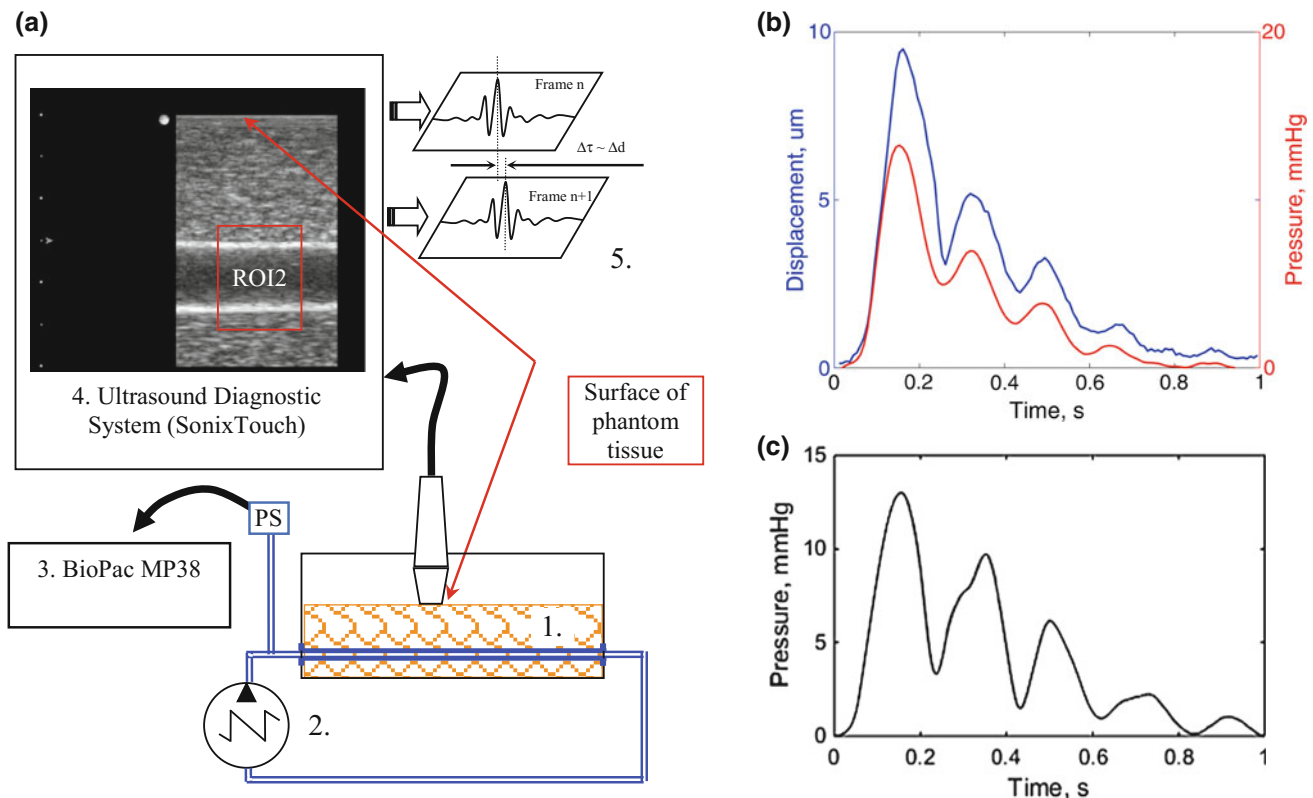


**Fig. 1** Experimental setup. **a1** Agar based phantom with embedded vessel, **2.** Centrifugal pump, **3.** Signal acquisition unit from pressure sensor (PS), **4.** US RF diagnostic scanner; **b** Pressure pulse generated in

phantom input and pulse generated displacements in agar based tissue mimicking material, and **c** excitation signal recorded by pressure sensor

centrifugal pump circulated water. Tubing was primed with water ensuring that all naked eye viewed air pockets were escaped. On the input to phantom, the T shaped junction was used to connect MP38 (BioPac) pressure sensor (PS). We ensured air pocket in this tube to protect pressure sensor from wetting.

The pulsatile water flow in vessel was produced by centrifugal pump MultiFlow (Gampt) at 3000 RPM speed with period of 1 s. With used tubing this speed ensured flow peak speed of 1.5 l/min. The pressure pulsations in phantom input were 13–15 mmHg peak-peak. The experimental setup is presented in Fig. 1a. The phantom and scanning probe were fixed during the experiment and the B mode image of longitudinal cross-section of the tube was obtained (Fig. 1a4).

### 2.3 RF Ultrasound Signals Processing Algorithm

Displacements were evaluated in two phantoms at three distances from vessel surface, which displaced because of pulsating flow. Distances from vessel surface were 2, 4 and 10 mm. Automatically selected regions of interest for displacement evaluation (ROI1) were  $1 \times 1$  mm in size. Distances between centers of these ROI1 were 4 mm in vertical and horizontal direction. Only RF signals in these ROI1 had been used for further analysis with phase correlation and sub-sample algorithm. After RF US signal extraction in ROI1, Hanning 2D window was applied.

Phase correlation is a frequency domain technique used to estimate shift between two images. This method based on the Fourier shift theorem and states that the shift between two images will cause a phase shift in the Fourier domain [6]. For example, shift between two RF signal matrixes  $a_1(x, y)$  and  $a_2(x, y)$  will cause a phase shift in the Fourier domain. RF signal matrixes  $a_1(x, y)$ ,  $a_2(x, y)$  and their 2D discrete

Fourier transforms (DFT) are denoted as  $A_1(u, v)$  and  $A_2(u, v)$ . The phase correlation is defined as:

$$r(x, y) = \mathcal{F}^{-1} \left( \frac{A_1(u, v)A_2^*(u, v)}{|A_1(u, v)A_2^*(u, v)|} \right) = \delta(x - \Delta x, y - \Delta y), \quad (1)$$

where  $*$  is the complex conjugate,  $\mathcal{F}^{-1}$  is 2D inverse DFT and  $\delta$  is so-called a 2D impulse (Dirac delta) function located at  $[\Delta x, \Delta y]$ . Then the displacement between two RF signal matrixes  $a_1$  and  $a_2$ :

$$(\Delta x, \Delta y) = \arg \max_{x, y} |r(x, y)|. \quad (2)$$

Because the estimated displacement had integer accuracy, phase correlation method was extended with sub-sample algorithm [7]. According to it, second degree surface was fitted to phase-correlation matrix maximum and neighborhood values to obtain displacement at sub-sample accuracy. Finally, displacement between the two RF signal matrixes  $a_1$  and  $a_2$ :

$$\begin{cases} x_{displacement} = x_{sub} + \Delta x \\ y_{displacement} = y_{sub} + \Delta y \end{cases} \quad (3)$$

Pulsation amplitude of channel diameter was estimated analyzing RF US signals in ROI2, which were manually selected and covered both edges of the phantom channel. From the center of ROI2, algorithm was searching for the maximums and their indices in RF US signals. Maximums were hold when they were above preset threshold and assumed as boundary between channel and vessel. Maximums indices found on lower wall were subtracted from indices of upper wall and channel diameter was estimated. Estimate of channel diameter is obtained as mean value of diameters estimated in ROI2. Size of ROI2 was  $1 \times 14$  mm.

**Fig. 2** Experimental data: B-mode image and selected ROI1 **a**, pressure pulsations in phantom input **(b, top)** and detected displacements in agarose gel **(b, bottom)** when ROI1 selected at three distances (2 (green), 6 (blue) and 10 (red) mm) from vessel surface **(a)**. The pressure pulse of irregular amplitude was induced manually at moment of 2 s (color figure online)

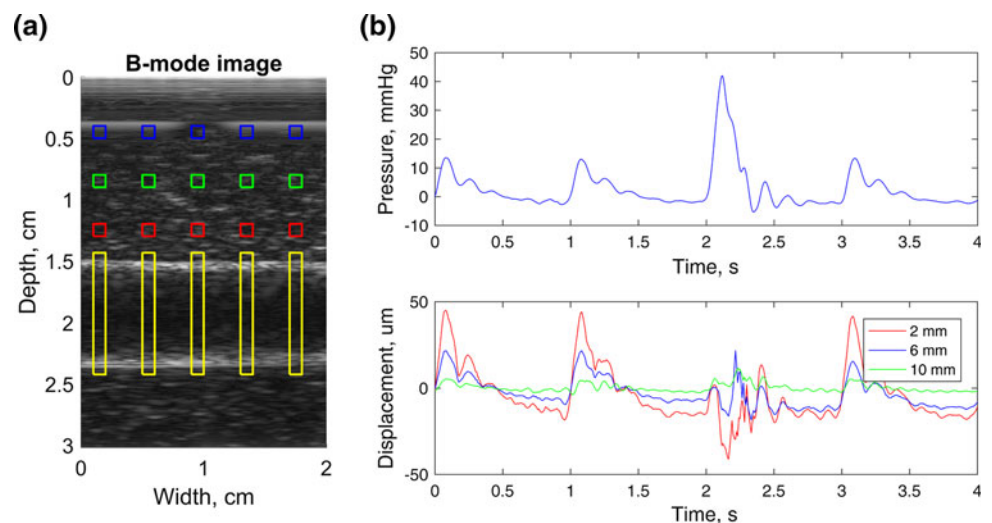


**Table 1** Comparison of pulsations of channel diameter and soft tissue mimicking material microdisplacements in phantoms

	Phantom 1	Phantom 2
Young modulus, kPa	7	10
Double amplitude of pressure, mmHg	13.44 ± 2.39	14.47 ± 5.87
Pulsation amplitude of channel diameter, μm (n = 5)	182.81 ± 11.11	138.34 ± 3.39
<i>Estimated microdisplacements (n = 15)</i>		
Displacement at 2 mm distance, μm	63.61 ± 10.36	43.27 ± 4.39
Displacement at 6 mm distance, μm	45.49 ± 5.76	20.64 ± 1.91
Displacement at 10 mm distance, μm	27.96 ± 3.71	9.42 ± 0.97
<i>Normalized microdisplacements (n = 15)</i>		
Displacement at 2 mm distance, μm	0.34 ± 0.06	0.31 ± 0.03
Displacement at 6 mm distance, μm	0.25 ± 0.03	0.15 ± 0.01
Displacement at 10 mm distance, μm	0.15 ± 0.02	0.07 ± 0.01

The pulsation of diameter and displacements of material were parametrized extracting peak to peak amplitudes. Amplitudes of displacements of soft tissue mimicking material were normalized according to pulsation amplitude of channel diameter:

$$A_{normalized(n)} = \frac{1}{n} \sum_{i=1}^p \frac{A_{displacement}(p)}{A_{diameter}(p)}, \quad (4)$$

where  $n = 1:15$ ,  $p = 1:5$ . There was 3 estimates of displacement at 5 positions in horizontal direction.

### 3 Results

Implemented algorithms were applied on RF US signals acquired from Phantom 1 and Phantom 2. Pressure pulsations and detected displacements are presented in Fig. 2. We selected 5 ROI1 at each 2, 6 and 10 mm distances.

In detected displacement waveforms, three periods were used to evaluate peak-to-peak amplitude of displacement. Mean values and standard deviations were calculated from  $n = 5 \times 3 = 15$  displacement estimates (results are presented in Table 1).

We found that displacements are dependent on phantom elasticity, i.e. with increase of phantom stiffness decrease displacement amplitude. In addition, displacement amplitude reduce with increase of distance from surface of channel.

### 4 Conclusions

The obtained in vitro results confirmed that the proposed method is technologically feasible and hypothesis was confirmed because tissue displacement showed negative

correlation with tissue stiffness. The method may provide the technological background for future in vivo studies examining relationships between blood pulse in arteries and generated microdisplacements surrounding soft tissues.

It should be noted that the detected microdisplacements were obtained even applying pulsating flow, which is closer to venous pressure in magnitude. Thus, even larger contrast could be expected for the arteries.

**Acknowledgements** This research was supported by the Research, Development and Innovation Fund of Kaunas University of Technology (grant No. MTEPI-L-17003, grant. No. MTEPI-L-16012) and the Research Fund of Lithuanian University of Health Sciences (SV5-074/BN17-99, grant No. LSMU-21).

**Conflict of interest** The authors declare that they have no conflict of interest.

### References

1. SARVAZYAN, A., et al. An Overview of Elastography-an Emerging Branch of Medical Imaging. *Current Medical Imaging Reviews*, 2011, vol. 7, no. 4. pp. 255–282.
2. MAHMOUD, A.M., et al. Detecting Hepatic Steatosis using Ultrasound-Induced Thermal Strain Imaging: An Ex Vivo Animal Study. *Physics in Medicine & Biology*, 2014, vol. 59, no. 4. pp. 881.
3. SCHENK, J.P., et al. Measurement of Real-Time Tissue Elastography in a Phantom Model and Comparison with Transient Elastography in Pediatric Patients with Liver Diseases. *Diagnostic and Interventional Radiology (Ankara, Turkey)*, Jan–Feb, 2014, vol. 20, no. 1. pp. 90–99 ISSN 1305-3612; 1305-3825.
4. OLSEN, D., SONG, P., GLASER, K. and EHMAN, R. *Cardiac-Gated Hepatic MR Elastography with Intrinsic Transient Waveforms.*, 2011.
5. HALL, T.J., BILGEN, M., INSANA, M.F. and KROUSKOP, T.A. Phantom Materials for Elastography. *IEEE Transactions on*

- Ultrasonics, Ferroelectrics, and Frequency Control*, 1997, vol. 44, no. 6. pp. 1355–1365.
6. MOHAMED, S., HELMI, A., FKIRIN, M. and BADWAI, S. Subpixel Accuracy Analysis of Phase Correlation Shift Measurement Methods Applied to Satellite Imagery. *Editorial Preface*, 2012, vol. 3, no. 12.
  7. SUN, C. Fast Optical Flow using 3D Shortest Path Techniques. *Image and Vision Computing*, 2002, vol. 20, no. 13. pp. 981–991.



# Basic Cardiovascular Computer Model Shows System Degeneracy When Used in Reverse on Standard Measured Parameters

Borut Kirn

## Abstract

Physiology-based computer models are used to simulate the cardiovascular system. When used in reverse the state of a cardiovascular system is determined from measured values and results are used in patient-specific medicine. However, reverse approach is limited by system degeneracy—a situation where the measured values are same but the system states are different. By using uniqueness analysis we explored the origin of system degeneracy by studying it in the most basic two parameter cardiovascular physiological models: Wind-Kessel model of aortic flow. From the model a parameter space of compliance, resistance and a measurement space of peak, mean pressure were generated. Pairs in the parameter space were obtained by gradually increasing each parameter throughout its physiological range. Pairs in the measurement space were equidistant and within the physiological range. Then in parameter space, a family of values was found such that yield peak, the mean pressure within measurement error distance from measurement space pair. The family members when present in the parameter space formed connected components. Number and shape of these components served us to determine the degree of degeneracy. We found that the component in parameter space remains non-divided for all values in measurement space. However, the shape of the component is asymmetrical and depends on the measured value. Compliance showed large uncertainty up to  $\pm 31\%$  of its physiological range while uncertainty in peripheral resistance was well  $\pm 5\%$ . The large uncertainty in one parameter is a form of degeneracy and we found that it exists already when using the simplest physiological two-parameter model. Models and measured parameters used in reverse engineering need to be carefully evaluated for degeneracy.

## Keywords

Computational modeling • Reverse engineering  
System degeneracy

## 1 Introduction

The extraction of tissue and system properties from measured observable could be achieved by directly comparing measured and computationally simulated values [1, 2]. A prerequisite for reverse engineering is a relevant computational model which provides realistic simulations within both physiological and pathological ranges. In theory, it works such that the model is fed with tissue and system properties and observable which is to be measured is simulated. The simulated and measured values are then compared and tissue and system properties are estimated from the signals that match.

There are several challenges with this approach. One is that computational simulations can be time intensive when using finite element models however when lumped parameter models are used each situation is simulated in a fraction of a second thus a large range of parameter values can be simulated within a reasonable time.

The computational model needs to be a relevant representation of the biological system. To achieve that it should include all main physiological characteristics of the system. However, an increase of parameter number exponentially increases the time of simulations and drastically increases the complexity of results interpretation. Thus the first step in complex system analysis is to study the simplest version of the model which incorporates only the crudest characteristics of the biological system. In the presenting study, the most elementary format for a physiological model of the aortic vessel (Windkessel) is used.

A common phenomenon in complex biological systems is degeneracy [3, 4]. In a computational model, the degeneracy is observed when a different set of input variables

B. Kirn (✉)

University of Ljubljana, Zaloska 4, 1000 Ljubljana, Slovenia  
e-mail: borut.kirn@mf.uni-lj.si

returns similar simulated observables. That is the simulated observables differ for less than expected value of measurement error.

Each system that is analyzed in reverse should thus be tested for degeneracy in addition to parameter sensitivity. In this study, a novel—graphical approach for system degeneracy and sensitivity is presented.

The simplest model of a segment of the circulatory system is a two-element Windkessel model (Eq. 1) [5]. In this model peripheral resistance  $R$ , arterial compliance  $C$ , and the flow of blood into the vessel  $I(t)$  determine the pressure in the artery during a cardiac cycle. Accordingly,  $R$ ,  $C$ , and  $I(t)$  are system variables.

$$I(t) = \frac{P(t)}{R} + C \frac{dP(t)}{dt} \quad (1)$$

We studied how uniquely observables  $P_{\max}$ ,  $P_{\text{mean}}$  translate into model parameters  $R$ ,  $C$  at a given  $I(t)$  while assuming that observables  $P_{\max}$ ,  $P_{\text{mean}}$  are measured with given measurement error.

## 2 Methods

The study is designed in a way to use forward simulation for studying sensitivity of parameter extraction in reverse. To achieve that two spaces are created a parameter space and a measurement space. The parameter space consists of the parameters ( $R$ ,  $C$ ) that are gradually changed in the simulation which is used to calculate predicted measured values. The measurement space is a space of all possible measured values ( $P_{\max}$ ,  $P_{\text{mean}}$ ).

The sensitivity and degeneracy of the parameter extraction in reverse is studied so that for a measured value we find all similar simulated values. Thus each pair  $P_{\max}$ ,  $P_{\text{mean}}$  that is measured with measurement error yields a group of simulated  $P_{\max}$ ,  $P_{\text{mean}}$  values which further yield a group of parameter values in parameter space ( $R$ ,  $C$ ).

All values mentioned in the study are computational. This is self-evident for parameter space but also the measurement space is constructed, however, within realistic measurement range and with realistic level of measurement error which enables us to study inherent relations that are characteristic for the observed model.

A parameter space was composed of  $32 \times 32$  pairs of  $R$ ,  $C$  values ranging from 20 to 180% of normal value in steps of 5% ( $R_{\text{normal}} = 0.95 \text{ mmHg} \times \text{s/ml}$ ;  $C_{\text{normal}} = 1.1 \text{ ml/mmHg}$ ) [6–8]. For each  $R_i$ ,  $C_j$  pair, a model value of  $P_{\max\_ij}$ ,  $P_{\text{mean\_ij}}$  was calculated with a two-element Windkessel model (MatLab, ode45). The  $I(t)$  applied in the calculations was the sine function  $I(t) = I_0 \times \sin(2\pi \times t/t_0)$  ( $I_0 = 424 \text{ ml}$ ,  $t_0 = 60 \text{ s/72}$ ) and was kept the same in all calculations.

A measurement space was composed of  $P_{\max\_ref}$  and  $P_{\text{mean\_ref}}$  values, which were divided into 29 equidistant values ranging from 60 to 200 mmHg and 30–170 mmHg, respectively.

Then, for each point of measurement space ( $P_{\max\_ref}$ ,  $P_{\text{mean\_ref}}$ ), a map in the parameter space was obtained such that in the map only those  $R_i$ ,  $C_j$  pairs were included that satisfied the criterion

$$(P_{\max\_ref} - P_{\max\_i})^2 + (P_{\text{mean\_ref}} - P_{\text{mean\_i}})^2 < E^2 \quad (2)$$

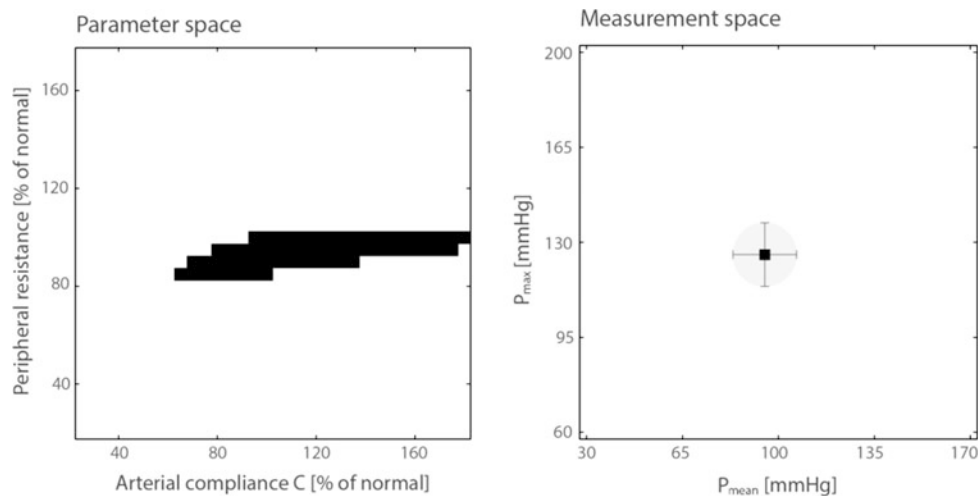


**Fig. 1** Parameter space (left) with  $32 \times 32$   $R_i$ ,  $C_j$  pairs and measurement space (right) with  $29 \times 29$  pairs of  $P_{\max\_ref}$ ,  $P_{\text{mean\_ref}}$ . All highlighted  $R$ ,  $C$  pairs in the parameter space yield calculated  $P_{\max}$ ,  $P_{\text{mean}}$  values within the marked circle in the measurement space

( $P_{\max\_ref} = 125 \text{ mmHg}$  and  $P_{\text{mean\_ref}} = 95 \text{ mmHg}$  with measurement error  $\pm 12 \text{ mmHg}$ ). Note that the marked  $R$ ,  $C$  pairs have similar  $R$  but drastically different  $C$  values

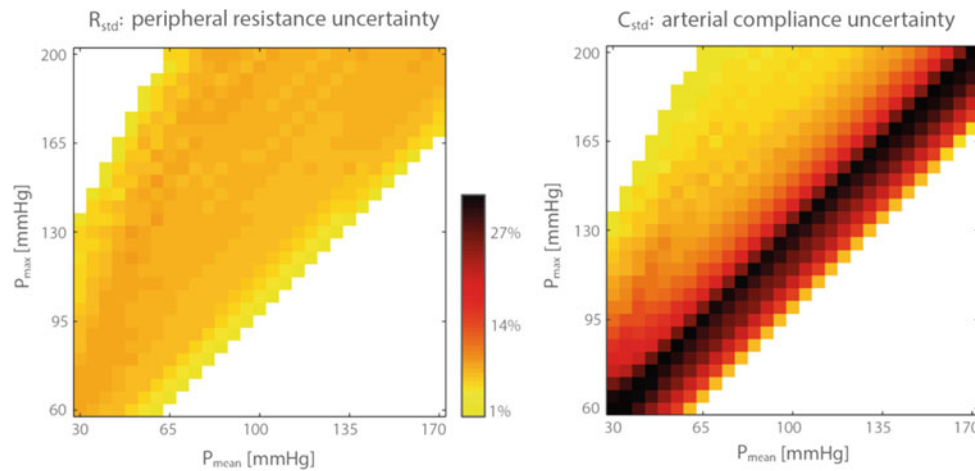


**Fig. 2** Uncertainty  $R_{std}$  (left),  $C_{std}$  (right) of  $R$ ,  $C$  values, respectively, calculated from  $P_{max}$ ,  $P_{mean}$  with measurement error  $\pm 12$  mmHg. The uncertainty is found as the standard deviation of island height and width in the  $R$ ,  $C$  map, respectively. Note that  $R_{std}$  is

where  $E$  is the measurement error  $\pm 12$  mmHg [6] and  $P_{max\_ij}$ ,  $P_{mean\_ij}$  are the model values for a pair  $R_i$ ,  $C_j$ . Uncertainty ( $R_{std}$ ,  $C_{std}$ ) for  $R$  and  $C$  were determined as the standard deviation of all  $R_i$  and  $C_j$  values that were included in the map.

### 3 Results

Figure 1 shows a value in the measurement space ( $P_{max\_ref} = 125$  mmHg,  $P_{mean\_ref} = 95$  mmHg) with a measurement error  $\pm 12$  mmHg (circular ring) together with a corresponding map in the parameter space. The values in the map form one island (blob), which is asymmetric and much wider in the  $C$ -axis direction as compared to the  $R$ -axis direction.

The narrow shape of the island in the  $R$ -axis direction indicates that resistance  $R$  has low uncertainty ( $R_{std} = \pm 5\%$ ). In contrast, the width of the island covers two-thirds of the total range of the  $C$ -axis. Hence  $C$  could be anything between 60 and 180% and thus uncertainty is large ( $C_{std} = \pm 31\%$ ).

When observing shapes of islands for all pairs in measurement space we confirmed that in all cases only one island in parameter space exists. The relation between the values in the measurement space and values in the parameter space is such that a decrease in  $P_{max}$  is associated with higher  $C$  values and increasing standard deviation, whereas an increase in  $P_{mean}$  is associated with higher  $R$  values at constant standard deviation.

The average  $R_{std}$ ,  $C_{std}$  for all system variable space was  $\pm 6$  and  $\pm 14\%$ , respectively. The distribution of uncertainty (Fig. 2) is relatively even for  $R$  but varies considerably for

low for any combination of  $P_{max}$ ,  $P_{mean}$ , whereas the  $C_{std}$  diagonal region, which includes physiological values, shows uncertainty in  $C$  up to  $\pm 35\%$

$C$ . Some combinations of  $P_{max}$ ,  $P_{mean}$  could not be calculated from the given range of system variable space, and so islands for these combinations are non-existent and have been removed from the statistics.

### 4 Discussion

In this computational study, it has been shown that measurement error of  $P_{max}$ ,  $P_{mean}$  translates unevenly into  $R$ ,  $C$ . The uncertainty of evaluating  $R$  from “measured”  $P_{max}$ ,  $P_{mean}$  is low, however, the uncertainty for evaluating  $C$  is up to six times greater, particularly in the physiological range of  $P_{max}$ ,  $P_{mean}$  values.

High uncertainty in  $C$  indicates a degree of degeneracy in the system, in which similar measured values of  $P_{max}$ ,  $P_{mean}$  will have similar values of  $R$  but could have largely different values of  $C$ .

By using the computational approach, the basic inherent characteristics of the biological system are revealed, given that basic physical tissue characteristics are used in the model. The next step is to study the influence of changing  $I(t)$ , which represents the flow of the blood from the ventricle into the artery. The duration of ejection, peak flow, and stroke volume each add a dimension of complexity. Furthermore, by upgrading the two-element Windkessel model with additional elements [5, 7, 9], including pulse wave bouncing, the level of degeneracy revealed here is not likely to disappear; on the contrary, each level of complexity of the model is likely to add a new dimension in degeneration. In case of increased model complexity, it can be expected that there will be more than one island in the parameter space. That kind of development would require additional

measurement in order to uniquely define the state of the system. In medicine, the approach of this kind is named differential diagnostics.

Patient-specific modelling is a developing approach that could both aid in diagnosis and support therapeutic decision-making in a clinical situation. The basic concept is that a model's functional and structural properties are adjusted until simulation matches a given set of measurements obtained from an individual patient. Therapeutic options can then be simulated to establish whether a proposed therapy is likely to succeed.

The main contribution of this study is thus the investigation into the uniqueness of parameter values in patient-specific modelling approaches. Our study addresses this issue by introducing parameter space exploration enabled by a fast, lumped-parameter model. Our simulation and analysis approach enables a scan across all states of the modelled system and, thus, detection of cases when a given measured value of the system could be simulated by more than one set of model parameters and thus could lead to more than one possible diagnosis. Graphical approach improves visual comprehension of sensitivity and degeneracy characteristics of a biological system. It translates complex system into maps which enables new analytical techniques for studying complex system like Manifold learning for dimension reduction.

This study revealed that  $P_{max}$ ,  $P_{mean}$  is a good representation of peripheral resistance  $R$ , whereas the uncertainty of arterial compliance  $C$  shows impractically high levels. Future studies should show how the great uncertainty in  $C$  influences understanding of the state of the cardiovascular system. High uncertainty in  $C$  is potentially important in physiological control for example in the control of the total artificial heart. A computer simulation with incorporated

high uncertainty in  $C$  should reveal consequences of high uncertainty in  $C$  for regulation of the total artificial heart.

**Acknowledgements** The authors acknowledge the project (J3-7312) was financially supported by the Slovenian Research Agency

**COI Disclosure** The authors declare that they have no conflict of interest.

---

## References

1. Villaverde, Alejandro F., and Julio R. Banga.: Reverse Engineering and Identification in Systems Biology: Strategies, Perspectives and Challenges. *Journal of the Royal Society Interface*, 11(91): 20130505 (2014).
2. Csete E.C., Doyle J.C.: Reverse engineering of biological complexity. *Science*, 295(5560): 1664–1669 (2002).
3. Tononi, G., Sporns, O., Edelman, G.M.: Measures of degeneracy and redundancy in biological networks. *Proc Natl Acad Sci USA*, 96(6):3257–3262 (1999).
4. Li, Y., Dwivedi, G., Huang, W., Kemp, M.L., Yi, Y.: Quantification of degeneracy in biological systems for characterization of functional interactions between modules. *J Theor Biol*, 302:29–38 (2012).
5. Westerhof, N., Lankhaar, J.W., Westerhof, B.E.: The arterial Windkessel. *Med Biol Eng Comput*, 47(2):131–141 (2009).
6. Reuben, S.R.: Compliance of the human pulmonary arterial system in disease. *Circ Res*, 29(1):40–50 (1971).
7. Stergiopoulos, N., Westerhof, B.E., Westerhof, N.: Total arterial inertance as the fourth element of the windkessel model. *Am J Physiol*, 276(1 Pt 2):H81–88 (1999).
8. Komet, L., Jansen, J.R., Nijenhuis, F.C., Langewouters, G.J., Versprille, A.: The compliance of the porcine pulmonary artery depends on pressure and heart rate. *J Physiol*, 512 (Pt 3):917–926 (1998).
9. Burkhoff, D., Alexander, J., Jr., Schipke, J.: Assessment of Windkessel as a model of aortic input impedance. *Am J Physiol*, 255(4 Pt 2):H742–753 (1988).

# Quantifying the Spatial and Angular Distribution of Lethal Neutrons for Treating Planning

Jonathan Jian Wei Yeo, Hong Qi Tan, Khong Wei Ang, James Cheow Lei Lee, and Andrew Anthony Bettiol

## Abstract

It is known that high energy protons in proton therapy generate secondary particles. Of which, secondary neutrons are a main concern as they deposit out-of-field doses and can have long-term health effects on cancer patients. In this paper, the energy, 3-D spatial and angular distribution of the production yield of neutrons is scored along the proton beam path in different types of tissue medium. The degree of biological damage is then quantified through factoring in the relative biological effectiveness of neutrons. This systematic study involved simulating 70, 150 and 200 MeV proton beam transport in various tissue compositions with the GEANT4 code. System specifications of the Hitachi proton therapy system were used in this study. Simulation results showed that the neutrons are forward facing and are generally emitted at a preferential angle. With considerations on the RBE variation with neutron's energy, the spatial and angular distribution of the production of lethal neutrons were identified along the proton track. Non-trivial relations between biological damage in different tissue medium were observed. Such comprehensive simulation studies have not been reported and this input information can be useful for treatment planning in reducing out-of-field neutron dose in sensitive organs.

## Keywords

Proton therapy • Neutrons • Monte carlo

## 1 Introduction

Proton therapy will soon be breaking into the Singapore market, with the completion of the Goh Cheng Liang Proton Therapy Centre in Singapore in 2022 [1]. The interest in proton therapy stems from the ability of proton beams to deliver a more targeted dose as compared to radiotherapy [2]. However, not all is perfect, as concerns over secondary cancer development due to the secondary neutrons doses arises [3].

Neutrons are produced as secondary particles during proton therapy and can contribute to the out-of-field dose of the patient. It has been intensively studied by several research groups [3–5], and it is worthy to note that current risk models predict a reduction in secondary cancer risk for active protons versus photons and a similar risk for passive protons versus photons [3]. However, from a physical standpoint, neutrons are harmful because of their high Relative Biological Effectiveness (RBE) and high Linear Energy Transfer (LET) properties [3]. Hence the risk of secondary cancer is still present in proton therapy.

This is a cause for concern because at the time of writing, commercial proton therapy treatment planning systems do not have the capabilities to determine neutron doses. As a result, we conducted a comprehensive study of neutron production in various tissue models to provide information of the angular distribution, spatial distribution and energy distribution of these secondary neutrons.

## 2 Materials and Methods

To perform this study, a Monte Carlo simulation, derived from GEANT4 [6–8], was used to simulate the yield of neutrons produced during proton therapy on various tissue models available from the GEANT4 materials database [9]. This simulation was originally developed for the commissioning of the upcoming proton therapy center in Singapore,

J. J. W. Yeo (✉) · H. Q. Tan · A. A. Bettiol  
Department of Physics, National University of Singapore, Center for Ion Beam Applications, Singapore, Singapore  
e-mail: jonayeo@hotmail.com; jyeo@u.nus.edu

K. W. Ang · J. C. L. Lee  
National Cancer Centre of Singapore, Singapore, Singapore



and the details on the detector geometry can be found in the corresponding conference paper (Geant4 Simulation for Commissioning of Proton Therapy Centre).

Proton pencil beams of energies 70, 150 and 200 MeV were used in this study to monitor the secondary neutron production in various blocks of  $30 \times 30 \times 30$  cm tissue phantoms. A total of 10 million protons were simulated in each run. The energy, momentum, position of the secondary neutrons were scored and analysed. Transport of the neutrons were killed right after production, to reduce the computing power needed; the information of the neutron transport was not required because this is a preliminary study.

## 2.1 Physics Model

In our simulation, the QGSP\_BIC\_EMY physics model [10] in GEANT4 was used to obtain the data of the neutron's position and momentum. The QGSP physics model was chosen because it is highly recommended for medical application [10]. The QGSP model can simulate nuclear excitation through high energy interactions and subsequently the nuclear de-excitation, using the pre-compound model and generate secondary particles. The BIC component replaces the LEP model in QGSP with a binary cascade, which is better at describing the production of secondary particles produced in the interactions of protons with the nuclei. The EMY option refers to the emstandard\_opt3 for the electromagnetic model and was chosen to achieve a higher accuracy.

## 2.2 Tissue Phantoms

A total of 24 blocks of tissue phantoms were used for this study [9], and the neutron yield from each phantom was compared against each other. Each phantom was made up of a  $30 \times 30 \times 30$  cm block of tissue, ranging from bone to adipose tissues. The full list of the tissue materials used can be found in Table 1.

## 2.3 Angular Distribution

The angular distribution was determined based on the information of the momentum vector of the neutrons. The angle of the direction of the neutron was calculated from the direction of pencil beam using the Eq. (1),

$$\theta = \cos^{-1} \frac{P_x}{\sqrt{P_x^2 + P_y^2 + P_z^2}} \quad (1)$$

where  $P_x$ ,  $P_y$ ,  $P_z$  are the momentum of the neutron in the x, y and z direction respectively and x is the initial direction of the pencil beam.

## 2.4 Lethality Factor

In this preliminary study, a lethality factor was defined as the track-summed RBE of the neutrons in each voxel of  $1 \text{ mm}^3$ . The lethality factor is a measure of the maximum risk of localized DNA damage from neutrons at the moment of production, and it follows Eq. (2),

$$L(i) = \sum_E R(E) \times N(E, i) \quad (2)$$

where R is the Relative Biological Effectiveness study value of the neutron based on its energy, N is number of neutrons of energy E in the i-th voxel and L is the sum across all neutron energies to get the lethality factor.

The RBE values of the neutrons used in this paper considers double strand break clusters caused by the neutrons and is dependent on the energy of the neutrons [11]. The highest lethality factor in a voxel for each material is then collated and presented in Fig. 3. The highest lethality factor reflects the relative concentration of lethal neutrons produced amongst the different tissue medium.

## 3 Results

A total of 72 runs were conducted, simulating the neutron production in various tissue phantoms with proton beams of different energies. The results from each run were collated and analyzed. Values of the maximum lethality calculated are presented in Fig. 3. The mode of energy distribution of the secondary neutrons and the most probable direction it is travelling towards are presented in Table 1.

### 3.1 Proton Beam on Water Phantom

Results from proton beams of energies 70, 150 and 200 MeV directed towards a water phantom are presented in this section. Figure 1 shows the distribution of the angular direction of the neutrons and Fig. 2 shows the distribution of the energy of the neutrons in a water phantom.

In Fig. 1, it is observed that majority of the neutrons produced are forward facing, with the mode of the angle  $\theta$  being  $(44.0 \pm 0.05)^\circ$  for a 70 MeV proton beam,  $(34.8 \pm 0.05)^\circ$  for a 150 MeV proton beam and  $(32.6 \pm 0.05)^\circ$  for a 200 MeV proton beam. The results suggest that a lower energy proton

**Table 1** The mode of the angular distribution of the neutrons (uncertainty of  $\pm 0.05^\circ$ ) and mode of the energy of the neutrons (uncertainty of  $\pm 0.05$  MeV) produced from 70, 150 and 200 MeV proton beam in the 24 materials used in the study. (\*) represents materials where results are not statistically significant due to the low number of counts

Tissue name	70 MeV		150 MeV		200 MeV	
	Mode angle ( $\pm 0.05^\circ$ )	Mode energy ( $\pm 0.05$ MeV)	Mode angle ( $\pm 0.05^\circ$ )	Mode energy ( $\pm 0.05$ MeV)	Mode angle ( $\pm 0.05^\circ$ )	Mode energy ( $\pm 0.05$ MeV)
G4 A150 tissue	48.3	0.7	31.1	0.7	30.3	0.9
G4 adipose tissue	44.3	0.6	32.0	0.9	34.0	0.7
G4 air *	26.7	1.1	55.6	0.6	32.5	1.7
G4 B100 bone	35.7	0.5	33.4	0.8	33.4	0.7
G4 blood ICRP	56.4	0.4	35.6	0.6	34.9	0.8
G4 Bone compact ICRU	43.9	0.6	29.1	0.6	31.9	0.7
G4 Bone Cortical	50.0	0.7	33.0	0.6	32.8	0.7
G4 brain	44.7	0.6	32.0	0.6	30.0	0.8
G4 C552 tissue	45.9	0.7	30.7	0.7	35.0	0.7
G4 eye lens ICRP	57.6	0.7	26.9	0.9	33.3	0.8
G4 lung ICRP	47.8	0.5	37.1	0.8	27.6	0.8
G4 MS20 tissue	38.4	0.7	29.0	0.7	34.1	0.8
G4 muscle skeletal ICRP	57.2	0.6	32.0	0.7	31.0	0.8
G4 Muscle Striated ICRU	53.9	0.9	34.5	0.6	28.9	0.6
G4 muscle without sucrose	38.4	0.4	32.2	0.7	34.2	0.8
G4 muscle with sucrose	46.4	0.8	33.0	0.8	30.6	0.7
G4 skin ICRP	34.7	0.7	34.1	0.9	34.4	0.7
G4 testes ICRP	38.6	0.7	35.9	0.8	31.6	0.9
G4 tissue methane *	104.0	0.8	38.7	0.3	28.5	3.1
G4 tissue propane *	33.9	0.4	18.0	0.9	17.6	2.0
G4 tissue soft ICRP	40.8	0.7	35.4	0.8	37.1	0.7
G4 tissue soft ICRU	57.9	0.6	31.9	0.8	29.2	0.7
G4 urea	45.6	0.6	34.1	0.8	33.0	0.8
G4 water	44.0	0.6	34.8	0.8	32.6	0.6

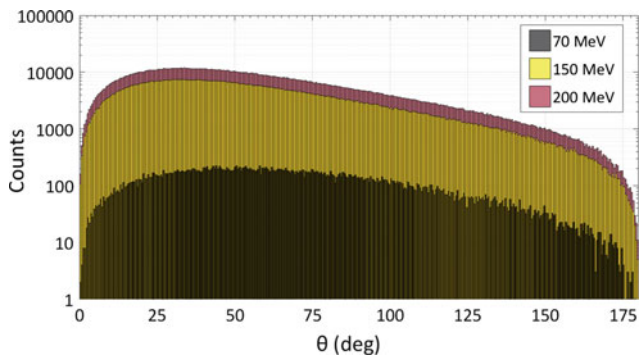


**Fig. 1** Histogram of the angular distribution of neutrons produced from an incident proton beam of energy 70 MeV (grey), 150 MeV (yellow) and 200 MeV (pink) on a water phantom with a bin width of  $1^\circ$  (Color figure online)

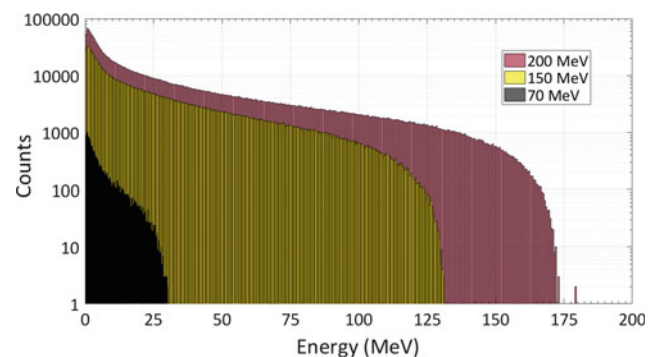


**Fig. 2** Histogram of the energy of neutrons produced from an incident proton beam of energy 70, 150 and 200 MeV on a water phantom

beam will produce neutrons that are more isotropic (histogram resembles a uniform distribution).

Figure 2 shows that when protons of energies 70, 150 and 200 MeV interact with water, most of the secondary neutrons produced are intermediate neutrons ( $<1$  MeV). The mode of the energy distribution of the neutrons are  $(0.6 \pm 0.05)$  MeV,  $(0.8 \pm 0.05)$  MeV and  $(0.6 \pm 0.05)$  MeV respectively. Intermediate neutrons are known to have high RBE and LET values [11], thus the effect of secondary neutron dose on biological materials cannot be neglected.

### 3.2 Collated Results

This preliminary study shows a non-trivial relation of the localized damage between the different tissue models, and it serves as a motivation to investigate the maximum risk of damage from transport of the neutrons. The lethality factor shown in Fig. 3 is a measure of the localized risk at the point of production, hence directing a proton beam into bone cortical is riskier than directing the beam towards soft tissues. This suggest that one should avoid directing the proton beam through bone cortical during treatment planning.

Like the results obtained from the water phantom, results from other tissue phantoms in Table 1 suggest that a higher energy proton beam would result in a less isotropic distribution and produce more neutrons that are forward facing. In addition, no distinguishable trend can be seen between the

mode of the energy of the neutrons and the energy of the proton beam.

## 4 Conclusion

In our study, the results show that most of the neutrons produced in the 24 tissue phantoms are intermediate neutrons ( $<1$  MeV). This is a cause for concern because intermediate neutrons have a high RBE value and can result in a high localized damage. Moreover, the angular distribution of the neutrons have a correlation to the energy of the incident proton beam. Treatment planners should also avoid directing the proton beam towards tissues such as bone cortical if possible, to reduce the risk of DNA damage due to secondary neutrons.

**Disclosures** No Conflict of interest, financial or otherwise, are declared by the authors.

## Appendix

The total lethality factor is calculated by summing up the lethality values of all the voxels in one run. It is presented in this section to give the reader a sense of the total relative biological effectiveness from the production of secondary neutrons in different tissue medium (Fig. 4).

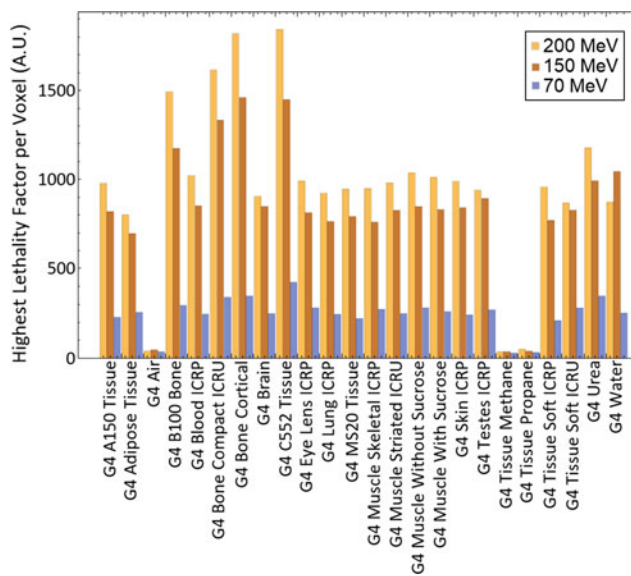


**Fig. 3** Bar chart showing the highest lethality factor of neutrons produced from 70 MeV (blue), 150 MeV (brown) and 200 MeV (orange) proton beam. The 24 materials used in this study are shown in the chart (Color figure online)

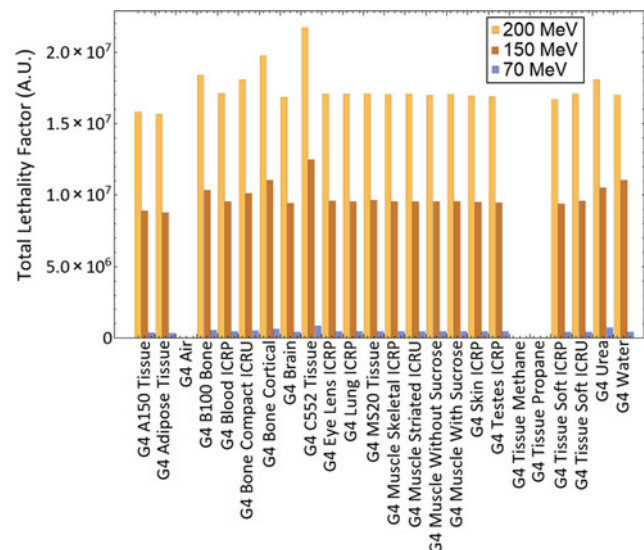


**Fig. 4** Bar chart showing the total lethality factor of neutrons produced from 70 MeV (blue), 150 MeV (brown) and 200 MeV (orange) proton beam. The 24 materials used in this study are shown in the chart (Color figure online)

## References

1. National Cancer Centre Singapore Facilities, <https://www.nccs.com.sg/ABOUTUS/OURFACILITIES/Pages/NewNCCSBuildingProtonTherapyCentre.aspx>, last accessed 2018/01/25.
2. Newhauser, W. D. and Zhang, R.: The physics of proton therapy. *Phys. Med. Biol.* 60, pp. R155 (2015).
3. Schneider, U. and Hälgl, R.: The impact of neutrons in clinical proton therapy. *Front. Oncol.* 5(October:235) (2015).
4. Hall, E. J.: Intensity-modulated radiation therapy, protons, and the risk of second cancers. *Int. J. Radiat. Oncol Biol Phys* 65, pp. 1–7 (2006).
5. Brenner, D. J., Hall, E. J.: Secondary neutrons in clinical proton radiotherapy: A charged issue. *Radiotherapy and Oncology* 86, pp. 165–170 (2008).
6. Agostinelli, S., Allison, J., Amako, K., Apostolakis, J., et. Al.: Geant4 – a simulation toolkit. *Nuclear Instruments and Methods in Physics Research Section A: Accelerators, Spectrometers, Detectors and Associated Equipment*. Volume 506, Issue 3, pp. 250–303 (2003).
7. Allison, J., Amako, K., Apostolakis, J., et. Al.: Geant4 developments and applications. *IEEE Transactions on Nuclear Science*, 53, pp. 270–278 (2006).
8. Allison, J., Amako, K., Apostolakis, J., et. Al.: Recent developments in Geant4. *Nuclear Instruments and Methods in Physics Research Section A: Accelerators, Spectrometers, Detectors and Associated Equipment*. Volume 835, pp. 186–225 (2016).
9. Geant4 Materials Database, [http://geant4.web.cern.ch/geant4/workAreaUserDocKA/Backup/Docbook\\_UsersGuides\\_beta/ForApplicationDeveloper/html/apas08.html](http://geant4.web.cern.ch/geant4/workAreaUserDocKA/Backup/Docbook_UsersGuides_beta/ForApplicationDeveloper/html/apas08.html), last accessed 2018/03/07.
10. Cirrone, G. A. P., Cuttone G., Guatelli S., Lo Nigro S., et. al.: Implementation of a new Monte Carlo simulation tool for the development of a proton therapy beam line and verification of the related dose distributions. *IEEE Transactions on Nuclear Science*, 52, pp. 1756–1758 (2005).
11. Baiocco, G., Barbieri, S., Babini G., et. Al.: The origin of neutron biological effectiveness as a function of energy. *Sci Rep.* 6 (1):34033 (2016).

# Effect of Left-Right Heart During Biventricular Assist Device Support by Speed Synchronization: A Computer Study

Phornphop Naiyanetr 

## Abstract

Biventricular assist device (BiVAD) is a treatment for the end-stage heart failure patients. Normally, after left ventricular assist device (LVAD) implanted in the end-stage heart failure patients, a right heart failure immediately appeared. Then, the right ventricular assist device (RVAD) was implanted. Both LVAD and RVAD implanted so call BiVAD. Additionally, the speed synchronization is a novel concept for remaining the high preload and increasing the cardiac output. It is a potential to promote a bridge to recovery treatment. The cardiovascular, RVAD, LVAD and speed synchronization models (co-pulse mode) are implemented using MATLAB. The normal heart and pathology heart are used in this study. The pathology level of the heart was regulated by a level of maximum elastance ( $E_{max}$ : 30% of normal heart value) in the heart model. The constant speed mode and co-pulse mode (increasing pump speed in systolic period between 8,000–11,000 rpm) are simulated using the MicroMed-DeBakey VAD model. The hemodynamics, ejection fraction, pressure-volume loop and pressure volume area (PVA) of different heart condition and pump mode are simulated. The results indicated the aortic pressure, pulmonary artery pressure and ejection fraction in co-pulse mode are similar to the constant speed mode. However, PVA in co-pulse mode are higher than the constant speed mode on pathology heart. In conclusion, this computer simulation can re-generated the effect of BiVAD under the pathological condition. The optimal ratio of RVAD support is important to prevent the suction event. Speed synchronization can maintain the high PVA than constant speed. Therefore, partial support with co-pulse mode can potentially use for the bridge to recovery treatment.

## Keywords

BiVAD • Biventricular assist device • Speed synchronization

## 1 Introduction

Biventricular assist device (BiVAD) is increasingly used in end-stage heart failure patient. By 30% of left ventricular assist device (LVAD) recipients, a right ventricular failure clinically presented. Therefore, a right ventricular assist device (RVAD) is immediately implanted. The conditions of patient who implanted both LVAD and RVAD so call BiVAD recipient [1]. For the first generation of VAD, pulsatile system was introduced as BiVAD. Nowadays, the second generation of VAD, a non-pulsatile system are currently use. In Germany, HeartWare HVAD (HeartWare Inc, Framingham, MA, USA) has been successfully implanted as BiVAD support [2, 3]. The non-pulsatile system is a rotary blood pump that provides a good device reliability and signification improvement of life quality.

BiVAD management needs an experienced person according to the difference pressure at aorta (related to LVAD support) and pulmonary artery of RVAD (related to RVAD support). A continuous-flow VAD is pressure dependent device. The flow of both LVAD and RVAD should be balance [4–6]. For training, animal model is expensive. The computer simulation of hemodynamic during BiVAD support is an alternative training that can reduce the cost of training [7]. Normally, each VAD has different characteristic. It needs the correct model of each VAD for simulation. For clinical education, the effect of left-right heart interaction has been implement using computer simulation with and without VADs [8, 9]. A speed synchronization (so call co-pulse) of BiVAD is a novel control system for destination therapy (DT) and bridge to recovery (BTR). For BTR concept, the speed control of BiVAD can induce the pulsatility that associates to the reverse

P. Naiyanetr (✉)  
Faculty of Engineering, Mahidol University, Nakorn Pathom,  
73170, Thailand  
e-mail: phornphop.nai@mahidol.ac.th



remodeling of heart during VAD support [10, 11]. For reverse remodeling, pressure-volume loop area (PVA) also be the indicator for heart energy monitoring [12]. Therefore, the computer simulation that can re-generated the effect of BiVAD under the pathological condition is important. Additionally, the optimal ratio of BiVAD support is important to prevent the suction event.

In this present study, the effect of left-right heart during BiVAD support by speed synchronization was investigate using numerical simulation.

## 2 Materials and Methods

In this study, cardiovascular system, RVAD, and LVAD models was developed base on lump-analog parameter model theory using MATLAB<sup>®</sup> and Simulink<sup>®</sup> (Math Works, Inc., Natick, MA, United States). The cardiovascular system model was implemented base on a study of Sun Y. et al. [8] and the time-varying elastance model was implemented base on Liang F. and Liu H. [13]. The MicroMed-DeBakey VAD model was implement base on the experimental model from Schima H. group [14].

The cardiovascular system, RVAD and LVAD models was similar to the previous study of Naiyanetr P [7] by divided into 7 groups of model: (1) cardiac chamber group: right atrium, right ventricle, left atrium, and left ventricle; (2) cardiac valve group: tricuspid valve, pulmonary valve, mitral valve, and aortic valve; (3) coronary group: coronary artery, coronary capillary, and coronary vein; (4) pulmonary part: pulmonary arteries, pulmonary capillaries, and pulmonary veins; (5) systemic vascular system: aorta, descending aorta, systemic arteries, systemic vein and vena cava; (6) RVAD model and (7) LVAD model. The heart failure conditions were implement by reducing the level of maximum elastance parameter ( $E_{max}$ ) from 100% (normal heart) to 30% (pathological heart) in the time-varying elastance equations (both left and right ventricles).

The BiVAD construction, the LVAD model was connect an inflow cannula at left ventricular model and an outflow cannula at ascending aorta model. The RVAD model was connect an inflow cannula at right ventricular model and an outflow cannula at pulmonary artery model. The speed synchronization of pump speed was related to the heartrate using a sine-wave pattern at a pulse-amplitude of 1,000 rpm (peak-to-peak equal to 2,000 rpm).

The hemodynamics of cardiovascular system with/without BiVAD was simulated. First, the normal, LV-pathological and RV&LV-pathological conditions without BiVAD support were investigated. Second, the RV&LV-pathological conditions with BiVAD support were investigated during fully support (aortic valve always close during systole) and partial support (aortic valve open during

systole). In fully support condition, BiVAD was set: (1) LVAD speed: 11,000 rpm and RVAD speed: 9,000 rpm. (2) LVAD speed: 11,000 rpm and RVAD speed: 11,000 rpm. In partial support condition, BiVAD was set as LVAD speed: 8,000 rpm and RVAD speed: 9,000 rpm. For speed synchronization, a sine-wave pattern at a pulse-amplitude of 1,000 rpm (peak-to-peak equal to 2,000 rpm) was applied on each condition.

In this study, the aortic pressure (AOP), left ventricular pressure (LVP), pulmonary artery pressure (PAP), right ventricular pressure (RVP), left ventricular volume (LVV), right ventricular volume (RVV), ejection fraction (EF), pressure-volume loop and pressure volume loop area (PVA) were investigated in all conditions.

## 3 Results

From simulation, the pressure-volume loop of normal heart, left heart failure and left-right heart failure were show in Figs. 1 and 2. PVA of left ventricle decreased related to the heart conditions: 6843.1, 6230.5 and 2879.4 (mmHg x ml), respectively. However, PVA of right ventricle show a different trend: 990.7, 1116.6 and 465.5 (mmHg x ml), respectively. EF decreased related to the heart condition; left heart-EF 59, 28 and 29%; right heart-EF 69%, 56% and 34%, respectively. The hemodynamics and pressure volume loop parameters wese show in Table 1. From simulation, the pressure-volume loop of: Full support I (LVAD 11,000 rpm and RVAD 9,000 rpm), Full support with co-pulse I, Full support II (LVAD 11,000 rpm and RVAD 10,000 rpm), Full support with co-pulse II, Partial support (LVAD 8,000 rpm and RVAD 9,000 rpm)and Partial support with co-pulse were show in Figs. 3 and 4. The hemodynamics and pressure volume loop parameters during BiVAD support was show in Table 2.

## 4 Discussion

The computer simulation use as an alternative study and training for clinician. The cardiovascular system model that can mimic the effect of left-right heart interaction was proposed [8]. The effect of LVAD support was investigated using computer study for both constant speed and co-pulse [9]. For speed synchronization of LVAD alone, LV-PVA is increased in comparison with constant speed [9]. However, the effect of BiVAD support for constant speed variation and speed synchronization was challenging to control.

The effect of left-right heart during biventricular assist device (BiVAD) support by speed synchronization is an important for BiVAD control system. In this study, the effect of speed synchronization mainly effect on both PVA and

**Fig. 1** Pressure volume loop of left ventricle: Normal heart, left and right heart failure, and left heart failure conditions

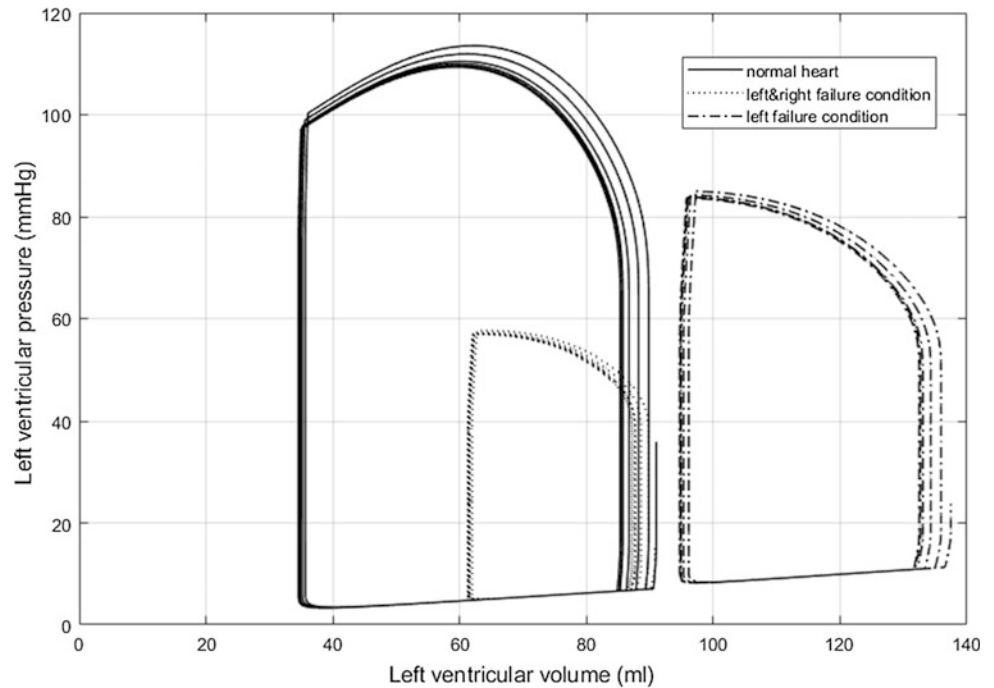
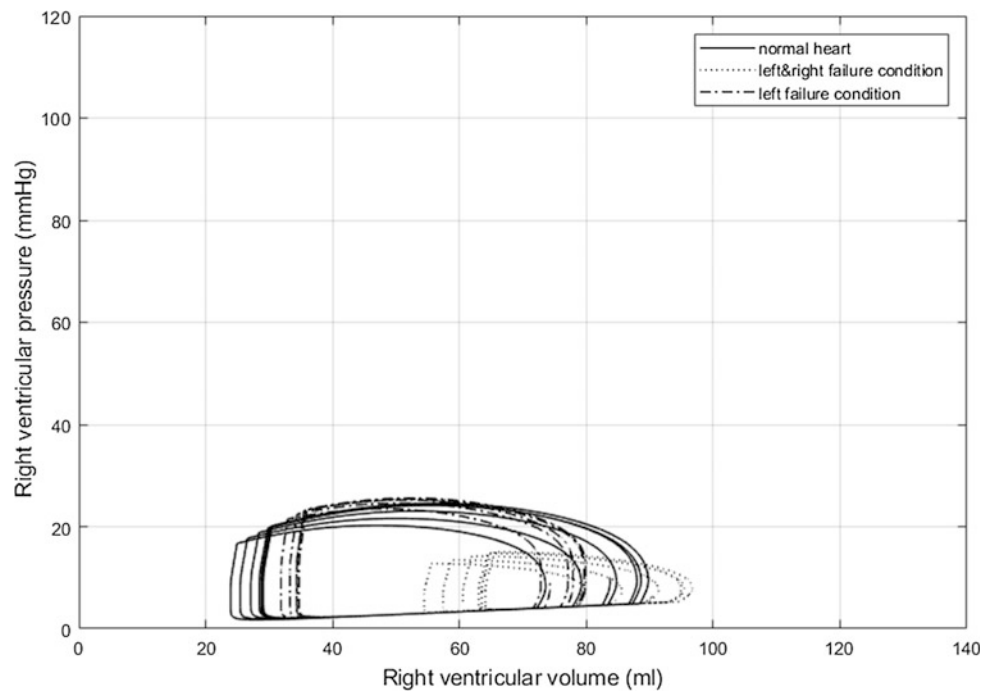


**Fig. 2** Pressure volume loop of right ventricle: Normal heart, left and right heart failure, and left heart failure conditions

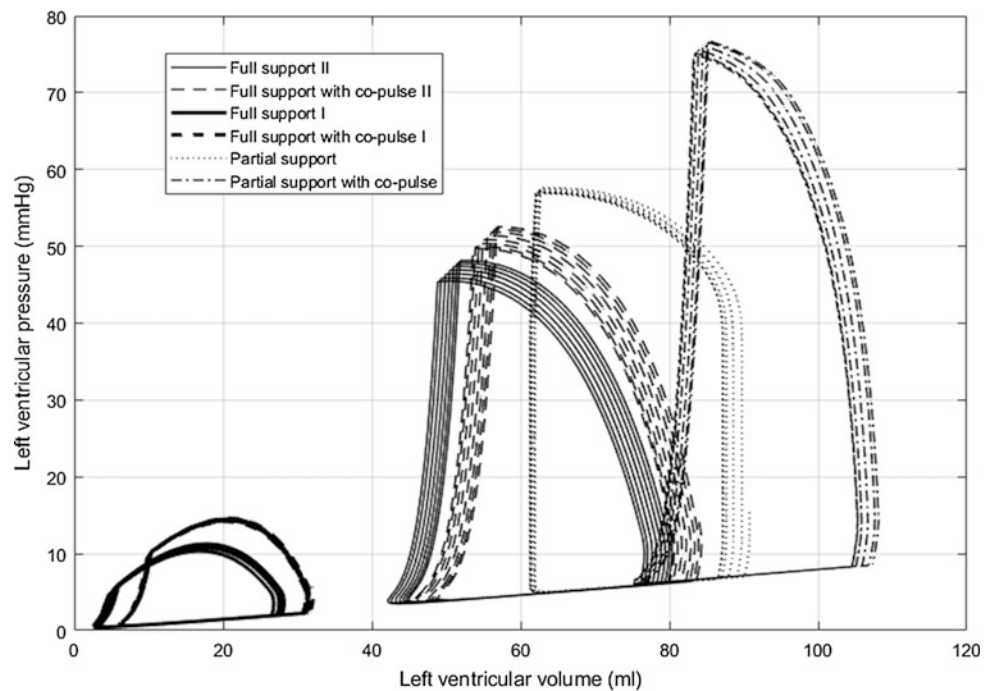


EDV. The speed synchronization increase both PVA and EDV of left ventricle in comparison with a constant speed mode as show in Table 2. On the right side of the heart, both PVA and EDV are not significantly change. However, in Fig. 4, the variation of RVAD mode are not effect to the EDV of right ventricle. The intrathoracic pressure that induced by breathing cycle effect on both PVA and EDV of right ventricle more than speed variation of RVAD.

The pump speed of RVAD is a mainly effect of left ventricular volume as shown in Fig. 3. The left ventricular volume is immediately increased after increase RVAD speed from 9,000 rpm to 10,000 rpm at the constant speed of LVAD. Increase the left ventricular volume can prevent the suction event of left ventricle. Therefore, the optimal ratio between LVAD and RVAD support is an important for BiVAD recipients.

**Table 1** Hemodynamics and pressure volume loop parameters without BiVAD support

Parameters	Normal heart	LV-failure	LV and RV failure
PVA-LV (mmHg ml)	6843.1	6230.5	2879.4
PVA-RV (mmHg ml)	990.7	1116.6	465.5
EDV-LV (ml)	85.7	132.6	87.63
EDV-RV (ml)	77.8	72.8	83.5
AOPmax (mmHg)	92.8	73.8	51.8
LVPmax (mmHg)	109.9	83.9	57.1
EF-LV (%)	59.3	28.4	29.7
EF-RV (%)	69.2	56.2	45.0

**Fig. 3** Pressure volume loop of left ventricle with BiVAD support: Full support I, Full support with co-pulse I, Full support II, Full support with co-pulse II, Partial support and Partial support with co-pulse

Application of BiVAD can be a bridge to transplant (BTT), destination therapy (DT) and bridge to recovery (BTR). For BTT, the optimal speed of both VAD can provide a high cardiac output and prevent suction event. For DT and BTR, only an optimal speed, the cardiac function and aortic valve open/close need to be consider, because the patient heart remain for long time. For BTR, cardiac monitoring for maintaining the quality of the heart or tracking the recovery of the heart need to be consider. For aortic valve open/close during support, the partial support need to be consider for keeping the aortic valve open during support (LVPmax higher than AOPmax). Cardiac function index

derived from pressure-volume relationship such as end-systolic pressure relationship (ESPVR), the maximum time varying elastance ( $E_{max}$ ), Pre-load-recrutable stroke work (PRSW), and the maximum derivative of ventricular pressure ( $dp/dt_{max}$ ) vs. EDV. However, all pressure-volume derived indexes need an invasive sensor. It is difficult for continuous monitoring. An alternative index such as pump flow derived index ( $I_q$ ) already proposed, but it depend on each model of VAD [15]. The computer model, which can re-create the physiological behavior of cardiovascular system, is important for both investigate the effect of BiVAD control system and train the VAD management staffs.

**Fig. 4** Pressure volume loop of right ventricle with BiVAD support:: Full support I, Full support with co-pulse I, Full support II, Full support with co-pulse II, Partial support and Partial support with co-pulse

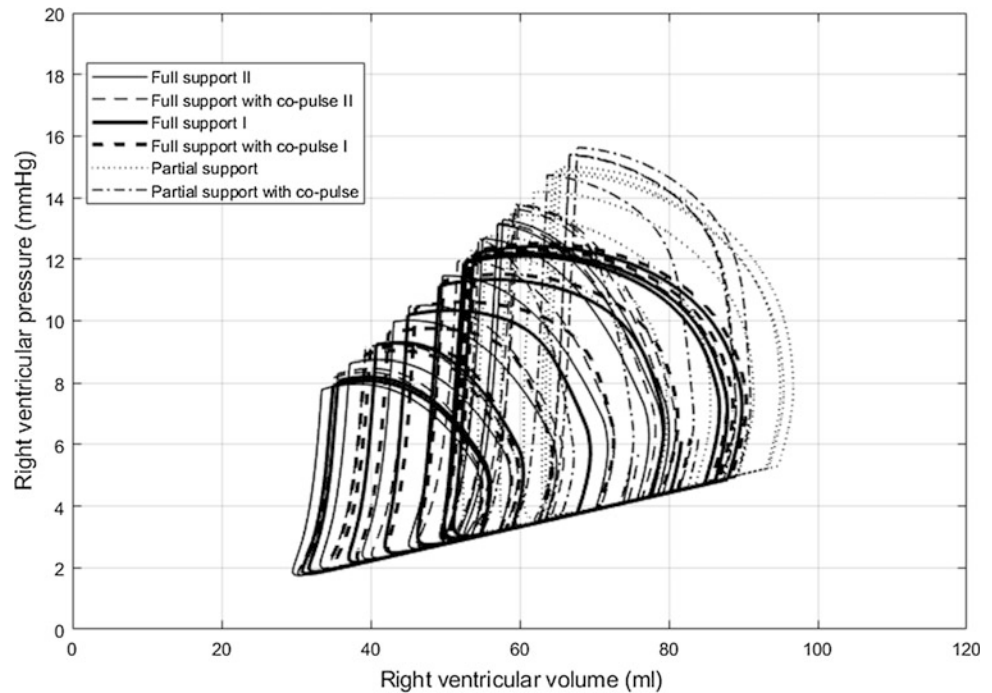


**Table 2** Hemodynamics and pressure volume loop parameters during BiVAD support

Parameters	Full support I	Full support with co-pulse I	Full support II	Full support with co-pulse II	Partial support	Partial Support with co-pulse
PVA-LV (mmHg ml)	347.9	360.2	2059.2	3086.4	3749.9	4141.3
PVA-RV (mmHg ml)	307.9	284.0	242.9	315.3	570.2	362.8
EDV-LV(ml)	27.5	31.2	77.0	80.6	88.4	108.1
EDV-RV(ml)	56.0	59.9	58.7	55.7	79.7	75.2
AOPmax (mmHg)	92.7	94.1	102.3	102.2	52.0	71.6
LVPmax (mmHg)	10.7	14.1	45.4	49.9	57.4	76.7
EF-LV(%)	90.6	80.7	45.3	43.2	30.4	28.9
EF-RV(%)	45.0	43.1	49.7	45.7	34.2	34.2

## 5 Conclusion

This computer simulation can re-generated the effect of BiVAD under the pathological condition. The optimal ratio of RVAD support is important to prevent the suction event during BiVAD support. Speed synchronization (co-pulse mode) can maintain the high PVA than constant speed. Therefore, partial support with co-pulse mode can potentially use for the bridge to recovery treatment in BiVAD heart failure patients.

## References

1. Krabatsch T., Potapov E., Stepanenko A., et al.: Biventricular circulatory support with two miniaturized implantable assist devices. *Circulation* 124(11 Supp.), S179–86 (2011).
2. Potapov E., Schweiger M., Vierecke J., et al.: Discontinuation of HeartWare RVAD support without device removal in chronic BIVAD patients. *ASAIO J.* 58(1), 15–18 (2012).
3. Stepanenko A., Krabatsch T., Hennig E., et al.: Retrospective hemolysis comparison between patients with centrifugal biventricular assist and left ventricular assist devices. *ASAIO J.* 57(5), 382–7 (2011).

4. Radovancevic B., Gregoric ID., Tamez D., et al.: Biventricular support with the Jarvik 2000 axial flow pump: a feasibility study. *ASAIO J.* 49(5), 604–7 (2003).
5. Gregory SD., Timms D., Gaddum N.: Biventricular assist device: a technical review. *Ann Biomed Eng.* 39(8), 2313–28 (2011).
6. Gregory SD., Percy MJ., Timms D., et al.: Passive control of a Biventricular assist device with compliant inflow cannulas. *Artif Organs.* 36(8) 683–90 (2012).
7. Naiyanetr P.: Effect of Continuous Flow Biventricular Assist Device on Pressure-Volume Loop: A Simulation Study. In: Boccaccini A.R. (eds.) 10th IASTED Internatiponal Conference on Biomedical Engineering on Proceedings, 791–089, ACTApress, Ausria (2013).
8. Sun Y., Beshara M., Lucariello RJ., and Chiaramida SA. A comprehensive model for right-left heart interaction under the influence of pericardium and baroreflex. *Am J Physiol* 272:H1499–515 (1997).
9. Htet ZL., Aye TPP., Singhavilai T and Naiyanetr P.: Hemodynamics during Rotary Blood Pump Support with Speed Synchronization in Heart Failure Condition: A Modelling Study. In 37th Annual International Conference of the IEEE Engineering in Medicine and Biology Society on proceedings, pp 3307–3310, IEEE, Milan, Italy (2015).
10. Cheng A., Willianitis C. A., and Slaughter M. S.: Comparison of continuous-flow and pulsatile flow left ventricular assist devices: is there an advantage to pulsatility?. *Ann. Cardiothorac.Surg.*, vol. 3, pp. 573581 (2014).
11. Burkhoff D., Klotz S., and Mancini D. M.: LVAD induced reverse remodeling: basic and clinical implications for myocardial recovery, *J. Card. Fail.*,vol. 12, pp. 227239, (2006).
12. Schima H., Vollkron M., Boehm H., et al.: Weaning of rotary blood pump recipients after myocardial recovery: a computer study of changes in cardiac energetic. *J Thirac Cardiovasc Surg.* 127(6), 1743–50 (2004).
13. Liang F. and Liu H. Simulation of hemodynamic response to the valsava maneuver: an intergrative computational model of the cardiovascular system and the autonomic nervous system. *J Physiol Sci* 56:45–65 (2006).
14. Vollkron M., Schima H., Huber L., and Wieselthaler G.: Interaction of the cardiovascular system with an implanted rotary assist device: simulation study with a refined computer model. *Artificial Organs.* 26: 349–59 (2007).
15. Naiyanetr P., Moscato F., Vollkron M., et al.: Continuous assessment of cardiac function during rotary blood pump support: a contractility index derived from pump flow. *J Heart Lung Transplant.* 29(10), 37–44 (2010).



# PCA-QDA Model Selection for Detecting NS1 Related Diseases from SERS Spectra of Salivary Mixtures

N. H. Othman, Khuan Y. Lee, A. R. M. Radzol, W. Mansor, and N. I. A. Hisham

## Abstract

Of recent, non-structural protein (NS1) in saliva has emerged to be engaging as a detection biomarker for diseases related to NS1 at febrile stage. Non-invasive detection of NS1 in saliva, free from risk of blood infection, further will make the approach more preferred than the current serum based ones. Our work here intends to define an optimal classifier model for Quadratic Discriminant Analysis (QDA), optimized with Principal Component Analysis (PCA), to distinct between positive and negative NS1 adulterated samples from salivary SERS spectra. The adulterated samples are acquired from our UiTM-NMRR-12-1278-12868-NS1-DENV database. Then, PCA extracts significant features from the database after pre-processing, based on three stopping criteria, which are served as inputs to the QDA classifiers. It is found that the PCA-QDA pseudo model with 5, 70 and 115 principal components from the three criterion achieves performance of 100% (Scree), 84.2% (CPV) and 55.3% (EOC) in accuracy. Higher accuracy at 100% (Scree), 97.3684% (CPV) and 97.3684% (EOC) are observed with QDA diagonal model.

## Keywords

Non-structural protein 1 • Surface Enhanced Raman Spectroscopy • Principal Component Analysis Quadratic Discriminant Analysis

## 1 Introductions

Dengue fever is a viral disease that infects people through female carrier *Aedes* mosquito. When a mosquito bites a person with dengue virus in their blood, the mosquito becomes infected and is enabled to spread the virus to another person. The World Health Organization (WHO) reports that more than 70% of the disease outbreak is in the South East Asia and Western Pacific. Symptoms of dengue fever usually start in four to six days after infection and can stay up to 10 days. In cases where the symptoms are moderate, it can be misdiagnosed for basic influenza or other viral diseases. For this reason, the need for a rapid and early biomarker for dengue detection is required. From literature, it is found that NS1 could be a biomarker for early and rapid detection. This is because it appears on the first day of fever, in comparison to antibodies which show up 5 or more days later [1]. The current methods for detecting of NS1 are such as enzyme-linked immunosorbent assay [2, 3], RT-PCR [2, 3], rapid diagnostic test [4] and virus isolation [2].

Raman spectroscopy founded by C.V. Raman and K.S. Krisnan in 1928 [5] claims capable of giving each molecule, a unique fingerprint spectrum and detection with sensitivity up to a single molecule [6]. It is a vibration based spectroscopy, making use of the inelastic dissemination of monochromatic light. Notwithstanding, the extremely weak signals that it delivered, renders its application disfavored until the discovery of SERS. SERS is able to amplify the signal intensity by  $10^4$  at the least [7]. Additional advantages of SERS are, measure of test required is negligible; preparation for spectroscopy is simple; analysis is rapid; test is harmless to humans and effortlessly reproducible [7]. These make the application of SERS prevalent amongst researchers, such as in genome sequencing [6], detection of DNA [5], detection of variants of cancer [8] and diagnosis of periodontitis [9]. Contemplating SERS with its wide acknowledgment as a disease discovery technique, it is hypothesized that SERS could be a promising detection technique for NS1, offering an

N. H. Othman · K. Y. Lee (✉) · A. R. M. Radzol · W. Mansor  
N. I. A. Hisham  
Faculty of Electrical Engineering, Universiti Teknologi MARA,  
Shah Alam, Malaysia  
e-mail: leeyootkhuan@salam.uitm.edu.my

K. Y. Lee · A. R. M. Radzol · W. Mansor  
Computational Intelligence Detection RIG, Pharmaceutical &  
Lifesciences Communities of Research, Universiti Teknologi  
MAR A, Shah Alam, Selangor DE, Malaysia

early and non-invasive recognition approach for flaviviral diseases, which to the best of our knowledge, has never been explored, besides our team.

In this study, it is aimed to define an optimal QDA Classifier model for detecting NS1 from salivary SERS spectra. In view of the volume of sample features, PCA is used to extract the most significant features residing in the SERS spectra before the classification stage [10]. PCA has the ability to identify a smaller number of uncorrelated variables from a larger set of data and represent the maximum amount of variance with that fewer number of variables. Classifier models from QDA are designed, examined and compared. Section 2 elaborates on the theoretical background of QDA. Section 3 describes the procedure and analysis methods. Section 4 examines, compares and discusses results from performance evaluation of the different classifier models with the different PCA stopping criteria.

## 2 Theoretical Background

Discriminant Analysis is a statistical procedure adopted to analyze a dataset when the criterion or the dependent variables is categorical and the independent variable is interval in nature. This multivariate technique offers two different types of classifier model, linear and quadratic. QDA is identical to LDA classifier, where it is accepted that the estimations from each class are conveyed. However, unlike LDA, QDA does not make the assumption that the covariance of each class is identical [11]. At the point where the typicality assumption is valid, the most ideal test for the hypothesis that a given estimation is from a given class, is the probability proportion test. Equation (1) gives the posterior probability equation [12]:

$$P(y|x) = \frac{P(x|y)P(y)}{P(x)} \quad (1)$$

where  $P(x|y)$  is a posterior probability that a point  $x$  belongs to a class  $y$ .  $P(y)$  is the prior probability for class  $y$  and  $P(x)$  is normalization constant, namely, the sum over  $y$  of  $P(x|y)P(y)$ . Statistical decision theory states that the posterior probability is the quantity of interest. Based on symmetric loss function, if the posterior probability of class 2 is more than posterior probability of class 1, then class 2 can be predicted. The steps to execute the QDA are shown in the following. Initially, the decision surface of the two classes data is retrieved. The set of the data at which the two posterior probability in Eqs. (2) and (3) are equally large, indicates where the decision surface lies, from which Eq. (4) is produced.

$$\text{Posterior probability of Class 2} = p(2|x) \quad (2)$$

$$\text{Posterior probability of Class 1} = p(1|x) \quad (3)$$

$$p(2|x) = p(1|x) \quad (4)$$

Then, Eq. (6) is derived from (4) using Eq. (5) and Bayes' theorem. Equation (7) is obtained by re-arranging Eq. (6) and ignoring the normalizing constant  $C_1$  and  $C_2$ , while  $\mu_1$  is the mean for class 1 and  $\mu_2$  is the mean for class 2.

$$p(x|2)p(2) = p(x|1)p(1) \quad (5)$$

$$\begin{aligned} p(2) \times C_2 \times \exp\left(-\frac{1}{2}(x - \mu_2)^T \sum_2^{-1} (x - \mu_2)\right) \\ = p(1) \times C_1 \times \exp\left(-\frac{1}{2}(x - \mu_1)^T \sum_1^{-1} (x - \mu_1)\right) \end{aligned} \quad (6)$$

$$-2 \ln \frac{P(2) \times C_2}{P(1) \times C_1} = (x - \mu_1)^T \sum_1^{-1} (x - \mu_1) - (x - \mu_2)^T \sum_2^{-1} (x - \mu_2) \quad (7)$$

Next, Eq. (7) are simplified to yield Eq. (8).

$$x^T \left( \sum_2^{-1} - \sum_1^{-1} \right) x + (\mu_2^T \sum_2^{-1} - \mu_1^T \sum_1^{-1}) x - 2 + \left( \mu_2^T \sum_2^{-1} \mu_2 + \mu_1^T \sum_1^{-1} \mu_1 \right) \quad (8)$$

Finally, Eq. (8) is converted into a general form as shown in Eq. (9), representing the decision surface [12].

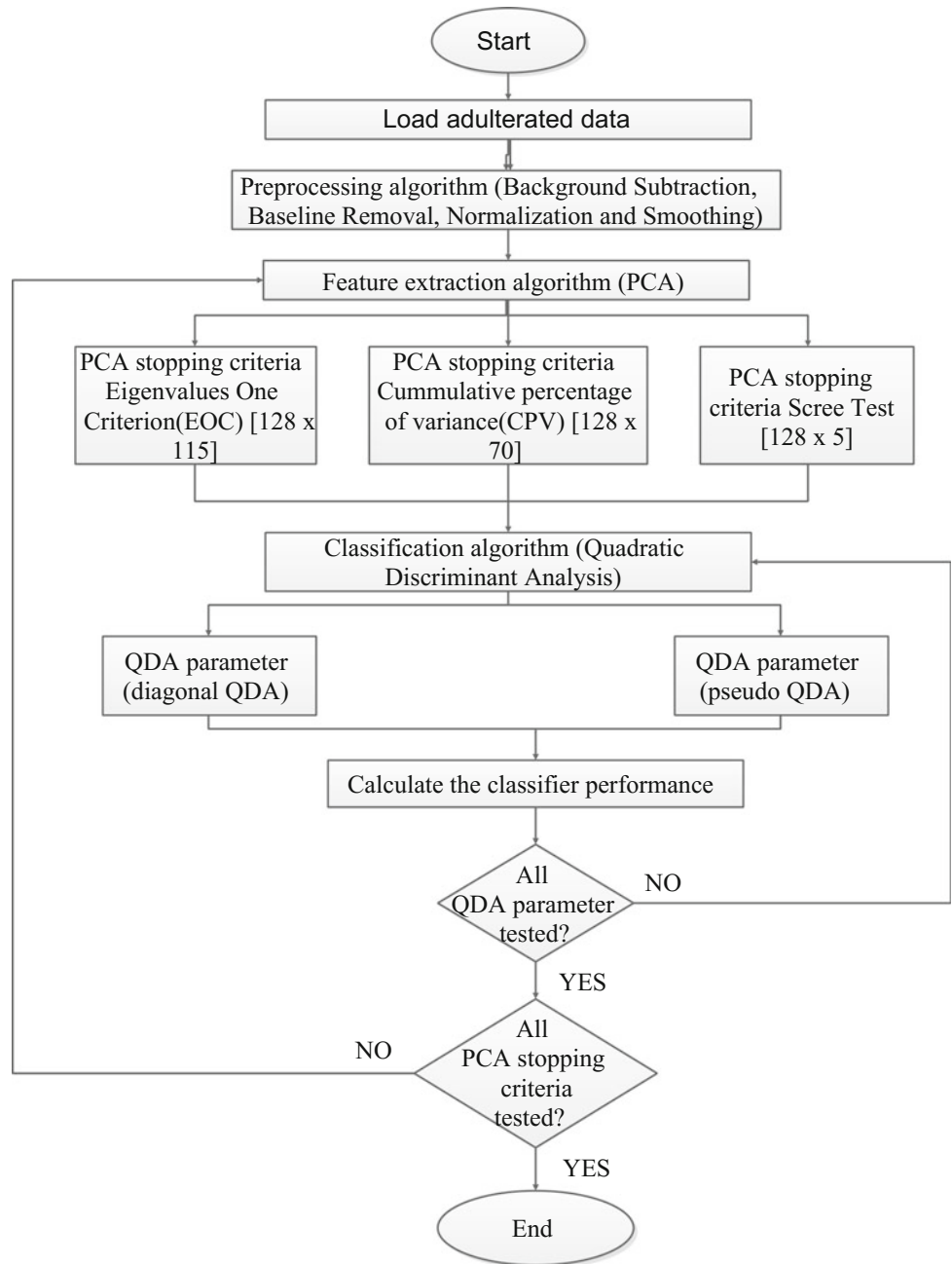
$$x^T A_x + b^T x + c \quad (9)$$

## 3 Methodology

Data used in this study were obtained from the UiTM-NMRR-12-1278-12868-NS1-DENV database. There were [64 × 1801] control group Raman spectra without NS1 and [64 × 1801] adulterated Raman spectra with NS1. The saliva samples were collected from healthy volunteers according to procedure detailed in [13].

With reference to Fig. 1, classification starts with pre-processing of the NS1 Raman spectra to eliminate noise and unwanted signal, for SNR enhancement. Pre-processing involved background subtraction, baseline removal, normalization, and smoothing [7, 14]. Then, SERS spectra of adulterated NS1 were transformed into a dataset of linearly uncorrelated PCs: 5PC's for Scree, 70PC's for CPV and 115 PC's for EOC criterion [10], which were served as inputs to the classifiers. For classification, QDA with diagonal and pseudo structure types were used. Performance of the classifier is calculated based on accuracy, precision, specificity and sensitivity and compared to determine an optimal classifier.

**Fig. 1** Flowchart of NS1 detection by quadratic discriminant analysis



### 4 Result and Discussion

Figures 2, 3 and 4 illustrate performance of QDA classifier integrated with different PCA stopping criteria.

With reference to Fig. 2, it can be observed that specificity of 100% is achieved with the three PCA stopping criteria, across the board. The only exception to this is the EOC-QDA pseudo model, with a low specificity of 42.1%. The performance of QDA classifier models equal to that of LDA [15].

**Fig. 2** Specificity for different PCA stopping criteria and DA classifier models

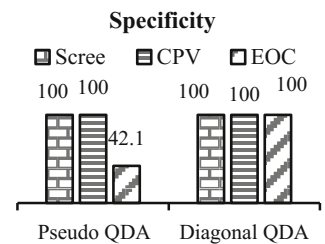
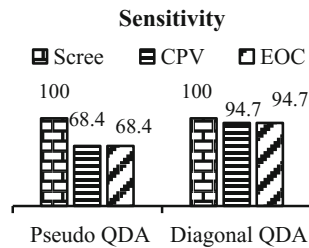
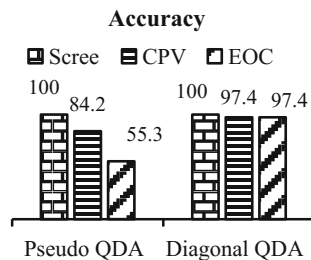


Figure 3 shows the sensitivity performance for QDA model. With Scree as the stopping criterion, both the QDA

**Fig. 3** Sensitivity for different PCA stopping criteria and DA classifier models



**Fig. 4** Accuracy for different PCA stopping criteria and DA classifier models



classifier models score 100%, higher than LDA (93.8%) [15]. With CPV stopping criterion, QDA diagonal (94.7%) and pseudo model (68.4%) perform lower than LDA (96.9%) [15]. It also shows that QDA diagonal model attains the highest (94.7%), followed by LDA (90.7%) [15] and QDA pseudo model (68.4%), with EOC stopping criteria.

The accuracy performance is shown in Fig. 4. Using Scree criterion, all the models achieve an accuracy of 100%. As the number of retained PCs is increased to 70 from CPV, the highest accuracy is with LDA (98.4%) [15] followed by QDA diagonal (97.4%) and pseudo (55.26%) model. Increasing the retained PCs to 115 as proposed by EOC, the highest accuracy at 97.4% is attained with QDA diagonal model, followed by LDA (95.3%) [15] and QDA pseudo model (55.26%).

For all the stopping criterion, it can be observed that QDA diagonal model performs in tandem with LDA, while QDA pseudo model is not performing. It can also be concluded 100% is attained for all the classifier models, except for LDA (96.9% in accuracy and 93.8% in sensitivity [15]), even though Scree produces the lowest number of PCs, as compared to CPV and EOC. This is in concordance to our previous works [13, 15]. It is also observed that, for QDA pseudo model, increasing the number of retained PCs decreases the performance, particularly specificity, which causes a lower accuracy performance. Similar effect is not observed in QDA diagonal and LDA model.

## 5 Conclusion

This paper examines the PCA-QDA classifier models with diagonal and pseudo discriminative structures for detection of NS1 from SERS salivary spectra. The performance is also

compared with our previous works on PCA-LDA. For all the criterion, the QDA diagonal classifier performs as good as the LDA classifier, in fact better in accuracy. The QDA diagonal model works efficiently with Scree criterion in achieving 100% in accuracy and sensitivity, with the addition benefit of lesser principal components and hence implied computation load. The QDA pseudo model is found unsuitable for our application.

**Acknowledgements** The author would like to thank the Ministry of Education (MOE), Malaysia, for providing the research funding 100-RMI/SF 16/6/2 (14/2015); the Research Management Institute, Universiti Teknologi MARA, Malaysia and the Faculty of Electrical Engineering, Universiti Teknologi MARA, Malaysia, for the support and assistance given to the authors in carrying out this research.

## References

1. Yap, G., Sil, B. K., Ng, L. C.: Use of saliva for early dengue diagnosis. *PLoS Negl. Trop. Dis.* 5(5), 1–8 (2011).
2. Ahmed, N. H., Broor, S.: Comparison of NS1 antigen detection ELISA, real time RT-PCR and virus isolation for rapid diagnosis of dengue infection in acute phase. *J. Vector Borne Dis.* 51(3), 194–199 (2014).
3. Korhonen, E. M., Huhtamo, E., Virtala, A. M. K., Kantele, A., Vapalahti, O.: Approach to non-invasive sampling in dengue diagnostics: Exploring virus and NS1 antigen detection in saliva and urine of travelers with dengue. *J. Clin. Virol.* 61(3), 353–358 (2014).
4. Aparna, D. A., Vinod Kumar, D. R., Muralikrishna, D. V., Kumar, D. R. P.: Diagnostic utility of saliva as non-invasive alternative to serum in suspected dengue patients. *J. Dent. Med. Sci.* 14(9), 26–32 (2015).
5. Carpignano, F., Grant-Jacob, J. A., Lamb, J., Pechstedt, K., Brocklesby, W. S., Melvin, T.: Direct detection of DNA on gold structured planar substrates by Raman microscopy. In: 2014 Fotonica AEIT Ital. Conf. Photonics Technol., pp. 1–4. IEEE, Naples Italy (2014).
6. Chen, C., Li, Y., Kerman, S., Neutens, P., Maes, G., Lagae, L., Stakenborg, T., Dorpe, P. V.: Plasmonic nanoslit for fluidic SERS: A strategy towards genome sequencing. In: 13th Proc. IEEE Conf. Nanotechnol., pp. 553–556. IEEE, Beijing China (2013).
7. Radzol, A. R. M., Lee, K. Y., Mansor, W., Azman, A.: Optimization of Savitzky-Golay smoothing filter for salivary surface enhanced Raman spectra of non structural protein 1. In: IEEE Reg. 10 Annu. Int. Conf. Proceedings/TENCON, pp. 9–14. IEEE, Bangkok Thailand (2015).
8. Xu, Z., Ge, X., Huang, W., Lin, D., Wu, S., Lin, X., Wu, Q., Sun, L.: Nasopharyngeal carcinoma detection by tissue smears using surface-enhanced Raman spectroscopy. *International Journal for Rapid Communication.* 50(1), 17–22 (2017).
9. Gonchukov, S., Sukhinina, A., Bakhmutov, D., Minaeva, S.: Raman spectroscopy of saliva as a perspective method for periodontitis diagnostics. *Laser Phys. Lett.* 9(1), 73–77 (2012).
10. Radzol, A. R. M., Lee, K. Y., Mansor, W., Othman, N. H.: Principal component analysis for detection of NS1 molecules from Raman spectra of saliva. In: Proc. - 2015 IEEE 11th Int. Colloq. Signal Process. Its Appl. CSPA, pp 168–173. IEEE, Kuala Lumpur Malaysia (2015).
11. Kon, M. A., Nikolaev, N.: Empirical normalization for quadratic discriminant analysis and classifying cancer subtypes. In: 10th Int.

- Conf. Mach. Learn. Appl. ICMLA, vol. 2, pp. 374–379. IEEE, Honolulu HI USA (2011).
12. Smarajit, B., Amita, P., Rita, S., Jitadeepa, N.: Generalized quadratic discriminant analysis. *Pattern Recognit.* 48(2015), 2676–2684 (2015).
  13. Othman, N. H., Lee, K. Y., Radzol, A. R. M., Mansor, W.: Termination Criterion for PCA with ANN for Detection of NS1 from Adulterated Saliva. *J. Teknol.* 78(6–8), 13–20 (2016).
  14. Radzol, A. R. M., Lee, K. Y., Mansor, W., Saadun, N.: Baseline Correction Customized for NS1 Salivary Raman Spectra with Piecewise Cubic Hermite Interpolation. In: *IEEE Symp. Ind. Electron. Appl.*, vol. 1, pp. 1–5. IEEE, Sabah Malaysia (2014).
  15. Othman, N. H., Lee, K. Y., Radzol, A. R. M., Mansor, W., Ramlan, N. N. M.: Linear discriminant analysis for detection of salivary NS1 from SERS spectra. In *Proc. of the 2017 IEEE Region 10 Conference (TENCON)*, pp. 2876–2879. IEEE, Penang Malaysia (2017).



# A Novel Concept of the Management of Coronary Artery Disease Patients Based on Machine Learning Risk Stratification and Computational Biomechanics: Preliminary Results of SMARTool Project

Antonis I. Sakellarios, Nikolaos Tachos, Elena Georga, George Rigas, Vassiliki Kigka, Panagiotis Siogkas, Savvas Kyriakidis, Georgia Karanasiou, Panagiota Tsompou, Ioannis Andrikos, Silvia Rocchiccioli, Gualtriero Pelosi, Oberdan Parodi, and Dimitrios I. Fotiadis

## Abstract

Coronary artery disease (CAD) is one of the most common causes of death in western societies. SMARTool project proposes a new concept for the risk stratification, diagnosis, prediction and treatment of CAD. Retrospective and prospective data (clinical, biohumoral, computed tomography coronary angiography (CTCA) imaging, omics, lipidomics, inflammatory and exposome) have been collected from ~250 patients. The proposed patient risk stratification, relying on machine learning analysis of non-imaging data, discriminates low and medium-to-high risk patients. The CAD diagnosis module is based on the 3D reconstruction and automatic blood flow dynamics of the coronary arteries, and the non-invasive estimation of smartFFR, an index correlated with invasively measured fractional flow reserve (FFR). CAD prediction is based on complex computational models of plaque growth considering the blood rheology, the lipoproteins transport and the major mechanisms of plaque growth, such as the

inflammation and the foam cells formation. Finally, the treatment module is based on the simulation of virtual stent deployment. Preliminary analysis of 101 patients yielded an overall accuracy of 85.2% with the sensitivity of Class II reaching 98%. The reconstruction methodology is validated against intravascular ultrasound data and the correlation of the geometry derived metrics such as the degree of stenosis, minimal lumen area, minimal lumen diameter, plaque burden are 0.79, 0.85, 0.81 and 0.75, respectively. SmartFFR has been validated compared to invasively measured FFR with a correlation coefficient of 0.90. Plaque growth modelling demonstrates that the inclusion of variables such as the macrophages and foam cells concentrations can increase to 75% the prediction accuracy of regions prone to plaque formation.

## Keywords

Coronary artery disease • Risk stratification  
Computational modelling

A. I. Sakellarios (✉) · N. Tachos · E. Georga · G. Rigas  
V. Kigka · P. Siogkas · S. Kyriakidis · G. Karanasiou  
P. Tsompou · D. I. Fotiadis

Department of Biomedical Research, Institute of Molecular  
Biology and Biotechnology – FORTH, University Campus  
of Ioannina, Ioannina, Greece  
e-mail: ansakel13@gmail.com

E. Georga · V. Kigka · P. Siogkas · P. Tsompou  
I. Andrikos · D. I. Fotiadis  
Unit of Medical Technology and Intelligent Information Systems,  
Department of Materials Science and Engineering,  
University of Ioannina, Ioannina, Greece

S. Rocchiccioli · G. Pelosi · O. Parodi  
Institute of Clinical Physiology, National Research Council,  
56124 Pisa, Italy

## 1 Introduction

Despite the improvements in the practice for the prevention of coronary artery disease (CAD), CAD is still considered as one of the leading causes of death in west societies [1]. Several factors contribute to CAD evolution including pathologic comorbid conditions such as hypertension, diabetes, hyperlipidemia, but also epigenetics and environmental influences such as the family history, gender and age. A major advance in CAD prevention is the use of computed tomography coronary angiography (CTCA) for visualizing

and assessing the CAD severity. The continuously improvement of CTCA spatial resolution will enhance its capability to prevent future events [2]. Besides the advances in imaging of CAD non-invasively, further achievements are made in understanding of the pathophysiology of plaque progression. In particular, several clinical trials attempt to collect patients' data under well-defined protocols aiming to search predictors and potential biomarkers, which are related to disease establishment and/or progression [3]. The main finding from large scale studies is that hemodynamics and especially low endothelial shear stress (ESS) affects the local phenotype of endothelial membrane promoting the atherosclerotic process [4]. Besides low ESS, other predictors of plaque progression are the increased plaque burden and lumen reduction at the baseline [5]. The recent years, computational modelling has been used further for simulating pathways and mechanisms of atherosclerosis initiating from the modelling of LDL transport and proving the association of LDL accumulation with disease progression [6]. Furthermore, complex models have been developed, which simulate the major steps of atherosclerosis such as the inflammation and the formation of smooth muscle cells [7].

Over the recent years, there has been major progress in systems medicine and multi-scale modelling approaches to human disease, boosted by the advent of high throughput omics technologies and the generation of genetic and

molecular big data specific to an individual's personal profile. Although these offer huge potential for improving human health, reducing healthcare demand and promoting sustainable healthcare systems, they have only sporadically been used to explore well-being, disease prevention or rehabilitation. In this work we present a novel concept for the management of CAD patients non-invasively utilizing CTCA imaging. In particular, our concept is based on machine learning algorithm for the risk stratification of patients and continues with the computationally assessment of diagnosis, prognosis and treatment. This work is performed under the SMARTool project.

## 2 Materials and Methods

### 2.1 Concept of SMARTool

The SMARTool project aims to deliver an idealized platform for the risk stratification, diagnosis, prognosis and treatment decision support for CAD patients. For this purpose retrospective patients' data are acquired from the EVINCI database [8] and prospective from the same patient population after a follow-up period of  $5 \pm 2$  years. Baseline and follow-up data from 263 patients are collected. CTCA imaging and clinical, molecular, biohumoral, inflammatory,

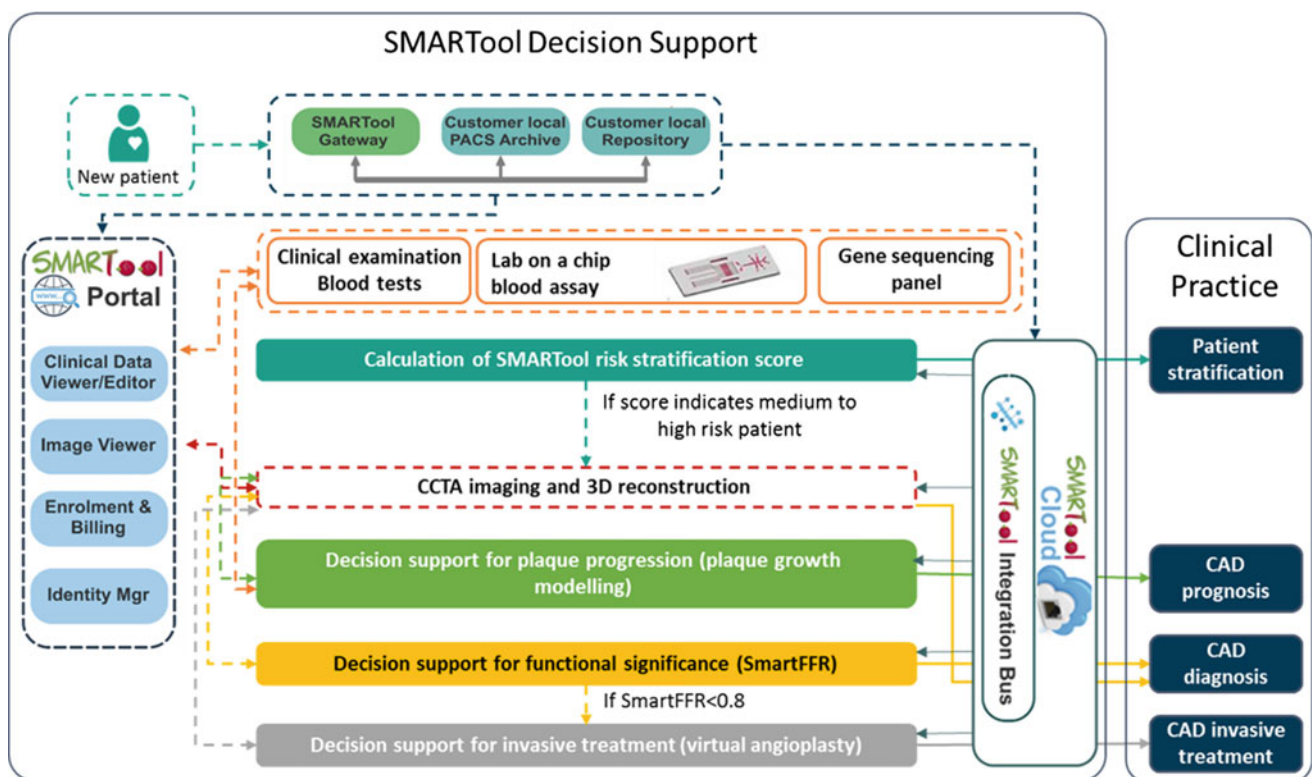


**Fig. 1** The proposed overall concept of SMARTool

omics and lipidomics information are included. The first step of the proposed concept is to provide a risk stratification scoring system based on machine learning techniques in order to identify in parallel biomarkers and predictors of CAD existence or not. The second step is to build decision support systems (DSS) for the diagnosis, prognosis and treatment of CAD in realistic patient's scenarios (Fig. 1).

## 2.2 CAD Risk Stratification

A multiclass classification problem is defined based on an established risk score of coronary atherosclerosis combining markers of stenosis severity, plaque location and composition, as assessed by computed tomography angiography. A multimodal architecture approach is selected whose generalization capability, with respect to CAD stratification, is currently evaluated. First, the following feature classes (or views) were defined: (View 1) demographics, (View 2) clinical data, risk factors, symptoms, (View 3) molecular variables (i.e. biohumoral, inflammatory markers and lipids profile), (View 4) gene expression data, (View 5) exposome, and (View 6) monocytes. The multimodal architecture consists of two processing layers which are defined according to late or intermediate data integration strategies. Late data integration consists in the construction of: (i) an ensemble of decision tree-based prediction models (i.e. random forests, boosted decision trees) for each data view, whose individual decisions are effectively merged using simple mechanisms (e.g. weighted voting), or (ii) a multimodal deep neural network comprising appropriate deep learning subnetworks for each separate data view and, unifying their output into higher network layers. Intermediate data integration is based on multiple kernel learning. Kernel matrices are computed for each data view, and then they are combined, through a parametric linear function, in order to generate the final kernel matrix. Kernel-based classification is subsequently applied to predict CAD risk stratification. Finally, early integration schemes, which concatenate all features into a single vector, accompanied by appropriate feature selection algorithms were implemented for comparison purposes.

## 2.3 CAD Diagnosis DSS

SmartFFR is our proposed new index for the assessment of the significance of coronary stenoses in coronary bifurcations. The aim of the current study is to compare SmartFFR with the Fractional Flow Reserve (FFR) values deriving from direct invasive pressure measurements from a dedicated pressure wire. In the context of the SMARTool study, 22 patients with chest pain symptoms and intermediate pre-test likelihood of CAD underwent CCTA as well as FFR

measurement. The 24 left arterial branches which included the LAD and the LCx were reconstructed using our in-house developed software. We performed two computational blood flow simulations for each case to calculate the SmartFFR for each 3D model. Assuming a myocardial blood flow of 2 ml/s and 6 ml/s during rest and under stress for the Left Main artery, respectively, we calculated the flow for each branch using Murray's law and applied it as outlet boundary conditions. SmartFFR was calculated for each branch by computing the ratio of distal to proximal pressure for a range of flows between 0 and 4 ml/s, normalized by the respective ratio of a normal artery.

## 2.4 CAD Prognosis DSS

The prognosis DSS of SMARTool is based on the prediction of site-specific plaque growth. This is achieved by implementing a multi-level modelling approach. The first level of our approach is the utilization of CTCA images for the 3D reconstruction of coronary arteries. The methodology was presented in [9]. In the second level, blood flow is modelled by using the Navier-Stokes equations. In the third level mass transport modelling is performed considering as mass the LDL, the high density lipoproteins (HDL) and the monocytes. The mass is transported in the lumen and in the arterial wall by employing the convection-diffusion equations [10]. The fourth level of prognosis DSS is the modelling of plaque growth and more specifically, the modelling of the atherosclerotic pathways of disease evolution. These pathways are representing the oxidation of LDL molecules, considering however the atheroprotective effect of HDL. The transformation of monocytes to macrophages is also modelled applying a diffusion equation, while in parallel the endocytosis of oxidized LDL by macrophages is modelled. The formation of foam cells and plaque is modelled after considering the density of each molecule in combination with their concentration.

## 2.5 CAD Treatment DSS

The treatment DSS of SMARTool is based on the modelling of stent deployment in stenosed coronary arteries. More specifically, the finite element model consists of the reconstructed artery and the stent, in their unexpanded configurations. The stent is inflated through a pressure driven approach as following: (i) loading ( $P = 0$  to 1.8 MPa), (ii) holding ( $P = 1.8$  MPa constant) and, (iii) unloading ( $P = 1.8$  to 0 MPa). Appropriate boundary conditions are imposed in the ends of the artery and the stent. A frictionless contact is assumed for the inner arterial wall-stent contact pair. The results show that the stent design characteristics

and the material influence the resulting stress field imposed on the arterial wall. From the analysis of the models the following parameters are examined: (i) Von Mises stress in the arterial wall, (ii) Von Mises stress in the stent scaffold, and (iii) Stent directional deformation.

### 3 Results

For the risk stratification tool the following cases are tested: (i) Case 1: Demographics, Risk Factors, (ii) Case 2: Demographics, Risk Factors, Symptoms, (iii) Case 3: Demographics, Risk Factors, Symptoms, Molecular Systemic Variables, (iv) Case 4: Feature ranking according to the InfoGain criterion. Also the following machine learning algorithms are implemented: (i) Feed-forward neural network; (ii) Support vector machine; (iii) Random forest. The Table 1 shows that for the current dataset of 101 patients the SVM algorithm outperforms the other especially for the Case 4. The main outcome, however, is that the inclusion of more kinds of data moving from Case 1 to Case 4 increases the accuracy results of all classification algorithms.

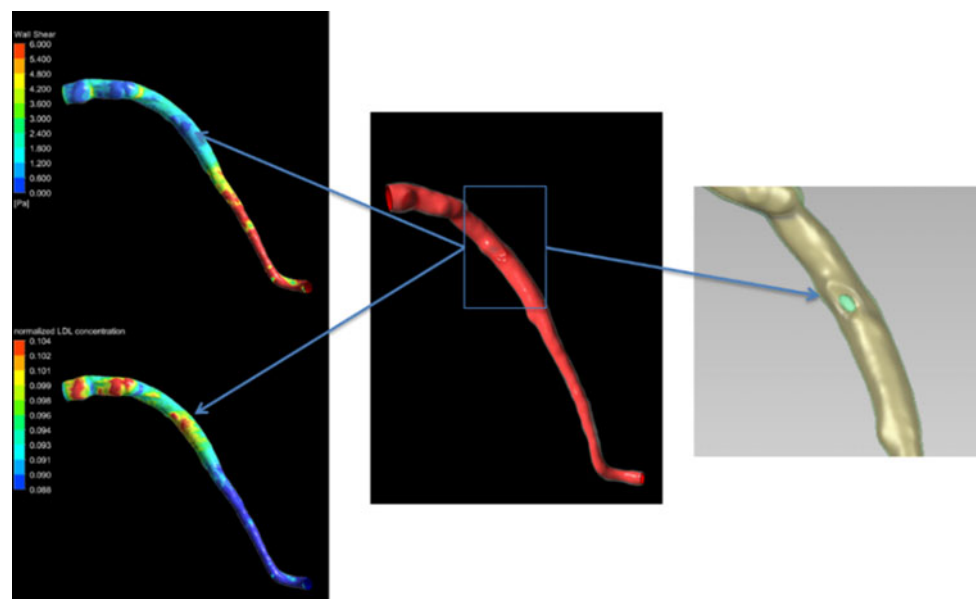
The 3D reconstruction methodology is validated using IVUS-VH images. The correlation coefficients of the IVUS based reconstruction with the proposed methodology for the degree of stenosis, the plaque burden, the minimal lumen area and the minimal lumen diameter, were 0.79, 0.75, 0.85, 0.81, respectively. The reconstructed arteries are used for the modelling of blood flow, mass transport and plaque growth. The preliminary analysis of about 60 patients demonstrate that a multivariate model which include all computational variables such as the macrophages and foam cells concentrations increase the prediction accuracy of regions prone to plaque formation to 75%. Figure 2 shows a case example, where baseline calculations predict the *de novo* plaque at the follow-up (right panel).

We implement a novel approach named SmartFFR in order to assess the hemodynamic status of coronary bifurcations. In the context of the SMARTool study, 24 patients with chest pain symptoms and intermediate pre-test likelihood of CAD underwent CCTA as well as FFR measurement. The 24 left arterial branches (29 arteries) which included the LAD and the LCx were reconstructed using our in-house developed software. Strong correlation

**Table 1** Accuracy, sensitivity and specificity for the various algorithms for the four cases

	MLP			SVM			RF		
	Acc.	Se.	Sp.	Acc.	Se.	Sp.	Acc.	Se.	Sp.
Case 1	66.3	78.9	28.0	77.2	97.4	16.0	73.3	85.5	36.0
Case 2	70.3	81.6	36.0	81.2	94.7	40.0	75.2	88.2	36.0
Case 3	74.3	84.2	44.0	<b>84.2</b>	<b>97.4</b>	<b>44.0</b>	77.2	97.4	16.0
Case 4	78.2	90.8	40.0	<b>85.1</b>	<b>98.7</b>	<b>44.0</b>	81.2	92.1	48.0

**Fig. 2** A patient example where the simulated results of shear stress and high LDL concentration are related to a new formed plaque at the follow-up



( $r = 0.87$ ,  $P < 0.0001$ ) was found between the two methods, while all pathological cases presenting ischemia, were correctly categorized by our method as hemodynamically significant lesions.

#### 4 Discussion and Conclusions

SMARTool aims to the development of a cloud-based platform which is based on a novel concept for the management of atherosclerosis. The excellence of SMARTool arises from the unique attempt to address the most recent guidelines and directions proposed by the European Society of Cardiology (ESC) [11]. ESC argues that CAD risk must be assessed in younger ages (<50 years old). American Heart Association proposes to consider also the genetic profile for prevention of CAD. Moreover, ESC proposes that risk factor intervention must be at the individual level and ideally non-invasively. SMARTool attempts to identify novel biomarkers of disease progression and integrate them in models and tools for the early diagnosis and prevention of CAD. The preliminary results show that SMARTool can provide a comprehensive platform for the risk stratification as well as DSS for the diagnosis, prognosis and treatment of CAD. In particular, it provides a novel risk stratification scheme taking in consideration the molecular and genetic patient's profile. Additionally, it delivers validated algorithms and tools for the 3D reconstruction of arteries using CTCA, which allows the non-invasive estimation of SmartFFR index (highly correlated to FFR for diagnosis), but also the site-specific prediction of plaque growth.

**Acknowledgements** This work is partially funded by the European Commission: Project SMARTOOL, "Simulation Modeling of coronary ARtery disease: a tool for clinical decision support—SMARTool" GA number: 689068).

#### References

1. (WHO) WHO. The atlas of heart disease and stroke [Available from: [http://www.who.int/cardiovascular\\_diseases/en/cvd\\_atlas\\_16\\_death\\_from\\_stroke.pdf](http://www.who.int/cardiovascular_diseases/en/cvd_atlas_16_death_from_stroke.pdf)].
2. Papadopoulou SL, Neeffjes LA, Garcia-Garcia HM, Flu WJ, Rossi A, Dharampal AS, et al. Natural History of Coronary Atherosclerosis by Multislice Computed Tomography. *Jacc-Cardiovasc Imag* 5(3):S28–S37 (2012).
3. Stone PH, Maehara A, Coskun AU, Maynard CC, Zaromytidou M, Siasos G, et al. Role of Low Endothelial Shear Stress and Plaque Characteristics in the Prediction of Nonculprit Major Adverse Cardiac Events: The PROSPECT Study. *JACC Cardiovascular imaging* (2017).
4. Chatzizisis YS, Coskun AU, Jonas M, Edelman ER, Feldman CL, Stone PH. Role of endothelial shear stress in the natural history of coronary atherosclerosis and vascular remodeling - Molecular, cellular, and vascular behavior. *J Am Coll Cardiol* 49(25):2379–93 (2007).
5. Bourantas CV, Papadopoulou SL, Serruys PW, Sakellarios A, Kitslaar PH, Bizopoulos P, et al. Noninvasive Prediction of Atherosclerotic Progression: The PROSPECT-MSCT Study. *JACC Cardiovascular imaging* 9(8):1009–11 (2016).
6. Sakellarios A, Bourantas CV, Papadopoulou SL, Tsirka Z, de Vries T, Kitslaar PH, et al. Prediction of atherosclerotic disease progression using LDL transport modelling: a serial computed tomographic coronary angiographic study. *European heart journal cardiovascular Imaging* (2016).
7. Sakellarios A, Raeber L, Bourantas C, Exarchos T, Athanasiou L, Pelosi G, et al. Prediction of Atherosclerotic Plaque Development in an in Vivo Coronary Arterial Segment Based on a Multi-level Modeling Approach. *IEEE transactions on bio-medical engineering* (2016).
8. Liga R, Vontobel J, Rovai D, Marinelli M, Caselli C, Pietila M, et al. Multicentre multi-device hybrid imaging study of coronary artery disease: results from the EVALuation of INtegrated Cardiac Imaging for the Detection and Characterization of Ischaemic Heart Disease (EVINCI) hybrid imaging population. *European heart journal cardiovascular Imaging* 17(9):951–60 (2016).
9. Sakellarios AI, Rigas G, Kigka V, Siogkas P, Tsompou P, Karanasiou G, et al. SMARTool: A tool for clinical decision support for the management of patients with coronary artery disease based on modeling of atherosclerotic plaque process. *Conf Proc IEEE Eng Med Biol Soc* 2017:96–9 (2017).
10. Sakellarios AI, Papafaklis MI, Siogkas P, Athanasiou LS, Exarchos TP, Stefanou K, et al. Patient-specific computational modeling of subendothelial LDL accumulation in a stenosed right coronary artery: effect of hemodynamic and biological factors. *Am J Physiol-Heart C* 304(11):H1455–H70 (2013).
11. Piepoli MF, Hoes AW, Agewall S, Albus C, Brotons C, Catapano AL, et al. 2016 European Guidelines on cardiovascular disease prevention in clinical practice: The Sixth Joint Task Force of the European Society of Cardiology and Other Societies on Cardiovascular Disease Prevention in Clinical Practice (constituted by representatives of 10 societies and by invited experts) Developed with the special contribution of the European Association for Cardiovascular Prevention & Rehabilitation (EACPR). *Eur Heart J* 37(29):2315–81 (2016).



# Estimating Cardiac Intensive Care Patients' Responsiveness to Late Conservative Fluid Management Using Systems Analysis

Katharina Bergmoser, Sonja Langthaler, Alexander Lassnig, Martin Horn, and Christian Baumgartner

## Abstract

Fluid overload is a common problem in critically ill patients who underwent surgery and is accompanied by a range of risks for severe organ damage. Therefore, in stable patients excess water should be removed using fluid-restricting treatment strategies in order to reach a neutral fluid balance as early as possible. Within this work, second order discrete-time transfer function models were identified for 10 selected cardiac patients staying at the intensive care unit for at least 5 days. For model estimation, the cumulative fluid intake and the cumulative fluid balance time series were used as model input and output parameters. Each individual model is capable of describing the respective patient's cumulative fluid balance trajectory as response to the actually applied fluid therapy. In the context of decision support, systems analysis can therefore offer valuable tools not only for describing an individual patient's reaction to a certain fluid therapy, but also for identifying patients with rebalancing issues at an early stage of recovery. In daily clinical practice, patient-specific transfer function models can be used for predicting the responsiveness to planned medical interventions, improving the fluid intake regime by focusing on the avoidance of a further increasing fluid overload and returning patients' fluid balances to an acceptable level before release from the intensive care unit.

## Keywords

Fluid balance • Transfer function • Decision support

K. Bergmoser (✉) · S. Langthaler · A. Lassnig · C. Baumgartner  
Institute of Health Care Engineering with European Testing Center  
of Medical Devices, University of Technology, Graz, Austria  
e-mail: Katharina.bergmoser@tugraz.at

K. Bergmoser · A. Lassnig  
CBmed – Center for Biomarker Research in Medicine, Graz,  
Austria

M. Horn  
Institute of Automation and Control, Graz University  
of Technology, Graz, Austria

## 1 Introduction

When talking about fluid balance (FB) in humans, two different types need to be distinguished: the external FB and the internal FB [1]. While the internal FB describes the fluid distribution between the extracellular and intracellular space, the external FB of a patient is defined as the difference between the total fluid intake and all ongoing fluid losses. In contrast to healthy humans, who only have to compensate for normal ongoing losses, patients recovering from surgery also lose water and electrolytes in form of hemorrhages, drainages or dialysate (see Fig. 1).

Despite raised doubts [2], in the intensive care unit (ICU) the external cumulative fluid balance (CFB) should be considered as an important parameter when assessing a patient's stability [3]. The CFB is usually calculated as the cumulative fluid intake (CFI) in milliliters since admission to the ICU minus the cumulative fluid loss in milliliters since ICU admission. The assessment and calculation of the daily FB is nowadays routinely done in the ICU—either by manually recording fluid intakes and ongoing losses or by using electronic medical records (EMR). However, in contrast to a visualized daily FB course, in the CFB course long-term trends are clearly recognizable.

### 1.1 Fluid Overload

Due to physiological reactions to surgery and following early goal-directed fluid therapy aiming to compensate lost intravascular fluids, fluid overload (FO) is common in critically ill patients [4, 5]. Basically, a FO of 10% of the baseline body weight is associated with increased probability of death [6–8]. Once a patient reached hemodynamic stability, further increasing the FO should be avoided [9] and excess fluid—which might lead to serious complications such as acute renal failure—should be removed [4, 10, 11].

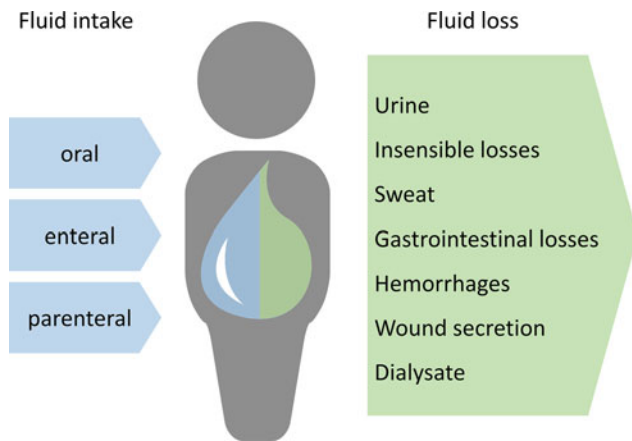


**Fig. 1** Ways for administering fluids to critically ill patients and fluid losses to be considered when defining fluid management strategies

Several studies [9, 12–14] describe the CFB course during fluid management after severe injury, which might be divided into two main stages, based on the patient's shock phases: (i) the Ebb phase and the (ii) Flow phase [9]. The Ebb phase follows directly after injury and is characterized by a reduced metabolic activity causing water retention and possibly edema. Usually after approximately three days, the Flow phase sets in, in which metabolism and therefore diuresis normalize and excess water is removed. If patients do not transit to the Flow phase on their own and are not responding to late conservative fluid therapy (LCFT) as expected, excess fluids should actively be removed from the body by applying late goal-directed fluid therapy (LGFT) [9]. Therefore, either administration of adequate diuretics [13] or application of renal replacement therapy [15] need to be considered. Regarding fluid administration, recent literature suggests an early goal-directed therapy followed by a more conservative fluid administration regime once the patient is stable in order to reach a neutral to negative balance early during ICU stay [11, 16, 17].

During a cardiac ICU stay, a wide range of different fluids and electrolytes are administered to the patient. In the study by Hessels et al. [18] the mean cumulative amount of fluids administered to 39 heart patients after 4 days was 14 L causing a positive CFB of 4 L in average. Daily fluid intakes might not only include oral, enteral and parenteral preparations for resuscitation, replacement or nutrition purposes, but also medications such as analgesics, diuretics or antibiotics.

## 2 Methods

Once a patient is stable, it is important to estimate whether LCFT will be effective or switching to LGFT is necessary [13, 15]. However, in times of big data, selecting the right

variable(s) for developing models being capable of assisting in fluid therapy planning is challenging. Therefore, a holistic approach described in our previous work [19] was used. Linear second order models with discrete-time transfer function (TF)

$$H[z] = (b_0 + b_1 * z^{-1}) / (a_0 + a_1 * z^{-1} + a_2 * z^{-2}) \quad (1)$$

were identified for describing individual patient's fluid transfer characteristics and estimating the CFB trajectory in 10 cardiac patients staying at the ICU for at least 5 days. For model identification, only the respective preliminary CFI and CFB are required. For simulation, each CFI was approximated using linear regression and used as model input. The models' outputs were then analyzed regarding their usefulness for describing the actual CFB course of individual patients and, thereby, to prove their ability to estimate the respective patient's responsiveness to LCFT.

Within the study population five patients responded to LCFT with—if needed at all—minor support through diuretics. The remaining five patients may have required fluid management strategies specifically focusing on lowering the CFB since the applied individual conservative approaches were not sufficient.

## 3 Results

All 10 built unique TF models delivered the expected outputs, which sufficiently describe the main CFB trajectory of the respective patient. Figure 2 shows the actual CFB and CFI courses of two exemplary patients and their models' outputs as well as the step responses of the systems. After a more liberal administration of fluids during the first post-operative hours, fluid therapy was changed to a more conservative regime in both patients.

## 4 Discussion

When comparing the actual CFI and CFB courses of the two exemplary patients in Fig. 2, the difference between responsive and non-responsive patients becomes obvious. Patient 1 showed a typical CFB course of a patient being responsive to LCFT. After a CFB rise during resuscitation and stabilization, the balance decreased and even reached the neutral level. However, this patient finally left the ICU with a strongly negative balance of approximately  $-2$  L. The point for stopping de-resuscitation [9] was missed and LGFT could have been applied in order to avoid dehydration. In Patient 2 the amount of fluids administered was already reduced after approximately 12 h, which can be interpreted

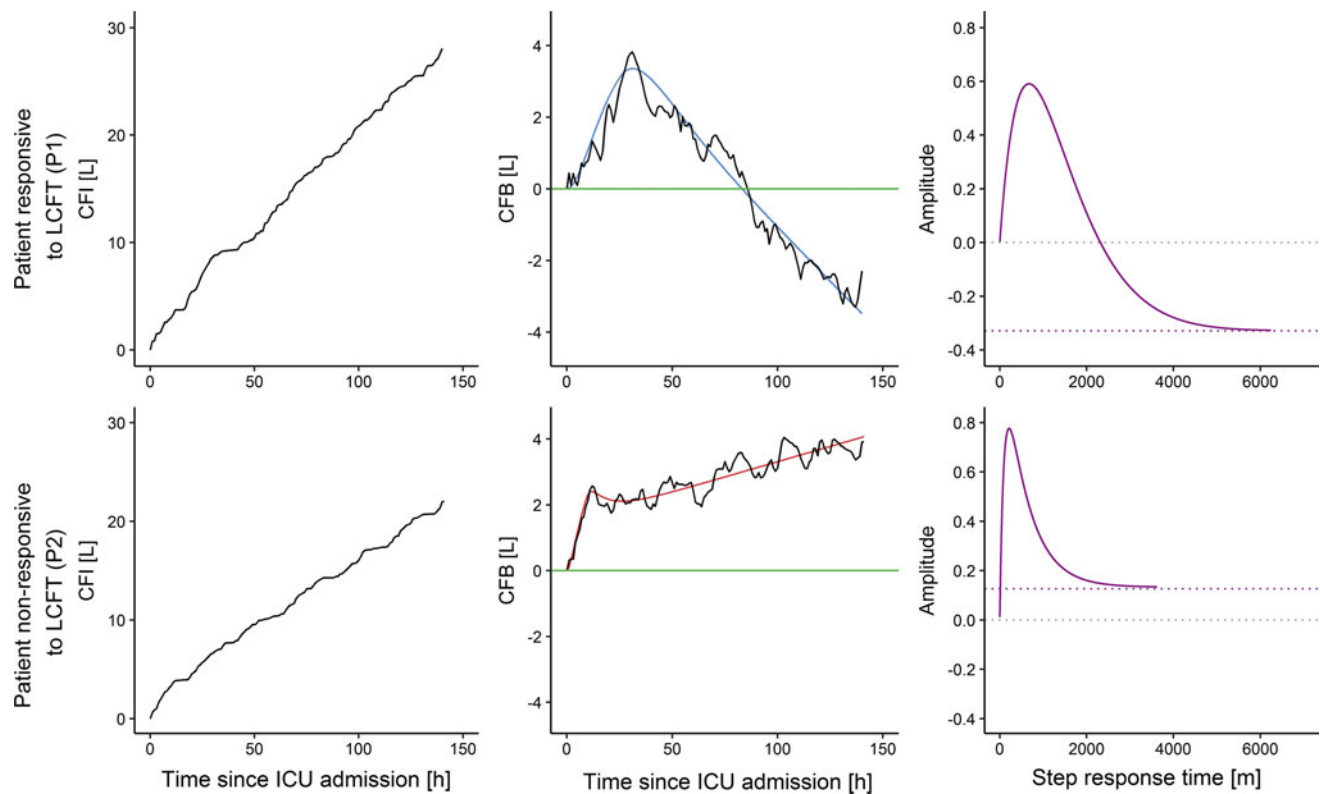


**Fig. 2** The actual cumulative fluid intakes (CFI) in liters of a patient being responsive (P1) and a patient being non-responsive (P2) to late conservative fluid therapy (LCFT). The actual cumulative fluid balance (CFB, black) of P1 decreased after restricting fluids. P2 did not return

towards a neutral balance (green) until discharge from the intensive care unit (ICU). The model outputs (blue, red) sufficiently describe the CFB trajectories. The step responses of the two transfer function models (purple) are shown in the right column (Color figure online)

as the patient's early progress to the so-called Flow phase. However, this patient's CFB steadily kept rising and did not return towards a neutral level during the remaining ICU stay. The patient's CFB at ICU discharge was approximately +4 L. Taking into account the patient's perioperative CFB, the patient left with a positive balance of approximately +6 L. Assuming a baseline body weight of 70 kg, an FO of that amount would already be close to a critical range.

In this work, each individual model is capable of describing the respective patient's CFB trajectory as response to the actually applied fluid therapy. In the time-domain, responders and non-responders differ in several characteristics of the step response curve. Therefore, it seems to be possible to define two general TFs describing the trajectory of the respective group.

During the resuscitation phase, whose character is shaped by the patient's instability, the administered amount of fluids or agents and the accompanied fluid imbalance completely depend on the severity of the disease and the individual recovery process. During this phase, the prediction of CFBs is neither helpful nor reasonable. However, once a patient enters a stable phase, the described approach can be used for

predicting the responsiveness to planned interventions and for adjusting daily FB targets.

When repeatedly or recursively calculating the TF using the FB data available so far throughout the ICU stay, changes in the model properties might indicate changing patient characteristics or even ongoing deteriorations. In case that a patient returns to the ICU, it would be interesting to investigate whether each stay results in the same TF.

Currently we are validating the proposed approach within a large study population of more than 200 patients by implementing a control loop, which can then be used as a decision support tool aiding in fluid management in critically ill patients.

## 5 Conclusion

Fluids make up a large part of administered medications in hospitals and therefore type and dosage have an essential influence on a patient's recovery process. FO may lead to severe complications such as edema or acute kidney injury and needs to be prevented. However, especially the first

hours after surgery often require a range of different medical interventions, whereby the goal is to stabilize the patient rather than to correct fluid dysbalances. Once a patient reaches a stable point, an individual TF model might be used for identifying the best possible fluid administration strategy and predicting the necessity for active fluid removal at an early stage of postoperative care.

**Acknowledgements** “CBmed” is cooperating together with B. Braun Melsungen AG for this research project. Work done in “CBmed” was funded by the Austrian Federal Government within the COMET K1 Centre Program, Land Steiermark and Land Wien.

## References

- Lobo, D., Lewington, A., Allison, S.: Basic Concepts of Fluid and Electrolyte Therapy. Bibliomed – Medizinische Verlagsgesellschaft mbH Melsungen, Melsungen (2013).
- Perren, A., Markmann, M., Merlani, G., Marone, C., Merlani, P.: Fluid balance in critically ill patients Should we really rely on it?. *Minerva Anestesiologica* 77(8), 802–811 (2011).
- Bagshaw, S., Brophy, P., Cruz, D., Ronco, C.: Fluid balance as a biomarker: impact of fluid overload on outcome in critically ill patients with acute kidney injury. *Critical Care* 12(4), 169 (2008).
- Gosling, P., Salt of the earth or a drop in the ocean? A pathophysiological approach to fluid resuscitation. *Emergency Medicine Journal* 20(4), 306–315 (2003).
- Cunha, A., Lobo, S.: What happens to the fluid balance during and after recovering from septic shock?. *Revista Brasileira de Terapia Intensiva* 27(1), 10–17 (2015).
- Bouchard, J., Soroko, S., Chertow, G., Himmelfarb, J., Ikizler, T., Paganini, E., Mehta, R., Program to Improve Care in Acute Renal Disease (PICARD) Study Group: Fluid accumulation, survival and recovery of kidney function in critically ill patients with acute kidney injury. *Kidney International* 76(4), 422–427 (2009).
- Vaara, S., Korhonen, A., Kaukonen, K., Nisula, S., Inkinen, O., Hoppu, S., Laurila, J., Mildh, L., Reinikainen, M., Lund, V., Ilkka, P., Pettilä, V.: Fluid overload is associated with an increased risk for 90-day mortality in critically ill patients with renal replacement therapy: data from the prospective FINNAKI study. *Critical Care* 16(5), R197 (2012).
- Hoste, E., Maitland, K., Brudney, C., Mehta, R., Vincent, J., Yates, D., Kellum, J., Mythen, M., Shaw, A.: Four phases of intravenous fluid therapy: a conceptual model. *British Journal of Anaesthesia* 113(5), 740–747 (2014).
- Malbrain, M., Marik, P., Witters, I., Cordemans, C., Kirkpatrick, A., Roberts, D., Van Regenmortel, N.: Fluid overload, de-resuscitation, and outcomes in critically ill or injured patients: a systematic review with suggestions for clinical practice. *Anaesthesia Intensive Therapy* 46(5), 361–380 (2014).
- Besen, B., Gobatto, A., Melro, L., Maciel, A., Park, M.: Fluid and electrolyte overload in critically ill patients: An overview. *World Journal of Critical Care Medicine* 4(2), 116–129 (2015).
- Prowle, J., Echeverri, J., Ligabo, E., Ronco, C., Bellomo, R.: Fluid balance and acute kidney injury. *Nature Reviews Nephrology* 6(2), 107–115 (2010).
- Ogbu, O., Murphy, D., Martin, G.: How to avoid fluid overload. *Current Opinion in Critical Care* 21(4), 315–321 (2015).
- Goldstein, S., Bagshaw, S., Cecconi, M., Okusa, M., Wang, H., Kellum, J., Mythen, M., Shaw, A.: Pharmacological management of fluid overload. *British Journal of Anaesthesia* 113(5), 756–763 (2014).
- McDermid, R., Raghunathan, K., Romanovsky, A., Shaw, A., Bagshaw, S.: Controversies in fluid therapy: Type, dose and toxicity. *World Journal of Critical Care Medicine* 3(1), 24–33 (2014).
- Rosner, M., Ostermann, M., Murugan, R., Prowle, J., Ronco, C., Kellum, J., Mythen, M., Shaw, A.: Indications and management of mechanical fluid removal in critical illness. *British Journal of Anaesthesia* 113(5), 764–771 (2014).
- Barmparas, G., Liou, D., Lee, D., Fierro, N., Bloom, M., Ley, E., Salim, A., Bukur, M.: Impact of positive fluid balance on critically ill surgical patients: A prospective observational study. *Journal of Critical Care* 29(6), 936–941 (2014).
- Elofson, K., Eiferman, D., Porter, K., Murphy, C.: Impact of late fluid balance on clinical outcomes in the critically ill surgical and trauma population. *Journal of Critical Care* 30(6), 1338–1343 (2015).
- Hessels, L., Lansink, A., Renes, M., van der Horst, I., Hoekstra, M., Touw, D., Nijsten, M.: Postoperative fluid retention after heart surgery is accompanied by a strongly positive sodium balance and a negative potassium balance. *Physiological Reports* 4(10), e12804 (2016).
- Bergmoser, K., Pflanzl-Knizacek, L., Langthaler, S., Baumgartner, C.: Describing Cardiac ICU Patients’ Fluid Transfer Characteristics Using System Analysis – a Proof of Concept. *Medical Fluids* 5(1), 87–88 (2017).

# Non-invasive Quantification of Coronary Artery Disease in Arterial Bifurcations Using CCTA and CFD: Comparison to Fractional Flow Reserve Measurements

Panagiotis K. Siogkas, Antonis I. Sakellarios, Lampros K. Michalis, and Dimitrios I. Fotiadis

## Abstract

Recent advances in coronary computed tomography angiography (CCTA) allow the calculation of various functional indices of coronary artery disease (CAD). smartFFR is our proposed new index for the assessment of the significance of coronary stenoses in coronary bifurcations. The aim of the current study is to compare smartFFR with the Fractional Flow Reserve (FFR) values deriving from direct invasive pressure measurements from a dedicated pressure wire. In the context of the SMARTool study, 22 patients with chest pain symptoms and intermediate pre-test likelihood of CAD underwent CCTA as well as FFR measurement. The 22 left arterial branches which included the LAD and the LCx were reconstructed using our in-house developed software. We performed two computational blood flow simulations for each case to calculate the smartFFR for each 3D model. Regarding the inlet, the average patient-specific pressure at rest was applied as a boundary condition. Assuming a myocardial blood flow of 2 ml/s and 6 ml/s during rest and under stress for the Left Main artery, respectively, we calculated the flow for each branch using Murray's law and applied it as outlet boundary conditions. smartFFR was calculated for each branch by computing the ratio of distal to proximal pressure for a range of flows between 0

and 4 ml/s, normalized by the respective ratio of a normal artery. The required average process time was less than 20 min. Strong correlation ( $r = 0.88$ ,  $P < 0.0001$ ) was found between the two methods. All pathological cases presenting ischemia, were correctly categorized by our method as hemodynamically significant lesions. smartFFR demonstrated a high diagnostic accuracy for distinguishing hemodynamically significant lesions in a matter of minutes, and may represent a valid non-invasive tool for comprehensive characterization of CAD.

## Keywords

smartFFR • FFR • CCTA

## 1 Introduction

The modern lifestyle in westernized societies has constituted cardiovascular diseases as one of the most common causes of death. Thus, the development of non-invasive techniques for the hemodynamic assessment of coronary arteries is of tremendous importance in modern clinical practice.

So far, the technique which is considered as the gold standard in the functional assessment of coronary arteries is the fractional flow reserve measurement (FFR). FFR is an invasive technique which requires the use of a dedicated pressure-flow wire, as well as the induction of hyperemia after the intravenous administration of adenosine. FFR is the ratio of the intravascular pressure distal of the stenosis divided by the respective aortic pressure. An FFR value 0.80 is considered as the threshold below which, the diseased artery is in need of a percutaneous coronary intervention (PCI).

Regarding coronary imaging modalities, the most commonly used in everyday clinical practice is the traditional invasive coronary angiography (ICA). ICA is a semi-invasive imaging technique which allows the 2-dimensional representation of the coronary vasculature after the insertion of the proper contrast media. Another coronary imaging modality

P. K. Siogkas (✉) · D. I. Fotiadis  
Unit of Medical Technology and Intelligent Information Systems,  
University of Ioannina, 45110 Ioannina, Greece  
e-mail: psiogkas4454@gmail.com

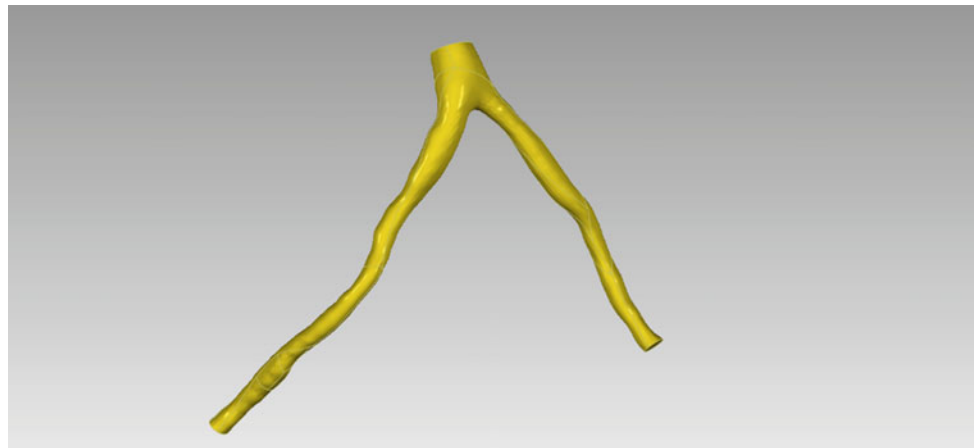
D. I. Fotiadis  
e-mail: fotiadis@cc.uoi.gr

P. K. Siogkas · A. I. Sakellarios · D. I. Fotiadis  
Department of Biomedical Research, Foundation for Research and  
Technology- Hellas (FORTH), 45110 Ioannina, Greece  
e-mail: ansakel13@gmail.com

L. K. Michalis  
Department of Cardiology in Medical School, Michaelideion  
Cardiac Center, University of Ioannina, 45110 Ioannina, Greece  
e-mail: lamprosmihalidis@gmail.com



**Fig. 1** Final 3D reconstructed model of a left arterial branch



that has gained substantial ground during the past decade due to its non-invasive nature is the coronary computed tomography angiography (CCTA). CCTA manages to give a visual representation of the coronary vasculature and provide useful information on the severity of a coronary stenosis, as well as, the type and extent of any possible atherosclerotic plaques.

The ongoing development of 3D reconstruction methods, combined with the application of computational fluid dynamics (CFD) on the 3D models has allowed the calculation of important hemodynamic parameters such as intravascular pressures, therefore allowing also the hemodynamic assessment of the artery of interest. Numerous studies have been published regarding the computational assessment of coronary stenosis [1–5]. The aforementioned methods suffer mainly of two drawbacks, the long computational time that is required to execute the flow simulations and the need of a remote core-laboratory analysis. Another drawback of other methods is the inability to be applied on bifurcating arterial models, since they can only generate results segmentally.

In the current study, we propose a new method for the computational functional assessment of coronary stenosis on 3D models of bifurcating arteries, and more specifically on models that include the left coronary artery (i.e. Left Anterior Descending and Left Circumflex). 18 patients were used to reconstruct in 3D their respective left coronary vasculature using our in-house developed algorithm and the smartFFR index was calculated in all 18 branches. The smartFFR values of the 22 arteries was compared against the invasively measured FFR.

## 2 Materials and Methods

### Dataset

In the context of the SMARTool project, a group of 18 symptomatic patients with intermediate pre-test probability (20–90%) of CAD underwent a CCTA exam (64-slice

General Electric Medical Systems Discovery PET/CT 690@ scanner) and a FFR measurement (ComboWire, Volcano Corp, Rancho Cordova, CA). All 18 left coronary branches were reconstructed. However, the smartFFR was calculated only for the branches that had an invasively measured FFR value (i.e. 22 cases).

## 3 3D Reconstruction Process

The 3D reconstruction of the 18 arterial branches was performed using our in-house developed reconstruction algorithm [6].

In brief, the reconstruction algorithm is based on a six-stage approach:

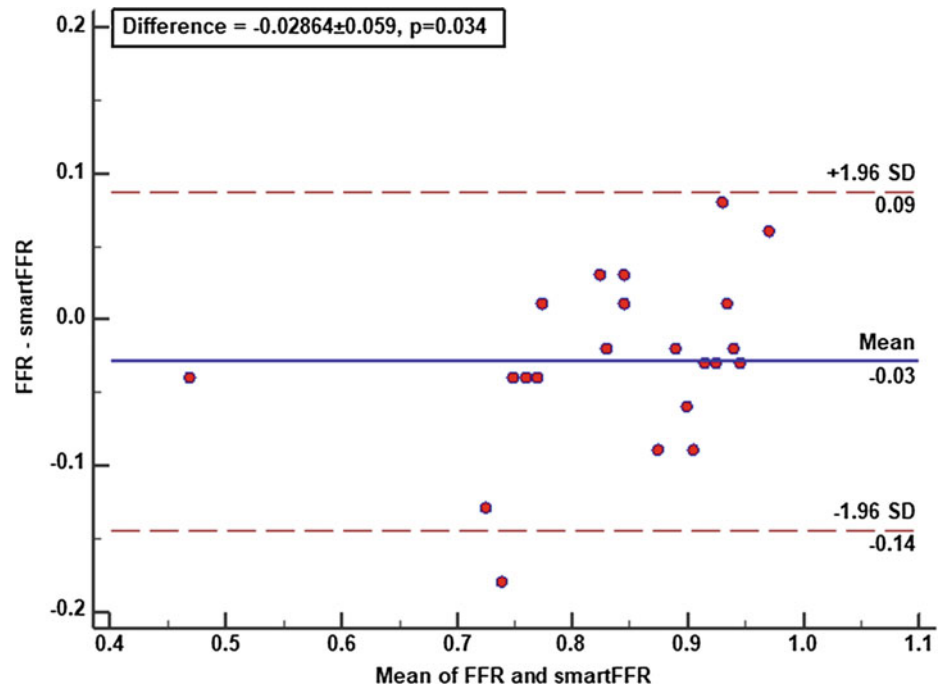
- (a) The CCTA images are pre-processed
- (b) The arterial borders are initially detected
- (c) The arterial centerline is extracted using a minimum cost path approach
- (d) The lumen parameters are translated and adapted into Hounsfield units (HU)
- (e) An enhancement of the active contours model is implemented for the lumen segmentation
- (f) The 3D surface for the lumen is created (Fig. 1).

The coronary branches were reconstructed using the same landmarks for all patients. The segmentation of the branches was based on the SYNTAX SCORE chart. More specifically, regarding the LAD we included segments 1–3, whereas for the LCx we included segments 11–13.

### smartFFR calculation process

To validate the proposed method, we performed the smartFFR calculations on 18 arterial branches, having 22 vessels in total (i.e. also with an invasive FFR measured). Our simulations were performed under the assumption that

**Fig. 2** Bland-Altman plot comparing smartFFR to the invasively measured FFR



the arterial wall was rigid, thus not taking into account its interaction with the blood flow. Blood flow was modelled using the Navier-Stokes and the continuity equations:

$$\rho \frac{\partial \mathbf{v}}{\partial t} + \rho(\mathbf{v} \cdot \nabla) \mathbf{v} - \nabla \cdot \boldsymbol{\tau} = 0, \quad (1)$$

$$\nabla \cdot (\rho \mathbf{v}) = 0, \quad (2)$$

where  $\mathbf{v}$  is the blood velocity vector and  $\boldsymbol{\tau}$  is the stress tensor, which is defined as:

$$\boldsymbol{\tau} = -p\boldsymbol{\delta}_{ij} + 2\mu\boldsymbol{\varepsilon}_{ij}, \quad (3)$$

where  $\boldsymbol{\delta}_{ij}$  is the Kronecker delta,  $\mu$  is the blood dynamic viscosity,  $p$  is the blood pressure and  $\boldsymbol{\varepsilon}_{ij}$  is the strain tensor calculated as:

$$\boldsymbol{\varepsilon}_{ij} = \frac{1}{2} (\nabla \mathbf{v} + \nabla \mathbf{v}^T), \quad (4)$$

Blood was modelled as a Newtonian fluid with density  $1050 \text{ kg/m}^3$  and dynamic viscosity  $0.0035 \text{ Pa s}$ . Blood flow was considered laminar and the Reynolds number ranged from 245–1832.

#### Boundary Conditions

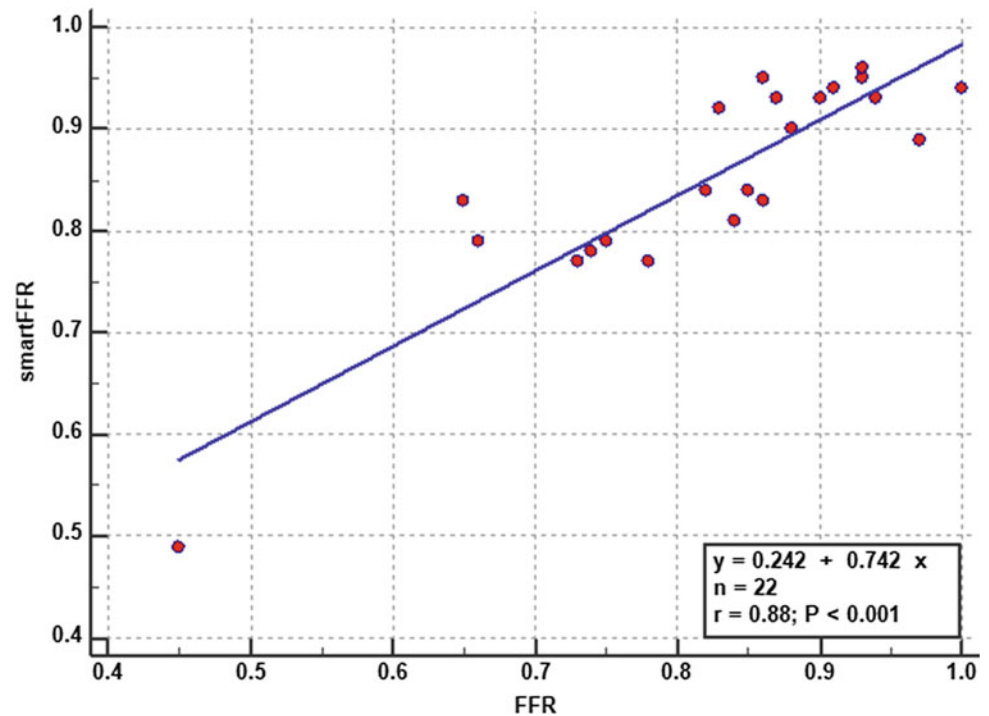
For each case, we performed two blood flow simulations. In the inlet, we applied an average pressure of 100 mmHg which is considered as the average aortic pressure of a human under rest. At the wall a no-slip, no penetration boundary condition was imposed, thus assuming that the velocity of blood at the interface between the blood and the arterial wall is zero.

Regarding the outlet, we used two different flow rates as an outflow boundary condition. According to several flow measurements deriving from PET perfusion, the average flow during rest at the left coronary artery (i.e. starting from the Left Main branch and bifurcating to the respective LAD and LCx arteries) is 2 ml/s, whereas under stress, the respective value reaches an average of 6 ml/s. In order for us to determine the ratio under which flow is divided at the bifurcation site, we applied Murray's law for each case.

In general, Murray's law correlates the flow ratio through the side branches with the diameters of the branches. This relation is given by:

$$\frac{q_{D2}}{q_{D1}} = \left( \frac{d_{D2}}{d_{D1}} \right)^3, \quad (5)$$

**Fig. 3** Regression plot for smartFFR and the invasively measured FFR



with  $q_{D1}$  and  $q_{D2}$  the flow through and  $d_{D1}$  and  $d_{D2}$  the diameters of the branches which are calculated directly from the 3D models.

The calculated flow rates were then imposed as outflow boundary conditions for each of the two simulations. Then, for each simulation the pressure gradient of each branch was calculated in order to build the patient-specific  $P_d/P_a$  versus flow curve [6]:

$$\frac{P_d}{P_a} = 1 - f_v \frac{Q}{P_a} - f_s \frac{Q^2}{P_a} \quad (6)$$

where  $Q$  is the flow rate,  $f_v$  is the coefficient of pressure loss due to viscous friction and  $f_s$  is the coefficient of pressure loss due to flow separation. Using  $P_a = 100$  mmHg in Eq. (6) allows the calculation of the two previously unknown coefficients, thus leading to the calculation of the area under the patient-specific  $P_d/P_a$  versus flow curve. Finally, smartFFR is then calculated as the ratio of the area under the patient-specific  $P_d/P_a$  versus flow curve to the respective reference area (i.e. the respective curve of a healthy artery).

### Mesh

All 3D models were discretized using the same mesh parameters. In general, the arterial models were discretized into tetrahedral elements with a face size between 0.09 and 0.1 mm, resulting to models of around 5 million elements. This specific element size was chosen after a mesh sensitivity analysis.

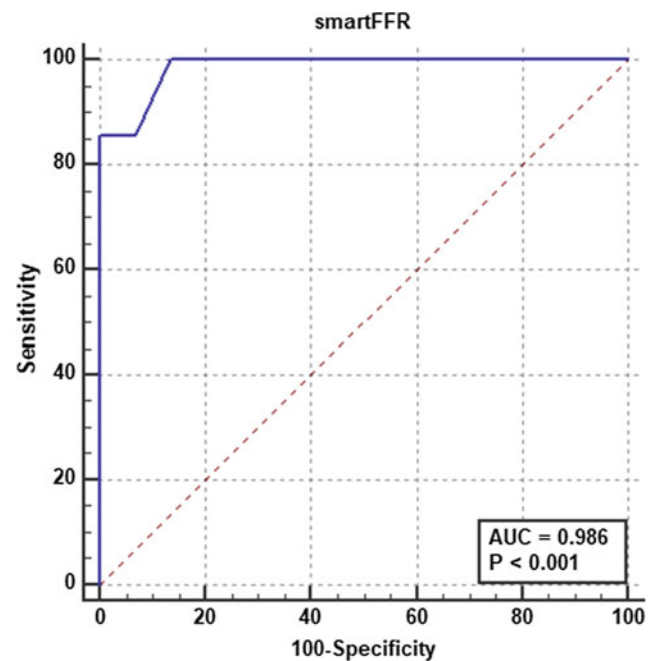


**Fig. 4** ROC curve for the smartFFR method

## 4 Results

We examined the validity of our newly proposed method by comparing the smartFFR values against the respective invasively measured FFR values. Strong correlation was found between the two methods (Pearson correlation coefficient

**Table 1** Per-vessel diagnostic performance for smartFFR  $\leq 0.83$ 

Accuracy (%)	Sensitivity (%)	Specificity (%)	PPV (%)	NPV (%)
90.9	100	86.7	77.8	100

$r = 0.88$ ,  $P < 0.001$ ) (Fig. 3). Moreover, good agreement was also observed, using the Bland-Altman method of comparison (Difference =  $-0.02864 \pm 0.059$ ,  $p = 0.034$ ) (Fig. 2). A small overestimation of smartFFR was also observed (Mean difference =  $-0.02864$ ). Finally, we also performed a Receiver Operator Curve (ROC) analysis to identify the optimal threshold for smartFFR to identify ischemic lesions that require a PCI (Fig. 4). The smartFFR threshold was  $\leq 0.83$  (i.e. deriving from the Youden index) to identify cases with FFR  $\leq 0.8$  (AUC = 0.986,  $P < 0.001$ ). The accuracy, sensitivity, specificity, Positive Predictive Value (PPV) and Negative Predictive Value (NPV) were 90.9%, 100%, 86.7%, 77.8% and 100%, respectively (Table 1).

## 5 Discussion

In this work we presented our newly proposed computational functional assessment index which can be applied on 3D models of coronary branches. 18 patients were selected for this study that underwent a CCTA exam and FFR measurement in at least one of the two main left arterial branches. 22 smartFFR values were compared to the invasively measured FFR values in order to validate the proposed method. The results were very promising, presenting strong correlation and good agreement between the two methods. smartFFR presented a slight overestimation of the FFR. This can be attributed to the fact that our method strictly relies on geometrical factors and does not take into account the microcirculatory system. The unique advantage of the proposed method is the very low computational time that is needed for each case, since less than an average of 20 min is required for the whole procedure. Moreover, the induction of hyperemia is redundant since the whole procedure is fully computational. Another point that needs to be noted is the fact that the whole process does not require a remote core-laboratory analysis and can be performed on any computer with average computational power.

One limitation of the present study is the rather modest dataset that was used which however, was counterbalanced by the quality of the dataset, since 7 of the 22 cases were pathological (i.e. 32%). A second limitation of the whole procedure is that in heavily calcified cases, the arterial lumen is underestimated because of the so-called blooming effect, thus affecting the final calculated smartFFR value.

## 6 Conclusions

The results of the current study suggest that the smartFFR can be accurately applied in coronary branches and can correctly discriminate a stenosis as hemodynamically significant or non-significant.

**Acknowledgments** This work is part-funded by the European Commission. SMARTool simulation modelling in coronary artery disease: a tool for clinical decision support. GA 689068.

**Conflict of Interest** The authors declare that there are no conflicts of interest.

## References

1. M. Renker, U. J. Schoepf, R. Wang, F. G. Meinel, J. D. Rier, R. Bayer, et al., "Comparison of Diagnostic Value of a Novel Noninvasive Coronary Computed Tomography Angiography Method Versus Standard Coronary Angiography for Assessing Fractional Flow Reserve," *American Journal of Cardiology*, vol. 114, pp. 1303–1308, Nov 1 2014.
2. M. Kruk, L. Wardziak, M. Demkow, W. Pleban, J. Pregowski, Z. Dzielinska, et al., "Workstation-Based Calculation of CTA-Based FFR for Intermediate Stenosis," *Jacc-Cardiovascular Imaging*, vol. 9, pp. 690–699, Jun 2016.
3. J. K. Min, J. Leipsic, M. J. Pencina, D. S. Berman, B. K. Koo, C. van Miegheem, et al., "Diagnostic Accuracy of Fractional Flow Reserve From Anatomic CT Angiography," *Jama-Journal of the American Medical Association*, vol. 308, pp. 1237–1245, Sep 26 2012.
4. P. D. Morris, D. Ryan, A. C. Morton, R. Lycett, P. V. Lawford, D. R. Hose, et al., "Virtual fractional flow reserve from coronary angiography: modeling the significance of coronary lesions: results from the VIRTU-1 (VIRTUal Fractional Flow Reserve From Coronary Angiography) study," *JACC Cardiovasc Interv*, vol. 6, pp. 149–57, Feb 2013.
5. M. I. Papafaklis, T. Muramatsu, Y. Ishibashi, L. S. Lakkas, S. Nakatani, C. V. Bourantas, et al., "Fast virtual functional assessment of intermediate coronary lesions using routine angiographic data and blood flow simulation in humans: comparison with pressure wire - fractional flow reserve," *EuroIntervention*, vol. 10, pp. 574–83, Sep 2014.
6. L. Athanasiou, G. Rigas, A. I. Sakellarios, T. P. Exarchos, P. K. Siogkas, C. V. Bourantas, et al., "Three-dimensional reconstruction of coronary arteries and plaque morphology using CT angiography-comparison and registration with IVUS," *BMC Med Imaging*, vol. 16, p. 9, 2016.

# Modelling Details for Electric Field Simulations of Deep Brain Stimulation

Johannes D. Johansson<sup>✉</sup>, Fabiola Alonso<sup>✉</sup>, and Karin Wårdell<sup>✉</sup>

## Abstract

Deep brain stimulation is a well-established technique for symptomatic treatment of e.g. Parkinson's disease and essential tremor. Computer simulations using the finite element method (FEM) are widely used to estimate the affected area around the DBS electrodes. For the reliability of the simulations, it is important to match used simulation parameters with experimental data. One such parameter is the electric field magnitude threshold  $EF_t$  required for axon stimulation. Another is the conductivity of the perielectrode space (PES) around the electrode. At the acute stage after surgery the PES will be characterized by an increased conductivity due to inflammation and edema while the later chronic stage will be characterized by a lower conductivity due to gliosis and minor scar formation. In this study, the  $EF_t$  and the electric conductivity of the PES have been estimated by comparing FEM simulations with clinical studies of activation distance, pulse length and electrode impedance. The resulting estimates are an  $EF_t$  of 0.2 V/mm at the common pulse width of 60  $\mu$ s and a chronaxie of 62  $\mu$ s. Estimated electric conductivities for the PES are 0.14 S/m in the acute stage and 0.05 S/m in the chronic stage, assuming a PES width of 250  $\mu$ m. These values are thus experimentally justified to use in FEM simulations of DBS.

## Keywords

Deep brain stimulation (DBS) • Finite element method (FEM) • Electric field (EF)

## 1 Introduction

Deep brain stimulation (DBS) is an established technique for the disruption of pathologic neural overactivity in e.g. Parkinson's disease, essential tremor and dystonia. The exact mechanism of DBS is not known but it has been found to have similar clinical effects as lesioning techniques in the same targets for these disorders when a sufficiently high pulse frequency is used [1–4]. This is possibly due to depletion of neurotransmitters from the synapses of axons triggered with high frequency [5, 6] or more complex network effects from the interaction between different brain structures [7].

Typical parameters that can be changed in DBS are amplitude (voltage or current), pulse width and pulse frequency. Increasing the pulse width decreases the required amplitude for both therapeutic and side effects according to the chronaxie in the Weiss-Lapicque model [8]. Pulse frequency has a more complicated effect where sufficiently high frequency as mentioned has a similar effect as lesioning while lower frequencies require a higher voltage for the effect [9] and sufficiently low frequency stimulation of e.g. 4–20 Hz on the contrary can worsen the pathological effect in overactive areas [9–11].

One way to estimate the tissue affected in the immediate vicinity of the active DBS contacts is to use finite element method (FEM) simulations to calculate the electric field around them [12]. The electric field magnitude ( $EF$ ) of 0.2 V/mm at a pulse width of 60  $\mu$ s has been used in several studies [13–15] as a threshold value for tissue activation but it has so far not been thoroughly justified.

The insertion of the DBS lead in the brain may cause a small, localized inflammation, which seems to contribute to the effect of DBS and could explain why inserting a DBS lead has clinical effect even when off [16]. Another result is that an edema will form in the immediate vicinity of the lead

J. D. Johansson (✉) · F. Alonso · K. Wårdell  
Linköping University, Linköping, Sweden  
e-mail: johannes.johansson@liu.se



[17], a vicinity often called the perielectrode space (PES) [18, 19]. The increase in tissue fluid of the edema will cause the electric conductivity of the PES to increase and thus affect the electric field around it. With time, the edema will subside and gliosis will form around the lead instead [20, 21]. However, the electric conductivity for the PES is not known for either the acute edema or the chronic gliosis, making it an unknown parameter for FEM modelling.

The aim of this paper is to calculate realistic values for the electric field magnitude threshold, including its rheobase and chronaxie, and to estimate reasonable conductivities for the perielectrode space during acute postoperative edema and later chronic gliosis formation.

## 2 Methods and Results

### 2.1 Estimation of Activation Threshold

Alexis Kuncel et al. [22] have made an estimate of the distance,  $r$  (mm), from the electrode contact center to the ventrocaudal nucleus (Vc) of the thalamus at which a certain stimulation amplitude triggers side effects from stimulation of the Vc. A pulse width of 90  $\mu$ s and a pulse frequency of 160 Hz had been used in this study. They arrived at a relation of threshold voltage,  $V_{th}$  (V), and  $r$  as

$$V_{th} = 0.1 + 0.22r^2 \quad (1)$$

and from this an effective activation distance can be calculated as

$$r = \sqrt{\frac{V - 0.1}{0.22}} \quad (2)$$

giving an effective activation radius of 2.0–3.9 mm for amplitudes of 1–3.5 V. Åström et al. found the average  $EF$  at these distances for the different voltages to be 0.165 V/mm [12]. This electric field magnitude threshold,  $EF_t$ , can be fitted to the Weiss-Lapicque model according to

$$EF_t = EF_{rheo} \left( 1 + \frac{T_{chr}}{T} \right) \quad (3)$$

where  $EF_{rheo}$  is the rheobase (V/mm),  $T_{chr}$  the chronaxie ( $\mu$ s) and  $T$  the pulse width ( $\mu$ s). With  $T = 90 \mu$ s and a  $T_{chr}$  for axon stimulation assumed to be 62  $\mu$ s after least squares fitting (lsqnonlin, Matlab, Mathworks, USA) to the average result from a clinical study by Mario Rizzone et al. (Table 2) [9], this gives an  $EF_{rheo}$  of  $0.165/(1 + 62/90) = 0.098$  V/mm. The estimated  $EF_t$  at the standard pulse width of 60  $\mu$ s then becomes  $0.098 \cdot (1 + 62/60) = 0.20$  V/mm. The

corresponding strength-duration curve is presented in Fig. 1a.

### 2.2 Estimation of the Conductivity of the Perielectrode Space

A study by Codrin Lungu et al. [23] was used to estimate the electric conductivity of the perielectrode space under the assumption that it has a characteristic thickness of 250  $\mu$ m [18, 19]. The electric conductivity was set between 0.01 and 0.2 S/m in a parametric sweep in steps of 0.01 S/m with a surrounding tissue domain assumed to be a mixture of gray and white matter with a conductivity of 0.09 S/m. Bipolar stimulation at a voltage,  $U$ , of 3 V between contacts 0 and 1 of a 3389 lead (Medtronic Inc., USA) was simulated for the parametric sweep. Modelling and simulation (Fig. 1b) was done in Comsol Multiphysics 5.2a (COMSOL, Sweden). For details, see [18]. The impedance,  $R$  ( $\Omega$ ), was calculated according to Ohm's law with the current calculated as the integration of the current density,  $\mathbf{J}$  (A/m<sup>3</sup>), normal to the surface of contact 0.

$$R = U / \left| \int \mathbf{n} \cdot \mathbf{J} dS \right| \quad (4)$$

In the Lungu study, the average measured impedance in the first week after implantation was 1530  $\Omega$  and after 3 weeks it had risen to 2530  $\Omega$  [23]. The parametric sweep gave corresponding closest impedances of 1551  $\Omega$  for a PES conductivity of 0.14 S/m and 2619  $\Omega$  for a PES conductivity of 0.05 S/m. The PES conductivities of 0.14 and 0.05 S/m are thus suitable values to use for the acute and chronic phases respectively.

## 3 Discussion

In this study, suitable rheobase and chronaxie to describe the electric field magnitude threshold,  $EF_t$ , as well as suitable conductivities of the perielectrode space have been estimated from experimental studies [22, 23].

Hemm et al. [24] had associated the 0.1 V/mm isolevel from 1.5 V stimulation to the lateral extent of the GPi in a dystonia patient. However, they had used a very long pulse width of 450  $\mu$ s. Putting that pulse width in Eq. (3) with  $EF_{rheo} = 0.098$  V/mm and  $T_{chr} = 62 \mu$ s gives an  $EF_t$  of 0.11 V/mm, in good agreement with the 0.2 V/mm level for 60  $\mu$ s in this study. Åström et al. [12] have studied the impact of the pulse width on  $EF_t$  with neuron model simulations. Least squares fitting to their results (Table 3 [12])

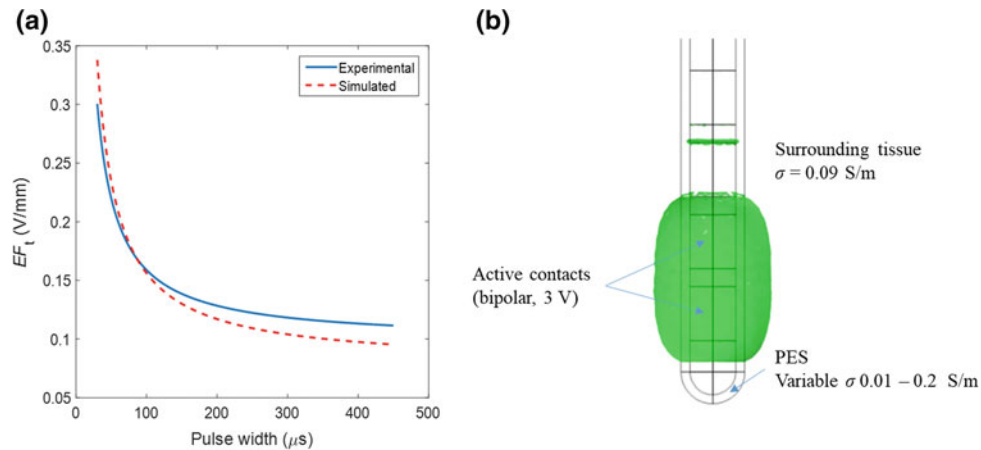


**Fig. 1** **a** Strength-duration curves with chronaxies fitted to Rizzone's experimental [9] and Åström's simulated [12] data, assuming an  $EF_t$  of 0.2 V/mm at a pulse width of 60  $\mu$ s. **b** Three-dimensional bipolar

model for estimation of PES conductivity. The green isosurface corresponds to  $EF = 0.2$  V/mm

gives a  $T_{chr}$  of 100  $\mu$ s (Fig. 1a), which would give an  $EF_{theo}$  of  $0.165/(1 + 100/90) = 0.078$  V/mm and thus an  $EF_t$  of  $0.078 \cdot (1 + 100/60) = 0.21$  V/mm at  $T = 60$   $\mu$ s when comparing to Kuncel's study [22].

Comparing the  $EF_t$  of 0.2 V/mm at 60  $\mu$ s with simulations of activation of axons with different fiber diameters [12] indicate that the typical diameter of axons stimulated by DBS should be around 3.5  $\mu$ m, which is among the larger axons in the deep brain structures although still smaller than the value of 5.7  $\mu$ m used in many DBS simulation studies [25]. Median axon diameters for different nuclei and white matter tracts have been found to be around 0.5  $\mu$ m in human (range: 0.16–9  $\mu$ m) and rhesus monkey brains [26, 27].

The 250  $\mu$ m thickness of the PES may vary between patients. A larger distance would result in a lower increase in the electric conductivity due to the inflammation/edema and a lower decrease due to the gliosis when estimating the conductivity from measured impedance.

It is interesting to note that the most energy-efficient stimulation occurs at pulse widths equal to the chronaxie [8]. The optimal pulse width to maintain a long battery lifetime is thus the default 60  $\mu$ s when the chronaxie of the triggered tissue is the same as in Rizzone's study [9].

In conclusion, based on the experimental studies used, suitable rheobase and chronaxie for axon activation seem to be 0.98 V/mm and 62  $\mu$ s respectively, giving a threshold electric field of 0.20 V/mm for the default pulse width of 60  $\mu$ s. Suitable values for a 250  $\mu$ m PES are 0.14 S/m for the acute edema phase and 0.05 S/m for the chronic gliosis phase. More experimental studies similar to those of Kuncel [22] and Lungu [23] would be desirable in order to further increase the reliability of these estimates and to see if there are differences in them between different parts of the brain.

**Acknowledgements** This work is funded by the Swedish Research Council (Vetenskapsrådet, Dnr. 2016-03564), the Swedish Foundation for Strategic Research (Project BD15-0032), and the Knut and Alice Wallenberg Foundation (Project Seeing Organ Function). The authors declare that they have no conflicts of interest.

## References

- Blomstedt, P., Hariz, G. M., and Hariz, M. I., Pallidotomy versus pallidal stimulation, *Parkinsonism Relat Disord*, 12(5) pp. 296–301, (2006).
- Schuurman, P. R., Bosch, D. A., Merkus, M. P., and Speelman, J. D., Long-term follow-up of thalamic stimulation versus thalamotomy for tremor suppression, *Mov Disord*, 23(8) pp. 1146–53, (2008).
- Eltahawy, H. A., Saint-Cyr, J., Giladi, N., Lang, A. E., and Lozano, A. M., Primary dystonia is more responsive than secondary dystonia to pallidal interventions: Outcome after pallidotomy or pallidal deep brain stimulation, *Neurosurgery*, 54 (3) pp. 613–619, (2004).
- Marin, C., Jimenez, A., Tolosa, E., Bonastre, M., and Bove, J., Bilateral subthalamic nucleus lesion reverses L-dopa-induced motor fluctuations and facilitates dyskinetic movements in hemiparkinsonian rats, *Synapse*, 51(2) pp. 140–50, (2004).
- Galarreta, M. and Hestrin, S., Frequency-dependent synaptic depression and the balance of excitation and inhibition in the neocortex, *Nat Neurosci*, 1(7) pp. 587–94, (1998).
- Urbano, F. J., Leznik, E., and Llinás, R. R., Cortical activation patterns evoked by afferent axons stimuli at different frequencies: an in vitro voltage-sensitive dye imaging study, *Thalamus & Related Systems*, 1(4) pp. 371–378, (2002).
- Brocker, D. T., Swan, B. D., So, R. Q., Turner, D. A., Gross, R. E., and Grill, W. M., Optimized temporal pattern of brain stimulation designed by computational evolution, *Sci Transl Med*, 9(371) 2017).
- Geddes, L. A., Accuracy limitations of chronaxie values, *IEEE Trans Biomed Eng*, 51(1) pp. 176–81, (2004).
- Rizzone, M., Lanotte, M., Bergamasco, B., Tavella, A., Torre, E., Faccani, G., *et al.*, Deep brain stimulation of the subthalamic

- nucleus in Parkinson's disease: effects of variation in stimulation parameters, *J Neurol Neurosurg Psychiatry*, 71(2) pp. 215–9, (2001).
10. Gradinaru, V., Mogri, M., Thompson, K. R., Henderson, J. M., and Deisseroth, K., Optical deconstruction of parkinsonian neural circuitry, *Science*, 324(5925) pp. 354–9, (2009).
  11. Hassler, R., Riechert, T., Munding, F., Umbach, W., and Ganglberger, J. A., Physiological observations in stereotaxic operations in extrapyramidal motor disturbances, *Brain*, 83 pp. 337–50, (1960).
  12. Åström, M., Diczfalusy, E., Martens, H., and Wårdell, K., Relationship between Neural Activation and Electric Field Distribution during Deep Brain Stimulation, *IEEE Transactions on Biomedical Engineering*, 62(2) pp. 664–672, (2015).
  13. Hemm, S., Pison, D., Alonso, F., Shah, A., Coste, J., Lemaire, J. J., *et al.*, Patient-Specific Electric Field Simulations and Acceleration Measurements for Objective Analysis of Intraoperative Stimulation Tests in the Thalamus, *Front Hum Neurosci*, 10 p. 577, (2016).
  14. Alonso, F., Latorre, M. A., Göransson, N., Zsigmond, P., and Wårdell, K., Investigation into Deep Brain Stimulation Lead Designs: A Patient-Specific Simulation Study, *Brain Sciences*, 6 (3) 2016).
  15. Horn, A., Reich, M., Vorwerk, J., Li, N. F., Wenzel, G., Fang, Q. Q., *et al.*, Connectivity Predicts Deep Brain Stimulation Outcome in Parkinson Disease, *Annals of Neurology*, 82(1) pp. 67–78, (2017).
  16. Perez-Caballero, L., Perez-Egea, R., Romero-Grimaldi, C., Puigdemont, D., Molet, J., Caso, J. R., *et al.*, Early responses to deep brain stimulation in depression are modulated by anti-inflammatory drugs, *Mol Psychiatry*, 19(5) pp. 607–14, (2014).
  17. Kozai, T. D., Jaquins-Gerstl, A. S., Vazquez, A. L., Michael, A. C., and Cui, X. T., Brain tissue responses to neural implants impact signal sensitivity and intervention strategies, *ACS Chem Neurosci*, 6(1) pp. 48–67, (2015).
  18. Alonso, F., Hemm-Ode, S., and Wårdell, K., Influence on Deep Brain Stimulation from Lead Design, Operating Mode and Tissue Impedance Changes – A Simulation Study, *Brain Disorders & Therapy*, 4(3) 2015).
  19. Yousif, N., Bayford, R., Bain, P. G., and Liu, X., The peri-electrode space is a significant element of the electrode-brain interface in deep brain stimulation: A computational study, *Brain Research Bulletin*, 74(5) pp. 361–368, (2007).
  20. Nielsen, M. S., Bjarkam, C. R., Sorensen, J. C., Bojsen-Moller, M., Sunde, N. A., and Ostergaard, K., Chronic subthalamic high-frequency deep brain stimulation in Parkinson's disease - a histopathological study, *European Journal of Neurology*, 14(2) pp. 132–138, (2007).
  21. Haberler, C., Alesch, F., Mazal, P. R., Pilz, P., Jellinger, K., Pinter, M. M., *et al.*, No tissue damage by chronic deep brain stimulation in Parkinson's disease, *Annals of Neurology*, 48(3) pp. 372–376, (2000).
  22. Kuncel, A. M., Cooper, S. E., and Grill, W. M., A method to estimate the spatial extent of activation in thalamic deep brain stimulation, *Clin Neurophysiol*, 119(9) pp. 2148–58, (2008).
  23. Lungu, C., Malone, P., Wu, T., Ghosh, P., McElroy, B., Zaghloul, K., *et al.*, Temporal macrodynamics and microdynamics of the postoperative impedance at the tissue-electrode interface in deep brain stimulation patients, *J Neurol Neurosurg Psychiatry*, 85(7) pp. 816–9, (2014).
  24. Hemm, S., Mennessier, G., Vayssiere, N., Cif, L., and Coubes, P., Co-registration of stereotactic MRI and isofieldlines during deep brain stimulation, *Brain Res Bull*, 68(1–2) pp. 59–61, (2005).
  25. McIntyre, C. C., Mori, S., Sherman, D. L., Thakor, N. V., and Vitek, J. L., Electric field and stimulating influence generated by deep brain stimulation of the subthalamic nucleus, *Clin Neurophysiol*, 115(3) pp. 589–95, (2004).
  26. Liewald, D., Miller, R., Logothetis, N., Wagner, H. J., and Schuz, A., Distribution of axon diameters in cortical white matter: an electron-microscopic study on three human brains and a macaque, *Biological Cybernetics*, 108(5) pp. 541–557, (2014).
  27. Mathai, A., Wichmann, T., and Smith, Y., More Than Meets the Eye-Myelinated Axons Crowd the Subthalamic Nucleus, *Movement Disorders*, 28(13) pp. 1811–1815, (2013).

# A Highly-Detailed 3D Model of the Human Atria

Sara Rocher, Alejandro López, Ana Ferrer, Laura Martínez, Damián Sánchez, and Javier Saiz

## Abstract

The underlying mechanisms of atrial fibrillation and the involved factors in the chronicity of the disease are object of great interest nowadays. Multiscale cardiac modelling has become a powerful tool since it can help to better understand the physiopathology of arrhythmias. In this study we present a “true” 3D model of the human atria with anatomical and functional heterogeneity. The model includes a realistic definition of the atrial wall thickness and transmural in fibres orientation. The electrical behaviour of the new model was validated by comparing the propagation sequence in sinus rhythm with respect to experimental activation times. The model was used for arrhythmogenic studies by adding electrical remodelling. We compared the fibrillatory activity of the new model with two models less detailed anatomically but with the same electrophysiological properties. The three models reproduced different fibrillatory patterns with the appearance of rotors in different areas, demonstrating that the anatomical properties of the model affect the electrical behaviour of the simulation. Our results suggest that it is very important to implement highly-detailed models to obtain results as close as possible to the real system.

## Keywords

Atrial fibrillation • Cardiac modelling  
 Computational simulation • Electrophysiology  
 Wall thickness • Fibers

S. Rocher · A. López · A. Ferrer · L. Martínez · J. Saiz (✉)  
 Centro de Investigación e Innovación en Bioingeniería,  
 Universitat Politècnica de València, Valencia, Spain  
 e-mail: jsaiz@ci2b.upv.es

D. Sánchez  
 Faculty of Medicine, Department of Anatomy and Cell Biology,  
 Universidad de Extremadura, Badajoz, Spain

## 1 Introduction

Atrial fibrillation (AF) is the most prevalent sustained arrhythmia and it is expected that its prevalence will continue to increase as the population ages. It is considered a major cause of morbidity and mortality, since it is clinically associated with an increase of embolic strokes, heart failure and impaired quality of life [1]. The recurrent hospitalizations for AF and the cost of its management result in a significant impact in public healthcare systems budget. Nevertheless, the physiopathology of the disease remains incompletely understood and the available treatments are partially effective.

AF burden has motivated during last years a deep research in cardiac electrophysiology, trying to clarify the arrhythmogenesis and maintenance mechanisms at the whole atria level. For this purpose, computational modelling provides a powerful tool to integrate multiscale data and study atrial activity under different conditions.

The rapid increase in the amount of experimental data and computational resources has allowed great advances in cardiac modelling. Several generic atrial models have already been published incorporating important features, such as morphological, histological, electrophysiological and functional information [2–4]. However, to the best of our knowledge, any of them consider atrial wall thickness and fibers transmural. Both features have been suggested as relevant factors in atrial activation and arrhythmias, and therefore, should be taken into account when developing computer models to study AF [5, 6].

The main objective of this work is to present a highly-detailed three-dimensional model of the human atria, by improving our previously atrial model [4] anatomically and histologically. For the first time, the model includes a realistic definition of the atrial wall thickness and transmural in fibres orientation. The developed model was used to study how the new geometrical and functional properties affect the electrical behavior during AF.

## 2 Methods

In the present work, we developed a new atrial model that improves our previous 3D model of the human atria [4]. The new model has enhanced the anatomical description of the atrial wall thickness and the description of fibers direction. As in our previous model [4], the mesh was divided into 21 regions and subdivided into 56 subregions for a detailed anatomical, electrophysiological and fiber orientation description.

### 2.1 Atrial Wall Thickness Definition

Atrial anatomy has been directly related with mechanisms of initiation and maintenance of cardiac arrhythmias. Furthermore, an exhaustive knowledge of cardiac anatomy can help interventional cardiologist to improve the safety and the rate success of ablation treatments. Thus, several authors have analyzed in detail the normal anatomy of the atria [7].

The atrial wall thickness of the right atrium (RA) is very heterogeneous because of the presence of the Crista Terminalis (CT) and the pectinate muscles (PMs). The thickest region is in the upper part of the CT with a thickness between 5 and 8 mm. The RA wall becomes extremely thinner towards the vestibule of the tricuspid valve (TV), where has a mean thickness of 2 mm [7].

The atrial wall thickness of the left atrium (LA) is much more uniform and measures on average 3 mm in thickness. It is thicker than the RA when we exclude considerations of the CT. The thickest region is the anterior wall with 4–5 mm, while the thinnest region is the vestibule of the mitral valve (MV), with a mean thickness of 2 mm [7].

Starting from our previous model, we developed a methodology to incorporate the anatomical information described in the bibliography for defining the wall thickness in each region. Firstly, as the transmural cardiac wall thickness is the distance between the epicardium and the endocardium, we manually separated the epicardium layer and the endocardium layer from the surface mesh. For redefining the thickness corresponding to each region, we moved the nodes coordinates until reach the anatomical thickness. Once the distance between both layers was established, the meshes were manually smoothed and joined.

### 2.2 Fibers Definition

The architecture of muscle fibers has a major impact on the cardiac electrical activity, since it defines the excitation wave propagation. In human models, fiber orientation is usually analyzed from ex vivo histological information [6, 8].

The RA has a complex fibrous structure, characterized by the abundant PMs, the prominent CT and a large appendage (RAA). In contrast, the LA has a smooth uniform appearance but presents marked transmural variations in fiber orientation. Several studies suggest that in both anterior and posterior walls this change in fiber angles takes place abruptly from epicardium to endocardium at the midwall, resulting in two fiber layers with nearly perpendicular directions [9–11].

In order to define different fiber directions transmurally in the atrial wall, we differentiate two layers in the atrial model. We labelled as epicardium from the midwall to the external surface and as endocardium from the midwall to the inner surface.

To the epicardium we assigned the same fiber orientation as in our previous model [4]. We employed a rule-based algorithm which computes fiber as the cross product between a main vector direction and the normal to the external surface of each element. For the endocardium, we used the same vectors as in the epicardium, except for the elements belonging to the posterior wall and the anterior wall. In these two regions, we rotated the epicardial fiber vector  $45^\circ$  in the y-axis.

### 2.3 Electrophysiological Properties

The electrophysiological properties determine the electrical behavior of the simulation. In this study, the cellular electrical activity is modelled by the Courtemanche ionic model [12], since it is the model with best performance in electrical remodeling. To reproduce the heterogeneity in action potential (AP) morphology and duration of the different atrial regions we defined nine cellular models by adjusting the maximum conductance of the ionic channels  $I_{to}$ ,  $I_{CaL}$  and  $I_{Kr}$ . Additionally, tissue heterogeneity was modelled by tuning in each region the longitudinal conductivities and the anisotropy ratios, as in [4].

In chronic AF (cAF), the recurrent episodes of fibrillation force the cardiovascular system to develop several mechanisms of adaptation resulting in alterations in atrial properties and stabilization of AF. In the present study, the electrical remodeling was included through the variation of the maximum conductance of  $I_{to}$ ,  $I_{CaL}$ ,  $I_{K1}$ ,  $I_{Kur}$  and  $I_{Ks}$ , as in [13]. On average, the electrical remodeling reduces a 56% the APD90 in our model. That means a decrease in the refractory period, increasing the vulnerability for AF genesis.

### 2.4 Stimulation Protocol

With the aim of stabilizing the electrophysiological properties of the model, smoothing differences between adjacent



regions and achieving a computational compromise, we applied to the sinoatrial node (SAN) 20 continuous beats with a basic cycle length (BCL) of 500 ms, 2 ms of duration and 28 pA/pF of amplitude (rectangular pulse above the stimulation threshold). We saved the state to use it as starting point in next simulations.

In order to validate the physiological propagation of the new model, we applied a single stimulus to the SAN. Then, to generate fibrillatory activity, we paced the coronary sinus (CS) using a continuous high-frequency train (BCL = 110 ms) for 6 s.

## 2.5 Computational Method

The electrical propagation in the atria was described by the monodomain model:

$$\nabla \cdot (D\nabla V) = C_m \cdot \frac{\partial V_m}{\partial t} + I_{ion} \quad \text{in } \Omega_H \quad (1)$$

$$\mathbf{n} \cdot (D\nabla V) = 0 \quad \text{in } \partial\Omega_H \quad (2)$$

where  $D$  is the equivalent conductivity tensor,  $V_m$  is the transmembrane potential,  $I_{ion}$  is the transmembrane ionic current that depends on the cellular model,  $C_m$  is the membrane capacitance and  $\Omega_H$  is the heart domain.

The monodomain Eqs. (1–2) were solved using the operator splitting numerical scheme with ELVIRA software [14] with a constant time step of 0.01 ms. The simulations were run on a computing node with forty-eight 6-core AMD Opteron Processors 6234 clocked at 2.4 GHz.

## 3 Results

### 3.1 3D Model

The new 3D model of the human atria has 1.945.101 hexahedral elements with spatial resolution of 300  $\mu\text{m}$  and 2.174.034 nodes. The RA presents a mean thickness of 3 mm while the LA has 3,4 mm on average (Fig. 1a). The range of thickness values for all the regions in the model are consistent with the experimental data.

Figure 1b shows the resulting bilaminar structure of fibers in the anterior and posterior walls of the LA. The posterior wall fibers in the epicardium descend perpendicularly from the superior wall to the MV, while in the endocardium are oriented mainly circumferentially from the right pulmonary veins (RPV) to the left pulmonary veins (LPV). On the other

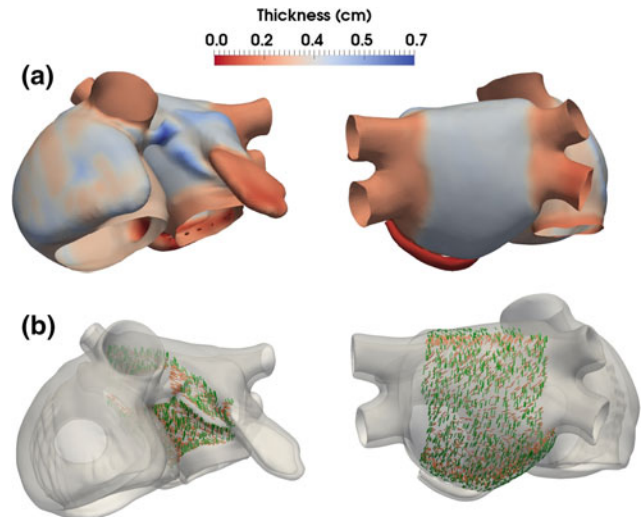


**Fig. 1** Properties of the atrial model. **a** Atrial wall thickness of the model after the smoothing. **b** Fiber transmuralities at the anterior wall (first column) and at the posterior wall (second column). Green fibers represent the epicardium fibers while the orange ones correspond to the endocardium

hand, the fibers from the epicardium of the anterior wall are aligned parallel to the right septum, while in the endocardium fibers run parallel to the left appendage from the Bachman bundle (BB) to the MV.

### 3.2 Model Validation

So as to validate the model, we compared the activation sequence from the model in sinus rhythm with experimental activation times measured by Lemery et al. [15].

After the SAN is depolarized, regions from the RA simultaneously start their respective depolarizations and two wavefronts appear towards the TV. The TV is the last RA region activated at  $t = 82$  ms. The activation moves from the RA to the LA through the fossa ovalis (FO) and the BB, registering the first activation of the LA at  $t = 42$  ms. Once in the LA, two wavefronts are responsible for the depolarization of the different regions in the LA. Finally, the last activation takes place at the left inferior pulmonary vein at  $t = 123$  ms. All the simulated activation times are within experimental ranges (Table 1).

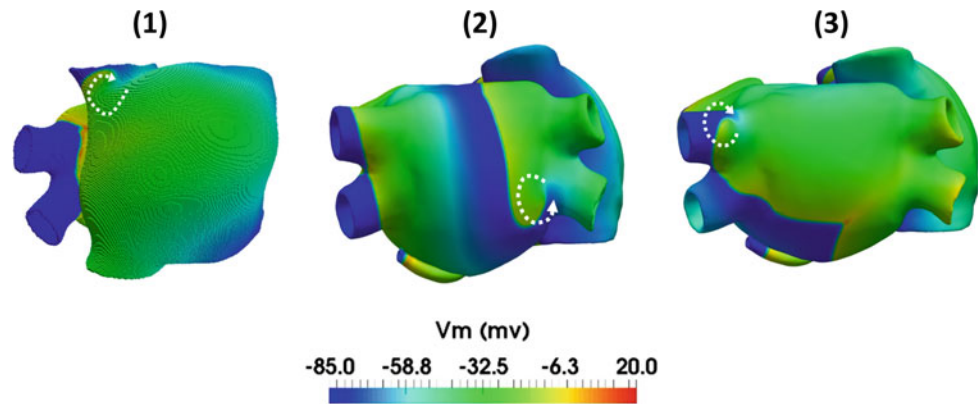
### 3.3 Atrial Fibrillation Simulations

From the stabilized model in electrical remodeling, we simulated AF episodes. With the aim of analyzing the fibrillatory

**Table 1** Activation times of atrial regions. Comparison of the simulated activation times with the experimental activation times at different points of the atria

	SAN	SCV	BB	FO	RAA	TV	RPV	LPV	Last
Model (ms)	0	22	36	37	42	82	72	101	123
Experimental (ms)	0	26 ± 22	31 ± 13	45 ± 14	39 ± 21	87 ± 25	75 ± 24	89 ± 25	116 ± 18

**Fig. 2** Electrical propagation of the simulated atrial fibrillation. **1** Model with homogeneous thickness. **2** Model with anatomical thickness. **3** New atrial model



pattern depending on the anatomical properties of the model, we launched three simulations: in our previous model with homogenous thickness (1), in an intermediate model with anatomical thickness (2) and in the new atrial model (3).

The three models show a recurrent fibrillatory activity with the appearance of a rotor. In the model 1 the rotor is established on the superior cava vein (SCV), in the model 2 the rotor appears on the right inferior pulmonary vein and in the model 3 the rotor emerges on the left superior pulmonary vein (Fig. 2).

## 4 Conclusions

At the present study, we have developed a new 3D model of the human atria, with, important advances with respect to our previous model: heterogeneous thickness and fiber transmural thickness.

The simulations carried out during AF activity allowed us to demonstrate that the anatomical definition of the model affects atrial activation, especially in abnormal rhythms. This highlights the need for using computer models taking into account the real structure of the atrium for the study of atrial arrhythmias. Our highly-detailed model is an excellent tool to analyze both physiological and pathologic conditions, guarantying reliable results. Therefore, it is a promising model to progress in the evaluation and treatment of arrhythmias, allowing to consider effects of transmural thickness in fibrosis and ablation.

**Conflict of Interest** None declared.

## References

1. J. Andrade, P. Khairy, D. Dobrev, and S. Nattel, "The clinical profile and pathophysiology of atrial fibrillation: relationships among clinical features, epidemiology, and mechanisms," *Circ. Res.*, vol. 114, pp. 1453–1469, 2014.
2. G. Seemann, C. Höper, F. B. Sachse, O. Dössel, A. V. Holden, and H. Zhang, "Heterogeneous three-dimensional anatomical and electrophysiological model of human atria," *Philos. Trans. R. Soc.*, vol. 364, pp. 1465–1481, 2006.
3. O. V. Aslanidi *et al.*, "3D virtual human atria: A computational platform for studying clinical atrial fibrillation," *Prog. Biophys. Mol. Biol.*, vol. 107, no. 1, pp. 156–168, 2011.
4. A. Ferrer *et al.*, "Detailed anatomical and electrophysiological models of human atria and torso for the simulation of atrial activation," *PLoS One*, vol. 10, no. 11, pp. 1–29, 2015.
5. M. Varela, C. Kolbitsch, A. Theron, R. Morgan, M. Henningsson, and T. Schaeffter, "3D high-resolution atrial wall thickness maps using black-blood PSIR," *J. Cardiovasc. Magn. Reson.*, vol. 17, no. Suppl 1, pp. 1–2, 2015.
6. S. Y. Ho and D. Sánchez-Quintana, "The importance of atrial structure and fibers," *Clin. Anat.*, vol. 22, no. 1, pp. 52–63, 2009.
7. D. Sánchez-Quintana, G. Pizarro, J. R. López-Mínguez, S. Y. Ho, and J. A. Cabrera, "Standardized review of atrial anatomy for cardiac electrophysiologists," *J. Cardiovasc. Transl. Res.*, vol. 6, no. 2, pp. 124–144, 2013.
8. K. C. Wang, S. Y. Ho, D. G. Gibson, and R. H. Anderson, "Architecture of atrial musculature in humans," *Heart*, vol. 73, no. 6, pp. 559–565, 1995.
9. S. Y. Ho, D. Sánchez-Quintana, J. A. Cabrera, and R. H. Anderson, "Anatomy of the Left Atrium: Implications for Radiofrequency Ablation of Atrial Fibrillation," *J. Cardiovasc. Electrophysiol.*, vol. 10, pp. 1525–1534, 1999.
10. S. Y. Ho, R. H. Anderson, and D. Sánchez-Quintana, "Atrial structure and fibres: Morphologic bases of atrial conduction," *Cardiovasc. Res.*, vol. 54, no. 2, pp. 325–336, 2002.

11. F. Pashakhanloo *et al.*, "Myofiber architecture of the human atria as revealed by submillimeter diffusion tensor imaging," *Circ. Arrhythmia Electrophysiol.*, vol. 9, no. 4, 2016.
12. M. Courtemanche, R. J. Ramirez, and S. Nattel, "Ionic mechanisms underlying human atrial action potential properties : insights from a mathematical model," *Am J Physiol Hear. Circ Physiol.*, vol. 275, pp. 301–321, 1998.
13. L. Martínez-Mateu *et al.*, "Factors affecting basket catheter detection of real and phantom rotors in the atria: A computational study," *PLoS ONE (Man. subm.)*, 2017.
14. E. Heidenreich, J. M. Ferrero, M. Doblaré, and J. F. Rodríguez, "Adaptive macro finite elements for the numerical solution of monodomain equations in cardiac electrophysiology," *Ann Biomed Eng.*, vol. 38, pp. 2331–2345, 2010.
15. R. Lemery *et al.*, "Normal Atrial Activation and Voltage During Sinus Rhythm in the Human Heart: An Endocardial and Epicardial Mapping Study in Patients with a History of Atrial Fibrillation," *J. Cardiovasc. Electrophysiol.*, vol. 18, pp. 402–408, 2007.

# The Correlation Between Central Corneal Thickness and Glaucomatous Optic Nerve Damage in a Human Eye

Chai Yee Loke, Ean Hin Ooi, Norlina Ramli, and Amir Samsudin

## Abstract

Results from clinical studies suggest a strong correlation between central corneal thickness (CCT) and glaucomatous optic nerve damage. A 3D model is developed to carry out structural investigation of the IOP-induced posterior displacement of the lamina cribrosa (LC), under the influence of CCT. The cornea, the sclera and the LC are assumed to exhibit nonlinear material properties. The numerical results suggest a higher glaucoma progression rate with a lower CCT, which supports the clinical trend. The low influential rate of CCT towards optic nerve damage suggests that CCT may not be a dominant factor in structural injury of the nerve bundles. The results indicate that CCT measurement can be significant in the diagnostic system of glaucoma.

## Keywords

Central corneal thickness • Glaucoma • Optic nerve damage

## 1 Introduction

Glaucoma is an eye disease associated with intraocular pressure (IOP) elevations. Elevated IOP at the anterior segment of the human eye is considered as a major risk factor towards optic nerve damage at the posterior segment [1]. Excessive stress is claimed to transfer to the optic nerve head (ONH) via in-wall hoop stress borne within the outer corneo-scleral shell. The stress is concentrated at the relatively less dense structure, the lamina cribrosa (LC), which is

considered as the weak spot in the study of ONH biomechanics. The IOP-induced posterior displacement of the LC is deemed to impose retinal ganglion cells injury, which eventually leads to blindness [2].

Recent clinical studies suggest that central corneal thickness (CCT) is an independent risk factor in glaucoma progression [3]. Past data demonstrates a strong correlation between lower CCT with higher progression rate [4]. Due to the sensitivity of the human eye to physical touch, in silico study is considered to be a powerful alternative of in vivo study. Numerous numerical studies have been carried out to investigate IOP-imposed ONH injury [5, 6]. Nevertheless, past numerical models mostly consider only the outer corneo-scleral shell and exclude the internal components in their eye models, such as the lens and the vitreous [7, 8]. The IOP is modeled as a pressure loading subjected directly on the inner surface of the retinal layer, which may be an oversimplification [7, 8]. In addition, the cornea is normally prefixed with zero displacement, in which the CCT is not under investigation [6, 8]. Motivated by this, the present study aims to investigate the influence of CCT towards glaucomatous posterior displacement of the LC. In the present study, a 3D computational model of the human eye is developed to investigate the ONH biomechanics correlated to CCT. The simulations are carried out using the commercial software COMSOL Multiphysics 5.3<sup>®</sup>.

## 2 Materials and Methods

### 2.1 The 3D Eye Model

The 3D human eye model is built in COMSOL Multiphysics 5.3<sup>®</sup>, with the dimensions follow closely to the model developed by Ooi and Ng [9]. The eye model includes the cornea, the sclera, the iris, the lens and the vitreous. It is modified to suit the purpose of the present study. The ONH, consists of the LC, the pre-laminar and post-laminar neural tissues, is added to the geometry, approximately 3.8 mm to

C. Y. Loke (✉) · E. H. Ooi  
School of Engineering, Monash University Malaysia, 47500  
Bandar Sunway, Selangor, Malaysia  
e-mail: loke.chai.yee@monash.edu

N. Ramli · A. Samsudin  
Faculty of Medicine, Department of Ophthalmology, University  
of Malaya, 50603 Kuala Lumpur, Malaysia

the nasal side of the fovea. The dimensions adopted for constructing the ONH follow closely to Sigal's study [8]. It is important to note that the ONH built represents a healthy eye, which is assumed to have an initial IOP within the physiological range, i.e. 9–20 mmHg [10]. The eye model with the incorporated ONH is assumed to represent a healthy eye under its equilibrium state.

A retinal layer is added, which is combined with the pre-laminar neural tissue as a single homogeneous domain. The zonular fibres, which hold the lens in place, are added to enhance the capability of the model to capture the IOP-induced stress-strain distribution across the eye globe. Three interfaces representing the contact surfaces of the ocular muscles (lateral, medial and inferior rectus) and the sclera are added to the model. The ocular muscles hold the eye in place, in which these interfaces are needed to prescribe a fixed boundary condition at later stage. The dimensions for all of the components are summarized in Table 1. To reduce computational burden and to save the computation time needed for each simulation, only one-half of the geometry is built. The symmetrical plane is set on the transverse plane of the eye model due to the physical location of the optic disc. The resulting structure representing a right eye is demonstrated in Fig. 1.

## 2.2 Boundary Conditions

The IOP is modeled as a boundary pressure load acting in the direction normal to the inner wall of the anterior and posterior chambers, as depicted in Fig. 1a (shaded in blue). The normal load is applied on the surface such that:

$$\boldsymbol{\sigma} \cdot \mathbf{n} = P_{\text{elev}}, \quad (1)$$

where  $\boldsymbol{\sigma}$  is the Cauchy stress tensor and  $P_{\text{elev}}$  is the acting boundary load. As mentioned in Sect. 2.1, the eye model is assumed to have an initial IOP that represents a healthy eye. Note that  $P_{\text{elev}}$  does not represent the IOP inside the anterior and posterior chambers, but the elevated IOP on top of the initial IOP under its equilibrium state. The elevated IOP,

$P_{\text{elev}}$  acting on the model represents an eye under glaucomatous condition.

A symmetrical plane is prescribed on the transverse plane of the eye model, with a zero displacement condition, such that:

$$\mathbf{u} = 0, \quad (2)$$

where  $\mathbf{u}$  represents the total displacement in  $x$ -,  $y$ - and  $z$ -directions, as depicted in Fig. 1c (shaded in blue). The interfaces representing the contact surfaces between the sclera and the ocular muscles are prefixed with a prescribed displacement, which allows tangential displacement but restricts normal displacement, as shown in Fig. 1d (shaded in blue). The remaining surfaces are allowed to deform freely in all directions.

## 2.3 Material Properties

The material properties of all the components in the eye model except for the cornea, the sclera and the LC, are assumed to be linear elastic, as glaucoma is a long term disease that develops over years [6, 8]. The cornea, the sclera and the LC are assumed to exhibit nonlinear material properties, as reported in the study by Woo et al. [12]. The Young's moduli,  $E$  of the three mentioned components are prescribed in nonlinear exponential functions of the first principal strain,  $\varepsilon$  based on Woo's study. The Poisson's ratio of each domain is adopted from the literatures [6, 8]. The vitreous, which is a gel-like substance, is prescribed with the shear and the bulk moduli. Table 2 summarizes the material properties of each component of the eye model.

## 2.4 Mesh Convergence Study

The eye model is discretized into tetrahedral elements to obtain the mesh-independent solutions. The total displacement, the Tresca shear stress and the maximum principle strain are examined at the reference points preset on the symmetrical plane of the cornea, the sclera and the LC. The deformation measured at the reference points show high consistency with less than 1% of discrepancy throughout the test, when the number of elements is increased slowly. On the other hand, the results for the Tresca shear stress and the principal strain are highly dependent on the mesh density. A threshold of discrepancy less than 10% is set for the two outcome measures. The final test results reveal a model with approximately 1.34 million elements is required to achieve mesh convergence. A CPU with 6 cores and a RAM of 120 GB is required to complete a single run, within 12–20 h per simulation.

**Table 1** Geometrical dimensions adopted for the construction of the ONH

Input factor	mm	Source
Scleral thickness at canal	0.50	[8]
Retinal thickness	0.20	[8]
LC thickness at axis	0.30	[8]
Peripapillary rim height	0.30	[8]
Cup depth	0.33	[8]
Optic disc diameter	1.84	[11]



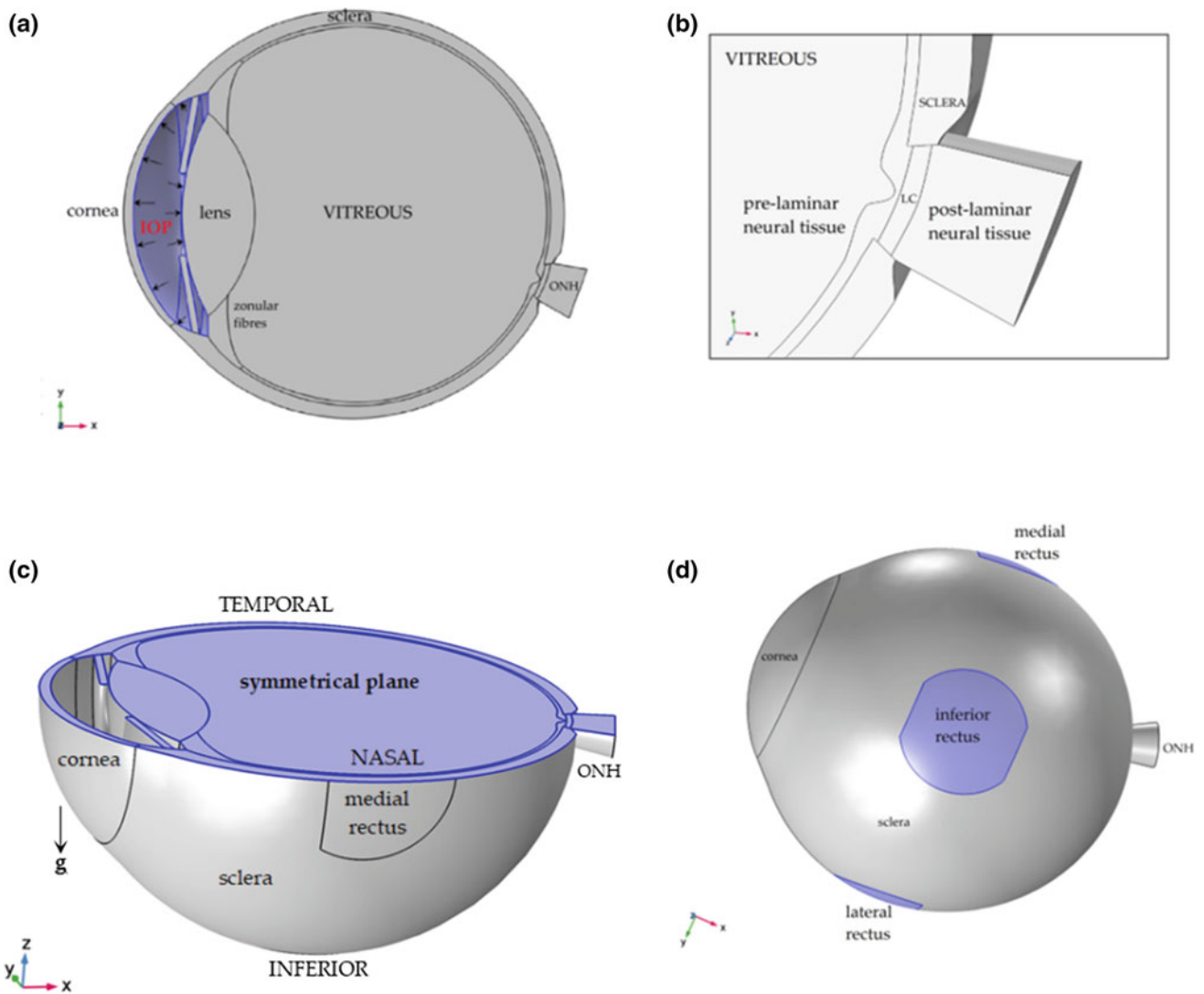


**Fig. 1** **a** The 3D eye model with the incorporated ONH; **b** Inset shows the constituent tissues of the ONH; **c** Symmetrical boundary condition applied on the model (shaded in blue); and **d** Prescribed displacement on the sclera-ocular muscle interfaces (shaded in blue) (Colour figure online)

**Table 2** Material properties for each component of the eye model adopted from past literatures

Ocular tissues	Young’s modulus, $E$ (MPa)	Bulk modulus, $K$ (GPa)	Shear modulus, $G$ (Pa)	Poisson’s ratio, $\nu$	Source
Cornea	$0.1512e^{28.0e}$			0.49	[8, 12]
Sclera	$0.7524e^{41.8e}$			0.47	[8, 13]
LC	$0.08855e^{11.5e}$			0.49	[8, 12]
Pre-LNT	0.03			0.40	[8]
Post-LNT	0.03			0.49	[8]
Iris	0.0861			0.49	[8, 14]
Lens	1.45			0.47	[12, 15]
Zonular fibres	5			0.45	[12, 16]
Vitreous		2	10		[15]

Abbreviations: *Pre-LNT* pre-laminar neural tissue; *Post-LNT* post-laminar neural tissue

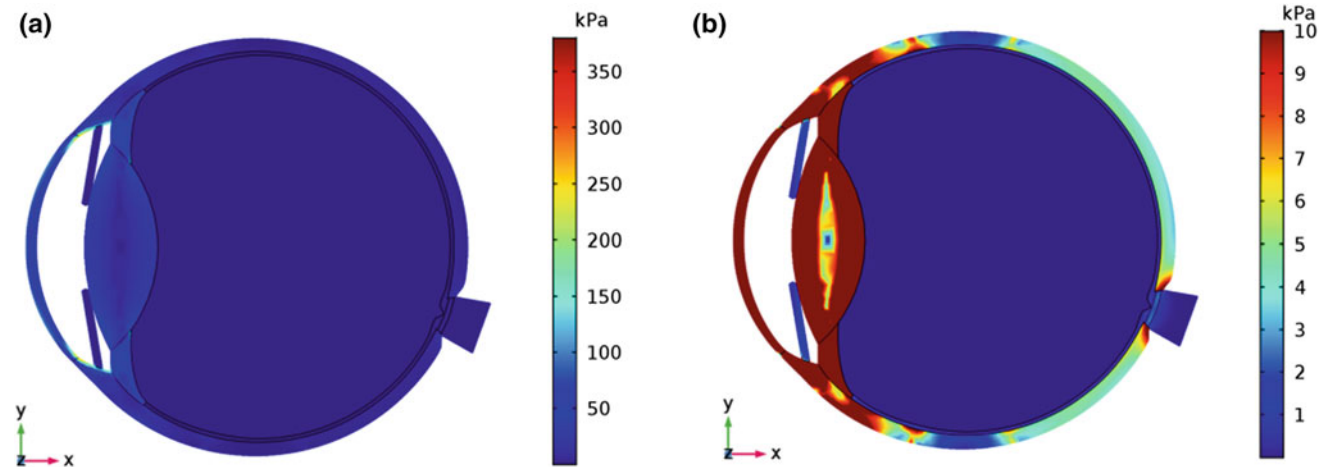


**Fig. 2** Tresca shear stress **a** plotted on the transverse plane of the eye model; and **b** re-plotted with the color bar capped at 10 kPa for better visualization of the in-wall hoop stress transfer

**Table 3** Posterior displacement of the LC and the corresponding Tresca shear stress for model CCT560 at  $P_{\text{elev}} = 50$  mmHg

Outcome measures	Max	Min	Mean
Total displacement, $\mu\text{m}$	77.13	68.48	74.53
Tresca shear stress, kPa	2.78	0.91	2.14

**Table 4** Mean Tresca shear stress borne within the corneo-scleral shell for each model at  $P_{\text{elev}} = 50$  mmHg

Model	Mean Tresca shear stress, kPa		
	Cornea	Sclera	LC
CCT380	79.28	8.14	2.18
CCT560	67.88	8.02	2.14
CCT740	55.67	7.88	2.10

### 3 Results and Discussion

Tresca shear stress, which is deemed to cause the damage of the ONH, is chosen as the principal outcome measure of the model [6]. The peak value is taken at 95th percentile to avoid potential numerical errors [8]. The total displacement of the LC, a surrogate indicator of the optic nerve damage, is examined.

#### 3.1 Generic Model

A generic model is constructed, with a CCT of 560  $\mu\text{m}$  (hereafter described as Model CCT560) to examine the validity of the eye model. Simulation is run at an input  $P_{\text{elev}}$  of 50 mmHg. Figure 2a depicts the Tresca shear stress borne within the ocular tissues. The numerical results show that the cornea bears the highest stress among the domains in the model, with a value up to 350 kPa. This may be due to its

vicinity to the source of pressure load. The results are re-plotted to better visualize the stress distribution across the eye model, where the color bar is capped at 10 kPa, as depicted in Fig. 2b. It could be observed that the stress is transferred from the cornea to the sclera shell, concentrated at the scleral canal and finally reaches the LC. This is in agreement with many of the past studies that suggest an IOP-induced in-wall hoop stress that is transmitted from the anterior to the posterior segment across the eye globe.

The transferred hoop stress together with the hydraulic pressure exerted by the vitreous onto the pre-laminar neural tissue cause the LC to displace posteriorly. The maximum, mean and minimum displacements of the LC are examined and tabulated in Table 3. The corresponding Tresca shear stress borne within the LC is recorded as well. From the results, the posterior displacement of the LC is predicted in the range approximately from 68 to 78  $\mu\text{m}$ . This result is very close to that reported in the clinical study carried out by Yan et al., which recorded a posterior displacement of the LC at 79  $\mu\text{m}$  with an increase of IOP at 50 mmHg [17].

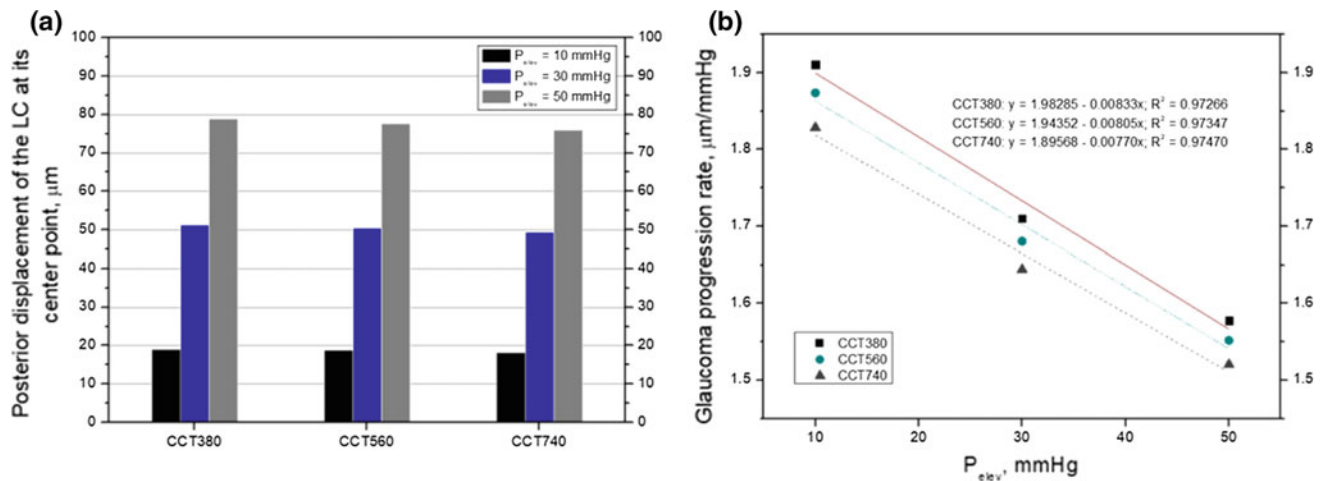


**Fig. 3** With an increasing input value of  $P_{\text{elev}}$  for all models, the predicted numerical results are plotted for **a** the posterior displacement of the LC at its center point; and **b** the estimated glaucoma progression rate

Hence, the numerical results suggest that the eye model of the present study is capable of capturing the IOP-imposed LC displacement.

### 3.2 The Effects of CCT on Glaucomatous Posterior Displacement of the LC

To investigate the influence of CCT towards optic nerve damage, two additional models with different values of CCT are constructed. The models are hereafter named CCT380 and CCT740; correspond to a model with a CCT of 380 and 740  $\mu\text{m}$ . Again, each model is applied with an increase in IOP,  $P_{\text{elev}}$  of 50 mmHg to simulate a glaucomatous condition. The in-wall hoop stress transferred from the cornea to the LC is examined for all models. Table 4 tabulates the predicted mean Tresca shear stress across the corneo-scleral shell structures, namely the cornea, the sclera and the LC.

From Table 4, Model CCT380 has the highest Tresca shear stress borne within the cornea, the sclera and the LC. This suggests that a lower CCT may lead to a greater rate of optic nerve damage. Simulations are repeated for all three models with an input  $P_{\text{elev}}$  at 10 and 30 mmHg to simulate the progression of optic nerve damage from early to end stage. The posterior displacement of the LC at its center point is recorded, as plotted in Fig. 3a. It is observed that Model CCT380 demonstrates the greatest posterior displacement of the LC at its center point, for all values of  $P_{\text{elev}}$ . The numerical results supports the clinical trend that reports greater glaucoma progression rates for the patients with lower CCTs [3, 4].

To further investigate the effects of CCT on glaucoma progression, the progression rate defined by unit posterior

displacement per unit increase of  $P_{\text{elev}}$ , are calculated. Figure 3b depicts the results. The highest progression rate is found in Model CCT380, with a progression rate up to approximately 1.91  $\mu\text{m}/\text{mmHg}$ . It could be observed that CCT is inversely correlated to glaucoma progression rate. This predicted result again supports the clinical trend, in which lower CCT may cause greater glaucomatous optic nerve damage [3, 4].

## 4 Conclusion

A 3D eye model is developed, aims to investigate the effects of CCT on glaucomatous optic nerve damage in a human eye. The in silico results suggest that a lower CCT may lead to a higher progression rate in glaucomatous optic neuropathy. In contrast, a thicker cornea has a stronger structure that may assist in maintaining the structural stability of the eye globe, hence less IOP-imposed damage to the optic nerve bundles. The results are in agreement with the present clinical trend, which reports lower CCTs recorded among glaucoma patients [3, 4]. Nevertheless, the results obtained indicate low influential rate of the CCT towards the estimated damage of the optic nerve. This suggests that CCT may not be the dominant factor in glaucomatous neuropathy.

**Acknowledgements** This project is supported by the Ministry of Education Malaysia through the Fundamental Research Grant Scheme under the project FRGS/2/2014/SG02/MUSM/02/1.

**Conflict of Interest** None declared.

## References

1. Burgoyne, C.F., Downs, J.C., Bellezza, A.J., Suh, J.-K.F., Hart, R. T.: The optic nerve head as a biomechanical structure: a new paradigm for understanding the role of IOP-related stress and strain in the pathophysiology of glaucomatous optic nerve head damage: *Progress in Retinal and Eye Research* 24, 39–73 (2005).
2. Downs, J.C., Roberts, M.D., Burgoyne, C.F.: Mechanical environment of the optic nerve head in glaucoma: *Ophthalmol. Vis. Sci.* 85, E425–E435 (2008).
3. Sng, C.C.A., Ang, M., Barton, K.: Central corneal thickness in glaucoma: *Current Opinion in Ophthalmology* 28(2), 120–126 (2017).
4. Lester, M., Telani, S., Frezzottie, P.: Differences in central corneal thickness between paired eyes and the severity of the glaucomatous damage: *Eye (Lond)* 26, 1424–1430 (2012).
5. Sigal, I.A.: Interactions between geometry and mechanical properties on the optic nerve head: *Ophthalmol. Vis. Sci.* 50, 2785–2795 (2009).
6. Ko, M.W.L.: Effect of corneal, scleral and lamina cribrosa elasticity, and intraocular pressure on optic nerve damages: *JSM Ophthalmology* 3(1), 1024 (2015).
7. Sigal, I.A., Flanagan, J., Tertinegg, I., Ethier, C.R.: Finite element modeling of optic nerve head biomechanics: *Ophthalmol. Vis. Sci.*, 45, 4378–4387 (2004).
8. Sigal, I.A., Flanagan, J., Ethier, C.R.: Factors influencing optic nerve head biomechanics: *Ophthalmol. Vis. Sci.*, 46, 4189–4199 (2005).
9. Ooi, E.H., Ng, E.Y.K.: Simulation of aqueous humor hydrodynamics in human eye heat transfer. *Computers in Biology and Medicine* 38(2), 252–262 (2008).
10. Murgatroyd, H., B.J.: Intraocular pressure: *Continuing Education in Anaesthesia, Critical Care & Pain* 8(3) (2008).
11. Sing, T., Noelani, M., Anderson, F., Sheila, Townsend, C., John: The normal optic nerve head: *Optometry and Vision Science* 77(6), 293–301 (2000).
12. Woo, S.L-Y., Kobayashi, A.S., Schlegel, W.A., Lawrence, C.: Nonlinear material properties of intact cornea and sclera: *Experimental Eye Research* 214, 29–39 (1972).
13. Salimi, S., Park, S.S., Freiheit, T.: Dynamic response of intraocular pressure and biomechanical effects of the eye considering fluid-structure interaction: *Journal of Biomechanical Engineering* 133/091009–1 (2011).
14. Zhang, K., Qian, X., Mei, X., Liu, Z.: An inverse method to determine the mechanical properties of the iris in vivo: *Biomedical Engineering Online* 13, 66 (2014).
15. Karimi, A., Rzaghi, R., Navidbakhsh, M., Sera, T., Kudo, S.: Quantifying the injury of the human eye components due to tennis ball impact using a computational fluid-structure interaction: *Sports Engineering* 19, 105–115 (2016).
16. Watson, R., Gray, W., Sponset, W.E., Lund, B.J., Glickman, R.D., Groth, S.L., Reilly, M.A.: Simulations of porcine eye exposure to primary blast insult: *TVST* 4(4), 8 (2015).
17. Yan, D.B., Coloma, F.M., Metheetraitut, A., Trope, G.E., Heathcote, J.G., Ethier, C.R.: Deformation of the lamina cribrosa by elevated intraocular pressure: *British Journal of Ophthalmology* 78(8), 643–648 (1994).

# Computer Simulation in the Analysis of Computed Tomography Exam Times

Rogério Santos, Andrei Pires, Wagner Pereira, and Renan Almeida

## Abstract

Computed Tomography (CT) is one of the most important tools in diagnostic imaging. In Brazil, among medical imaging devices, 4.7% were CTs, representing eighth place in exam numbers and first in costs. The aim of this study was to evaluate the effect of faster CT equipment on total exam time (from patient arrival to departure). To this end, exams were divided into six steps: patient arrival, patient movement in the examination room, patient positioning, data entry, image acquisition and patient exit. Step duration was measured on 84 exams with 1, 4 and 128-slices CTs in 5 private clinics/hospitals, in 2014/2015. Models were created in the MedModel<sup>®</sup> software and thirty days were simulated for a hospital operating 24 h/day. Scenarios were simulated for three types of CTs using the average times obtained from the exams. In the model, except for the acquisition stage, the times from each step were the same for all CT types. Simulations showed that, for example, a single slice CT running inpatient examinations at night (8:00 PM–7:00 AM) and adding another dressing room could decrease total exam time by approximately 33%; while replacement of a single slice CT by a 4 slices model (more expensive) would result in a much smaller overall time reduction. In conclusion, productivity gains may be smaller than expected when replacing simpler models by more sophisticated ones, and patient care time is not only a function of the speed of data

acquisition, and organizational changes can produce decreases in these times.

## Keywords

Discrete event simulation • Scheduling • Computed Tomography

## 1 Introduction

Computed Tomography (CT) is one of the most important diagnostic tools in medicine, with wide scope for clinical use [1]. CTs' diagnostic capability increased while examination times and radiation doses diminished. In 2009, Brazil had 15.6 CT scanners per million people, a density comparable to Canada (14.2) and New Zealand (15.8). However, Brazil's southeastern region had 21.8 CTs per million people, more than Luxembourg (19.7); and its northeastern region had 8.1 CTs per million people, fewer than Tunisia (9.3). Of all medical imaging devices in Brazil in 2009, 4.7% were CTs, ranking eighth in the number of installed devices [2–4]. In the US, the percentage of patients using CTs in emergency departments increased from 2.4% in 1992 to 13.9% in 2007 and, only 0.7% of patients in these departments used magnetic resonance imaging [5, 6], underscoring the importance of CT availability.

However, even in the cities where CTs are more available, large queues in public services are common, sometimes extending into months of waiting. Hence, increasing productivity also means increasing the availability and number of patients in the public services; as well as profitability in the private ones. Thus, one can see the importance of studying these processes, since performance gains may not produce productivity increases if stages of the process do not change [7].

Computer simulation is as an important tool to study the behavior of computed tomography sectors. It has been applied successfully in decision making in many areas, and,

---

R. Santos (✉)  
CEFET “CSF” - RJ, Rio de Janeiro, RJ, Brazil  
e-mail: rogeriopires1@uol.com.br

R. Santos · A. Pires · W. Pereira · R. Almeida  
Programa de Engenharia Biomédica, COPPE/UFRI, Rio de Janeiro, RJ, Brazil  
e-mail: andreilenine@uol.com.br

W. Pereira  
e-mail: wcap58@gmail.com

R. Almeida  
e-mail: renan.m.v.r.almeida@gmail.com



in the health sector [8, 9], allowed for the optimization of physical, financial and human resources in many hospital settings [10, 11]. Therefore, the objective of the present study was to simulate simple and inexpensive scenarios that could decrease the CTs patients' care time or increase the productivity in a general hospital.

## 2 Materials and Methods

### 2.1 Studied Devices

To provide a broad overview of the equipment, and considering that even single-slice models are still used in many countries [5], models with 1, 4 and 128 slices were studied. Therefore, a convenience sample of five devices, from brands A (1, 4-slice) and B (128-slice), in five private health facilities located in four cities of the state of Rio de Janeiro, Brazil (one specialized radiology clinic, one general medicine clinic and three general hospitals). Three single-slice CTs were studied, one manufactured in 2003 and two devices in 2009. The 4-slice model was manufactured in 2005 and the 128-slice model in 2014. All studied technologies are used in Brazil and remain in production in several countries [6, 7]; and all studied equipment are still in use.

### 2.2 Measurements

Exam procedures were divided into: 1. Patient entrance to the examination room; 2. Patient changing clothes; 3. Patient positioning; 4. Patient's data input into the CT's computer; 5. Image acquisition; and 6. Patient departure.

Two researchers measured the times using a stopwatch application with a precision of one hundredth of a second. Values were rounded, resulting in measured times in minutes and seconds. So it was converted to the decimal mode to use in MedModel<sup>®</sup> software. Exam procedures have not changed since their collection.

### 2.3 The Simulation

Models were created in the MedModel<sup>®</sup> software using as parameters:

- **Locations:** In/Out, Waiting room (capacity: 10 patients), Dressing room (one or two), CT Scanner e Console;
- **Entities:** Patients (scheduled, emergency and scheduled with radio-contrast);
- **Arrival cycles:** thirty scheduled patients without radio-contrast, seventeen emergency patients (24 h

non-scheduled) and five scheduled patients using radio-contrast per day;

- **Resources:** Operator and Nurse; and
- **Process times:** 1. Patient entrance to the examination room ( $6.47e-002 + L(0.62, 0.82)$ ), using one resource; 2. Patient clothes change ( $0.13 + E(1.04)$ ); 3. Patient positioning at the CT scanner ( $1.13e-002 + L(1.13, 0.62)$ ) using one resource; 4. Patient's data input into the CT computer ( $-1.21 + L(2.27, 0.48)$ ) using one resource; 5. Image acquisition: single-slice ( $1.4 + E(1.95)$ ), 4-slice ( $0.13 + L(1.75, 0.55)$ ) and 128-slice ( $0.37 + E(0.60)$ ) using one resource; and 6. Patient departure ( $-0.11 + L(2.08, 1.4)$ ).

Above, "L" and "E" are the Lognormal and Exponential probability distributions, and times are reported as "minimum + L((Mean - minimum), SD)" and "minimum + E (SD)"; all times in decimal minutes.

For exams using radio-contrast, two more data acquisition (with the same duration of the first) and venous access placement/remove are needed; these processes use one resource each. Priority of care was defined as higher for emergency patients.

Five scenarios were created and studied for the three CT technologies:

- **Scenario 1:** The default: one operator, one dressing room and scheduling patients from 7:00 AM to 8:00 PM;
- **Scenario 2:** Adding 24 h scheduling to the default model;
- **Scenario 3:** The default model with 2 dressing rooms;
- **Scenario 4:** Adding 24 h scheduling to the third model;
- **Scenario 5:** Adding a nurse to the fourth model.

The simulation focused on patients' mean time in the system, from arrival to departure. One month of a CT sector operation located inside a fictitious hospital was simulated; operating 24 h/day. Average exam times were based on the weighted average of the number of monthly exams for each patient type (840 exams without venous contrast, 140 with contrast and 476 non-scheduled emergency exams).

## 3 Results

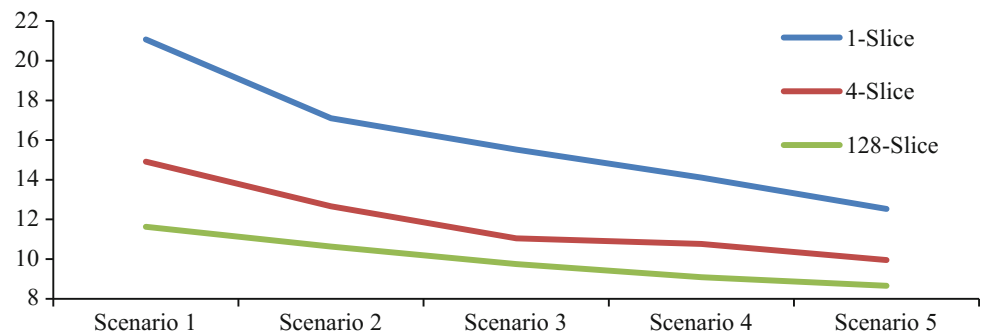
Table 1 shows the patients' mean time in the system for the three CT technologies studied in five simulated scenarios. Figure 1 shows the weighted average times for each CT model in the five proposed scenarios.

Introducing exams between 8:00 PM and 7:00 AM produces a decrease in the system mean time of 18.84%, 15.09% and 8.60%, for single, 4 and 128 slice CTs, respectively. The addition of another dressing room reduced

**Table 1** Patients mean time in the system for the three CT types in five simulated scenarios. Weighted average times for each CT model in five scenarios. Scenario 1: Default: 1 operator, 1 dressing room and scheduling from 7:00 AM to 8:00 PM. Scenario 2: Adding 24 h scheduling to the default. Scenario 3: Default with 2 dressing rooms. Scenario 4: 24 h scheduling and 2 dressing rooms. Scenario 5: Adding a nurse to the fourth model. Time in decimal minutes

	Scenario 1	Scenario 2	Scenario 3	Scenario 4	Scenario 5
<b>1-Slice</b>					
No Contrast	21.16	16.35	14.99	13.11	11.73
Emergency	17.56	15.40	13.39	12.64	11.46
Contrast	32.44	27.44	25.99	25.14	21.02
<b>4-Slice</b>					
No Contrast	14.82	12.18	10.51	10.12	9.16
Emergency	12.48	11.44	9.74	9.57	9.50
Contrast	23.72	19.68	18.77	18.64	16.20
<b>128-Slice</b>					
No Contrast	11.30	10.01	9.30	8.53	8.14
Emergency	10.14	9.79	8.66	8.19	8.07
Contrast	18.64	17.18	16.17	15.49	13.72
<b>Weighted</b>					
<b>1-Slice</b>	21.07	17.10	15.52	14.11	12.53
<b>4-Slice</b>	14.91	12.66	11.05	10.76	9.95
<b>128-Slice</b>	11.63	10.63	9.75	9.09	8.65

**Fig. 1** Weighted average times (in decimal minutes) for each CT model in five scenarios



these times in 26.34%, 25.89% and 16.17%, while the combination of the two strategies generated a decrease of 33.03%, 27.83% and 21.84%, respectively. Finally, the models with two dressing rooms, night scheduling and one nurse implied in a decrease of 40.53, 33.27 and 25.62% for the three TC technologies studied.

## 4 Discussion

The aim of this study was to simulate and compare scenarios that could reduce the average system time for patients using hospital CT services. Since our focus was specifically on equipment productivity, cost and image quality were not included here. However, it is known that 1 mm slice resolution (used in studied models) can still yield a degree of detail sufficient for many clinical applications [7].

As mentioned, medical equipment productivity is important for both private and public health services, in which waiting lists sometimes may extend for months. Faster exams can represent more exams/time, but the idea that doubling the number of CT slices per unit of time could reduce to half the system time (a linear decrease) is not realistic, since exam times are not exclusively dependent to the image acquisition/reconstruction time [7, 12].

In fact, this study indicates that the CT exam duration do not proportionally decrease by using models with “more slices”. For instance, exchanging a single-slice for a 128-slice model implies in a decrease in system time of 45%. These results draw attention to the importance of process optimization as whole, if larger productivity gains are desired. Similarly, it could be seen that adding another dressing room and introducing night scheduling for the single-slice device allowed an average time in the system

smaller than that of a 4-slice. Thus, changing patient scheduling strategy can greatly reduce patient waiting times and increase productivity, and, considering that no new resources are needed (both operator and equipment are already available) night scheduling is an especially interesting option. Finally, hiring a nurse would reduce the time of patient care even more, but, in this case, the costs thus incurred would have to be taken into account for the analysis.

It must be noted that a CT sector with a single-slice CT with 24 h of scheduling, two dressing rooms and one nurse would have an average service time (12.53 min) lower than a default sector with a 4-slice (14.91 min) or slightly larger than a default sector with a 128-slice (11.63 min). This result should be contrasted with the investment for the replacement of a single-slice CT by another 128-slice CT, which can easily surpass US\$ 500,000.00.

## 5 Conclusion

This study shows that productivity gains may be smaller than expected when replacing simpler CT models with more “sophisticated” ones, and patient care time is not only a function of the speed of data acquisition, since organizational changes can produce considerable decreases in these times. Thus, increases in productivity due to the number of CT slices are not linear, and without organizational changes, a large productivity increase cannot be expected from changes to “faster” models. CT equipment acquisition should consider variables such as the number and types of exams; keeping in mind that, in this context, “more” is not necessarily “better” [7].

**Conflict of Interest Statement** The authors declare that they have no conflict of interest.

## References

1. Seeram, E. *Computed tomography: physical principles, clinical applications, and quality control*. 4th ed. St Louis, MO: Elsevier Health Sciences. 2015.
2. Instituto Brasileiro de Geografia e Estatística (IBGE). *Estatísticas da Saúde - Assistência Médico-Sanitária-2009*. Rio de Janeiro: IBGE. 2009. Portuguese.
3. World Health Organization (WHO). 2011. Density of computed tomography units. [Cited 2016 Aug 14]. Available from <http://tinyurl.com/j33eh9a>.
4. Organization for Economic Co-operation and Development (OECD), 2011. [Cited 2016 Aug 14]. Available from <http://www.oecd-ilibrary.org/>.
5. Ginde, A.A., Foianini, A., Renner, D.M., Valley, M., Camargo, Jr, C.A. Availability and quality of computed tomography and magnetic resonance imaging equipment in US emergency departments. *Academic emergency medicine*. 2008; 15(8), 780–783.
6. Niska, R., Bhuiya, F., Xu, J. National hospital ambulatory medical care survey: 2007 emergency department summary. *Natl Health Stat Report*. 2010; 26(26), 1–31.
7. Santos, R.P., Pires, A.L.A., Pereira, W.C.A., Almeida, R.M.V.R. (2017) “Computed Tomography Scanner Productivity and Entry-Level Models in the Global Market.” *Journal of healthcare engineering*.— vol. 2017, Article ID 1304960, 5 pages. <https://doi.org/10.1155/2017/1304960>.
8. Jacobson, S.H., Hall, S.N., Swisher, J.R. (2006), “Discrete-Event Simulation of Health Care Systems”. In: *Int Series in Operations Research & Management Science*. v.91 p. 211–52.
9. Ferreira, R.B., Coelli, F.C., Almeida, R.M.V.R, Pereira, W.C.A. (2008) “Optimizing patient flow in a large hospital surgical centre”, In: *Journal of Evaluation in Clinical Practice*, v. 14, p. 1031–1037.
10. Villamizar, J.R., Coelli, F.C., Pereira, W.C.A., Almeida, R.M.V.R. (2011) “Discrete-event computer simulation methods in the optimization of a physiotherapy clinic”. *Physiotherapy* v. 97, 71–77.
11. Coelli, F.C., Almeida, R.M.V.R., Pereira, W.C.A. (2010) “A cost simulation for mammography examinations taking into account equipment failures and resource utilization characteristics”, In: *Journal of Evaluation in Clinical Practice* v.16, p. 1198–1202.
12. Jhaveri, K.S., Saini, S., Levine, L.A., Piazzo, D.J., Doncaster, R.J., Halpern, E.F. et al. Effect of multislice CT technology on scanner productivity. *American Journal of Roentgenology*. 2001; 177(4), 769–772.

# Genetic Algorithms Applied to Estimate 6-Parameters Model Which Define Analytical Function to Simulate the Motor Unity Force from Experimental Measures

J. P. Bermeo, F. Sanchez, J. Bravo, L. Bueno, J. D. Jara, and R. Rodas

## Abstract

An individual twitch of motor unity MU force can be simulated by 6-parameters model, then a train of repeated pulses evokes a tetanic contraction. However, is a hard issue to estimate the parameters for one twitch, and the way to put many of them, such that can reproduce a shape tailored a muscle contraction generated by a set of stimulation pulses. In this work, genetic algorithms are applied to estimate nine parameters from experimental measures, where six are used to define a 6-parameters model, and the other three are used to generate a train of pulses, which simulate muscle contraction. The measured data by dynamometer were used with genetic algorithms to estimate the nine parameters, after that, their information was compared with data measured by electromyograph. The results show that calculated parameters, like as latency time, contraction time, repetition time, half contraction, intermediate time of relaxation force and number of pulses, can be applied to generate a set of successive twitches to simulate the muscle contraction, with an error less than 5%. Besides, the simulation results prove that force level depends directly on repetition frequency, number of pulses and amplitude of stimulation signal. finally, in this work the genetic algorithms worked like an excellent tool to optimize and validate a theoretical model with the experimental data, a despite the process last more than 40 h for each training, the method was friendly to apply and to reconfigure many options before to find the best solution.

## Keywords

Genetic algorithms • Motor unity • 6-parameters model  
Electromyograph • Optimization

J. P. Bermeo (✉) · F. Sanchez · J. Bravo · L. Bueno · J. D. Jara  
R. Rodas  
Universidad Politécnica Salesiana, Cuenca, 010105, Ecuador  
e-mail: jbermeo@ups.edu.ec

## 1 Introduction

### 1.1 Muscle's Anatomy and Physiology

Human body has 650 muscles, and all of them are commanded by the Central Nervous System (CNS). According to the neural signal which activates it, muscles can be classified as *voluntary muscle* when the activation route is the pyramidal system by motor axons; or *involuntary muscle* when the activation route is by parasympathetic nervous system [1]. The force generated by muscles depends on the next factors:

- Activation degree: CNS make the recruit of fibers, according al model claimed by [2]
- Stimulation frequency or temporary sum: one stimulus has a muscle response called twitch, while repeated stimuli cause an increase in strength, so muscle strength also depends on how often the stimulus is repeated [3]
- Shortening speed—is the speed with muscles contract against a stimulus, speed is around 15 mm/s for slow fibers and 45 mm/s for fast fibers [4].
- Initial muscle length at rest.
- Cross-sectional area of muscle [5].

### 1.2 Force of Contraction and 6 Parameters Model

Force contraction depends on summation of individual twitches. There are many models for twitch's simulation. The Fig. 1 shows a comparison between two models and an experimental measure of force for single stimulus [6], for this work, the force is simulated using the summation of twitches, where a six parameters model is applied to simulate one twitch.

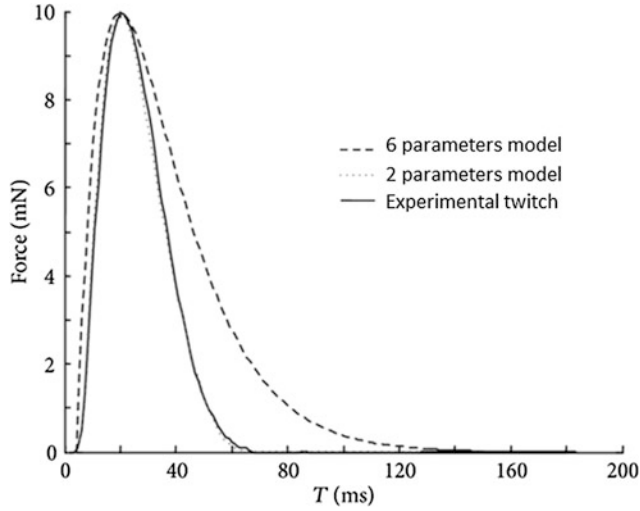


**Fig. 1** Comparison between models and experimental force for one twitch [6]

The six parameters model [7] define the muscle force generated by the  $i$ th stimulus through the following equation:

$$F^i(t) = \frac{f_1(t)}{f_2(t)} \quad (1)$$

where:

$$f_1(t) = F_0 \left[ P1^{c1} e^{(c1-c1 \cdot P1(t))} + (P2 - 1) P1^{c2} e^{(c2-c2 \cdot P1(t))} \right] \quad (2)$$

$$f_2(t) = P2 \cdot (1 - e^{4eP3}) \quad (3)$$

$$P1(t) = \frac{t - T_i - T_{lead}}{T_c} \quad (4)$$

$$P2(t) = 1 + e^{2e(P1(t)-1)} \quad (5)$$

$$P3(t) = \frac{t - T_i - 0.5(T_{tot} + T_{hr})}{T_{tot} - T_{hr}} \quad (6)$$

$$c1 = \frac{\ln(2)T_c}{T_{hc} + T_c \cdot \left[ \ln\left(\frac{T_c}{T_{hc}}\right) - 1 \right]} \quad (7)$$

$$c2 = \frac{\ln(2)T_c}{T_{hr} + T_c \cdot \left[ \ln\left(\frac{T_c}{T_{hr}}\right) - 1 \right]} \quad (8)$$

The  $c1$ ,  $c2$ ,  $P1(t)$ ,  $P2(t)$  and  $P3(t)$  are auxiliary variables to reduce the main equation, and the six parameters used in equations are defined such as  $T_{lead}$ : latency time to start de contraction;  $T_c$ : contraction time until get the maximum force;  $T_{hc}$ : half of contraction time;  $T_{hr}$ : half time relax;

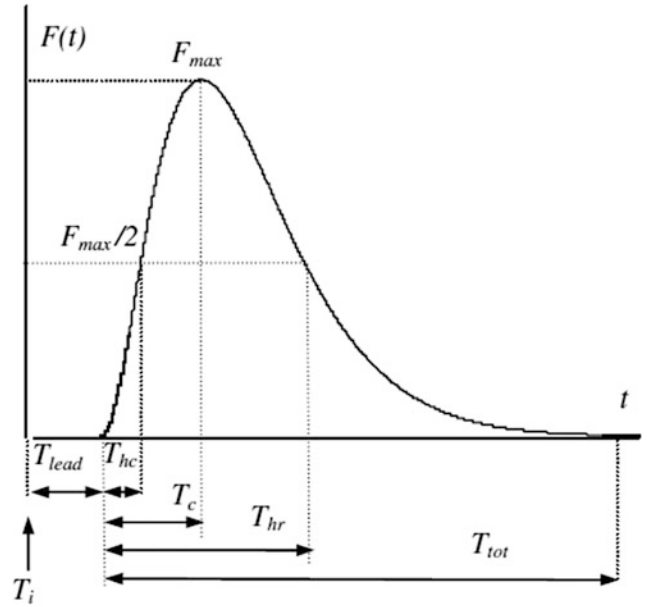


**Fig. 2** Analytical function to six parameters model [7]

$T_{tot}$ : total contraction time and  $F_{max}$ : maximum force. In the Fig. 2 is showed each parameter to simulate the force for one twitch.

## 2 Measurement and Optimization by Genetic Algorithms

### 2.1 Measurement of Muscle Force

Muscle force was measured by dynamometer of equipment of Biomedical Engineering Group of Salesian Polytechnic University. Eleven tests were done, nine short pulses and two large pulses, in Fig. 3 four short pulses are showed. Every pulse was simulated like as summation of elements defined in Eq. (1), to obtain the total force showed in the Eq. (9)

$$F_T(t) = \sum_{i=1}^N F^i(t) \quad (9)$$

### 2.2 Optimization by Genetic Algorithms

Genetic algorithms have many application like as find the best route to supply chain [8], for this work, Genetic Algorithms are used to optimize the analytic function.

Genetic Algorithms GA is applied to calculate repetition time ( $R_{time}$ ), number of pulses, resolution and the six parameters ( $T_{lead}$ ,  $T_{hc}$ ,  $T_c$ ,  $T_{hr}$ ,  $T_{tot}$  and  $T_i$  showed in Fig. 2)



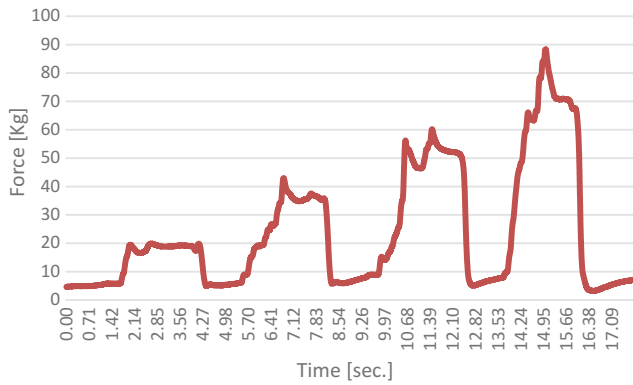


Fig. 3 Four pulses measured by dynamometer to simulation

to model the muscle force, the Table 1 shows the calculated parameters for each pulse by GA, the parameters were estimated (optimized) to get the minimal RMS error between simulation of six parameters model and the experimental measures. The stopping criteria applied was the average change in RMS error (fitness function) lower to  $1e-6$ , furthermore that parameters must meet with constraints like as  $T_{hc} < T_c$  and others.

With the tabulated information, basic statistics were estimated like as mean, standard deviation and confidence intervals of 99%, the results obtained are within the statistics reported by previous works [9].

Table 1 Calculated parameters by genetic algorithms

Pulse number	T_lead [s]	T_c [s]	T_hc [s]	T_hr [s]	T_tot [s]	R_time [s]	Number of pulses
P01	0.0022	0.0493	0.0206	0.1500	0.2727	0.0423	62
P02	0.0025	0.0464	0.0298	0.1480	0.2750	0.0511	52
P03	0.0049	0.0523	0.0351	0.1483	0.2710	0.0478	51
P04	0.0040	0.0476	0.0411	0.1407	0.2713	0.0282	79
P05	0.0035	0.0465	0.0420	0.1487	0.2803	0.0270	99
P06	0.0034	0.0480	0.0410	0.1173	0.2861	0.0312	80
P07	0.0024	0.0475	0.0197	0.1204	0.2572	0.0331	66
P08	0.0034	0.0506	0.0342	0.1170	0.2525	0.0231	91
P09	0.0046	0.0709	0.0333	0.1499	0.2176	0.0275	74
P10	0.0040	0.0596	0.0370	0.1409	0.2815	0.0237	80
P11	0.0042	0.0498	0.0283	0.1491	0.2824	0.0287	108

Table 2 Calculated parameters by genetic algorithms

Pulse number	T_lead [ms]	T_c [ms]	T_hc [ms]	T_hr [ms]	T_tot [ms]	R_time [ms]
Average	3.54	51.69	32.92	139.11	267.95	33.06
Standard deviation	0.9	7.4	7.7	13.8	19.6	9.6
Confidence interval 99%	0.87	7.05	7.37	13.20	18.76	9.22

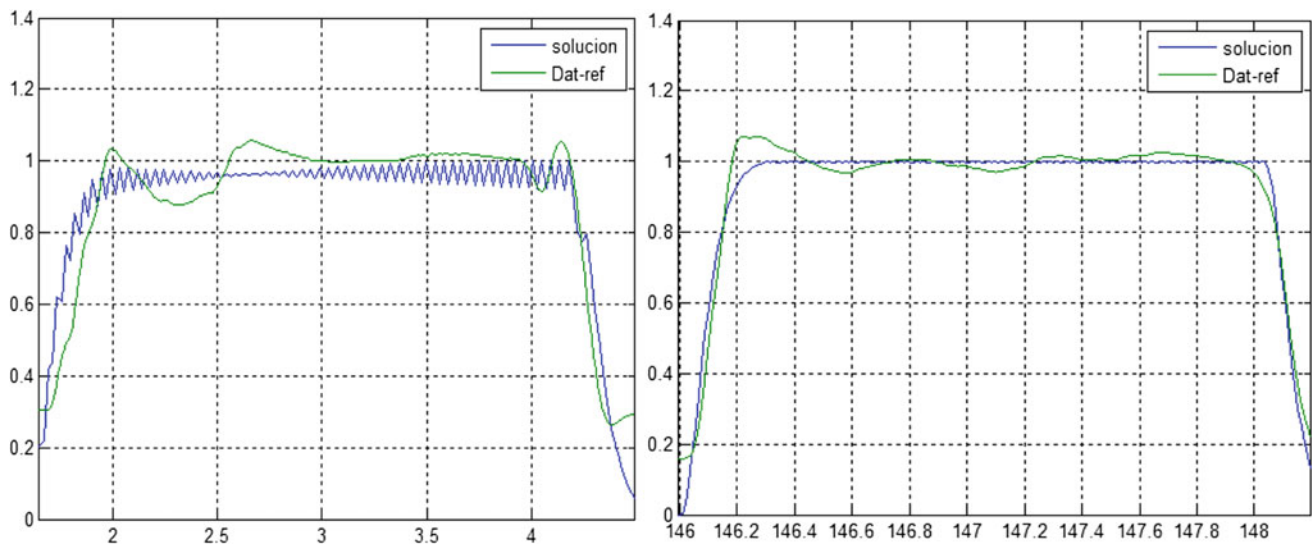


Fig. 4 Comparison between simulation with values optimized by GA and experimental measures from dynamometer

The basic statistics showed in Table 2, like as mean of latency time ( $T_{lead}$ ), contraction time ( $T_c$ ), half contraction time ( $T_{hc}$ ), half time relax ( $T_{hr}$ ) and total contraction time ( $T_{tot}$ ), values which correspond with those obtained by [10]. Figure 4 displays a comparison between simulation with values optimized by GA and experimental measures from dynamometer of pulses 1 and 10.

### 3 Conclusions and Future Works

#### 3.1 Conclusions

Given the need to validate the theoretical model with the experimental measurements, it was necessary to use an optimization method. For this reason, we analyzed the different optimization methods, which can be classified between classical or heuristic methods, being that the first seeks and guarantee an optimal solution and the others seek an “acceptably good” solution in an “acceptably fast” time, for our case of optimization of parameters from the theoretical model, GA was used.

With the aim to model the muscle response, two-parameter model [11] and the six-parameter model [7] were analyzed. Where the six-parameter model has better approximates the simulations with the experimental results, see Fig. 1. And GA was applied to optimize the parameters (such as repetition frequency,  $T_{lead}$ ,  $T_{hc}$ ,  $T_c$ ,  $T_{hr}$ ,  $T_{tot}$  and  $T_i$ ) from the experimental data, see Fig. 4 where the results obtained between the simulation and the experimental data are shown.

The parameters calculated by GA are shown in Table 1, to complete the analysis, the average, standard deviation and confidence interval were estimate; values obtained agree with the ranges reported by other studies from the analyzed bibliography.

#### 3.2 Future Works

From the results obtained from the modeling of force, the model of six parameters can be applied to evaluate the tensor associated to the muscular contraction, then with this tensor could be multiplied by the tensor of elastic deformation, to define the muscular behavior like as a continuous medium.

An electromyograph could be used to measure where the contraction started, to increase the precision of model for each stimulation and simulation.

**Conflict of Interest Statement** The authors have no conflict of interest.

### References

1. J. A. Kent-Braun y A. Ng., «Specific strength and voluntary muscle activation in young and elderly women and men.» *Journal of Applied Physiology*, vol. 87, n° 1, pp. 22–29, 1999.
2. E. Henneman, «Relation between size of neurons and their susceptibility to discharge.» *Science*, vol. 126, n° 12, pp. 1345–1347, 1957.
3. A. M. Ramirez Martínez y B. Calvo Calzada, Modelado y simulación del tejido músculo esquelético. Validación experimental con el músculo tibial anterior de rata, Zaragoza: Centro Politécnico Superior, Universidad de Zaragoza, 2011.
4. W. Gittings, J. Bunda y R. Vandenboom, «Shortening speed dependent force potentiation is attenuated but not eliminated in skeletal muscles without myosin phosphorylation.» *Journal of Muscle Research and Cell Motility*, vol. 38, n° 2, pp. 157–162, 2017.
5. M. Narici, G. S. Roi, L. Landoni, E. Minetti y P. Cerretelli, «Changes in force, cross-sectional area and neural activation during strength training and detraining of the human quadriceps.» *European Journal of Applied Physiology and Occupational Physiology*, vol. 59, n° 4, pp. 310–319, 1989.
6. Hindawi, «Hindawi Open Research.» 30 Agosto 2017. [En línea]. Available: <https://www.hindawi.com/journals/cmmm/2013/625427/fig1/>. [Último acceso: 30 agosto 2017].
7. R. Raikova, M. Pogrzebna, J. Celichowski y H. Aladjov, «Variability of successive contractions subtracted from unfused tetanus of fast and slow motor units.» *Journal of Electromyography and Kinesiology*, vol. 18, n° 5, pp. 741–751, 2008.
8. J. Bermeo, H. Castillo y S. Serrano, «Neural Networks and Genetic Algorithms Applied for Implementing the Management Model “triple A” in a Supply Chain. Case: Collection Centers of Raw Milk in the Azuay Province.» *MATEC Web of Conferences*, vol. 68, pp. 68–75, 2016.
9. D. Rodríguez, J. García, S. Sarmiento, Y. Saa, D. Vaamonde y M. E. Da Silva, «Assessment of muscle response as a control tool in the area of physical activity. health. and sports.» *Revista Andaluza de Medicina del Deporte*, vol. 5, n° 1, pp. 28–40, 2015.
10. O. García-García, A. Hernández Mendo, V. Serrano Gómez y V. Morales Sánchez, «Aplicación de la teoría generalizabilidad a un análisis de tensiomiografía en ciclistas profesionales de ruta.» *Revista de Psicología del Deporte*, vol. 22, n° 1, pp. 53–60, 2013.

# Quality Assurance in Medical 3D-Printing

Djim Kanters, Anke de Vries, Henk Boon, Joost Urbach, Arjen Becht, and Homme-Auke Kooistra

## Abstract

In the strive towards patient specific healthcare, medical 3D-printing has proven to be of great value. With the growing possibilities in applicability of these 3D-prints, quality control of the complete surgical 3D-printing workflow: (1) case selection, (2) image acquisition, (3) segmentation, (4) engineering, (5) 3D-printing and (6) preparation, has never been of more importance. The objective of this study was to provide a quality control methodology to assess the reproducibility, accuracy and stability of a medical 3D-printing workflow. With computer-aided-design (CAD) software a quality control (QC)-phantom was designed with dimensional characteristics based on commonly used surgical guides. Seven identical QC-phantoms were 3D-printed and labeled ( $n = 1, \dots, 7$ ). Their dimensional parameters were determined by physical measurements. Through comparison with the CAD-drawing, information was gained on the performance of the 3D-printer. The seventh phantom was scanned six times on a CT-scanner with a slice thickness of 0.4 mm. The 3D-segmented phantom was 3D-printed and its characteristics compared to the original. The other six phantoms ( $n = 1, \dots, 6$ ) underwent a number of sterilization cycles (3 min, 134 °C) corresponding with their label. The overall 3D-printer accuracy due to solely printing was found to be within 0.2 mm deviation with an average of 0.04 mm and a standard deviation of 0.06 mm. Image acquisition and segmentation induced shrinkage of the slots and holes. Thereby, a deviation of maximum 0.4 mm occurred compared to the original phantom, the average deviation was 0.06 mm with a standard deviation of 0.06 mm. Furthermore, within a cycle of six sterilizations ( $n = 1, \dots, 6$ ) the

accuracy and durability of the materials did not deteriorate. By design of this phantom, a method to implement overall QC of a medical 3D-printing workflow was developed. Execution of this method showed that the quality of the complete medical 3D-printing workflow can be assured and that it provides insight in the influences of each of the different steps in the workflow. In this study the strongest effect on the dimensional characteristics was observed in the image acquisition step.

## Keywords

3D-printing • Quality assurance • Phantom

## 1 Introduction

Three-dimensional printing (3D-printing) was first patented in 1986 by C.W. Hull [1]. In his patent Hull described a process he called stereolithography. In this process, 3D-objects are formed by a step by step process of locally curing thin layers of a specific medium by photopolymerization. By focusing a beam of light on the surface of the medium, cross-linking of the polymer chains within the medium occurs. With aid of a moveable platform, successive layers of the hardened medium build up the cross sections of a computer-aided design (CAD) drawing. Presently, dozens of different 3D-printing techniques co-exist, of which three main categories can be identified: (1) extrusion, (2) resin and (3) powder printing.

In recent years the development of relatively cheap desktop 3D-printers has led to a booming 3D-printing industry. Now, with the arrival of commercially available biocompatible and sterilizable 3D-prints, local medical 3D-printing labs emerge in hospitals worldwide [2]. Studies show that medical 3D-printing can be in many different ways of great added-value for all kind of specializations. Three main applications are defined: (1) anatomic models, (2) surgical guides, and (3) implants and prostheses [3].

D. Kanters (✉) · A. de Vries · H. Boon · J. Urbach · A. Becht  
H.-A. Kooistra  
Gelre ziekenhuizen, 7334 DZ Apeldoorn, The Netherlands  
e-mail: d.kanters@gelre.nl

- (1) The added-value of 3D-printed anatomical models is three-fold:
  - they provide a valuable tool for physicians in patient-doctor communication [4, 5];
  - they serve as a tool for resident education [6] and surgical training [7] and
  - they allow development for optimal surgical planning [8, 9]. Furthermore, the quality of the preoperative plans based on 3D-prints is shown to be higher than that of digital 3D-rendered images [10].
- (2) 3D-printed surgical guides are widely used in specializations as orthopedics, traumatology [11], oral and maxillofacial surgery [12], plastic surgery [13] and several other invasive surgical fields. Patient specific surgical guides offer a boost in surgical precision and reduction of surgical time, leading to lesser chance for infection and a faster recovery [14].
- (3) Development of implants and personalized prostheses is the most important and most valuable direction when applying 3D-printing in the field of orthopedics [15]. Several individual cases of 3D-printed cranial, dental and spinal implants have been reported.

With this rapidly growing new in-hospital technology, there's an urge and necessity for methods of quality control and quality assurance. Apart from a recent paper from Leng et al. [16], where a methodology is provided for quality control of the in-house 3D-printing workflow for unsterilized anatomical models, no literature on the quality control of the complete process, with all applicabilities is known. By providing guidelines for the workflow and by the design and exercise of a phantom study this paper gives a framework for the quality assurance methodology of this complete 3D-printing workflow.

## 2 Quality Assurance of Medical In-house 3D-Printing

In the 3D-printing workflow, several error inducing steps are bound to take place. These errors partly arise due to human factors such as miscommunication. For the other part, the induced errors are inherent to the workflow step. By optimizing the workflow and a proper definition of the responsibilities, the human errors can be minimized or completely taken away, whereas the inherent errors can only be minimized and monitored.

### 2.1 Qualitatively Induced Errors

Without a well defined 3D-printing workflow the quality of the 3D-printing process cannot be assured. The process

definition should at least include the workflow steps, definitions of the different stakeholders and the distribution of responsibilities.

**Process definition.** In general the 3D-printing workflow consists of six steps: (1) the selection of 3D-printing cases, (2) image acquisition, (3) segmentation, (4) engineering, (5) 3D-printing and (6) preparation for use.

Case selection (1) is based on the clinical value, cost-effectiveness and a risk assessment. The involved health-care professionals are the treating physician and a medical physicist. Image acquisition (2) lies within the responsibility of the radiologist and medical physicist. Segmentation (3) of the reconstructed images is a joint work between a technologist with anatomical knowledge, the requesting physician and a medical engineer. The output of this step is commonly a printable file format. The engineering step (4) is typically a task for the medical technologist. This step includes the development of molds or guides, the smoothing and the supporting of the printable. 3D-printing (5) requires technological and material knowledge and is therefore a task for the medical engineer. Lastly, in the preparation for use (6), the print is discomposed of its supports by a medical engineer, checked and validated by the requesting physician and if necessary sterilized at the central sterile service department (CSSD). For an overview of the process see Fig. 1.

### 2.2 Quantitatively Induced Errors

**Image acquisition and segmentation.** A critical step in each patient specific 3D-print is the image acquisition. As the commonly used imaging modalities already own a QC program the quality control of the image acquisition is left out of the scope of this report. However, it is evident that from patient to digital scan, this is the first inherently error inducing step in the process. Slice thickness and reconstruction kernel are the most important parameters at this stage.

The process of restricting the reconstructed volumetric images into the region of interest only is called segmentation. Segmentation is possible with numerous software packages. Within each of these packages a segmentation can be achieved through various methods. These range from threshold segmentation based on the Hounsfield units to slice per slice contouring. It should be clear that different software and different methods lead to different segmentations. For a successful quality assurance program these induced errors should be insightful and easily be monitored over time.

Step	1. Selection	2. Scan	3. Segment	4. Engineer	5. Print	6. Prepare
Competence	Value/cost Risk analysis	Anatomy Pathology Technical Dosimetry	Anatomy Pathology Technical	Technical	Technical	Anatomy Technical
Responsibility	Physician Physicist	Radiologist Physicist Technologist	Technologist	Engineer Physician	Engineer	Engineer Physician CSSD

**Fig. 1** 3D-printing process definition with a definition of steps and distribution of responsibilities

**3D-printing.** It is evident that from CAD-drawing to 3D-print the 3D-printer induces errors due to the discrete layers that build up the model. The printers resolution and accuracy are the determining factors in this step but curing effects, ageing of the printer or resin could lead to unexpected dimensional errors.

**Sterilization.** For several 3D-printing purposes, sterilization of the finished product is necessary. Possibilities are surgical instruments, surgical guides and implants. In high temperature steam sterilization the 3D-print is exposed for three minutes to temperatures of 134 °C [17]. Although only print material fit for sterilization should be used, at this moment it is unclear if significant shrinkage, expansion or deterioration of the print occurs at these temperatures.

### 3 Phantom Study

To gain control over the quantitatively induced errors of the in-house 3D-printing process, a phantom was designed and a phantom study was developed and exercised. In the following paragraphs a description of the design and an outline of the study is given.

#### 3.1 Phantom Design

The designed ‘Gelre Surgical Guide (GSG)’ - phantom (See Fig. 2), contains more than fifty measurable parameters, these parameters can be categorized by: (1) outer dime-

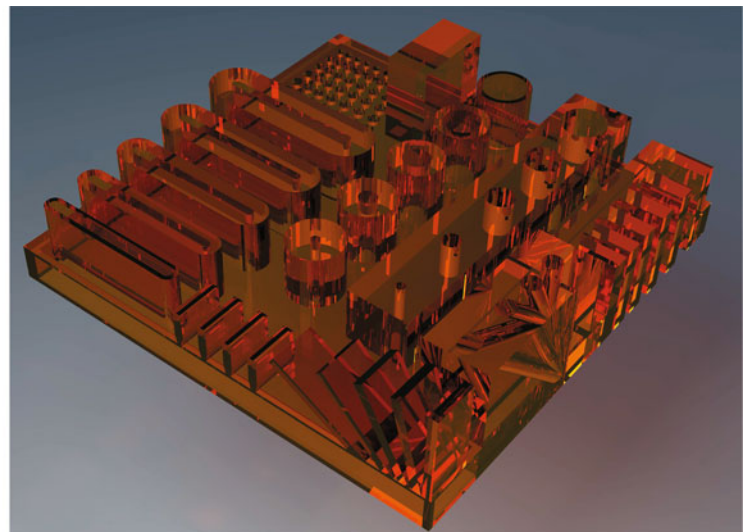
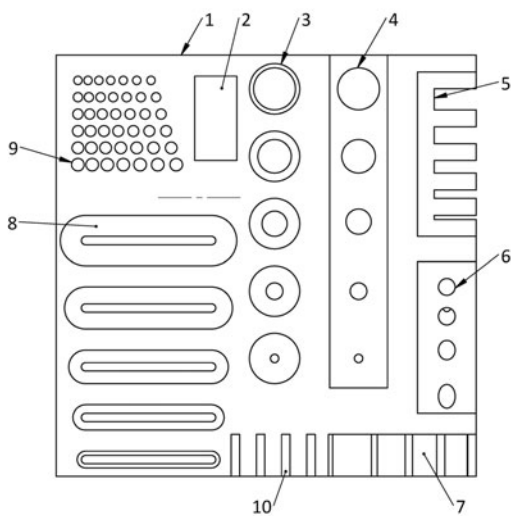


**Fig. 2** Design of the 3D-printing QC-Phantom



**Table 1** Phantom parameters

#	Name	Parameter	Notes
1	Outer dimensions	Width: 50.0 mm	
		Depth: 50.0 mm	
2	Solid cube	Width: 5.0 mm	
		Depth: 10.0 mm	
		Height: 10.0 mm	
3	Drill guide (tub.)	Inner diameter: 5.0–1.0 mm	Steps of 1.0 mm
		Outer diameter: 6.0 mm	
4	Drill guide (emb.)	Inner diameter: 5.0–1.0 mm	Steps of 1.0 mm
5	Saw guide (notch)	Gap width: 2.5–0.5 mm	Steps of 0.5 mm
		Gap depth: 5.0 mm	
		Border thickness: 2.0 mm	
6	Angled holes	Angles: 90°–45°	Steps of 15°
		Diameter: 2.0 mm	
7	Overhang	Angles: 90°–30°	Steps of 15°
8	Saw guide (bulge)	Outer width: 6.0–2.0 mm	Steps of 1.0 mm
		Inner width: 1.0 mm	
9	Raster	Hole diameter: 1.5–1.0 mm	Steps of 0.1 mm
10	Binary numbering	–	Labeling tool

nsions, (2) solid cube, (3, 4) drill-guides (tubular and embedded), (5, 8) saw-guides (notch and bulge types), (6) angled holes (7) angled overhangs, (9) rasterised holes and (10) a binary numbering tool. The GSG-phantom was designed with CAD-software SolidWorks [18]. Table 1 gives the measurable parameters.

Through this phantom, the printers resolution, shrinkage or expansion effects and angular defects can be monitored by performing physical measurements after each 3D-printing workflow step. The dimensions of the design are based on typical surgical drills and saws. These surgical drill-bits are available with diameters typically ranging from 0.5 mm to several millimeters [19]. Surgical saw blades generally vary in thickness ranging from 0.5 to 2.0 mm.

### 3.2 Study

The designed phantom was printed seven times with a Formlabs Form 2 stereolithography (SLA) printer in the material NextDent Surgical Guide (SG). The phantoms were printed at a printing resolution of 0.05 mm. Each phantom was made identifiable by breaking the numbering pillars in a binary order. By measuring the dimensions of the GSG-phantoms, the achievable resolution of the 3D-printing step could be determined. The dimensions of the GSG-phantoms were measured with a HBM 150 ± 0.02 mm caliper and a variety of feeler gauges (HBM02695).

To monitor the induced errors of the image acquisition and segmentation, the phantom labeled  $n = 7$  was scanned in 6 positions on a Siemens Somatom Definition FLASH CT with 120 kV, a slice thickness of 0.4 mm and reconstructed with kernel U70u. The six reconstructed 3D-volumes were segmented via the threshold segmentation of the open-source software 3D-slicer. The range of Hounsfield Units was chosen between  $-700$  and  $700$  HU. Each of these segmentations was reprinted with the Formlabs Form 2 printer. Again, in the material NextDent SG. By comparing the dimensions with the original phantom the induced dimensional errors by image acquisition and threshold segmentation could be determined.

To investigate the effects of steam sterilization, the six GSG-phantoms labeled  $n = 1, \dots, 6$  underwent a number of sterilization cycles corresponding to their label. After their respective number of sterilization cycles the dimensional parameters are measured and compared with their parameters prior to sterilization. A complete overview of the developed phantom study is shown in Fig. 3.

## 4 Results

### 4.1 3D-Printing

The overall integrity of the printed phantoms was shown to be good. There were no chipped or rounded edges, the

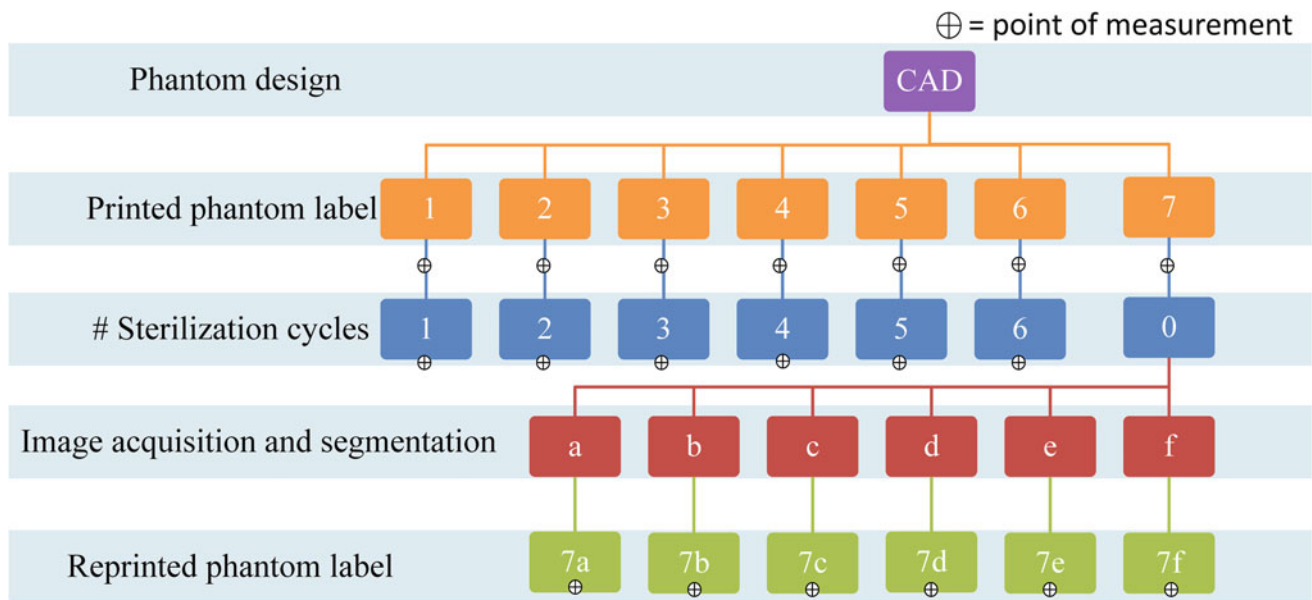


**Fig. 3** Outline of the phantom study, each point of measurement is marked

surface was smooth and the protrusions were rigid and strong. The maximum measured deviation from the CAD-drawing was measured in the 1.0 mm drill guide of phantom  $n = 1$  and was found to be 0.2 mm. The average deviation of all prints was 0.04 mm with a standard deviation of 0.06 mm. For all found deviations the inner dimensions print turned out smaller than intended. Furthermore, phantom  $n = 3$  showed clogging of the smallest embedded drill guide.

#### 4.2 Image Acquisition and Segmentation

For all measured parameters of the scanned and reprinted GSG-phantoms, the maximum deviation was found to be 0.4 mm. The average deviation was 0.06 mm with a standard deviation of 0.2 mm. The image acquisition and segmentation induced an increase in surface roughness. For two out of six reprinted phantoms this resulted in clogging of the smaller sized (1.0 mm) guides. Through advanced visualization software: Sectra, it was shown that the increase in surface roughness was induced in the image acquisition step.

#### 4.3 Sterilization

The maximum dimensional difference due to the sterilization process was found to be 0.2 mm. This maximum was found at the smallest notch type saw guide for phantoms sterilized 3 times and up. The average deviation was found to be 0.04 mm and the standard deviation was 0.07 mm. Although

all maximum deviation were found in phantoms sterilized for three times and up, no general trend was discovered over all measured parameters. Therefore, correlation with the number of sterilization cycles and size of the induced deviations could not be shown.

### 5 Discussion and Conclusion

Quality control of the in-house 3D-printing workflow was assessed by design of a GSG-phantom and development of a phantom study. Exercise of this study resulted in quantitative quality indicators of the in-house 3D-printing workflow. For the printing workflow assessed, the image acquisition step was shown to have the largest influence on the dimensional precision of the 3D-workflow. However, the induced errors are shown to be smaller than 0.5 mm when a high resolution scanning protocol is used.

For the assessed workflow the 3D-printing and sterilization steps were shown to have lower impact on the dimensional errors. No trend in dimensional differences versus number of sterilization cycles could be shown for a total of six sterilization cycles. Furthermore holds that the overall expected error is not a superposition of the individual error inducing steps. Image acquisition results in deviation between the patient and the adjacent plane, whereas 3D-printing and sterilization contributes to deviations in surgical guides.

It should be noted that by performing stated phantom study, each unique 3D-printing workflow, with its own technical specifications, can come to different conclusions. The GSG-phantom designed for this study was found to be

sufficient for its purpose. However, the design was not optimized and should not be considered as fixed. Future research for optimizing the phantom design is advised.

With the found maximum deviation, the quality of the in-house 3D-printing workflow was determined as sufficient and in control. To remain in control and assure the quality of medical 3D-printing at all time, this phantom study should be exercised periodically.

**Conflict of Interest** None

## References

- Hull, C.W.: Apparatus for production of three-dimensional objects by stereolithography. US4575330 A, 1986.
- Sheikh, A., Chepelev L., Christensen A.M., Mitsouras D., Schwarz B.A., Rybicki F.J.: Beginning and Developing a Radiology-Based In-Hospital 3D Printing Lab. In: Rybicki F., Grant G. (eds) 3D Printing in Medicine (2017).
- Malik H.H., Darwood, A.R.J., Shaunak S., Kulatilake, P., El-Hilly, A.A., Mulki, O. Baskaradas, A.: Three-dimensional printing in surgery: a review of current surgical applications. *Journal of Surgical Research* 199 (2) 512–522 (2015).
- Yang, L., Grottkau, B., He, Z., Ye, C.L.: Three dimensional printing technology and materials for treatment of elbow fractures. *Int Orthop.* 41 (11) 2381–2387 (2017).
- Atalay HA, Canat HL, Ülker V, Alkan İ, Özkuvanci Ü, Altunrende F. Impact of personalized three-dimensional (3D) printed pelvicalyceal system models on patient information in percutaneous nephrolithotripsy surgery: a pilot study. *International Brazilian Journal of Urology: official journal of the Brazilian Society of Urology.* 43(3):470–475 (2017).
- Bartellas, M.: Three-Dimensional Printing and Medical Education: A Narrative Review of the Literature. *mededpublish.org/manuscripts/1010/v1.*
- Li K, Kui C, Lee E, Ho C, Wong S, Wu W, Wong W, Voll J, Li G, Liu T, Yan B, Chan J, Tse G, Keenan I.: The role of 3D printing in anatomy education and surgical training: A narrative review. *MedEdPublish* 6 (2) 31 2017.
- Sodian, R., Weber, S., Markert, M., Loeff, M., Tim Lueth, T., Weis, F.C., Daebritz, S., Malec, E., Schmitz, C., Reichart, B.: Pediatric cardiac transplantation: Three-dimensional printing of anatomic models for surgical planning of heart transplantation in patients with univentricular heart. *The Journal of Thoracic and Cardiovascular Surgery* 136 (4) 1098–1099 (2008).
- Yang L, Shang X-W, Fan J-N, et al. Application of 3D Printing in the Surgical Planning of Trimalleolar Fracture and Doctor-Patient Communication. *BioMed Research International.* (2016).
- Zheng, Y., Yu, D., Zhao, J., Wu, Y. Zheng, B.: 3D Printout Models vs. 3D-Rendered Images: Which Is Better for Preoperative Planning? *Journal of Surgical Education* 73(3), 518–523 (2016).
- Auricchio F, Marconi S. 3D printing: clinical applications in orthopaedics and traumatology. *EFORT Open Reviews.* 1(5), 121–127 (2016).
- Coppen, C., Weijs, W., Bergé, S.J., Maal, T.J.J., Oromandibular reconstruction using 3D planned triple template method. *American Association of Oral and Maxillofacial Surgeons* (71), 243–247 (2013).
- Chae, M.P., Rozen, W.M., McMenamin, P.G., Findlay M.W., Spychal, R.T., Hunter-Smith D.J., Emerging applications of bedside 3D printing in plastic surgery. *Frontiers in Surgery*, June 2015.
- Parthasarathy J. 3D modeling, custom implants and its future perspectives in craniofacial surgery. *Annals of Maxillofacial Surgery.* 4(1), 9–18 (2014).
- Hong, C.: Application of 3D printing in orthopedics: status quo and opportunities in China. *Annals of Translational Medicine* 3 (S1):S12 (2015).
- Leng, S., McGee, K., Morris, J., Alexander, A., Kuhlmann, J., Vrieze, T., McCollough, C.H., Matsumoto, J.: Anatomic modeling using 3D printing: quality assurance and optimization. *3D Printing in Medicine* 3–6 (2017).
- WIP richtlijn, <http://www.rivm.nl/dsresource?objectid=330dd0f8-e6b8-4621-86b1-7a039ac83d42&type=pdf&disposition=inline>, Last accessed: 2018/01/31.
- Solidworks software, <http://www.solidworks.nl/>, Last accessed: 2018/01/31.
- Bertollo, N., Walsh, W.R: Drilling of Bone: Practicality, Limitations and Complications Associated with Surgical Drill-Bits, INTECH Open Access Publisher (2011).

# Validation of Geant4 Nuclear Reaction Models for Hadron Therapy and Preliminary Results with BLOB

C. Mancini-Terracciano, B. Caccia, M. Colonna, M. De Napoli, A. Dotti, R. Faccini, P. Napolitani, L. Pandola, E. Solfaroli Camillocci, G. Traini, and G. A. P. Cirrone

## Abstract

Reliable nuclear fragmentation models are of utmost importance in hadron therapy, where Monte Carlo (MC) simulations are used to compute the input parameters of the treatment planning software, to validate the deposited dose calculation, to evaluate the biological effectiveness of the radiation, to correlate the  $\beta +$  emitters production in the patient body with the delivered dose, and to allow a non-invasive treatment verification. Despite of its large use, the models implemented in Geant4 have shown severe limitations in reproducing the measured secondaries yields in ions interaction below 100 MeV/A, in term of production rates, angular and energy distributions. We present a benchmark of the Geant4 models with double-differential cross section of the secondary fragments produced in the  $^{12}\text{C}$  fragmentation at 62 MeV/A on thin carbon target. Such a benchmark includes the recently implemented model “Liège Intranuclear Cascade”. Moreover, we present the preliminary results, obtained in simulating the same interaction, with the “Boltzmann-Langevin One Body” model

(BLOB). BLOB is a semiclassical one-body approaches to solve the Boltzmann-Langevin equation. It includes a mean-field propagation term, on the basis of an effective interaction. In addition to the mean field term, BLOB introduces fluctuations in full phase space through a modified collision term where nucleon-nucleon correlations are explicitly involved. It has been developed to simulate the heavy ion interactions in the Fermi-energy regime. In this work, we show the BLOB capabilities in describing  $^{12}\text{C}$  fragmentation, in the perspective of a direct implementation in Geant4. Monte Carlo simulation, nuclear interaction, nuclear fragmentation, hadron therapy.

## Keywords

Monte Carlo simulation • Nuclear interaction  
Nuclear fragmentation • Hadron therapy

C. Mancini-Terracciano (✉) · R. Faccini · E. Solfaroli Camillocci  
G. Traini  
INFN, Sez. di Roma, Rome, Italy  
e-mail: carlo.mancini.terracciano@roma1.infn.it

B. Caccia  
National Center for Radiation Protection and Computational  
Physics, Istituto Superiore di Sanità, Rome, Italy

M. Colonna · L. Pandola · G. A. P. Cirrone  
INFN, Laboratori Nazionali del Sud, Catania, Italy

M. De Napoli  
INFN, Sez. di Catania, Catania, Italy

A. Dotti  
SLAC National Accelerator Laboratory, Menlo Park, USA

R. Faccini · E. Solfaroli Camillocci · G. Traini  
Dip. di Fisica, Università di Roma La Sapienza, Rome, Italy

P. Napolitani  
CNRS/IN2P3, Orsay, France

## 1 Introduction

Nuclear interaction and fragment production in the energy range between 15 MeV/A and 200 MeV/A are of utmost importance in hadron therapy [1]. Hadron therapy is the treatment of tumours with Protons (p), or heavier ions like Carbon (C) and Oxygen (O).

Full MC simulations are considered the gold standard for dosimetric calculations in conventional radio therapy and hadron therapy, hence the high relevance of a reliable MC simulation between few hundreds and few tens of MeV/A, the typical energy range of such a therapy [2]. For instance, MC codes are used in hadron therapy to:

- generate input parameters, such as the depth-dose distribution in water for different ions, of the deterministic codes (pencil beam algorithms [3]) in treatment planning for regular clinical use [4];

- validate the dose calculation of the pencil beam algorithms, especially in cases with great tissue heterogeneities [5];
- estimate the risk of secondary cancer induction [6];
- estimate the production of beta emitters, such as  $^{11}\text{C}$  and  $^{15}\text{O}$ , which would allow for a non-invasive verification of

the treatment via Positron Emission Tomography (PET) imaging during, or shortly after, the treatment itself. However, the density of activated isotopes is not directly proportional to the delivered dose, and MCs are used to infer the dose as a function of the measured density of annihilation photons [7, 8].

**Fig. 1** Double differential cross section of H production in the interaction of  $^{12}\text{C}$  with a thin  $^{nat}\text{C}$  target at 62 MeV/A emitted at the angles  $\theta_{lab} = 11.4^\circ, 14.4^\circ, 17.2^\circ,$  and  $19.4^\circ$ . The green functions shows the BIC prediction, in red the QMD and in blue INCL. For BIC and QMD the lighter colours are for Geant4 version 10.4, while the darker are for Geant4 version 9.4.p1. In black the experimental data (Color figure online)

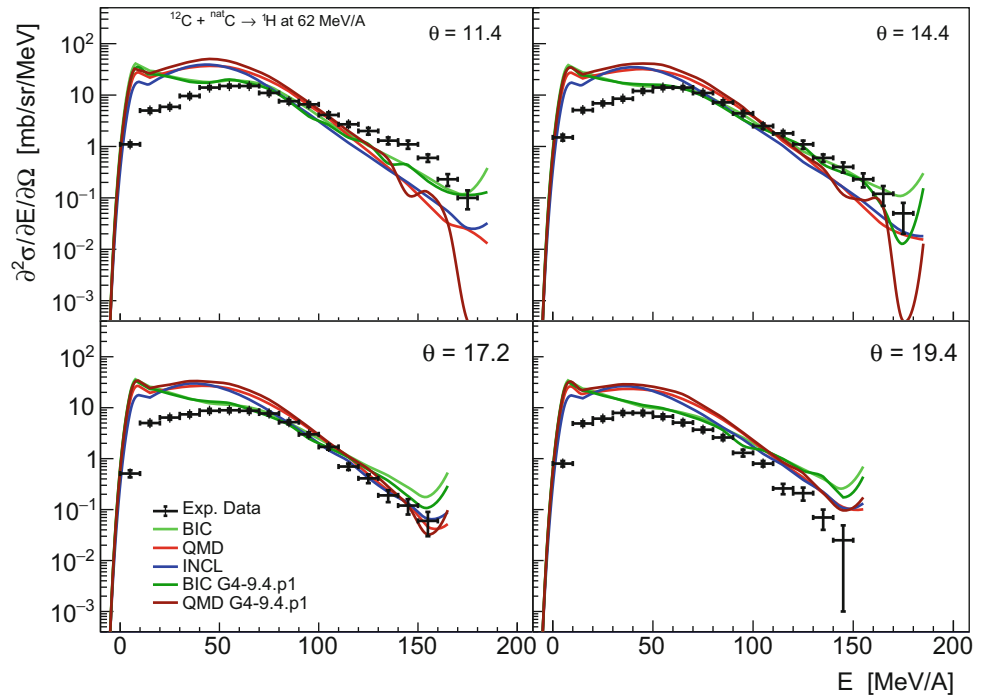


**Fig. 2** Double differential cross section of  $^2\text{H}$  production in the interaction of  $^{12}\text{C}$  with a thin  $^{nat}\text{C}$  target at 62 MeV/A emitted at the angles  $\theta_{lab} = 11.4^\circ, 14.4^\circ, 17.2^\circ,$  and  $19.4^\circ$ . The green functions shows the BIC prediction, in red the QMD and in blue INCL. For BIC and QMD the lighter colours are for Geant4 version 10.4, while the darker are for Geant4 version 9.4.p1. In black the experimental data

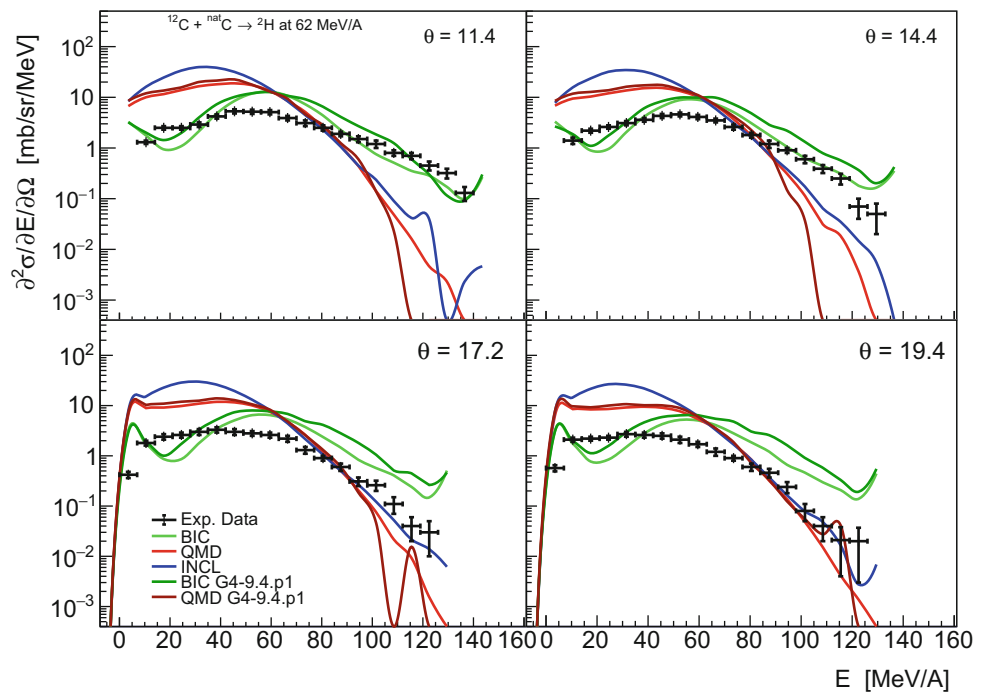




**Fig. 3** Double differential cross section of  ${}^3\text{H}$  production in the interaction of  ${}^{12}\text{C}$  with a thin  ${}^{\text{nat}}\text{C}$  target at 62 MeV/A emitted at the angles  $\theta_{\text{lab}} = 11.4^\circ, 14.4^\circ, 17.2^\circ,$  and  $19.4^\circ$ . The green functions shows the BIC prediction, in red the QMD and in blue INCL. For BIC and QMD the lighter colours are for Geant4 version 10.4, while the darker are for Geant4 version 9.4.p1. In black the experimental data

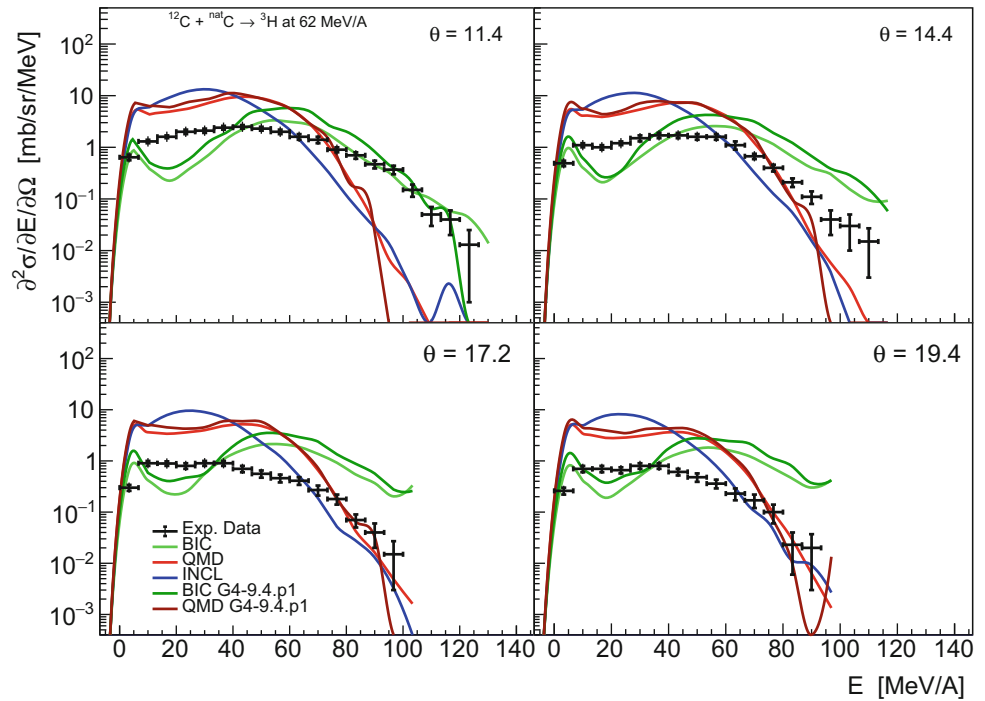
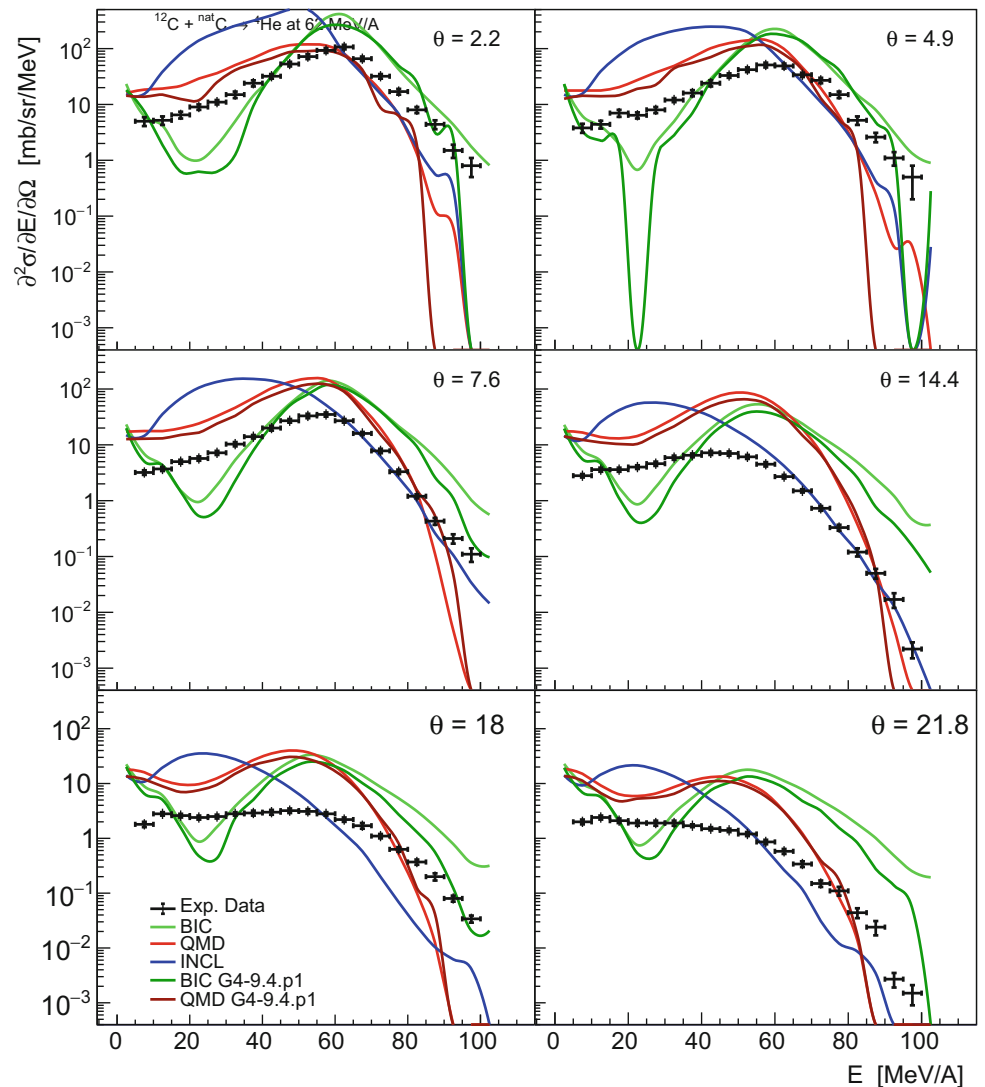


**Fig. 4** Double differential cross section of  ${}^4\text{He}$  production in the interaction of  ${}^{12}\text{C}$  with a thin  ${}^{\text{nat}}\text{C}$  target at 62 MeV/A emitted at the angles  $\theta_{\text{lab}} = 2.2^\circ, 4.9^\circ, 7.6^\circ, 14.4^\circ, 18^\circ,$  and  $21.8^\circ$ . The green functions shows the BIC prediction, in red the QMD and in blue INCL. For BIC and QMD the lighter colours are for Geant4 version 10.4, while the darker are for Geant4 version 9.4.p1. In black the experimental data



MC codes are also used in radiobiology to link the physical dose deposited to the biological effectiveness. Indeed, biological effects are a function not only of the dose but also of the quality of incident radiation [9].

Besides the importance for medical applications, these models are used also in simulations for space radiation dosimetry and nuclear spallation sources.

In this paper we present an update of the comparison between measured fragmentation of  $^{12}\text{C}$  ions at 62 MeV/A and the Geant4 predictions published by De Napoli et al. [10].

Geant4 [11] is one of the most widely used MC toolkit, both in Nuclear and Particle Physics and in medical application. It simulates radiation transport and interaction with matter and has the capability to import the Computed Tomography scan (CT) of a patient in DICOM format [12], allowing to simulate the interaction of the beam with a specific patient. Moreover, two programs specifically

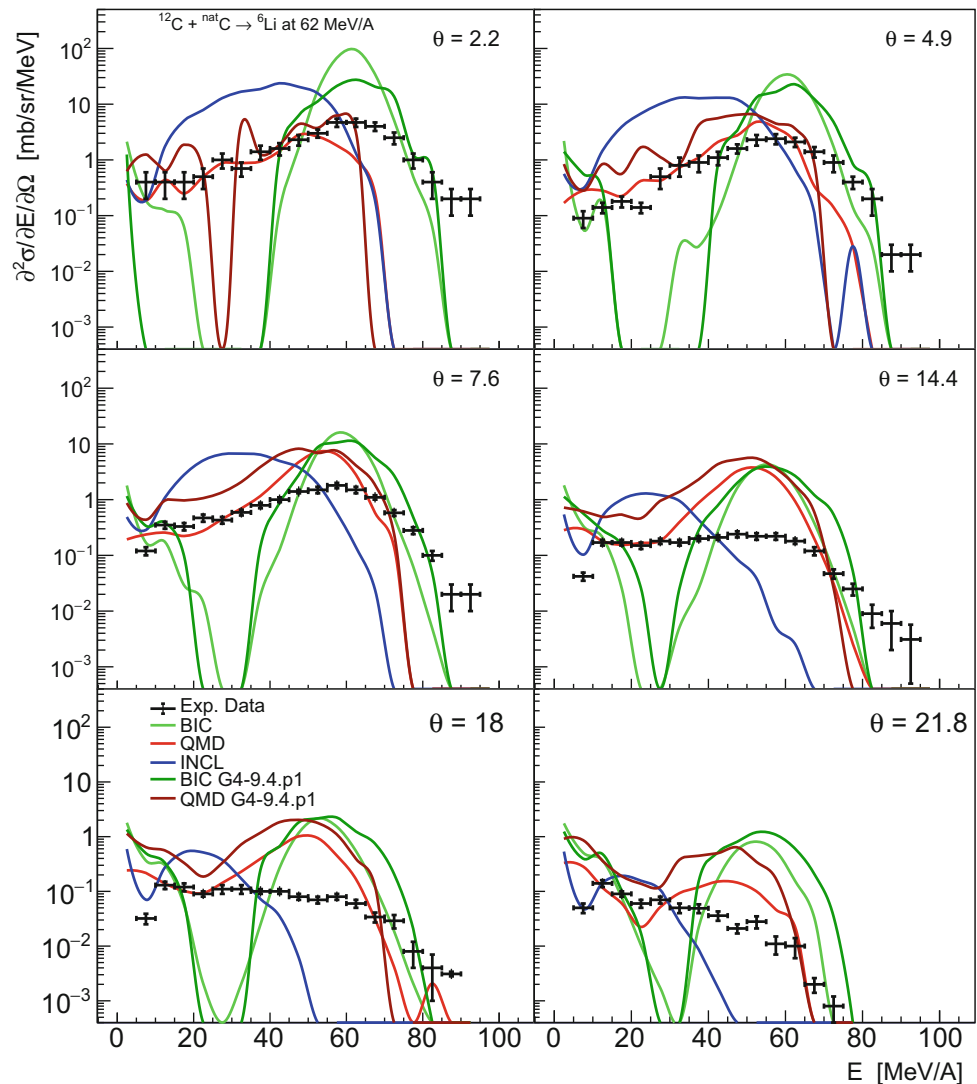
developed for medical simulations have been built using Geant4, and therefore use its nuclear reaction models. There also exist a Geant4 package dedicated to simulation of early biological damage induced by ionizing radiation at the DNA scale: Geant4-DNA [13].

## 2 Geant4 Models

The data shown in this paper have been acquired in the interaction of  $^{12}\text{C}$  with thin targets, these data are of particular interest as the fragmentation of the secondary products and the electromagnetic interaction in the target are not relevant. Therefore, they are the perfect test for the Nuclear Reaction models implemented in Geant4 relevant for hadron therapy.

The nuclear interactions are described in two steps, usually called “entrance channel” and “exit channel”. The first

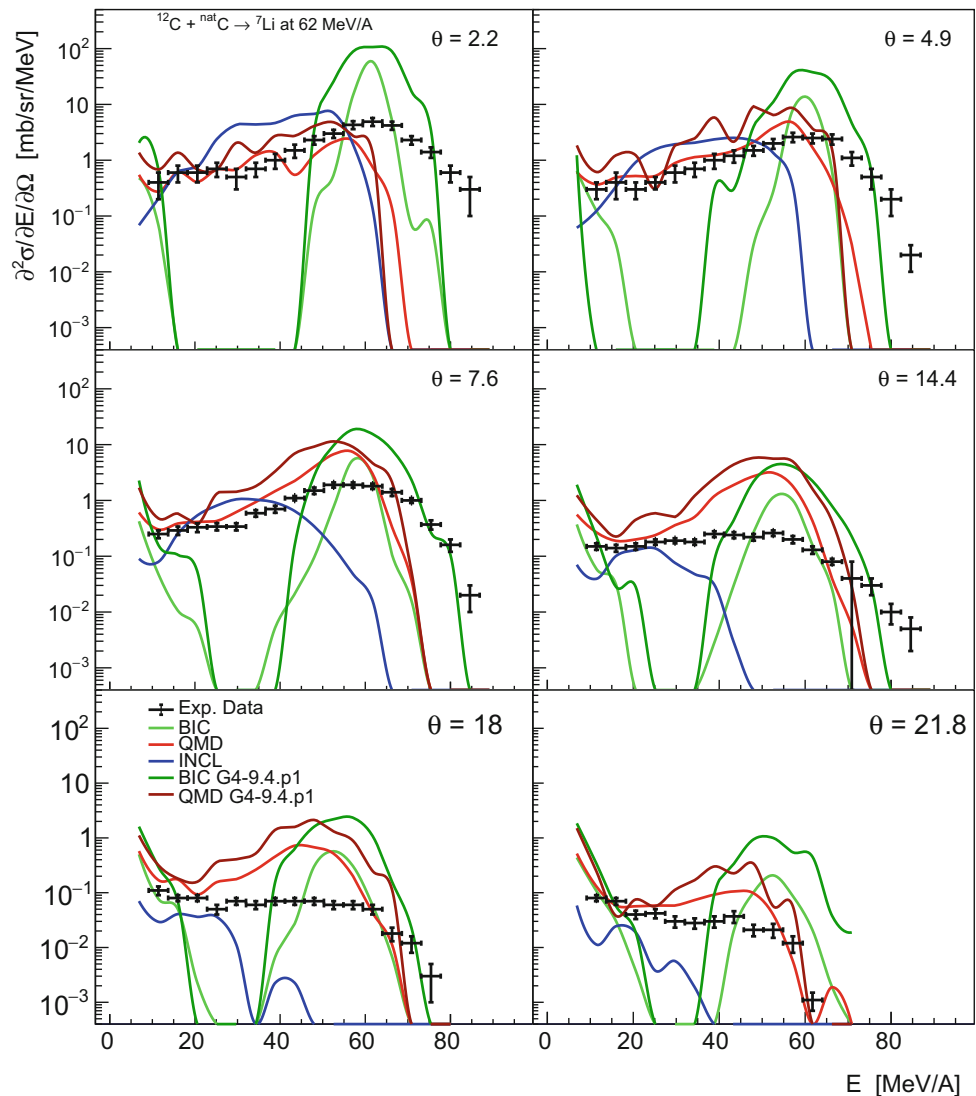
**Fig. 5** Double differential cross section of  $^6\text{Li}$  production in the interaction of  $^{12}\text{C}$  with a thin  $^{nat}\text{C}$  target at 62 MeV/A emitted at the angles  $\theta_{lab} = 2.2^\circ, 4.9^\circ, 7.6^\circ, 14.4^\circ, 18^\circ,$  and  $21.8^\circ$ . The green functions shows the BIC prediction, in red the QMD and in blue INCL. For BIC and QMD the lighter colours are for Geant4 version 10.4, while the darker are for Geant4 version 9.4.p1. In black the experimental data



step describes the collision, the production of excited nuclear states, their possible pre-equilibrium emission, and the sharing of the energy among the nucleons, process usually called “thermalization”. The second step deals with the decays of such excited states after the thermalization. In the energy range of interest of hadron therapy, in Geant4 there are three different models for the entrance channel:

- Binary Intra-nuclear Cascade (BIC) [14]: This is an extension of the Binary Cascade model [15], a model in which primary or secondary particles, usually called “participating” particles, are tracked in the nucleus. The interactions are between them and an individual nucleon of the nucleus, thus the name. The model can be seen as a hybrid between a classical cascade code and a Quantum molecular Dynamics (QMD) model, as the participating particles are described by Gaussian wave functions. The cross sections are the ones for free particles and
- Quantum Molecular Dynamics (QMD) [16]: Similarly to the BIC model, each nucleon is described by an independent Gaussian wave function. However, in QMD all the nucleons are considered as “participants”, and the scattering between participants is included. The time evolution is followed in steps of 1 fm/c up to a given time, typically 100 fm/c.
- Liège Intranuclear Cascade (INCL) [17]: The nucleons are modelled as a free Fermi gas in a static potential well. The radius of the well depends on the nucleon

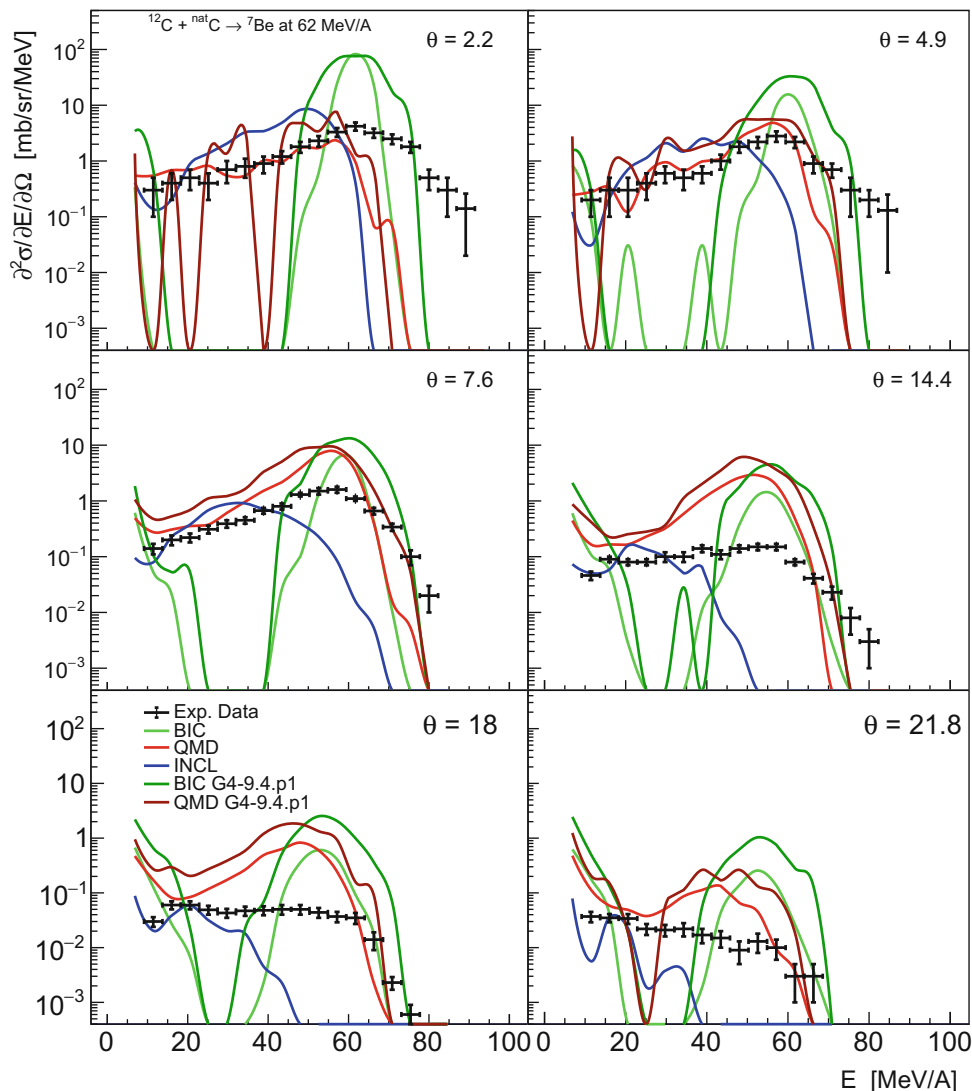
**Fig. 6** Double differential cross section of  ${}^7\text{Li}$  production in the interaction of  ${}^{12}\text{C}$  with a thin  ${}^{nat}\text{C}$  target at 62 MeV/A emitted at the angles  $\theta_{lab} = 2.2^\circ, 4.9^\circ, 7.6^\circ, 14.4^\circ, 18^\circ,$  and  $21.8^\circ$ . The green functions shows the BIC prediction, in red the QMD and in blue INCL. For BIC and QMD the lighter colours are for Geant4 version 10.4, while the darker are for Geant4 version 9.4.p1. In black the experimental data



momentum. The particles are assumed to propagate along straight-line trajectories. The algorithm calculates the time at which events will happen, and propagates the particles directly to their positions at that particular point in time. This means that the length of the time step in simulation is not constant. The stopping time is a function of the target nucleus mass. If the projectile is a nucleus, a random impact parameter is sampled and an overlap volume between the two nuclei is calculated accordingly to it. The participants are all the nucleons from projectile and target inside this volume. The participants that traverse the nucleus without undergoing any collision are coalesced with any existing geometrical spectators to form an excited projectile-like pre-fragment. A particle-hole model generates the excitation energy of the pre-fragment. This model was not available in the version 9.4.p1 of Geant4, the one used for the first benchmark of the Geant4 models with this data-set [10].

As already mentioned, after the thermalization, the particle emission from the excited nuclear species produced in the entrance channel is simulated with the so-called exit channels modes. In this stage, the excitation energy is supposed to be shared among all the nucleons, and the nucleus is described only by its mass, charge, and excitation energy, neglecting the steps that led to its formation. The most relevant model implemented in Geant4 in this energy domain is the Generalized Evaporation Model (GEM) [18]. It is based on the first statistical theory of compound nuclear decay made by Weisskopf and Ewing [19], and it is an application of the balance principle. It associates the probability that a nucleus with  $A$  nucleons emits one of them, remaining with  $A - 1$  nucleons, to the probability that the produced nucleus, with  $A - 1$  nucleon, captures the nucleon in object. The latter probability is calculated using the energy level density of the evaporating nucleus and an empirical cross section for the inverse reaction. It takes into account also the emission

**Fig. 7** Double differential cross section of  ${}^7\text{Be}$  production in the interaction of  ${}^{12}\text{C}$  with a thin  ${}^{\text{nat}}\text{C}$  target at 62 MeV/A emitted at the angles  $\theta_{\text{lab}} = 2.2^\circ, 4.9^\circ, 7.6^\circ, 14.4^\circ, 18^\circ,$  and  $21.8^\circ$ . The green functions shows the BIC prediction, in red the QMD and in blue INCL. For BIC and QMD the lighter colours are for Geant4 version 10.4, while the darker are for Geant4 version 9.4.p1. In black the experimental data



of fragments heavier than  $\alpha$  particles and uses an accurate level density function, based on the Fermi gas model, for total decay width.

### 3 Geant4 Simulations

As mentioned in the previous section the models that could be used to simulate  $^{12}\text{C}$  fragmentation below 100 MeV/A in Geant4 are three: BIC, QMD and INCL. While the default energy range of BIC and INCL range from 0 MeV/A, the minimum energy at which QMD is used by default is 100 MeV/A. Therefore, for this benchmark we manually modified the lower threshold at which QMD is used. The simulations presented in this work have been done with the last stable version of Geant4, namely the 10.4. To compare the results obtained with the actual Geant4 version with the original results published by De Napoli et al. [10], we

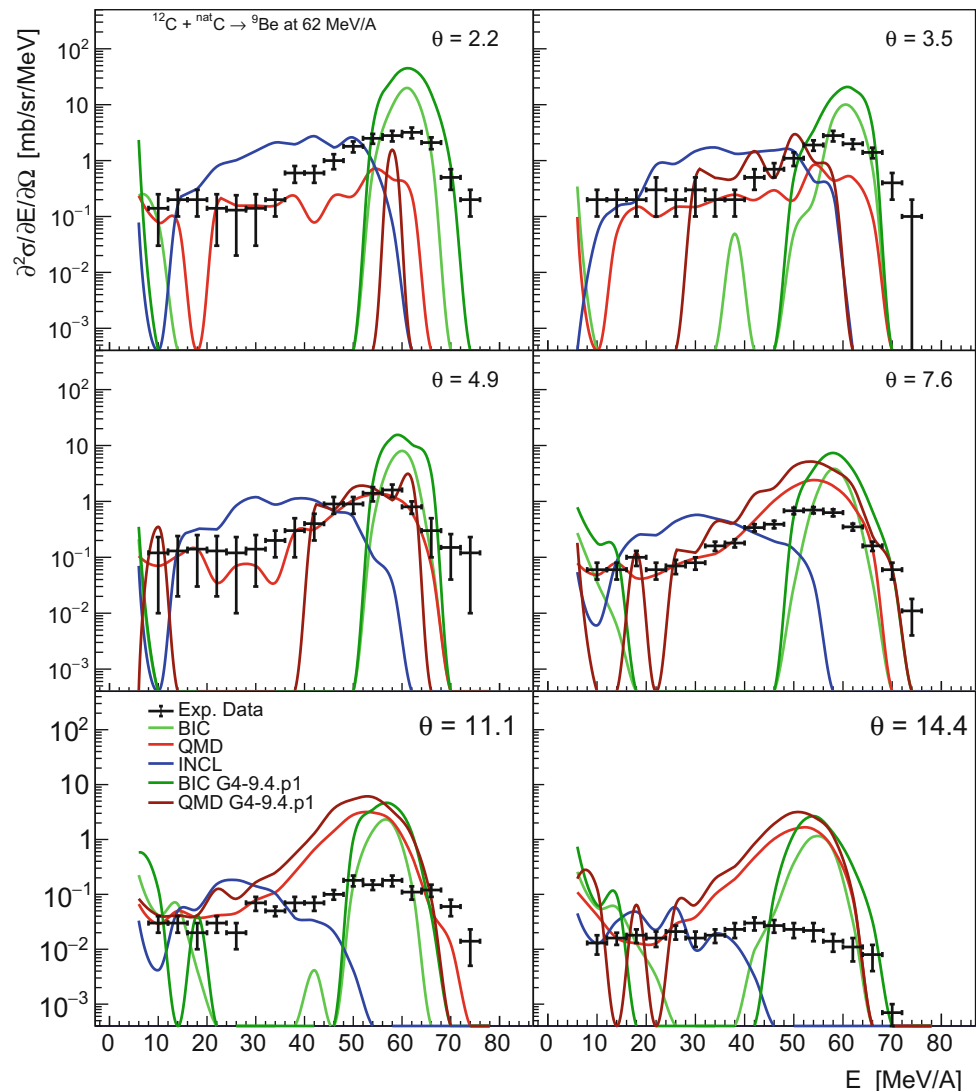
computed the cross section also with the version 9.4.p1 of Geant4, the one used by De Napoli et al. in their publication.

In order to reduce the computation time, all interactions, but the hadronic inelastic, have been switched off. All secondaries are discarded after being produced and the target is much longer than the hadronic inelastic interaction length. In this way all primaries undergo inelastic interaction, which is also the only process simulated. The results are then scaled by the total inelastic cross section and processed to reproduce the experimental angular resolution, geometrical acceptance and energy resolution.

### 4 Geant4 Results

In Figs. 1, 2, 3, 4, 5, 6, 7, 8, 9 and 10, the double-differential cross sections of several isotopes are compared with the Geant4 models predictions. As mentioned before, INCL was

**Fig. 8** Double differential cross section of  $^9\text{Be}$  production in the interaction of  $^{12}\text{C}$  with a thin  $^{nat}\text{C}$  target at 62 MeV/A emitted at the angles  $\theta_{lab} = 2.2^\circ, 4.9^\circ, 7.6^\circ, 14.4^\circ, 18^\circ,$  and  $21.8^\circ$ . The green functions shows the BIC prediction, in red the QMD and in blue INCL. For BIC and QMD the lighter colours are for Geant4 version 10.4, while the darker are for Geant4 version 9.4.p1. In black the experimental data





not available in the version 9.4.p1. For the curves where the Geant4 version is not specified the last one is intended, namely the 10.4.

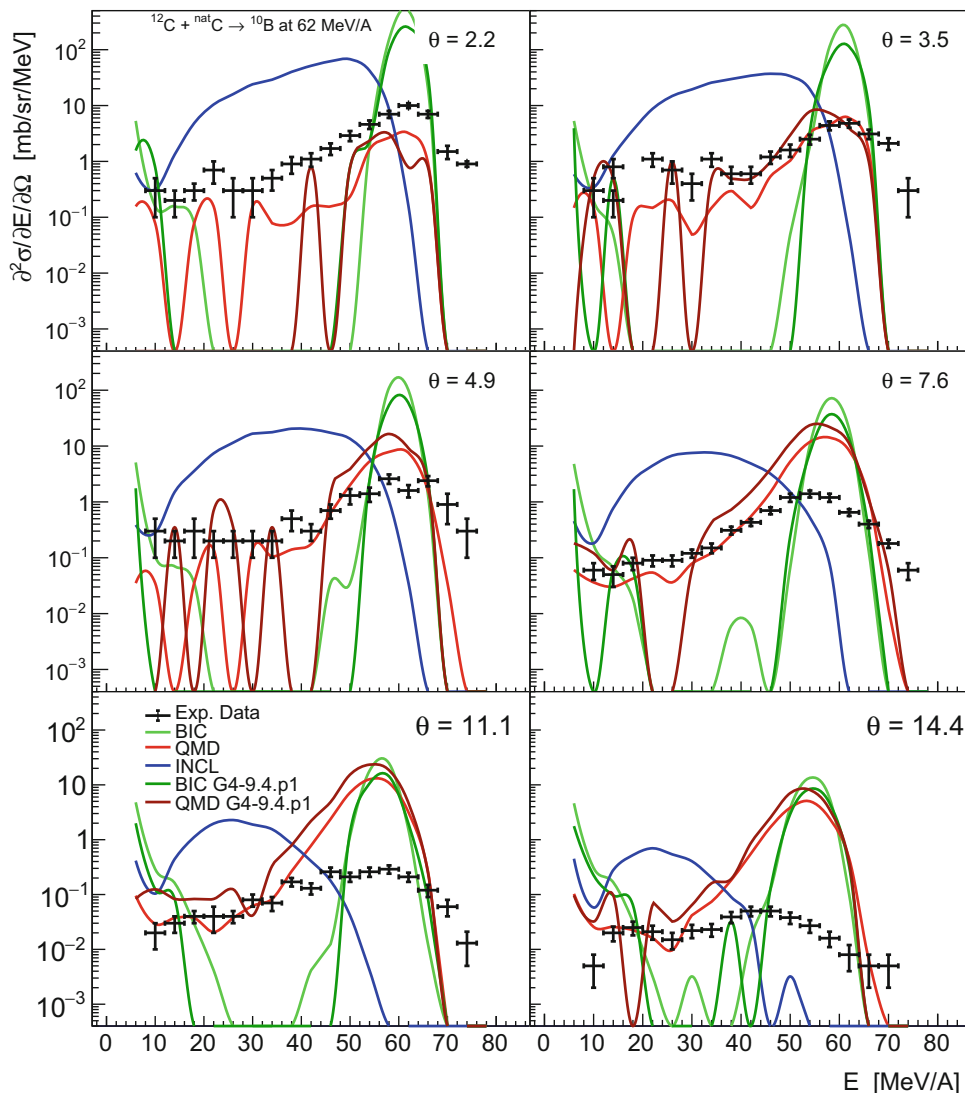
Despite the numerous updates of the code, especially of the de-excitation model [20], the BIC and QMD did not change significantly from the version 9.4.p1 to the 10.4. As noted in the first benchmark of Geant4 with this data-set, BIC reproduces better the emission cross section of fragments with high energy at a small angle with respect to the beam direction, i.e. the peripheral interactions [10]. The recently implemented model, INCL, shows results similar to QMD for the emission of secondaries with  $Z = 1$ , namely H (Fig. 1), deuterium (Fig. 2), and tritium (Fig. 3). For the emission of the most probable ejectile,  ${}^4\text{He}$ , (Fig. 4) BIC shows two separate distributions, one at low energy, produced by the fragments emitted by the target, and one at high energy, produced by the projectile. This doubly peaked

distribution seems mitigated in QMD but still present, especially at large angles. Therefore, these two models underestimate the production of  ${}^4\text{He}$  as an intermediate mass fragment. Conversely, INCL overestimates this possibility, showing a large peak at energy lower than the beam. All the three models overestimate the total production of  ${}^4\text{He}$ .

## 5 Preliminary Results with BLOB

BLOB (Boltzmann-Langevin One-Body) [21, 22] is a recent one-body approach to solve the Boltzmann-Langevin (BL) equation [23] in full phase space. The model describes the time evolution of the semiclassical one-body nucleon distribution function in a self-consistent mean field potential. Two-body correlations are explicitly taken into account by introducing hard nucleon-nucleon (n-n)

**Fig. 9** Double differential cross section of  ${}^{10}\text{B}$  production in the interaction of  ${}^{12}\text{C}$  with a thin  ${}^{\text{nat}}\text{C}$  target at 62 MeV/A emitted at the angles  $\theta_{\text{lab}} = 2.2^\circ, 4.9^\circ, 7.6^\circ, 14.4^\circ, 18^\circ,$  and  $21.8^\circ$ . The green functions shows the BIC prediction, in red the QMD and in blue INCL. For BIC and QMD the lighter colours are for Geant4 version 10.4, while the darker are for Geant4 version 9.4.p1. In black the experimental data



scattering, governed by the residual nuclear interaction, with Pauli blocking strictly fulfilled in the final states. Many-body correlations are recovered by introducing a fluctuating term, which acts as a continuous source linked to the nucleon-nucleon collision term, and which is exploited to produce phase-space fluctuations through a stochastic treatment. This model can provide a dynamical description of dissipative nuclear processes, tracking the formation of fragments and clusters from mean-field instabilities since the earliest instants. It is well suited to simulate nuclear collisions and fragment production between 15 MeV/A and 200 MeV/A. BLOB, as BIC, QMD and INCL, is made to describe the out-of-equilibrium entrance channel and the successive dynamical path towards thermalisation.

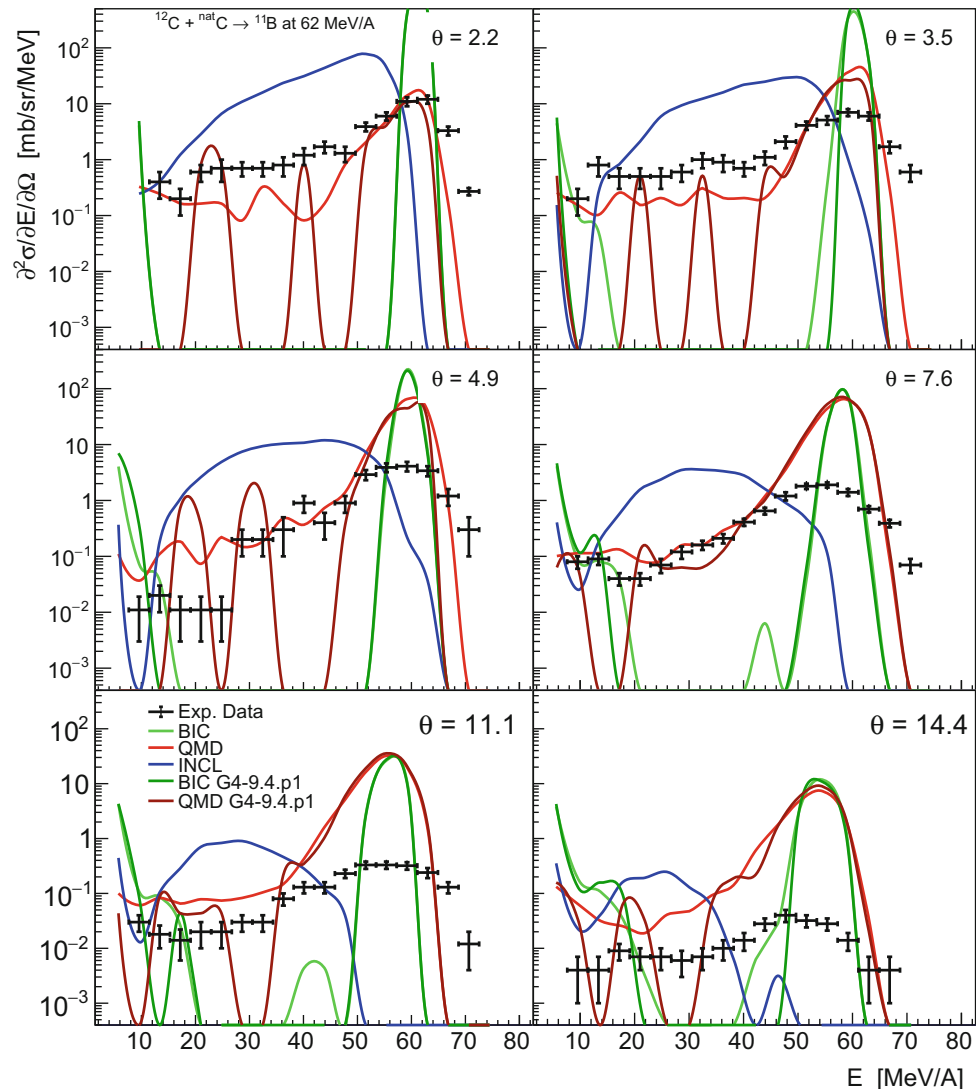
Foreseeing an implementation of BLOB in Geant4, we performed a simulation of  $^{12}\text{C}$  fragmentation coupling BLOB with a stand alone de-excitation model called Simon

[24]. We computed the total yields of the secondaries in the interaction of  $^{12}\text{C}$  with  $^{12}\text{C}$  at 62 MeV/A and compared this result with the total yields we extrapolated from the angular distribution published by De Napoli et al. [10]. The comparison is shown in Fig. 11. It has to be noted that at this level we neglected the fact that the target was natural Carbon and not pure  $^{12}\text{C}$ . Data are normalised so that the sum of Deuterium and Tritium yields equals the corresponding calculated quantity.

The BLOB simulation was stopped in a time window from 80 to 140 fm/c, when the last split is registered. Therefore, all the sequence of hot fragments is de-excited using the Simon code. More details about the simulation can be found in the work presented by P. Napolitani [25].

The agreement between the BLOB results and the experimental points is very good for light fragments yields up to  $^9\text{Be}$ . The production of  $^{10}\text{B}$  and  $^{11}\text{B}$  is underestimated

**Fig. 10** Double differential cross section of  $^{11}\text{B}$  production in the interaction of  $^{12}\text{C}$  with a thin  $^{nat}\text{C}$  target at 62 MeV/A emitted at the angles  $\theta_{lab} = 2.2^\circ, 4.9^\circ, 7.6^\circ, 14.4^\circ, 18^\circ, \text{ and } 21.8^\circ$ . The green functions shows the BIC prediction, in red the QMD and in blue INCL. For BIC and QMD the lighter colours are for Geant4 version 10.4, while the darker are for Geant4 version 9.4.p1. In black the experimental data



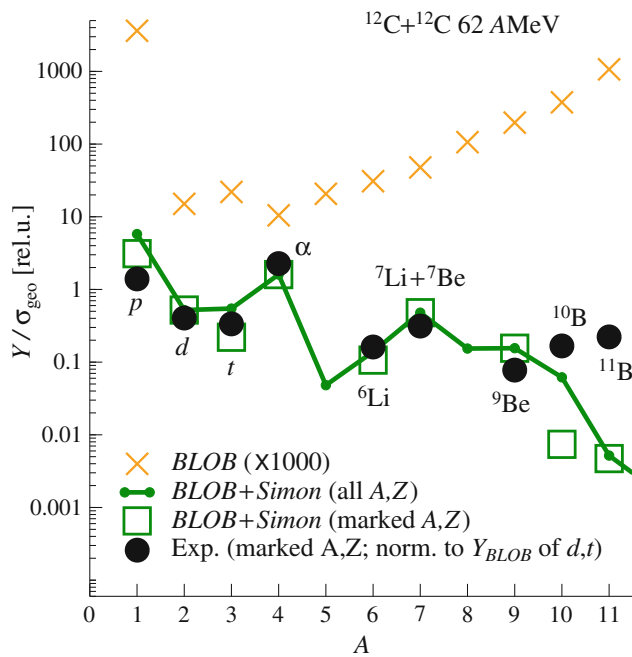


**Fig. 11** Fragment yields ( $Y$ ) from the interaction of  $^{12}\text{C}$  with  $^{12}\text{C}$  at 62 MeV/A divided by the geometric cross section ( $\sigma_{\text{geo}}$ ). The BLOB results are shown with crosses and are multiplied by a factor 1000. The green line shows the mass distribution of the fragments as calculated coupling Simon to BLOB while the squares are the yields predictions for the isotopes for which an experimental measure is available. Data are normalised so that the sum of Deuterium ( $d$ ) and Tritium ( $t$ ) yields (called  $Y_{\text{BLOB}}$  in the figure) equals the corresponding calculated quantity

by more than an order of magnitude, these fragments are produced in peripheral reaction. As is possible to see from the crosses in Fig. 11, BLOB produces these ejectiles, however their excitation energy is too high and so they are made to emit nucleons by Simon. This explains also the overestimation of the proton production.

## 6 Summary and Conclusions

This work shows an update of the benchmark done with double differential cross section of  $^{12}\text{C}$  fragmentation interacting with a thin  $^{nat}\text{C}$  target at 62 MeV/A. These reactions are necessary for the use of Geant4 in hadron therapy. In the current version of Geant4, three models are able to simulate the interactions of ions at such energy, namely BIC QMD and INCL. The last one was not available when De Napoli et al. [10] published the first benchmark of Geant4 with this data-set and therefore, this is the first benchmark of INCL with this data-set.

The results show that the performances of BIC and QMD in simulating this reaction did not improve from the version 9.4.p1 to the 10.4 of Geant4 and INCL does not show clear better results. It has to be noted that 62 MeV/A is lower than

the energy range where the QMD model has been designed to work.

Besides the work from which we took the data-set by De Napoli et al. [25], other works showed the limitation of the Geant4 models in simulating the  $^{12}\text{C}$  fragmentation below 100 MeV/A, such as Braunn et al. [26] and Doudet et al. [27]. For this reason we investigated the potentiality of another model that could simulate the entrance channel of nuclear reaction in such energy domain. We performed a preliminary simulation of the interaction of two  $^{12}\text{C}$  at 62 MeV/A and the agreement with experimental data is encouraging.

## References

1. U. Amaldi and G. Kraft. "Radiotherapy with beams of carbon ions". In: Reports on Progress in Physics 68.8 (2005), pp. 1861-1882.
2. D. W. O. Rogers. "Fifty years of Monte Carlo simulations for medical physics". In: Physics in Medicine and Biology 51.13 (2006), R287-R301.
3. M. Krämer et al. "Treatment planning for heavy-ion radiotherapy: physical beam model and dose optimization". In: Physics in Medicine and Biology 45.11 (2000), p. 3299.
4. K. Parodi et al. "Monte Carlo simulations to support start-up and treatment planning of scanned proton and carbon ion therapy at a synchrotron-based facility". In: 57.12 (2012), pp. 3759-3784.
5. S. Molinelli et al. "Dosimetric accuracy assessment of a treatment plan verification system for scanned proton beam radiotherapy: one-year experimental results and Monte Carlo analysis of the involved uncertainties". In: Physics in Medicine and Biology 58.11 (2013), pp. 3837-3847.
6. S. Yonai, N. Matsufuji, and M. Namba. "Calculation of out-of-eld dose distribution in carbon-ion radiotherapy by Monte Carlo simulation". In: Medical Physics 39.8 (2012), p. 5028.
7. G. Battistoni et al. "The FLUKA code and its use in hadron therapy". In: Nuovo Cimento Della Societa Italiana Di Fisica C-Colloquia on Physics 31.1 (2008), pp. 69-75.
8. A. C. Kraan. "Range Verification Methods in Particle Therapy: Underlying Physics and Monte Carlo Modeling". In: Frontiers in Oncology 5 (2015), pp. 1-27.
9. J. Kraft. "Tumor therapy with heavy charged particles". In: Progress in Particle and Nuclear Physics 45 (2000), S473-S544.
10. M. De Napoli et al. "Carbon fragmentation measurements and validation of the Geant4 nuclear reaction models for hadrontherapy". In: Physics in Medicine and Biology 57.22 (2012), pp. 7651-7671.
11. S. Agostinelli et al. "Geant4, a simulation toolkit". In: Nuclear Instruments and Methods in Physics Research Section A: Accelerators, Spectrometers, Detectors and Associated Equipment 506.3 (2003), pp. 250-303.
12. <https://twiki.cern.ch/twiki/bin/view/Geant4/Geant4MedicalPhysics>.
13. M. Bernal et al. "Track structure modeling in liquid water: A review of the Geant4-DNA very low energy extension of the Geant4 Monte Carlo simulation toolkit". In: Physica Medica 31.8 (2015), pp. 861-874.
14. Geant4 Physics Reference Manual.
15. G. Folger, V. N. Ivanchenko, and J. P. Wellisch. "The Binary Cascade". In: The European Physical Journal A - Hadrons and Nuclei 21.3 (2004), pp. 407-417.
16. T. Koi et al. "New native QMD code in Geant4," in: Proceedings of the MC2010 Monte Carlo Conference (2010).

17. S. Leray et al. "Recent Developments of the Li<sub>ège</sub> Intranuclear Cascade Model in View of its Use into High-energy Transport Codes". In: Nuclear Data Sheets 118 (2014), pp. 312–315.
18. S. Furihata. "Statistical analysis of light fragment production from mediumenergy proton induced reactions". In: Nucl. Instrum. Meth. B171 (2000), pp. 251–258.
19. V. F. Weisskopf and D. H. Ewing. "On the Yield of Nuclear Reactions with Heavy Elements". In: Phys. Rev. 57 (6 1940), pp. 472–485.
20. [http://geant4.cern.ch/support/source/geant4/source/processes/hadronic/models/de\\_excitation/History](http://geant4.cern.ch/support/source/geant4/source/processes/hadronic/models/de_excitation/History).
21. P. Napolitani and M. Colonna. "Bifurcations in Boltzmann-Langevin one body dynamics for fermionic systems". In: 726 (2013). Ed. by P. L. B, pp. 382–386.
22. P. Napolitani and M. Colonna. "Inhomogeneity growth in two-component fermionic systems". In: Phys. Rev. C 96 (5 2017), p. 054609.
23. M. Colonna et al. "Fluctuations and dynamical instabilities in heavy-ion reactions". In: Nuclear Physics A 642.3–4 (1998), pp. 449–460.
24. D. Durand. "An event generator for the study of nuclear collisions in the Fermi energy domain (I). Formalism and first applications". In: Nuclear Physics A 541.2 (1992), pp. 266–294.
25. P. Napolitani, M. Colonna, and C. Mancini-Terracciano. "Cluster formation in nuclear reactions from mean-field inhomogeneities". In: submitted to: Journal of Physics: Conference Series - IOP. 2018. [arXiv:1801.07623](https://arxiv.org/abs/1801.07623) [nucl-th].
26. B. Braunn et al. "Comparisons of hadrontherapy-relevant data to nuclear interaction codes in the Geant4 toolkit". In: Journal of Physics: Conference Series 420 (2013), p. 012163.
27. J. Dudouet et al. "Benchmarking Geant4 nuclear models for hadron therapy with 95 MeV/nucleon carbon ions". In: Phys. Rev. C 89 (2014), p. 054616.

# Prototype Measurement System for the Eye-Hand Coordination Test of the Developmental Test of Visual Perception

Daniel Alejandro Quiroga-Torres, Juan S. Lara, Antonio Miguel-Cruz, and Adriana María Ríos-Rincón

## Abstract

The current version of the Developmental Test of Visual Perception (DTVP-3) is one of the most commonly used tests to identify the presence and degree of visual-perceptual and visual-integration deficits in children from 4 to 12 years of age. This test consists of five main sub-tests including a eye-hand coordination test (EHCT). Currently, the EHCT is based on observations by a therapist and requires a post-hoc analysis using the DTVP normative data, a time-consumption task that is not free of therapist error. Thus, a medical device is needed to automatically measure, score and report the test scores obtained from the DTVP-3. This device will lead to an overall decrease in the time taken for the post-hoc analysis and an improvement in the accuracy of the EHCT score. We determined that the device must allow a stylus position to be tracked in two dimensions with a resolution of 1 mm and the system must be small in size in order not to interfere with the test. In this study, we proposed a system based on Hall-effect technology sensors, which allows distances from the magnetic field magnitudes to be indirectly estimated using small sensors. A first prototype consisted of a matrix array of sensors. A radial basis function was used to model the

magnitude-distance response of each sensor. The model was estimated by using a multivariate linear regression, and it was found that the proposed model for 1 mm resolution tests, had an average  $r^2$  of 99%.

## Keywords

DTVP-3 • Eye-hand coordination test • Hall-effect technology • Measurement system

## 1 Introduction

Reading and writing difficulties at an early age can lead to future learning disabilities and difficulty with performing tasks as simple as a literary composition [1]. Eye-hand coordination (EHC) is one of the components that affects reading and writing processes, because problems such as illegible handwriting, and the inversion or disappearance of letters can be caused [2]. EHC assessment is usually performed by an occupational therapist using paper and pencil, although it is currently a process that requires considerable effort on the part of the therapist, who has to pay continual attention to the child's performance, i.e. even if the occupational therapist loses attention momentarily the validity of the results will be affected due to the lost information [3]. In addition, depending on the age range, the applicable test and the resulting score, standardized tables have to be consulted and analyzed [4], which limits the test in that the result is not generated immediately.

In this context, the Frostig Developmental Test of Visual Perception (DTVP-3) is one of the measures used to evaluate a patient's level of visual and motor perception [4, 5]. The DTVP-3 has five sub-tests of visual perception, in this study we are focusing on sub-test 1, which is a eye-hand coordination test (EHCT). This sub-test consists of a set of tracks where a line must be drawn along a certain path, if the patient leaves the demarcated area or lifts the pencil from the paper, his/her score for the sub-test will decrease.

D. A. Quiroga-Torres (✉) · J. S. Lara · A. Miguel-Cruz  
Biomedical Engineering Program, School of Medicine and Health Sciences, Universidad del Rosario, Calle 63D # 24-31, 7 de Agosto, Bogotá D.C., Colombia  
e-mail: daniel.quiroga@urosario.edu.co

J. S. Lara  
e-mail: juan.lara@urosario.edu.co

A. Miguel-Cruz  
e-mail: antonio.miguel@urosario.edu.co

A. M. Ríos-Rincón  
Occupational Therapy Program, School of Medicine and Health Sciences, Universidad del Rosario, Calle 63D # 24-31, 7 de Agosto, Bogotá D.C., Colombia  
e-mail: adriana.rios@urosario.edu.co



With regard to the abovementioned test, in this work a measurement system for the EHCT is proposed, which must be able to detect the slightest variation in the position of the pencil during the test. In addition, the aim of this study is to validate a prototype based on sensors that are small in size, which allows the minimum resolution necessary for the evaluation of sub-test 1. The proposed device could help occupational therapists to accurately assess a patient's performance during the test. Likewise, one of the main purposes of the system is data storage capacity over time; this information could be useful for therapists, as they would not need to perform a post-hoc analysis.

## 2 Methodology

Hall-effect technology is used for its two main advantages: (1) This kind of technology allows a magnetic field's magnitude to be measured, which in turn is related to the location of the magnetic source. (2) A Hall-effect sensor acts like a magnetic field transducer, i.e. this kind of sensor provides a voltage output in response to a magnetic field. For this reason, these sensors can be integrated into a digital system and the data can be stored and processed in an electronic device.

### 2.1 Experimental Setup

A first prototype consisting of a matrix array of four Hall-effect sensors is shown in Fig. 1. With this configuration, the measurements allow the distance between the

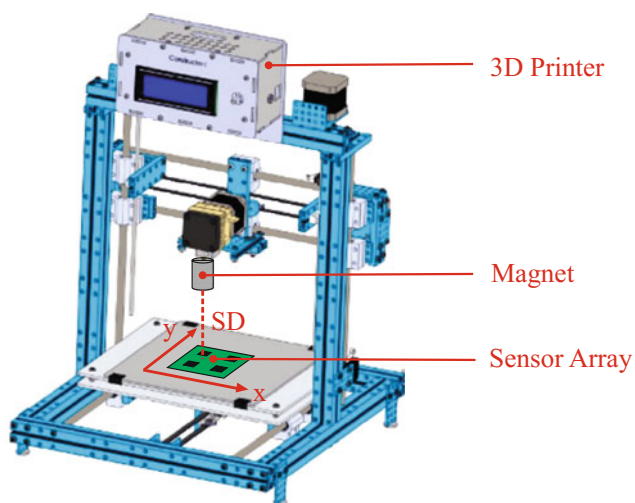


**Fig. 1** Diagram of the setup used in the experiments. The two main metrics are shown: The coordinate system ( $x, y$ ) and the separation distance (SD)

magnetic source and each sensor to be estimated, although the source is located within the square formed by the sensors (i.e. when the four sensors are detecting the magnetic source).

In this study, a neodymium cylindrical magnet ( $1 \times 2$  cm, N45) was used as the magnetic source. Likewise, the magnet is placed (see Fig. 1) on a MakeBlock Constructor I 3D printer (MakeBlock, China), allowing accurate three-dimensional movements.

Finally, the matrix array was built using 49E linear Hall-effect sensors (YZPST, China) due to their sensibility ( $1.4\text{--}3.0$  mV/GS) and compatibility with the 3D printer's electrical features.

Taking into account the fact that the stylus position in two dimensions is one of the most important metrics during the EHCT, the system must be set up to track the  $x$  and  $y$  position of the magnet. Nevertheless, the magnetic magnitude also depends on the separation distance (the  $z$ -axis position of the magnet), therefore, if the magnet's movements are constrained within a certain separation distance and the relationship between the distance and the magnetic magnitude is known, it is possible to track the magnet's two-dimensional position.

### 2.2 Model Selection

With regard to the distance-magnetic magnitude relationship, a model was selected according to the experimental data. In the first instance, in order to observe changes in the measurements due to variations in the magnet's position, the magnet moved around a sensor on a  $40 \times 40$  mm grid using 1 mm steps and a fixed separation distance of 10 mm.

This procedure allows two relevant features to be identified that must be included in the model. On one hand, as shown in Fig. 2a, the measured equipotential lines are circular in shape and are centered on the sensor's position, thus, it is simple to use a Radial Basis Function (RBF) as a model. On the other hand, as shown in Fig. 2b, c, the changes' behavior in the measured voltage is exponential, more precisely, the curves have a Gaussian shape. Therefore, the model must include an exponential part.

With regard to the aforementioned, the proposed model is shown in Eq. 1. Where  $s_i$  is the magnitude response of a sensor  $i$ ,  $A$  is the scale factor in the exponential part,  $(x, y)$  is a point in space,  $(\mu_x, \mu_y)$  is the sensor's location,  $\alpha$  and  $\beta$  are the scale factors in the radial part.

$$s_i = Ae^{\alpha(x-\mu_x)^2 + \beta(y-\mu_y)^2} \quad (1)$$

The  $\mu_x$  and  $\mu_y$  parameters can be estimated as the Center of Mass (CoM) in each dimension of the measured data, as shown in Eq. 2, where  $n$  and  $m$  are the total number of

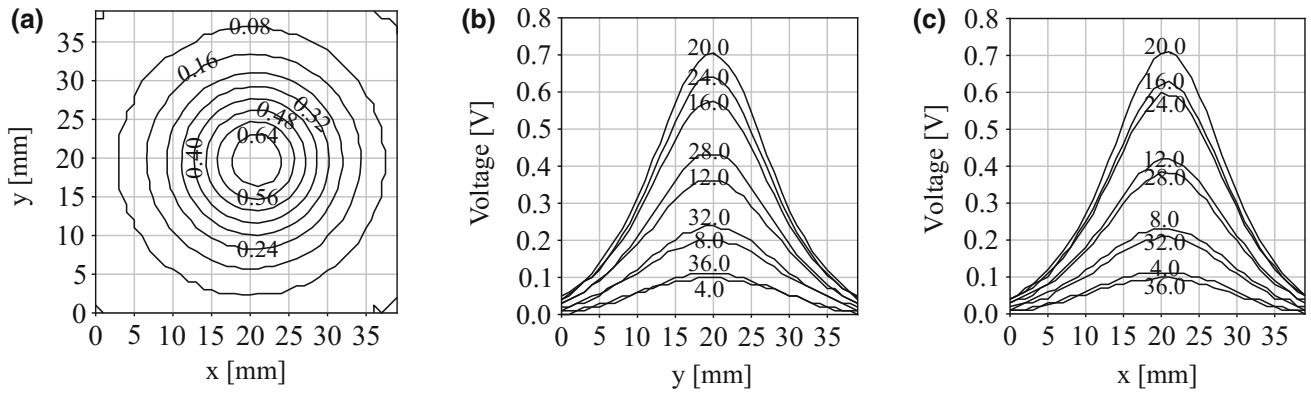


**Fig. 2** The experimental data used to identify the behavior of the measured magnetic magnitude. In **a** are shown the equipotential lines and their respective values. In **b** are shown the measured magnitude's

responses at different  $y$  values with scalars representing the  $x$  value. In **c** is shown the same response, but at different  $x$  values with scalars representing the  $y$  value

observations on each axis and  $z[i,j]$  is the measured value in the point  $(i,j)$ .

$$\mu_x = \frac{\sum_{i=1}^n (i \sum_{j=1}^m (z[i,j]))}{\sum_{i=1}^n \sum_{j=1}^m (z[i,j])}; \quad \mu_y = \frac{\sum_{j=1}^m (j \sum_{i=1}^n (z[i,j]))}{\sum_{i=1}^n \sum_{j=1}^m (z[i,j])} \quad (2)$$

One of the main advantages of the proposed model is that it can be easily converted into a generalized linear model (GLM) through parameterization, i.e. if  $z_i = \ln(s_i)$ ,  $\epsilon = \ln(A)$ ,  $x' = (x - \mu_x)^2$  and  $y' = (y - \mu_y)^2$ ; then the model will be in a GLM form, as shown in Eq. 3; thus, parameters such as  $\epsilon$ ,  $\alpha$  and  $\beta$  can be estimated using linear regression. Nevertheless, considering that there are multiple sensors, the model's parameters for each sensor can be estimated with multivariate linear regression.

$$z_i = \alpha x' + \beta y' + \epsilon \quad (3)$$

Finally, it is possible to estimate the distance between a sensor  $i$  and the magnet if  $\alpha \approx \beta$ , which means that there is symmetry in the exponential behavior between the  $x$  and  $y$  axes. Therefore, the estimated distance  $r_i$  depends on the model's parameters ( $\epsilon$ ,  $\alpha$  and  $\beta$ ) and the measured voltage ( $s_i$ ), as shown in Eq. 4.

$$r_i = \sqrt{\frac{\ln(s_i/A)}{|0.5\alpha + 0.5\beta|}} \quad (4)$$

### 3 Results

As already mentioned in Sect. 2.2, the RBF model was selected experimentally; moreover, it is possible to assess the quality of the predictions. For instance, in the proposed prototype the separation distance between the sensors is

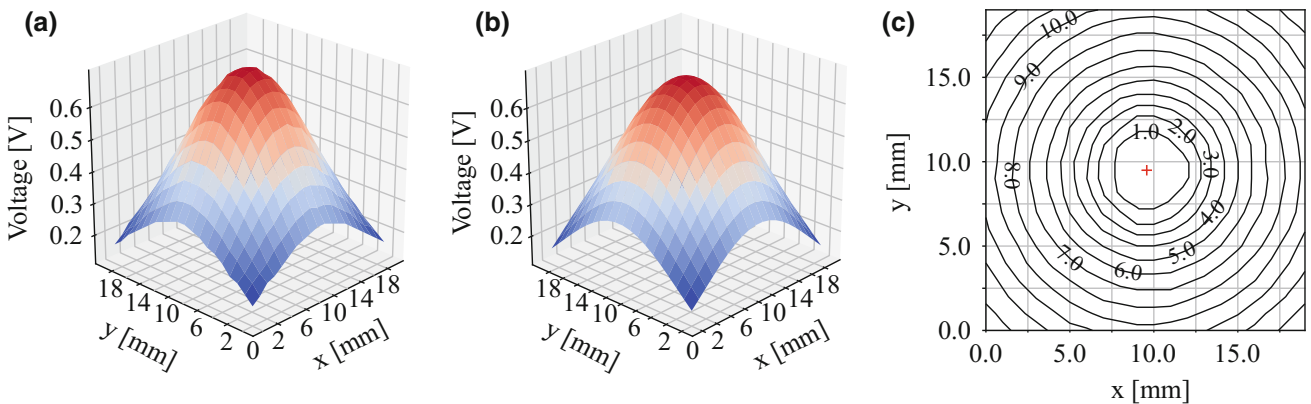


**Fig. 3** Example of a distance estimation using the proposed model. In **a** are shown the voltage measurements of one sensor at a fixed separation distance, in **b** are shown the voltage predictions using the

RBF model and in **c** are shown the CoM of the data and different distance level curves estimated with the model

**Table 1** Linear regression analysis of the model's  $\alpha$  and  $\epsilon$ . The three main metrics are shown: the coefficient of determination ( $r^2$ ), the regression's estimated parameters ( $\theta_1$  and  $\theta_0$ ) and the Pearson correlation coefficient ( $\rho$ )

Sensor	$\alpha$				$\epsilon$			
	$r_\alpha^2$	$\theta_{1\alpha}$	$\theta_{0\alpha}$	$\rho_\alpha$	$r_\epsilon^2$	$\theta_{1\epsilon}$	$\theta_{0\epsilon}$	$\rho_\epsilon$
1	0.98	$75 \times 10^{-5}$	$-16 \times 10^{-3}$	0.99	0.99	-0.15	1.39	-0.99
2	0.98	$76 \times 10^{-5}$	$-16 \times 10^{-3}$	0.99	0.99	-0.14	1.38	-0.99
3	0.98	$72 \times 10^{-5}$	$-16 \times 10^{-3}$	0.99	0.99	-0.14	1.25	-0.99
4	0.98	$73 \times 10^{-5}$	$-16 \times 10^{-3}$	0.99	0.99	-0.14	1.36	-0.99

10 mm; therefore, the measurements were sampled on a  $20 \times 20$  mm grid because it is more convenient that the model fits better within ranges where the voltage is higher (i.e. the nearest points to the sensor that it is measuring).

To illustrate, in Fig. 3a is shown an example of the measurements from one sensor; likewise, in Fig. 3b is shown a graph of the estimated model for the data that is shown in Fig. 3a. It is possible to observe the similarity between the model's predictions and the measurements, which in turn is reflected in a  $r^2$  of 0.99. Finally, in Fig. 3c are shown the distances estimated through the expression of Eq. 4.

The proposed model is intended to be used at a fixed separation distance, which corresponds to the normal usage of the prototype during the EHCT, although the model varies depending on the design parameters, or more precisely, the separation distance. For this reason, the model was evaluated at different separation distances within a range of between 9 and 14 mm and with a resolution of 0.1 mm.

With regard to the relationship between the model's parameters and the separation distance, in Table 1 are shown the values related to a linear regression analysis. It was found that the  $r^2$  values are equal for all the sensors and close to 1; in addition, the Pearson correlation coefficients are always positive between the  $\alpha$  parameter the separation distance (SD), while they are negative between the  $\epsilon$  parameter and the SD. In addition, these two parameters ( $\alpha$  and  $\epsilon$ ) show a linear behavior with regard to the SD.

## 4 Discussion

As shown in Fig. 3c, the RBF model allows distances from magnetic magnitude measurements to be estimated. Most importantly, the estimated distances show linear behavior, which can be observed in two ways. On one hand, each distance level curve is similar to a circumference, i.e. the model preserves the radial behavior of the magnetic magnitude after the distance estimation; on the other hand, each level curve is located equidistantly to the others and the estimated distances correspond to the real distances between the magnet and the estimated sensor's position (CoM) [6].

One of the key concepts to come out of this work is the need for a measurement system that allows the stylus position to be tracked with a resolution of 1 mm. Hence, the proposed model allows distances to be predicted within the specified ranges with a high  $r^2$ , showing that the error variance ratio is around 1%, which in part is related to unwanted events such as electromagnetic noise, temperature changes and manufacturing defects, among others.

One of the main advantages of the prototype is that there are multiple sensors located at different points, thus making it possible to estimate the position of the magnet from different perspectives, which is expected to allow the measuring error to decrease using an individual sensor. Equally important, considering that the location of each sensor is known and the method allows the distance between the magnet and each sensor to be estimated, it is possible to estimate the magnet's two-dimensional position through triangulation [7].

It is important to highlight that the coefficient of determination ( $r^2$ ) has an average of around 0.99 for all the sensors, showing that the RBF model can be used properly within the specified range. However, choosing a separation distance outside of this range could lead to two unwanted events: (1) When the separation distance is below the lower limit, there may be saturation in the sensors and it will not be possible to differentiate between distances when the magnet is within a range closer to the sensor's location. (2) When the separation distance is greater than the upper limit, the magnitude will be within a low range and the measurements are subject to noise interference.

The device allows the pen to be used in standardized tests. While it is true that a tablet with a stylus can perform the same activity, in the case of pencil and paper, specialized body functions are needed to perform the strokes effectively. The table allows you to have an infinite number of test options to do, something you can't have on paper [8]. However, the important thing about the DTVP-3 test is to evaluate hand-eye coordination, and with pencil and paper these skills are better developed [9]. Finally, we find cases of children who do not have their skills fully developed and the use of pencil and paper helps them properly [10].

## 5 Conclusions and Future Work

With regard to the obtained results, the proposed prototype allows the stylus position to be detected with a resolution of 1 mm, thus making this prototype suitable for the evaluation of the EHCT of the DTVP-3 test. This study shows that it is possible to accurately estimate distances using Hall-effect technology; therefore, it is possible to design devices based on this proposal for similar tracking applications.

The aim of future works is to determine the trajectory of a magnet with a larger sensor array using triangulation techniques. In addition, kinematic models will be implemented in order to improve the measurement results. Finally, the final version of the system will be subject to clinical validation, thus ensuring it can be used clinically.

**Acknowledgements** We would like to thank the Universidad del Rosario for the resources they provided and the internal grant for financing the innovation and technological entrepreneurship projects with the number IV-FCS005.

**Conflicts of Interest** The authors report no conflicts of interest.

---

## References

1. Spira, E.G., Bracken, S.S., Fischel, J.E.: Predicting Improvement after first-grade reading difficulties: The effects of oral language, emergent literacy, and behavior skills. *Developmental Psychology* 41(1), 225–234 (2005)
2. Iglesias, R.: La lectoescritura desde edades tempranas, consideracion teóricas-prácticas. In: Congreso Mundial de Lecto-escritura. vol. 1, pp. 1–41. Valencia (2000)
3. Brown, T., Rodger, S., Davis, A.: Factor Structure of the Four Motor-Free Scales of the Developmental Test of Visual Perception, 2nd Edition (DTVP-2). *The American Journal of Occupational Therapy* 62(5), 502–513 (2008)
4. Hammil, D.D., Pearson, N.A., Voress, J.K.: *Developmental Test of Visual Perception (DTVP-3)*. Pro ed Inc, Texas, third edn. (2014)
5. Clutten, C.S.: The development of a visual perception test for learners in the foundation phase (2009), <http://hdl.handle.net/10500/2613>
6. Ocaña, M., Bergasa, L.M., Sotelo, M.A., Nuevo, J., Flores, R.: Indoor robot localization system using WiFi signal measure and minimizing calibration effort. In: *IEEE International Symposium on Industrial Electronics*. vol. IV, pp. 1545–1550. IEEE, Dubrovnik (2005)
7. Niculescu, D., Nath, B.: Position and orientation in ad hoc networks. *Ad Hoc Networks* 2(2), 133–151 (2004)
8. Kunz, A.M., Pfadenhauer, M.: One Campus Many Ways to Go?! A methodological comparison of paper-pencil and electronic log-books when exploring students' patterns of spatial use. *Journal of New Frontiers in Spatial Concepts* 6, 21–27 (2014)
9. Haßler, B., Major, L., Hennessy, S.: Tablet use in schools: A critical review of the evidence for learning outcomes. *Journal of Computer Assisted Learning* 32(2), 139–156 (2016)
10. Taherbhai, H., Seo, D., Bowman, T.: Comparison of paper pencil and online performances of students with learning disabilities. *British Educational Research Journal* 38(1), 61–74 (2012)

1. Spira, E.G., Bracken, S.S., Fischel, J.E.: Predicting Improvement after first-grade reading difficulties: The effects of oral language,

# The Implications of the Lead Theory on the Patch ECG Devices Positioning and Measurement

Ivan Tomasic, Aleksandra Rashkovska, Roman Trobec, and Maria Lindén

## Abstract

Currently we are witnessing fast development of patch ECG devices, some of which have already been extensively evaluated and shown to be useful for detecting arrhythmias. The research about using the patch ECG devices for purposes other than arrhythmia detection has been scarce. The efficiency of patch electrocardiography for a specific purpose can depend on the devices location on the body surface. It is still an open question where to position the ECG patch devices, and should the position depend on the specific purpose and perhaps even be personalized. We present the lead theory of differential leads (ECG leads obtained by patch ECG devices) and discuss its implications on the patch ECG devices positioning on the body surface.

## Keywords

Electrocardiography • ECG • Lead theory  
Differential lead • Bipolar lead • Patch monitors  
Remote monitoring • Telemonitoring

## 1 Introduction

For the purpose of detecting arrhythmias in normal daily activities, Holter monitors are traditionally used. Recently however, there has been an intensive development of wireless bi-potential patch ECG devices (PECGs) [1–3], which are starting to challenge the Holters since they are unobtrusive, wire free, and with much longer recording capabilities (weeks to months). The PECGs can also be used for monitoring fetal ECGs [4], obtaining breathing rate

[5], or even for obtaining electromyography (EMG) measurements [6].

The Savvy monitor ([www.savvy.si](http://www.savvy.si)) has been certified as a medical device and has recently become available on the market (Fig. 1), whereas the ZIO® XT Patch ([irhythmtech.com/products-services/zio-xt](http://irhythmtech.com/products-services/zio-xt)), and SEEQ® MCT patch device from Medtronic, have already been extensively evaluated. The evaluations show evidence of an increased diagnostic lead in both adult and pediatric patients, compared to Holters [2]. One additional example is the ePatch from BioTelemetry Inc. Denmark. Compared to the before mentioned PECGs which can record one lead, the ePatch® can record up to 3 leads but it does not provide wireless data transmission. In addition to Savvy and SEEQ, the Spyder BT sensor ([www.web-biotech.com](http://www.web-biotech.com)) and Cortrium C3 ([cortrium.com](http://cortrium.com)) also provide wireless data transmission. The LifeTouch Patient Surveillance System ([isansys.com/en/products/sensors](http://isansys.com/en/products/sensors)), is a device which provides heart rate and respiratory rate (derived from the ECG), and has a wireless data connection. For a direct comparison of Savvy, SEEQ, and ZIO patch monitors technical characteristics, the reader is referred to [7].

The ECG leads produced by patch ECG monitors are often called differential leads (DLs) [8]. The DLs can provide ECG signals with satisfactory signal-to-noise ratio [9] and can even be used for synthesizing the 12-lead ECG, the sole standard in today's electrocardiography. The synthesis can be performed with linear and nonlinear methods [10, 11]. Recent publications, besides traditional methods, like multiple linear regression [12], report also some novel approaches for ECG leads synthesis, like genetic algorithm optimized neural networks [13], support vector regression [14], regression trees [15], and state-space models [16]. Some researchers apply linear transformation on independent [17] or principal components [18–23], or on derived characteristics in the wavelet domain [24, 25], instead of transforming original signals.

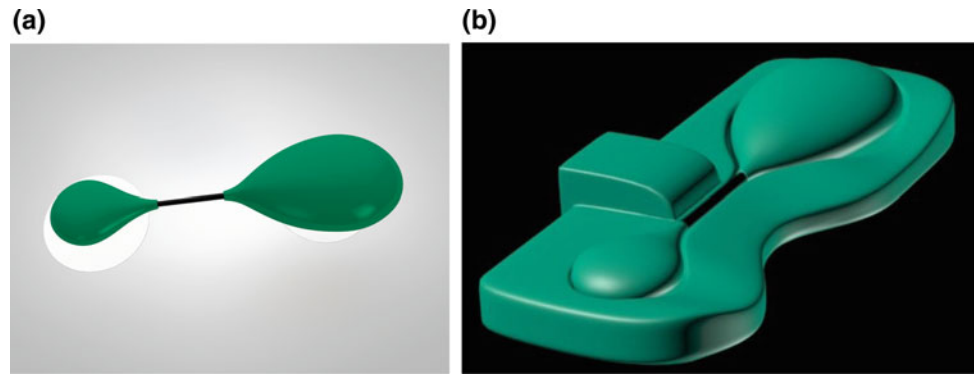
The deterministic method of synthesis [10, 26] was used by Cao et al. to synthesize the 12-lead ECG from three DLs

I. Tomasic (✉) · M. Lindén  
Mälardalen University, Västerås, Sweden  
e-mail: [ivan.tomasic@mdh.se](mailto:ivan.tomasic@mdh.se)

A. Rashkovska · R. Trobec  
Jožef Stefan Institute, Ljubljana, Slovenia



**Fig. 1** Savvy sensor. **a** The wearable body sensor in biocompatible housing with two self-adhesive electrodes attached. **b** The body sensor during charging, placed in the charging dock



[27], whereas a number of investigations [8, 28–31] used linear transformation for the same purpose, with comparable results. Lee et al. used both linear regression and artificial neural networks to synthesize 12-lead ECG from 3 DLs that can be implemented as a single patch device [32].

### 1.1 Evaluations of the PECG Monitors

A Philips experimental device featuring three DLs has been shown to provide high agreement with the EASI Holter monitor, in terms of “evaluation of atrial activity, ventricular morphology, rhythm diagnosis” [33], as well as for “recognition of ventricular ectopic activity and ventricular fibrillation” [34]. Similarly, an evaluation of the Imec’s ECG patch on ten subjects, showed that “the new ECG patch has the same performance as a medical gold standard Holter” for atrial fibrillation detection [35]. Zio Patch [36] evaluations however show that during one day it detects significantly less arrhythmic events than a Holter monitor, but over the total wear time, it detects more arrhythmic events than the Holter monitor. A clinical evaluation of the WPR Medical monitor shows that “recorded ECG signals obtained from the wireless ECG system had an acceptable quality for arrhythmia diagnosis” [37]. Additionally, the ePatch [38] has been shown to be adequate for rhythm analysis.

There has been very little research about applicability of DLs for specific purposes other than arrhythmia detection. It has been shown [39, 40] that a DL can provide better sensitivity for detecting left ventricular hypertrophy compared to the 12-lead ECG. Furthermore, the so-called CM5 lead—a specific lead between the manubrium and the V5 position—has been shown to contribute to increased sensitivity of the exercise ECG to the coronary artery disease [41]. Haddad et al. have shown a possible application of DLs for detecting acute transmural myocardial ischemia [42].

Here we present the DLs’ theory, understanding of which can leverage future research in applying patch ECG devices, as well as facilitate interpreting DLs obtained from them.

## 2 ECG Theory for Patch Electrocardiography

### 2.1 Lead Field of a DL

By using the electromagnetic reciprocity theorem, it can be shown that the lead field of an ECG lead with electrodes on positions  $Q_1$  and  $Q_2$  (see Fig. 2), is equal to the gradient of the potential field  $\phi_0$ , caused by a pair of a unit current source and a sink of equal strength  $I_0$ , placed at the lead’s electrodes positions [43]:

$$\vec{L}_{Q_1 Q_2}(x, y, z) = \frac{\nabla \phi_0}{I_0}, \quad (1)$$

where  $\vec{L}_{Q_1 Q_2}(x, y, z)$  is the lead field for the lead defined by the points  $Q_1$  and  $Q_2$ .

To easily illustrate the lead field, we can consider that the current density in a volume conductor is directly proportional to the gradient of the potential  $\vec{J}_0^L = -\sigma \nabla \phi_0$ . If we apply this to Eq. 1, we get:

$$\vec{L}_{Q_1 Q_2}(x, y, z) = \frac{\nabla \phi_0}{I_0} = \frac{-\vec{J}_0^L(x, y, z)}{I_0 \sigma}, \quad (2)$$

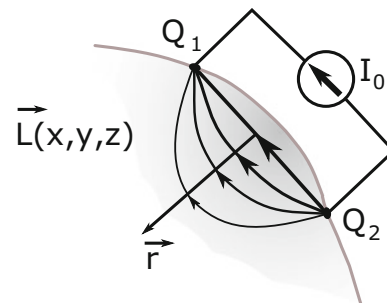


**Fig. 2** The lead field of a DL. The lines with arrows within the volume conductor (gray space) represent the lead field  $\vec{L}$ . The lead field is proportional to the current flow field arising from a unit current introduced at  $Q_1$  and removed at  $Q_2$ , and has the opposite direction. The bowing of the field increases with  $r$ , whereas the field magnitude (i.e., the current strength) decreases with  $r^3$

where  $\vec{J}_0^L(x, y, z)$  denotes the current density due to unit reciprocal current  $I_0$  and  $\sigma$  is the conductivity distribution through the volume conductor. Hence the lead field amplitude and direction, for the lead defined by two electrodes, is equivalent to the structure of the current density between the same two electrodes, but respecting that the current and the potential gradient have opposite directions (see Fig. 2).

The lead field is a sensitivity distribution of a lead, as its role is to weight (i.e. multiply in terms of scalar product) each current source element  $\vec{J}^i$  in myocardium, before it is summed into the lead voltage [43]. A larger magnitude of  $\vec{J}_0^L$  at a part of myocardium  $dV$ , and a smaller angle between  $\vec{J}^i$  and  $\vec{J}_0^L$  at  $dV$ , result in a larger contribution of  $\vec{J}^i$  at  $dV$  to the measured voltage. The equation that describes this is [43]:

$$V_{Q_1 Q_2} = \int \frac{\nabla \phi_0}{I_0} \cdot \vec{J}^i dV = \frac{1}{I_0} \int \left( \frac{-\vec{J}_0^L}{\sigma} \right) \cdot \vec{J}^i dV. \quad (3)$$

$V_{Q_1 Q_2}$  is the measured voltage,  $\sigma$  is in general a function of position and time:  $\sigma = \sigma(x, y, z, t)$  through the myocardium, and  $\vec{J}^i$  is the volume source impressed current vector field, which also depends on position and time:  $\vec{J}^i = \vec{J}^i(x, y, z, t)$ .

## 2.2 Differential Lead Positioning

For a closely spaced electrode pair, i.e. for a DL, according to Eq. 1, the lead field can be represented with the gradient of a dipole field. This is because a dipole can represent the current source and the sink at the electrodes  $Q_1$  and  $Q_2$  of a DL, since it is a pair of a current source and a current sink of the same current strength  $I_d$ , separated by a small displacement  $d$ . The mathematical definition of a dipole requires  $d \rightarrow 0, I_d \rightarrow \infty$ , with  $p = I_d \cdot d$  remaining finite. The quantity  $p$  is the moment or magnitude of the dipole. The dipole is a vector  $\vec{p}$  with magnitude  $p$  and direction from the negative source (sink) towards the positive source [44].

The potential field of a dipole  $\vec{p}$  and its gradient [45] are given by:

$$\phi_D = \frac{\vec{a}_r \cdot \vec{p}}{4\pi\sigma r^2}, \quad \nabla \phi_D = -\frac{1}{4\pi\sigma r^3} [3(\vec{a}_r \cdot \vec{p})\vec{a}_r - \vec{p}], \quad (4)$$

where  $\vec{r}$  is the radius vector for a point in space at which the field is evaluated, and  $\vec{a}_r$  is the unit vector in the direction of  $\vec{r}$ . The Eq. 4 shows that a DL lead field weakens with the cube of the distance, which is faster compared to the field of a point electrode which varies with a square of the distance [43]. Consequently, the source elements closer to the DLs electrodes' positions are weighted more strongly, by a factor of  $\frac{1}{r^3}$ . Figure 2 illustrates the lead field of a DL.

## 3 Conclusion

A PEGC measures potential difference between two body surface electrodes, on a distance which is usually less than 10 cm. The lead theory presented justifies the PEGCs to be considered as focused cardiac electrical activity detection devices. This is because the magnitude of a DL's lead field drops with a cube of the distance from the PEGC measuring the DL.

There are still no established and widely accepted guidelines as to how to position the PEGCs on the body surface. In contrast to the 12-lead electrode positioning which is fixed, the PEGCs can potentially have different placing depending on a specific purpose. For instance, PEGCs can be placed so that they pick up more "information" about a specific side or part of the heart, or perhaps placed with an intention of achieving a better accuracy for detecting a specific type of arrhythmia.

The presented theoretical consideration can facilitate interpreting DLs obtained from PEGCs, and leverage the future research in applying PEGCs for specific purposes, the research which has been scarce so far.

**Acknowledgements** I. Tomasic gratefully acknowledges the funding by the Swedish Knowledge Foundation (KKS), project name: CCOPLD (reference number 20160029), and support by the Embedded sensor systems for health research profile, also funded by the KKS. R. Trobec and A. Rashkovska acknowledge the financial support of the Slovenian Research Agency under Grant P2-0095.

## References

1. Baig, M.M., Gholamhosseini, H., Connolly, M.J.: A comprehensive survey of wearable and wireless ECG monitoring systems for older adults. *MBEC* **51**(5), 485–495 (2013)
2. Fung, E., Jrvelin, M.R., Doshi, R.N., Shinbane, J.S., Carlson, S.K., Grazette, L.P., Chang, P.M., Sangha, R.S., Huikuri, H.V., Peters, N.S.: Electrocardiographic patch devices and contemporary wireless cardiac monitoring. *Front Physiol* **6**, 149 (2015)
3. Guzik, P., Malik, M.: ECG by mobile technologies. *J Electrocardiol* **49**(6), 894–901 (2016)
4. Rashkovska, A., Avbelj, V.: Abdominal fetal ECG measured with differential ECG sensor. In: *MIPRO*, pp. 289–291 (2017)
5. Trobec, R., Rashkovska, A., Avbelj, V.: Two proximal skin electrodes—a respiration rate body sensor. *Sensors (Basel)* **12**(10), 13,813–13,828 (2012)
6. Tomasic, I., Avbelj, V., Trobec, R.: Smart wireless sensor for physiological monitoring. *Studies in Health Technology and Informatics* **211**, 259–301 (2015)
7. Trobec, R., Tomasic, I., Rashkovska, A., Depolli, M., Avbelj, V.: Commercial ECG systems. In: *Body Sensors and Electrocardiography*, chap. 6, pp. 101–114. Springer International Publishing (2018)
8. Trobec, R., Tomasic, I.: Synthesis of the 12-lead electrocardiogram from differential leads. *IEEE Trans Inf Technol Biomed* **15**(4), 615–621 (2011)

9. Puurtinen, M., Viik, J., Hyttinen, J.: Best electrode locations for a small bipolar ECG device: signal strength analysis of clinical data. *Ann Biomed Eng* **37**(2), 331–336 (2009)
10. Tomašić, I., Trobec, R.: Electrocardiographic systems with reduced numbers of leads-synthesis of the 12-lead ECG. *IEEE Rev Biomed Eng* **7**, 126–142 (2014)
11. Vozda, M., Cerny, M.: Methods for derivation of orthogonal leads from 12-lead electrocardiogram: A review. *Biomed. Signal Proces.* **19**, 23–34 (2015)
12. Figueiredo, C.P., Mendes, P.M.: Towards wearable and continuous 12-lead electrocardiogram monitoring: Synthesis of the 12-lead electrocardiogram using 3 wireless single-lead sensors. In: *BIODEVICES*, pp. 329–332 (2012)
13. Chen, F., Pan, Y., Li, K., Cheng, K.T., Huan, R.: Standard 12-lead ECG synthesis using a GA optimized BP neural network. In: *ICACI*, pp. 289–293 (2015)
14. Yodjaiphet, A., Theera-Umpon, N., Auephanwiriyakul, S.: Electrocardiogram reconstruction using support vector regression. In: *ISSPIT*, pp. 269–273 (2012)
15. Tomasic, I., Trobec, R., Lindén, M.: Can the regression trees be used to model relation between ECG leads? In: *Internet of Things. IoT Infrastructures*, pp. 467–472. Springer International Publishing (2016)
16. Lee, J., Kim, M., Kim, J.: Reconstruction of precordial lead electrocardiogram from limb leads using the state-space model. *IEEE J Biomed Health* **20**(3), 818–828 (2016)
17. Tsouri, G.R., Ostertag, M.H.: Patient-specific 12-lead ECG reconstruction from sparse electrodes using independent component analysis. *IEEE J Biomed Health* **18**(2), 476–482 (2014)
18. Tomašić, I., Skala, K., Trobec, R.: Principal component analysis and visualization in optimization and personalization of lead's set for generation of standard 12-leads ECG. In: *MIPRO*, pp. 307–313 (2008)
19. Mann, S., Orglmeister, R.: PCA-based ECG lead reconstruction. *Biomedizinische Technik. Biomedical engineering* **58**(Suppl. 1), 24–25 (2013)
20. Dawson, D., Yang, H., Malshe, M., Bukkapatnam, S.T.S., Benjamin, B., Komanduri, R.: Linear affine transformations between 3-lead (Frank XYZ leads) vectorcardiogram and 12-lead electrocardiogram signals. *J Electrocardiol* **42**(6), 622–630 (2009)
21. Padhy, S., Dandapat, S.: Synthesis of 12-lead ECG from a reduced lead set using singular value decomposition. *PCITC* pp. 316–320 (2015)
22. Padhy, S., Dandapat, S.: SVD analysis on reduced 3-lead ECG data. In: *Advances in Communication and Computing*, pp. 253–260. Springer India, New Delhi (2015)
23. Maheshwari, S., Acharyya, A., Schiariti, M., Puddu, P.E.: Personalized reduced 3-lead system formation methodology for remote health monitoring applications and reconstruction of standard 12-lead system. *Int Arch Med* **8** (2015). <https://doi.org/10.3823/1661>
24. Nallikuzhy, J.J., Dandapat, S.: Enhancement of the spatial resolution of ECG using multi-scale linear regression. In: *Proceedings of NCC*, pp. 1–6 (2015)
25. Nallikuzhy, J.J., Dandapat, S.: Spatial enhancement of ECG using diagnostic similarity score based lead selective multi-scale linear model. *Comput Biol Med* **85**, 53–62 (2017)
26. Kors, J.A.: Lead transformations and the dipole approximation: Practical applications. *J. Electrocardiol.* **48**(6), 1040–1044 (2015). <https://doi.org/10.1016/j.jelectrocard.2015.08.015>
27. Cao, H., Li, H., Stocco, L., Leung, V.C.M.: Wireless three-pad ECG system: Challenges, design, and evaluations. *J Commun Netw* **13**(2), 113–124 (2011)
28. Hansen, I.H., Hoppe, K., Gjerde, A., Kanters, J.K., Sorensen, H.B. D.: Comparing twelve-lead electrocardiography with close-to-heart patch based electrocardiography. In: *EMBC*, pp. 330–333 (2015)
29. Farotto, D., Atallah, L., van der Heijden, P., Grieten, L.: ECG synthesis from separate wearable bipolar electrodes. In: *EMBC*, pp. 5058–5061 (2015)
30. Tomašić, I., Frljak, S., Trobec, R.: Estimating the universal positions of wireless body electrodes for measuring cardiac electrical activity. *IEEE Trans Inf Technol Biomed* **60**(12), 3368–3374 (2013)
31. Hsu, C.H., Wu, S.H.: Robust signal synthesis of the 12-lead ECG using 3-lead wireless ECG systems. In: *ICC*, pp. 3517–3522 (2014)
32. Lee, H., Lee, D., Kwon, H., Kim, D., Park, K.: Reconstruction of 12-lead ECG using a single-patch device. *Method Inform Med* **56** (4), 319–327 (2017)
33. Janata, A., Lemmert, M.E., Russell, J.K., Gehman, S., Fleischhackl, R., Robak, O., Pernicka, E., Sterz, F., Gorgels, A.P.: Quality of ECG monitoring with a miniature ECG recorder. *Pace* **31**(6), 676–684 (2008)
34. Lemmert, M.E., Janata, A., Erkens, P., Russell, J.K., Gehman, S., Nammi, K., Crijns, H.J., Sterz, F., Gorgels, A.P.: Detection of ventricular ectopy by a novel miniature electrocardiogram recorder. *J. Electrocardiol.* **44**(2), 222–228 (2011)
35. Torfs, T., Smeets, C.J., Geng, D., Berset, T., der Auwera, J.V., Vandervoort, P., Grieten, L.: Clinical validation of a low-power and wearable ECG patch for long term full-disclosure monitoring. *J. Electrocardiol.* **47**(6), 881–889 (2014)
36. Barrett, P.M., Komatireddy, R., Haaser, S., Topol, S., Sheard, J., Encinas, J., Fought, A.J., Topol, E.J.: Comparison of 24-hour Holter monitoring with 14-day novel adhesive patch electrocardiographic monitoring. *Am. J. Med.* **127**(1), 95.e11–7 (2014)
37. Fensli, R., Gundersen, T., Snaprud, T., Hejlesen, O.: Clinical evaluation of a wireless ECG sensor system for arrhythmia diagnostic purposes. *Med Eng Phys* **35**(6), 697–703 (2013)
38. Saadi, D., Fauerskov, I., Osmanagic, A., Sheta, H., Sorensen, H., Egstrup, K., Hoppe, K.: Heart rhythm analysis using ECG recorded with a novel sternum based patch technology: A pilot study. In: *CARDIOTECHNIX*, pp. 15–21 (2013)
39. Väisänen, J., Puurtinen, M., Hyttinen, J., Viik, J.: Short distance bipolar electrocardiographic leads in diagnosis of left ventricular hypertrophy. *Computing in Cardiology* **37**, 293–296 (2010)
40. Puurtinen, M., Väisänen, J., Viik, J., Hyttinen, J.: New precordial bipolar electrocardiographic leads for detecting left ventricular hypertrophy. *J Electrocardiol* **43**(6), 654–659 (2010)
41. Puurtinen, M., Nieminen, T., Kähkönen, M., Lehtimäki, T., Lehtinen, R., Nikus, K., Hyttinen, J., Viik, J.: Value of leads V4R and CM5 in the detection of coronary artery disease during exercise electrocardiographic test. *Clin Physiol Funct I* **30**(4), 308–312 (2010)
42. Haddad, M.E., Vervloet, D., Taeymans, Y., Buyzere, M.D., Bov, T., Stroobandt, R., Duytschaever, M., Malmivuo, J., Gheeraert, P.: Diagnostic accuracy of a novel method for detection of acute transmural myocardial ischemia based upon a self-applicable 3-lead configuration. *J. Electrocardiol.* **49**(2), 192–201 (2016)
43. Trobec, R., Tomasic, I., Rashkovska, A., Depolli, M., Avbelj, V.: Lead theory of differential leads and synthesis of the standard 12-lead ECG. In: *Body Sensors and Electrocardiography*, chap. 5, pp. 77–100. Springer International Publishing (2018)
44. Malmivuo, J., Plonsey, R.: Dipole. In: *Bioelectromagnetism*, chap. 8.2. Oxford University Press (1995)
45. Griffiths, D.J.: The electric field of a dipole. In: *Introduction to Electrodynamics*, 3 edn., chap. 3.4.4, pp. 153–155. Prentice Hall (1999)

# VirRespir—An Application for Virtual Pneumonological Experimentation and Clinical Training

Krzysztof Zieliński<sup>✉</sup>, Anna Stecka<sup>✉</sup>, and Tomasz Gólczewski<sup>✉</sup>

## Abstract

Computer models are a useful tool in research and education. They have a particular value in medicine and biology due to legal and ethical restrictions. Considering the above, a general-purpose virtual patient (ViP) has been developed in the Nalecz Institute of Biocybernetics and Biomedical Engineering to be used for various kinds of simulations, both in analyses of cardio-respiratory problems and staff training, including distal e-learning. ViP is a system of mutually cooperating models, the main of which are models of the respiratory system mechanics, pulmonary circulation, and gas transfer and exchange. The VirRespir system containing ViP was developed in the form of a web application accessible from <http://virrespir.ibib.waw.pl/> to enable other users to use it in their works. Although there are several complex models of the cardiovascular system, their pulmonary part is usually simplified in comparison with the other parts. Therefore the end-user of VirRespir has two options: he/she either can use VirRespir with an embedded simple model the heart and systemic circulation or can unite ViP and own complex model. The latter is a unique feature and may be very useful for scientists being experts in cardiovascular modeling but not familiar with pulmonary issues.

## Keywords

Virtual patient • Modeling and simulation  
Cardio-respiratory model

## 1 Introduction

Computer models are a powerful tool in research, medical training and education. In particular, simulations of medical procedures can help to understand phenomena observed in real patients (e.g. [1]). Although there are several more or less complex numerical models of the cardiovascular system (e.g. [2–4]), their pulmonary parts are usually simplified in comparison to the other parts. Thus, important respiratory system properties are not taken into account despite that interactions between the cardiovascular and respiratory systems can be extremely important in some cases; dyspnea in heart failure is an example. Merging models of various parts of the cardiovascular and respiratory systems may give a one but complex model, which can be treated as Virtual Patient (ViP).

VirRespir is such a ViP free accessible through Internet from <http://virrespir.ibib.waw.pl/>, as a web application [5]. It can be used either as a stand-alone complex model or as a kind of pulmonary supplement to a model of the heart and systemic circulation (HSC) developed by the end-user.

## 2 VirRespir Presentation

### 2.1 VirRespir Overview

The VirRespir system in the form of a web application has been developed in the C# language using Microsoft® Silverlight™ technology and is hosted in the server of the Nalecz Institute of Biocybernetics and Biomedical Engineering. It consists of four modules represented by four panels in the graphical user interface.

The PATIENT panel enables the user to manage general information of simulations and ViP (such as sex, height and hemoglobin concentration, for example), and to load and save data.

The SPIROMETRY panel can be used to diagnose the respiratory system by means of virtual forced spirometry.

K. Zieliński (✉) · A. Stecka · T. Gólczewski  
Nalecz Institute of Biocybernetics and Biomedical Engineering,  
Polish Academy of Sciences, Ks. Trojdena 4, 02-109 Warsaw,  
Poland  
e-mail: kzielinski@ibib.waw.pl



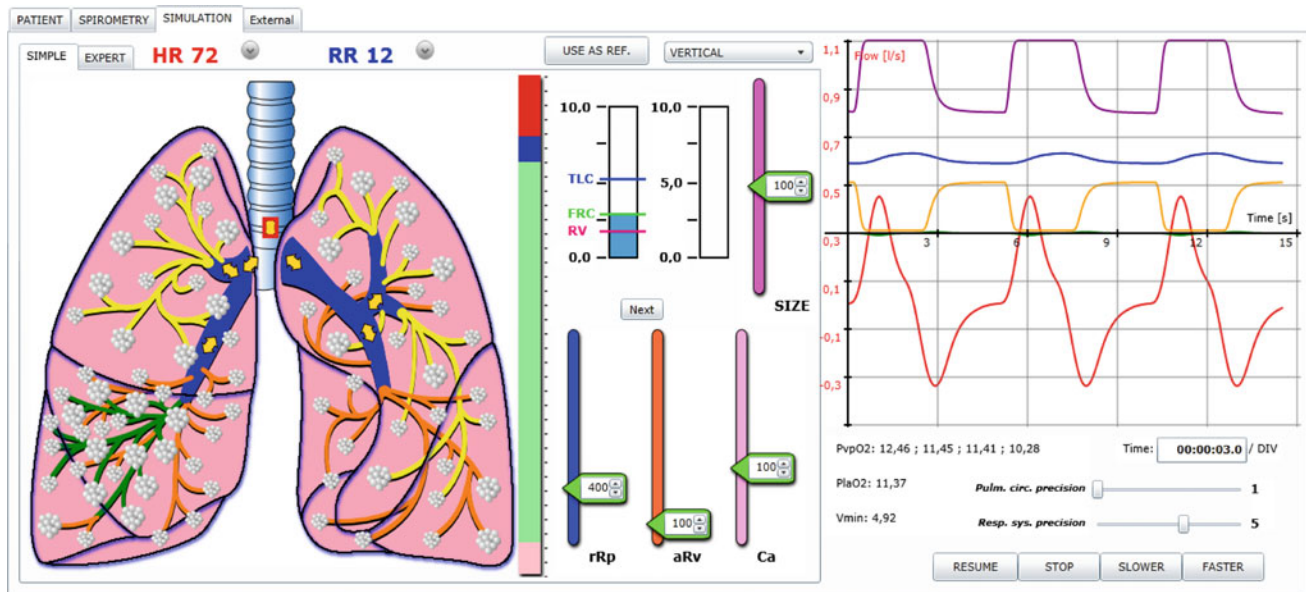


**Fig. 1** The SIMULATION panel of the VirRespir web application [5]

The flow-volume loop and such spirometric indices as forced expiratory volume in 1 s ( $FEV_1$ ), forced vital capacity (FVC), peak expiratory flow, for example, are presented. Some parameters that could be obtained from plethysmography are also accessible.

The SIMULATION panel (Fig. 1) is the main one. It enables: (a) to change values of chosen parameters of the respiratory system and some others; (b) to perform simulations; (c) to observe several respiratory and circulatory variables related to chosen lung areas, such as airflow, air pressure,  $O_2$  and  $CO_2$  partial pressures and tensions, and blood flow, for example; (d) to export the results of simulation to an excel file.

The EXTERNAL panel enables the end-user to unity ViP and his/her own model of HSC and/or of a respirator.

According to the results of forced spirometry and Polish reference values [6], ViP with the default values of models parameters corresponds to the average middle-aged Polish women.

## 2.2 Models

ViP consists of the following, previously developed and described in details models of the respiratory mechanics [1, 7], gas transfer and exchange in the respiratory system [8], pulmonary circulation mechanics [9] and gas transport with blood [8]. In VirRespir, the lungs are divided into 80 parts (16 per lobe), however different partition was also used in some ViP applications [1]. The partition is taken into account in all models related to lungs (i.e. respiratory

mechanics, pulmonary circulation, etc.). Each part is characterized by its coordinates (with the pulmonary trunk as the origin) and its size, which enables to calculate the hydrostatic pressure in pulmonary vessels or influence of gravity on ventilation, for example. In VirRespir, ViP can be supplemented with an embedded HSC model or a model elaborated by the user.

## 2.3 Parameters of Models and Changes of Their Values

Although some parameters have no direct physiological meaning (they are just coefficients in mathematical equations), their changes can be physiologically interpreted. For that reason, although the end-user cannot fix an absolute value of such a parameter, he/she can introduce a change in the form of the percentage of the default value. And thus, for example, to introduce mild, moderate, severe or very severe chronic obstructive pulmonary disease (COPD), the value of a relevant parameter has to be increased at least 2, 4, 8, or 16 times, respectively. Certainly, the user can fix absolute values of parameters having direct physiological meaning (e.g. age or pH of blood).

## 2.4 VirRespir Communication with External Software

VirRespir is provided with a simple embedded HSC model based on [10]. However the user can modify only the heart



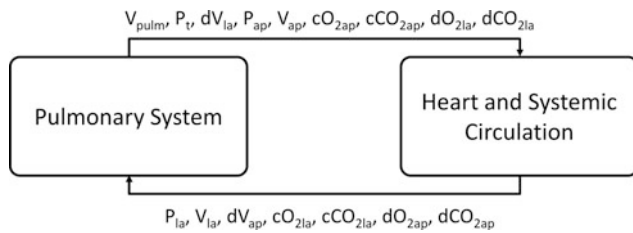


**Fig. 2** Mutual communication in VirRespir between ViP and an external HSC model developed by user (abbreviations are explained in the text)

rate. To have full control, the user should use own HSC model. ViP and user's model uniting is realized by a client-server software architecture. VirRespir is a web application executed in a web browser environments as client in a local machine. The user's external software must be executed as the server. The mutual communication is realized by TCP/IP connection by local ports. Data are exchanged between ViP and an external model every 1 ms of the simulated time with a specified protocol. The structure of data-packages is determined and the variables must be sent in the restricted order.

Every 1 ms (of the simulated time), VirRespir sends the following current values to the external application (Fig. 2): total blood volume in the pulmonary system ( $V_{pulm}$ ), intrathoracic pressure ( $P_t$ ), the blood volume that flowed into the left atrium during the last 1 ms ( $dV_{la}$ ), pulmonary trunk blood pressure ( $P_{ap}$ ), total blood volume in the pulmonary trunk ( $V_{ap}$ ),  $O_2$  and  $CO_2$  concentration in the trunk ( $cO_{2ap}$  and  $cCO_{2ap}$ ) and amount of  $O_2$  and  $CO_2$  in  $dV_{la}$  ( $dO_{2la}$ ,

$dCO_{2la}$ , respectively). The external application sends (Fig. 2): the left atrial pressure ( $P_{la}$ ), total blood volume in the left atrium ( $V_{la}$ ), flow from the right ventricle to the pulmonary trunk over 1 ms ( $dV_{ap}$ ),  $O_2$  and  $CO_2$  concentration in the left atrium ( $cO_{2la}$  and  $cCO_{2la}$ ) and amount of  $O_2$  and  $CO_2$  in  $dV_{ap}$  ( $dO_{2ap}$ ,  $dCO_{2ap}$ , respectively).

### 3 Examples of Simulations

#### 3.1 Diagnosis of the Respiratory System

After changes in respiratory system parameters, ViP should be diagnosed before further virtual experiments. The SPIROMETRY panel enables a user to determine whether ViP with particular values of the parameters can be treated as suffering from an obstructive lung disease or a restrictive one or it is healthy. Both absolute values of spirometric indices and those values presented as the percentages of reference values (predicted for fixed sex, age and height) are shown in the table at the SPIROMETRY panel. Figure 3 presents examples of the volume-airflow loop for tidal breathing and during forced spirometry in healthy ViP and suffering from severe COPD.

#### 3.2 Ventilation to Perfusion Ratio

The ventilation to perfusion ratio ( $V/Q$ ) is the fundamental index describing cooperation between the respiratory system and circulation. The ideal  $V/Q$  ratio equal to 1 would mean

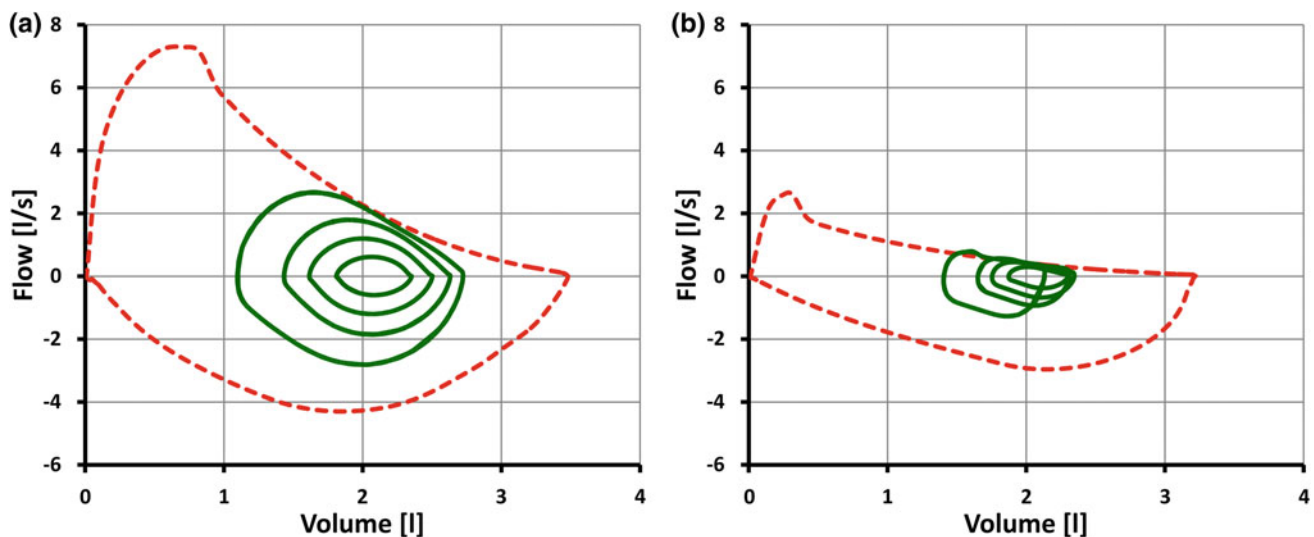


**Fig. 3** Examples of the flow-volume loop: **a** for the default (healthy) ViP and **b** for suffering from severe COPD. Solid loops—respiratory cycles for various respiratory efforts, dashed—results of the forced spirometry. The loops for COPD: expiratory flow limitation during

physical activity is present in patients with COPD, and the shift to the left of the solid loop means dynamic hyperinflation. A slightly decrease of FVC in COPD is caused by air-trapping

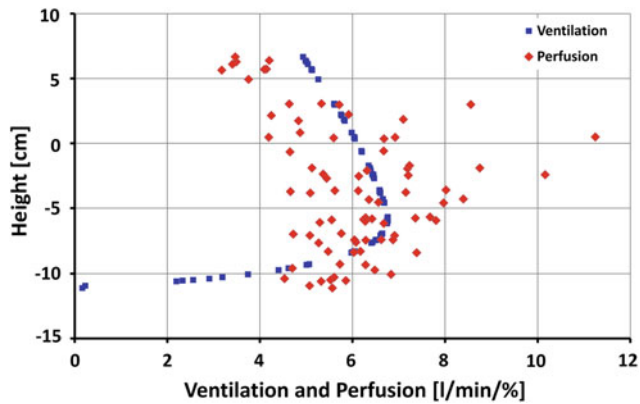


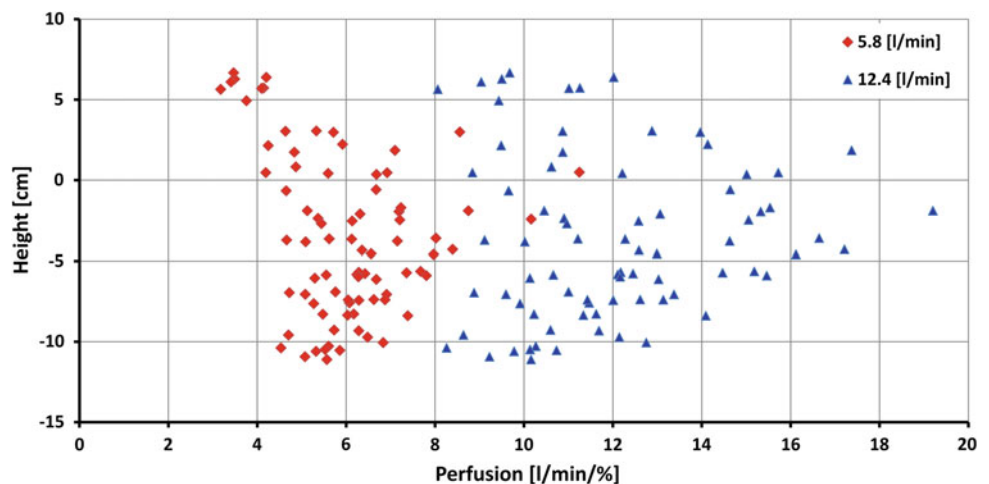
**Fig. 4** Dependence of ventilation (■) and perfusion (◆) of particular lung areas on their vertical position relative to the pulmonary trunk in ViP with the default values of models parameters in the standing position. Note that since the vascular resistance depends on the vessels length, i.e. the distance from the trunk, points related to perfusion are dispersed (bigger perfusion of lung areas being closer to the trunk) (Color figure online)

exact matching between respiration and blood flow. Unfortunately, both ventilation of particular lung areas and their perfusion depend differently on various factors. Gravity is the main such factor but it influences perfusion more than ventilation. Additionally, also the distance of a lung area from the pulmonary trunk influences the perfusion [11]. Therefore, examination of the V/Q ratio (Fig. 4) is also important in diagnosing the ViP state.

### 3.3 Perfusion for Different Hemodynamic Conditions

Figure 5 presents simulations with the use of an external HSC model for two cardiac outputs. The difference between those two outputs were caused by different values of the

**Fig. 5** Dependence of perfusion of particular lung areas on their vertical position relative to the pulmonary trunk in ViP in the standing position, for two values of the cardiac output



heart rate, left and right end-systolic maximal elastance, systemic peripheral resistance and venous tone (resting volume of systemic venous compartment).

## 4 Conclusions

VirRespir is a freeware application accessible from web browser, and thus it can be used both in research and for educational purposes by each end-user. It enables to unite ViP and users' models of the heart and systemic circulation, which is a unique feature and may be very useful for scientists being experts in cardiovascular modeling but not familiar with pulmonary issues.

**Compliance with Ethical Standards Funding:** The study received financial support from the European Regional Development Fund (grant POIG 02.03.00-00-003/09) and the Nalecz Institute of Biocybernetics and Biomedical Engineering, Polish Academy of Sciences. **Ethical approval:** This article does not contain any studies with human participants or animals performed by any of the authors.

## References

- Gólczewski, T., Stecka, A.M., Michnikowski, M., et al.: The use of a virtual patient to follow pleural pressure changes associated with therapeutic thoracentesis. *Int J Artif Organs* 40(12), 690–695 (2017).
- Fresiello, L., Ferrari, G., Di Molfetta, A., Zieliński, K., et al.: A cardiovascular simulator tailored for training and clinical uses. *J Biomed Inform* 57, 100–112 (2015).
- Broomé, M., Maksuti, E., Bjällmark, A., Frenckner, B., Janerot-Sjöberg, B.: Closed-loop real-time simulation model of hemodynamics and oxygen transport in the cardiovascular system. *Biomed Eng Online* 12:69 (2013).
- Albanese, A., Cheng, L., Ursino, M., Chbat, N.W.: An integrated mathematical model of the human cardiopulmonary system: model validation under hypercapnia and hypoxia. *Am J Physiol Heart Circ Physiol* 310(7), H899–921 (2016).

5. VirRespir Homepage. <https://virrespir.ibib.waw.pl>, last accessed 2018/03/14.
6. Lubiński, W., Gólczewski, T.: Physiologically interpretable prediction equations for spirometric indexes. *J Appl Physiol* 108(5), 1440–1446 (2010).
7. Gólczewski, T., Darowski, M.: Virtual respiratory system for education and research: simulation of expiratory flow limitation for spirometry. *Int J Artif Organs* 29(10), 961–972 (2006).
8. Gólczewski, T.: Gas exchange in a virtual respiratory system - simulation of ventilation without lung movement. *Int J Artif Organs* 30(12), 1047–1056 (2007).
9. Stecka, A.M., Gólczewski, T., Grabczak, E.M., et al.: The use of a virtual patient to follow changes in arterial blood gases associated with therapeutic thoracentesis. *Int J Artif Organs* [in press].
10. Ferrari, G., Kozarski, M., Zieliński, K., et al.: A modular computational circulatory model applicable to VAD testing and training. *Artif Organs* 15(1), 32–43 (2012).
11. Glenny, R.W., Bernard, S., Robertson, H.T., Hlastala, M.P.: Gravity is an important but secondary determinant of regional pulmonary blood flow in upright primates. *J Appl Physiol* 86(2), 623–632 (1999).

# A Hybrid Cardio-Pulmonary Simulation Platform—An Application for Extracorporeal Assist Devices

Krzysztof Zieliński<sup>✉</sup>, Piotr Okrzeja<sup>✉</sup>, Anna Stecka<sup>✉</sup>, Maciej Kozarski, and Marek Darowski

## Abstract

U.S. Food and Drug Administration agency is encouraging to use modeling and simulation in medical device evaluation, in order to reduce validation process and reduce a number of animal and human trials. To address this challenge, a variety of models and simulators is developed, playing the role of artificial/virtual patients or animals. There is a lack of simulators enabling interaction with real extracorporeal devices and also offering more advanced models of the cardiovascular/respiratory systems, available in pure computer simulators. A previously elaborated hybrid (hydro-computer), cardio-pulmonary simulation platform was adapted for extracorporeal applications. An extracorporeal membrane oxygenation (ECMO) mechanical assistance was simulated using this simulation platform and specially designed hydraulic model of ECMO. In these simulations veno-arterial (V-A) and veno-venous (V-V) basic ECMO configurations were considered. The preliminary results demonstrate the left ventricular afterload increasing for V-A configuration and blood recirculation effect for V-V one. Taking into account cannulas position, geometrical structures of the systemic vessels and real oxygenation gives more realistic and prospective approach. The application for extracorporeal assist devices (like ECMO) extends the whole hybrid cardio-pulmonary simulation platform functionalities in terms of the heart and lungs assistance simulations. The configuration for cardio-pulmonary bypass is also possible to be introduced. This simulation platform is a flexible tool and can be used by a wide range of stakeholders as a test-bench for various medical assist devices, as well as for educational purposes.

## Keywords

Cardiovascular simulator • Circulatory assistance  
Modeling and simulation

## 1 Introduction

Food and Drug Administration (FDA) USA agency is encouraging to use modeling and simulation in medical device evaluation, in order to reduce validation process and reduce a number of animal and human trials. FDA Center for Devices and Radiological Health published the set of regulatory science priorities [1]. It “serves as a catalyst to improving the safety, effectiveness, performance and quality of medical devices...” [1]. One of the priorities for 2017 is “Develop computational modeling technologies to support regulatory decision-making” [1].

To address this challenge, a variety of models and simulators is developed, playing the role of artificial/virtual patients or animals. In the case of cardiovascular and respiratory systems, the popular approach is to develop hydraulic or pneumatic mock-up simulators, allowing the interaction with physical cardiovascular (ventricular assist devices, heart valves prosthesis etc.) and respiratory (respirator, spirometer etc.) devices. The evolution of mock-up systems leads to so-called hybrid (physical-computer) simulators [2], inheriting an interaction with physical medical devices, from mock-up systems, and moreover, inheriting also the advantages of numerical models like flexibility and accuracy of cardio-pulmonary physiology reproduction [2]. There is a variety of “hybrid” simulators of the cardiovascular and respiratory systems [2]. Concerning only that one dedicated to extracorporeal circulation purposes, especially for the extracorporeal membrane oxygenation (ECMO) applications, the solutions presented in [3, 4] are simple devices offering rather basic physiology reproduction for educational purposes. Computer simulators, like e.g. in [5, 6], offer more sophisticated numerical cardiovascular

K. Zieliński (✉) · P. Okrzeja · A. Stecka · M. Kozarski  
M. Darowski

Nalecz Institute of Biocybernetics and Biomedical Engineering,  
Polish Academy of Sciences, Ks. Trojdena 4, 02109 Warsaw,  
Poland  
e-mail: kzielinski@ibib.waw.pl

models, including also gas transport and exchange, but they are purely numerical, thus an extracorporeal assist device must be also numerical and often very simplified. It is far from the real clinical situations. There is a lack of simulators enabling interaction with the real extracorporeal devices and also offering more advanced models of the cardiovascular/respiratory systems, available in computer simulators. It can be fulfilled only by hybrid hydraulic-computer simulators.

Therefore, the aim of this paper was to introduce, to a previously elaborated hybrid cardio-pulmonary simulation platform, an application for extracorporeal assistance.

## 2 Materials and Methods

### 2.1 The Hybrid Cardio-Pulmonary Simulation Platform Overview

In our Institute, the pneumo-hydro-numerical cardio-pulmonary simulation platform (HCPSP) was developed. It consists of the hybrid comprehensive cardiovascular and respiratory simulators, designed for different applications connected with mechanical circulatory and respiratory assistances. Thanks to the implemented numerical cardio-pulmonary model, various heart and lungs diseases are possible to be simulated.

The hybrid, hydro-numerical cardiovascular simulator, exploited in this paper, consists of two main modules: a computer model of the cardiovascular system and a hydro-numerical interface.

**The Computer Cardiovascular Model** The computer model of the cardiovascular system mechanics is based on the model presented in [7]. The heart ventricles systole is described by means of the time-varying elastance model by Suga and Sagawa, while the ventricular filing phase is simulated by the sum of exponentials. Atria are described by passive, linear compliances. The systemic and pulmonary circulation are described by 4 Windkessel models for arterial systemic, venous systemic, arterial pulmonary and venous pulmonary circulation, respectively. Each Windkessel model reproduces resistive, inertial and elastic properties of the simulated vessels.

**The Hydro-numerical Interface** The hydro-numerical interface consists of 4 sections. Each section, called “impedance transformer” (TR), converts bidirectionally pressure and flow signals from the physical (hydraulic) domain to the numerical (circulatory model) one. Thanks to it, the mutual interaction of physical assist devices and the computer circulatory model is enabled. 4 sections allow connection of physical medical assist device or prosthesis up to 4 points to the numerical model. For example, LVAD equipping with

one input and one output cannula allocates 2 sections in hybrid interface while BVAD system requires 4 sections. The hybrid interface was described in more details in [8, 9].

### 2.2 The Hybrid Cardiovascular Simulator Configuration for Extracorporeal Applications

ECMO circuit in basic configuration is connected to the patient by 2 cannulas. To connect ECMO to the hybrid cardiovascular simulator, in this configuration, only 2 hydraulic sections are required. The hardware configuration is the same for both veno-venous (V-V) and veno-arterial (V-A) “cannulation”. In the case of V-A the drainage cannula was connected to the right atrium of the numerical model by TR1, while the infusion cannula was connected to the aorta by TR2 (Fig. 1a). In the case of V-V the drainage cannula was connected (by TR1) to the systemic venous compartment (due to only one-compartment model of the systemic venous circulation), while the infusion cannula was connected (by TR2) to the right atrium (Fig. 1b).

To test the hybrid cardiovascular simulator for ECMO applications, an ECMO model was elaborated. It consists of an industrial centrifugal flow pump and a mechanical clamp. The last component was introduced to regulate the ECMO model circuit resistance and to regulate the centrifugal pump flow. The ECMO model was presented in Fig. 2. The simulations for V-A assistance were performed in 3 steps: 1. The physiological condition of the circulatory system was simulated. 2. The left ventricular pathology was introduced by the end-systolic left ventricular elastance decreasing and the left ventricular rest volume increasing. 3. The same pathological circulatory condition was retained but the ECMO model was introduced. The simulations were performed for different ECMO model flows—an extracorporeal “blood” flow (EBF). The simulations for V-V assistance were performed in 2 steps: 1. The physiological condition of the circulatory system was simulated. 2. The ECMO model was introduced and the simulation were performed for different EBF.

## 3 Results and Discussion

V-A ECMO is used as a partial or full support in the heart failure. Therefore, in Fig. 3, V-A ECMO mechanical assistance is presented, in the form of left ventricular pressure-volume (p-v) loops, describing its assistance effect.

The physiological condition is represented by red (◆ marked) loop, while the left ventricular pathology is described by blue (▲ marked) one. The left ventricular external work (a p-v loop surface) decreasing and p-v loop shifting towards the right are typical effects of the left



**Fig. 1** The scheme of the hybrid (physical-numerical) simulator of the cardiovascular system for ECMO applications:

- a Veno-arterial configuration;
- b Veno-venous configuration

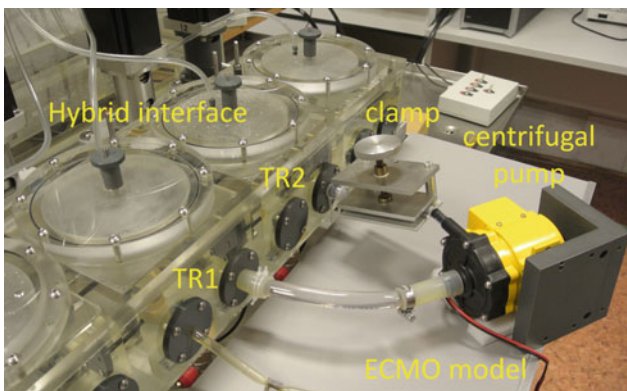
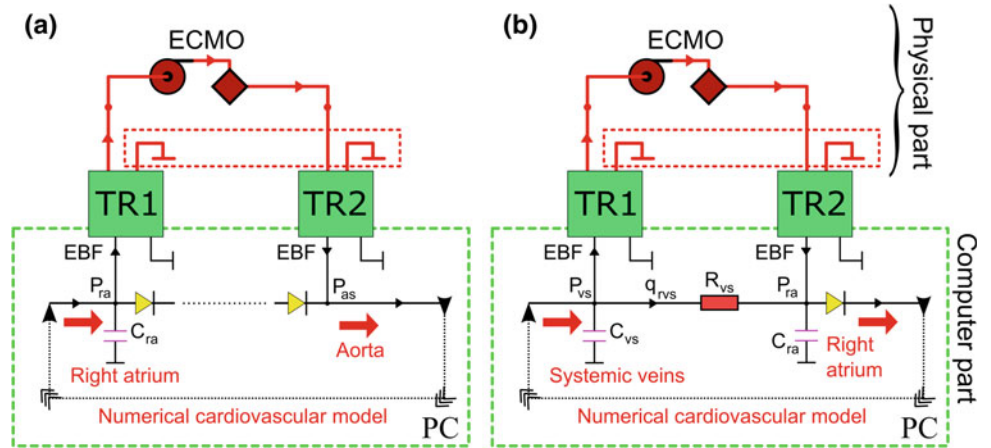


**Fig. 2** A laboratory set-up for the hybrid cardiovascular simulator with the ECMO model

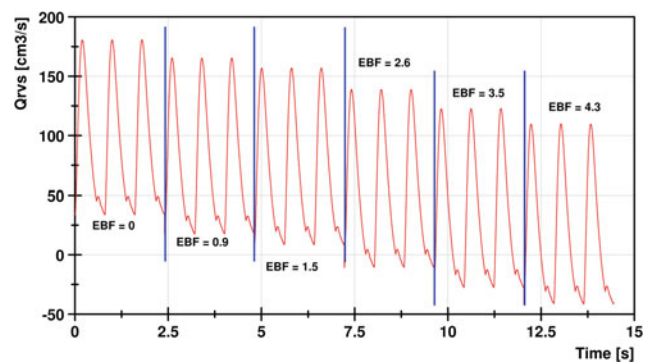


**Fig. 4** A venous systemic flow ( $Q_{rvs}$ ) for V-V ECMO mechanical assistance

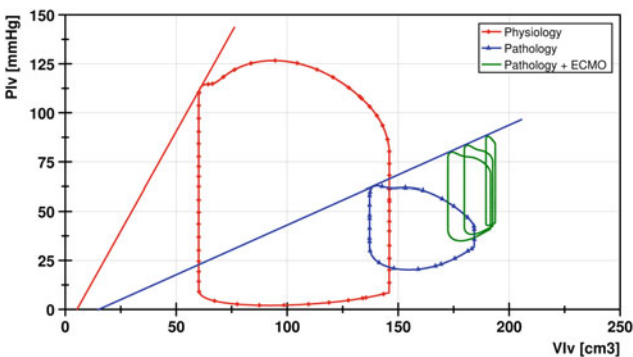


**Fig. 3** Left ventricular pressure-volume loops for V-A ECMO mechanical assistance

ventricular disease. V-A ECMO assistance effect, for selected EBF = 2.5, 3.3 and 4.4 l/min, is represented by green loops. This V-A ECMO effect is visible by the left ventricular stroke volume (SV) decreasing, while EBF increases, and the systolic blood pressure increasing from 50 mmHg (EBF = 0) to 85 mmHg (EBF = 4.4). However, increasing EBF increases also left ventricular end-diastolic

and end-systolic volumes due to afterload increasing by V-A ECMO. This negative loading effect is known and reported by others in [5, 10, 11].

The main function of V-V ECMO is to support lungs functions by blood oxygenation, in the respiratory failure. However, for this configuration the blood recirculation effect is observed [6, 12]. The V-V ECMO simulation results, presented in Fig. 4, demonstrate it. From the hybrid cardiovascular simulator point of view, the drainage cannula flow decreases venous systemic pressure ( $P_{vs}$ ) and the infusion cannula flow increases right atrial pressure ( $P_{ra}$ ) while EBF is increasing, what decreases venous systemic flow ( $Q_{rvs}$ ). In Fig. 4 is well visible that for EBF over  $\sim 2$  l/min,  $Q_{rvs}$  is negative in some phases. It is the returning blood from the right atrium to the venous systemic compartment and then draining again by the input ECMO cannula.

This study has several limitations. Only basic ECMO configurations were presented. The numerical model of the cardiovascular system was simple. More appropriate is to use that one presented in [9], where systemic circulation is at least divided by inferior and superior vena cava compartments. The last but not least is that only mechanical ECMO assistance effect is only possible reproduced by real device.

Taking into account cannulas position, geometrical structures of the systemic vessels and real oxygenation gives more realistic and prospective approach.

## 4 Conclusions

The application for extracorporeal assist devices like ECMO extends the HCPSP functionalities in terms of the heart and lungs assistance simulations. There is also possible to “un-cut” heart and pulmonary circulation by changing only numerical model parameters, to obtain the configuration for a cardio-pulmonary bypass without any hardware rearrange. HCPSP is a flexible tool, that can be used by a wide range of stakeholders, as a test-bench for various medical assist devices, as well as for educational purposes.

### Compliance with Ethical Standards

**Funding** The study received financial support from the Nalecz Institute of Biocybernetics and Biomedical Engineering, Polish Academy of Sciences.

**Ethical approval** This article does not contain any studies with human participants or animals performed by any of the authors.

## References

1. FY2017 Regulatory Science Priorities, <https://www.fda.gov/MedicalDevices/ScienceandResearch/ucm467550.htm>, last accessed 2018/03/14.
2. Zieliński, K., Darowski, M., Kozarski, M., et al.: The need for hybrid modeling in analysis of cardiovascular and respiratory support. *Int J Artif Organs*. 39(6), 265–271 (2016).
3. Tokumine, A., Momose, N., Tomizawa, Y.: Use of an extracorporeal circulation perfusion simulator: evaluation of its accuracy and repeatability. *J Artif Organs* 16(4), 417–424 (2013).
4. Lansdowne, W., Machin, D., Grant, D.J.: Development of the orpheus perfusion simulator for use in high-fidelity extracorporeal membrane oxygenation simulation. *J Extra Corpor Technol* 44(4), 250–255 (2012).
5. Broomé, M., Donker, D.W.: Individualized real-time clinical decision support to monitor cardiac loading during venoarterial ECMO. *J Transl Med* 14, 4 (2016).
6. Broman, M., Frenckner, B., Bjällmark, A., et al.: Recirculation during veno-venous extra-corporeal membrane oxygenation - a simulation study. *Int J Artif Organs* 38(1), 23–30 (2015).
7. Ferrari, G., Kozarski, M., Zieliński, K., et al.: A modular computational circulatory model applicable to VAD testing and training. *J Artif Organs* 15(1), 32–43 (2012).
8. Darowski, M., Kozarski, M., Ferrari, G., et al.: A new hybrid (hydro-numerical) model of the circulatory system. *Bull. Pol. Ac.: Tech.* 61(4), 993–1003 (2013).
9. Fresiello, L., Zieliński, K., Jacobs, S., et al.: Reproduction of continuous flow left ventricular assist device experimental data by means of a hybrid cardiovascular model with baroreflex control. *Artif Organs* 38(6), 456–468 (2013).
10. Burzotta, F., Carlo, C., Doshi, S.N., et al.: Impella ventricular support in clinical practice: Collaborative viewpoint from a European expert user group. *Int J Cardiol* 201, 684–691 (2015).
11. Ostadal, P., Mlcek, M., Kruger, et al.: Increasing venoarterial extracorporeal membrane oxygenation flow negatively affects left ventricular performance in a porcine model of cardiogenic shock. *J Transl Med* 13, 266 (2015).
12. Abrams, D., Bacchetta, M., Brodie, D.: Recirculation in venovenous extracorporeal membrane oxygenation. *ASAIO J* 61(2), 115–121 (2015).

# Different Methods of Arterial Compliance Estimation Tested with Reservoir-Wave Model of Arterial System

Marek Żyliński, Wiktor Niewiadomski, Marta Sadowiec, and Gerard Cybulski

## Abstract

Arterial compliance ( $C$ ) describes the ability of the arterial system to increase volume ( $V$ ) with increasing pressure ( $P$ ). Compliance is a marker of preclinical vascular diseases and cardiovascular risk factor. There are many different methods estimating arterial compliance. The aim of this study was to find out whether three of them: diastolic decay time method, pulse pressure method and area method are able to recover assumed value of  $C$ , when applied to reservoir-wave model of arterial system. This model assumes that arterial pressure is sum of two components: pressure caused by blood flow and pressure resulting from change in arterial blood volume. We calculate aortic blood pressure using reservoir-wave model for given blood flow and different values of model parameters  $Z$ —arterial impedance ( $0.1 < Z < 0.4$ )  $C$ —compliance ( $0.6 < C < 2.0$ ),  $R$ —total peripheral resistance ( $0.5 < R < 3.0$ ) Next, we use above mentioned three methods of compliance estimation and compared recovered value of  $C$  with value of  $C$  used in reservoir—wave model. We found, that area method showed best agreement between assumed and calculated arterial compliance  $C$ . Also diastolic decay time method can be used but estimated  $R$  may be misleading. Pulse pressure method produced erroneous estimates of assumed  $C$  values.

## Keywords

Arterial compliance • Reservoir-wave model  
Area method • Pulse-pressure method • Diastolic decay time method

M. Żyliński (✉) · M. Sadowiec · G. Cybulski  
Faculty of Mechatronics, Institute of Metrology and Biomedical Engineering, Warsaw University of Technology, Warsaw, Poland  
e-mail: zyliniski@mchtr.pw.edu.pl

W. Niewiadomski  
Mossakowski Medical Research Centre, Polish Academy of Sciences, Warsaw, Poland

## 1 Introduction

Arterial compliance ( $C$ ) describes the ability of the arterial to increase volume ( $V$ ) with increasing pressure ( $P$ ) [1].  $C$  is defined as:

$$C = \frac{\Delta V}{\Delta P} \quad (1)$$

Compliance is a marker of preclinical vascular disease and cardiovascular risk factor [2, 3]. Arterial compliance decreases with age, resulting in increased pulse pressure (PP).

There are many different methods estimating arterial compliance, some are based on shape of blood pressure time course, like diastolic decay time, pulse pressure or area method.

We wanted to see, how well these methods could recover assumed  $C$  value, when blood pressure is calculated using assumed blood inflow ( $Q(t)$ ) with reservoir-wave model of arterial system. This model [4] assumes that blood pressure is sum of two components:  $P_{ex}$ —pressure caused by arterial flow and  $P_w$ —pressure resulting from change in arterial volume.

## 2 Method

### 2.1 Reservoir-Wave Model

Reservoir-wave model of aortic circulation assumes that aortic pressure ( $P_{ao}$ ) is a sum of wave pressure ( $P_{ex}$ ) and reservoir pressure ( $P_{wk}$ ):

$$P_{ao} = P_{ex} + P_{wk} \quad (2)$$

$P_{ex}$  is a product of blood flow ( $Q$ ) and aortic impedance ( $Z$ ).  $P_{wk}$ —reservoir component is related to pressure caused by change of blood volume in arterial system.  $P_{wk}$  is described by two element Windkessel model (arterial resistance

(R) connected in parallel with arterial compliance (C)), as proposed by Frank [5].  $P_{wk}(t)$  changes according to the formula:

$$P_{wk}(t) = (P_0)e^{\frac{-t}{RC}} + e^{\frac{-t}{RC}} \int_{t_0}^t \frac{Q(t')}{C} e^{\frac{t'}{RC}} dt' \quad (3)$$

Reservoir-wave model was verified in dog by Wang et al. [6], they measure blood flow, blood pressure and aortic volume and show good agreement between measured signal and model predictions.

Aortic pressure in reservoir-wave model is described by equation:

$$P_{ao}(t) = Q(t) * Z + (P_0)e^{\frac{-t}{RC}} + e^{\frac{-t}{RC}} \int_{t_0}^t \frac{Q(t')}{C} e^{\frac{t'}{RC}} dt' \quad (4)$$

where  $P_0$  is diastolic pressure. We use this equation in our simulations for given blood flow and model parameters values from following ranges ( $0.1 < Z < 0.4$ ,  $0.6 < C < 2.0$ ,  $0.5 < R < 3.0$ ).

## 2.2 Compliance Estimation Methods

### Diastolic decay time method ( $C_{dias}$ )

In post-ejection period of heart cycle blood inflow ceases but outflow continues and arterial volume and pressure decline exponentially. During this period  $P_{ao}$  is described by two-element Windkessel model and changes according to equation:

$$P_{ao}(t) = P_0 * e^{\frac{-t}{\tau}} \quad (5)$$

where:  $P_0$  is pressure at end of systole.  $\tau$  is time constant of pressure decay, it equals the product of R and C.

With diastolic decay time method aortic compliance is computed in two steps:

1.  $\tau$  is estimated from the  $P_{ao}(t)$  in late diastole, by fitting exponential decay curve
2.  $C_{dias}$  is determined by dividing  $\tau$  by R.

Where R is usually calculated, as follows:

$$R = \frac{\text{mean blood pressure}}{\text{mean blood flow}} \quad (6)$$

### Pulse pressure method ( $C_{pp}$ )

In this method [7], resistance (R) value was calculate as quotient of mean arterial pressure and mean blood flow. Next, using two-element Windkessel model and assumed compliance ( $C_{pp}$ ) blood pressure was estimated for given Q (t). Pulse pressures (PP) from both pressure curves first-calculated with reservoir-wave model and second produced with two-element Windkessel model were compared, and if error between PPs were too big value of compliance was changed until error declined below pre-set limit, usually after few iterations. The algorithm is shown in Fig. 1.

### Area method ( $C_{area}$ )

Area method was proposes by Liu et al. [8]. This method is based on hypothetical arterial P-V relations. If linear P-V relation is assumed compliance is obtained as:

$$C = \frac{SV}{K(P_1 + P_2)} \quad (7)$$

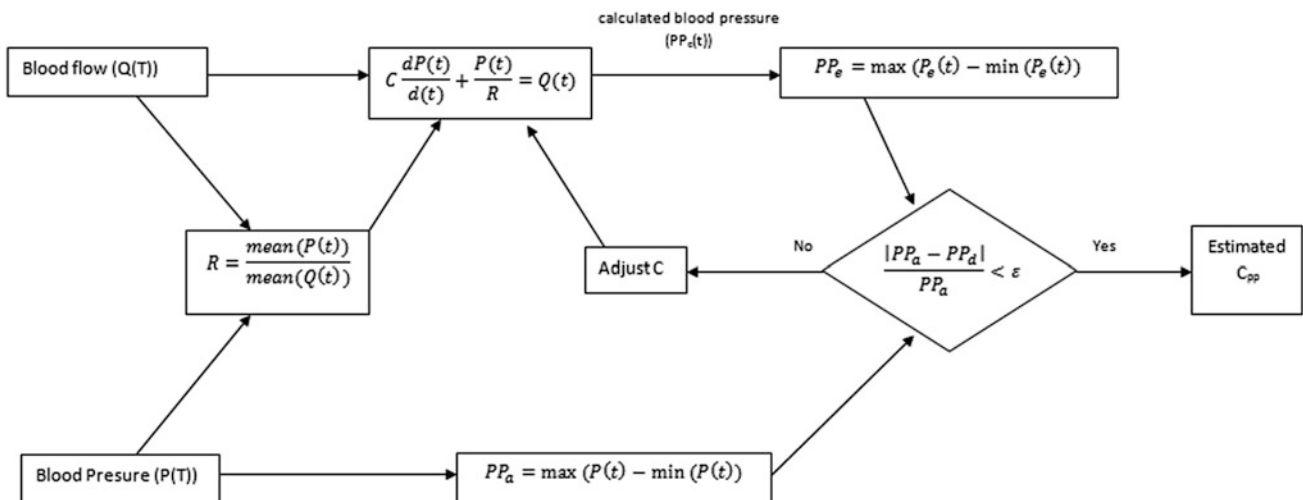


Fig. 1 Schematic diagram of the pulse pressure estimation method

where  $P_1$  is diastolic pressure and  $P_2$  is pressure at the end of systole.  $K$  is area index defined as:

$$K = \frac{(A_s + A_d)}{Ad} \tag{8}$$

where:  $A_s$  is area under systolic part of blood pressure,  $A_d$  is area under diastolic part of blood pressure.

Compliance in this method can be also calculated using more physiological exponential P-V relation:

$$C(P) = \frac{b * SV * e^{bP}}{K(e^{bP_1} - e^{bP_2})} \tag{9}$$

$b$  is given as  $-0.0131$  [8]. Segers et al. [9] showed in animal model that this method is sensitive to wave reflection and can overestimate compliance value.

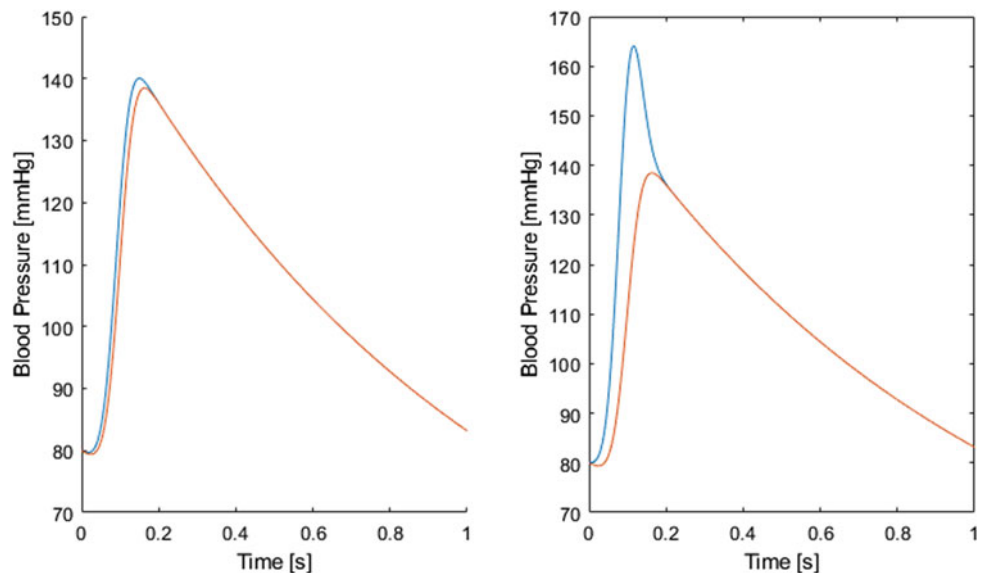
### 3 Results

For each method, percentage error of estimated compliance value with respect to the one used in reservoir-wave model was calculated and obtained values are shown in Table 1.

**Table 1** Mean percentage error and standard deviation for three methods of compliance estimation

Compliance estimation method	Mean percentage error	Standard deviation
$C_{dias}$	22.4	41.8
$C_{arealin}$	3.3	21.8
$C_{areaeks}$	11.2	14.6
$C_{pp}$	69.6	13.5

**Fig. 2** Impact of  $Z$  on calculated aortic blood pressure. Purple line is aortic pressure, green reservoir pressure (Color figure online)



### 4 Discussion

Results of our simulation showed that area method of compliance estimation gave best agreement with  $C$  for used in reservoir-wave model. Linear equation in area method is slightly better, than exponential one as the latter overestimates  $C$ , but difference is not significant.

It is not a surprise that pulse pressure method resulted in very poor agreement of calculated  $C$  with  $C$  used in reservoir-wave model calculation. Occurrence of wave pressure ( $P_{ex}$ ) led to compliance underestimations by pulse pressure method. Impact of  $P_{ex}$  on aortic pressure is shown in Fig. 2. Pulse pressure method gave good result when aortic impedance are low ( $P_{ex}$  is small), in this case, this method produces same error as area method (Fig. 3). Probably  $C_{pp}$  should be good estimator of  $C$  if two-element Windkessel model would be replaced with reservoir pressure.

Poor result of the diastolic time method is somewhat surprising, as in late diastole reservoir-wave model reduces to two-element Windkessel model and we should expect perfect agreement between input and output  $C$ s and  $R$ s. The key to such discrepancy may be that calculated TPR did not equal  $R$  used for simulation. First step to resolve this discrepancy is to check, whether formula (6) really returns assumed  $R$  value in reservoir-wave model and in two-element Windkessel model.

We assume that in terms of reservoir-wave model to estimate arterial compliance area method should be preferred. Diastolic time method can be used but estimation of TPR need same caution. Pulse pressure method should be avoided.

It need to be highlighted that this statements should be treated only as hints when using these methods in analysis of real aortic system as they stem from wave-reservoir model



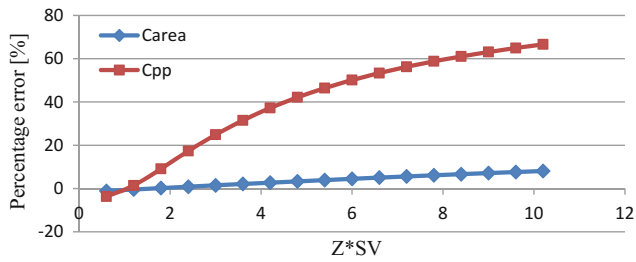


**Fig. 3** Impact of Z on percentage error of  $C_{area}$ ,  $C_{pp}$  method. C, R, and SV are constant and Z varies in range (0.1–0.4)

simulation, and the latter model may represent imperfectly reality.

**Conflict of Interest** The authors declare that they have no conflict of interest.

## References

- Dart, Anthony M., and Bronwyn A. Kingwell. "Pulse pressure—a review of mechanisms and clinical relevance." *Journal of the American College of Cardiology* 37.4 (2001): 975–984.
- van der Giezen AM, Schopman-Geurts van Kessel JG, Schouten EG, Slotboom BJ, Kok FJ, Collette HJ. Systolic blood pressure and cardiovascular mortality among 13,740 Dutch women. *Prev Med* (1990); 19:456–465.
- Domanski MJ, Mitchell GF, Norman JE, Exner DV, Pitt B, Pfeffer MA. Independent prognostic information provided by sphygmomanometrically determined pulse pressure and mean arterial pressure in patients with left ventricular dysfunction. *J Am Coll Cardiol* (1999); 33:951–958.
- Tyberg, John V., et al. "The case for the reservoir-wave approach." *International journal of cardiology* 172.2 (2014): 299–306.
- Frank O. Die grundform des arteriellen pulses. *Z Biol* 1899; 37:483–526.
- Wang J. J., O'Brien A. B., Shrive N. G., Parker K. H., Tyberg J. V. Time-domain representation of ventricular-arterial. *Am J Physiol Heart Circ Physiol* 2003; 284: H1358–H1368.
- Stergiopoulos, N., J-J. Meister, and N. Westerhof. "Simple and accurate way for estimating total and segmental arterial compliance: the pulse pressure method." *Annals of biomedical engineering* 22.4 (1994): 392–397.
- Liu, Zhaorong, Kenneth P. Brin, and F. C. Yin. "Estimation of total arterial compliance: an improved method and evaluation of current methods." *American Journal of Physiology-Heart and Circulatory Physiology* 251.3 (1986): H588–H600.
- Segers, Patrick, et al. "Pulse pressure method and the area method for the estimation of total arterial compliance in dogs: sensitivity to wave reflection intensity." *Annals of biomedical engineering* 27.4 (1999): 480–485.

# Breathing Experiments into the Simulated Avalanche Snow: Medical and Technical Issues of the Outdoor Breathing Trials

Lenka Horáková<sup>1</sup>, Karel Sýkora<sup>2</sup>, Ladislav Sieger<sup>3</sup>,  
and Karel Roubík<sup>4</sup>

## Abstract

Avalanche burials represent one of the most dangerous risks associated with winter activities in the mountains. Asphyxiation occurs as a consequence of blocked airways; or, due to a severe hypoxia and hypercapnia resulting from rebreathing previously exhaled gas. Recently, outdoor breathing experiments with healthy volunteers were conducted in order to investigate the gas exchange limitations and work of breathing effects on the probability of survival under avalanche snow. Ambient conditions during the experiments differ significantly from the recommended operating conditions of the medical devices. Therefore, special measures need to be applied during the experiments not only to assure proper functioning of the devices used for the monitoring of the breathing subjects, but also ensuring their required precision and accuracy. As the subject starts to suffer from hypoxia and hypercapnia short after beginning of the breathing trial, careful and detailed monitoring and advanced safety precautions must be adopted. Using our experience from real outdoor breathing trials, we aim to recommend both the technical and medical precautions that should be undertaken in future studies.

## Keywords

Avalanche victims • Snow burial • Survival  
Hypercapnia • Hypoxia • Work of breathing  
Technical limits • Outdoor experiments

L. Horáková (✉) · K. Roubík  
Faculty of Biomedical Engineering, Czech Technical University  
in Prague, nám Sítěná 3105, 272 01 Kladno, Czech Republic  
e-mail: horakle5@fbmi.cvut.cz

K. Sýkora  
Faculty of Physical Education and Sport, Charles University  
in Prague, J. Martího 31, 162 52 Prague 6, Czech Republic

L. Sieger  
Faculty of Electrical Engineering, Czech Technical University  
in Prague, Technická 2, 166 27 Prague 6, Czech Republic

## 1 Introduction

Avalanche burials represent one of the most dangerous risks associated with winter activities in the mountains. The survival chances depend on multiple factors: on trauma sustained during the accident, on the length and depth of the snow burial, and the presence of an air pocket [1–3]. The most common cause of death in avalanche victims is suffocation. Up to 90% of the casualties die because of asphyxia, as was analysed in numerous studies [4–6]. This occurs as a consequence of blocked airways, or due to a severe hypoxia and hypercapnia resulting from rebreathing previously exhaled gas. However, the mechanism of gas exchange in a snow buried avalanche victim has not yet been fully elucidated and is a subject of worldwide research activities. Recently, outdoor breathing trials with healthy volunteers have been conducted in order to investigate the gas exchange limitations and work of breathing effects on the probability of survival under avalanche snow.

In these studies, the endpoints and safety limits of the breathing trials are specified using oxygen ( $O_2$ ) and carbon dioxide ( $CO_2$ ) concentrations in the inhaled or exhaled gas and peripheral oxygen saturation ( $SpO_2$ ). The set limits vary among the studies. Brugger et al. [7] used monitoring of end-tidal  $CO_2$  content ( $EtCO_2$ ) to describe the effect of an air pocket of a different size in front of the subject's airways. The endpoint was based on  $SpO_2$  monitoring, which was set at  $SpO_2$  75%. Many studies set their limits on values  $SpO_2$  of less than 85% [8, 9]. In study of Roubík et al. [10] much lower pulse oximetry readings were recorded. In some studies, combined limits have been used, based on both  $SpO_2$  and  $CO_2$  concentration. Strappazon et al. [11] used for example  $SpO_2$  limit of 75% with an additional criterion of inspired  $CO_2$  concentration ( $FiCO_2$ ) higher than 8%. An overview of the physiological parameters used for safety monitoring of the subjects during breathing experiments is presented in Table 1.

**Table 1** Physiological parameters used for safety monitoring of the tested subjects during breathing experiments

Parameter	Meaning	Nomal/Physiological values	Comments
FiO <sub>2</sub>	Fraction of oxygen in inspired gas	20.9476%	Dry air
EtO <sub>2</sub>	End tidal fraction of oxygen in expired gas	16%	Value after a single breath expiration when inhaling FiO <sub>2</sub> of 21% and negligible FiCO <sub>2</sub>
FiCO <sub>2</sub>	Fraction of carbon dioxide in inspired gas	0.0314%	Dry air
EtCO <sub>2</sub>	End tidal fraction of carbon dioxide in expired gas	4%	Value after a single breath expiration when inhaling FiO <sub>2</sub> of 21% and negligible FiCO <sub>2</sub>
SpO <sub>2</sub>	Peripheral haemoglobin oxygen saturation	94–98%	
PaO <sub>2</sub>	Arterial partial pressure of oxygen	10–13 kPa (75–100 mmHg)	Can be obtained only via arterial blood analysis
PaCO <sub>2</sub>	Arterial partial pressure of carbon dioxide	4.7–6.0 kPa (35–45 mmHg)	Can be obtained only via arterial blood analysis

For monitoring of the subjects throughout these experiments, medical vital sign monitors are commonly used. Nevertheless, these monitors are designed mainly for the use in critical care units, and a direct use in the field can cause errors and misinterpretation of data. Furthermore, when they are taken into the outdoor environment, unquestioning operation in such experiments may pose the participants of the study into threat.

The aim of this study is to analyse possible peculiarities, risks and limitations of the use of medical devices in outdoor breathing experiments simulating avalanche snow burial and to help in designing of future experiments in order to avoid erroneous results and their misinterpretation.

## 2 Outdoor Breathing Experiments and Their Technical Management

### 2.1 The Environmental Condition Effects on Correctness of the Methodology

As the breathing experiments to the snow are usually conducted in the mountain areas, the effect of high altitude should be considered. The most important parameter is a reduced ambient pressure that may be significantly lower

than the atmospheric pressure measured at the sea level. This situation may have serious consequences for both safety of the participants and for evaluation of the experiment results.

Medical devices usually allow the user to select several forms of result presentations and units for one particular measure. For example, composition of respiratory gases (FiO<sub>2</sub>, EtO<sub>2</sub>, FiCO<sub>2</sub> and EtCO<sub>2</sub>) may be expressed as a fraction of the corresponding gas in the gas mixture (i.e., expressed in %), or, as a partial pressure of the corresponding gas in the mixture (expressed in kPa or mmHg). Furthermore, the partial pressure may be expressed by the monitor under several conditions denoted as B.T.P.S. (body temperature, ambient pressure and saturated with water vapour), A.T.P.D. (ambient temperature and pressure, dry) or recalculated to standard conditions at standard temperature of 0 °C and standard pressure of 101.325 kPa (760 mmHg), denoted as S.T.P.D. (standard temperature and pressure, dry). S.T.P.D. makes the comparison of different subjects even from different test sites possible, but is not optimal for assessment of the vital signs of the subjects, whereas the parameters expressed in B.T.P.S. describe the real physiological state of the organism optimally. The detailed description of standardized conditions of measurement is presented in Table 2.

**Table 2** The detailed description of standardized conditions of measurement

Abbreviation	Meaning	Values	Comments
B.T.P.S.	Body temperature, ambient pressure, saturated with water vapour	Body temperature (estimated 37 °C), ambient barometric pressure, saturated with water vapour of 6.3 kPa (47 mmHg) at 37 °C <sup>a</sup>	Gas under conditions in the human body, i.e. heated to body temperature and saturated with water vapours at this temperature
A.T.P.D.	Ambient temperature and pressure, dry	Ambient temperature (estimated as room temperature 20 °C), ambient barometric pressure, dry air (not saturated with water vapour)	Gas volumes obtained during spirometry at ambient conditions
S.T.P.D.	Standard temperature and pressure, dry	Standard temperature 0 °C, standard pressure 101.3 kPa (760 mmHg), dry air (not saturated with water vapour)	Gas volume under standard conditions—enables to compare results obtained under different conditions

<sup>a</sup>Variations in the range of 35–39 °C are of a little importance

If, for example, the maximum allowed  $\text{EtCO}_2$  value set for termination of a breathing experiment for safety reasons is 8%, it represents  $\text{EtCO}_2$  of 8 kPa at sea level, whereas it is 7.2 kPa at 1 000 m and only 6.4 kPa at 2 000 m above sea level. Vice versa, if the set  $\text{EtCO}_2$  limit is 8 kPa, it corresponds to  $\text{EtCO}_2$  of 8% at sea level but to 8.9% at 1000 m and even 10% at 2 000 m.

For snow-based experiments, in addition to the density of snow, its temperature is also important. Changes in weather often do not provide stable climate conditions for the experiment. Snow has a large heat capacity; therefore, the temperature at a depth of 50 cm and more is minimally affected by the daily changes in air temperature. Snow temperature measurement is wise to carry out continuously (e.g., for the whole week of experiments) by a data-logger at reasonable (e.g. 5-min) time intervals. According to the international standard ISO 2533:1975/Add.2:1997 [12], the air temperature is recommended to be measured 5 cm above the snow surface and the temperature of snow at depths of 10, 20, 30, 40 and 50 cm. An example of such record of temperature development over four days is presented in Fig. 1. The graph documents that the snow temperature variability significantly decreases with the increasing depth of snow.

In general, the measuring technique is influenced by sudden temperature fluctuations, especially at lower temperatures. For this reason, a thermal comfort for the devices is pivotal. In a shelter, all the devices should be individually thermo-insulated and heated.

A deleterious source of measurement errors is the leakage in a circuit that may occur at any time during the measurement (leakage of the nasal clip, mask, experimental set in the snow, etc.). Nitrous oxide ( $\text{N}_2\text{O}$ ) can be used as the tracing gas during the experiments. The anaesthesia monitors are capable of detecting  $\text{N}_2\text{O}$  even at very low concentrations, which are lower than the values affecting the subject's

cognition.  $\text{N}_2\text{O}$  may be administered to the space in the vicinity of the breathing subject with a respiratory circuit. The absence of  $\text{N}_2\text{O}$  in the respiratory circuit carries the information about its tightness [10].

## 2.2 Performance of Medical Devices During Outdoor Breathing Experiments

Vital sign monitors are often used for both assuring safety of the subjects and for measuring parameters that may serve as study endpoints or providing data suitable for subsequent analysis and evaluation. If a non-standard breathing circuit is used (e.g. two arms equipped with one-way valves), a significant distortion of the gas concentration curves may occur compared to a standard configuration. This deformity may represent a problem for the breath detection algorithm present in the monitor that may affect evaluation of parameters derived from the measured concentration curves. The monitors are designed for monitoring of critically ill patients; therefore, their measuring capability covers a wide range of each parameter well exceeding normal physiological limits. Nevertheless, during extreme breathing experiments, the physiological parameters exhibit very rapid changes and their values may temporarily fall outside the measuring range of vital sign monitors.

In their experiments, Roubík et al. [10] discovered that values of end-tidal  $\text{CO}_2$  concentrations ( $\text{EtCO}_2$ ) displayed on the screen of Datex-Ohmeda S/5 anaesthesia monitor often did not correspond with the  $\text{CO}_2$  concentration curve displayed on the same screen of the monitor. After analysis of other parameters, the same disproportion was documented for all the parameters evaluated from the  $\text{CO}_2$  and  $\text{O}_2$  concentration curves, i.e.  $\text{EtCO}_2$ ,  $\text{FiCO}_2$ ,  $\text{EtO}_2$  and  $\text{FiO}_2$  values. An example documenting the observed error is presented in Fig. 2.

In order to explain this disproportion, Roubík and Filip [13] conducted a detailed analysis and several additional laboratory experiments. The results show that the error of  $\text{EtCO}_2$  and  $\text{EtO}_2$  occurred in 39% and in 30% of the total experimental time of breathing into snow, with and without an air pocket respectively (range from 13 to 93% of time). The breathing experiments with simulated avalanche snow, conducted in order to find the cause of the error determined that the error occurs immediately after a significant increase of  $\text{CO}_2$  in the breathing circuit as a consequence of expired gas rebreathing and is independent of other breathing parameters. The study confirmed that a newer model of the monitor (Carescape B650) is prone to this error as well. The last experiment conducted with a standard anaesthesia machine confirmed that the error occurs even in a standard clinical setup, in the presence of rebreathing simulated by removing soda lime from the  $\text{CO}_2$  absorber.

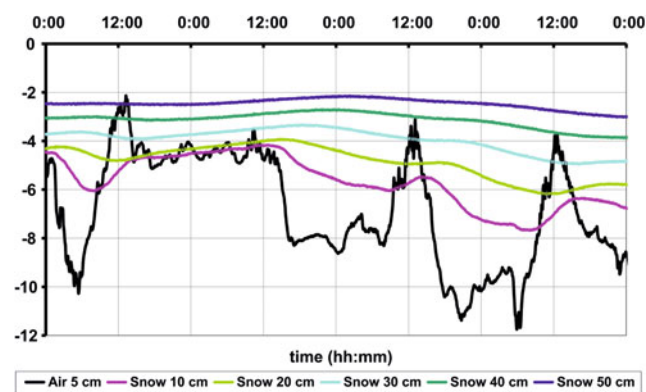
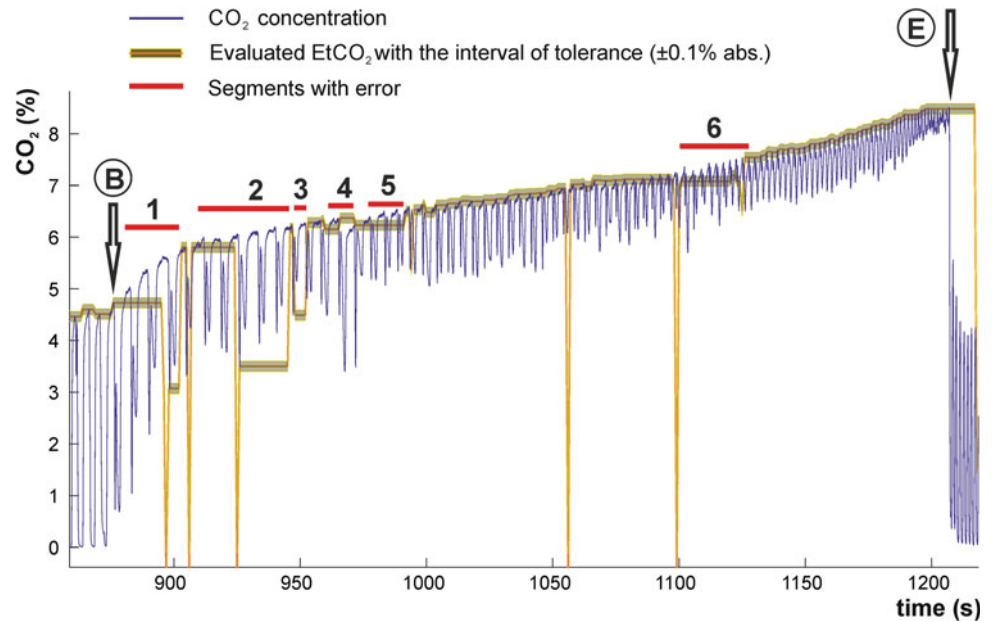


**Fig. 1** Variation of air temperature during a four day experiment measured 5 cm above the snow surface (the black line) and its effect on temperature of snow measured at different depths of 10, 20, 30, 40 and 50 cm below the surface

**Fig. 2** Example of a curve of measured CO<sub>2</sub> concentration (blue line) and the values of EtCO<sub>2</sub> (yellow line) evaluated by the monitor. Segments where EtCO<sub>2</sub> does not correspond to the CO<sub>2</sub> concentration curve are marked with red horizontal lines. B—beginning of breathing trial in the snow after the initial stabilization period; E—end of the breathing trial. Reprinted from [13] under CC BY license (Colour figure online)



During the same outdoor breathing experiments [10], tidal volumes of majority of participants in the most pronounced hypercapnia state went beyond the maximum value of tidal volume that the monitor is able to record. As a consequence, the flow rate signal was distorted and the correct tidal volume could not be calculated. To prevent this situation, a modified flow sensor might be used, but due to the sensor nonlinearity, the recalculation cannot be accomplished by a simple correction with a constant. Actual tidal volumes should be calculated directly from the flow rate curves after their non-linear correction using an experimentally acquired calibration curve.

Inaccessibility of the correct flow signal and thus correct tidal volumes makes it impossible to calculate the Work of Breathing (WoB) that is typically expressed in J, J/ breath or J/min. As a surrogate of WoB, another measure may be used for evaluation of breathing effort of the subject: Pressure-Time Product (PTP) expressed typically in Pa·s or Pa·s/min. According to physiological studies, PTP is even more reliable in assessment of energy cost of breathing because it is a good indicator of the metabolic work of breathing [14]. Field et al. [15] documented that oxygen consumption of the respiratory muscles is only weakly correlated with the mechanical WoB (the product of  $\Delta P \cdot V$ ), whereas it is well reflected by the PTP. PTP takes into account the isometric phase of muscle contraction [16] and represents a good indicator of energy expenditure [17].

A proper care should be devoted to the optimum setting of the individual pieces of equipment. Each vital sign monitor for example allows selection of data averaging and display refreshment time, usually referred to as 'response', i.e. how fast the SpO<sub>2</sub> value follows the measurement.

Concerning SpO<sub>2</sub>, several modes of the value presentation may be selected from beat-to-beat presentation to averaging results for 20 s, which is the default setting for Datex S/5 monitors. The long averaging is preferred at intensive care unit (ICU) setup, where stable readings are convenient as the patient physiological parameters do not change rapidly. During extreme breathing experiments, averaging with such a long time base may cause a significant delay in reaction to the current state of the volunteer that may represent a threat to the volunteer's health.

### 3 Medical Aspects of Extreme Outdoor Experiments

While conducting outdoor clinical trials, it is essential to minimise any medical risks posed on the subjects of the experiment. This can be primarily ensured by meticulous selection of participants. Most of the studies are designed for healthy volunteers, scoring ASA 1 according to the American Society of Anaesthesiologists, without any known cardio-respiratory disease and non-smokers. One study had two volunteers suffering from asthma, both treated with beta-agonist inhalers. Prior to a breathing experiment, both self-administered their usual inhalers and no bronchoconstriction has been manifested [8]. In case of any emergencies, a presence of a skilled physician is crucial conjointly with advanced vital sign monitoring, as mentioned above.

Fortunately, only minimal medical issues have been reported during outdoor breathing experiments. On the other hand, the participants need to face the conditions seen in snow burial victims: the triad of hypoxia, hypercapnia and



hypothermia. The protocol design and end point parameters should help to prevent any deleterious effects of these states. The value limits for each trial are conventionally approved by an ethical committee based on the emergency medicine criteria and they might not reflect brief changes in healthy volunteers' physiology.

### 3.1 Hypoxia and Hypercapnia

The main medical risks are associated with the consequences of hypoxia and hypercapnia. The end-tidal O<sub>2</sub> (EtO<sub>2</sub> in %) and end-tidal CO<sub>2</sub> (EtCO<sub>2</sub> in %) in some of the trials reached values that would be considered as critical in ICU setting. Extreme alveolar gas partial pressures were documented in other sports and outdoor experiments.

For instance, a similar situation in terms of short lasting profound changes in arterial partial pressures of gases as in an avalanche victim can be seen in breath-hold divers: a combination of hypoxia and hypercapnia together with a concomitant acidosis due to cumulation of blood and tissue CO<sub>2</sub>. For example, Willie et al. [18] measured the end-apnoea end-tidal partial pressure of oxygen (pO<sub>2</sub>) and carbon dioxide (pCO<sub>2</sub>) during a static dry apnoea reaching  $37 \pm 14$  mmHg and  $45 \pm 7$  mmHg respectively. SpO<sub>2</sub> fell down to  $56.7 \pm 11.3\%$ . Obviously, there is a great deal of adaptation to these derangements among elite free-divers.

Another example of hypoxia observed in healthy young sportsmen is the hypobaric hypoxia, typical for the high altitude where the hypoxemia is in general accompanied by respiratory alkalosis and hypocapnia due to a compensatory hyperventilation. The lowest values of arterial partial pressure of O<sub>2</sub> (PaO<sub>2</sub>) recorded during a simulated high altitude ascent to 8 848 m in a hypobaric chamber was  $30.6 \pm 1.4$  mmHg ( $4.08 \pm 0.19$  kPa) with the lowest recorded values of PaCO<sub>2</sub>  $11.9 \pm 1.4$  mmHg ( $1.59 \pm 0.19$  kPa); the lowest recorded SpO<sub>2</sub> measured from arterialized capillary blood was 67.9% in 8 000 m above sea level [19]. In the course of an experiment conducted on Mt. Everest in Himalaya, there were arterial blood samples obtained at the altitude of 8 400 m following a successful summit ascent. Four climbers were tested while breathing ambient air. A mean PaO<sub>2</sub> of 24.6 mmHg (3.28 kPa) and a mean PaCO<sub>2</sub> of 13.3 mmHg (1.77 kPa) were measured by a bench-top blood gas analyser placed at 6 400 m [20].

In all these experiments, conducted on mountaineers, free-divers and other healthy volunteers, there were measured short time excursions to alarming levels of hypoxia and hypo/hypercapnia mainly seen in critically ill patients. However, the recovery was always rapid back to normal.

These outstanding changes in subjects' physiology necessitate a detailed monitoring. Apart from the technical means, the clinical observation is of a high priority.

Perception of both hypoxia and hypercapnia is highly subjective. A continuous assessment of the awareness and cognition of the subject may help to recognize changes in consciousness.

After their experiments, Roubik et al. [10] conducted a short interview with each of the volunteers to evaluate their subjective perception of the changes in their consciousness. From the answers it was clear that the subjective sensation of the arterial gas changes differed a lot. The sentence of losing control of the situation occurred in two men out of twelve. One of them was disconnected from a zero air pocket by the supervising physician after 330 s when his EtCO<sub>2</sub> reached 8.4%. Another one was describing a worsening dyspnoea which suddenly started to improve and he had experienced a sensation of relief. He was also disconnected at this point and reached a maximum EtCO<sub>2</sub> of 10.2%; compare to another subject, who at the level of CO<sub>2</sub> of 9.5% did not have any problems with dizziness, changes in mental state or headache.

From the above mentioned reasons, it is clear that one isolated value of any parameter is not sufficient itself for overall assessment of the participant's physiology during a breathing experiment. Inter-individual differences are considerable. When defining endpoints for safety and ethical reason, not just one isolated physiological limit should be considered.

### 3.2 Hypothermia

Although only 1–2% avalanche victims die on account of hypothermia [4], the changes in core temperature of outdoor breathing experiment participants may occur. Despite a careful heat protection, a temperature drop happens. Grissom et al. had one subject who requested an experiment termination because he was cold and shivering [8]. Another subject in Radwin's snow burial trial had to be removed from the snow, as his core body temperature dropped after 73 min below 35 °C [9].

### 3.3 Arrhythmias

As a side effect of both hypoxia and hypercapnia, different types of arrhythmias have been reported. In one study, participants were studied for haemodynamic changes at end-tidal CO<sub>2</sub> of 7 kPa and an increase in QT dispersion has been showed [21]. Occasional premature ventricular beats developed during the last minute of the experimental snow burial in the AvaLung study and the testing of the same subject had to be terminated prematurely due to hypoxia [8].

In case of the experiments conducted by Roubík et al. [10] one of the volunteers had to be excluded due to frequent bigeminal ventricular extrasystoles. The medical literature suggests that frequent premature ventricular complexes (PVCs) can evolve into malignant ventricular arrhythmias, ventricular tachycardia or even ventricular fibrillation [22]. These changes in electric cardiac activity have been found to increase a risk of sudden cardiac death not only in patients with structural heart disease [23], but also among young healthy athletes with concealed cardiopathy [24]. As these rhythms rank among the shockable ones, the availability of emergency equipment and drugs as per Advanced Life Support (ALS) guidelines should be mandatory, including the Automated External Defibrillator (AED) [25].

### 3.4 Hygiene During Experiments

The availability and affordability of plastic single-use kits for the health care made the expensive and labour-extensive decontamination of reusable equipment falling out of favour. On the other hand, this applies mainly to hospital setting.

In case that an outdoor breathing trial includes any sort of breathing circuits, the antimicrobial filters should be used to prevent a cross contamination of the equipment. The Heat and Moisture Exchangers (HME), used mainly in anaesthesia and critical care settings, are not convenient. Firstly, humidification is not necessary in snow breathing experiments as the natural moisture of this substance provides some humidity. In addition, the artificial moisture and heat conserved by the filter would change the microclimate in the designed air pocket. A significant heat exchange between the filter and the snow would occur. In a real avalanche burial, the breath causes thawing of the snow in a close proximity to the victim's airway and hence changing the properties of the air pocket. Despite its disadvantages, the sterilisation of breathing circuits appears to be a better solution.

## 4 Conclusion

During outdoor breathing experiments, the intensive care monitors and devices are used in conditions substantially different from a standard ICU. Safety limits of physiological parameters must be interpreted considering these conditions; otherwise the intended safety ranges may be falsely interpreted and safety of the subjects may be impaired. The measuring principle used in these devices is essential to consider when evaluating and interpreting the measured data. Along with technical issues, medical precautions must be applied during the breathing experiments. The physiological parameters of the subjects get quickly out of normal range which increases a risk of complications.

**Acknowledgements** The study was supported by Czech Technical University in Prague grant No. SGS17/203/OHK4/3T/17.

**Compliance with Ethical Requirements** The authors declare that they have no conflict of interest.

## References

1. Falk, M., Brugger, H. and Adler-Kastner, L., 1994. Avalanche survival chances. *Nature*, 368(6466), p. 21.
2. Brugger H, Falk M, Adler-Kastner L., 2003. Der Lawinennotfall. Eine aktuelle Übersicht. *Wiener Klinische Wochenschrift* 9(8), pp. 691–701.
3. Stalsberg, H., Albretsen, C., Gilbert, M., Kearney, M., Moestue, E., Nordrum, I., Rostrup, M. and Ørbo, A., 1989. Mechanism of death in avalanche victims. *Virchows Archiv A*, 414(5), pp. 415–422.
4. Hohlrieder, M., Brugger, H., Schubert, H.M., Pavlic, M., Ellerton, J. and Mair, P., 2007. Pattern and severity of injury in avalanche victims. *High altitude medicine & biology*, 8(1), pp. 56–61.
5. Logan, N., Atkins, D., 1996. The snowy torrents: Avalanche accidents in the United States 1980–1986. *Colorado geological survey* pp. 240–243.
6. Grossman, M.D., Saffle, J.R., Thomas, F., Tremper, B., 1989. Avalanche trauma. *Trauma* 29, pp. 1705–1709.
7. Brugger, H., Sumann, G., Meister, R., Adler-Kastner, L., Mair, P., Gunga, H.C., Schobersberger, W. and Falk, M., 2003. Hypoxia and hypercapnia during respiration into an artificial air pocket in snow: implications for avalanche survival. *Resuscitation*, 58(1), pp. 81–88.
8. Grissom, C.K., Radwin, M.I., Harmston, C.H., Hirshberg, E.L. and Crowley, T.J., 2000. Respiration during snow burial using an artificial air pocket. *Jama*, 283(17), pp. 2266–2271.
9. Radwin, M.I., Grissom, C.K., Scholand, M.B. and Harmston, C. H., 2001. Normal oxygenation and ventilation during snow burial by the exclusion of exhaled carbon dioxide. *Wilderness & environmental medicine*, 12(4), pp. 256–262.
10. Roubík, K., Sieger, L. and Sykora, K., 2015. Work of breathing into snow in the presence versus absence of an artificial air pocket affects hypoxia and hypercapnia of a victim covered with avalanche snow: a randomized double blind crossover study. *PloS one*, 10(12), p. e0144332.
11. Strapazon, G., Paal, P., Schweizer, J., Falk, M., Reuter, B., Schenk, K., Gatterer, H., Grasegger, K., Dal Cappello, T., Malacrida, S. and Riess, L., 2017. Effects of snow properties on humans breathing into an artificial air pocket—an experimental field study. *Scientific reports*, 7(1), p. 17675.
12. ISO 2533:1975/Add 2:1997. Standard Atmosphere ADDENDUM 2: Extension to –5000 m and standard atmosphere as a function of altitude in fe. Swiss, 1997. 123 p.
13. Roubík, K. and Filip, J., 2017. Reliability and source of errors in end-tidal gas concentration evaluation algorithms during avalanche snow and rebreathing experiments. *Lékař a technika-Clinician and Technology*, 47(3), pp. 73–80.
14. Bellani, G., Patroniti, N., Weismann, D., Galbiati, L., Curto, F., Foti, G. and Pesenti, A., 2007. Measurement of pressure–time product during spontaneous assisted breathing by rapid interrupter technique. *Anesthesiology: The Journal of the American Society of Anesthesiologists*, 106(3), pp. 484–490.
15. Field, S., Sanci, S. and Grassino, A., 1984. Respiratory muscle oxygen consumption estimated by the diaphragm pressure-time index. *Journal of Applied Physiology*, 57(1), pp. 44–51.

16. Sassoone, C.S.H. and Mahutte, C.K., 1998. Work of breathing during mechanical ventilation. *Lung biology in health and disease*, 118, pp. 261–310.
17. Collett, P.W., Perry, C. and Engel, L.A., 1985. Pressure-time product, flow, and oxygen cost of resistive breathing in humans. *Journal of Applied Physiology*, 58(4), pp. 1263–1272.
18. Willie, C.K., Ainslie, P.N., Drvis, I., MacLeod, D.B., Bain, A.R., Madden, D., Maslov, P.Z. and Dujic, Z., 2015. Regulation of brain blood flow and oxygen delivery in elite breath-hold divers. *Journal of Cerebral Blood Flow & Metabolism*, 35(1), pp. 66–73.
19. Richalet, J.P., 2010. Operation Everest III: COMEX'97. *High altitude medicine & biology*, 11(2), pp. 121–132.
20. Grocott, M.P., Martin, D.S., Wilson, M.H., Mitchell, K., Dhillon, S., Mythen, M.G., Montgomery, H.E. and Levett, D.Z., 2010. Caudwell xtreme Everest expedition. *High altitude medicine & biology*, 11(2), pp. 133–137.
21. Kiely, D.G., Cargill, R.I. and Lipworth, B.J., 1996. Effects of hypercapnia on hemodynamic, inotropic, lusitropic, and electrophysiologic indices in humans. *Chest*, 109(5), pp. 1215–1221.
22. Carrim, Z.I., Khan, A.A., 2005. Mean frequency of premature ventricular complexes as predictor of malignant ventricular arrhythmias. *Sinai J Med* 2005, 72, pp. 374–380.
23. Lerma, C. and Glass, L., 2016. Predicting the risk of sudden cardiac death. *The Journal of physiology*, 594(9), pp. 2445–2458.
24. Corrado, D. and Zorzi, A., 2017. Sudden death in athletes. *International journal of cardiology*, 237, pp. 67–70.
25. Resuscitation Council UK. *Advanced Life Support*, Sixth Edition, 2011.

# Technique and Gender Specific Conversion Coefficients for Estimation of Effective Dose from Kerma Area Product During X-Ray Radiography of Chest

Asen Dimov, Ivan Tsanev, and Dimitar Penev

## Abstract

**Purpose:** The purpose of this research is to assess Kerma Area Product (KAP) to Effective dose (E) conversion coefficients (CC) specific to gender of patient and type of radiography technique applied during X-ray radiography of Chest. **Methods and materials:** A sample of 1723 adult and paediatric patient records examined on 81 X-ray systems was included in present study. Effective dose for each patient examination was assessed using Monte Carlo simulation software PCXMC, version 2.0.1. CC in  $\mu\text{Sv } \mu\text{Gy}^{-1} \text{ m}^{-2}$  were determined using linear fit for “soft”—below 100 kV and “hard” radiography techniques with respective tube filtration for males and females respectively. **Results:** CC obtained for adult males and females were 1.14 ( $R^2 = 0.93$ ) and 1.25 ( $R^2 = 0.97$ ) respectively when using the “soft” techniques. For “hard” techniques CC values were 2.15 ( $R^2 = 0.98$ ) and 2.25 ( $R^2 = 0.97$ ) for males and females respectively. **Conclusion:** Present study shows technique and gender related differences in conversion coefficients estimated for standard adult patients. CC obtained for paediatric patients contribute to assessment of patient effective doses and hence the risk in individual and population exposures cases.

## Keywords

Effective dose • Conversion coefficient • Chest Radiography

## 1 Introduction

Radiography of chest is the most often examination in X-ray diagnostic radiology. Radiation risk for the patient is calculated based on assessment of the corresponding Effective dose (E). Availability of proper methodology for estimation of effective dose for variety of patient anatomies and exposure conditions could help to professionals engaged in assessment of radiation exposure during this examination. It can also be used for purposes of assessment of Collective effective dose from this examination received by population consisting of adults and children belonging to different age groups as required by European Basic Safety Standards (BSS) Directive and United Nations Scientific Committee on the Effects of Atomic Radiation (UNSCEAR) [1, 2]. Such assessments could aid to process of justification of: screening programmes directed to groups of asymptomatic individuals for purposes of early detection of lung diseases; medical exposure as part of medical or biomedical research programmes; practices for radiological health assessment for employment, immigration, insurance purposes; etc., as specified by international standards and local legislation [1, 3, 4].

## 2 Materials and Methods

Effective dose (E) was calculated for a real sample consisting of 1723 patients: 1244 adult and 479 paediatric exposure records collected during Third National Survey (TNS) of patient doses in diagnostic and interventional radiology organized by Laboratory of Radiation Protection at Medical Exposure (LRPME) at the National Centre of Radiobiology and Radiation Protection (NCRPP) [5]; The children were divided into four age categories: 0–1; 1–5; 5–10; 10–15 years old.

Radiation exposure of each patient was simulated via Monte Carlo calculation software PCXMC [6, 7]. The

A. Dimov (✉) · I. Tsanev · D. Penev  
National Centre of Radiobiology and Radiation Protection, 3, Sv.  
Georgi Sofiyski Str., 1606 Sofia, Bulgaria  
e-mail: adimov\_sl@yahoo.com; a.dimov@ncrrp.org;  
a.dimov07@gmail.com

definition files for PCXMC simulation are generated automatically with an especially designed programme script from an electronic table with patient anthropomorphic and exposure data collected during TNS. The script was elaborated according to PCXMC requirements for patient definition files [7]. Phantom size and weight presented in the table were modified to approximate actual patient morphology using a scaling factor recommended by Tapiovaara [6]. The X-ray field size was also scaled accordingly, as all phantom exposures were set in Posterior-Anterior (PA) projection only, as they were reported for collected patient's sample.

PCXMC software was set to simulate automatically all 1723 patient definition files. Each patient simulation was performed by employing 20,000 photon histories. X-ray spectrum was then modified using reported anode potential applied at patient radiograph. The filtration of tube was not always reported to NCRRP, so standard recommended filtrations were chosen for the specified tube potential: 2 mm Al for tube kilovoltage below 75 kV; 3 mm Al for 76–100 kV; 4 mm Al for 101–125 kV; and 5 mm Al for tube potential over 125 kV. Effective dose was further calculated via standard PCXMC procedures using tissue weighting factors recommended by Publication 103 of International Commission of Radiological Protection (ICRP) [8].

Conversion coefficient (CC) from Kerma Area Product (KAP) to E, expressed in  $[\mu\text{Sv } \mu\text{Gy}^{-1} \text{m}^{-2}]$  were determined using linear approximation of their relation. Different conversion coefficients were calculated for male and female adults. For children CC were obtained despite of their gender.

Dependence of the calculated CCs from applied tube potential was also approximated using a liner fitting.

### 3 Results

Calculated effective dose as a function of reported patient KAP during Chest PA radiography of adult males and females is shown on Fig. 1. Different linear fits are elaborated and displayed for males and females exposed with different anode potential at different filtrations, as specified above. Thus following six linear fits (Linear) are elaborated and displayed on the same figure for: males at 2 mm Al; females at 2 mm Al; males at 3 mm Al; females at 3 mm Al; males at 4 mm Al; females at 4 mm Al. For each of those fits the corresponding linear coefficient and  $R^2$  is determined.

Conversion coefficients from KAP to E are obtained also for children using same approach. Results for all CCs are shown in Table 1.

**Fig. 1** Values of effective dose as a function of Kerma area product to patient

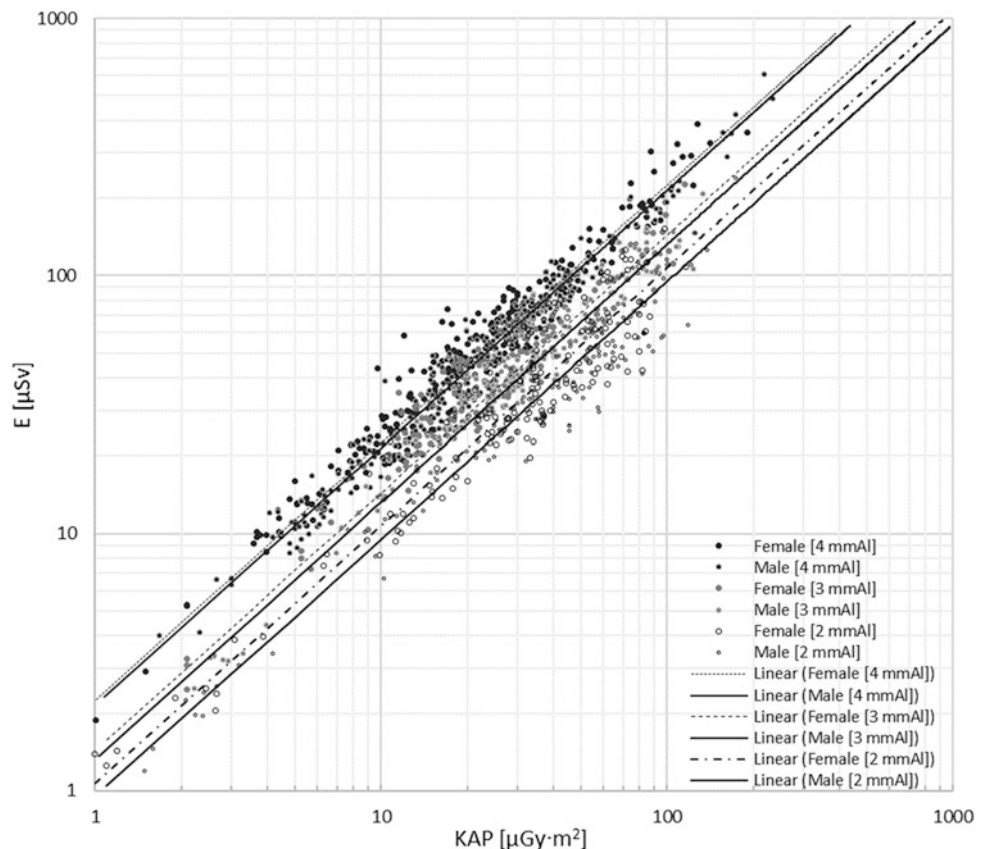




**Table 1** Results for CCs calculated for adults (Male and female); adult males; adult females; and children for Chest radiography

X-ray tube voltage			Sample			Conversion coefficient	
Range	$U_{\text{mean}}$ [kV]	SD	Subgroup	Sample size	No of X-ray systems	E/DAP [ $\mu\text{Sv}/(\mu\text{Gy m}^2)$ ]	$R^2$
50–75 kVp	67	7	Male	120	26	0.91	0.91
	68	7	Female	159	29	1.07	0.89
	67	7	Male and female	279	31	1.00	0.90
	59	10	Children (0y–1y)	93	18	11.03	0.85
	59	10	Children (1y–5y)	101	20	6.66	0.86
	60	10	Children (5y–10y)	64	16	2.80	0.77
	59	8	Children (10y–15y)	43	14	3.47	0.74
75–100 kVp	85	6	Male	159	32	1.37	0.97
	85	7	Female	175	35	1.44	0.96
	85	7	Male and female	334	37	1.39	0.96
	89	8	Children (0y–1y)	33	4	20.66	0.94
	89	8	Children (1y–5y)	20	5	14.46	0.97
	89	9	Children (5y–10y)	27	8	4.24	0.68
	88	7	Children (10y–15y)	23	6	1.93	0.92
100–125 kVp	120	6	Male	318	31	2.15	0.98
	120	7	Female	313	29	2.25	0.97
	120	7	Male and female	631	31	2.20	0.97
	113	8	Children (0y–1y)	13	5	18.21	0.94
	112	8	Children (1y–5y)	24	8	10.82	0.97
	112	8	Children (5y–10y)	19	5	5.03	0.97
	112	5	Children (10y–15y)	19	5	3.72	0.93

The column of  $U_{\text{mean}}$  represent the average tube potential calculated from kVp values reported in patient exposure records for each subgroup. Standard Deviation (SD) of kilovoltage and  $R^2$  of CC for each subgroup of patients are displayed in this table also.

Relative statistical uncertainty calculated by PCXMC for simulation of exposure for our patient sample lies in an interval and has a mean value as follows:

- for adult phantom: from 0.5 to 1.3%; mean: 0.7%;
- for 15 years old children phantom: from 0.6 to 1.3%; mean: 0.8%;
- for 10 years old children phantom: from 0.6 to 3.5%; mean: 2.0%;
- for 5 years old children phantom: from 0.8 to 8.6%; mean: 4.3%;
- for 1 years old children phantom: from: 2.4 to 9.7%; mean: 4.7%.

CCs for adult males and females were 1.14 ( $R^2 = 0.93$ ) and 1.25 ( $R^2 = 0.97$ ) respectively when using the “soft” techniques. For “hard” techniques CC values were 2.15 ( $R^2 = 0.98$ ) and 2.25 ( $R^2 = 0.97$ ) for males and females respectively.

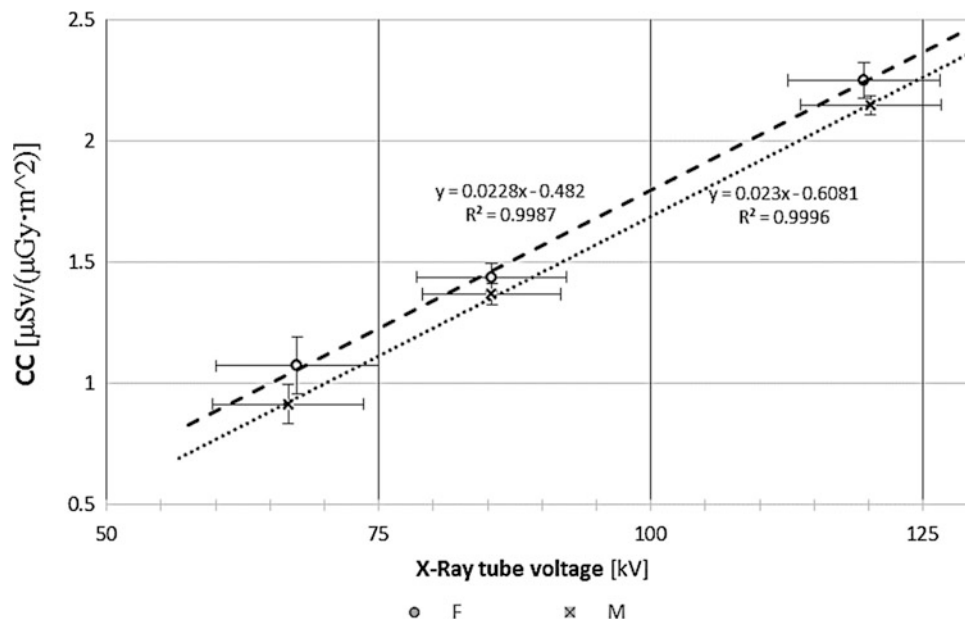
From Table 1 it is seen that for high kV technique (with tube potential of over 100 kV) the CC for Chest PA equals to  $2.20 \mu\text{Sv} (\mu\text{Gy m}^2)^{-1}$  ( $R^2 = 0.97$ ), which differs from often quoted value of  $1.8 \mu\text{Sv} (\mu\text{Gy m}^2)^{-1}$  obtained by Hart et al. for Chest (PA + Lat), recommended by [9–11]. For low kV technique (with tube potential of less than 100 kV) our CC is assessed to  $1.19 \mu\text{Sv} (\mu\text{Gy m}^2)^{-1}$  ( $R^2 = 0.87$ ), which also differs to value of 1.0 for Chest (PA + Lat) obtained by Hart [9].

Values of CCs for adult males and females against the tube potential are plotted in Fig. 2. The standard deviations of mean kVp and the corresponding values of  $[1 - R^2]$ , expressed in %, are displayed on the figure for each coefficient on horizontal and vertical direction respectively.

## 4 Discussion

Deviations of our results for CCs values and values recommended by European guidance and UNSCEAR manual are related with the fact that Hart calculates CCs for combined Chest X-ray procedure including PA plus Lateral projection radiographs [9, 10, and 11]. In addition there are differences between our and Hart’s methodology of CCs

**Fig. 2** Plot of conversion coefficient against mean tube potential for males and females



calculation. Although based on same phantom model (Christy 1980)—adopted by Hart and Tapiovaara, there is a modification prepared by Tapiovaara and implemented in the PCXMC software [6, 9, 12].

Other reason for discrepancy is related to tissue weighting factors recommended by ICRP 60 (1991) and applied by Hart in contrast with ICRP 103 definition of effective dose employed in this study [8, 13].

Main uncertainties in CCs assessment in this study are related to limitations of phantom model to represent different real human anatomies as well as to the fact that actual filtration of the tube was not always reported for this examination during TNS. Since reliable information on tube potential or filtration is not always available when assessment of patient exposure is requested retrospectively, the proposed CCs might be considered as appropriate for use.

Relative statistical uncertainty calculated by PCXMC for simulation of exposure and assessment of effective dose is dependant of total number of photon histories limited to 20,000 in present study and to differences between adult and paediatric anatomies modelled. It is smaller for adults and is bigger for children, but it does never exceed 5% in the present study.

## 5 Conclusion

Calculated conversion coefficients are suitable for determination of effective dose to different subgroups of patients

examined at different exposure conditions for X-ray radiography of Chest, performed in PA projection.

In cases when assessment of effective dose to population is being undertaken by radiation protection authorities and no detailed information for all individual exposures is available additional mean CCs based on present study might be calculated and used.

The automatic generation of patient definition files via designed software script avoids manual way for input of patient and exposure data to be simulated by the PCXMC software and saves time and efforts for the user.

Calculation of effective dose with PCXMC programme would be faster in case an automatic option is provided by software developers for “Compute doses” module in a similar way as it is realized in capabilities of “Simulate” and “Risk assessment” modules.

**Conflict of Interest** The authors declare that they have no conflict of interest.

### Statement of Informed Consent

Informed consent was obtained from all individual participants included in the study.

### Protection of Human Subjects and Animals in Research

All procedures performed in studies involving human participants were in accordance with the ethical standards of the institutional and/or national research committee and with the 1964 Helsinki declaration and its later amendments or comparable ethical standards.

## References

1. Council Directive 2013/59/Euratom of 5 December 2013 laying down basic safety standards for protection against the dangers arising from exposure to ionising radiation, and repealing Directives 89/618/Euratom, 90/641/Euratom, 96/29/Euratom, 97/43/Euratom and 2003/122/Euratom. Official Journal of the European Union, L 13, 17 January 2014, 1–73. ISSN 1977-0677.
2. UNSCEAR Homepage, <http://www.unscear.org>, last accessed 2018/01/20.
3. International Atomic Energy Agency (2014). IAEA Safety Standards for protecting people and the environment. Radiation Protection and Safety of Radiation Sources: International Basic Safety Standards. General Safety Requirements Part 3, No. GSR Part 3. IAEA, Vienna, 2014.
4. Ordinance No. 2 of the Ministry of Health for protection of individuals at medical exposure, promulgated in State Gazette № 13 of February 9 (2018) (in Bulgarian).
5. Dimov A., Ivanova D., Vassileva F. Design, methodology and purposes of the third national patient dose survey in diagnostic radiology. In: Scientific works of the union of scientists in Bulgaria – Plovdiv. Series G. Medicine, Pharmacy and Dental Medicine, Vol. XIX, pp. 130–134, House of Scientists, Plovdiv (2016). ISSN 1311 – 9427.
6. Tapiovaara M, Siiskonen T. A Monte Carlo program for calculating patient doses in medical x-ray examinations. Radiation and Nuclear Safety Authority (STUK), Helsinki (2008). ISBN 978-952-478-393-4.
7. Tapiovaara M, Siiskonen T. PCXMC 2.0 User's Guide. Radiation and Nuclear Safety Authority (STUK), Helsinki (2008). ISBN 978-952-478-397-2.
8. International Commission on Radiological Protection. The 2007 recommendations of the ICRP. Publication 103. Ann ICRP. 2007; 37:2–4.
9. Hart D, Jones DG and Wall BF. (1994a) Estimation of effective dose in diagnostic radiology from entrance surface dose and dose-area product measurements. NRPB-R262 (Chilton, UK: National Radiological Protection Board).
10. European Commission. European guidance on estimating population doses from medical X-ray procedures. Radiation protection No 154, Brussels: 2008.
11. UNSCEAR. Unscear's global survey of radiation exposure. Medical Exposure, a user manual (version October, 2017), available online at: [http://www.survey.unscear.org/lib/exe/fetch.php/unscear\\_medical\\_exposure\\_survey\\_manual\\_v2.pdf](http://www.survey.unscear.org/lib/exe/fetch.php/unscear_medical_exposure_survey_manual_v2.pdf), last accessed 2018/02/21.
12. Christy- Cristy M and Eckerman KF. Specific absorbed fractions of energy at various ages from internal photon sources. I. Methods. Report ORNL/TM-8381/V1. Oak Ridge: Oak Ridge National Laboratory; 1987.
13. ICRP, 1991. 1990 Recommendations of the International Commission on Radiological Protection. ICRP Publication 60. Ann. ICRP 21 (1–3).

# Design and Demonstration of a Complex Neonatal Physiological Model for Testing of Novel Closed-Loop Inspired Oxygen Fraction Controllers

Jakub Rafl<sup>✉</sup>, Thomas E. Bachman, Tomas Martinek, Leos Tejkl, Veronika Huttova, Petr Kudrna, and Karel Roubik<sup>✉</sup>

## Abstract

Recently published clinical trials document that manual control of oxygen fraction in the inspiratory gas in neonates is not prompt enough to react to the rapidly changing physiological status of a neonate. As a result, the arterial blood oxygen saturation exhibits significantly long periods when the actual oxygen saturation level goes outside the desired safe range. Simple closed-loop systems are able to optimize the inspiratory oxygen fraction in steady-state situations, but they do not perform well in the context of rapidly changing physiological parameters. As a consequence, new algorithms for the closed-loop control of the inspired oxygen fraction are being developed and are becoming available. The aim of our study was to create a physiologically-realistic model of a neonatal organism allowing more extensive bench testing of newly developed algorithms for oxygen control in neonates. The design of the model is based both on the theoretical and up-to-date knowledge of the physiological principles, as well as on the well-documented observations by the authors in the neonatal intensive care units. The simulated outputs of the model correlate well with the real situations observed in the clinical environment.

## Keywords

Oxygenation • Closed-loop control • Neonatal model

## 1 Introduction

Oxygen therapy represents an essential treatment technique both in critical care and in patients with chronic respiratory diseases. Supplemental oxygen has long been used to prevent hypoxia which is associated with detrimental effects on the brain, pulmonary vasculature, patency of the ductus arteriosus and other tissues and organs in premature infants [1–4]. No less important as prevention of hypoxia is a protection of the organism against excessive and prolonged oxygen exposure due to the oxygen toxicity. Oxidative damage and serious complications affecting the central nervous system, eye, and lungs are associated with hyperoxemia [5–7].

Several studies documented that clinical staff responds more carefully on episodes of lower SpO<sub>2</sub> levels while they tend to tolerate higher levels of SpO<sub>2</sub> than the predetermined target limits [8, 9]. In order to minimize the periods when measured SpO<sub>2</sub> levels are outside the target limits, automated closed-loop control of inspired fraction of oxygen (FiO<sub>2</sub>) have been developed recently. Many studies document benefits of this approach to FiO<sub>2</sub> regulation over the manual one [10–13].

Various algorithms for automated control of FiO<sub>2</sub> have been proposed including rule-based controllers with or without fuzzy logic involved, PID controllers, adaptive controllers, and several other algorithms [14]. For assessment of their efficiency and performance and for their comparison, human physiological models are being developed. Despite the sufficient numbers of models describing the response of adult patients to FiO<sub>2</sub> changes, we are aware of only one model developed for simulation of infants [15]. The existing model works satisfactorily in general but reflects only a limited set of physiological principles needed for realistic scenarios observed in neonatal intensive care units. The aim of the study is to enhance the current neonatal FiO<sub>2</sub> response model and to demonstrate the model's utility by reporting the distribution of

J. Rafl (✉) · T. E. Bachman · T. Martinek · L. Tejkl · V. Huttova  
P. Kudrna · K. Roubik  
Faculty of Biomedical Engineering, Department of Biomedical  
Technology, Czech Technical University in Prague, nam. Sitna  
3105, 272 01 Kladno, Czech Republic  
e-mail: rafl@fbmi.cvut.cz

V. Huttova  
e-mail: huttover@fbmi.cvut.cz

oxygen exposure during simulations of a typical manual  $\text{FiO}_2$  titration scheme.

## 2 Methods

Our model is based on an existing lumped-parameter model of neonatal oxygen transport, published by Morozoff [15, 16]. It was implemented in the Matlab–Simulink environment (Mathworks, Natick, USA). Our model was enhanced from that of Morozoff in a number of ways. First, it was scaled to simulate very small neonates most often deserving respiratory support in the neonatal Intensive Care Unit (ICU) and the most vulnerable to hyperoxemia and hypoxemia. Potential shifts in the oxyhemoglobin dissociation curve were implemented. The known bias between  $\text{SpO}_2$  and  $\text{SaO}_2$  was addressed. Subtleties in the respiratory system associated with a respiratory support were added. We developed a set of realistic scenarios for various categories of neonates. Finally, we added an output module that collected the aggregate exposure to  $\text{SpO}_2$  and  $\text{PaO}_2$ .

The model is divided into the respiratory system model and the circulatory model, connected by the gas exchange section. Another section, the pulse oximeter, represents the measurement of  $\text{SpO}_2$ . The respiratory system model consists of four RC compartments (mouth, trachea, bronchi, and alveoli) connected in series. Instantaneous total pressures of the inhaled/exhaled gas mixture are calculated for all compartments as well as are the gas flows between the compartments. The partial pressure of oxygen in the compartments is derived from the total gas flows between compartments and the oxygen fraction. Spontaneous breathing is mimicked using a

sinusoidal driving function. The circulatory system is modeled as nine perfect mixing chambers and four delay compartments. The concentration of oxygen bonded to hemoglobin is traced in each chamber and expressed as oxygen saturation. Oxygen consumption in the model is directly related to the oxygen concentration in the tissue compartment. Gas exchange between the alveolar compartment and the pulmonary capillaries is calculated under the assumption of the perfusion limited diffusion, that is, the equal partial pressure of oxygen in the alveoli and in the pulmonary capillaries [17]. The oxyhemoglobin dissociation curve (OHDC) links the oxygen partial pressure and saturation of oxygen. The pulse oximeter compartment adds noise and motion artifacts to the  $\text{SaO}_2$  (arterial saturation of oxygen) signal as well as the  $\text{SpO}_2$ – $\text{SaO}_2$  bias that is an issue in case of neonates [18, 19]. We included the bias as an enhancement of the original Morozoff’s model.

Three shunts are incorporated in the model: an atrial right-to-left shunt (patent foramen ovale), a right-to-left shunt from the pulmonary artery to the aorta (patent ductus arteriosus, PDA), and a pulmonary shunt that includes both the true shunt and the ventilation/perfusion mismatch. The model implements two different OHDC: the adult hemoglobin OHDC, based on Kelman’s model [20], and a left-shifted fetal hemoglobin OHDC.

We defined “neonates” of three different types: (1) very stable, (2) typical, and (3) unstable; that differed in the PDA shunt level, the pulmonary shunt level and the number and duration of apneic episodes, as characterized in Table 1. For each of the neonates, we ran a 1-h simulation, each with two different OHDC. As a baseline for a steady-state without clinical exacerbations,  $\text{FiO}_2$  21% was sufficient for

**Table 1** Characteristics of the infant scenarios

Condition or event	Property	Scenario		
		Very stable	Typical	Unstable
PDA shunt	Baseline	10%	15%	20%
	Change	No change	No change	80%
	Occurrence	No change	No change	At the 15th and 45th min
	Duration	n/a	n/a	5 min
Pulmonary shunt	Baseline	20%	30%	30%
Apnea (severe)	Occurrence	At the 30th min	At the 20th and 40th min	Every 12 min
	Duration	60 s	60 s	90 s
Apnea (minor)	Occurrence	Every 4 min	Every 3 min	Every 2 min
	Duration	20 s	30 s	45 s
Noise ( $\text{SpO}_2$ )	Baseline	$\pm 1$ $\text{SpO}_2$ unit	$\pm 1$ $\text{SpO}_2$ unit	$\pm 1$ $\text{SpO}_2$ unit
	Change	Minus 10%	Minus 10%	Minus 10%
	Occurrence	Every 10 min starting at the 5th min	Every 10 min starting at the 5th min	Every 10 min starting at the 5th min
	Duration	3 min	3 min	3 min



maintaining SpO<sub>2</sub> 92–95%, in all three scenarios. We used the model in a closed-loop arrangement with a simple rule-based controller that adjusted the oxygen fraction FiO<sub>2</sub> in the input gas mixture. The FiO<sub>2</sub> titration scheme changed FiO<sub>2</sub> with a magnitude and timing depending on whether the SpO<sub>2</sub> was <80, <90 or >95%. In addition, as a baseline to see the impact of the strategy, we ran each simulation with no adjustment from the initial FiO<sub>2</sub> baseline.

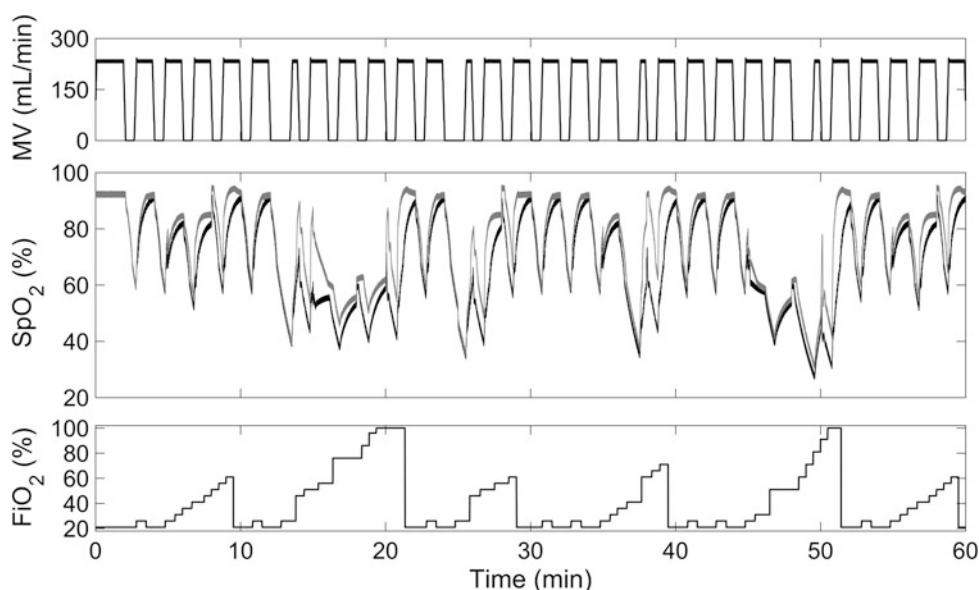
### 3 Results

Figure 1 compares the SpO<sub>2</sub> waveforms with and without the FiO<sub>2</sub> adjustment during a 1-h simulation of the unstable neonate with adult hemoglobin. The figure shows that the

increase of FiO<sub>2</sub> does not have an effect during the apnea as the increased partial pressure of oxygen cannot reach alveoli with no breathing activity. On the other hand, the SpO<sub>2</sub> recovers faster with the FiO<sub>2</sub> increase after the spontaneous breathing is reestablished. The increase of the magnitude and duration of the FiO<sub>2</sub> intervention with a deeper or longer desaturation is also illustrated.

The SpO<sub>2</sub> histogram for the three scenarios in Fig. 2 characterizes their differences with no FiO<sub>2</sub> adjustment. The SpO<sub>2</sub> histogram for the same scenarios in Fig. 3 demonstrates the effect of the FiO<sub>2</sub> adjustment and is especially pronounced in case of the unstable neonate. In this case, the time of SpO<sub>2</sub> below 81% was reduced by 18% and the time with SpO<sub>2</sub> 90–95% improved by 11%. In all three

**Fig. 1** SpO<sub>2</sub> course during 1-h simulated unstable scenario. Comparison of no FiO<sub>2</sub> control (middle panel, black) with FiO<sub>2</sub> control (middle panel, gray). Minute ventilation (MV, top) reduced to zero marks the apneic episodes. The FiO<sub>2</sub> adjustments are shown in the bottom panel. Normal hemoglobin OHDC



**Fig. 2** SpO<sub>2</sub> histogram for no FiO<sub>2</sub> adjustment. Normal hemoglobin OHDC

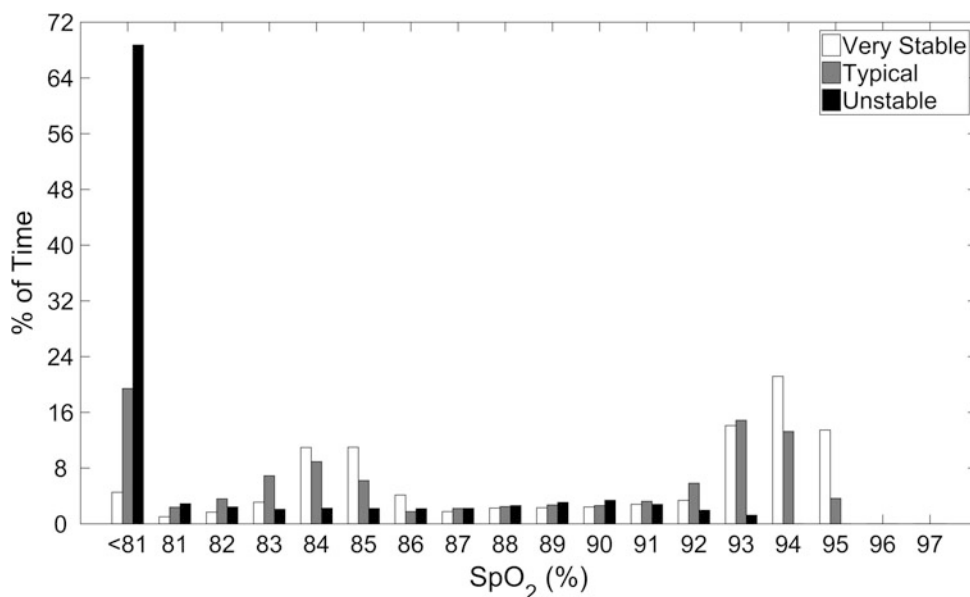
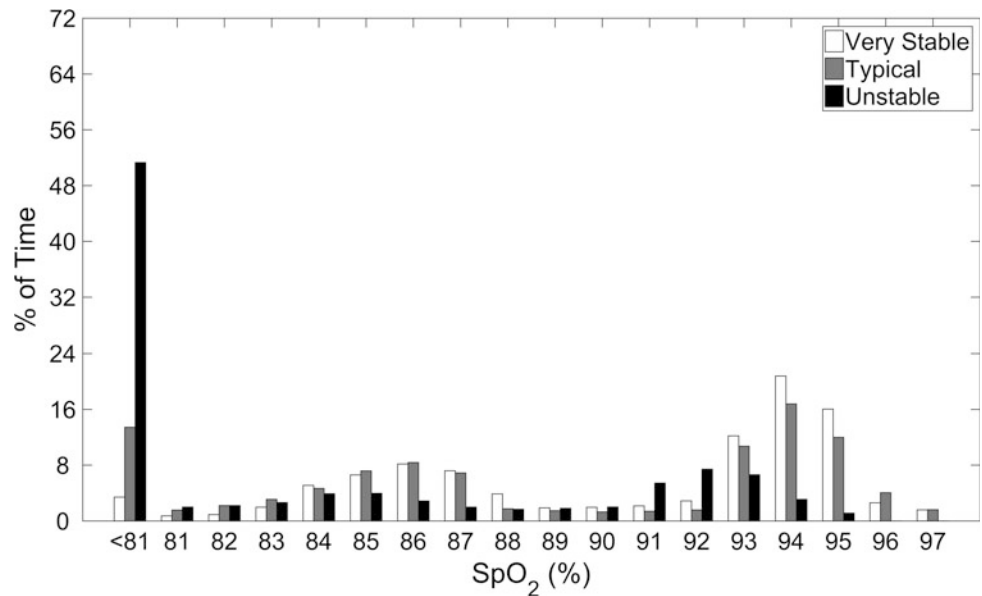


**Fig. 3** SpO<sub>2</sub> histogram for controlled FiO<sub>2</sub>. Normal hemoglobin OHDC



neonates, the SpO<sub>2</sub> is shifted to the higher values due to the closed-loop FiO<sub>2</sub> adjustment.

The distribution of PaO<sub>2</sub> for the three infant profiles is reported in Table 2 (no FiO<sub>2</sub> adjustment) and in Table 3 (the closed-loop FiO<sub>2</sub> adjustment). The shift in PaO<sub>2</sub> with OHDC was marked. As compared to no adjustments, the titration scheme improved the time with PaO<sub>2</sub> < 40 mmHg by 1%, 3%, and 16% (adult OHDC), and by 1%, 5%, and 17% (fetal OHDC) for the very stable, typical, and unstable scenario, respectively.

**Table 2** PaO<sub>2</sub> distribution with different oxyhemoglobin dissociation curves with no FiO<sub>2</sub> adjustments

% Time PaO <sub>2</sub>	Scenario		
	Very stable	Typical	Unstable
50–80 mmHg	85/80	65/58	13/3
>100 mmHg	0/0	0/0	0/0
<40 mmHg	2/7	11/26	60/76

OHDC normal/fetal

**Table 3** PaO<sub>2</sub> distribution with different oxyhemoglobin dissociation curves with FiO<sub>2</sub> adjustments

% Time PaO <sub>2</sub>	Scenario		
	Very stable	Typical	Unstable
50–80 mmHg	79/84	74/69	35/29
>100 mmHg	0/0	0/0	0/0
<40 mmHg	1/6	8/21	44/59

OHDC normal/fetal

## 4 Discussion

Contrary to numerous models available for modeling of a response to FiO<sub>2</sub> changes in adults, equivalent neonatal models are very rare. One important contributing factor is the relative inaccessibility of neonatal physiological data and their interrelationships. The lack of such data is caused by the fact that an experimental physiological research in neonates is not only technically complicated, but safety and ethical reasons play an important role.

The precision and accuracy of models depend on their complexity and the number and quality of parameters included in the calculations. Complex models, that do require the input of patient-specific data and tuning, show in general better accuracy than less complex universal models, but the patient-specific tuning represents a meaningful obstacle for their routine use. The goal of our work was to create a model that is able to simulate realistically the ICU scenarios, but still be simple enough so that it does not require detailed patient-specific data. The three ICU scenarios differing by their stability of SpO<sub>2</sub> response represent typical patterns present at neonatal ICU and document the ability of the developed model to compare different FiO<sub>2</sub> closed-loop control algorithms. We speculate that they could also be used to refine manual FiO<sub>2</sub> titration guidelines.

## 5 Conclusions

An improved neonatal model suitable for studying automatic closed-loop FiO<sub>2</sub> control algorithms has been described. Using the model, distribution of PaO<sub>2</sub> for

different infant profiles and different forms of hemoglobin with no  $\text{FiO}_2$  adjustment and with an adjustment of  $\text{FiO}_2$  may be conducted. The model is suitable for testing, validation, and comparison of  $\text{FiO}_2$  closed-loop control algorithms.

**Acknowledgements** The work was supported by grant SGS17/203/OHK4/3T/17 of the Czech Technical University in Prague.

**Compliance with Ethical Requirements** The authors declare that they have no conflict of interest.

## References

1. Silverman, W. A.: A cautionary tale about supplemental oxygen: the albatross of neonatal medicine. *Pediatrics* 113(2), 394–396 (2004).
2. Skinner, J. R., Hunter, S., Poets, C. F., Milligan, D. W., Southall, D., Hey, E. N.: Haemodynamic effects of altering arterial oxygen saturation in pre-term infants with respiratory failure. *Arch Dis Child Fetal Neonatal Ed* 80(2), F81–F87 (1999).
3. Noori, S., Patel, D., Friedlich, P., Siassi, B., Seri, I., Ramanathan, R.: Effects of low oxygen saturation limits on the ductus arteriosus in extremely low birth weight infants. *J Perinatol* 29(8), 553–557 (2009).
4. Claire, N., Bancalari, E.: Automated closed loop control of inspired oxygen concentration. *Respiratory care* 58(1), 151–161 (2013).
5. Collins, M. P., Lorenz, J. M., Jetton, J. R., Paneth, N.: Hypocapnia and other ventilation-related risk factors for cerebral palsy in low birth weight infants. *Pediatr Res* 50(6), 712–719 (2001).
6. Flynn, J. T., Bancalari, E., Snyder, E. S., Goldbert, R. N., Feuer, W., Cassady, J., et al.: A cohort study of transcutaneous oxygen tension and the incidence and severity of retinopathy of prematurity. *N Engl J Med* 326(16), 1050–1054 (1992).
7. Askie, L. M., Henderson-Smart, D. J., Irwig, L., Simpson, J. M.: Oxygen-saturation targets and outcomes in extremely preterm infants. *N Engl J Med* 349(10), 959–967 (2003).
8. Clucas, L., Doyle, L. W., Dawson, J., Donath, S., Davis, P. G.: Compliance with alarm limits for pulse oximetry in very preterm infants. *Pediatrics* 119(6), 1056–1060 (2007).
9. Sink, D. W., Hope, S. A., Hagadorn, J. I.: Nurse: patient ratio and achievement of oxygen saturation goals in premature infants. *Arch Dis Child Fetal Neonatal Ed* 96(2), F93–F98 (2011).
10. Van Zanten, H. A., Kuypers, K. L. A. M., Stenson, B. J., Bachman, T.: The effect of implementing an automated oxygen control on oxygen saturation in preterm infants. *Arch Dis Child Fetal Neonatal Ed*. 102(5), F395–F399 (2017).
11. Wilinska, M., Bachman, T., Swietlinski, J., Jakiel, G.: Quicker response results in better  $\text{SpO}_2$  control - a comparison of 3  $\text{FiO}_2$ -titration strategies in ventilated preterm infants. *Annals of agricultural and environmental medicine* 22(4), 708–712 (2015).
12. van Kaam, A. H., Hummler, H. D., Wilinska, M., Swietlinski, J., Bachman, T.: Automated versus manual oxygen control with different saturation targets and modes of respiratory support in preterm infants. *Journal of Pediatrics* 167(3), 545–550.e2 (2015).
13. Bachman, T., Roubik, K.: Crossover from automated to manual titration of  $\text{FIO}_2$  in the nicu: Is there a transition lag? *Lekar a technika – Clinician and Technology* 46(2), 37–40 (2016).
14. Fathabadi, O. S., Gale, T. J., Olivier, J. C., Dargaville, P. A.: Automated control of inspired oxygen for preterm infants: what we have and what we need. *Biomedical Signal Processing and Control* 28 (Jul 1), 9–18 (2016).
15. Morozoff, E. P., Saif M.: Oxygen therapy control of neonates – part I: A model of neonatal oxygen transport. *Control and Intelligent Systems* 36(3), 227–237 (2008).
16. Morozoff, E. P., Saif M.: Oxygen therapy control of neonates: part II – Evaluating manual, PID and fuzzy logic controller design. *Control and Intelligent Systems* 36(3), 238–249 (2008).
17. Rideout, V. C.: *Mathematical and computer modeling of physiological systems*. 1st edn. Prentice Hall, Englewood Cliffs, N. J. (1991). ISBN 01–356-3354-0.
18. Ross, P. A., Newth, C. J. L., Khemani, R. G.: Accuracy of pulse oximetry in children. *Pediatrics* 133(1), 22–29 (2014).
19. Bachman, T. E., Newth, C. J. L., Ross, P. A., Iyer, N. P., Khemani, R. G.: Characterization of the bias between oxygen saturation measured by pulse oximetry and calculated by an arterial blood gas analyzer in critically ill neonates. *Lekar a technika – Clinician and Technology* [Article in press].
20. Kelman, G. R.: Digital computer subroutine for the conversion of oxygen tension into saturation. *Journal of Applied Physiology* 21 (4), 1375–1376 (1966).

# Radionuclide Internal Dosimetry Using GATE and PENELOPE for Experimental Validation in Geometrical Phantoms

Nícollas Gonçalves Cavedini<sup>✉</sup>, Caroline Machado Dartora<sup>✉</sup>,  
Luís Vinícius de Moura<sup>✉</sup>, Marcelo Menna Barreto Schwarcke<sup>✉</sup>,  
and Ana Maria Marques da Silva<sup>✉</sup>

## Abstract

The aim of this study is to investigate the use of two freely available Monte Carlo (MC) codes to model simple geometrical radionuclide configurations, which could be compared to experimental measurements or analytical calculus for internal dosimetry. Three spherical geometries were simulated using GATE 7.1 and PENELOPE 2008: (1) a point source centered in a 10 cm radius sphere; (2) a 5 cm radius sphere with homogeneous radioactive distribution inside a 10 cm radius sphere; (3) two separated spheres (5 and 10 cm radius) 5 cm apart, the first acting as source and the second as target. All spheres were filled with water and sources produced  $10^8$  primary gamma emissions from  $^{99m}\text{Tc}$ . Total absorbed doses were analyzed using 3D Dose Point Kernel (DPK). Results obtained with GATE and PENELOPE simulations were, respectively: (1) 15 and 14.25 mGy, with 5.2% difference; (2) 7.4 and 8.51 mGy, showing higher difference (13.04%); (3) 0.93 and 0.97 mGy, in target sphere. Concluding, GATE and PENELOPE MC codes can be easily used to simulate simple geometries, allowing for comparison against experimental measurements or analytical calculations. Further studies are required to compare these simulation results with experimental data designed to the clinical practice.

## Keywords

Monte carlo • GATE • PENELOPE • Dose DPK

N. G. Cavedini (✉) · C. M. Dartora · L. V. de Moura  
A. M. Marques da Silva  
PUCRS, Laboratory of Medical Imaging, School of Science,  
Porto Alegre, RS 90619900, Brazil  
e-mail: nicollas.cavedini@acad.pucrs.br

M. M. B. Schwarcke  
Department of Exact and Social Applied Sciences,  
Federal University of Health Science of Porto Alegre,  
Porto Alegre, RS 90050170, Brazil

## 1 Introduction

Nuclear Medicine (NM) is a specialty in which the radioactive source is internally distributed in the patient. Internal dosimetry has been one of the greatest difficulties and challenges in NM.

Many difficulties are found in internal dosimetry studies related to radiopharmaceutical temporal distributions in the organ source and target irradiation processes. Some techniques have been published by the Committee on Medical Internal Radiation Dose (MIRD) [1]. One of most successful software for mathematical modeling for internal dosimetry in NM using MIRD techniques is OLINDA [2]. Most dose calculations are based on standard subjects, anthropomorphic mathematical models, also called anthropomorphic phantoms, which display the target organs masses and the energy fractions absorbed in tissues. It has been widely used in several internal dosimetry studies in SPECT and PET studies [3].

Concepts of deposited energy and absorbed dose are of particular interest in NM in imaging applications and radiopharmaceutical therapy. Due to patient-specific internal characteristics, the discrepancy between the patient body geometry and that of the dosimetry model, as well as the individual variation in time-activity biodistribution introduce inaccuracies into the absorbed dose calculation [4].

Several MC simulation codes have been used in the estimation of internal dosimetry in NM. Among them, the following codes can be highlighted: EGS4, MCNP, GEANT4 [5] and PENELOPE [6]. GEANT4 and PENELOPE are those with more applications in NM [7–11].

GATE (Geant4 Application for Tomographic Emission) is a simulation platform based on the GEANT4 toolkit for radiation therapy and dosimetry applications [12]. This application is used in medical imaging and dosimetry fields. It simulates the interaction between matter and radiation of energy between 1 keV and 100 TeV. Available interaction libraries include photoelectric effect, Compton scattering,

Rayleigh scattering, electron ionization, gamma conversion, Bremsstrahlung, positron annihilation, multiple scattering and muon electromagnetic processes.

PENELOPE (PENetration and Energy Loss of Positron and Electrons) is a MC simulation code written in FORTRAN programming language, which simulates photon, electron and positron interactions with energy between 250 keV and 1 GeV. It uses a library of interactions of photoelectric effect, Rayleigh scattering, Compton scattering, electron-positron pair, elastic collisions, inelastic collisions, Bremsstrahlung emission and positron annihilation [6].

To obtain the average estimate of deposited energy and absorbed dose, usually a standard patient is considered [4]. Models of standardized patients can be based on morphological information in geometrical or voxelized virtual phantoms. Standardized patients based models are accepted to estimate the dose average value, but in clinical practice, it does not show accurate results or can be experimentally validated. To improve accuracy, MC simulations allow individualizing the physical processes and geometries, producing more realistic data [3]. This technique enables to model the radionuclide disintegration, the attenuation probabilities in the tissues and the detailed values of individual organ volumes, giving the dosimetry data in a volumetric matrix [13]. However, MC is time consuming for clinical practice. One feasible approach is the use of dose point kernels (DPKs) [8, 14], which give the absorbed dose deposited at a certain distance from a point source, assuming a homogeneous transport medium.

The aim of this study is to investigate the use of two freely available Monte Carlo (MC) codes to allow radionuclide internal dosimetry with simple geometries, which can be compared to experimental measurements or analytical calculation, using DPK method.

## 2 Materials and Methods

This study is based on GATE 7.1 and PENELOPE 2008 Monte Carlo simulation codes of three geometries modeled and simulated (Fig. 1): (a) a point source inside a 10 cm radius water spherical target; (b) a 5 cm radius water spherical source inside a 10 cm radius water spherical target; and (c) a 5 cm water radius spherical source separated 5 cm of the border of a 10 cm radius water spherical target. Spherical geometry was chosen due to the future practicality in experimental studies.

For all simulations, 140 keV photons from a  $^{99m}\text{Tc}$  isotropic source with  $1 \times 10^8$  primary histories were simulated. Sources and targets materials were defined as water. Absorbed dose analysis was performed based on 3D Dose Point Kernel (DPK) [8, 14], using a house made code, developed in MATLAB R2014b.

In GATE, the smallest element volume in absorbed dose matrix is a cubic voxel called *dosel*, and it defines the dose map spatial resolution. We used a  $121 \times 121 \times 121$  *dosel* matrix (0.17 cm/pixel). Two libraries of electromagnetic processes on Geant4.10.1 [15] were used: standard (photoelectric effect, Compton scattering, electron ionization, gamma conversion, Bremsstrahlung, positron annihilation, electron and positron multiple scattering and muon) and Penelope (Rayleigh scattering).

For PENELOPE simulation, we used the standard simulation (photoelectric effect, Compton scattering, electron ionization, Bremsstrahlung, positron annihilation, electron-positron pair, elastic and inelastic collisions) with 3D dose map with  $121 \times 121 \times 121$  bins matrix (0.17 cm/pixel).

### 2.1 Point Source Simulation

For the analysis of point source simulation inside the spherical target, the total absorbed dose in GATE and PENELOPE was compared to the theoretical approach, based on Prestwich et al. [16] and Loevinger and Berman [17].

### 2.2 Spherical Sources Simulation

For the volumetric sources simulation, profile doses were delineated in the central axis plan of both simulations. An exponential fitting was applied in a central axis of the target 3D dose distribution central slice, in order to compare the simulated results.

## 3 Results and Discussion

### 3.1 Point Source

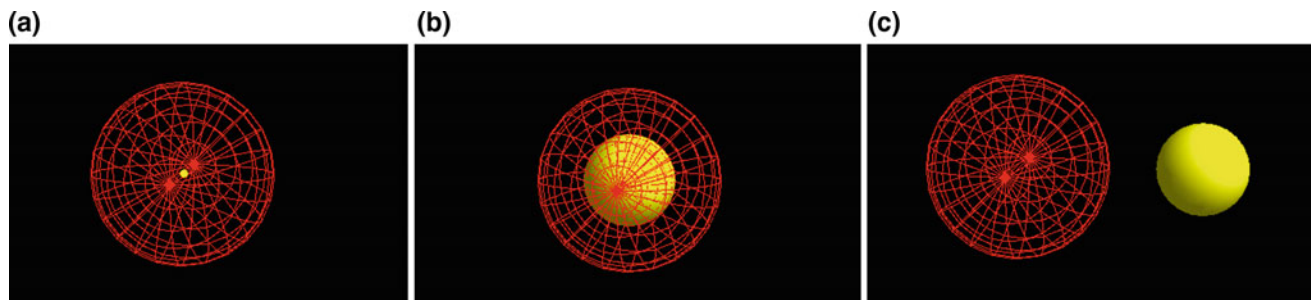
For GATE and PENELOPE, the total absorbed dose was 15 mGy and 14.25 mGy, respectively, with a difference of 5.2%. Compared with the theoretical approach (12.54 mGy), codes differences were 16.4 and 12%, in GATE and PENELOPE.

Figure 2 shows the dose distribution obtained with GATE and PENELOPE, and the dose distribution profile, normalized for the maximum in each simulation.

### 3.2 Spherical Source Inside Spherical Target

Results of the total absorbed dose in GATE were 7.4 and 8.51 mGy in PENELOPE, with a difference of 13.0%. This geometry does not allow an analytical approach.





**Fig. 1** Three geometries modeled: **a** point source (yellow dot) inside a water sphere (red grid), **b** Spherical water source surrounded by a water spherical target, and **c** Spherical water source detached from a spherical water target. All sources are represented in yellow and targets are represented in red grids (Color figure online)

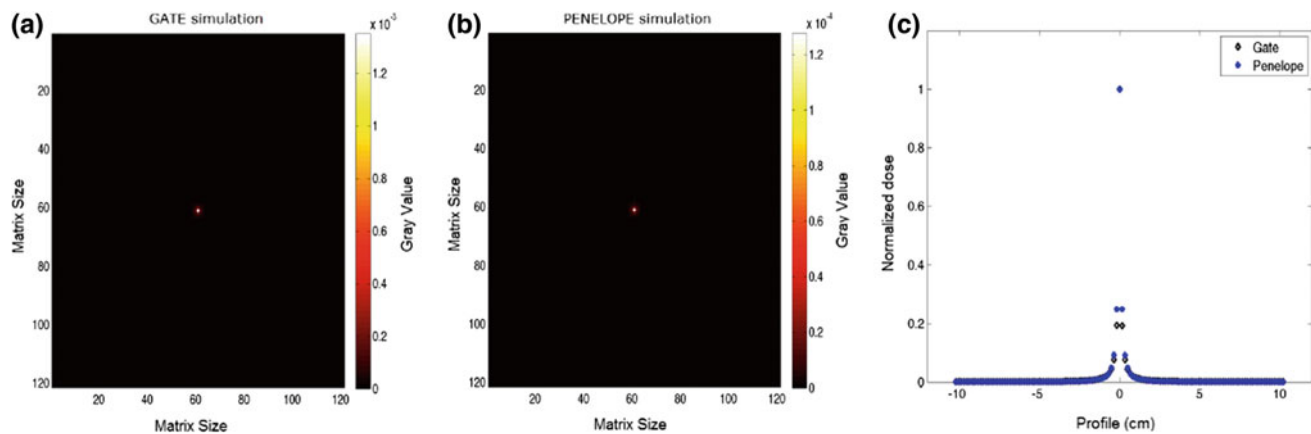


**Fig. 2** Dose distribution obtained in GATE (a) and PENELOPE (b). c Dose distribution profiles in GATE (black) and PENELOPE (blue) (Color figure online)

Figure 3 shows the results of 2D dose distribution in the spherical water target due to the inner spherical source in GATE and PENELOPE (Fig. 3a, b) and the absorbed dose profile, normalized for the maximum in each simulation (Fig. 3c).

### 3.3 Spherical Source Detached from Spherical Target

For the irradiation geometry where the spherical source is situated 5 cm apart the spherical target, it is possible to visually observe a similarity between GATE and PENELOPE results (Fig. 4a, b). Total absorbed dose for the spherical target was 0.93 mGy for GATE and 0.97 mGy for PENELOPE. Dose difference between the two MC codes is 4.03%. Figure 4c shows the dose distribution profile in the central axis of the spherical target. The dose values are normalized for the maximum value of each simulation.

GATE has been initially designed for the simulation of NM imaging systems. However, the latest versions extend its applications to the dosimetry, thus making validation against other existing MC codes a necessary process. GATE's tools allow importing medical images for making patient specific 3D absorbed dose calculations. Although without complex imaging tools, PENELOPE MC simulation of coupled electron-photon transport can be easily defined for arbitrary materials and complex quadric geometries.

The differences in point source simulations results are compatible with previous studies comparing MC codes [2, 8]. The slightly higher discrepancies observed for volumetric sources are acceptable [18], as different algorithms are applied in each MC code and the result depends on the simulation libraries and parameters. Some discrepancies could be due to the boundary effect in cubic voxels.

Further studies are required to compare both MC codes in particles, like alpha and beta emitters, and multispectral sources. Modeling cylindrical phantoms also will allow

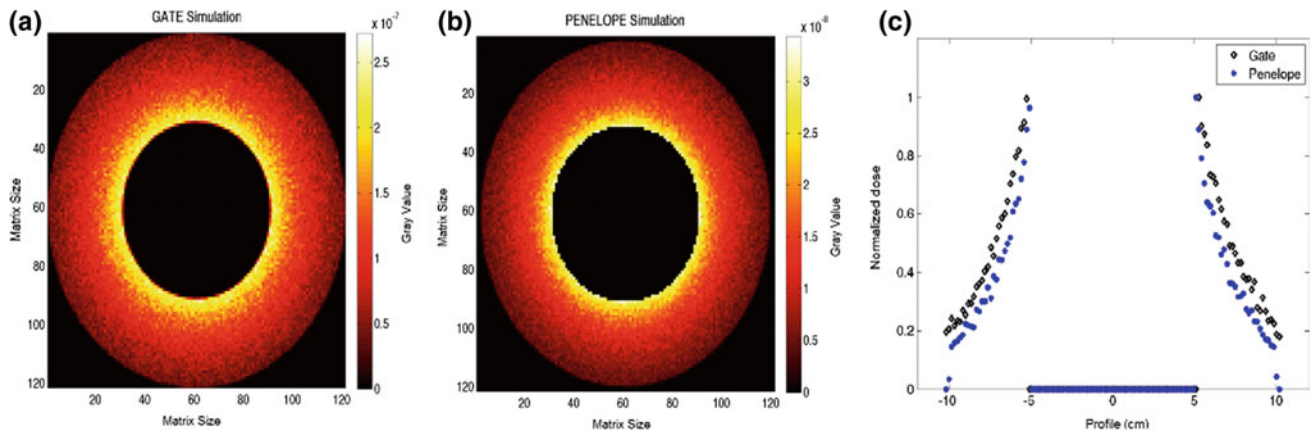


**Fig. 3** Dose distribution in GATE (a) and PENELOPE (b) in the spherical target with inner spherical source. c Dose profile in GATE (black) and PENELOPE (blue) (Color figure online)

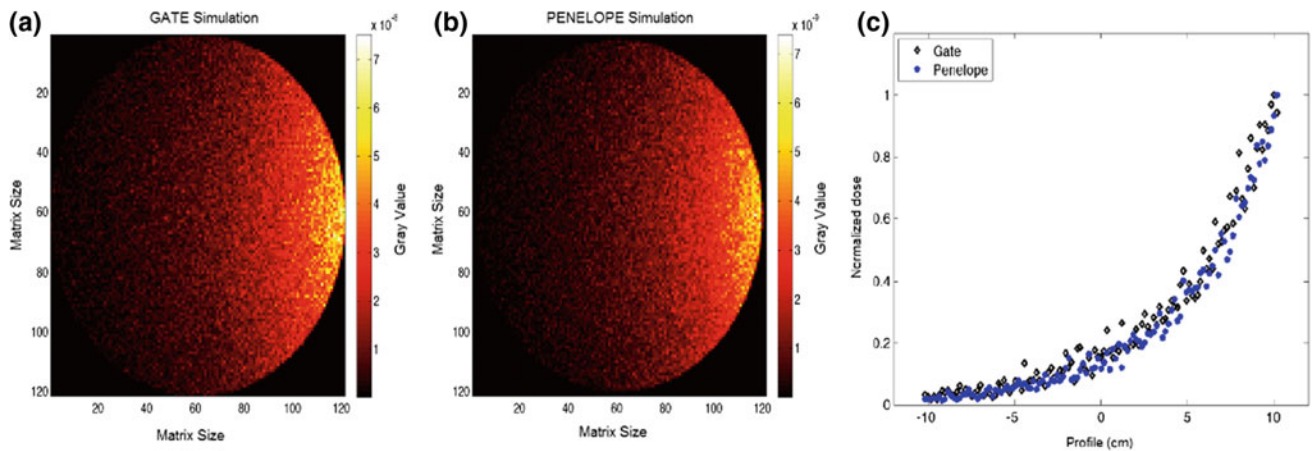


**Fig. 4** Absorbed dose distribution in the target sphere using GATE (a) and PENELOPE (b). In c absorbed dose profile of GATE (black) and PENELOPE (blue) (Color figure online)

more feasible designs for experimental data collection using TLD or polymeric gel dosimetry in clinical practice.

## 4 Conclusions

In this study, we have performed a comparison between GATE and PENELOPE in simulating a monoenergetic gamma source and simple geometries that can be compared with theoretical and experimental approaches. In all cases both MC codes dose results were comparable to previously published data to demonstrate the appropriateness of MC as an adequate tool for dose calculations in NM field. Concluding, GATE and PENELOPE MC codes can be easily used to simulate simple geometries, allowing for comparison against experimental measurements or analytical calculations.

## Compliance with Ethical Standards

**Conflicts of interest:** The authors declare that they have no conflict of interest.

## References

1. Committee on Medical Internal Radiation Dose (MIRD) Homepage, <http://www.snmmi.org/ClinicalPractice/content.aspx?ItemNumber=4212>, last accessed 2017/01/24.
2. Stabin, M., Sparks, R., Crowe, E.: OLINDA/EXM: The Second-Generation Personal Computer Software for Internal Dose Assessment in Nuclear Medicine. *J Nucl Med* (48), 1023–1027 (2005).
3. Zaidi, H., Sgouros, G.: Therapeutic Applications of Monte Carlo Calculations in Nuclear Medicine. 1<sup>st</sup> ed Institute of Physics Publishing, London (2003).
4. Stabin, M.: Uncertainties in Internal Dose Calculations for Radiopharmaceuticals. *J Nucl Med* (49), 853–860 (2008).

5. Allison, J. et al.: Recent developments in Geant4. *Nuclear Instruments and Methods A* 835, 186–225 (2016).
6. Salvat, F., Fernández-Varea: J. M.: Penelope-2008: A code system for Monte Carlo simulation of electron and photon transport. Nuclear Energy Agency, (2008).
7. Flux, G., Bardies, M., Monsieurs, M., Savolainen, S., Strand, S., Lassmann, M.: The Impact of PET and SPECT on Dosimetry for Targeted Radionuclide Therapy. *Med Phys* (16) 1, 47–59 (2006).
8. Papadimitroulas, P., Loudos, G. et al. Photon dose kernels dataset for nuclear medicine dosimetry, using the GATE Monte Carlo toolkit. *Med Phys* 39 (8):5238–5247 (2012).
9. Falzone, N. Fernández-Varea, J.M., Flux, G. and Vallis, K.A. Monte Carlo Evaluation of Auger Electron-Emitting Theranostic Radionuclides. *J Nucl Med*, 56 (9):1441–1446 (2015).
10. Zanotti-Fregonara, P. et al. New Fetal Dose Estimates from <sup>18</sup>F-FDG Administered During Pregnancy: Standardization of Dose Calculations and Estimations with Voxel-Based Anthropomorphic Phantoms. *J Nucl Med* 57 (11):1760–1763 (2016).
11. Dartora, C.M., Cavedini, N.G., and Marques da Silva, A.M.: Comparison between fetal dose estimates for [<sup>18</sup>F] FDG PET imaging in pregnant patient using static and dynamic bladder voiding models. In: 30th Annual Congress of the European Association of Nuclear Medicine, 2017, Viena. EJNMMI, Berlin: Springer Berlin, 2017. v. 44. p. S290–S291.
12. Sarrut, D., Bardiès, M., Boussion, N.: A review of the use and potential of the GATE Monte Carlo simulation code for radiation therapy and dosimetry applications. *Med Phys* (41) 6: 064301 (2014).
13. Tagesson, M., Ljungberg, M., Strand, S.: A Monte Carlo Program Converting Activity Distributions to Absorbed Dose Distributions in a Radionuclide Treatment Planning System. *Acta Oncologica* (35) 3, 367–372 (1996).
14. Furhang, Eli., Sgouros, G., Chui, Chen-Shou.: Radionuclide photon dose kernels for internal emitter dosimetry. *Med Phys* (23) 5, 759–764 (1996).
15. GEANT4 Homepage, <http://geant4.web.cern.ch/geant4/UserDocumentation/UsersGuides/PhysicsReferenceManual/BackupVersions/V10.1/fo/PhysicsReferenceManual.pdf>, last accessed 2018/01/24.
16. Prestwich, W.V., Nunes, J. and Kwok, C.S.: Beta dose point kernels for radionuclides of potential use in radioimmunotherapy. *J Nucl Med* 30:1036–1046 (1989).
17. Loevinger, R. and Berman, M.: A formalism for calculation of absorbed dose from radionuclides. *Physics in Medicine and Biology* 13 (2), 205–217 (1968).
18. Zanotti-Fregonara, P. and Stabin, M.G.: New Fetal Radiation Doses for <sup>18</sup>F-FDG Based on Human Data. *J Nucl Med* 58:1865–1866 (2017).

# Development of Low Cost Central Monitoring Platform by Modeling and Simulation for Patients Care in Low Middle Income Countries

Md. Ashrafuzzaman, Md. Sakib Abrar Hossain,  
A. F. M. Mohaimenul Joaa, and Md. Tareq Aziz

## Abstract

This study discusses and presents a medical engineering approach for developing a cost effective central monitoring platform for underprivileged patients in hospitals of the low to middle income countries. Over decades, the developed countries have improved their patients care through medical engineering by establishing Central Monitoring Station (CMS). Whereas, low middle income countries like Bangladesh is yet to introduce CMS for standard patients care in most of hospitals due to lack of local expertise and awareness about the technological advancement and their potential benefits. The main focus is on the development and application of advanced and proven vital parameters measuring technologies by modeling and simulation in the biomedical engineering laboratory. Central monitoring platform is designed and tested for centralized monitoring of vital patient information to observe basic parameters i.e. ECG, SpO<sub>2</sub>, NIBP, Temp, RR using simulation. A set of UniPort was connected to expand the function modules providing monitor of IBP, CO<sub>2</sub>, AAg, BIS, PiCCO and noninvasive ICG which is presently found as very unpleasant. We have seen that the patient care from medical equipment in the middle income countries is found unsafe, unreliable and costly. But simulation results using such CMS has shown that the life-threatening influences can be monitored from a single platform by quick check of patient's status directly from a standard PC, Mac or tablet PC, a

wireless PDA or smartphone. Patients care will be enhanced in many folds with safe and convenient method in cost effective manner. It is an urgent issue to produce and introduce such medical engineered CMS in hospitals of low and middle income countries which will improve patients care and HTM at overall.

## Keywords

CMS • Patients care • Health technology management  
Modeling and simulation

## 1 Introduction

### 1.1 Local Context

Currently, there are 593 government, 467 community and 126 secondary and tertiary levels hospitals in Bangladesh. There are 2,983 hospitals and 5,220 diagnostic centers run by the private stake holder [1]. Bangladesh Government and private NGOs have taken many initiatives in e-health and m-health sectors [2]. Recent surveys have suggested that, central monitoring systems have not been implemented in most of the hospitals in Bangladesh though GDP per capita is of \$958 and population is of 156.6 million in 2013 [3, 4]. This population is expected to rise to 218 million by 2030 [4]. Bangladesh is now on path of a rapid urbanization. The population of the capital city has grown to 10.2 million by 2000 and 16.8 million by 2015 from just 5.8 million in 1990 [5] with current rate of urbanization 3.19% [6]. At present 70% of the population live in the rural areas of Bangladesh [6]. The health sector profoundly support by the government by spending 3% of the Gross Domestic Product (GDP), according to World Health Organization (WHO 2010) report and current expenditure on health is 34% of the health expenditure (THE) and rest 66% is Out Of Pocket (OOP) expense [7]. Due to such socio economic structure, CMSs are unaffordable in most hospitals of Bangladesh at

Md. Ashrafuzzaman (✉) · Md. S. A. Hossain  
A. F. M. Mohaimenul Joaa · Md. T. Aziz  
Department of Biomedical Engineering, Military Institute  
of Science & Technology, Dhaka, 1216, Bangladesh  
e-mail: ashezaman@gmail.com

Md. S. A. Hossain  
e-mail: blksakib@gmail.com

A. F. M. Mohaimenul Joaa  
e-mail: afmjoaa@gmail.com

Md. T. Aziz  
e-mail: tareqazizmist@gmail.com

cost of \$1850–\$3950 per clinical device [8]. A central monitoring system consisting of only 10 devices would cost huge in the local perspective. Some local research work was done for developing low cost central monitoring systems in the past but none of these have seen in clinical use.

## 1.2 Central Monitoring Systems

The central monitoring system uses advance data transfer technology to monitor patients effectively. These systems can be integrated with the Healthcare Information System (HIS) of the hospitals. These features give clinicians an edge in patients' data access and share with potential to reduce physical contact time between physicians and patients. As doctors can access patients' real time data through this system, it reduces the need of stationed physicians for the same time. There are only 3.05 physicians per 10,000 populations in Bangladesh. Bangladesh has also been suffering from proper management of human resource in health sector [9]. Recent survey by INMAS (INSTITUTE OF NUCLEAR MEDICINE AND ALLIED SCIENCE), DMCH (Dhaka Medical College and Hospital) has shown that a doctor must need to attend almost 40 patients daily but in rural areas a doctor attends only 4/5 patients daily which is due to fragile management of stationed doctors in hospitals. A CMS connected with wide or medium area network can improve the current distribution of medical service across local areas. All of these circumstances strongly uphold that, CMSs are indispensable for hospitals in this region (Figs. 1 and 2).

## 1.3 Low Cost Central Monitoring System

As discussed earlier, in context of Bangladesh CMSs are essential but the current market prices have kept these away

from clinical use. The main motive for this research is to derive a stable solution for this complex problem. Currently the prototype is in clinical testing with effective modeling and simulation techniques.

## 2 Methods

Our plan is to develop low cost CMS for hospitals in the local areas. The expected production cost is of \$100 per clinical device with initial server/master establishment cost of \$125. First generation prototype has been developed using Raspberry Pi 3 boards and Arduino Mega board whole programming on python. The OS was used on LINUX with some modification. The Raspberry Pi 3 comes with a 1.2 GHz 64-bit quad-core ARMv8 CPU, Built in 802.11n Wireless LAN and shared specifications to the Raspberry Pi 2 which runs on Raspbian OS. The pi also supports other OS like LINUX [10]. The Arduino mega microcontroller board based on atmega 2560 with 54 digital i/o pins, 16 analog pins, 16 MHz crystal oscillator was used and can communicate with raspberry pi board through USB or I2C connections [11]. PYQT is an integrated developing environment where Python wrapper was used around the QT framework for creating graphical user interfaces or GUIs.

### 2.1 Class

The monitoring system comes with two classes of implementations. These two types/classes have been modeled by analyzing current clinical situation in local areas (Fig. 3).

#### 2.1.1 Module

The class module comes with some predefined modules. Modules are considered to be different clinical instruments.

**Fig. 1** Central monitoring system in hospitals (LAN)

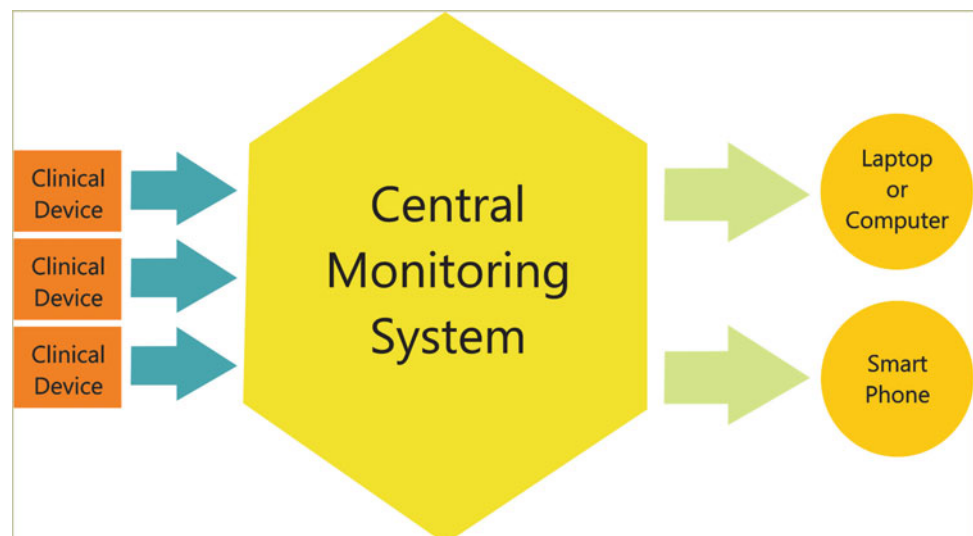
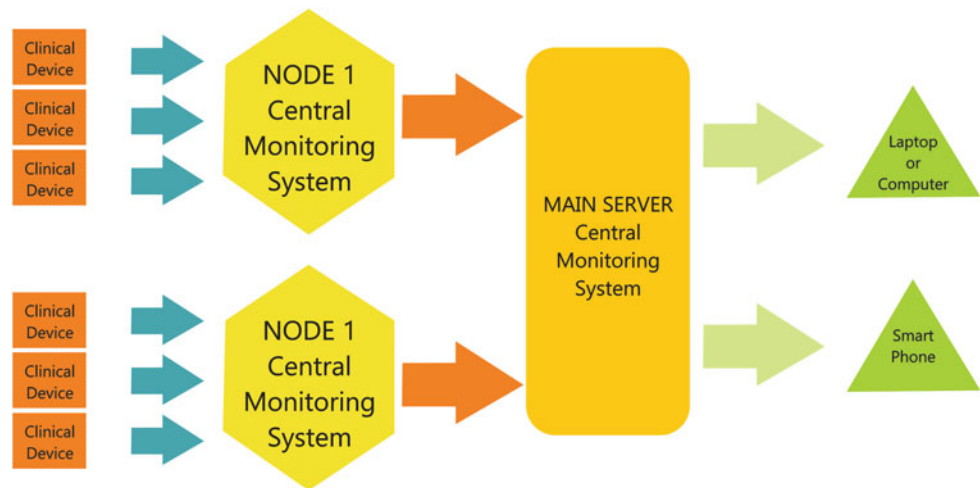




**Fig. 2** Central monitoring system in hospitals (MAN or WAN)



The master has access to all modules under the local area network (Fig. 4).

A node RASPBERRY PI 3 was connected to four modules where ARDUINO MEGA was attached to each and modules communicated with the node via I2C connection. The nodes upload data to the MASTER using fixed IP address for dedicated modules in the integrated system (considering each ARDUINO MEGA's MASK IP). Connecting more than 4 modules may raise obscure during real time data transfer as the ARDUINO and Raspberry Pi communicates via I2C connection (Fig. 5).

Each module was developed to communicate with an Arduino Mega board through USB and also connected to a Raspberry Pi 3 board through I2C connection. The Raspberry Pi 3 board was considered to be a node for the system. The Arduino boards (modules) were connected with each node of the system. The node was connected to a router to prepare Local Area Network (LAN). LAN usually assigns an arbitrary IP address for any device connected to it but Arduino mega boards IP address is different and fixed as per their MASK address of each node. Then nodes were

connected to the MASTER through LAN where connections with other external devices will become convenient during use of this integrated system within a hospital. Only the connected devices have access to the system for ensuring crucial issue with data security in the covered areas. Control of a module by any external device follows the flow chart as shown in Fig. 6.

When any device connected to the LAN requests for access to run a module, the device asked permission to the MASTER. As the device selects an arbitrary module, node connected to the module is then automatically selected by the MASTER as per LINUX protocol considering the users information with certain IP address of Arduino board connected to the module. As the MASTER redirects user to the required node for specific module, the external device (user) is then connected to that certain nodal IP address. The external device (user) then sends the data to the node (raspberry pi 3 board). The data then is uploaded on Arduino board, which IP address was selected at the beginning of the process. The Arduino board then controls the module as per the defined data. Application will be developed using PYQT for each system separately based on hospital requirements to operate locally.

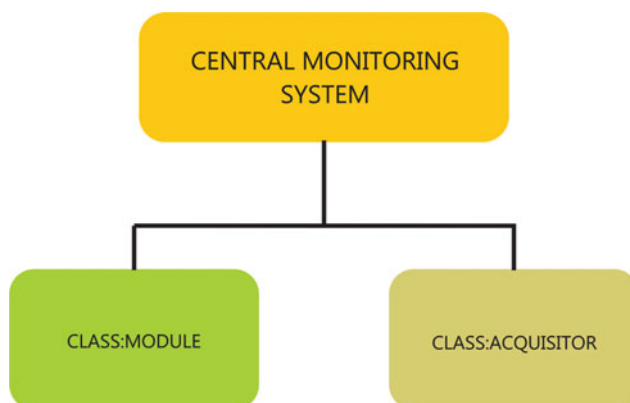


**Fig. 3** Class

### 2.1.2 Acquisitor

The class acquisitor is the second class clinical device which connected to a server. The server is the part of Wide Area Network (WAN) and has the access in processed data of the devices (Fig. 7).

In the acquisitor class an acquisition circuit RASPBERRY PI 3 board was integrated with each clinical device. Then it was connected with the external computer of the clinical device through USB which collects data and uploads in the server. In this case, IP address of each acquisitor is fixed and assigned (considering the Raspberry Pi 3 Mask IP). Each acquisitor was assigned with specific web address

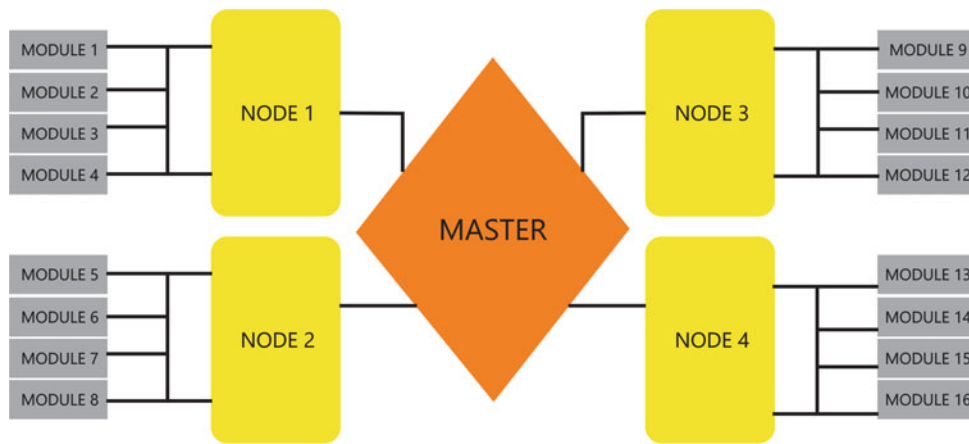


Fig. 4 Class: module

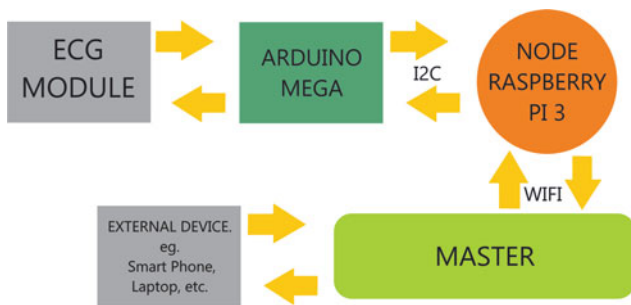


Fig. 5 Class: module block diagram

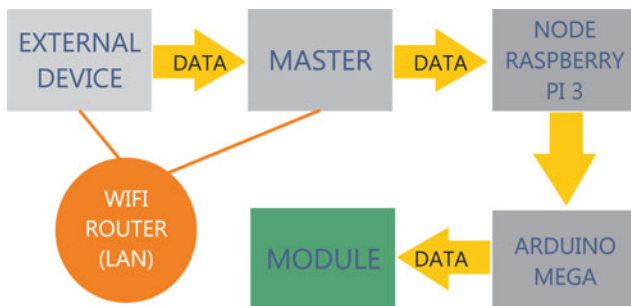


Fig. 6 Class: for chart for module control

which helps to view data of each clinical device in a page. The server has access to all the processed data of the attached clinical devices and the data flow is unidirectional. The whole network is being integrated under a single WAN which allows the users to gain access from anywhere through a website and thus hospitals can be inter-connected. All clinical data will be uploaded in a website. After receiving permission from server (verification of user’s IP address), the user can view the web address specified for the clinical device (Fig. 8).

When connected with clinical device, the raspberry pi extracts all imaging data from the device and then uploads to the server with authentication. Once the server approved, the raspberry pi board uploads all diagnosis data on a specific

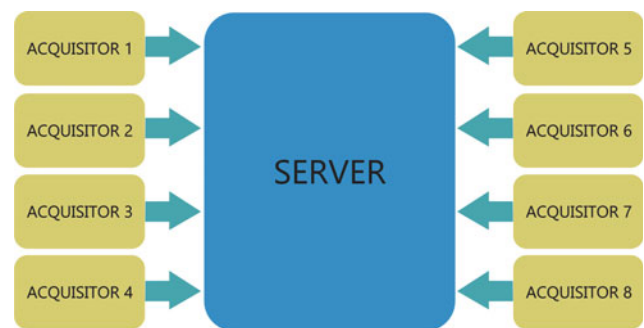


Fig. 7 Class: acquirer

web address. Through this, hospitals can be interconnected among themselves which provides connection between as different clinical devices from different hospitals under a single server with minimum expenditure (Fig. 9).

### 3 Development Cost

Currently available CMSs for hospitals cost about \$1850–\$3950 per clinical device as shown in Fig. 10 [8]. The class acquirer installation would cost \$60 per medical device with initial server establishment cost is about \$125 only.

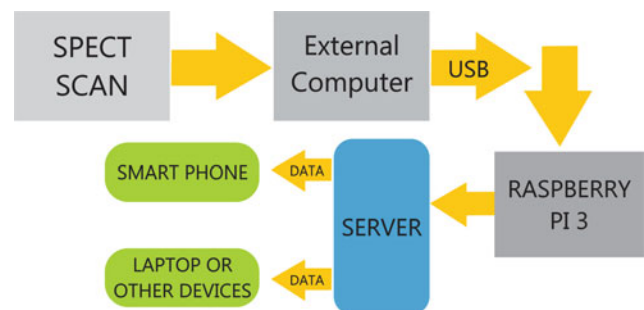


Fig. 8 Class: acquirer block diagram

The class module cost varies with the type of modules but the initial master establishment cost is about \$60. For a 50 device system, available CMSs would cost about \$92,500–\$197,500 whereas, class acquirer will cost maximum \$3000 which is much less than the cost of single unit of present CMS. In terms of class module, the cost varies with the type of modules being developed but initial cost is about \$60. In this case class module for EEG, ECG, EMG, Syringe pump, infusion pump etc. will be much cheaper than conventional system if total instrumentation cost is considered.

### 4 Results and Discussion

The first generation prototype of both the classes have been developed and tested for two ECG modules which were developed earlier. The Arduino mega of each module is connected to the controller via I2C connection. In the first generation prototype the whole node and master system have been replaced with a Raspberry Pi 3 board controller connected to a LAN. External devices connected to the LAN can access the controller and further access gain by the external devices through VNC viewers and this prototype showed an excellent performance during its function (Fig. 11).

The ECG module replicates the ECG device and designed in an easy way to communicate with an Arduino mega. When the module was turned on (or start to receive ECG signals) through Arduino program it sent signal to the Arduino. The Arduino fed the signal to the raspberry pi 3 board through I2C connection. The signal was then fed to a python program and displayed the signal in a python GUI. The Fig. 12 demonstrated the instrumentation amplifier was used [12–14] which was designed with an AD620 IC.

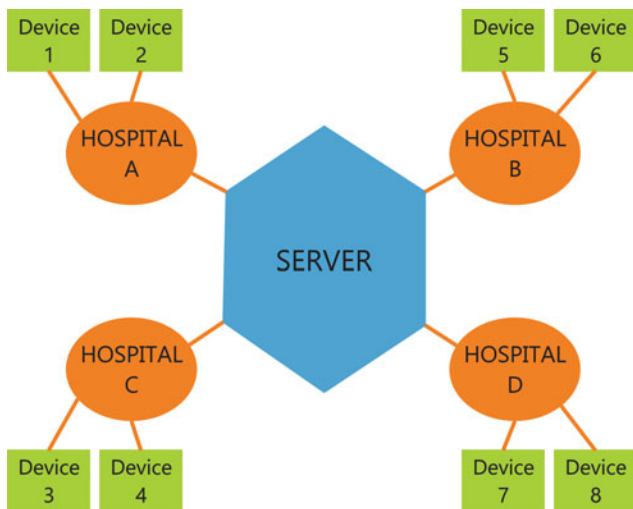


Fig. 9 Class: acquirer interconnecting hospitals

Conventional Central Monitoring System	VS	CLASS: ACQUISITOR
Cost \$1850-\$3950 per clinical device. For a 50 medical device network it would cost \$92,500-\$197,500.		Cost \$60 per device. Comes with an initial server establishment cost of \$125. For a 50 medical device network it would cost \$3,125.
	VS	CLASS: MODULE
		Comes with an initial Master establishment cost of \$60. Total cost varies with the type of module being developed.

Fig. 10 Comparison between systems

When any device is connected to a LAN, the network automatically assigns an IP address for that specific device where the Raspberry Pi IP address is fixed. When VNC viewers attempted to gain access from the connected Raspberry Pi board, its home screen was displayed on the connected devices. From that Arduino terminal the ECG module was turned on and thus the ECG signal was viewed with real time data through the GUI (Fig. 13).

For the first generation prototype an acquirer has been developed to extract data from a SPECT SCAN machine. A second generation prototype was also develop to evaluate the further progress of the data accumulated from several medical devices (Fig. 14).

An Arduino mega was attached to SPECT SCAN’s external computer via USB to extract all SPECT images and was fed the Raspberry Pi 3 connected with I2C. Two Raspberry Pi 3 were connected on a LAN so that the second Raspberry Pi 3 easily expanded its access to the first Raspberry Pi via VNC viewers. The Raspberry Pi then extracts all SPECT SCAN imaging data and stores and uploads all imaging data in the server following the same. External devices connected to the server got an access to the imaging data if certain criteria are achieved after verification. The server is on progress to improve its capacity for numerous connections with huge data storage (Fig. 15).

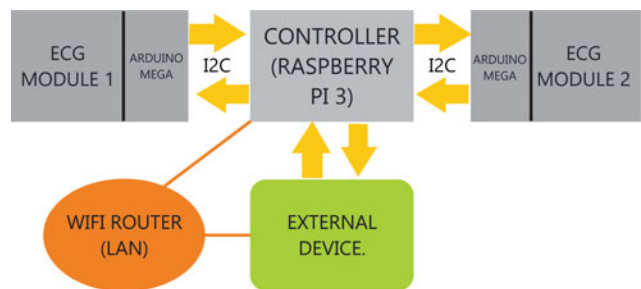


Fig. 11 Class module prototype block diagram

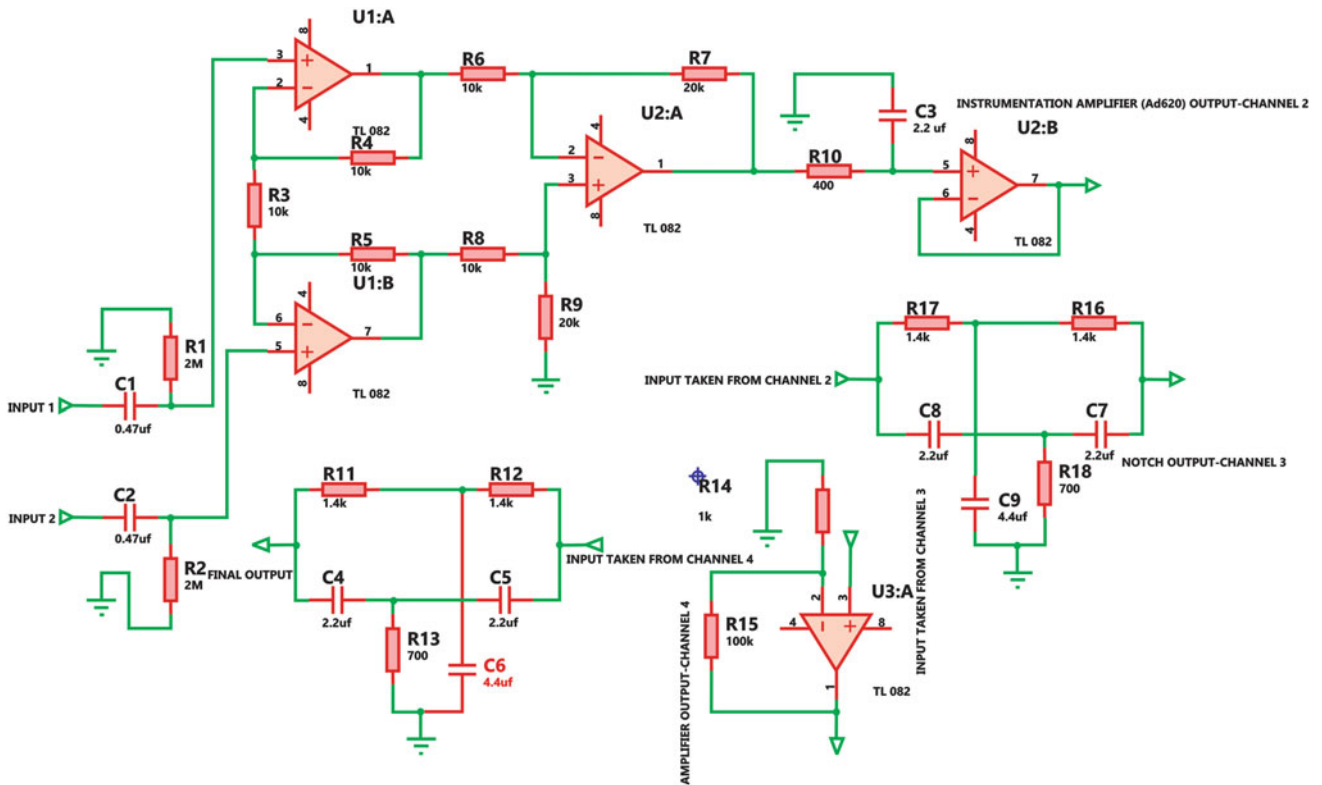


Fig. 12 Instrumentation amplifier PROTEUS schematic

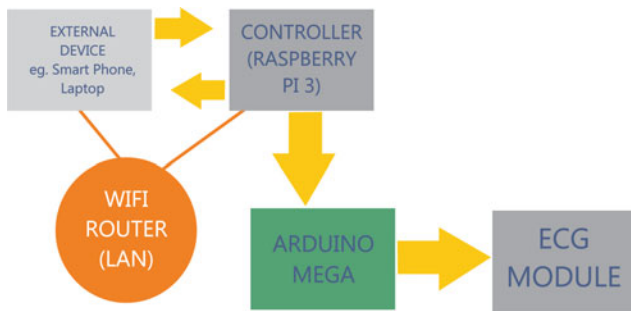
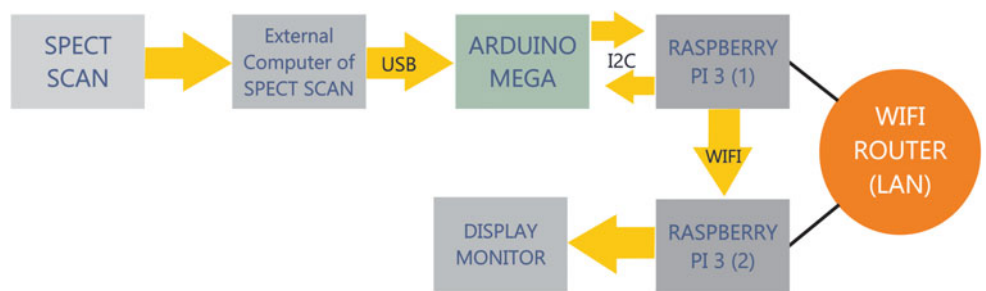


Fig. 13 ECG module communication flow chart

The first generation class module prototype costs \$60 for establishment of controller. Each ECG module costs \$90

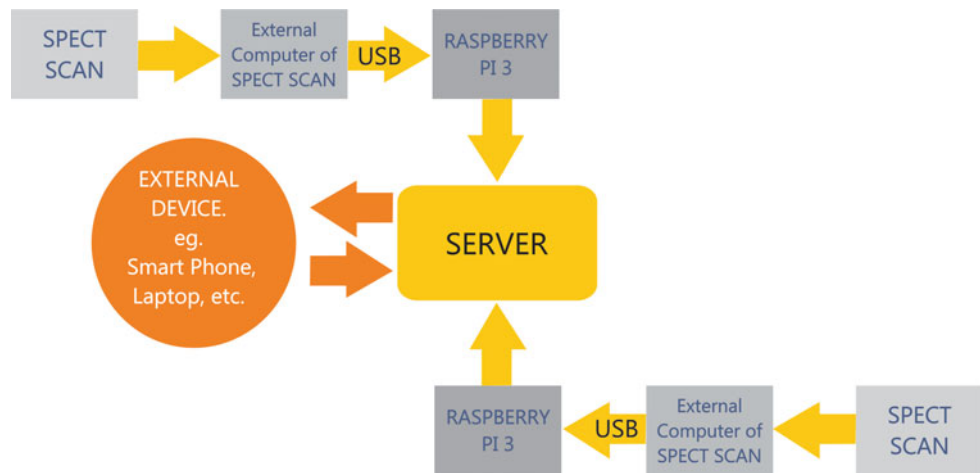
along with the Arduino mega board. The whole set of equipment was developed with an expenditure of about \$300 only. Besides, the first generation class acquirer prototype costs about \$250. The acquirer costs \$160 and the second generation class acquirer prototype has been estimated to cost about \$245 and the server establishment costs around \$125. Class acquirer has great potential for clinical use. The second generation prototype has been scheduled for testing in INMAS, Bangladesh. For smaller clinical devices like ECG, EKG, EMG, Infusion pump, Syringe pumps the class module can be applied effectively, as some these clinical devices are being developed and manufactured locally. Most importantly both of these classes provide cheap alternatives in the local perspective.

Fig. 14 First generation class: acquirer prototype block diagram





**Fig. 15** Acquisitor second generation prototype block diagram and communication flow chart



## 5 Conclusion

From the publications and literature review results, we examine that development of central monitoring system is expensive and technology involved with experts from various fields. Whereas, economically developing countries like Bangladesh is focusing on the medical equipment maintenance and management through biomedical/clinical engineering only. Development of medical equipment is far to think and implement successfully with specific research laboratories and vendors from private sectors. It is also revealed that the health care technologies and health services are very inferior in Bangladesh with respect to standards of developed countries. However, despite all challenges discussed above, the department of biomedical engineering of MIST has started to perform research on device development for medical applications but the health care technology to ensure the safe and efficient health care services through indigenously developed equipment like CMS is yet to satisfy. Notwithstanding, the crying needs of local development with collaborative knowledge from the international universities and organizations our researchers have developed and tested the prototype of CMS platform which is considered as very low cost development. Such low cost platform may have potential to move forward for original device development through the support from government and private organizations which will definitely contribute to save the life of enormous populations in near future if implemented nationwide. In this regards, we believe that active cooperation of ACCE/IFMBE/IUPESM/JACE/CEASA will excel such project and will be implemented in hospitals of low to middle income countries. It concluded that it was very necessary to develop a module to produce CMS platform for

use in middle income countries like Bangladesh. Shortly, the original device development project will initiate for successful development of low cost CMS and will serve in most of the hospitals of Bangladesh. It will facilitate the quality and standard of patients monitoring system and HTM in Bangladesh effectively in near future.

**Acknowledgements** Authors would like to acknowledge the support from the Biomedical Engineering Department, Military Institute of Science and Technology (MIST), Bangladesh; Bangabandhu Sheikh Mujib Medical University (BSMMU), Bangladesh.

**Conflict of Interest** The Authors declare that they have no conflict of interest.

## References

1. Health Bulletin, Ministry of Health and Family Welfare, Government of the People's Republic of Bangladesh. (2016) and World health statistics (2012).
2. Tanvir Ahmed, Gerald Bloom, Mohammad Iqbal, Henry Lucas, Sabrina Rasheed, Linda Waldman, Azfar Sadun Khan, Rubana Islam and Abbas Bhuiya.: E-health and M-Health in Bangladesh: Opportunities and Challenges. Evidence Report 60: (2014).
3. Bangladesh 2016 Politics, Governance and Middle Income Aspirations Realities and Challenges: An Empirical Study (2016).
4. Ramesh Govindaraj, Dhushyanth Raju, Federica Secci, Sadia Chowdhury, Jean-Jacques Frere.: Health and Nutrition in Urban Bangladesh Social Determinants and Health Sector Governance. ISBN (paper): 978-1-4648-1199-9 (2018).
5. Baker JL.: Dhaka: Improving living conditions for the urban poor. Popline. Document Number: 332534 (2007).
6. The World Bank. <https://www.cia.gov/library/publications/the-world-factbook/fields/2212.html>.
7. Anwar Islam1, Tuhin Biswas.: Health system in Bangladesh: Challenges and opportunities. American Journal of Health Research 2(6): 366–374 (2014).



8. Retrieved from: [https://www.alibaba.com/product-detail/Central-monitor-system-MS-PM28-multi\\_60492514554.html?spm=a2700.7724857.main07.57.6d4a192vNNTU2](https://www.alibaba.com/product-detail/Central-monitor-system-MS-PM28-multi_60492514554.html?spm=a2700.7724857.main07.57.6d4a192vNNTU2).
9. Global health workforce alliance. <http://www.who.int/workforcealliance/countries/bgd/en/>.
10. Retrieved from official website of Raspberry Pi: <http://www.raspberrypi.org/project/raspbian/docs/35/userguide/hardware-specifications.md>.
11. Retrieved from official website of Arduino: <https://store.arduino.cc/usa/arduino-mega-2560-rev3>.
12. Pankaj K. Gakare, Abhilasha M. Patel, Jignesh R. Vaghela, R.N. Awale.: Real Time Feature Extraction of ECG Signal on Android Platform|| IEEE Conference on Communication, Information & Computing Technology, Mumbai, India (2012).
13. K Siddique-e Rabbani.: Neuro-Physiological Measurements for Diagnosis using Evoked Responses. Bangladesh Journal of Medical Physics 5(1): 1–24 (2012).
14. Emmanuel Kobina Payne, Dennis Joe Harmah.: Multi-parametric Telemetry Patient Monitoring System. International Journal of Scientific and Research Publications 5(11), 272–276 (2015).

# Assistance Ratio: An Approach to Quantify the Hydraulic Load Distribution in LVAD Therapy

Philip von Platen, Daniel Rüschen, Steffen Leonhardt, and Marian Walter

## Abstract

Left ventricular assist devices (LVADs) have grown in popularity for treating patients with severe heart failure. In many cases rotary blood pumps (RBPs) are used as LVADs, which are set to a fixed rotational speed in the clinical environment. The physicians rely on practical guidelines, available measurements and experience in choosing the rotational pump speed. This can lead to poor or unfavourable patient support, possibly even dangerous operating conditions. Hence, there exists great potential to implement closed-loop control of LVADs to overcome these problems. However, the choice of the control variable is not trivial. This paper presents a methodological approach to deriving a suitable control variable for closed-loop LVAD therapy. To simplify the setpoint choice for clinicians, an assistance ratio is introduced to represent the sharing of hydraulic workload between the LVAD and the native heart. Available measurements include the left ventricular and aortic root pressure, pump flow and aortic flow rate, with the latter estimated using a Kalman filter. Based on these measurements, assistance ratios based on flow, work and pulsatility are proposed. The merits of different assistance ratios are assessed based on their ability to provide insight into hemodynamic support, myocardial protection and left ventricular unloading, along with their ease of implementation and robustness of their calculation. Their implementation is tested in a hybrid mock circulatory loop and retrospectively on data from animal experiments. An assistance ratio based on flow is shown to be the most robust, whilst giving some indication of hemodynamic support. The closed-loop control using an assistance ratio therefore makes it easier to achieve different therapeutic goals. This

approach has the potential to reduce interventions by the clinician and could eventually lead to a versatile definition of LVAD therapy protocols, independent of pump-type or patient.

## Keywords

Left ventricular assist device • Physiological control  
Hydraulic load distribution

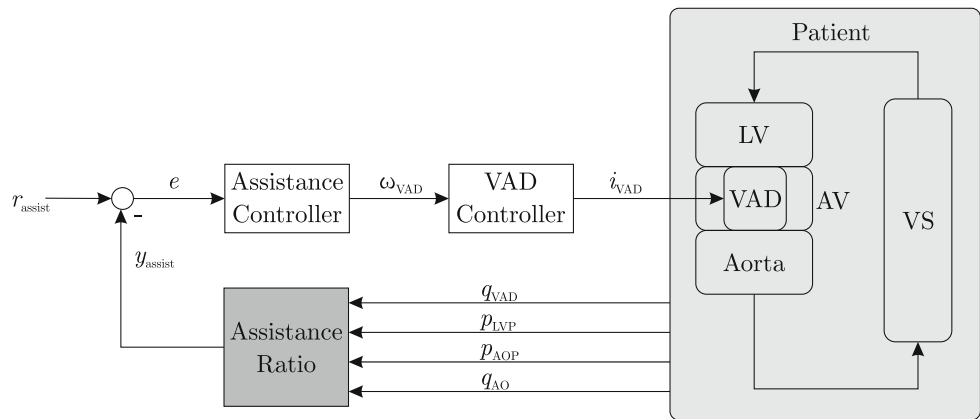
## 1 Introduction

The use of left ventricular assist devices (LVADs) in patients suffering heart failure is becoming more common, most notably due to the cost and lack of available heart transplants [1]. Recent developments in continuous-flow rotary blood pumps have made these smaller, more durable and simpler to use. They are able to stabilize the patient's hemodynamics and further give myocardial support. This is of particular interest in the application of LVADs as bridge-to-recovery devices. This application of LVADs has been shown in literature by Frazier et al. in [2]. It is however non-trivial for the attending physician to properly adjust the pump speed for optimal recovery.

For an improved use of the LVAD, the concept of physiological (closed-loop) control has been applied. Various strategies have been described in literature, including: controlling the pressure difference between aorta and left ventricle [3], reproduction of the Frank-Starling mechanism [4] and maximum flow with suction control [5]. For the latter case, setting a maximum flow achieves hemodynamic support, but possibly has adverse effects on or hinders myocardial recovery [6]. Firstly, suction or ventricular collapse may occur. Secondly, excessive unloading of the LV may impair the pumping action of the right ventricle due to a septum shift [6]. A common factor in many of the other physiological control strategies is that these require a physiological reference value. This is problematic as the

P. von Platen (✉) · D. Rüschen · S. Leonhardt · M. Walter  
Philips Chair for Medical Information Technology,  
Helmholtz-Institute for Biomedical Engineering, RWTH Aachen  
University, Aachen, Germany  
e-mail: platen@hia.rwth-aachen.de  
URL: <https://www.medit.hia.rwth-aachen.de/>

**Fig. 1** Block diagram of the proposed assistance control strategy, with VAD—ventricular assist device, LV—left ventricle, AV—aortic valve, VS—vascular system,  $p_x$ —pressure,  $q_x$ —flow,  $\omega$ —speed and  $i$ —current. Focus lies on the “Assistance Ratio” block



reference value will vary depending on the patient, the patient state and the environment.

Since the majority of the native physiological control mechanism of the patient are still functioning, a new control strategy is proposed in [7]. Hereby the native heart and LVAD function in parallel, meaning the LVAD does not replace the function of the native heart, but rather supports it by reducing its hydraulic load. A block diagram of this control structure is shown in Fig. 1. Central to this strategy is the definition of the degree of assistance, also called assistance ratio, and this paper considers different options and their applicability in bridge-to-recovery therapy.

## 2 LVAD Therapy Goals

The main goals of LVAD therapy are hemodynamic support and myocardial protection. Hemodynamic support is provided by an increased blood flow and associated stabilization of blood pressure. It has also been discussed that a certain pulsatility in the blood flow is a requirement for correct hemodynamic support [8]. The concept of Energy Equivalent Pressure and Surplus Hemodynamic Energy have been used to quantify pulsatility of blood flow and pressure [9]. Myocardial protection can be provided by simultaneously unloading the left ventricle, by decreasing myocardial oxygen demand and increasing coronary blood flow, which increases myocardial oxygen supply. A visual tool for evaluating ventricular unloading is the reduction of the pressure-volume loop area in a cardiac cycle [10].

It is important to remember here that the native physiological control loops are considered to remain functioning, despite the heart failure. A functioning venous return shows this. As such, the body still regulates the cardiac output, as long as the sum of flow from the native heart and LVAD is adequate. The remaining question therefore is how to quantify the hydraulic load distribution between native heart and the LVAD. Since flow is inherently measured, it is used as a first assistance ratio ( $r_{\text{flow}}$ —flow assist ratio). The area

of the PV loop (and the associated work) is important when considering LV unloading, and it is therefore also considered ( $r_{\text{work}}$ —work assist ratio). Finally, since the question of pulsatility remains a question in literature, a ratio based on surplus hemodynamic energy (SHE) is also considered ( $r_{\text{pulsatility}}$ —pulsatility assist ratio).

Once these assistance ratios have been established and validated, therapeutic protocols can be envisioned. Effective myocardial recovery could for example be detected by keeping the pump speed constant and monitoring an assistance ratio. If the assistance ratio decreases, the native heart takes on more hydraulic load, which could be related to a recovering ventricle. A further example is the process of weaning a patient off the LVAD, which can be defined by the stepwise reduction of the assistance ratio, thereby steadily increasing the hydraulic load of the native heart.

## 3 Materials and Methods

### 3.1 Assistance Ratio Calculation

Different assistance ratios are calculated according to the following formulas:

$$r_{\text{flow}} = \frac{q_{\text{VAD}}}{q_{\text{AO}}} \quad (1)$$

$$r_{\text{work}} = 1 - \frac{A_{\text{Px}}}{A_{\text{P0}}} \quad (2)$$

$$r_{\text{pulsatility}} = \frac{\text{SHE}_x}{\text{SHE}_0} \quad (3)$$

where  $q_{\text{VAD}}$  is the pump flow,  $q_{\text{AO}}$  is the aortic flow,  $A_{\text{Px}}$  is the area of the pressure-volume loop with LVAD support and  $A_{\text{P0}}$  is the pressure-volume loop of the pathological heart without LVAD support. Similarly,  $\text{SHE}_x$  is the surplus hemodynamic energy of the heart with LVAD support and  $\text{SHE}_0$  is the surplus hemodynamic energy of the pathological heart.

### 3.2 Experimental Setup

The Impella CP (Abiomed Inc, Danvers, USA) is used as the LVAD in this study. The device is a catheter-mounted micro-axial flow pump, which pumps blood from the left ventricle into the aortic root. The device has been modified to include two optical pressure sensors mounted on the device at the inlet and outlet cannula, allowing for the measurement of the left ventricular pressure,  $p_{LVP}$ , and the aortic pressure,  $p_{AOP}$ , respectively. The LVAD is controlled via an Automated Impella Controller (AIC). The AIC allows for different levels of support to be chosen ranging from P1 (min) to P8 (max). Via a controller area network (CAN bus) connection, the measured variables are available at a sample rate of 250 Hz. All algorithms are implemented in Simulink (The MathWorks Inc., Natick, USA) and are executed on a real-time computer (MicroAutoBox II, dSPACE GmbH, Paderborn, Germany).

## 4 Results and Discussion

The different assistance ratios were first evaluated in vitro using the hybrid mock circulatory loop described in [11]. This hardware-in-the-loop simulation of a numerical CVS model [12] was connected to an Impella CP via a hydrodynamic interface. The simulation was modified to simulate heart failure by reducing the myocardial contractility to 25% of its nominal value. After simulating the pathological heart without LVAD support, the LVAD support was increased stepwise. The results of these tests are shown in Table 1. The LVAD flow is calculated by the AIC, whilst the aortic flow is taken from the simulation.

Clearly with increasing LVAD support, the degree of flow assistance increases to a maximum of 85%. Similarly, the degree of work assistance also increases. This can also be seen in Fig. 2, whereby the area of the PV-loop decreases with increasing support. Lastly, the degree of pulsatility assistance decreases with increasing support. This is due to the fact that the LVAD is pumping continuously and hence with increasing support, the pulsatility of the flow and

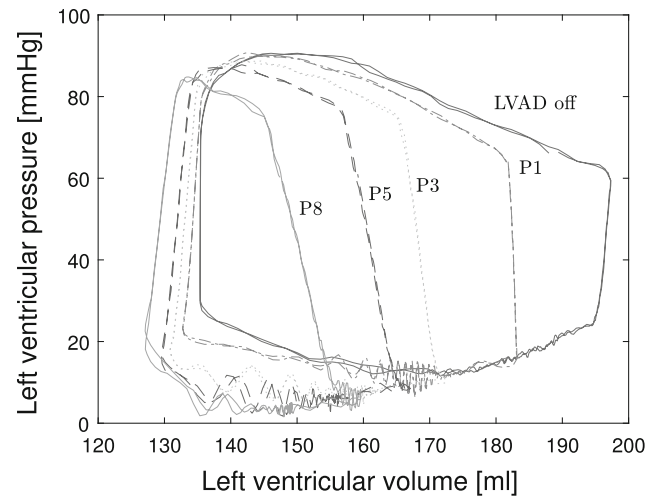


**Fig. 2** Pressure volume loops for different pump speed settings in the mock circulatory loop experiment

pressure decreases, which is visible in the reduced pulsatility assist ratio.

After the initial validation in the mock circulatory loop, data from previous animal studies was used to evaluate the flow assist ratio. In this case, an accurate instantaneous measurement of the aortic blood flow was not present, making calculation of the other assistance variables impossible. An observer based on a Kalman filter was used to estimate the cardiac output, see [13], and allowed for the calculation of the flow assist ratio. The experiments were performed on adult sheep (*Ovis aries*, Röhn, female, approx. 63 kg) with experimentally induced myocardial infarction through balloon occlusion. The LVAD was implanted when first symptoms of the myocardial infarction appeared and the results shown here are form taken from data measured 12 h after the infarction. Figure 3 shows the results for different LVAD support settings from the animal experiment. Importantly, the combined blood flow from the native heart and LVAD remains almost constant at 8 l/min, despite the step change in flow supplied by the LVAD. This shows the validity of the assumption concerning the functionality of the native control loops for cardiac output regulation. The increase in LVAD support

**Table 1** Degree of assistance for different LVAD support settings in the mock circulatory loop experiment

LVAD level	Aortic flow l/min	LVAD flow l/min	Flow assist %	Work assist %	Pulsatility assist %
LVAD off	2.73	NA	0	0	100
P1	3.02	0.48	16	15	62
P3	3.26	1.72	53	31	54
P5	3.37	2.26	67	42	24
P7	3.47	2.79	80	54	14
P8	3.51	2.98	85	59	3

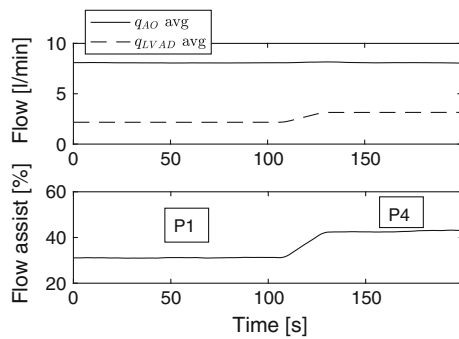


**Fig. 3** Degree of assistance shown by the flow assist for different LVAD speed settings during an animal experiment

from P1 (low) to P4 (mid) support, increases the degree of assistance from 30 to 45%. This level of support can be calculated without any further knowledge of the patient or state.

## 5 Conclusions

The hydraulic load distribution between the native heart and LVAD can be conveniently presented by the use of an assistance ratio. Different ratios have been shown to give insight into ventricular unloading and myocardial recovery, which are important goals of LVAD therapy. The calculation of these assistance ratios can in future be incorporated into LVAD control loops to simplify and individualize the pump settings and therapeutic protocols.

**Acknowledgements** In the ongoing in vivo study, all national and European laws, guidelines and policies for the care and use of laboratory animals are followed. This work has been funded by the Federal Ministry of Education and Research (BMBF, Germany) and is part of the project “inHeart” (grant number 13GW0118C).

**Conflict of Interest** The authors declare that they have no conflict of interest.

## References

1. P. Ponikowski, A.A. Voors, S.D. Anker, B. Héctor, J.G. Cleland, A.J. Coats, V. Falk, J.R. González-Juanatey, Veli-PekkaHarjola, E. A. Jankowska, et al., *European Heart Journal* **37**(27), 2129 (2016).
2. H. Frazier, T. Myers, *The Annals of Thoracic Surgery* **68**(2), 734 (1999). [https://doi.org/10.1016/s0003-4975\(99\)00801-2](https://doi.org/10.1016/s0003-4975(99)00801-2).
3. G.A. Giridharan, G.M. Pantalos, K.J. Gillars, S.C. Koenig, M. Skliar, *ASAIO Journal* **50**(5), 403 (2004).
4. R.F. Salamonsen, E. Lim, N. Gaddum, A.H.H. AlOmari, S.D. Gregory, M. Stevens, D.G. Mason, J.F. Fraser, D. Timms, M.K. Karunanithi, N.H. Lovell, *Artificial Organs* **36**(9), 787 (2012). <https://doi.org/10.1111/j.1525-1594.2012.01457.x>.
5. A.H.H. AlOmari, A.V. Savkin, M. Stevens, D.G. Mason, D.L. Timms, R.F. Salamonsen, N.H. Lovell, *Physiological Measurement* **34**(1), R1 (2013).
6. A. Arndt, P. Nüsser, K. Graichen, J. Müller, B. Lampe, *Artificial Organs* **32**(10), 761 (2008). <https://doi.org/10.1111/j.1525-1594.2008.00628.x>.
7. D. Rüschen, S. Leonhardt, M. Walter, in *24th Congress of the International Society for Rotary Blood Pumps (ISRBP)* (Mito, Japan, 2016).
8. K.G. Soucy, S.C. Koenig, G.A. Giridharan, M.A. Sobieski, M.S. Slaughter, *The Journal of Heart and Lung Transplantation* **32**(6), 581 (2013).
9. A. Ündar, B. Ji, B. Lukic, C.M. Zapanta, A.R. Kunselman, J.D. Reibson, W.J. Weiss, G. Rosenberg, J.L. Myers, *ASAIO Journal* **52**(6), 712 (2006).
10. L.D. Sauren, R.E. Accord, K. Hamzeh, M. De Jong, T. Van Der Nagel, F.H. Van Der Veen, J.G. Maessen, *Artificial Organs* **31** (11), 839 (2007).
11. B. Misgeld, D. Rüschen, S. Schwandtner, S. Heinke, M. Walter, S. Leonhardt, *Biomedical Signal Processing and Control* **20**, 35 (2015). <https://doi.org/10.1016/j.bspc.2015.04.004>.
12. S. Heinke, C. Pereira, S. Leonhardt, M. Walter, *Medical & Biological Engineering & Computing* **53**(10), 1049 (2015).
13. D. Rüschen, M. Rimke, J. Gesenhues, S. Leonhardt, M. Walter, *Computer Methods and Programs in Biomedicine* (2016). <https://doi.org/10.1016/j.cmpb.2016.08.020>. [Epub aop].



# Analysis of Left Ventricular Unloading by Double Lumen Arterial Cannula During ECMO Assessed by Mathematical Modeling

Svitlana Strunina<sup>✉</sup>, Jiri Hozman<sup>✉</sup>, and Petr Ostadal<sup>✉</sup>

## Abstract

Extracorporeal membrane oxygenation is increasingly used for the therapy of the cardiogenic shock. However, it has been repeatedly shown that increased afterload associated with extracorporeal membrane oxygenation significantly deteriorates left ventricular performance. A number of approaches suggested how to deal with left ventricular unloading. Each of these methods requires extra interventions, which increase invasiveness of the method and thus does not correspond with current trends in the mini-invasive performance. Therefore, the development of a mini-invasive method of left heart decompression is a significant issue in extracorporeal membrane oxygenation therapy. The study presents an alternative mini-invasive method for the left ventricular unloading during extracorporeal membrane oxygenation. The draft of double lumen arterial cannula for left ventricular unloading during extracorporeal membrane oxygenation was created in AutoCAD software. The Modelica modeling language was used for modeling and simulations. The initial parameter values were derived from measurements on a female swine. Our simulation results indicate that drainage lumen of the presented double lumen arterial cannula for veno-arterial extracorporeal membrane oxygenation is capable of withdrawing 0.374 L/min during extracorporeal blood flow 1 L/min, 0.441 L/min during 2 L/min, 0.481 L/min during 3 L/min, 0.532 L/min during 4 L/min, 0.560 L/min during 5L/min. The double lumen arterial cannula presents an alternative and perspective solution. It is less invasive than the currently used methods for the left ventricle decompression during veno-arterial extracorporeal membrane oxygenation. The

double lumen arterial cannula is capable of achieving left ventricle decompression and blood return while requiring only one single puncture.

## Keywords

Extracorporeal membrane oxygenation • Double lumen Cannula • Left ventricular • Decompression

## 1 Introduction

One of the main problems and tasks of the extracorporeal membrane oxygenation (ECMO) is the prevention and treatment of complications caused by stagnation of the blood in the left heart. An inadequate drainage of the left ventricle (LV) can highly impair patient outcome during ECMO.

ECMO is a technology used to support failing hearts and lungs. It provides sufficient support to enable adequate tissue perfusion even in cardiac arrest.

Extracorporeal membrane oxygenation in veno-arterial configuration (VA-ECMO) represents the most effective minimally invasive circulatory support system. However, it has been repeatedly shown that increased afterload associated with ECMO significantly deteriorates left ventricular performance [1, 2]. In the presence of severe LV dysfunction, the left ventricle is unable to eject a sufficient volume of blood against the increased afterload caused by the ECMO flow [3].

Overflow LV, leads to stagnation of blood. This results in LV overload with distension [1, 2, 4–7], and increased pressure in the pulmonary circulation causing the development of edema [4, 5, 7, 8].

Various techniques have been proposed to decrease left ventricular distension and improve its function, including insertion of intra-aortic balloon pump or percutaneous left ventricular assist device, left atrial and left ventricular venting, or switch to surgically inserted left ventricular support with or without oxygenator [3]. All of these methods

S. Strunina (✉) · J. Hozman  
Faculty of Biomedical Engineering, Czech Technical University in Prague, Nám. Sítná 3105, 272 01 Kladno, Czech Republic  
e-mail: svitlana.strunina@fbmi.cvut.cz

P. Ostadal  
Cardiovascular Center, Na Homolce Hospital, Roentgenova 37/2,  
150 30 Prague, Czech Republic

require extra interventions, which increase invasiveness of the methods and thus does not correspond with current trends in the mini-invasive performance. Therefore, the less invasive method is a significant issue of the ECMO therapy. As a less invasive approach, a double lumen cannula can be used.

Over the past years, the double-lumen cannulas were widespread in the ECMO therapy. This type of cannula is less invasive, reduces circuit size and minimizes interaction between blood cells and the circuit [9].

The purpose of this paper is to present a double lumen arterial cannula (DLAC) for VA-ECMO and analyze the capability of a double lumen arterial cannula to unload left ventricle during ECMO.

## 2 Methods

The draft of double lumen arterial cannula for left ventricular unloading during extracorporeal membrane oxygenation was created in AutoCAD software. The Modelica modeling language was used for modeling and simulations. Each compartment of the model (see Fig. 1) is modeled using a mathematical relationship between blood volume  $V_i(t)$ , input flow rate  $F_{in}(t)$  and output flow rate  $F_{out}(t)$  relative to the  $i$ -th compartment given as

$$\frac{dV_i(t)}{dt} = F_{in}(t) - F_{out}(t) \quad (1)$$

With flow rate  $F_{ij}(t)$  between compartments  $i$  and  $j$  defined by

$$F_{ij}(t) = \frac{P_i(t) - P_j(t)}{R_{ij}} \quad j = i - 1 \quad (2)$$

The law sum-to-zero is applies in the hydraulic domain to the flow variables. The sum of all mass flows at a point is zero

$$F_{in} - F_{out} = 0 \quad (3)$$

The left ventricular pressures were established according to a single cycle of cardiac activity time given as

$$pressure = \begin{cases} diaPressure & \text{if } tc < TD1 \\ diaPressure + \sin\left(\frac{(tc-TD1)}{(TD2-TD1)}\pi\right)(sysPressure - diaPressure) & \text{if } tc < TD2 \\ diaPressure & \text{else} \end{cases} \quad (4)$$

where  $diaPressure$  is diastolic blood pressure,  $sysPressure$  is systolic blood pressure,  $tc$  is relative time of cardiac cycle,  $TD1$  is relative time of start of systole,  $TD2$  is relative time of end of systole.

The blood flow in the system components was described by Hagen–Poiseuille equation

$$Q = \frac{\pi \Delta P r^4}{8 \mu L} \quad (5)$$

where  $Q$  is volumetric flow rate,  $\mu$  is dynamic viscosity,  $r$  is pipe radius,  $L$  is length of pipe,  $\Delta P$  is pressure reduction. The radius and length of components were various, as a consequence of required quantities. The dynamic viscosity of blood was 0.001 Pa s [10].

The pump element was used from Modelica library for physiological calculations—Physiolibrary. For the purpose of simulation, a pump flow rate was gradually increased from 1 to 5 L/min.

The oxygenator was modeled as a compartment with a pressure gradient

$$\Delta P = P_{in} - P_{out} \quad (6)$$

**Fig. 1** System diagram. CCP cardiac cycle pressure, A aorta, OL outflow lumen, ACP arterial circuit part, LV left ventricle, RA right atrium, IL inflow lumen, VS volume sensor, VCP venous circuit part, P pump, OX oxygenator, IC inflow cannula

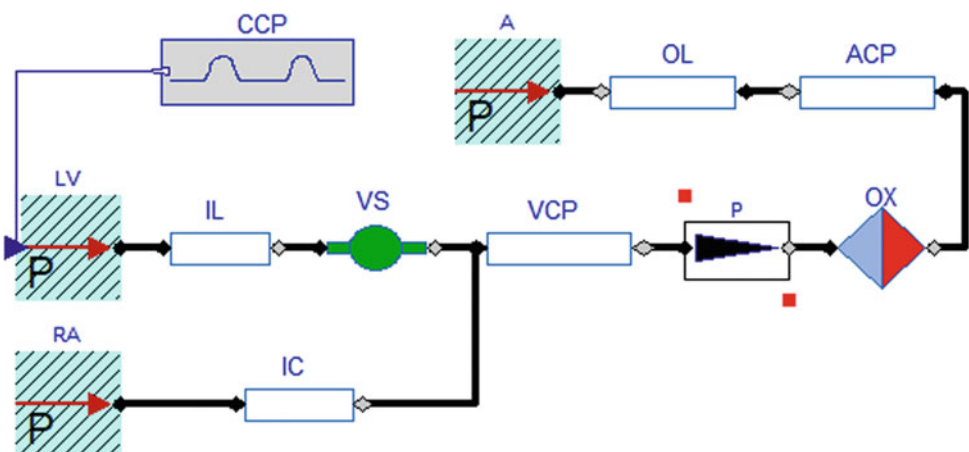


**Table 1** Initial values of state variables and parameters of the model in Modelica

Extracorporeal blood flow [L/min]	1	2	3	4	5
End-systolic volume [mL]	64 ± 11	70 ± 11	74 ± 11	78 ± 12	83 ± 14
Systolic blood pressure [mmHg]	60 ± 7	72 ± 7	81 ± 6	89 ± 7	97 ± 8
LV end-diastolic pressure [mmHg]	17.2 ± 1.4	18.2 ± 0.7	18.6 ± 1.5	18.9 ± 2.4	19.0 ± 2.9
Heart rate	94 ± 4	89 ± 3	84 ± 3	80 ± 2	77 ± 2

The simulation in this study is based on data from standard in vivo experiment in large animal models. The initial parameter values were derived from measurements on female swine [2]. The parameters for the simulations are presented in Table 1.

The blood flow value in drainage lumen of the double lumen arterial cannula during various extracorporeal blood flow (EBF) values (from 1 to 5 L/min) were investigated.

### 3 Results

The drafting of the double lumen arterial cannula for VA-ECMO, which is capable of achieving left ventricle decompression and to return the oxygenated blood with only one puncture, is presented in Fig. 2.

The relationship between the flow in the drainage lumen of the double lumen arterial cannula and the EBF is shown in Fig. 3. Table 2 presents the simulation results of flow values in the drainage lumen of the double lumen arterial cannula. The size of drainage lumen of the double lumen arterial cannula is 10 Fr.

### 4 Discussion

The present study reports a double lumen arterial cannula for VA-ECMO, which unload left ventricle during ECMO. In the conducted simulation study, the flow rate in the drainage

lumen was increased with increasing EBF. DLAC withdraws from 0.374 to 0.560 L/min in accordance to EBF. The present invention requires just one single puncture to achieve unloading LV and to return the oxygenated blood to the circulation.

Insufficient decompression of the left ventricle during the VA-ECMO is considered to be a major factor preventing an adequate LV recovery [11]. The LV decompression, during the ECMO therapy seems to be associated with a significant improvement of the LV function [12].

A number of studies mention successful LV unloading by drainage catheter, inserted in the LV and connected to venous circuit of VA-ECMO [13–17]. Nevertheless, inserting the catheter to the LV requires extra interventions, which increases invasiveness of the method and thus does not correspond with the current trends in the mini-invasive performance. Therefore, DLAC is a less-traumatic and effective alternative method.

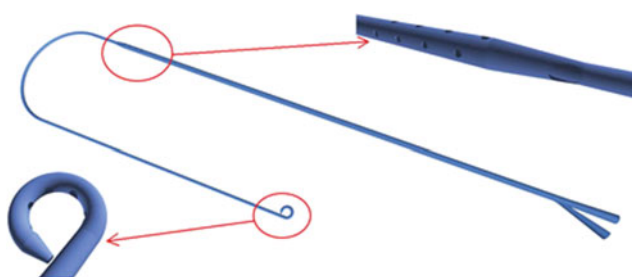
DLAC consists of two contiguous lumens; one is longer than the other. The shorter lumen, the end of which is positioned in the aorta, serves as a blood return lumen. The longer lumen, the end of which is introduced in the LV, serves as a blood intake lumen.

An elongated tube has a pigtail tip with multiple side holes. The pigtail tip prevents the wall of the heart chamber from being drawn to the catheter tip.

The inserted length of the cannula can be changed according to the requirements. Therefore, the present invention is suitable for patients with different anatomical parameters.

Our simulation results indicate that drainage lumen of the double lumen arterial cannula for VA-ECMO is capable of withdrawing  $0.478 \pm 0.074$  L/min during the EBF from 1 to 5 L/min (Table 2). Based on the data from an experiment with big animal model [2] we assume, that flow  $0.478 \pm 0.074$  L/min in drainage lumen of the double lumen arterial cannula is sufficient to unload LV during ECMO. Nevertheless, the results have to be verified experimentally and further validation is required.

A double lumen arterial cannula for VA-ECMO presents a promising solution to achieve the LV unloading during the

**Fig. 2** Drafting of the double lumen arterial cannula

**Fig. 3** The flow rate value in the drainage lumen of the double lumen arterial cannula according to EBF. The values can be found in Table 2

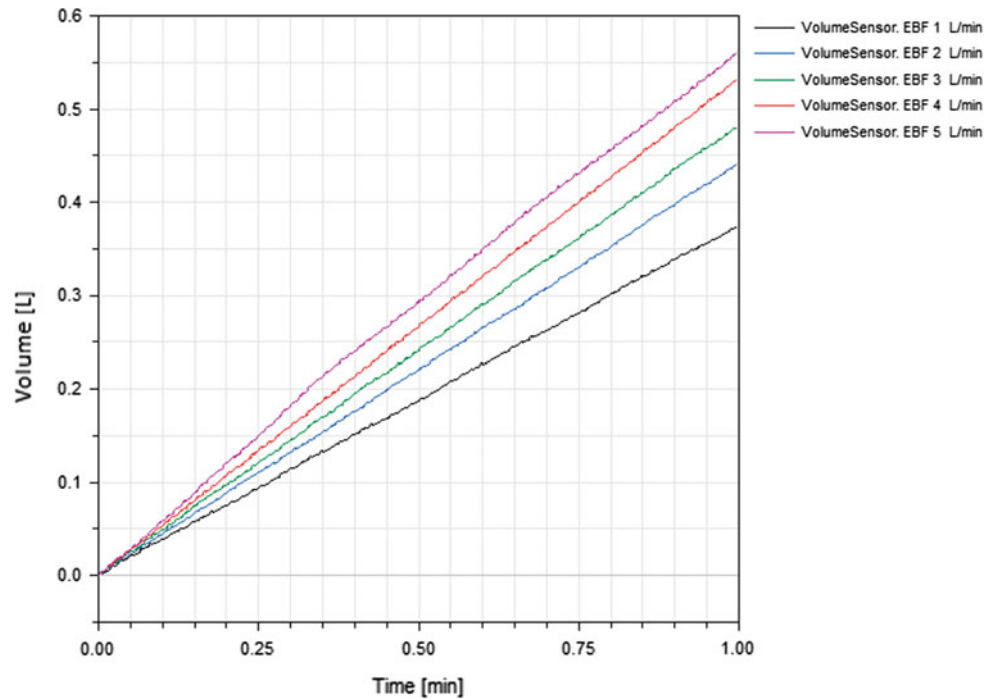


**Table 2** The flow rate value in the drainage lumen of the double lumen arterial cannula during VA-ECMO in Modelica

Extracorporeal blood flow [L/min]	1	2	3	4	5
Drainage lumen flow [L/min]	0.374	0.441	0.481	0.532	0.560

ECMO and corresponds with the current trends in the mini-invasive performance.

## 5 Conclusion

The study presents a less-traumatic method of LV unloading during ECMO. The double lumen arterial cannula is capable of achieving left ventricle decompression and blood return while requiring a single puncture. The simulation study was conducted to analyze the capability of a double lumen arterial cannula to unload left ventricle during ECMO. DLAC presents an alternative and perspective solution for LV unloading during the ECMO therapy.

**Acknowledgements** The authors thank Eva Motyčková from Faculty of Biomedical Engineering, Czech Technical University in Prague and Eva Poncová for help and support.

## References

1. Aissaoui N, Guerot E, Combes A, Delouche A, Chastre J, Leprince P, et al. Two-Dimensional Strain Rate and Doppler Tissue Myocardial Velocities: Analysis by Echocardiography of Hemodynamic and Functional Changes of the Failed Left Ventricle during Different Degrees of Extracorporeal Life Support. *Journal of the American Society of Echocardiography*;25(6):632–640.
2. Ostadal, Mlcek, Kruger, Hala, Lacko, Mates, et al. Increasing venoarterial extracorporeal membrane oxygenation flow negatively affects left ventricular performance in a porcine model of cardiogenic shock. *Journal of Translational Medicine* 2015 8;13 (1).
3. Strunina S, Ostadal P. Left ventricle unloading during veno-arterial extracorporeal membrane oxygenation. *Current Research: Cardiology* 2016;3(1):5–8.
4. Soleimani, B, and WE Pae. Management of left ventricular distension during peripheral extracorporeal membrane oxygenation for cardiogenic shock. *Perfusion* 2012;27(4):326–331.
5. Massetti M, Gaudino M, Crea F. How to transform peripheral extracorporeal membrane oxygenation in the simplest mid-term paracorporeal ventricular assist device. *Int J Cardiol* 2013;166 (3):551–553.
6. Kotani Yasuhiro, Chetan Devin, Rodrigues Warren, Sivarajan V. Ben, Gruenwald Colleen, Anne-Marie Guerguerian, et al. Left Atrial Decompression During Venarterial Extracorporeal Membrane Oxygenation for Left Ventricular Failure in Children: Current Strategy and Clinical Outcomes. *Artificial Organs* 2013;37(1):29–36.

7. Fouilloux V, Lebrun L, Macé L, Kreitmann B. Extracorporeal Membranous Oxygenation and Left Atrial Decompression: A Fast and Minimally Invasive Approach. *Ann Thorac Surg* 2011;91(6):1996–1997.
8. Seib PM, Faulkner Sherry C, CCP, Erickson C. Christopher, Stephen H. Van Devanter, James E. Harrell, et al. Blade and Balloon Atrial Septostomy for Left Heart Decompression in Patients With Severe Ventricular Dysfunction on Extracorporeal Membrane Oxygenation. *1999 Catheter Cardiovasc Interv*;46(2):179–186.
9. Kohler K, Valchanov K, Nias G, Vuylsteke A. ECMO cannula review. *Perfusion* 2013;28(2):114–124.
10. Uggla B, Nilsson TK. Whole blood viscosity in plasma cell dyscrasias. *Clin Biochem* 2015;48(3):122–124.
11. Hong TH, Byun JH, Yoo BH, Hwang SW, Kim HY, Park JH. Successful Left-Heart Decompression during Extracorporeal Membrane Oxygenation in an Adult Patient by Percutaneous Transaortic Catheter Venting. *Korean J Thorac Cardiovasc Surg* 2015 /06/05;48(3):210–213.
12. Douflé G, Roscoe A, Billia F, Fan E. Echocardiography for adult patients supported with extracorporeal membrane oxygenation. *Critical Care* 2015;19(1):1–10.
13. Hong, Byun, Yoo, Hwang, Kim, Park. Successful Left-Heart Decompression during Extracorporeal Membrane Oxygenation in an Adult Patient by Percutaneous Transaortic Catheter Venting. *The Korean Journal of Thoracic and Cardiovascular Surgery* 2015 06;48(3):210–213.
14. Kitamura M, Hanzawa K, Takekubo M, Aoki K, Hayashi J. Pre-clinical Assessment of a Transaortic Venting Catheter for Percutaneous Cardiopulmonary Support. *Artificial Organs* 2004 March 1;28(3):298–302.
15. Guirgis M, Kumar K, Menkis AH, Freed DH. Minimally invasive left-heart decompression during venoarterial extracorporeal membrane oxygenation: an alternative to a percutaneous approach. *Interact CardioVasc Thorac Surg* 2010 05/01;10(5):672–674.
16. Barbone A, Malvindi PG, Ferrara P, et al. Left ventricle unloading by percutaneous pigtail during extracorporeal membrane oxygenation. 2011;13(3):293–295.
17. Hong TH, Byun JH, Lee HM, Kim YH, Kang G, Oh JH, et al. Initial Experience of Transaortic Catheter Venting in Patients with Venous Arterial Extracorporeal Membrane Oxygenation for Cardiogenic Shock. *ASAIO Journal* 2016;62(2). Author, F.: Article title. *Journal* 2(5), 99–110 (2016).



# Electromagnetic Compatibility of Cardiac Stimulation Technology in Relation to Human Body—The Introductory Study

Jan Morava, Aleš Richter, and Pavel Kučera

## Abstract

The session deals with interdisciplinary topic of the electromagnetic compatibility of cardiac stimulation devices that are used in patients with cardiac pathology. This study is thematically interested in physical and energy impacts of artificial electromagnetic fields, particularly in the influence of strong energy time-variable fields, on cardiac stimulation system implanted into human organism. We consider implanted electronic device, pacemaker or cardioverter-defibrillator with fixed electrodes, and human heart, especially cardiac conduction system, as a whole. In this article we present the functional principles of implantable cardiac pacemakers and describe its interaction with the source of external interference by using modelling and simulation methods by electric circuit substitution. Subsequently, we discuss the physical mechanisms of disturbance signals and methods to minimize its consequences. The aim of the study is the theoretical analysis and the introduction to this issue and also the definition of the terms. This session does not occupy with medical clinical problems but the emphasis is put on physical and energy aspects of external electromagnetic fields on heart implanted device and to refer and analyze the possible risks of interaction.

## Keywords

Electromagnetic interference • Cardiac stimulation  
Implantable device • Electrophysiology

## 1 Introduction

The issue of electromagnetic compatibility of pacemaker devices combines knowledge from the field of electronic microprocessor-controlled systems and cardiac electrophysiology. Our attention is put on the devices that are used in cardiac patients with defect of cardiac conduction system or with higher risk of malignant ventricular arrhythmia caused by other structural changes. A patient with an implanted pacemaker is every day exposed to various sources of interference whose interaction with this system can result in its wrong functioning. Certainly it can affect the patient's health. The risks depend on various factors and cannot be predicted easily. There are different innovative technologies including software and hardware mechanisms that can minimize, but not totally eliminate, these risks.

## 2 Theoretical Premises

This article does not solve medical problems in any case and presents mainly theoretical physical point of view. The following text makes an effort to explain possible practical aspects of external electromagnetic field into human tissue. The principles of electromagnetic induction in human tissue are briefly presented.

### 2.1 A Physical Aspects

The electromagnetic field is completely described by four Maxwell equations. This theory is appropriate to describe the inner electromagnetic field in human bodies and in the

J. Morava (✉) · A. Richter  
Institute of Mechatronics and Computer Engineering, Technical  
University of Liberec, Liberec, Czech Republic  
e-mail: jan.morava@tul.cz

J. Morava · P. Kučera  
Department of Cardiology, Regional Hospital Liberec, Liberec,  
Czech Republic

tissues. The law of electromagnetic induction, or Faraday's law, has the form and it is valid in living tissues too.

$$\text{rot } \mathbf{E} = - \frac{\partial \mathbf{B}}{\partial t} \left[ \frac{\text{V}}{\text{m}} \right] \quad (1)$$

$$\oint_C \mathbf{E} dr = - \frac{\partial}{\partial t} \iint_S B_n dS [\text{V}] \quad (2)$$

It is important to give in the integral form where  $C$  is closed curve embracing part of body and  $S$  is any surface having the curve  $C$  as its periphery. The symbol  $B_n$  denotes the normal component of magnetic flux density  $\mathbf{B}$  with respect to the surface  $S$ . Both the forms (1) and (2) of Faraday's law say that the time varying magnetic field produces electric field having closed lines of force. The integral form is more illustrative.

The induced electric field in the body, due to the time varying magnetic field, generates the current that forms the magnetic field according to the Ampere law where  $H$  is the magnetic field strength [A/m],  $J$  is the current density, due to the induced electric field [A/m<sup>2</sup>] and  $D$  is the electric field flux density [C/m<sup>2</sup>] or [A s/m<sup>2</sup>].

$$\text{rot } \mathbf{H} = \mathbf{J} + \frac{\partial \mathbf{D}}{\partial t} [\text{A}] \quad (3)$$

$$\mathbf{J} = \gamma \mathbf{E} \quad (4)$$

The equations above are complete for the next analysis. The electric field  $\mathbf{E}$  produces current of volume density  $i$  according to the differential Ohm's law where  $\gamma$  is the conductivity of biologic medium [S/m] or [m<sup>-3</sup> kg<sup>-1</sup> s<sup>3</sup> A<sup>2</sup>].

The examples of tissue conductivity show that human or animal body is strongly heterogeneous surrounding from electromagnetic view. We can speculate about low intensity of external electromagnetic field so the conductivity of individual tissue is linear. The ones of tissues (particularly muscle and brain) are anisotropic.

The magnetic quantities (magnetic field strength  $H$  and magnetic flux density  $\mathbf{B}$ ) are connected by the relation where  $\mu = \mu_r \mu_0$  is absolute permeability,  $\mu_r$  is relative permeability and  $\mu_0 = 4\pi \times 10^{-7}$  [H/m] or [m kg s<sup>-2</sup> A<sup>-2</sup>] means permeability of vacuum.

The tissues and human bodies mainly consist of diamagnetic substances. The diamagnetism is too weak that is

why we can count in permeability of vacuum  $\mu_0$ . The metal implants are made from magnetic neutral materials too.

Analogically the electric quantities (electric field strength  $\mathbf{E}$  and electric flux density  $\mathbf{D}$ ) are connected by the relation where  $\varepsilon = \varepsilon_r \varepsilon_0$  is absolute permittivity,  $\varepsilon_r$  is relative permittivity and  $\varepsilon_0 = 8.86 \times 10^{-12}$  [F/m] or [m<sup>-2</sup> kg<sup>-1</sup> s<sup>4</sup> A<sup>2</sup>] means permittivity of vacuum.

$$\mathbf{B} = \mu \mathbf{H} [\text{T}], [\text{kg s}^{-2} \text{A}^{-1}] \quad (5)$$

$$\mathbf{D} = \varepsilon \mathbf{E} \quad (6)$$

Relative permittivity characterizes dielectric properties of tissues and human and animal bodies and its range is approximately from 2 to 70. We can exclude the ferroelectric materials in the living bodies and in implants.

We suppose that there is only exciting magnetic field, which is affecting human. We do not consider any external electric field, external current density and external electric charges. Of course the magnetic field must be generated by external current, for instance. Therefore we suppose that the sources of external magnetic field  $\mathbf{B}_{\text{ex}}$  are outside the volume with investigated medium. The magnetic and electric fields are coupled. The external magnetic field  $\mathbf{B}_{\text{ex}}$  produces the electric field according to the Faraday law (2). The induced electric field forms the current according to Ohm's law (5) and the magnetic field using the Ampere's law (4). The detailed analysis shows that the acting magnetic field in Faraday's law (2) decreases. Then the loop is repeated.

The above explained coupling leads to wave equations for both the electric and magnetic field derived from Maxwell Eqs. (1), (3) and material conditions. They are quite general, but analytical solution can be found only for several simple cases of small technical importance. Fortunately, practical simplifications exist.

All the quantities in Eqs. (1)–(3) depend on used frequency. Usually the harmonic excitation with angular frequency  $\omega$  is used. The following Table 1 contains values for the electrical conductivity for frequencies up to 1 MHz for all tissues, including statistical information on the standard deviation and the spread in the values. The low frequency parameters are based on a combination of the Gabriel dispersion relations and a review of the available literature. The following Table 1 describes values for the electrical conductivity of heart tissues for frequencies up to 1 MHz and is

**Table 1** Low frequency electrical conductivity of heart tissues

Conductivity (S/m)	Average	Standard deviation	Number of studies	Minimum	Maximum
Heart lumen	6.60E-1	1.39E-1	19	4.33E-1	9.46E-1
Heart muscle	3.81E-1	1.75E-1	28	1.04E-1	6.46E-1
Heart muscle longitudinal	3.94E-1	7.62E-2	3	3.19E-1	4.72E-1
Heart muscle transversal	2.16E-1	4.47E-2	3	1.77E-1	2.65E-1

also including statistical information. The electrical conductivity of metals used in implant construction, titanium and stainless steel, is  $1.8 \times 10^6$  and  $1.1 \times 10^6$  S/m. References [1, 2] are used in this Sect. 2.1.

### 3 Basic Principles of Cardiac Stimulation Technique

A cardiac stimulation implantable device (CIED) is a medical device for the treatment of bradyarrhythmias and tachyarrhythmias. It consists of the pacemaker (located subcutaneously above the pectoral muscle) containing the battery, capacitors and control circuits, and electrodes (1–3) leading from the head of stimulator through the subclavia vein into the right heart (Fig. 1).

Electrodes are mostly actively fixed to the endomyocardium. We always check the electrical parameters of each electrode during the implantation process or during the periodic check-up. Electrical parameters of each chamber electrode give us overall information about the correct system functioning.

#### 3.1 Stimulation Parameters

We usually check these following electrical parameters of implanted electrodes: stimulation threshold, impedance, sensitivity (sensing), eventually slew-rate. The stimulation threshold reflects the minimum amount of delivered energy that can cause depolarization of myocardium. The electrical impulse is characterized by its amplitude programmed in volts [V] or [mA], and the pulse width in [ms]. Ideal parameters of stimulation threshold during the implantation process is the value under the half of battery voltage (under 1.5 V) at pulse width 0.4 ms. Delivered current will vary

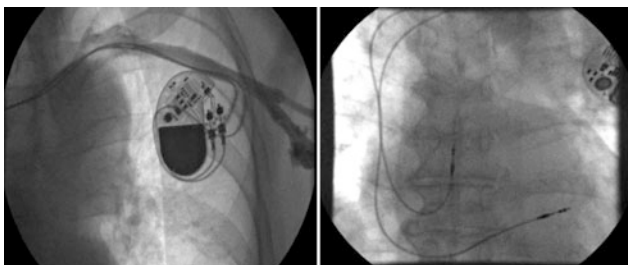


**Fig. 1** X-ray images of implanted dual chamber pacemaker with two actively fixed intracardiac electrodes

according to the impedance by the Ohm's law. The impedance of stimulation electrode, that combines wire and tissue resistance, should be in the range of 200–2000  $\Omega$ . Sensing is the ability of device to detect its own cardiac action. The value is measured in units to tens of [mV]. It depends on the monitored channel. In atrium we detect the P-waves (action potential of sinoatrial node) and in ventricle the R-waves (depolarization of ventricles). The sensitivity setting corresponds to the threshold for the lowest signal amplitude that can be detected. The slew rate value refers to sensitivity and gives us information about the sensing quality. It represents the amplitude change of the scanned signal over time [3, 4].

#### 3.2 Cardiac Stimulation Devices

The main function of CIED is the therapeutic ability, it means the delivering of stimulation or defibrillation pulse, and diagnostics including recording of clinical and technical data. The systems can be divided according to several aspects. All devices are able to monitor cardiac action and, in the case of pacemakers, adequately compensate the patient's own action by an electrical impulse. For good clinical effect and proper electrical activation of heart, it is necessary to synchronize patient's own cardiac activity with pacemaker timing algorithms. These timers derive from the interpretation of the IEGM (intracardiac ECG) signals. Devices with cardioversion and defibrillation function are more advanced systems. These devices also have pacemaker function and in case of dangerous ventricular arrhythmia, they are able to terminate the arrhythmia by a sequence of electrical impulses or by electrical discharge (shock) of energy up to 40 J. The devices also differ in the number of electrodes as single chamber, dual chamber and devices for resynchronization therapy (3 electrodes). For single chamber devices is one electrode actively fixed into the right ventricle, for dual chamber device there is next electrode in the right atrium and for the resynchronization therapy devices there is the third electrode passively fixed into the coronary sinus to stimulate the myocardium of left ventricle [5].

The pacemaker configuration is distinguished by the location of the anode the unipolar and bipolar. The cathode is always located at the distal end of electrode (tip). In the unipolar configuration leads the vector to the device (can) as anode and in the bipolar configuration to a proximal pole (ring) located proximally also on conductor. The stimulation and sensing vector setting can be selected individually, on

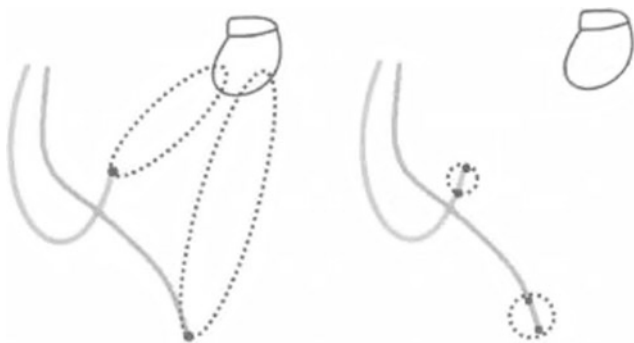


**Fig. 2** The difference between position of cathode and anode in bipolar and unipolar configuration of pacemaker

each channel. Due the distance of sensing poles, it can be inferred that the bipolar configuration is more resistant to interference caused by myopotentials or EMI than the unipolar setting [6] (Fig. 2).

An important feature of cardiostimulation device is its programmability. Device interrogation and programming can be done thanks to a special computer (programmer) when the programming head is attached near the device. Modern pacemakers and defibrillators allow wireless telemetry in a frequency band 402–405 MHz (called MICS—Medical Implant Communication Service). Thanks to the programmer we can measure the electrical parameters of electrodes, check battery, read diagnostics or we can program the pacing mode of the device. The mode is described by NBG code that consists of several characters. The first character indicates the stimulated chamber, the second one is sensed chamber (A = Atrium, V = Ventricle, D = Dual, O = None) and the third mark reflects the response to the sensed event (I = Inhibited, T = Triggered, D = Dual, O = None) [4, 5].

## 4 Electromagnetic Interference

Electromagnetic compatibility (EMC) reflects the ability of the device to work properly in an environment with other sources of interference. Also, at the same time, the device is not a source of interference signals for its surroundings that could be influenced by it. We can divide EMC property into electromagnetic susceptibility (EMS) and electromagnetic interference (EMI).

A patient with implanted pacemaker is exposed to various sources of electromagnetic fields every day. This may have

consequences clinical or technical. Interaction with the implanted system can be detected by the device as its own cardiac action. Induction of local currents on the electrodes, an increase in the current density in the tissue around the device (electrode poles) and the heating of the implant may occur. This may have fatal consequences such as the inhibition of stimulation or inappropriate therapy (discharge) in cardioverter-defibrillator patient. Also it can cause the damage of the device electronics or changes in pacemaker programming. The risk of the interaction with the patient depends on a number of factors such as the distance from the source (intensity decreases with the square of the distance), the exposure time or the position of the system. It also depends on configuration (unipolar or bipolar sensing) and programming of the pacemaker. If a strong EMI (electrocautery, external defibrillation, radiofrequency ablation) occurs, the device can be reset to Power-On reset, because the communication between the microprocessor and the device memory can be interrupted. In a defibrillator, when the Power-On reset occurs, therapies are deactivated [3, 4].

In daily life there are many different sources of interference. It could be the radio communication devices, metal detectors or other power hand tools. In healthcare the EMI interferes, for example, in magnetic resonance imaging, ionizing radiation photons in oncology patients during radiation (linear accelerator), but also with electrocautery and other appliances of electric current (electromyography), or capsule endoscopy. In these cases, temporary reprogramming of the device is required to a suitable pacing mode.

The risk of EMI cannot be predicted very well. The components or hardware, software mechanisms used against the EMI includes filtering (bandpass), bipolar sensing, shielding, reed switch (magnetic relay in ICD), Zener diode, feed through filter of capacitor, Hall sensor. Despite these, the risks can be minimized, but not completely eliminated. The mechanisms to minimize the risks for the CIED associated with EMI are included in the European directives or in the National technical standards [3] (Fig. 3).

## 5 Discussion

The relevance of this issue is growing with the rapidly increasing number of cardiac patients using this kind of electrophysiological treatment. Patients are exposed



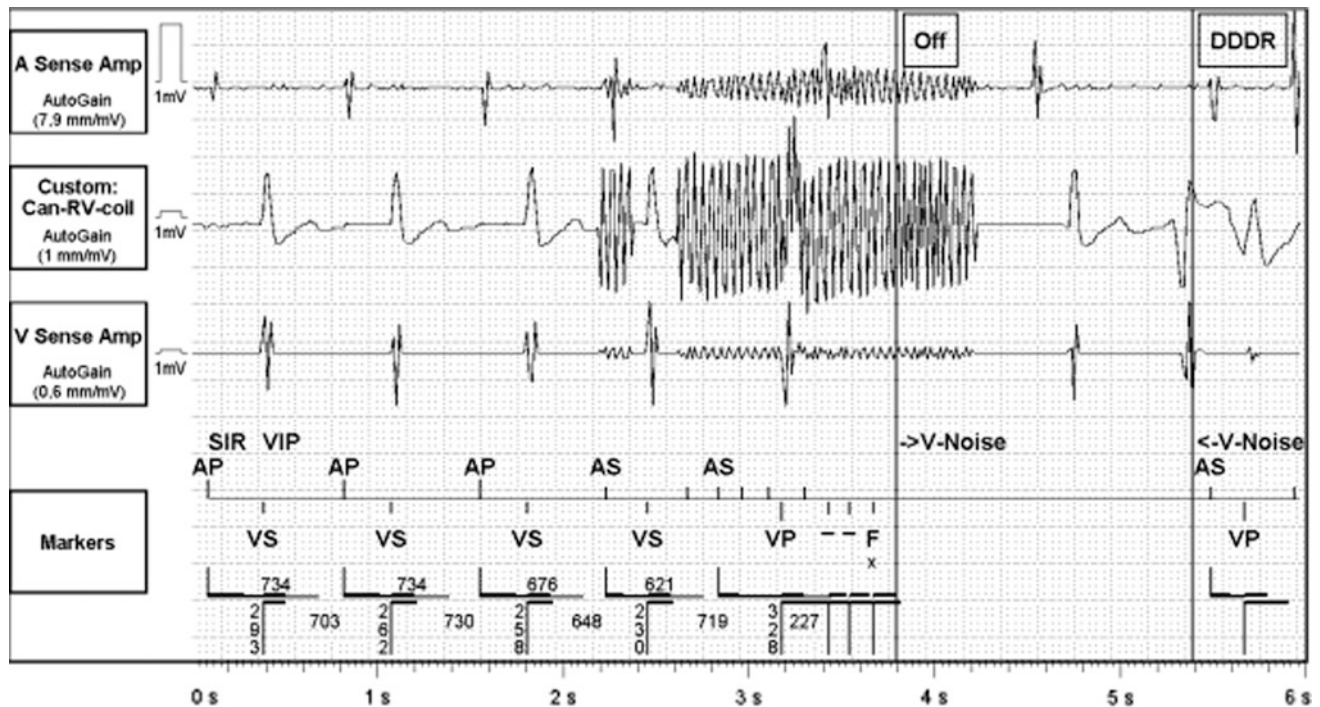


**Fig. 3** The intra-cardiac recording of interference signals in atrial and ventricular channel

to the influence of external electromagnetic sources, potential sources of interference, in daily life or during hospitalization. These risks are very often overlooked or are not taken seriously. It is necessary to remember that these medical systems also have its own limits as other electronic devices. For modern and currently applied devices are these risks greatly minimized in comparison to devices implanted in previous years, but it can't be neglected.

## 6 Conclusion

The aim of the study is to describe and experimentally verify the limits of implantable devices and the risks associated to the interaction with external sources of electromagnetic interference. An important part represents discussion about mechanisms and procedures related to the prevention of interference. The principle of this ARTICLE is to clarify the basic physical aspects of cardio stimulation from non-medical, technical view and the possible influence on the correct functioning of the system caused by external fields. We believe that this aim of our study will contribute to the knowledge of medical staff and patients and will also bring us a number of practical findings and answers to the unanswered questions. This article represents the initial part of long-term research realized in cooperation of the Technical University of Liberec and Regional Hospital Liberec.

**Acknowledgements** This article is result of cooperation between Technical University of Liberec and Regional Hospital Liberec. This work was supported by MŠMT funds on institutional support for long-term conceptual development the Faculty of Mechatronics and Computer Engineering and Student grant competition of the Technical University of Liberec.

## References

1. S. U. Inan, S. A. Inan: *Engineering Electromagnetics*, Addison-Wesley, Menlo Park, CA, USA, 1999 (ISBN 0-201-47473-5)
2. A. Richter, Ž. Ferková: *Physical and energy analysis of therapy applying low-dynamic magnetic fields*, Conference Paper May 2017, <https://doi.org/10.1109/ecmsm.2017.7945889> Conference: 2017 IEEE International Workshop of Electronics, Control, Measurement, Signals and their Application to Mechatronics (ECMSM)
3. Ellenbogen, Kenneth A., Bruce L., Wilkoff and G. Neal Kay.: *Clinical cardiac pacing, defibrillation, and resynchronization therapy*. Philadelphia, PA: Elsevier, 2017. ISBN 978-0-323-37804-8
4. Hayes, David L., and Paul A. Friedman.: *Cardiac pacing and defibrillation: a clinical approach*. Oxford: Wiley-Blackwell, 2008. ISBN 978-1-4051-6748-2
5. Korpas D.: *Kardiostimulační technika*. Praha: Mladá fronta, 2011. Aeskulap. ISBN 978-80-204-2492-1.
6. Love, Charles J.: *Handbook of cardiac pacing*. Austin, TX: Landes Bioscience, 1998. ISBN 1-57059-492-9
7. Brodeur, P.: *Annals of Radiation: The hazards of electromagnetic fields*. Parts 1–3. New Yorker, 12 June, 51–88; 19 June, 47–73; 26 June, 39–68, 1989. (Later published as *Currents of death: Power*



- lines, computer terminals and the attempt to cover up their threat to your health. New York: Simon and Schuster, 1989
8. Reference of ICNIRP committee: *Guidelines for Limiting Exposure to Time-Varying Electric, Magnetic, and Electromagnetic Fields (up to 300 GHz)*. Health Physics 74/ 4: 494–522, 1998
  9. *Tissue properties - Low Frequency (Conductivity)* [online], <https://www.itis.ethz.ch/virtual-population/tissue-properties/database/low-frequency-conductivity/>
  10. Eisenberger M., Bulava A. and Martin Fiala.: *Základy srdeční elektrofyzologie a katérových ablací*. Praha: Grada, 2012. ISBN 978-80-247-3677-8

# Computational Fluid Dynamics Analysis of Coronary Stent Malapposition

Iuliana-Claudia Hudrea, Alin-Florin Totorean, and Dan Gaita

## Abstract

Numerous pathological and intravascular imaging studies have been conducted on the attempt of identifying the mechanisms underlying stent thrombosis in percutaneous coronary interventions (PCI). Stent under expansion and undersizing have been associated with early thrombosis, while delayed endothelization and late malapposition (related to vessel positive remodelling or clot lysis) have been linked to late and very late thrombosis. It has been suggested that flow disturbances leading to increased thrombogenicity are likely to occur at the site of stent malapposition. These flow alterations include zones with high Wall Shear Stress (WSS) that induce platelet activation and recirculation regions associated with low WSS and endothelium denudation, conditions susceptible to high thrombogenic risk. This paper aims to analyze the effect of stent malapposition on flow conditions in relation to stent thrombosis, using computational fluid dynamics (CFD) techniques. The findings may improve the understanding of the mechanisms correlating stent malapposition and stent thrombosis, a severe and multifactorial complication of coronary artery stenting.

## Keywords

Stent malapposition • Stent thrombosis • Wall shear stress

I.-C. Hudrea · D. Gaita  
Victor Babes University of Medicine and Pharmacy,  
Timisoara, Romania  
e-mail: claudia\_hudrea@yahoo.com

D. Gaita  
e-mail: dgaita@cardiologie.ro

I.-C. Hudrea · D. Gaita  
Cardiology Department, Institute for Cardiovascular  
Diseases, Timisoara, Romania

A.-F. Totorean (✉)  
Department of Mechanics and Strength of Materials,  
Politehnica University of Timisoara, Timisoara, Romania  
e-mail: alin.totorean@upt.ro

## 1 Introduction

Stent malapposition or incomplete stent apposition (ISA) is defined by a gap between at least one stent strut and the underlying innermost layer of the vessel wall, and is more frequently associated with drug eluting stents (DES) than with bare metal stents (BMS) [1, 2]. Some authors have classified ISA depending on the gap distance, into: mild,  $\leq 100 \mu\text{m}$ ; moderate,  $100\text{--}300 \mu\text{m}$ ; intermediate,  $300\text{--}500 \mu\text{m}$ ; and severe,  $>500 \mu\text{m}$  [3]. Many factors contribute to stent malapposition, either procedure-related (stent underexpansion, undersizing), plaque-related (thrombus dissolution, positive vessel remodeling), or stent-related (delayed endothelization, chronic stent recoil) [1–6].

Studies comprising optical coherence tomography (OCT) and intravascular ultrasound (IVUS) as diagnosis tools revealed that ISA is the most common finding in stent thrombosis (ST) cases [2, 7]. Stent under expansion and undersizing have been associated with early thrombosis, while delayed endothelization and late malapposition (related to vessel positive remodeling or clot lysis) have been linked to late and very late thrombosis [4]. Strut dimensions and positioning relative to the vessel wall are considered critical factors in modulating stent thrombogenicity [3, 5].

Computational fluid dynamics (CFD) has emerged as a powerful tool in the study of the mechanisms underlying stent thrombosis. CFD investigations showed that the luminal protrusion of stent struts modify the local hemodynamic environment. It has been suggested that these flow disturbances tend to worsen with increasingly higher degrees of strut malapposition, resulting in enhanced thrombogenicity [3–6]. Several authors propose that high WSS ( $>2.5 \text{ Pa}$ ) induce platelet activation near thrombogenic struts and impede strut endothelizations (neointimal coverage and stent healing). Also, these authors correlate recirculation regions and associated low WSS ( $<1 \text{ Pa}$ ) developed at the

malapposition site with endothelium dysfunction (denudation), a highly thrombogenic condition [3–9].

**The aim of the present paper** is to analyze the effect of stent malapposition on flow conditions in relation to stent thrombosis, using CFD techniques.

## 2 Numerical Approach

Numerical investigations of the haemodynamic changes associated with different degrees of stent malapposition were conducted in this study, in comparison with the well-apposed stent situation. For these purposes, a simplified stented coronary artery model was used with a uniform internal diameter  $D = 4$  mm [10]. The stent geometrical characteristics were established according to literature [11]. The stent was inserted at the distance  $10D$  relative to artery edges for proper simulation purposes and it was assumed to be rigid, without mechanical deformation. The stent length was  $L_{\text{stent}} = 18$  mm. The struts were simplified as a series of rectangular of 0.1 mm thick and 0.1 mm wide; each strut was separated 1 mm from each other [11]. The artery and stent geometry details are found in Figs. 1 and 2.

The flow was computed for the well-apposed stent geometry and for three stent malapposition geometries, respectively gap distance ( $H$ ) between the vessel wall and strut of 100, 200 and 400  $\mu\text{m}$  (corresponding to ISA classification above-mentioned) [3]. We aimed to investigate a particular case of proximal malapposition where struts S1–S4 have a constant gap distance of  $H$ , strut S5 of  $H/2$  and struts S6–S17 were considered well-apposed relative to vessel wall (Figs. 1 and 2). The simulations were performed under steady-state conditions. Flow field visualizations along the vessel wall and in the vicinity of stent struts were carried out. The main hemodynamic parameters investigated

were: WSS distribution, velocity field and the corresponding recirculation regions.

## 2.1 Boundary Conditions

The blood flow dynamics entail numerous geometric and mechanical characteristics. In order to simplify the model while remaining close to physiological conditions, boundary conditions used for numerical simulations were imposed, as follows:

- Inlet: mean physiological flow rate  $Q_{\text{in}} = 200$  ml/min.
- Outlet: outlet pressure of 0 Pa.
- Walls: assumed to be nonslip and rigid.

The fluid was assumed to be incompressible, similar to blood with density of  $1050$  kg/m<sup>3</sup> and dynamic viscosity of  $0.00368$  kg/ms. The physical properties remain constant and gravitational effects were negligible during all the analysis. The numerical simulations were performed using the commercial CFD software Fluent 6.3 [12], under steady-state and laminar conditions and the Navier-Stokes governing equations were solved iteratively until the residual of continuity and velocity reached the convergence criterion of  $10^{-9}$ .

## 3 Results

A number of four flow analyses under steady state conditions were performed: for normal stent position and for three malapposition geometries of 100, 200 and 400  $\mu\text{m}$  (Fig. 3).

As it can be observed in Fig. 3, for normal position of the stent, the protrusion of stent struts inside de artery lumen

**Fig. 1** Computational domain used for stent numerical simulations.  $L_{\text{stent}}$ —stent length,  $D$ —artery internal diameter,  $Q_{\text{in}}$ —inlet flow ratio

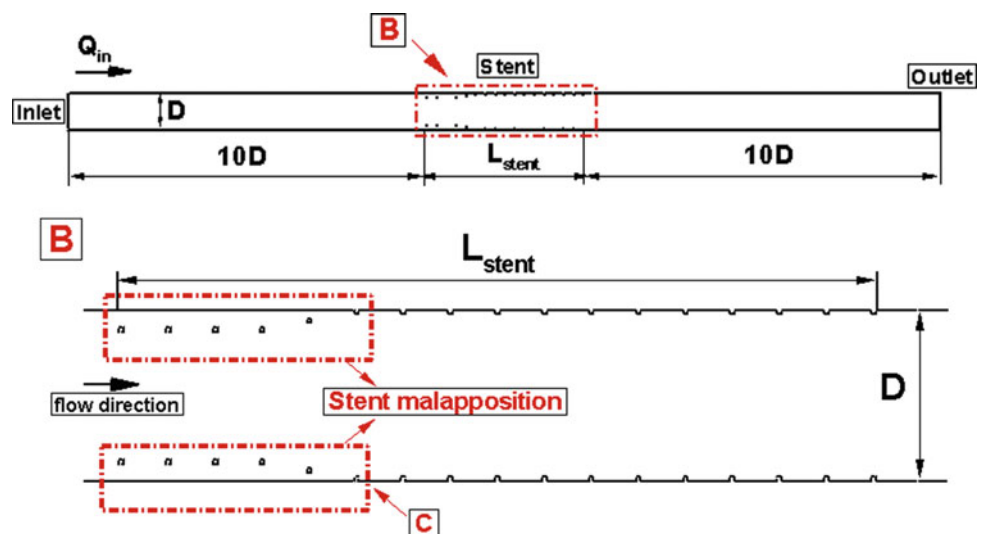


**Fig. 2** Stent geometry detail (detail C in Fig. 1):  $h$ —strut height,  $w$ —strut width,  $H$ —gap distance between bottom artery wall and strut,  $L_{interstrut}$ —distance between consecutive struts

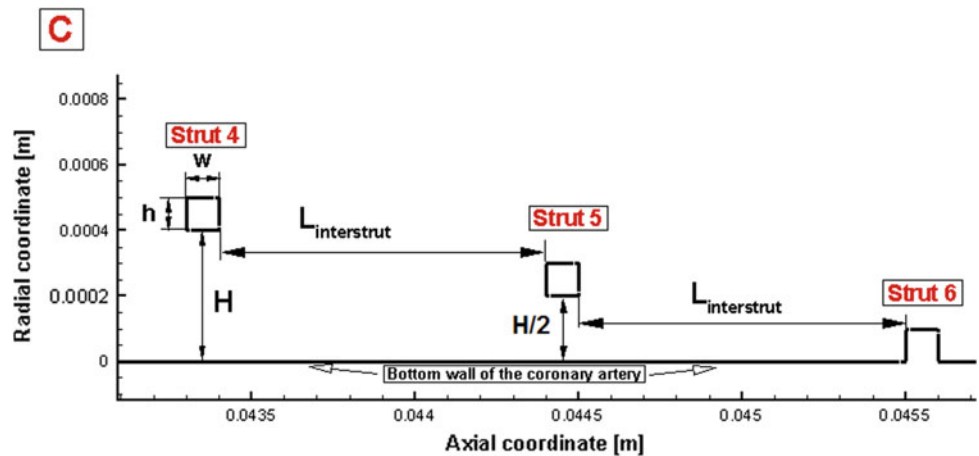
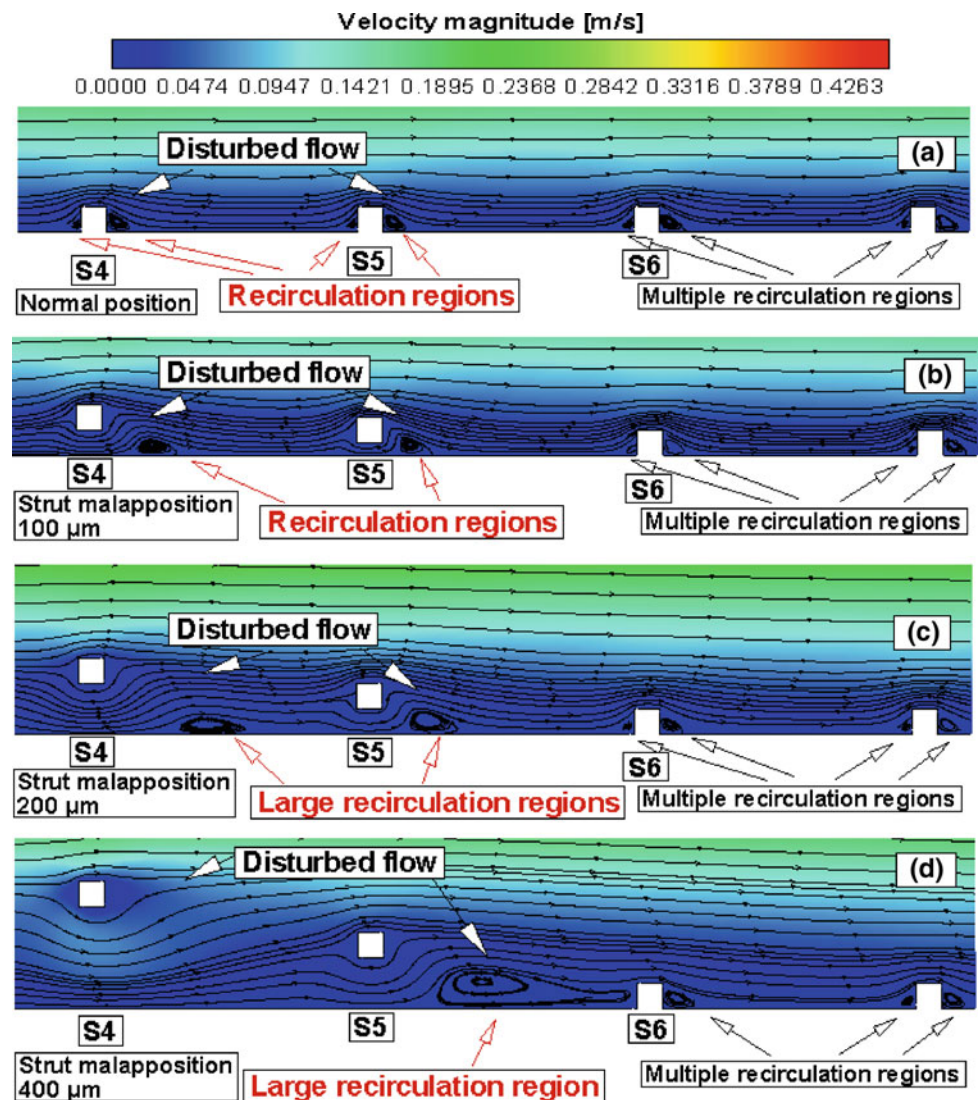


**Fig. 3** Impact of strut-wall malapposition distance on blood flow velocity field. Velocity field associated to fluid flow in the vicinity of struts 4–6 at the bottom artery wall, in the cases of: **a** well-apposed stent, **b** stent malapposition of 100  $\mu\text{m}$ , **c** stent malapposition of 200  $\mu\text{m}$ , and **d** stent malapposition of 400  $\mu\text{m}$



promotes fluid perturbations. Flow separation occurs and recirculation regions form immediately adjacent to each strut [14]. Strut position relative to vessel wall significantly

affects the flow field [3, 5, 13, 14]. Flow field patterns of recirculation vary with each malapposition degree. The most noticeable disturbances are observed around struts S4 and S5

(Fig. 3). As the gap distance increases, recirculation zones initially grow in size and then shift downstream, losing contact with the strut. At maximal strut displacement the recirculation even ceases, as it can be observed in Fig. 3d (between S4 and S5).

Flow perturbations function as modulators of the artery wall, leading to mechanical being forces translated into biological and molecular signals. Recirculation is associated with low values of WSS ( $<1$  Pa) downstream of struts, condition presumed to induce endothelial denudation (dysfunction), thus exposing the underlying thrombogenic structures to blood flow particles. Large recirculation zones in contact with vessel wall may in this way promote clot formation [3, 5].

Furthermore, several studies have raised the concern that the high shear stress levels detected on top of the struts may impede strut endothelialization (and delay stent healing) and that the even higher shears stress levels around strut edges may induces platelets activation. These disturbances are directly correlated to strut position into the flow stream [3–6, 8, 9]. Figure 4 confirms these considerations, as it can be observed that WSS tends to attain high values around and on the top of struts. WSS reaches highest values around the first strut, particularly in case of maximal gap distance ( $H = 400 \mu\text{m}$ ) as seen in Fig. 5.

## 4 Conclusions and Discussions

Stent thrombosis is a multifactorial phenomenon that cannot be explained by malapposition alone. Stent-related thrombogenicity is among others a function of strut-wall detachment distance and emerging flow disturbances.

Our results revealed that stent struts position relative to the vessel wall affects flow field patterns and impacts the recirculation zones extent and position. As recirculation increases in size, larger parts of endothelium are being

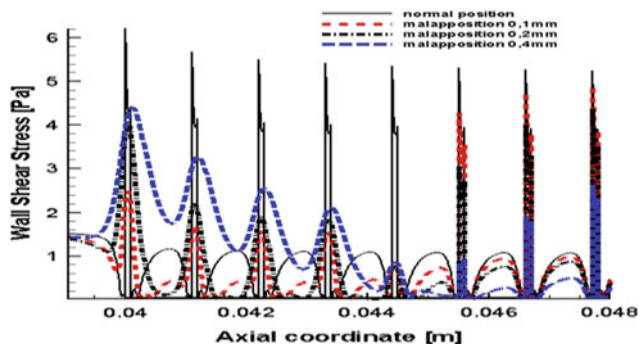


**Fig. 4** WSS evolution along the stented artery bottom wall in the vicinity of the first 8 struts for normal stent position and for stent malapposition of 100, 200 and 400  $\mu\text{m}$

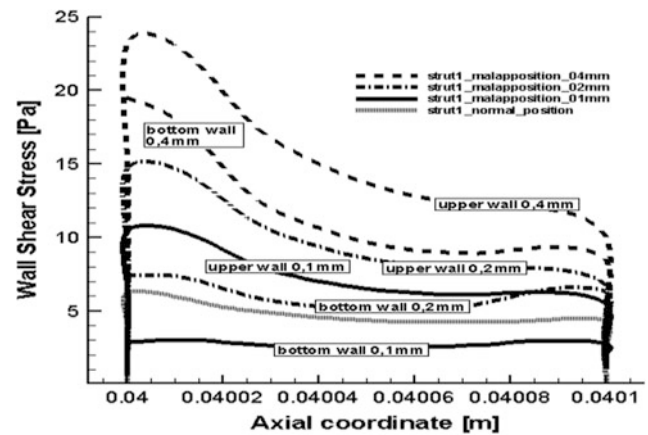


**Fig. 5** WSS distribution around the first strut

exposed to low WSS and clot may form as described in the scientific literature. Also, considering the high shear stress hypothesis, our findings suggested that larger wall-strut gap distances may account for higher thrombogenic risk, through delayed endothelization and platelet activation. However, these observations require further more complex and methodical investigations for experimental and clinical validation.

The present paper included the analysis of a two-dimensional idealized stented coronary artery, thus the limitations are easily appreciable. Future research should include patient-specific three-dimensional investigations in order to better understand the haemodynamic changes associated with stent malapposition. Nevertheless, the results provide useful information that could potentially guide future stent designs and deployment techniques, in order to limit stent thrombosis in PCI.

**Acknowledgements** This work was supported by a grant of the Romanian National Authority for Scientific Research and Innovation, CNCS/CCCDI UEFISCDI, project number PN-III-P2-2.1-PED-2016-0293, within PNCDI III.

**Conflict of Interest** The authors declare that they have no conflict of interest.

## References

- Otsuka, F., Nakano, M., Ladich, E., Kolodgie, F.D., Virmani, R.: Pathologic etiologies of late and very late stent thrombosis following first-generation drug-eluting stent placement. *Thrombosis* 2012, 608593 (2012).
- Im, E., Kim, B.K., Ko, Y.G., et al.: Incidences, predictors, and clinical outcomes of acute and late stent malapposition detected by optical coherence tomography after drug-eluting stent implantation. *Circ Cardiovasc Interv* 7, 88–96 (2014).
- Foin, N., Gutiérrez-Chico, J.L., Nakatani, S.: Incomplete Stent Apposition Causes High Shear Flow Disturbances and Delay in



- Neointimal Coverage as a Function of Strut to Wall Detachment Distance. Implications for the Management of Incomplete Stent Apposition. *Circulation: Cardiovascular Interventions* 7, 180–189 (2014).
4. Chesnutt, J.K.W., Han H.C.: Computational simulation of platelet interactions in the initiation of stent thrombosis due to stent malapposition. *Phys Biol* 13(1), 016001 (2016).
  5. Kolandaivelu, K., Swaminathan, R., Gibson, W.J., et.al.: Stent thrombogenicity early in high-risk interventional settings is driven by stent design and deployment and protected by polymer-drug coatings. *Circulation* 123, 1400–9 (2011).
  6. Koskinas, K.C., Chatzizisis, Y.S., Antoniadis, A.P., Giannoglou, G.D.: Role of endothelial shear stress in stent restenosis and thrombosis: pathophysiologic mechanisms and implications for clinical translation. *J Am Coll Cardiol* 59, 1337–49 (2012).
  7. Fuentes, L., Gomez-Lara, J., Salvatella, N., et.al.: IVUS Findings in Late and Very Late Stent Thrombosis. A Comparison Between Bare-metal and Drug-eluting Stents. *Rev Esp Cardiol* 2017 (article in press).
  8. Casa, L.C., Ku, D.: High shear thrombus formation under pulsatile and steady flow. *Cardiovasc Eng Technol* 5, 154–63 (2014).
  9. Holme, P.A., Orvim, U., Hamers, M.J., et.al.: Shear-induced platelet activation and platelet microparticle formation at blood flow conditions as in arteries with a severe stenosis. *Arterioscler Thromb Vasc Biol* 17, 646–653 (1997).
  10. Dodge, J.T., Bolson E.L., Dodge, H.T.: Lumen diameter of normal human coronary arteries. Influence of age, sex, anatomic variation, and left ventricular hypertrophy or dilation. *Circulation* 86, 232–246 (1992).
  11. Ng, J., Foin, N., Sen, S., et. al.: Over-expansion capacity and stent design model: An update with contemporary DES platforms. *International Journal of Cardiology* 221, 171–179 (2016).
  12. FLUENT 6.3 User's Guide, ANSYS-Fluent Incorporated (2006).
  13. Bernad, S.I, Totorean, A., Bosioc, A., Crainic, N., Hudrea, I.C., and Bernad, E.S: Fluid mechanics in stented arterial model. *AIP Conference Proceedings* 1702, 080008 (2015).
  14. Totorean, A.F., Hudrea, C.I., Bosioc, A.I., Bernad, S.I., Flow field evolution in stented versus stenosed coronary artery, *Proceedings of the Romanian Academy Series A-Mathematics, Physics, Technical Sciences, Information Sciences* 18(3), 248–255 (2017).

# Local Hemodynamics in Coronary Bypass in the Presence of Competitive Flow and Different Diameter Ratios Between Graft and Host Artery

Alin-Florin Totorean and Iuliana-Claudia Hudrea

## Abstract

Coronary bypass graft patency is strongly influenced by local hemodynamics in the anastomosis region. Graft failure is mainly caused by intimal hyperplasia development which is associated to low values of Wall Shear Stress (WSS). Several factors are known to alter the local hemodynamic environment, such as: type of graft, suture configuration, anastomosis angle, ratio between graft and native artery diameters and the presence of competitive flow. The aim of this paper was to analyze the influence of competitive flow on local hemodynamics at the anastomosis region in bypass configurations with different ratio between graft and native stenosed artery diameters, for a coronary stenosis of 75%. The results indicated that the most significant flow alterations and WSS variation occur at the anastomosis site and are strongly influenced by the presence of the fluid jet through the partially stenosis in case of competitive flow. Graft diameter influences these hemodynamic alterations to a further extent, especially when coupled with the negative effects of competitive flow. These findings provide a better understanding of the phenomena that occur in the bypass anastomosis region and may potentially contribute to the improvement of the coronary bypass surgical approach in order to increase long-term graft patency.

## Keywords

Competitive flow • Graft diameter • Wall shear stress

A.-F. Totorean (✉)

Department of Mechanics and Strength of Materials, Politehnica University of Timisoara, Timisoara, Romania  
e-mail: alin.totorean@upt.ro

I.-C. Hudrea

Victor Babes University of Medicine and Pharmacy, Timisoara, Romania  
e-mail: claudia\_hudrea@yahoo.com

I.-C. Hudrea

Cardiology Department, Institute for Cardiovascular Diseases, Timisoara, Romania

## 1 Introduction

CABG is one of the most effective treatment options for coronary stenosis, preferable in patients with severe three-coronary vessel disease, left main coronary artery (LMCA) disease, diabetes mellitus and left ventricular dysfunction.

Early coronary bypass graft failure (<30 days) is mostly attributable to surgical errors, while the development of intimal hyperplasia (IH) is responsible for late graft failure. The IH process resides in smooth muscle cell growth and proliferation generated by an injured or dysfunctional endothelium. It has been observed that IH develops predominantly at the toe and heel of the distal anastomosis and on the artery bed across the junction, where flow disturbances and altered haemodynamic factors appear. One of the most important haemodynamic factor investigated in relation to genesis of IH is Wall Shear Stress (WSS). Low WSS values (<0.5 Pa) are known to induce endothelial dysfunction, favoring IH genesis and development [1–6].

Studies analyzing flow behavior at distal anastomosis site indicated several factors that contribute to graft failure through IH, such as: type of graft, suture configuration, angle of anastomosis (the angle of the graft relative to the native artery), the distance between stenosis and graft suture position, the ratio between graft and native artery diameters and the presence of competitive flow [5–7].

Competitive flow is defined by native blood flow through the stenosed coronary artery to which the bypass graft has been previously sutured and depends on the degree of host artery stenosis [6]. Competitive flow leads to disturbed graft flow and triggers a decrease in WSS levels. Higher competitive flow produce increased haemodynamic alterations in terms of unfavorable WSS which is consistent with endothelial dysfunction and graft failure. There is substantial evidence correlating graft failure to competitive flow. Clinical findings suggest that partial competitive flow associated with functionally significant stenosis (stenosis degrees

higher than 75%) are better tolerated by coronary grafts than major competitive flow associated to non-significant stenosis (stenosis degrees lower than 75%) [7–11]. Nevertheless, the effect of competitive flow is gradual and there has not been reported a degree of coronary stenosis below which graft patency declines abruptly [7]. Arterial grafts are more susceptible to competitive flow induced negative effects than venous ones. Several studies revealed that unlike the internal mammary artery grafts, saphenous vein graft patency does not decrease with increasing competitive flow. A possible explanation of this phenomenon may be related to the difference in diameters between these vessels [7–11].

Computational fluid dynamics (CFD), as a method for complex fluid investigations, constitutes a powerful tool for competitive flow analyses in different coronary bypass settings and provides a better understanding of the phenomena associating competitive flow and graft failure.

**The aim** of this paper is to analyze the effects of the presence of competitive flow and different graft diameters on the local hemodynamics associated to the anastomosis region, by using CFD techniques. The parameters considered for investigation were the distribution of the WSS along the bed region of the bypassed artery and the pressure drop along the graft and host vessel.

## 2 Numerical Approach

### 2.1 Bypass Configuration

The simplified vascular models used in this paper are associated to bypassed stenosed coronary artery with 75%

stenosis degree in relation with vessel diameter, as described by the formula (1):

$$\text{stenosisdegree } \% = \left( 1 - \frac{D_{\text{minimumofstenosis}}}{D_{\text{nativeunstenosedartery}}} \right) \cdot 100 \quad (1)$$

The grafts considered for bypass configurations have variable diameters between 3 mm and 6 mm, in correlation with the most used grafts (radial and internal mammary arteries, respectively saphenous vein), as described in the scientific literature [12]. Table 1 presents the geometrical details associated to bypass configurations.

Figure 1 shows the geometrical configuration of bypass with 30° anastomosis angle and graft diameter of 3 mm. All the investigated configurations have the anastomosis angle of 30°, and the graft suture position situated at distance 3D from the stenosis.

All the models were meshed with an average value of 700.000 tetrahedral cells.

### 2.2 Boundary Conditions

The numerical analyses were performed using the commercial CFD software Fluent 6.3 [13], under steady-state and laminar regime using the boundary conditions:

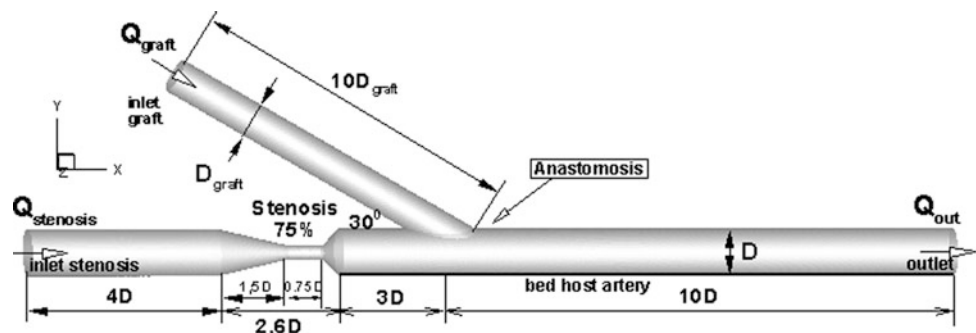
- (a) Inlet: input flow rates associated to the graft and host artery inlet sections, described by the following ratios, considering the output flow rate  $Q_{\text{out}}$  to be the mean physiological flow rate of 200 ml/min:

$$Q_{\text{out}} = Q_{\text{stenosis}} + Q_{\text{graft}} \quad (2)$$

**Table 1** Bypass configuration geometrical details

	Case 1 $D_{\text{graft}} < D$	Case 2 $D_{\text{graft}} = D$	Case 3 $D_{\text{graft}} > D$
Graft diameter $D_{\text{graft}}$	3 mm	4 mm	6 mm
Host artery diameter $D$		4 mm	
Stenosis degree		75%	
Anastomosis angle		30°	

**Fig. 1** Geometrical configuration of bypass with anastomosis angle of 30° and competitive flow associated to stenosis degree of 75%



$$Q_{stenosis} = \frac{1}{4} Q_{graft} \quad (3)$$

- (b) Outlet: pressure to be 0 Pa;  
 (c) Walls: rigid, non-slip and impermeable, considering that calcified stenosis and artificial grafts suffer very small deformations under pressure.

The fluid is assumed to be homogenous and incompressible, with properties similar to blood having the density of  $1050 \text{ kg/m}^3$  and dynamic viscosity of  $0.00368 \text{ Pa s}$ . In numerical simulation, to ensure that the flow through the region of interest, respectively anastomosis region was not affected by the flow conditions at the boundaries, the inlets and outlet of the models were extended as follows:

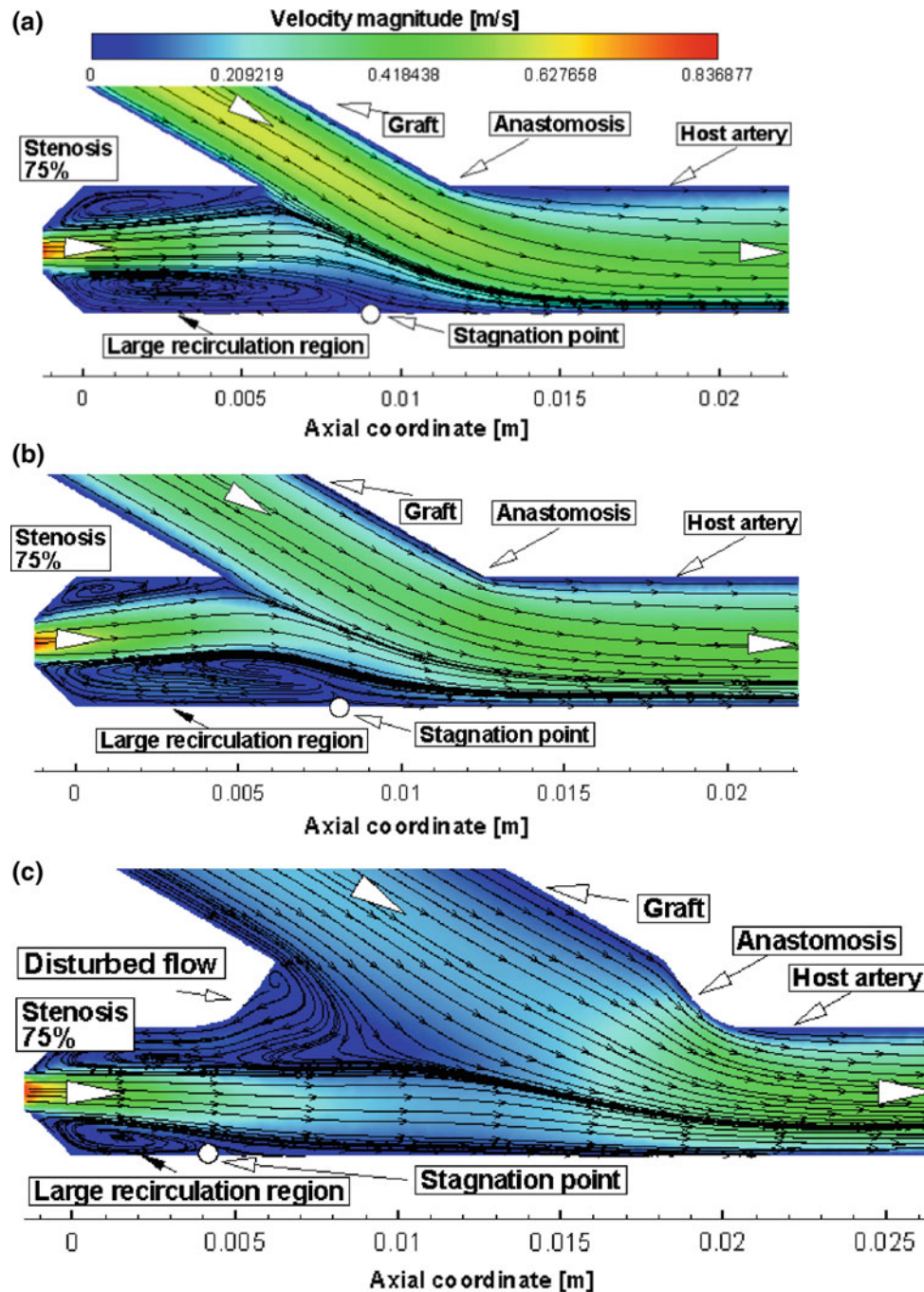


**Fig. 2** Velocity field associated to the anastomosis region in case of bypass configurations with stenosis degree of 75%, anastomosis angle of 30° and variable graft diameter: **a** 3 mm; **b** 4 mm; **c** 6 mm

- (a) Stenosis inlet: 4 host artery diameters from the stenosis inlet;
- (b) Graft diameter inlet: 10 graft diameters from the anastomosis region;
- (c) Outlet: 10 host artery diameters from the anastomosis region.

The Navier-Stokes equations were iteratively solved until the residual of the continuity and velocity reached the convergence criterion of  $10^{-9}$ .

### 3 Results

Velocity field was investigated in the anastomosis region for all bypass configurations, as presented in Fig. 2. Accelerated fluid jet through the narrowed host coronary artery influence the extension of recirculation regions formed between the stenosis and the anastomosis region. Stagnation point associated to the anastomosis region situated in the vicinity of the bed host artery modifies its position in correlation with the graft diameter. The largest recirculation zone appears in case of 3 mm bypass configuration, the stagnation point being situated in this case at the bed host artery approximately in the middle of corresponding anastomosis region.

The stagnation point moves its position in the direction of stenosis as the graft diameter increases. Fluid velocity through the graft increases with the reduction of graft diameter, being the highest in case of 3 mm bypass configuration. In the situation of 6 mm graft, because of the significant diameter variation, fluid jet accelerates in the distal vicinity of the anastomosis, and in combination with the fluid jet accelerated through the stenosis, the recirculation region from the lower host artery wall is the less extended. On the other hand, the local hemodynamics environment is disturbed at the upper wall near the junction in the direction of stenosis, compared to the other configurations.

Regions with low values of WSS are associated to disturbed flow and recirculation regions formation. Figure 3 shows the WSS distribution along the bed host artery in all the investigated configurations. It can be observed that the less extended region with low WSS is associated to the 6 mm model, in correlation to the velocity field presented in the Fig. 2. The regions with low WSS increase when the graft diameter is lower.

Pressure drop has the highest value of 504 Pa in case of bypass configuration with the lowest graft diameter of 3 mm, being associated to a high flow resistance given by the graft. The pressure decreases dependently on the

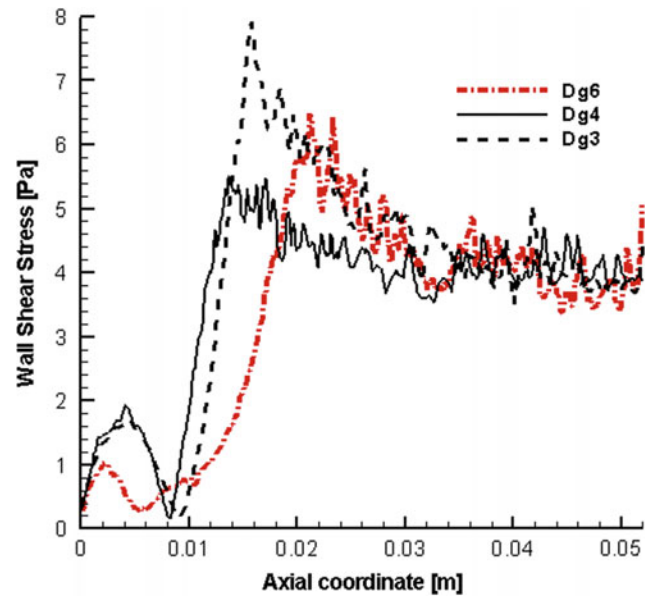


Fig. 3 WSS distribution along the bed host artery with variable graft diameters of 3, 4 and 6 mm

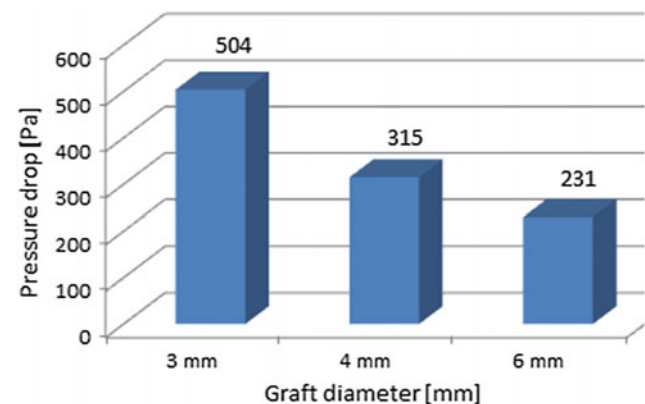


Fig. 4 Pressure drop associated to fluid flow across grafts with different diameters and host artery

lowering the graft diameter, being the lowest with the value of 231 Pa in case of the 6 mm graft diameter vascular investigated model, as described in Fig. 4.

### 4 Conclusions

Graft diameter influences the local hemodynamics associated to the anastomosis region in the presence of competitive flow. Pressure drop along the graft and the host artery increases as the graft diameter reduces. Regions with low



WSS associated to recirculation regions decrease when using grafts with high diameters, assuming that could reduce the intimal hyperplasia development and increase the graft patency as described in the scientific literature.

**Acknowledgements** This work was supported by a grant of the Romanian National Authority for Scientific Research and Innovation, CNCS/CCCDI UEFISCDI, project number PN-III-P2-2.1-PED-2016-0293, within PNCDI III.

**Conflict of interest** The authors declare that they have no conflict of interest.

## References

- Bertolotti, C., Deplano, V.: Three-dimensional numerical simulations of flow through a stenosed coronary bypass. *Journal of Biomechanics* 33, 1011–1022 (2000).
- Totorean, A.F., Bosioc, A.I., Bernad, S.I., Susan-Resiga, R.: Critical Flow Regions In The Coronary By-Pass Graft Anastomosis. *Proceedings Of The Romanian Academy, Series A*, 16 (2): 201–208 (2015).
- Deplano, V., Bertolotti, C., Boiron, O.: Numerical simulations of unsteady flows in a stenosed coronary bypass graft. *Biol. Eng. Comput.* 39, 488–499 (2001).
- Hamedani, B.A., Navidbakhsh, M.: Blood Flow Pattern in Bending Coronaries in Coronary Artery Bypass Grafts. *J Forensic Biomed* 6, 122 (2015).
- Do, H., Owida, A., Yang, W., Morsi, Y.S.: Numerical simulation of the haemodynamics in end-to-side anastomoses. *Int. J. Numer. Meth. Fluids* 67, 638–650 (2011).
- Ghista, N., Kabinejadian, F.: Coronary artery bypass grafting hemodynamics and anastomosis design: a biomedical engineering review. *BioMedical Engineering Online* 12: 129 (2013).
- Sabik III, J.F.: Should Coronary Artery Bypass Grafting Be Performed in Patients With Moderate Stenosis of the LAD. *Circulation* 8 (2015).
- Totorean, A. F., Bernad, S.I., Hudrea, I.C., Susan-Resiga, R.F.: Competitive flow and anastomosis angle influence on bypass hemodynamics in unsteady flow conditions. *AIP Conference Proceedings* 1863, 030013 (2017).
- Nordgaard, H., Swillens, A., Nordhaug, D., et. al.: Impact of competitive flow on wall shear stress in coronary surgery: computational fluid dynamics of a LIMALAD model. *Cardiovascular Research* 88, 512–519 (2010).
- Swillens, A., De Witte, M., Nordgaard, H., et.al.: Effect of the degree of LAD stenosis on “competitive flow” and flow field characteristics in LIMA-to-LAD bypass surgery. *Med Biol Eng Comput* 50, 839–849 (2012).
- Ding, J., Liu, Y., Wang, F., Bai, F.: Impact of Competitive Flow on Hemodynamics in Coronary Surgery: Numerical Study of ITA-LAD Model. *Computational and Mathematical Methods in Medicine* (2012).
- Martínez-González, B., Reyes-Hernández, C.G., Quiroga-Garza, A., et.al.: Conduits Used in Coronary Artery Bypass Grafting: A Review of Morphological Studies. *Annals of Thoracic and Cardiovascular Surgery* 23(2), 55–65 (2017).
- FLUENT 6.3 User’s Guide, ANSYS-Fluent Incorporated (2006).

# The Electrical Conductivity of Human Cerebrospinal Fluid In Vivo

Juha Latikka and Hannu Eskola

## Abstract

Cerebrospinal fluid (CSF) is a clear, highly conductive liquid. Due to its much higher electric conductivity compared to other intracranial tissues, its influence is significant, for example, on volume conductor models, current distribution and heat generation in RF surgery. It has already been shown previously that it is important to include CSF in models to achieve more accurate results. Conductivity values measured in vitro are commonly used in modelling because in vivo values are not available. We have developed a method for taking calibrated in vivo human CSF conductivity measurements with a needle electrode. We used this method to take CSF conductivity measurements from four patients during brain surgeries that were conducted to remove tumours. The patients were selected so that the surgical path went through a ventricle to make sure that there was enough CSF volume to take the measurements. Two of the patients had meningiomas and the other two had gliomas. Measurements taken from clear CSF with our method resulted in conductivity values of 1.79–1.81 S/m. Impurities such as blood or the presence of cystic brain tumour decreased the measured electrical conductivity of CSF. Our results support the findings that the previously suggested conductivity value of 1.79 S/m for human CSF at 37 °C taken from in vitro measurements is applicable for modelling purposes.

## Keywords

Brain tissue • Electrical properties • Measurements Modelling

## 1 Introduction

Cerebrospinal fluid (CSF) is a clear, electrically highly conductive liquid that surrounds the central nervous system and is also found in four cavities inside the brain known as the ventricles. CSF circulates slowly with a pulsating motion and it has several functions. For example, it supports the brain physically and therefore prevents the brain from damaging itself under its own weight; it provides some protection for the brain against mechanical injury; and it takes part in transporting metabolic waste products from the brain. It is similar to blood plasma, but it has fewer proteins and different electrolyte concentrations. CSF is constantly reabsorbed and the brain produces new CSF roughly 3–4 times of its 125–150 ml total volume each day [1]. The size of the ventricular system can vary, due to intersubject variation or medical conditions such as a hydrocephalic brain [2].

From an electrical point of view, CSF is similar to a weak solution of NaCl. As an ionic liquid, CSF's electrical conductivity is temperature-dependent. The conductivity increases when the temperature increases, because the ions in the CSF become more mobile. Although 25 °C is the commonly used reference temperature for liquid electrical conductivities, values measured at body temperature should be used for modelling purposes. The temperature coefficient of CSF has been reported to be 1.9–2 %/°C in in vitro measurements [3, 4]. Typically, ionic salts have a temperature correction coefficient of about 2 %/°C, while acids, alkalis and concentrated salt solutions have coefficients of 1.5–1.9 %/°C.

As an ionic liquid, CSF is not expected to have significant reactive capacitance or to show anisotropy. The electrical conductivity of tissues depends on frequency, and since all bioelectrical sources produce frequencies below 1 kHz only, a low measurement frequency is necessary especially for source localisation modelling purposes. Baumann et al. [4] reported no systematic difference in CSF conductivity across

J. Latikka (✉) · H. Eskola  
Faculty of Biomedical Sciences and Engineering, Tampere  
University of Technology, Tampere, Finland  
e-mail: juha.latikka@student.tut.fi

the frequency range of 10 Hz–10 kHz, and CSF did not show significant reactive capacitance.

Compared to the most intracranial tissues, CSF has a substantially higher electrical conductivity. This feature has been used in neuronavigation during stereotactic surgeries in the treatment of Parkinson's disease [5]. In these surgeries, the relative resistivity changes informed the surgeon that a CSF-filled ventricle was reached or exited, thus giving information about the position of the probe tip inside the brain.

The higher electrical conductivity of CSF focuses current, as more current flows through high-conductivity areas in volume conductors. Therefore, CSF plays an important role in simulations. The realism of the volume conductor model, inter-individual differences and the conductivity values all affect the result of the modelling [6]. Ramon et al. [7] observed a significant change in the scalp potentials when the distinction between the CSF and the brain matter was eliminated, that is, when the CSF conductivity was set equal to the brain conductivity. The uncertainty of CSF influences much to the localisation error in source localisation [8, 9]. To produce accurate results, including CSF in models is important, whether the target application is transcranial magnetic stimulation (TMS), source location studies or cancer treatment [10]. In radiofrequency (RF) surgery, CSF might lead the current away from the surrounding tissues and thus affect the heating pattern and heat generation in tissue, which could ultimately affect the result of the surgery [11].

CSF can be relatively easily extracted from various locations and stored for later use, which makes it possible to estimate its conductivity by *in vitro* measurements. Baumann et al. [4] measured the electrical conductivity of human CSF at room (25 °C) and body temperatures (37 °C). They collected CSF in sterile conditions in an operating room from seven neurosurgical patients. The samples were then refrigerated and stored usually for one to four weeks. Measurements were taken with a frequency range from 10 Hz to 10 kHz. They reported a room temperature conductivity of 1.45 S/m and a body temperature conductivity of 1.79 S/m. Ranck and BeMent [12] reported the conductivity of feline CSF to be 1.67 S/m. Gabriel et al. [13] took measurements from porcine CSF immediately after extraction and reported a measured conductivity of  $1.59 \pm 0.18$  S/m. Radvan-Ziemnowicz et al. [3] reported a CSF conductivity of 1.557 S/m at 1 kHz and 24.5 °C. Crile et al. [14] reported the conductivity of rabbit CSF at 39 °C to be 1.79 S/m (range 1.64–1.94 S/m) with a measurement frequency of 1 kHz.

In this study we measured the conductivity of human CSF *in vivo* during brain surgeries.

## 2 Methods and Material

### 2.1 Measurement Method

The electrical conductivity of a liquid is usually measured with a conductivity cell whose geometry or cell factor ( $K$ ) is known. Even then, the measurements are usually calibrated with an electrolyte of well-known electrical conductivity, because the cell factor  $K$  can change, for example due to the ageing of the electrode. Basically, taking a measurement from an unknown liquid is a comparative procedure.

For calibrated *in vivo* measurements, a new approach had to be developed. Due to the restrictions imposed by the operating room environment, it was not possible to introduce new or use bulky equipment for this study. Therefore, we chose to use the Neuro N50 lesion generator that has options for impedance and temperature measurements and has been approved for use in operating rooms. The Neuro N50 uses a monopolar needle electrode for the measurements with a large reference electrode, usually placed on the patient's hip. The same equipment was used in [15].

Based on the low 50 kHz measurement current and previous measurements on CSF [4], it was assumed that only the real part (resistance) was present in the impedance measurement, that is,  $Z = R$ . The measured  $R$  depends on the conductivity of the measured liquid ( $\kappa$ ) and the cell factor  $K$  of the measurement cell

$$R = \rho \left( \frac{l}{A} \right) = \left( \frac{1}{\kappa} \right) \left( \frac{l}{A} \right) = \frac{K}{\kappa} \quad (1)$$

where  $R$  is the measured resistance,  $\rho$  the resistivity of the liquid in measurement cell,  $l$  the length and  $A$  the area of the measurement cell, the conductivity of the measured liquid and  $K$  the cell factor. Thus, the conductivity can be presented as follows:

$$\kappa = \frac{K}{R} \quad (2)$$

Two comparative steps were needed to take calibrated *in vivo* CSF conductivity measurements. First, we calibrated a commercial conductivity cell with KCl solution, and then we measured the conductivity of Ringer's lactate *in vitro* with the cell over a temperature range from 25 to 40 °C. Then, during the surgeries, we took *in vivo* impedance and temperature measurements from Ringer's lactate and an impedance measurement from the CSF in the operating room with the monopolar needle electrode. Ringer's lactate was selected as the operating room reference liquid, since it was commonly used during brain surgeries as a rinsing liquid.

During the surgery, CSF measurements were taken from a cavity filled with CSF. The CSF was then removed by suction from the cavity and filled with the Ringer's lactate for rinsing. Then measurements were taken from the Ringer's lactate. When the Ringer's lactate was removed, the CSF started to slowly fill the cavity and the measurements could be taken again, if the surgery permitted it and there was no harm to the patient.

For in vivo measurements, the cell constant for Ringer's lactate reference measurements ( $K_{REF}$ ) is not directly known. However, it can be calculated as

$$K_{REF} = \kappa_{REF} * R_{REF} \quad (3)$$

where  $R_{REF}$  is the measured resistance in the reference liquid measurement, in this case Ringer's lactate and,  $\kappa_{REF}$  is the conductivity of the same reference liquid at a known temperature.

When the measurements are taken for both the CSF and Ringer's lactate in the same cavity during the surgery, the cell factor for the CSF measurement ( $K_{CSF}$ ), is the same as the  $K_{REF}$ :

$$K_{REF} = K_{CSF} \quad (4)$$

Using Eq. (2), the conductivity of the CSF ( $\kappa_{CSF}$ ) can be presented as follows:

$$\kappa_{CSF} = \frac{K_{CSF}}{R_{CSF}} \quad (5)$$

where the  $R_{CSF}$  is the measured resistance in the CSF measurement. Now, using Eqs. (3)–(5), the conductivity of the CSF ( $\kappa_{CSF}$ ) can be calculated:

$$\kappa_{CSF} = \kappa_{REF} * \frac{R_{REF}}{R_{CSF}} \quad (6)$$

## 2.2 Material

The CSF measurements were taken from four patients during brain surgeries that were performed to remove brain tumours. The patients were selected so that the surgical path went through a ventricle to make sure that there was enough CSF to be measured. Two of the patients had meningiomas and the other two had gliomas. Meningiomas are solid tumours with distinct boundaries whereas gliomas are cystic and may diffuse to the surrounding tissues, making the tumour boundaries unclear.

## 3 Results

From one of the patients with meningioma, we were able to take seven measurements from clear CSF. Using the Eq. (6) above, we calculated the CSF electrical conductivity to be from 1.79 to 1.81 S/m. From both patients with meningioma, we took measurements from CSF containing some blood, which caused the conductivity to decrease to 1.55–1.6 S/m. The CSF measurements taken from the two patients with gliomas resulted in conductivity values from 0.64 to 1.46 S/m.

## 4 Discussion

We have developed a method for obtaining calibrated in vivo measurements. The restrictions brought by the operating room environment prohibited us from using any new and unapproved measurement equipment. Our method uses two comparative steps to obtain calibrated in vivo CSF electrical conductivity values.

Because the measurements involved more than one step, there were also possible error sources caused by both reference liquids. How fresh was the KCl used as the first reference? How constant was the composition of the Ringer's lactate between infusion bags used in in vitro calibration and operating room measurements? A different infusion bag had to be used each time. There could also have been measurement errors when measuring KCl and Ringer's lactate conductivity in calibration, temperature measurement errors during calibration or during surgery, etc.

The pathological conditions affect the CSF. For example, Dallos et al. [16] concluded that the determination of the CSF glycoproteins is a more sensitive indicator for the existence of pathological conditions in the central nervous system than the measurement of the CSF in total proteins. The conductivity changes due to pathologic states may also affect the source location [6]. In our measurements, the presence of blood reduced the electrical conductivity of the CSF as expected, and with the presence of cystic brain tumours it was reduced even further.

With our method for taking calibrated in vivo human CSF electrical conductivity measurements with a needle electrode, the average of clear CSF was 1.8 S/m. It is close to previous results by Baumann et al. [4], and therefore our results are in agreement with the conductivity value of 1.79 S/m they obtained in vitro for human CSF at 37 °C. This kind of similarity of the in vivo and in vitro results was not

found for other intracranial tissues [17]. Our results suggest that the conductivity of CSF can be estimated reliably by in vitro measurements.

**Conflict of Interest** The authors declare that they have no conflict of interest.

## References

1. Wright, B. L. C., Lai, J. T. F., Sinclair, A. J.: Cerebrospinal fluid and lumbar puncture: a practical review. *Journal of Neurology* 259, 1530–1545 (2012).
2. Linninger, A.A., Xenos, M., Zhu, D. C., Somayaji, M. R., Kondapalli, S., Penn, R. D.: Cerebrospinal fluid flow in the normal and hydrocephalic human brain. *IEEE Trans Biomed Eng.* 54, 291–302 (2007).
3. Radvan-Ziemnowicz, S. A., McWilliams, J. C., Kucharski, W. E.: Conductivity versus frequency in human and feline cerebrospinal fluid. In *Proc. 17th Ann. Conf. Eng. Med. Biol.* 6, 108 (1964).
4. Baumann, S. B., Wozny, D. R., Kelly, S. K., Meno, F. M.: The electric conductivity of human cerebrospinal fluid at body temperature. *IEEE Trans Biomed Eng.* 44, 220–223 (1997).
5. Laitinen, L.V., Johansson, G. G.: Locating human cerebral structures by the impedance method. *Confin. Neurol.* 29, 197–201 (1967).
6. Van Uiert, R., Johnson, C., Zhukow, L.: Influence of head tissue conductivity in forward and inverse magnetoencephalographic simulations using realistic head models. *IEEE Trans Biomed Eng.* 51 (12), 2129–2137 (2004).
7. Ramon, C., Schimpf, P., Hauelsen, J., Holmes, M., Ishimaru, A.: Role of soft bone, CSF and grey matter in EEG simulations. *Brain topography* 16, 245–248 (2004).
8. Ramon, C., Schimpf, P. H., Hauelsen, J.: Influence of head models on EEG simulations and inverse source localizations. *BioMedical Engineering OnLine* 5, 10 (2006).
9. Wendel, K., Narra, N. G., Hannula, M., Kauppinen, P., Malmivuo, J.: The influence of CSF on EEG sensitivity distributions of multilayered head models. *IEEE Transactions on Biomedical Engineering* 55 (4), 1454–1456 (2008).
10. Miranda, P. C., Mekonnen, A., Salvador, R., Basser, P. J.: Predicting the electric field distribution in the brain for the treatment of glioblastoma. *Phys. Med. Biol.* 59, 4137–4147 (2014).
11. Johansson, J. D., Loyd, D., Wårdell, K., Wren, J.: Impact of cysts during radiofrequency lesioning in deep brain tissues - a simulation and in vitro study. *J. Neural Eng.* 4, 87–95 (2007).
12. Ranck, J. B., Bement, S. L.: The specific impedance of the dorsal columns of cat: an anisotropic medium. *Exp. Neurol.* 11, 451–63 (1965).
13. Gabriel, C., Peyman, A., Grant, E. H.: Electrical conductivity of tissue at frequencies below 1 MHz. *Phys. Med. Biol.* 54, 4863–4878 (2009).
14. Crile, Hosmer, Rowlan: the electrical conductivity of animal tissues. *Amer. J. Physiol.* 60, 59–106 (1922).
15. Latikka, J., Kuurne, T., Eskola, H.: Conductivity of living intracranial tissues. *Physics in Medicine & Biology* 46 (6), 1611–1616 (2001a).
16. Dallos, E., Oberman, Z., Herzberg, M., Streifler, M.: Cerebrospinal fluid glycoproteins in diseases of the central nervous system. *Confin. Neurol.* 29, 26–32 (1967).
17. Latikka, J. A., Hyttinen, J. A., Kuurne, T. A., Eskola, H. J., Malmivuo J. A.: The conductivity of brain tissues: comparison of results in vivo and in vitro measurements. *Engineering in Medicine and Biology Society, Proceedings of the 23rd Annual International Conference of the IEEE*, 910–912 (2001b).



# Time-Efficient Fourier Domain Evaluation of Pharmacokinetic Model in Dynamic Contrast-Enhanced Magnetic Resonance Imaging

Michal Bartoš<sup>✉</sup>, Michal Šorel<sup>✉</sup>, and Radovan Jiřík<sup>✉</sup>

## Abstract

Dynamic contrast-enhanced magnetic resonance imaging obtains information about tissue perfusion and permeability. Following the administration of a contrast agent, concentration-time curves measured in each voxel are fitted by a pharmacokinetic model formulated as a time-domain convolution of an arterial input function (AIF) and an impulse residue function (IRF). Since the measurement window contains hundreds of time samples, the discrete convolution is demanding, even when it is performed via discrete Fourier transform (DFT). Additionally, its discretization causes convergence complications in the curve fitting and it is not applicable to functions without a closed-form expression in the time domain, e.g. tissue homogeneity model IRF. Both issues can be solved by formulating the functions in a closed form in the Fourier domain. In the Fourier domain, the model transforms to multiplication of IRF and AIF, followed by the inverse DFT. To avoid time-domain aliasing, the number of samples in the Fourier domain must be higher than the sum of supports of the functions in the time domain. If the functions are slowly decaying exponentials, the support is theoretically infinite, which dramatically reduces the computational performance. In this contribution, we propose a modification of IRF in the Fourier domain to consider the measurement window. Our solution reduces the required number of samples to three times the measurement window compared to dozens needed without the modification and reduces the number of DFTs. This provides faster evaluation of the pharmacokinetic model and its derivatives for each voxel in each iteration of the curve fitting.

## Keywords

DCE-MRI • Tracer kinetic modelling • Tissue homogeneity model

## 1 Introduction

Dynamic contrast-enhanced magnetic resonance imaging has become an established tool to obtain information about tissue perfusion and capillary permeability. Following the administration of a contrast agent, a set of images in time is acquired using an MRI scanner. These images are related to concentration of the contrast agent in each voxel in each time-instant of the measurement. These concentration-time curves are fitted by a pharmacokinetic model to obtain the perfusion and permeability parameters of interest. These parameters are useful in diagnostics and monitoring of treatment effects, mostly in oncology.

The pharmacokinetic model is usually formulated as a time-domain convolution of an arterial input function (AIF) and an impulse residue function (IRF). Since each concentration-time curve contains hundreds of samples equal to the number of image frames, the discrete time-domain convolution is demanding, even when it is performed in the frequency domain via the discrete Fourier transform (DFT). Additionally, it causes convergence complications in the curve-fitting procedure, because the imprecise time-domain discretization causes local optima [1, 2, 3]. Furthermore, this approach is not applicable to the functions without closed-form expression in the time domain as e.g. the tissue homogeneity (TH) IRF model [4]. Despite these problems, the time-domain approach of evaluation of the pharmacokinetic model is widely used mostly in connection with basic IRFs such as the Kety/Tofts model and its extension containing a vascular contribution (see review [5]).

Use of advanced IRF models instead of the basic ones provides estimation of a more complete set of perfusion parameters. The requirement to use these advanced models

M. Bartoš (✉) · M. Šorel  
The Czech Academy of Sciences, Institute of Information Theory and Automation, Prague, Czech Republic  
e-mail: bartos@utia.cas.cz

R. Jiřík  
The Czech Academy of Sciences, Institute of Scientific Instruments, Brno, Czech Republic

however puts higher demands on the precise evaluation of the convolution. One possibility is to find a closed-form expression for the convolution and was shown in [2] for adiabatic approximation of TH model (ATH) [6] and a specific closed-form AIF [7]. Because the particular form of the functions involved can be limiting, a correction scheme for evaluation of the convolution was also proposed [2]. Another interesting approach of the pharmacokinetic model evaluation was introduced by Garpebring [1]. It also naturally overcomes the problem with the nonexistent closed-form expression of the IRF in the time domain. As above, the convolution is performed as a multiplication in the Fourier domain but the IRF is evaluated directly in the Fourier domain in contrast to the DFT case. Unfortunately, the remaining problem of this approach is the speed of its evaluation. Although it removes some of slow forward DFTs, the number of function samples must be increased to avoid a time-domain aliasing.

In this paper, we describe the above-mentioned approaches of pharmacokinetic model evaluation and propose an efficient modification of the Fourier domain approach (FDA) [1]. This eliminates the increase in the number of samples required to avoid the time-domain aliasing.

## 2 Pharmacokinetic Model

The pharmacokinetic model is in general described by a system of partial differential equations. Using the Laplace transform with boundary conditions taking the AIF into account, the solution has the form:

$$C_t(s) = c_a(s)h(s) \quad (1)$$

where  $C_t$  is contrast-agent concentration in a tissue unit,  $c_a$  is concentration in the arterial input of the tissue unit, i.e. the AIF, and  $h$  is the IRF.  $s$  is the Laplace variable. If the functions involved have a closed form in the time domain, (1) can be written as a time-domain convolution of AIF and IRF.

Equation (1) can also be formulated in the Fourier domain using the substitution:  $s \rightarrow j\omega$ , where  $j$  is the imaginary unit and  $\omega$  is the angular frequency. The substitution is possible for stable functions. It was used for the TH model [1] but it is valid for all IRFs because of their decaying-exponential-like character guaranteeing stability.

### 2.1 Time Domain Approach—Discrete Convolution

The most usual approach to evaluate (1) as the convolution is based on the DFT. Here, the IRF is parametrized in the

discrete-time domain. The AIF is either directly measured in the discrete-time domain or the discrete-time model is used. The discrete convolution is then solved using the multiplication of their DFTs and the subsequent inverse DFT. This approach is possible for any AIF and for IRFs with a closed-form temporal-domain formulation, i.e. not for the TH model.

### 2.2 Time Domain Approach—Analytic Evaluation

As the IRF models are mostly formulated and parametrized in the continuous-time domain, a straightforward approach to evaluation of (1) is to use an analytic expression of the convolution of the IRF and AIF. This is possible only when analytic time-domain formulations of both the AIF and IRF are available (i.e. not for the TH model nor for a measured nonparametric AIF). The feasibility of such solution was shown in [2] for the AIF of [7] (*Model 2*) and the ATH model [4]. Tractability of this approach for other AIF and IRF models is not guaranteed.

### 2.3 Fourier Domain Approach

Another option is to use Fourier version of (1) with the AIF and IRF represented directly in the Fourier domain with the subsequent inverse DFT as proposed in [1]:

$$C_t[n] = \mathcal{F}_{\text{DFT}}^{-1}\{c_a[w]h[w]\}, \forall w \in \left\{0, 1, \dots, \frac{N - \text{mod}(N, 2)}{2}\right\} \quad (2)$$

where “mod” is modulo. For an arbitrary function  $f$  in the Fourier domain holds:

$$f[w] = f(j\Delta\omega w), \Delta\omega = \frac{2\pi}{N\Delta t} \quad (3)$$

The output of  $\mathcal{F}_{\text{DFT}}^{-1}$  should be real, thus it is assumed that  $\mathcal{F}_{\text{DFT}}^{-1}$  also includes necessary complex conjugate symmetrization. The necessary number of samples  $N$  of the resulting function is analyzed in the following section.

*Time-domain aliasing.* The use of (2) requires special care about time-domain aliasing [1]. The aliasing effect (folding of the end of  $C_t[n]$  back to its beginning) is avoided, if the number of samples in the time domain is:  $N = N_{\text{AIF}} + N_{\text{IRF}}$ , where  $N_{\text{AIF}}, N_{\text{IRF}}$  are lengths of the respective functions in the time domain. In theory, the lengths  $N_{\text{AIF}}, N_{\text{IRF}}$  are infinite, because of their decaying-exponential-like character. In practice, the functions fall to zero with a time constant defined by the respective exponentials. As proposed in [1] for the TH model, this length of the IRF can be assumed:

$$N_{\text{IRF}} = \frac{6}{k_{\text{ep}} \Delta t} \quad (4)$$

where  $k_{\text{ep}}$  is one of the TH model parameters and the time constant of the decaying “exponential”. Because most of the known IRFs have similar decaying character, (4) can be used in general.

Although it is possible to represent the AIF in the Fourier domain as described in [8], here we assume, that  $c_a[w]$  is the DFT of measured  $K$  samples of the AIF zero-padded to length  $N = K + N_{\text{IRF}}$  as proposed in [1].

### 3 Methods

The drawback of the Fourier domain evaluation is the variable length of the functions in the Fourier domain, which depends on the support of the IRF,  $N_{\text{IRF}}$ , which changes during the iterations based on the current parameters of the IRF. The number of samples can become very high during the curve fitting. This reduces the performance, since the evaluation of  $C_t[k]$  is repeated several time for every voxel in every iteration to evaluate the criterion function and its partial derivatives with respect to its parameters. In this section, a closed-form expression for a windowed IRF is derived. This allows us to keep the number of samples to be:  $N = 2K$ , where  $K$  is the required number of samples in the time domain.

#### 3.1 Derivation of Windowed IRF

The windowed IRF in the time domain can be written as  $h^w(t) = h(t)\mathcal{H}(t_w - t)$ , where  $\mathcal{H}(x)$  is the Heaviside step function and  $t_w$  is a length of the measurement window. However, the transformation of  $h^w(t)$  to the Laplace domain can be intractable. Also if the IRF does not exist in the time domain in a closed form as the TH model, it can be impossible to find its Laplace-domain windowed variant.

The presented solution is based on a simple consideration that the Laplace transform of the windowed function is equal to the original function minus the original function outside the window.

The TH model IRF is parametrized by:  $\mathbf{p}_{\text{TH}} = \{F_p, v_p, v_e, PS, \tau\}$ , including the bolus arrival time  $\tau$  and it is defined by [1]:

$$h_{\text{TH}}(s, \mathbf{p}_{\text{TH}}) = \frac{(e^{-(a+bs)} - 1)(a+bs)(av_e + v_p(cbs+a))}{a^2(e^{-(a+bs)} - 1) - (a+bs)sb(c(a+bs)+a)} e^{-s\tau},$$

$$a = \frac{PS}{F_p}, b = \frac{v_p}{F_p}, c = \frac{v_e}{v_p} \quad (5)$$

To use the above-mentioned consideration, it is necessary to formulate the IRF part outside the window. It seems impossible to formulate it exactly but it can be approximated based on the general knowledge about the IRFs. All IRFs in the time domain have the form of a decaying-exponential-like function. Thus if this is assumed together with  $t_w \gg v_p/F_p$ , i.e. vascular phase takes only a short part of the measured window, the windowed version of the TH model can be approximated by the TH model minus decaying exponential:

$$h_{\text{TH}}^w(s, \mathbf{p}_{\text{TH}}, t_w) = h_{\text{TH}}(s, \mathbf{p}_{\text{TH}}) - FE e^{-k_{\text{ep}}(t_w - \tau - T_c)} \frac{e^{-st_w}}{s + k_{\text{ep}}} \quad (6)$$

where the extraction fraction:  $E = 1 - \exp(-PS/F_p)$  and the mean capillary transit time:  $T_c = v_p/F_p$ . The expression  $1/(s + k_{\text{ep}})$  is the Laplace transform of the decaying exponential,  $\exp(-st_w)$  is its time shift to  $t_w$  and the rest is a constant correcting its amplitude. The derived windowed function can be sampled using (3) with  $N = K + N_{\text{AIF}}$ , which turns into  $N = 2K$ , if used together with time-domain AIF.

#### 3.2 Experiments

**Validation.** To validate our windowed TH model (6), 10,000 evaluations using (3) was repeated and transformed to the time domain using the inverse DFT. The time axis was defined by,  $t = \{0, 1, \dots, N-1\} \cdot 1.5/60$  min, where  $N = 10000$  samples, i.e. 0–250 min, to simulate an infinitely long measurement avoiding aliasing effect. The length of the window was set  $t_w = 10$  min, i.e.  $K = 400$ . The IRF parameters were generated uniformly from intervals:  $F_p \in \langle 0.06, 0.75 \rangle$ ,  $v_p \in \langle 0.01, 0.20 \rangle$ ,  $v_e \in \langle 0.05, 0.70 \rangle$ ,  $PS \in \langle 0.05, 0.50 \rangle$ ,  $\tau = 0$  as in [1]. For each evaluated function, a ratio ( $R$ ) of energy of the folded part ( $E_f$ ) to energy inside the window ( $E_w$ ) as a function of the number of samples in multiples of the window length was computed:

$$R(q) = \frac{E_f[m]}{E_w} = \frac{\sum_{n=0}^{N-1} h_{\text{TH}}^w[n]^2 - \sum_0^m h_{\text{TH}}^w[m]^2}{\sum_{k=0}^{K-1} h_{\text{TH}}^w[k]^2}, \forall m < N-1,$$

$$q = \frac{m+K}{K} \quad (7)$$

If (6) is a sufficient approximation of the windowed IRF,  $R(2) \rightarrow 0$ , thus there will be no energy contaminating the result of the convolution with the AIF. This should hold for any combination of the parameters. The collected 10,000 ratios  $R(q)$  were statistically processed. The result was plotted and visually analyzed.

**Table 1** Tested variants of the pharmacokinetic model

Variant		IRF				No. of DFT
#	Description	Model	$h(\cdot)$	Equation	No. of samples	Forward/inverse
2.1	TDA—DFT	DCATH	$t$	[10] (2)	$K$	1/1
2.2	TDA—closed form	ATH	$t$	[2] (A1)	$K$	0/0
2.3	FDA—[1]	TH	$\omega$	(5)	$(K + f(k_{ep}))/2$	0/1
3.1	FDA—proposed	TH <sub>w</sub>	$\omega$	(6)	$3K/2$	0/1

**Evaluation time.** The evaluation time of (6) in (2) was compared to other evaluation variants discussed (see Table 1). For each variant and each parameter set, 1000 function evaluations were repeated to stabilize the measurement of the evaluation time. Their average represented the evaluation time. The time scale  $t$  was generated similar to previous experiment with  $N_{IRF}$  defined in Table 1 (Number of samples). The AIF model and its parameters were fixed and same as in [7] (Model 2). The IRF parameters were fixed to:  $F_p = 0.06 \text{ min}^{-1}$ ,  $v_p = 0.04$ ,  $PS = 0.031 \text{ min}^{-1}$ ,  $\tau = 0.1 \text{ min}$ ; except  $k_{ep}$ , where 10 values were generated on a logarithmic scale from  $10^{-2}$  to  $1 \text{ min}^{-1}$ . In variants “2.1” and “2.2”, the TH model had to be replaced by the distributed capillary adiabatic tissue homogeneity model (DCATH) [9] and the ATH model [2], [6], respectively. The DCATH IRF instead of the ATH was used, because the ATH in the time-domain approach (TDA) using DFT causes convergence problems in practice. The additional DCATH parameter was set to approximate the ATH model,  $\sigma = \Delta t$ , as explained in [10, 11]. The number of samples in the variant “3.1” reflects the result of the previous validation experiment.

## 4 Results

**Validation.** The plot (Fig. 1) of the approximation error based on the folding energy revealed that in most cases, the derived windowed TH model is sufficient. Only in less than 10% of the cases, the result of the convolution inside the measurement window would be contaminated by the ratio of folding energy ranging from  $10^{-4}$  to  $10^{-2}$ . It was discovered, that this happened for the cases where the extraction fraction  $E$  was close to 1 in combination with low flow  $F_p$ . It is a regime, where the contrasted agent travels mainly through an extracellular extravascular space. Although the ratio is small and such cases are rare, it is recommendable to use  $N = 3K$  for sampling of the windowed TH model.

**Evaluation time.** The evaluation times for each variant in Table 1 are plotted in Fig. 2. As expected, only method “2.3” does not have a constant evaluation time. That is caused by (4) defining the necessary number of samples to

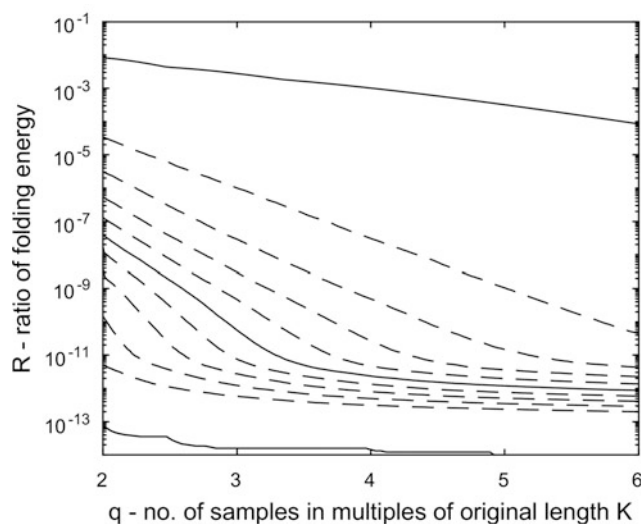


**Fig. 1** Ratio of folding energy as a function of the addition of samples. Solid lines are maximum, median, minimum and the dashed lines are the resting 10-quantiles

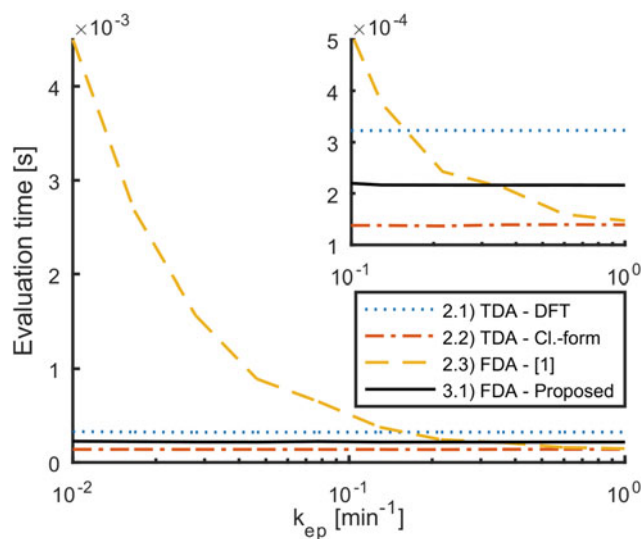


**Fig. 2** Comparison of the possible variants of the pharmacokinetic model evaluation in terms of their evaluation time. The top-right plot is a close-up

avoid aliasing. Other variants have a constant number of samples as listed in Table 1. The number of samples with its

type (real/complex) is not the only factor influencing the evaluation time. The second factor is the number of needed DFT operations, which is the most demanding operation and its speed depends on the number of samples. The faster evaluation of “2.3” in comparison with “3.1” for high  $k_{ep}$  is in the area, where the proposed windowing is not needed and thus can be eliminated in practice.

## 5 Discussion and Conclusion

It was shown, that the fastest approach to evaluate the pharmacokinetic model in DCE-MRI is to use the closed-form evaluation “2.2” [2]. This is not surprising, since it does not use the DFT and the number of real samples is the lowest possible, i.e. equal to the number of the time-domain samples. The limitation of this variant is the necessity to have a specific parametrized form of AIF (it is not possible to use measured AIF directly) and also the IRF is limited to specific models to derive a closed-form formula.

Our Fourier domain approach “3.1” allows both to use a measured AIF or a parametrized one. Our derived closed-form expressions for windowed IRF dramatically speed up the evaluation in comparison with the original FDA “2.3” [1] and with the conventional time domain approach “2.1” using the DFT, although only 1.5 times. However, this factor grows with the time resolution because of the DFT. Additionally, the evaluation of the pharmacokinetic model together with its derivatives is repeated many times in the iterative estimation procedure for each voxel, thus even a slight speed up can save a lot of time.

**Acknowledgements** This work has been supported by the projects of the Czech Science Foundation and the Czech Academy of Sciences (projects: GA16-13830S and MSM100751802).

### Disclosure

**Conflict of Interest** The authors declare that they have no conflict of interest.

## References

1. Garpebring, A., Ostlund, N., Karlsson, M.: A Novel Estimation Method for Physiological Parameters in Dynamic Contrast-Enhanced MRI: Application of a Distributed Parameter Model Using Fourier-Domain Calculations. *IEEE Trans. Med. Imaging.* 28(9), 1375–1383 (2009).
2. Koh, T.S., Cheong, D.L.H., Hou, Z.: Issues of discontinuity in the impulse residue function for deconvolution analysis of dynamic contrast-enhanced MRI data. *Magn. Reson. Med.* 66(3), 886–92 (2011).
3. Bartoš, M., Keunen, O., Jiřík, R., Bjerkvig, R., Taxt, T.: Perfusion Analysis of Dynamic Contrast Enhanced Magnetic Resonance Images Using a Fully Continuous Tissue Homogeneity Model with Mean Transit Time Dispersion and Frequency Domain Estimation of the Signal Delay. In: *Analysis of Biomedical Signals and Images*. pp. 269–274. Brno University of Technology, Brno, Czech Republic (2010).
4. Lawrence, K.S. St., Lee, T.-Y.: An Adiabatic Approximation to the Tissue Homogeneity Model for Water Exchange in the Brain: I. Theoretical Derivation. *J. Cereb. Blood Flow Metab.* 18(12), 1365–1377 (1998).
5. Sourbron, S.P., Buckley, D.L.: Classic models for dynamic contrast-enhanced MRI. *NMR Biomed.* 26, 1004–27 (2013).
6. Johnson, J.A., Wilson, T.A.: A model for capillary exchange. *Am. J. Physiol. Heart Circ. Physiol.* 210(6), 1299–1303 (1966).
7. Orton, M.R., D’Arcy, J.A., Walker-Samuel, S., Hawkes, D.J., Atkinson, D., Collins, D.J., Leach, M.O.: Computationally efficient vascular input function models for quantitative kinetic modelling using DCE-MRI. *Phys. Med. Biol.* 53(5), 1225–39 (2008).
8. Bartoš, M.: Advanced Signal Processing Methods in Dynamic Contrast Enhanced Magnetic Resonance Imaging, [https://www.vutbr.cz/www\\_base/zav\\_prace\\_soubor\\_verejne.php?file\\_id=93420](https://www.vutbr.cz/www_base/zav_prace_soubor_verejne.php?file_id=93420), (2014).
9. Koh, T.S., Zeman, V., Darko, J., Lee, T.-Y., Milosevic, M.F., Haider, M., Warde, P., Yeung, I.W.: The inclusion of capillary distribution in the adiabatic tissue homogeneity model of blood flow. *Phys. Med. Biol.* 46(5), 1519–38 (2001).
10. Kratochvíla, J., Jiřík, R., Bartoš, M., Standara, M., Starčuk, Z., Taxt, T.: Distributed capillary adiabatic tissue homogeneity model in parametric multi-channel blind AIF estimation using DCE-MRI. *Magn. Reson. Med.* 75(3), 1355–1365 (2016).
11. Bartoš, M., Jiřík, R., Kratochvíla, J., Standara, M., Starčuk, Z., Taxt, T.: The precision of DCE-MRI using the tissue homogeneity model with continuous formulation of the perfusion parameters. *Magn. Reson. Imaging.* 32(5), 505–13 (2014).



# Proton Therapy Treatment Plan Verification in CCB Krakow Using Fred Monte Carlo TPS Tool

M. Garbacz, G. Battistoni, M. Durante, J. Gajewski, N. Krah, V. Patera, I. Rinaldi, A. Schiavi, E. Scifoni, A. Skrzypek, F. Tommasino, and A. Rucinski

## Abstract

Monte Carlo (MC) methods account for many details of the interactions of particles with human tissue in proton beam therapy. The accuracy and fast dose calculation time offered by GPU-accelerated MC treatment planning systems (TPS) pushed development of such tools to support experimental treatment plan verification in the clinical routine. The GPU-accelerated MC-TPS Fred (Schiavi et al, *Phys Med Biol* 62:7482, 2017, [4]; University of Rome) is currently investigated in Cyclotron Centre Bronowice (CCB) Krakow proton beam therapy centre (Poland) that is in clinical operation from October 2016. The Krakow proton centre physical beam model has been implemented in Fred and was validated against Eclipse TPS calculations and patient Quality Assurance (QA) measurements in water phantom. We analyzed depth-dose distributions of single proton pencil beams and dose cubes of varying range and modulation in water. We used the gamma index

method as quantitative measure and obtained a good agreement between Fred and analytical TPS calculations. We have also found that Fred reach proton tracking rates over  $10^6$  primaries per second. In the future, the proposed fast MC methods can help to reduce the time needed for experimental patient treatment plan verification measurements in water phantoms that are part of clinical routine procedures.

## Keywords

Proton therapy • Treatment planning system  
Monte Carlo simulations • GPU

## 1 Introduction

Cancer treatment is one of the greatest challenges of modern medicine. Treatment with ionizing radiation, particularly protons, is an efficient method to treat malignant tissues located deeply in patient body and close to organs at risk (OARs). Contrary to photons, the dose deposited by protons is increasing with depth and has a finite range. Proton beams can therefore achieve a precise dose delivery during radiotherapy due to their specific depth-dose distribution (DDD). This property of proton (and heavier ion) beams reduces dose in healthy tissues and allow to spare surrounding OARs [1].

The advantages of using proton beams for radiotherapy of neoplastic diseases has lead to a rapid growth of the number of proton beam therapy (PBT) facilities. In 2016, the first PBT centre in Poland—Cyclotron Center Bronowice (CCB)—started clinical operation. CCB is equipped with an IBA Proteus C-235 cyclotron providing proton beam energies up to 226.1 MeV in two rotational gantries with pencil beam scanning (PBS), the eye treatment room and the

M. Garbacz (✉) · J. Gajewski · A. Rucinski  
Institute of Nuclear Physics PAN, Kraków, Poland  
e-mail: Magdalena.Garbacz@ifj.edu.pl

G. Battistoni  
INFN, Sezione di Milano, Milan, Italy

M. Durante · E. Scifoni · F. Tommasino  
Trento Institute for Fundamental Physics and Applications,  
Povo, Italy

N. Krah  
CNRS, CREATIS, UMR 5220, Lyon, France

V. Patera · A. Schiavi  
Sapienza University of Rome, Rome, Italy

I. Rinaldi  
CNRS/IN2P3 and Lyon 1 University, UMR 5822, Lyon, France

A. Skrzypek  
AGH University of Science and Technology, Kraków, Poland

F. Tommasino  
Department of Physics, University of Trento, Trento, Italy

experimental hall. Eclipse treatment planning system (TPS) is used at CCB to plan the irradiation of head and neck as well as ocular tumors. Eclipse TPS uses an analytical algorithm to predict and calculate the dose distribution in the patients body.

In PBT, Monte Carlo (MC) simulations are considered to be the most reliable dose calculation tool [2]. They take into account physical interactions of protons in heterogeneous material, in particular nuclear interactions and multiple Coulomb scattering, and therefore offer increased accuracy regarding the contribution of single beams to the total dose field. Detailed description of ion interaction in the patient allows to achieve significant uncertainty reduction of lateral dose and proton range calculations. MC TPS can be used to support dose computations with analytical TPS and experimental treatment plan verification in water phantom [3].

## 2 Commissioning of Fred Monte Carlo TPS in Krakow Proton Beam Therapy Centre

Transporting a large number of particles through the patient geometry while simulating their interactions with the medium causes long dose calculation times with generic MC codes. The trimmed-down MC-based dose calculation engine Fred (Fast paRticle thErapy Dose evaluator) was developed at the Sapienza University of Rome to reduce dose calculation time [4]. MC Fred was implemented to run on general-purpose programming GPU cards, which gives a possibility to reach tracking rates over  $10^6$  primaries per second and reduce the simulation time to a few minutes per patient treatment plan.

Fred code was previously commissioned against proton beam model used in a synchrotron based facility, CNAO, Pavia, Italy and FLUKA MC code [4]. Currently Fred is being commissioned with respect to Eclipse TPS in Krakow. Fred uses as an input data obtained during the facility commissioning measurements. These are the lateral beam profiles measured in air at isocentre as well as DDDs acquired in water phantom at energies from 70 to 226.1 MeV in 10 MeV steps. The phase space parameters, which characterize the proton beam model at CCB, need to be tuned through MC simulations in order to achieve the best agreement between commissioning measurements and TPS dose calculations. We implemented Matlab tools [5] that support finding suitable Fred input parameters like beam energy, momentum spread, lateral beam size and number of protons corresponding to the monitor units (MUs) prescribed in TPS. The simulation setup was implemented in accordance with the experimental setup at CCB. A water phantom of lateral size of  $10\text{ cm} \times 10\text{ cm}$  with 0.6 mm spacing and 40 cm length with 1 mm spacing was located 200 cm downstream from the virtual source of the proton beam (see Fig. 1).

### 2.1 Single Beams from TPS and Fred Simulations

In this contribution, examples of the comparison of single beam depth dose distribution calculated with TPS Eclipse and Fred MC code at 100, 150 and 200 MeV are shown. An overlap of the Bragg peaks locations was achieved between Fred and TPS simulations in water phantom (Fig. 2, left panel). The lateral beam size agrees within less than 0.2 mm (Fig. 2, right panel).

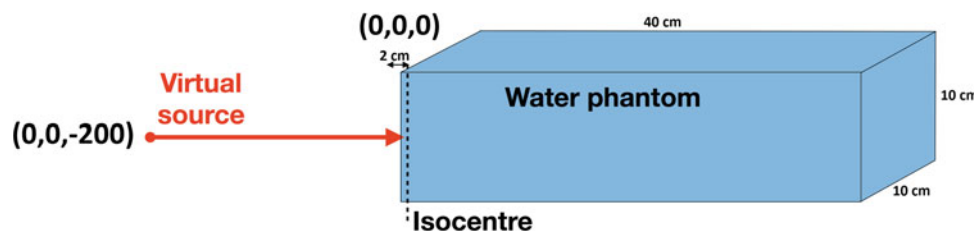


**Fig. 1** Simulation setup used in Fred to reproduce commissioning measurements

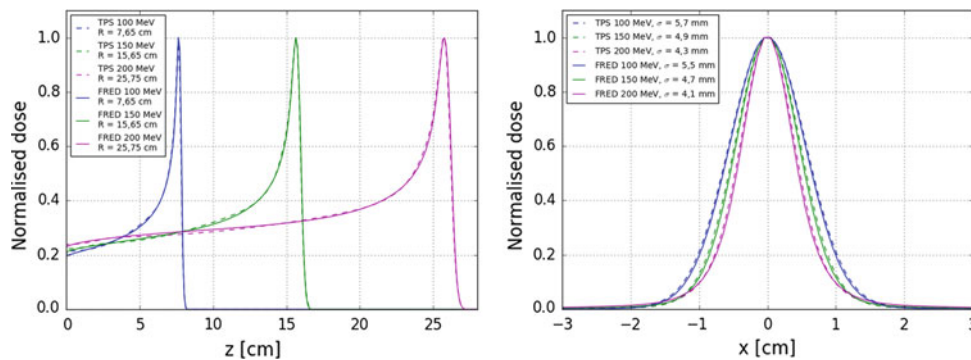


**Fig. 2** Comparison of depth dose distributions (left side) and lateral profiles (right side) for TPS (dashed lines) and Fred simulations (solid lines)

### 2.2 Dose Cubes from TPS and Fred Simulations

The treatment plans of dose cubes generated with Eclipse TPS are routinely used to verify geometry and dose characteristic of the beam in water phantom quality assurance (QA) measurements. An example of such a treatment plan was recalculated in Fred using the beam model phase space parameters developed for single beams. The dose cube treatment plan presented here contained 8001 pencil beams, a modulation of 10 cm and a range of 20 cm. The proton beams energy was in a range from 114.9 to 172.8 MeV. The simulation of dose cubes was performed in a 40 cm × 40 cm × 40 cm water phantom. The dose computation on a high resolution grid was performed with a total number of  $1.6 \times 10^9$  particles within 440 s.

A comparison of DDD in the spread-out Bragg peak (SOBP) region and lateral dose profiles showed a good agreement between Fred and Eclipse with a variation of less than 5% of the maximum dose value (see Fig. 3).

Three dimensional gamma index analysis [6] with the dose-difference and distance-to-agreement passing criteria was used to evaluate and compare dose distributions computed with Eclipse (Fig. 4, top row) and with Fred (Fig. 4, middle row). Only dose exceeding 5% of the maximum dose value was evaluated. A passing rate of 96.6% and 81.7% (percentage of voxels which meet the acceptance criteria) was obtained for the passing criteria 3%/3 mm (see Fig. 4, bottom row) and 2%/2 mm, respectively.

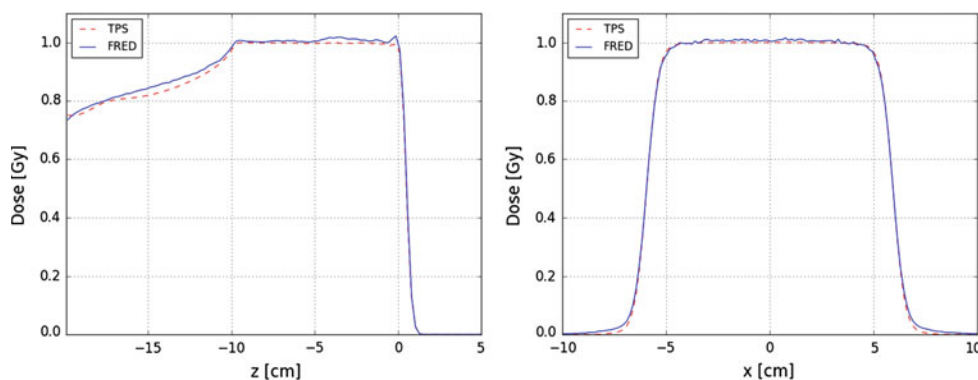


**Fig. 3** Comparison of depth dose distributions (left side) and lateral profiles (right side) for TPS (red dashed line) and Fred simulations (blue solid line) (Color figure online)

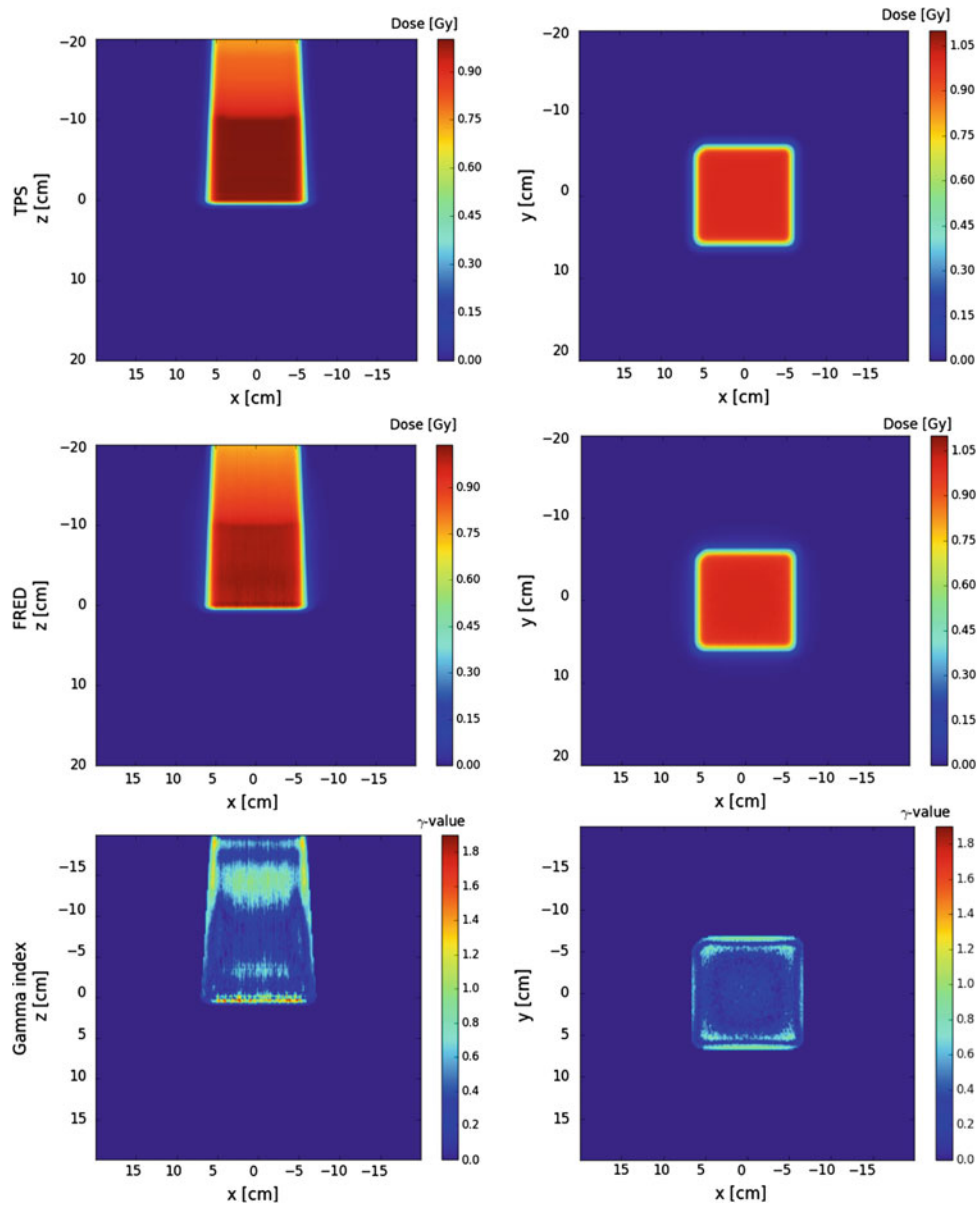


**Fig. 4** The planes for a cube-shaped treatment plan obtained in TPS (top row), in Fred simulations (middle row) and gamma index map 3%/3 mm (bottom row) in the longitudinal (left column) and lateral (right column) planes, all intersecting the center of the cube

### 3 Conclusions

The GPU-accelerated Fred MC TPS allows to achieve high accuracy of treatment plan dose recalculation and increased time performance with respect to the generic MC codes, like FLUKA or GEANT4. Fred is intended to support treatment plan verification and medical physics research in CCB Krakow PBT center.

This contribution reports on the ongoing works aiming at the commissioning of the Fred MC TPS in the cyclotron based PBT centre in Krakow, Poland. Examples of dose

distributions computed with Eclipse TPS and Fred MC TPS were shown for single pencil beams at three energies and for a QA treatment plan of a cube. A good agreement of beam profiles and dosimetric values was obtained for single beams and SOBP (see Figs. 2 and 3). We are currently tuning the phase space parameters through additional commissioning measurements in air at isocenter and by implementing a beam emittance model [7]. This is expected to improve the gamma index passing rate. Further analysis will include simulation of cubes with various modulations and located at different depths in water and will be followed by a comparison of patient treatment plans.

**Acknowledgements** This project is carried out within the Reintegration programme of the Foundation for Polish Science co-financed by the European Union under the European Regional Development Fund. This research was supported in part by the PL-Grid Infrastructure.

**Conflicts of Interest** The authors declare that they have no conflict of interest.

---

## References

1. Durante, M., Orecchia, R., Loeffler, J. S.: Charged-particle therapy in cancer: clinical uses and future perspectives. *Nature Reviews Clinical Oncology* vol. 14, pages 483495 (2017), <https://doi.org/10.1038/nrclinonc.2017.30>.
2. Paganetti, H.: Range uncertainties in proton therapy and the role of Monte Carlo simulations. *Phys. Med. Biol.* 7;57(11):R99–117, (2012), <https://doi.org/10.1088/0031-9155/57/11/r99>.
3. Bauer, J. et al: Integration and evaluation of automated Monte Carlo simulations in the clinical practice of scanned proton and carbon ion beam therapy. *Phys. Med. Biol.* 21;59(16):4635–59, (2014), <https://doi.org/10.1088/0031-9155/59/16/4635>.
4. Schiavi, A. et al: Fred: a GPU-accelerated fast-Monte Carlo code for rapid treatment plan recalculation in ion beam therapy. *Phys. Med. Biol.* 62 7482, (2017), <https://doi.org/10.1088/1361-6560/aa8134>.
5. Gajewski, J., Bragg Peak Analysis, MATLAB Central File Exchange, (2017).
6. Low, D. A. et al: A technique for the quantitative evaluation of dose distributions. *Med. Phys.* 25 (5), (1998), 0094-2405/98/25(5)/656/6/\$10.00.
7. Grevillot, L. et al: A Monte Carlo pencil beam scanning model for proton treatment plan simulation using GATE/GEANT4. *Phys. Med. Biol.* 21;56(16):5203–19 (2011), <https://doi.org/10.1088/0031-9155/56/16/008>.



# Investigating Ballistic Gelatin Based Phantom Properties for Ultrasound Training

Mertcan Özdemir<sup>✉</sup>, Galip Özdemir, and Osman Eroğul<sup>✉</sup>

## Abstract

The simulation has become an important tool for healthcare practitioners who have difficulty in accessing patients to learn ultrasound imaging modes. The ultrasound phantoms are specially designed objects that are used or imagined to evaluate, analyze and adjust the performance of test devices. These phantoms for ultrasonography devices are expensive, and low-cost alternatives have provided an educational experience that does not give the best result. Ballistic gelatin is a member of the 250-Bloom hydrogel family that resembles human muscle tissue in terms of its mechanical properties. The 250-Bloom Ballistic Gelatin (BG) is prepared with different mixing ratios to be made the mechanical tests such as gunshot, compression and electrical conductivity measurement. The results are compared with the mechanical results of human muscle tissue in order to measure the similarity of the 250-Bloom BG we prepared to human muscle tissue. It is showed that the 250-Bloom BG phantom model has very close mechanical properties to human muscle tissue at time-dependent characteristics of mechanical test results. It is also measured how long it can last without degradation with the time required to use it in the simulation and it is coated with the thermal insulation material needed to extend the degradation period. Based on these results, 250-Bloom BG phantom is recommended as a model for the creation of phantom limb model. Consequently, this model is a much more affordable alternative and easy to produce, it facilitates to work with any organ model in ultrasound imaging for healthcare practitioners.

## Keywords

Ultrasound • Phantom • Medical education  
Ballistic gelatin

## 1 Introduction

Ultrasound Imaging is a modality which can be effective especially in emergency conditions, for evaluation and treatment of patients. However, there is a need for sonography training and ultrasound-expert doctors in developing countries [1]. Therefore, simulation has become an important tool for healthcare practitioners to learn ultrasound imaging modes, to provide them a practice tool in an ideal environment, and to gain experience before attempting to patients [2]. Operational simulation requires a model that provides a realistic tactile, haptic, visual, and cognitive experience to the healthcare practitioners [3]. Commercial phantoms are available in the market, but costs between \$200 and \$19000 (Blue Phantom Corporation, WA/Universal Medical, GT Simulators) depending on quality of the phantom and the desired body part. These price levels are still considered high for many low and middle income countries. To reduce relatively higher cost, researchers use low-cost tissue mimicking phantom models generated by using metamucil, gelatin, chicken breasts, or bologna [4–7]. Nevertheless, some may reveal the risk of infection by pathogens such as Salmonella and Campylobacter, and all phantom models have limited reuse capacity.

Gelatin powder contains biological proteins extracted from the natural protein collagen which are present in skin, bone tissues and tendons of mammals through extraction using hot water in an acidic (type A) or alkaline (type B) environment [8]. Gelatin stiffness is defined by the Bloom number (running from 50 to 300). The higher a Bloom number, gel will have higher melting and gelation points, where required gelatinisation time will be shorter [9]. Type A and 250 Bloom Gelatin are the most commonly utilized phantoms for mimicking human muscle tissue.

The rates of preparation of BG have changed considerably recently. 10% at 4 °C (Fackler gelatin) and 20% at 10 °C (NATO gelatin) are two common gelatin mixture with water

M. Özdemir (✉) · G. Özdemir · O. Eroğul  
TOBB University of Economics and Technology, Ankara, Turkey  
e-mail: m.ozdemir@etu.edu.tr

rates available in the literature [10]. The stiffness of gelatin is generally investigated by gunshot test. This test procedure is usually noted as calibration in the literature; it is carried out at a constant temperature of the gelatin. Gunshot test is one of the most common test used to measure the resemblance to human tissue.

Another method of measuring compliance to human muscle tissue is the compression test. Various studies have been carried out to measure the effect of strain rate on the mechanical properties of ballistic gelatin. It is known that the mechanical properties of gelatin are sensitive to gelatin temperature, conditioning or aging [11].

In addition to these tests, electrical conductivity may be a necessary method to compare the similarity of human muscle tissue. Therefore, in addition to mechanical tests, BG's conductivity was measured on electrical conductivity testing and results compared with human muscle tissue.

In this study, 250A-Bloom Ballistics Gelatin (BG), mimicking the human muscle tissue, is used for the creation of simulating phantoms for healthcare practitioners to understand ultrasound image generation and device operation, image optimization, image interpretation, and needle insertion and injection. Gunshot, compression tests and electrical conductivity measurement are implemented to demonstrate the similarity between human muscle tissue and BG based phantom model.

## 2 Materials and Methods

Equipments used in this study are: Ultrasound-Siemens Sonoline Adara, Instron 3360 Series Dual Column Tabletop Testing Systems, Laboratory hot plate heater and magnetic stirrer, Cylindrical Plastic Mold, Hatsan Mod 25 Airgun, 4.5 mm airgun pellets, Needle, Plastic casting molds (100 mm × 110 mm × 50 mm and 84 mm × 83 mm × 3 mm).

Refrigerator

Materials used for preparing the phantom model are: 250A Bloom Gelatin, Winkel Silicone Spray, Cinnamon Leaf Oil, Tap water (pH = 8.0).

### 2.1 BG Test Sample Preparation

Ballistic gelatin is prepared by using 250 Bloom BG powder as core ingredient. The gelatin production process is implemented according to gelatin preparation guideline [10] which corresponds to 10% concentration (powder-water ratio) at 4 °C. The first BG phantom sample, meant to use in uniaxial compression test, placed into cylindrical molds of

30 mm diameter and 25 mm thickness. The second sample group was prepared for gunshot testing on plastic testing molds of 100 mm × 110 mm × 50 mm in size and the third group with the size of 84 mm × 83 mm × 3 mm for electrical conductivity measurement.

### 2.2 Gunshot Testing

The calibration blocks were made in a mold (100 mm × 110 mm × 50 mm) and evaluated using the standard 4.5 mm pellet impact test at a temperature of 4 °C. The penetrations of the pellets were examined on calibration blocks of BG. The penetration depth ( $L_p$ ) of the pellets is calculated.

### 2.3 Compression Test

The main purpose of the performing a compression test on a material is to evaluate the mechanical behavior or response of the material while experiencing a compression load by measuring mechanical variables such as stress, strain and deformation. By understanding these different parameters and the values associated with a particular material, it can be determined whether the material is suitable for the specific application or whether it fails under desired stress levels. In this study, several trials made to equate the graphical values of [12] through compression test (Fig. 1). Cylindrical BG samples of 30 mm diameter and 25 mm length BG was used for compression test. The effect of temperature on

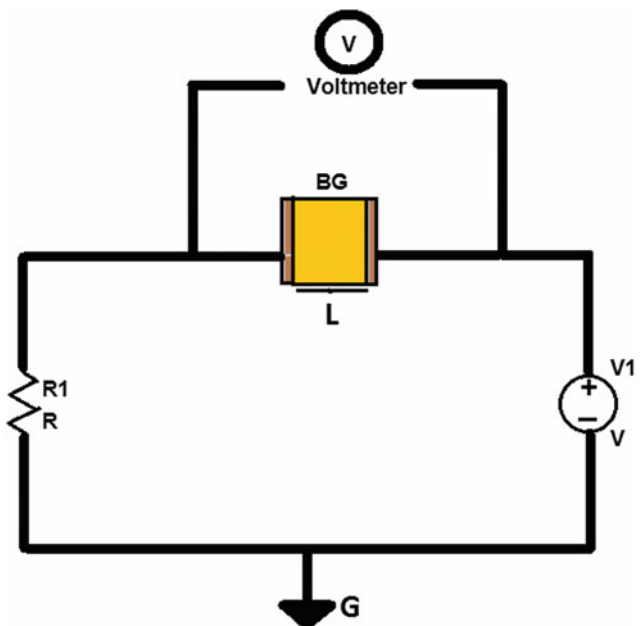


Fig. 1 Basic electrical conductivity measurement circuit

stress-strain curve was investigated at a compression rate of 0.01 mm/s. The mechanical test data at different test conditions were compared by investigating stress-strain curves.

## 2.4 Electrical Conductivity Measurement

The purpose of the measurement of electrical conductivity of the BG phantom is to show that the tissue model is also suitable for electrical device applications. Size of 84 mm  $\times$  83 mm  $\times$  3 mm BG sample is used in this manner. Figure 1 illustrates how the electrical conductivity is measured. Total resistance of gelatin is calculated by using the ohm law (1).

$$R = V/I \quad (1)$$

The electrical resistivity (specific electrical resistance)  $\rho$  ( $\Omega$  m) is defined as (2):

$$\rho = R \times A/L \quad (2)$$

Electrical conductivity,  $\sigma$  ( $\text{Sm}^{-1}$ ), is defined as the inverse of resistivity (3):

$$\sigma = 1/\rho \quad (3)$$

where R (ohm) is the resistance of BG specimen, V (Volts) is the measured electrical potential of BG phantom, I (Amps) is the current flowing through the BG phantom, L (m) is the length of the BG phantom, A ( $\text{m}^2$ ) is the cross-sectional area of the BG phantom.

## 2.5 Phantom Preparation

60 g of powder was mixed with 540 g of tap water (at 58.5 °C) to obtain 10% concentrated gelatin. The mixture was stirred by using hot plate heater and paramagnetic stirrer at a constant temperature of 58.5 °C. To prevent foaming a number of cinnamon leaf oil (anti-foaming agent) drops were added into the mixture. Final BG solution was poured into phantom mold and were left for solidification in room temperature (23 °C) for 12 h. A plastic serum vessel was placed into the solution for vascular imaging. Top surface of the phantom covered with plastic wrap and was placed in the refrigerator (4 °C set) for 24 h. The preserved solutions are solidified and reached to the desired stiffness level after 36 h. This phantom can also be shredded into smaller pieces and can properly be reused after reapplying the heating process. The material can be remolded multiple times.

## 2.6 Ultrasound Imaging of the Phantom

Ultrasound phantom image was obtained from a Siemens Sonoline device.

## 3 Results

Calibration block was shot with air gun 4 times, lengths of penetration to the BG block were measured with photomacrographic scale. The average penetration depth was measured as  $72 \pm 2$  mm for 10% concentrated BG block. The muzzle velocity of the air gun was  $154 \pm 5$  m/s and gun was located adjacent to the surface of BG phantom block. The purpose of repeating same procedure multiple times for the same calibration block is to show the homogeneity and experimental consistency by obtaining similar results. Previous studies indicate that for the human muscle tissue mimicking phantoms, air gun pellet penetration depth was found as  $70 \pm 3$  mm [13]. Equation 4 explains the relation between the penetration depth and muzzle velocity of the air gun for a diameter of 4.5 mm pellet [10].

$$L_p = 0.594 \times V_i - 21.92 \pm 5 \quad (4)$$

where  $L_p$  is the penetration depth (mm) and  $V_i$  is the muzzle velocity (m/s).

The theoretical penetration depth is calculated as  $70 \pm 5$  mm by using this equation. These theoretical and experimental results on gunshot test suggest that %10 BG phantom is suitable for a model for human muscle tissue.

Compression test was undertaken on the gelatin after aging for 72 h. The samples were evenly compressed between the plates during the test. At a constant strain rate of  $0.01 \text{ s}^{-1}$ , no significant change in mechanical properties was observed in the first 30 min in terms of stress-strain response (Fig. 2).

The resistance of gelatin is calculated with the ohm law as 282  $\Omega$ . The total body resistance of human consists of 300  $\Omega$  [14]. It has been found that BG is close to human tissue resistance value. Electrical resistivity and conductivity were calculated as 6558  $\Omega\text{m}$  and 0.15 mS/m respectively.

No significant change of penetration depth has been observed during the first 15 min at ambient temperature of about 23 °C. After 15 min, due to changes in BG's mechanical properties, penetration depth increases, however but there was no deformity observed on BG.

A probe with frequency of 5 MHz is used to visualize the phantom sample (Fig. 3).

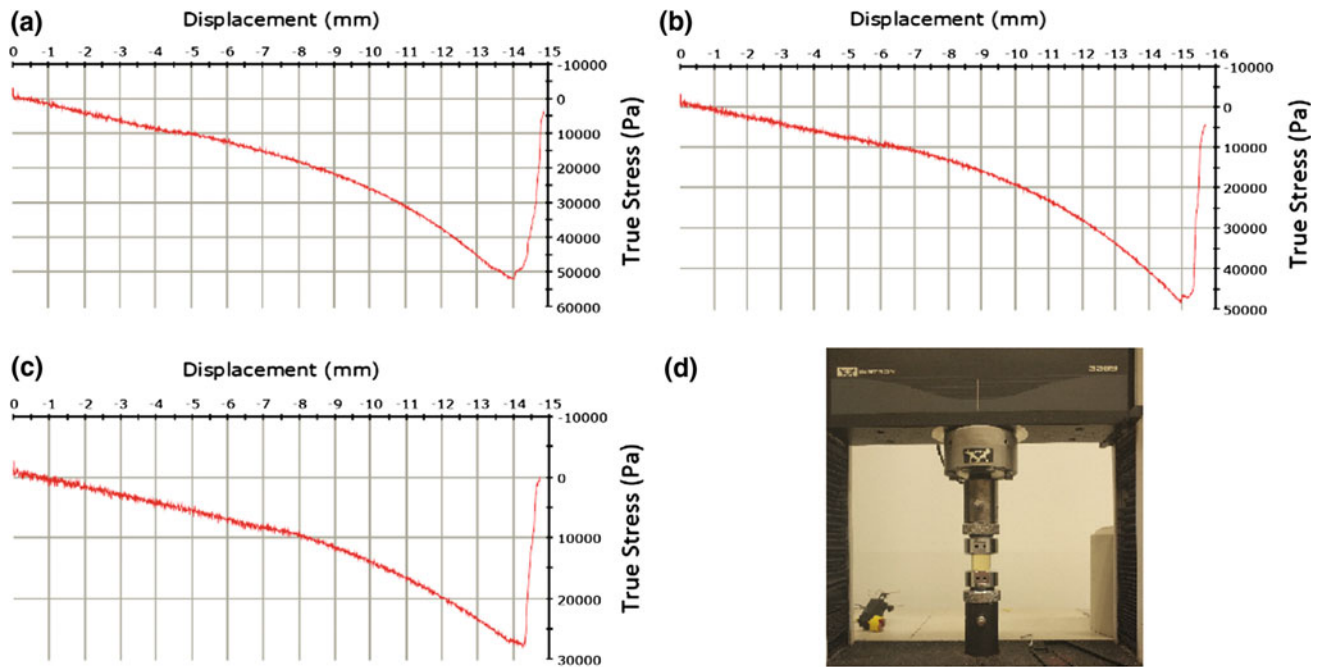


**Fig. 2** a 5 min, b 30 min, c 60 min after BG sample was removed from the refrigerator, d Compression test setup

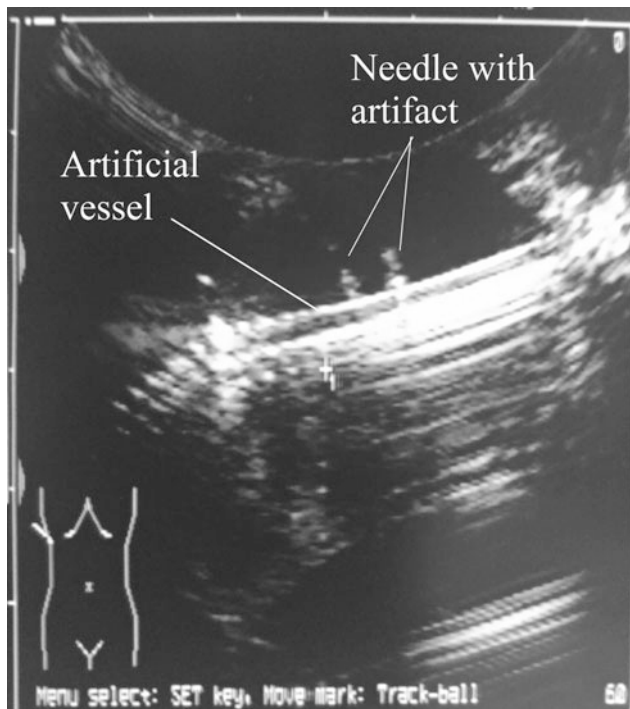


**Fig. 3** Ultrasound BG phantom image

## 4 Discussion

Our results suggest that concentration ratio for BG phantom mimicking human muscle tissue should not exceed 10% of the BG concentration [12]. Phantom can be prepared in any shape since it is in the form of a liquid mixture during preparation procedure. Once the phantom is successfully prepared, it is sturdy enough and does not require excessive care. The tube inside BG is a model representing a blood vessel. The serum wall offers resistance to needle advancement, similar to actual vessel layer, and allows aspiration and injection of fluid into the tube. Various potential errors can be investigated on these phantoms during medical education which may contribute to medical expert training. Test results show similarity to available studies in compression and gunshot tests. In this study 50 kPa failure stress is observed as Cronin and Falzon also noted similar levels at constant 23 °C temperature [12]. As for the gunshot test,  $72 \pm 2$  mm for 10% concentrated BG block is consistent with the calculated theoretical  $70 \pm 5$  mm value for our block as Jussila proposed [10].

There is also a question about how much time is needed to use a BG phantom following the removal from

refrigerator. It basically depends on both the BG phantom size and the ambient temperature of the training area [10]. The mechanical test result of BG samples, which left at room temperature after 5, 30, and 60 min, compared respectively. No significant change in mechanical properties was observed in the first 30 min of cylindrical BG sample of size 30 mm diameter and 25 mm thickness in room temperature (23 °C) (Fig. 2). However, it is clear that the BG phantom should only be used within 30 min after removal from refrigerator to mimic human muscle tissue properly.

## 5 Conclusion

In our study, a BG phantom model may be useful for healthcare practitioners who require training or courses on peripheral nerve block in ultrasound guidance. We believe it would be useful to officially examine the educational value in an ultrasound training program for healthcare practitioners. This simple training model also has the advantages of production, reusability and low cost. Therefore, for ultrasound training, that kind of phantom could be a cost-effective alternative.

**Conflict of Interest** The authors declare that they have no conflict of interest.

## References

- Shah, S., Bellows, B. A., Adedipe, A. A., Totten, J. E., Backlund, B. H., Sajed, D.: Perceived barriers in the use of ultrasound in developing countries. *Critical ultrasound journal* 7(1), 11 (2015).
- Sites, B. D., Chan, V. W., Neal, J. M., Weller, R., Grau, T., Koscielniak-Nielsen, Z. J., Zbigniew J., Ivani, G.: The American Society of Regional Anesthesia and Pain Medicine and the European Society of Regional Anaesthesia and Pain Therapy joint committee recommendations for education and training in ultrasound-guided regional anesthesia. *Regional anesthesia and pain medicine* 35(2), 74–80 (2010).
- Hocking, G., Hebard, S., Mitchell, C. H.: A review of the benefits and pitfalls of phantoms in ultrasound-guided regional anesthesia. *Regional anesthesia and pain medicine* 36(2), 162–170 (2011).
- Kendall, J. L., Faragher, J. P.: Ultrasound-guided central venous access: a homemade phantom for simulation. *Canadian Journal of Emergency Medicine* 9(5), 371–373 (2007).
- Morrow, D. S., Broder, J.: Cost-effective, reusable, leak-resistant ultrasound-guided vascular access trainer. *Journal of Emergency Medicine* 49(3), 313–317 (2015).
- Budak, E., Beytar, F., Ozdemir, M., Susam, B. N., Goker, M., Unlu, A., Erogul, O.: Lower limb phantom design and production for blood flow and pressure tests. *The Eurobiotech Journal* 1(4), 278–284 (2017).
- Wells, M., Goldstein, L.: The polony phantom: a cost-effective aid for teaching emergency ultrasound procedures. *International journal of emergency medicine* 3(2), 115–118 (2010).
- Sellier, K. G., Kneubuehl, B. P.: *Wound ballistics and the scientific background*. Elsevier Health Sciences, Amsterdam (1994).
- Schrieber, R., Herbert G.: *Gelatine handbook: theory and industrial practice* Wiley-VCH-Verl, Weinheim (2007).
- Jussila, J.: Preparing ballistic gelatine—review and proposal for a standard method. *Forensic science international* 141(2–3), 91–98 (2004).
- Jusilla J.: *Wound ballistic simulation: Assessment of the legitimacy of law enforcement firearms ammunition by means of wound ballistic simulation*. University of Helsinki, Helsinki (2005).
- Cronin, D. S., Falzon, C.: Characterization of 10% ballistic gelatin to evaluate temperature, aging and strain rate effects. *Experimental mechanics* 51(7), 1197–1206 (2011).
- Uzar, A. I., Dakak, M., Ozer, T., Ogunç, G., Yigit, T., Kayahan, C., Oner K, Sen, D.: A new ballistic simulant “transparent gel candle” (experimental study). *Turkish journal of trauma & emergency surgery* 9(2), 104–106 (2003).
- Fish, R. M., Geddes, L. A.: Conduction of electrical current to and through the human body: a review. *Eplasty* 9 (2009).



# Physical Breast Model as a Simulator of Pathological Changes

J. Biernat, M. Biernat, W. Łukasik, T. Pałko, A. Jung, and M. Trzyna

## Abstract

It's well known that there is a relationship between skin temperature and many pathological changes. Local increase of temperature on a skin surface can represent symptoms of such diseases as: bacteria or viral infections, viral diseases as well as it might indicate an occurrence of a tumor. For verification and validation medical devices and products based on the registration of local temperature changes, a simplified physical breast model was designed and constructed. Therefore, the physical breast model can work with medical devices equipped with thermometer, infrared camera, contact thermography device or thermo-optic indicators. In this study we present a simulation of breast cancer for a need of contact thermography (Braster) and simulation of inflammation for needs of thermo-optic indicator (thermochromic pigment).

## Keywords

Physical breast model • Temperature monitoring device  
Contact thermography • Simulation of breast cancer  
Simulation of inflammation • Thermo-optic indicator

J. Biernat (✉) · W. Łukasik · T. Pałko  
Faculty of Mechatronics, Warsaw University of Technology,  
Boboli 8, 02-525 Warsaw, Poland  
e-mail: j.biernat@onet.pl

W. Łukasik  
e-mail: w.lukasik@mchtr.pw.edu.pl

T. Pałko  
e-mail: t.palko@mchtr.pw.edu.pl

J. Biernat · M. Biernat · M. Trzyna  
Braster S.A., Cichy Ogród 7, 05-580 Ozarów Mazowiecki, Poland  
e-mail: m.biernat@braster.eu

M. Trzyna  
e-mail: m.trzyna@braster.eu

A. Jung  
Military Institute of Medicine, Szaserów 128, 04-141 Warsaw,  
Poland  
e-mail: a.jung@spencer.com.pl

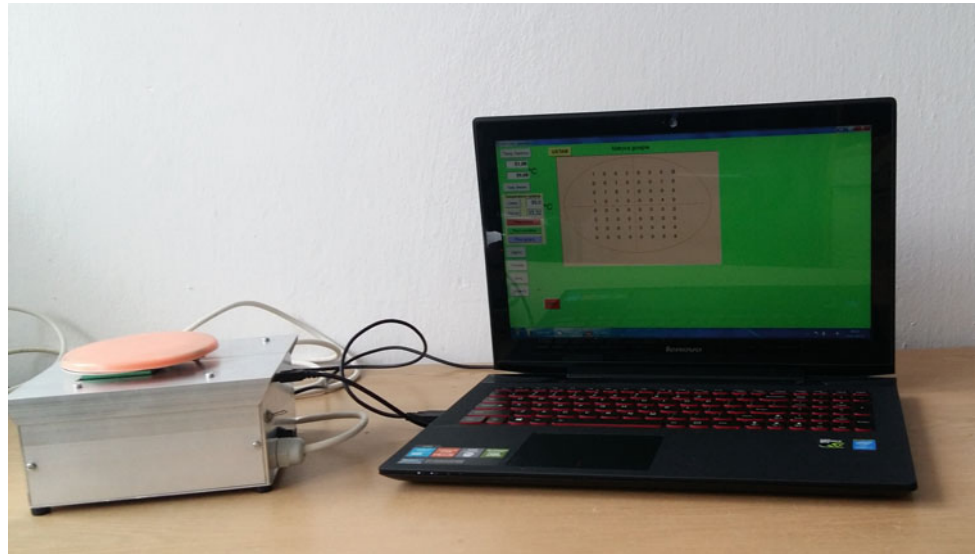
## 1 Introduction

Human body's surface temperature has been an indicator of health since 400 B.C. Hippocrates, the Greek physician, wrote that "In whatever part of the body excess of heat or cold is felt, the disease is there to be discovered" [1]. Nowadays, the demand of continuous monitoring of physiological parameters by means of wearable instruments is rising, but the analysis of the relevant literature reveals the lack of wearable devices for skin thermography. As a result the need of wearable devices for the thermal monitoring is increasing. Skin temperature imaging could be used during medical continuous monitoring, for instance in breast cancer detection or for the monitoring of vascular, dermatological, rheumatic disorders, as well as inflammation or viral disease [2, 3].

It is well known that there is a difference in energy consumption between normal and cancerous tissue [4]. Blood vessel activity and heat indicate the presence of pre-cancerous cells or cancer cells in their early stages of development. The following factors cause cancerous cells to generate heat: higher metabolic activity of cancerous cells compared to normal cells and the neoangiogenesis - a cancer tumor builds dense net of blood vessels in order to provide nutrition and increase metabolism which results in faster and uncontrolled growth. These energy consumption differences lead to small but detectable local temperature changes, which is why the thermography is a potential early breast cancer detection method [1, 4, 5]. Contact thermography (used in BRASTER system) is based on the thermal conductivity between a body and a cholesteric liquid crystal foil placed directly on the skin, as a result of which it provides a colourful imaging of temperature distribution across the three colours: red, green and blue [6].

Increased local temperature is one of the typical symptoms of wound infection, its quantitative measurement may have a potential to improve assessment and diagnosis of chronic wound infection at the bedside. Marjorie Fierheller,

**Fig. 1** Test station for simulations



R. Gary Sibbald showed that in the presence of infection, the mean temperature difference between wound skin and an equivalent contralateral control site was found to be more than  $2\text{ }^{\circ}\text{C}$  [3], what confirms the possibility of using thermo-optic materials as an indicator of inflammation.

The purpose of this work is to present the simplified physical breast model as a simulator of breast cancer for a needs of contact thermography and simulator of skin inflammation for a need of thermo-optic indicator. The model is able to simulate a thermal effect on the surface close to temperature distribution of skin.



**Fig. 2** Thermograms register process

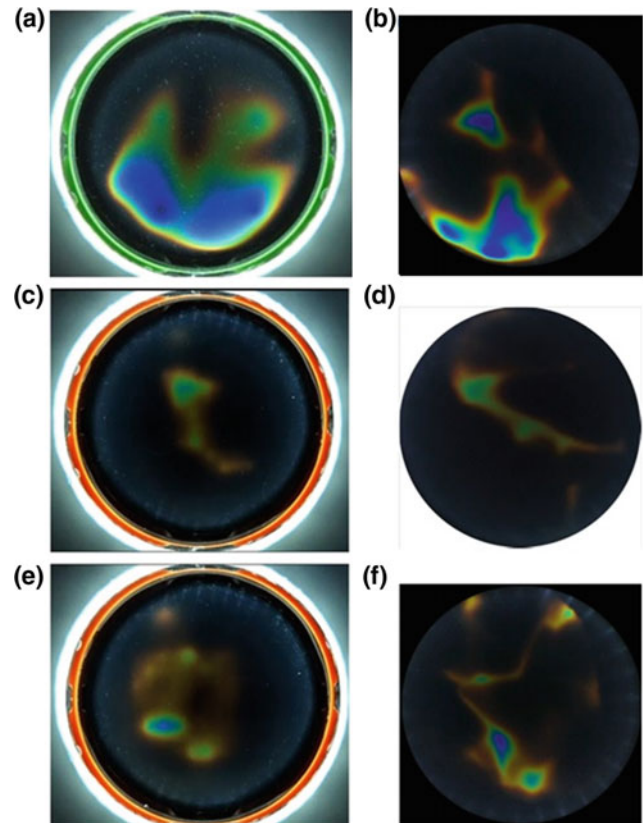


**Fig. 3** Sample results of breast cancer simulation (a), (c) and (e), thermograms of cancerous breast (b), (d) and (f)

## 2 Materials and Methods

Researchers conducted two experiments using physical breast model as a simulator:

1. Simulation of breast cancer
2. Simulation of skin inflammation

The complete test station is shown in Fig. 1. Experiments were held in laboratory conditions at ambient temperature of  $23\text{ }^{\circ}\text{C} \pm 1\text{ }^{\circ}\text{C}$ .

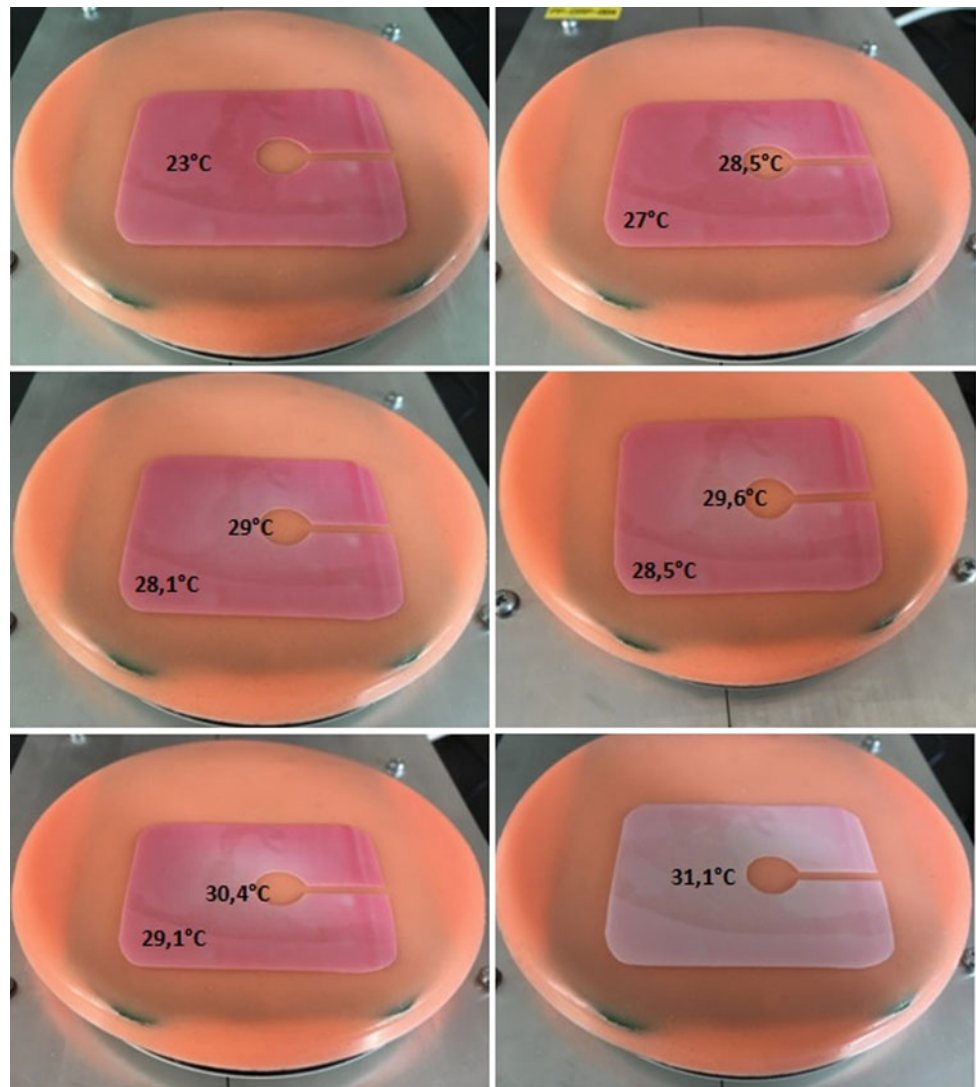
Physical breast model is based on PCBA with matrix of resistors (local temperature generating system) which generate areas of temperature higher than surrounding parts of the phantom within range from 0.25 to  $2\text{ }^{\circ}\text{C}$  and are treated as a local heat sources. Simulation of temperature distribution is caused by conversion an electrical energy into thermal energy in controlled way dependent on a value of current

flow. The thin layer (2 mm) of additive silicone (thermal conductivity:  $0.22\text{ W/m K}$ ) provides heat conduction to the top surface of the phantom. Physical breast model enables thermal surface reaction based on activation particular local heat sources (single or multiple resistors) which is why it can simulate inflammation, local skin changes connected with temperature increase e.g. hormones variation or cancer.

### 2.1 Simulation of Breast Cancer

In this experiment the phantom simulates a temperature distribution of a breast. During tests several resistors configuration (heating level, number, position) and two value of breast phantom initial temperature ( $31.5\text{ }^{\circ}\text{C}$ ,  $33\text{ }^{\circ}\text{C}$ ) were programmed. Each test consisted of: choosing model work's configuration, stabilizing of model's temperature response, applying BRASTER device to breast model (Fig. 2), and

**Fig. 4** Sample results of inflammation simulation



acquiring thermograms. The experiments were aimed at obtaining thermograms similar to thermograms of cancerous breast, taken from medical images database collected in clinical trials by Braster company.

## 2.2 Simulation of Skin Inflammation

In this experiment the phantom simulates a temperature distribution on human skin. As an indicator of inflammation, researchers used thin polyurethane foil (100  $\mu\text{m}$ ) covered by thermochromic pigment (chromazone®, activation temperature: 31 °C) and with an adhesive layer on the other side of the foil. During tests the thermo-optic indicator was placed on the surface of the phantom. The test consisted of: programming value of phantom initial warming (29.5 °C), increasing power of local heat sources, stabilizing model's thermal response, acquiring thermo-optic indicator response and value of phantom surface temperature.

## 3 Results and Discussion

Thermograms, a result of breast model performance, was recorded by Braster testprogram.exe PC software. A sample of the registered thermograms and comparative thermograms of cancerous breast are shown in Fig. 3.

The experiments showed that physical breast model is able to simulate a temperature distribution similar to a cancerous breast. The functionality of programming several resistor configuration and values of phantom initial warming enables simulation of many diverse cases.

Results of inflammation simulation are shown in Fig. 4.

The experiments proved that the breast phantom is able to simulate a temperature distribution of skin with presence of wound infection which confirms the color change of the thermo-optic indicator.

## 4 Conclusions

Physical breast model is a simulator of temperature distribution. The original application of the model was breast simulation for contact thermography. However, abovementioned experiments showed that the physical breast model could be used also with other products, such as thermo-indicators. Breast model various work configurations enables projection of different cases. Additionally, thanks to the high repeatability of simulation results gives new possibilities for the breast model to be used by researchers to test new solutions, devices or medical products based on the registration of local temperature changes.

**Conflict of Interest** The authors declare that they have no conflict of interest.

## References

1. EtehadTavakol M., Sadri S., Ng E.Y., Application of K- and Fuzzy c-Means for Color Segmentation of Thermal Infrared Breast Images, *Journal of Medical Systems*, 2010, 34(1): 35–42.
2. Giansanti S., Maccioni G., Development and testing of a wearable Integrated Thermometer sensor for skin contact thermography, *Medical Engineering & Physics*, 2007, 29(5): 556–565.
3. Fierheller M., Sibbald R.G., A Clinical Investigation into the Relationship between Increased Periwound Skin Temperature and Local Wound Infection in Patients with Chronic Leg Ulcers, *Adv Skin Wound Care*, 2010, 23(8): 369–379.
4. González F.J.: Thermal simulation of breast tumors, *Revista Mexicana De Fisica*, 2007, 53(4): 323–326.
5. SalmanOgli A, Rostami A., Modeling and Improvement of Breast Cancer Site Temperature Profile by Implantation of Onion-Like Quantum-Dot Quantum-Well HeteronanoCrystal in Tumor Site, *IEEE Transactions on Nanotechnology*, 2012, 11(6): 1183–1191.
6. Małyska J., Biernat M., Łukasik W., Pałko T., Physical Breast Model Design for Contact Thermography, *Recent Global Research and Education: Technological Challenges*, Jabłoński R., Szewczyk R. (red.), *Advances in Intelligent Systems and Computing*, Springer International Publishing, 2017, 519: 217–222.



# Activation Propagation in Cardiac Ventricles Using the Model with the Conducting System

Elena Cocherova<sup>✉</sup>, Jana Svehlikova<sup>✉</sup>, and Milan Tysler<sup>✉</sup>

## Abstract

The characteristics of the activation propagation in a geometrical model of cardiac ventricles formed by several ellipsoids, with or without a fast conducting endocardial layer representing the Purkinje fibers and with activation started in one or several endocardial locations were compared in this study. The activation propagation was simulated by two approaches. In the first one, temporal and spatial changes of the membrane potential were numerically modeled by a reaction-diffusion (RD) equation of the propagation with the transmembrane ionic current density defined by modified FitzHugh-Nagumo equations. The propagation was numerically solved in Comsol Multiphysics environment. In the second approach, the electrical excitation of the working ventricular myocardium was simulated by a cellular automaton (CA) model that was implemented in Matlab environment. Local activation times in both ventricles were computed by both approaches in ventricular models with and without the fast conducting layer representing Purkinje fibers (heterogeneous and homogeneous model). In both models, the activation was initiated either in a single starting position or gradually in nine starting positions imitating more physiological conditions. Despite some differences in the activation sequences, by both approaches acceptable activation times of the whole ventricles were obtained for the homogeneous model with nine starting points and for the model with conducting layer regardless of number of starting positions.

## Keywords

Cardiac ventricles • Purkinje fibers • Local activation times • Reaction-diffusion propagation model  
Cellular automaton

E. Cocherova (✉) · J. Svehlikova · M. Tysler  
Institute of Measurement Science, Slovak Academy of Sciences,  
Bratislava, Slovakia  
e-mail: elena.cocherova@savba.sk

## 1 Introduction

The propagation velocity of the activation front in the human cardiac ventricles depends on the myocardial tissue parameters, as well as on the local shape of the front [1, 2]. The propagation velocity is smaller for the convex shape of the front than for the planar or concave one.

The activation propagation in the can be modeled using the approach based on reaction-diffusion (RD) equations (in monodomain or bidomain tissue models) [3, 4], or by using the approach with less time-consuming models based on the cellular automaton (CA) [5, 6]. If the RD equations are used, the realistic dependence of the propagation velocity on the activation front curvature is preserved, while constant propagation velocity, independent from the front shape is supposed in the CA approach.

The geometry of heart ventricles can be derived from CT or MRI scans [3] or some simplified ventricular geometry can be defined analytically, using ellipsoidal or spherical segments. In this article, analytically described ventricles defined by ellipsoidal segments were used [6, 7] and the local activation times when the activation front arrived in particular points in the ventricles were computed for homogeneous ventricular myocardium and for myocardium with conducting endocardial layers representing the branches of Purkinje fibers. The results for approaches using the RD and CA propagation models were compared.

## 2 Subject and Methods

### 2.1 Monodomain RD Model and CA Model

In the RD monodomain model, the electrical activation of the cardiac tissue [3, 4] is described by the partial differential equation:

$$\frac{\partial V_m}{\partial t} = \nabla \cdot (D \nabla V_m) - i_{ion} + i_s \quad (1)$$



where  $V_m$  is the membrane potential,  $D$  is the tissue diffusivity,  $i_{ion}$  is the ionic transmembrane current density,  $i_s$  is the stimulation current density. Current densities are normalized to membrane capacitance with units A/F. The ionic transmembrane current density  $i_{ion}$  is modeled using the modified FitzHugh-Nagumo (FHN) equations [4, 7, 8].

The tissue diffusivity  $D$  is mainly dependent on the tissue conductivity  $\sigma$ , and also on the membrane surface-to-volume ratio  $\beta$  and the membrane capacitance per unit area  $C_m$ :

$$D = \sigma / (\beta C_m) \quad (2)$$

In the CA propagation model, ventricular tissue is represented by a finite regular grid of elements, in which the activation states are calculated [6, 7].

## 2.2 Models of the Ventricular Tissue

The electrical activation of the ventricles simulated by the RD and CA approaches was computed in four different models of the ventricular tissue. In all of them the geometry

was defined analytically by several ellipsoidal segments that are described in details in [5–7]. Their size from apex to base was 80 mm and diameters at the base were 84 and 60 mm. When the RD approach was used, the stimulations were applied to spheres with their centers in desired starting positions and with a radius of  $r = 2$  mm. When the CA approach was used, the stimulations were applied to single points in the same desired positions.

Two homogeneous models of the ventricular myocardium were defined (Fig. 1, left). In the first one, a single starting position (marked by blue circle) was defined near the endocardial surface of the left ventricular septum (at the x, y, z position: 42, 35, 32 mm). In the second one, nine physiologically substantiated starting positions were defined near the endocardial surfaces of the left and right ventricular septum, and lateral walls of both ventricles (all marked circles).

Another two ventricular models were heterogeneous: They had the same geometry defined by ellipsoidal segments and the same two configurations of the starting positions of activation but they had also fast conducting layers (highlighted areas in Fig. 2, right) representing the Purkinje fibers

**Fig. 1** Ellipsoidal geometry of homogeneous ventricles with nine starting points of activation. The single starting point is marked by blue color (left). The posterior view of the geometry of ventricles with highlighted fast conducting layers representing the Purkinje fibers (right)

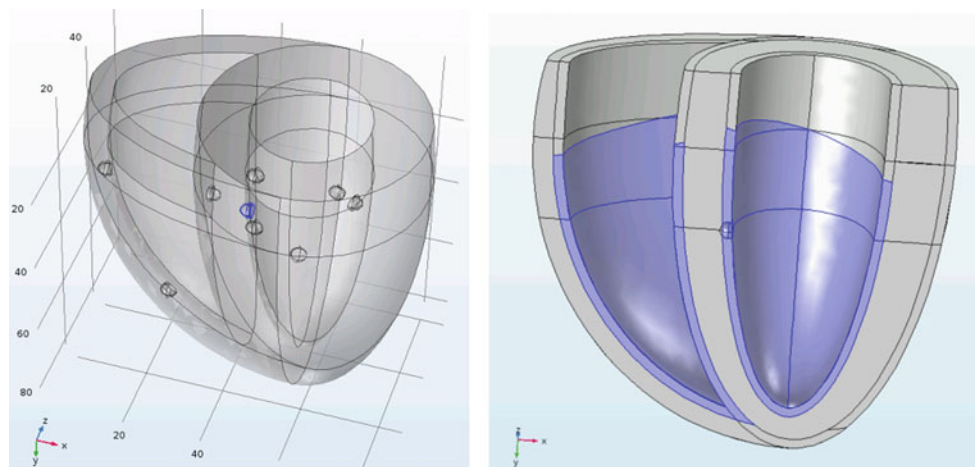
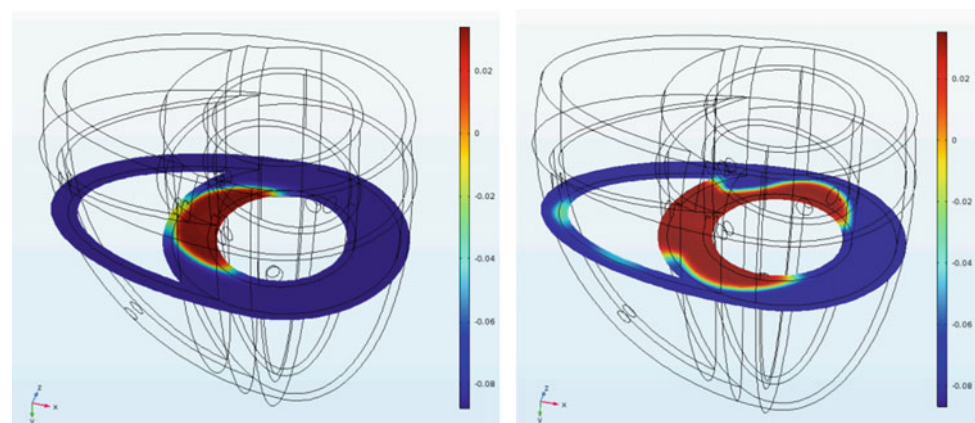


**Fig. 2** Spatial distribution of the membrane potential  $V_m$  [V] in the ventricular model with the conducting layer in time  $t = 23$  ms obtained from the RD propagation model for one starting position (left) and for nine starting positions (right)



with higher conduction velocity. These conducting layers (2 mm thick) were set apart at the endocardium of the left and right ventricle, spreading from apex to about 70% of the apex-to-base distance. The remaining ventricular volume represented the working myocardium.

### 2.3 Parameters of CA and RD Propagation Models

The activation propagation computed using the CA model [6] was performed in Matlab. To resemble the conduction system (the Purkinje fibers), the activation propagation velocity in the conducting layer was defined three times higher than in the working myocardium tissue:  $v_M = 0.52$  m/s for the working myocardium and  $v_P = 3 \cdot v_M$  for the conducting layer.

In the RD propagation model, the same parameters of the ventricular tissue as in [7] were used in the homogeneous ventricular model. The tissue diffusivity of the working myocardium was  $D = 0.0004$  m<sup>2</sup>/s (relating to the tissue conductivity  $\sigma = 0.4$  S/m). The tissue diffusivity of the conducting layer was nine times higher than in the myocardium, as the conduction velocity in a one-dimensional fiber is proportional to the square root of the tissue conductivity.

in ventricles with the conducting layer for one and nine starting positions are shown in Fig. 2.

Spatial distributions of activation times in the model with the conducting layer and nine starting positions in plane  $y = 45$  mm obtained from the RD and CA propagation model are shown in Fig. 3.

Maximal activation times in the ventricular models with the conducting layer (heterogeneous models) were considerably shorter than in the homogeneous models because the activation is spreading much faster along the endocardium (Table 1).

Maximal activation times, when the whole homogeneous model with single starting position was activated, were out of the physiological range (higher values than 120 ms, [9–12]) when both, the CA and RD propagation models were used. Physiologically acceptable maximal activation times (in the range from about 80 to 120 ms) were obtained in the homogeneous model with nine starting positions and also in the heterogeneous ventricular model with single starting position.

Still acceptable total activation times, slightly shorter than physiological values for adult people (values lower than 80 ms [10]) were obtained in the ventricular model with conducting layer and nine starting positions when both, the CA and RD propagation models were used.

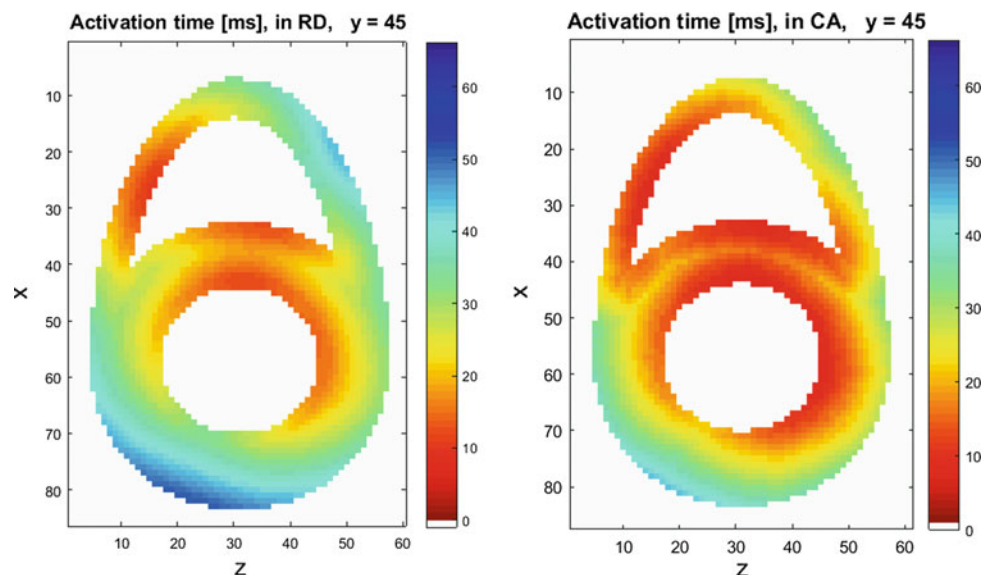
## 3 Results

In the RD propagation model, the membrane potential  $V_m$  was numerically solved in Comsol (Mesh Finer) and the activation times were subsequently evaluated from the time courses of  $V_m$  in Matlab. Spatial distributions of the membrane potential  $V_m$  obtained from the RD propagation model

**Table 1** Maximal activation times in ms

Model	DR	CA
Homogeneous, one starting position	137	145
Homogeneous, nine starting positions	85	89
Heterogeneous, one starting position	101	90
Heterogeneous, nine starting positions	66	63

**Fig. 3** Spatial distribution of activation times in the ventricular model with the conducting layer in the plane  $y = 45$  mm obtained from the RD (left) and CA (right) propagation models



## 4 Conclusions

Maximal activation times higher than 120 ms were obtained by both, RD and CA approaches in the homogeneous ventricular model with one starting position. More physiological activation times of the whole ventricles in the range from about 80 ms to 120 ms were obtained by RD and CA approach in the homogeneous ventricular model with nine starting positions. Similar values were obtained also for models with the conducting layer and one starting position. Slightly shorter values were obtained for models with the conducting layer and nine starting positions.

The differences between activation times obtained by the RD and CA approaches in heterogeneous models were caused by delayed activation propagation through the tissue boundary in the RD approach and changing velocity of propagation due to curvature of the activation front.

**Acknowledgements** This work was supported by grants APVV-14-0875 from the Slovak Research and Development Agency and 2/0071/16 from the VEGA grant agency. Conflict of Interest The authors declare that they have no conflict of interest.

## References

1. Fast, V.G., Kleber, A.G.: Role of wavefront curvature in propagation of cardiac impulse. *Cardiovascular Research* 33, 258–271 (1997).
2. Cocherová, E.: Analysis of the activation propagation velocity in the slab model of the cardiac tissue. In: Maňka, J., Tyšler, M., Witkovský, V., Frollo, I. (eds.) MEASUREMENT 2015, Proceedings of the 10th International Conference on Measurement, pp. 105–108. Institute of Measurement Science, Slovak Academy of Sciences, Bratislava (2015).
3. Potse, M., Dube, B., Richer, J., Vinet, A., Gulrajani, R.M.: A comparison of monodomain and bidomain reaction-diffusion models for action potential propagation in the human heart. *IEEE Transactions on Biomedical Engineering* 53(12), 2425–2435 (2006).
4. Sovilj, S., Magjarevic, R., Lovell, N.H., Dokos, S.: A Simplified 3D Model of Whole Heart Electrical Activity and 12-Lead ECG Generation. *Computational and Mathematical Methods in Medicine*, 2013, 10 (2013).
5. Szathmáry, V., Osvald, R.: An interactive computer model of propagated activation with analytically defined geometry of ventricles. *Computers and Biomedical Research* 27(1), 27–38 (1994).
6. Švehlíková, J., Zelinka, J., Szathmáry, V., Bachárová, E., Tyšler, M.: Modeling as a tool for understanding of changes in ECG signals. In: Maňka, J., Tyšler, M., Witkovský, V., Frollo, I. (eds.) MEASUREMENT 2015, Proceedings of the 10th International Conference on Measurement, pp. 101–104. Institute of Measurement Science, Slovak Academy of Sciences, Bratislava (2015).
7. Cocherová, E., Švehlíková, J., Zelinka, J., Tyšler, M.: Activation propagation in cardiac ventricles using homogeneous monodomain model and model based on cellular automaton. In: Maňka, J., Tyšler, M., Witkovský, V., Frollo, I. (eds.) MEASUREMENT 2017, Proceedings of the 11th International Conference on Measurement, pp. 217–220. Institute of Measurement Science, Slovak Academy of Sciences, Bratislava (2017).
8. Durrer, D. et al.: Total excitation of the isolated human heart. *Circulation* 41(6), 899–912 (1970).
9. Rijnbeek, P.R. et al.: Normal values of the electrocardiogram for ages 16–90 years. *Journal of Electrocardiology* 47(6), 914–921 (2014).
10. Macfarlane, P.W. et al.: *Comprehensive electrocardiology*. Springer-Verlag, Berlin (2011).
11. Mirvis, D.M., Goldberger, A.L.: In: Mirvis D.M. (ed) *Electrocardiography: a physiologic approach*, Ch. 9, 532, Mosby (1993).
12. Pullan, A.J., Cheng, L.K., Buist, M.L.: *Mathematically modelling the electrical activity of the heart: from cell to body surface and back again*. World Scientific, Singapore (2005).

# Comparison of ECRES Algorithm with Classical Method in Management of Diabetes Type 1 Exercise-Related Imbalances

Miloš Ajčević, Maria Pia Francescato, Mario Geat, and Agostino Accardo

## Abstract

Nutrition and physical activity are important parts of a healthy lifestyle and management of diabetes. Regular moderate-intensity physical activity in type 1 diabetes patients can enhance insulin sensitivity, reduce the risk of cardiovascular disease and improve psychological well-being. Nevertheless, the risk of exercise-induced hypoglycemia is a great challenge for patients with type 1 diabetes and represents an important barrier to physical activity in these patients. Recently, an algorithm called ECRES has been developed with the aim of estimating, depending on patient's own therapy and specific physical activity, the glucose supplement required by the patient to maintain safe blood glucose levels. The aim of this study is to compare the ECRES algorithm to classical quantitative approach. Therefore, we measured and compared glycaemia in 23 patients (mean age:  $43 \pm 12$  years) during 1-h treadmill walk/run maintaining heart rate at 65% of his/her theoretical maximum value for age. For each subject two separate tests were performed: with carbohydrates supplement estimated by ECRES algorithm and by classical approach, respectively. The average heart rate observed during exercise (average progression speed:  $5.8 \pm 0.8$  km/h at  $4.2 \pm 2.3\%$  inclination) was  $111.5 \pm 9.4$  bpm. Glycaemia measured by portable glucometer showed no significant differences between tests managed with ECRES algorithm and with classical approach, both before ( $149 \pm 47$  vs.  $128 \pm 41$  mg/dL) and at the end of the performed exercise ( $134 \pm 66$  vs.  $138 \pm 54$  mg/dL). The ECRES algorithm, however, estimated a significantly lower amount of carbohydrate needed for physical activity as compared to that suggested by the classical approach

( $14.8 \pm 12.0$  g vs.  $23.4 \pm 4.7$  g;  $p < 0.05$ ), while maintaining patients' blood glucose within optimal clinical limits. The study results confirmed the validity of the estimates made by the ECRES algorithm.

## Keywords

Physiological modelling • Type 1 diabetes  
Glycaemia • Algorithm • Exercise

## 1 Introduction

Type 1 diabetes is an autoimmune disorder which prevents the body from being able to produce enough insulin to adequately regulate blood glucose levels. Despite significant advancements in blood glucose monitoring and improved insulin therapy, large excursions in blood glucose concentration remain a major challenge for the active person with type 1 diabetes mellitus [1]. Physical activity and adequate nutrition, together with insulin therapy, are very important milestones of a healthy lifestyle and management of diabetes. Regular moderate-intensity physical activity in type 1 diabetes patients can enhance insulin sensitivity, reduce the risk of cardiovascular disease and improve psychological well-being [2–4]. Nevertheless, the risk of exercise-induced hypoglycemia is a great challenge for patients with type 1 diabetes and represents the most important barrier to physical activity in these patients [5].

Exercise-associated glycemic imbalances are often difficult to manage. Hypoglycemia during exercise can be dangerous and decreases performance; on the other hand, excessive carbohydrates intake before or during physical activity can result in hyperglycemia and negate some of the metabolic and cardiovascular benefits of exercise [6]. Existing guidelines for minimizing the risk of a hypoglycemia are still inexplicit. Thus, the patient has to determine his/her self-management strategy by trial-and-error. The exercise-induced excessive fall of blood glucose level

M. Ajčević (✉) · A. Accardo  
Department of Engineering and Architecture, University of Trieste, Trieste, Italy  
e-mail: majcevic@units.it

M. P. Francescato · M. Geat  
Department of Medicine, University of Udine, Udine, Italy

has generally been attributed to the large exercise-induced rise in muscle glucose uptake not matched by a simultaneous increase in hepatic glucose production [4]. Energy consumption during physical activity, as well as carbohydrate oxidation rate, varies with the type, duration and intensity of exercise.

Perkins proposed management of exercise-related imbalances by estimating carbohydrate needed to avoid hypoglycemia according to type of activity and patient weight [7]. This classical quantitative method is based on standardized tables, that have been developed to help athletes estimating their carbohydrate requirements for many different types of exercise, a few times also with varying intensities, according to body weight. However, patient's insulin sensitivity, the state of physical conditioning of the subject and the timing of the exercise relative to the last meal and insulin bolus are additional factors that require consideration [1].

Recently, an algorithm called ECRES has been developed with the aim of estimating, depending on patient's own therapy and specific physical activity, the glucose supplement required by the patient to maintain safe blood glucose levels [8]. This method is based on the patient's habitual therapy and diet, and changes in the insulin dose are not mandatory. The patient's insulin sensitivity is taken into account through the individual dietary carbohydrates-to-insulin ratio. The actual exercise intensity and duration are used for the estimate and the patient's physical fitness is considered when the overall amount of glucose oxidized is estimated. This algorithm also takes into account the timing of the activity relative to the last meal and insulin bolus, allowing the estimation of the carbohydrates supplement for any time of day the exercise is performed. The method was preliminary evaluated in the previous study showing promising results [8]. However, this innovative approach has not yet been compared to classical quantitative method. Therefore, the aim of this study is to compare the ECRES algorithm to the classical approach.

## 2 Materials and Methods

### 2.1 Experimental Protocol

Patients with type 1 diabetes diagnosed for at least 2 years and with no evidence of diabetes complications contraindicating physical activity, were recruited at Diabetes Center, ASUITS, Trieste, Italy. For each subject two separate tests were performed: with carbohydrates supplement estimated by ECRES algorithm and by classical approach, respectively. The two tests were performed at a distance of one week in random order. Patients were recommended to maintain their usual therapy (i.e. diet and insulin regimen)

and to control their blood glucose levels according to the self-management procedures to avoid the occurrence of hypoglycemic events 24 h before the tests. All tests started 4 h after the lunch (midday) insulin treatment. Each test consisted in 1-h treadmill walk/run maintaining heart rate at 65% of patient's theoretical maximal value (HRmax):

$$\text{HRmax} = 220 - \text{Age} \quad (1)$$

where Age is expressed in years. Treadmill speed and/or slope were adjusted to maintain the target heart rate. Before each test patients were administered the amount of carbohydrates supplement, calculated by one of the two methods, in the form liquid dietary supplement Glucosprint (Harmonium Pharma, Milan, Italy).

### 2.2 Quantitative Method

Amount of carbohydrates required (reqCHO) to avoid exercise-induced imbalances according to quantitative classical approach for 1 h walking at a progression speed of 5 km/h (which, according to our previous experience, elicits 65% of HRmax) can be calculated by the following equation derived from standardized tables [7].

$$\text{reqCHO} = 0.31 \text{ g/kg } w + 1 \text{ g} \quad (2)$$

where W is patient weight expressed in kg.

### 2.3 ECRES Algorithm

The ECRES algorithm, described in detail previously [8], calculates the amount of carbohydrates supplement required to avoid glycemic imbalances (reqCHO) as a fraction (Ft) of the overall amount of carbohydrates burned during the exercise (CHOox) and further corrects it by subtracting or adding the excess or lack of glucose contained in the extracellular compartment (Gb) as follows:

$$\text{reqCHO} = (\text{CHOox} \cdot \text{Ft}) \pm \text{Gb} \quad (3)$$

Gb is derived from the actual capillary glucose level measured before the start of the exercise (aGL):

$$\text{Gb} = (\text{aGL} - \text{theoGL}(t)) \cdot \text{ECF} \quad (4)$$

where theoGL(t) is the theoretical glycaemia the patient should have at the time of day the exercise is performed. This value is estimated taking into account the time distance from last meal and therapy; ECF is the volume of the extracellular fluid compartment. The CHOox is calculated as the product of exercise duration (exD), and the whole-body carbohydrate oxidation rate. The latter is estimated on the



basis of the expected exercise intensity, represented by the average expected HR, and the patient's fitness levels (sedentary or active):

$$\text{CHO}_{\text{ox}} = (m \cdot \text{HR} + q) \cdot \text{exD} \quad (5)$$

where the  $m$  and  $q$  values are those reported previously [9] for trained and untrained patients. The  $F_t$  is almost proportional to the prevailing insulin concentration throughout the effort ( $\text{IC}(t, j)$ ). This is estimated on the basis of the patient's usual therapy data and on standard pharmacokinetic profiles of the insulin analogues loaded in the system. It is also corrected for the patient's insulin sensitivity ( $S(j)$ ), inferred from the patient's usual dietary carbohydrate-to-insulin ratio:

$$F_t = ((\text{IC}(t, j) * S(j)) \cdot e + f \quad (6)$$

where  $t$  is the time of day and  $j$  is the day period (i.e. morning, afternoon or evening) when the exercise is performed; the  $e$  and  $f$  values have been reported in previous work [8]. According to the description above, the following data were uploaded in the algorithm to obtain  $\text{reqCHO}$  for all patients: (a) their usual therapy (i.e. insulin types, doses and time scheduling, together with the dietary carbohydrates); (b) the time of day of exercise; (c) the capillary blood glucose level measured just before the start; (d) the average heart rate and duration foreseen for the particular exercise.

## 2.4 Data Acquisition and Analysis

Capillary blood glucose concentrations were measured using a handheld glucometer (Accu-Chek Aviva, Roche Diagnostics, Indianapolis, Indiana, United States) 30 min before ( $-30'$ ), just before the start ( $0'$ ), at the middle ( $30'$ ), at the end ( $60'$ ) of 60-min exercise, and, finally, also 1 h thereafter. Glycaemia in the range of 70–180 mg/dL was defined as being on target. Heart rate was measured by heart rate monitor (Polar, Kempele, Finland) during of the whole experimental session. Amount of carbohydrates administered before the start of the exercise were recorded in detail. Mean velocity and slope were measured by treadmill.

## 3 Results

Twenty-three patients were recruited (mean age:  $43 \pm 12$  years). Average heart rate observed during exercise was  $111.5 \pm 9.4$  bpm, significantly higher than the mean heart rate measured at rest  $75.4 \pm 9.9$  bpm ( $p < 0.001$ ). The average treadmill progression speed was  $5.8 \pm 0.8$  km/h at  $4.2 \pm 2.3\%$  inclination. Cases of hypoglycemia were not observed during and after tests, either by applying classical approach or by applying the ECRES algorithm. On the other

**Table 1** Mean  $\pm$  1SD blood glucose levels measured before during and after exercise in two tests managed with classical and ECRES method

Time from exercise start (min)	Classical approach (mg/dL)	ECRES algorithm (mg/dL)
$-30'$	$128 \pm 41$	$149 \pm 47$
$0'$	$146 \pm 46$	$160 \pm 45$
$30'$	$157 \pm 50$	$152 \pm 54$
$60'$	$138 \pm 64$	$134 \pm 66$

side, too high glucose levels ( $>180$  mg/dL) were observed in 7 of 23 subjects during the tests managed with classical method, while this occurred in only 5 cases during the tests managed with ECRES. Mean glycaemia measured values before during and after exercise in the two tests managed with classical and ECRES method are reported in Table 1; no significant difference was observed at any time point.

The mean difference between glycaemia before the test (i.e.; before exercise and carbohydrates administration) and after test ( $60'$ )  $\Delta$ Glycaemia ( $-30'$ )–( $60'$ ) was positive for ECRES (15 mg/dL), and negative for classical method ( $-10$  mg/dL). Thus, on the average the classical method tended to result in higher glucose blood levels at the end than before the exercise; vice versa was observed for ECRES. Moreover, the ECRES algorithm estimated a significantly lower amount of carbohydrate needed for physical activity as compared to that suggested by the classical approach ( $14.8 \pm 12.0$  g vs.  $23.4 \pm 4.7$  g;  $p < 0.05$ ), while maintaining patients' blood glucose within safe clinical range.

## 4 Discussion

Appropriate self-management of type 1 diabetes is crucial for the prevention of diabetes-related complications and other adverse outcomes. Patients affected by this disorder may benefit from the many valuable effects of regular physical activity. Anyhow, the frequent metabolic imbalances experienced by these patients during exercise discourage them from regular physical activities [5]. So far, only general strategies have been suggested and no well-defined guidelines have been proposed to help patients maintain a glycaemia within optimal clinical range for activities performed at any time of day and under a rather wide range of intensities. In order to overcome this problem, recently ECRES model for self-management of exercise-associated glycemic imbalances was proposed.

Our study compared classical and ECRES algorithm to estimate the amount of supplemental carbohydrates to avoid hypoglycaemia during the 1-h walk performed 4 h after midday therapy and meal. There was no significant difference in glycaemia at the end of exercise between the

two methods and there were no cases of hypoglycaemia during and after the tests. ECRES maintained patients' glycaemia level within optimal clinical range in 87% of cases, while the classical approach was successful in 78%. If glycaemic imbalances, either hypoglycaemia or hyperglycaemia are avoided, exercise will give benefits also on long-term glycaemic control [8].

The amount of carbohydrates supplement estimated by classical quantitative method was significantly higher compared to that suggested by the ECRES algorithm. Higher carbohydrates administration than real exercise needs can partially cancel the beneficial effects of physical activity. In fact, patient managed with classical method had higher glucose blood levels at the end than before the exercise, while this was not the case with ECRES algorithm.

The results of this study should be interpreted bearing in mind that the tests were performed 4 h after the therapy, which represents the best condition for the classical approach. However, in case of exercise performed earlier or after this time, ECRES would suggest a higher or lower carbohydrate supplement, respectively, while the classical approach does not take into account this variable. Previous study showed that ECRES maintained patients' blood glucose level within optimal range in 70% of the walks, independently of the time distance (3, 4 and 5-h) from the insulin injection [6].

## 5 Conclusions

The study results confirmed the validity of the estimates made by the ECRES algorithm. This method estimated a significantly lower amount of carbohydrate needed for physical activity as compared to the amount suggested by the classical approach, while maintaining patients' blood glucose within safe clinical limits. The results should be confirmed in future clinical study performing the tests at a different time distance from the insulin injection.

**Acknowledgements** The study was partially funded by University of Udine and Trieste research project—PoCN and University of Trieste research funds—FRA2015.

**Conflict of Interest** The authors declare that they have no conflict of interest.

**Compliance with Ethical Requirements** The study was approved by the ethics committee of the Friuli-Venezia-Giulia region (Italy) and was conducted according to the Declaration of Helsinki. All patients gave their voluntary written consent after having been informed about the nature, purpose and possible risks involved.

## References

1. Riddell, MC., Perkins, BA.: Type 1 diabetes and vigorous exercise: applications of exercise physiology to patient management. *Canadian Journal of Diabetes* 30(1), 63–71 (2006).
2. Stallknecht, B., Larsen, JJ., Mikines, KJ., Simonsen, L., Bulow, J., Galbo, H.: Effect of training on insulin sensitivity of glucose uptake and lipolysis in human adipose tissue. *Am J Physiol* 279, 376–385 (2000).
3. Lehmann, R., Kaplan, V., Bingisser, R., Bloch, K., Spinaz, G.: Impact of physical activity on cardiovascular risk factors in IDDM. *Diabetes Care* 20, 1603–1611 (1997).
4. Steppel, JH., Horton, ES.: Exercise in the management of type 1 diabetes mellitus. *Rev Endocr Metab Disord* 4, 355–360 (2003).
5. Brazeau, AS., Rabasa-Lhoret, R., Strychar, I., Mircescu, H.: Barriers to physical activity among patients with type 1 diabetes. *Diabetes care* 31(11), 2108–2109 (2008).
6. Francescato, MP., Carrato, S.: Management of exercise-induced glycaemic imbalances in type 1 diabetes. *Current diabetes reviews* 7 (4), 253–263 (2011).
7. Perkins, BA., Riddell, MC.: Type 1 diabetes and exercise: using the insulin pump to maximum advantage. *Canadian Journal of Diabetes* 30(1), 72–79 (2006).
8. Francescato, MP., Geat, M., Accardo, A., Blokar, M., Cattin, L., Noacco, C.: Exercise and glycaemic imbalances: a situation-specific estimate of glucose supplement. *Med Sci Sports Exerc* 43(1), 2–11 (2011).
9. Francescato, MP., Cattin, L., Geat, M., Tosoratti, E., Lazzar, S., Noacco, C., Di Prampero, PE.: Glucose pulse: A simple method to estimate the amount of glucose oxidized during exercise in type 1 diabetic patients. *Diabetes Care* 28, 2028–2030 (2005).

# Application of Computational Aerodynamics on the Risk Prediction of PM<sub>2.5</sub> in Congenital Tracheal Stenosis

L. M. Zhu, X. L. Gong, J. Y. Shen, L. P. Liu, J. F. Liu, J. L. Liu, and Z. M. Xu

## Abstract

PM<sub>2.5</sub> is one of the particulate pollutants in atmosphere. It refers to the matter size smaller than 2.5 μm. Long-term exposure can lead to health problems, especially to the respiratory system. Although many reports have been published on its harm, there are little researches focused on its risk prediction to the children with congenital tracheal stenosis (CTS). In the present study, we used the method of computational fluid dynamics (CFD) to investigate the aerodynamic characteristics of airflow with PM<sub>2.5</sub> in the trachea. The motion of airflow and the risk of PM<sub>2.5</sub> were predicted in a normal tracheal model and a patient-specific CTS model, respectively. Compared with the tracheal aerodynamics and PM<sub>2.5</sub> distributions in the main airway, the potential risk of PM<sub>2.5</sub> to the CTS were disclosed. The results indicated that more deposited areas of PM<sub>2.5</sub> were observed at the downstream of the trachea stenosis and the bronchus around the bridging bronchus were more likely affected by PM<sub>2.5</sub>. This implied that the

trachea with CTS was more vulnerable and PM<sub>2.5</sub> might aggravate the tracheal stenosis. The application of computational aerodynamic analysis could be used for the risk prediction of PM<sub>2.5</sub> in CTS.

## Keywords

Computational fluid dynamic • Congenital trachea stenosis • PM<sub>2.5</sub> • Particle deposition • Risk prediction

## 1 Introduction

Congenital tracheal stenosis (CTS) is a rare structural obstructive airway disease. The clinical symptoms of CTS include asthma, shortness of breath, cough and wheezing [1]. PM<sub>2.5</sub> refers to the micron particles with equivalent diameter smaller than or equal to 2.5 μm. It can enter the respiration tract by breathing, deposit on the bronchus and even permeate to the alveoli and blood. Many researches have confirmed long-term exposure to polluted air poses a serious threat to the respiration system [2–5]. However, there are little researches focused on its risk prediction to the children with CTS. Numerical computation has become an important way to study aerodynamics in the airway in recent years [6–9]. In the present study, our research focused on the aerodynamic characteristics of airflow with PM<sub>2.5</sub> in the trachea to predict the potential risk of PM<sub>2.5</sub> to a patient with CTS by the comparison of a normal trachea. In the simulation of the airflow, the DPM model was used to numerically analyze the deposition regularity of PM<sub>2.5</sub> in the trachea. The aerodynamic parameters, including wall shear stress (WSS), velocity streamlines, position of particles deposition and statistics of tracked, escaped and trapped particles were calculated to estimate the differences of aerodynamic characteristics between the normal trachea and the patient-specific CTS model.

Co-first author: L. M. Zhu, X. L. Gong and J. Y. Shen

L. M. Zhu (✉) · X. L. Gong · J. Y. Shen · L. P. Liu · J. F. Liu · J. L. Liu (✉) · Z. M. Xu (✉)

Department of Cardiothoracic Surgery, Shanghai Children's Medical Center, Shanghai Jiao Tong University School of Medicine, Shanghai, 200127, China  
e-mail: zhulimin121@hotmail.com

J. L. Liu  
e-mail: jinlong\_liu\_man@163.com

Z. M. Xu  
e-mail: zmxyfb@163.com

J. Y. Shen · J. F. Liu · J. L. Liu  
Shanghai Engineering Research Center of Virtual Reality of Structural Heart Disease, Shanghai Science and Technology Committee (STCSM), Shanghai, 200127, China

J. L. Liu  
Institute of Pediatric Translational Medicine, Shanghai Children's Medical Center, Shanghai Jiao Tong University School of Medicine, Shanghai, 200127, China

## 2 Materials and Methods

### 2.1 3D Model Reconstruction and Mesh Generation

In the present study, a 15-month-old male patient, was diagnosed CTS with three stenoses. Due to the small size of the tiny bronchi, only the stenosis in the main airway can be surgically corrected. A male normal child as control was selected. By obtaining written informed consent from all guardians and the approval of the local institutional ethical review board, our study was carried out. CT images in DICOM format were imported into a medical image processing software, Materialise®-Mimics Innovation Suite 18.0, (Belgium). A 3D tracheal object was transformed into 3D geometry from two-dimensional (2D) images. Then, we imported it into computer-aided design (CAD) software, Materialise®-3-Matic 10.0 (Belgium), to smooth the surface of model. The two 3D smoothed models have been shown in Fig. 1.

After the process of model reconstruction and smoothing, they were imported into the grid-generation software, ANSYS®-ICEM 14.5. Three-layer body-fitted hexahedral grids were generated for the accurate measurement of WSS near the wall, and tetrahedral grids in the interior. Hereinto, an average nodal space of hexahedral grids increased by a ratio of 1.2. In order to find a better mesh for the efficient calculations, grid sensitivity verification has been checked. The grid number of tracheal model with CTS and normal tracheal model is 1,412,781 and 1,021,855, respectively.

### 2.2 CFD Simulation

We assumed the airflow as a Newtonian and incompressible fluid. Navier-Stokes (N-S) equation and continuity equation as the governing equations were applied for the computational analysis of airflow in the trachea. We assumed the airflow with the constant density ( $\rho = 1.61 \text{ kg/m}^3$ ) [10] and viscosity ( $\mu = 1.864 \times 10^{-5} \text{ kg/m s}$ ) [11] in the present study. The airflow in the lower respiration tract was turbulence flow with a low Reynolds number. Wilcox k- $\epsilon$  model was considered to obtain the turbulence viscosity, which was verified perfectly for airflow simulation by CFD. We set PM 2.5 as solid spherical particles, and its constant density was far greater than the density of air. Discrete Phase Model (DPM) was applied to simulate the airflow with PM 2.5 in the trachea. The unit Stokes' drag force of particles, the gravity of particles and Saffman Lift Force were considered in calculations. The governing equations of particle velocity, in Lagrange method, were as follows:

$$\frac{dv_p}{dt} = \frac{18\mu}{d_p^2 \rho_p C_c} (v - v_p) + \frac{g_z(\rho_p - \rho)}{\rho_p} + \frac{2 \times 2.594 v^{1/2} \rho d_{ij}}{\rho_p d_p (d_{ik} d_{kl})^{1/4}} (\vec{v} - \vec{v}_p) \quad (3)$$

where  $v$  was the fluid velocity,  $v_p$  was the particle velocity,  $\mu$  was the dynamic viscosity,  $\rho$  was the fluid density,  $\rho_p$  was the particle density,  $d_p$  was the particle diameter.

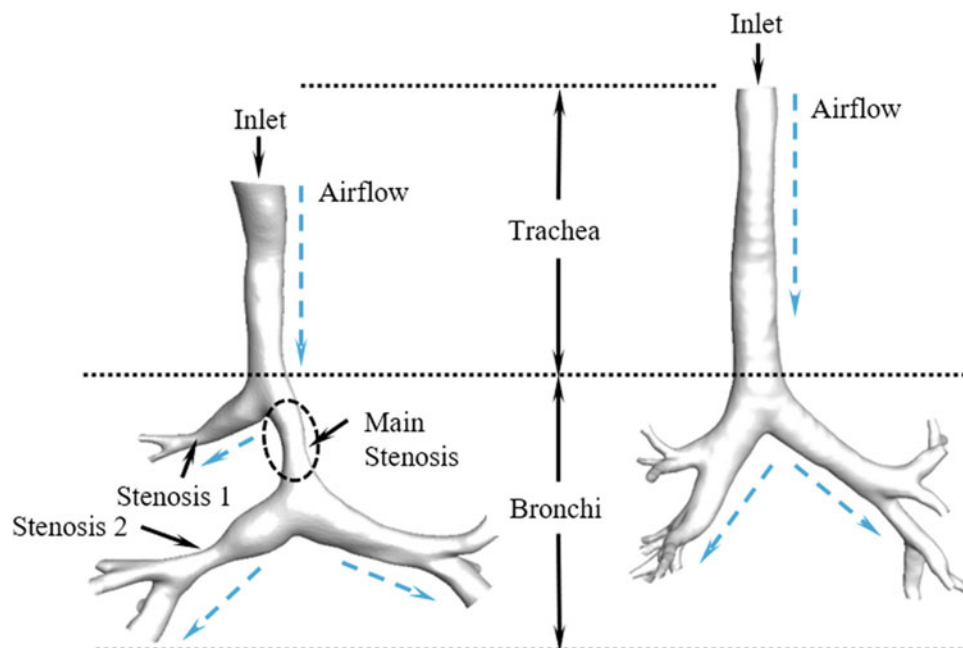


**Fig. 1** A 3D tracheal model with CTS and a normal tracheal model (Blue dotted lines indicate the direction of airflow in inspiration)

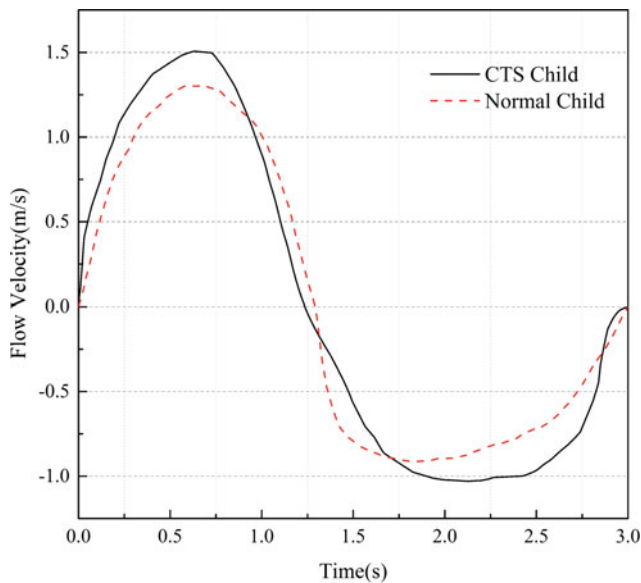


**Fig. 2** Respiration curves in the calculation

Monodispersed particles of diameters ( $d_p = 1 \mu\text{m}$ ) and density ( $\rho_p = 2000 \text{ kg/m}^3$ ) [3] were used for simulation of deposition efficiency,  $g_z$  was the gravity in  $z$  direction,  $\rho_p$  and  $\rho$  were density of particles and air, respectively,  $d_{ij}$  was the fluid deformation rate tensor,  $C_c$  was Cunningham correction factor.

The breathing curves of the child with CTS and normal child in these calculations have been showed in Fig. 2. The “trap” condition was used for the walls of calculation domain, which meant that when the edge of a particle touches the wall, the particle was deposited. The “escape” condition was used for inlet and outlets which were changed for inspiratory and expiratory parts of breathing. It meant that a particle passing this boundary (leaving domain) was lost for further calculations. The direction of the expiration was opposite.

### 3 Results

Figure 3 displayed the velocity streamlines and position contour of PM<sub>2.5</sub> deposition in the models of CTS and normal trachea (b) at the respiration with the highest velocity. The airflow was straight in the normal trachea. The turbulence flow was appeared in right upper lobe (RUL), bridging bronchus (BB) and left middle bronchi (LMB) in

the CTS model which were marked out with dotted circles. There was the turbulence airflow with higher velocity (10 vs. 3 m/s) in the CTS model. The highest value of the velocity was found in the main stenosis as well. It was obvious that the distribution of particles was more uniform in the normal tracheal model. The particles were mainly deposited in RUL, BB and LMB where the turbulence airflow was generated. Statistics of tracked, escaped and trapped particles were described in Fig. 4. The number of all the particles traced equaled to the sum of the number of particles trapped by the wall of the trachea and the number of particles escaped from the outlets of bronchus. In the model of CTS, there was 99.3% of PM<sub>2.5</sub> that would deposit in the trachea. While the most particles deposited in the trachea, the possibility of aggravating tracheal stenosis might increase. In the normal tracheal model, there was 91.5% of PM<sub>2.5</sub> that might transport to the next level bronchi and even the lungs. It indicated that the risk of potential injury to the lungs was higher for the normal child.

### 4 Discussion

CTS is a life-threatening congenital disease that often causes severe respiratory insufficiency. PM<sub>2.5</sub> is the most common particulate pollutants in atmosphere. The effects and risks caused by PM<sub>2.5</sub> in the trachea with CTS are still unclear. In the present study, the method of CFD was applied to simulate the movement of airflow with of PM<sub>2.5</sub> in trachea. Streamlines, the position of particles deposition and statistics of tracked, escaped and trapped particles were computed to estimate the aerodynamic differences and deposition regularity of PM<sub>2.5</sub> in the tracheal model CTS and the normal trachea. The streamlines of velocity indicated the tracks of airflow. The complex turbulence occurred in RUL, BB and LMB of the trachea with CTS. More deposited areas of PM<sub>2.5</sub> were observed at the downstream of the tracheal stenosis and the areas of bronchus around BB were more likely accumulated the particles of PM<sub>2.5</sub>. For the patient with CTS, there were 99.3% of PM<sub>2.5</sub> that would deposit in the trachea and bronchus. Long-term exposure to PM<sub>2.5</sub> would increase the infection rate and aggravate the tracheal stenosis because of a large number of deposited particles. However, for the normal patient, 91.5% of PM<sub>2.5</sub> might transport to the next level bronchi and even the lungs. It inferred that for the normal child, the possibility of injury to the lungs was larger than the children with CTS.



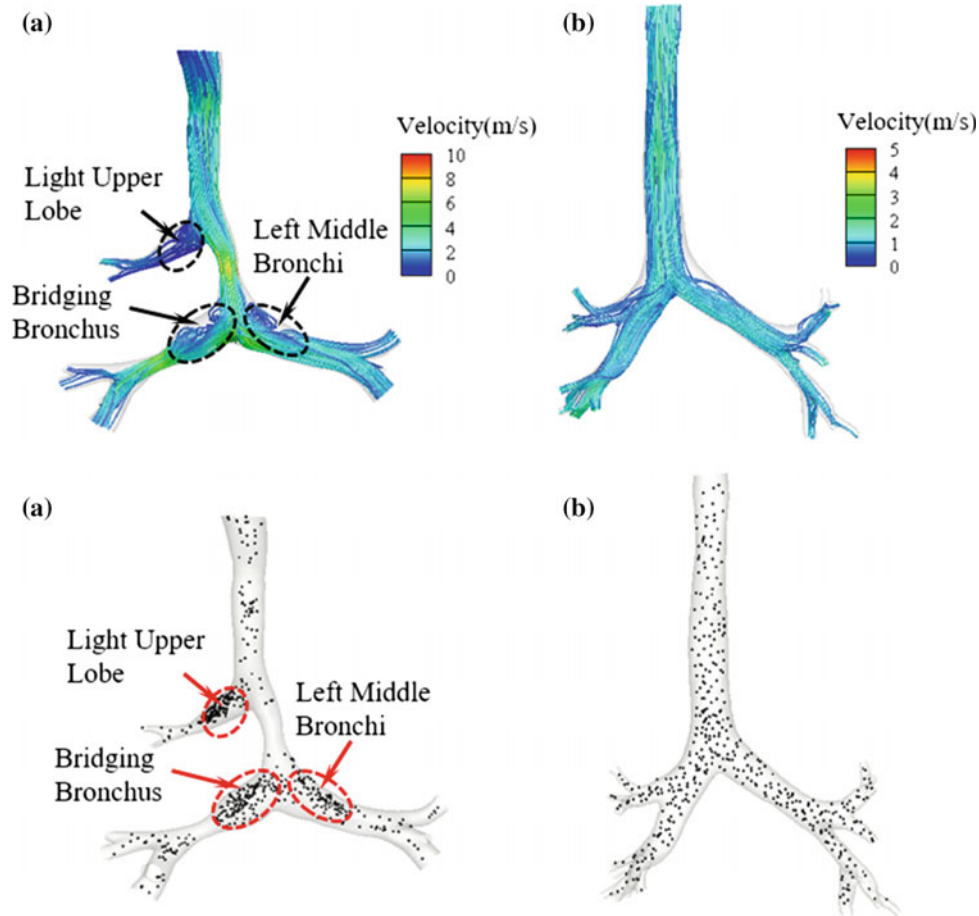


**Fig. 3** Streamlines of the patient and particles deposition contour of the patient with CTS (a) and normal child (b)

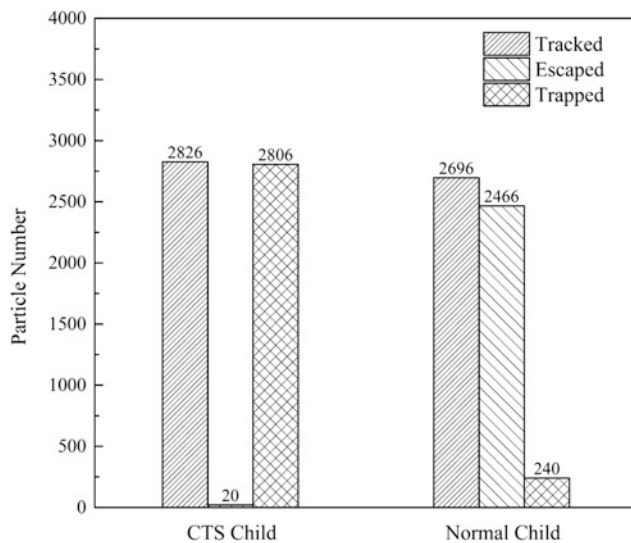


**Fig. 4** Statistics of tracked, escaped and trapped particles in the trachea of two children

The distribution of particle deposition was closely related to the tracheal geometry.

## 5 Conclusion

In order to disclose the potential risk of PM<sub>2.5</sub> to the CTS and the aerodynamic differences between the CTS and normal trachea, the numerical study was carried out by the method of CFD. The results showed the aerodynamic differences and different distributions of deposition of PM<sub>2.5</sub> in two tracheas of a patient with CTS and a normal child. For the patient with CTS, the probability of PM<sub>2.5</sub> deposited in the trachea was higher, and the location of particle deposition was distributed mainly in places where turbulence flow occurred. These regions were prone to aggravate the stenosis. Compared to the normal child, the possibility of PM<sub>2.5</sub> causing damage to the trachea was higher, which might further aggravate the stenosis.

**Acknowledgements** We have been genuinely appreciative of the support of the National Nature Science Foundation of China (No. 81602818 and No. 81501558), the Fund of The Shanghai Committee of Science and Technology (No. 15411967100 and No. 17DZ2253100) and the Biomedical and Engineering (Science) Inter-disciplinary Study Fund of Shanghai Jiaotong University (No. YG2014MS63).

**Conflict of Interest** The authors declare that they have no conflict of interest.

## References

1. Hofferberth S C, Watters K, Rahbar R, et al. Management of Congenital Tracheal Stenosis. *Pediatrics*, 136(3): e660–e669 (2015).
2. Dominici F, Peng R D, Bell M L, et al. Fine Particulate Air Pollution and Hospital Admission for Cardiovascular and Respiratory Diseases. *Jama the Journal of the American Medical Association*, 295(10): 1127–34 (2006).
3. Zhang T, Gao B, Zhou Z, et al. The movement and deposition of PM<sub>2.5</sub> in the upper respiratory tract for the patients with heart failure: an elementary CFD study. *Biomedical Engineering Online*, 15(2): 517–530 (2006).
4. Ostro B, Lipsett M, Reynolds P, et al. Long-Term Exposure to Constituents of Fine Particulate Air Pollution and Mortality: Results from the California Teachers Study. *Environmental Health Perspectives*, 118(3): 363 (2010).
5. Villeneuve P J, Weichenthal S A, Crouse D, et al. Long-term Exposure to Fine Particulate Matter Air Pollution and Mortality Among Canadian Women. *Epidemiology*, 26(4): 536 (2015).
6. Braunfahrländer C, Vuille J C, Sennhauser F H, et al. Respiratory health and long-term exposure to air pollutants in Swiss schoolchildren. SCARPOL Team. Swiss Study on Childhood Allergy and Respiratory Symptoms with Respect to Air Pollution, Climate and Pollen. *American Journal of Respiratory & Critical Care Medicine*, 155(3): 1042 (1997).
7. Rahimi-Gorji M, Pourmehran O, Gorji-Bandpy M, et al. CFD simulation of airflow behavior and particle transport and deposition in different breathing conditions through the realistic model of human airways. *Journal of Molecular Liquids*, 209: 121–133 (2015).
8. Sandeau J, Katz I, Fodil R, et al. CFD simulation of particle deposition in a reconstructed human oral extrathoracic airway for air and helium–oxygen mixtures. *Journal of Aerosol Science*, 41(3): 281–294 (2010).
9. Chen X, Zhong W, Zhou X, et al. CFD–DEM simulation of particle transport and deposition in pulmonary airway. *Powder Technology*, 228(3): 309–318 (2012).
10. O Mimouni-Benabu, L Meister, J Giordano, P Fayoux, N Loundon, et al., A preliminary study of computer assisted evaluation of congenital tracheal stenoses: a new tool for surgical decision-making. *Int J Pediatr Otorhinolaryngol*, 76: 1552–1557 (2012).
11. CY Ho, HM Liao, CY Tu, CY Huang, CM Shih, MY Su, JH Chen, TC Shih, Numerical analysis of airflow alteration in central airways following tracheobronchial stent placement. *Experimental hematology & oncology*, 1(1): 23–23 (2012).

# Hemodynamic Effects of Conduit Position on Systemic-to-Pulmonary Shunt: A Numerical Study Using Virtual Design

J. L. Liu, Q. Sun, Z. R. Tong, J. Y. Shen, and J. F. Liu

## Abstract

The systemic-to-pulmonary shunt is a widely used palliative procedure in the therapy of congenital heart defect (CHD). Although it improved over the years, the anastomosis position of the conduit related to the control of pulmonary flow in the procedure is still one of the controversial issues. Based on patient-specific medical images, a three-dimensional (3D) vascular model was reconstructed in the present study. Four possible surgical positions of the conduit implantation for the systemic-to-pulmonary shunt were virtually devised by computer-aided design (CAD). Pulsatile simulations were done by the technique of computational fluid dynamics (CFD) to capture the physiological information of blood flow. The results indicated that higher pressure and wall shear stress were generated in the conduit. It may increase the risk of blood cell damage. While, the quantitative analysis showed that a relatively good balance of blood flow distribution and appropriate pressure drop between systemic and pulmonary circulations were achieved when the conduit was anastomosed at the innominate artery or subclavian artery than it was at the ascending aorta. The numerical study based on the virtual design is a useful approach for the preoperative prediction of local

hemodynamics and provides more detailed information for the choice of patient-specific surgical design.

## Keywords

Systemic-to-pulmonary shunt • Conduit position  
Hemodynamics • Virtual design • Computational fluid dynamics

## 1 Introduction

The systemic-to-pulmonary shunt is one of the most widely used palliative procedures to lessen cyanosis and improve the oxygen saturation in the therapy of congenital heart defects (CHDs). By surgical connection between the subclavian artery (SA) or ascending aorta (AAO) and the pulmonary artery (PA) through a Gore-Tex conduit, the blood flow was diverted from the systemic circulation to the pulmonary arteries (PAs). Although various modifications of the systemic-to-pulmonary shunt have been described and applied to clinical treatment over the years, much debate regarding anastomosis position of the conduit are still concerned for the optimization.

Medical image-based virtual design of the procedures by the combination of the techniques of computational fluid dynamics (CFD) and computer-aided design (CAD) is a promising method for the surgical studies. Different schemes can be designed to find the optimal approach by the evaluation of hemodynamics [1–3].

Here, we used the medical image-based virtual design to investigate the conduit anastomosis position in the systemic-to-pulmonary shunt. A patient-specific three-dimensional (3D) vascular configures after the systemic-to-pulmonary shunt were reconstructed. The technique of CAD was utilized to change the conduit position to imitate three possible surgical implantations of the conduit. The local hemodynamics was compared to disclose the effects of the conduit

Co-first author: J. L. Liu and Q. Sun

J. L. Liu (✉) · Q. Sun · Z. R. Tong · J. Y. Shen · J. F. Liu  
Department of Cardiothoracic Surgery, Shanghai Children's  
Medical Center, Shanghai Jiao Tong University School  
of Medicine, Shanghai, 200127, China  
e-mail: jinlong\_liu\_man@163.com

J. L. Liu  
Institute of Pediatric Translational Medicine, Shanghai Children's  
Medical Center, Shanghai Jiao Tong University School  
of Medicine, Shanghai, 200127, China

J. L. Liu · Z. R. Tong · J. Y. Shen · J. F. Liu  
Shanghai Engineering Research Center of Virtual Reality  
of Structural Heart Disease, Shanghai Science and Technology  
Committee (STCSM), Shanghai, 200127, China

position of the systemic-to-pulmonary shunt by CFD. The objective of this study was to disclose the flow features of the different connections of the conduit and provide information for surgical optimal design of patient-specific treatment in clinic.

## 2 Materials and Methods

### 2.1 Generation of Geometric Models

Clinical studies were done with the approval of the local institutional review board and regional research ethics committee of Shanghai Children's Medical Center (SCMC) Affiliated Shanghai Jiao Tong University School of Medicine. A 3D patient-specific vascular model of the systemic-to-pulmonary shunt was reconstructed from a series of continuous 0.625 mm-thick CT images of a 10-month-old child.

The medical images from a 16-slice multi-detector row enhanced CT scanner (Bright Speed Elite, GE Medical System, General Electric, America) were compiled and reconstructed by the software Materialise®-Mimics 18.0 and 3-Matic 10.0 (Materialise, Haasrode, Belgium). Due to the pulmonary atresia, the blood flow of PAs was provided from systemic circulation through the systemic-to-pulmonary shunt. Figure 1 depicts the reconstructed geometry after surface smoothing. The stereo-lithography interface format (STL) format was used to export the 3D vascular geometry for model rebuilding by CAD software.

### 2.2 Model Rebuilding

The process of model rebuilding was done by the CAD software Materialise®-3-Matic 10.0. Based on our clinical experience and patient-specific anatomical structures of arteries, we modified the connection position of the conduit to three possible surgical positions. The same diameter of conduit was used. Figure 1 shows the results of our virtual design.

### 2.3 CFD Analysis

**Mesh Generation.** A computational mesh was generated for the numerical solution of the equations governing blood motion. The five-layer body-fitted prismatic grids in the near-wall regions were employed to catch the hemodynamic characteristics of wall shear stress (WSS). The tetrahedral grids were created in the rest domain. The grid-independent verification was performed in our previous study to find the best mesh for CFD analysis [4].

**Boundary Conditions.** Due to the pulmonary atresia, we used the pulsatile velocity measured by echocardiography at the AAO as the inlet condition. Sixty times of vessel diameter were extended for sufficient recovery of blood pressure at each branch. A zero pressure gradient with the estimated pressure wave reflections from peripheral vessels at diastolic phase proposed in our previous study of Norwood procedure [4] was applied at the outlets. Details of our methods and validations were reported in the previous studies [4–6].

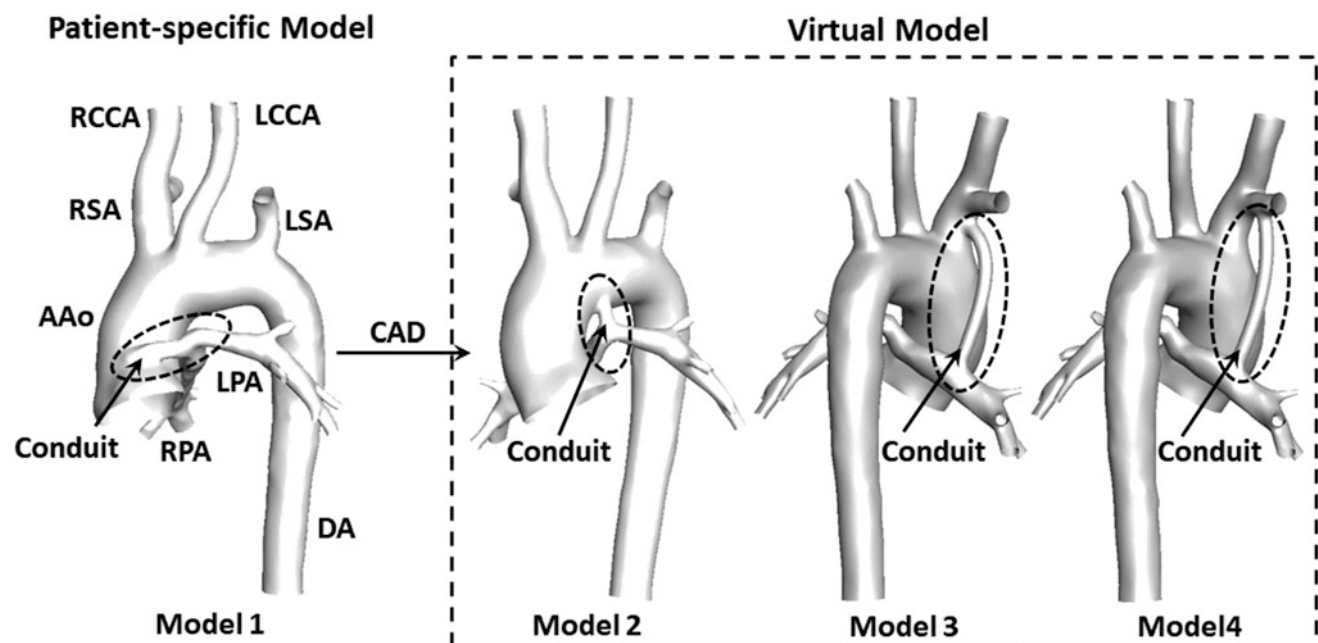


**Fig. 1** The 3D patient-specific vascular model of the systemic-to-pulmonary shunt and three virtual models created by CAD (AAo: Ascending Aorta; DA: Descending Aorta; LPA: Left Pulmonary

Artery; RPA: Right Pulmonary Artery; LSA: Left Subclavian Artery; RSA: Right Subclavian Artery; LCCA: Left Common Carotid Artery; RCCA: Right Common Carotid Artery)

**Calculations.** The 3D incompressible Navier-Stokes equations governing the motion of blood flow was solved by the software, ANSYS®-FLUENT 14.5, for the simulation of the physiologic flow in the models. We assumed the blood was a Newtonian fluid with a constant kinematic viscosity of  $4.0 \times 10^{-3}$  Pa s and the density of  $1060 \text{ kg m}^{-3}$ , and the vessels were rigid. For the detailed methodology of calculation, it was described in our previous studies [4–6].

### 3 Results

Due to the relatively close position of the anastomosis in the systemic and pulmonary circulation in Model 1 and Model 2, Model 3 and Model 4, the pressure distribution of these models is relatively close as well. The pressure gradient of the systemic-to-pulmonary shunt in Model 1, Model 2, Model 3 and Model 4 is about 6000 Pa, 7000 Pa, 8000 Pa

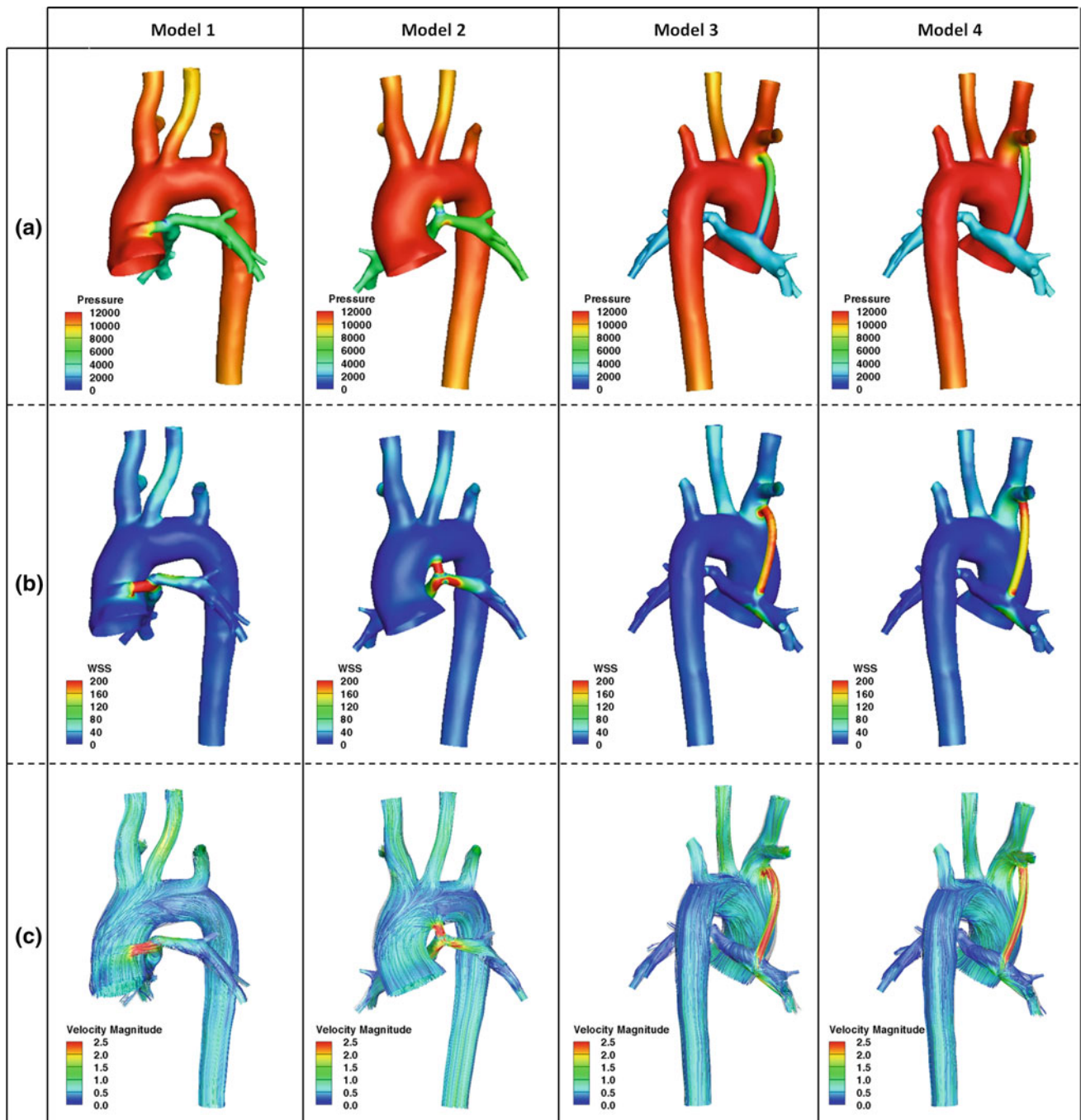


**Fig. 2** The contour plots of the distribution of pressure (a), WSS (b) and streamlines (c) (Unit: Pressure-Pa; WSS-Pa; Velocity Magnitude-m/s)



and 10000 Pa, respectively. Figure 2a shows the results of Pressure.

The highest WSS regions are mainly located in the systemic-to-pulmonary shunt and its anastomotic areas, which increases the possibility of damage to endothelial cells. Figure 2b displays the contour plots of WSS.

High speed regions are mainly appeared in the systemic-to-pulmonary shunt, and low speed areas are distributed in the PA and the DA. Turbulence occurred in anastomotic region of the systemic-to-pulmonary shunt and RPA in Model 3 and Model 4, respectively. Figure 2c shows the streamlines of each model.

## 4 Discussion

In the present study, we used the technology of CAD to virtually modify the conduit position of the systemic-to-pulmonary shunt. Compared with the original vascular model reconstructed from medical images, local hemodynamic characteristics were investigated by the analysis of CFD simulation results. Based on our clinical experience, the anastomosis position of the conduit was rebuilt. The same boundary conditions were imposed and the same calculation methods were applied in the CFD calculations. Obviously different WSS distribution was found in the conduit, while relatively equal pressure drop was obtained from systemic circulation to PAs.

WSS is considered to be the main reasons on the formation of thrombosis and occlusion. Studies have shown a strong correlation in the magnitude of WSS, endothelial cell function, and vessel wall remodeling [7, 8]. High WSS can damage the endothelial layer of blood vessels. Therefore, to control the WSS is critical for the reduction of thrombosis formation.

The systemic-to-pulmonary shunt should keep the balance of the blood supply to PAs. Otherwise, it might result in low coronary perfusion pressure or cannot lessen cyanosis efficiently. The balance of blood flow distribution ratio (FDR) between systemic and pulmonary circulations was critical to evaluate the outcomes of the systemic-to-pulmonary shunt. The oxygen saturation would be changed together with the distribution of blood flow between the pulmonary and systemic circulations. Studies implied that when the value of the FDR reached between 0.5 and 1 [9], the maximal oxygen delivery would be achieved in the procedure. In the present study, the FDR was 0.893, 0.883, 0.916, and 0.917, respectively. Based on previous studies [9, 10], a relatively good balance of blood flow distribution between systemic and

pulmonary circulations were achieved when the conduit was anastomosed at the innominate artery or subclavian artery than it was at the ascending aorta.

## 5 Conclusion

In the present study, we modified the conduit connection position of the systemic-to-pulmonary shunt and investigated the local flow features. We found the surgical design of the conduit connected at Model 3 and Model 4 might be the ideal design to achieve the better hemodynamics. Large scale verification and validation will be done in the future work. The combined technology of CAD and CFD is a possible promising tool for the patient-specific surgical design of the systemic-to-pulmonary shunt.

**Acknowledgements** We have been genuinely appreciative of the support of the National Nature Science Foundation of China (No. 81501558, P.I.: J.L. Liu), the Project-sponsored by the Scientific Research Foundation for the Returned Overseas Chinese Scholars, State Education Ministry (No. 20144902, P.I.: J.L. Liu), and the Fund of The Shanghai Committee of Science and Technology (No. 17DZ2253100, P.I.: J.F. Liu).

**Conflict of Interest** The authors declare that they have no conflict of interest.

## References

1. Sun, Q., Liu, J.L., Qian, Y., Zhang H.B., Wang, Q., Sun, Y.J., Hong, H.F., Liu, J.F.: Computational Haemodynamic Analysis of Patient-specific Virtual Operations for Total Cavopulmonary Connection with Dual Superior Venae Cavae. *European Journal of Cardio-Thoracic Surgery*, <https://doi.org/10.1093/ejcts/ezt394>, (2013).
2. Liu, J.L., Qian, Y., Itatani, K., Murakami, A., Shiurba, R., Miyaji, K., Miyakoshi, T., Umezu, M.: Image-Based Computational Hemodynamics of Distal Aortic Arch Recoarctation Following the Norwood Procedure. In: 4th International Congress on Image and Signal Processing 2011, pp. 318–323. IEEE Press, New York (2011).
3. Wang, Q., Hong, H.F., Sun, Q., Sun, Y.J., Liu, J.F., Liu J.L., Qian, Y. Umezu, M., Hemodynamic Influence of Surgical Methods on Systemic-to-Pulmonary Shunt: Modified Blalock-Taussig Shunt Versus Melbourne Shunt, Proceeding of “The 10th Asian Control Conference 2015 (ACSS 2015)”, Kota Kinabalu, Sabah, Malaysia (2015).
4. Qian, Y., Liu, J.L., Itatani, K., Miyaji, K., Umezu, M.: Computational Hemodynamic Analysis in Congenital Heart Disease: Simulation of the Norwood Procedure, *Ann. Biomed. Eng.*, 38, 2302–2313 (2010).
5. Liu, J.L., Sun, Q., Qian, Y., Hong, H.F., Wang, Q., Sun, Y.J., Umezu, M., Liu, J.F., Medical Image-Based Hemodynamic

- Analysis for Modified Blalock-Taussig Shunt, *Journal of Mechanics in Medicine and Biology*, 15(3), 1550035 (2015).
6. Liu, J.L., Sun, Q., Qian, Y., Hong, H.F., Liu, J.F., Numerical Simulation and Hemodynamic Analysis of the Modified Blalock-Taussig Shunt, Proceeding of "The 35th Annual International Conference of the IEEE Engineering in Medicine and Biology Society", Osaka, Japan (2013).
  7. Adel, M.M., Seth, L.A., Seigo, I., Hemodynamic shear stress and its role in atherosclerosis, *JAMA*, 282(21): 2035–2042 (1999).
  8. Gimbrone, M.A., Resnick, N., Nagel, T., Hemodynamics, Endothelial Gene Expression, and Atherogenesis, *Ann N Y Acad Sci*, 811(1): 1–10 (1997).
  9. Barnea, O., Santamore, W.P., Rossi, A., Salloum, E., Chien, S., Austin, E.H., Estimation of oxygen delivery in newborns with a univentricular circulation, *Circulation*, 98(14): 1407–1413 (1998).
  10. Odum, J., Portzky, M.D., Zurakowski, G., Wernovsky, R.P., Burke, R.P., Jr Mayer, J.E., Castaneda, A.R., Jonas, R.A., Sternotomy approach for the modified Blalock-Taussig shunt, *Circulation*, 92(9): II256–261(1995).

# Parameter Search to Find Ranges of Activation and Inhibition of Wound Healing Rate in a Mathematical Model with Introduced Photobiomodulation

Alistair McQueen, Jacquelyn Dawn Parente, Sean McGinty, and Knut Moeller

## Abstract

When light stimulation is used for wound healing therapy, a biphasic dose-response curve is observed, where cells are activated below and inhibited above a treatment dose threshold. Light treatment-dose responses are not yet incorporated into mathematical models of wound healing—yet these relationships would support optimization of wound healing treatment protocols. This work adapts an existing wound healing mathematical model by exploring parameter values and introducing exogenous photobiomodulation treatment inputs for future applications in model-based experimental research. A wound healing mathematical model, created by Sherratt and Murray in 1990, includes proliferation, migration, and activating and inhibitory chemical terms. This model was implemented and discretized by Forward Euler (FE) in time and the Central Difference Method (CDM) in space in 1D. Travelling wave solutions of cell density and chemical concentration were obtained and used to plot wound closure in time and to estimate the wound healing rate. A parameter search was conducted to identify ranges where model simulations resulted in activation, inhibition, saturation, or numeric instability of wound healing. Published results of photobiomodulation treatment-control studies reporting a percentage change in proliferation were used to scale proliferation terms, thus serving as a proxy for light stimulation. Results showed the inhibition model was more sensitive to parameter variation than the activation model. Changes in the cell migration parameter are most sensitive overall. Most model parameters were bounded by saturation or numeric instabilities, while

otherwise demonstrating activating and/or inhibitory effects on the rate of wound healing. Light stimulation simulations were consistent with expectations that increasing the proliferation term increased wound healing rate. To support photobiomodulation model-based experimental wound healing research, the model parameter search identified threshold values categorizing activation or inhibition of wound healing rate and this work also adapted a model proliferation term consistent with photobiomodulation biological effects.

## Keywords

Mathematical model • Photobiomodulation  
Sensitivity analysis • Wound healing

## 1 Introduction

Mathematical models of wound healing represent coordinated biological processes depending on chemically mediated multi-cellular interactions. Advanced model-based wound healing therapies apply knowledge of these relationships to guide individually optimized treatment protocols [1]. To understand parameter relationships in a wound healing model, we conduct a parameter sensitivity analysis on a species conservation mechanochemical model by Sherratt and Murray [2]. In addition, no existing mathematical models of wound healing incorporate light treatment. Therefore, this work introduces exogenous photobiomodulation treatment inputs to the model.

Equation 1 illustrates the change in cell density, with Eq. 2 demonstrating how the chemical concentration varies with time during the wound healing process. The model's equations are presented below in dimensionless form [2]:

A. McQueen (✉) · S. McGinty  
University of Glasgow, University Avenue, Glasgow, G12 8QQ,  
Scotland  
e-mail: 2076772m@student.gla.ac.uk

A. McQueen · J. D. Parente · K. Moeller  
Institute for Technical Medicine, Jakob-Kienzle Strasse 17, 78054  
Villingen-Schwenningen, Germany  
e-mail: pjd@hs-furtwangen.de

$$\frac{\partial n}{\partial t} = D\nabla^2 n + \left( \frac{2c_m(h-\beta)c}{c_m^2 + c^2} + \beta \right) n(2-n) - n, \text{ with}$$

$$\beta = \frac{1 + c_m^2 - 2hc_m}{(1 - c_m)^2} \quad (1)$$

$$\frac{\partial c}{\partial t} = D_C \nabla^2 c + \delta \left( \frac{n(1 + \alpha^2)}{n^2 + \alpha^2} \right) - \delta c, \quad (2)$$

where  $n$  is cell density, and  $c$  is chemical concentration. In the first term on the right-hand side of Eq. 1,  $D$  portrays cell migration by a diffusive term. Several terms represent cell mitosis:  $h$  is the difference in mitosis rates between wounded and unwounded dermis; and  $c_m$  is the maximum rate of mitosis, as controlled by the chemical mediator.  $\beta$  is used to group parameters for simplification. The chemical mediator,  $D_C$ , represents diffusion, where  $\delta$  is chemical decay, a first order kinetic parameter. The chemical production term,  $\alpha$ , dictates the maximum rate of chemical production.

The inhibitor model below implements similar fundamental equations as the activator model above; with altered cell proliferation and chemical production terms. Equations 3 and 4 describe a chemical inhibitor model in dimensionless form [2]:

$$\frac{\partial n}{\partial t} = D\nabla^2 n + \left( \frac{(h-1)c+h}{2(h-1)c+1} \right) n(2-n) - n, \quad (3)$$

$$\frac{\partial c}{\partial t} = D_C \nabla^2 c + \delta n - \delta c. \quad (4)$$

The parameters in the inhibitor model have the same characteristics as described within the activator model. Both the activator and inhibitor models employ Dirichlet boundary conditions at the wound centre, equivalent to the unwounded tissue value, and a zero-flux Neumann boundary condition at the wound centre, preventing the movement of cells and chemicals to and from the wound [2].

## 2 Method and Materials

The model equations were discretized in time by Forward Euler and in space by the Central Difference Method. The algebraic equations progress forward in time when plotting travelling wave solutions; illustrating how both species migrate through the wound space during the healing process. From this, the minimal healing time was devised, allowing for the relative time taken for the wound to close be demonstrated.

A sensitivity analysis was conducted to demonstrate the effect on healing time by, relative to the original healing time

(relative healing time), altering individual parameters; providing insight into how the model parameters alter wound healing characteristics. Minimum and maximum parameter values were defined for a fixed mesh size, where the results illustrated behaviour which was numerically unstable or stagnated. Stagnation was defined upon observing a 1% (or less) change in relative heal time after varying the parameter by a single order of magnitude. The total heal time was selected as a marker point for comparison. The extensive sensitivity analysis depicts the change in relative wound healing time to variations of individual parameters within the model, thus providing an initial concept into understanding the effect of light stimulation for wound healing; illustrated through a mathematical model.

After implementing a generic mathematical model portraying wound closure, a simplistic approach into understanding photobiomodulation was addressed in the model. Within the literature, cells proliferation is often noted as a cellular response to light stimulation. Relevant literature was found using the Web of Science (WoS) database, searching for keywords including: 'Light Stimulation', 'LED', 'Wound Healing' and 'Proliferation'. The search was limited to papers published since July 2007. Additionally, most methodologies involving wound healing via light stimulation implement different parameters involving the irradiation of light. Therefore, the fundamental inclusion criteria were to present results from experimental publications which kept irradiation parameters as similar as possible.

The effect of light stimulation was incorporated into the mathematical model by scaling the proliferation term by the percentage increase documented experimentally. This procedure was only applied to the activator model because all experiments documenting positive results to wound healing by the stimulation of red light. Therefore, parameters  $h$  and  $c_m$  were those primarily effected, illustrating the change in mitosis rate between wounded and unwounded skin and by a chemical mediator, respectively. Five papers in total were used, reporting changes in cell proliferation upon light stimulation, and is documented within Table 3 [3–7].

## 3 Results

The mathematical models were implemented in 1D to obtain travelling wave solutions to the activator and inhibitor models using original parameter values [2]. The solutions demonstrate cell density and chemical concentration throughout the wound space, and how these levels vary in time. The interval spacing defines the wave speed.

Tables 1 and 2 present parameter sensitivity analysis results for the activator and inhibitor models. Decreased healing time was observed in both models upon decreasing parameters  $D_C$ ,  $c_m$ , and  $\alpha$ . However, increasing these values

**Table 1** Sensitivity analysis of activator model (dimensionless results). For each parameter value, the minimum, original [2], and maximum parameter values are shown in bold, below which are the corresponding times to wound closure, relative to the original heal time. At parameter values beyond the limits, the model results were characterized as saturated (S) or numerically unstable (U)

Parameter	Minimum	Original [2]	Maximum
D heal time	– increasing	<b>0.0005</b> 1	– decreasing
$D_C$	<b>0.0005</b> (S) 0.69	<b>0.45</b> 1	<b>0.9</b> 1.04 (U)
$\delta$	<b>0.03</b> (S) 1.18	<b>30</b> 1	<b>~14900</b> 0.69 (U)
$h$	<b>0.1</b> (S) 1.24	<b>10</b> 1	<b>100</b> 0.79 (–)
$c_m$	<b>~5</b> (U) 0.79	<b>40</b> 1	<b>1000</b> 1.18 (S)
$\alpha$	<b>0.0001</b> (U) 0.70	<b>0.1</b> 1	<b>10</b> 2.49 (S)

**Table 2** Sensitivity analysis of inhibitor model (dimensionless results)

Parameter	Minimum	Original [2]	Maximum
D heal time	– increasing	<b>0.0001</b> 1	– decreasing
$D_C$	<b>~0.4</b> (U) 0.4	<b>0.85</b> 1	<b>1.7</b> 2.3 (U)
$\delta$	<b>0.05</b> (S) 1.14	<b>5</b> 1	<b>~10</b> 0.74 (U)
$h$	<b>0.5</b> (U) 1.37	<b>10</b> 1	<b>10,000</b> 0.9 (U)

increased the relative heal time. Alternatively, relative heal time increased when decreasing  $D$ ,  $\delta$ , and  $h$ , while increasing these parameters produced a decreased heal time. Overall, parameter behaviours trends are similar for chemical activator and chemical inhibitor models. Yet, the inhibitor is more sensitive to parameter variation; numerical results tend towards numerical instability, over stagnation. Unstable model results are noted at fixed mesh values, therefore the parameter bounds observed vary upon altering the mesh.

**Table 3** Scaling the model proliferation term by documented proliferation increase (at various irradiation parameters) decreases healing time. The original parameter values were used [2]

Dose [J/cm <sup>2</sup> ]	Wavelength [nm]	Proliferation increase [%]	Closure time [%]	Travelling wave [mm/h]
Control	–	–	100	$2.20 \times 10^{-3}$
4 [3]	627	52.0	72.0	$3.30 \times 10^{-3}$
5 [4]	670	27.5	81.20	$2.75 \times 10^{-3}$
6 [5]	640	25.0	83.11	$2.75 \times 10^{-3}$
10 [6]	700	11.6	90.87	$2.70 \times 10^{-3}$
16 [7]	640	10.0	92.31	$2.68 \times 10^{-3}$

For example, the result of varying parameter  $h$  for the activator model is described. Murray and Sherratt used  $h = 10$ , based upon experimental results [2]. Decreasing  $h$  from the original value increased heal time, while increasing the value decreased heal time. A minimum bound at  $h = 0.1$  with a relative heal time of 1.24, where the result stagnated. A maximum bound was observed at  $h = 100$ , with a relative heal time of 0.79, where increasing  $h$  beyond this value increased healing time.

Table 3 presents the time taken for the wound to close and travelling wave speed when stimulated by varying doses of red light. The results agree with conclusions drawn from Chaves et al. [8]. A minimum value is observed at 4 J/cm<sup>2</sup>, illustrating an overall decrease in wound healing time by 28.00%. For two successive singular increments in dosage, the healing time only reduced by 18.8 and 16.89% respectively. Increasing the dosage to 10 and 16 J/cm<sup>2</sup> illustrates only slight decreases in the healing time by 9.13 and 7.59% respectively. The results represent a positive response, where increases in the proliferation scaling decrease heal time.

## 4 Discussion

The parameter sensitivity analysis demonstrates activating or inhibiting behaviour towards maximum and minimum value bounds, where unstable or stagnant behaviour was observed. The results portrayed the sensitive behaviour of  $D$  which, unlike other parameters, is independent of chemical mediators and hence, heavily influences the travelling wave speed and heal time directly.

Altering cellular proliferation parameters,  $h$  and  $c_m$  of the activator model has opposite effects. Increasing  $h$  saw cell density levels fall below the chemical concentration, thus decreasing heal time; with cell density levels increasing above the chemical concentration for increments beyond  $h = 100$ . Decreasing  $c_m$  illustrated stability issues, with interval spacing at the wound centre increasing for decreased values of  $c_m$ . Increasing  $c_m$ , unlike other parameter variations, saw the chemical concentration increase gradually towards the wound centre, whilst also decreasing the



travelling wave speed, possibly explaining why healing time increased.

For chemical mediator parameters, increasing  $D_c$  and  $\alpha$  increased heal time, while increasing  $\delta$  decreased heal time. The former two noted decreased levels of chemical concentration when their values were decreased, resulting in an increased heal time. Whereas, increasing  $\delta$  demonstrated the opposite effect.

An initial approach to incorporating the effects of photobiomodulation into wound healing illustrates the positive effects red light had on relative healing time. Scaling the proliferation term influences  $c_m$  and  $h$ , which dictate chemical activity and mitosis rates, respectively. Increasing the scale reduced healing time, which reflects experimental results documenting increased proliferation rates and reduced healing times.

When compared to Arndt-Schulz curve (which portrays bi-phasic cellular activation and inhibition at a threshold dosage [8]) the results do not demonstrate a sharp decrease in cell proliferation. Only doses of  $4 \text{ J/cm}^2$  and greater are presented. Thus, the activation increase towards a maximum is not represented. Lastly, the light doses, irradiation parameters, and experimental models are not similar [3–7].

## 5 Conclusion

Understanding wound healing mathematical model parameter behaviour aids the development of advanced model-based therapies to modulate wound healing processes. This work identified the numerical behaviour of model parameters and their effects on wound healing time. Additionally, an initial methodology to incorporate

photobiomodulation was introduced, to account for documented cellular proliferation responses to red light as a positive influence on decreasing wound closure rate.

**Acknowledgements** This study was partially supported by the German Federal Ministry of Research and Education (BMBF under project OWID/IP1 CoHMED grant number FKZ 13FH5I01IA

**Conflict of Interest** The authors declare they have no conflict of interest

## References

1. Parente, J. D. & Möller, K., 'A control system design to establish dose-response relationships in wound healing therapy', *J Biomed Sci Eng*, 10(5), 76–85, 2017.
2. Sherratt, J.A. & Murray, J. D., 'Models of epidermal wound healing', *Proc Biol Sci.*, 241, 29–36, 1990.
3. Komine et al, 'Activation of the extracellular signal-regulated kinase signal pathway by light emitting diode irradiation', *Lasers Med Sci*, 25, pp. 531–537, 2010.
4. Lanzafame. J.R et al, 'Reciprocity of Exposure Time and Irradiance on Energy Density During Photo radiation on Wound Healing in a Murine Pressure Ulcer Model', *Lasers in Surgery and Medicine*, 39, pp. 534–542, 2007.
5. Agnol. D.A.M, 'Comparative analysis of coherent light action (laser) versus non-coherent light (light-emitting diode) for tissue repair in diabetic rats', *Lasers Med Sci*, 24, pp. 909–916, 2009.
6. Susana. C.P et al, 'Effect of laser and LED phototherapies on the healing of cutaneous wound on healthy and iron-deficient Wistar rats and their impact on fibroblastic activity during wound healing', *Lasers Med*, 28, pp. 799–806, 2013.
7. Nogueira. C.V et al, 'Biomodulation effects of LED and therapeutic ultrasound combined with semipermeable dressing in the repair process of cutaneous lesions in rats', *Acta Cir. Bras*, 29, pp. 588–595, 2014.
8. Chaves et al, 'Effects of low-power light therapy on wound healing: LASER x LED', *An Bras Dermatol*, 89(4), pp. 616–623, 2014.

# The Effects of Expiratory Flow Limitation and Different Inspiratory and Expiratory Airway Resistances on Dynamic Hyperinflation of the Lungs: A Bench Study

Václav Ort and Lukáš Konupka

## Abstract

Dynamic hyperinflation occurs when mean alveolar pressure exceeds the mean airway pressure measured in the airway opening. The dynamic hyperinflation develops as a consequence of insufficiently long expiration terminated by the subsequent inspiration. Two main principles are supposed to create the dynamic hyperinflation during high frequency oscillatory ventilation (HFOV): expiratory flow limitation and different inspiratory and expiratory airway resistances ( $R_e > R_i$ ). The aim of the study is to design and test a physical model of the respiratory system comprising both the mechanisms causing dynamic hyperinflation and to characterize their effect upon dynamic hyperinflation or hypoinflation development during HFOV. The models were created using a rigid volume and passive pneumatic components mimicking the required characteristics of the airway resistance. The models were connected to a HFOV ventilator and different ventilator settings were applied in order to investigate the parameters having the most significant effect on dynamic hyperinflation development. The main result of the study is that the expiratory flow limitation corresponds better with the observed and published properties of the respiratory system during HFOV. The magnitude of dynamic hyperinflation depends on ventilator setting. The acquired results are supported by recently published studies using mathematical-physical modeling and correspond with results of the published clinical trials.

## Keywords

Expiratory flow limitation • Dynamic hyperinflation  
High-frequency oscillatory ventilation

## 1 Introduction

High frequency oscillatory ventilation (HFOV) is an unconventional ventilatory regimen that is characterized by using very small tidal volumes applied with a high ventilatory frequency (2–15 Hz). As the tidal volumes are small, comparable to the dead space volume of the respiratory system (RS), HFOV is supposed to be a typical representative of so called protective ventilatory techniques. On the other hand, HFOV is associated with several adverse phenomena. A possibility of development of a lung dynamic hyperinflation (DH) belongs to them and was documented in several published studies [1–3].

DH can be characterized as a state where the mean alveolar pressure ( $mPalv$ ) is higher than the mean airway pressure ( $mPaw$ ) measured in the airway opening [1]. The pressure gradient between the alveolar space and the airway opening develops due to the asymmetry of the inspiratory and expiratory flow resistance. As a consequence, an insufficient expiration occurs, interrupted by the subsequent inspiration [4]. DH can affect safety and efficiency of mechanical ventilation. Several studies, both theoretical and experimental, documented even opposite effect called dynamic hypoinflation, when  $mPalv$  may be lower than  $mPaw$ , under certain conditions [5, 6].

Using a computer model, Solway et al. [3] proposed two principal mechanisms, how the dynamic hyper- or hypo-inflation may develop. First, higher expiratory flow resistance than the inspiratory flow resistance ( $R_e > R_i$ ) may generate the pressure difference; second, a limitation of expiratory flow rate, pronounced and been typical for example in chronic obstructive pulmonary disease (COPD) patients, may significantly contribute to the creation of the pressure difference between  $mPalv$  and  $mPaw$ .

The aim of this study is to design and to test passive models of the respiratory system mimicking both the principal ways of creation of dynamic hyper/hypo-inflation and

V. Ort (✉) · L. Konupka  
Faculty of Biomedical Engineering, Czech Technical University  
in Prague, nám Sítná 3105, 272 01 Kladno, Czech Republic  
e-mail: ortvacla@fbmi.cvut.cz

to validate the model during high-frequency oscillatory ventilation.

## 2 Methods

Three sets of models have been created corresponding to three main types of patients with a respiratory insufficiency or limitation: a normal healthy subject, an adult patient with a mild airway obstruction, and an adult patient with severe COPD. Each set of models comprised several models of the respiratory system and the expiratory flow limitations. Except for one, where  $Re = Ri$ , all others were characterized by  $Re > Ri$ .

Preferably, the inspiratory flow resistance characteristics were identical in all the models, whereas they differed in expiratory flow characteristics, as documented in Fig. 1.

The compliance of all the models of the RS was realized by a rigid glass container with a predetermined volume.

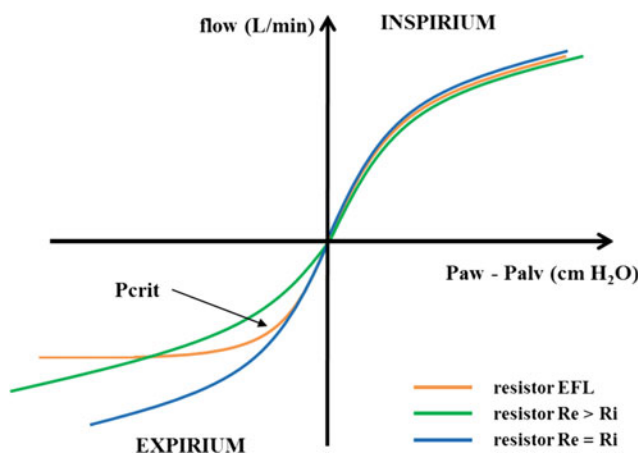


**Fig. 1** The measured pressure-flow characteristics of the modeled airways.  $P_{crit}$  stands for a point where the expiratory flow limitation starts to develop. EFL—expiratory flow limitation

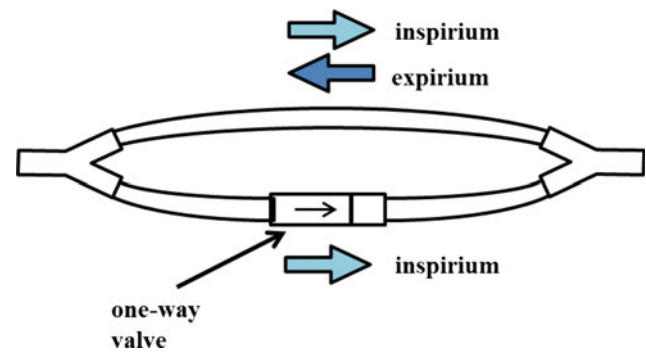


**Fig. 2** Schematics of the airway part of the RS model with  $Re > Ri$ . Inspirium occurs thru both limbs of the model, expirium only at limb without one-way valve

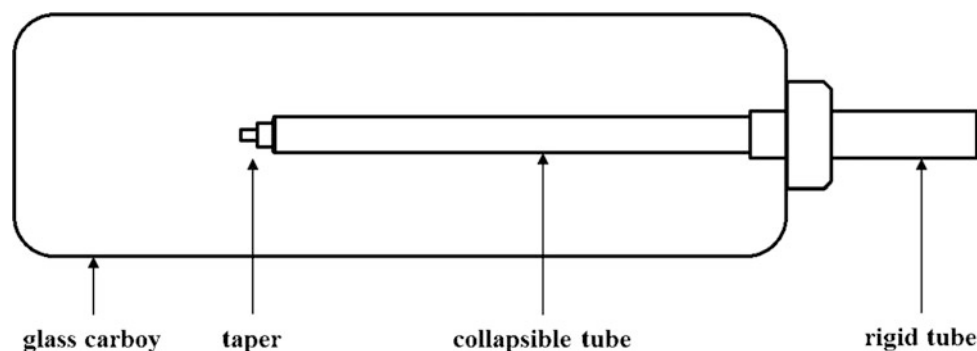
While the uniform model (the symmetric one, where  $Re = Ri$ ) consisted of a simple endotracheal tube, the asymmetric model with  $Re > Ri$  consisted of a parallel combination of two different cannulas; one rigid and the second collapsible equipped with a one-way valve as documented in Fig. 1.

The assembling of the model of the airways comprising the mechanical parts is depicted in Fig. 2. The collapsible part of the airway model is situated inside the compliance model so that the alveolar pressure can affect the expiratory flow resistance by compressing the compressible airways, as depicted in Fig. 3.

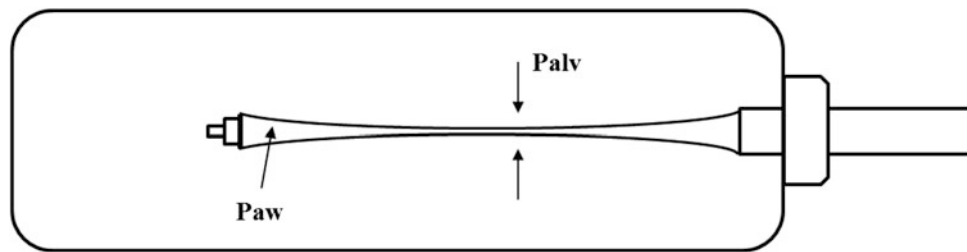
In this physical model, when  $P_{alv}$  becomes higher than  $P_{aw}$ , the collapse of the airways occurs and the expiratory flow limitation develops as a consequence.

Figure 4 demonstrates that increasing expiratory effort pronounces the expiratory flow limitation and further increases the expiratory flow resistance.

Using the constructed set of models (details are presented in Table 1), the pressure-flow characteristics of the corresponding models were measured. The simulations were conducted for different alveolar pressures related to the airway pressure measured at the airway opening.



**Fig. 3** Scheme of the RS model with expiratory flow limitation



**Fig. 4** Principle of the expiratory flow limitation when alveolar pressure exceeds the airway pressure

**Table 1** Overview of the created models of the RS and their measured characteristics

Set	Label	Inspiratory resistance (cm H <sub>2</sub> O · s/L) at 1 L/s	Expiratory resistance (cm H <sub>2</sub> O · s/L) at 1 L/s	Pcrit (cm H <sub>2</sub> O)	Maximal flow (L/min)
A	A1 (EFL)	6.4	–	4.0	0.37
	A2 (EFL)	3.7	–	3.5	0.5
	A3 (Re > Ri)	4.0	9.0	–	–
	A4 (Re = Ri)	4.2	4.3	–	–
B	B1 (EFL)	13.1	–	4.2	0.38
	B2 (Re > Ri)	12.8	15.6	–	–
	B3 (Re = Ri)	12.3	12.3	–	–
C	C1 (EFL)	21.0	–	6.5	0.31
	C2 (EFL)	20.4	–	5.0	0.42
	C3 (EFL)	19.3	–	12.0	0.43
	C4 (Re > Ri)	20.8	43.3	–	–
	C5 (Re = Ri)	21.6	21.3	–	–

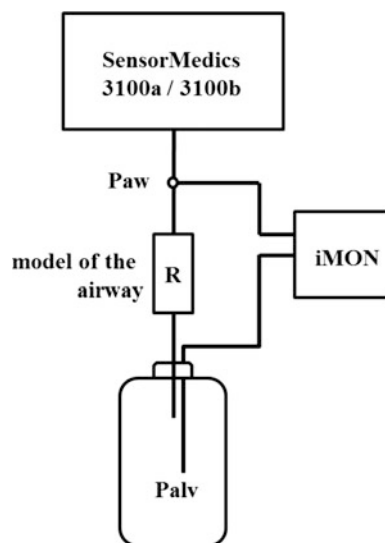


**Fig. 5** The overall scheme of the experiment testing the effects of Ri to Re relations upon development of dynamic hyper- or hypo-inflation

So that the simulations resembles the real clinical scenarios, the measurement was conducted using two most common HFOV ventilators: SensorMedics 3100a and 3100b (CareFusion, Yorba Linda, California, USA). Paw and Palv were measured using a custom made system iMON [7]. The measuring assembly is depicted in Fig. 5. The HFOV ventilator setting was as follows: bias flow = 25 L/min, inspiratory time  $T_i/T$  (%Ti) was 33% and 50%, power of oscillations ( $\Delta P$ ) were 50, 75 and 100 cm H<sub>2</sub>O, oscillatory frequency was 5 Hz.

### 3 Results

The results of simulation are presented in the following graphs for different characteristics of the respiratory system. Results for normal airways of an adult are presented in Fig. 6, whereas the results for mild airway obstruction are presented in Fig. 7 and for an adult with COPD are presented in Fig. 8.

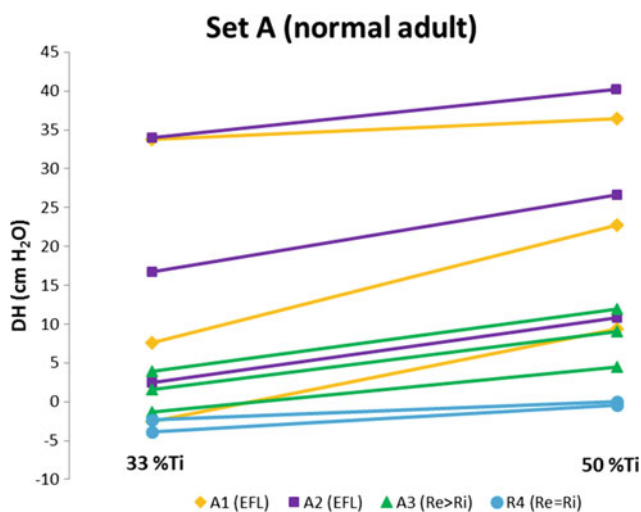


**Fig. 6** Dependence of dynamic hyperinflation upon relative inspiratory time ( $T_i/T$ , or % $T_i$ ) for oscillatory amplitudes of 50, 75 and 100 cm  $H_2O$  for healthy adult subject

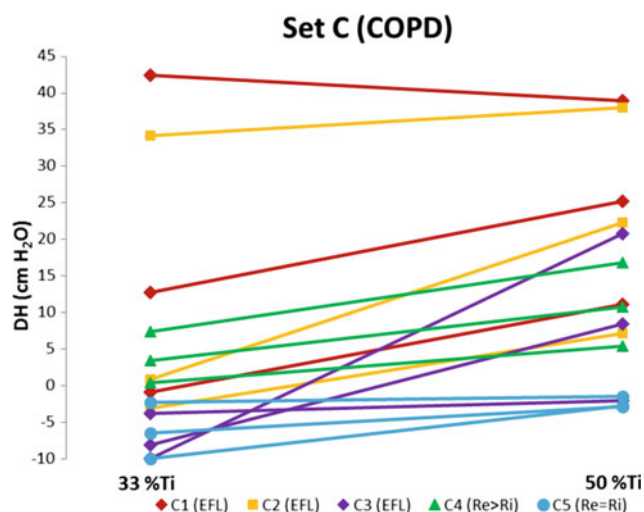


**Fig. 8** Dependence of dynamic hyperinflation upon relative inspiratory time ( $T_i/T$ , or % $T_i$ ) for oscillatory amplitudes of 50, 75 and 100 cm  $H_2O$  for a COPD patient model

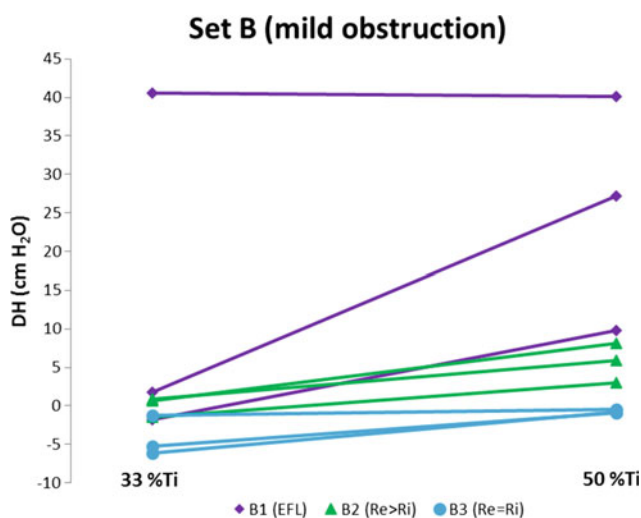


**Fig. 7** Dependence of dynamic hyperinflation upon relative inspiratory time ( $T_i/T$ , or % $T_i$ ) for oscillatory amplitudes of 50, 75 and 100 cm  $H_2O$  for a subject with mild airway obstruction

The above presented results demonstrate that the principal cause of the DH development consists in collapsible airways causing the expiratory flow limitation.

## 4 Discussion

The main finding of the study is that the highest dynamic hyperinflation occurs in the model with the expiratory flow limitation. According to the analysis of the measured pressure-flow characteristics, the hyperinflation occurs for pressures higher than the critical pressure  $P_{crit}$  and  $Re > Ri$ ,

whereas the model develops a hypoinflation for pressures less than  $P_{crit}$  and  $Re = Ri$ . These results correspond with the formerly published studies about mathematical and physical modeling [3] and laboratory experiments with models where  $Re = Ri$  [5, 8].

The fact that the expiratory flow limitation model may develop both dynamic hyperinflation and dynamic hypoinflation can help to explain different results of clinical trials, when some authors confirmed development of dynamic hyperinflation during HFOV [1–3] whereas others confirmed development of dynamic hypoinflation during HFOV [5, 6, 8].

The current study was designed in order to investigate the effects of various resistors (i.e. expiratory flow limitation resistors,  $Re = Ri$  and  $Re > Ri$ ) upon development of dynamic hyperinflation. To investigate development of dynamic hypoinflation in models with the expiratory flow limitation a separate study should be conducted, focused on this phenomenon.

## 5 Conclusion

Using a set of created models of the respiratory system mimicking the real inspiratory-to-expiratory resistance asymmetry and expiratory flow limitation, the ventilatory parameters affecting creation of dynamic hyper- or hypo-inflation were identified. The expiratory flow limitation plays the major role in the DH creation. DH increases also with increasing  $T_i/T$  time (% $T_i$ ) and the amplitude of HFOV oscillations. These findings suggest that for a rationale clinical use of HFOV, preferably without adverse pressure



effects, the effect of dynamic hyper- or hypo-inflation development must be considered for a safety of a patient.

**Acknowledgements** The study was supported by Czech Technical University in Prague grant No. SGS16/258/OHK4/3T/17.

**Conflict of Interest** The authors declare no conflict of interest.

---

## References

1. Simon B, Weinmann G, Mitzner W (1984) Mean airway pressure and alveolar pressure during high-frequency ventilation. *Journal of Applied Physiology* 57:1069–1078.
2. Pepe P, Marini J (1982) Occult Positive End-Expiratory Pressure in Mechanically Ventilated Patients With Air-Flow Obstruction - The Auto-PEEP Effect. *American Review of Respiratory Disease* 126:166–170.
3. Solway J, Rossing T, Saari A, Drazen J (1986) Expiratory flow limitation and dynamic pulmonary hyperinflation during high-frequency ventilation. *JOURNAL OF APPLIED PHYSIOLOGY* 60:2071–2078.
4. Kimball W, Leith D, Robins A (1982) Dynamic Hyperinflation and Ventilator Dependence in Chronic Obstructive Pulmonary Disease. *American Review of Respiratory Disease* 126:991–995.
5. Pillow J, Neil H, Wilkinson M, Ramsden C (1999) Effect of I/E ratio on mean alveolar pressure during high-frequency oscillatory ventilation. *JOURNAL OF APPLIED PHYSIOLOGY* 87:407–414.
6. Easley R, Lancaster C, Fuld M, Custer J, Hager D, Kaczka D, Simon B (2009) Total and regional lung volume changes during high-frequency oscillatory ventilation (HFOV) of the normal lung. *Respiratory Physiology* 165:54–60. <https://doi.org/10.1016/j.resp.2008.10.010>.
7. Roubik K Measuring and evaluating system designed for high frequency oscillatory ventilation monitoring.
8. Ort V, Roubik K (2015) The Effect of Dynamic Hypoinflation during High Frequency Oscillatory Ventilation in an in Vitro Model of the Respiratory System. 5th IEEE International Conference on E-Health and Bioengineering.

---

**Part V**

**BME and MP Education, Training and Professional  
Development**

# A Novel Online Training Platform for Medical Image Interpretation

S. M. da Silva, S. C. M. Rodrigues, M. A. S. Bissaco, T. Scardovelli,  
S. R. M. S. Boschi, M. A. Marques, M. F. Santos, and A. P. Silva

## Abstract

One of the major problems in the health area is false positive and negative diagnoses, especially in the interpretation of radiological images. Several papers affirm that the radiologist experience helps in accurate diagnosis, reducing inter-observer and intra-observer variability. We assume that the lack of training is causing this problem and if a good training process is on place can reduce the level of false positive and false negative diagnosis, and this training should start at the undergraduate level. Thus, this paper aims to show an online training platform applied to of interpretation imaging learning. The platform was developed using the *php* language and is hosted on the 000webhost server, consisting of an image base (format, *png, jpg, tiff and DICOM*), diagnostic imaging tests and user training quiz (students/residents) about radiographic images interpretation. The teacher can add images, prepare diagnostic tests and create questionnaires. The users perform the diagnostic tests and answer the questionnaires, obtaining a score in real time. This platform can be used inside and outside the classroom, where they can train the diagnosis by image to improve their knowledge. The platform was tested by 20 medical students that, after use it, answered the usability tests based on the SUS scale. The usability tests results showed that 90 of the users gave the maximum concept to the platform.

## Keywords

Learning • Interpretation medical images • Image diagnostic

S. M. da Silva (✉) · S. C. M. Rodrigues · M. A. S. Bissaco  
T. Scardovelli · S. R. M. S. Boschi · M. F. Santos · A. P. Silva  
Biomedical Engineering, University of Mogi das Cruzes, São  
Paulo, Brazil  
e-mail: simone.silva14@fatec.sp.gov.br

M. A. Marques  
Instituto de Ciência e Tecnologia, São Paulo State University,  
Sorocaba, Brazil

## 1 Introduction

Medical error due to misinterpretation of clinical exams is a delicate issue and happens frequently [1], especially when these exams require images interpretation and it shows the difficulty of evaluating the medical images structure that leads to false positive and negative diagnoses. These misinterpretations are related to many factors, including the lack of knowledge of the professional that lead us to the importance of a good training process for the medical student.

The use of technological resources such as computers, projectors and even mobile phones to support classroom teaching has become increasingly common [2] as well the training [3]. These features enable the teacher to upload a video using the Youtube platform and share instantly with their students, or ask them to answer to a quiz, using their own mobile phone, for example. This facilitates the teacher's work, because it is practical and often more illustrative, contributing positively to improve their skills [4].

The objective of this work was to develop an online training platform that can be applied to teach medical imaging and can be used inside and outside the classroom.

In a study carried out in the United States, the researchers compared ten most used learning techniques and concluded that among them the quiz technique and the distributed study were the techniques classified as "High Efficiency" [5]. Based on this study the quiz techniques and the idea of the distributed study were added to the platform.

### 1.1 Background

In the recent literatures several papers directly related to this research were found.

The Table 1 shows a summary of the analysis performed.

Some important parameters were observed to develop this platform, such as:

**Table 1** Problems encountered on the searched platforms

Name	Lack of interactivity	Paid	Mammography images only	Quiz	Score feedback
QualIM [6]			×		
Mamodb [7]			×		
Web-based Mammography [8]			×		×
Capricorn [9]					
Radiopaedia	×			×	×
RADPrimer (Elsevier 2016)		×		×	×

- The importance of initiatives related to teaching medical image analysis;
- The importance of medical images interpretation training;
- All software and web sites analyzed are applied to radiologists, none were applied to use during the medical image analysis classes;
- The free ones are “incomplete” and have lack of interactivity, which suggests more studies of practical applications to understand their real benefits.

## 2 Materials and Methods

The first stage of the project was to define the learning content of the platform, therefore it was defined that the platform will have two test modules: (a) diagnostic imaging tests to mark the image area requested by the teacher. (b) questionnaires on subjects addressed by the teacher.

The actors, who will use the platform, will be the Students and Teachers and based on this, it was defined that the teacher would be allowed to insert images, prepare the tests and questionnaires with templates and the student to carry out the tests and questionnaires requested by the teacher.

The Fig. 1 illustrates this process through a use case diagram:

The platform does were:

- The teacher uploads the image, marks the area to be studied, confirms the marking;
- The marking is saved in the database and only the original image becomes available to the student;
- The student analyzes the image and marks the area of interest requested;
- The system will check if the student’s mark matches with the area of interest marked by the teacher;

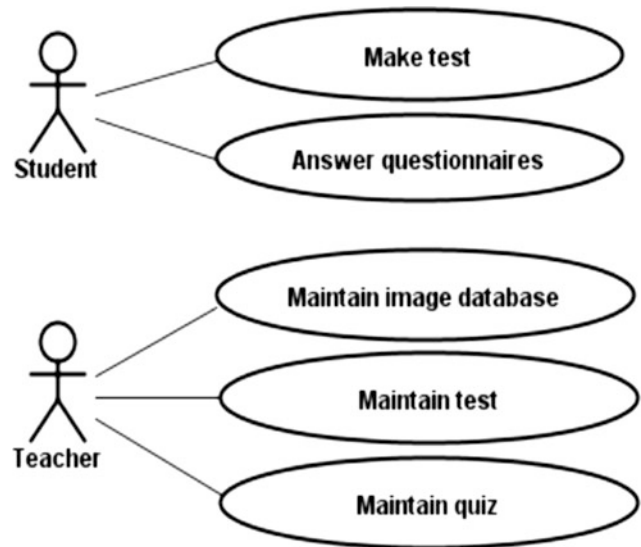


**Fig. 1** Use case of the actors illustrating the interactions of each one with the platform

- If yes, a message appears saying that the student has hit;
- Otherwise, a message appears saying that the student has missed.

The quiz development was based on the Google Forms questionnaires, where the teacher can insert the questions, the answers, the value of each question and the system will calculate the final score.

Once the questionnaire has being saved it will become available to the student, that could answer the questions and at the end will receive the score.

### 2.1 Sample Description

For the platform tests were invited 20 medical students from University of Mogi das Cruzes (Brazil), attending the

discipline of medical images, which after using the platform answered the usability and functionality tests.

## 2.2 Usability Test

The Usability Test was applied based on the SUS (System Usability Scale) scale [10] and the purpose of this test is to measure the platform usability.

The SUS results are calculated using the answers that may be between 1 and 5, where 1 represents “strongly disagree” and 5 “completely agree”. To calculate the final score, it is necessary to conduct the follow actions:

- For odd answers (1, 3 and 5): subtract one from the user response.
- For even answers (2 and 4): subtract the user responses from 5.
- Once done the items above it is necessary to add all values and multiply by 2.5.

The final calculation should be between 0 and 100 and this number will be used to classify the platform according to the grade scale F, D, C, B and A, being the scale “A” a of greater usability. See Fig. 2 [11].

## 2.3 Functionality Test

The Functionality Test was based on the Likert scale, being rated from 1 to 5, with 1 “completely disagree” and 5 “I completely agree”. The difference is that in this case, the more questions get closer to grade 5, greater is the platform functionality.

For the data analysis, we use the statistical value of mode the statistical value.

## 3 Results

The platform developed addresses the two most efficient learning techniques, the questionnaire and distributed study by being online.

It is possible to upload images using *png*, *jpg*, *tiff* and *DICOM* formats. After uploading the image, the teacher can select the area of interest that he wants the student to work on, once the area of interest by the teacher is marked the image becomes available for the student use. The Fig. 3 show this process:

Likewise, the questionnaire is developed by the teacher and become available to the student. The Fig. 4 show this process:

After the student answers the questionnaire, the score is obtained in real time, that allows him to verify his performance.

The platform tests obtained a score of 90, which results in a classification A. This means that the platform has “best imaginable” rating, according to Fig. 2.

The Functionality Test shows that the platform must have more functionalities.

## 4 Discussion and Conclusion

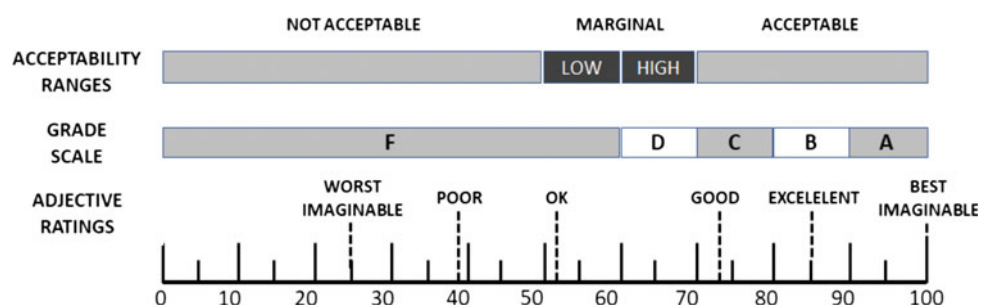
According to some authors, it can be observed that there is a high incidence of medical misinterpretation in the diagnostic imaging [12–14]. The goal of this platform is to reduce these errors and could be a differential for users. A better imaging diagnoses training for the students (radiologists), will support this errors reduction.

There are several initiatives to develop technological content to help the radiologist training, however, there are some shortcomings such as: lack of interactivity, paid platforms, only mammography images available, no questionnaires available and the end results are not show right away.

Some efficient teaching techniques, such as, questionnaires and distributed practice [5] have been studied trying to relate neuroscience to the act of learning to learn. The proposal platform uses these techniques besides testing the student’s skills through questionnaires and diagnostic imaging tests, that can be executed anywhere and anytime.

With this work, it was possible to develop an online training platform to aid the medical image analysis teaching. As future work, tests need to be applied to measure the teaching efficiency of the platform.

Fig. 2 SUS scale





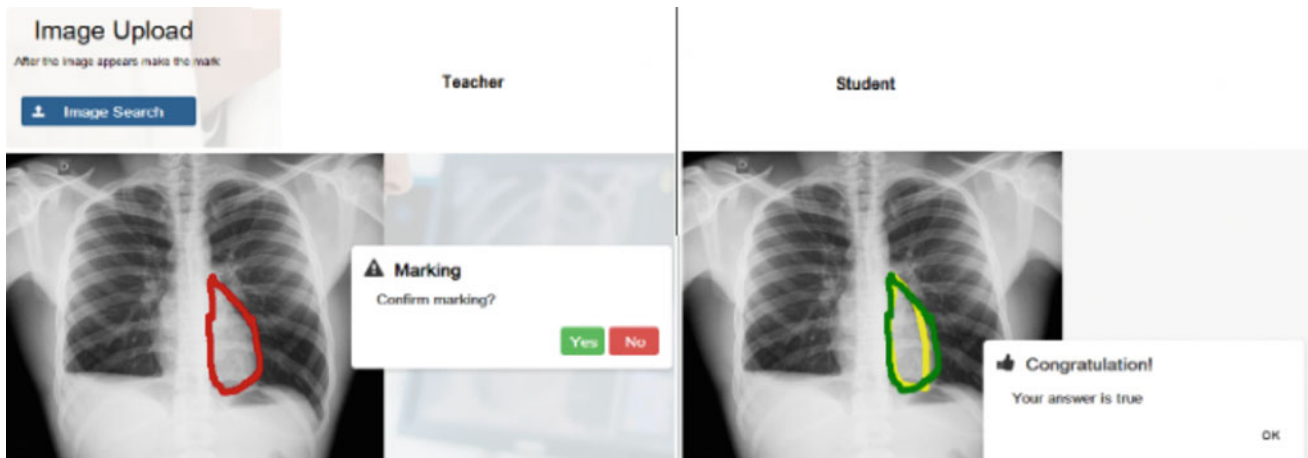


Fig. 3 Teacher and student screen

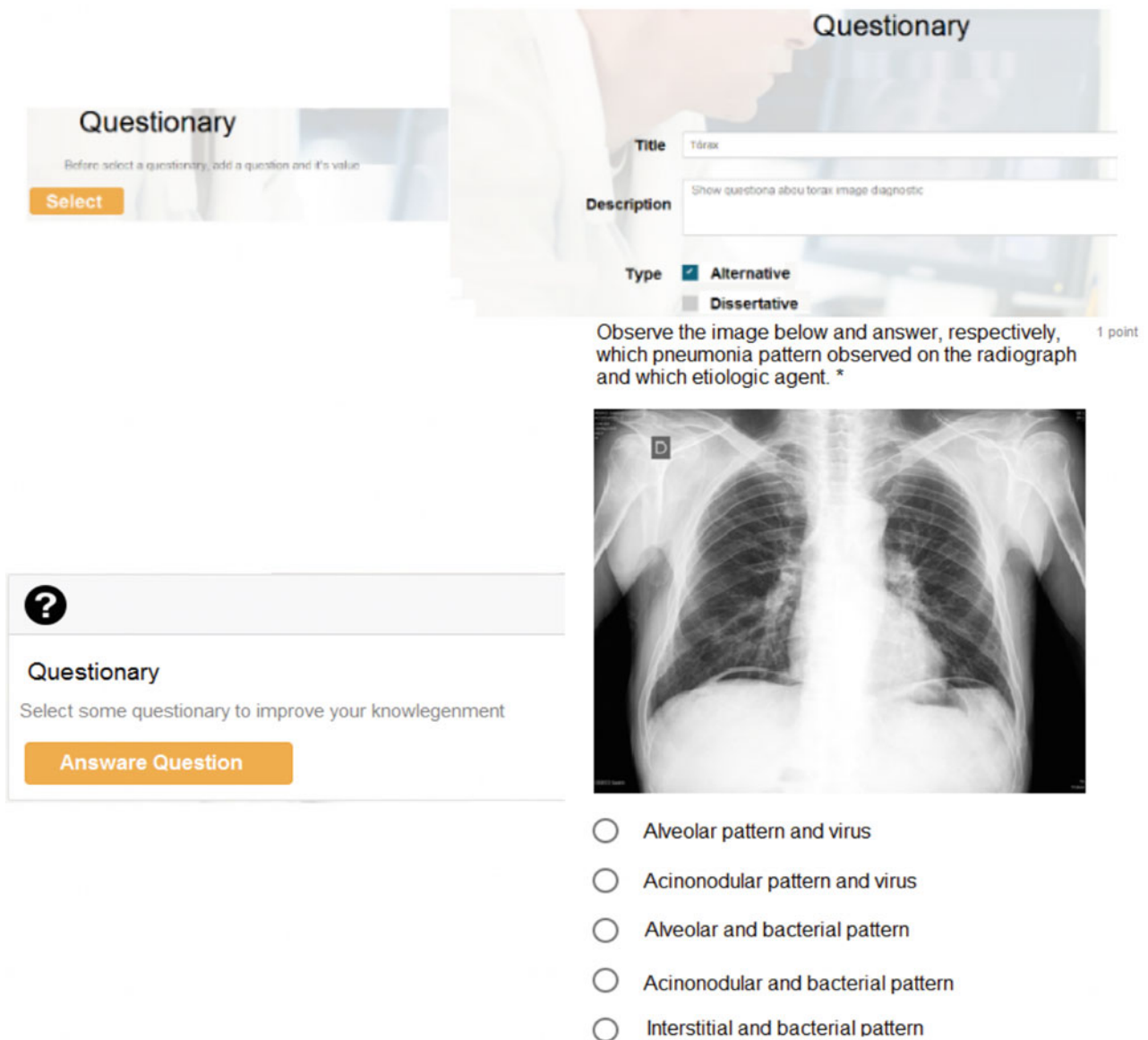


Fig. 4 Questionnaire screen

**Acknowledgements** The FAEP—Foundation for Support to Education and Research of University of Mogi das Cruzes, financial support from FAPESP—São Paulo Research Foundation (Grant No. 2017/14016-7) and CAPES (Coordenação de Aperfeiçoamento de Pessoal de Nível Superior).

**Conflict of Interest** The authors declare that they have no conflict of interest.

## References

1. Brandão, P. e Reis, A. M.: Erro Médico em Imagiologia - Performance e Sistemas de Detecção Computorizada. *Qualidade e Saúde. Acta Med Port.* 19:235–238. (2006).
2. Silva, J. M.: Novas tecnologias em sala de aula. *Revista ciencia, salud, educación y economía - nº 11* (2017).
3. Pezzuol, J. L.; Abreu, F. D. L.; Silva, S. M.; Tendolini A.; Bissaco, M. A. S.; Rodrigues, S. C. M.: “Virtual setting for training in interpreting mammography images”, *Proc. SPIE 10138, Medical Imaging 2017: Imaging Informatics for Healthcare, Research, and Applications*, 101380U. <https://doi.org/10.1117/12.2254677> (2017).
4. Toledo, B. S.: O uso de softwares como ferramenta de ensino aprendizagem na educação do ensino médio/técnico no instituto federal de minas gerais. *Dissertação de Mestrado. Univesidade FUMEC. Belo Horizonte - MG.* (2016).
5. Dunlosky, J.; Rawson, K. A.; Marsh, E. J.; Nathan, M. J. e Willingham, D. T.: Improving Students’ Learning With Effective Learning Techniques: Promising Directions From Cognitive and Educational Psychology. *Psychological Science in the Public Interest.* (2013).
6. Pires, S. R.; Medeiros, R. B.; Elias, S.: QualIM<sup>®</sup>: a software for training in the reading of digital medical images. *Rodiol Bras.* 41(6):391–395 (2008).
7. Martí, J., Mata, C., Lladó, X., e Oliver, A.: Mamodb: A Web-Based Tool For Training Radiologists In The Diagnosis Of Digital Mammography. *Proceedings of Edulearn 11 Conference.* Barcelona, Spain. (2011).
8. Geller B, Ichikawa L, Miglioretti D, Eastman D.: Web-based Mammography Audit Feedback. *AJR American journal of roentgenology.* 198(6):W562–W567. <https://doi.org/10.2214/ajr.11.7971> (2013).
9. Chen, P.; Chen, Y. e Cook. T. S.: Capricorn—A Web-Based Automatic Case Log and Volume Analytics for Diagnostic Radiology Residents. *Academic Radiology*, Vol 22, No 10, Out. (2015).
10. Brooke, John. SUS: a “quick and dirty” usability scale. In P.W. Jordan, B. Thomas, B.A. Weerdmeester, and I.L. McClelland (Eds.) *Usability Evaluation in Industry (189–194).* London: Taylor and Francis. 1996.
11. Bangor, A.; kortum, P.; Miller, J. A. The system usability scale (SUS): An empirical evaluation. *International Journal of Human-Computer Interaction*, v. 24, n. 6, p. 574–594, 2008.
12. Neto, L. L. S.: O Erro diagnóstico. *BBSNM – Brasília Médica.* 34: 44–46 (1997).
13. Goldman, L.; Sayson, R.; Robbins, S.; Cohn, L. H.; Bettmann, M.; Weisberg, M.: The Value of the Autopsy in Three Medical Eras. *New England Journal of Medicine.* (1983).
14. Fenelon, S.: Aspectos ético-legais em Imaginologia. *Radiol Bras [online].* vol. 36, n. 1 pp. 03–06 (2003).



# Biomedical Engineering Education in Georgia

Irine Gotsiridze and Giorgi Gigilashvili

## Abstract

In the paper Study Program in Biomedical Engineering (BME) and Medical Informatics (MI) in Georgia is described. This program is realized in Georgian Technical University, at Biomedical Engineering Department. Implementation and sustainability activities are presented. The broad fields of Biomedical Engineering (BME) and Medical Informatics (MI) are among the most prominent and fastest developing scientific areas. These are considered as key, out of a few, challenges within crucial research and innovation strategies worldwide. Almost every university wanting to be in accordance with a technological progress offers a curriculum in BME&MI at master and doctoral levels, and numerous offer bachelor level degrees as well. Where it is not the case, state and universities authorities are making efforts to open dedicated study programs. Following the evident needs European Commission promotes such actions through its educational strategies and corresponding projects, Tempus being one of these. Department of GTU is one of the participant of BME-ENA—Biomedical Engineering Education Tempus Initiative in Eastern Neighbouring Area, Project Number: 543904-TEMPUS-1-2013-1-GR-TEMPUS-JPCR, is a Joint Project within the TEMPUS IV program and is 90% financed by the Commission of the European Communities. The following short study highlights the main guidelines of BME&MI study programs development, respecting European good practice.

## Keywords

Biomedical engineering • High education Georgia

## 1 Introduction and Aim

Biomedical Engineering Department was established at Georgian Technical University in 1983. Biomedical Engineering Department has produced more than 500 professionals who were successfully employed in the Georgia Health Care Organizations. Implementation of Georgia's health care reforms requires the preparation of biomedical engineering specialists at higher education levels. Graduate students of Biomedical Engineering discipline will be capable to work as not only biomedical engineers, but as health information specialists and solve healthcare management and control-related problems.

Graduates of this Department contribute the country's total health care engineering and maintain functioning of Healthcare Information Systems, that in turn promotes the field's economics.

Biomedical Engineering Department of Georgian Technical University promoted an initiative based on which the Medical Systems and Technologies Department was established in the Ministry of Healthcare of Georgia.

According the LAW OF GEORGIA ON HIGHER EDUCATION higher education.

**Higher education in Georgia consists of three stages:** Bachelor program, master program and doctorate program [1].

Educational program in the institution of higher education during one educational year includes averagely 60 credits. Educational program of first stage of teaching (bachelor) consists of no less than 240 credits. First stage of higher education may include educational program of teacher's training. Only holders of state certificates confirming full general education or persons equalized with them, have a right to study in a bachelor programs. Educational program of second stage of teaching (master) consists of no less than 120 credits. Only bachelors or persons with degrees equalized with them have a right to study in a master programs. Medical/dentist educational program is one-stage higher

I. Gotsiridze (✉) · G. Gigilashvili  
Georgian Technical University, Tbilisi, Georgia  
e-mail: irgocci@gmail.com

educational program which ends with awarding academic degree of certified physician/dentist. Academic degree received after completing educational program of physician with 360 credits or dentist with 300 credits, is equalized with academic degree of master. Third stage of studying (doctorate program) consists of no less than 180 credits. Only masters or persons with degrees equalized with them, have a right to study in doctoral programs [2].

After completion of each stage of higher education, respective diploma is issued. Institution of higher education is authorized to award student with intermediate qualification, in case of completing a part of educational program. Awarding an intermediate qualification is allowed after reaching of results in studying, defined for completing a part of educational program which should not be less than half of credit number defined for educational program.

Obtaining a status of institution of higher education and implementation of respective educational activity is possible only in case of authorization of higher education institution defined by the rules of authorization provision. Authorization is a procedure of obtaining a status of higher education institution purpose of which is to ensure compliance with standards necessary for implementation of respective activity required for issuing of education confirming document recognized by the state. Authorization is carried out by the National Center for Educational Quality Enhancement, according to the rules defined by the authorization provision. The state recognizes only diplomas issued by accredited or equalized with them educational institutions.

#### **Acceptance:**

In the institutions of higher education, in bachelor, certified physician/dentist educational programs, only those enrollees have a right to study who completed respective Unified National Exams according to the rule defined by the Ministry of Education and Science of Georgia.

National Examinations Center is a legal entity of public law which ensures execution of Unified National and Joint Master Exams, is authorized to carry out national estimations and international researches, carrying out other authorities defined by the Georgian legislation (Fig. 1).

In order to be admitted to the BME program at Georgian Technical University, a student should pass Mathematics along with other exams organized by the National Assessment and Examinations Center (NAEC) through “Unified National Exams” and receive enough scores to be admitted to the Informatics and Control Systems Faculty. “Unified National Exams” is provided through Computer Adaptive Testing (CAT) created by the experts of NAEC [3]. Non-resident applicant has the right to apply for BME educational program, in accordance with Georgian

legislation. The applicant must have the certificate confirming the knowledge of English on the level not less than B1 or must present international certificate TOEFL (The Test of English as a Foreign Language) of II certification level. The applicant is free from the necessity of presenting a certificate confirming his/her competence at having completed course in the foreign language in case educational language of the program was English. At not having appropriate certificate or other analogous document, the applicant will have an interview in English. The interview will be implemented with the temporary commission of GTU.

At this time at the Department of Biomedical Engineering students are able to apply for admission for Bachelor degree, Master degree and Doctoral degree programs. Students are offered to be trained on various accredited programs on Georgian and English languages. From the beginning of its foundation, Biomedical Engineering department has had exchange programs with various European universities like Friedrich Schiller Jena University, Warsaw Biomedical Research Centre in Warsaw, Almena Technical University. In 2012–2013 memorandum was signed by the Georgian Technical University and Alabama University, United States to promote collaboration in the field of Biomedical Engineering. Above mentioned memorandum involves possibilities of exchange programs between two universities. Cooperation agreement is signed between West Pomeranian University of Technology, Szczecin and Georgian Technical University, which include mobility of teaching staff, research personal and student, implementation of joint research and development projects and exchange of scientific and technological information.

The broad fields of Biomedical Engineering (BME) is among the most prominent and fastest developing scientific areas. University authorities are making efforts to open dedicated study programs. Following the evident needs European Commission promotes such actions through its educational strategies and corresponding projects, Tempus being one of these. Department of GTU is one of the participant of BME-ENA—Biomedical Engineering Education Tempus Initiative in Eastern Neighbouring Area, Project Number: 543904-TEMPUS-1-2013-1-GR-TEMPUS-JPCR, is a Joint Project within the TEMPUS IV program and is 90% financed by the Commission of the European Communities. The following short study highlights the main guidelines of BME&MI study programs development, respecting European good practice [4–6].

Educational objectives of Biomedical Engineering Program are giving students knowledge how to apply their fundamental engineering skills to solving problems in medicine and biology [7]. Program covered include, medical

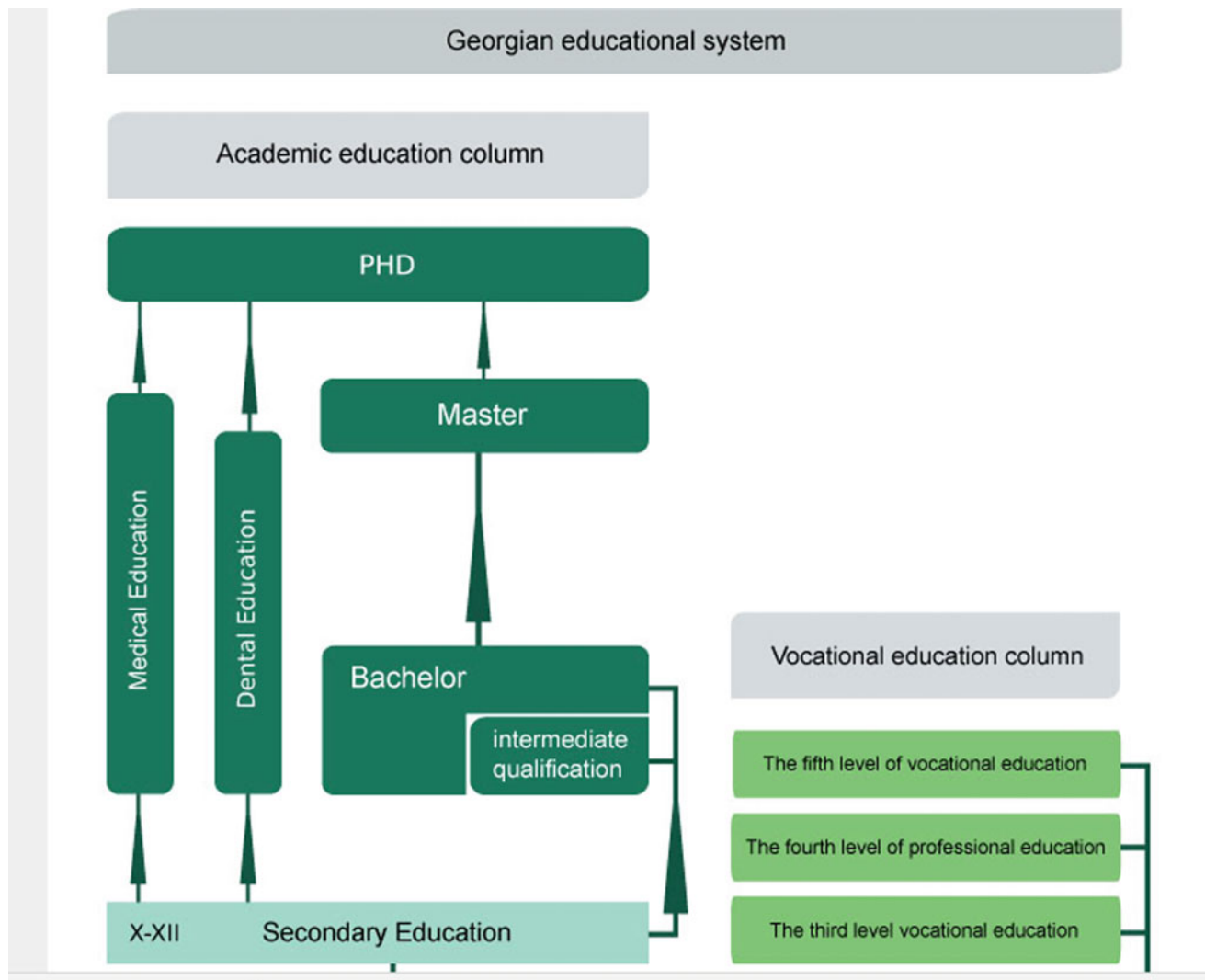


**Fig. 1** Educational system of Georgia

instrumentation and design, physiology, biomaterials, mass transport, application of computers in medicine, artificial implants, and medical imaging. Anatomy and physiology as they relate to specific to bioengineering will be reviewed. It is intended to facilitate the student's understanding in all areas of Biomedical Engineering so that they can appreciate the collaborative nature of the field, provide an empowering professional degree for students who intend to become a practicing engineering.

The number of students who are willing to apply for the bachelor course of Biomedical Engineering increases annually. During the last enrollment process the number of applicants exceeded the available quota three times. Compared to other engineering disciplines afore mentioned demand is substantially higher. Currently the number of students listed on the Biomedical Engineering department is 140 students, including foreign students.

The main aims of the biomedical engineering education in Georgia are:

- To provide interdisciplinary education based mostly on engineering disciplines, information technologies and life sciences;
- To integrate engineering and medical knowledge with principles of computing technologies for understanding and control of the processes in human organism.

Forms and methods of achieving of the learning outcomes of all levels of study are Lectures, Seminars (working in the group) Practical classes, Laboratory classes, Practice Course Work/Project, Independent Work and consultations. For Bachelors the period of theoretical study and practical work takes 4 years. The students who became Bachelors can be admitted to Master of Sciences degree programs.



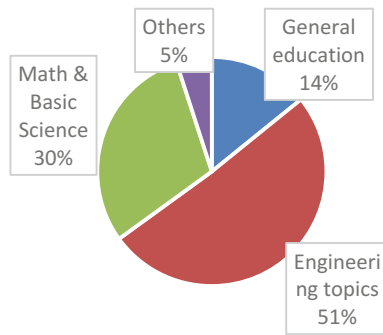


**Fig. 2** Relative sizes of the different courses in BM B.Sc. programs at Georgian Technical University

To obtain the B.S. in Biomedical Engineering, a student must obtain different course credits in: Mathematics, Basic Sciences, Engineering Analysis, Engineering Design, Basic engineering, Statistics and quality control, Biomedical Engineering core and elective courses, Social sciences and humanities courses (Fig. 2).

The distribution of hours is presented in the educational plan. The duration of the program is 4 years (8 semesters) and it contains not less than 240 credits. Educational program consists from required and elective courses. Elective courses consist of University elective and professional elective courses (Table 1).

### Program Constituencies

The constituencies of Biomedical Engineering program include students, current and potential employers, program graduates, faculty members, administration of Controls and Informatics faculty and Biomedical Advisory Board. The primary relationship of each of these constituencies with our program is described below (Fig. 3).

For developing of Biomedical Engineering Programs at GTU “Committee of Support for Developing of BME study” as Biomedical Engineering Advisory Board, has been founded at the “Biomedical and Clinical Society” which is comprised with 5 permanent members. Employers are constituents because we supply them with well-educated and high quality employers. Our relationship with employers in turn benefits our students by keeping them in high demand.

Education of the future engineers within the university curriculum could not be accomplished without sound practical training; laboratory experiments being the most valuable part of it. Despite of fast development of computer technologies, one should not switch university labs to purely virtual experiments. Technical students have to have direct contact with the “hardware” that gives them sense of how the equipment is designed. Modern Engineering Tools also help students develop the ability to use modern engineering tools, provides graduates with skills that a potential employer views as immediately applicable. In cases where

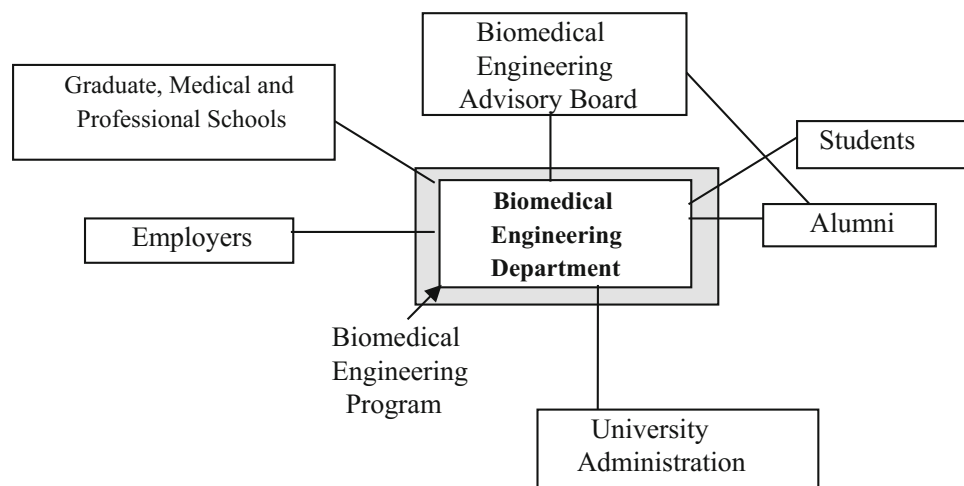
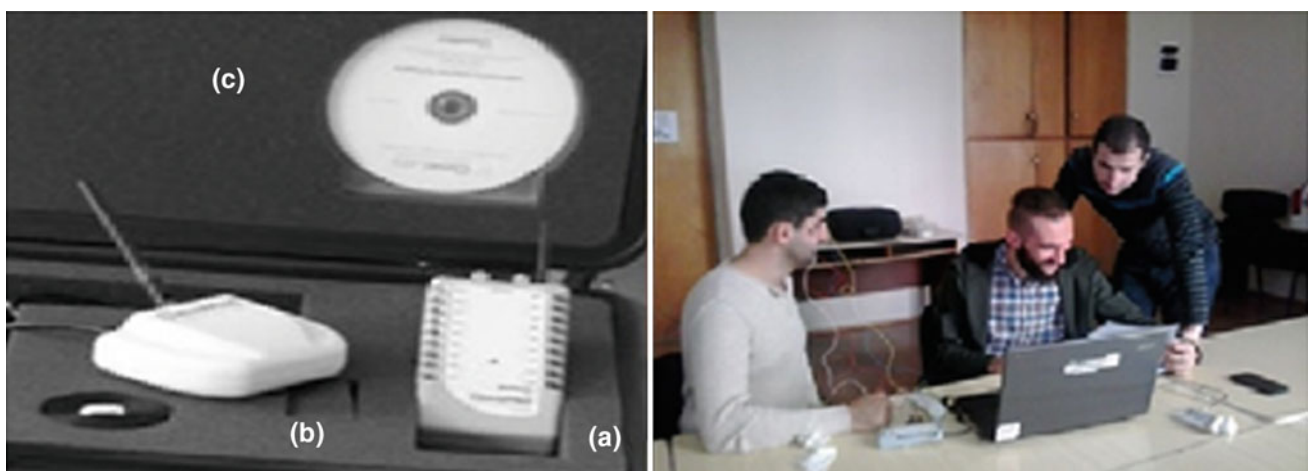
employers expect that some training will be necessary for a given job, they will be interested in an applicant who can produce useful work during the training process. Also, experience with tools like MATLAB, LabView, and Math-Cad [8] can help students to learn other tools. Equipping a good teaching lab is a tough task that requires substantial financial investment. Such question as “what instruments and methods to select” and would we use rather expensive clinically used samples of equipment, or cheaper functional prototype models” should be addressed as well.

**Requirement to the laboratory equipment.** Initial purpose of the laboratory at the Department of Biomedical Engineering of Georgian Technical University was delivery of the laboratory-based course—“Physiological measurements”. The following criteria were used to select appropriate equipment: (1) The lab experiments should cover typical clinically used types of equipment and methods and have possibilities to go beyond routine clinical practice to some experimental research. Laboratory experiments were selected from those ones, described in the existing physiology laboratory courses for medical students [9]. Selection of labs covered electrophysiology (ECG, EMG, EEG), circulatory system physiology (blood pressure and photoplethysmography), respiration system physiology (respiratory monitoring, spirometry, pulse-oximetry), motion physiology (gait analysis). Preference was given to non-invasive clinically used methods. Any labs, based on preparative or animal experiments were avoided, as well as electrical stimulation experiments. (2) Number of laboratory experimental kits should be enough to have about 5 student groups working simultaneously. This last requirement appeared due to confidence that in a lab course consisted from separate laboratory experiments, students must work individually, at least in groups not more than 2 persons. CleveLab<sup>®</sup> Biomedical measurement system (Cleveland Medical Device Inc) CleveLab<sup>®</sup> system was selected mainly on the base of 2nd criteria as most cost effective solution. Courses “Biomedical Measurements” and “Biomedical instrumentation”, poses such questions as how and with which instrument the measurement should be performed, therefore this laboratory is employed to illustrate measurement principles, functional design and data processing peculiarities (Fig. 4).

**Bio-Radio Capture Lite<sup>®</sup>** is a LabView<sup>®</sup> [10] based software that provides data acquisitions functions for the BioRadio<sup>®</sup> unit. Software has integrated unit-programming utility, that allows selecting channels to display, channel input ranges, sampling rate. Using built-in digital filter utility, low-pass, high-pass, band-pass or band stop filters may be applied to each channel, alongside with additional 50/60 Hz notch filter. Data may be saved into text file. Spectral analysis of separate channels may be performed as

**Table 1** The part of plan of study for students in the Biomedical Engineering

Year; semester	List all courses in the program by term starting with the first term of the first year and ending with the last term of the final year	Indicate whether course is required, elective or a selected elective by an R, an E or an SE	Subject areas credits			
			MATH and Basic Science	Engineering topics check if contains significant design	General education	Other
	PHYS 195-General Physics I Mechanics Laboratory	R	4			
	CHEM 100-Introduction to General Chemistry		3			
	ENGL 001-English literature	R			2	
	BIOL 100-General Biology	R	1			
	MATH 151-Calculus II	R	4			

**Fig. 3** The relationship between these stakeholders and the program (lines in the figure represent lines of communication between stakeholders)**Fig. 4** Left: Measurement kit BioRadio® 150: **a** patient unit, **b** computer unit; **c** course software. Right: Fragment of laboratory classes

**Table 2** Purpose for Fluke Biomedical testing devices

Preventive maintenance (PM)	Design validation	Quality assurance
Physiological parameter testing	Troubleshooting	Clinical education
Physiological simulation	Test automation	Bench testing

well. Main disadvantage of the software is that even with filters applied, only raw data is saved into file. CleveLab<sup>®</sup> laboratory course kit is flexible and budget solution for the teaching lab within Biomedical engineering curricula with the emphasis on physiological measurements and data processing, but not on the equipment design. Another Laboratory course that is concerned for supporting students to get practical skills is Medical Equipment Quality Assurance based on Fluke Biomedical testing devices [11].

Medical equipment testing is a critical task to ensure medical devices are performing correctly for patients, doctors, nurses and technologists alike. Fluke Biomedical offers a complete line of biomedical test and simulation products for biomedical/clinical engineers and technicians. Students have access to standalone electrical-safety testers, x-ray analyzers and dosimeter measurement, patient simulators and performance analyzers to fully-integrated and automated performance-testing and documentation systems, test and simulation products. By making practical and laboratory work with Fluke Biomedical ProSim Vital Signs Simulators transform physiological simulation by adding multi-parameter functionality in a single patient simulator device, helping meet patient monitor testing and medical device quality requirements to ensure patient safety (Table 2).

Bachelor and Master Degree Programs in Biomedical Engineering are based on development of student's ability to function on multidisciplinary teams as team-based projects are prevalent in Engineering at GTU that begins in the ENGR 120-122 sequence. By the time the students are seniors, they have had multiple experiences on engineering teams, particularly in ENGR 220, BIEN 325 and BIEN 425.

They have also become multidisciplinary in the sense that each student has a different track (Electrical, Mechanical, Chemical, Computer Information, or Pre-medicine). Senior design team selection for considers the multidisciplinary

nature of the students. In addition, the students have the opportunity to work on a broader team that includes members other than students (such as mentors and the user of the device being designed). Students also work in teams in the Biomedical Senior Laboratory course, where the makeup of each team differs for each of the four laboratories.

After completion of Bachelor and Master levels of Biomedical Engineering Courses our graduates will understand the application of engineering principles to biological systems and will receive specific technical training in one of the following areas: electrical engineering, mechanical engineering, biomedical engineering, Career opportunities also include clinical engineering.

## References

1. Facts to Know about Georgian Education System [www.mes.gov.ge](http://www.mes.gov.ge).
2. [http://mes.gov.ge/higher\\_edu.php?id=2&lang=eng](http://mes.gov.ge/higher_edu.php?id=2&lang=eng).
3. Gotsiridze I., Gigilashvili G.; Biomedical Engineering and Medical Informatics Education in Georgia: Experience and Challenge <http://atsu.edu.ge/EJournal/HENTI/index.html>.
4. Bliznakov Z., Pallikarakis N.: Review of the Biomedical Engineering education programs in Europe within the framework of TEMPUS IV, CRH-BME project. Medicon 2010 Conference, Porto Carras, Chalkidiki, Greece, 27–30 May 2010, [www.springerlink.com](http://www.springerlink.com).
5. Penkala K.: Tempus Project CRH-BME “Curricula Reformation and Harmonisation in the field of Biomedical Engineering as example of structural cooperation enhancing mobility”. Eastern.
6. Sanikidze T., Gotsiridze I., Gigilashvili G.: and others: Development of the BME MSc Study Program in Georgia within the BME-ENA TEMPUS IV Project [https://link.springer.com/chapter/10.1007/978-981-287-736-9\\_117](https://link.springer.com/chapter/10.1007/978-981-287-736-9_117).
7. Thomas R. Harris1, John D. Bransford, and Sean P. Brophy; Roles for Learning Sciences and Learning Technologies In Biomedical Education. Annu. Rev. Biomed. Eng. 2002. 4:29–48 <https://doi.org/10.1146/annurev.bioeng.4.091701.125502>.
8. Clemens Brunner, Arnaud Delorme and Scott Makeig: EEGLAB – AN OPEN SOURCE MATLAB TOOLBOX FOR ELECTROPHYSIOLOGICAL RESEARCH Biomed Tech 2013; 58 (Suppl. 1) © 2013 by Walter de Gruyter · Berlin · Boston. <https://doi.org/10.1515/bmt-2013-4182>.
9. <https://glneurotech.com/bioradio/bioradio-wireless-physiological-monitor/human-physiology-signal-processing-software>.
10. <http://www.ni.com/academic/students/learn-labview>.
11. <http://www.flukebiomedical.com/biomedical/usen/Home/default.htm>.

# Education System for Biomedical Technicians, Biomedical Engineers and Clinical Engineers in the Czech Republic

Jaromir Cmiral

## Abstract

Biomedical Technician, Biomedical Engineer and Clinical Engineer are professions that are included among controlled professions. Education system for these professions is defined by state legislation (one law, two state decrees, one government regulation and two Ministry of Health guidelines). The education system has 3 levels of qualification. First level (bachelor's degree) is for biomedical technician, second level (master's degree) for biomedical engineers and third level (postgraduate specialised education for biomedical engineers with attestation examination) for clinical engineers. The law defines the study programs at Technical Universities to obtain the Biomedical Technicians and Biomedical Engineers qualification. The minimum requests for the content of these study programs are defined by one state decree and more detailed requests (number of ours for individual study subjects) by one Ministry of Health guideline. The government regulation defines the branches of postgraduate specialised education. The education program for obtaining the clinical engineer qualification is defined by the Ministry of Health guideline. One state decree defines works activities that the professions mentioned above may exercise.

## Keywords

Education • Biomedical technician • Biomedical engineer • Clinical engineer • Legislation

## 1 Introduction

In the Czech Republic, the superior governmental office in relation to universities in the state administration is the Ministry of Education, Youth and Sports (MEYS). University education was defined in the Higher Education Act No. 111/1998 Coll. [1] till 2016. The amendment to the higher education act No. 137/2016 Coll. [2] was approved by the government and adopted by the Parliament in 2016.

The amendment formulates rules for accreditation of study programmes. Newly formulated rules for institutional accreditation allow develop new study programmes in the approved areas of education without applying to the National Accreditation Office for each individual study programme. If the higher education institution (HEI) does not have the institutional accreditation or wants to apply for accreditation of a study programme outside the approved areas of education the HEI must submit application for accreditation of the study programme. The same rule holds for study programmes, which need approval based on other legal regulations. This is the case of all study programmes leading to regulated professions. Biomedical technicians and biomedical engineers as health care professions are among them.

Not only the undergraduate education, but also qualification, accreditation, and occupations are regulated by special legal provisions. During 2004 and 2005 new law and related regulations became effective. List of the legal provisions and currently accredited study programmes in the Czech Republic was presented in [3]. Since their introduction some of them were amended. They define requirements also for postgraduate and lifelong learning, which is mostly organized by the Institute for Postgraduate Medical Education (IPVZ) [4]. The Institute is responsible for postgraduate education of physicians, pharmacists, dentists and non-medical professionals (university graduates). In this paper we focus on the legal provisions in more detail.

J. Cmiral (✉)

Czech Society for Biomedical Engineering and Medical Informatics, Prague, Czech Republic  
e-mail: zdena.cmiral@seznam.cz

## 2 The Basic Legislative Document: The Act No. 96/2004 Coll

The basic legislative document is the Act No. 96/2004 Coll. on the Conditions for the Obtaining and Recognition of Qualifications for Pursuing Paramedical Professions and for Carrying out Activities in Connection with the Provision of Health Care and on the Amendments of Some of the Related Acts (Act on Paramedical Professions) [5]. A paramedical profession shall be the sum of activities carried out during the provision of health care according to this Act. A paramedical professions is divided in two categories:

- A Health Care Professional—physical persons pursuing a paramedical professions according to this Act,
- Another professional shall be a physical person carrying out activities different from the provision of health care which are, however, directly related to the provision of health care,

Biomedical Technicians, Biomedical Engineers and Clinical Engineers are included in the health care professional category.

In this Act there are defined the following professional qualifications for pursuing the profession of Biomedical Technician, Biomedical Engineer and Clinical Engineer.

Professional qualifications for pursuing the profession of biomedical technician shall be acquired by completing

1. An accredited healthcare study programme (study programme leading to a bachelor's degree shall be the field of study that has been approved by the Ministry of Health) for the training of biomedical technicians leading to a bachelor's degree, or
2. An accredited study programme (study program leading to a bachelor's degree shall be the field of study within a particular study programme that has been accredited by the Ministry of Education) of electrical engineering courses leading to a bachelor's degree or at least three-years' study at higher vocational colleges of electrical engineering subjects and an accredited qualification course of biomedical technology.

Activities within diagnostic and treatment care in the field of biomedical technology in cooperation with a biomedical engineer or a doctor shall be considered as pursuing the profession of biomedical technician.

Professional qualifications for pursuing the profession of biomedical engineer shall be acquired by completing

1. An accredited healthcare study program for the training of biomedical engineers leading to a master's degree, or

2. An accredited study programme in electrical engineering leading to a master's degree and an accredited qualification course in biomedical engineering.

Activities within the framework of diagnostic and therapeutic care performed in cooperation with the physician shall be considered as pursuing the profession of biomedical engineer.

The persons that passed an accredited study programme at a university leading to a master's or bachelor's degree in electrical engineering field of study or a higher-level vocational schools in electrical engineering field of study or a secondary vocational schools in the electrical engineering field of study are include among "Another professionals".

Upon a successful completion of specialised education by an in-specialisation exam, a health care professional shall acquire specialised qualification for carrying out specialised activities of a particular paramedical profession. Specialised education shall be provided by an accredited facility according to a study programme. The accreditation for specialised education is giving out by the special rules of Ministry of Health. The study programme of specialised education shall specify the total duration of training, extent and content of the training, especially the duration of compulsory practice in the field and places of work where the training takes place. Further, it shall specify the requirements for theoretical knowledge and practical skills, completion of educational events, courses, workshops, traineeships and other requirements for acquiring specialised qualifications. The study programme shall contain a list of recommended study literature and characteristics of activities, specified for particular modules, of the persons who completed specialised training.

The Ministry of Health may decide on granting specialised qualification in the field of specialisation to graduates of an accredited course leading to a doctor's degree (Ph.D.) which is a follow-up course to the course in health-care leading to a master's degree, if it complies with a particular study programme of specialised education issued by the Ministry of Health.

## 3 The Decree No. 39/2005 Coll

The Decree No. 39/2005 Coll. [5] stipulates the minimal requirements on the study programmes for obtaining professional qualification for performance of a paramedical health-care profession.

This Decree incorporates the relevant regulations of the European Commission and provides for the minimal requirements on the study programmes, the study of which results in professional qualification for performance of a



paramedical health-care profession; these minimum requirements constitute a list of the theoretical and practical fields necessary for performance of regulated activities.

*Study programmes for obtaining the professional qualification for the profession Biomedical Technicians shall provide the following knowledge and skills:*

In the basic following fields:

- in the ethics of a medical profession in the field,
- in administrative activities in medical care, particularly in keeping documents related to the field, including the electronic form of these documents,
- in organization and management of medical care,
- in the fundamentals of support for and protection of health, including prevention of nosocomial contagion,
- in first aid and provision of medical care in emergencies and crises,
- in legal relations on the provision of medical care in the field.

Moreover the study programmes shall contain:

The theoretical courses providing knowledge in:

- fields that form the basis necessary for performance of a technical medical profession, on the basis of anatomy, physiology and pathology,
- technical fields, i.e. in the processing of signals and images (introduction to the theory of signal processing, analysis and interpretation of biosignals, biomedical sensors), in medical apparatuses (fundamentals of electrical circuits, diagnostic medical apparatuses, therapeutical medical apparatuses, laboratory medical apparatuses, complexes of medical apparatuses, imaging systems in clinical practice), in computer science and cybernetics (fundamentals of statistics in medicine, computer support for diagnostics, telemedicine, information systems in medical care, introduction to the theory of simulation and modelling), electrical engineering subjects (mathematics, physics, theoretical electrotechnology, electronics, electrical measurements, programming),
- related fields, i.e. in management of medical technology, in technical legal regulations and standards valid in medical care and in the fundamentals of the methodology of scientific research,

The practical training providing skills and knowledge in the fields mentioned in previous subparagraph; practical training shall take place in school laboratories and in medical facilities; practical training in medical facilities shall include at least 50 h at workplaces employing diagnostic medical apparatuses, at least 30 h at workplaces employing

therapeutical medical apparatuses and at least 20 h at workplaces employing laboratory medical apparatuses.

The more detailed requirements (number of hours for individual study subjects) are included in the special guideline of Ministry of Health. A special decree defines the activities that the biomedical technicians may exert.

*Study programmes for obtaining the professional qualification for the profession Biomedical Engineer shall have a total standard period of study of:*

- at least 5 years in a certified master's study program after obtaining complete secondary education, of which practical training shall correspond to at least 100 h after obtaining complete secondary education,
- at least 2 years in a certified master's study program following on from a certified bachelor's study program in a field of electrical engineering, of which practical teaching shall correspond to at least 100 h; the requirements on the number of hours of practical training and the requirements stipulated in the basic field (the same as for Biomedical Technicians) may also be fulfilled during prior study in a certified bachelor's study program.

If basic electrical engineering education, i.e. in mathematics, physics, theoretical electrical principles, electronics, electrical measurement, theory of electromagnetic field and programming was not part of the previous study in a certified study program it shall be part of this study programme.

Study in the programmes shall provide the knowledge and skills specified as the basic fields (the same as for the Biomedical Technicians) and shall further contain:

The theoretical courses providing knowledge in:

- fields that form the basis required for performance of a technical medical profession, i.e. in the fundamentals of anatomy, physiology and pathology, in defining systems on biological objects, biophysics, and physical methods in therapy,
- technical fields, i.e. in the processing of signals and images (the theory of signals, digital processing of signals and images, analysis and interpretation of biosignals, biomedical sensors), in medical apparatuses (theory of circuits, diagnostic medical apparatuses, therapeutical medical apparatuses, laboratory medical apparatuses, complexes of medical apparatuses, theory of imaging systems, imaging systems in clinical practice), in computer science and cybernetics (statistics in medicine, computer support for diagnostics, telemedicine, information systems in medicine, the theory of simulation and modelling in medicine),
- related fields, i.e. in technical legal regulations and standards valid in medicine, in management of medical

technology, fundamentals of computer science and methodology of scientific research, methodology of scientific research.

The practical training providing skills and knowledge in the fields mentioned in previous subparagraph; practical training shall take place in school laboratories and in medical facilities; practical training in medical facilities shall include at least 30 h at workplaces employing diagnostic medical apparatuses, at least 20 h at workplaces employing therapeutical medical apparatuses and at least 10 h at workplaces employing laboratory medical apparatuses.

The more detailed requirements (number of hours for individual study subjects) are included in the special guideline of the Ministry of Health.

If the certified master's study program is following on from a certified bachelor's study program for Biomedical Technicians, the courses of this study programme are partly credited in Biomedical Engineering study programme.

#### 4 Special Legal Regulations

In addition to the Act No. 96/2004 Coll. and Decree No. 39/2005 there are legal regulations that specify accompanying issues, in particular:

- details about holding the attestation examination, examination for issuing the certificate, final examinations of accredited qualification courses, approbation examinations and examination rules for these examinations;
- health capability for performing the occupations of health service professional and another specialist;
- activities of health service professionals and other employees;
- fields of specialized education and specification of the expertise of health service professionals. The special government regulation defines the branches of post-gradual specialised education. One of them is the Clinical Engineering. For graduates after the attestation examination this regulation defines the official attribute "Clinical Engineer". The education programme for obtain the clinical engineers qualification is defined by Ministry of Health guideline.

#### 5 Conclusion

The whole education system has 3 levels of qualification. First level (bachelor's degree) is for biomedical technician, second level (master's degree) for biomedical engineers and third level (postgraduate specialised education for biomedical engineers with attestation examination) for clinical engineers. All levels are focused on preparing students for the work in hospital clinics. The special decree defines the activities that the professions mentioned above may exert (separate for each profession).

The Act No. 96/2004 Coll. and all related legal regulations and provisions have a number of consequences both for undergraduate study and for postgraduate study and lifelong learning. Biomedical technicians and biomedical engineers who will be working in the Health Care sector will be involved in a system of education and lifelong learning for acquiring specialized competence that is similar to present system of education and training of medical doctors. The greatest benefit of this system is that it clearly defines skills and knowledge that biomedical technicians and biomedical and clinical engineers should have. Especially for the potential employers it is necessary to know which competences the graduates possess.

**Conflict of Interest Statement** Author declares that he has no conflict of interest.

#### References

1. Act No. 111/1998 Coll. (amended and consolidated) on Higher Education Institutions and on Amendments and Supplements to Some Other Acts (THE HIGHER EDUCATION ACT), Ministry of Education, Youth and Sports of the Czech Republic, 2009. [Online]. Available: <http://www.msmt.cz/areas-of-work/tertiary-education/the-higher-education-act>, last accessed 2018/03/15.
2. Amendment to the Higher Education Act – published as No. 137/2016 Coll. (documents in Czech). [Online]. Available: <http://www.msmt.cz/vzdelavani/vysoke-skolstvi/seminar-k-novele-zakona-o-vysokych-skolach>, last accessed 2018/03/15.
3. Lhotska, L., Hozman, J.: Biomedical Engineering Education in the Czech Republic. In *XIV Mediterranean Conference on Medical and Biological Engineering and Computing MEDICON 2016*. New York: Springer, 2016, pp. 1323–1328. IFMBE Proceedings. vol. 57.
4. Institute for Postgraduate Medical Education [Online]. Available: <http://foreigner.ipvz.cz/en> last accessed 2018/03/15.
5. Collection of Laws of the Czech Republic [Online]. Available: <http://www.mvcr.cz/sbirka/index.html>, last accessed 2018/03/15.

# Implementation of Project-Based Learning in Biomedical Engineering Course in ITB: Opportunities and Challenges

Agung W. Setiawan

## Abstract

Introduction to Biomedical Engineering is an elective course for final year undergraduate student. For the last two years, 2015–2016, the traditional learning was implemented in this course. In 2017, project-based learning (PBL), was applied to the course. The goal is to enable students to take initiative, identify and solve the problems, work and communicate ideas in team, build responsibility and confidence. This paper will focus on implementation of PBL, specifically on the opportunities and challenges. The students choose their own topic, identify and explain what is the topic, why they choose that, and how they solve the problem. They have to review the existing solution and they should propose a new solution. Finally, they have to submit a report, then present their work in class attended by all the students and instructor. Using this learning approach, the students become more active to present their ideas, give some comments and questions.

## Keywords

Project-based learning • Biomedical engineering  
Developing country

## 1 Introduction

Introduction to Biomedical Engineering is an elective course for final year undergraduate student in School of Electrical Engineering and Informatics, Institut Teknologi Bandung (ITB), Indonesia. In the Electrical Engineering Study Program curriculum, the category of the course is elective depth

A. W. Setiawan (✉)  
Biomedical Engineering, School of Electrical Engineering and Informatics, Institut Teknologi Bandung, Bandung, 40132, Indonesia  
e-mail: awsetiawan@stei.itb.ac.id; agungws@gmail.com  
URL: <https://biomed.stei.itb.ac.id>

course. For the last two years (2015–2016), the traditional learning (TL) was implemented in this course. The student outcomes for the course is adopted from the Accreditation Board for Engineering and Technology (ABET), that are: (a) an ability to apply knowledge of mathematics, science, and engineering (high); and (k) an ability to use the techniques, skills, and modern engineering tools necessary for engineering practice (medium). After completion of the course, the student is expected to: Understand the field of biomedical engineering, Identify and analyze problems in the field of biomedical engineering, Identify and review the current implementation (solution), Solve and design the new solution.

According to the previous experience, the students are so passive, their activities are just listening, the majority of the students indicate they are bored. To improve the quality of the lecture, project based learning (PBL) was introduced to this course. In this learning scheme, the main goal is to get students actively engaged in the learning process. PBL is introduced to increase the student interest [1]. In PBL, students are usually provided with specifications for a desired end product [2]. The main issue is how to make the learning process more effective in engineering education, the answer is using PBL [3]. This paper will focus on implementation of PBL in Introduction to Biomedical Engineering course in ITB, specifically focus on the opportunities and challenges.

## 2 Course Details

In 2017, for the first time, PBL was introduced to the course. Due to this reason, the PBL was conducted in the last four weeks of the course schedule, this is part of the management of change from previous learning method to PBL. This is the detail of the course outline:

1. Introduction to biomedical engineering (2 weeks)
2. Biomedical signal and systems (2 weeks)
3. Biomedical modelling and simulation (1 week)

4. Control & feedback in physiology (2 weeks)
5. Biomedical Instrumentation (2 weeks)
6. Biomedical Signal Processing: ECG and EEG (2 weeks)
7. Project (4 weeks)

In the first five weeks of the course, the lecturer give some lecture about definition and scopes of biomedical engineering, signal and systems in biomedical engineering and biomedical modelling and simulation. The goal of these lessons is to provide strong foundation in basic science and engineering thats applied in biomedical engineering.

For topics 4 and 5, lecture-discussion method was used to involve the students actively in class. After short lecture, a task is given to the students. The task is to review related papers or book chapters in the area of biomedical engineering. In biomedical signal processing topic, the student use their knowledge in digital signal processing that is applied in biomedical engineering. The students have to process ECG and EEG signals. The objective is to give the student an opportunity to use modern engineering tools.

Finally, the project (PBL) was introduced to the students at week #12. So, the students has 4 weeks to do the project. In this learning scheme, the students need to be active to acquire hard and soft skills [4]. The lecturer act as mentor that provide suggestion, feedback, and expert guidance [2].

### 3 Framework of the Project

To avoid and minimize free rider problem in a team, student teams have only two members. And to build a solid team, they are free to choose a teammate, organize and assign tasks, and manage their conflict. After forming a team, they should choose their own topic. They have very limited time, just two days, to search and review the project topic, then select and decide it.

The students have to write a resume about project description, max 2 pages. The contents of the project resume or proposal are what is the problem, why the problem is important, and how to solve the problem. The role of instructor is to determine the project feasibility, give some advice, and approve the project proposal. When required, the instructor can suggest project topic.

In the tutoring sessions, the student should attend this session to report their project progress and present their progress. During this session, the instructor can monitor and evaluate the project progress.

In the end of the semester, they have to submit a report. The most important part of the report is the students have to review the existing solution and they should propose a new solution according to their review. Also, they have to present their work in class attended by all the students and instructor.

### 4 Resources

The university has some facilities that can be used by the students to do the project, for example access to some publication portals, study rooms at library and student halls. Another facility is some licensed software can be accessed in university computer labs. The students need to provide the sensors, electronic components, and circuit board by their own. Oscilloscope, function generator, power supply, and other equipments can be accessed in laboratory.

### 5 Assessment

The teams have to submit project report and present their work in the class. The oral presentation, including question-answer session, is an individual evaluation. It is used to assess the individual contribution and students

**Table 1** Oral presentation and project report rubric

Criterion	Weight	4	3	2	1
<b>Oral Presentation</b> Clear, Proper grammar, On time	3	3 out of 3	2 out of 3	1 out of 3	0 out of 3
<b>Question &amp; Answer</b> Clear, Effective, Relevant	1	3 out of 3	2 out of 3	1 out of 3	0 out of 3
<b>Slide Structure and Design</b> Clear, Attractive, Systematic	3	3 out of 3	2 out of 3	1 out of 3	0 out of 3
<b>Introduction</b> What, Why, Objective	3	3 out of 3	2 out of 3	1 out of 3	0 out of 3
<b>Review</b> Relevant, Appropriate, Useful	3	3 out of 3	2 out of 3	1 out of 3	0 out of 3
<b>Specification</b> Clearly stated with(out) description, Detail	3	3 out of 3	2 out of 3	1 out of 3	0 out of 3
<b>Block Diagram</b> Showing Software, Hardware, All input-output	3	3 out of 3	2 out of 3	1 out of 3	0 out of 3
<b>Detail Design</b> Well defined, organized & planned	3	3 out of 3	2 out of 3	1 out of 3	0 out of 3
<b>Conclusion or Discussion</b> Clearly stated, Re-state the objective, Show the result	1	3 out of 3	2 out of 3	1 out of 3	0 out of 3
<b>References</b> Relevant, Appropriate, Citation style	1	3 out of 3	2 out of 3	1 out of 3	0 out of 3
<b>Language</b> No Punctuation, Spelling, Grammatical errors	1	3 out of 3	2 out of 3	1 out of 3	0 out of 3

comprehension of basic science and engineering. The oral presentation will represent the 12%, slide structure and design 4%, and question-answer 12% of the mark for each student.

The main output of the project is a report, the objective of this evaluation is to assess the complete knowledge of how to apply basic science and engineering to solve problem in the real-world. Introduction will represent 12%; product or paper review (positioning) 12%; system specification 12%; system block diagram 12%, detailed design and results 12%; conclusion 4%; references 4%; and grammar 4% of the mark for each team. The rubric for oral presentation and project report is shown in Table 1.

One example of the project topics is “Portable Cholesterol Monitoring”. The score for oral presentation is 3, due to

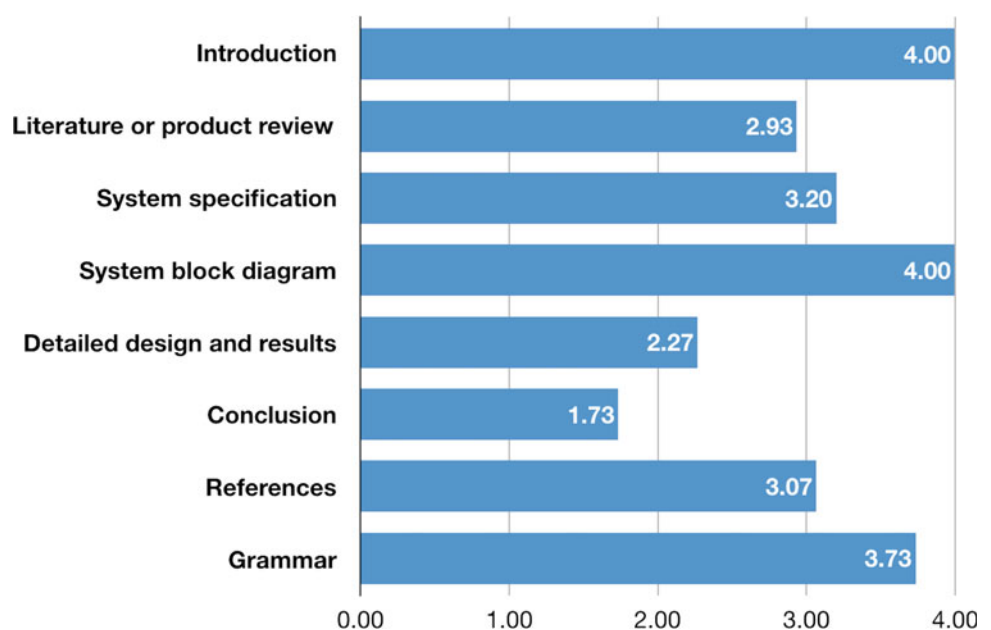
the use of proper grammar, on time, and mumbling (comply 2 out of 3). The subtotal for oral presentation is  $score \times weight = 3 \times 3 = 9$ . In question-answer session, the answer is unclear and irrelevant, the score is 2 (comply only 1 criterion). The subtotal is  $2 \times 3 = 6$ . For slide structure and design, they comply all criterion. They earn maximum score: 4, the subtotal is  $4 \times 1 = 4$ . The overall score can be seen in Table 2. The total score for this team is 75.

The average score of project report is shown in Fig. 1. It can be seen that all teams have maximum score for introduction and system block diagram. It means that the projects background, why its important, objective of the project, and system block diagram are very well described by them. All teams has clearly state system specification with description and/or explain the specification details, and some of them

**Table 2** Scoring: Portable cholesterol monitoring

Criterion	Score	Weight	Subtotal
<b>Oral Presentation</b> Proper grammar, On time	3	3	9
<b>Question and Answer</b> Unclear, Effective, Irrelevant	2	3	6
<b>Slide Structure and Design</b> Clear, Attractive, Systematic	4	1	4
<b>Introduction</b> What, Why, Objective	4	3	12
<b>Review</b> Relevant	2	3	6
<b>Specification</b> Clearly stated with description, Detail	4	3	12
<b>Block Diagram</b> Showing software and Hardware, All input-output signals are well defined	4	3	12
<b>Detail Design</b> Clearly defined	2	3	6
<b>Conclusion or Discussion</b> Re-state the objective	2	1	2
<b>References</b> Relevant, Appropriate, Citation style	4	1	4
<b>Language</b> No spelling errors	2	1	2
Total			75

**Fig. 1** The average score of project report





didn't describe and/or explain it. Some teams write irrelevant reference and the amount of the reference is inappropriate. The score of detailed design & results is very low, majority of the teams didn't clearly defined the detailed design. The conclusion criterion has lowest score, almost of the teams didn't clearly stated their objective result or their contribution.

## 6 Evaluation

The evaluation of PBL is analyzed using two quantitative assessment: 1. Academic results, from students final grades, and 2. student impression as extracted from student questionnaire. The grade distribution of traditional learning and PBL is shown in Fig. 2. In PBL, the average of grade-point is 3.3 (out of 4), higher than using TL (3.2 out of 4). Using PBL approach, the number of students that have grade A & AB is 65%, higher than TL (52%).

From the assessment, some teams have failed in describing the detailed design & result and conclusion. There is two hypotheses: 1. The duration of the project is too short, just three weeks. 2. The lack of facilities, especially in

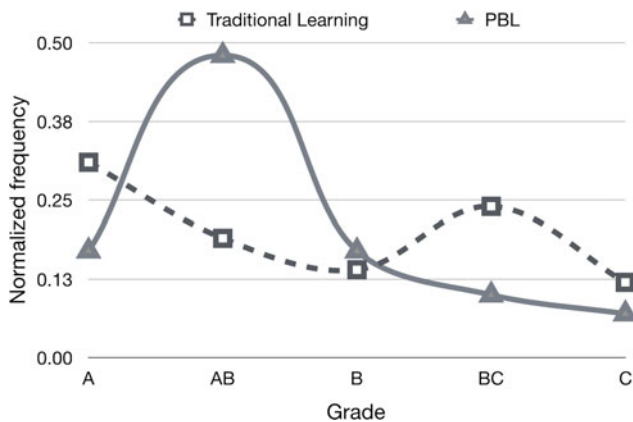


**Fig. 2** Grade distribution of traditional learning and project-based learning

availability of sensors, electronic components, and micro-controller. This is inline with questionnaire result about Facilities for the course are adequately, the point is decrease traditional learning (TL): 3.4 and PBL: 3.2 (out of 4). The students impression to the PBL is the same as TL: 3.5 (out of 4).

## 7 Concluding Remarks

The course has partially implemented using PBL in 2017. There are some opportunities to increase the course quality using PBL: increasing student mastered the learning outcome, give student an opportunity to create their own project. Another opportunity is that the students become more active. The challenges for implementing PBL are the lack of facilities, especially in electronic components, due to the budget limitation; the duration of the project is too short, due to the some lecture topics should be delivered to give student the definition and scope of biomedical engineering. The overall grade-point average and the number of students that have grade A & AB with PBL is higher than TL.

## References

1. Macias-Guarasa, J., Montero, J.M., San-Segundo, R., Araujo, A., Nieto-Taladriz, O.: A project-based learning approach to design electronic systems curricula. *IEEE Transactions on Education*, vol. 49(3), 389–397 (2006). <https://doi.org/10.1109/te.2006.879784>.
2. Savery, J.R.: Overview of Problem-based Learning: Definitions and Distinctions. *Interdisciplinary Journal of Problem-Based Learning*, vol. 1(1), 9–20 (2006). <https://doi.org/10.7771/1541-5015.1002>.
3. Galand, B., Milgrom, E., Raucent, B.: Effectiveness of Problem-Based Learning In Engineering Education: A Comparative Study on Three Levels of Knowledge Structure. *International Journal of Engineering Education*, vol. 28(4), 939947 (2012).
4. Iturregi, A., Mate, E., Larruskain, D.M., Abarrategui, O., Etxegarai, A.: Work in Progress: Project-based learning for electrical engineering. In: 2017 IEEE Global Engineering Education Conference (EDUCON), pp. 464–467. IEEE, New York (2017). <https://doi.org/10.1109/educon.2017.7942888>.

# Monte Carlo Simulation of a Linac Using PRIMO: User-Friendly Educational Tool Which Can Be Taken to the Cloud for Free

Angelina M. Bacala

## Abstract

PRIMO is a free, self-contained linac simulator and dose calculation software based on the Monte Carlo code PENELOPE 2011. Windows-based, it is user-friendly and does not require any programming tasks by the end user. PRIMO comes with an intuitive graphical interface which guides the configuration and execution of the linac simulation in seemingly natural stages: from the primary electron source in the linac head to the collimators then down to a binned water phantom or patient computed tomography. We report here the simulations done with PRIMO of a 6 MV Varian Clinac 2100 and the dose deposition in a water phantom using student desktop computers with Pentium type processors. The program is then ported to the Amazon Elastic Compute Cloud. Here abnormal program termination due to power outages which is a common occurrence in developing countries is no longer a concern. Without the need to invest in expensive hardware upfront, the PRIMO simulations can be deployed reliably and faster in the Amazon Cloud and which for some time can be free.

## Keywords

Monte Carlo linac simulation • PRIMO • Amazon Elastic Compute Cloud

## 1 Introduction

The Monte Carlo method of radiation transport is generally regarded as the gold standard for obtaining the most accurate estimate of the dose distribution in external photon and

electron beam radiotherapy. It is however characterized by long computation time which can exceed the normal clinical requirements. Another encumbrance is that it typically requires a significant experience and an overall great effort to set up a Monte Carlo simulation from scratch. A self-contained, windows-based software package called PRIMO is designed to overcome these limitations [1, 2].

PRIMO is an automated, full Monte Carlo-based linac simulator and dose calculator for a variety of Varian and Elekta linacs. The linac geometries are included in the package hence the user does not input any geometrical information into the program. PRIMO can produce phase-space files (PSFs) as output of the linac simulation and it can also import compliant external PSFs written by other Monte Carlo codes to commence a linac simulation. It comes with a user-friendly, intuitive graphical interface for one to seamlessly configure and execute the linac simulation. Once completed the numerical tools within the interface can be accessed to analyze the output PSFs and the absorbed dose tallied in a binned water phantom or in a patient's computerized tomography. PRIMO also provides comparison with experimental values of the percent depth dose and lateral profiles using gamma analysis, all accessible within the user interface.

PRIMO simulates the radiation transport and estimates the absorbed dose based on the general purpose Monte Carlo code PENELOPE 2011; a set of subroutines that model the physics of the electromagnetic shower in a wide energy range from a few hundred eV up to GeV [3]. Prior knowledge of the physics of Monte Carlo is not required to configure and execute the PRIMO program although advanced users are given access to modify the configuration files governing the simulation. To reduce simulation time, a number of variance-reduction techniques are incorporated where a user is given the option to choose which to apply. In addition, the simulations can be distributed among the cores in a single computer. PRIMO is not open source software but it is freely distributed through its website [4].

A. M. Bacala (✉)  
Department of Physics, Mindanao State University-Iligan Institute  
of Technology, 9200 Iligan City, Philippines  
e-mail: angelina.bacala@g.msuiit.edu.ph

## 2 Linac Simulation Using PRIMO

In PRIMO, the linac simulation can be separated by geometrical segments. The photon beam generated from the linac head proceeds in three stages: starting from the source upstream of movable collimators (s1) then through the collimators themselves and all components of the lower part of the linac (s2). Then finally the dose distribution is computed in a binned water phantom located downstream (s3). In s2, the splitting-roulette variance-reduction option is chosen and fitted to the chosen field size while in s3, splitting in the phantom is also enabled. In this study, the simulations s1,s2 and s3 are done in succession.

Using PRIMO version 0.1.5.1307, a 6 MV Varian Clinac 2100 is simulated with nominal energy of 6.26 MeV for the primary electron beam while all other beam parameters are set to default values of zero. Using one field of size  $10 \times 10 \text{ cm}^2$ , the dose is tallied on a homogeneous water phantom with dimensions  $16.2 \times 16.2 \times 31.0 \text{ cm}^3$  at a source-to surface distance of 95.0 cm. The dose-scoring bin size was set to  $0.2 \times 0.2 \times 0.2 \text{ cm}^3$ .

The simulations are run using typical student desktop computers with Pentium type processors. In a 4-core computer, it took more than 52 h to completely simulate 25 million histories yielding an average statistical uncertainty of 3.7% in the absorbed dose distribution. Increasing the number of histories reduces the average statistical uncertainty in the absorbed dose calculations as shown in Table 1.

To simulate 80 million histories, an 8-core computer is used in which it took more than 3 days to complete the s1 simulation alone. This particular simulation was done soon after an scheduled power interruption was implemented in our locality.

Many of our simulation attempts were aborted due to unscheduled power outages. As is usually the case for any software program that is terminated abnormally, no files are output and the simulation needs to be restarted again. This provides the motivation to port to the cloud the PRIMO simulations especially when  $10^8$  histories are involved.

**Table 1** The average statistical uncertainty of the absorbed dose distribution in the water phantom for different number of histories

Number of histories	Average statistical uncertainty in absorbed dose (%)
$10.7 \times 10^6$	5.58
$25 \times 10^6$	3.70
$80 \times 10^6$	2.09
$100 \times 10^6$	1.97

## 3 PRIMO in the Amazon Elastic Compute Cloud

Amazon.com's on-demand cloud-computing platform is called the Amazon Web Services (AWS) and its central core is the Amazon Elastic Compute Cloud (EC2). Amazon EC2 provides scalable computing capacity where one can launch as many or as few virtual servers as one needs, configure security and networking, and manage storage through a web-based user interface [5]. The Amazon EC2 virtual computers, termed as instances, come with preconfigured templates which includes the operating system and other software that allows a user to install and run specific applications in just a few minutes. It is available all the time through the Internet and accessible in a client computer via the remote desktop protocol.

Access to Amazon EC2 is on a subscription basis and one is charged for the usage typically on a per-hour basis. For the first 12 months of use there is a free-tier option for new account holders. Amazon EC2 not only eliminates the need to invest in expensive hardware upfront but the free-tier option also allows a new user to run a micro-sized server, with storage and bandwidth completely free of charges for one year, provided the monthly usage does not exceed 720 h. One key difference however between a real server and an Amazon EC2 server is that when an instance is terminated, the virtual server and its data are no longer available.

In order to overcome our problem of power outages, the PRIMO program of the same version is installed and run in the AWS EC2 cloud in a Windows 2016 base server instance type in the free-tier option. The simulation of a 6 MV Varian C2100 linac was configured to run for 720 h. After a full 30 days of non-stop calculations, the s1 simulation is completed. Since the EC2 instance is of the free-tier option, only 1 core with 1 GB memory is attached to the EC2 Windows server when launched. The total number of events simulated consisted of  $1.07 \times 10^7$  histories and at the end of s3 simulations, this gives an average statistical uncertainty of 5.58% for the absorbed dose distribution in the water phantom.

The average statistical uncertainty in the dose calculation can be reduced to less than 2% if the number of histories simulated is of the order of  $10^8$ . To simulate a hundred million histories in a much shorter period, a faster EC2 is launched—the C5 instance, introduced by AWS EC2 in 2017, described as the next generation of EC2 instances powered by 3.0 GHz Intel Xeon scalable processors. With this type of architecture, using a Windows 2016 base server with 32 cores and 64 GB memory, it took some 21.2 h to complete the s1 simulation of  $10^8$  histories. To minimize the usage of this EC2 instance which is now metered, the linac

PSFs output from the completed s1 simulations and other files were transferred to our desktop computer where the s2 and s3 simulations were migrated to complete the dose tallying in the binned water phantom.

It is remarkable to note that the entire simulations done at AWS EC2 are totally free of charge. Although outside of the free-tier option, the AWS Educate Portal [6] has given enough educational credits to pay for the usage of a c5.9xlarge instance and the bandwidth incurred in the file transfer to the local computer.

### 3.1 Comparison with Experiment

Default configuration values for the primary beam parameters for each available linac are provided by PRIMO software and the user can change any of these values. However it does not provide a beam configuration algorithm. Therefore several simulations have to be performed by the user to

fine-tune the simulation parameters to obtain a better match between the simulated and the experimentally measured depth dose distribution and lateral profiles of reference fields.

The simulated dose distributions are compared to a given experimental result consisting of a lateral profile and percent depth dose (PDD) curves measured on a Varian Clinac iX. These measurements are also included in the PRIMO software package distribution. The gamma analysis method that combines the dose-difference and the distance-to-agreement criteria is used in the comparison. The acceptance criteria for the gamma analysis is set at 2% and 2 mm, for the dose and the distance-to-agreement respectively. The comparison of simulated and measured values for the PDD and profile curves and their corresponding gamma indices are shown in Figs. 1 and 2. There is just one difference in the linac simulation of the data set with  $10^8$  histories compared with the rest of the data sets given in Table 1. The s1 simulation is configured for the primary

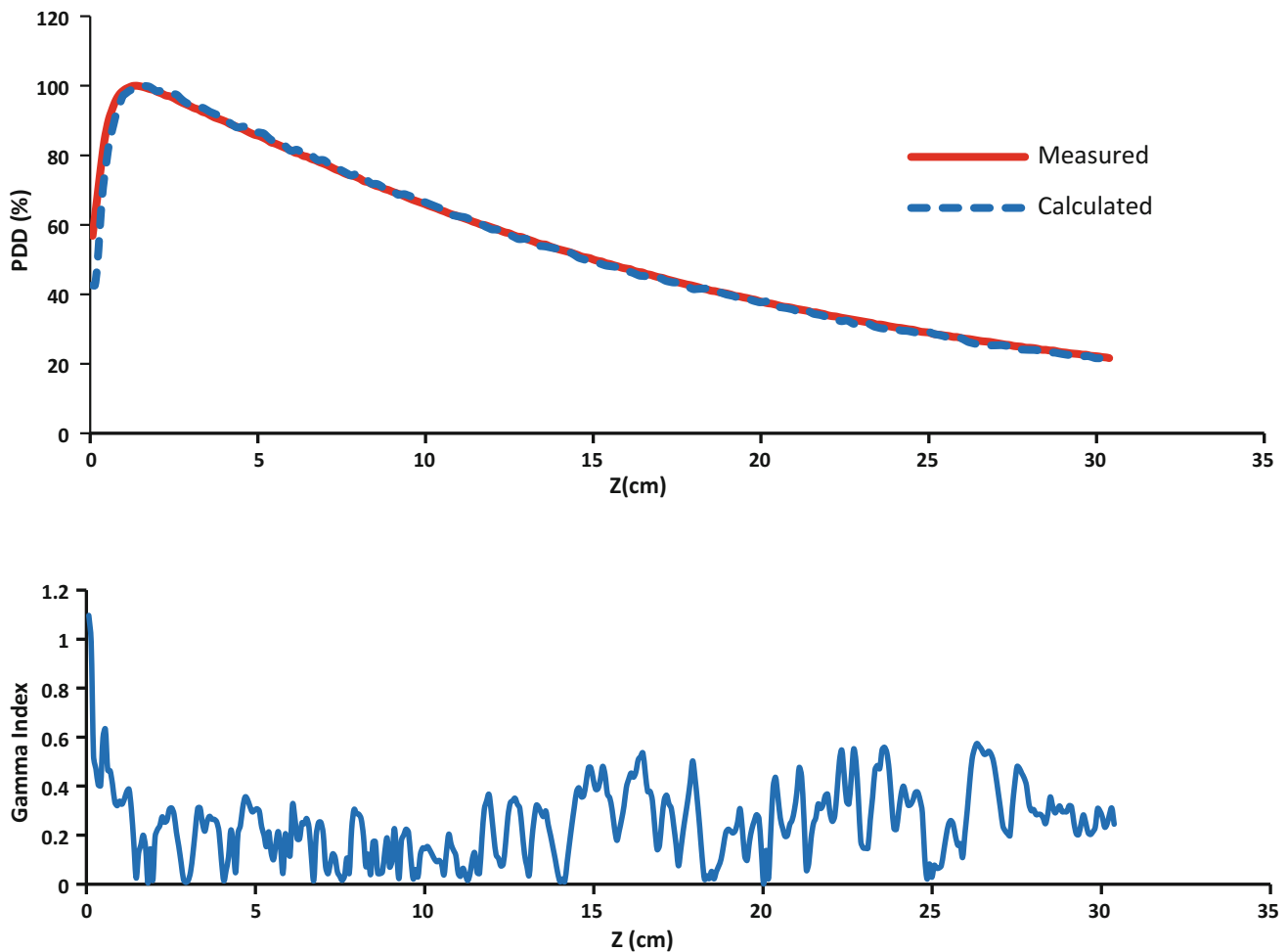


**Fig. 1** The calculated percent depth dose (PDD) compared with the measured values and the associated gamma index as a function of depth for the simulation of  $10^8$  histories

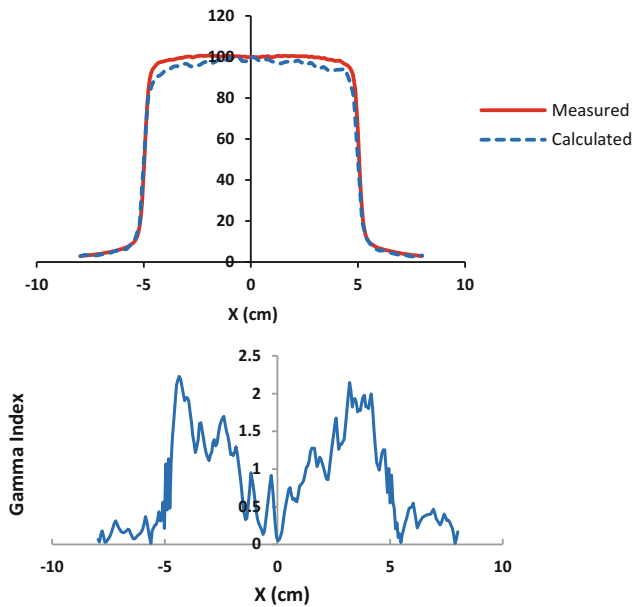


**Fig. 2** The calculated lateral profile compared with the measured value and the associated gamma index as a function of position for the simulation of  $10^8$  histories

electron beam to have a full-width-half-maximum focal spot size of 0.10 cm while all the other data sets are configured to have zero values.

## 4 Conclusion

The PRIMO system is a user-friendly, self-contained, windows-based software pack-age that allows one to configure, execute and analyze the Monte Carlo simulation of a linac without requiring any programming task from the user.

Using PRIMO, a 6 MV Varian C2100 linac is simulated and the average statistical uncertainties of the absorbed dose on a binned water phantom are compared for different number of histories. Less than 2% statistical uncertainty is reached when the number of histories is of the order of  $10^8$ . Simulations of this order is taken to the Amazon EC2 cloud where the calculations are faster and steady and for sometime are free of charges.

**Acknowledgements** I express my gratitude and appreciation to the following organizations who have provided support for this study: the Mindanao State University-Iligan Institute of Technology through the Office of the Chancellor, the National Research Council of the Philippines and Amazon.com's AWS Educate Educator Collaboration Portal. Also deeply appreciated is the assistance given by the International Organization for Medical Physics and the Society of Medical Physicists in the Republic of the Philippines.

**Conflict of Interest Statement** The author declares that she has no conflict of interest.

## References

1. Rodriguez, M, Sempau, J, Brualla, L: PRIMO: A graphical environment for the Monte Carlo simulation of Varian and Elekta linacs. *Strahlenther Onkol* 189, 881–886 (2013).
2. Brualla, L, Rodriguez, M, Lallena, A: Monte Carlo systems used for treatment planning and verification: *Strahlenther Onkol* 193, 243–259 (2017).
3. Salvat, F, Fernández-Varea, JM, Sempau, J: PENELOPE 2011—a code system for Monte Carlo simulation of electron and photon transport. Issy-les- Moulineaux, France: OECD Nuclear Energy Agency (2011).
4. PRIMO project website: <https://www.primoproject.net/primoin>.
5. Amazon.com AWS EC2: <https://aws.amazon.com/ec2/>.
6. Amazon.com AWS Educate: <https://aws.amazon.com/education/awseducate/>.



# Interdisciplinary Work as a Pedagogical Innovation for Biomedical Engineering and Health Science Students

William Ricardo Rodríguez Dueñas and Adriana María Ríos Rincón

## Abstract

The real world requires new professionals who know how to work in interdisciplinary teams to solve different types of problems efficiently. However, at university students have few scenarios where they can acquire and consolidate these necessary skills. One way to approach this problem is to offer interdisciplinary elective courses where different active and collaborative learning techniques (AcoLTs) can be applied, simulating “real” professional contexts. The aim of this study is to implement and evaluate AcoLTs to promote significant learning environments and communities of practices on an interdisciplinary course (Assistive Technology—AT) for health science and biomedical engineering students. Among the selected and adapted AcoLTs are: Project-based learning, Role-play, Hands-on technology and Hackathons. A combination was used of an only post-test one-group design using a survey and a semi-structured interview to find out the students’ perceptions about the AcoLTs implemented on the AT course. The constructs measured in the survey were Satisfaction with Learning (SL) and Communities of Practice (CoP) using a 7-point Likert scale. Descriptive statistics were used and a Spearman correlation between CoP and SL constructs was calculated. As a result, we found a strong correlation between SL and CoP, and that the students were satisfied with the opportunity to solve problems through interdisciplinary team-work relating to the project they were developing. Placing the students in “real” simulated situations of their professional practice

allowed them to acquire competences such as team-work, problem solving and critical thinking skills.

## Keywords

Pedagogical innovation • Active learning  
Interdisciplinary work • Professional skills

## 1 Introduction

The real world requires new professionals who know how to work in interdisciplinary teams to solve different types of problems efficiently. This situation requires the development of skills for multi and interdisciplinary interactions, as well as skills for how to address problems related to unequal participation, students’ resistance to group work and their different levels of ability [1]. However, at university few courses are designed to develop these kinds of skills and students from different disciplines are not always allowed to integrate. It is rare to find courses that are designed with an interdisciplinary approach, a situation that makes students feel unprepared for team work [2].

Using traditional ‘passive’ learning techniques on regular or elective courses (i.e. students just listen to the teacher’s lecture and take notes), means that the students’ learning outcomes at the end of the academic process are not fully exploited. On the other hand, when teachers use AcoLTs as an alternative they can create natural critical learning environments [3–7] that improve student learning. There is evidence that AcoLTs are effective at improving critical-thinking and problem-solving skills, thus reducing attrition [6], closing the gap between the students’ current and desired performance [8], and fostering a generation of Communities of Practice [9].

The above situations show that strengthening these kinds of skills in interdisciplinary groups is a relevant issue in higher education. One way to approach this problem is to offer interdisciplinary elective courses where different

W. R. R. Dueñas (✉) · A. M. R. Rincón  
School of Medicine and Health Sciences, Biomedical Engineering Program, Universidad del Rosario, Bogotá, Colombia  
e-mail: william.rodriguez@urosario.edu.co

A. M. R. Rincón  
e-mail: adriana.rios@urosario.edu.co

A. M. R. Rincón  
Department of Rehabilitation Sciences, University of Alberta, Alberta, Canada

AcoLTs can be applied, thus simulating ‘real’ professional contexts. The aim of this study is to implement and evaluate AcoLTs to promote significant learning environments and communities of practices on an interdisciplinary course called Assistive Technology (AT) for health science and biomedical engineering students.

## 2 Materials and Methods

### 2.1 Study Design and Participants

For this study, the constructs measured were Satisfaction with learning (SL) and Communities of Practice (CoP). SL is the extent to which students perceive how well a learning environment supports academic success [10], while CoP is the extent to which students perceive they are part of a community of peers who share the same interests and who work together to learn [9].

The instruments include a survey with 7-point Likert scale with 36 items divided into three sections. The first section asked about the participants’ demographics, and the second and third sections inquired about SL and CoP. SL (17 items) included items related to the students’ level of satisfaction with the materials, equipment, activities and instructor’s support, as well as their motivation and sense of control during the learning process, while CoP (12 items) included items related to the students’ sense of connectedness with their peers and instructors. Each item had the same weight in each construct. The scales and items that measured the two constructs, SL and CoP, had already been validated [9]. The other instrument was a semi-structured interview designed to assess the students’ perceptions about the AcoLT implemented and to obtain general opinions and recommendations about this pedagogical innovation. The interview was conducted at the end of each academic period.

With regard to the participants, this study included undergraduate students enrolled on the AT course for three academic periods (three semesters 2016–17). The University Ethics Committee endorsed this research and the students signed their informed consent.

### 2.2 The AT Course and AcoLT Implemented

The AT elective course is offered to students of biomedical engineering and health science at the School of Medicine and Health Sciences. The course is taught in English, it has three academic credits (48 h of work per semester) and focuses on the implementation, adaptation and development of assistive technologies for people with disabilities using an inter-professional approach.

Based on the results of a pilot study [11], four AcoLTs were selected and implemented. These AcoLTs were selected to improve skills such as communication with professionals from different disciplines, hands-on skills, working under pressure, problem solving and communication in an academic environment [11].

**Project-based learning.** Students have to use a hypothetical case of an individual with a disability throughout the course and design an assistive technology device for this person.

**Role-play.** In this activity, the students simulate different roles: patients with disabilities, health or engineering professionals, patients’ families and social services professionals, all in a ‘real’ life situation. They prepare their role-play based on an assigned case study. The final aim is to raise awareness among students about ‘real’ professional experiences as well as the needs of patients and their families.

**Hands-on Technology.** This is an activity where the students find, set up, test and compare different technologies as an input text interface. They compare their performance by writing/typing a sentence using different interfaces such as head trackers, adapted keyboards and keyboards on the screen.

**Hackathon.** Here the students have to solve a real technical problem within a set time. Similar to the Hands-on Technology technique [12], with this activity the students can gain a more in-depth understanding of the related concepts, but under pressure (See Fig. 1). This is an example: “*TASK: You will have the challenge of creating an assistive technology device. It will allow you to emulate the left mouse click of a person with reduced mobility by means of a ‘switch’. You have three hours to finish the activity. You can use the elements provided (e.g. springs, magnets, levers, aluminum bars, Arduino boards, and electronic elements and sensors). The design requirements are: the device cannot use batteries, and it should be as small as possible.*” Figure 1 shows an interdisciplinary group working during a Hackathon activity (three occupational therapy students and one biomedical engineering student).

### 2.3 Data Analysis

Descriptive statistics were used. The mean and standard deviation of the SL and CoP constructs were calculated. If these constructs have mean values higher than 5 points, this indicates good perceptions with the AcoLTs implemented on the AT course. In addition, a Spearman’s correlation between the CoP and SL constructs was calculated. The alpha level of significance for all the tests was set at  $p < 0.05$  (two-sided) and an SPSS V 22.0 statistics package was used. We carried out a non-parametric statistical analysis in



**Fig. 1** Interdisciplinary group working during a Hackathon activity (three occupational therapy students and one biomedical engineering student)

this study due to the ordinal nature of the variables and because we wanted to identify how the SL and CoP constructs behaved in the learning environment we had created.

### 3 Results

#### 3.1 Participants' Demographics

Of the 17 questionnaires distributed, 16 students filled them out, which provided a 94% response rate. The students were mostly young people, most aged between 20 and 22 years old (68.8%), female (87.5%), studying a bachelor's degree in health sciences (81.3% including occupational therapy, physical therapy, speech language pathology and psychology). Three students (18.8%) were enrolled on a biomedical engineering bachelor's degree program.

#### 3.2 About the Survey

The means and standard deviations of all the items of SL and CoP sections were calculated. In addition, a summative scale with all the items from both constructs (SL and CoP) were calculated, and then the mean and standard deviation of this new scale were obtained. With regard to SL, the mean and SD of the average of all the items were 6.30 (SD = 0.46. Median = 6.47. Mode = 6.65), while for the summative

scale they were 107.25 (SD = 7.85. Median = 110. Mode = 113), which means that the SL construct measured by 17 items (maximum score = 119) was located in the top third of the summative scale. This indicates that the students' SL on the AT course was high. In relation to the CoP construct, the mean was 6.26 (SD = 0.63. Median = 6.33. Mode = 6.25), the mean and SD of the summative scale were 75.1 and 7.58, respectively, with a median of 76 and a mode of 75, which means that this construct measured by 12 items (maximum score = 84) was located in the top third of the summative scale. This reveals that the students believed that the AT course contributed to the creation of communities of practice. Finally, the correlation coefficient (Spearman's Rho = +0.865,  $p = 0.000$ ) indicates a significantly strong correlation between SL and CoP.

#### 3.3 The Semi-structured Interview

Different qualitative contributions were obtained from the interviews. With regard to the AcoLT/Project-based learning, the students valued the opportunity to contribute to solving the case from the point of view of their own careers, but also from the points of view of other disciplines. In the AcoLT/Role-play, the students mentioned how useful it was to put themselves into 'another's shoes' (e.g. a person with disability); they reflected on the feelings, motivations and frustrations of being a person with a disability, or on his/her

responsibility as a professional for the patient or his/her family. With regard to the AcoLT/Hands-on technology, they liked the method of comparing their own performance when doing the same activity that involved using different input text interfaces, and sharing their scores, problems and possible improvements with the interdisciplinary group. With regard to the AcoLT/Hackathon, the students highlighted the time pressure they felt during the activity and the difficulty of quickly deciding how to solve the problem. They recognized the usefulness of listening to every member's opinion in order to select the best solution. The students mentioned that at the start they felt that the challenge was impossible, but after the three-hour session they realized that they had been able to create a simple switch, which was rewarding for them.

## 4 Discussion

The qualitative results obtained and the strong positive correlation between SL and CoP indicates that the students were very satisfied with this pedagogical innovation. The fact that the students had the opportunity to create their basic community of practice around the 'real' project, prepared them to face future interdisciplinary challenges and gave clues that they were working using an interdisciplinary approach, which is crucial in the field of assistive technology [13].

With regard to the general comments, one of the most relevant was that after finishing the AT course, the health science students felt they had the capacity to contribute to the technical aspects of any given project and, vice versa, the engineering students felt more comfortable participating in the steps of training patients as part of the assistive technology delivery process. The fruitful discussions by the students, which took place at the end of the course (semi-structured interview), also included proactive proposals for the project; for instance, the possibility of having more courses with this type of innovation, of improving some of the guidelines in the lab procedures, of having more time for their final projects (related to the case) and of continuing to create space for discovering opinions and experiences from other disciplines.

## 5 Conclusion

The students who participated in this study believed that the AT course contributed to the creation of communities of practice; they were satisfied with the learning process

carried out during the course and considered the AcoLTs implemented were useful for the pedagogical proposal. Placing the students in 'real' simulated situations of their professional practice allowed them to acquire competencies such as team-work, problem-solving and critical-thinking skills using an interdisciplinary approach. These results will encourage us to continue with this strategy in the future with larger courses.

**Conflicts of interest** The authors of this work declare that they have no conflicts of interest.

## References

1. E. F. Barkley, K. P. Cross, and C. H. Major, Collaborative learning techniques: a handbook for college faculty. Jossey-Bass, 2005.
2. B. Williams, T. Brown, R. Scholes, J. French, and F. Archer, "Can interdisciplinary clinical DVD simulations transform clinical field-work education for paramedic, occupational therapy, physiotherapy, and nursing students?" *J. Allied Health*, vol. 39, no. 1, pp. 3–10, Jan. 2010.
3. E. F. Barkley, K. P. Cross, and C. H. Major, Collaborative learning techniques: a handbook for college faculty. Jossey-Bass, 2005.
4. UNC, "Classroom activities for active learning," Suggestions and reflections on teaching and learning, 2009. [Online]. Available at: <http://cfe.unc.edu/files/2014/08/FYC2.pdf>.
5. P. Murcia, CEAP, "Reflexiones pedagógicas No1 - Aprendizaje activo," Bogotá, 2015.
6. T. A. Angelo and K. P. Cross, Classroom assessment techniques: a handbook for college teachers. Jossey-Bass, 1993.
7. K. Bain, What the Best College Teachers Do. Harvard University Press, 2004.
8. J. Charles, M.-D. Debra, M. Bob, N. David, R. David, and S. Brenda, "Enhancing student learning through effective formative feedback," 2004.
9. L. Liu, A. M. Rios Rincón, S. Esmail, E. Taylor, and A. Miguel Cruz, "Usability of mobile technologies in an occupational therapy" in CAOT, Banff, Canada, 2016.
10. C. C. Lo. "How student satisfaction factors affect perceived learning." *Journal of the Scholarship of Teaching and Learning*, vol. 10, no. 1, pp. 47–54, January 2010.
11. W. R. Rodríguez, A. Ríos, and A. Miguel (2017). How Can Biomedical Engineering and Health Science Students Learn Together? BT - VII Latin American Congress on Biomedical Engineering CLAIB 2016, Bucaramanga, Santander, Colombia, October 26th–28th, 2016. In I. Torres, J. Bustamante, & D. A. Sierra (Eds.) (pp. 50–53). Singapore: Springer Singapore.
12. CRLT-Engin. (n.d.). Active Learning Continuum. Retrieved January 24, 2018, from [http://www.crlt.umich.edu/sites/default/files/resource\\_files/Active\\_Learning\\_Continuum.pdf](http://www.crlt.umich.edu/sites/default/files/resource_files/Active_Learning_Continuum.pdf).
13. J. Bogera, P. Jackson, M. Mulvenna, J. Sixsmith, A. Sixsmith, A. Mihailidis, and Kontos, "Principles for fostering the transdisciplinary development of assistive technologies," *Disability And Rehabilitation: Assistive Technology*, p. online 10 March, 2016.



# Overseeing the Growth of Medical Physics: Indonesia Case

S. A. Pawiro, L. E. Lubis, A. N. Oktavianto, and D. S. Soejoko

## Abstract

As a nation of 261 million people (2015 survey), Indonesia has been in constant need of improvement in healthcare services which includes clinical medical physics services. A growth in number of clinical medical physicists, particularly in the field of radiation therapy, has been observed since the last thirty years. However, it is not until the last decade that a major increase took place owing to three main reasons; (1) the increase in number of radiotherapy facilities, (2) the founding of more medical physics programs in universities, and (3) the fusion of two previously-independent professional societies into one government-acknowledged professional body. All the three main reasons have positive linkage to another, allowing the field to grow even more in the future. This paper discusses the contribution of the three reasons to the growth status in medical physics profession, their relation and two-way impact to the academic aspect, as well as the future opens as consequence of this growth. Immediate plans and ongoing schemes will also be described to elaborate the chances of medical physics to thrive in Indonesia.

## Keywords

Medical physics education • Clinical training  
Professional organization

## 1 Introduction

Medical Physics service in Indonesia has been present since the era of radiotherapy with Cobalt-60 machines started in the early 1960s. The historical context is described by Soejoko et al. [1]. She also described the challenge of medical physics development in Indonesia from the beginning up to the situation in early 2015. The paper describes achievements and challenges of medical physics education and plans to establish the schemes for enabling Clinically Qualified Medical Physicists (CQMP) through clinical training.

Indonesian medical physics community consists of medical physicists in academic, clinical, and regulatory setting who has all worked together to establish the medical physics field in Indonesia. This paper aims to describe the achievements of medical physics as a growing field in Indonesia from 2015 to present.

## 2 Professional Organization

Until 2015, Indonesia has two medical physics organizations; Himpunan Fisikawan Medis dan Biofisika Indonesia (HFMBI), and Ikatan Fisikawan Medik Indonesia (IKAFMI). HFMBI was affiliated to the International Organization for Medical Physics (IOMP) and mainly focused on education and research, while IKAFMI, whose members mostly work on clinical setting, served as a partner to the Ministry of Health and dealt with regulations drafting.

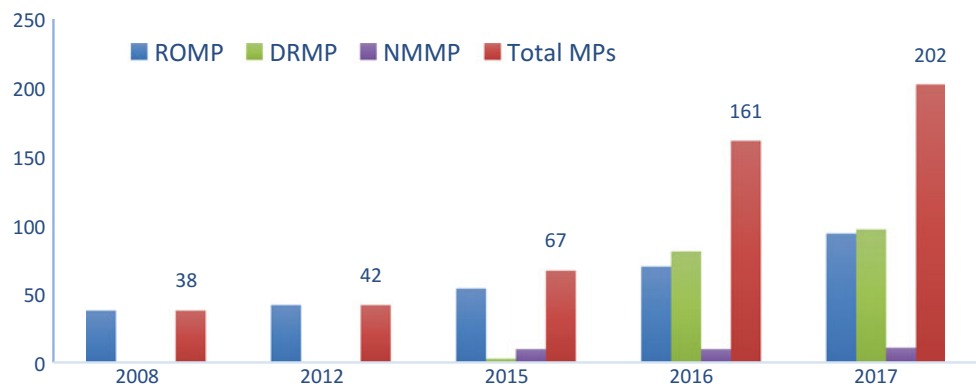
The situation of that time was not convenient, since many issues could not be solved with two separate organizations. As the society grew along with the increase of medical infrastructure number and complexity, the community sensed the need for the two professional organizations to fuse together—and so it was declared that the two parties are merged on October 31th 2015.

S. A. Pawiro · L. E. Lubis · D. S. Soejoko  
Department of Physics, Faculty of Mathematics and Natural  
Sciences, Universitas Indonesia, 16424 Depok, Indonesia

S. A. Pawiro (✉) · A. N. Oktavianto  
Aliansi Fisikawan Medik Indonesia (AFISMI), Semarang,  
Indonesia  
e-mail: supriyanto.p@sci.ui.ac.id



**Fig. 1** The number clinical medical physicists from 2008 to 2017 before and after the fusion of two organizations



Abiding the regulation regarding associations/societies from the Ministry of Law, Republic of Indonesia, all members agreed to dissolve the two organizations and establish a new one, named 'Aliansi Fisikawan Medik Indonesia' (abbreviated as AFISMI) with 'Indonesian Association of Physicists in Medicine' as its English name. In 2016, the new organization begun its labor by first re-registering members of two previous organizations and then proceed with the long-run effort for the recognition and development of medical physics in Indonesia.

During the re-registration, the total members of the society was 298 with 161 clinical medical physicists in 2016. The number grew in 2017 to be 381 members with 202 clinical medical physicists. Beside clinical medical physicists, members of the society included bureaucrats at Ministry of Health and Nuclear Regulatory Agency, academics, and other professionals at manufacturers and their representatives. Figure 1 indicated that the number of the new society's members significantly increased after the fusion of two organizations took place. The number of medical physicists from 2008 to 2015 is predicted and only Radiation Oncology Medical Physicists (ROMPs) are presented. Figure 1 also displays that the number of Diagnostic Radiology Medical Physicists (DRMPs) was significantly increased in 2016 and 2017. Unfortunately, the number of Nuclear Medicine Medical Physicists (NMMPs) has not changed from 2015 to 2017.

### 3 Recognition of Medical Physics as a Discipline

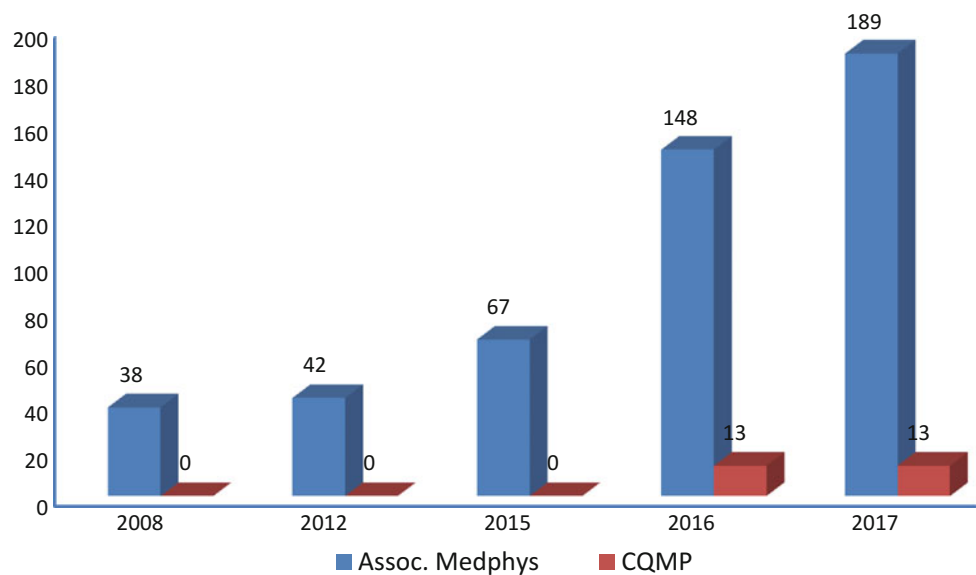
Medical physicist as profession in Indonesia has been recognized in 2007 by Ministry of Health in Decree No. 48/2007. Currently, medical physicist has been mentioned in Government Regulation No. 36/2014, classified under Biomedical Technology cluster together with radiographer and biomedical engineer. By law, medical physicists has to be present in Radiotherapy, Diagnostic and

Interventional Radiology, and Nuclear Medicine services as one of the prerequisites for medical devices to be licensed for clinical use. It is regulated by both the Nuclear Energy Regulatory Agency and Ministry of Health under separate decrees.

According to Government Regulation No. 12/2012 about higher education, medical physics education comprises of academic and professional training. In line with international recommendations, the Clinically Qualified Medical Physicist (CQMP) has academic qualification of postgraduate level with minimum 2 years of additional clinical training at hospital [2, 3]. However, a challenge is present to directly adopt the international recommendation concerning the demography of population and also medical devices distribution. To answer the quantity demand of medical physicists of around 1600 (according to Nuclear Regulatory Agency calculation), it is decided that two levels of medical physicists are to be recognized nationally; they are Associate Medical Physicist (Assoc. Medphys) and Clinically Qualified Medical Physicist (CQMP). This leveling scheme follows the directives from Indonesian regulation according to Government Regulation No. 12/2012. The Associate Medical Physicist level falls on the category of Indonesian Qualification Framework (IQF) in Level 7, whereas Clinically Qualified Medical Physicist is categorized in IQF as Level 8.

An Associate Medical Physicist essentially holds a bachelor's degree in Physics and completed the additional professional training for 6–12 months. Based on the Competence Standard of Medical Physicist developed by AFISMI and Ministry of Health, Associate Medical Physicists are dedicated to play limited role in physics service; i.e. related with simple equipment for radiotherapy, diagnostic radiology, and nuclear medicine. For the use of advanced techniques and devices in radiotherapy, diagnostic and interventional radiology, and nuclear medicine, the Clinically Qualified Medical Physicist (CQMP) must be present. The Associate Medical Physicist also served as a bridge to match the current national capacity with the international qualification of medical physicist in the future.

**Fig. 2** The number of Indonesian clinical medical physicist belonging to each levels



Currently, our CQMPs are experienced medical physicist with master's degree in medical physics who passed grandfather certification/exam conducted in May 2016 by Indonesian Board of Medical Physics (IBMP). The IBMP consists of universities, professional organization, and related stakeholders. Those with master's degree who have not passed the grandfather certification are categorized as Associate Medical Physicists. In addition to them, currently existing Associate Medical Physicists are those experienced in medical physics practice with only bachelor's degree in physics, or closely-related sciences, who had also passed similar examination. Figure 2 displays the number of Associate Medical Physicist and Clinically Qualified Medical Physicist from 2008 to 2017. The number of medical physicist in 2008 are as mentioned by Kron et al. [4] and Gondowihardjo [5]. For 2012, the data is adapted from Kron et al. [6], whereas the number of medical physicist was taken from document RCA RAS6077 which was published online at IAEA Website [7]. From 2016, data was taken from AFISMI's data and has been published by Pawiro [8].

### 3.1 Professional Training and Specialist Clinical Training

In order to harmonize and standardize the clinical medical physicist in terms of competence, we have commenced the specialist clinical training for CQMP in October 2016 and professional training for Associate Medical Physicist in January 2018. We developed modules for professional training based on the national competency standard of medical physicists that comprises of the following; radiation protection and emergency response, acceptance and commissioning of new equipment, quality control of equipment,

**Table 1** The number of trainee for AMP training and CQMP training

Batch	AMP training	CQMP training
I	23 (January 2018)	7 (October 2016)
II	25 (June 2018)	6 (October 2017)

radiotherapy planning, and dose audit. On the other hand, the specialist training used entirely the IAEA Training Course Series 37 [9], 47 [10], and 50 [11] for ROMP, DRMP, NMMP, respectively. Table 1 described the number of trainees of both training programs.

### 3.2 Certification

According to Ministry of Education Regulation No. 83/2010, the competency certificate has to be issued and signed by a representative of higher education institution and the professional organization. Abiding the regulation, the certification of medical physicist is performed by Indonesian Board of Medical Physics and is currently administered by the Indonesian Alliance of Universities with Medical Physics Program (in Indonesian; Aliansi Institusi Pendidikan Fisika Medis Indonesia, AIPFMI). Currently, the members of AIPFMI are Universitas Indonesia, Bandung Institute of Technology, Diponegoro University, Brawijaya University and Hasanuddin University.

The Alliance served to arrange written, oral, and/or practical exams for the examinee. In addition, this organization also provides the competency certificates signed by the Dean of one of its members (depends on where the certification examinations are held) and AFISMI president. Beside playing roles in the certification, AIPFMI also

harmonizes curricula for medical physics programs in both undergraduate and graduate levels.

### 3.3 Registration and Licensing

The registration of clinical medical physicists in Indonesia is regulated under the National Council of Allied Health Professional (KTKI). AFISMI as the official professional organization for medical physics will place two representatives in the council and will help to register the clinical medical physicists. As a requirement to register as clinical medical physicist, candidates must have competency certificate and recommendation from AFISMI. Upon successful application, clinical medical physicists belonging to both levels will get the certificate of registration and registration number as medical physicist valid for five years. After five years, clinical medical physicists has to re-new their registration to the council with 25 Continuous Professional Development (CPD) credits and a recommendation from AFISMI.

After the registration, the Ministry of Health is planned to issue the license for medical physicists to practice. Until recently, the Ministry of Health and AFISMI are still working on the drafting of the regulation.

## 4 Capacity Building in Medical Physics

Based on the number of radiotherapy machines, diagnostic X-rays machines, and nuclear medicine machines in Indonesia, the nation is currently in short of approximately 1600 medical physicists. This data is in line with the calculation by Datta [12] which calculated the need of medical physicists based on cancer data and ideal radiotherapy equipment of around of 469 ROMPs. Additionally, the documents of RAS6077 [6] mentioned the need of ROMP, DRMP, NMMP in Indonesia are 122, 271, and 22 clinical medical physicists. Based on this data, we have tried to enhance and strengthen medical physics in Indonesia in education, clinical training and continuous professional development.

### 4.1 Medical Physics Education

Soejoko [1] has described that the establishment of medical physics education has been supported by IAEA Project through Technical Cooperation Project No. INS6013, INS6014, and INS6015. This project supported the equipment, training of faculty members, training of candidate of clinical supervisors, training of nuclear regulatory staffs, and scientific visit for senior staffs from 2007 to 2012. The professional training for Associate Medical Physicist and specialist clinical training for CQMP could have only be

initiated due to success stories of our previous IAEA projects from 2007 to 2015.

The next focus of our IAEA projects will be the establishment the clinical medical physicists and training for diagnostic radiology medical physicists in University Hospitals through INS6020 for 2018 to 2019. The project will procure equipment for Bandung Institute of Technology and Brawijaya University, provide fellowships for young staff members, and scientific visit for benchmarking senior staffs. Universitas Indonesia, Diponegoro University, and Hasanuddin University already have equipment from previous IAEA and Government projects, so they only need human resources funding for fellowships and scientific visits. It is highly expected that the project will enhance the quality of education and professional trainings for Associate Medical Physicist in the near future.

For education, we are fortunate that Indonesia government provide scholarships for students to pursue master's and doctorate through Endowment Fund for Education (LPDP) and Beasiswa Unggulan (BU) scholarships from the Ministry of Education (under collaboration framework with the Ministry of Finance). This scheme has increased the number and quality of graduate students in Medical Physics. From 2012, 17 awardees of government scholarship schemes have pursued master's degree in Medical Physics at Universitas Indonesia, 6 awardess at Bandung Institute of Technology, and 1 awardee have obtained master's degree in Medical Physics at Imperial College London. Beside scholarships for young student, the government also provide scholarships lecturers to pursue their Ph.Ds. Under this scheme, around 10 young lecturers from several universities are currently finishing their Ph.Ds. in Medical Physics.

### 4.2 Clinical Training

Specialist training to achieve Clinically Qualified Medical Physicist level has been initiated under IAEA regional project RAS6077 and is continued through regional project RAS6087. This project, provides resources for the trainers of clinical training supervisor, remote supervisor from overseas for participants with limited number of supervisor on certain medical physicist specialist, and e-learning system. We also appreciate the vendor who donated Treatment Planning System units for professional training of Associate Medical Physicist that enables trainees to explore the system's capabilities prior to clinical placement.

### 4.3 Continuous Professional Development

Continuous Professional Development (CPD) is described as a mechanism to maintain and improve the quality of medical

physicist through seminars, workshops, trainings, or publication. By regulation, medical physicists have to collect 25 CPD credits from AFISMI in order to be re-registered every 5 years.

The Ministry of Health provides funding support for CPD activities every year, with the main objective being to support professional organizations to conduct activities for CPD and upgrade the knowledge and competency in new techniques and technology. On the other hand, IAEA, from several projects also enable expert missions to share and upgrade the knowledge of Indonesian medical physicists.

## 5 Conclusion

We conclude that the fusion of professional organization gave significant impact to the acceleration of Medical Physics development in Indonesia. The fusion fueled our efforts for recognition, capacity increase, certification, and registration of medical physicist in Indonesia. The international and government incentives are also of significant positive influence to the improvement of the quantity and quality of medical physicist through academic education, clinical training, and continuous professional development.

**Acknowledgements** We express gratitude to Indonesian Ministry of Health and Nuclear Energy Regulatory Agency for recognizing the medical physicist profession and many supports in the form of not only administrative, but also incentives to improve the quality of medical physicists. We also recognize and highly appreciate the International Atomic Energy Agency and Indonesian Nuclear Energy Agency who has facilitated projects to provide equipment and build the capacity of Indonesian medical physicists.

**Conflict of Interest Disclosure** The authors have no conflict of interest to report.

## References

1. Soejoko, DS., Pawiro, SA., Lubis, LE.: Medical Physics in Indonesia: Current Status and Plan. In: IFMBE Proceeding Vol 51, pp. 1601–1603. Springer International Publishing Switzerland (2015).
2. International Organization for Medical Physics. Basic Requirements for Education and Training of Medical Physicist. Policy Statement No. 2, IOMP, [www.iomp.org](http://www.iomp.org).
3. International Atomic Energy Agency.: Postgraduate Medical Physics Academic Programmes. IAEA, Vienna (2013).
4. Kron, T et al.: Medical physics aspects of cancer care in the Asia Pacific region. *Biomed Imaging Interv J* 4(3):e33 (2008).
5. Gondhowiardjo, SA.: History and growth of radiation oncology in Indonesia. *Biomed Imaging Interv J* 4(3):e42 (2008).
6. Kron, T et al.: Medical physics aspects of cancer care in the Asia Pacific region: 2011 survey results. *Biomed Imaging Interv J* 8(2): e10 (2012).
7. IAEA Homepage, [https://humanhealth.iaea.org/HHW/MedicalPhysics/The MedicalPhysicist/ Educationand Training Requirements/Accreditationand Certification/ Recommendations\\_for\\_accreditation\\_and\\_certification\\_in\\_medical\\_physics.pdf](https://humanhealth.iaea.org/HHW/MedicalPhysics/The%20MedicalPhysicist/EducationandTrainingRequirements/AccreditationandCertification/Recommendations_for_accreditation_and_certification_in_medical_physics.pdf), last accessed 2018/1/30.
8. Pawiro, SA et al.: Current Status of Medical Physics Recognition in SEAFOMP Countries. *MPI Journal* 5(1), 11–13 (2017).
9. International Atomic Energy Agency: Clinical Training Medical Physicists Specializing in Radiation Oncology. IAEA, Vienna (2009).
10. International Atomic Energy Agency: Clinical Training Medical Physicists Specializing in Diagnostic Radiology. IAEA, Vienna (2010).
11. International Atomic Energy Agency: Clinical Training Medical Physicists Specializing in Nuclear Medicine. IAEA, Vienna (2011).
12. Datta, NR et al.: Radiation Therapy Infrastructure and Human Resources in Low-and Middle-Income Countries: Present Status and Projections for 2020. *Int J Radiat Oncol Biol Phys* 89(3): 448–57 (2014).

# Enhance Medical Education and Training Using Interactive Autostereoscopic 3D Display by In Situ 3D Interaction

Guowen Chen, Cong Ma, Xinran Zhang, and Hongen Liao

## Abstract

In this study, we proposed to combine autostereoscopic 3D display and interactive display to enhance medical education and training, which could be an alternative to the traditional medical education. We developed an enhanced 3D rendering algorithm for medical education and training based on the traditional lens based rendering algorithm (LBR). We used the system to perform a user study of medical visualization and education with a heart phantom, and a human-computer interaction device to capture hand motions, rotations, and gestures. Structure of the heart was labeled and validated by physician ahead. Furthermore, we divided 40 users (20 women and 20 men) into two groups: control group and experimental group, to operate a user study on anatomical structure of the heart phantom. Experimental results showed that our algorithm can achieve higher rendering performance than the traditional LBR. User test showed that 3D education system equipped by the enhanced LBR can achieve interactive display, and can thus promote education experience and reduce education time consuming. Further work includes more user studies on medical education and increasing frame rate of rendering for more versatile hardware configurations.

## Keywords

Medical education • Human-computer interaction  
In situ interaction

## 1 Introduction

In the traditional medical education scenario, anatomical models, experimental animals and books are utilized to convey the knowledge of anatomical structures. However, the anatomical models are bulky to carry and expensive, experimental animals are not always available, while the books are not intuitive and vivid. One solution for this problem is medical simulation [1, 2]. In medical simulation, the main sense input of human are vision [3], while the control information outputs of human relies on hand. Currently, people mainly rely on two-dimensional display as visual input and the mouse as the corresponding output device, default. In an interactive display system, human coordination includes: spatial coordination which is the relationship between the spatial position of display and control and the human expectation, coordination of motion which refers to the movement of the controlled variables is coordinate with the movement of the visual feedback variables, the conceptual coordination that refers to the consistency of display and control conceptually with human expectations and habitual mode which refers to subconscious and automatic behavior as a conditioned reflex. For human vision, 3D display can provide motion and binocular parallax as depth cue directly. Thus, it can cater for the spatial coordination than the traditional 2D display [4, 5]. Furthermore, hand tracking devices can provide 3D control information by spatial movements and can provide conceptual coordination and habitual control by hand gesture.

## 2 Methods

### 2.1 Interaction Model Design

In multi-channel interactions, users can communicate with computer systems using natural interactions such as voice, gestures, eyes, emoticons, and more. In this study, we use

G. Chen (✉) · C. Ma · X. Zhang · H. Liao  
Department of Biomedical Engineering, School of Medicine,  
Tsinghua University, Beijing, 100084, China  
e-mail: liu-j15@mails.tsinghu.edu.cn

H. Liao  
e-mail: liao@tsinghua.edu.cn



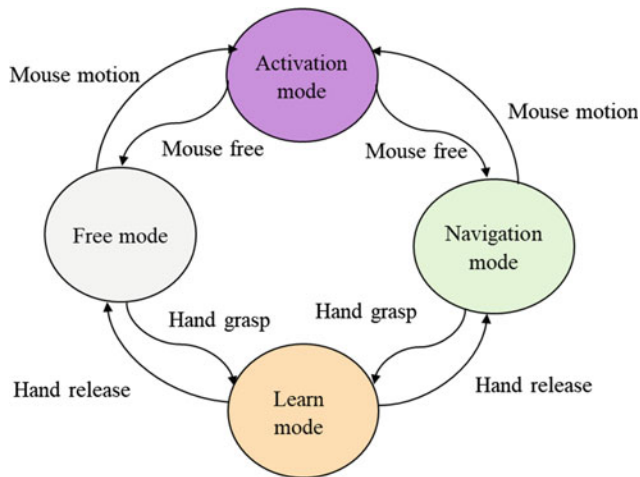


**Fig. 1** Diagram of state machine model

mouse and the Leap motion controller as interactive inputs of multi-channel information [6]. In the application, we offer the 2D and 3D visualization information by 2D and 3D displayer. We use the state machine principle. We set the system as four modes: navigation mode, activation mode, learn mode and free mode. The navigation mode consists of translation, rotation operation. Under the navigation mode, different perspectives of the model can be observed by mouse. In the idle mode, the program stops rendering. After capturing the right hand by the Leap Motion camera, the

state machine jumps from the idle mode to the activation state, and if the hand gesture has been registered, it enters the learn mode. If the hand is released or the gesture is unregistered, it went back to the free mode if the mouse button is up, or navigation mode if the mouse button is push down. In the learn mode, the user can pick up the region of interest (ROI) to view the denotation of anatomical structure (Fig. 1).

## 2.2 Rendering Algorithm

To meet the image quality and interactivity of the system, we proposed an enhanced lens based rendering algorithm for autostereoscopic 3D displays to achieve higher frame rates and better image quality without pixel resampling [7]. We adopted Octree to manipulate the mesh load and undertake viewport based minimal indexing before sending the meshes to GPU, as shown in Fig. 2, to accelerate the rendering. The details of Octree based index shuffling and viewport based minimal indexing are shown in Fig. 3a, b. In the viewport based minimal indexing, the visibility of vertices are determined by Octree to achieve the index range. The range can be used to cull most of the invisible vertices. The pre-processing of meshes introduce a small overhead on CPU but can provide a great time cost cut on GPU based primitive processing.

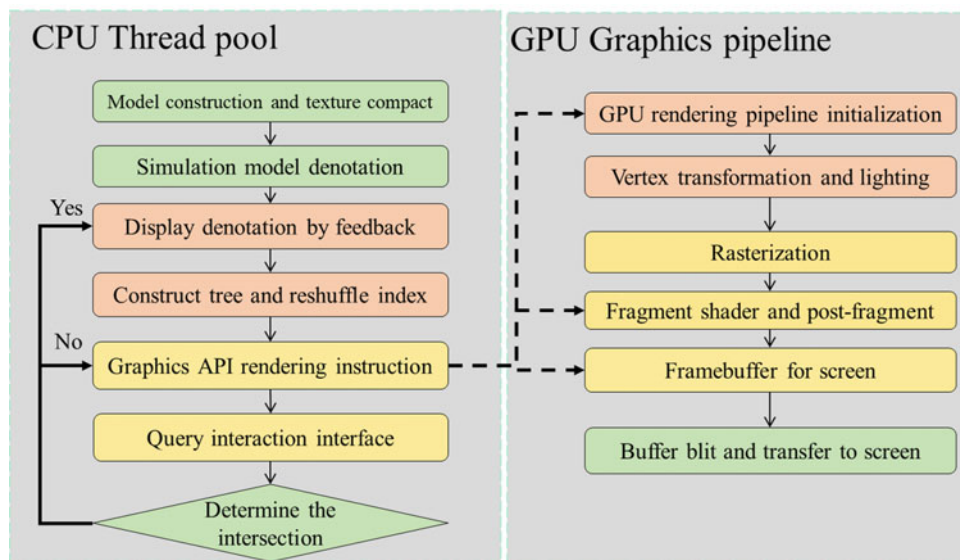


**Fig. 2** Flowchart of the rendering and display

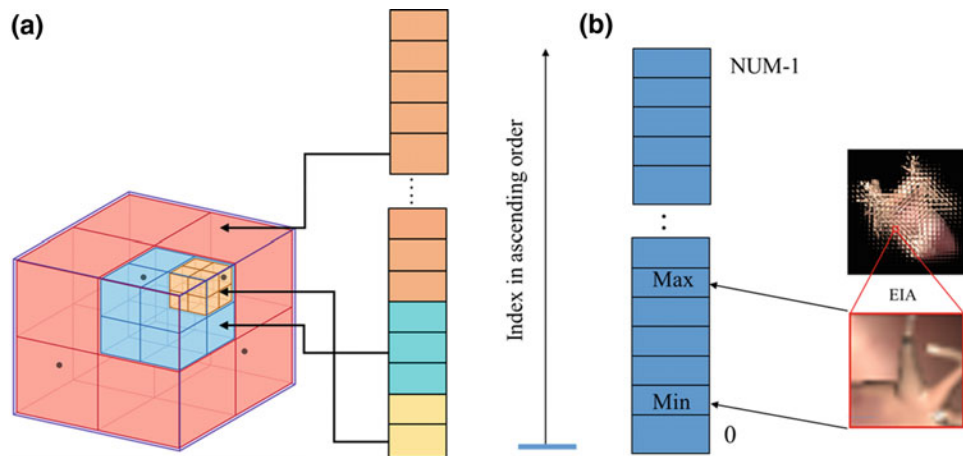


**Fig. 3** a Octree based vertex shuffling and b viewport based minimal indexing

### 3 Experiments and Results

#### 3.1 System Setup

To evaluate the proposed algorithm, we fabricated one IV display and implemented the algorithm by C++ with omp OpenGL and GLSL. We implemented the proposed LBR algorithm to render IP images on a NVIDIA GTX 1080Ti platform. For studying the anatomy, the structure of heart should be of fine precision. Therefore, we adopt a heart phantom with 53400 triangular primitives in this experiment. The 3D display consists of a LCD of  $3840 \times 2400$  resolution and micro-lens array with  $84 \times 73$  lenses as shown in Fig. 4c. The resolution specification of the 2D display is  $3840 \times 2160$  as shown in Fig. 4b.

#### 3.2 Experiment Design

In this study, we should prove the usability of the proposed education system. Usability is an important part of the human-computer interaction system. It relates to whether human-computer interaction can meet the user's

expectations and the efficiency and convenience of achieving this goal. The research on the feasibility analysis and evaluation of human-computer interaction system mainly involves the convenience and the efficiency of the system. The convenience of the system refers to simplicity in learning and using in simple tasks. The efficiency of the system can be evaluated by the time cost to finish a specific task after professional training. In this experiment, we design the easy task as that to know how to navigate through the heart phantom and the advanced task as to learn through ten denoted anatomical structures as shown in the Fig. 4a.

#### 3.3 Results

In this experiment, we achieved rendering rate of approximately 50 FPS and achieved fluent interactivity (grasps and scratches), with the enhanced LBR as shown in Fig. 4d, while rendering frame rate of the traditional method is 9.8 FPS. Specifically, the overhead of minimal primitive indexing introduced an overhead of 0.003 s and have a cut-off on general rendering time cost by more than a half. In the user study, the experimental group cost 34.7 s on the 3D display, while the control group used 44.5 s on the 2D

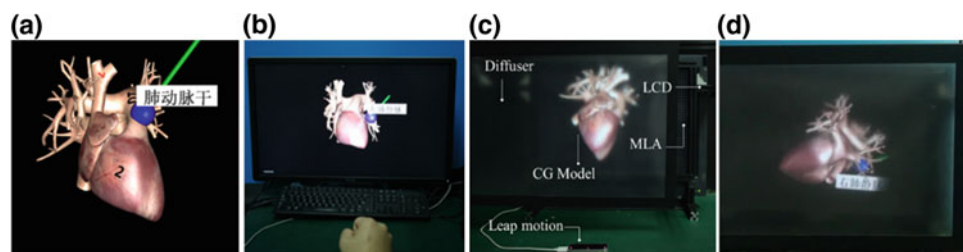


**Fig. 4** a Ten denoted structures b human interaction by 2D display c configuration of interactive 3D display d demonstration of interactive 3D display

**Table 1** Results of user study

Groups	Introductory task (s)	Advanced tasks (s)
Experimental group	34.7	32.2
Control group	44.5	34.9

display under the advanced tasks. The experimental group cost 32.2 s in the introductory task in average, while the control group cost 34.9 s in average (Table 1).

## 4 Conclusions

In this paper, according to the requirements of medical visualization, we proposed and implemented an enhanced LBR algorithm, and evaluated rendering performance by benchmarking against the traditional LBR. Evaluation experiments show the 3D interactive medical learn system is more convenient and efficient for educatees to navigate and learn through the anatomical structures than the traditional interactive 2D display system.

**Acknowledgements** The authors acknowledge supports from National Key Research and Development Program of China (2017YFC0108000), National Natural Science Foundation of China

(81427803, 81771940), National Key Technology R&D Program of China (2015BAI01B03), Soochow-Tsinghua Innovation Project (2016SZ0206), and Beijing Municipal Science & Technology Commission (Z151100003915079).

## References

1. Basdogan, C., Ho, H., Srinivasan, M.: Virtual environments for medical training: graphical and haptic simulation of laparoscopic common bile duct exploration, *IEEE/ASME Trans. Mechatronics* 6, 269–285 (2001).
2. Okuda, Y., Bond, W., Bonfante, G., et al.: National growth in simulation training within emergency medicine residency programs, 2003–2008 [J]. *Academic emergency medicine*, 15(11), 1113–1116 (2008).
3. Loomis, M., Klatzky, L., and Giudice, N.: Sensory substitution of vision: importance of perceptual and cognitive processing. *Assistive technology for blindness and low vision*: 162–191(2012).
4. Van, K., and Broyles, J.: Visuospatial task performance as a function of two-and three-dimensional display presentation techniques. *Displays*, 21(1), 17–24 (2000).
5. Dodgson, N.: Autostereoscopic 3D Displays. *Computer* 38(8), 31–36 (2005).
6. Leap motion, Inc., Leap motion, <https://www.leapmotion.com>, last accessed 2018/01/27.
7. Chen, G. et. al.: Real-time Lens based Rendering Algorithm for Super-multiview Integral Photography without Image Resampling, *IEEE transactions on visualization and computer graphics* (2017).

# Public-Private Partnership Strategy in Acquiring Facilities for Radiotherapy Services and for Education and Training of Medical Physicists in Southern Philippines

Angelina M. Bacala and Agnette de Perio Peralta

## Abstract

The Philippines is an archipelagic country with an estimated 105 M people. Although cancer is the third leading cause of mortality, only a few radiotherapy centers are in operation and majority of these are located in the capital region of Manila in the island of Luzon. There is only a single school, a private university, located in Manila, offering the master's degree in medical physics. Mindanao Island, considered the breadbasket of the nation, is the second largest island of the Philippines. It is located in the south and has a population of about 22 M people. Only four hospitals in Mindanao provide radiotherapy services using a linear accelerator (linac) while four radiation oncologists and seven medical physicists serve the needs of the entire island. We describe in this paper the public-private partnership (PPP) strategy we are proposing in order to acquire a medical linac to be used for radiotherapy at a local private hospital, for research, and for a planned medical physics education and training program in the largest state university in Mindanao.

## Keywords

Medical physics graduate program • Mindanao Philippines • Public-private partnership

## 1 Overview

Located in Southeast Asia, the Philippines is an archipelago of 7,107 islands. As it is completely surrounded by water, the islands are accessible only by sea and air. It is estimated that the current Philippine population consists of about 105 million persons based on the 2015 Census of Population with an annual population growth rate of 1.72% between the years 2010–2015 [1].

As to the leading cause of mortality among the Filipino population, cancer is the third. The Globocan (2012) data showed that around 100,000 people are newly diagnosed with cancer each year. The Philippines has the highest breast cancer prevalence in Asia. Cancers common in the country are breast cancer, colorectal cancer, nasopharyngeal cancers, laryngeal cancers, and gynecologic cancers [2, 3].

There are at present 34 licensed facilities with linear accelerators in the country that offer radiation therapy services (Fig. 1) and seven (7) facilities in the pre-licensing phase with more being planned. Of these 34, two (2) also have a cobalt 60 teletherapy unit [4]. Additionally, there are five (5) hospitals which have only a cobalt-60 teletherapy unit, one of which is a gamma knife [5].

About half of those hospitals are located in the capital region of Manila in Luzon, the largest island in the country. The second largest island in the Philippines is Mindanao Island. It is considered the breadbasket of the nation with a population of about 22 million people. Only four (4) hospitals offer linear accelerator radiotherapy services in the whole island. Four (4) radiation oncologists and seven (7) medical physicists serve the needs of the entire Mindanao. All of the medical physicists studied in the University of Santo Tomas (UST), a private university located in Manila, the only university that offers the master's program in medical physics (MP) in the Philippines.

---

A. M. Bacala  
Department of Physics, Mindanao State University-Iligan Institute of Technology, 9200 Iligan City, Philippines

A. de Perio Peralta (✉)  
The Graduate School, University of Santo Tomas, Manila, Philippines  
e-mail: apperalta2004@yahoo.com

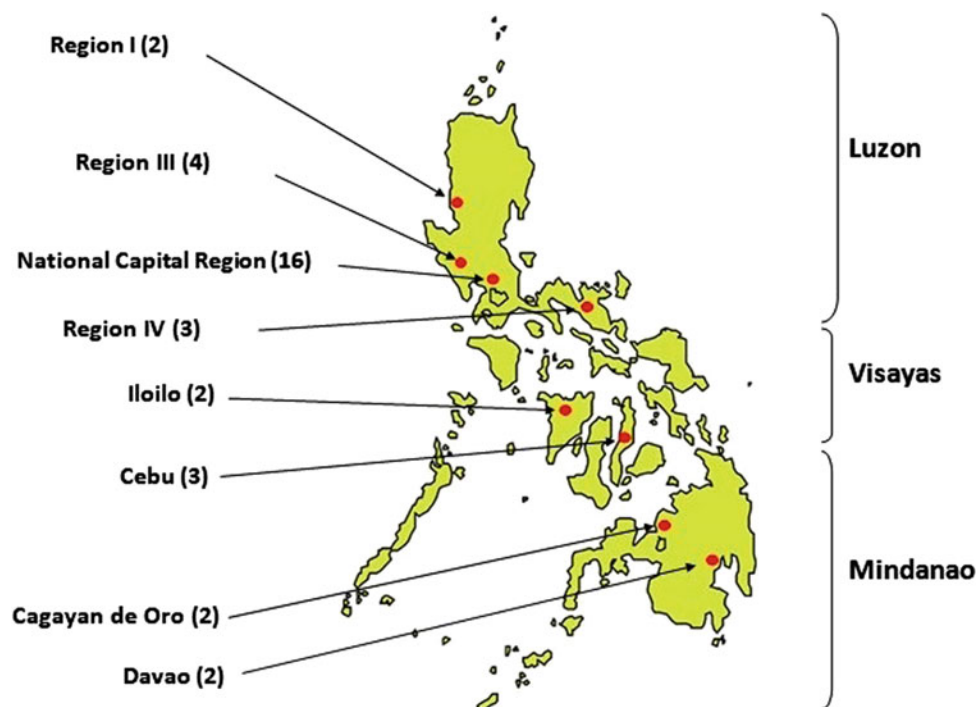


**Fig. 1** Licensed linac teletherapy facilities in the Philippines

## 2 Radiation Oncology Medical Physics Practice in the Philippines

The Philippine Organization of Medical Physicists (POMP) was established in 1986. It became the Society of Medical Physicists in the Republic of the Philippines (SMPRP) in 2016. POMP created the Philippine Board of Medical Physics Section of Radiation Oncology Medical Physics in 2010. To date, there are twenty (20) Board-certified radiation oncology medical physicists and sixty-eight (68) practicing radiation oncology medical physicists in the country, almost all with a master's degree from UST [6]. Practicing MPs have gone through a mentoring or a residency program with the senior physicists in major hospitals. The clinical training modules developed by the International Atomic Energy Agency are used in the residency programs in radiation oncology medical physics and also in those of nuclear medicine medical physics and diagnostic radiology medical physics. However, with regards to other certifying boards, there is still no existing certifying board for the other fields of medical physics.

## 3 Public-Private Partnership for Southern Philippines

### 3.1 Education, Clinical and Research Applications

Significant improvement in radiotherapy services in Mindanao can be effected if an advanced education and training program in medical physics is initiated. An indispensable tool in the implementation of this program is the existence of a medical linac for the treatment of patients which can also be used for the training and education of medical physics graduate students [7, 8].

A major cancer treatment modality is called external beam radiation therapy which uses a linac. Linacs are devices that accelerate electrons to high kinetic energies using microwave radio-frequency fields through specially evacuated linear structures called accelerating waveguides.

In this project, when the linac is not being used for therapeutic purposes, it will be used for education, training, and research. Besides research in medical physics, several



research projects can be undertaken such as testing the radiation hardness of new materials for the semiconductor and nanoparticle laboratories, analysis of protein structures leading to the development of new drugs, and image processing with applications to materials characterization, among others. This arrangement is possible since the linac will be used for cancer treatment for eight (8) h in a day, five (5) days in a week.

To surmount the huge challenges in present-day Philippines, a private-public partnership (PPP) is proposed with a local private hospital in Iligan City to host the radiotherapy operations of a medical linac. In the PPP, the linac will be acquired through government funds by a university research community which is going to maintain the linac as a research facility with pre-arranged schedule of access given to university researchers.

### 3.2 Mercy Community Hospital and Mindanao State University-Iligan Institute of Technology

Iligan City, with a population of more than 350,000 is located in Northern Mindanao and is home to the Mindanao State University-Iligan Institute of Technology (MSU-IIT), a state university, and Mercy Community Hospital (MCH), a private tertiary hospital. MCH lacks the huge capital investment required to set up a radiotherapy center but has agreed to provide the land requirement for free inside their hospital campus and the use of their diagnostic equipment such as CT, MRI and other machines once the linac is available.

MSU-IIT, on the other hand, has been running one of the country's most active physics programs for several years now. It is the only institution in Mindanao that offers the Ph.D. Physics program and has the highest concentration of advanced manpower in physics in southern Philippines. The same can be said of its graduate programs in mathematics, chemistry, biology, engineering, and materials sciences. MSU-IIT has been tasked to submit the proposal for funding to the Department of Health (DOH) for the acquisition of a medical linac and the construction of the facility. The funding required however for the training of personnel and the setup of the master's program in medical physics will be sourced from the Department of Science and Technology funds as the DOH does not provide such kind of grants.

## 4 Conclusion

There is a shortage of radiotherapy facilities in the country. Although this situation is due to a number of factors, any intervention would be extremely helpful. The acquisition of a medical linac by a university planning to offer a medical physics master's course would be greatly advantageous.

In the PPP strategy, the linac will be used in a local hospital to treat cancer patients. When it is not used for radiotherapy, research personnel from the university will be given access to the linac to enable them to do research. In addition to education, training, and research and development in medical physics, the linear accelerator can also be used by researchers in materials science, nanotechnology, radiobiology, chemistry, advanced mathematics, statistics, and agriculture.

PPP is one of the most viable ways to address the immense shortfall of medical linacs in the country while at the same time providing for the urgent need of educating and training future practicing medical physicists to serve the needs of the patients in the southern island of Mindanao. It is imperative for this model to succeed so that it can be replicated in other areas of the country, all of which are in need of a medical linac. It is an innovative approach which we think other countries can use for development in education and research, especially in medical physics.

**Acknowledgements** We appreciate and are grateful to the following for the support given to us in this undertaking: Sr. Rose Palacio, RSM of Mercy Community Hospital, Iligan City, the Department of Research, Mindanao State University-Iligan Institute of Technology, Iligan City, the University of Santo Tomas Graduate School, the Department of Health, Manila, the Philippine Nuclear Research Institute of the Department of Science and Technology, and the Society of Medical Physicists in the Republic of the Philippines. The assistance from the International Organization for Medical Physics is also gratefully acknowledged.

**Conflict of Interest** The authors declare that they have no conflict of interest.

## References

1. Philippine Statistics Authority POPCEN 2015, <https://psa.gov.ph/tags/popcen-2015>, last accessed 2018/01/18.
2. Department of Health, <http://www.doh.gov.ph/Statistics/Leading-Causes-of-Mortality>, last accessed 2018/01/18.
3. Canal, J.P.A., Limkin, E.J.C.: Radiation Therapy in the Philippines: A Challenge in Resourcefulness. *Int J Radiation Oncol Biol Phys* 94 (1), 7–10 (2016).

4. Center for Device Regulation Radiation Health and Research (CDRRHR), <http://www.fda.gov.ph/fda-corner/center-for-device-regulation-radiation-health-research/>.
5. Philippine Nuclear Research Institute, Department of Science and Technology, <http://www.pnri.dost.gov.ph>.
6. Society of Medical Physicists in the Republic of the Philippines Database.
7. Abdel-Wahab, M., Zubizarreta, E., Polo, A., Meghzifene, A.: Improving Quality and Access to Radiation Therapy – An IAEA Perspective. *Semin Radiat Oncol* 27, 109–117 (2016).
8. Zubizarreta, E.H., Fidarova, E., Healy, B., Rosenblatt, E.: Need for Radiotherapy in Low and Middle Income Countries – The Silent Crisis Continues. *Clinical Oncology* 27, 107–114 (2015).

# Evaluation of the Impact of an International Master of Advanced Studies in Medical Physics

Giorgia Loreti, Hossein Aslian, Antonio Brito, Harry Delis, Renata Longo, and Renato Padovani

## Abstract

The Master of advanced studies in Medical Physics (MMP) has been jointly organized since 2014 by the International Centre for Theoretical Physics (ICTP) and Trieste University and supported by the International Atomic Energy Agency (IAEA), through the work of the Dosimetry and Medical Radiation Physics Section (DMRP), Division of Human Health (NAHU) and the IAEA Technical Cooperation Programme. The MMP, offers one academic year of theoretical classes followed by one year of structured clinical training in hospitals. It aims at addressing the scarcity of formal education and training schemes for medical physics studies, through an internationally harmonized programme that provides graduates with an academic knowledge and practical skills and competencies, to effectively practice medical physics once back to their home countries and Regions. Adequate academic education and structured clinical training of medical physicists play an important role in ensuring the safe and effective use of nuclear technologies in the diagnosis and treatment of patients. To evaluate the impact of the MMP, an online survey was developed and distributed to the graduates of the first two cycles of the

programme, in March 2017, considering different aspects contributing to the overall fulfilment of the MMP aims. Criteria comprised: the activity of the graduates before and after the MMP, return rate to their home country and work activities performed after the degree. Specific feedback was also analysed about the MMP programme. The analysis of the 22 received answers (85% of all graduates at the time of the survey) is presented in this article.

## Keywords

Medical physics education • Postgraduate education  
Clinical training

---

The original version of this chapter was revised: This chapter has been changed as Open Access licensed under the terms of the Creative Commons Attribution 3.0 IGO License. The correction to this chapter can be found at [https://doi.org/10.1007/978-981-10-9035-6\\_166](https://doi.org/10.1007/978-981-10-9035-6_166)

---

G. Loreti (✉) · H. Delis

International Atomic Energy Agency (IAEA), Vienna, Austria

e-mail: g.loreti@iaea.org

H. Aslian · R. Longo

Dipartimento Di Fisica, Università Di Trieste, Trieste, Italy

A. Brito

Hospital Metropolitano, Quito, Ecuador

R. Padovani

International Centre for Theoretical Physics (ICTP), Trieste, Italy

---

## Introduction and Historical Background

### 1.1 Establishment of the Joint ICTP—University of Trieste Master of Advanced Studies in Medical Physics Supported by IAEA

The Master of Advanced Studies in Medical Physics (MMP) programme has been established in 2013 thanks to an agreement between the Abdus Salam International Centre for Theoretical Physics (ICTP) and the Trieste University and the contribution of the Trieste University Hospital. The ICTP, a United Nations Educational, Scientific and Cultural Organization (UNESCO) and IAEA institution, has been for more than 50 years a driving force behind global efforts to advance scientific expertise worldwide.

In January 2018 the MMP began its 5th cycle, composed by 19 students from 17 different countries. The international and unique profile of the programme is better understood knowing that the 87 students of the 5 cycles come from 48 different countries, 22 from Africa, 13 from Asia and the Pacific, 5 from Europe and 8 from Latin America and the Caribbean.

Implementation of the MMP programme requires significant financial resources and thus the financial support of different stakeholders has been crucial; these include: American Cancer Society (ACS), European Federation of Organisations For Medical Physics (EFOMP), ICTP, International Organization for Medical Physics (IOMP), Kuwait Foundation for the Advancement of Sciences (KFAS), The World Academy of Sciences (TWAS), Secretaría de Educación Superior, Ciencia, Tecnología e Innovación of Ecuador (SENESCYT), but mainly the IAEA, through the work of the Dosimetry and Medical Radiation Physics Section (DMRP) [1], Division of Human Health (NAHU) and the IAEA Technical Cooperation Programme.

## 1.2 The MMP Structure

The two-year programme is designed to provide promising graduates in physics or in related fields with one year of postgraduate academic education and one year of clinical training. The clinical training network comprises 19 medical physics departments: 18 Italian and one Croatian. The residency focuses on a specific area of medical physics: medical physics for diagnostic imaging or medical physics for radiation therapy, with elements in cross cutting fields. The programme and the assessment methodology of the acquired competencies constitute the resident's portfolio, derived adapting the IAEA [2–6]—including AFRA [7–9]—guidelines. At the end of the programme, the resident defends a thesis on a specific activity developed during the clinical training.

The programme has received accreditation in 2016 by the IOMP [10]. Thanks to the collaboration with the International Medical Physics Certification Board (IMPCB) [11], from December 2018 selected graduates can undertake the IMPCB certification exams at the ICTP.

## Materials and Methods

### 2.1 The Survey

The survey was developed exclusively online and consisted of 27 main questions. It was circulated through email and social media from April 2017 until May 2017, with a peak of received answers in April (68%).

### 2.2 Sample

22 among the graduates of 2 cycles answered to the survey, 85% of the whole graduates at the time of the survey. 55% of respondents are graduates of the year 2015, 45% of 2016.

50% and 27% were sponsored respectively by ICTP and IAEA, one participant by KFAS and the other students participated at their own expenses or supported by their countries.

The provenance of the graduates that answered to the survey includes 17 countries in 4 Regions, with a maximum of participants (41%) coming from Africa (7 countries), 27% of participants from Asia and the Pacific (5 countries), 23% from Latin America and the Caribbean (3 countries) and 9% from Europe (2 countries). This reflects the scope of the MMP: offer the programme in priority to candidates from Regions where there is lack of opportunities to acquire the necessary competencies to become clinical medical physicists.

## Results

### 3.1 Impact Evaluation

To analyse the impact of the MMP, four indicators have been considered:

- (1) rate of graduates returning to their home country (which can be considered the best-case scenario),
- (2) rate of graduates returning to a different country, but in the same Region the participant originated from,
- (3) rate of graduates working as clinical medical physicists and
- (4) rate of graduates working in a non-clinical environment, but in an area related to medical physics.

**Rate of graduates returning to their home country or Region.** One of the main risks connected to the provision of such education and training during a 2 years programme abroad is that it can result in brain drain. The data from the survey show that this phenomenon is minimal within the analysed sample (91% of the participants went back to their home country). Only 9% (2 graduates, both from the Middle East) remained in Italy, both enrolled in a Ph.D. in Radiotherapy Medical Physics. According to these data, across 2 cycles of the MMP, countries were consistently returned trained professionals able to contribute to work in the clinic, thus supporting and developing the national and regional medical physics activities.

**Rate of graduates working in clinical medical physics or related areas.** To fulfil its main purpose, the MMP should provide professionals that can work in the field of their specialization and support clinical activities.

It is often the case that candidates that apply to the MMP programme already have some experience working in medical physics at the time of the application. Among the

respondents of the survey 77% were workers before the MMP. After the MMP 73% of participants were workers, 14% unemployed and 14% students. A follow up done in fall 2017 showed that the situation of unemployment had changed: only 1 unemployed, 82% workers.

41% of the respondents were working in the clinic as medical physicists before enrolling in the MMP. The role of the MMP programme in these cases is to expand the professional competence of participants. After the programme, the results showed that 55% of respondents worked in the clinic and 86% have activities related to medical physics, versus 50% before the MMP.

**Areas of activity.** The most frequent area of activity was diagnostic radiology (10 respondents), followed by radiotherapy (9 respondents). Respondents could select more than one answer to this question. The results showed that half of the respondents worked in several areas at the same time. This is understandable, considering that in countries without an established clinical medical physics department, the few available medical physicists will have to cover the whole spectrum of applications of radiation in medicine.

### 3.2 Local Title Registration and Certification

Programmes of higher education in the European Higher Education Area (EHEA) are offered at three levels or cycles: undergraduate, graduate and postgraduate. The Trieste MMP is a third-cycle program (“Master of Second level” in the Italian system). One of the questions of the survey aimed at exploring how the MMP diploma was recognized in their home countries. Most graduates (59%) underwent the process with different results. Most of the survey’s respondents that underwent the process of title recognition were already working in medical physics or related fields (71%) before entering the MMP. In general, in most countries of the graduates of the MMP there is little or no established path to become a clinical medical physicist, which is one of the reasons why these participants were considered for the Trieste MMP in the first place.

For the graduates that attempted the local registration of the title, the local recognition appeared not to be an issue in most cases (62% of participants that underwent the process) and the equivalence proposed has been in each case an M.Sc (Ecuador, Ghana, Nicaragua, Nepal, Togo, Sudan). Although, as explained previously, the title has a different meaning in the Italian system. 38% of the graduates that underwent the process faced difficulties in the process of local recognition of the title (Guatemala, Iran, Montenegro, Morocco and Qatar). In the case of Morocco, no equivalence was proposed. For example, in Guatemala and Qatar, the equivalence proposed was respectively of a Master’s

Programme (6–7 years of University) and a “diploma” (2–3 years Master’s).

### 3.3 Professional Development and Support to Local Medical Physics

The formal recognition of the profession of clinical medical physicist is a challenge internationally. From the survey it emerges that 36% of the respondents report one medical physics national professional society, active in their country and 18% more than one. With the aim of supporting the recognition of the profession of clinical medical physicist, a national professional certification should be considered. Certification demonstrates the ability of the resident to be an independent medical physics practitioner or Clinically Qualified Medical Physicist (CQMP). Certification is normally awarded by a national body. Respondents of the survey for the most part (91%) declared not to have a national board for certification and, among those, answers were mostly positive (90%) to the possibility of taking part in an international certification process.

According to internationally recognized guidelines [2] certification should be followed by registration as a CQMP and the maintenance of registration achieved through Continuing Professional Development (CPD). This is the case for the two respondents that report having a national certification board. In some cases, CPD can be a national requirement, independent from the process of certification retention (59% of respondents). Among all the respondents that participate in a CPD programme 55% have plans to participate in educational activities as participants, while 32% as lecturers. 18% of respondents ignore whether there are requirements in their country for medical physicists to participate in a CPD.

### 3.4 Participants Feedback

The survey also contained specific questions to evaluate the MMP and its impact on the participant’s career. Most respondents declared that the MMP had helped them improve their career (59% highest appreciation mark). It was specified that the MMP helped increase the participant’s competence level in medical physics (77% highest marks). The self-assessment of the capacity of performing medical physics procedures after the MMP was of score 4 over 5 for 68% of participants and the highest for the remaining. The lectures and materials, assignments and activities part of the MMP were rated relevant (86%) to the participant’s current careers and the quality of the clinical training excellent (36%) and good (50%). Most respondents (82%) declared that they are still using documents collected during the



clinical training (for example QC protocols), generally to develop updated protocols in their hospital 59%.

Furthermore, most participants (95%) keep in touch with the colleagues of the hospital where the clinical training took place, for example to discuss professional issues (55%) and develop research projects jointly (41%). The opportunity of maintaining and enlarging a network of peers for knowledge exchange and research purposes is an added value of the MMP.

## Conclusions and Future Directions

The MMP offers to its participants a highly appreciated academic programme and one year of structured clinical training, thanks to its hospital network. The programme has proven to participate to provide the needed competencies to the participants, that in most cases regress to their home countries and Regions (91% of the graduates responding to the survey). The MMP programme has received the international IOMP Accreditation in 2016 and, since 2017, with the collaboration of IMPCB offers graduates that fulfil the needed requisites, the opportunity of undertaking examinations to achieve international certification.

Since the 2015–16 cycle, the MMP has received an increasing support from the IAEA, both technical for the selection of candidates and financial with the largest number of awarded fellowships. The MMP is continuing in the upcoming year and there are plans to extend the same survey to the new graduates of 2017.

**Conflict of Interest** The authors declare that they have no conflict of interest.

**Open Access** This chapter is licensed under the terms of the Creative Commons Attribution 3.0 IGO License (<https://creativecommons.org/licenses/by/3.0/igo/>), which permits use, sharing, adaptation, distribution and reproduction in any medium or format, as long as you give appropriate credit to the International Atomic Energy Agency, provide a link to the Creative Commons licence and indicate if changes were made.

The use of the International Atomic Energy Agency's name, and the use of the International Atomic Energy Agency's logo, shall be subject to a separate written licence agreement between the International

## References

1. Loreti, G., Delis, H., Healy, B., Izewska, J., Poli, G.L., Meghifene, A., IAEA Education and Training Activities in Medical Physics, *Journal Medical Physics International* 3(2), 81–86, (2015)
2. INTERNATIONAL ATOMIC ENERGY AGENCY Roles and Responsibilities, and Education and Training Requirements for Clinically Qualified Medical Physicists IAEA Human Health Series 25, IAEA, Vienna (2013)
3. INTERNATIONAL ATOMIC ENERGY AGENCY Postgraduate Medical Physics Academic Programmes, Training Course Series 56, IAEA, Vienna (2013)
4. INTERNATIONAL ATOMIC ENERGY AGENCY, Clinical Training of Medical Physicists Specializing in Radiation Oncology, Training Course Series 37, IAEA, Vienna (2009)
5. INTERNATIONAL ATOMIC ENERGY AGENCY Clinical Training of Medical Physicists Specializing in Diagnostic Radiology, Training Course Series 47, IAEA, Vienna (2010)
6. INTERNATIONAL ATOMIC ENERGY AGENCY, Clinical Training of Medical Physicists Specializing in Nuclear Medicine, Training Course Series 50, IAEA, Vienna (2011)
7. INTERNATIONAL ATOMIC ENERGY AGENCY, Report of a Task Force Meeting on a Regional Postgraduate Medical Physics Syllabus for Academic Programmes, Recommendations for Medical Physics Education in AFRA Member States, (2013)
8. INTERNATIONAL ATOMIC ENERGY AGENCY, A Regional Clinical Training Programme for Radiotherapy Medical Physics Report of a Task Force Meeting, (2013)
9. INTERNATIONAL ATOMIC ENERGY AGENCY, Clinical Training Programmes and Portfolios for the Regional Training in Nuclear Medicine and Diagnostic/Interventional Radiology Medical Physics Report of a Task Force Meeting, IAEA, Vienna (2014)
10. International Organization for Medical Physics (IOMP), Accreditation policies, <http://www.iomp.org/?q=content/accreditation-home>
11. International Medical Physics Certification Board (IMPCB), Certification policies, <http://www.impcbdb.org/policies/>

Atomic Energy Agency and the user and is not authorized as part of this CC-IGO licence. Note that the link provided above includes additional terms and conditions of the licence

The images or other third party material in this book are included in the book's Creative Commons licence, unless indicated otherwise in a credit line to the material. If material is not included in the book's Creative Commons licence and your intended use is not permitted by statutory regulation or exceeds the permitted use, you will need to obtain permission directly from the copyright holder.



# UDA- $\mu$ BioLab: Teaching Microcontrollers with Bioinstrumentation

O. Alvarado-Cando, H. Torres-Salamea, and D. A. Almeida

## Abstract

This paper presents the development, implementation and assessment of a practice guide designed to support the course of microcontrollers named UDA- $\mu$ BioLab. This guide allows to consolidate the knowledge about the different peripherals of the microcontroller and introduces the students in the area of Bioinstrumentation through the acquisition of biosignals and actuators for prosthetics. Practices begin with the use of the A/D converter for the acquisition of EMG signals and flashing of a LED, then it is integrated with a DC motor to control the opening and closing of a commercial “Ottobock” prosthetics. To learn the PWM module, the prosthetics must pick up different objects such as a wood cube, a plastic ball and an egg without damage. The ECG signal and pulse oximeter are acquired by the microcontroller too. The final project is the control of a robotic hand with 5 DOF (servomotor) and controlled by the EMG signals of a student and the computer. The outcomes of the course development presented here may be used as a guideline for the creation of multidisciplinary courses.

## Keywords

Microcontrollers • Bioinstrumentation • Biomedical engineering education • Multidisciplinary courses

## 1 Introduction

The Ecuadorian biomedical sector has a major shortcoming in Latin America because the lack of specialization at the undergraduate level and postgraduate level. There is only one university that offers the biomedical engineer degree but it still does not have graduate students [1]. The School of Electronic Engineering at “University of Azuay (UDA)” in Cuenca-Ecuador has been offering the subject of Bioelectronics (6 credits) for more than 10 years [2], but this is not enough to improve the biomedical sector. Also, the employers in the Biomedical Engineering (BME) servicing industries and health care institution in Ecuador demands engineers with some expertise in medical equipment because the majority of the works are in the field of clinical engineering.

In 2016, aware that students need more knowledge in the BME area and the high rate of academic failure in the Microcontroller course, a multidisciplinary curriculum was proposed for this course. It combines the acquisition of biosignals, control of actuators and C programming for Microchip’s PIC microcontrollers.

The course CTE0209 Microcontroller is a core unit for the 4th year in Electronic Engineer Degree. The previous curriculum studied the GPIO, PWM, ADC, Timers, Interrupts, and UART. The credits were divided into 4 h of lectures and 2 h of laboratory a week during a sixteen weeks semester. The laboratories were focus on the use of the peripheral’s library, LEDs’ control and alphanumeric dot matrix LCD  $16 \times 2$ . This could not represent a significant learning in the students because they used everything separate and in a real embedded system the peripherals work together. The methodology is out of date because it is focused on presenting more theoretical content and it does not help the students to develop other skills, know-how.

Students need to think critically and be able to solve real-world problems, so the three competence (knowledge, know-how and how to be) has to be development in classroom [3–5]. In order to achieve this competences, all

O. Alvarado-Cando (✉) · H. Torres-Salamea  
Escuela de Ingeniería Electrónica, Universidad del Azuay,  
Cuenca, Ecuador  
e-mail: oalvarado@uazuay.edu.ec

D. A. Almeida  
Escuela Técnica Superior de Ingenieros de Telecomunicaciones,  
Universidad Politécnica de Madrid, Madrid, Spain

laboratories are design to introduce bioinstrumentation to the electronics' students by the resolve of biosignals acquisition or control prosthetic motors problems. The students need prerequisite knowledge about programming in C language, digital and analog circuits which are learn in the 3rd year of electronic engineering.

The paper is organized as follows. The structure of the microcontroller and hardware is described at Sect. 2, followed by the result Sect. 3. Finally, the conclusions are in Sect. 4.

## 2 Structure Course and Methodology

The microcontroller course emphasizes the active learning where students are the principal actor of the education process. The course objectives are:

- (1) Use microcontroller as the core of an embedded system, using internal peripherals and interrupts.
- (2) Design and implement algorithms to acquired electrical biosignals and control actuators.
- (3) Develop and simulate clean code using finite state machine in C programming.

### 2.1 Course Structure

The six-credit Microcontroller course consists of one lecture and two laboratory session each week during a sixteen weeks semester, this is the first change made in the new curriculum. Each 2 h lecture is structure to provide a description of the peripheral of the microcontrollers and an electronic refresher of the electronic need to perform the laboratory via interactive activities. One of these activities is the design of the hardware, where the students apply their previous knowledge and in group through discussions they propose a design.

The laboratory sessions, twice a week for 2 h each, provide hands-on learning which reinforce the theoretical

knowledge of microcontroller's internal peripherals; students work in two or three person teams to encourage collaborative work between them. The laboratories are six and each one consist of pre-lab exercises, lab procedure, self-work and questionnaire. In the pre-labs, students apply course concept to configure and initialize the peripherals of the microcontroller, demonstration code or to pre-design the hardware for sensor or actuator. For example, for an electromyography (EMG) pre-lab exercise, students had to design a pre-amplifier using the AD620 instrumental amplifier with appropriated gain for EMG measurement. The lab procedure activities gives student hands-on experience with microcontroller programming and hardware design. It's important to mention than not all the hardware is design by the students some commercial shields are used. The self-work activities give students the opportunity to do something without a guide. For example, expand the program to acquire mores analog-digital-converter (ADC) channels or to control for that one motor. At the end, the achievements learning are verify by a questionnaire.

### 2.2 Course Modules and Laboratories

The course has six learning modules, each related to a Bioinstrumentation topic, shown Table 1.

Module I focuses on the MPLABX integrated development environment and the Curiosity board by Microchip. The students learn how to build and download a program to flash light on the Curiosity board. The lesson proceeds with a discussion of the utility of simulation, debugger and the syntax of the compiler. There is no laboratory in this module, but there are some exercises about breakpoints, programming from scratch, modify code and analysis demo codes.

Module II focuses on configuration register of the pins of the microcontrollers as digital input or output. The students write and test code to configure the I/O ports to control the rotation of a DC motor with an H-bridge driver with two switches. Also, the students are introducing to biosignals, and refreshment of instrumental amplifier, noise and filters.

**Table 1** Microcontroller course modules and laboratories

Module	Topic (s)	Laboratories
I	Software basis	1. EMG signal to control (On/Off) a LED.
II	Peripheral basics and port I/O	2. Ottobock prosthetics I: open and close control with EMG signal
III	Analog interfacing, Timer and counters	
IV	Concurrency and interrupts	3. Ottobock prosthetics II: picked up objects (PWM)
V	Communication	4. ECG signal with computer interface 5. Pulse oximeter
VI	Advanced programming	6. Robotic hand 5DOF with EMG

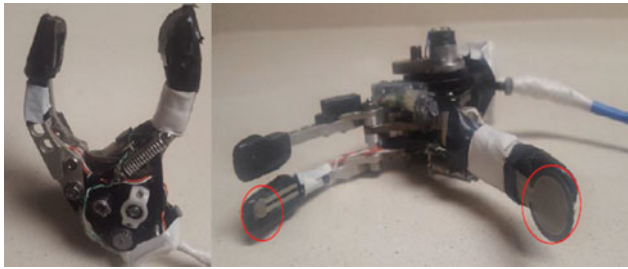


**Fig. 1** Ottobock prosthetics used in course CTE0209 microcontroller

During Module III, the analog interfacing, timers and counters are studied. The student learns (pre-labs) how to configure, initialize and control de ADC and comparators peripheral to convert analog signal to digital, also they learn to count internal or external event by the timer peripheral. Finally, the characteristics of the EMG signal are presented and analyzed in the classroom and how EMG has been used to control upper limb prosthetics for many years. Students carry out laboratories 1 and 2, for which they must build two electronic PCB for acquisition and control; they have expertise in design PCB for the previous curse in the career.

Module IV focuses on concurrency and interrupts which are an important concept in microcontroller's world [6]. Students perform codes to manage the interrupt service routine (ISR) to respond to external and internal events in the ISR and not in the normal flow of program. Students design an ON/OFF control system, laboratory 3, using the EMG signals and pressure sensor as an inputs and the DC motor of the prosthetic as an output (Fig. 1).

In Module V, students are introduces to serial, I<sup>2</sup>C and SPI communication. They used the UART (universal synchronous-asynchronous) to connected the microcontroller to a PC and visualize 2-lead ECG signal in LabVIEW interface, laboratory 4. The SPI module is studied by using the "heart rate click" from MikroElektronika which integrated a pulse oximetry and a heart-rate-sensor.

Finally, Module VI focuses on programming technics like advanced concurrency and using FSM (Finite State Machine), multiple interrupts and peripherals. The final laboratory is the control of the InMoov robotic hand with 5 DOF, previously built using 3D print, using EMG signals (Fig. 2).

### 2.3 Students Assessment

Student performance is assessed by the following

- Lab reports (1–5): 40%.
- Robotic hand presentation: 20%.
- Midterm exam: 15%.
- Peer assessment: 5%.
- Final exam: 20%.



**Fig. 2** InMoov robotic hand used for the final laboratory

The labs report has to communicate the laboratory work, hardware design and code programming, so it includes Abstract, Introduction, Materials and Methods, Results and Discussion sections. The reports are written in IEEE templates for Conference Proceedings [7], this help students to prepare their paper in the future.

The robotic hand need a control system, digital filters and a good EMG PCB so it is evaluating with a report and a presentation, showing: that the 5 DOF are working and can be controlled by a computer interface; and that the robotic hand can imitate the move of the fingers of the student who has connected the electrodes for EMG. These demonstrations proof that students are able to design a biosignals acquired system.

The midterm examination and final exam are a combination of code programming exercises and theoretical questions about microcontroller architecture. The examination is divided in two periods on 45 min each for practical and writing exam with a break of 15 min. This assessment is individual so students can demonstrate their skill about microcontrollers design and develop solutions.

There is two peer assessment evaluation during the course at the midterm and at the end of term. This is very useful to know who works and who don't during the laboratories.

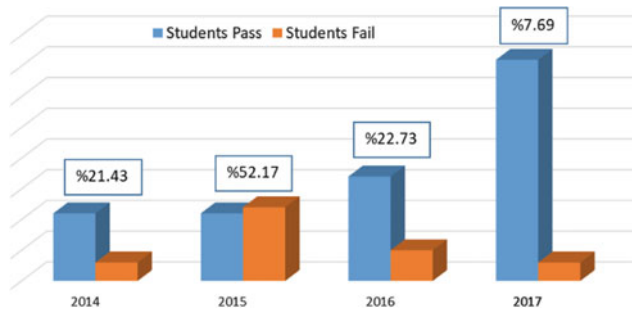
## 3 Results

This new course has been offers by two years to the electronic engineer students (2016, 2017). The available laboratory facilities allows a maximum of 24 students; the first time 22 students enrolled. The number of interested students grew so much that in the last semester of 2017 two parallels had to be opened, where 39 students were enrolled.

In the 2015, the 52% of students enrolled at the Microcontrollers course failed, it was 30.7% more than the 2014.

**Table 2** Average and maximum grade from the course CTE0209 microcontroller

Year	Average grade (%)	Max. grade (%)
2014	60.82	82.6
2015	42.86	80.4
2016	64.82	87.4
2017	73.06	96.8

**Fig. 3** Historical percentage of failed students in the course CTE0209 microcontroller

The main objective of renewing the curriculum was to reduce the large index of students who failed in the subject. The first year of the new Microcontroller curriculum the fail index reduces from %52.17 to %22.73. The last semester of 2017 only the %7.69 of the students enrolled in the course fail it.

The minimum grade to a student approve any course according to the regulations at University of Azuay is 30/50 points which is the 60%. The average and maximum grade of the course is increasing as time passes, it's calculate with fail and pass students' notes, Table 2 (Fig. 3).

## 4 Conclusion

This new multidisciplinary curriculum combines theoretical teaching and the emphasis on applying concepts to bioinstrumentation laboratories. A strength of the methods used

here is the protagonist that the students have in learning process through active learning; they design, simulate, program and take biomedical signals by themselves.

Several offering of the course have shown that the vast majority (92.31%) of the students have achieved successful results. Students have gained a great understanding of microcontrollers' architecture, embedded programming and they know how to integrate several peripheral with sensors and actuators in bioinstrumentation area.

The approaches of this curriculum proves that active learning and multidisciplinary mini project-based learning is a good educational model for undergraduate students.

**Conflict of Interest** The authors declare that they have not conflict of interest.

## References

1. Secretaria de Educación Superior, Ciencia, Tecnología e Innovación, «Sistema Nacional de Información de Educación,» 2018. [En línea]. Available: <https://infoeducacionsuperior.gob.ec/#/>.
2. University of Azuay, «Ingeniería Electrónica,» 2017. [En línea]. Available: <http://www.uazuay.edu.ec/carreras/ingenieria-electronica>. [Último acceso: 3 1 2018].
3. H. J. Passow y C. H. Passow, «What Competencies Should Undergraduate Engineering Programs Emphasize? A Systematic Review,» *Journal of Engineering Education*, vol. 106, n° 3, pp. 475–526, 2017.
4. J. Walther, N. Kellam, N. Sochacka y D. Radcliffe, «Engineering Competence? An Interpretive Investigation of Engineering Students' Professional Formation,» *Journal of Engineering Education*, vol. 100, n° 4, pp. 703–740, 2011.
5. A. L. Guzzomi, S. A. Male y K. Miller, «Students' Responses to Authentic Assessment Designed to Develop Commitment to Performing at Their Best,» *European Journal of Engineering Education*, vol. 42, n° 3, pp. 219–240, 2017.
6. D. Ibrahim, *Advanced PIC Microcontroller Projects in C: from USB to RTOS with the PIC18F*, Oxford: Elsevier, 2008.
7. IEEE, «Manuscript Templates for Conference Proceedings,» 2017. [En línea]. Available: [https://www.ieee.org/conferences\\_events/conferences/publishing/templates.html](https://www.ieee.org/conferences_events/conferences/publishing/templates.html). [Último acceso: 5 12 2017].



# Development of a Blended and eLearning Course on Anatomy and Physiology for Engineers in Indonesia: Lessons Learned and Future Developments

Yoke Saadia Swito, Allya Paramita Koesoema,  
and Amanatulhay Pribadi

## Abstract

Human anatomy and physiology is an essential part of biomedical engineering (BME) curriculum. This is because while BME consists of diverse subdisciplines such as biomechanics, bioelectronics and biophysics, at the core of it BME is the application of engineering principles to solve problems related to the human body. However, for new BME departments, especially in developing countries like Indonesia, there is often a lack of anatomy and physiology courses tailored for BME students, with students taking courses from other departments such as medicine or pharmacology. This is not ideal, as these courses are designed for different learning outcomes requirements. This paper describes the development and implementation of a course on human anatomy and physiology for engineers that has been implemented both in blended and pure eLearning mode in two universities in Indonesia. It focuses on analogies of the human physiological systems as engineering systems, including tie-in of physiological systems to engineering based quantitative models, as well as BME applications of anatomy and physiology principles. In addition to learning the fundamentals of anatomy and physiology, as a final class project, students are required to conduct a simple design exercise in developing a design applying engineering principles to solve a medical problem. This allows them to start integrating engineering and medical knowledge, which is a key part of BME education. In terms of implementation, the course has been run successfully between the two universities for three semesters, with generally satisfactory learning outcomes. However, there are still some hurdles that merits

improvement, notably technical issues related to ICT infrastructure and some pedagogical issues related to higher level learning outcomes in pure eLearning modes. It is hoped that this course and the lessons learned from its development and implementation will contribute to the growth of BME education in Indonesia and beyond.

## Keywords

BME education • eLearning • Anatomy and physiology

## 1 Introduction

Human anatomy and physiology is a key element in any biomedical engineering (BME) higher education program curriculum. While BME is multidisciplinary by nature, the understanding the human body is always the cornerstone of BME, i.e. the application of engineering principles to solve problems related to the human body. Ideally, human anatomy and physiology learning in BME programs should be tailored to the specific needs of BME students, bridging engineering and medical fields and thinking frameworks. However, this is not always the case.

The historical diversity of BME departments, often stemming out from various engineering disciplines with their associated staff and resources, may result on the lack of anatomy and physiology courses tailored for BME students. This is especially true for newer BME programs in developing countries such as Indonesia. While each program may have a group of faculty members with a strong specific expertise related to BME, individual programs often has gaps in their set of expertise configuration vital for a comprehensive BME education, such as anatomy and physiology education. To solve this issue, programs may have students follow courses from other programs (e.g. taking human physiology courses from biology or medical programs). However, this arrangement is not optimal, as these courses are designed for students with different educational

Y. S. Swito (✉) · A. P. Koesoema  
Indonesian eHealth and Telemedicine Society, Bandung,  
Indonesia  
e-mail: yokesaadia@gmail.com

Y. S. Swito · A. P. Koesoema · A. Pribadi  
Biomedical Engineering Research Group, Institut Teknologi  
Bandung, Bandung, Indonesia

backgrounds and learning outcomes requirements. For example, engineering-based BME students following a medical program's anatomy course may find it too detailed and memorization based. More importantly, it may be difficult to connect the physiological concepts learned in the course to their potential engineering applications and frameworks.

To contribute in addressing this issue, this paper describes the development and implementation of a series of Anatomy and Physiology courses for engineers that has been implemented both in blended and pure eLearning mode in two universities in Indonesia. The course adjusts traditional medical-school based course on human physiology by approaching the topic using analogies of the human physiological systems as engineering systems, including tie-in of physiological systems to engineering based quantitative models, as well as BME applications of anatomy and physiology principles.

---

## 2 Course Design

### 2.1 Context in the Curriculum and Institution

The authors in Institut Teknologi Bandung's (ITB) BME program has developed a series of anatomy and physiology courses for engineers, each tailored for a specific target audience. There is (i) a condensed one semester course covering the basic principles of anatomy and physiology aimed for general engineering students, (ii) a more detailed two-courses sequence specifically for BME students, who needs more in depth knowledge of human anatomy and physiology, and finally (iii) a graduate course of anatomy and physiology.

The three series of courses have similar approaches to teaching and learning, but differ in the depth of knowledge and focus. The condensed one semester course is intended to be a brief introduction for non BME engineering students who may have an interest in BME or projects involving the human body. The course is designed to be taken as an elective for third or fourth year engineering undergraduate student, with a solid background in basic engineering. In addition to implementation at ITB, the condensed one semester course has also been implemented three times with blended learning methodology at Udayana university, an Indonesian state university in Bali as an elective course in their Electrical Engineering Program [1–4]. The two-course series is part of the ITB's core BME undergraduate curriculum, intended to be taken through two semesters in the second year of BME program. The course are taught concurrently with other basic core BME courses such as Fundamentals of Biomedical Engineering, Biomedical Electronics, and Biochemistry. In addition, BME students in

the second year stage follows a series of BME lab courses that integrates lab modules from the different courses, including anatomy and physiology. Finally, the graduate course goes into more depth to the integration between body systems and engineering applications in anatomy and physiology.

The development and implementation of these courses has been supported by multiple academic grants, including the SPADA grant from the Indonesian government office for higher education (DIKTI), the INHERENT K-1 grant and the GDLN grant [1–4]. The course has been implemented and improved over time since 1999, and is also part of an initiative to develop a more comprehensive course repository on BME for Indonesia [5].

### 2.2 Course Content

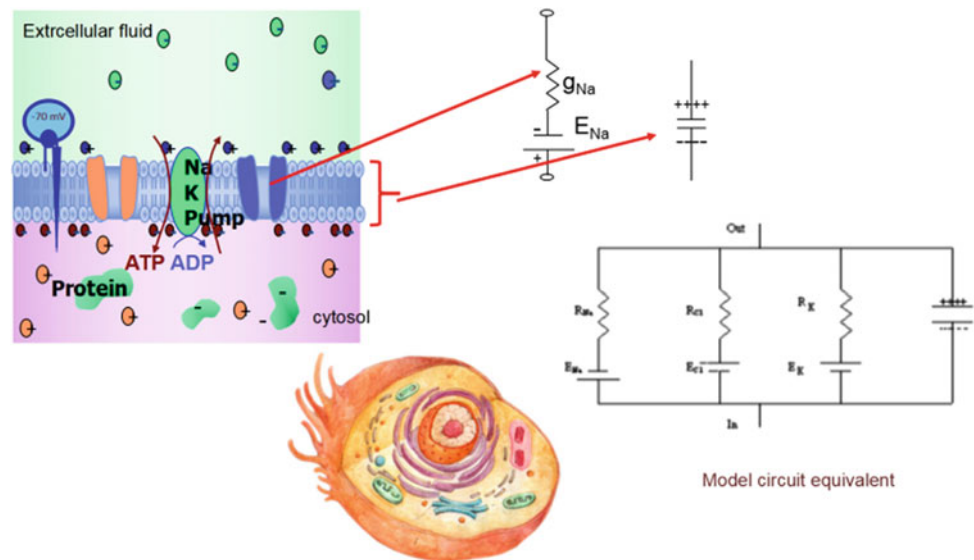
The course opens with an introduction to living systems, homeostasis, and basics of physiological modeling, emphasizing the connection between biology and engineering frameworks. While not the core of the course, a short introduction of ethics in BME is also given, and reinforced throughout the course in topic relevant cases. It then follows the system based approach in teaching anatomy and physiology, proceeding with the major systems of the human body, including the nervous, musculoskeletal, cardiovascular, respiratory, respiratory and urinary system. Each chapter is accompanied by a module discussing BME applications of anatomy and physiology principles. The course is capped with a major assignment to integrate their anatomy physiology knowledge with an engineering application.

### 2.3 Delivery Methodology and Learning Approaches

The delivery method for the course is in general blended learning, with a combination of in-class instruction, discussion, and online learning and interaction. Online learning materials are designed to prepare students for active classroom discussions and activities, including video, picture, and textual materials. Students study online materials, submit assignments and conduct short quizzes online. This is aimed to provide students with a more efficient, flexible learning environment that also allows them to better track their progress [6–8]. This approach is supplemented with face-to-face or synchronized online meetings for distance learning implementations.

In terms of learning approach, the course approaches anatomy and physiology learning through the lenses of engineering student learning styles, using flowcharts and block diagrams to illustrate physiological processes and the connections between physiological elements, focusing on

**Fig. 1** Example of engineering analogy for physiological system: electrical circuit model for human cell membrane



quantitative models of physiological systems, and when possible using analogies of the human physiological systems as engineering systems. In addition, each chapter is accompanied by a module discussing BME applications of anatomy and physiology principles. This can range from a discussion of windkessel models in cardiovascular system, to practical lab sessions with EMG. Figure 1 gives an example of engineering analogy used to describe physiological systems, in this case the electrical circuit equivalent to a human cell membrane.

Matching the teaching approach, student performance was assessed by a balance of examinations, problem sets and design assignment. The written examinations are a combination of online, multiple choice knowledge based questions and more open ended problem-solving or critical-thinking based essay materials done on class in an open book manner. To complement the traditional exams, as a final class project, students are required to conduct a simple design exercise applying engineering principles to solve a medical problem. This allows them to start integrating engineering and medical knowledge, which is a key part of BME education.

### 3 Results and Future Developments

In general, throughout the iterations of their implementation, the courses have satisfied its learning objectives and general objective of improving BME anatomy and physiology education in their implementation sites. Student enrollment are generally to maximum capacity of the class for elective courses, and full attendance for compulsory courses. This generally amounts to between 25 and 32 student enrollment per course for undergraduate courses and between 5 and 10 student enrollments for the graduate course.

Student performance is generally high in problem solving and design based assessments. They are somewhat more varied in the knowledge based assessments (e.g. quiz and written examinations), but this is within normal pedagogical parameters, with 100% of the students passing the course. Moreover, the primary objective of the courses is to give basic grounding for engineering students to understand the basic principles of human anatomy and physiology, to be able to use them as a framework to use engineering skills and knowledge in solving medical based issues. Detail knowledge was not the main objective, and can be acquired over time as needed. Table 1 shows student assessment results from the 2016 iteration of the course.

In terms of student based course assessments, a student questionnaire on a 5 level Likert scale was distributed at the end of each course iteration [9, 10]. Results showed that in 2016, the blended learning mode of teaching is new to slightly more than half the students, and 100% of the students recommends that this method of pedagogy should be repeated for the next semester. In terms of class activity, students primarily uses the online learning management system (LMS) to view class materials and submit assignments, with forums being the least used online tool in the LMS (average score 1.4).

In general, students agree that the blended learning method increases learning effectiveness, flexibility, and aids in controlling study progress (average scores >3.8), but think less that online learning can replace face to face interactions completely (average score 2.8). In terms of presentation of content and study method, students agree that learning media (pictures, animations, models) help course understanding (average score 4.1), the course was well structured (average score 3.8) and that the course motivates them to explore the field in more depth (average score 3.8).

**Table 1** Example grade distribution for undergraduate courses on semester 1 2016/2017

Grades	EB2103 (First of a sequence of two for BME students)	EB2207 (One semester general engineering course)
A	5	4
AB	9	9
B	11	16
BC	5	2
C	3	1
Total students	33	32

Having said that, there are still some hurdles that merits improvement, notably technical issues related to ICT infrastructure and some pedagogical issues related to higher level learning outcomes in pure eLearning modes. Multi-university/distance learning implementation was particularly affected by this issue. It is hoped that this course and the lessons learned from its development and implementation will contribute to the growth of BME education in Indonesia and beyond.

**Acknowledgements** The authors would like to thank and acknowledge the grant funders that has made the development and implementation of the courses possible. The development and implementation of these courses has been supported by multiple academic grants, including the SPADA grant from the Indonesian government office for higher education (DIKTI), the INHERENT K-1 grant and the GDLN grant.

## References

1. Irawan, Y. S., Koesoema, A. P.: "Development Results Document, Development Of A Customized Anatomy & Physiology E-Learning Courseware For Engineering Students: Application In Udayana University", Global Development Learning Network Indonesia Content Development Grant Batch-2 (2007).
2. Irawan, Y. S., Koesoema, A. P.: "Final Report Document, Development Of A Customized Anatomy & Physiology E-Learning Courseware For Engineering Students: Application In Udayana University", Global Development Learning Network Indonesia Content Development Grant Batch-2 (2007).
3. Irawan, Y. S., Koesoema, A. P.: "Research Proposal, Development Of A Customized Anatomy & Physiology E-Learning Courseware For Engineering Students: Application In Udayana University", Global Development Learning Network Indonesia Content Development Grant Batch-2 (2007).
4. Irawan, Y. S., Koesoema, A. P. "Project Proposal: Development Results Document, Development Of A Customized Anatomy & Physiology E-Learning Courseware For Engineering Students", INHERENT K1 Grant (2006).
5. Saadia Irawan, Y., Paramita Koesoema, A., Aridarma, A., & Setiawan, A. W. Design of an open knowledge repository and communication Forum for biomedical engineering education and research in Indonesia (2008).
6. Fainholc, B., & Scagnoli, N. Blended learning through interuniversity collaboration interaction. In 23rd ICDE World Conference on Open Learning and Distance Education. Retrieved February (Vol. 4, p. 2010) (2009).
7. Romano, P., Giugno, R., & Pulvirenti, A.: Tools and collaborative environments for bioinformatics research. Briefings in bioinformatics, 12(6), 549–561 (2011).
8. Davis, H. C., Carr, L. A., Hey, J. M., Howard, Y., Millard, D., Morris, D., & White, S.: Bootstrapping a culture of sharing to facilitate open educational resources. IEEE transactions on learning technologies, 3(2), 96–109 (2010).
9. Lonn, S., & Teasley, S. D.: Saving time or innovating practice: Investigating perceptions and uses of Learning Management Systems. Computers & Education, 53(3), 686–694 (2009).
10. Katzlinger, E., & Herzog, M. A.: Wiki Based Collaborative Learning in Interuniversity Scenarios. Electronic Journal of e-Learning, 12(2), 149–160 (2014).

# Cultural Aspects in Technology-Enhanced Education

Tatjana Welzer, Marjan Družovec, and Aida Kamišalići

## Abstract

Information and communication technologies helped make our world global a long time ago. Developed global models thus influenced education including teaching and mobility. Technology-enhanced education became one of the possible popular approaches used at different levels of education. For educational institutions, technology-enhanced education introduced new types of learners and the potential to share resources with other institutions. Learners can be involved in blended learning, and thereby choose when and where they learn. Opportunities for personalized learning, where learners find their own way through learning material appears and, last but not least, a wide range of devices and systems among which learners can choose their preferred platform is available. By using the mentioned approaches, being virtually involved, we can easily cross geographical borders. Participants can span across continents, countries, regions, cultures and languages easily, without having to step out of the classroom or office, or even be aware that they are crossing geographical borders. The learners became virtually mobile, but at the same time, participants in the same system can be of a different cultural and linguistic background. This requires a new understanding and for the preparation of educational materials as well as educational modules. The needs and expectations of participants from different environments and countries, as well as from different languages and culture groups can be different even with regard to some well-known and developed topics. These differences can influence the complete educational process and participants have to be aware of cultural aspects in technology-enhanced education. Cultural aspects and awareness help them to avoid communicational misunderstandings and other disappointments during the educational process. In this paper, we will introduce some basic cultural aspects and connect them to

technology-enhanced education. Through case studies, our experiences with cultural aspects in different situations, expert topics and environments including technology-enhanced education tools will also be presented.

## Keywords

Cultural aspects • Cultural awareness • Education  
Technology-enhanced education

## 1 Introduction

In the available literature, we may find many definitions of culture: Culture as an art, culture as a culture of groups or societies and countries. Culture has a complex history and diverse range of meanings. The word culture has grown over the centuries to reach today's broad understanding [21]. Nevertheless, culture is not something that we simply know, it is something that we have to learn and absorb [18]. In our contribution, we refer to Hofstede [6] and Lewis [10] as leading researchers in the field of culture and cultural communications. Hofstede defines culture as a collective phenomenon, because culture is shared with people who live or have lived within the same social environment. According to his definition, culture consists of unwritten rules of a social game. The collective programming of the mind distinguishes the member of one group or category of people from other groups or categories [7]. On the other hand, Lewis presents culture as an integrated pattern of human knowledge, core belief, and behavior that depends upon the capacity for symbolic thought and social learning [20]. In his model, Lewis focuses on communication and interaction skills. Cultural behavior is not coincidental, but more the final product of centuries of collected wisdom, passed along through many generations to its final presently known form. Lewis also classifies cultures into three categories: Multi-active, linear-active and reactive, or dialogue-oriented, data-oriented and listeners [11]. Besides definitions given by both mentioned leading researchers, we can find many other

T. Welzer (✉) · M. Družovec · A. Kamišalići  
Faculty of Electrical Engineering and Computer Science,  
University of Maribor, Maribor, Slovenia  
e-mail: tatjana.welzer@um.si



descriptions of culture as well. The cumulative deposit of knowledge, experience, beliefs, values, meanings, hierarchies, religion, notions of time, roles, spatial relations, concepts of the universe and material objects and possessions acquired by a group of people in the course of a generation through individual and group striving is also defined as culture [18]. Culture has also been defined as a shared pattern of behavior, but observing behavior is not enough. The meaning of the behavior is important [9]. All in all, culture can also be defined as a particular way of life of a group of people, comprising the deposit of knowledge, experience, beliefs, values, traditions, religion, notions of time, roles, spatial relations, worldviews, material objects and geographic territory [12, 20]. Besides culture, we also have to clarify the needs of our contribution to cultural awareness. Poor or no cultural awareness means a poor understanding of cross-cultural dialogue, which can lead to blunders and damaging consequences, especially in business, management and advertising, where cultural awareness seems to be of key importance for success [21]. The foundation of communication and the ability to observe our cultural values, beliefs and perceptions from the outside are defined as cultural awareness [14]. For culture and cultural awareness, cultural groups are also interesting. They introduced different units, sometimes also presented as layers, within the concept of culture [19]: Culture in societies and nations, regional and local culture, business cultures, organizational and corporate culture, functional subcultures at an organizational level, social groups in the organization, professional and functional cultures [12, 20]. The numbered groups present specific cultures according to social life, geographical location and business domain. Such a definition of culture is probably more convenient to engineers and other businesses, as well as technical groups, because they are more familiar with the presentation of culture through groups and layers. For that reason, it corresponds quite well to expert groups of teachers and the educational system itself as well as to technology-enhanced education [4, 5, 8, 16]. Furthermore, we will point out some of our experiences in teaching according to the different cultures with which we are confronted in technology-enhanced education as well as in the world. Solutions can be quite different in the sense of very basic information up to the deep knowledge that participants can collect in different ways [21].

## 2 Cultural Aspects in Technology-Enhanced Education

Education and teaching are currently global activities, which are performed for the same institution all around the world, and in which we have to deal with many associates including learners and teachers from different cultures and language groups [21]. Not only this, but they also belong to different expert domains and cooperate and work together [4]. If we summarize this, we can conclude that we have to deal with

many cultural differences in education and teaching, that can have a strong influence on competencies and even work, including research and also research results [21]. We have to be aware about this and have to prepare scenarios of how to cope with this. The influence of these scenarios can also be based on technology (distance learning, e-learning, using Skype as well as e-mails, Moodle and similar tools), strictly speaking on technology-enhanced education. Furthermore, in this chapter, we will examine teaching and mobility challenges during the educational period, that are also based on technology-enhanced education.

### 2.1 Educational Cases

In Educational cases, we will deal with education and teaching, connected to technology-enhanced education primarily within the framework of the Erasmus+ exchange and similar mobility projects (CEEPUS). In at least last 15 years, we have identified the following problems of cultural awareness in teaching: Home students on mobility, host students on mobility, home teachers either on mobility, either at home, or dealing with host mobile students (Erasmus+, CEEPUS). Probably the less problematic cultural aspects, is cultural shock, by host students that are coming to Slovenia to our institution. The period that students select to stay with us is short enough, in that they are mostly coping with the honeymoon phase of cultural shock, in which they are impressed by the country, people and their study mates. Those full of enthusiasm and with clear goals are also able to deal easily with frustrations that can appear, because nothing is as they expected or believed it was in the beginning. For some of the host students, this situation appears first at the end, when they recognize that they did not achieve the results that they planned or that they are obligated to achieve [21]. We can then recognize a lot of frustration, but not because of cultural differences, even though students claim that they are not familiar with habits and rules in our country or institution with regard to obligations. Of course, all this information is given to them upon arrival. So far we do not have any particular cultural preparations for arriving students, but it would also be useful for them to experience some possible cultural preparations at their home institution. We would invest in their cultural knowledge as well. In some cases, the frustrations can also be caused by using technology in the sense of technology-enhanced education they do not know the principles and tools and are probably out of the cultural understanding that they have from their home country. In cases where they were involved in technology-enhanced education at their home institution, problems should not appear or should be much smaller and not relevant. On the other side, more cultural preparation is available for our home students going on mobility. Depending on the faculties inside the University of Maribor, students are getting instructions on how to prepare themselves for mobility. They have to start already during the

selection of the institution and country where they plan to go. If they are not used to a lot sun or extreme cold and especially if they have some health problems in connection with both, it is, of course, not the best idea to select a country in either the north or south, while probably, for health reasons, the frustration can be provoked much faster than by other students [21]. Such students also need to think about possibilities like blended and/or personalized learning and virtual mobility, which technology-enhanced education can make possible. The next phase of preparation is language preparation [18], which is supported by the Erasmus+ tool (technology-enhanced education), as well as by the institution with some language courses. The Online Linguistic Support (OLS) supports language learning for Erasmus+ mobility participants. The OLS offers participants in Erasmus+ long-term mobility activities the opportunity to assess their skills in the foreign language(s) they will use to study, work or volunteer abroad. In addition, the international office of the University of Maribor, from time to time organizes some short courses. They are working now on some new ideas that are the result of research that was done by a member of the office within the framework of her master's thesis [13]. Main idea are technology-enhanced cases where the IT based tools would be used like gamification. The advantage of gamification should be also in the content (cultural differences). Namely, gamification can also improve an individual's ability to comprehend digital content and understand a certain area of teaching and education. We should not overlook that it gamification has been applied to almost every aspect of life. In the case of home students, we also have to be aware about reverse cultural shock after students return back home to Slovenia and their family, while, on the basis of mobility experiences, they have experienced a different point of view on many things and have to cope with them. Preparation for life back home would be needed and could be based first of all on technology-based approaches in the sense of technology-enhanced education. Namely, students who are still abroad and would need the preparation for their returning home are not available for face-to face communication, while virtual environments and technologically supported solutions are very suitable for them. Actually, the biggest challenge are teachers [20, 21]. It is easy for those who are going on mobility abroad, are hosts at partner institutions, and are not particularly confronted with the partners' culture while they are bringing their own culture with them and use it in the classroom; however, when networking with partners, this has no strong influence. Problems can appear mostly if they are staying for a longer time and have to deal with daily life in the country and the institution. If they are using technology-enhanced education, the aforementioned problems can be more minimized. And last but not least, technology can minimize cultural aspects so that even some expert topic based problems can appear, for example: technology-oriented topics are probably more easier presented in that way than, for example, some medical ones. Much greater challenge is the teachers who meet

with Erasmus+ visiting students within their own institution. Unfortunately, it happens too often that teachers use stereotypes about Erasmus+ students, their habits, plans and capabilities. The first designation is very often that students have arrived as tourists and that they want to see the country and the neighboring countries and, after that, perhaps want to study [21]. Of course, such students can also be found, but we hope and expect that teachers be more positive and that they do not mark students first by stereotypes, and that they have to work even harder to overcome such designations [19]. Technology can again minimize the cultural aspects in a way that we described before. Because teachers are on one side busy with their daily activities, teaching and researching, as well they do not want to be exposed in public with others, while on the other side they do not believe, that they need or would need cultural preparation, actually the only possibility is preparation based on the literature or supported by the technology using Moodle or other tools. Namely, technology-enhanced education enable teacher that they do this in private, when they have time and self-tests are possible as well. Tools like these are actually useful for all participation groups, either as a main or side preparation. In one of the projects we built up the VCE (Virtual Centre of Entrepreneurship) in which we built up the Cross Cultural module used for preparations [19]. In that case, VCE is an example of technology-enhanced education [1, 15, 21], developed on the Moodle platform. The main activities supported by the VCE are the following:

- E-learning system that individuals can register and select a module that would like to work on it. Whereby learners can also develop their language skills in a foreign language as part of their learning;
- Teaching resources (VCE e-modules) available for user for freely use for their own teaching purposes;
- A reference repository of relevant publications in the field [16, 19].

---

### 3 Conclusion

Our main duty when using technology-enhanced education is that we are aware of the importance of cultural aspects also in cases where technology is in the foreground. Namely, the concept of culture does not represent an entity in an independent objective world; it is more production and exchange of meaning or signifying practice, leading to what is distinctive about a way of life [2]. Cultural aspects can also be recognized as an interdisciplinary or post-disciplinary field of inquiry, which explores the production, and inculcation of maps of meaning [2]. This is also, what we can understand as cultural awareness [14]. When we have to deal with bigger groups of students who are multilingual and multicultural, it is best to have right away at the beginning a Cross-cultural

communication course to present a framework of cultural aspects and awareness to all associates [17], meaning students as well as teachers. Namely, sometimes teachers need even more help and support [21]. The same or similar course can be used for students who will take part in mobility and will visit partner institutions all around the world, or will take part in a placement or internship [19, 21]. At last but not least, we also have to take care of students coming back from mobility, to solve their possible reverse cultural shock and collect their experiences for future mobile associates [21]. In all these cases, technology-enhanced education can be of great service, while as mentioned, teachers supported the idea of taking a course in their own environment based on technological solutions and also post-mobility students mostly prefer a similar approach. In the paper, described experiences are mostly based on the engineering education, more precisely Informatics and Computer Science education. According to the fact that Biomedical engineering education is the application of engineering principles and design concepts to medicine and biology for healthcare purposes, we expect very similar situations and scenarios so long that the engineering is in foreground. If the medicine is in the foreground it would be necessary that the influence of medical culture would be introduced in research of described cases and proposals. Each profession has namely its own culture. For further work professional cultures and its influence has to be taken into consideration as well as pedagogical approaches connected to the technology-enhanced education. We would like to point out just few of them: personalised learning—tailoring the learning experience to an individual learners needs and desires, further flexible learning—similar to personalised but with a greater focus on how the material adapts to an individuals progress, as well as in the paper mentioned gamification the use of game techniques to encourage and motivate activities, that can be especially relevant to learning. Finally, we have to mentioned also online learning—the use of Internet-based e-learning to deliver content supports at anytime and anywhere and as a last of our selected approaches the blended learning—a mix of face-to-face interaction complemented by e-learning, this hybrid is especially relevant to introducing elements of flexibility into traditional courses [3]. Numbered pedagogical approaches that are using the benefits of technology-enhanced education we have to observe through different cultural awareness from national to professional one.

**Conflict of Interest Statement** The authors declare that they have no conflict of interest.

## References

1. Application Form I-ACE: Erasmus+ KA2 I-ACE project, ISEP, Porto, Portugal, 2016.
2. Barker C.: *Cultural Studies*, Sage Publication, London, 2012.
3. Christensen S.H., Delahousse B.: *Profession culture and Communication*, Institute of Business Administration and Technology Press, Herning, 2003.
4. Gordon N.: *Flexible Pedagogies: technology-enhanced learning*, University of Hull, January 2014, [https://www.heacademy.ac.uk/system/files/resources/tel\\_report\\_0.pdf](https://www.heacademy.ac.uk/system/files/resources/tel_report_0.pdf), last accessed 2018/03/15.
5. Heimbürger A.: *When Cultures Meet: Modelling Cross-Cultural Knowledge Spaces*, In: *Proceedings of the 17th European-Japanese conference on information modelling and knowledge Pori*, Tampere University of Technology, 2007.
6. Hofstede G.: *Cultures Consequences, Comparing Values, Behaviors, Institutions and Organizations Across Nations*, Sage Publications, Thousand Oaks, 2001.
7. Hofstede G., Hofstede G.J., Minkov M.: *Cultures and Organizations: Software of the Mind: Intercultural Cooperation and its Importance for Survival*, McGraw-Hill, New York, 2010.
8. Jakkola H., Heimbürger A.: *Cross-Cultural Software Engineering*, In: *MIPRO 2009*, Opatija, 2009.
9. Jandt F.W.: *An introduction to Intercultural Communication Identities in a Global community*, Sage Publication, Thousand Oaks, 2004.
10. Lewis R.D.: *When Cultures Collide, Leading Across Cultures*, Nicholas Brealey Publishing, London, 2006.
11. Lewis R.D.: *When Teams Collide, Managing Successfully Across Cultures*, Nicholas Brealey Publishing, London, 2012.
12. Magnan M.: *Valeurtech, a Leonardo Pilot Project: Highlighting Professional Experience Acquired in Undergraduate Technology Programmes*, In: *EAIE Vienna Conference, Session 4.14*, Vienna, 2003.
13. Milovan A.: *Kulturni ok in kulturna priprava*, Master Thesis, University of Maribor-FERI, (only in Slovenian language), Maribor, 2017.
14. Quappe S., G. Cantatore (2005), *What is Cultural Awareness, anyway? How do I build it?*, Culturocity.com, <http://www.culturocity.com/pdfs/What%20is%20Cultural%20Awareness.pdf>, last accessed 2018/02/05.
15. SALEIE project, University of York, York, 2016, <http://www.saleie.co.uk/projectsite/index.php> last accessed 2018/02/05.
16. Welzer T., Bonacic M., Zoric-Venuti M.: *Cultural Awareness in Information Society*, In: *20th EAEEIE Annual Conference Innovation in Education for Electrical and Information Engineering*, Valencia.
17. Welzer T., Jaakkola H., Bonačić M., Družovec M.: *Cultural awareness for the 21st century IT teaching*, In: *Grundspenkins J. (eds.) Proceedings of 13th East-European Conference Advances in databases and information systems, ADBIS 2009*, Riga, Latvia, pp. 209–213, 2009.
18. Welzer T., Jaakkola H., Družovec M., Hölbl M.: *Cultural and lingual awareness for the global conceptual modeling*, In: *Information modelling and knowledge bases XXIV*, IOS Press, pp. 271–276, 2013.
19. Welzer T., Družovec M., Nemec L., Hölbl M.: *Importance of Intercultural preparation for mobility: Teachers and staff need it as well*, In: *Papadourakis G.M. Proceedings of the 24th International Conference on European Association for Education in Electrical and Information Engineering - EAEEIE*, Chania, 2013.
20. Welzer T., Družovec M., Nemec Zlatolas L., Hölbl M., Jaakkola H., Ivanović M., Radovanović M.: *Introducing cultural issues and cultural awareness in conceptual modeling education*, In: *Information modelling and knowledge bases XXVII*, IOS Press, 2016.
21. Welzer T., Družovec M.: *Cultural awareness in research and teaching*, In: *Überwimmer M., Gaisch M., Füreder R., Costa Y. (eds.) Proceedings Cross-Cultural Business Conference 2017*, Shaker Verlag, Aachen, pp. 289–296, 2017.



---

## Correction to: Evaluation of the Impact of an International Master of Advanced Studies in Medical Physics

Giorgia Loreti, Hossein Aslian, Antonio Brito, Harry Delis, Renata Longo, and Renato Padovani

---

### Correction to:

**Chapter “Evaluation of the Impact of an International Master of Advanced Studies in Medical Physics” in: L. Lhotska et al. (eds.), *World Congress on Medical Physics and Biomedical Engineering 2018*, IFMBE Proceedings 68/1, [https://doi.org/10.1007/978-981-10-9035-6\\_162](https://doi.org/10.1007/978-981-10-9035-6_162)**

The original version of the chapter “Evaluation of the Impact of an International Master of Advanced Studies in Medical Physics” was published non-open access. This has now been changed to the copyright holder “International Atomic Energy Agency” and open access under the terms of the Creative Commons Attribution 3.0 IGO License (<https://creativecommons.org/licenses/by/3.0/igo/>). For further details see license information in the chapter. The chapter and the book have been updated with the change

---

The updated version of this chapter can be found at [https://doi.org/10.1007/978-981-10-9035-6\\_162](https://doi.org/10.1007/978-981-10-9035-6_162)

## Author Index

### A

Abdala, Nitamar, [173](#)  
Abdullah-Al-Harun, Md., [405](#)  
Abe, Shuji, [45](#)  
Abiwinanda, Nyoman, [183](#)  
Abtahi, Farhad, [433](#)  
Accardo, Agostino, [475](#), [803](#)  
Adam, Vojtech, [255](#)  
Ahmed, Azza, [57](#)  
Ajčević, Miloš, [475](#), [803](#)  
Akagawa, Takuya, [147](#)  
Alam, Mohammad Tareq, [405](#)  
Albrechtova, Denisa, [81](#)  
Almeida, D.A., [877](#)  
Almeida, Renan, [661](#)  
Alonso, Fabiola, [645](#)  
Altemani, João Maurício Carrasco, [173](#)  
Alvarado-Cando, O., [877](#)  
Alves, Allan Felipe Fattori, [151](#), [173](#)  
Amadori, Elena, [155](#)  
Andrade, Adriano O., [303](#), [421](#)  
Andrikos, Ioannis O., [191](#), [207](#), [629](#)  
Ang, Khong Wei, [583](#), [589](#)  
Antonelli, Adriana, [135](#)  
Anyz, Jiri, [255](#)  
Aoki, Hirooki, [341](#)  
Aootaphao, Sorapong, [63](#)  
Arao, Shinichi, [29](#)  
Ashrafuzzaman, Md., [405](#), [737](#)  
Aslian, Hossein, [873](#)  
Assef, Amauri A., [233](#)  
Aulia, Masyithah Nur, [471](#)  
Aymerich, Xavier, [227](#)  
Azhar, Tauhid Nur, [471](#)  
Aziz, Md. Tareq, [737](#)

### B

Babic, Ankica, [347](#), [439](#), [457](#), [463](#), [467](#)  
Babič, František, [311](#)  
Bacala, Angelina M., [851](#), [869](#)  
Bachman, Thomas E., [725](#)  
Bai, Hongmin, [143](#)  
Baldo, Amani, [57](#)  
Ballarin, Virginia, [135](#)  
Balvan, Jan, [239](#)  
Banaszewski, Jacek, [249](#)  
Barbieri, Giovanni, [475](#)

Barbounaki, S.G., [381](#)  
Bariciak, E., [307](#)  
Barta, P., [489](#)  
Bartoš, Michal, [267](#), [777](#)  
Battistoni, G., [783](#)  
Baumgartner, Christian, [635](#)  
Becht, A., [669](#)  
Bednařík, Josef, [3](#)  
Bednařík, Petr, [3](#)  
Belardinelli, A., [321](#), [559](#)  
Benassi, A., [321](#)  
Benavides, Oriana, [53](#)  
Bergmoser, Katharina, [635](#)  
Bermeo, J.P., [665](#)  
Bernard, Vladan, [87](#)  
Bettiol, Andrew Anthony, [583](#), [589](#), [611](#)  
Biernat, J., [795](#)  
Biernat, M., [795](#)  
Bissaco, M.A.S., [831](#)  
Bjerkvig, Rolf, [267](#)  
Bliznakov, Zhivko, [213](#)  
Bliznakova, Kristina, [213](#)  
Boon, Henk, [669](#)  
Boschi, S.R.M.S., [831](#)  
Bravo, J., [665](#)  
Brioschi, Marcos Leal, [15](#)  
Brito, Antonio, [873](#)  
Brombal, Luca, [109](#)  
Brun, F., [123](#)  
Bueno, L., [665](#)  
Buhl, Sebastian, [21](#)  
Buliev, Ivan, [213](#)  
Burša, Miroslav, [427](#)  
Buzkova, Kristyna, [81](#)

### C

Caccia, B., [675](#)  
Cardenas, Diego Armando Cardona, [177](#)  
Carpini, C., [559](#)  
Casar, Josef, [351](#)  
Castaldo, Rossana, [335](#)  
Castonguay-Henri, Aude, [283](#)  
Castro, Carlos, [531](#)  
Castro, Carolina, [53](#)  
Cavanagh, Jonathan, [91](#)  
Cavedini, Nicollas Gonçalves, [731](#)  
Cerny, Martin, [505](#)



Cervantes, David, 531  
 Cesarelli, M., 567  
 Chagas, Luciene, 303  
 Chang, Feiyan, 499  
 Chantrel, Steeve, 201  
 Cheimariotis, G.A., 261  
 Chen, Fang, 297  
 Chen, Guowen, 865  
 Chen, Wei-Ling, 519  
 Chen, Yinsheng, 143  
 Cheng, Chun-An, 331  
 Cheng, Kuo-Sheng, 371  
 Cheng, Yanyan, 515, 563  
 Chien, Pei-Fang, 371  
 Chiu, Hung-Wen, 331  
 Chmelik, Jiri, 155, 223  
 Chudáček, Václav, 427  
 Chukwudebe, G., 445  
 Chunkiri, Thossapol, 63  
 Ciagli, E., 321, 559  
 Cifrek, M., 411  
 Cirone, D., 559  
 Cirrone, G.A.P., 675  
 Clemente, F., 567  
 Cmiral, Jaromir, 843  
 Cocchi, D., 321, 559  
 Cocherova, Elena, 799  
 Colonna, M., 675  
 Condon, Barrie, 91  
 Costa, Ana Paula Christakis, 15  
 Costa, Eduardo T., 233  
 Cui, Xiwen, 297  
 Cybulski, Gerard, 707

**D**

Dadunashvili, Sergo, 315  
 Darowski, Marek, 703  
 Dartora, Caroline Machado, 731  
 da Silva, Ana Maria Marques, 731  
 da Silva, Marcos Antonio Salvino, 525  
 da Silva, S.M., 831  
 Daskalaki, A., 9  
 Davis, Alberto, 227  
 de Almeida, Rosimary Terezinha, 357  
 De Dea, Federica, 475  
 de Freitas, Carlos Clayton Macedo, 173  
 de Guise, Jacques A., 201, 283  
 de Melo Mafra Machado, José Eduardo, 15  
 de Moura, Luís Vinícius, 731  
 De Napoli, M., 675  
 de Perio Peralta, Agnette, 869  
 de Pina, Diana R., 151  
 de Souza, Marcio Nogueira, 525  
 de Vries, Anke, 669  
 Delgado, Efren, 531  
 Delis, Harry, 873  
 Delogu, P., 123  
 Detmar, Klaus, 21  
 Deutsch, Elena, 75, 97  
 Dimitrioglou, N.G., 381, 539, 547  
 Dimov, Asen, 719  
 Ding, Ning, 499  
 Di Trapani, V., 123  
 Donato, Sandro, 109  
 Dong, Tong, 515, 563

Doskocil, Radek, 351  
 Dotti, A., 675  
 Dreossi, D., 123  
 Drosatos, George, 481  
 Druzgalski, Christopher, 103  
 Družovec, Marjan, 885  
 Dueñas, William Ricardo Rodríguez, 855  
 D'Uffizi, A., 567  
 Duitama-Muñoz, John F., 367  
 Dukov, Nikolay, 213  
 du Raan, Hanlie, 573  
 Durante, M., 783

**E**

Eichenlaub, Manuel, 577  
 Ejeh, John E., 573  
 Ekwonwune, E., 445  
 Eroğul, Osman, 243, 789  
 Eskola, Hannu, 773  
 Esty, A., 307

**F**

Faccini, R., 675  
 Faiella, G., 567  
 Farlik, Jan, 351  
 Fatah, Ahmed, 57  
 Ferrer, Ana, 649  
 Flores, Dora-Luz, 531  
 Flores, Mabel Bustos, 117  
 Fojnica, Adnan, 197  
 Folador, João Paulo, 303  
 Fonseca-Ruiz, Nelson J., 367  
 Fotiadis, Dimitrios I., 191, 207, 375, 629, 639  
 Francescato, Maria Pia, 803  
 Freire, Sergio Miranda, 357  
 Friganovic, K., 411  
 Frize, M., 307  
 Frosini, F., 321, 559  
 Furuie, Sergio Shiguemi, 177  
 Fusco, Roberta, 129

**G**

Gaita, Dan, 761  
 Gajewski, J., 783  
 Gao, Xiang, 515, 563  
 Garbacz, M., 783  
 García, Felipe, 227  
 García-Gallo, Javier E., 367  
 Gautam, Kumar, 103  
 Gavelli, Giampaolo, 155, 223  
 Geat, Mario, 803  
 Gelman, Sigita, 601  
 Georga, Elena, 629  
 Gesicho, Milka, 467  
 Gigilashvili, Giorgi, 837  
 Gilchrist, J., 307  
 Gólczewski, Tomasz, 697  
 Gollée, Henrik, 49  
 Gong, X.L., 807  
 Gordillo, Nelly, 227  
 Gorovoy, Sergei, 535  
 Górski, Filip, 249  
 Gotanda, Rumi, 29, 45, 147

Gotanda, Tatsuhiro, 29, 45, 147  
 Gotsiridze, Irine, 837  
 Granado, Diogo W., 233  
 Grendarova, P., 273  
 Gromilić, Zehra, 197  
 Gumulec, Jaromir, 239

**H**

Hagiwara, Naoki, 327  
 Halilović, Sabina, 197  
 Handayani, Astri, 183  
 Handel, Till, 397  
 Hanif, Muhammad, 183  
 Hantos, Zoltán, 553  
 Harauchi, Hajime, 29  
 Harrison, Jerome, 201  
 Harrold, J., 307  
 Hatala, Robert, 97  
 Hattersley, John, 577  
 Hatziavramidis, D.T., 539, 547  
 Hayashi, Akiko, 29  
 Hayashida, Tae, 387  
 Hejda, Jan, 351  
 Hesaputra, S. Tafwida, 183  
 Higuchi, Masakazu, 327  
 Hisham, N.I.A., 623  
 Hluštik, Petr, 3  
 Hok, Pavel, 3  
 Holguin, Alfonso, 53  
 Holmerová, Iva, 393  
 Horáková, Lenka, 711  
 Horák, Tomáš, 3  
 Horak, Vratislav, 255  
 Horn, Martin, 635  
 Hossain, Md. Sakib Abrar, 737  
 Hou, Xiaoxu, 499  
 Hozman, Jiri, 749  
 Hracho, Michal, 239  
 Hruban, Lukáš, 427  
 Huang, Yu-Ting, 331  
 Hudrea, Iuliana-Claudia, 761, 767  
 Huerta, Monica, 401  
 Huptych, Michal, 427  
 Huttova, Veronika, 725

**I**

Idris, Ibrahim, 57  
 Ilah, Layla Abdel, 197  
 Inaji, Hideo, 45  
 Iomdina, E.N., 495  
 Ivanova, Galina, 397

**J**

Jakubicek, Roman, 155, 223  
 Jan, Jiri, 155, 223  
 Janků, Petr, 427  
 Jara, J.D., 665  
 Jennane, Rachid, 173  
 Jiřík, Radovan, 267, 777  
 Jitsaard, Jaturong, 63  
 Johansson, Johannes D., 645  
 Johari, J., 597  
 Jovic, A., 411

Jozic, K., 411  
 Juhong, Aniwat, 165  
 Jung, A., 795  
 Junior, Nivaldo S., 233  
 Jurkonis, Rytis, 601

**K**

Kabancova, Oksana, 535  
 Kajihara, Mariko, 45  
 Kamišalići, Aida, 885  
 Kaldoudi, Eleni, 481  
 Kan, Chung-Dann, 519  
 Kanters, Djim, 669  
 Karanasiou, Georgia, 629  
 Kardaras, D., 381  
 Katsaggelos, A., 261  
 Katsuda, Toshizo, 45, 147  
 Kavousanakis, M.E., 539  
 Kavvadias, Spyridon, 481  
 Kawaji, Yasuyuki, 147  
 Kawamura, Hiraku, 35  
 Keunen, Olivier, 267  
 Khashabh, Ibrahim Abou, 427  
 Khovanova, Natasha, 577  
 Kiang-ia, Atthasak, 63  
 Kigka, Vassiliki I., 191, 207, 629  
 Kim, Borut, 607  
 Kneppo, Peter, 75  
 Koesoema, Allya Paramita, 471, 881  
 Kolar, Radim, 239  
 Konupka, Lukáš, 823  
 Kooistra, Homme-Auke, 669  
 Korenbaum, Vladimir, 535  
 Korpas, D., 489  
 Kostiv, Anatoly, 535  
 Kourou, Konstantina, 375  
 Kozarski, Maciej, 703  
 Kozuka, Takahiro, 45  
 Krah, N., 783  
 Krishnadas, Rajeev, 91  
 Krivanek, Vaclav, 351  
 Krumsvik, Ole Andreas, 347, 439  
 Kučera, Pavel, 755  
 Kuczko, Wiesław, 249  
 Kudrna, Petr, 725  
 Kukulja, D., 411  
 Kutilek, Patrik, 351  
 Kuwano, Tadao, 147  
 Kuznetsova, S., 273  
 Kyriakidis, Savvas, 629

**L**

Labounek, René, 3  
 Lambert, Lukas, 155, 223  
 Langthaler, Sonja, 635  
 Lara, Juan S., 687  
 Lassnig, Alexander, 635  
 Latikka, Juha, 773  
 Lee, James, 583  
 Lee, Khuan Y., 623  
 Lei, James Lee Cheow, 611  
 Lell, Michael, 21  
 Lenglet, Christophe, 3  
 Leonhardt, Steffen, 745

Liang, Chaofeng, 143  
 Liao, Hongen, 159, 297, 865  
 Li, Deyu, 499  
 Lindecrantz, Kaj, 433  
 Lindén, Maria, 693  
 Li, Qihua, 143  
 Liu, J.F., 807, 813  
 Liu, J.L., 807, 813  
 Liu, Jia, 159  
 Liu, L.P., 807  
 Liu, Lei, 143  
 Li, Zhi-Cheng, 143  
 Loke, Chai Yee, 509, 655  
 Longo, Renata, 109, 123, 873  
 Lopera, Wilson, 53  
 Lopes, Andrei Guilherme, 417  
 López, Alejandro, 649  
 Lopez-Gonzalez, Maria Rosario, 91  
 Loreti, Giorgia, 873  
 Lubis, L.E., 859  
 Łukasik, W., 795  
 Lu, Ke, 433  
 Luo, Ronghui, 143  
 Luzhnov, P.V., 495

## M

Ma, Cong, 297, 865  
 Maglaveras, N., 261  
 Maia, Joaquim Miguel, 15, 233  
 Mancini-Terracciano, C., 675  
 Mangová, Marie, 267  
 Mansor, W., 597, 623  
 Margani, Hind, 57  
 Marques, M.A., 831  
 Martinek, Tomas, 725  
 Martínez, Laura, 649  
 Matenine, Dmitri, 283  
 Matthies, Philipp, 279  
 McGinty, Sean, 819  
 McLean, John, 91  
 McQueen, Alistair, 819  
 Mejía, José, 227  
 Mengko, Tati Rajab, 183  
 Meschino, Gustavo, 135  
 Michalis, Lampros K., 191, 207, 639  
 Miguel-Cruz, Antonio, 687  
 Miniati, R., 321  
 Mitsuyoshi, Shunji, 327  
 Moeller, Knut, 819  
 Mohaimenul Joaa, A.F.M., 737  
 Morava, Jan, 755  
 Morgun, O., 39  
 Mornstein, Vojtěch, 87  
 Mourão, Arnaldo Prata, 117  
 Mroczka, Janusz, 593  
 Mugisha, Alice, 347, 439, 463  
 Mumuni, Abdul Nashirudeen, 91

## N

Naiyanetr, Phomphop, 617

Nakamura, Mitsuteru, 327  
 Nan, Qun, 515, 563  
 Napolitani, P., 675  
 Narkbuakaew, Walita, 63  
 Nascimento, Aline, 357  
 Nasifoglu, Huseyin, 243  
 Neba, Julius, 279  
 Nemchenko, K., 39  
 Niewiadomski, Wiktor, 707  
 Nishi, Toshio, 45  
 Nkuma-Udah, K.I., 445  
 Noury, Norbert, 505  
 Nova, Michaela, 363

## O

Okrzeja, Piotr, 703  
 Oktavianto, A.N., 859  
 Okura, Yasuhiko, 29  
 Oliveira, Fábio Henrique M., 421  
 Omiya, Yasuhiro, 327  
 Ono, Atsushi, 29  
 Ooi, Ean Hin, 509, 655  
 Orozco-Morales, Rubén, 219  
 Ort, Václav, 823  
 Osmancik, Pavel, 75, 97  
 Osmanović, Ahmed, 197  
 Ostadal, Petr, 749  
 Østergaard, Lasse Riis, 69  
 Othman, N.H., 623  
 Ourednicek, Petr, 155, 223  
 Özdemir, Galip, 243, 789  
 Özdemir, Mertcan, 789

## P

Pałko, T., 795  
 Pabiszczak, Maciej, 249  
 Pacile', Serena, 109  
 Padovani, Renato, 873  
 Pallewela, A.L., 451  
 Pallikarakis, N., 9  
 Pandola, L., 675  
 Papaloukas, Costas, 375  
 Paralič, Ján, 311  
 Parameshwaran, V., 451  
 Parente, Jacquelyn Dawn, 819  
 Parodi, Oberdan, 629  
 Patera, V., 783  
 Pavan, Ana Luiza Menegatti, 151, 173  
 Pawiro, S.A., 859  
 Pecchia, Leandro, 335  
 Pelosi, Gualtriero, 629  
 Penev, Dimitar, 719  
 Pepino, Alessandro, 129  
 Perdomo, César A., 289  
 Perdomo, óscar J., 289  
 Pereira, Wagner, 661  
 Pérez-Díaz, Marlen, 219  
 Peter, Lukas, 505  
 Petrillo, Antonella, 129  
 Phua, Jun Hao, 583

Pina, Diana, 173  
 Pino, Alexandre Visintainer, 525  
 Pinto, Francisco A., 279  
 Pires, Andrei, 661  
 Pirrone, Jose, 401  
 Piskořová, Zuzana, 3  
 Pitavirooj, Chuchart, 165  
 Plocharski, Maciej, 69  
 Ploquin, N., 273  
 Pokorná, Jana, 87  
 Polak, Adam G., 553, 593  
 Porumb, Mihaela, 335  
 Pribadi, Amanatullah, 881  
 Purahong, Boonchana, 165  
 Pusztová, Ludmila, 311  
 Puttawibul, Puttisak, 63

## Q

Qi, Tan Hong, 611  
 Quiroga-Torres, Daniel Alejandro, 687

## R

Radzol, A.R.M., 623  
 Rafl, Jakub, 725  
 Raja Mohd Radzi, R.U.K., 597  
 Ramírez, Emmanuel, 53  
 Ramli, Norlina, 509, 655  
 Rashkovska, Aleksandra, 693  
 Regolini, J., 321  
 Richter, Aleš, 755  
 Riga, M., 261  
 Rigas, George, 207, 629  
 Rigon, L., 123  
 Rinaldi, L., 783  
 Rincón, Adriana María Ríos, 855  
 Ringler, Ralf, 21  
 Ríos-Rincón, Adriana María, 687  
 Riyani, Annisa, 471  
 Rocchiccioli, Silvia, 629  
 Rocher, Sara, 649  
 Rodas, R., 665  
 Rödby, Kristian, 433  
 Rodrigues, S.C.M., 831  
 Rodríguez-Gallo, Yakdiel, 219  
 Rothmaler, Katrin, 397  
 Roubik, Karel, 711, 725  
 Rucinski, A., 783  
 Rüschen, Daniel, 745

## S

Sadowiec, Marta, 707  
 Saiz, Javier, 649  
 Sakalauskas, Andrius, 601  
 Sakellarios, Antonis I., 191, 207, 629, 639  
 Salih, Isam, 57  
 Samsudin, Amir, 509, 655  
 Sanches, Elizabeth Gomes, 525  
 Sánchez, Damián, 649  
 Sanchez, F., 665  
 Sansone, Mario, 129  
 Santos, M.F., 831  
 Santos, Rogerio, 661  
 Sawai, Yuka, 45

Scardovelli, T., 831  
 Scherer, Daniel, 417  
 Schiavi, A., 783  
 Schmittbuhl, Matthieu, 201, 283  
 Schneider, Fabio K., 233  
 Schreiber, Max, 397  
 Schuller, Karina, 21  
 Schwarcke, Marcelo Menna Barreto, 731  
 Scifoni, E., 783  
 Seoane, Fernando, 433  
 Setiawan, Agung W., 847  
 Shamaev, D.M., 495  
 Shen, J.Y., 807, 813  
 Shiells, Kate, 393  
 Shiga, Tsuyoshi, 341  
 Shi, Huabei, 159  
 Shimada, Makoto, 45  
 Shimono, Tetsunori, 147  
 Shinohara, Shuji, 327  
 Shiryayev, Anton, 535  
 Sieger, Ladislav, 711  
 Silva, A.P., 831  
 Simonetti, M., 567  
 Siogkas, Panagiotis K., 191, 629, 639  
 Skrzypek, A., 783  
 Slawig, Anne, 21  
 Smrcka, Pavel, 351  
 Soejoko, D.S., 859  
 Solfaroli Camillocci, E., 675  
 Šorel, Michal, 267, 777  
 Sosnowska, Anna, 49  
 Spilka, Jiří, 427  
 Staffa, Erik, 87  
 Stecka, Anna, 697, 703  
 Štěpánková, Olga, 255, 363, 393  
 Stich, Manuel, 21  
 Strunina, Svitlana, 749  
 Sun, Qiuchang, 143, 813  
 Suriyal, Shorav, 103  
 Suwan, Supakorn, 165  
 Suzuki, Atsushi, 341  
 Svátková, Alena, 3  
 Svehlikova, Jana, 75, 97, 799  
 Swito, Yoke Saadia, 471, 881  
 Sýkora, Karel, 711

## T

Tabuchi, Akihiko, 29  
 Tachos, Nikolaos, 629  
 Tagiltcev, Alexandr, 535  
 Takanashi, Takaoki, 35  
 Takayama, Eiji, 327  
 Takeda, Yoshihiro, 45  
 Tan, Hong Qi, 583, 589  
 Tanki, Nobuyoshi, 45, 147  
 Tan, Lloyd, 583  
 Tejkl, Leos, 725  
 Thajchayapong, Pairash, 63  
 Thanasupsombat, Chalinee, 63  
 Thind, K., 273  
 Thongvigitmanee, Saowapak S., 63  
 Tian, Zhen, 515, 563  
 Tipo, V., 567  
 Tito, Thâmmara Lariane Henriques, 417  
 Tokuno, Shinichi, 327

Tomasic, Ivan, 693  
 Tommasino, F., 783  
 Tong, Z.R., 813  
 Tonheim, Aleksander Nygård, 457  
 Torres-Salamea, H., 877  
 Tortoli, P., 321, 559  
 Totorean, Alin-Florin, 761, 767  
 Tousoulis, D., 261  
 Toutouzas, K., 261  
 Traini, G., 675  
 Trindade, Andre P., 151  
 Trobec, Roman, 693  
 Tromba, Giuliana, 109  
 Trzyna, M., 795  
 Tsanev, Ivan, 719  
 Tsiounia, K., 381  
 Tsobou, Panagiota, 207  
 Tsompou, Panagiota I., 191, 629  
 Tysler, Milan, 75, 97, 799

## U

Urbach, Joost, 669  
 Utama, Dody Qori, 471

## V

Vacavant, Antoine, 151  
 Vaculovic, Tomas, 255  
 Vaisburd, A., 39  
 Valošek, Jan, 3  
 van Staden, Johan A., 573  
 Vargas, Eunice, 531  
 Vicar, Tomas, 239  
 Vieira, Marcus Fraga, 303, 421  
 Viteckova, Slavka, 351  
 Vojtech, Zdenek, 363  
 Vojtíšek, Lubomír, 3  
 Volf, Petr, 351  
 von Platen, Philip, 745  
 Vuckovic, Aleksandra, 49  
 Vyslouzilova, Lenka, 255, 363

## W

Wakholi, Peter, 463  
 Walner, Hynek, 267  
 Walter, Marian, 745  
 Wangkaoom, Kongyot, 63  
 Wang, Sheei-Meei, 371  
 Wårdell, Karin, 645  
 Wei, Ang Khong, 611  
 Wei, Jonathan Yeo Jian, 611  
 Welzer, Tatjana, 885  
 Wichniarek, Radosław, 249  
 Wilches, Carlos A., 289  
 Wu, Chiu-Chin, 519  
 Wuestemann, Jan, 279  
 Wu, Jia-Yun, 371  
 Wysoczański, Dariusz, 593

## X

Xie, Sheng, 499  
 Xu, Z.M., 807

## Y

Yamauchi, Yasushi, 387  
 Yang, Jinfeng, 499  
 Yang, Liyun, 433  
 Yatake, Hidetoshi, 45

## Z

Zambacevičienė, Monika, 601  
 Zaruz, Thaila Ferreira, 421  
 Zdarska, Jana, 75  
 Zhang, Chi, 499  
 Zhang, Xinran, 865  
 Zhao, Zhe, 297  
 Zhu, L.M., 807  
 Zieliński, Krzysztof, 697, 703  
 Zimbico, Acacio J., 233  
 Zimolka, Jakub, 3  
 Żyliński, Marek, 707